


THE FILE COPY

ARO 26304.1-EL-6



 SPIE—The International Society for Optical Engineering

AD-A217 343

*Conference Digest*  
**Thirteenth International  
Conference on  
Infrared and Millimeter Waves**

Richard J. Temkin  
Editor

5-9 December 1988  
Honolulu, Hawaii

Sponsored by  
SPIE—The International Society for Optical Engineering  
With the cooperation of  
U.S. Army Research Office



1988



Volume 1039

DISTRIBUTION STATEMENT A  
Approved for public release  
Distribution Unlimited

90 01 22 1311

## REPORT DOCUMENTATION PAGE

1a. REPORT SECURITY CLASSIFICATION Unclassified		1b. RESTRICTIVE MARKINGS	
2a. SECURITY CLASSIFICATION AUTHORITY		3. DISTRIBUTION/AVAILABILITY OF REPORT Approved for public release; distribution unlimited.	
2b. DECLASSIFICATION/DOWNGRADING SCHEDULE		5. MONITORING ORGANIZATION REPORT NUMBER(S) ARO 26304.1-EL-CF	
4. PERFORMING ORGANIZATION REPORT NUMBER(S)		7a. NAME OF MONITORING ORGANIZATION U. S. Army Research Office	
6a. NAME OF PERFORMING ORGANIZATION Georgia Institute of Technology	6b. OFFICE SYMBOL (If applicable)	7b. ADDRESS (City, State, and ZIP Code) P. O. Box 12211 Research Triangle Park, NC 27709-2211	
6c. ADDRESS (City, State, and ZIP Code) Atlanta, Georgia 30332	9. PROCUREMENT INSTRUMENT IDENTIFICATION NUMBER DAAL03-88-G-0044		
8a. NAME OF FUNDING/SPONSORING ORGANIZATION U. S. Army Research Office	8b. OFFICE SYMBOL (If applicable)	10. SOURCE OF FUNDING NUMBERS	
8c. ADDRESS (City, State, and ZIP Code) P. O. Box 12211 Research Triangle Park, NC 27709-2211	PROGRAM ELEMENT NO.	PROJECT NO.	TASK NO.
11. TITLE (Include Security Classification) Thirteenth International Conference on Infrared and Millimeter Waves			
12. PERSONAL AUTHOR(S) James C. Wiltse			
13a. TYPE OF REPORT Final	13b. TIME COVERED FROM 8/22/88 TO 8/21/89	14. DATE OF REPORT (Year, Month, Day) 1989	15. PAGE COUNT 469
16. SUPPLEMENTARY NOTATION The view, opinions and/or findings contained in this report are those of the author(s) and should not be construed as an official Department of the Army position, policy, or decision, unless so designated by other documentation.			
17. COSATI CODES		18. SUBJECT TERMS (Continue on reverse if necessary and identify by block number)	
FIELD	GROUP	SUB-GROUP	
		Millimeter Wave Conference	
19. ABSTRACT (Continue on reverse if necessary and identify by block number) The conference was held as scheduled. A conference digest has been published by SPIE-The International Society for Optical Engineering, P.O. Box 10, Bellingham, Washington 98227-0010.			
20. DISTRIBUTION/AVAILABILITY OF ABSTRACT <input type="checkbox"/> UNCLASSIFIED/UNLIMITED <input type="checkbox"/> SAME AS RPT. <input type="checkbox"/> DTIC USERS		21. ABSTRACT SECURITY CLASSIFICATION Unclassified	
22a. NAME OF RESPONSIBLE INDIVIDUAL		22b. TELEPHONE (Include Area Code)	22c. OFFICE SYMBOL



*Conference Digest*

**Thirteenth International  
Conference on  
Infrared and Millimeter Waves**

**Richard J. Temkin**  
*Editor*

**5-9 December 1988**  
**Honolulu, Hawaii**

*Sponsored by*  
SPIE—The International Society for Optical Engineering  
*With the cooperation of*  
U.S. Army Research Office

*Published by*  
SPIE—The International Society for Optical Engineering  
P.O. Box 10, Bellingham, Washington 98227-0010 USA  
Telephone 206/676-3290 (Pacific Time) • Telex 46-7053

**1988**  
  
**IR MM**

**Volume 1039**

SPIE (The Society of Photo-Optical Instrumentation Engineers) is a nonprofit society dedicated to advancing engineering and scientific applications of optical, electro-optical, and optoelectronic instrumentation, systems, and technology.

The papers appearing in this book comprise the proceedings of the meeting mentioned on the cover and title page. They reflect the authors' opinions and are published as presented and without change, in the interests of timely dissemination. Their inclusion in this publication does not necessarily constitute endorsement by the editors or by SPIE.

Please use the following format to cite material from this book:

Author(s), "Title of Paper," *Thirteenth International Conference on Infrared and Millimeter Waves*, Richard J. Temkin, Editor, SPIE Vol. 1039, page numbers (1988).

Library of Congress Catalog Card No. 88-63146  
ISBN 0-8194-0074-2

Copyright © 1988, The Society of Photo-Optical Instrumentation Engineers.

Copying of material in this book for sale or for internal or personal use beyond the fair use provisions granted by the U.S. Copyright Law is subject to payment of copying fees. The Transactional Reporting Service base fee for this volume is \$2.00 per article and should be paid directly to Copyright Clearance Center, 27 Congress Street, Salem, MA 01970. For those organizations that have been granted a photocopy license by CCC, a separate system of payment has been arranged. The fee code for users of the Transactional Reporting Service is 0-8194-0074-2/88/\$2.00.

Individual readers of this book and nonprofit libraries acting for them are permitted to make fair use of the material in it, such as to copy an article for teaching or research, without payment of a fee. Republication or systematic or multiple reproduction of any material in this book (including abstracts) is prohibited except with the permission of SPIE and one of the authors.

Permission is granted to quote excerpts from articles in this book in other scientific or technical works with acknowledgment of the source, including the author's name, the title of the book, SPIE volume number, page number(s), and year. Reproduction of figures and tables is likewise permitted in other articles and books provided that the same acknowledgment of the source is printed with them, permission of one of the original authors is obtained, and notification is given to SPIE.

In the case of authors who are employees of the United States government, its contractors or grantees, SPIE recognizes the right of the United States government to retain a nonexclusive, royalty-free license to use the author's copyrighted article for United States government purposes.

Address inquiries and notices to Director of Publications, SPIE, P.O. Box, Bellingham, WA 98227-0010 USA.

## CONFERENCE PROGRAM

### Thirteenth International Conference on Millimeter and Infrared Waves

5-9 December 1988

Pacific Beach Hotel

Waikiki Beach, Honolulu, Hawaii 96815 USA

Sponsored by SPIE—The International Society for Optical Engineering

With the cooperation of U.S. Army Research Office

	Ballroom (Mauka)	Mahimahi Room	Papio Room	Ballroom (Makai)
MON AM	MMW Sources I	MMW Modulation of Light	MMW Antennas	FEL I
MON PM	MMW Sources II	Optical Tech. for MMW	Astronomy	FEL II
TUE AM	MMW Systems I	Microwave-Optical Interactions Plasma Diagnostics I	MMW Guides	FEL III
TUE PM	MMW Systems II MMW Detectors & Mixers	Plasma Diagnostics II	Atmospheric Phys.	Gyrotron I
WED AM	Guided Prop. I	High $T_c$ Superconductors I	Submm Detectors	Gyrotron II
WED PM	Guided Prop. II	High $T_c$ Superconductors II	Submm Devices	Gyrotron III
THR AM	MMW Integ.Ct.I	Near MMW Meas.& Tech.	Lasers I	Gyrotron IV
THR PM	MMW Integ.Ct.II	Materials Characterization I	Lasers II	Gyrotron V
FRI AM	MMW Devices I	Semiconductors	Lasers III	Gyrotron VI
FRI PM	MMW Devices II	Materials Characterization II	SubMM Waves	Gyrotron & FEL

Morning sessions begin at 0900 hours. Afternoon sessions begin at 1400 hours. Friday afternoon sessions begin at 1300 hours.

*Invited Keynote* papers are allotted 40 minutes; contributed papers 20 minutes. Speakers are expected to allow some of their time for discussion, but they rarely do that. Therefore, several opportunities have been provided for listeners to question the speakers personally, namely, between 0800 and 0900 hours when we have all gathered for breakfast, between 1000 and 1100 hours when some delegates will be having coffee (also 1500 to 1600 hours), and at the late afternoon receptions.

A convenient gathering place will be the exhibit area on Tuesday and Wednesday.



By _____	
Distribution/	
Availability Codes	
Dist	Avail and/or Special
A-1	

## NOTES FROM THE PROGRAM CHAIR

When this conference is held in North America, it is essentially The Millimeter Wave Conference. Thirty of the thirty-six sessions lie exclusively in the realm of millimeter waves, that is, 35 to 300 GHz. Measures are being devised by the Program Chair to increase the submillimeter component, but his appeal to the submillimeter scientists remains his strongest measure.

A glance at the program (previous page) shows that we have our usual Millimeter Wave Week and our usual Free Electron Laser and Gyrotron Week. But we now have another symposium on millimeter wave measurement techniques applied to the characterization of materials and the tabulation of their millimeter wave properties. Another new, and growing, component is the Microwave-Optical Interactions.

This Program has been organized through the diligent and sustained efforts of the following individuals:

### Program Council

James C. Wiltse, Georgia Tech Research Institute  
Richard J. Temkin, MIT  
Koji Mizuno, Tohoku University (Japan)  
Kenneth J. Button, MIT  
M. von Ortenberg, Universität Würzburg (FRG)

### Special Program Topics

Mohammed N. Afsar, Tufts University & MIT  
Tatsuo Itoh, University of Texas at Austin  
Jerald R. Izatt, University of Alabama  
Chi H. Lee, University of Maryland  
George J. Simonis, U.S. Army Harry Diamond Laboratories

### Program Advisors

Igor Alexeff, University of Tennessee  
Frank DeLucia, Duke University  
Margaret Frerking, Jet Propulsion Laboratory, California Institute of Technology  
V. Granatstein, University of Maryland  
Armand Hadni, Université Nancy (France)  
Fritz Kneubuhl, ETH, Zurich (Switzerland)  
Li Si-fan, Nanjing Institute of Technology (China)  
R. W. McMillan, Georgia Tech Research Institute  
J. Nishizawa, Tohoku University (Japan)  
K. Sakai, Osaka University (Japan)  
U. Strom, Naval Research Laboratory  
F. Strumia, Università di Pisa (Italy)

**Digest Editor:** Richard J. Temkin, MIT Plasma Fusion Center

**Exhibit Manager and Executive Secretary:** Mohammed N. Afsar, Tufts University and MIT

**Program Chair:** Kenneth J. Button, Massachusetts Institute of Technology

**Liaison in Japan:** T. Matsui, Communications Research Laboratory (Japan)

## NOTES FROM THE PROCEEDINGS EDITOR

The Proceedings of this Conference can be obtained for \$50 by subscribing through the Editor, Ken Button, to the 12 issues of the *International Journal of Infrared and Millimeter Waves* to be published in the year 1989, namely, Volume 10. This special rate is available only to individuals during the month of the Conference when the bulk subscription is prepared. Otherwise, direct subscription through Plenum Publishing Company is about \$300. The Proceedings papers appear throughout the year along with additional papers in the millimeter and submillimeter (far-infrared) area. The Journal contains about 1500 pages each year.

The Journal was established about ten years ago to serve as an economical method of publishing the Proceedings and also to provide a central source for literature that is unique to this region of the electromagnetic spectrum. Each speaker at the annual Conference is expected to submit a definitive Proceedings paper. The paper should be comprehensive because there is no deadline; the paper is published in the next monthly issue after it is received.

Under normal circumstances, an annual subscription to a monthly journal is not an economical way to provide a Proceedings. Thus one never sees this done for other conferences. But a specially negotiated arrangement was made between the Editor and the Publisher at the time the Journal was started. Once each year, at the time of the Conference, the Editor must collect \$50 from each subscriber and make up a bulk subscription. The Publisher, Plenum Publishing Company, must be spared the paperwork, billing, and so on, the Editor must do all the work. The Editor, in turn, appeals to each delegate, please, to make this process simple.

If you wish to take advantage of this special rate for the Proceedings, please prepare a check (payable to Ken Button), a money order, or cash and convey it to the Editor *during the month of December*.

## MILLIMETER WAVE BOOKS

Eighteen books have been published by Academic Press. Now the series of books will be reorganized and published at about one-third the previous prices. Moreover, the topics will be selected in millimeter-wave engineering where a larger circulation can be expected.

## FUTURE CONFERENCES

The next conference (the Fourteenth Annual SPIE International Conference on Infrared and Millimeter Waves) will be held at the University of Würzburg, in the City of Würzburg, Federal Republic of Germany, 23-27 October 1989. Würzburg is located about two hours east of Frankfurt, by train. Some of us will recall the excellent Fifth Conference held in Würzburg in October 1980. Our host will be:

Prof. Dr. Michael von Ortenberg  
Physikalisches Institut der Universität Würzburg  
Röntgenring 8  
87 Würzburg  
Federal Republic of Germany

The lecture halls of the University in the center of the city will be used. The delegates will have their choice of a variety of very comfortable hotels nearby. The General Chair of this series of conferences and the Editor of the Proceedings is

Kenneth J. Button  
Box 72, M.I.T. Branch  
Cambridge, MA 02139 USA  
(617)489-4353 or (617)253-5561  
Telex 92-1473; FAX (617)253-0807

(winter address)  
Box 2455  
Satellite Beach, FL 32937 USA  
(407)777-7293

The 1990 Conference will be held in North America. The Program Chair has nearly completed the arrangements at this writing.

It should be obvious that the main objective of the planners of these conferences is to provide an opportunity for everyone in our profession to attend frequently. For example, the 1988 Conference is intended to be the "Japan Conference in Honolulu," where the delegates from Japan will be specially invited.

## TECHNICAL EXHIBIT

The second annual trade show will be held this year on Tuesday and Wednesday, 6-7 December. This exhibit will be held on a modest scale at an exhibit hall adjacent to the lecture halls. It is hoped that each delegate will take a few moments to look at the few exhibits by way of welcoming our friends and colleagues who help us ultimately with their professionally designed and engineered instruments.

## NOTES FROM THE DIGEST EDITOR

The Conference Digest for this Thirteenth International Conference again attests to the dynamic growth in the field of infrared and millimeter waves.

The Digest is a convenient, timely reference work in the field of infrared and millimeter waves. Copies of the Digest may be purchased from SPIE at the address given on the title page. Papers in the Digest may be referred to in journal articles by citing the SPIE Volume Number. Many libraries throughout the world acquire SPIE publications for their collections. For this reason a paper contributed to this Digest represents an important research contribution.

The Digest Editor would like to thank Ms. Carol Arlington for her outstanding effort in organizing and arranging the material in this Digest and for serving as Assistant Registrar.

# EXHIBITION GUIDE

The second annual millimeter wave exhibit will be held in the AHI / MAHI room (3rd floor), at the Pacific Beach Hotel, Waikiki Beach, Honolulu for two full days, Tuesday and Wednesday, December 6 and 7, 1988 from 8 AM to 8 PM. The list below represents information available at press time.

Mohammed N. Afsar  
Exhibit Manager

**DORADO COMPANY, SEATTLE, WASHINGTON**

Antennas, Attenuators, Bends, Detectors, E-H tuners, Ferrite Devices, Filters, Frequency Meters, Hybrid Tees, Loads, Mixers, Gunn Oscillators, Phase Shifters, Power Meter, Shorts, Straights, Switches, etc. 18 - 170 GHz

**W. L. GORE ASSOCIATES, NEWARK, DELWARE**

GORE-TEX Dielectric Waveguide Assemblies from 18 to 100 GHz with flexibility, Long flex life and low insertion loss. GORE-TEX Microwave cables

**HEWLETT-PACKARD COMPANY, SANTA ROSA, CALIFORNIA**

Millimeter Wave Network Analyzer

**HUGHES AIRCRAFT COMPANY, TORRANCE, CALIFORNIA**

Millimeter Wave Sources, Millimeter Wave Devices, Millimeter Wave Components and Submillimeter Wave Products

**MICRO-NOW INSTRUMENTS COMPANY, SKOKIE, ILLINOIS**

Millimeter Wave Instrumentation

**MM-WAVE TECHNOLOGY INC., WALNUT, CALIFORNIA**

Millimeter Wave Components, Antennas, Subassemblies and Subsystems

**SYSTRON DONNER CORPORATION, CONCORD, CALIFORNIA**

Microwave and Millimeter Wave Frequency Counters and Signal Generators and Microwave Repeater Checker

**WATKINS-JOHNSONS COMPANY, PALO ALTO, CALIFORNIA**

Millimeter Wave Products

**WILTRON COMPANY, MORGAN HILL, CALIFORNIA**

Millimeter Wave Vector Network Analyzer

---

---

## SESSION M1

---

---

---

Ballroom (Mauka) 7<sup>th</sup> Floor

---

Monday AM

December 5, 1988

---

R. W. McMillan, Presider

---

---

### MMW SOURCES I

---

- M1.1 MMW GRID OSCILLATORS - (*Invited Keynote, 40 min.*) - D. Rutledge, Z.B. Popovic and M. Kim, Cal Tech, Pasadena, CA 91125
- M1.2 A FEEDBACK MODEL OF MILLIMETRE WAVE HARMONIC OSCILLATORS AND ITS APPLICATION - J-P. Xu and S-F. Li, Southeast Univ, Nanjing, P.R. China
- M1.3 TIME DEPENDENT SIMULATION OF THE QUANTUM WELL INJECTION TRANSIT TIME DIODE - D.R. Miller, V.P. Kesan, R.L. Rogers, C.M. Maziar, and D.P. Neikirk, Dept of Elec and Cmptr Engr, U of Texas at Austin, Austin, TX 78712
- M1.4 LINEAR ANALYSIS OF THE HIGH-POWER MAGNETRON - R. Stark and H. Uhm, Naval Surface Warfare Center, Silver Spring, MD
- M1.5 POWER COMBINING FET OSCILLATOR USING COUPLED RAMPART LINE ANTENNAS - J. Birkeland and T. Itoh, Dept EE, University of Texas, Austin, TX
- M1.6 A 94/47 GHz FREQUENCY HALVER USING A GaAs GUNN-DEVICE - H. Barth, AEG Aktiengesellschaft, Sedanstrasse 10/Post-box 1730, 7900Ulm/F.R.Germany
- M1.7 DESIGN OF A Ka-BAND TWO-WAY POWER COMBINING SOURCE MODULE USING PLANAR CIRCUIT APPROACH - F-M. Yang and C-K. C. Tzuang, I of Comm Engr, Natl Chiao Tung U, Hsinchu, Taiwan, R.O.China
- M1.8 PARAMETRIC ANALYSIS OF GaInAs DEVICES FOR MM-WAVE APPLICATIONS - A.R. Jha, JHA Technical Consulting Services, 12345 Charlwood St, Cerritos, CA 90701
- M1.9 LARGE SIGNAL CHARACTERISTIC OF GUNN DIODE IN FUNDAMENTAL MODE AND HARMONIC MODE MMW OSCILLATOR - N. Chen, S.F. Li, Z.L. Sun, Dept Radio Engineering, Southeast Univ, Nanjing, PRC

---

---

## SESSION M2

---

---

---

Mahimahi Room, 3<sup>rd</sup> Floor

---

Monday AM

December 5, 1988

---

### MMW MODULATION OF LIGHT

---

---

Chi Lee, Presider

---

- M2.1 ADVANCED LIGHTWAVE TECHNOLOGY - VERY LARGE CAPACITY OPTICAL COHERENT COMMUNICATIONS - (*Invited Keynote, 40 min*) - K. Nosu, NTT Labs, Take 1-2356, Tokosuka-shi, Kanagawa-ken, Japan 238-03
- M2.2 MICROWAVE MODULATION OF LIGHT (*Invited, 30 min*) - T. Seuta, Dept of Elec Engr, Osaka Univ, Toyonaka-Shi, Osaka 560 Japan
- M2.3 GENERATION AND DETECTION OF MILLIMETER WAVE MODULATED LIGHT WITH HIGH SPEED DIODE LASERS AND PHOTODETECTORS - (*Invited, 30 min*) - J. Bowers, Dept Elec And Cmptr Engr, U of California, Santa Barbara, CA 93106
- M2.4 MMW MODE-LOCKING OF SEMICONDUCTOR LASERS - (*Invited, 30 min*) - R. Tucker, U. Koren, G. Raybon, C. A. Burrus, G. E. Eisenstein, Bell Telephone Laboratories, Holmdel, NJ 07733
- M2.5 OPTICALLY CONTROLLED MILLIMETER WAVE PHASED ARRAY ANTENNAS - (*Invited, 30 min.*) - P. R. Herczfeld and A. S. Daryoush, Center for Microwave/Lightwave Engineering, Drexel Univ., Philadelphia, PA 19101
- M2.6 GaAs TRAVELING-WAVE OPTICAL MODULATOR USING A MODULATED COPLANAR STRIP ELECTRODE WITH PERIODIC CROSS-TIE OVERLAY - H.-Y. Lee and T. Itoh, Dept Elec and Cmptr Engr, The U of Texas at Austin, Austin, TX



---

---

### SESSION M3

---

---

---

Papio Room, 3<sup>rd</sup> Floor

---

Monday AM December 5, 1988

---

#### MMW ANTENNAS

---

J. M. Mink, Presider

---

- M3.1 A NEW CLASS OF SCANNABLE MILLIMETER WAVE ANTENNAS (*Invited Keynote*) - Arthur A. Oliner, Polytechnic University, 333 Jay St, Brooklyn, NY 11201
- M3.2 INTEGRATED CIRCUIT ACTIVE ANTENNA ELEMENTS AND SPATIAL POWER COMBINING (*Invited Keynote*) - Kai Chang, K.A. Hummer and J.L. Klein, Texas A&M Univ., College Station, TX 77843
- M3.3 DETECTOR ANTENNA ARRAY WITH A DIELECTRIC LENS FOR MILLIMETER-WAVE IMAGING - K. Uehara, T. Yonekura, H. Nishimura, K. Mizuno, Research Inst of Elec Communication, Tohoku Univ, Sendai, 980 JAPAN; D. B. Rutledge, California I of Technology, Pasadena, CA 91125
- M3.4 OMNI-DIRECTIONAL PERIODIC ROD ANTENNA T<sub>Mon</sub> MODE EXCITATION - S. Xu, Dept of Radio and Electronics, U of Science and Technology of China, Hefei, Anhui, P. R. CHINA
- M3.5 EFFICIENCY OF MM-WAVE HORN IMAGING ARRAYS - G. M. Rabeiz, Y. Guo, P. A. Stimson and D. B. Rutledge, California I of Technology, Pasadena, CA 91125
- M3.6 ANTENNAS ON LAYERED SUBSTRATES - R. L. Rogers, D. P. Neikirk, H. Ling and T. Itoh, Univ. Texas, Austin, TX 78712

---

---

### SESSION M4

---

---

---

Ballroom (Makai), 7<sup>th</sup> Floor

---

Monday AM December 5, 1988

---

#### FEL I

---

A.K. Ganguly, Presider

---

- M4.1 NEW DIRECTIONS IN MMW VACUUM ELECTRONIC RESEARCH - (*Invited Keynote*) R.J. Barker, U.S. Air Force Office of Scientific Research, AFOSR/NP Bolling Air Force Base, DC 20332-6448
- M4.2 SHORT-PERIOD WIGGLER FREE ELECTRON LASER WITH A SHEET ELECTRON BEAM - (*Invited Keynote*) J.H. Booske, Lab for Plasma Research, U of Maryland, College Park, MD 20742
- M4.3 TUNABLE MICRO-UNDULATORS FOR FREE ELECTRON LASERS - S.C. Chen, G. Bekefi and S. DiCecca, Dept Physics and Plasma Fusion Center, MIT, Cambridge, MA 02139
- M4.4 THE EFFECT OF WIGGLER FIELD ERRORS ON THE PERFORMANCE OF FELs - E. Esarey, W. Marable, Berkeley Research Associates, Springfield, VA; C.M. Tang and P. Sprangle, Plasma Physics Div, Naval Research Lab, Washington, DC 20375-5000
- M4.5 COLLECTIVE INSTABILITY IN CIRCULAR FREE ELECTRON LASER - Y. Kawai, H. Saito, Inst. of Space and Astron. Science, Yoshinodai, Sagamihara, Japan 229; J. Wurtele, MIT Plasma Fusion Center, 167 Albany St NW16, Cambridge, MA 02139
- M4.6 THE ANALYSIS OF RADIATION HARMONICS IN THE FEL USING THE SOURCE DEPENDENT EXPANSION METHOD - C.M. Tang, P. Sprangle, Plasma Physics Div, Naval Research Lab, Washington, DC 20375-5000; S. Riyopoulos, Science Applications Intl. Corp, McLean, VA
- M4.7 SUPPRESSION OF SIDEBANDS BY DIFFRACTION IN A FEL - T.M. Antonsen, Jr., Lab for Plasma Research, U of Maryland, College Park, MD 20742; G. Laval, Ecole Polytechnique, France
- M4.8 ANALYSIS AND NONLINEAR SIMULATION OF A HELICAL QUADRUPOLE WIGGLER FOR MILLIMETER WAVES - J.E. Scharer, S.F. Chang, and O.C. Eldridge, Univ of Wisconsin, Madison, WI

---

---

## SESSION M5

---

---

---

Ballroom (Mauka), 7<sup>th</sup> Floor

---

Monday PM

December 5, 1988

---

### MMW SOURCES II

---

S-F. Li, Presider

- M5.1 DEVELOPMENT OF HIGH EFFICIENCY FREQUENCY MULTIPLIERS FOR 130-350 GHz - T. Tolmuncen, A. Raisanen and M. Sironen, Helsinki U of Tech, Radio Lab, Otakaari 5 A, SF-02150 Espoo, Finland
- M5.2 PERIODIC MONOLITHIC MILLIMETER-WAVE QUANTUM WELL OSCILLATOR - A. Mortazawi, V.P. Kesan, D.P. Neikirk, and T. Itoh, Dept Elec & Cmptr Engr, The U of Texas at Austin, Austin, TX 78712
- M5.3 RIGOROUS FIELD ANALYSIS OF IMPEDANCES OF SOME MILLIMETER WAVE OSCILLATOR CAVITIES - W. Hong and S-F. Li, Southeast U, Nanjing, P.R. China
- M5.4 THEORY OF THE DIOTRON INSTABILITY IN HIGH POWER MAGNETRON - H.S. Uhm and H.C. Chen, Naval Surface Warfare Center, White Oak, Silver Spring, MD 20903-5000; H.E. Brandt, Harry Diamond Laboratory, Adelphi, MD 20783-1197
- M5.5 POWER COMBINING SYSTEM USING TWO PUSH PULL POWER AMPLIFIERS - S. Toyoda, Dept Elec Engr, Osaka I of Tech, 5-16-1 Omiya Aaahi-ku, Osaka 535, Japan
- M5.6 QUASI-OPTICAL RESONATOR FOR MILLIMETER AND SUB-MILLIMETER WAVE SOLID-STATE SOURCES - M. Hieda, M. Nakayama, K. Mizuno, T. Ajikata and D.B. Rutledge\*, Research I of Elec Comm, Tohoku U, Sendai 980, Japan; \*California I of Tech, Pasadena, CA 91125
- M5.7 NUMERICAL SIMULATION OF THE DIOTRON INSTABILITY IN PLANAR DIODE GEOMETRY - H.C. Chen and H.S. Uhm, Naval Surface Warfare Center, White Oak, Silver Spring, MD 20903-5000
- M5.8 RESONANT-TUNNELING DEVICES FOR MILLIMETER-WAVE GENERATION - R.K. Mains and G.I. Haddad, Ctr for High-Frequency Microelectronics, Dept Elec Engr & Cmptr Science, The U of Michigan, Ann Arbor MI 48109
- M5.9 PARAMETRIC AMPLIFICATION USING SUPERCONDUCTING TUNNEL JUNCTIONS - H.K. Olsson and t. Claesson, Chalmers Univ of Tech, S-41296 Göteborg, Sweden

---

---

## SESSION M6

---

---

---

Mahimahi Room, 3<sup>rd</sup> Floor

---

Monday PM

December 5, 1988

---

### OPTICAL TECHNOLOGY FOR MMW

---

Tatsuo Itoh, Presider

- M6.1 PICOSECOND OPTOELECTRONICS AND MILLIMETER-WAVE TECHNOLOGY - (Invited, 40 min.) - C.H. Lee, Dept Elec Engr, U of Maryland, College Park, MD 20742
- M6.2 OPTICAL GENERATION AND CONTROL OF MILLIMETER WAVES - Invited, 30 min - L. Goldberg, Naval Research Labs, Washington, DC
- M6.3 EXPERIMENTAL PERFORMANCE OF AN OPTICALLY CONTROLLED COPLANAR WAVEGUIDE PHASE SHIFTER WITH A THICK GaAs BURIED LAYER - P. Cheung, D.P. Neikirk and T. Itoh, U of Texas, Austin, TX
- M6.4 STRUCTURAL CONTROL OF MICROSTRIP DISPERSION FOR SHAPING GIGA-HERTZ-BANDWIDTH PULSES - E. Yamashita, K. Atsuki and Y. Qian, U of Electro-comm., Chofu-shi, Tokyo, Japan 182
- M6.5 OPTOELECTRONICS AND ELECTROMAGNETICS: VIDEO TO VISIBLE - Invited, 30 min - A.P. DeFonzo, Dept of Elec & Cmptr Engr, U of Massachusetts, Amherst, MA 01003
- M6.6 INVERTED SLOT LINE FOR MILLIMETER-WAVE OPTICAL MODULATOR - T. Yoneyama and T. Kato, Research I of Elec Comm, Tohoku U, 2-1-1 Katahira, Sendai, 980 Japan
- M6.7 AN OPTOELECTRONIC TECHNIQUE FOR S-PARAMETER MEASUREMENTS OF GaAs MONOLITHIC INTEGRATED CIRCUITS - P. Polak-Dingels, H-L. A. Hung\*, K.J. Webb\*\*, T.T. Lee, T. Smith\*, and C.H. Lee\*\*, The Lab fo Physical Sciences, College Park, MD 20742; \*COMSAT Labs, Clarksburg, MD 20871; \*\*U of Maryland, College Park, MD 20742
- M6.8 EFFECT OF THE LIGHT ON THE ELEMENTS OF THE ELECTRIC SCHEME OF A HEMT - D. Pasquet, B. Zemour, J.L. Gautier, P. Pouvil, ENSEA, Les Chenes Pourpres, 95000 Cergy, France

---

---

## SESSION M7

---

---

---

Papio Room, 3<sup>rd</sup> Floor

---

Monday PM December 5, 1988

---

### ASTRONOMY

---

A. Räisänen, Presider

---

- M7.1 SYSTEMATIC SURVEY OF STAR FORMATION REGIONS WITH THE 4 m MILLIMETER-WAVE TELESCOPE AT NAGOYA UNIVERSITY - MOLECULAR OUTFLOWS AS THE EARLIEST STAGE OF STAR FORMATION - (*Invited Keynote*) - Y. Fujui, Dept of Astrophysics, Nagoya Univ, Chikusa, Nagoya 464, Japan
- M7.2 JOSEPHSON LOCAL OSCILLATOR FOR INTEGRATED RADIOASTRONOMICAL RECEIVERS - R. Monaco, S. Pagano, C. Costabile, Istituto di Cibernetica, I-80072 Arco Felice (NA), Italy
- M7.3 A BROADBAND LOW NOISE SIS RECEIVER FOR SUBMILLIMETER ASTRONOMY - T.H. Büttgenback<sup>1</sup>, R.E. Miller<sup>2</sup>, M.J. Wengler<sup>1,3</sup>, D.M. Watson<sup>1</sup>, T.G. Philips<sup>1</sup>, <sup>1</sup> Division of Physics, Mathematics and Astronomy, California I of Tech, Pasadena, CA 91125; <sup>2</sup> AT&T Bell Labs, Murray Hill, NJ 07974, <sup>3</sup> Dept of Elec Engr, U of Rochester, Rochester, NY 14627
- M7.4 BALLOON-BORNE OBSERVATIONS OF THE CYGNUS REGION IN THE FAR INFRARED - C.G. Degiacomi, A. Holenstein, F.K. Kneubühl, Infrared Physics Lab, ETH, 8093 Zurich, Switzerland; D. Huguennin, Geneva Observatory, 1290 Sauverny, Switzerland
- M7.5 490 GHz SOLID STATE SOURCE WITH VARACTOR-QUINTUPLER - R. Rüdiger and P. Zimmermann, Radiometer-physics, Bergerwiesenstr. 15, 5309 Meckenheim, West Germany

---

---

## SESSION M8

---

---

---

Ballroom (Makai), 7<sup>rd</sup> Floor

---

Monday PM December 5, 1988

---

### FEL II

---

J.E. Walsh, Presider

---

- M8.1 HIGH POWER, MILLIMETER WAVE FEL FOR PLASMA HEATING APPLICATIONS - (*Invited Keynote*) - R.A. Jong and T.J. Orzechowski, Lawrence Livermore Nat'l Lab, Livermore, CA
- M8.2 CURRENT THEORETICAL AND EXPERIMENTAL ISSUES ON FREE-ELECTRON LASERS - (*Invited Keynote*) - F. Hartmann, J.M. Buzzi, G. Mourier and M. Faillon, Thomson-CSF, 2 Rue Latecoere, B.P. 23-78141, Velizy-Villacoublay, France
- M8.3 MODE COMPETITION, SUPPRESSION AND CONTROL IN FEL OSCILLATORS - B. Levush and T. Antonsen, Jr., Lab for Plasma Research, U of Maryland, College Park, MD 20742
- M8.4 HIGH HARMONIC EMISSION IN THE UNIFORM MAGNETIC FIELD FREE-ELECTRON LASER - J. Soln, Harry Diamond Labs, 2800 Powder Mill Rd, Adelphi, MD 20783
- M8.5 A HIGH POWER, 600  $\mu$ m WAVELENGTH FREE-ELECTRON LASER - D.A. Kirkpatrick, NRL, Washington, DC 20375-5000; G. Bekefi, A.C. DiRienzo, Dept Physics and Research Lab of Electron., MIT, Cambridge, MA 02139; H.P. Freund and A.K. Ganguly, NRL, Washington, DC 20375-5000
- M8.6 3-D MOTION OF ELECTRONS IN COMBINED REALISTIC HELICAL WIGGLER WITH AXIAL GUIDE FIELD FOR FREE-ELECTRON LASER - S-C. Zhang, Z. Zhang and S. Zhou, Dept Physics, Chengdu I of Radio Engr, Chengdu, Sichuan, China
- M8.7 BETATRON-SYNCHROTRON RESONANCES IN FREE ELECTRON LASER - Y-J. Shi, I of Atomic Energy, P.O. Box 275(18), Beijing, China
- M8.8 HIGH-GAIN FREE ELECTRON LASER WITH VARIABLE PARAMETER WIGGLERS - Z-X. Hui, Xinan I of Elec Engr, P.O. Box 517, Chengdu, P.R.China
- M8.9 THE EFFICIENCY IMPROVEMENT OF A RAMAN FREE-ELECTRON LASER - Z. Wang, Z. Lu, L. Zhang, and J. Chen, Shanghai I of Optics and Fine Mechanics, Academia Sinica, P.O. Box 8211, Shanghai, PRC

---

---

## SESSION T1

---

---

---

Ballroom (Mauka), 7<sup>th</sup> Floor

---

Tuesday AM

December 6, 1988

---

### MMW SYSTEMS I

---

J. C. Wiltse, Presider

---

- T1.1** MILLIMETER WAVE RADAR-CURRENT STATUS AND FUTURE DIRECTIONS - (*Invited Keynote, 40 min.*) - E.K. Reedy, Georgia Tech Research Inst, GA Inst Tech, Atlanta, GA 30332
- T1.2** NEW TRENDS IN MILLIMETER WAVE MISSILE SEEKER DESIGN - (*Invited Keynote, 40 min.*) - T.T. Fong, TRW Inc, Redondo Beach, CA 90278
- T1.3** A PROTOTYPE COMMERCIAL ORBITRON MASER FOR MILLIMETER RADAR - M.G. Nilmira and R.J. Churchill, American Research Corp of Virginia; I. Alexeff, F. Dyer and M. Radar, University of Tennessee, Dept Elec and Cmpt Engr, Knoxville, TN 37996-2100
- T1.4** A LOW-LOSS HIGH-POWER FILTER FOR DIRECT BROADCAST SATELLITE TRANSPONDERS - T. Nomoto, Science and Technical Research Laboratories, 1-10-11, Kinuta, Setagaya, Tokyo, 157, Japan
- T1.5** MILLIMETRIC CHARACTERIZATION USING AN 80 GHz MONO-STATIC HIGH POWER POLARIMETRIC RADAR - G.N. Crisp, P.A. Blakelock, K.E. Potter, C.E. Burnett, MEDL Microwave, Doddington Rd, Lincoln, LN6 3LF, England
- T1.6** A MODEL BASED TECHNIQUE FOR MILLIMETER WAVE TARGET RECOGNITION - F.A. Sadjadi, Honeywell, Systems and Research Ctr MN65-2300, 3660 Technology Dr, Minneapolis, MN 55418
- T1.7** RECENT ADVANCES IN MILLIMETER WAVE UP AND DOWN CONVERTERS - C. Oleson, A. Larsen, R. Chew and W. Day, Varian Solid State Microwave Div, 3251 Olcott St, Santa Clara, CA 95054
- T1.8** 205 GHz SIS RECEIVER DEVELOPMENT FOR REMOTE SENSING APPLICATIONS - W.R. McGrath, C.N. Byrom, B.N. Elhison\*, M.A. Frerking, and R.E. Miller\*\*, Jet Propulsion Lab, Pasadena, CA; \*California Inst of Tech, Pasadena, CA; \*\*AT&T Bell Labs, Murray Hill, NJ
- 

---

---

## SESSION T2

---

---

---

Mahimahi Room, 3<sup>rd</sup> Floor

---

Tuesday AM

December 5, 1988

---

### MICROWAVE-OPTICAL INTERACTIONS

---

T. Sueta, Presider

---

- T2.1** OPTICAL TECHNOLOGY APPLIED TO SubMM/MMW - (*Invited Keynote, 40 min.*) - H.R. Fetterman, Dept Electrical Engineering, U of California, Los Angeles, CA
- T2.2** HIGH FREQUENCY MODULATION OF SEMICONDUCTOR LASERS - A.P. DeFonzo, Dept of Electrical and Computer Engineering, U of Massachusetts, Amherst, MA 01003
- T2.3** LIGHT-CONTROLLED MICROSTRIP LINE COUPLER - H. Shimazaki, Faculty of Engineering, Osaka Univ, Suita 564, Japan; M. Tsutsumi, Faculty of Engineering and Design, Kyoto I of Technology, Kyoto 606, Japan
- T2.4** OPTICAL GENERATION AND DISTRIBUTION OF MICROWAVE SIGNALS - G.J. Simonis and K.G. Purchase, LABCOM, Harry Diamond Lab, 2800 Powder Mill Road, Adelphi, MD 20783-1197
- 

---

---

## SESSION T3

---

---

---

Mahimahi Room, 3<sup>rd</sup> Floor

---

Tuesday AM

December 6, 1988

---

### PLASMA DIAGNOSTICS I

---

K. Kawahata, Presider

---

- T3.1** INFLUENCE OF WAVELENGTH ON THE PERFORMANCE OF COLLECTIVE THOMSON SCATTERING FOR ALPHA-PARTICLE DIAGNOSTICS - (*Invited Keynote*) - P.P. Woskov, D.R. Cohn, J.S. Machuzak and D.Y. Rhee, MIT Plasma Fusion Center, Cambridge, MA 02139
- T3.2** A CO<sub>2</sub> LASER THOMSON SCATTERING DIAGNOSTIC FOR THE MEASUREMENT OF FUSION PRODUCT ALPHA PARTICLES - R.K. Richards, C.A. Bennett\*, L.K. Fletcher\*\*, H.T. Hunter and D.P. Hutchinson, Oak Ridge Natl Lab, Oak Ridge, TN 37831; \*On sabbatical leave from U of North Carolina of Asheville; \*\*Tennessee Technological Univ, Cookeville, TN
- T3.3** ECRH OF TRAPPED ELECTRONS IN TOKAMAKS - S.P. Kuo, Polytechnic U, Farmingdale, NY 11735; M.C. Lee, MIT, Cambridge, MA 02139
- T3.4** PLASMA DENSITY PROFILE IMAGING BY MICROWAVE HETERODYNE SYSTEM AND ELECTRON ACCELERATION IN CROSS FIELD ACCELERATION SCHEME - (*30 min.*) Y. Nishida, H. Okazaki, Y. Yamada, T. Shinozaki and N.C. Luhmann, Dept Elec Engr, Utsunomiya Univ Utsunomiya, Tochigi 321 JAPAN
-

---

---

## SESSION T4

---

---

---

---

Papio Room, 3<sup>rd</sup> Floor

---

---

Tuesday AM December 6, 1988

---

---

### MMW GUIDES

---

---

S. T. Peng, Presider

---

---

- T4.1 MEGAWATT CW MILLIMETER WAVE TRANSMISSION SYSTEMS - (*Invited Keynote*) - M. Thumm, H. Barkley, W. Kasparek, G.A. Müller and P.G. Schuller, Institut für Plasmaforschung, Universität Stuttgart, Pfaffenwaldring 31, D-7000 Stuttgart 80, West Germany
- T4.2 LOW LOSS, BROADBAND, MULTIMODE, CIRCULAR CORRUGATED WAVEGUIDE PERFORMANCE - A. Cavallo, J. Doane, R. Cutler, Princeton Plasma Physics Lab, Princeton University, Princeton, NJ 08540; J. Brenner, Brenner Tool and Die, Croydon, PA 19020
- T4.3 INITIAL OPERATION OF A POLARIZATION-CONTROLLED BEAMED ECH LAUNCHER - T.S. Bigelow, C.R. Schaich and T.L. White, Oak Ridge Nat'l Lab, P.O. Box Y, MS-2, Bldg. 9101-2, Oak Ridge, TN 37831
- T4.4 VERY SHORT QUASI-PERIODIC AND APERIODIC MODE CONVERTERS FOR 60 AND 140 GHz GYROTRONS - M.J. Buckley, G.H. Luo, R.J. Vernon, Dept Electrical and Cmptr Engr, U of Wisconsin, Madison, Wisconsin 53711
- T4.5 AN X-BAND VLASOV-TYPE MODE CONVERTOR - B.G. Ruth, D. Schlesiger and R.K. Dahlstrom, Harry Diamond Laboratories, ATTN: SLCHD-NW-RI, 2800 Powder Mill Rd, Adelphi, MD 20783-1197
- T4.6 A QUASI-OPTICAL CONVERTER FOR EFFICIENT CONVERSION OF WHISPERING GALLERY MODES INTO NARROW BEAM WAVES - A. Möbius, K. Kreischer and R. Temkin, MIT Plasma Fusion Center, 167 Albany St NW16, Cambridge, MA 02139
- T4.7 REALISTIC PROSPECTS FOR SUPERCONDUCTING GYROTRON RESONATORS - J. Halbritter, G. Hochschild, J. Jödicke, Kernforschungszentrum Karlsruhe, Inst. f. Technische Physik, D-7500 Karlsruhe, Fed Rep Germany
- T4.8 DESIGN OF THE CIT GYROTRON ECRH TRANSMISSION SYSTEM - J.A. Casey, P. Woskov, D. Cohn, R. Temkin, MIT Plasma Fusion Center, 167 Albany St NW16, Cambridge, MA 02139
- T4.9 PRELIMINARY LOW-POWER INVESTIGATION OF TE<sub>0n</sub> MODE VLASOV LAUNCHERS - P.J. Sealy and R.J. Vernon, Dept Elec and Cmptr Engr, U of Wisconsin, Madison, WI 53711

---

---

## SESSION T5

---

---

---

---

Ballroom (Makai), 7<sup>th</sup> Floor

---

---

Tuesday AM December 6, 1988

---

---

### FEL III

---

---

W.M. Manheimer, Presider

---

---

- T5.1 OBSERVATION OF UBITRON FUNDAMENTAL MODE AMPLIFICATION - (*Invited Keynote*) - R.H. Jackson, D.E. Pershing and H. Bluem, Vacuum Electronics Branch, Code 6842, Naval Research Lab, Washington, DC 20375-5000
- T5.2 FREQUENCY SPECTRUM OF THE UCSB FEL - (*Invited Keynote*) - L. Elias, CREOL, U Central Florida, (12424 Research Parkway, Suite 400), Orlando, FL 32826
- T5.3 OPTIMIZATION OF A PLANAR OROTRON - J.E. Walsh, J.A. Jackson, E.M. Marshall, Dartmouth College, Hanover, NH 03755
- T5.4 THE CIRCULAR ORBIT LINEAR THEORY OF AXIAL INJECTION ORBITRON MASER OSCILLATORS - J.M. Burke, Burke Technologies, Inc., San Diego, CA 92111-1316
- T5.5 PULSED AND STEADY-STATE MULTIANODE ORBITRON MASERS - I. Alexeff, F. Dyer, and M. Rader, U of Tennessee, Knoxville, TN 37996-2100
- T5.6 HIGH EFFICIENCY OPERATION OF THE MODIFIED PENIOTRON USING TE<sub>11</sub> RECTANGULAR WAVEGUIDE CAVITY - K. Yokoo, M. Razeghi, N. Sato and S. Ono, Research I of Elec Communication, Tohoku U, Sendai 980, Japan
- T5.7 AUTO-RESONANT PENIOTRON FOR HIGH POWER MILLIMETER WAVE GENERATION WITH AN EXTREMELY HIGH EFFICIENCY - K. Yokoo, S. Ono, N. Sato, Research I of Elec Communication, Tohoku U, Sendai 980, Japan

---

---

## SESSION T6

---

---

---

---

Ballroom (Mauka), 7<sup>th</sup> Floor

---

---

Tuesday PM December 6, 1988

---

---

### MMW SYSTEMS II

---

---

E. Reedy, Presider

---

---

- T6.1 MMW COMMUNICATIONS TECHNOLOGY - (*Invited Keynote*) - R. Ying, Hughes Aircraft Co., Torrance, CA
- T6.2 MEASUREMENT OF COHERENCE BANDWIDTH FOR AN URBAN MILLIMETER WAVE RADIO LINK - R.S. Cole, H.J. Thomas, G.L. Siqueira, University College, London WC1F 7SE, England

---

---

## SESSION T7

---

---

Ballroom (Mauka), 7<sup>th</sup> Floor

Tuesday PM

December 6, 1988

---

### MMW DETECTORS & MIXERS

---

J. Archer, Presider

- T7.1** MILLIMETER-WAVE SIS RECEIVERS OF NOBEYAMA RADIO OBSERVATORY - (*Invited Keynote*) - J. Inatani, Nobeyama Radio Observatory, Nobeyama, Nagano 384-13, Japan
- T7.2** A NEW FUNDAMENTALLY PUMPED BALANCED MIXER FOR G-BAND (140-220 GHz) - I. Galin, Aerojet ElectroSystems Company, Azusa, CA 91702
- T7.3** LARGE-AREA BOLOMETERS FOR MILLIMETER-WAVE POWER CALIBRATION - G.M. Rebeiz, C. Ling, Univ of Michigan, Ann Arbor, MI 48109; D.B. Rutledge, Div of Engr and Appl Science, California I of Tech, Pasadena, CA 91125
- T7.4** SERIES-CONNECTED JOSEPHSON-EFFECT MIXERS FOR MILLIMETER-WAVE RADIATION - H. Ohta\*, T. Matsui and B. Komiyama, Radio Res Lab, Ministry of Posts and Telecomm, Nukui-ki tamachi 4-2-1, Koganei-shi 184, Tokyo, Japan; \*The I of Physical and Chem Research, Hirosawa 2-1, Wako-shi Saitama 351-01, Japan
- T7.5** A QUASI-OPTICAL SLOT-RING MIXER MONOPULSE ARRAY - R. Gingras<sup>1</sup>, G.M. Hegazi<sup>2</sup>, T.L. Korzeniowski<sup>1</sup>, K.D. Stephan<sup>3</sup>, J. Wolverson<sup>4</sup>, and K.S. Yngvesson<sup>3</sup>, <sup>1</sup> Missile Systems Div, Raytheon Co, Tewksbury, MA; <sup>2</sup> COMSAT Labs, Clarksburg, MD; <sup>3</sup> Dept Elec & Cmptr Engr, U of Massachusetts, Amherst, MA; Air Force Armament Labs, Air to Ground Systems Div, Eglin Airforce Base, FL
- T7.6** PLANAR SUBHARMONIC MIXER FOR 183 GHz - N.J. Cronin, S.P. Marsh, P.J. Reece, U of Bath, School of Physics, Claverton Down, Bath BA2 7AY England

---

---

## SESSION T8

---

---

Mahimahi Room, 3<sup>rd</sup> Floor

Tuesday PM

December 6, 1988

---

### PLASMA DIAGNOSTICS II

---

Y. Nishida, Presider

- T8.1** A MULTICHANNEL SUBMILLIMETER WAVE INTERFEROMETER SYSTEM ON ATF - (*Invited Keynote, 40 min*) - D.P. Hutchinson, C.H. Ma, K.L. Vander Sluis, C.A. Bennett\* and J. Lee\*\*, Oak Ridge Natl Lab, Oak Ridge, TN
- T8.2** DEVELOPMENT OF STABLE, HIGH POWER CW FIR LASER FOR PLASMA DIAGNOSTIC - Q. Zu, S. Ruan, F. He, B. Li, Y. Xu, Inst. Physics, Chinese Acad. Sci, Beijing, PRC
- T8.3** FIR POLARIMETER/INTERFEROMETER FOR JIPP T-II U - A. Yasuda, Tokyo U of Mercantile Marine, Etchujima, Koto-ku, Tokyo 135, Japan; K. Kawahata and J. Fujita, I of Plasma Physics, Nagoya University; S. Okajima, Chubu Univ; Y. Nagayama, The U of Tokyo, Japan
- T8.4** A MULTICHANNEL HCN LASER INTERFEROMETER FOR ELECTRON DENSITY MEASUREMENTS ON THE JIPP T-IIU TOKAMAK - K. Kawahata and J. Fujita, I of Plasma Physics, Nagoya U, Nagoya, Japan; A. Yasuda, Tokyo U of Mercantile Marine, Tokyo Japan; S. Okajima, Chubu U, Ksaugai 487, Japan
- T8.5** SCATTERING OF MILLIMETER-SUBMILLIMETER RADIATION FROM THE TORTUS TOKAMAK PLASMA - M.D. Bowden, P.W. Fekete, M.J. Ballico, G.F. Brand, I.S. Falconer, B.W. James and K.J. Moore, School of Physics, U of Sydney, NSW 2006, Australia; T. Idehara, Fukui University, Japan
- T8.6** A HIGH POWER CH<sub>3</sub>OH LASER SYSTEM USING STARK STABILIZED CO<sub>2</sub> PUMP LASERS - D.P. Hutchinson, C.A. Bennett\*, J. Lee\*\*, L.K. Fletcher, C.H. Ma and K.L. Vander Sluis, Oak Ridge Nat' Lab, Oak Ridge, TN
- T8.7** SIMULTANEOUS MULTILINE OPERATION OF A FORMIC ACID LASER AND APPLICATIONS - M.D. Bowden, I.S. Falconer, B.W. James, U of Sydney, NSW, Australia; L.B. Whitbourn, CSIRO Lindfield, NSW 2070, Australia; J.C. Macfarlane, CSIRO, Australia
- T8.8** ION TEMPERATURE MEASUREMENTS IN A TOKAMAK BY COLLECTIVE THOMSON SCATTERING OF FIR LASER RADIATION - R. Behn, D. Dicken\*, J. Hackmann\*, S.A. Salito and M.R. Siegrist, Ecole Polytechnique Federale Lausanne, Switzerland
- T8.9** DESIGN AND CALIBRATION OF A TWO-CHANNEL LOW NOISE HETERODYNE RECEIVER AT 10.6  $\mu$ m - C.A. Bennett, R.K. Richards, and D.P. Hutchinson, Oak Ridge Natl Lab, Oak Ridge, TN 37831
- T8.10** CALIBRATION OF 10-CHANNEL GRATING POLYCHROMATOR - K. Kawahata, M. Sakamoto, J. Fujita, Inst of Plasma Physics, Nagoya Univ, Chikusa-ku, Nagoya 464-01, Japan; H. Matsuo, Dept of Astrophysics, Nagoya Univ; K. Sakai, Dept of Applied Physics, Osaka Univ, Suita, Osaka 565, Japan
- T8.11** A STARK-TUNED CH<sub>3</sub>OH LASER FOR USE IN HIGH FREQUENCY MODULATED INTERFEROMETRY - D.K. Mansfield, M. Vocaturo, L. Guttadora, Princeton Univ. Plasma Physics Lab, Princeton, NJ 08543

---

---

**SESSION T9**

---

---

---

**Papio Room, 3<sup>rd</sup> Floor**

---

**Tuesday PM****December 6, 1988**

---

**ATMOSPHERIC PHYSICS**

---

---

**E. E. Altshuler, Presider**

---

- T9.1** THE EFFECTS OF TURBULENCE IN CLEAR AND TURBID ATMOSPHERES ON MILLIMETER WAVE PROPAGATION - R.W. McMillan and R.A. Bohlander, GA Inst of Tech, Atlanta, GA 30332; R.J. Hill and S.F. Clifford, Natl Oceanic and Atmos Admin, Boulder CO 80303
- T9.2** ATMOSPHERIC ATTENUATION AND DELAY RATES BETWEEN 1 GHz AND 1 THz - (*Invited Keynote*) - H. Liebe, NTIA/ITS, 325 Broadway, Boulder, CO 80803
- T9.3** AN ALGORITHM FOR ESTIMATING CLOUD ATTENUATION AT MILLIMETER WAVELENGTHS - E.E. Altshuler, R.A. Marr, Rome Air Devlmt Center/EECP, Electromagnetics Directorate, Hanscom AFB, MA 01731-5000
- T9.4** MILLIMETER WAVE ATMOSPHERIC PROGAGATION STUDY AT CRL - T. Ihara\*, T. Manabe\*\*, J. Awaka\*\*, Y. Furuhashi\*\*\*, \*Kashima Space Res Ctr, Comm Res Lab, Ministry of Posts and Telecomm, 893-1 Hirai, Kashima-machi, Ibaraki-ken, 314 Japan; \*\*Comm Res Lab, Ministry of Posts and Telecomm, 2-1, Nukuiikita-machi 4-chome, Koganei-shi, Tokyo 184, Japan; \*\*\*ATR Optical and Radio Comm Res Lab, Twin21 MID Tower, 2-1-61, Shiromi, Higashi-ku, Osaka 540 Japan
- T9.5** FOR FUTURE METEOROLOGICAL MILLIMETER-WAVE RADIATIVE TRANSFER MODEL AND AN AIRBORNE CAMPAIGN - C. Prigent, Dept de radioastronomie Millimetrique, Observatoire de Meudon, 92190 Meudon, France; P. Abba, Alcatel-Espace, France; N.A. Scott, Lab de Météorologie Dynamique, France
- T9.6** MESOSPHERIC RADIOWAVE PROPAGATION IN THE 60GHz BAND AFFECTED BY PROPERTIES OF ZEEMAN-SPLIT OXYGEN LINES - H.J. Liebe, G.A. Hufford and A.S. Katz, Natl Telecomm and Info Admin, I for Telecomm Sciences, 325 Broadway, Boulder, CO 80303

---

---

**SESSION T10**

---

---

---

**Ballroom (Makai), 7<sup>th</sup> Floor**

---

**Tuesday PM****December 6, 1988**

---

**GYROTRON I**

---

---

**V.L. Granatstein, Presider**

---

- T10.1** STATUS AND FUTURE PLANS OF HIGH POWER SOURCES FOR PLASMA HEATING - (*Invited Keynote*) - T.V. George, U.S. Dept of Energy, Office of Fusion Energy, Washington, DC 20545
- T10.2** MEGAWATT GYROTRONS FOR ECR HEATING - (*Invited Keynote*) - K. Felch, C. Hess, E. Jongewaard, H. Jory, H. Huey and R. Pendleton, Varian Associates, Inc., 611 Hansen Way, Palo Alto, CA 94303
- T10.3** EXPERIMENTAL STUDIES ON THE 120 GHz GYROTRON OF MITSUBISHI ELECTRIC CORP. - T. Kikunaga, T. Shimozuma, H. Asano, Y. Yasojima, Y. Murai, K. Nakashima and T. Tsukamoto, Central Research Laboratory, Mitsubishi Electric Corp., Amagasaki, Hyogo, 661 Japan
- T10.4** THE DESIGN OF MEGAWATT GYROTRONS FOR THE COMPACT IGNITION TOKAMAK - K.E. Kreischer, T. Grimm, A.W. Mobius, and R.J. Temkin, MIT Plasma Fusion Center NW-16, 167 Albany St, Cambridge, MA 02139
- T10.5** 8 GHz HIGH POWER GYROTRON WITH DEPRESSED COLLECTOR - P. Muggli, H.-G. Mathews\*, M.Q. Tran, G. Agosti\*, S. Alberti\*, A. Perrenoud, T.M. Tran, Ecole Polytechnique Federale de Lausanne, 1007 Lausanne, Switzerland; \*Asea Brown Boveri Ltd., Dept EKR, 5401 Baden, Switzerland
- T10.6** DEPRESSED COLLECTORS FOR GYROTRONS - M.E. Read and Alan J. Dudas, Physical Sciences, Inc., 635 Slaters Lane, Suite G101, Alexandria, VA 22314; W. Lawson and A. Singh, Lab for Plasma and Fusion Energy Studies, U of Maryland, College Park, MD 20742
- T10.7** MADEY THEOREM IN GYROTRON - S.-C. Zhang, Dept of Physics, Chengdu I of Radio Engr, chengdu, Sichuan, P.R.China
- T10.8** GYROTRON IV - A NEW TUNABLE GYROTRON - G.F. Brand, School of Physics, U of Sydney, NSW 2006, Australia

---

---

## SESSION W1

---

---

---

Ballroom (Mauka), 7<sup>th</sup> Floor

---

Wednesday AM

December 7, 1988

---

### GUIDED PROPAGATION I

---

A. A. Oliner, Presider

---

- W1.1** MODELLING OF MMW STRUCTURE IN THE TIME DOMAIN USING TRANSMISSION LINE MODELLING (T.L.M.) - (*Invited Keynote*) W. Hoefer, Electrical Engineering, University of Ottawa, Ottawa, Ontario, Canada
- W1.2** CHARACTERISTICS OF COUPLED PLANAR STRIP-SLOT RESONATORS WITH MULTIPLE-LAYER DIELECTRICS - A. Rong and S. Li, Dept of Radio Engineering, Southeast U, Nanjing, P.R.China
- W1.3** EXCITATION AND TRANSMISSION MEASUREMENTS OF DIELECTRIC ROD WAVEGUIDE  $HE_{11}$ -MODE IN THE 50-150 GHz RANGE - Y. Yamamoto and K. Fujisawa, Dept of Electrical Engineering and Electronics, Faculty of Engineering, Osaka Sangyo U, Daito, Osaka, 574, Japan
- W1.4** A NEW APPROACH FOR THE ANALYSIS OF WAVEGUIDES WITH MULTIPLY CONNECTED CROSS SECTION - A.S. Omar and K. Schünemann, Technische Universität Hamburg-Harburg, Arbeitsbereich Hochfrequenztechnik, Postfach 90 14 03, D-2100 Hamburg 90, West Germany
- W1.5** MODAL ANALYSIS OF CIRCULAR BIFURCATION FOR CCTWTs - F. Lin and A.S. Omar, Technische Universität Hamburg-Harburg, Arbeitsbereich Hochfrequenztechnik, Postfach 90 14 03, D-2100 Hamburg 90, West Germany
- W1.6** ANALYSIS OF ECCENTRIC ANNULAR WAVEGUIDES - Y. Xu and A.S. Omar, Technische Universität Hamburg-Harburg, Arbeitsbereich Hochfrequenztechnik, Postfach 90 14 03, D-2100 Hamburg 90, West Germany
- W1.7** CHARACTERISTICS OF DOUBLE GROOVE GUIDE FOR 100 GHz OPERATION - Y.M. Choi, Hong Kong Polytechnic, Kowloon, Hong Kong

---

---

## SESSION W2

---

---

---

Mahimahi Room, 3<sup>rd</sup> Floor

---

Wednesday AM

December 7, 1988

---

### HIGH $T_c$ SUPERCONDUCTORS I

---

Mohammed N. Afzar, Presider

---

- W2.1** PROCESSING AND ELECTRICAL PROPERTIES OF HIGH  $T_c$  SUPERCONDUCTORS - (*Invited Keynote*) - R.B. Poeppel, M.T. Lanagan, J.P. Singh, K.C. Goretta, J.T. Dusek, S.E. Dorris, U Balachandran, C. Bohn and J.R. Delayen, Ceramic Technology Div, Argonne Natl Laboratory, Argonne IL 60439
- W2.2** EXPLORING THE LOW LYING EXCITATION SPECTRA OF HIGH  $T_c$  SUPERCONDUCTORS - (*Invited Keynote*) - A.J. Sievers, Dept of Physics, Cornell U, Ithaca, NY
- W2.3** AN OPEN RESONATOR FOR TESTING SURFACE RESISTIVITY OF SUPERCONDUCTOR FILMS AND METALLIC SAMPLES AT 100-120 GHz - (*Invited Keynote*) - T. Matsui, M. Kiyokawa and B. Komiyama, Communications Research Lab, Koganei, Tokyo 134, Japan
- W2.4** ANTIFERROMAGNETIC ORDER IN HIGH  $T_c$  SUPERCONDUCTOR OXIDES - S. Yoshimori and M. Kawamura, Dept of Physical Elec, Faculty of Engr, Tokyo Inst of Technology, Japan
- W2.5** MEASUREMENT OF SUPERCONDUCTOR SURFACE IMPEDENCE BY USING A PARALLEL PLATES OPEN CAVITY RESONATOR EXCITED BY DIELECTRIC ROD  $HE_{11}$ -MODE - F. Fujisawa, Y Yamamoto and F. Okuda, Dept of Elec Engr and Electron, Faculty of Engr, Osaka Sangyo Univ, Osaka 574, Japan
- W2.6** OPEN TUBE RESONATORS FOR MILLIMETER/SUBMILLIMETER-WAVE SURFACE RESISTIVITY MEASUREMENTS - P.P. Woskov, D.Y. Rhee and D.R. Cohn, MIT Plasma Fusion Center, Cambridge, MA 02139
- W2.7** MMW DETECTION BY SUPERCONDUCTING FILMS - APPLICATIONS OF HIGH TEMPERATURE SUPERCONDUCTING FILMS - Y.-Y. Jeong and K. Rose, Center for Integrated Electron, Rensselaer Polytechnic Inst, Troy, NY



---

---

## SESSION W3

---

---

Papio Room 3<sup>rd</sup> Floor

Wednesday AM

December 7, 1988

---

### SubMM DETECTORS

---

B. J. Clifton, Presider

---

- W3.1** A FAST, WIDE-SPECTRAL RANGE PHOTOCONDUCTIVITY FIR-DETECTOR SYSTEM - M. von Ortenberg and J. Geiger, Physikalisches Institut der Universitaet Wuerzburg, D-8700 Wuerzburg, F.R. Germany
- W3.2** HIGH DYNAMIC RANGE INFRARED DETECTORS - A.G.U. Perera and D.D. Coon, U of Pittsburgh, Pittsburgh, PA
- W3.3** PYROELECTRIC INFRARED DETECTORS FOR PRECISION EARTH SENSOR - K. Nakamura, T. Ishigaki, A. Kaneko, S. Takahashi, J. Nishida, Matsushita Research I Tokyo, Inc., R&D Project Teams, 3-10 1 Higashimita Tama-ku Kawasaki-Shi, Japan 214; Y. Wakabayashi and H. Nakamura, National Space Devl'mt Agency of Japan, Tsukuba Space Center, 2-1-1 Sengen Tsukuba-Shi Ibaraki, Japan 305
- W3.4** THE DEPENDENCE OF GaAs SCHOTTKY DIODE NOISE ON DRY ETCHING DAMAGE - T. Suzuki, T. Iinuma and K. Mizuno, Research I Electrical Communication, Tohoku U, Sendai 980, Japan
- W3.5** MINIMIZATION OF HEATING EFFECTS OF A MECHANICALLY STABLE MOM POINT CONTACT DIODE FOR HIGH POWER CO<sub>2</sub> LASER DETECTION - C. Yu and S. Tan, Dept of Electrical Engineering, North Carolina A&T State University, Greensboro, NC 27411
- W3.6** CHARACTERISTICS OF A SCHOTTKY BARRIER DIODE MIXER WITH CONICAL HORN ANTENNA FOR SUBMILLIMETER WAVELENGTHS - H. Nett, Max-Planck-Institut für Radioastronomie, Auf dem Hügel 69, 5300 Bonn 1, West Germany; and B.J. Clifton, M.I.T. Lincoln Laboratory, P.O. Box 73, Lexington, MA 02173
- W3.7** CONVERSION LOSS AND NOISE FIGURE THEORETICAL ESTIMATION OF A SINLE MIM DIODE SUBMILLIMETER MIXER - W.N.A. Pereira, Instituto Militar de Engenharia, Rio de Janeiro, Brazil; and M. Pyee, ENSAE, 10, Av E.Belin - 31055 Toulouse Cedex, France
- W3.8** ADIABATIC DEMAGNETIZATION COOLER FOR FAR INFRARED DETECTOR - A. Sato, T. Yazawa, Toshiba Research and Development Center, Ukishima, Kawasaki, Japan; J. Yamamoto, Low Temperature Center, Osaka University, Suita, Osaka, Japan
- W3.9** THE STUDY OF ANTIREFLECTION DIELECTRIC FILM MATERIAL ON MERCURY CADMIUM TELLURIDE ir DETECTOR SURFACE - Shu Yuwen and Luo Yuanhai, North China Research Institute of Electro-Optics, P.O. Box 8511, Beijing, China
- W3.10** ON THE WORK MECHANISM OF MIM POINT CONTACT DIODE - G. Carelli, N. Ioli, A. Moretti, D. Pereira, M. Prevedelli, F. Strumia, Dept di Fisica, Univ di Pisa-Italy; M. Inguscio, Univ di Napoli, Italy

---

---

## SESSION W4

---

---

Ballroom (Makai), 7<sup>th</sup> Floor

Wednesday AM

December 7, 1988

---

### GYROTRON II

---

T.V. George, Presider

---

- W4.1** MODE CAPTURE EXPERIMENTS ON THE 150 GHz GYROTRON - (Invited Keynote) - KfK Gyrotron Team, presented by G. Hochschild, Kernforschungszentrum Karlsruhe, Institut für Technische Physik, Postfach 3640, D-7500 Karlsruhe, Fed Rep Germany
- W4.2** PRELIMINARY RESULTS FROM THE UNIVERSITY OF MARYLAND X-BAND GYROKLYSTRON - W. Lawson, J. Calame, D. Welsh, M. Skopec, B. Hogan, M. Naimann, J. Renbaum, and M.E. Read\*, Lab for Plasma Research, U of Maryland, College Park, MD 20742; \*Physical Sciences, Inc., Alexandria, VA 22314
- W4.3** MODE INTERACTION IN A PRIMED GYROTRON - A.H. McCurdy, Omega-P Inc., 2008 Yale Station, New Haven, CT 06520; C.M. Armstrong, Code 6842, Naval Research Lab, Washington, DC 20375-5000
- W4.4** 85 GHz TE<sub>1,3</sub> PHASE-LOCKED GYROKLYSTRON OSCILLATOR EXPERIMENT - J.M. Burke\*, M.A. Czarnaski\*\*, R.P. Fischer\*\*, M. Giangrave, A.W. Fliflet and W.M. Manheimer, Plasma Physics Div, Naval Research Lab, Washington, DC 20375-5000; \*Burke Technologies, Inc., San Diego, CA 92111; \*\*Jaycor, Inc., Vienna, VA 22180
- W4.5** FEASIBILITY OF 30 GHz GYROKLYSTRON AMPLIFIERS FOR DRIVING LINEAR SUPERCOLLIDERS - V.L. Granatstein, W. Lawson and P.E. Latham, Lab for Plasma Research, U of Maryland, College Park, MD 20742
- W4.6** AC SPACE CHARGE IN MODERATELY RELATIVISTIC GYROTRONS - P.E. Latham and T.M. Antonsen, Jr., Lab for Plasma Research, U of Maryland, College Park, MD 20742
- W4.7** THE THEORY OF LARGE-ORBIT GYRO-KLYSTRON WITH INCLUSION OF SPACE CHARGE EFFECT - H-B. Jiang and S. Yu, High Energy Electronics Research Institute, Chengdu I of Radio Engr, Chengdu, Sichuan, P.R.China
- W4.8** CALCULATION OF LIMITING CURRENT IN CONNECTION WITH APPLICATION TO GYROTRON - H.S. Uhm and C. Grebogi, Naval Surface Warfare Center, White Oak, Silver Spring, MD 20903-5000

---

---

## SESSION W5

---

---

Ballroom, 7<sup>th</sup> Floor

Wednesday PM

December 7, 1988

---

### GUIDED PROPAGATION II

---

Y. Kobayashi, Presider

- W5.1** NONRADIATIVE SYMMETRICAL DIELECTRIC GRATING WAVEGUIDE FOR MMW DBR GUNN OSCILLATORS - Z.-W. Li, Dept of Radio Engr, Southeast U, Nanjing, Jiangsu, P.R.China
- W5.2** NUMERICAL RESULTS ON DIELECTRIC RESONATORS INSIDE WAVEGUIDES - A. Jöstingmeier and A.S. Omar, Technische U, Hamburg-Harburg, Hamburg 90 FRG
- W5.3** NON-LINEAR TLM MODELLING OF HIGH-FREQUENCY VARIATOR MULTIPLIERS AND HALVERS - S. Kosmopoulos and W.J.R. Hoefer, U of Ottawa, Ottawa, Canada; A. Gagnon, Telemus Inc., Nepean, Ont. Canada
- W5.4** NUMERICAL MODELING OF GENERALIZED MILLIMETER-WAVE TRANSMISSION MEDIA WITH FINITE ELEMENT AND TRANSMISSION LINE MATRIX METHODS - Eswarappa, G. Costache, W. Hoefer, U of Ottawa, Ottawa, Ont. Canada
- W5.5** POLARIZATION CONVERSIONS IN DIELECTRIC STRIP WAVEGUIDES - Z.M. Lu, S.L. Wang, S.T. Peng, New York I of Tech, Old Westbury, NY; H. Jenkinson, US Army Armament Res, Devlmt & Engr Ctr, Picatinny, NJ 07806
- W5.6** THE SOLUTION OF END EFFECTS OF SLOT LINE BY OPEN CAVITY METHOD - Y. Chen, Southeast, Nanjing, PRC
- W5.7** SPECIALLY CONFIGURED ULTRA-LOW-LOSS DIELECTRIC WAVEGUIDES FOR MM/Sub-MM WAVES - C. Yeh, UCLA, Los Angeles, CA; F. Shinabukuro, Aerospace Corp, Los Angeles, CA
- W5.8** ANALYSIS OF MICROSTRIP LINES ON FERRITE AND ANISOTROPIC DIELECTRIC SUBSTRATES - M.R.M.L. Albuquerque, A.G. D'Assuncao, M.R.G. Maia, UFRN-Natal, RN, Brazil; A.J. Giarola, State U of Campinas, Campinas, Brazil
- W5.9** ANALYSIS OF FINLINES ON BIAXIAL ANISOTROPIC DIELECTRIC - F.D.A.F. Tejo, UFPB-DEE-C.P. Campina Grande; A.G. D'Assuncao, UFRN-DEE-Natal; A.J. Giarola, UNICAMP-FEE-DMO-Campinas, Brazil
- W5.10** SINGLE MODE PROPAGATION IN MAGNETOOPTICAL WAVE GUIDES - J.H. Marco, L. Grau, F. Canal, Univ. Politecnica de Catalunya, Barcelona, Spain

---

---

## SESSION W6

---

---

Mahimahi Room, 3<sup>rd</sup> Floor

Wednesday PM

December 7, 1988

---

### HIGH T<sub>c</sub> SUPERCONDUCTORS II

---

A.J. Sievers, Presider

- W6.1** MAKING SENSE OF SUPERCONDUCTING INFRARED SENSORS - (Invited Keynote, 40 min) - S. Wolf, Naval Research Lab, Washington, DC
- W6.2** FAR-IR REFLECTIVITY AND MAGNETIC FIELD DEPENDENCE OF HIGH T<sub>c</sub> SUPERCONDUCTORS - M.N. Afsar and H. Chi, Tufts Univ, EE Dept, Medford, MA 02155
- W6.3** FAR INFRARED REFLECTIVITY OF CERAMIC HIGH T<sub>c</sub> SUPERCONDUCTORS - K.F. Renk, W. Ose, J. Schützmann, T. Zetterer, H.H. Otto, J. Keller and K.F. Renk, Fakultät f Physik, Univ Regensburg, Regensburg, W. Germany; B. Roas and L. Schultz, Siemens AG, FRG
- W6.4** FAR INFRARED OPTICAL PROPERTIES OF HIGH T<sub>c</sub> SUPERCONDUCTORS - S. Onari, T. Hiroaki, A. Oro, S. Hidaka and T. Arai, Inst of Applied Physics, Univ of Tsukuba, Tsukuba, Ibaraki 305, Japan
- W6.5** FAR INFRARED PHOTORESPONSE OF GRANULAR SUPERCONDUCTING FILMS - U. Strom and S.A. Wolf, NRL, Washington, DC; S. Perkowitz and G.L. Carr, Emory Univ, Atlanta, GA
- W6.6** MICROWAVE CHARACTERISTICS OF BULK AND POWDERED HIGH T<sub>c</sub> SUPERCONDUCTORS - A. Meulenbergh, H.-L. Hung, and G. Tough, COMSAT Labs, Clarksburg, MD 20871
- W6.7** RF MEASUREMENTS OF HIGH TEMPERATURE SUPERCONDUCTING MATERIAL - J. Chang, R.K. Pandey, M.K. Skrehot, M. Li, G.R. Gilbert, K.W. Goeking, B.L. Gries, D.L. Mabus J.C. McCleary, Dept of EE, Texas A&M Univ, College Station, TX 77843
- W6.8** FTIR ABSORBANCE STUDIES OF Cu-O BANDS OF YBa<sub>2</sub>Cu<sub>3</sub>O<sub>7</sub> IN SEMICONDUCTING AND SUPERCONDUCTING PHASE - M.M. Pradhan, R.K. Garg and M. Arrora, Natl Physical Lab, New Delhi 110012, India
- W6.9** PERMITTIVITY OF HIGH T<sub>c</sub> CERAMICS AT CENTIMETER AND MILLIMETER WAVELENGTHS - R.L. Moore and J.M. Bourgeois, GTRI, GA Inst Tech, Atlanta, GA 30332

---

---

## SESSION W7

---

---

Papio Room, 3<sup>rd</sup> Floor

Wednesday AM

December 7, 1988

---

### SubMM DEVICES

---

K. Mizuno, Presider

- W7.1** CHARACTERISTICS AND PERFORMANCE OF THE NATIONAL SYNCHROTRON LIGHT SOURCE INFRARED BEAMLINE - (Invited, 30 min.) - G. P. Williams, C. J. Hirschmugl, D.P. Sidons and E.A. Sullivan, Brookhaven Natl. Lab, Upton, NY 11973; K.D. Moeller, P. Petrone and E. Angelides, Fairleigh Dickinson Univ, Teaneck, NJ 07666; and Y.J. Chabal AT&T Bell Labs, Murray Hill, NJ 07974; F.M. Hoffman, Exxon Research Labs, Annandale, NJ 08801
- W7.2** OPTICALLY-PUMPED NH<sub>3</sub> LASERS - A VERY STABLE FREQUENCY SOURCE - J. Reid and K.J. Siemsen, McMaster U and Natl Research Council of Canada
- W7.3** PRESSURE EFFECTS ON THE FREQUENCY OF OPFIR LASERS - R.L. Crownover and F.C. DeLucia, Duke University; D.D. Skatrud, Army Research Office, P.O. Box 12211, Research Triangle Park, NC 27709-2211
- W7.4** TUNABLE 690 GHz SIXTUPLER WITH FUNDAMENTAL GUNN-OSCILLATOR - R. Rüdiger and P. Zimmermann, Radiometer-physics, Bergerwiesenstr. 15, 5309 Meckenheim, West Germany
- W7.5** LASER RADAR RANGE IMPROVED OPTIMIZATION FOR DETECTING AND TRACKING AIRBORNE COOPERATIVE TARGETS - J. Gavan, Center for Technological Education Holon, P.O.B. 305, Holon 58102, Israel; A. Korman, Techno Science Ltd, P.O.B. 1784, Ramat Gan, Israel
- W7.6** INITIAL ATTEMPTS TO OBSERVE LONG WAVELENGTH PHASE CONJUGATION IN AN ARTIFICIAL KERR MEDIUM - P.A. Krug, School of Physics, U of Sydney, NSW 2006, Australia; D.K. Mansfield, Plasma Physics Lab, Princeton Univ, Princeton, NJ 98544
- W7.7** SUBMILLIMETER WAVE LOW TEMPERATURE ADMITTANCE OF N-GaAs AND InP DIODE STRUCTURES USING TRANSPORT ANALYSIS - C.M. Krowne, Electronics Science and Tech Div, Naval Research Lab, Washington, DC 20375-5000
- W7.8** ANALYSIS OF SCATTERING FROM OIL FILM ON SEA SURFACE WITH MODEL OF STRATIFIED MEDIUM WITH SLIGHTLY ROUGH INTERFACES - Shanjia Xu and Liguao Sun, Dept of Radio and Elec, U of Science and Tech of China, Hefei, Anui 230029, P.R.China
- W7.9** MICROFABRICATED SUBMILLIMETER BWO EXPERIMENTS - L.R. Barnett, J.M. Baird, R.W. Grow, Dept of Elec Engr, U of Utah, Salt Lake, UT 84112
- W7.10** STUDY OF OPTICAL OUTPUT COUPLERS FOR SUBMILLIMETER WAVELENGTH BACKWARD-WAVE OSCILLATORS (BWO's) - J.D. Cook, Dept of Physics, Eastern Kentucky U, Richmond, KY 40474; N. Stankiewicz, NASA/Lewis Research Ctr, Cleveland, OH 44135

---

---

## SESSION W8

---

---

Ballroom (Makai), 7<sup>th</sup> Floor

Wednesday PM

December 7, 1988

---

### GYROTRON III

---

J.M. Baird, Presider

- W8.1** OPERATION AND PROSPECTS OF HIGH-POWER, HIGH-FREQUENCY QUASI-OPTICAL GYROTRONS - (Invited Keynote) - CRPP and ABB Quasi-Optical Gyrotron Development Group, presented by M.Q. Tran, CRPP, Lausanne, Switzerland
- W8.2** OPERATION OF A QUASI-OPTICAL GYROTRON WITH VARIABLE OUTPUT COUPLING - A.W. Fliflet, T.A. Hargreaves\*, W.M. Manheimer, R.P. Fischer\*\*, and M.L. Barsanti\*\*, NRL, Washington, DC 20375-5000
- W8.3** NONLINEAR THEORY OF A QUASI-OPTICAL GYROTRON WITH AN ELECTRON BEAM AT AN OBLIQUE ANGLE - C.Y. Wang\*, K.E. Kreischer, R.J. Temkin, MIT Plasma Fusion Center NW16, 167 Albany St, Cambridge, MA 02139;
- W8.4** 120 GHz AXISYMMETRIC QUASI-OPTICAL GYROTRON - Y. Itoh, M. Komuro, K. Hayashi and T. Sugawara, Toshiba Corp., 4-1, Ukishimacho, Kawasaki-ku, Kawasaki 210 Japan
- W8.5** DESIGN OF A QUASI-OPTICAL GYROTRON WITH A SHEET ELECTRON BEAM - M.E. Read and A.J. Dudas, Physical Sciences, Alexandria, VA; J. Petillo and A. Drobot, Science Applications Int'l Corp, McLean, VA
- W8.6** MODE STABILITY IN A QUASI-OPTICAL GYROTRON - W.M. Manheimer, NRL, Washington, DC; T.M. Antonsen and B. Levush, U of Maryland, College Park, MD
- W8.7** MODE COMPETITION IN QUASI-OPTICAL GYROTRONS - S. Riyopoulos, Science Applications Int'l Corp, McLean, VA; W.M. Manheimer and A. Fliflet, NRL, Washington, DC
- W8.8** FREQUENCY STEP-TUNABLE GYROTRON - O. Dumbrajs, Arbeitsbereich Hochfrequenztechnik, Technische U, Hamburg-Harburg, D-2000 Hamburg 90, FRG, B. Piosczyk, Kernforschungszentrum Karlsruhe, I fur Technische Physik, Karlsruhe FRG
- W8.9** SIMULATION OF THE ELECTROSTATIC CYCLOTRON INSTABILITY ON AN ANNULAR ELECTRON BEAM - F.S. Kuo, Dept of Physics, Nat'l Central U, Chung-Li Taiwan, P.R. China; J.J. Su, Dept of Physics, Los Angeles, CA; K.R. Chu, Physics Dept, Nat'l Tsing Hua U, Hsinchu, Taiwan ROC

---

---

## SESSION Th1

---

---

---

Ballroom (Mauka), 7<sup>th</sup> Floor

---

Thursday AM                      December 8, 1988

---

### INTEGRATED CIRCUITS I

---

C. Seashore, Presider

---

- Th1.1** MILLIMETRE-WAVE MONOLITHIC AND HYBRID INTEGRATED CIRCUIT TECHNOLOGY - (*Invited Keynote*) - J.W. Archer, CSIRO, Epping NSW 2121, Australia
- Th1.2** AN EFFECTIVE MODEL OF E-PLANE METAL SEPTUM FOR MILLIMETER WAVE INTEGRATED CIRCUIT DESIGN - J. Hong, 98 Market Road, Gu Lang Yi, Xiamen, Fujian, P.R.China
- Th1.3** BROADBAND PHASE MODULATORS IN INTEGRATED FIN-LINE TECHNIQUE FOR MILLIMETRE-WAVE APPLICATIONS - E. Kpodzo, Bell-Northern Research, P.O. Box 3511, Station C, Ottawa, Canada K1Y 4H7
- Th1.4** GaAs TRAVELLING WAVE SCHOTTKY CONTACT COPLANAR WAVEGUIDE WITH APPLICATIONS TO MIMIC - D.R. Singh, Honeywell, MN38-3300, 10400 Yellow Circle Dr, Minnetonka, MN 55434; K.S. Champlin, Dept Elec Engr, U of Minnesota, Minneapolis, MN 55454
- Th1.5** OPTIMAL DESIGN OF MILLIMETER WAVE INTEGRATED E-PLANE DIPLEXERS - J. Hong and J. Shi, Dept of Radio Engr, Fuzhou Univ, Fujian, P.R.China
- Th1.6** INTEGRATED CIRCUIT ACTIVE ARRAYS AND SPATIAL POWER COMBINERS USING APERTURE COUPLED PATCH ANTENNAS - K. Chang, K.A. Hummer and J.L. Klein, Dept of Elec Engr, Texas A&M Univ, College Station, TX 77843-3128
- Th1.7** UNIVERSAL TEST FIXTURE FOR MONOLITHIC MM-WAVE INTEGRATED CIRCUITS USING A NOVEL DEEMBEDDING PROCEDURE - R.R. Romanofsky and K.A. Shalkhauser, NASA Lewis Research Center, Cleveland, Ohio 44135
- Th1.8** ON THE MEASUREMENT OF MM-WAVE PROPAGATION CHARACTERISTICS OF GaAs MICROSTRIP LINES - R.R. Romanofsky, K.L. Adaway, and K.B. Bhasin, NASA Lewis Research, Cleveland, Ohio 44135
- Th2.1** INTERNATIONAL SAMPLE EXCHANGE FOR THE COMPARISON OF NEAR-MILLIMETER WAVE CHARACTERIZATIONS OF MATERIALS - (*Invited Keynote, 40 min*) - G.J. Simonis and J.R. Birch\*, Harry Diamond Labs, Adelphi, MD; \*Nat'l Physical Lab, Div of Elec Science, Middlesex, U.K.
- Th2.2** SOLID STATE SPECTROSCOPY IN FAR IR AND MM WAVES REGIONS BY SYNCHROTRON RADIATION - (*Invited Keynote, 40 min*) - T. Nanba, Dept of Physics, Tohoku U, Sendai 980, Japan
- Th2.3** MILLIMETER WAVE MEASUREMENT OF COMPLEX PERMITTIVITY BY IMPROVED DIELECTRIC DISK RESONATOR METHOD - Y. Kobayashi and J. Sato, Dept Elec Engr, Saitama U, Urawa, Saitama 338, Japan
- Th2.4** NEAR MMW DIELECTRIC MEASUREMENTS BY MEANS OF A NON-DISPERSIVE FOURIER TRANSFORM SPECTROMETER OPTIMIZED BELOW 15cm<sup>-1</sup> REGION - K. Sakai, T. Nakano and Y. Ichioka; Dept Applied Physics, Osaka U, Suita, Osaka 565, Japan; H. Matsuo and K. Kawahata, Nagoya U, Chikusa, Nagoya 464, Japan
- Th2.5** THE MARPLE ALGORITHM FOR THE AUTOREGRESSIVE SPECTRAL ESTIMATES OF SMMW FOURIER TRANSFORM SPECTROSCOPY DATA - G. Zhang and G. Zhou, Elec Dept, Zhongshan U, Guangzhou, P.R.C.
- Th2.6** SOME NEW PROPERTIES OF LOADED RESONATORS - L.F. Libelo and G.E. Pisane, Harry Diamond Labs, Adelphi, MD
- Th2.7** NEAR-MILLIMETER WAVELENGTH MEASUREMENTS OF COMPLEX INDEX VALUES OF SEVERAL POLYMER MATERIALS - G.J. Simonis and M. Stead, Harry Diamond Labs, Adelphi, MD
- Th2.8** THEORY AND PRACTICE IN OPEN RESONATOR MEASUREMENTS OF MULTI-LAYER SAMPLES - T. Weils, GTRI, GA Inst Tech, Atlanta, GA
- Th2.9** DIELECTRIC PROPERTIES OF COMPOSITE STRIPLINE/RADOME MAT'LS - R.L. Moore and A. MacDonald, GTRI, GA Inst Tech, Atlanta, GA

---

---

## SESSION Th2

---

---

---

Mahimahi Room, 3<sup>rd</sup> Floor

---

Thursday AM                      December 8, 1988

---

### NEAR MMW MEASUREMENTS & TECHNIQUES

---

T. Matsui, Presider

---

---

---

### SESSION Th3

---

---

---

Papio Room, 3<sup>rd</sup> Floor

---

Thursday AM                      December 8, 1988

---

#### LASERS I

---

K. M. Evenson, Presider

---

- Th3.1 PHYSICAL PROCESSES AND DEVELOPMENT OPPORTUNITIES IN FAR-INFRARED LASERS - *(Invited Keynote)* Frank C. LeDucia, Duke University, Durham, NC 27706
- Th3.2 WIDE-BAND GERMANIUM LASERS IN THE RANGE FROM FAR-INFRARED TO MILLIMETER WAVES - *(Invited Keynote)* S. Komiyama, Dept of Pure and Applied Sciences, University of Tokyo, Kamaba, Tokyo 153, JAPAN
- Th3.3 OPTICALLY PUMPED MID-INFRARED NH<sub>3</sub> LASERS - *(Invited Keynote)* J. Reid, Lumonics Inc., Kanata, Ontario, CANADA K2K 1Y3
- Th3.4 <sup>15</sup>NH<sub>3</sub> RAMAN FIR LASER - W. Zhu and J.R. Izatt, Dept of Physics and Astronomy, University of Alabama, Tuscaloosa, AL 35487
- Th3.5 SUBMILLIMETER-WAVE LASER PUMPED BY AN EMQ-SWITCHED CO<sub>2</sub> LASER - H. Shirai, J. Bae, T. Nishida, K. Mizuno, Research Institute of Electrical Communication, Tohoku University, Sendai 980, JAPAN
- Th3.6 LINEWIDTH AND POLARIZATION OF AN OPTICALLY-PUMPED GAAS SURFACE-EMITTING LASER WITH INTEGRATED BRAGG REFLECTORS - J. Faist, F. Morier-Genoud, D. Martin, M.A. Dupertuis, J.D. Ganiere, F.K. Reinhart, Inst. Optoelectronics, PHB-Ecublens, CH-1015, Lausanne, Switzerland

---

---

### SESSION Th4

---

---

---

Ballroom (Makai), 7<sup>th</sup> Floor

---

Thursday AM                      December 8, 1988

---

#### GYROTRON IV

---

N.C. Luhmann, Presider

---

- Th4.1 MILLIMETER WAVE CARM AMPLIFIER EXPERIMENT - *(Invited Keynote)* - B.G. Danly, K.D. Pendergast and R.J. Temkin, MIT Plasma Fusion Center, Cambridge, MA 02139
- Th4.2 DESIGN AND ANALYSIS OF A 1 GIGAWATT 250 GHz CARM AMPLIFIER USING AN INDUCTION LINAC - M. Caplan and J.K. Boyd, Lawrence Livermore Nat'l Lab, P.O. Box 808, Livermore, CA
- Th4.3 THE NRL 100 GHz COLD-CATHODE CARM - R.B. McCowan, C.A. Sullivan, A.W. Fliflet, D.A. Kirkpatrick, Science Applications Int'l Corp, McLean, VA 22101; W.M. Manheimer, S.H. Gold, W.M. Manheimer, W.M. Black, A.K. Kinkead and M. Sucey, Code 4740, Plasma Physics Div, Naval Research Lab, Washington, DC 20375
- Th4.4 CYCLOTRON AUTORESONANCE MASER (CARM) EC HEATING SOURCE FOR HIGH FIELD TOKAMAKS - Q.S. Wang, A.T. Lin, N.C. Luhmann, Jr. and D.B. McDermott, UCLA, Los Angeles, CA; K.R. Chu, Nat'l Tsing Hua U Taiwan, Rep of China
- Th4.5 OPTICAL GUIDING IN THE CYCLOTRON AUTORESONANCE MASER - R.G. Kieva and B. Levush, U of Maryland, College Park, MD 20742; P. Sprangle, Naval Research Lab, Washington, DC 20375
- Th4.6 INITIAL OPERATION OF A CHERENKOV CARM - H. Cao, D.B. McDermott and N.C. Luhmann, Jr., UCLA, Los Angeles, CA
- Th4.7 HIGH POWER, MULTI-CAVITY PHASE-LOCKED GYROTRON OSCILLATOR EXPERIMENT - S.H. Gold, A.W. Fliflet, W.M. Black, D.A. Kirkpatrick, SAIC, McLean, VA 22101; W.M. Manheimer, Plasma Physics Div, Naval Research Lab, Washington, DC 20375-5000

---

---

## SESSION Th5

---

---

---

Ballroom (Mauka), 7<sup>th</sup> Floor

---

Thursday PM

December 8, 1988

---

### INTEGRATED CIRCUITS II

---

W. Hoefer, Presider

---

- Th5.1 MMW MONOLITHIC INTEGRATED CIRCUITS: IMPLICATIONS AND APPLICATIONS - *(Invited Keynote)* - C.R. Seashore, Honeywell, Inc., 10400 Yellow Circle Dr, Minnetonka, MN 55343
- Th5.2 DOMINANT MODE PROPAGATION CHARACTERISTICS FOR DIELECTRIC TAPE IMAGE LINE - J.C. Wiltse, GTRI, Georgia Inst. Tech, Atlanta, GA 30332
- Th5.3 MONOLITHIC WATT-LEVEL MILLIMETER-WAVE BARRIER-INTRINSIC-N<sup>+</sup> (BIN) DIODE-GRID FREQUENCY TRIPLER ARRAY - R.J. Hwu, N.C. Luhmann, Jr., Dept of Elec Engr, U of CA, Los Angeles, CA 90024; D.B. Rutledge, CIT, Pasadena; D. Streit, T. O'Neill, TRW, Redondo Beach, CA; B. Hancock, U. Lieneweg, JPL, Pasadena, CA
- Th5.4 ANALYSIS OF A NOVEL MONOLITHIC GaAs MIS PHASE SHIFTER - M.E. McCaughan and F.C. Jain, U of Connecticut, Dept Elec and Systems Engr, U-157, Room 312, 260 Glenbrook Rd, Storrs, CT 06268
- Th5.5 MILLIMETER-WAVE MMIC PACKAGING DESIGN - M.J. Gawronski, J.R. Lamberg, D.R. Singh, Honeywell Inc, 10400 Yellow Circle Dr, Minnetonka, MN 55343
- Th5.6 SCATTERING OF PLANE WAVE BY MICROSTRIP LINES - S.T. Peng, NY Inst of Technology, Old Westbury, NY 11568; R.T. Kinasewitz, US Army Armament Research, Dev't and Engr Ctr, Picatinny, NJ 07806-5000
- Th5.7 FINLINE-DISPLACEMENT ISOLATOR - THE THEORETICAL AND EXPERIMENTAL INVESTIGATION - J. Huang and Q. Yang, Dept of Radio Engr, Southeast University, Nanjing, China
- Th5.8 DESIGN AND PERFORMANCE OF 20 AND 45 GHz MMIC LANGE COUPLERS - J.E. Wallace and G.A. Ellis, Boeing Electronics Company, High Tech Center, P.O. Box 24969, M/S 7J-65, Seattle, WA 98124

---

---

## SESSION Th6

---

---

---

Mahimahi Room, 3<sup>rd</sup> Floor

---

Thursday PM

December 8, 1988

---

### MATERIALS CHARACTERIZATION

---

G. J. Simonis, Presider

---

- Th6.1 FAR-INFRARED AND SURFACE LAYERS - *(Invited Keynote, 40 min)* - A. Hadni and X. Gerbaux, U of Nancy 1, Nancy, France
- Th6.2 CHARACTERIZATION OF THE INFRARED AND FAR-INFRARED PROPERTIES OF SAPPHIRE AND QUARTZ - M.E. Thomas and R.I. Joseph, The John Hopkins U, Applied Physics Lab, Laurel, MD 20707; G.J. Simonis and M. Stead, LABCOM Harry Diamond Labs, Adelphi, MD 20783
- Th6.3 SOFT MODE SPECTROSCOPIC STUDY OF FERROELECTRIC PHASE TRANSITION IN Li<sub>2</sub>Ge<sub>2</sub>O<sub>15</sub> - M. Wada, A. Sawada\*, and Y. Ishibashi\*, Dept of Physics, Faculty of Liberal Arts, Shinshu U, Matsumoto 390, Japan; \*Synthetic Crystals Res Lab, Faculty of Engr, Nagoya U, Nagoya 464, Japan
- Th6.4 FAR IR TRANSMISSION SPECTRA OF ROCHELLE SALT AT 5K - X. Gerbaux and A. Hadni, U of Nancy 1, Nancy, France
- Th6.5 MEASUREMENT OF THE SPECTRAL THERMAL EMISSION FROM TECHNICAL INFRARED RADIATORS - A. Leupin, H. Vetsch and F.K. Kneubühl, Infrared Physics Lab, ETH, Aarich, Switzerland
- Th6.6 THE RELATION BETWEEN IR AND VIS SPECTRAL PROPERTIES OF GLASSES AND THE ENERGY TRANSFER THROUGH WINDOWS - R. Furler, P. Williams and F.K. Kneubühl, ETH, Zurich, Switzerland
- Th6.7 EFFECT OF TEMPERATURE OF IR-ABSORPTION OF DIPHENYL - M.I. Nasser and M.A. Moharram, Physics Dept, Natl Research Ctr, Dokki, Cairo, Egypt
- Th6.8 MEASUREMENT OF THE DIELECTRIC CONSTANT OF FERROELECTRIC KH<sub>2</sub>PH<sub>4</sub> AT 35 GHz BY TRANSMISSION IN A WAVEGUIDE - M. Horioka, Dept Electronics, Kanazawa Inst Tech, Kanazawa 921, JAPAN
- Th6.9 TEMPERATURE INDEPENDENT PERMITTIVITIES IN COMPOSITES OF TWO OR MORE DIELECTRICS - R.L. Moore and J. Estrada, GTRI, Atlanta, GA

---

---

## SESSION Th7

---

---

---

Papio Room, 3<sup>rd</sup> Floor

---

Thursday PM                      December 8, 1988

---

### LASERS II

---

F. K. Kneubühl, Presider

---

- Th7.1 FAR-INFRARED LASER SPECTROSCOPY - *(Invited Keynote)* K. M. Evenson, National Bureau of Standards, Boulder, CO 80303
- Th7.2 SPECTROSCOPY AND FIR LASER EMISSION: PERISCOPE TO THE VIBRATIONAL WORLD OF METHANOL AND METHYLAMINE - *(Invited Keynote)* R. M. Lees, U of New Brunswick, Fredericton, NB, Canada E3B 5A3
- Th7.3 TEMPERATURE AND PRESSURE DEPENDENCE OF CH<sub>3</sub>F RAMAN FIR LASER EMISSION - Yu Guan and J. R. Izatt, Dept of Physics and Astronomy, U of Alabama, Tuscaloosa, AL 35487
- Th7.4 HOMOGENEOUS LINEWIDTHS AND LEVEL-CROSSING SIGNALS OF SOME PUMP TRANSITIONS OF <sup>12</sup>CH<sub>3</sub>OH cw LASER LINES - N. Sokabe, K. Matsushima and A. Murai, Dept of Applied Physics, Osaka City University, Osaka, Japan
- Th7.5 IR SPECTRA AND FIR LASER ASSIGNMENTS FOR 0-18 METHANOL - R.M. Lees, W. Lewis-Bevan, J.W.C. Johns and D.P. Donovan, Physics Department, U of New Brunswick, Box 4400, Fredericton, NB, Canada E3B 5A3
- Th7.6 FIR LASER ASSIGNMENTS FOR METHYLAMINE - R.M. Lees, Physics Department, U of New Brunswick, Box 4400, Fredericton, NB Canada E3B 5A3; W. Lewis-Bevan, So. Illinois Univ, Carbondale, IL 62901
- Th7.7 DETERMINISTIC CHAOS IN OPTICALLY PUMPED FAR-INFRARED RAMAN LASERS - S. Rai and J.R. Izatt, Dept Physics, U of Alabama, Tuscaloosa, AL 35487; J. Rai and C. M. Bowden, Research Directorate Research, Development, and Engineering Ctr., U.S. Army Missile Command, Redstone Arsenal, AL 35898-5248

---

---

## SESSION Th8

---

---

---

Ballroom (Makai), 7<sup>th</sup> Floor

---

Thursday PM                      December 8, 1988

---

### GYROTRON V

---

R.J. Barker, Presider

---

- Th8.1 EXPERIMENTAL RESULTS ON RELATIVISTIC GYRO-DEVICES - R. McCowan, S. Gold, W.M. Black and W.M. Manheimer, Plasma Physics Div, Naval Research Lab, Washington, DC 20375-5000
- Th8.2 INTENSE ELECTRON BEAM CYCLOTRON MASERS WITH MICROSECOND PULSELENGTHS - R.M. Gilgenbach, J.G. Wang, J.J. Choi, C. Outten and T. Spencer, Intense Energy Beam Interaction Lab, Nuclear Engr Dept, The U of Michigan, Ann Arbor, MI 48109-2104
- Th8.3 EXPERIMENTAL INVESTIGATION OF THE EFFECTS OF A NEUTRALIZING BACKGROUND PLASMA ON THE OPERATION OF A HIGH CURRENT GYROTRON - D.A. Kirkpatrick\*, S.H. Gold, A.K. Kinkad, W.M. Manheimer, C.A. Sullivan\*, Plasma Physics Div, Naval Research Lab, Washington, DC 20375-5000; \*Science Applications Int'l Corp, McLean, VA 22102
- Th8.4 DESIGN OF A 1 MW GYRO-TWT - C.S. Kou, D.B. McDermott, C.K. Chong and N.C. Luhmann, Jr., UCLA, Los Angeles, CA
- Th8.5 EFFICIENCY ENHANCEMENT IN GYRO-BWO BY TAPERED MAGNETIC FIELD - A.K. Ganguly and S. Ahn, US Naval Research Lab, Washington, DC 20375-5000
- Th8.6 OPERATION OF A 140 GHz TUNABLE BACKWARD-WAVE GYROTRON OSCILLATOR - W.C. Guss, K. Kreischer, R. Temkin, MIT Plasma Fusion Center NW16, Cambridge, MA 02139; M. Caplan, Lawrence Livermore Nat'l Lab, P.O. Box 808, Livermore, CA; D. Pirkle, Varian Associates, 611 Hansen Way, Palo Alto, CA
- Th8.7 A GYROTRON TWT AMPLIFIER EXPERIMENT DESIGNED FOR HIGH STABILITY - L.R. Barnett, K.R. Chu, C.C. Tu, L.H. Chang and H.N. Liu, Dept of Physics, National Tsing Hua U, Hsinchu, Taiwan 30043, Rep of China
- Th8.8 AN EXPERIMENTAL SIXTEENTH HARMONIC CUSPTRON DEVICE - S.P. Kuo, K.K. Tiong, and P.E. Miller, Polytechnic U, Farmingdale, NY 11735
- Th8.9 RESONATOR WITH A CURVED WALL FOR A GYROTRON - O. Dumbrajs, Arbeitsbereich Hochfrequenztechnik, Technische U, Hamburg-Harburg, D-2000 Hamburg 90, FRG; H. Wenzelburger, Kernforschungszentrum Karlsruhe, I für Datenverarbeitung in der Technik, Karlsruhe, FRG

---

---

## SESSION F1

---

---

Ahi Room, 3<sup>rd</sup> Floor

Friday AM

December 9, 1988

---

### MMW DEVICES I

---

K. Chang, Presider

- F1.1** MODULATION OF INTENSE RELATIVISTIC ELECTRON BEAMS FOR HIGH POWER MICRO- AND MILLIMETER WAVE GENERATION - THEORY AND SIMULATION - J. Krall, Science Applications Intl. Corp, McLean, VA; Y.Y. Lau, M. Friedman and V. Serlin, NRL, Washington, DC
- F1.2** MILLIMETER-WAVE SUSPENDED PARALLEL-COUPLED FILTERS AT Ka AND W-BAND - T.C.-C. Ho and K. Chou, Chung Shan I of Science, Lung-Tan, Taiwan, ROC
- F1.3** THE PRINTED-CIRCUIT RAT-RACE-TYPE DIRECTIONAL COUPLER FOR LARGER POWER-SPLIT RATIO - I. Ohta, I. Hagino, and T. Kaneko, Faculty of Engr, Himeji I of Tech, 2167 Shosha, Himeji-shi, 671-22, Japan
- F1.4** CIRCULATOR USING GaAs DUAL-GATE FET - S. Toyoda, Dept Elec Engr, Osaka I of Tech, Osaka, Japan
- F1.5** AN EXPERIMENTAL STUDY OF JOSEPHSON EFFECT IN BULK YBaCuO - S.Z. Cai, Y.S. Hou and E.X. Yu, E.E. Dept, Fudan Univ, Shanghai, P.R.China
- F1.6** A SIMPLE AND LOW COST 3-PROBE MEASUREMENT TECHNIQUE USING MICROSTRIP CIRCUITS - K. Chang, M. Li and T. Sauter, Dept Elec Engr, Texas A&M Univ, College Station, TX
- F1.7** EXPERIMENTAL RESULTS OF A HIGH Q QUASI-OPTICAL REFLECTION CAVITY - K.A. Lee and M.A. Frerking, JPL, California I of Tech, Pasadena, CA 91109
- F1.8** CW DOPPLER SYSTEMS FOR EXTERNAL URODYNAMIC STUDY, COMPARISON BETWEEN ELECTROMAGNETIC WAVE AND AIRBORNE ULTRASOUND - Yasuhito Takeuchi, Yokogawa Medical Systems, Ltd., Tokyo, 190 Japan
- F1.9** DEVELOPMENT OF A BROADBAND 3-mm PHF H-PLANE WAVEGUIDE CIRCULATOR - D. Zhang and Z. Wu, Applied Phys. Inst, Box 83, Chengdu, Sichuan, P.R.China
- F1.10** DETERMINATION OF I-V CHARACTERISTICS OF NEGATIVE CONDUCTANCE DEVICES FROM MICROWAVE REFLECTION COEFFICIENTS - P. Huang, A. Botula, N.C. Luhmann, Jr, and D.S. Pan, UCLA, Los Angeles, CA 90024

---

---

## SESSION F2

---

---

Mahimahi Room, 3<sup>rd</sup> Floor

Friday AM

December 9, 1988

---

### SEMICONDUCTORS

---

M. von Ortenberg, Presider

- F2.1** SUBMILLIMETER WAVE EMISSION FROM SEMICONDUCTOR SUPERLATTICES - (*Invited Keynote, 40 min*) - M. Helm, E. Colas, P. England, F. DeRosa, S.J. Allen, Jr, Bell Communications Research, Red Bank, NJ 07701-7020
- F2.2** FAR-INFRARED NON-ASTIGMATIC CZERNY-TURNER MONOCHROMETER FOR STRESSED Ge:Ga PHOTOCONDUCTOR EXPERIMENTS - N. Hiromoto and T. Itabe, Communications Research Laboratory, Koganei, Tokyo 184, Japan; H. Takami, Nat'l Astron. Sci; H. Okuda, H. Matsuhara, H. Shibai and T. Nakagawa, I Space & Astron Sci., Japan
- F2.3** HIGH FREQUENCY SEMICONDUCTOR HETEROSTRUCTURE DEVICE ANALYSIS - C.M. Krowne and G.B. Tait, NRL, DC
- F2.4** FAR INFRARED ABSORPTION SPECTRA OF AMORPHOUS (As<sub>2</sub>S<sub>3</sub>)-(Sb<sub>2</sub>S<sub>3</sub>) SEMICONDUCTORS AND THE SPATIAL CHARGE FLUCTUATION - K. Matsushita, T. Anzaki, S. Onari and T. Arai, Inst of Applied Physics, U of Tsukuba, Tsukuba, Ibaraki 305, Japan
- F2.5** INFRARED ABSORPTION SPECTRUM OF Ge(Na) - L.T. Ho, Inst of Physics, Academia Sinica, Taipei, Taiwan, R.O.China
- F2.6** EFFECTS OF ANNEALING ON THE ELECTRICAL PROPERTIES OF Cd<sub>0.2</sub>Hg<sub>0.8</sub>Te GROWN BY LPE - I. Yasumura and K. Sato, Mitsubishi, Elec Corp, Amagasaki 661, Japan; Y. Yoshida and Y. Komine, Mitsubishi Elec Corp, Itami 664, Japan
- F2.7** MILLIMETER AND SUBMILLIMETER WAVE OPTICAL AND DIELECTRIC PROPERTIES OF SINGLE CRYSTAL HIGH PURITY SILICON - M.N. Afsar, Tufts U, Dept of EE, Medford, MA
- F2.8** INVESTIGATION OF ELECTRONIC SUB-BAND STRUCTURES IN PbTe/Pb<sub>1-x</sub>Sn<sub>x</sub> SUPERLATTICES BY SUB-MM MAGNETOABSORPTION SPECTRA - S. Shimomura, Y. Urakawa, S. Takaoka and K. Murase, Osaka U, Toyonaka 560, Japan
- F2.9** BAND EDGE STRUCTURE OF Pb<sub>1-x</sub>Sn<sub>x</sub>Te DOPED WITH INDIUM BY FAR-INFRARED MAGNETOPLASMA REFLECTION METHOD - S. Takaoka, S. Shimomura, H. Takahashi and K. Murase, Osaka U, Toyonaka 560, Japan
- F2.10** LOW FREQUENCY IMPURITY VIBRATION MODES IN II-VI SEMICONDUCTORS - W. Lu, H. Ye, W. Xu, S.C. Shen, and W. Giriat, Centra de Fisica, Caracas, Venezuela



---

---

## SESSION F3

---

---

---

Papio Room, 3<sup>rd</sup> Floor

---

Friday AM

December 9, 1988

---

### LASERS III

---

J. R. Izatt, Presider

---

- F3.1 NOVEL ASPECTS OF FAR-INFRARED GAS LASERS** (*Invited Keynote*) - F. K. Kneubühl, Infrared Physics Laboratory, ETH, 8093 Zurich, Switzerland
- F3.2 THEORY OF OPTICALLY PUMPED FAR INFRARED LASERS** (*Invited Keynote*) - Y. Lin, Zhongshan University, Quanzhou, P.R.China
- F3.3 LINE SELECTION IN OFF-RESONANTLY PUMPED SYSTEMS** (*Invited Keynote*) - M.A. Dupertuis, Swiss Federal Institute of Technology, Lausanne, Switzerland
- F3.4 THE INVERSE SMITH-PURCELL EFFECT AT SUBMILLIMETER WAVELENGTHS** - J. Bac, K. Furuya, H. Shirai, T. Nozokido, and K. Mizuno, Research Institute of Electrical Communication, Tohoku University, Sendai, 980 Japan
- F3.5 UNTUNED CAVITY RESONATOR FOR THE FAR INFRARED** - Hong Tang and J.R. Izatt, Dept of Physics and Astronomy, U of Alabama, Tuscaloosa, AL 35487
- F3.6 COPPER AND MOLYBDENUM MIRRORS FOR HIGH POWER TEA CO<sub>2</sub> LASER** - Y. Tsunawaki\*, K. Yoshida\*\*, K. Ohta\*\*\*, S. Aramaki\*\*\*, H. Okamoto\*\*\*, M. Yamanaka\*\* and S. Nakai\*\*, \*Dept of Elec Engr and Electronics, Osaka Industrial U, Nakagaito, Daito, Osaka 574, Japan; \*\*Institute of Laser Engineering, Osaka U, Yamada-oka, Suita, Osaka 565, Japan; \*\*\*Central Research Laboratory, Nippon Mining Company, Toda, Saitama 335, Japan
- F3.7 DOUBLE-GRATING 10-ATMOSPHERE CO<sub>2</sub>-TE LASER** - W. Zhu and J.R. Izatt, Dept of Physics and Astronomy, U of Alabama, Tuscaloosa, AL 35487
- F3.8 MICROWAVE AND MILLIMETER-WAVE SPECTRA OF <sup>13</sup>CD<sub>3</sub>OH** - K.V.L.N. Sastry, I. Mukhopadhyay, R.M. Lees, J. VanderLinde and D. Donovan, Dept of Physics, U of N.B., Fredericton, N.B. Canada

---

---

## SESSION F4

---

---

---

Ballroom (Makai), 7<sup>th</sup> Floor

---

Friday AM

December 9, 1988

---

### GYROTRON VI

---

M.Q. Tran, Presider

---

- F4.1 SOME PHYSICS ISSUES OF GYRO-TWT AND CARM AMPLIFIERS** - (*Invited Keynote*) - K.R. Chu, Nat'l Tsing Hua U, Hsinchu, Taiwan, ROC; A.T. Lin, N.C. Luhmann, UCLA, CA
- F4.2 LARGE SIGNAL OPERATION OF A TAPERED GYRO-TWT AMPLIFIER** - S.Y. Park\*, R.H. Kyser\*\*, C.M. Armstrong and R.K. Parker, NRL, Washington, DC; \*Omega-P, New Haven, CT; \*\*B-K Systems, Inc., Rockville, MD
- F4.3 HIGH CURRENT DENSITY CATHODES FOR MICROWAVE TUBES** - M.E. Read and A.J. Dudas, Physical Sciences, Alexandria, VA; P. Oettinger, Thermo Electron, Waltham, MA
- F4.4 A NON-ADIABATIC ELECTRON GUN FOR GYROTRONS** - B. Piosczyk, Kernforschungszentrum Karlsruhe, I fur Technische Physik, Postfach 3640, D-7500 Karlsruhe 1, Fed Rep Germany
- F4.5 FREQUENCY DOMAIN ANALYSIS OF A GYROTRON** - E. Jensen and K. Schünemann, Technische U Hamburg-Harburg, Postfach 90 14 03, D-2100 Hamburg 90, West Germany
- F4.6 EXPERIMENTS WITH A 35 GHz CYCLOTRON AUTORESONANCE MASER (CARM) AMPLIFIER** - G. Bekefi, A. DiRienzo, C. Leibovitch and B. Danly, MIT, Cambridge, MA
- F4.7 OPERATION OF HARMONIC GYROTRONS IN THE SUB-MILLIMETER REGION** - S. Spira, K.E. Kreischer and R.J. Temkin, MIT Plasma Fusion Center NW16, Cambridge, MA 02139
- F4.8 PARAMETER SPACE SEARCH FOR PENIOTRON MODES** - V. Ayres, J.Y. Choe, K. Boulais, and H.S. Uhm, Naval Surface Warfare Center, Silver Spring, MD; S. Ahn and A. Ganguly, NRL
- F4.9 NON-LINEAR ANALYSIS OF A GYRO-PENIOTRON OSC.** - P. Vitello, Science Applications Int'l, McLean, VA
- F4.10 PREBUNCHED HIGH HARMONIC GYROTRON** - C.S. Kou, D.B. McDermott and N.C. Luhmann, Jr., UCLA, CA
- F4.11 LINEAR ANALYSIS OF THE HIGH-POWER MAGNETRON** - R. Stark and H. Uhm, Silver Spring, MD

---

---

## SESSION F5

---

---

---

Ahi Room 3<sup>rd</sup> Floor

---

Friday PM

December 9, 1988

---

### MMW DEVICES II

---

(15 minute papers, 1300 hours)

---

M. Frerking, Presider

---

- F5.1** DIRECT PROBING OF HIGH-FREQUENCY GaAs ICs BY PICOSECOND ELECTRO-OPTIC SAMPLING - *Invited Keynote* - R.K. Jain, Amoco Tech Co, PO Box 400, Naperville, IL 60566
- F5.2** INVERTED L DIELECTRIC GUIDE FOR MILLIMETER WAVE FREQUENCIES - A.K. Tiwari and R.P. Singh, Dept of Electron Engr, Maulana Azad College of Tech, BHOPAL - 462 007 (M.P) India
- F5.3** SYMMETRY AND PERIODICITY FOR MILLIMETER-WAVE DEVICES - W.N. Cain and R.W. Grow, Microwave Dev and Phys Electron, Dept of EE, U of Utah, Salt Lake City, UT 84112

---

---

## SESSION F6

---

---

---

Mahimahi Room, 3<sup>rd</sup> Floor

---

Friday PM

December 9, 1988

---

### MATERIALS CHARACTERIZATION II

---

(15 minute papers, 1300 hours)

---

K. Sakai, Presider

---

- F6.1** MILLIMETER WAVE CHARACTERIZATION OF HIGH  $T_c$  SUPERCONDUCTING MATERIALS - L. Wade, I. Galin, S. Gillespie, P. George, R. Haas, E. Witteles, Aerojet Electro Systems, 1100 W. Hollyvale St, P.O. Box 296, Azusa, CA 91702
- F6.2** MICROWAVE LOSSES IN HIGH- $T_c$  SUPERCONDUCTING MICROSTRIP RING RESONATORS - J. Takemoto, F. Oshita, H. Fetterman, Dept Elec Engr, U of California, Los Angeles, CA 90024; P. Kobrin, E. Sovero, Rockwell Intl Science Ctr, 1049 Camino dos Rios, Thousand Oaks, CA 91360
- F6.3** MICROWAVE PHASE CONJUGATION IN ARTIFICIAL KERR MEDIA - R. Shih, H.R. Fetterman, B. Bobbs, Dept Elec Engr, U of California, Los Angeles, CA 90024; W.W. Ho, R. McGraw, D. Rogovin, Rockwell Intl Science Ctr, 1049 Camino dos Rios, Thousand Oaks, CA 91360
- F6.4** DIELECTRIC PROPERTIES OF COMPOSITE STRIPLINE/RADOME MATERIALS - R.L. Moore and A. MacDonald, GTRI, GA I of Tech, Atlanta, GA 30332
- F6.5** TEMPERATURE INDEPENDENT PERMITTIVITIES IN COMPOSITES OF TWO OR MORE DIELECTRICS - R.L. Moore and J. Estrada, GTRI, GA I of Tech, Atlanta, GA 30332
- F6.6** THEORY AND PRACTICE IN OPEN RESONATOR MEASUREMENTS OF MULTI-LAYER SAMPLES - T. Wells, GTRI, GA I of Tech, Atlanta, GA 30332
- F6.7** MAGNETOPOLARON EFFECTS IN CdTe - J. Oberti, M. Goiran, M. Bouchelagem, J. Léotin, Lab de Physique des Solides, associé au CNRS INSA, Ave de Rangueil, 31077 Toulouse-Cedex, France; R. Triboulet, Meudon, France
- F6.8** QUANTUM LIMIT ELECTRON-PHONON SCATTERING STUDIES IN SEMICONDUCTORS BY FAR-INFRARED CYCLOTRON RESONANCE - H. Kobori, T. Ohyama and E. Otsuka, College of General Education, Osaka Univ, Toyonaka, Osaka 560 Japan
- F6.9** FAR-INFRARED CYCLOTRON RESONANCE STUDIES OF IMPURITY SCATTERING IN Ge, GaAs AND InSb - H. Kobori, T. Ohyama and E. Otsuka, College of General Education, Osaka Univ, Toyonaka, Osaka 560, Japan
- F6.10** BROADBAND DIELECTRIC MEASUREMENTS WITH PICOSECOND TRANSIENT RADIATION - G. Arjavalingam, Y. Pastol, J.-M. Halbout and G.V. Kopcsay, IBM, P.O. Box 218, Yorktown Heights, NY 10598
- F6.11** WAVEFRONT DIVIDING INTERFEROMETERS FOR INFRARED SYNCHROTRON RADIATION - K.D. Moeller\*, D.P. Siddons, C.J. Hirschmugl, P. Petrone\*, and G.P. Williams, Natl Synchrotron Light Source, Brookhaven Natl Lab, Upton, NY 11973; \*Physics Dept, Fairleigh Dickinson U, Teaneck, NJ 07666

---

---

## SESSION F7

---

---

---

Papio Room, 3<sup>rd</sup> Floor

---

Friday PM

December 9, 1988

---

### ATMOSPHERIC PROPAGATION

---

(1300 hours; 15 minute papers)

---

K. J. Button, Presider

---

- F7.1 MILLIMETRE-WAVELENGTH PULSE PROPAGATION THROUGH THE EARTH'S ATMOSPHERE - C.J. Gibbins, Rutherford Appleton Lab, Chilton, Didcot, Oxfordshire, OX11 0QX, UK
- F7.2 STATISTICS OF PROPAGATION AT MILLIMETRIC, INFRARED AND OPTICAL WAVELENGTHS - C.J. Gibbins, Rutherford Appleton Lab, Chilton, Didcot, Oxfordshire, OX11 0QX, UK

---

### SUBMILLIMETER WAVES

---

(15 minute papers; 1415 hours)

---

- F7.3 FAR-INFRARED DETECTOR USING  $\text{BaPb}_{0.7}\text{Bi}_{0.3}\text{O}_3$  THIN FILM JOSEPHSON ELEMENT - A. Sawada, K. Sato, Y. Enomoto\* and T. Murakami\*, Synthetic Crystal Res Lab, Faculty of Engr, Nagoya Univ, Nagoya 464-01 Japan; \*NTT Electrical Commtn Lab, Tokai, Ibaraki-ken 319-11 Japan
- F7.4 GaAs SCHOTTKY BARRIER MIXER DIODES FOR THE FREQUENCY RANGE FROM 1 - 10 THz - T.W. Crowe, Dept of Elec Engr, Thornton Hall, Univ of Virginia, Charlottesville, VA 22901
- F7.5 MICROWAVE ATTENUATION TECHNIQUES APPLICABLE TO INFRARED WINDOWS FOR USE ON ELECTRO-OPTICAL SENSORS - W. Hasan, The Perkin-Elmer Corp, 761 Main Ave, Norwalk, CT 06859
- F7.6 FABRICATION AND ANALYSIS OF GaAs SCHOTTKY BARRIER DIODES FABRICATED ON THIN MEMBRANES FOR TERAHERTZ APPLICATIONS - L.K. Seidel and T.W. Crowe, Dept of Elec Engr, Thornton Hall, Univ of Virginia, Charlottesville, VA 22901
- F7.7 WAVEFRONT DIVIDING INTERFEROMETERS FOR INFRARED SYNCHROTRON RADIATION - K.D. Moeller D.P. Sidons\*, C.J. Hirschmugl\*, P. Petrone and G.P. Williams\*, National Synchrotron Light Source, Brookhaven Natl Lab, Upton, NY 11973; \*Physics Dept, Fairleigh Dickinson Univ, Teaneck, NJ 07666
- F7.8 COHERENT MECHANICAL FIR DOPPLER SHIFTING FOR HETERODYNE APPLICATIONS - U.H.W. Lammers, R.A. Marr, J.B. Morris, Rome Air Development Center, Hanscom AFB, MA
- F7.9 DPR IN  $\text{DyAl}$  GARNET AT MM AND SUBMM WAVELENGTHS - P. Janssen, Lab Temperaturen en Hoge-Veldenfysica, Leuven, Belgium; W.P. Wolf, Yale Univ, Becton Ctr, New Haven, CT 06520

---

---

## SESSION F8

---

---

---

Ballroom (Makai), 7<sup>th</sup> Floor

---

Friday PM

December 9, 1988

---

### GYROTRON AND FREE ELECTRON LASERS

---

(15 minutes, 1300 hours)

---

K.R. Chu, Presider

---

- F8.1 CIRCULAR ELECTRIC HYBRID CAVITY FOR THE HARMONIC AUTO-RESONANT PENIOTRON (HARP) - J.M. Baird, R.C. Freudenberger, R.W. Grow, and L.R. Barnett, Dept Elec Engr, Univ of Utah, Salt Lake City, UT
- F8.2 SELF-CONSISTENT TRANSMISSION LINE ANALYSIS OF THE GYROTRON TRAVELING-WAVE AMPLIFIER - J.E. Arrington, R.W. Grow, J.M. Baird, and L.R. Barnett, Dept Elec Engr, Univ of Utah, Salt Lake City, UT
- F8.3 SIMULATION OF THE ELECTROSTATIC CYCLOTRON INSTABILITY ON AN ANNULAR ELECTRON BEAM - F.S. Kuo, Dept of Physics, Natl Central U, Chung-Li, Taiwan, R.O.China; K.R. Chu, Dept Physics, Natl Tsing Hua U, Hsinchu, Taiwan 30043, R.O.China
- F8.4 THE SURFACE-MATCHING METHOD FOR SOLVING PERIODIC AND HELICALLY-PERIODIC SLOW WAVE STRUCTURES FOR TRAVELING-WAVE SIMULATION - K.J. Bunch and R.W. Grow, Dept Elec Engr, Univ Utah, Salt Lake City, UT 84112
- F8.5 RADIATION PATTERNS WITH SUPPRESSED SIDELOBES FOR QUASI-OPTICAL MODE CONVERTERS - M. Thumm, L. Rebuffi\*, H.J. Barkley, A. Jacobs, G.A. Müller, Inst für Plasmaforschung, Univ Stuttgart, Pfaffenwaldring 31, D-7000 Stuttgart 80, FRG
- F8.6 IN-WAVEGUIDE TE<sub>01</sub>-TO-WHISPERING GALLERY MODE CONVERSION USING PERIODIC WALL PERTURBATIONS - M. Thumm and A. Jacobs, Univ Stuttgart, FRG
- F8.7 THE DIRECT CONVERSION TO A GAUSSIAN BEAM FROM TE<sub>03</sub> GYROTRON MODES - H.J. Barkley, Univ Stuttgart, FRG
- F8.8 SERPENTINE WAVEGUIDE TRAVELING WAVE TUBE (TWT) WITH FULL GAIN AND BROAD BANDWIDTH AT MILLIMETER WAVE FREQUENCIES - G. Dohler, D. Gallagher, R. Moats, Northrop Defense Syst Div, 600 University Dr, Arlington Heights, IL 60004
- F8.9 SPACE CHARGE EFFECTS IN THE BALLISTIC MODEL OF FREE ELECTRON LASER INTERACTIONS - G. Dohler, Northrop, IL
- F8.10 WINDOW MATERIALS FOR 280 GHz CONTINUOUS WAVE GYROTRON - M.N. Afsar, Dept Elec Engr, Tufts Univ, Halligan Hall, Medford, MA and MIT/PFC
- F8.11 SMALL-SIGNAL ANALYSIS OF A FREE ELECTRON CYCLOTRON RESONANCE LASER - C. Wang, Res Lab of Microwave Electron, Chengdu I of Radio Engr, PRChina
- DESIGN AND OPERATION OF RIBBON BEAMS FOR GYROTRONS - A.M. Ferendeci, ECE Dept, Univ Cincinnati, Cincinnati, Ohio 45221

# INDEX TO AUTHORS

Author	Session	Page	Author	Session	Page
Abba, P.	T9.5	169	Bohlander, A.	T9.1	162
Adaway, Kim	Th1.8	296	Bohn, C.L.	W2.1	197
Afsar, M.N.	F2.7	400a	Booske, J.H.	M4.2	37
Afsar, M.N.	F8.10	468a	Botula, A.	F1.10	389
Afsar, M.N.	W6.2	254a	Bouchelagem, M.	F6.7	443
Agosti, G.	T10.5		Boulais, K.	F4.8	
Ahn, S.	Th8.5	367	Bourgeois, J.M.	W6.9	
Ajikata, Toshihiro	M5.6	55	Bowden, C.M.	Th7.7	
Alberti, S.	T10.5		Bowden, M.D.	T8.5	150
Albuquerque, M.R.M.L.	W5.8	247	Bowden, M.D.	T8.7	153
Alexeff, I.	T1.3	92	Bowers, J.E.	M2.3	17
Alexeff, I.	T5.5	133	Boyd, J.K.	Th4.2	
Allen, S.J. Jr.	F2.1	391	Brand, G.F.	T10.8	183
Altshuler, Edward E.	T9.3	165	Brand, G.F.	T8.5	150
Angelides, E.	W7.1	263	Brandt, Howard E.	M5.4	51
Antonsen, T.M.	Th8.3	364	Brenner, J.	T4.2	113
Antonsen, T.M. Jr.	M4.2	37	Buckley, M.J.	T4.4	117
Antonsen, T.M. Jr.	M4.7	43	Bunch, K.J.	F8.4	461
Antonsen, T.M. Jr.	W4.6	232	Burke, J.M.	W4.4	228
Antonsen, Thomas	W8.6	281	Burnett, C.E.	T5.4	131
Antonsen, Thomas M. Jr.	M8.3	83	Burrus, C.A.	T1.5	
Anzaki, T.	F2.4	397	Burrus, C.A.	M2.3	17
Arai, T.	F2.4	397	Buttgenback, T.H.	M2.4	
Arai, T.	W6.4	257	Buzzi, J.M.	M7.3	
Aramaki, S.	F3.6	414	Byrom, C.N.	M8.2	81
Archer, J.W.	Th1.1	284	Cai, S.Z.	T1.8	98
Arjavalasingam, G.	F6.10	449	Cain, W.N.	F1.5	
Armstrong, C.M.	F4.2	418	Calame, J.	F5.3	437
Armstrong, C.M.	W4.3	226	Canal, F.	W4.2	224
Arrington, J.E.	F8.2	459	Cao, H.B.	W5.10	251
Arrora, M.	W6.8		Caplan, M.	Th4.6	324
Asano, H.	T10.3	177	Caplan, M.	Th4.2	
Atsuki, Kazuhiko	M6.4	65	Carelli, G.	Th8.6	369
Awaka, J.	T9.4	167	Carr, G.L.	W3.10	222
Ayres, V.	F4.8		Casey, J.A.	W6.5	
Bae, Jongsuck	F3.4	412	Cavallo, A.	T4.8	123
Bae, Jongsuck	Th3.5	312	Chabal, Y.J.	T4.2	113
Baird, J.M.	F8.1		Champlin, K.S.	W7.1	263
Baird, J.M.	F8.2	459	Chang, Kai	Th1.4	288
Baird, J.M.	W7.9		Chang, Kai	F1.6	381
Balachandran, U.	W2.1	197	Chang, Kai	M3.2	25
Ballico, M.J.	T8.5	150	Chang, Kai	Th1.6	292
Barker, R.J.	M4.1	35	Chang, Kai	W6.7	261
Barkley, H.J.	F8.5	463	Chang, L.H.	Th8.7	
Barkley, H.J.	F8.7	467	Chang, S.F.	M4.8	44a
Barkley, H.J.	T4.1	111	Chen, H.C.	M5.4	51
Barnett, L.R.	F8.1		Chen, H.C.	M5.7	57
Barnett, L.R.	F8.2	459	Chen, Jizhong	M8.9	91
Barnett, L.R.	Th8.7		Chen, N.	M1.9	
Barnett, L.R.	W7.9		Chen, S.C.	M4.3	39
Barsanti, M.L.	W8.2	273	Chen, Yi-yuan	W5.6	245
Barth, Helmut	M1.6	9	Cheung, P.	M6.3	63
Behn, R.	T8.8	155	Chew, Richard	T1.7	96
Bekefi, G.	F4.6	426	Chi, H.	W6.2	
Bekefi, G.	M4.3	39	Choe, J.Y.	F4.8	
Bekefi, G.	M8.5	87	Choi, J.J.	Th8.2	362
Bennett, C.A.	T3.2	107	Choi, Yat Man	W1.7	195
Bennett, C.A.	T8.1	145	Chong, C.K.	Th8.4	365
Bennett, C.A.	T8.6	152	Chou, Kan	F1.2	375
Bennett, C.A.	T8.9	157	Chu, K.R.	F4.1	
Bhasin, Kul B.	Th1.8	296	Chu, K.R.	F8.3	
Bigelow, T.S.	T4.3	115	Chu, K.R.	Th4.4	320
Birch, James R.	Th2.1	298	Chu, K.R.	Th8.7	
Birkeland, Joel	M1.5	7	Chu, K.R.	W8.9	
Black, W.M.	Th4.3	318	Churchill, R.J.	T1.3	92
Black, W.M.	Th4.7	326	Claeson, T.	M5.9	59
Black, W.M.	Th8.1	360	Clifford, S.F.	T9.1	162
Blakelock, P.A.	T1.5		Clifton, B.J.	W3.6	217
Bluem, Hans	T5.1	127	Cohn, D.	T4.8	123
Bobbs, Bradley	F6.3	441	Cohn, D.R.	T3.1	104

# INDEX TO AUTHORS

Author	Session	Page	Author	Session	Page
Cohn, D.R.	W2.6	205	Fletcher, L.K.	T3.2	107
Colas, E.	F2.1	391	Fletcher, L.K.	T8.6	152
Cole, R.S.	T6.2		Fliflet, A.W.	Th4.3	318
Cook, J.D.	W7.10		Fliflet, A.W.	Th4.7	326
Coon, D.D.	W3.2	209	Fliflet, A.W.	W4.4	228
Costabile, G.	M7.2	73	Fliflet, A.W.	W8.2	273
Costache, G.	W5.4	241	Fong, T.T.	T1.2	
Crisp, G.N.	T1.5		Frerking, M.A.	T1.8	98
Cronin, N.J.	T7.6		Frerking, Margaret A.	F1.7	383
Crowe, T.W.	F7.4		Freudenberger, R.C.	F8.1	
Crowe, T.W.	F7.6		Freund, H.P.	M8.5	87
Crownover, Richard L.	W7.3	266	Friedman, M.	F1.1	
Cutler, R.	T4.2	113	Fujisawa, K.	W1.3	187
Czarnaski, M.A.	W4.4	228	Fujisawa, K.	W2.5	203
d'Assuncao, A.G.	W5.8	247	Fujita, J.	T8.10	159
d'Assuncao, A.G.	W5.9	249	Fujita, J.	T8.3	146
Dahlstrom, R.K.	T4.5	119	Fujita, J.	T8.4	148
Danly, B.	F4.6	426	Fujui, Y.	M7.1	
Danly, B.	Th4.1	316	Furler, R.	Th6.6	348
Daryoush, A.S.	M2.5	19	Furuhama, Y.	T9.4	167
Day, Walter	T1.7	96	Furuya, Kazuyuki	F3.4	412
DeFonzo, A.P.	M6.5		Gagnon, A.	W5.3	239
DeFonzo, A.P.	T2.2		Galin, I.	F6.1	
Degiacomi, C.G.	M7.4	75	Galin, I.	T7.2	139
Delayen, J.R.	W2.1	197	Gallagher, D.	F8.8	
DeLucia, Frank C.	Th3.1	308	Ganguly, A.K.	F4.2	418
DeLucia, Frank C.	W7.3	266	Ganguly, A.K.	M8.5	87
DeRosa, F.	F2.1	391	Ganguly, A.K.	Th8.5	367
Destler, W.W.	M4.2	37	Ganiere, J.D.	Th3.6	314
DiCecca, S.	M4.3	39	Garg, R.K.	W6.8	
Dicken, D.	T8.8	155	Gautier, J.L.	M6.8	71
DiRienzo, A.	F4.6	426	Gavan, J.	W7.5	267
DiRienzo, A.C.	M8.5	87	Geiger, Jurgen	W3.1	207
Doane, J.	T4.2	113	George, P.	F6.1	
Dohler, G.	F8.8		George, T.V.	T10.1	173
Dohler, G.	F8.9		Gerbaut, X.	Th6.1	338
Donovan, D.	F3.8	416	Gerbaut, X.	Th6.4	344
Donovan, D.P.	Th7.5	356	Gerbaut, X.	W4.4	228
Dorris, S.E.	W2.1	197	Giangrave, M.	W5.8	247
Drobot, A.	W8.5	279	Giarola, A.J.	W5.9	249
Dudas, A.J.	F4.3	420	Gibbins, C.J.	F7.1	451
Dudas, A.J.	T10.6	181	Gibbins, C.J.	F7.2	453
Dumas, O.	W8.5	279	Gilbert, G.R.	W6.7	261
Dumas, O.	Th8.9	373	Gilgenbach, R.M.	Th8.2	362
Dupertuis, M.A.	W8.8	282	Gillespie, S.	F6.1	
Dupertuis, M.A.	F3.3	410	Gingras, R.	T7.5	
Dusek, J.T.	Th3.6	314	Giriat, W.	F2.10	403
Dyer, F.	W2.1	197	Goeking, K.W.	W6.7	261
Dyer, F.	T1.3	92	Goiran, M.	F6.7	443
Dyer, F.	T5.5	133	Gold, S.H.	Th4.3	318
Eisenstein, G.E.	M2.4		Gold, S.H.	Th4.7	326
Eldridge, O.C.	M4.8	44a	Gold, S.H.	Th8.1	360
Elias, L.	T5.2		Gold, S.H.	Th8.3	364
Ellis, Grant A.	Th5.8	336	Goldberg, L.	M6.2	
Ellison, B.N.	T1.8	98	Goretta, K.C.	W2.1	197
England, P.	F2.1	391	Goulding, R.R.J.	Th7.5	356
Enomoto, Y.	F7.3	455	Granatstein, V.L.	M4.2	37
Esarey, E.	M4.4		Granatstein, V.L.	W4.5	230
Estrada, J.	Th6.9		Grau, L.L.	W5.10	251
Eswarappa	W5.4	241	Grebogi, Celso	W4.8	233
Evenson, K.M.	Th7.1		Gries, B.L.	W6.7	261
Faillon, G.	M8.2	81	Grimm, T.L.	T10.4	179
Faist, J.	Th3.6	314	Grow, R.W.	F5.3	437
Falconer, I.S.	T8.5	150	Grow, R.W.	F8.1	
Falconer, I.S.	T8.7	153	Grow, R.W.	F8.2	459
Fekete, P.W.	T8.5	150	Grow, R.W.	F8.4	461
Felch, K.	T10.2	175	Grow, R.W.	W7.9	
Fetterman, H.R.	T2.1		Guan, Yu	Th7.3	
Fetterman, Harold	F6.2	439	Guo, Yong	M3.5	31
Fetterman, Harold, R.	F6.3	441	Guss, W.C.	Th8.6	369
Finn, J.M.	M4.2	37	Guttadora, L.	T8.11	161
Fischer, R.P.	W4.4	228	Haas, R.	F6.1	
Fischer, R.P.	W8.2	273	Hackmann, J.	T8.8	155

# INDEX TO AUTHORS

Author	Session	Page	Author	Session	Page
Haddad, G.I.	M5.8		Izatt, J.R.	Th3.4	
Hadni, A.	Th6.1	338	Izatt, J.R.	Th7.7	
Hadni, A.	Th6.4	344	Jackson, J.A.	T5.3	129
Hagino, Ichiro	F1.3	377	Jackson, Robert H.	T5.1	127
Halbout, J.-M.	F6.10	449	Jacobs, A.	F8.5	463
Halbritter, J.	T4.7		Jacobs, Annmarie	F8.6	465
Hargreaves, T.A.	W8.2	273	Jain, F.C.	Th5.4	330
Hartemann, F.	M8.2	81	Jain, R.K.	F5.1	
Hasan, W.	F7.5		James, B.W.	T8.5	150
Hayashi, K.	W8.4	277	James, B.W.	T8.7	153
He, F.	T8.2		Janssen, P.	F7.9	
Hegazi, G.M.	T7.5		Jenkinson, H.	W5.5	243
Helm, M.	F2.1	391	Jensen, Erk	F4.5	424
Herczfeld, P.R.	M2.5	19	Jeong, Y-Y.	W2.7	
Hess, C.	T10.2	175	Jha, A.R.	M1.8	11
Hidaka, S.	W6.4	257	Jiang, H-B.	W4.7	
Hieda, Morishige	M5.6	55	Jodicke, J.	T4.7	
Hill, R.J.	T9.1	162	Johns, J.W.C.	Th7.5	356
Hiroaki, T.	W6.4	257	Jong, R.A.	M8.1	79
Hiromoto, N.	F2.2	393	Jongewaard, E.	T10.2	175
Hirschmugl, C.J.	F6.11		Jory, H.	T10.2	175
Hirschmugl, C.J.	F7.7		Joseph, Richard I.	Th6.2	339
Hirschmugl, Carol J.	W7.1	263	Jostingmeier, A.	W5.2	237
Ho, L.T.	F2.5		Kaneko, A.	W3.3	211
Ho, Thomas Chen-Chou	F1.2	375	Kaneko, Takenori	F1.3	377
Ho, William W.	F6.3	441	Kasperek, W.	T4.1	111
Hochschild, G.	T4.7		Kato, Tomoaki	M6.6	67
Hochschild, G.	W4.1		Katz, A.S.	T9.6	171
Hoefler, W.	W1.1		Kawahata, K.	T8.10	159
Hoefler, W.	W5.3	239	Kawahata, K.	T8.3	146
Hoefler, W.J.R.	W5.4	241	Kawahata, K.	Th2.4	
Hoffmann, F.M.	W7.1	263	Kawai, Yasushi	M4.5	41
Hogan, B.	W4.2	224	Kawamura, M.	W2.4	201
Hollenstein, A.	M7.4	75	Kawhata, K.	T8.4	148
Hong, J.	Th1.2		Keller, J.	W6.3	255
Hong, Jia Sheng	Th1.5	290	Kesan, V.P.	M1.3	5
Hong, Wei	M5.3	49	Kesan, V.P.	M5.1	45
Horioka, M.	Th6.8	351	Kesan, V.P.	M5.2	47
Hou, Y.S.	F1.5		KfK Gyrotron Team	W4.1	
Huang, Jifu	Th5.7	334	Kikunaga, T.	T10.3	177
Huang, P.	F1.10	389	Kim, Moonil	M1.1	1
Huey, H.	T10.2	175	Kinasewitz, R.T.	Th5.6	332
Hufford, G.A.	T9.6	171	Kinthead, A.K.	Th4.3	318
Huguenin, D.	M7.4	75	Kinthead, A.K.	Th3.3	364
Hui, Z-X.	M8.8		Kirkpatrick, D.A.	M8.5	87
Hummer, K.A.	M3.2	25	Kirkpatrick, D.A.	Th4.3	318
Hummer, Kenneth A.	Th1.6	292	Kirkpatrick, D.A.	Th4.7	326
Hung, H-L. A.	W6.6	259	Kirkpatrick, D.A.	Th8.3	364
Hung, H-L.A.	M6.7	69	Kiyokawa, M.	W2.3	199
Hunter, H.T.	T3.2	107	Klein, J.L.	M3.2	25
Hutchinson, D.P.	T3.2	107	Klein, James L.	Th1.6	292
Hutchinson, D.P.	T8.1	145	Kleva, Robert G.	Th4.5	322
Hutchinson, D.P.	T8.6	152	Kneubuhl, F.K.	F3.1	406
Hutchinson, D.P.	T8.9	157	Kneubuhl, F.K.	M7.4	75
Hwu, R.J.	Th5.3	328	Kneubuhl, F.K.	Th6.5	345
Ichioka, Y.	Th2.4		Kneubuhl, F.K.	Th6.6	348
Idehara, T.	T8.5	150	Kobayashi, Yoshio	Th2.3	302
Ihara, T.	T9.4	167	Kobori, H.	F6.8	445
Iinuma, Toshihiko	W3.4	213	Kobori, Hiromi	F6.9	
Inatani, J.	T7.1		Kobori, Hiromi	F6.9	447
Inguscio, M.	W3.10	222	Kobrin, Paul	F6.2	439
Ioli, N.	W3.10	222	Komine, Y.	F2.6	399
Ishibashi, Yoshihiro	Th6.3	342	Komiyama, B.	W2.3	199
Ishigaki, T.	W3.3	211	Komiyama, Bokuji	T7.4	143
Itabe, T.	F2.2	393	Komiyama, S.	Th3.2	
Itoh, T.	M2.6	21	Komuro, M.	W8.4	277
Itoh, T.	M3.6	33	Kopcsay, G.V.	F6.10	449
Itoh, T.	M5.1	45	Koren, U.	N2.4	
Itoh, T.	M5.2	47	Korman, A.	W7.5	267a
Itoh, Tatsuo	M6.3	63	Korzeniewski, T.L.	T7.5	
Itoh, Y.	M1.5	7	Kosmopoulos, S.A.	W5.3	239
Izatt, J.R.	W8.4	277	Kou, C.S.	F4.10	433
Izatt, J.R.	F3.5		Kou, C.S.	T8.4	
Izatt, J.R.	F3.7		Kpodzo, Elias	Th1.3	286

# INDEX TO AUTHORS

Author	Session	Page	Author	Session	Page
Krall, J.	F1.1		Luhmann, N.C. Jr.	Th5.3	328
Kreischer, K.	T4.6	121	Luhmann, N.C. Jr.	Th8.4	365
Kreischer, K.E.	F4.7	429	Luo, G.H.	T4.4	117
Kreischer, K.E.	T10.4	179	Luo, Yuanhai	W3.9	221
Kreischer, K.E.	Th8.6	369	Ma, C.H.	T8.1	145
Kreischer, K.E.	W8.3	275	Ma, C.H.	T8.6	152
Krowne, Clifford M.	F2.3	395	Mabius, D.L.	W6.7	261
Krowne, Clifford M.	W7.7	269	MacDonald, A.	Th2.9	
Krug, Peter A.	W7.6	268	Macfarlane, J.C.	T8.7	153
Kuo, F.S.	F8.3		Machuzak, J.S.	T3.1	104
Kuo, F.S.	W8.9		Maia, M.R.G.	W5.8	247
Kuo, S.P.	T3.3	109	Mains, R.K.	M5.8	
Kuo, S.P.	Th8.8	371	Manabe, T.	T9.4	167
Kyser, R.H.	F4.2	418	Manheimer, W.M.	Th4.3	318
Lammers, U.H.W.	F7.8	457	Manheimer, W.M.	Th4.7	326
Lanagan, M.T.	W2.1	197	Manheimer, W.M.	Th8.1	360
Larsen, Arthur	T1.7	96	Manheimer, W.M.	Th8.3	364
Latham, P.E.	M4.2	37	Manheimer, W.M.	W4.4	228
Latham, P.E.	W4.5	230	Manheimer, W.M.	W8.2	273
Latham, P.E.	W4.6	232	Manheimer, W.M.	W8.7	
Lau, Y.Y.	F1.1		Manheimer, Wallace	W8.6	281
Laval, G.	M4.7	43	Mansfield, D.K.	T8.11	161
Lawson, W.	T10.6	181	Mansfield, Dennis K.	W7.6	268
Lawson, W.	W4.2	224	Marable, W.	M4.4	
Lawson, W.	W4.5	230	Marco, Hernandez, J.	W5.10	251
Lee, C.H.	M6.7	69	Marr, R.A.	F7.8	457
Lee, Chi H.	M6.1	61	Marr, Richard A.	T9.3	165
Lee, H.-Y.	M2.6	21	Marsh, S.P.	T7.6	
Lee, J.	T8.1	145	Marshall, E.M.	T5.3	129
Lee, J.	T8.6	152	Martin, D.	Th3.6	314
Lee, Karen A.	F1.7	383	Mathews, G-G.	T10.5	
Lee, M.C.	T3.3	109	Matsuhara, H.	F2.2	393
Lee, T.T.	M6.7	69	Matsui, T.	W2.3	199
Lees, R.M.	F3.8	416	Matsui, Toshiaki	T7.4	143
Lees, R.M.	Th7.2	353	Matsuishi, K.	F2.4	397
Lees, R.M.	Th7.5	356	Matsuo, H.	T8.10	159
Lees, R.M.	Th7.6	358	Matsuo, H.	Th2.4	
Leibovitch, C.	F4.6	426	Matsushima, K.	Th7.4	354
Leotin, J.	F6.7	443	Mayergoyz, I.D.	M4.2	37
Leupin, A.	Th6.5	345	Maziar, C.M.	M1.3	5
Levush, B.	Th8.3	364	McCleary, J.C.	W6.7	261
Levush, Barach	M8.3	83	McCowan, R.B.	Th4.3	318
Levush, Baruch	Th4.5	322	McCowan, R.B.	Th8.1	360
Levush, Baruch	W8.6	281	McCurdy, A.H.	W4.3	226
Lewis-Bevan, W.	Th7.5	356	McDermott, D.B.	F4.10	433
Lewis-Bevan, W.	Th7.6	358	McDermott, D.B.	Th4.4	320
Li, B.	T8.2		McDermott, D.B.	Th4.6	324
Li, M.	W6.7	261	McDermott, D.B.	Th8.4	365
Li, Ming-Yi	F1.6	381	McGrath, W.R.	T1.8	98
Li, S.F.	M1.9		McGraw, Robert	F6.3	441
Li, Sifan	M1.2	3	McKaughan, M.E.	Th5.4	330
Li, Sifan	M5.3	49	McMillan, R.W.	T9.1	162
Li, Sifan	W1.2	185	Meulenberg, A.	W6.6	259
Li, Zong-Wen	W5.1	235	Miller, D.R.	M1.3	5
Libelo, Louis F.	Th2.6	304	Miller, P.E.	Th8.8	371
Liebe, H.J.	T9.6	171	Miller, R.E.	M7.3	
Liebe, Hans J.	T9.2	164	Miller, R.E.	T1.8	98
Lieneweg, U.	Th5.3	328	Mizuno, Koji	F3.4	412
Lin, A.T.	F4.1		Mizuno, Koji	M3.3	27
Lin, A.T.	Th4.4	320	Mizuno, Koji	M5.6	55
Lin, F.	W1.5	191	Mizuno, Koji	Th3.5	312
Lin, Yikun	F3.2	409	Mizuno, Koji	W3.4	213
Ling, Curtis C.	T7.3	141	Moats, R.	F8.8	
Ling, H.	M3.6	33	Mobius, A.	T4.6	121
Liu, H.N.	Th8.7		Mobius, A.W.	T10.4	179
Lu, Wei	F2.10	403	Moeller, K.D.	F6.11	
Lu, Z.M.	W5.5	243	Moeller, K.D.	F7.7	
Lu, Zaitong	M8.9	91	Moeller, K.D.	W7.1	263
Luhmann, N.C.	F4.1		Moharram, M.A.	Th6.7	350
Luhmann, N.C.	T3.4		Monaco, R.	M7.2	73
Luhmann, N.C. Jr.	F1.10	389	Moore, K.J.	T8.5	150
Luhmann, N.C. Jr.	F4.10	433	Moore, R.L.	Th6.9	
Luhmann, N.C. Jr.	Th4.4	320	Moore, R.L.	Th2.9	
Luhmann, N.C. Jr.	Th4.6	324	Moore, R.L.	W6.9	

# INDEX TO AUTHORS

Author	Session	Page	Author	Session	Page
Moretti, A.	W3.10	222	Pan, D.S.	F1.10	389
Morier-Genoud, F.	Th3.6	314	Pandey, R.K.	W6.7	261
Morris, J.B.	F7.8	457	Park, S.Y.	F4.2	418
Mortazawi, A.	M5.1	45	Parker, R.K.	F4.2	418
Mortazawi, A.	M5.2	47	Pasquet, D.	M6.8	71
Mourier, G.	M8.2	81	Pastol, Y.	F6.10	449
Muggli, P.	T10.5		Pendergast, K.D.	Th4.1	316
Mukhopadhyay, I.	F3.8	416	Pendleton, R.	T10.2	175
Muller, G.A.	F8.5	463	Peng, S.T.	Th5.6	332
Muller, G.A.	T4.1	111	Peng, S.T.	W5.5	243
Murai, A.	Th7.4	354	Pereira, D.	W3.10	222
Murai, Y.	T10.3	177	Pereira, W.N.A.	W3.7	
Murakami, T.	F7.3	455	Perera, A.G.U.	W3.2	209
Murase, K.	F2.8		Perkowitz, S.	W6.5	
Murase, K.	F2.9	401	Pershing, Dean E.	T5.1	127
Nagayama, Y.	T8.3	146	Petillo, J.J.	W8.5	279
Naimann, M.	W4.2	224	Petrone, P.	F6.11	
Nakagawa, T.	F2.2	393	Petrone, P.	F7.7	
Nakai, S.	F3.6	414	Petrone, P.	W7.1	263
Nakamura, H.	W3.3	211	Philips, T.G.	M7.3	
Nakamura, K.	W3.3	211	Piosczyk, B.	F4.4	422
Nakano, T.	Th2.4		Piosczyk, B.	W8.8	282
Nakashima, K.	T10.3	177	Pirkle, D.	Th8.6	369
Nakayama, Masatoshi	M5.6	55	Pisane, Guy	Th2.6	304
Nanba, Takao	Th2.2	300	Poeppel, R.B.	W2.1	197
Nasser, M.I.	Th6.7	350	Polak-Dingels, P.	M6.7	69
Neikirk, D.P.	M1.3	5	Popovic, Zorana B.	M1.1	1
Neikirk, D.P.	M3.6	33	Potter, K.E.	T1.5	
Neikirk, D.P.	M5.1	45	Pouvil, P.	M6.8	71
Neikirk, D.P.	M5.2	47	Pradhan, M.M.	W6.8	
Neikirk, D.P.	M6.3	63	Prevedelli, M.	W3.10	222
Nett, H.	W3.6	217	Prigent, C.	T9.5	169
Niimura, M.G.	T1.3	92	Purchase, Kenneth G.	T2.4	102
Nishida, J.	W3.3	211	Pyee, M.	W3.7	
Nishida, Takashi	Th3.5	312	Qian, Yongxi	M6.4	65
Nishida, Toshiyuki	F3.4	412	Radack, D.J.	M4.2	37
Nishida, Y.	T3.4		Rader, M.	T1.3	92
Nishimura, Hiroshi	M3.3	27	Rader, M.	T5.5	133
Nomoto, Toshihiro	T1.4	94	Rai, J.	Th7.7	
Nosu, Kiyoshi	M2.1	13	Rai, S.	Th7.7	
Nozokido, Tatuo	F3.4	412	Raisanen, A.	M5.1	45
O'Neill, T.	Th5.3	328	Raybon, G.	M2.4	
Oberti, J.	F6.7	443	Razeghi, M.	T5.6	135
Oettinger, P.E.	F4.3	420	Read, M.E.	F4.3	420
Ohta, Isao	F1.3	377	Read, M.E.	T10.6	181
Ohta, K.	F3.6	414	Read, M.E.	W4.2	224
Ohya, T.	F6.8	445	Read, M.E.	W8.5	279
Ohya, Tyuzi	F6.9	447	Rebeiz, Gabriel	T7.3	141
Okajima, S.	T8.3	146	Rebeiz, Gabriel M.	M3.5	31
Okajima, S.	T8.4	148	Rebuffi, L.	F8.5	463
Okamoto, H.	F3.6	414	Reece, P.J.	T7.6	
Okazaki, H.	T3.4		Reedy, E.K.	T1.1	
Okta, Hiroshi	T7.4	143	Reid, J.	Th3.3	310
Okuda, F.	W2.5	203	Reid, J.	W7.2	265
Okuda, H.	F2.2	393	Reinhart, F.K.	Th3.6	314
Oleson, Charles	T1.7	96	Renbaum, J.	W4.2	224
Oliner, Arthur A.	M3.1	23	Renk, K.F.	W6.3	255
Olsson, H.K.	M5.9	59	Rhee, D.Y.	T3.1	104
Omar, A.S.	W1.4	189	Rhee, D.Y.	W2.6	205
Omar, A.S.	W1.5	191	Richard, R.K.	T3.2	107
Omar, A.S.	W1.6	193	Richards, R.K.	T8.9	157
Omar, A.S.	W5.2	237	Riyopoulos, S.	M4.6	
Onari, S.	F2.4	397	Riyopoulos, S.	W8.7	
Onari, S.	W6.4	257	Roas, B.	W6.3	255
Ono, A.	W6.4	257	Rodgers, J.	"4.2	37
Ono, S.	T5.6	135	Rogers, R.L.	"3	5
Ono, S.	T5.7	137	Rogers, R.L.	M3.6	33
Ose, W.	W6.3	255	Rogovin, Dan	F6.3	441
Oshita, Floyd	F6.2	439	Romanofsky, Robert R.	Th1.7	294
Otsuka, E.	F6.8	445	Romanofsky, Robert R.	Th1.8	296
Otsuka, Eizo	F6.9	447	Rong, Aosheng	W1.2	185
Otto, J.H.	W6.3	255	Rose, K.	W2.7	
Outten, C.	Th8.2	362	Rosenbury, E.T.	M4.2	37
Pagano, S.	M7.2	73	Ruan, S.	T8.2	



# INDEX TO AUTHORS

Author	Session	Page	Author	Session	Page
Rudiger, Ralph	M7.5	77	Spencer, T.A.	Th8.2	362
Ruth, B.G.	T4.5	119	Spira, S.E.	F4.7	429
Rutledge, D.B.	M3.3	27	Sprangle, P.	M4.4	
Rutledge, D.B.	Th5.3	328	Sprangle, P.	M4.6	
Rutledge, David B.	M1.1	1	Sprangle, P.	Th4.5	322
Rutledge, David B.	M3.5	31	Stankiewicz, N.	W7.10	
Rutledge, David B.	M5.6	55	Stark, R.	M1.4	
Rutledge, David B.	T7.3	141	Stark, R.A.	F4.11	435
Rutledge, David B.	T1.6	95a	Stead, Michael	Th2.7	306
Sadjadi, F.A.	M4.5	41	Stead, Michael	Th6.2	339
Saito, Hirobumi	T8.10	159	Stephan, K.D.	T7.5	
Sakai, K.	Th2.4		Stimson, Philip A.	M3.5	31
Sakai, K.	T8.10	159	Storz, F.G.	M2.3	17
Sakamoto, M.	T8.8	155	Streit, D.	Th5.3	328
Salito, S.A.	F3.8	416	Strom, U.	W6.5	
Sastry, K.V.L.N.	W3.8	219	Strumia, F.	W3.10	222
Sato, Akio	Th2.3	302	Su, J.J.	W8.9	
Sato, Junya	F2.6	399	Sucy, M.	Th4.3	318
Sato, K.	F7.3	455	Sueta, Tadasi	M2.2	15
Sato, K.	T5.6	135	Sugawara, T.	W8.4	277
Sato, N.	T5.7	137	Sullivan, C.A.	Th4.3	318
Sato, N.	F1.6	381	Sullivan, C.A.	Th8.3	364
Sauter, Thomas	F7.3	455	Sullivan, Erin A.	W7.1	263
Sawada, A.	Th6.3	342	Sun, Ligu	W7.8	271
Sawada, Akikatsu	T4.3	115	Sun, Z.L.	M1.9	
Schaich, C.R.	M4.8	44a	Suzuki, Tetsu	W3.4	213
Scharer, J.E.	T4.5	119	Tait, Gregory B.	F2.3	395
Schlesiger, C.D.	T4.1	111	Takahashi, H.	F2.9	401
Schuller, P.G.	W5.3	255	Takahashi, S.	W3.3	211
Schultz, L.	W1.4	189	Takami, H.	F2.2	393
Schunemann, K.	F4.5	424	Takaoka, S.	F2.8	
Schunemann, Klaus	W6.3	255	Takaoka, S.	F2.9	401
Schutzmann, J.	T9.5	169	Takemoto, June	F6.2	439
Scott, N.A.	T4.9	125	Takeuchi, Y.	F1.8	385
Sealy, P.J.	Th5.1		Tan, C.S.	W3.5	215
Seashore, C.R.	F7.6		Tang, C.M.	M4.4	
Seidel, L.K.	F1.1		Tang, C.M.	M4.6	
Serlin, V.	Th1.7	294	Tang, Hong	F3.5	
Snalkhauser, Kurt A.	F2.10	403	Tejo, F.A.F.	W5.9	249
Shen, Xuchu (S.C.)	Th1.5	290	Temkin, R.	M4.3	39
Shi, Jun Ming	M8.7	89	Temkin, R.	T4.6	121
Shi, Yi-jin	F2.2	393	Temkin, R.	T4.8	123
Shibai, H.	F6.3	441	Temkin, R.J.	F4.7	429
Shih, Robert	T2.3	100	Temkin, R.J.	T10.4	179
Shimasaki, Hitoshi	F2.8		Temkin, R.J.	Th4.1	316
Shimomura, S.	F2.9	401	Temkin, R.J.	Th8.6	369
Shimomura, S.	T10.3	177	Temkin, R.J.	W8.3	275
Shimozuma, T.	T3.4		Thomas, H.J.	T6.2	
Shinozaki, T.	F3.4	412	Thomas, Michael E.	Th6.2	
Shirai, Hirokazu	Th3.5	312	Thumm, M.	F8.5	463
Shirai, Hirokazu	W3.9	221	Thumm, M.	T4.1	111
Shu, Yuwen	F6.11		Thumm, Manfred	F8.6	465
Siddons, D.P.	F7.7		Tiong, K.K.	Th8.8	371
Siddons, D.P.	W7.1	263	Tiwari, A.K.	F5.2	
Siddons, Peter D.	T8.8	155	Tolmunen, T.	M5.1	45
Siegrist, M.R.	W7.2	265	Torner, Ll.	W5.10	251
Siemens, K.J.	W2.2		Tough, G.H.	W6.6	259
Sievers, A.J.	T2.4	102	Toyoda, Sachihiro	F1.4	379
Simonis, George J.	Th2.1	298	Toyoda, Sachihiro	M5.5	53
Simonis, George J.	Th2.7	306	Tran, M.Q.	T10.5	
Simonis, George J.	Th6.2	339	Tran, M.Q.	W8.1	
Simonis, George J.	T10.6	181	Triboulet, R.	F6.7	443
Singh, A.	Th1.4	288	Tsukamoto, T.	T10.3	177
Singh, D.R.	W2.1	197	Tsunawaki, Y.	F3.5	414
Singh, J.P.	F5.2		Tsutsumi, Makoto	T2.3	100
Singh, R.P.	T6.2		Tu, C.C.	Th3.7	
Siqueira, G.L.	M5.1	45	Tucker, R.	M2.4	
Sironen, M.	W7.3	266	Tzuang, C-K. C.	M1.7	
Skatrud, David D.	W4.2	224	Uehara, Kazuhiro	M3.3	27
Skopec, M.	W6.7	261	Uhm, H.	M1.4	
Skrehot, M.K.	M6.7	69	Uhm, H.S.	F4.11	435
Smith, T.	Th7.4	354	Uhm, H.S.	F4.8	
Sokabe, N.	M8.4	85	Uhm, H.S.	M5.7	57
Soln, Josip	F6.2	439	Uhm, Han S.	M5.4	51
Sovero, Emilio					

# INDEX TO AUTHORS

Author	Session	Page	Author	Session	Page
Uhm, Han S.	W4.8	233	Young, C.	Th7.5	356
Urakawa, Y.	F2.8		Yu, C.	W3.5	215
Vander Sluis, K.L.	T8.1	145	Yu, E.X.	F1.5	
Vander Sluis, K.L.	T8.6	152	Yu, S.	W4.7	
VanderLinde, J.	F3.8	416	Zemour, B.	M6.8	71
Vernon, R.J.	T4.4	117	Zetterer, T.	W6.3	255
Vernon, R.J.	T4.9	125	Zhang, Dengguo	F1.9	387
Vetsch, H.	Th6.5	345	Zhang, G.	Th2.5	
Vitello, P.	F4.9	431	Zhang, Lifan	M8.9	91
Vocaturro, M.	T8.11	161	Zhang, S-C.	M8.6	
von Ortenberg, Michael	W3.1	207	Zhang, S-C.	T10.7	
Wada, Mitsuo	Th6.3	342	Zhang, Z.	M8.6	
Wade, L.	F6.1		Zhang, Z.X.	M4.2	37
Wakabayashi, Y.	W3.3	211	Zhou, G.	Th2.5	
Wallace, Jack E.	Th5.8	336	Zhou, S.	M8.6	
Walsh, J.E.	T5.3	129	Zhu, W.	F3.7	
Wang, C.	F8.11	469	Zhu, W.	Th3.4	
Wang, C.Y.	W8.3	275	Zimmermann, Peter	M7.5	77
Wang, J.G.	Th8.2	362	Zu, Q.	T8.2	
Wang, Q.S.	Th4.4	320			
Wang, S.L.	W5.5	243			
Wang, Zhijiang	M8.9	91			
Watson, D.M.	M7.3				
Webb, K.J.	M6.7	69			
Wells, T.	Th2.8				
Welsh, D.	W4.2	224			
Wengler, M.J.	M7.3				
Wenzelburger, H.	Th8.9	373			
Whitbourn, L.B.	T8.7	153			
White, T.L.	T4.3	115			
Williams, G.P.	F6.11				
Williams, G.P.	F7.7				
Williams, Gwyn P.	W7.1	263			
Williams, P.	Th6.6	348			
Wiltse, J.C.	Th5.2				
Witteles, E.	F6.1				
Wolf, S.A.	W6.1	253			
Wolf, S.A.	W6.5				
Wolf, W.P.	F7.9				
Wolverton, J.	T7.5				
Woskov, P.	T4.8	123			
Woskov, P.P.	T3.1	104			
Woskov, P.P.	W2.6	205			
Wu, Zhengde	F1.9	387			
Wurtele, Jonathan S.	M4.5	41			
Xu, Jinping	M1.2	3			
Xu, Shanjia	M3.4	29			
Xu, Shanjia	W7.8	271			
Xu, Wenlan	F2.10	403			
Xu, Y.	T8.2				
Xu, Y.	W1.6	193			
Yamamoto, Junya	W3.8	219			
Yamamoto, Y.	W1.3	187			
Yamamoto, Y.	W2.5	203			
Yamanaka, M.	F3.6	414			
Yamashita, Eikichi	M6.4	65			
Yang, F-M.	M1.7				
Yang, Quanrang	Th5.7	334			
Yasojima, Y.	T10.3	177			
Yasuda, A.	T8.3	146			
Yasuda, A.	T8.4	148			
Yasumura, K.	F2.6	399			
Yazawa, Takashi	W3.8	219			
Ye, Hongjuan	F2.10	403			
Yeh, C.	W5.7				
Ying, R.	T6.1				
Yngvesson, K.S.	T7.5				
Yokoo, K.	T5.6	135			
Yokoo, K.	T5.7	137			
Yonekura, Takeshi	M3.3	27			
Yoneyama, Tsukasa	M6.6	67			
Yoshida, K.	F3.6	414			
Yoshida, Y.	F2.6	399			
Yoshimori, S.	W2.4	201			

# MILLIMETER WAVE GRID OSCILLATORS

David B. Rutledge, Zorana B. Popović, Moonil Kim

Division of Engineering and Applied Science  
California Institute of Technology  
Pasadena, Ca.

## ABSTRACT

Loading a two-dimensional grid with active devices offers a means of combining the power of solid-state oscillators in the microwave and millimeter-wave range. The grid structure allows a large number of negative resistance devices to be combined. In this approach, the combining is done in free space, and the active devices do not require an external locking signal. The loaded grid is a planar structure amenable to monolithic integration. Measurements on a 25-MESFET grid at 9.7 GHz show power-combining and frequency-locking without an external locking signal, with an ERP of 37 W. Experimental far-field patterns agree with theoretical results obtained using reciprocity.

## INTRODUCTION

Solid-state oscillators in the millimeter-wave range have limited RF powers. Kesan *et al.* [1] predict the output power of quantum-well oscillators to be about 10  $\mu$ W at 400 GHz. Since radar and imaging array applications require higher power levels, coherent power combining of a large number of solid-state devices becomes attractive. Wandinger and Nalbandian [2] proposed and demonstrated power-combining using a quasi-optical resonator with Gunn-diodes at 60 GHz. Mink [3] gave a theoretical analysis, and Stephan [4] and Mizuno *et al.* [5] demonstrated power-combining and injection-locking in a quasi-optical resonator of two and three devices. Here we demonstrate a grid loaded with GaAs microwave transistors which allows the power of a large number of devices to be combined. The approach is similar in spirit to the diode grid phase shifters, multipliers, and oscillators investigated by Lam *et al.* [6], Jou *et al.* [7], and Popović *et al.* [8]. Lam and Jou fabricated grids with 1600 Schottky diodes, and showed that the grids can be accurately modeled as a component in a simple transmission-line equivalent circuit.

## GRID OSCILLATOR

The oscillator configuration is shown in Fig. 1. This configuration is analogous to a maser, where the loaded grid, which is the active medium, is placed inside a Fabry-Perot resonator. The idea is that the active devices couple through the mode of the cavity, and self-lock. One resonator plate is a metal mirror, and the other is a partially transparent reflector (with a transmittance of 37% in our case).

Figure 2 shows a X-band model of a five-by-five active grid. Simple scaling applies for higher frequencies. The grid is fabricated on a microstrip substrate (Rogers Corporation, Duroid,  $\epsilon_r = 10.5$ , thickness 2.35 mm). The vertical lines connected to the transistor drain and gate terminals support the flow of RF currents, and the radiated electric field vec-

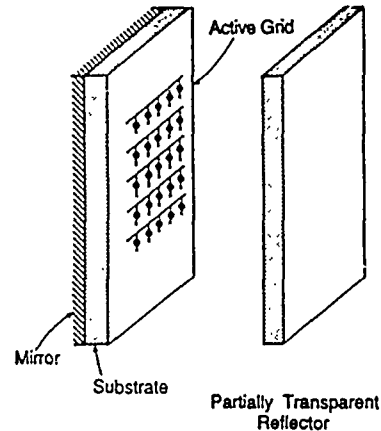


Fig. 1 Resonator configuration.

tor is parallel to them. The horizontal lines are used for DC bias. The transistors are Fujitsu FSC-11 MESFET's, and they typically produce 20 mW in single-transistor microstrip oscillator circuits. When biased at a voltage of 4 V, the transistors oscillate at a frequency of 9.7 GHz. The spacing between substrate and reflector for which the devices lock varies from 5 to 7 mm, which is about  $0.2\lambda_0$  at the oscillating frequency. Varying this spacing shifts the frequency over a 1% range, and produces large changes in the power. The largest

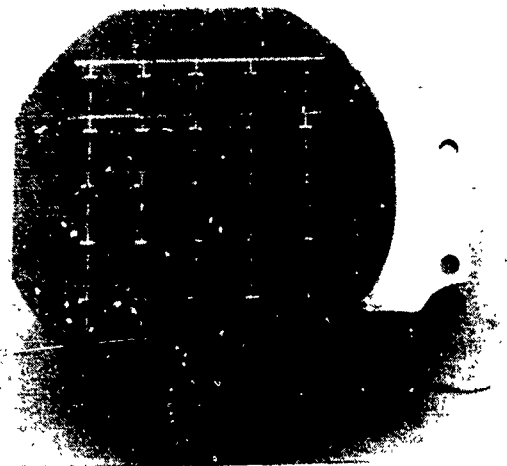


Fig. 2. Photograph of the 25-transistor oscillator grid at 9.7 GHz.

effective radiated power relative to an isotropic source (ERP) that we measured was 37 watts at a spacing of 4.8 mm. Fig. 3 shows the measured far-field pattern where the peak ERP was 20.7 watts. From the measured pattern, we can deduce the total radiated power, which is 464 mW. This is roughly 25 times the power that we typically get from a single transistor oscillator. The DC to RF conversion efficiency is 14.5%. The cross-polarized signal is 20 dB down from the peak. We noticed that the beam position can be shifted 15° by tilting the reflector.

Figure 4 shows the comparison with theory for our best E and H plane patterns. The theoretical pattern is that of an array of 25 infinitesimal current elements on an infinite dielectric sheet. It can be found by reciprocity [9]. To get the pattern for the entire array, we multiply the individual element pattern by the array factor. The theoretical and experimental patterns agree well. The substrate and reflector were not parallel, which resulted in a shift of 7° in the E-plane.

### ACKNOWLEDGEMENTS

This research was supported by the Army Research Office and the Jet Propulsion Laboratory.

### REFERENCES

- [1] V. P. Kesan, D. P. Neikirk, T. D. Linton, P. A. Blakey, B. G. Streetman, "Influence of the Transit Time Effects on the Optimum Design and Maximum Oscillation Frequency of Quantum Well Oscillators," *12th International Conference on Infrared and Millimeter Waves*, Orlando, Florida, December 1987.
- [2] L. Wandering, V. Nalbandian, "Millimeter-Wave Power Combiner Using Quasi-Optical Techniques," *IEEE Transactions on Microwave Theory and Techniques*, Vol. MTT-31, No. 2, pp. 189-193, February 1983.

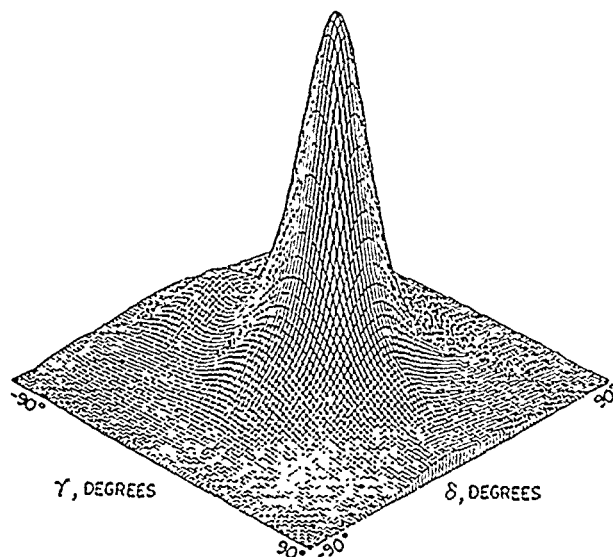


Fig. 3. Two-dimensional far-field pattern of the transistor grid. The vertical scale is linear in power, the peak ERP is 20.7 W, and the directivity is 16.4 dB.

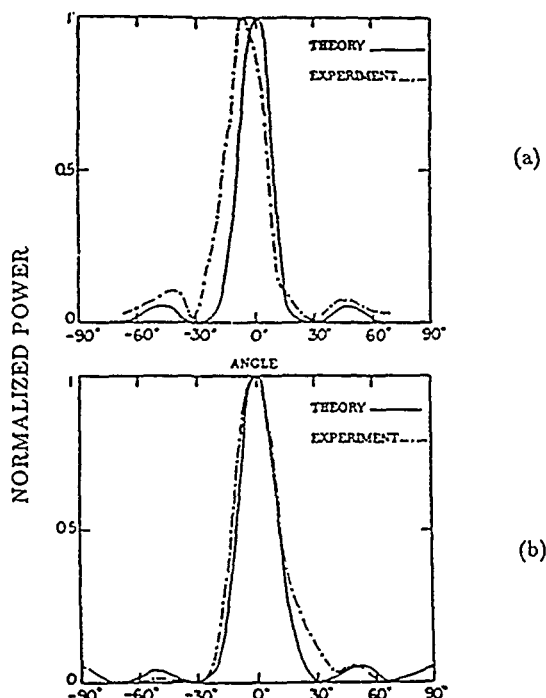


Fig. 4. (a) E-plane, (b) H-plane of transistor grid, theory and experiment. The scale is linear in power.

- [3] J. W. Mink, "Quasi-Optical Power Combining of Solid-State Millimeter-Wave Sources," *IEEE Transactions on Microwave Theory and Techniques*, Vol. MTT-34, pp. 273-279, February 1986.
- [4] K. D. Stephan, "Inter-Injection-Locked Oscillators for Power Combining and Phased Arrays," *IEEE Transactions on Microwave Theory and Techniques*, Vol. MTT-34, pp. 1017-1025, October 1986.
- [5] K. Mizuno, T. Ajikata, M. Hieda, and N. Nakayama, "Quasi-Optical Resonator for Millimeter and Submillimeter Wave Solid-state Sources," submitted for publication to *Electronics Letters*.
- [6] W. W. Lam, C. F. Jou, H. Z. Chen, K. S. Stolt, N. S. Luhmann, D. B. Rutledge, "Millimeter-Wave Diode-Grid Phase-Shifters," To be published in the *IEEE Transactions on Microwave Theory and Techniques*.
- [7] C. F. Jou, W. W. Lam, H. Z. Chen, K. S. Stolt, N. C. Luhmann, D. B. Rutledge, "Millimeter-Wave Diode-Grid Frequency Doubler," To be published in the *IEEE Transactions on Microwave Theory and Techniques*.
- [8] Z. B. Popović, D. B. Rutledge, "Diode-Grid Oscillators," 1988 *IEEE Antennas and Propagation Symposium*, Syracuse, New York, June 1988.
- [9] D. B. Rutledge, D. P. Neikirk, D. P. Kasilingam, "Integrated Circuit Antennas," *Infrared and Millimeter Waves*, vol. 10, Academic Press, 1983, pp. 1-90.
- [10] Z. B. Popović, M. Kim, D. B. Rutledge, "Grid Oscillators," *International Journal of Infrared and Millimeter Waves*, vol. 9, No. 7, pp. 647-654 July 1988.

# A FEEDBACK MODEL OF MILLIMETRE WAVE HARMONIC OSCILLATORS AND ITS APPLICATION

Jinping Xu      Sifan Li  
Southeast University  
Nanjing, P.R. China

## ABSTRACT

In this paper a feedback model of second harmonic oscillators is developed. By using describing functions of nonlinearity of active devices, the performances of second harmonic oscillators are studied. Frequency dependence of I-V characteristics of active element are taken into account. The ratio of maximum output power of second harmonic to fundamental is given. The maximum harmonic locking bandwidth of injected harmonic oscillator is derived. The theoretical prediction is compared with experimental results.

## INTRODUCTION

Millimetre wave harmonic oscillators have been studied and applied extensively in recent years. However, the theoretical study of Gunn diode harmonic oscillators is not sophisticated enough to meet the needs of its design and testing. In the theoretical circuit models established by K. Solbach [1] and R. Knöchel [2], frequency dependence of I-V characteristic of active element was not taken into account. In this paper, a feedback model of second harmonic oscillator is developed. Using describing function method, which was successfully used to analyse microwave oscillators and amplifiers [3], and taking frequency dependence of I-V characteristic of active element into account, the expressions of fundamental and harmonic voltages are obtained. Maximum power conditions and power ratio are given. Harmonic synchronization bandwidth of injected second harmonic oscillator are obtained.

## FEEDBACK MODEL OF HARMONIC OSCILLATOR

A feedback model for both fundamental and second harmonic of harmonic oscillator is established, which is partly based on the circuit model in [1]. Fig.1 shows an equivalent circuit model of a harmonic oscillator, in which  $G_1$ ,  $L_1$ ,  $C_1$  and  $G_2$ ,  $L_2$ ,  $C_2$  denote circuit parameters of fundamental and second harmonic frequency, respectively. N is a frequency-multiplexing network.  $I_{e1}$  and  $I_{e2}$  are injecting signal sources, in case of free-running state,  $I_{e1}=I_{e2}=0$ . The voltage across the active element is assumed to contain only fundamental

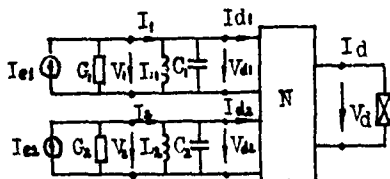


Fig.1 Equivalent circuit of harmonic oscillator

and second harmonic components, i.e.,  $v_d = v_{d1} + v_{d2}$ .

Let the resonant elements  $L_1$ ,  $C_1$  or  $L_2$ ,  $C_2$  be

treated as a coupling circuit between load conductance and active element, and it is described by voltage-current transmission matrix T. When injecting current exists,  $G_i V_i = I_{ei} - I_i$ , where  $i=1$  and  $i=2$

corresponds to fundamental and second harmonic mode, respectively. The following relation can be derived [3]

$$V_{di} = \frac{1}{G_i T_{11}(j\omega_i) + T_{21}(j\omega_i)} [I_{ei} - [G_i T_{12}(j\omega_i) + T_{22}(j\omega_i)] I_{di}] \quad (1)$$

A general feedback model of harmonic oscillator can now be established based on (1) and Fig.1, as shown in Fig.2

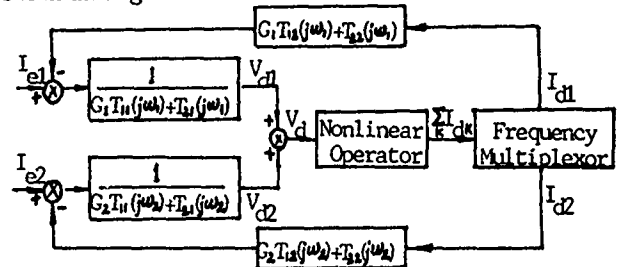


Fig.2 Feedback model of second harmonic oscillator

## DESCRIBING FUNCTIONS OF NONLINEARITY

Suppose the I-V characteristic of active device is described by

$$i_d = c_1 v_d + c_2 v_d^2 + c_3 v_d^3 \quad (2)$$

Because the active element does not possess a negative conductance when it operates at harmonic frequency, it means that the I-V characteristic of an active element does dependent on frequency. Therefore, it is more reasonable to express the coefficients  $c_j$  as  $c_j = a_j$  for fundamental frequency and  $c_j = b_j$  for harmonic frequency, where  $j=1,2,3$ .

The voltage across the active element is  $v_d = v_{d1} + v_{d2} = V_{d1} \cos \omega t + V_{d2} \cos(2\omega t + \phi)$ , where  $V_{d1}$  and  $V_{d2}$  are the amplitude of fundamental voltage and second harmonic voltage. Substituting  $v_d$  into (2), fundamental current  $i_{d1}$  and second harmonic current  $i_{d2}$  can be derived. According to definition, the describing functions for fundamental frequency  $\omega_1$  and harmonic frequency  $\omega_2$  can be obtained as follows

$$N_1 = I_{d1}/V_{d1} = a_1 + \frac{3}{4} a_3 V_{d1}^2 + \frac{3}{2} a_3 b_3 V_{d2}^2 + (a_2 b_2) V_{d2} e^{j\phi} \quad (3)$$

$$N_2 = I_{d2}/V_{d2} = b_1 + \frac{3}{2} a_3 b_3 V_{d1}^2 + \frac{3}{4} b_3 V_{d2}^2 + \frac{1}{2} a_2 V_{d1}^2 e^{j\phi} \quad (4)$$

If the nonlinear operator together with the frequency-multiplexing network is replaced by

describing function  $N_1$  and  $N_2$ , the feedback model shown in Fig.2 can be separated into two, one corresponding to fundamental circuit and the other to harmonic circuit.

#### OUTPUT POWER OF HARMONIC OSCILLATOR

If the harmonic circuit is omitted, the circuit equation for a free-running fundamental oscillator ( $I_{e1}=0$ ) is easily obtained from the separated feedback model of fundamental circuit

$$N_1 \frac{G_{12}T_{12}(j\omega_1)+T_{22}(j\omega_1)}{G_{11}T_{11}(j\omega_1)+T_{21}(j\omega_1)} + 1 = 0 \quad (5)$$

The transmission parameters of the parallel coupling circuit are  $T_{11}=1$ ,  $T_{12}=0$ ,  $T_{21}=j(\omega_1 C_1 - 1/\omega_1 L_1)$  and  $T_{22}=1$ . Substituting (3) into (5), the fundamental voltage  $V_{d1}$  is obtained in terms of  $V_{d2}$  and device parameters  $a_j$  and  $b_j$ .

If the conductance of a Gunn diode at second harmonic frequency is considered to be linear and positive, we assume  $b_2=b_3=0$ , but  $b_1>0$ . The expression of  $V_{d1}$  is reduced to

$$V_{d1}^2 = 4(-G_1 - a_1)/3a_3 \quad (6)$$

which is in agreement with that in [1].

The circuit equation of free-running harmonic oscillator is obtained from the separated feedback model of harmonic circuit. It has the same form as that of fundamental circuit except  $N_1$ ,  $G_1$  and  $\omega_1$  being replaced by  $N_2$ ,  $G_2$  and  $\omega_2$ . It can be solved to obtain

$$V_{d2} = a_2 V_{d1}^2 / 2(-b_1 - G_2) \quad (7)$$

The condition of maximum output power can then be found as  $G_1 = -a_1/2$ ,  $G_2 = b_1$ . The power ratio of harmonic to fundamental is

$$P_2/P_1 = a_2^2 / (-4a_1 b_1) \quad (8)$$

It is obvious from (7) that, the harmonic output power depends closely on nonsymmetrical coefficient  $a_2$ , and it is inversely proportional to positive conductance  $b_1$  at harmonic frequency.

As for Gunn diodes, according to reference [4], the real part of fundamental source impedance is  $R_1 = (10 \sim 50)R_0$ , where  $R_0$  is low field resistance of diode. The Gunn diodes used in harmonic oscillators at W-band in our experiment have  $R_0 \approx 0.5$  ohm. A rigorous field analysis [5] shows that, at harmonic frequency the real part of impedance of a Gunn diode mounted in a specific cavity is approximately  $(1 \sim 5)$  ohm. Combining with the condition of maximum power, we have  $b_1 = (1 \sim 5)|a_1|$ .

If the coefficients  $a_j$  are chosen to be the typical value presented in [1], then  $P_2/P_1 = (-4.26 \sim -11.25)$  dB. It shows that more than -11 dB power ratio is possible. But in [1]  $P_2/P_1$  is not high than -11 dB. It is due to neglecting the frequency dependence of I-V characteristic. In fact, the experiments done in our research institute show that a Gunn diode in a radial line-to-waveguide cavity having maximum output power 110 mW at 45 GHz, delivers 12.5 mW power at 90 GHz. Another Gunn

diode oscillator has  $P_2/P_1 = -8.37$  dB. The value of  $P_2/P_1$  of most Gunn oscillator range from -7 dB to -10 dB.

#### HARMONIC SYNCHRONIZATION

When a harmonic oscillator operates in harmonic injection locked state,  $V_{d2}$  and  $I_{e2}$  have the same frequency. The circuit equation describing the locked state is obtained from feedback model of harmonic circuit

$$N_2 \frac{G_2 T_{12}(j\omega) + T_{22}(j\omega)}{G_2 T_{11}(j\omega) + T_{21}(j\omega)} + 1 = \frac{|I_{e2}| e^{j\theta}}{|V_{d2}|} \frac{1}{G_2 T_{11}(j\omega) + T_{21}(j\omega)} \quad (9)$$

where  $\theta$  is the phase difference between  $I_{e2}$  and  $V_{d2}$ .

Let  $\nu = \omega/\omega_2 = 1 + \Delta\nu$ , where  $\omega$  is injecting frequency and  $\Delta\nu \ll 1$ . The maximum locking bandwidth is derived from (9)

$$\Delta\nu_{\max} = \frac{1}{2} \sqrt{\frac{L_2}{C_2}} \frac{|I_{e2}|}{|V_{d2}|} = \frac{1}{Q_{\text{ex2}}} \sqrt{\frac{P_i}{P_2}} \quad (10)$$

where  $Q_{\text{ex2}}$  is external quality factor of harmonic circuit,  $P_2$  is harmonic power,  $P_i$  is injected power.

Due to the high value of  $Q_{\text{ex2}}$ , the maximum locking bandwidth of a harmonic oscillator is much smaller than that of fundamental ones. Experimental result obtained at W-band is about 30 GHz [6]. Therefore, harmonic power combining, harmonic injection frequency stabilization are much more difficult. In such cases, fundamental injection locking in harmonic oscillators is preferable.

#### CONCLUSION

A general theoretical feedback circuit model is established for the first time. Voltage and current of fundamental mode and that of second harmonic mode are related by describing functions  $N_1$  and  $N_2$ . Frequency dependence of active element is taken into account. The condition for maximum power delivered to load has been investigated. High ratio of second harmonic power to fundamental power is theoretically predicted and has been proved by experiments. For second harmonic oscillators, if injection locking is needed, it is preferable to inject signal of fundamental frequency instead of harmonic frequency.

#### REFERENCES

- [1] K. Solbach, IEEE Trans., Vol.MTT-30, 1982, pp.1233-1237
- [2] R. Knöchel, et al, IEEE Trans., Vol.MTT-26, 1978, pp.939-944
- [3] L. Gustafsson, et al, IEEE Trans., Vol.MTT-20, 1972, pp.402-409
- [4] J.A. Copeland, IEEE Trans., Vol.ED-14, 1967, pp.55-58
- [5] Wei Hong and Sifan Li, "Rigorous field analysis of impedances of some millimeter wave oscillator cavities," (in this digest)
- [6] Zhong-Liang Sun, Si-Fan Li, IEEE MTT-S, Inter. Microwave Symp. Digest, 1984, pp.172-174

## Time Dependent Simulation of the Quantum Well Injection Transit Time Diode

D. R. Miller, V. P. Kesan, R. L. Rogers, C. M. Maziar, D. P. Neikirk  
Department of Electrical and Computer Engineering  
The University of Texas at Austin, Austin, Texas 78712

### Introduction:

The quantum well injection transit time (QWITT) diode is a transit time device that couples a heterojunction barrier structure as an injector with a depleted epitaxial drift region, as shown in Figure 1. The device, which was originally proposed by Kesan et al. [1], is a promising solid state source with potential for operation at the higher millimeter wave frequencies. Both large and small signal analyses of the device have shown that the specific negative resistance due to transit time effects from the drift region are on the order of, or are significantly greater than, the intrinsic negative differential negative resistance of the quantum well double barrier diode. This paper presents results of a large signal simulation which uses a full set of semiconductor time dependent transport equations, and solves self-consistently for the electric field as well as for the electron and hole populations throughout the device.

Kesan et al. [2, 3] provided the first small and large signal analyses of the QWITT structure. The analysis assumed that the carriers traverse the drift region at their saturation velocity with no diffusion. The quantum well injector was characterized by specifying its current density versus electric field relationship. For the small signal analysis only the slope of the J-E curve was used, while the large signal result assumed a more realistic J-E curve for the quantum well. Song and Pan [4] have also presented large signal analysis which includes diffusion and transient velocity effects. The transient velocity effect was attributed to a highly non-equilibrium carrier population being ejected from the quantum well into the drift region. More recently, Brown et al. [5] presented an optimized QWITT structure based on many considerations including transit time effects, and differential quantum well, spreading, and contact resistances. Since each of the semi-analytical analyses used above incorporate many simplifying assumptions, their usefulness is limited in actual device design and optimization. This is because device optimization requires proper design of the drift region electric field profile, as controlled by the doping profile in the drift region. They also cannot account for epitaxial losses, carrier generation, and other transport issues that could have an impact on the device operation.

### Analysis:

To circumvent the above limitations, it is necessary to solve the full set of semiconductor transport equations; i.e., solve Poisson's equation self consistently with some form of the Boltzmann equation. However, near the heterostructure region, quantum mechanical reflections and transmission begin to dominate carrier transport processes. This invalidates use of the semi-classical Boltzmann formalism. Past analyses of this region have relied on simple Schrödinger type models [6] or solutions to the quantum Liouville equation through the use of Wigner functions [7]. Even if these techniques accurately describe the quantum region, they completely ignore real transport issues (such as phonon scattering, impurity scattering, generation, recombination, etc.) for the vast majority of the device where the "classical" transport equations remain valid. For devices such as the QWITT, these outside regions may significantly determine overall operational characteristics. Thus, for this study we will apply the drift/diffusion formalism to the entire structure so that the drift region can be properly quantified.

The electron and hole drift/diffusion/continuity equations as well as Poisson's equations were discretized using the standard Scharfetter and Gummel methods [8]. The quantum heterostructure region was replaced with a "black box" whose transport parameters are chosen to provide an accurate description of the measured dc device behavior and are consistent with the drift/diffusion formalism. From Frensky's [7] work, it is obvious that the current through the quantum region is a function of the quantum distribution functions and the applied potential across the quantum well. However, the distribution functions are also a function of the applied potential. Thus to first order, it is natural to assume that the particle current  $J_n$  and  $J_p$  through the quantum region are given by the relationships:

$$J_n = \sigma_n(E_w) E_w \quad J_p = \sigma_p(E_w) E_w$$

where  $E_w$  is the effective electric field in the quantum well and is assumed spatially constant within the well. The quantum region electron conductance,  $\sigma_n$ , is experimentally determined from a dc J-V curve for a quantum well grown

in our laboratory. The quantum hole conductance is set to some finite small value and was included for future studies. The structure used in this simulation is shown in Figure 2. The dc IV curve was corrected for a specific contact resistance of  $10^{-5}$  ohms-cm<sup>2</sup> which was determined from independent experimental investigation. The equivalent quantum well electric field can then be related to the terminal voltage using the relationship [5]:

$$V_{\text{contact}} = x_w E_w + \frac{\epsilon_s}{2q \left( N_d - \frac{J}{q v_{\text{sat}}} \right)} E_w^2$$

where  $x_w$  is the quantum well width,  $\epsilon_s$  is the permittivity,  $q$  is the electron charge, and  $v_{\text{sat}}$  is the magnitude of the saturation velocity of the carriers. This expression is different from that found in [5] since we adjusted for free carriers in the drift region. Once the quantum well conductances were determined, a dc JV trace was computed. Agreement between the simulated and measured JV trace was excellent. Shown in Figure 3 is the measured J-V trace corrected for contact resistance with the deconvolved J-E<sub>w</sub> data.

The widths of a drift region doped n-type to  $10^{17}$  cm<sup>-3</sup> were then varied from 0Å to 2000Å and temporal calculations were performed at 100 GHz to determine the specific negative resistance. The bias point of each simulation was maintained approximately at the same J-E<sub>w</sub> point for the quantum well. This point was approximately in the middle of the differential negative resistance region. The terminal ac voltage amplitude was adjusted so that the quantum well electric field stayed in the differential negative resistance portion of the J-E<sub>w</sub> curve. This was done to allow direct comparisons with small signal analysis. The corresponding ac modulation was approximately 15% of the dc terminal voltage.

Shown in Figure 4 is a plot of specific negative resistances versus drift region length. The length was determined from the addition of the buffer region, the  $10^{17}$  cm<sup>-3</sup> drift region, and from any depleted  $10^{18}$  cm<sup>-3</sup> contact region that would provide an electric field sufficiently high to ensure the saturation velocity of carriers. Also shown in Figure 4 are the results from the small signal analysis. As can be seen, the fully self-consistent numeric simulation compares very favorably with the small signal analysis. This is an encouraging result since the numeric simulation incorporates most of the physical transport processes of the drift region. Thus, the assumptions made for the small signal analysis are valid. More importantly, it must also be noted from this figure that the transit time effects of the drift region provide a considerably higher specific negative resistance than that of a bare quantum well. This confirms the results of earlier analysis [2].

The simulated field profiles for  $10^{17}$  cm<sup>-3</sup> drift region lengths of 0Å, and 300Å, are shown in Figure 5. This figure also shows a field profile of a structure where the lightly doped  $10^{14}$  cm<sup>-3</sup> buffer region and  $10^{17}$  cm<sup>-3</sup> drift region is replaced with  $10^{18}$  cm<sup>-3</sup> doped material. We note with interest that even for the structure with  $10^{18}$  cm<sup>-3</sup> doped material adjacent to the quantum well, a portion (~100Å) of the material is depleted. This 100Å is sufficiently long that the transit time negative resistance is comparable to the intrinsic quantum well negative resistances.

### Conclusions:

In conclusion, we have developed a fully self-consistent semiconductor numerical simulation tool capable of analyzing the impact of classical transport regions on quantum well oscillator performance. We have applied this tool to understanding QWITT behavior and have found excellent agreement with previous small signal analysis. Finally, from the results presented, it is doubtful that recently reported oscillator results for heterostructure devices can be attributed solely to the intrinsic negative resistance of the quantum well. In fact, most quantum well oscillator structures reported in the literature probably exhibit significant transit time effects, and their performance is most likely due to QWITT like operation.

This work was supported by the Texas Advanced Research Program and the Joint Services Electronics Program.

## References:

1. V. Kesan, D. Neikirk, B. Streetman, P. Blakey, IEEE Electron Device Letters, Vol 8, pp. 129 (1988).
2. V. Kesan, D. Neikirk, P. Blakey, B. Streetman, T. Linton, IEEE Transaction on Electron Devices, Vol. 35, No. 4, pp. 405-413 (1988).
3. V. Kesan, T. Linton, C. Maziar, D. Neikirk, P. Blakey, B. Streetman, 1987 IEEE International Elect. Dev. Meeting Dig., pp. 63-65, Dec 6-9 (1987).
4. I. Song, D. Pan, IEEE Electron Device Letters, EDL-8, pp. 560-562 (1987).
5. E. Brown, W. Goodhue, T. Sollner, Journal of Applied Physics, Vol. 64, No. 3, (1988).
6. R. Tsu, L. Esaki, Applied Physics Letters, Vol 22, p. 562 (1973).
7. W. Frensley, Picosecond Electrons and Optoelectronics II, Springer-Verlag, Berlin, pp. 109-112 (1987).
8. D. Scharfetter, H. Gummel, IEEE Trans. Electron Devices, ED-16, pp. 64-77 (1969).

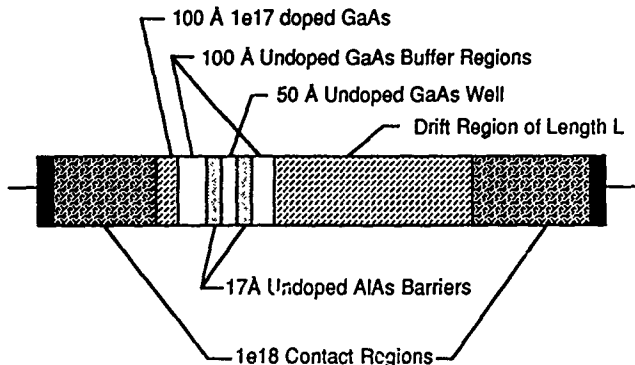


Figure 1. QWITT structure.

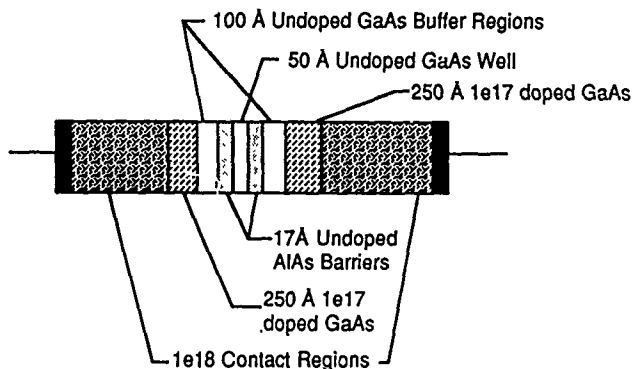
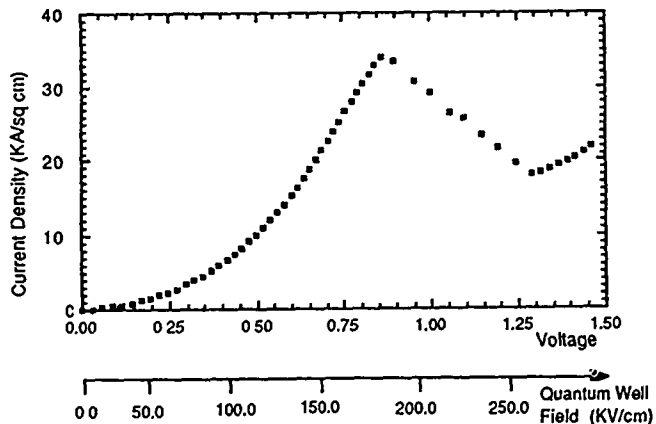
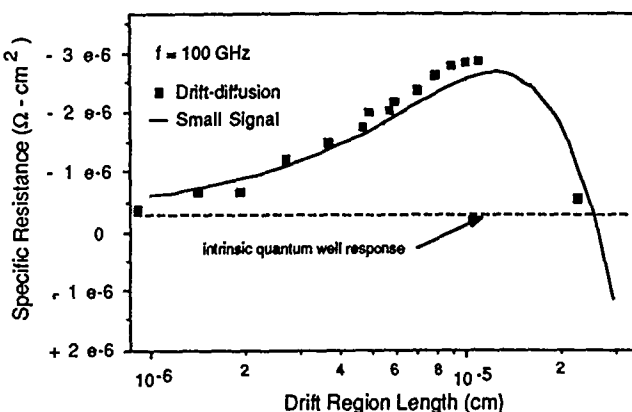
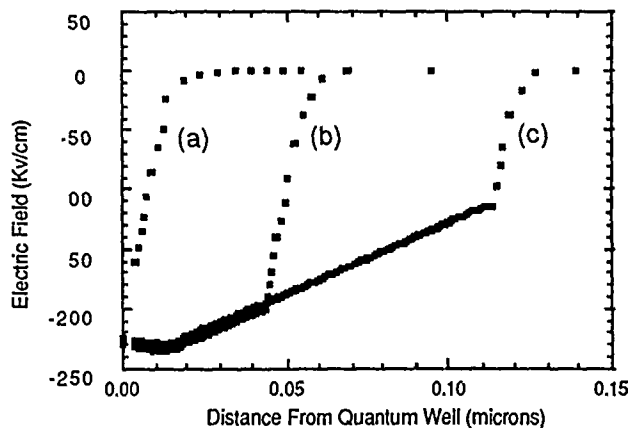
Figure 2. Structure used in obtaining the  $J-E_w$  characteristics for the simulation.Figure 3. Measured JV curve adjusted for contact resistance with the corresponding quantum well electric field  $E_w$ .

Figure 4. Specific negative resistances versus total drift region length.

Figure 5. Electric field profile at the beginning of the ac cycle with (a) no  $10^{14} \text{ cm}^{-3}$  or  $10^{17} \text{ cm}^{-3}$  layers, (b)  $100 \text{ Å}$  of  $10^{14} \text{ cm}^{-3}$  followed by  $300 \text{ Å}$  of  $10^{17} \text{ cm}^{-3}$ , and (c)  $100 \text{ Å}$  of  $10^{14} \text{ cm}^{-3}$  followed by  $1000 \text{ Å}$  of  $10^{17} \text{ cm}^{-3}$ .



# POWER COMBINING FET OSCILLATOR USING COUPLED RAMPART LINE ANTENNAS\*

Joel Birkeland and Tatsuo Itoh

Department of Electrical and Computer Engineering  
The University of Texas at Austin  
Austin, Texas 78712

## ABSTRACT

Circuits in which oscillators are integrated with antennas to form quasi-optical sources have applications in phased array radar (1), quasi-optical local oscillators (2), and a variety of obstruction detection and process control applications (3). In this paper we describe a low-cost planar oscillator circuit in which 2 FETs are coupled by microstrip rampart line antennas and operate in a push-pull power combining configuration. Prototype circuits have been constructed which operate at X-band; the same principle may be applied at higher frequencies.

## INTRODUCTION

In a previous paper we described a microstrip quasi-optical oscillator which used a single FET as the negative resistance element and a periodic microstrip patch array as a resonant element and antenna (4). In that instance the leaky-wave stopband of the antenna was used to reflect energy to the FET and sustain oscillation while simultaneously radiating in the broadside direction.

In the circuit described in the present paper, the leaky-wave resonator/antenna is formed by coupling two rampart line antennas at intervals of  $\lambda_g$  along their length. In this way the even and odd mode impedances of the coupled sections may be used to control the mode of oscillation of the two FETs.

## ANTENNA DESIGN

The microstrip rampart line antenna has been described by Hall (5). The antenna consists of sections of microstrip line connected by mitred right angle bends. For propagation directions close to broadside, the radiation may be considered to arise from a magnetic current element lying at the edge of the mitred bend. If the lengths of the lines between the bends are equal to  $\lambda_g/4$ , the radiation will be in the broadside direction, with the E field polarized perpendicular to the axis of the antenna.

In our case, two such antennas are placed side by side as shown in Figure 1. In this case it can be seen that the antenna will radiate in the broadside direction if it is excited in the odd mode, that is, with the voltages at ports one and two 180 degrees out of phase.

The coupled sections exhibit even and odd mode impedances,  $Z_{0e}$  and  $Z_{0o}$ , which are dependent on the width and spacing of the lines. If we choose  $Z_{0o} < Z_0$  and  $Z_{0e} = Z_0$ , then reflective stopbands will exist in the odd mode due to the periodic impedance variations, but none will occur in the even mode. This is the configuration that we use. In addition, the widths and spacings of the coupled sections may be varied for each section to alter the shape of the stopband.

When this type of antenna is operated in the leaky-wave stopband, the total field radiated from the mitred bends at the terminated end is shifted in phase from that at the feed end, thereby moving the radiated beam a few degrees off from the broadside direction. This effect is diminished as the antenna length is increased.

## CIRCUIT CONFIGURATION

A schematic view of the oscillator is shown in Figure 2. The FETs are connected to the coupled antennas in a symmetric fashion as shown. The operation of the circuit may be understood in the following way:

Since the circuit is symmetric, we may consider separately the even and odd modes of operation. In the odd mode, (at the frequency of oscillation), the coupled antenna appears as a transmission line of impedance  $Z_0$  which is periodically loaded with sections of impedance  $Z_{0o} < Z_0$ , hence it presents a large return loss to the FET. By adjusting the lengths of the open circuit microstrip lines on the FETs, we can satisfy the oscillation condition for the device. Conversely, in the even mode, the impedances of the coupled sections are  $Z_{0e} = Z_0$ , therefore the drains of the FETs are effectively terminated in 50  $\Omega$ . This causes the FETs to operate in a more stable region than in the odd mode case. In this way we force the FETs to oscillate in the odd mode.

Finally, it is necessary to insure that the circuit will oscillate only at the desired operating frequency. For this reason, it may be necessary to add resistive elements to the circuit to remove any unwanted instabilities.

## CIRCUIT CONSTRUCTION

The X-band prototype circuits were fabricated using .020 inch thick Rogers Duroid 5880, with a relative dielectric constant of 2.2. The FETs used were NEC 710 packaged devices, which were soldered in place.

The electrical design was performed using the FET small signal parameters and Touchstone microwave CAD program available from EEsof, Inc., of Westlake Village, CA. The design frequency was 10 GHz; the actual measured oscillation frequency was 9.5 GHz. Most likely the difference between the predicted and actual values was due to the error introduced by neglecting the nonlinear behaviour of the FETs as well as uncertainties in the electrical lengths of the rampart line mitred bends.

The measured radiation patterns in the principle planes are shown in Figures 3 and 4. The one sided 3dB beamwidths are 10 degrees in the H-plane and 38 degrees in the E-plane. The maximum cross polarization level is more than 20 dB below the main beam level. The lobes in the E-plane pattern are most likely due to finite ground plane effects.

As a measure of the overall efficiency of the quasi-optical source, we define the isotropic conversion gain as the ratio of radiated power in a particular direction to that of an isotropic source which converts dc power to rf at 100% efficiency. For this device we measure 6.1 dB isotropic conversion gain.

## CONCLUSION

We have described a quasi-optical power combining push-pull GaAsFET oscillator using coupled microstrip antennas. X-band prototypes have exhibited good isotropic conversion gain in a simple low-cost planar circuit. The prototype design may be scaled to higher frequencies.

## REFERENCES

- (1) K.D. Stephan, "Inter-injection-locked oscillators for power

\* This work was supported by the Texas Advanced Technology Program and the U.S. Army Research Office, contract no. DAAL03-88-K-0005

combining and phased arrays," *IEEE Trans. Microwave Theory Tech.*, vol. MTT-34, pp. 1017-1025, Oct. 1986.

- (2) K. Stephan, N. Camilleri, and T. Itoh, "A quasi-optical polarization duplexed balanced mixer for millimeter-wave applications," *IEEE Trans. Microwave Theory Tech.*, vol. MTT-31, pp. 164-170, Feb. 1987.
- (3) Alpha Industries, Inc., Semiconductor Division, Woburn, MA, *Microwave Sensing Modules and Sources*, Publication Number 50050200, 1987.
- (4) J. Birkeland and T. Itoh, "An integrated planar oscillator using a microstrip leaky-wave resonator/antenna," *18th Europ. Microwave Conf. Proc.*, Stockholm, September 1988.
- (5) P.S. Hall, "Microstrip linear array with polarization control," *IEE Proc.*, vol. 130, part H, no. 3, April 1983.

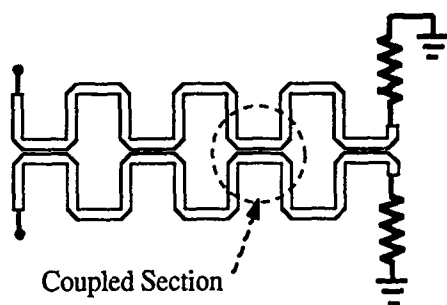


Figure 1. Four section coupled rampart line antenna.

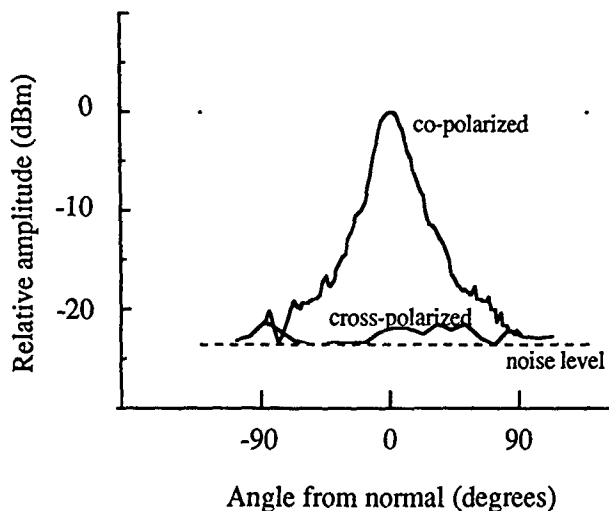


Figure 3. H-plane antenna pattern.

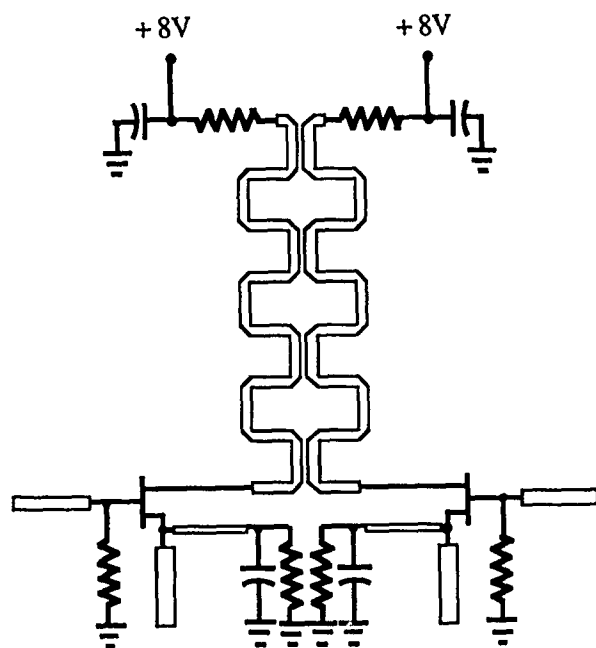


Figure 2. Schematic view of Oscillator Circuit

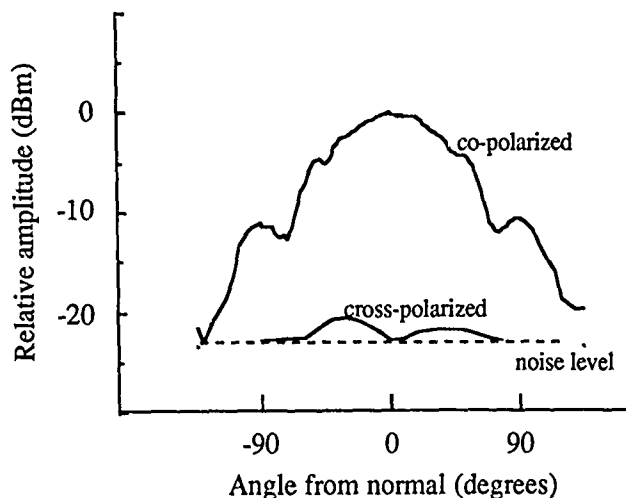


Figure 4. E-plane antenna pattern.

## A 94/47GHz FREQUENCY HALVER USING A GA AS GUNN-DEVICE

Helmut Barth

AEG Aktiengesellschaft  
Sedanstrasse 10/Postbox 1730  
7900 Ulm/F.R.Germany

## INTRODUCTION

Basically, frequency division is possible by synchronizing a harmonic mode oscillator at its harmonic frequency  $f_H$  while coupling out the fundamental frequency  $f_F$ . However, the very high virtually external Q-factor ( $>1000$  c.o. [1]) of standard type harmonic mode oscillators limits the bandwidth of operation to only a few hundred MHz at moderate input power levels.

This paper describes the application of an specifically tuned 2nd harmonic mode oscillator as a frequency halver showing a relatively large synchronisation bandwidth of 5GHz respectively 2.5GHz centered around 94GHz respectively 47GHz.

## BASIC PRINCIPLES

This broadband mode of operation occurs under the following conditions:

1. The bias voltage is slightly below threshold of the Gunn-device, the incident RF-power causes an additional voltage across the device exceeding the threshold-voltage (Fig.1). Hence, a dipole-domain arises and starts drifting through the crystal. Once a domain exists no other can be generated until the present domain has reached the anode of the Gunn-device after the transit time  $T_t$ . Here, the domain decays inducing a steep current rise [2]. The voltage across the device is now below threshold and the next domain arises (inducing a steep current drop) not till then the RF-voltage exceeds the threshold once more.

Consequently, only each second RF-cycle is causing a current pulse: the period of the resulting output current is twice the period of the input signal.

This so triggered (or primed) Gunn-oscillator is comparable to a frequency divider using a monostable multivibrator having a hold time of  $T_t$ . This mode of operation was proposed by Bosch and Pollmann in 1973 ([3]).

2. The bias voltage is adjusted above threshold. Hence, normal oscillator mode takes place. Now, the incident RF-voltage lowers the voltage across the device to a level below threshold. Between  $t_1$  and  $t_2$  (c.f. Fig. 2) no domain can arise. Then, -at  $t_2$ - the threshold voltage will be exceeded, a domain arises, travels through the crystal

and finally reaches the anode at  $t_3$  after the transit time  $T_t$ . Again, the RF-voltage hinders the generation of another domain until -at  $t_4$ - the threshold will be exceeded once again.

Consequently, one of two cycles of the RF-voltage has less influence on the current: it oscillates with half the incident frequency  $f_H/2$ .

This mode is adequate to the common "delayed domain mode" caused by tuning the resonator of a fundamental mode oscillator to frequencies lower than the transit frequency  $f_t$  of the Gunn-device.

Frequency halving occurs in both cases only in a frequency window, where

$$(2-d) \cdot f_t < f_H < 2 \cdot f_t$$

is valid. Herein, the domain delay is denoted by  $d = \Delta t \cdot f_H$  (refer Fig.2). It ranges between 0 and .5 and depends -as Fig.2 shows- on bias voltage, input power and circuit tuning. The input power level should not be too high to prevent quenching of drifting domains before they have arrived at the anode.

However, both modes are overlapping and not very critical about bias voltage.

## SET UP

The set up of the frequency halver is shown in Fig.3. The Q-Band (40-60GHz) waveguide of the oscillator mount supports both the fundamental frequency  $f_F$  and the harmonic frequency  $f_H = 2 \cdot f_F$ . The W-Band (75-110GHz) waveguide, where the input power is incident, totally reflects the fundamental wave. Hence the free running frequency of the oscillator is determined by the distance between the Q-R-Band interface and the device. It can be tuned by spacer 1.

A resonant iris [3] at the output port is used to stop the input wave ( $2 \cdot f_F$ ) but to pass the fundamental wave ( $f_F$ ). It has an insertion loss of .5dB at  $f_F$  and of  $\approx 25$ dB at  $f_H$ . The distance between device and iris is adjustable by spacer 2 to optimize the voltage swing across the device caused by the incident synchronisation power and the generated fundamental wave.

## RESULTS

Transit frequency of the device	$\approx 55\text{GHz}$
Input power (at $f_H$ )	$\approx 1\text{mW}$
Output power (at $f_F$ )	$\approx 50\text{mW}$
Conversion gain	$\approx 17\text{dB}$

The noise-to-carrier ratio (phase noise) at  $f_F=47\text{GHz}$  was measured to be 6dB lower than that of the input signal at  $f_H=94\text{GHz}$  (shown in Fig.4). The bandwidth of this frequency halver was found to be  $5\text{GHz}/2.5\text{GHz}$  centered around  $94\text{GHz}/47\text{GHz}$ .

## CONCLUSION

The basic principles and the set up of a new frequency halver for millimeter-wave applications are discussed briefly. A GaAs Gunn-device is used acting like a monostable multivibrator having a hold time adequate to the domain transit time of the device. An input power of about  $1\text{mW}$  is sufficient to achieve a bandwidth of  $5\text{GHz}$  respectively  $2.5\text{GHz}$  centered at  $94\text{GHz}$  respectively  $47\text{GHz}$ . An output power of  $50\text{mW}$  is generated. Thus, the frequency halver offers a conversion gain of  $17\text{dB}$ .

Possible applications are (i.e.):

- <> Frequency processing in mm-wave radars
- <> Bandcompression in surveillance receivers
- <> PLL's
- <> Frequency synthesizers
- <> Gigabit logics
- <> Counters

## References

- [1] Barth, H.: A Wideband, backshorttunable 2nd harmonic W-band oscillator. Conf. digest IEEE MTT-S 1981, pp 334-338
- [2] Warner, F.L.: Extension of the Gunn-effect theorie given by Robson and Mahrous. Electronics Letters, July 1966 Vol.2 No.7
- [3] Bosch, B.G.: Gunn-Effekt Elektronik. Die Telefunkenröhre, Heft 47 (1967)
- [4] Barth, H.: A high Q cavity stabilized Gunn-oscillator at  $94\text{GHz}$ . Conf. digest IEEE MTT-S 1986, pp 179-182

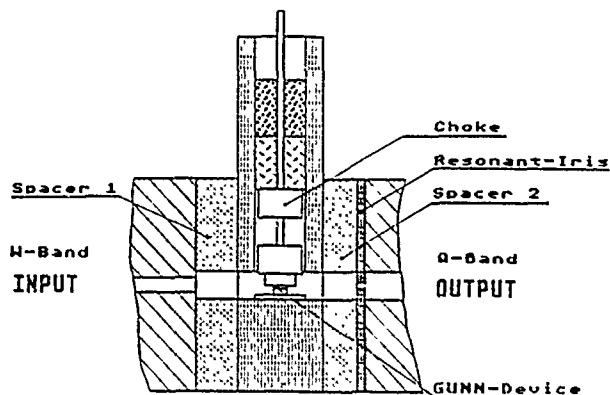


Fig.3 : Set-up of the frequency halver

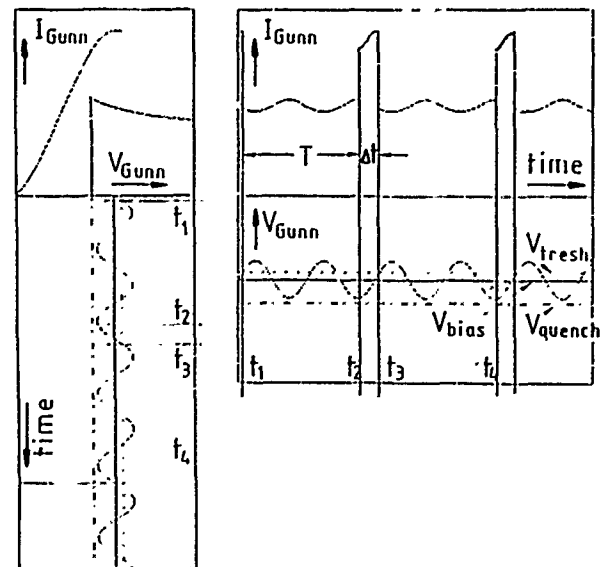


Fig.1 : Harmonically primed Gunn-oscillator

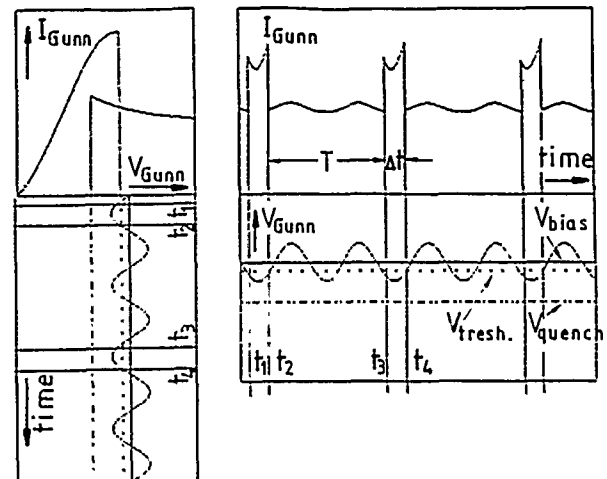


Fig.2 : Harmonically delayed Gunn-oscillator

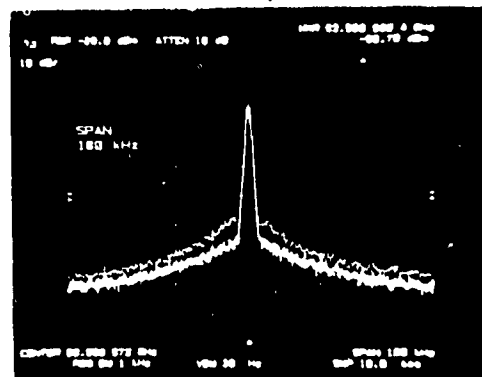


Fig.4 : Input-and output-spectra of the frequency halver

ve t. = 10dB/div ; span = 100 KHz  
br. ht curve : fundamental output  
weak curve : harmonic input

## PARAMETRIC ANALYSIS OF GaInAs DEVICES FOR MM-WAVE APPLICATIONS

A.R. JHA, TECHNICAL DIRECTOR

JHA TECHNICAL CONSULTING SERVICES  
12354 Charlwood Street  
Cerritos, CA 90701

### ABSTRACT

Metal-Insulator-Semiconductor FETs (MISFETs) when fabricated from GaInAs semiconductor material offer significant performance improvement at mm-wave frequencies. Higher electron velocity, power-added efficiency, device stability, transconductance and resistance to ionizing radiation are the outstanding features of these devices. Significant improvements in gain-bandwidth product, AM/PM performance, and third-order intermodulation distortion make GaInAs devices attractive for communication and radar equipment.

### INTRODUCTION

Low noise and high gain microwave devices are desirable for millimeter wave radars, radiometric sensors, and Electronic Support Measures (ESM) receivers. Theoretical studies performed indicate that MISFET devices have potential applications in mm-wave systems. It is important to mention that high electron mobility, saturation electron velocity, and transconductance of the MISFETs can provide low noise, high gain, and high power-added efficiency in mm-wave regions.

This paper identifies principal advantages and unique performance characteristics of the MISFETs based on peak drift electron velocity and advanced transport theory. The studies performed indicate that MISFET fabricated from GaInAs semiconductor material will yield excellent performance in mm-wave regions. The studies further indicate that such devices will be found potentially superior in some respects to conventional GaAs power MESFETs. Preliminary computations reveal that a MISFET with 1 micron gate length and fabricated with a self-aligned-gate process can deliver power output about 900 mw @ 4 GHz, 450 mw @ 12 GHz, 400 mw @ 20 GHz and 180 mw @ 35 GHz, with power-added efficiencies of 55, 42, 29, and 15 percent, respectively. However, at lower power levels, power-added efficiencies as high as 66, 58, 35, and 18 percent, respectively, are possible. The devices show high resistance to large doses of ionizing radiation (about  $10^8$  rad). Properties of potential materials that can be used in fabrication of MISFET devices are shown in Table 1. Note the average drift velocity ( $\bar{v}$ ) is directly proportional to transit time ( $t$ ). Furthermore, small transit time will yield large drift velocity, and, consequently, high device gain. Note higher electron drift velocity and small gate length will yield higher cutoff frequencies, and, thus higher device gain. The performance behavior of GaInAs compound improves significantly compared with GaAs and InP compounds, as the device gate length decreases. It is important to mention that the intrinsic properties of GaInAs compound

such as low-field mobility, peak drift velocity and intervalley separation are higher than those for GaAs, thereby making it most ideal compound for fabrication of MISFET devices. The metal-insulator-semiconductor (MIS) provides independent optimization of channel doping, high gate-to-drain breakdown voltage, and higher current swings, which are responsible for improved power output density. The RF performance of a MISFET is inherently more linear than a conventional MESFET device, because of nearly constant transconductance and input capacitance of the MIS gate, irrespective of the RF drive.

### DEVICE CONFIGURATION AND FABRICATION

The cross-section of a MISFET<sup>2</sup> device using the self-aligned-gate construction<sup>2</sup> technique is shown in Figure 1. The device shown uses GaInAs compound as a fabrication material instead of conventional GaAs compound. This device configuration provides full-gate structure with minimum parasitic capacitances and drain current drift, which are considered the principal requirements for optimum microwave performance. GaInAs and Si InP are the important compounds and widely used in fabrication of MISFETs. The MISFET process used SiO<sub>2</sub> deposited at low temperature as the gate insulator and self-aligned-gate approach to minimize gate-overlap capacitances that impair RF performance, and at the same time retains a full-gate structure for satisfactory device stability. The starting wafer consists of an Si InP substrate with n- and n+ GaInAs layers grown by the vapor-phase-epitaxy (VPE) technique. After mesa etching to isolate the devices, the source and drain contact metalization (Ti/Pt/Au) is deposited and defined using lift-off techniques. The channel recess is defined with photoresist, and the recess is etched until the required drain current is obtained. SiO<sub>2</sub> is then deposited, which is immediately followed by the deposition of the Gate metalization (Ti/Pt/Au). After lift-off, the wafer is annealed, because annealing improves the already very low source and drain contact resistance. Gold plating of source posts and bridges for flip-chip mounting completes the fabrication process. The gate length of the MISFET is nominally 1 micron and the devices have a four-gate stripe geometry.

### MISFET PERFORMANCE CAPABILITY

The I-V characteristics of a typical GaInAs MISFET device with gate length of 1 micron, gate width of 600 microns and gate oxide layer of 0.05 micron yield a maximum frequency of oscillation around 45 GHz, transconductance of 171 ms, average carrier velocity of about  $4.2 \times 10^7$  cm/sec and transit time of less than 3 picoseconds. The predicted performance parameters of the device are summarized in Table 2. The device with a flip-flop structure provides the lowest thermal resistance and source inductance, both necessary for high power density and power-added efficiency. Maximum available gain (MAG) versus frequency for a MISFET, standard HEMT and pseudomorphic HEMT is shown in Figure 2. Note the MISFET performance falls between a standard HEMT and pseudomorphic HEMT (or MODFET). Recent research and development

activities indicate that a heterostructure-gated SIFET fabricated with InGaAs gate, InAlAs barrier, InGaAs channel and InP substrate seems to yield a peak intrinsic transconductance of about 325 ms/mm and drift velocity greater than  $4 \times 10^7$  cm/sec. (Figure 3). with moderate gate lengths.

### SUMMARY

GaInAs MISFET devices with moderate gate lengths yield high gain, improved power-added efficiency and enhanced power density in mm-wave regions. The fabrication cost of a MISFET device with gate lengths varying from 1 to 2 micron will be substantially lower than that for submicron FETs or HEMTs, which normally require gate lengths between 0.25 to 0.5 micron. GaInAs MISFET devices are superior to GaAs MESFETs for high power mm-wave amplifier applications due to higher current swings, power output density, and power-added efficiency. The MISFETs show an improvement of 12 to 13 dB in the third-order intermodulation distortion over MESFETs. Significant improvements in performance can be achieved by applying submicron gates to GaInAs MISFETs. Further research into characteristics of the semiconductor/insulator interface should result in considerable improvements to device stability.

### ACKNOWLEDGEMENT

The author is grateful to Miss Sarita Jha and Miss Vineeta Jha for computations of performance parameters and to Miss Rashmi Kumar for typing and editing.

### REFERENCES

1. Gardner, P.D., "GaInAs MISFETs Show Promise in Power Applications," Microwave and RF, January 1988, page 99.
2. Cappy, A. and others, "Comparative Potential Performance of Si, GaAs, GaInAs, InP Submicrometer-Gate FETs," IEEE Transactions on Electron Devices, Vol. ED-27, No. 11, November 1980, page 2158.

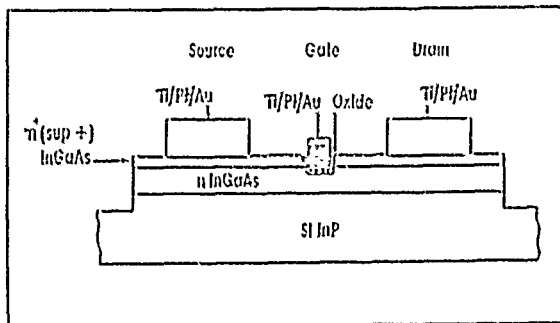


FIGURE 1 CROSS-SECTION OF THE MISFET SHOWING THE SELF-ALIGNED-GATE CONSTRUCTION OF THE DEVICE

TABLE 1

Semiconductor Compound	Energy Gap (eV)	Ave. Drift velocity (cm/sec)	Electron Mobility ( $\text{cm}^2/\text{V}\cdot\text{s}$ )
GaAs	1.42	$1.8 \times 10^7$	4,600
InP	1.35	$2.4 \times 10^7$	2,800
GaInAs	0.78	$2.1 \times 10^7$	7,800
InAs	0.35	$3.5 \times 10^7$	16,000
REMARKS	The average velocity, $v = L_g / \tau$		

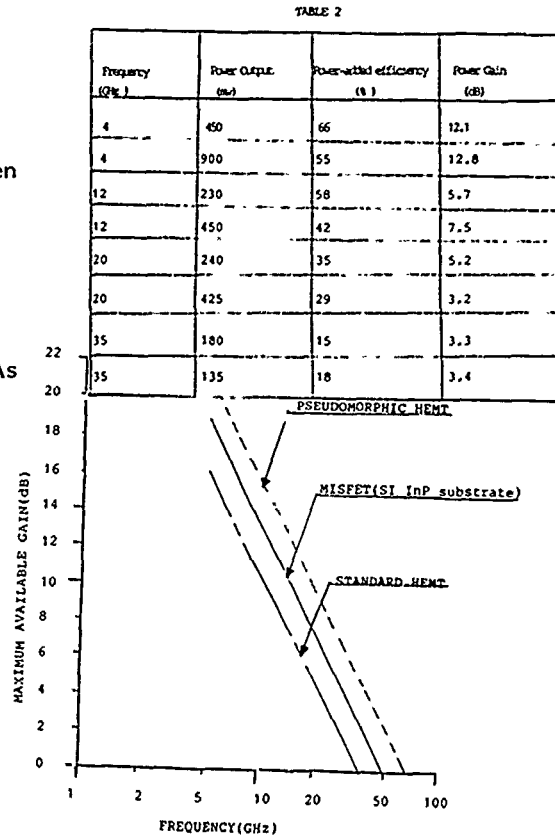


FIGURE 2 MAXIMUM AVAILABLE GAIN FOR VARIOUS DEVICES

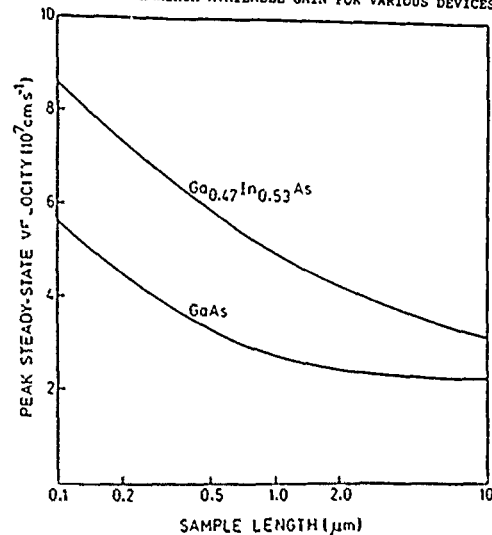


FIGURE 3 DRIFT VELOCITY FOR MISFET CHANNEL MATERIALS AS A FUNCTION OF GATE LENGTH

## Advanced Lightwave Technology - Very large Capacity Optical Coherent Communications

Kiyoshi Nosu, NTT Laboratories, 1-2356 Take, Yokosuka-shi, Kanagawa-ken, Japan 238-03

**ABSTRACT** Attempts are recommencing, after a ten year dormancy, to use lightwaves in as sophisticated manner as that in which radio waves are used. Technologies previously developed for radio wave systems are now being transferred to high speed/large capacity advanced lightwave communications. This paper reviews key technologies for advanced lightwave communications, especially optical heterodyne/homodyne detection and optical FDM (frequency division multiplexing).

**1. INTRODUCTION** Almost one hundred years have passed since Marconi invented radio communication, and about thirty years have passed since the invention of the laser. Present practical fiber optic communication systems convey information by changing optical "power". In other words, present optical communications are at the level of spark discharge radio communications in the 1890'.

With the recent development of coherent light sources, more sophisticated communication technologies which utilize the very large bandwidth potential of optical carriers are becoming feasible<sup>(1)-(4)</sup>. Advanced lightwave technologies using coherent light sources have potential for constructing large capacity communication systems, breaking through the present barrier of incoherent light communication performance. There are two ways to improve transmission capacity: (1) high speed transmission - time division multiplexing, and (2) multi-channel optical transmission - optical frequency division multiplexing. A key technology in high-speed transmission is optical heterodyne detection, and a key technology in optical multiplexing transmission is optical frequency division multiplexing (optical FDM). This paper describes the present state and perspectives of these advanced lightwave technologies.

**2. HETERODYNE DETECTION TECHNOLOGY** A block diagram of a communication system using heterodyne detection is shown in Fig.1. Figure 2 shows theoretical estimations of high speed transmission system repeater spans. The combination of FSK or PSK modulation and optical heterodyne detection permits significantly improved sensitivity, improved by more than 15dB over conventional direct detection.

As shown in Fig. 2, the direct detection system transmission speed is limited by fiber chromatic dispersion, while, in a heterodyne detection, optical signal waveform distortion due to fiber chromatic dispersion can be compensated for by an electrical delay equalizer in an electrical IF band. Accordingly, it is anticipated that heterodyne detection technology will be used not only for long-haul transmission but also for high-speed transmission and dense multiplexing transmission systems, although heterodyne detection employs sophisticated devices such as narrow spectrum lasers, broadband IF circuits etc..

Major research topics for high speed heterodyne detection systems are shown in Fig.3. Among them, broadband receiver electrical IF circuits, broadband photodetectors and their integration technology (OEIC) are most significant because heterodyne receiver's bandwidth must be about twice that of a direct detection receiver.

**3. OPTICAL FDM TECHNOLOGY** The schematic configuration of an optical FDM system is shown in Fig. 4. Frequency utilization efficiencies of optical multiplexing systems and radio systems are shown in Fig. 5.

Two technologies are important for optical FDM. One is multiplexing and demultiplexing of optical carrier waves with GHz-order intervals. The filter configurations developed for microwaves or millimeter waves, such as periodic filters (Mach-Zehnder interferometers) and ring resonators, are now being applied to FDM systems<sup>(5)</sup>. At present, the most promising is a planar waveguide periodic filter. The other key technology is light source frequency stabilization<sup>(5)-(6)</sup>. Thermally stabilized etalon and ring resonators are utilized as optical frequency references. A more accurate frequency references are atomic absorption lines of gases. Although LD frequency deviation of less than 1MHz has been achieved, frequency stabilization of a number of optical sources is an item for further research.

Nonlinear optical effects such as four-wave mixing in optical fiber and optical amplifiers cause interference waves<sup>(7)</sup>. These characteristics must be taken into account in designing systems. Figure 6 summarizes the major research topics for optical multiplexing with a large number channels.

**Acknowledgment** The authors would like to express their thanks to Drs. Sadakuni Shimada and Hidetoshi Kimura, NTT Laboratories, for their guidance on coherent lightwave transmission system research.

**REFERENCES** (1) Y. Yamamoto and T. Kimura, IEEE J. of QE, QE-17, 6, pp.919-941 (1981). (2) T. Okoshi, IEEE J. of LT, LT-2, 4, pp.341-346 (1984). (3) K. Iwashita et al. OFC 88, PD-15 (1988). (4) K. Emura et al., Elect. Lett., 22, 21, pp.1096-1097 (1986). (5) H. Toba et al., IEEE J. of SAC, SAC-4, 9, pp.1458-1467 (1986). (6) R. J. Bachus et al., Elect. Lett., 22, 19, pp.1002-1003 (1986). (7) N. Shibata et al., Electron. Lett., 23, p.675 (1986).

Figure 1. Optical heterodyne/homodyne detection system configuration.

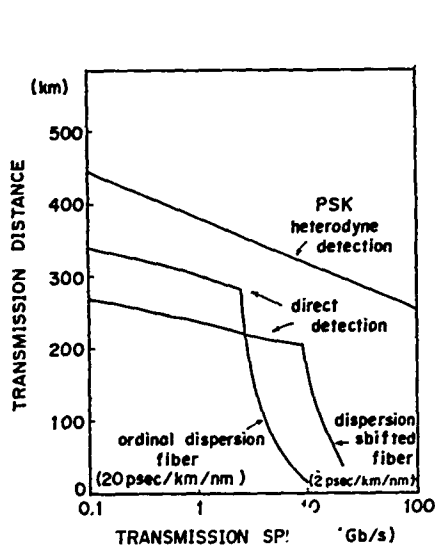
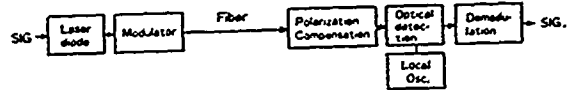


Figure 2. Repeaterless transmission distance of high-speed systems.

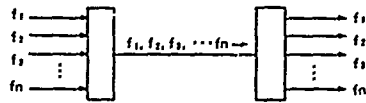


Figure 4. Optical FDM system configuration.

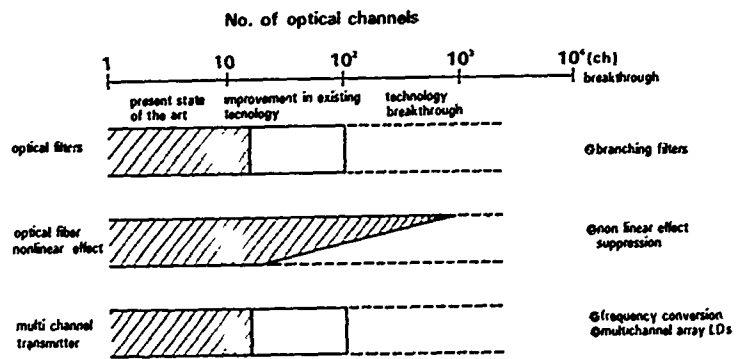


Figure 3. Factors limiting high-speed transmission.

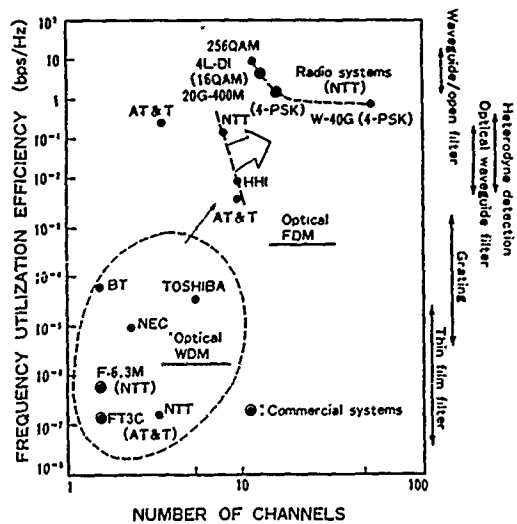
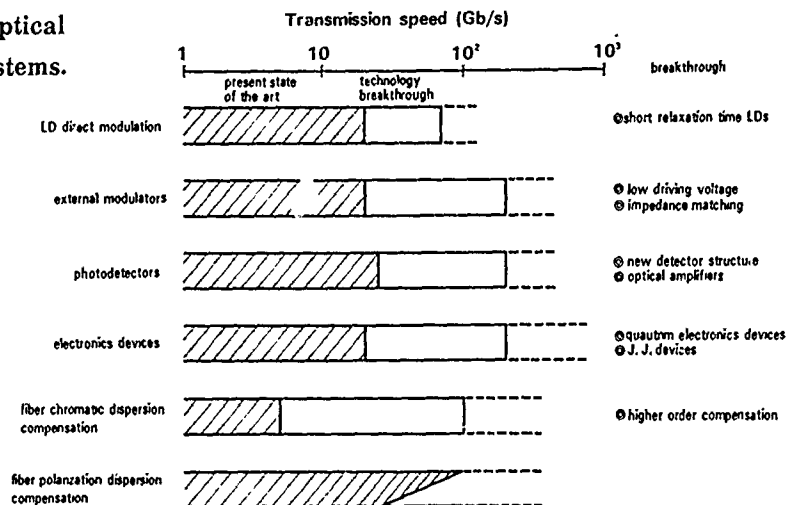


Figure 5. Performances of optical multiplexing systems.

Figure 6. Factors limiting optical multi-channel systems.





## MICROWAVE MODULATION OF LIGHT

Tadasi Sueta

Department of Electrical Engineering  
Osaka University  
Toyonaka-Shi, Osaka 560, Japan

### Abstract

High-speed or wide-band light modulators are described. It is shown that high-performance microwave light modulators are realized with the optical guided-wave structure and traveling-wave type operation. The integration of high-performance modulators is also discussed. Other topics include the efficient light modulation at millimeter-wave frequencies and the generation of extremely broad optical sideband (0.64 THz) by a microwave light modulator.

### Introduction

A natural advantage of the light wave is in its potentially large bandwidth or ultrafast property. In that respect, the modulation of light at microwave or millimeter-wave frequencies is one of the most important techniques in the optical electronics, and has attracted considerable attention.

### Guided-Wave Light Modulators

The introduction of waveguide techniques to coherent optical devices is the natural extension of successful microwave waveguide technology. Since the concept of optical guided-wave devices was introduced at the end of 1960's, various waveguide modulators have been demonstrated [1-2].

For ordinary bulk type electrooptic modulator, the  $P/\Delta f$  (i.e., modulating power/bandwidth) figure was the order of several mW/MHz due to the inevitable diffraction effect. With the guided-wave type scheme, this limitation was removed and the modulation efficiency was remarkably improved to several mW/GHz [3]. However, the bandwidth was not very large due to the capacitance of the modulator.

To increase the modulating frequency to the microwave region, we introduced the traveling-wave mode of operation for the guided-wave modulator, and showed that, in the case of  $\text{LiNbO}_3$ , this type of operation would give three-times efficient modulation even with the velocity mismatching between light and modulating waves. The first experimental phase modulator based on this concept proved the expected modulation frequency range from DC to 7.5 GHz [4].

For the first model the symmetrical coplanar strip line was used as electrodes/transmission line. Frequency characteristic, however, over such a wide range was not good due to the discontinuities at the

connecting points of electrodes and input/output coaxial lines. The use of asymmetric coplanar strip line reduced considerably this effect, thereby producing the smooth modulation characteristics [5]. Later the three-electrode coplanar line was also introduced as an effective electrodes [6].

While the scheme for the phase modulator is straightforward, there are different methods for the intensity modulator/switch. Of these, the directional coupler and push-pull interferometer types, as shown in Fig. 1, are promising for the high-speed and efficient modulation.

The maximum modulation frequency of the traveling-wave type modulator is limited by the velocity mismatching between light and microwave. In case of the ordinary  $\text{LiNbO}_3$  guided-wave modulator the product of maximum frequency  $f_m$  and length  $L$  is approximately given by

$$f_m \cdot L = 6.7 \text{ [GHz} \cdot \text{cm]} \quad (1)$$

It means that the modulator length should be reduced in order to obtain the large bandwidth. But with the shorter length the larger modulation power is required. Several methods for reducing the velocity mismatching have been proposed. In most cases, however, the larger modulating power is required in exchange of the bandwidth. Until now 24 GHz bandwidth [7] and 1.5 mW/GHz  $P/\Delta f$  at 633 nm [8] were achieved.

### Integration of High-Speed Light Modulators

Integration of high-speed modulators is interesting for applications. Only few examples, however, have been reported because of difficulties in integration. The first successful example is an SSB (single-sideband) modulator/frequency-shifter which is constructed by integrating two push-pull interferometer modulators and three optical phase shifters on a  $\text{LiNbO}_3$  substrate [9]. Frequency shift of 2 GHz for 633 nm light wave was observed in the experiment.

Another interesting example is a 1x4 optical switch array composed of three high-speed modulators as shown in Fig. 2 [10]. The basic operation of the array as a gigabit-rate time demultiplexer was experimentally confirmed.

### Resonant-Electrode Guided-Wave Modulator: An Efficient Millimeter-Wave Light Modulator

As seen from Eq. (1), if the modulation

at millimeter waves is desired, the length for the traveling-wave type modulator should be reduced to a few millimeters. As a result the modulating power reaches an impracticable level.

Recently a novel modulator with a resonant electrode structure was proposed and experimentally demonstrated at the modulation frequency of 35 GHz [11]. Unlike traveling-wave type modulators the present one works within certain frequency bands around its resonant frequencies. Although the bandwidth is limited to 5 GHz, the phase modulation of 0.76 rad was obtained with the modulating power of only 220 mW. This is perhaps the first millimeter wave light modulator workable at the realistic power level. Fig.3 shows the structure of the modulator and an example of the optical spectrum of the phase-modulated light measured by a scanning Fabry-Perot interferometer.

#### Generation of Extremely Broad Optical Sideband

The wideband modulation is a natural way to obtain widely spread optical sidebands. An alternate approach is to make use of the deep modulation. If a continuous light wave is phase modulated by a sinusoidal microwave signal of the frequency  $f_m$ , the spectral width of the modulated light is approximately given by

$$\Delta f = 2 f_m \cdot \Delta\theta \quad (2)$$

where  $\Delta\theta$  is the depth of phase modulation. A specially made  $\text{LiTaO}_3$  bulk-type two-stage modulator was used to modulate 514.5 nm light beam. A 9.35 GHz pulsed magnetron was used as a modulating source. Fig.4 shows an example of the measured optical spectrum, from which the modulation depth is estimated as 34 rad [12]. The observed spectral width of 640 GHz is one of the widest reported with the electrooptic method.

#### Conclusion

Guided-wave modulators at microwave or even millimeter wave frequencies are coming up to the stage of practical use. Some modulators have been used as the modulator and the demultiplexer for high-bit-rate optical transmission experiments [13]. Also their applications as a portion of microwave systems would be useful.

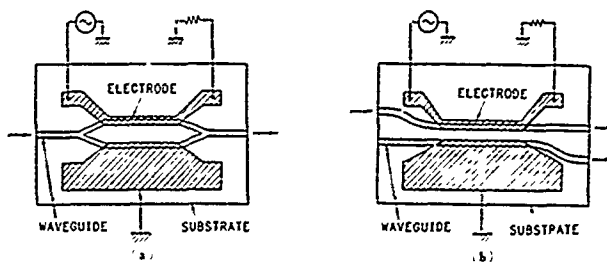


Fig.1 High-speed intensity modulators

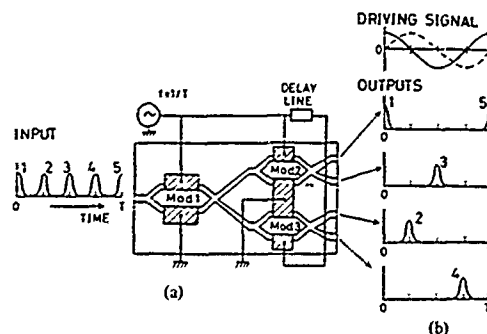


Fig.2 A 1x4 optical time demultiplexer[10]

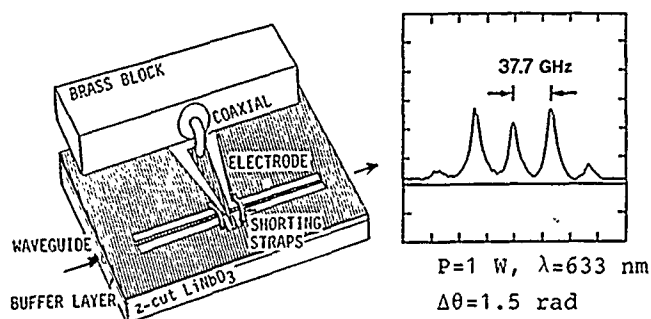


Fig.3 A MM-wave light modulator [11]

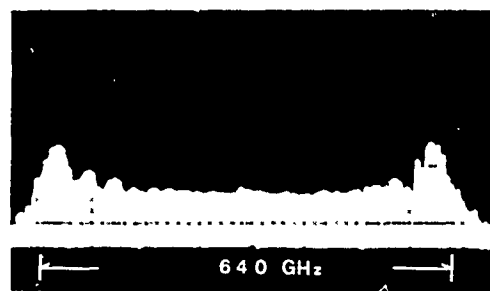


Fig.4 Observed optical spectrum of the deeply phase-modulated light[12]

- References** [1] T.Sueta et al., J.Opt.Comm., 3, 52 (1982). [2] S.K.Korotky et al., Integrated Optical Circuits and Components, ed. L.D.Hutcheson, Marcel Dekker, Inc., ch.6 (1987). [3] I.P.Kaminow et al., Appl.Phys.Lett., 27, 55 (1975). [4] M.Izutsu et al., IEEE J.Quantum Electron., QE-13, 287 (1977). [5] M.Izutsu et al., ibid., QE-14, 394 (1978). [6] P.S.Cross et al., Appl.Phys.Lett., 44, 486 (1984). [7] D.W.Dolfi et al., OFC/IOOC'87, PDP4 (1987). [8] H.Haga et al., IEEE J. Quantum Electron., QE-22, 902 (1986). [9] M.Izutsu et al., ibid., QE-17, 2225 (1981). [10] H.Haga et al., J.Lightwave Tech., LT-3, 116 (1985). [11] M.Izutsu et al., CLEO'88, PD14 (1988). [12] K.Amano et al., J. Lightwave Tech., LT-5, 1454 (1987). [13] R.S.Tucker et al., OFC'88, THB2 (1988).

# Generation and Detection of Millimeter Wave Modulated Light with High Speed Diode Lasers and Photodetectors

## INVITED PAPER

J. E. Bowers

Department of Electrical and Computer Engineering  
University of California  
Santa Barbara, CA 93106

C. A. Burrus and F. G. Storz

AT&T Bell Laboratories  
Crawford Hill and Holmdel Laboratories  
Holmdel, New Jersey 07733

### Abstract

The bandwidths of semiconductor lasers, modulators and photodetectors have dramatically increased recently, making it possible to directly modulate light with signals whose frequencies extend from dc to millimeter wave frequencies. Furthermore, the low attenuation of optical fiber and modulation-frequency-independent nature of the attenuation makes lightwave transmission of broadband microwave signals attractive.

Recent advances in generating subpicosecond optical pulses at microwave frequencies using semiconductor lasers has made it possible to generate combs of frequencies extending through the entire microwave and millimeter wave spectrum. With present and next generation photodetectors to detect these optical signals, many applications of optoelectronic devices to spectroscopy, analog and digital transmission, electro-optic sampling, and high speed electronics and optical computing have become important.

### Loss of Microwave Transmission Systems

Optical fiber transmission has many advantages over coaxial cable or waveguide, including lower attenuation and dispersion, light weight, small size, flexibility and greater immunity to crosstalk. The two major disadvantages of optical fiber transmission are the limited bandwidth of the microwave to optical and optical to microwave transducers, and the very significant conversion loss. This large conversion loss makes fiber runs unattractive for short lengths. The crossover point where less loss is incurred in fiber transmission is typically around 10 m, as shown in Fig. 1. The system losses for several transmission systems at 10 GHz are shown in this figure. The relatively steep curves are for semirigid coaxial cable and WR-90 waveguide with losses at 10 GHz of 1 and 0.1 dB/m, respectively. For optical fiber, the attenuation for optical transmission at 1.55  $\mu\text{m}$ , 1.3  $\mu\text{m}$  and 0.8  $\mu\text{m}$  is typically 0.0002, 0.0004, and 0.002 dB/m, respectively[1]. Even lower attenuation has been achieved with carefully spooled fiber before cabling.

The major differences in the optical curves in Fig. 1 are the optoelectronic transducers. The only optical source which can be directly modulated at these frequencies is a semiconductor laser. Bandwidths of 20 GHz have been demonstrated at several laboratories[2,3], and much higher bandwidths have been demonstrated by cooling the laser[4,5]. The small signal current loss of a simple system of length  $L$  coupled directly to the laser and to a pin or Schottky photodetector without matching is

$$\frac{I_D}{I_L} = \eta_L \eta_D C_L C_D e^{-\alpha L} \quad (1)$$

which has a maximum of 1. To obtain high efficiencies, the quantum efficiency of the laser ( $\eta_L$ ) and photodetector ( $\eta_D$ ) must both be high. The alternative to direct laser modulation is a cw optical source coupled with an external modulator. The small signal current loss is

$$\frac{I_D}{I_M} = \frac{e \eta_D C_D C_M C_{\text{Mod}} R_s P_{\text{in}} e^{-\alpha L}}{v_\pi \hbar \nu} \quad (2)$$

where the  $C$ 's are coupling coefficients,  $v_\pi$  is the half wave voltage of the modulator,  $\hbar \nu$  is the photon energy,  $e$  is the electron charge, and  $P_{\text{in}}$  is the input power to the modulator. Unlike the case for direct modulation, the current loss depends on the optical power. Presently, the loss of

external modulator systems is typically larger than the loss of direct modulation systems because of the large half-wave voltages of high bandwidth modulators and because of the loss associated with coupling in and out of the modulator. However, the current loss will probably decrease as higher power semiconductor lasers (greater  $P_{\text{in}}$ ) become available, and transmission systems with gain are possible.

Lower losses can be achieved in several ways. First, the quantum efficiency of the photodetector can be increased. The bandwidth efficiency product of pin and Schottky photodetectors are limited by an inherent bandwidth efficiency product which is independent of design parameters[6]:

$$f_{3dB} = 0.45 \alpha V_S \quad (3)$$

where  $\alpha$  is the absorption coefficient, and  $V_S$  is the saturation velocity. For a transmission system at 1.3  $\mu\text{m}$ , this limit is around 28 GHz. Bandwidths of 60 GHz with an efficiency of 33% have been demonstrated with GaInAs photodetectors at 1.3  $\mu\text{m}$ [7], while bandwidths of 110 GHz have been demonstrated with GaAs Schottky photodetectors at 0.8  $\mu\text{m}$  with an efficiency of 25%[8]. Bandwidths in excess of 200 GHz appear to be possible with proper design[6]. Higher bandwidth efficiency products should be possible with waveguide photodetectors[9].

Higher bandwidth efficiency products have been demonstrated with avalanche photodetectors. The highest gain bandwidth product demonstrated to date is 70 GHz. This is the gain over the quantum efficiency of the absorbing region of the APD, which in the case of [10] is 0.7 for an overall efficiency-bandwidth product of 50 GHz. One problem with APDs has been the limited absolute bandwidth, presently limited to 7 GHz[10]. Although higher bandwidths appear possible, pin or Schottky photodetectors appear necessary at millimeterwave frequencies. For transmission systems with limited bandwidth, much lower loss can be obtained with appropriate matching circuits to the laser and photodetector[11]. The reduction in loss for a given bandwidth for a passive network is of course limited by the extent the bandwidth is reduced[12].

Another way to decrease transmission loss is to coat the laser facets to minimize the light output from the back of the laser, and maximize the quantum efficiency out the front of the laser. We have used mirror coatings of 5% on the front and >90% on the back facet to increase the quantum efficiency of 1.3  $\mu\text{m}$  lasers to 70%. Using these lasers with avalanche photodetectors, the total system loss from microwave connector to microwave connector was reduced to under 5 dB, as measured with an HP 8510 vector network analyzer.

### Larger Bandwidth Transmission

The author has used 31 GHz 3 dB bandwidth lasers (at -40 °C) with 36 GHz photodetectors to transmit millimeter wave signals at 40 GHz over short lengths of optical fiber, which to our knowledge is the highest frequency transmission demonstrated to date. The bandwidth of the laser at that temperature was limited by laser parasitics. Smaller parasitics are certainly possible. This laser was limited at room temperature by highest resonance frequency that could be generated. The bandwidth is related to the resonance frequency by[13]

$$f_{3dB} = \sqrt{1 + \sqrt{2}} f_r \approx 1.55 f_r \quad (4)$$

while the resonance frequency is given by [14]

$$f_r = \frac{1}{2\pi} \sqrt{\frac{vgS}{\tau_p}} \quad (5)$$

where  $v$  is the group velocity,  $S$  is the photon density,  $g$  is the differential gain, and  $\tau_p$  is the cavity lifetime. Higher resonance frequencies can be generated by higher power lasers, narrower optical waveguides, higher differential gain coefficients (achieved by modulation doping[15] and quantum confinement in wells or wires[16]) and by cooling.

An alternative for high frequency modulation is to use external modulators. Presently modulators with 3 dB bandwidths to 20 GHz have been demonstrated using velocity matched traveling wave modulators in GaAs[17] as well as staggered LiNbO<sub>3</sub> modulators (although the microwave phase is distorted)[18] and conventional GaAs and LiNbO<sub>3</sub> modulators [19,20].

These relations between loss and carrier frequency are summarized in Fig. 2. Here we plot maximum transmission distance as a function of modulation frequency. The calculations assume a 2 Gbit/s signal is transmitted with  $10^{-9}$  bit error rate using broadband devices. Longer transmission is possible with narrow band resonant optoelectronic transducers. These loss estimates are conservative if lower bit rate transmission is used and optimistic if analog transmission with 60 dB dynamic range is desired. However, this curve includes the important effects and breaks in the distance versus bandwidth curve. Note that the microwave transmission distance decreases dramatically with frequency, typically as the square root of modulation frequency, while the optical attenuation stays about the same. This is because it is directly the carrier which is being transmitted in the microwave case. In the optical case, the carrier frequency is typically around 200,000 GHz, and transmission of the microwave subcarrier at 10, 26 or even 100 GHz is virtually identical (in fact the loss can even go down at higher modulation frequencies if a high power narrow line optical source is used so that nonlinear effects in the fiber are important). This figure also shows experimental results for 2 Gbit/s PSK transmission at 1.3  $\mu$ m over optical fiber[21]. Longer distance transmission at these bit rates is possible with properly designed receivers.

### Short Pulse Generation

A major new application of high speed optoelectronic devices is in the realm of short electrical pulse generation. With the use of mode locked semiconductor lasers, it is possible to generate subpicosecond pulses at repetition rates from 8 GHz to 20 GHz. Slightly wider pulses can be generated at lower repetition rates. These pulses are useful as compact sources for electrooptic sampling, for very high sampling rate analog to digital converters, and for sampling oscilloscopes using optically switched sampling gates. Presently, 100 mV electrical pulses can be generated with FWHMs of 8 ps, and pulses up to 1 V in amplitude can be generated with 12 ps FWHM, limited by space charge effects in the photodetector[22]. Other applications of these devices include low-jitter comb generators with significant frequency components beyond 50 GHz.

### References

- [1] P. Kaiser and D. B. Kock, in *Optical Fiber Telecommunications I*, eds. S. E. Miller and I. P. Kaminow, Academic Press (1988).
- [2] J.E. Bowers et al., *Electron. Lett.* 24 1263-1265 (1988).
- [3] R. Olshansky et al., *Electron. Lett.* 23 (1988).
- [4] J. E. Bowers, *Electron. Lett.* 21(25/26) 1195-1197 (1985).
- [5] J. E. Bowers et al., *Electron. Lett.* 21, 1090-1091 (1985).
- [6] J. E. Bowers and C. A. Burrus, *Electron. Lett.* 22(17) 905-906 (1986).
- [7] J. E. Bowers and C. A. Burrus, *J. Lightwave Tech.* LT-5(10), 1339-1350 (1987).
- [8] D. G. Parker et al., *Electron. Lett.* 23(10), 527-528 (1987).
- [9] J. E. Bowers et al., submitted to *J. Lightwave Tech.*
- [10] J. C. Campbell et al., *Appl. Phys. Lett.* 51(18) 1454-1456 (1987).
- [11] M. de la Chapelle et al., *Proc. SPIE* 716, 23-24 September, 1986.
- [12] R. M. Fano, *J. Franklin Inst.* 244(57) 139 (1950).
- [13] J. E. Bowers et al. *IEEE J. Quantum Electron.* QE-22(6) 833-843 (1986).
- [14] K. Y. Lau and A. Yariv, in *Semiconductors and Semimetals* (vol 22), ed.

- W. T. Tsang, pp. 69-152, Academic Press (1985)..
- [15] K. Uomi et al., *Appl. Phys. Lett.* 51(2) 78-80 (1987).
- [16] Y. Arakawa and A. Yariv, *IEEE J. Quantum Electron.* QE-22(9) 1887-1899 (1986).
- [17] J. Nees, CLEO paper PD15, April 1988.
- [18] D. W. Dolfi et al., Optical Fiber Commun. Conf., Reno, NV, paper PDP4 (1987).
- [19] S. K. Korotky et al., Top. Meet. Picosecond Electronics and Optoelectronics, Incline Village, NV, paper FB4 (1987).
- [20] S. Y. Wang and D. Bloom, *Electron. Lett.* 19 554-555 (1983).
- [21] J. E. Bowers, 10th IEEE Semiconductor Laser Conf., Kanagawa, Japan, paper M-3 (1986).
- [22] S. W. Corzine et al., *Appl. Phys. Lett.* 52 348 (1988).

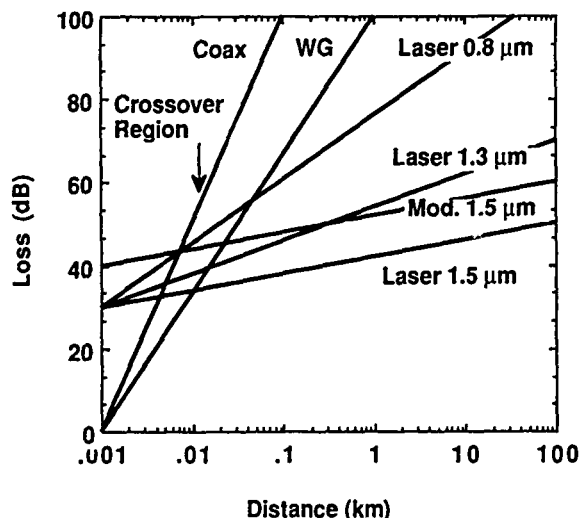


Figure 1. Loss of microwave and optical transmission systems as a function of length.

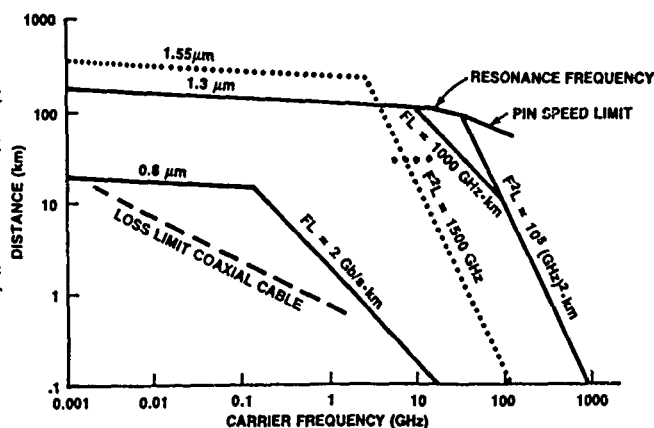


Figure 2. Dependence of maximum transmission distance on carrier frequency for a 2 Gbit/s digital amplitude shift keyed transmission with  $10^{-9}$  bit error rate. Also shown are some experimental results for 2 Gbit/s transmission[21].

# OPTICALLY CONTROLLED MILLIMETER WAVE PHASED ARRAY ANTENNAS.

P R Herczfeld and A S Daryoush

Center for Microwave-Lightwave Engineering, Drexel University, Philadelphia, Pa. 19104

This paper is concerned with recent developments related to optically controlled phased array antennas operating in the millimeter wave range. The antenna consists of three main elements: the central processing unit (CPU), the fiberoptic (FO) distribution system with optical signal processing capability, and the planar array. The antenna array is composed of a large number of distributed and independently powered transmit/receive (T/R) modules fabricated by monolithic microwave integrated circuit (MMIC) techniques. The function of the fiber optic distribution system is to distribute the carrier reference signals for the frequency synchronization of the T/R modules, to transmit the appropriate control signals for beam forming, and to route the information and data signals.

The replacement of coaxial cables or waveguides by the fiberoptic network reduces size and weight, and also provides large bandwidth, immunity to interference (EMI and EMP), excellent crosstalk isolation, and smaller transmission losses, particularly at millimeter wave frequencies.

The synchronization of the T/R modules can be achieved by placing a free oscillator (LO) on each T/R module and injection locking it to a reference signal transmitted from the master oscillator via a high speed fiberoptic link. Daryoush, et al [1], have demonstrated a 39 GHz FO link that utilizes the fourth harmonic of the laser modulation in conjunction with the third subharmonic of the LO. This method could be applied up to 60 GHz with presently available components.

The term beamforming applies to the steering of the beam in various directions and adjusting the beam shape (side lobe suppression, selective nulling, etc.) of the phased array. This can be performed by optically triggered phase shifters and gain controllers as demonstrated by Paoletta et al [2-3]. He controlled the biasing circuit of an amplifier and the control line of a variable bit phase shifter by optical means. The optical sensing element was a multi-finger MESFET illuminated by an LED source. The optical injection controlled the gate to source voltage of the FET, which in turn was used to adjust the bias voltage of the gain amplifier and/or the phase shifter, and

hence control of the gain and/or phase of the module. This approach is independent of the operating frequency of the microwave components thus it can be used in the millimeter wave range, it is compatible with GaAs MMIC fabrication processes and with parallel optical processing (spatial filters).

In order to use the transmitted signal for communication or radar applications, suitable modulation of the carrier must be provided. In communication, an analog or digital baseband signal is superimposed on the carrier, usually via AM or FM technique. There are two broad categories of implementation possible for fiberoptic distribution networks. The conventional FO configuration is referred to as *Central Data Mixing* (CDM). In this architecture, the FO link is directly substituted for the coaxial cable. The information or data is first upconverted by the reference signal at the CPU level and then transmitted to a remote element, such as a T/R module. This puts severe restraints on the laser since it is expected to be linear and free of noise very close to its relaxation oscillation frequency. This results in high attenuation and limited dynamic range. To reduce the link noise figure and thus increase the dynamic range, an alternate link architecture was developed [4]. It is noted that most applications require a relatively narrow bandwidth information/data signal, (typically 0.5-1.0GHz), modulating a high frequency carrier (10GHz or higher). By separating the information/data signal from the carrier, significant improvements can be achieved. This alternate configuration, called *Remote Data Mixing* (RDM), uses two FO links, one for the data and one for the carrier. Each link can then be independently optimized.

The performance of the two configurations, CDM and RDM, were experimentally compared by Koffman, et al[26]. The RDM configuration proved superior in terms of bandwidth, dynamic range and noise.

While the progress in optical techniques applied to phased array antennas has been very impressive it is also clear that more research will be required before large scale implementation of these ideas becomes a reality. High speed FO links must be extended to still higher frequencies, their losses must be reduced and their dynamic range improved. This will require component and subsystem level studies. Optical beamforming of phased arrays should be investigated in more detail. Compatibility with established MMIC fabrication and optical processing must be emphasized.

1. A. Daryoush et al., "Optical Control of Millimeter Wave Phased Array Antennas for Communications," European Microwave Conference Proc., pp. 864-870, Dublin, September, 1986.
2. Herczfeld, P. R., Paoella, A., Daryoush, A., Jemison, W., Rosen, A., "Phase and Gain Control of a GaAs MMIC Transmit-Receive Module by Optical Means", European Microwave Conference, Stockholm, Sweden, Sept. 11-15, 1988
3. Herczfeld, P. R., Paoella, A., "Optical Gain Control of a GaAs MMIC Transmit-Receive Module Compatible with Optical Spatial Filters", IEEE AP-S Int.Symp., Syracuse, N.Y., June 1988.
4. Koffman, et al., "High Speed Fiber Optic Links for Short-haul Microwave Applications," 1988 IEEE MTT-S International Symposium Digest, pp. 983-986, New York, NY, May 1988.

# GaAs TRAVELING-WAVE OPTICAL MODULATOR USING A MODULATED COPLANAR STRIP ELECTRODE WITH PERIODIC CROSS-TIE OVERLAY

H.-Y. Lee and T. Itoh

Department of Electrical and Computer Engineering  
The University of Texas at Austin, Austin, TX 78712

## ABSTRACT

This paper proposes and analyzes a GaAs traveling-wave optical modulator which uses a modulated coplanar strip electrode with periodic cross-tie overlay. This slow-wave structure can be designed to satisfy phase velocity and impedance matching conditions simultaneously. The dominant conductor loss in the slow-wave structure is reduced using the modulated coplanar strip electrode. The calculated modulation bandwidth is much wider than those of conventional electrode structures which are limited by phase velocity mismatch.

## INTRODUCTION

In the design of a traveling-wave electro-optic modulator phase velocity matching between modulation and light waves is an essential task because the upper frequency limit is limited by the inverse of the transit time difference of the two waves[1]. If the optical and modulation wave velocities are equal, the electro-optic modulator would offer the potential of a very wide modulation bandwidth. However, conventional coplanar traveling-wave electrodes on semiconductor materials cannot be designed to achieve this phase velocity matching because the phase velocity of the modulation wave is in all cases higher than that of the light wave due to the field in the air side of the electrodes. In a previous slow-wave structure on GaAs substrate using a coplanar waveguide electrode with periodic cross-tie overlay[2], the velocity and impedance matchings have been successfully satisfied over a very wide bandwidth by reducing the phase velocity of the modulation wave. However, the dominant conductor loss of the structure is relatively high and it limits the modulation bandwidth.

In this paper we propose and analyze a GaAs traveling-wave optical modulator using a modulated coplanar strip electrode with periodic cross-tie overlay. The strip width is periodically modulated in order to reduce conductor loss while satisfying the both matching conditions. The calculated 3dB bandwidth and modulation voltage are 100 GHz and 23 V, respectively, for 4mm long modulator at 1.3  $\mu\text{m}$  light wavelength. And the modulation characteristic slowly varies over the bandwidth because the phase velocity matching is satisfied.

## STRUCTURE AND ANALYSIS

The proposed optical modulator shown in Fig.1 is constructed with a coplanar strip slow-wave electrode on a GaAs ridge optical waveguide. The slow-wave electrode consists of an infinite array of a more capacitive Section A(with overlay) and a

more inductive Section B(without overlay) based on a modulated coplanar strip. Since the period chosen is much smaller than the propagation wavelength, this structure behaves as a uniform transmission line. In this structure, we can increase the effective capacitance(C) and inductance(L) of this transmission line independently by a spatial separation of electric and magnetic energies into two different sections. Therefore, the propagation constant( $\beta$ ), which is proportional to  $\sqrt{LC}$ , can be increased above that of common coplanar strip. In order to reduce dominant conductor loss the strip width is periodically modulated because wider strip width of the Section A results lower conductor loss for a given capacitance and strip gap. The both ends of the slow-wave electrode are extended and connected to coaxial lines through intermediate microstrip lines for wideband feeding and termination[3]. The GaAs ridge optical waveguide can be easily formed on thick (100) semi-insulating GaAs substrate using epitaxial and mesa etching techniques. Optical and modulation waves propagate along  $\langle 011 \rangle$  direction and the modulation field is in  $\langle 011 \rangle$  direction for the highest electro-optic effect. Silicon nitride layer insulates the cross-tie overlays from the strip electrode.

Numerical analysis of the slow-wave electrode has been carried out by quasi-static analysis of each section and by an application of Floquet's theorem to the periodic array[2]. The dominant conductor losses of the two sections are calculated using incremental inductance formula[4]. Overall complex propagation constant including loss, and characteristic impedance of the periodic array are approximately proportional to the ratio and the product of the characteristic impedances of the two sections, respectively[2]. This property can be used very effectively to achieve the simultaneous matching of the phase velocity and the impedance, which is required in the optimum electrode design of traveling-wave optical modulators. Furthermore, since this slow-wave structure is almost dispersionless due to the uniform transmission line behavior, the structure is very useful for the design of wideband traveling-wave optical modulators. The GaAs ridge optical waveguide is analyzed for a single  $\text{TE}_0$ -like mode propagation using effective index method. The mode size of the ridge waveguide is designed for good coupling to single mode fiber. Since the mode is not intrinsically leaky, the optical propagation loss is very small compared to the coupling loss.

## CALCULATED BANDWIDTH AND MODULATION VOLTAGE

The effective index, attenuation constant and characteristic impedance of the slow-wave structure are shown in Fig. 2 for the case of maximum figure-of-merit which is defined by bandwidth divided by modulation voltage. From this figure it can be seen that this slow-wave optical modulator has a very wide bandwidth for simultaneous phase velocity and impedance matching. However, the attenuation constant is much larger than those of conventional structures. Therefore, the modulation characteristics are limited not by phase velocity mismatch but by attenuation. In a 4mm long GaAs traveling-wave modulator using a conventional coplanar electrode[5], the modulation reduction factor[2][6] shown in Fig. 3 descends steeply over the 3dB bandwidth(30 GHz) because of its sync function behavior due to the phase velocity mismatch. However, for the same device length at 1.3  $\mu$ m light wavelength this slow-wave structure has much wider bandwidth(100 GHz) and the modulation reduction factor even varies slowly over the 3dB frequency. This characteristic is more significant at high frequencies and for a long modulator length.

Although the calculated  $V_{\pi}$  (23 V) is a little larger than that of the conventional electrode structure (20 V) due to the low field overlap between modulation and optical waves in section A, the figure-of-merit (4 GHz/V) is much higher than that of the conventional structure(1.5 GHz/V).

### CONCLUSIONS

In this paper we proposed and analyzed a GaAs traveling-wave optical modulator using a modulated coplanar strip electrode with periodic cross-tie overlay. The dominant conductor loss in the slow-wave structure is reduced using the modulated coplanar strip electrode. The calculated modulation bandwidth of the velocity-matched slow-wave structure is much wider than those of conventional electrode structures which are limited by phase velocity mismatch.

### ACKNOWLEDGEMENT

This work was supported by the U.S. Army Research Office under contract DAAL-03-88-K-0005 and the Texas Advanced Technology Program.

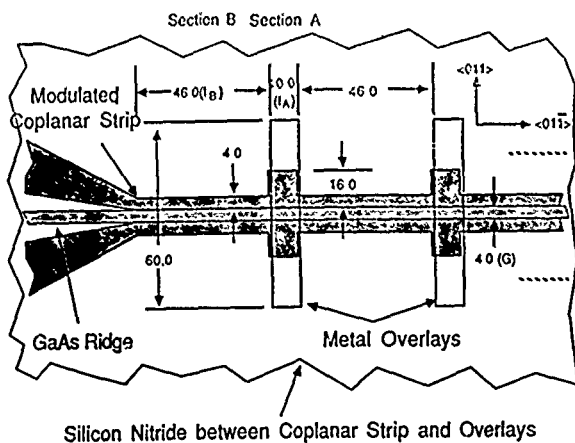


Fig. 1a - Top-View

### REFERENCES

- [1] R. C. Chen, *Proceedings of the IEEE*, Vol. 58, pp. 1440-1457, October 1970.
- [2] H.-Y. Lee et al, *Int. Journal of IR and MM Waves*, Vol. 9, No.1, pp.87-99, January 1988
- [3] H.-Y. Lee and T. Itoh, submitted to *Electronics Letters*
- [4] R. A. Pucel et al., *IEEE Trans. Microwave Theory Tech.*, Vol. MTT-16, pp. 342-350, 1968.
- [5] S. Y. Wang et al, *Appl. Phys. Lett.*, 51(2), 13, pp.83-85, July 1987.
- [6] K. Kubota et al, *IEEE J. Quantum Electron.* QE-16, pp. 754-760, July 1980.

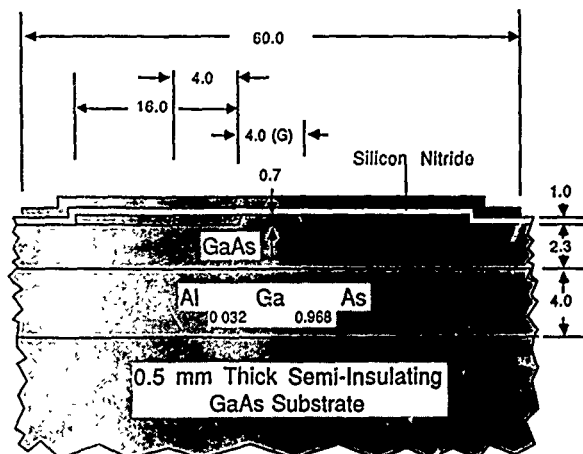


Fig. 1b - (011) Face Cross-Section

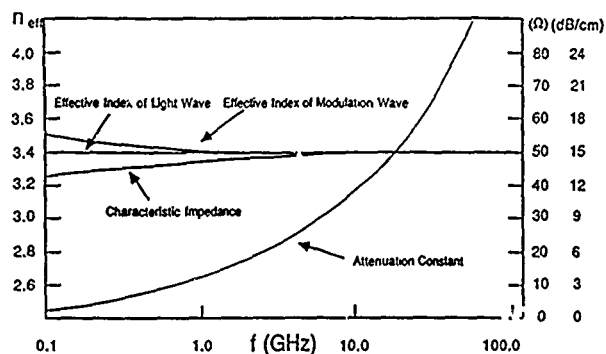


Fig. 2 - Dispersion, Attenuation and Chr. Impedance

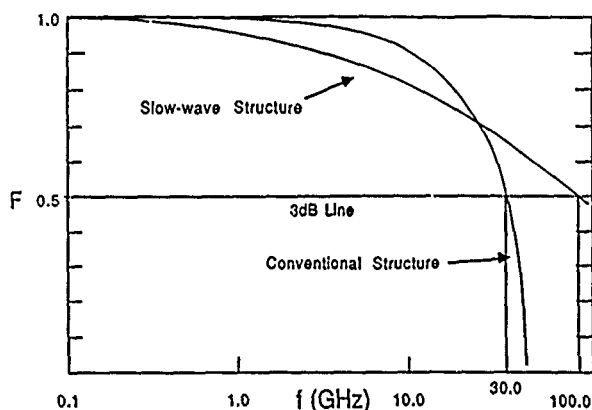


Fig. 3 - Modulation Reduction Factor



## A NEW CLASS OF SCANNABLE MILLIMETER WAVE ANTENNAS

Arthur A. Oliner

Polytechnic University  
Weber Research Institute  
333 Jay Street  
Brooklyn, NY 11201

### ABSTRACT

The complexity usually associated with scanning arrays at millimeter wavelengths produces fabrication difficulties, so that alternative methods are needed that employ simpler structures. This paper describes such an alternative scanning approach, and presents a group of *new and simpler radiating structures* suitable for millimeter-wave applications.

### INTRODUCTION

The new class of scanning arrays described in this paper achieves scanning in two dimensions by creating a one-dimensional array of *leaky-wave* line-source antennas. The individual line sources are fed from one end and are scanned in elevation by electronic means or by varying the frequency. Scanning in the cross plane, and therefore in azimuth, is produced by *phase shifters* arranged in the feed structure of the one-dimensional array of line sources.

Within the sector of space over which the arrays can be scanned, the radiation has *negligible cross polarization*, *no blind spots* and *no grating lobes*. These are significant, and also unusual, advantages. The novel features in the study reported here relate mainly to the new structures employed for the individual leaky-wave line sources and their combination into arrays, but also to analyses of the interactive effects produced when scanning occurs in both planes simultaneously.

The analyses of the various antenna structures are believed to be accurate, and for most of the antennas they are notable for resulting in transverse equivalent networks in which all the elements are in *closed form*, so that the dispersion relations for the propagation properties of the leaky-wave structures are also in closed form. It should be added that for all the array structures the analyses take *all mutual coupling effects* into account.

Although these studies are predominantly theoretical in nature, sets of careful *measurements* were made for two of the novel leaky-wave line-source antennas: the foreshortened NRD guide structure and the offset-groove-guide antenna. The agreement with the theoretical calculations was excellent in both cases.

In this paper, seven different novel antennas are described, of which four are leaky-wave line sources that scan in elevation, and three are arrays that scan in two dimensions. They represent *examples* of the new class of scannable antennas that are simple in configuration and suitable for millimeter wavelengths.

This study has been extensive in scope, and it has involved collaboration with colleagues in Italy and Japan, as well as students and colleagues at Polytechnic University. The principal (senior) colleagues are Prof. Paolo Lampariello of the University of Rome, Italy, and Prof. Hiroshi Shigesawa of Doshisha University, Kyoto, Japan. Performance results for some of these antennas have been presented at recent symposia, but all of the details will be issued soon in the form of a comprehensive report entitled "Scannable Millimeter Wave Arrays," to be issued by RADC at Hanscom Field, MA, the sponsor of this study, as the Final Report on Contract No. F19628-84-K-0025.

### LEAKY-WAVE LINE-SOURCE ANTENNAS

A leaky-wave line-source antenna is basically an open waveguide possessing a mechanism that permits a slow leakage of power along the length of the waveguide. This slow leakage is characterized by a phase constant  $\beta$  and a leakage constant  $\alpha$ , whose knowledge immediately yields the angle of the radiated beam and the beam width.

Leaky-wave antennas for the millimeter-wave range face two main problems. The first relates to the small wavelengths involved, which require small waveguide dimensions and pose fabrication difficulties. The second problem is higher metal loss; for antennas that are many wavelengths long, the leakage (which results in radiation) may compete with the intrinsic waveguide loss, and the antenna design can be adversely affected. We overcome the first of these problems by considering leaky-wave structures with *longitudinally continuous apertures*, and the second by basing the antennas on *low-loss waveguides*. Of the possible low-loss waveguides that have been proposed over the years, we have selected two on which to base our new leaky-wave antennas: the *groove guide* and the *nonradiative dielectric (NRD) guide*.

Several different *mechanisms* have been introduced to produce the necessary leakage from a waveguiding structure whose dominant mode is purely bound. These mechanisms include asymmetry, foreshortening of the structure's cross section, and the use of leaky higher modes. Of the four line-source antennas described here, one uses the foreshortening technique, one is based on leaky higher modes, and two employ asymmetry.

The two leaky-wave antennas based on NRD guide are shown in Figs. 1 and 2, whereas the groove guide antennas are indicated in Figs. 3 and 4. The radiation properties of these line-source antennas, and the physical principles that underlie the leakage mechanisms, will be described in the talk.

## TWO-DIMENSIONAL SCANNING ARRAYS

The two-dimensional arrays are comprised of linear arrays of leaky-wave line sources, which themselves yield scannable narrow beams in elevation in the longitudinal plane, with wide fan beams in the cross plane. When these line sources are arranged parallel to each other in an array, the array can then produce a pencil beam scannable in two dimensions within a specified region of space. Scanning in the cross plane in phased-array fashion is achieved by placing a given phase shift between successive line sources. This mode of operation is common to all three of the arrays discussed here.

The analyses for all of the arrays employ a *unit cell* for the external periodic environment, in which phase-shift walls take into account the effects of scan in the cross plane. The individual line sources are analyzed using a transverse equivalent network, in which the radiating open end is representative of the environment of a single lone line source. In the two-dimensional array, the environment of the line source is very different, and the unit cell now becomes the termination on the transverse equivalent network. The unit cell termination changes with scan and automatically takes into account all mutual coupling effects; the resonances of the complete network reveal the array performance as a function of scan angle in both scan planes.

The first of the three array structures is shown in Fig. 5. It is composed of a series of leaky NRD guides of the type shown in Fig. 2, where the line sources provide the elevation pattern, and the geometry in the plane shown specifies the cross-plane behavior.

The other two array structures, seen in Figs. 6 and 7, have a *printed-circuit form*. Their printed-circuit nature permits the detailed metal circuit to be deposited lithographically on the dielectric surface. The process is simple and can automatically, by employing an appropriate mask, accommodate the tapering in the aperture distribution required for accurate sidelobe control. In Fig. 6, the aperture is longitudinally uniform (except for slight tapering for sidelobe control), whereas in Fig. 7 it is periodic. The line source in the former array is essentially a printed-circuit version of the offset-groove-guide leaky-wave antenna shown in Fig. 4. For the latter array, the dominant mode is chosen to be slow, so that it is purely bound; the period is then selected relative to the wavelength so that only the  $n=-1$  space harmonic becomes radiating. As a result, the array provides greater scan coverage, since the uniform-aperture structures can scan only in the forward quadrant, but the  $n=-1$  beam can scan over the complete backward quadrant and part or all of the forward quadrant, depending on the parameters.

In all three arrays, scanning in the cross plane causes the beam to undergo conical scan, with the beam finally hitting the ground. A feature common to all the arrays is the presence of the set of parallel baffles, which serve two purposes. First, they produce a region of below-cutoff parallel-plate guide to eliminate the vertically polarized field and thus produce *essentially pure horizontally polarized radiation*. Second, they *eliminate* the possibility of *blind spots*, which are angles at which the antenna cannot radiate or receive any power. The baffle spacings are also chosen so that *no grating lobes* are present.

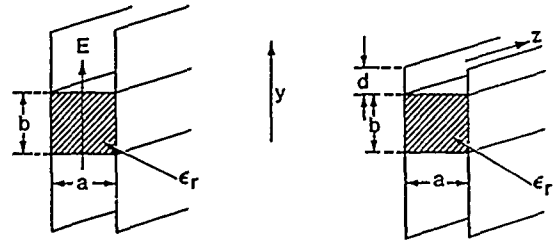


Fig. 1: The basic NRD guide (left) and the foreshortened-top leaky-wave antenna based on it.

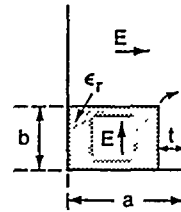


Fig. 2: The asymmetric leaky-wave NRD guide antenna.

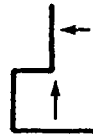


Fig. 3: The L-shaped leaky-wave antenna, based on the groove guide.

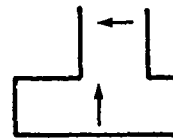


Fig. 4: The offset-groove-guide leaky-wave antenna.

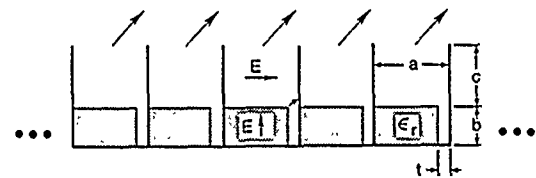


Fig. 5: Linear phased array of parallel NRD guide leaky-wave line sources of the type in Fig. 2.

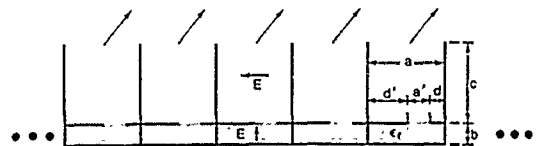


Fig. 6: Linear phased array in which the line source is a printed-circuit version of the antenna in Fig. 4.

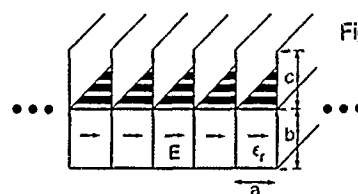


Fig. 7: Linear phased array of longitudinally periodic line sources to provide greater scan coverage.

# INTEGRATED CIRCUIT ACTIVE ANTENNA ELEMENTS AND SPATIAL POWER COMBINING

(Invited Keynote)

Kai Chang  
Department of Electrical Engineering  
Texas A&M University  
College Station, Texas 77843

## ABSTRACT

Recent developments in microwave/millimeter-wave solid-state devices and integrated circuits have made it possible to integrate the active sources directly with planar antennas. The circuits have advantages of low cost, small size and monolithic implementation. This paper summarizes the recent results, potential applications and future trends of active antenna elements.

## INTRODUCTION

Mounting an active device on a planar antenna to form an active antenna could be very challenging for both experimentalists and theoreticians. Recent advances in planar integrated circuit antennas and solid-state sources have made it possible to integrate the source directly on the antenna. The active antenna element can be used as a low cost transmitter.

Many of these elements can be combined to form a spatial power combiner or a quasi-optical power combiner. Recent activities in microwave and millimeter-wave have created an urgent need for high power solid-state transmitters. Compared with tubes, solid-state devices offer the potential for orders-of-magnitude improvement in reliability and reduction in size, weight, and power supply requirements. The output power from a single solid-state device is limited by fundamental thermal and impedance problems. To meet the high power requirements for many applications, it is necessary to combine many devices to achieve high power levels.

Many power combining approaches have been demonstrated in microwave and millimeter-wave frequency range in the past two decades. A review can be found in references 1 and 2 [1,2]. Most of these techniques are to combine the power for  $N$  individual devices in the circuit level. However, these conventional combining techniques have serious limitations due to the moding and size problems. Consequently, the maximum number of devices that can be combined is limited. To overcome these problems, spatial or quasi-optical combiners were recently proposed to combine the power in free space [2] or in a quasi-optical resonator [3]. An active device mounted directly on a planar antenna forms a module for spatial or quasi-optical combiner. Figure 1 shows a possible arrangement for spatial combiner. In order to achieve coherency and effective combining in free space the modules will be injection locked to each other through mutual coupling or through an external master source. Injection locking is not necessary if a Fabry-Perot resonator is used.

The single element active antennas should have applications in low cost electronic warfare decoys. Since the oscillating frequency is electronically tunable through bias or varactor tuning, the active antennas should also be useful for communication and radar systems. The power combiners will have applications in radar and communication systems.

## RECENT DEVELOPMENTS AND RESULTS

Thomas et. al. [4] reported a Gunn source integrated with a rectangular patch antenna at X-band. Perkin [5] used a circular patch antenna integrated with an IMPATT diode. Injection-locking through free space was also demonstrated. Hummer

and Chang [6,7] reported both the single element active antenna and two-element array. The circuits are shown in Figure 2. Gunn diodes and patch antennas were used for circuit construction. By varying the bias, over 9 percent electronic tuning range has been achieved at X-band for a single active patch element [7]. Injection-locked experiments were carried out to achieve frequency coherency and to calculate the Q-factor using either mutual coupling or an external source. With two-element array, a power combining efficiency of over 90 percent has been achieved. The measured pattern for a two-element array is shown in Figure 3. Also shown are the patterns with either antenna "off". It can be seen that when both antennas are "on", the beamwidth is narrower and the gain is higher. Recently, Stephan and Young have studied the effects of the separation between the two antennas for two active antenna elements [8]. Monolithic millimeter-wave IMPATT oscillators and active antennas were demonstrated at 43 GHz [9]. Active antenna elements using FETs have also been developed [10].

Power combining using two active antenna elements and an open resonator was also reported at 10 GHz using Gunn diodes [11]. A modified Fabry-Perot resonator was used to stabilize the circuit and to combine the power.

## CONCLUSIONS

Microwave/millimeter-wave integrated circuit active antenna elements used for low cost transmitters and power combiners have been developed in the past few years. Developments and results are summarized and applications are discussed in this paper.

## ACKNOWLEDGEMENTS

This work was supported in part by Army Research Office under contract No. DAAL03-88-K-0151 and by a grant from TRW. The author would like to thank Mr. Kenneth A. Hummer for helpful discussions.

## REFERENCES

- [1] K. J. Russell, "Microwave Power Combining Techniques", *IEEE Trans. on Microwave Theory and Tech.*, Vol. MTT-27, May 1979, pp. 472-478.
- [2] K. Chang and C. Sun, "Millimeter-Wave Power Combining Techniques", *IEEE Trans. on Microwave Theory and Tech.*, Vol. MTT-31, Feb. 1983, pp. 91-107.
- [3] J. M. Mink, "Quasi-Optical Power Combining of Solid-State Millimeter-Wave Sources", *IEEE Trans. on Microwave Theory and Tech.*, Vol. MTT-34, Feb 1986, pp. 273-279.
- [4] H. J. Thomas, D. L. Fudge and G. Morris, "Gunn Source Integrated with a Microstrip Patch", *Microwave & RF*, Feb. 1985, pp. 87-89.
- [5] T. O. Perkins, "Active Microstrip Circular Patch Antenna", *Microwave Journal*, March 1987, pp. 110-117.

- [6] K. A. Hummer and K. Chang, "Spatial Power Combining Using Active Microstrip Patch", *Microwave and Optical Technology Letters*, Vol. 1, March 1988, pp. 8-9.
- [7] K. A. Hummer and K. Chang, "Microstrip Active Antennas and Arrays", in 1988 *IEEE-MTT Int. Microwave Conference Technical Digest*, pp. 963-966.
- [8] K. D. Stephan and S. L. Young, "Mode Stability of Radiation-Coupled Interinjection-Locked Oscillators for Integrated Phased Arrays", *IEEE Trans. on Microwave Theory and Tech.*, Vol. MTT-36, May 1988, pp. 921-924.
- [9] N. Camillieri and B. Bayraktaroglu, "Monolithic Millimeter-Wave IMPATT Oscillator and Active Antenna", in 1988 *IEEE-MTT Int. Microwave Conference Technical Digest*, pp. 955-958.
- [10] K. Chang, K. A. Hummer and G. K. Gapalakrishnan, "Active Radiating Element Using FET Source Integrated with Microstrip Patch Antenna", To be published.
- [11] S-L. Young and K. D. Stephan, "Stabilization and Power Combining of Planar Microwave Oscillators with an Open Resonator", in 1987 *IEEE-MTT Int. Microwave Conference Technical Digest*, pp. 185-188.

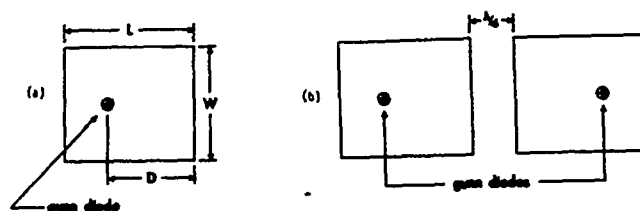


Figure 2. Single and two-element active antenna elements with devices mounted directly on antennas.

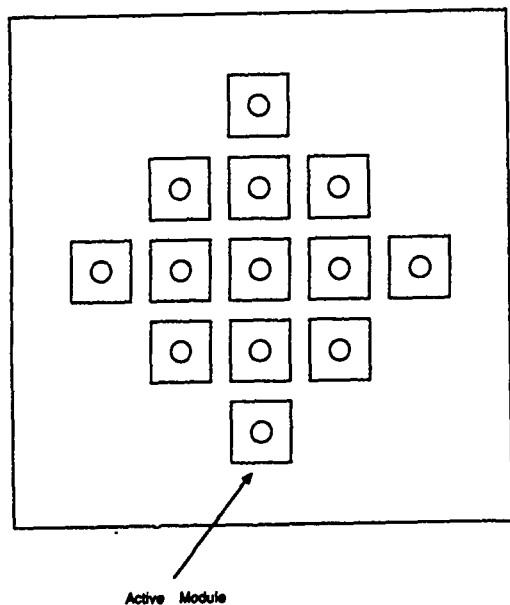


Figure 1. Spatial power combiner

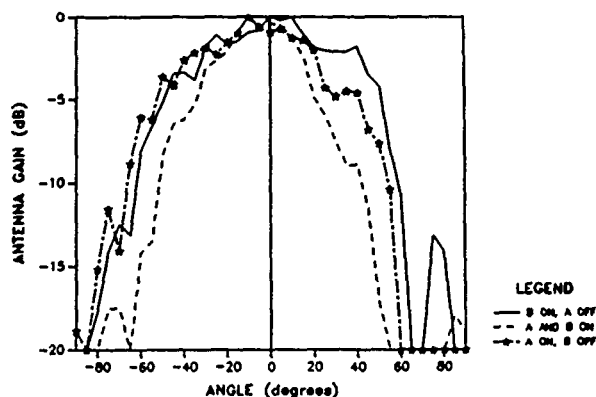


Figure 3. Measured power pattern for a two-element array.

## Detector Antenna Array with a Dielectric Lens for Millimeter-Wave Imaging

Kazuhiro Uehara, Takeshi Yonekura, Hiroshi Nishimura,  
Koji Mizuno and David B. Rutledge<sup>\*)</sup>

Research Institute of Electrical Communication  
Tohoku University, Sendai, 980 Japan

<sup>\*)</sup> California Institute of Technology, Pasadena, CA 91125, U.S.A.

### ABSTRACT

We are developing antenna arrays as detectors for millimeter-wave imaging. The antenna is a resonant dipole [1] with a director in a dielectric lens. Our goal is to measure the plasma density of the TSUKUBA GAMMA-10 plasma machine.

### INTRODUCTION

Recently millimeter-wave imaging is becoming increasingly important in plasma diagnostics, remote sensing, radiometry, astronomy and radar. In the plasma diagnostics, we have been measuring the plasma density of TSUKUBA GAMMA-10 plasma machine in collaboration with several university institutes. We have measured a low-density plasma with a 70 GHz imaging system constructed with a bow-tie antenna array [2,3] and beam-lead GaAs Schottky diode detectors. In order to improve the efficiency of the system, we have designed a Yagi-Uda antenna array with Schottky diode detectors on a dielectric hemisphere (Fig.1).

### IMAGING ARRAY

The hemispherical lens is made of TPX of  $\epsilon_r=2.13$ . The antenna can be easily fabricated as part of a monolithic integrated-circuit by a normal photolithography. The radiator and the director are on both sides of the substrate (3M Cu-Clad 217,  $\epsilon_r=2.17$ , with a thickness of  $0.0975\lambda_d$ ). The element length of the radiator is  $0.496\lambda_e$ , and the director is  $0.435\lambda_d$ . Here  $\lambda_d$  is the wavelength in the dielectric and  $\lambda_e=[(1+\epsilon_r)/2]^{-1/2}\lambda_0$ ,  $\lambda_0$  is the wavelength in a free space. A beam-lead GaAs Schottky diode (Sanyo Electric Co. Ltd., SBL-221) is bonded to the center of the radiator element. The optical configuration is a "reverse-microscope" design developed by Rutledge in 1982 [2]. This configuration has planar monolithic receptor array attached to the lens, and has other attractive properties; little spherical aberration or coma, and high resolution owing to the low f-number. In addition, the troublesome effects of substrate surface waves can be effectively eliminated. The system has proved to be efficient and having diffraction-limited resolution.

### MEASUREMENTS AND DISCUSSIONS

Fig.2 shows the measured radiation patterns of single element comparing with a dipole on the dielectric hemisphere. We can note that patterns are much improved; the central dip in the H-plane has disappeared, and the beam shapes of both planes are close to a  $(\cos\theta)^2$ -shape. The 3 dB beam widths are

63 degrees in the E-plane and 90 degrees in the H-plane. The gain is increased 5.9 dB up at normal incidence.

As to the mutual coupling [4] in the linear array, we have measured 5 GHz model of polyethylene substrate ( $\epsilon_r=2.32$ ) with a metal image plane [5] by using an HP-8510A network analyzer. The coupling is more than 30 dB down for antenna spacing of  $1.00\lambda_d$ , indicating that the effect of the mutual coupling should be neglected.

The lens-coupled arrays have a serious requirement of the matching of the antenna pattern to the beam incident angle at the array. The incident angle varies as a function of the position on the array, with the largest angle at the edges. This can be a particular problem if the diameter of substrate lens is small. We have solved this problem by fabricating a "shifted-director Yagi-Uda antenna" (Fig.3). The director is displaced along the element axis for a distance D, in order to shift the beam direction. Fig.4 shows the measured shifted beam directions. The maximum is 13 degrees for  $D=0.25\lambda_d$ . Both the power gain and the resonant frequency of the antenna also change (Fig.5, Fig.6). The power gain is not degraded more than 3 dB when D is smaller than  $0.3\lambda_d$ . The resonant characteristics were measured on 5 GHz models with a network analyzer. The resonant frequency is 10-20% higher when D is larger than  $0.2\lambda_d$ . Because the band-width of this Yagi-Uda antenna is 9%, we need to correct the antenna length when D is larger than about  $0.2\lambda_d$ . I can conclude from these results that it is possible to shift the beam direction of the antennas at the edges of the array, more than 10 degrees by shifting the director without gain losses or antenna length corrections.

### CONCLUSION

A Yagi-Uda antenna with a Schottky diode detector on the dielectric has been investigated as a receptor element for millimeter-wave imaging. This receptor has an excellent radiation pattern and high gain with low mutual coupling in the array. The significant advance is a "Shifted-director Yagi-Uda antenna." This antenna can compensate for shifts in the incident beam direction. These linear arrays are suitable for a substrate-lens-coupled monolithic imaging system at millimeter-wave-lengths.

### ACKNOWLEDGMENTS

The authors wish to thank Sanyo Electric Co., Ltd. for kindly providing Schottky diodes, and Fujitsu TDT Co., Ltd. for their helpful assistance in these measurements.

## REFERENCES

- [1] K. Mizuno, Y. Daiku and S. Ono, IEEE Trans. Microwave Theory Tech., vol. MTT-25, pp. 470-472, June 1977.
- [2] D. B. Rutledge and M. S. Muha, IEEE Trans. Antennas Propagat., vol. AP-30, pp. 535-540, July 1982.
- [3] R. C. Compton et al., IEEE Trans. Antennas Propagat., vol. AP-35, pp. 622-631, June 1987.
- [4] N. G. Alexopoulos and I. E. Rana, IEEE Trans. Antennas Propagat., vol. AP-29, pp. 106-111, Jan. 1981.
- [5] H. Jasik: Antenna Engineering Handbook, New York: Mc-GrawHill, 1961, Chapter 34-11.

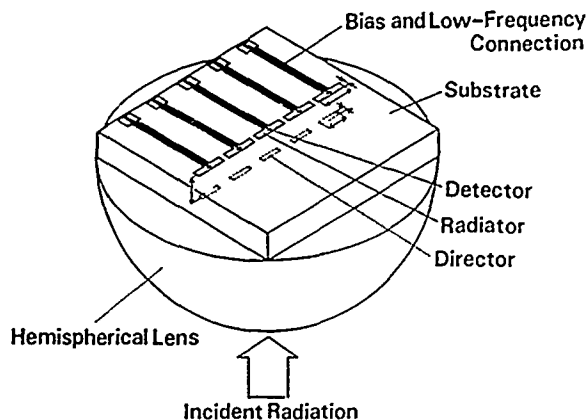


Fig.1. Yagi-Uda arrays on a substrate lens.

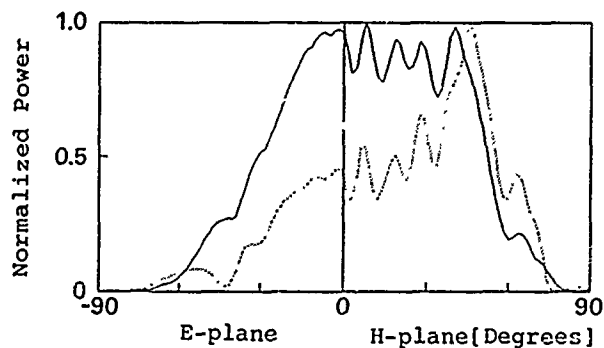


Fig.2. Antenna patterns of a single element in a dielectric hemisphere ( $\epsilon_r=2.13$ , ---- dipole, — Yagi-Uda) at 50 GHz.

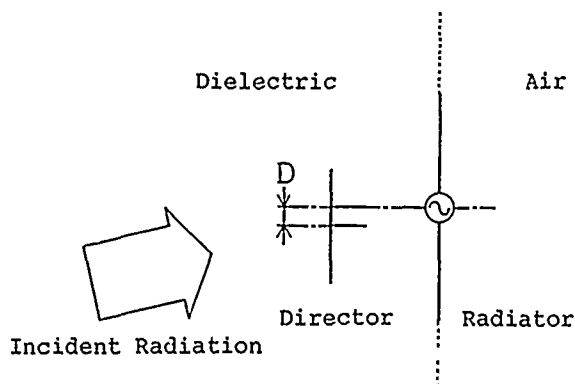


Fig.3. Geometry of a shifted-director Yagi-Uda antenna with a dielectric substrate.

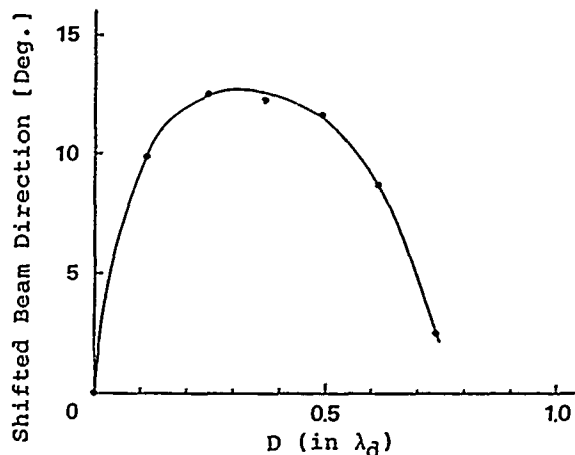


Fig.4. Shifted beam direction of the antenna versus director-shifted-length  $D$  (in  $\lambda_d$ ) in a dielectric hemisphere ( $\epsilon_r=2.13$ ) at 50 GHz.

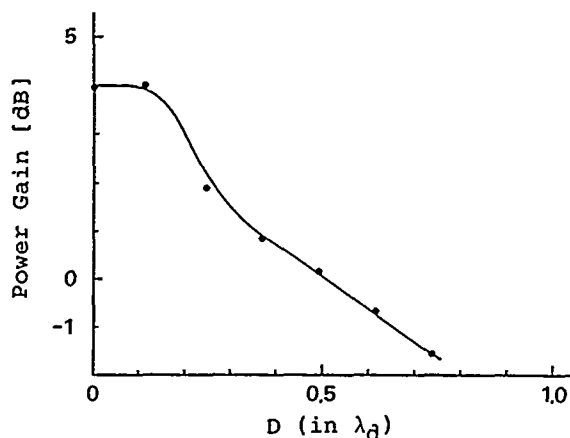


Fig.5. Power gain of the antenna versus director-shifted-length  $D$  (in  $\lambda_d$ ) in the dielectric hemisphere ( $\epsilon_r=2.13$ ) at 50 GHz.

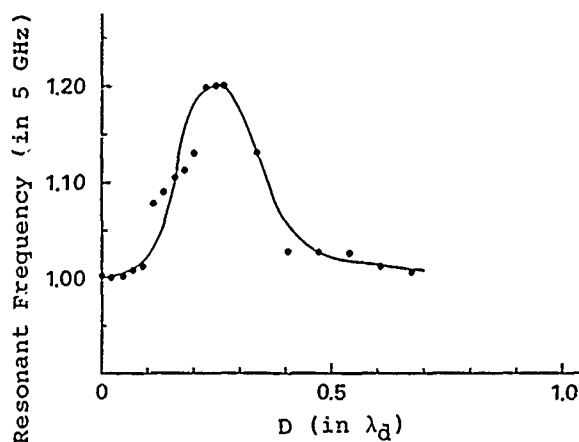


Fig.6. Resonant frequency of the antenna versus director-shifted-length  $D$  (in  $\lambda_d$ ) in a semi-infinite dielectric substrate ( $\epsilon_r=2.32$ ) at 5 GHz.

# OMNIDIRECTIONAL PERIODIC ROD ANTENNA — TMO<sub>1</sub> MODE EXCITATION

Xu Shan-jia

Department of Radio and Electronics  
University of Science and Technology of China  
Hefei, Anhui  
The People's Republic of China

## ABSTRACT

An Omni-directional periodic dielectric rod antenna operating in TMO<sub>1</sub> mode is investigated. As an eigenvalue problem, the structure is analyzed theoretically with mode matching technique. The radiation characteristics are calculated for different parameters with a particular attention directed to the Brewster angle effect on the performances of the antenna.

## INTRODUCTION

Rectangular and circular dielectric rod antennas have been extensively treated in the literature. In these kinds of antennas, the produce of radiation comes from the perturbation of the surface waves by means of tapering the dielectric rod progressively. However, the radiation from the antenna presented here is caused by the perturbation of surface waves on uniform dielectric rod through corrugating, not tapering, the rod periodically, and the circular symmetry of the antenna reminds unchanged. If the structure is excited by angularly uniform fields, the radiation will be angularly uniform. It means that the antenna is omni-directional, i.e. the radiation pattern will be in the shape of an umbrella, providing a uniform azimuthal coverage of 360°. Such an antenna is of particular interest, because of its simplicity in geometry and ease for fabrication. Hence, it is very suitable for millimeter wave applications.

The antenna operating in TEO<sub>1</sub> mode was discussed previously.[1] Here, starting with solving eigenvalue problem, the omni-directional periodic rod antenna operating in TMO<sub>1</sub> mode is theoretically analyzed, with a particular attention directed to the Brewster angle effect on the performances of the antenna. The numerical results indicate that the variation of leakage constant with the thickness of the periodic layer is quite different between TE and TM modes. The reason for that is explained in this paper.

## ANALYSIS METHOD

A circular dielectric rod with periodic corrugations is shown in Fig.1. The structure can be divided into three regions: a uniform inner dielectric core, a circular layer of periodic medium, and the outer free space. The rod has a relative dielectric constant

$\epsilon_0$ , the inner and outer radius and the period of the ring are denoted by  $a$ ,  $b$ , and  $d$ , respectively. Such a structure may be analyzed as a boundary value problem, whose eigenvalues determine the radiation characteristics of the antenna.

For using the method of mode matching to solve the boundary value problem, the general solutions of the electromagnetic fields in the three constituent regions are determined first and the fields are then required to satisfy the boundary conditions at the two surfaces of the periodic layer. Utilizing the general solutions of the three constituent regions, a system of homogeneous linear equations for the mode amplitudes is obtained according to the boundary conditions. The existence of a nontrivial solution requires the vanish of coefficient determinant. Such a determinantal equation defines the dispersion relation, from which the radiation characteristics of the antenna are determined.

## NUMERICAL RESULTS

For antenna applications, one is interested mostly in the case of a single beam radiation. Therefore, the case where only  $n=-1$  space harmonic of TMO<sub>1</sub> mode radiates into free space is investigated. Fig.2 shows the variation of leakage constant  $\alpha$  with the thickness of the periodic layer  $t$  for TEO<sub>1</sub> and TMO<sub>1</sub> modes, respectively. It can be seen from the figure that when  $t=0$ , the antenna becomes a uniform dielectric rod waveguide; no radiation occurs because none of perturbation is introduced to the structure. The fields of a surface wave supported by a uniform dielectric rod are evanescent in the air region. The increase of the thickness can be viewed as adding more periodic material to the structure. When the thickness  $t$  is increased from zero, but is not so large, say  $0 < t < 0.125\lambda$ , the perturbation is in a region with strong fields; its effect on leakage constant increases rapidly with the increasing thickness. However, as the thickness  $t$  increases to a large amount, for instance,  $t > 0.35\lambda$ , the additional material appears in a region where the fields are exponentially small, and would have very little effect on the radiation for both TEO<sub>1</sub> and TMO<sub>1</sub> modes.

Fig.2 shows that near  $t=0.22\lambda$ , completely different radiation characteristics of the  $n=-1$  space harmonic appear between TEO<sub>1</sub> and TMO<sub>1</sub> modes: The variation of  $\alpha$  with  $t$  for TEO<sub>1</sub> mode is flat, whereas it is drastically

reduced to zero at point  $t=0.225\lambda$ , For  $TM_0$  mode. Such a drastic change in radiation may be interpreted as the Brewster angle effect of TM modes. It is well known that when a TM plane wave impinges upon a dielectric interface at Brewster angle from one medium to another medium, the wave passes into the another medium completely without reflection. Brewster angle  $\theta_b$  is governed by:

$$\theta_b = \tan^{-1}(\epsilon_1/\epsilon_2)^{1/2} \quad (1)$$

where  $\epsilon_1$  and  $\epsilon_2$  are the dielectric constants in two regions, respectively. Substituting  $\epsilon_1 = \epsilon_a = 1.0$  and  $\epsilon_2 = \epsilon_c = 4.0$  into Eq.(1),  $\theta_b = 26.57^\circ$  is obtained. On the other hand, in dielectric periodic layer, the incident angle  $\theta_i$  for  $n=-1$  space harmonic of  $TM_0$  mode is determined by:

$$\theta_i = \sin^{-1} [(Kr/K_0)_{-1} / \sqrt{\epsilon_c}] \quad (2)$$

where  $Kr$  is wavenumber in radial direction,  $K_0$  is wavenumber in free space. Calculation shows that  $(Kr/K_0)_{-1} = 0.9075$  for  $a=0.35\lambda$  and  $t=0.225\lambda$ ; then from (2) one has:  $\theta_i = 26.98^\circ \approx \theta_b$ . It means that in the case of  $t=0.225\lambda$  the  $n=-1$  space harmonic of  $TM_0$  mode is perfectly propagating in dielectric periodic layer. Therefore, the action of the periodic layer just likes a cylindric ring sleeving on a dielectric rod of radius  $a$ , while the ring has the thickness of  $t=0.225\lambda$  and approximate dielectric constant of  $\epsilon_{ave} = (\epsilon_a + \epsilon_c)/2 = 2.5$ . That is to say, the perturbation of the periodic layer to the surface wave suddenly disappears at thickness  $t=0.225\lambda$ ; so the  $\alpha$  is drastically reduced to zero at this point. Such phenomenon does not happen to  $TE_0$  mode, because there is no Brewster angle effect for TE modes.

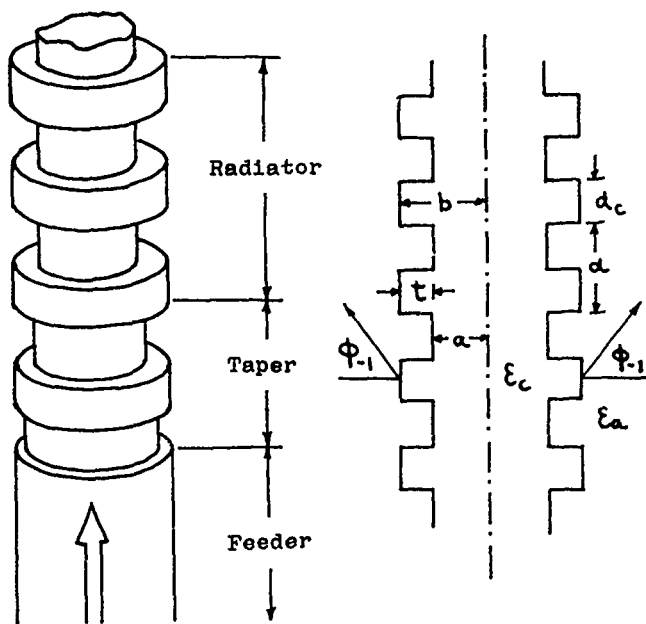


Fig.1 Dielectric rod antenna with periodic corrugations

A particular advantage of periodic antennas is that their radiation beam can be scanned electronically by changing frequency. We have calculated the variations of  $\alpha$  and  $\phi_1$  with the wavelength, for the antenna is operating over a frequency range with the center wavelength of 3.3 mm. The results show that for a change in wavelength from 3.0 mm to 3.6 mm, the main beam sweeps almost linearly over an angular range from  $15^\circ$  to  $35^\circ$ . Besides, the leakage constant peaks at the wavelength of about 3.3 mm and decreases almost symmetrically on both sides, as the wavelength is changed. This is very desirable characteristic, because it ensures a stable radiation pattern with little distortion, as the beam is being scanned.

The author would like to thank professor S. T. Peng of New York Institute of Technology for his help and very useful discussion. This work was supported by The National Natural Science Foundation of China under grant No. 6861004.

#### REFERENCES

- [1] S. T. Peng, S. J. Xu and F. K. Schwing, "Omni-directional Periodic Rod Antenna", 1986 IEEE-APS Symp. Dig. pp.697-700.

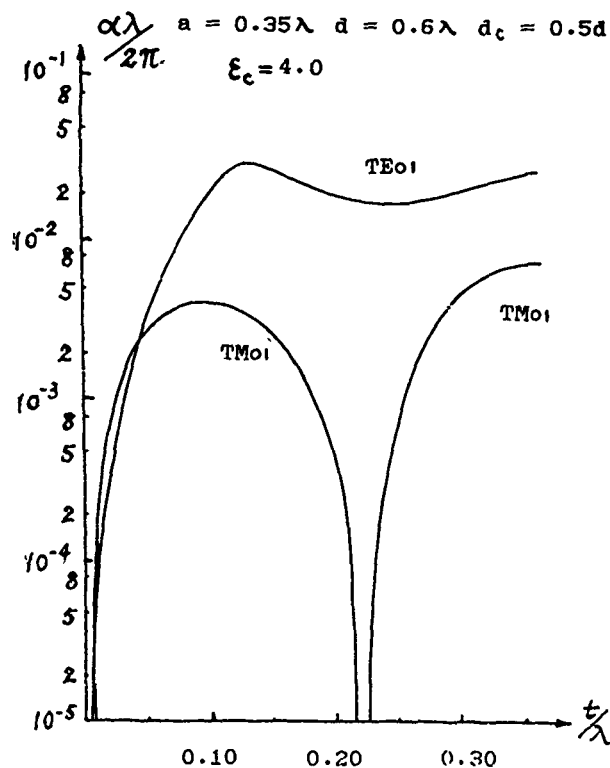


Fig.2 Effect of layer thickness on leakage constant



# EFFICIENCY OF MILLIMETER-WAVE HORN IMAGING ARRAYS

*Gabriel M. Rebeiz<sup>†</sup>, Yong Guo, Philip A. Stimson,  
and David B. Rutledge*

California Institute of Technology, Pasadena, CA.

## ABSTRACT

Two-dimensional horn-antenna arrays are monolithic, high-efficiency imaging detectors of millimeter-wave radiation. In this configuration, a dipole antenna is suspended in a pyramidal horn on a 1- $\mu\text{m}$  silicon oxynitride membrane. This approach leaves room on the wafer for low-frequency lines and processing electronics. Antenna pattern measurements on single elements agree well with theory, exhibiting 3-dB beamwidths of  $54^\circ$  and  $62^\circ$  for the E and H-planes respectively. Horn aperture efficiencies of  $44 \pm 4\%$  have been measured at 93 GHz. Loss processes include impedance mismatch loss, due to impedance mismatch between the antenna and the detector, resistive loss in the horn sidewalls, cross-polarization, intrinsic pattern loss, and horn-to-horn coupling loss. A system efficiency of 24% has been measured for a lens-coupled array.

## INTRODUCTION

Wideband log-periodic antennas and imaging arrays have been integrated on membranes for millimeter and sub-millimeter-wave applications [1]. These imaging arrays are limited to one dimensional designs, because focal plane array elements need to be as large as the spot size of the imaging optics to attain good coupling efficiencies. This limits the area available for supporting electronics. Arrays incorporating an antenna suspended on a membrane inside a horn however, are not limited in this manner. Such devices have recently been shown to exhibit favorable radiation patterns, as the membrane is so thin compared to the wavelength that the antenna effectively radiates in free space inside the horn and substrate dielectric losses are eliminated [2,3]. Previous experiments were performed at 242 GHz where absolute power measurements are difficult [2]. We present here measurements on an array designed for 93 GHz where absolute power calibration can be readily made.

## FABRICATION

The horn antenna array is composed of four stacked silicon wafers. The back two wafers act as a reflecting cavity, while the front wafer forms the mouth of the horn. The opening on the front wafer defines the aperture size. The thickness of the front two wafers determines the position of the antenna inside the horn. To produce the membrane, a silicon oxynitride film is grown on the rear of the second wafer by plasma enhanced chemical vapor deposition. The

<sup>†</sup> now with Department of Electrical Engineering and Computer Science, University of Michigan, Ann Arbor, MI, 48109.

deposition conditions are adjusted to produce a film with a small residual tensile stress. This produces the best membranes. The tensile stress in the film is determined from the bending of the wafer, which is measured with a profiling stylus [4]. The wafers are patterned and etched in an ethylenediamine pyrocatechol solution [5]. The etching process is anisotropic, and forms pyramidal cavities bounded by the  $\langle 111 \rangle$  crystal planes. These make an angle of  $54.7^\circ$  with the  $\langle 100 \rangle$  surface plane. The back wafer is etched until a closed pyramidal cavity is formed. The membrane wafer is etched until the transparent membrane appears. The other wafers are etched through, to form pyramidal sided holes. A silver antenna and a bismuth microbolometer are then lithographically defined on the membrane surface. The pyramidal cavities are gold coated and the wafers aligned and glued together to form the array (Figure 1).

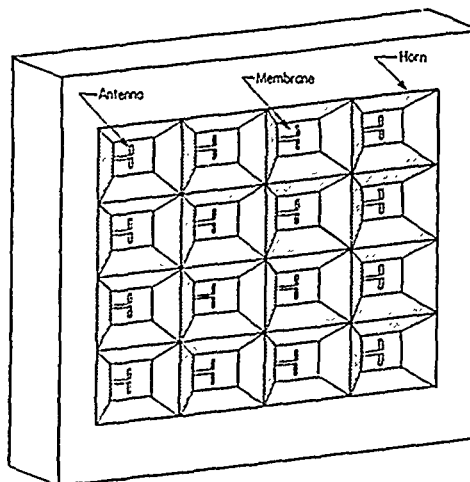


Figure 1. Perspective view of a two-dimensional horn imaging array.

## MEASUREMENTS

### A. Single Element Aperture Efficiency

The aperture efficiency of single elements of the array was determined by measuring the power received by the bolometers when the array was illuminated by a plane wave of known power density. This was found by recording the voltage across the bolometer when the array was illuminated with a source of known power and gain. The known responsivity of the bolometer allows the aperture efficiency to be calculated. The horn-aperture efficiency was measured to be  $44 \pm 4\%$ , or -3.6 dB. This may be compared to the total loss calculated from theory, which is -3.4 dB [7]. The gain of an array element is  $7.3 \pm 0.5$  dB.

It is important that the different contributions to the loss be determined, because this indicates the potential for improvements. Table 1 gives the loss breakdown. The biggest loss is the 2.2 dB dipole mismatch loss between the probe dipole and the bolometer. This is given by the formula  $4R_a R_b / |Z_a + R_b|^2$ , where  $R_a$  is the antenna radiation resistance (50  $\Omega$ ),  $R_b$  is the bolometer resistance (138  $\Omega$ ), and  $Z_a$  is the antenna impedance ( $54 + j95 \Omega$ ). These values were determined from measurements made at 7 GHz on a microwave model of the horn array which incorporated dipole antennas cut from thin copper sheet. The next biggest loss is resistive loss in the horn sidewalls, which is equal to 0.7 dB. The sidewalls of the two wafers defining the back-shorting cavity and the front wafer defining the horn aperture were gold coated, but the sidewalls of the membrane-wafer were not. The main contribution to the sidewall losses comes from the membrane wafer. It should be possible to reduce the mismatch and wall losses, if all the horn sidewalls are gold coated, and the antenna is matched. The aperture efficiency of a  $1.0 \lambda$  square horn should then be around 88%. Other minor losses include pattern losses due to taper loss, loss due to reception of the cross-polarized component and the coupling loss to neighbouring horns.

intrinsic pattern loss	-0.2 dB
mismatch loss	-2.2 dB
horn sidewall losses	-0.7 dB
cross-polarization loss	-0.2 dB
horn-to-horn coupling loss	-0.1 dB
total calculated losses	-3.4 dB
total measured losses	-3.6 dB

Table 1. Horn aperture-efficiency losses.

## B. System Efficiency

The coupling efficiency of a horn array to an imaging system is defined as the power received by a single element placed at the focal point of the imaging system, divided by the total power transmitted through the primary lens, when the lens is illuminated by a plane wave. The coupling efficiency of the 93-GHz array was measured for systems of different f-numbers (Figure 2). We found that 24% of the incident power was absorbed by a single detector for an f-number of 0.7, and 14% for an f-number of 1.1. An imaging system suffers from spillover loss, in addition to the losses given in Table 1. If matching and sidewall losses were eliminated, the coupling efficiency would be 54%. This agrees with the theoretical coupling-efficiency of 60% [4]. The distribution of the power in the focal plane, for a plane wave incident normal to the lens, was measured for these lenses. The result for the f/0.7 lens is shown in Figure 3. The lens Airy pattern has its first dark ring at  $0.61 \lambda$  and  $1.22 \lambda$  for the f/0.7 and f/1.1 lenses respectively. The center element receives 96% of the total power incident on the focal plane for the f/0.7 lens, and 56% for the f/1.1 lens. An f/0.7 optical system is therefore desirable for a diffraction-limited imaging system.

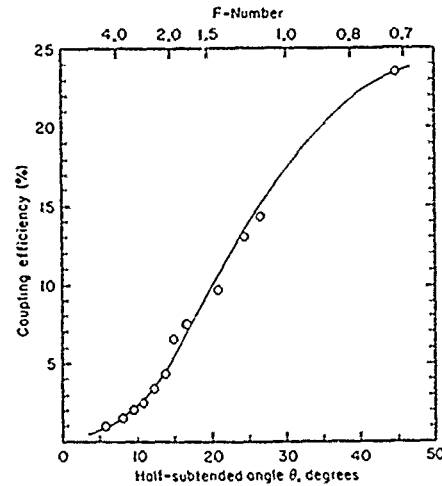


Figure 2. The coupling efficiency of a horn element. Measured points are indicated by circles.

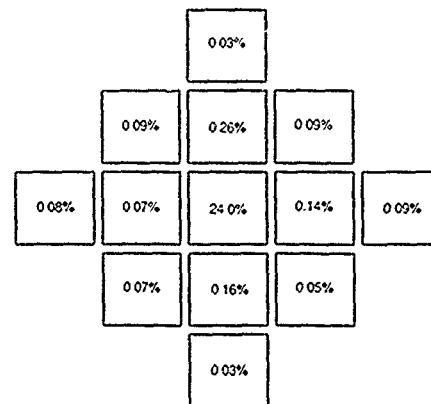


Figure 3. The distribution of the power in the focal plane as a percentage of the total power incident on the f/0.7 lens.

## ACKNOWLEDGEMENTS

This work was supported by contracts from the Army Research Office, the Department of Energy, the Innovative Space Technology Center at the Jet Propulsion Laboratory, the Innovative Science and Technology Program of the Strategic Defense Initiative Organization and Aerojet Electrosystems. P. A. Stimson is supported by a CSIRO of Australia Postdoctoral Award.

## REFERENCES

- [1] G. M. Rebeiz, W. G. Regehr, D. B. Rutledge, R. L. Savage and N. C. Luhmann Jr, *Int. J. of IR and MM Waves*, 8, pp. 1249-1255, 1987.
- [2] G. M. Rebeiz, Y. Guo, D. B. Rutledge and D. P. Kasilingam, *12th Annual IEEE Int. Conf. on IRMM Waves*, Lake Buena Vista, Florida, Dec 14-18, 1987.
- [3] G. M. Rebeiz, Y. Guo, P.A. Stimson, D. B. Rutledge and D. P. Kasilingam, "Monolithic Millimeter-Wave Two-Dimensional Horn Imaging Arrays", Submitted for publication in the *IEEE Transactions on Antennas and Propagation*, June 1988.
- [4] L. Maissel and R. Glang, *Handbook of Thin-Film Technology*, McGraw-Hill, New York, 1970.
- [5] K. Peterson, *Proc. of the IEEE*, 70, pp. 420-457, 1982.
- [6] D. P. Kasilingam, "Topics in Millimeter-Wave Imaging Arrays," Ph. D Thesis, California Institute of Technology, June 1987.
- [7] G. M. Rebeiz, "Monolithic Millimeter-Wave Two-Dimensional Horn Imaging Arrays," Ph. D Thesis, California Institute of Technology, June 1988.

## Antennas on Layered Substrates

R.L. Rogers, D.P. Neikirk, H. Ling, and T. Itoh  
Department of Electrical and Computer Engineering  
The University of Texas at Austin, Austin, TX 78712

### Introduction:

Electrically thick layered substrates using the resonant structures discussed in [2-4] offer the advantage of providing simple and efficient support for millimeter wave printed circuit antennas. They can also produce desirable beam patterns through the proper choice of dielectrics. There has been theoretical study of these layered structures [2-4], but experimental investigation has been limited. Also, the primary focus has been on the use of dipole antennas with these structures, while slot antennas have received little attention. Here we give results for efficiency calculations for both slots and dipoles, and experimental pattern measurements for slots on layered substrates which show that they can produce desirable beam patterns with high front-to-back ratio. We find good agreement between theory and 10GHz modeling experiments.

### Analysis:

The general substrate configurations studied here are shown in Fig. 1. For a dipole antenna (Fig. 1a) the dipole is placed on a grounded substrate (layer 1), and then covered by a "superstrate" (layers 2 through N). In contrast, the slot (Fig. 1b) is a simple aperture in the ground plane on the back of layer 1. Each layer is a quarter of a dielectric wavelength thick. The efficiency of the structures shown in Fig. 1 are calculated using the definition:

$$\eta = \frac{P_{\text{rad}}}{P_{\text{rad}} + P_{\text{sw}} + P_{\text{backside}}}$$

where  $P_{\text{rad}}$  is the total integrated power radiated through the dielectric to air,  $P_{\text{sw}}$  is the total integrated power coupled to guided (surface) waves, and  $P_{\text{backside}}$  is the total integrated power radiated directly to air for the slots. The calculation of these quantities, as well as the beam patterns, uses the techniques described in [1],[4],[5]. In this paper, the dielectric structures for the slot and dipole antennas are the same.

### Experiment:

To test the validity of the calculated beam patterns for these layered structures measurements were made at 10GHz. To construct a layered substrate Emerson and Cumming Stycast Hi-K dielectric and polyethylene sheets were used. The dielectrics were all machined to be nominally a quarter of a dielectric wavelength thick at 10GHz. The ground plane was made by placing strips of 3M copper foil tape on the back surface of the first layer of the substrate. Additional layers were then added as desired. The detectors used were zero-bias Schottky diodes made by MACOM. The detectors were soldered across the slot antenna. A motorized azimuth-elevation antenna positioner was used to hold and move the antenna. The ground plane was fairly small, being only 3.3 free space wavelengths on a side; consequently, there were some problems with finite ground-plane effects for E-plane measurements. Most of the H-plane patterns, however, did not show such effects.

### Results:

Measured and calculated H-plane beam patterns for a three dielectric layer substrate are shown in Figs. 2 and 3. For Fig. 2, the dielectrics used for layers 1 and 2 give  $\epsilon_1 = \epsilon_2 = 4$ , and for layer 3 gives  $\epsilon_3 = 13$ ; thus the slot is effectively on a  $\lambda_d/2$  thick,  $\epsilon_r = 4$  layer, followed by a  $\lambda_d/4$  thick,  $\epsilon_r = 13$  layer. The losses in the dielectric and ground plane have been included to calculate the beam patterns, although these effects are quite small. The agreement between theory and experiment clearly shows that the patterns are dominated by the dielectric. The calculated efficiency of a single slot on this structure assuming lossless dielectrics would be about 45%. If twin slots are employed in a manner similar to that described in [5]

the efficiency can be increased to about 72%. The calculated efficiency of a single dipole placed between layers 1 and 2 would be 79%, while broadside twin dipoles would give 85% [5]. Measurements and calculations with twin slot antennas show no appreciable difference in the beam pattern compared to a single element slot. Our calculations show that the beam patterns for slots and dipoles are nearly identical, which is true for all of the structures considered here.

Figure 3 shows the measured and calculated pattern for a three layer structure with  $\epsilon_1 = 13$ ,  $\epsilon_2 = 2.4$  and,  $\epsilon_3 = 13$ . Again we see that the agreement is fairly good. Because this three layer stack is more resonant than the three layer structure discussed above, the beam pattern is slightly narrower. The calculated efficiency of a single slot on this structure is about 32%, while a twin slot configuration [5] would give of 77%. The single dipole would have an efficiency of 46%, and broadside twin dipoles, 61%. Here the measured front-to-back ratio for the single slot is 36, with a predicted value of 70. This discrepancy is probably due to the fairly large detector diode on the backside of the substrate.

Figure 4 shows the measured and calculated H-plane patterns for a five layer structure with  $\epsilon_1 = 4$ ,  $\epsilon_2 = 2.4$ ,  $\epsilon_3 = 13$ ,  $\epsilon_4 = 4$ , and  $\epsilon_5 = 13$ . Here the beam pattern is much narrower than for the three layer cases. We also have measured a front-to-back ratio that is close to the value predicted by theory: 66 measured, 70 calculated. The E-plane pattern (not shown) is identical to the H-plane pattern and agrees with experiment equally well. In this case the lobes due to finite ground plane effects are conspicuously absent from the measured E-plane pattern because of the dielectric layers. Again assuming lossless dielectrics, the efficiency of a single slot antenna on this structure is calculated to be about 47%, while the twin elements would give about 79%. The single dipole would have an efficiency of 86%, and broadside twin dipoles 92%. The dipoles are more efficient than the slots because the initially low dielectric constant layer followed by the subsequent higher dielectric constant layers tends to suppress guided mode losses to the lower order TM modes.

In order to illustrate the sensitivity of antenna patterns on these layered structures we have also considered the effects of a small air-gap between the dielectric layers. Figure 5 shows the H-plane pattern of the same structure as that used in Fig. 3 with a 40mil ( $0.03\lambda_0$ ) air gap between the first and second layers. The rather dramatic result is the appearance of "horns" at  $28^\circ$  from boresight. In addition, in order to achieve the fit between experiment and theory, the assumed values of  $\epsilon_1$  and  $\epsilon_3$  were changed from 13 to 12.8 (the material is only guaranteed to be within 10% of the nominal value of 13). This small change in dielectric constant reduced the magnitude of the "horns" by a factor of 0.7. Both calculations and measurements show that the location and size of these peaks are more sensitive to parameter errors than when the beam is concentrated along boresight (i.e. no air-gap). For this dielectric structure our calculations show the same results in the case of the dipole when the same air-gap is placed at the interface between layer 1 and layer 2 (i.e. the interface containing the dipole). It is worth noting that this gap, scaled to 94GHz, would be approximately the thickness of a human hair.

### Conclusions:

We have found that preliminary experimental results show good agreement between theory and experiments for multi-layer, electrically thick planar substrates. Both theory and experiment indicates that the dielectric layers largely determine the radiation patterns of the structures. Dielectric and ground plane losses are generally small enough that they can be neglected in structures containing few layers. Small air gaps, however, are very

detrimental to the beam pattern, as shown by both theory and experiment. On structures with the first layer made of a lower density (dielectric constant) material than the subsequent layers, the dipole antenna is a more efficient radiator. When the first layer has the same dielectric constant as the highest dielectric constant material in the stack, however, twin slots should give better efficiency than twin dipoles because of TM guided mode loss reduction. We have also found that when broadside twin elements are employed, there is no appreciable difference between single and twin element beam patterns on the dielectric structures considered here.

This work was supported by the Joint Services Electronics Program under contract number AFOSR F49620-86-C-0045, and the National Science Foundation under grant ECS-8552868.

#### References:

- [1] D.B. Rutledge, D.P. Neikirk, and D.P. Kasilingam, 'Integrated Circuit Antennas,' Infrared and Millimeter Waves, vol. 10, Academic Press, 1983, pp. 1-90.
- [2] N.G. Alexopoulos, D.R. Jackson, 'Fundamental Superstrate Effects on Integrated Circuit Antennas,' IEEE Trans. Antennas and Propagation, vol. AP-32, no. 8, Aug. 1984, pp. 807-816.
- [3] H.Y. Yang and N.G. Alexopoulos, 'Gain Enhancement Methods for Printed Circuit Antennas Through Multiple Superstrates,' IEEE Trans. Antennas and Propagation, vol. AP-35, no. 7, July 1987, pp. 860-863.
- [4] R.L. Rogers, D.P. Neikirk, and H. Ling, 'Planar Matching of Antennas on Electrically Thick Dielectric Substrates,' 12th Intern. Conf. on Infrared and Millimeter Waves, Dec., 1987, pp 288-289.
- [5] R.L. Rogers, D.P. Neikirk, 'Use of Broadside Twin Elements to Increase Efficiency on Electrically Thick Dielectric Substrates,' Int. Journal of Infrared and Millimeter Waves, November, 1988 (to be published).

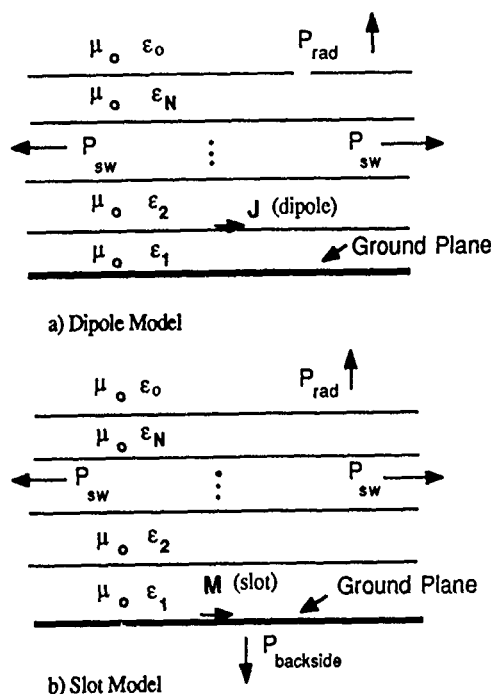


Figure 1 Printed slot and dipole antennas in layered substrates. For the resonant configurations, all layers are  $\lambda_d/4$  thick, where  $\lambda_d$  is the wavelength in the dielectric layer. The dielectric configurations of the layered structures are exactly the same for dipole and slot cases.

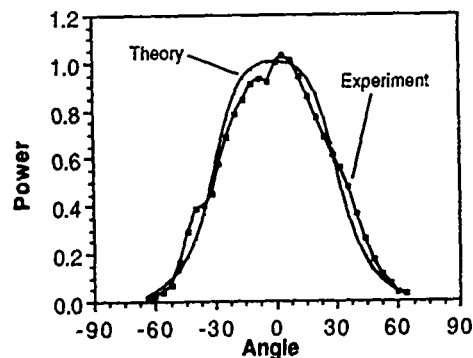


Figure 2 H-plane pattern for a slot with  $\epsilon_1=\epsilon_2=4$ , and  $\epsilon_3=13$ .

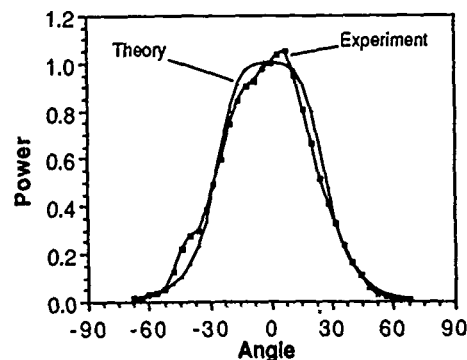


Figure 3 H-plane pattern for a slot with  $\epsilon_1=13$ ,  $\epsilon_2=2.4$ , and  $\epsilon_3=13$ .

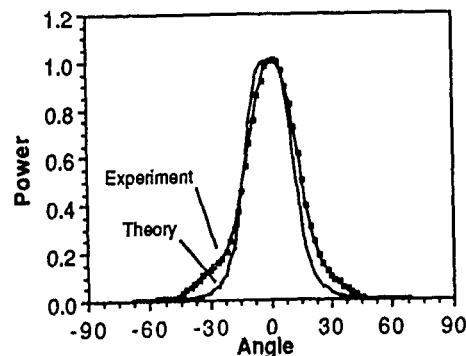


Figure 4 H-plane pattern for a slot with  $\epsilon_1=4$ ,  $\epsilon_2=2.4$ ,  $\epsilon_3=13$ ,  $\epsilon_4=4$ , and  $\epsilon_5=13$ .

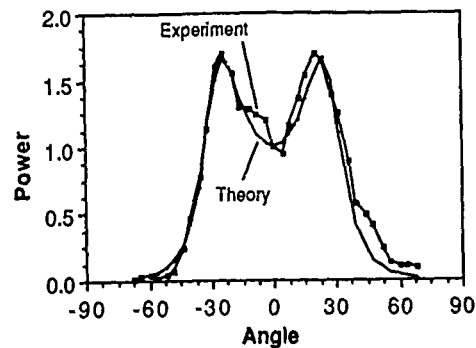


Figure 5 H-plane pattern for a slot with  $\epsilon_1=12.8$ ,  $\epsilon_2=2.4$ , and  $\epsilon_3=12.8$  with a 40mil ( $0.033\lambda_0$ , where  $\lambda_0$  is a wavelength in free space) air gap between layers 1 and 2.

## NEW DIRECTIONS IN MMW VACUUM ELECTRONICS RESEARCH

R.J. Barker

U.S. Air Force Office of Scientific Research  
 Bolling Air Force Base  
 Washington, DC, USA

## ABSTRACT

A technical review and appraisal of ongoing basic research in vacuum and plasma mm-wave sources sponsored by the Air Force Office of Scientific Research (AFOSR) will be presented. In all, the work of more than a dozen leading scientific laboratories will be discussed. Emphasis will be placed on individual project goals, recent results, and important technical issues.

## INTRODUCTION

On March first of this year, a workshop was held at AFOSR which brought together 14 government program managers from the DOD, DOE, and NSF. They represented all of the major federal agencies which were funding research in the field of high-power, mm-wave, vacuum-electronic devices. Each summarized the individual efforts within his respective program in the light of current and future objectives. The meeting proved so informative that attendees felt the technical highlights should be shared with the mmw-community at large. It is the objective of this presentation to cover as much of that technical material as possible.

Most of the research topics to be covered have their counterparts in efforts currently supported by AFOSR, which contributes over \$1.5 million per year to non-solid-state mmw studies. AFOSR funds work in the following three major sub-areas: vacuum devices, plasma devices, and numerical modeling. Although the scope of the sponsored research is kept as broad as possible, emphasis is placed on novel concepts which could lead to the eventual development of future rf oscillators and amplifiers in the 10-300 GHz range which can operate with reasonable efficiency at powers of 100 W to 1 GW. The potential applications to communications and radar are obvious.

## VACUUM DEVICES

Among the most promising topics of mmw research today is the cyclotron auto-resonance maser (CARM) [1]. Two of the leaders in that field are N.C. Luhmann and A.T. Lin of UCLA. They are currently using theory and experiment to examine a

400 kV, 140 GHz CARM amplifier as well as a low voltage, slow-wave CARM (Cherenkov CARM) [2]. G. Bekefi at M.I.T. similarly has work underway on a 35 GHz CARM [3]. Bekefi is also pursuing a broad variety of FEL studies, most notably in the areas of permanent magnet wigglers [4] and micro-wigglers [5].

Work is proceeding on the cusp-injected magnetron (CUSPTRON) at both the University of Maryland (Destler [6]) and the Polytechnic University (Kuo [7]). S.P. Kuo has now completed a 30 kW, 12.3 GHz version which will operate at the eighth harmonic.

Other areas of gyrotron research are being pursued by R.M. Gilgenbach (U. of Michigan) and A.M. Ferendeci (U. of Cincinnati). Gilgenbach is studying the possible use of 1 MV, 1-10 kA, microsecond pulsed e-beams in a gyrotron configuration to yield kJ-level, 2-8 GHz rf pulses [8]. Ferendeci, on the other hand, has been examining the use of intense ribbon beams in a planar geometry gyrotron (see Fig. 1) to amplify 90 GHz radiation [9].

The Orbitron [10] of I. Alexeff of the University of Tennessee has now left the basic research stage amid a flurry of new interest. Alexeff reports reliable operation at up to 10 GHz steady state and up to a terrahertz in pulsed mode.

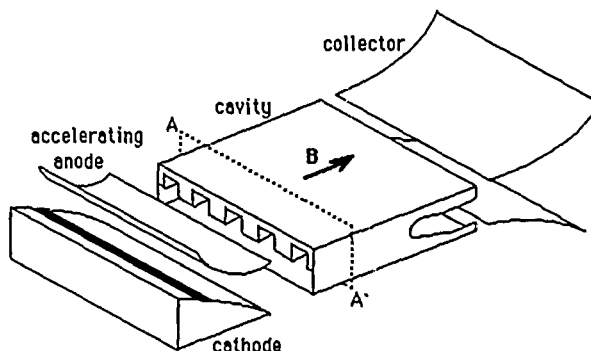


Figure 1.

The Rectangular High Harmonic Gyrotron  
 (A.M. Ferendeci, U. of Cincinnati)

## PLASMA DEVICES

The most famous of the plasma-based mmw concepts under active investigation revolves around the pioneer work of G. Benford at UC-Irvine [11]. Benford's present plasma/intense-e-beam interaction studies involve the careful examination of the plasma turbulence created by the beam. Meanwhile, R.W. Schumacher of the Hughes Research Labs has studied beam-plasma interactions at the lower end of the energy spectrum. His novel 3-wave-mixing mmw device [12], as depicted in Fig. 2, is now receiving widespread attention.

Using a quite different approach based on results obtained in early magnetic mirror plasma research, G.E. Guest and R.A. Dandl of AMPC, Inc., are studying plasmas as storage mediums for ordered populations of high energy electrons. In their Plasma Electron Microwave Source (PEMS), upper off-resonant electron heating is used to build up the electron energy which is then released in a short, intense rf burst by triggering a whistler wave [13]. A 1 GW, 3-35 GHz PEMS is the goal of a current joint study by AMPC and Varian.

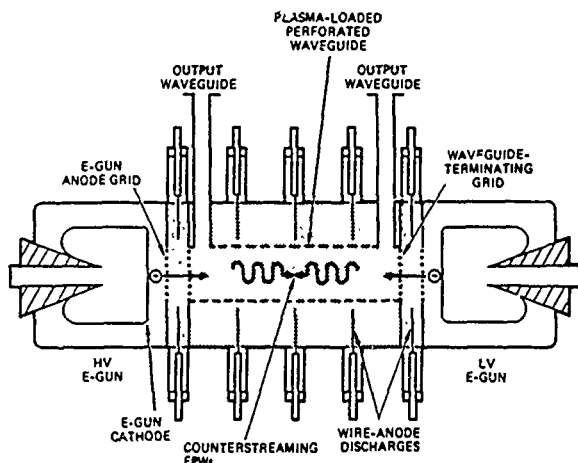


Figure 2.

Beam-Plasma 3-Wave Mixing Apparatus  
(R.W. Schumacher, Hughes Res. Labs)

## NUMERICAL MODELING

The physics involved in the current generation of vacuum mmw device concepts is extremely complex. Analytic theory is hard-pressed to give solid explanations or predictions for many high-power, short-wavelength devices. At the same time, comprehensive experimental studies of novel mmw concepts are becoming prohibitively expensive in both time and money. Even reliable diagnostics become an expensive luxury. Luckily, computer codes for numerical modeling have now reached a level of reliability and speed that make

them clear choices to fill the crucial gap between theory and experiment. High-risk, high-payoff ideas born of analysis can now be subjected to a next higher level of scrutiny and understanding before hundreds of thousands of dollars are invested in risky experiments.

To hasten the widespread use of these new numerical tools, the DOD and NASA have contracted with MRC and SAIC to perfect and release special versions of their powerful 3-D P.I.C. codes, SOS and ARGUS. On a smaller scale, AFOSR is sponsoring MRC to introduce four university research groups to the powerful 2-D P.I.C. code, MAGIC. To assist the code's acceptance, T. Gladd of JAYCOR is preparing a user-friendly, PC-based, graphics interface package which will help potential users who lack numerical simulation experience to actually be able to use MAGIC themselves.

## REFERENCES

- (1) A.T. Lin, *Inf. J. Electronics*, 1984, vol. 57, p.1097.
- (2) H. Cao, D.B. McDermott and N.C. Luhmann, Jr., Gyrotron IV Session, this conference.
- (3) G. Bekefi, A. DiRienzo, C. Leibovitch and B. Danly, Gyrotron VI Session, this conference.
- (4) G. Bekefi and J. Ashkenazy, *Appl. Phys. Lett.*, 1987, vol. 51, pp. 700-702.
- (5) S.C. Chen, G. Bekefi and A.C. Wang, to be published in *Appl. Phys. Lett.*, 1988.
- (6) E. Chojnacki, W.W. Destler, W. Lawson and W. Namkung, *J. Appl. Phys.*, 1987, vol. 61, pp. 1268-1275.
- (7) S.P. Kuo, K.K. Tiong and P.E. Miller, Gyrotron V Session, this conference.
- (8) R.M. Gilgenbach, J.G. Wang, J.J. Choi, C. Outten and T. Spencer, Gyrotron V Session, this conference.
- (9) A.M. Ferendeci, *IEEE MTT-S Digest*, 1983, p. 430.
- (10) I. Alexeff, "The Orbitron Microwave Maser," in *High Power Microwave Sources*, Granatstein & Alexeff, Eds., Artech House, Norwood, MA, 1987, pp. 293-305.
- (11) G. Benford, K. Kato and D. Tzsch, *Phys. Rev. Lett.*, 1983, vol. 50, p. 20.
- (12) J. Santoru and R.W. Schumacher, *Bull. Am. Phys. Soc.*, 1986, vol. 31, p. 1602.
- (13) G.E. Guest and R.L. Miller, *Nuclear Fusion*, 1988, vol. 28, pp. 419-432.

# SHORT PERIOD WIGGLER FREE ELECTRON LASER WITH A SHEET ELECTRON BEAM

J.H. Booske, D.J. Radack, T.M. Antonsen, Jr., W.W. Destler, J.M. Finn, V.L. Granatstein,  
P.E. Latham, I.D. Mayergoyz, J. Rodgers, E.T. Rosenbury, and Z.X. Zhang  
Laboratory for Plasma Research  
University of Maryland, College Park, Maryland 20742

## ABSTRACT

A review of recent progress at the University of Maryland's Laboratory for Plasma Research (LPR) on the development of millimeter-wave free electron lasers (FELs) using short period electromagnet planar wigglers and low voltage ( $V_{beam} \approx 500kV$ ) sheet electron beams will be given.

## INTRODUCTION

LPR's research program on short period wiggler FELs is devoted to the development of low cost, high power, tunable, coherent millimeter wave sources with applications for ECRH of fusion plasmas, space-based radar, and oscillator drivers for accelerator-based FEL amplifiers. The essential components for the concept include short-period planar wigglers ( $5mm \leq \ell_w \leq 10mm$ ), modest electron energies ( $V_{beam} < 1MeV$ ), sheet electron beams, and multi-stage depressed collectors (for spent beam energy recovery) [1]. The reasons for these features have been described in Ref. 1. It is particularly noteworthy, however, that with sheet electron beams, the planar wiggler not only drives the FEL interaction, but also provides strong ponderomotive beam focusing [1]. This obviates the need for axial guide magnetic fields. Since a detailed description of the FEL configuration has been provided in Ref. 1, the remainder of this paper shall be devoted to a discussion of recent research progress.

## OVERVIEW OF RECENT RESULTS

### A. Theory

During the past year we have made substantial progress in developing theoretical descriptions and predictive capabilities for short period wiggler FELs. A normalized nonlinear theoretical formulation has been developed for obtaining FEL oscillator designs which are optimized for maximum efficiency when operating in single mode equilibria [2]. Linear analyses of satellite stability in saturated oscillator equilibrium states have yielded an identification of stable regions of parameter space for single mode oscillation [3]. One important consequence of the work in Refs. 4 and 5 was the identification of a "golden rule" for FEL oscillator design. This rule states that to maximize efficiency while maintaining stable single mode operation one should choose the beam current equal to approximately three times the start oscillation current.

A model has been developed for simulating the nonlinear time evolution of FEL oscillator radiation fields from noise to saturation, including the effects of competition between multiple axial cavity modes [4]. This work has provided valuable information on the timescales necessary

to achieve oscillator saturation, the evolution of various competing modes during the start-up phase, as well as a method of programming the beam voltage turn-on in order to achieve the highest efficiency available to saturated single mode equilibria [5] (see also paper by B. Levush and T.M. Antonsen, Jr. in the FEL II session, this conference).

Finally, we have combined the (normalized theory) results of Refs. 2-5 with scaling laws for dimensionalized physical parameters to generate a procedure for synthesizing optimized FEL oscillators [6]. As examples, parameters for both tapered and untapered 1.0 MW, 300 GHz FEL oscillators are provided in the first two columns of Table 1.

The nonlinear analyses described above have been supplemented by linear calculations to survey the importance of such issues as magnet field errors as well as non-FEL instabilities that compete for the beam's free energy. Wiggler magnetic field errors, for example, can result in beam heating, beam disruption, and/or beam diffusion to the waveguide walls. For FELs with parameters similar to those in Table 1, however, most of these effects are negligible if errors in peak wiggler field amplitudes are less than 10% (rms) and errors in wiggler period lengths are less than 2.5% [7].

Two instabilities have been identified as possible competition for the basic FEL instability. The first of these is a second harmonic, FEL-like, electromagnetic instability arising from electron betatron motions in the narrow transverse-or wiggler-focused-dimension. This absolutely unstable mode has been called the "beta-FEL" instability [8]. Since the mode is suppressed by beam energy spreads in excess of 0.02%, however, it is not expected to be important for our devices. The second instability that we have been studying with linear analyses is an electrostatic "resistive wall" mode resulting from the coupling of a negative energy space charge wave to eddy currents in waveguide walls with finite conductivity [7]. Our calculations to date, however, indicate that the growth rate of this instability should be negligible for parameters similar to those presented in Table 1. As a final comment, it should be noted that there are no low frequency beam instabilities expected to arise from the wiggler focusing fields (such as diocotron instability) since the coupling to axial wiggler field components is weak and the beam is confined near the minimum of the ponderomotive well (i.e., on-axis) [1,?].

### B. Sheet Beam Propagation Experiments

In addition to a theoretical study of beam stability we are involved in an on-going series of experiments to verify the feasibility of propagating wiggler-focused sheet electron beams through narrow waveguide gaps between the short-period wiggler magnets. The measurements are conducted using a pulse line accelerator to generate a beam of ap-

proximately 300-500 keV, 20 A, and a beam cross-section of approximately 1 mm  $\times$  2-3 cm. The first of these experiments was completed using a five-period wiggler magnet with a 3 mm waveguide gap and  $\ell_w = 1$  cm [9]. The results of this study were promising in that they clearly demonstrated wiggler focusing without any observable beam disruption instabilities. Incomplete beam transport was observed, however, due to poorly matched entrance conditions associated with the wiggler field profile. More recently, we have completed a series of preliminary experiments using a ten-period wiggler whose field profile has been modified to improve beam entrance conditions. The initial results from this second effort have been illustrated in Fig. 1 along with data from the previous five-period wiggler run. It is evident that a larger percentage of injected current was transported and collected in the 10 period wiggler experiments. This increase can be attributed to the improved wiggler entrance conditions.

### PROOF OF PRINCIPLE EXPERIMENT

We are now in the process of designing and assembling a proof-of-principle (PoP) experiment to test the feasibility of some of the basic concepts associated with short-period wiggler FEL oscillators. A 450 kV thermionic Pierce electron gun has been obtained from the Stanford Linear Accelerator Center (SLAC) to provide a 1  $\mu$ s, 300-400 A beam with energy between 400-450 keV. Much of the beam will be masked with a tapered graphite and molybdenum beam scraper to yield a 1 mm  $\times$  2 cm cross-section sheet beam. Simulations of the masked beam using an electron trajectory code [10] indicate that the resultant beam has approximately 20 A of usable current within a  $\pm 1\%$  axial energy spread. Parameters for the PoP configuration are summarized in the third column of Table 1.

### ACKNOWLEDGEMENTS

The authors wish to acknowledge generous assistance by various personnel at SLAC, as well as many members of LPR's gyrokystron experimental staff and the Charged Particle Beam Group. This work is supported in part by the U.S. Department of Energy and by SDIO/IST through a grant administered by the Harry Diamond Laboratory.

### REFERENCES

- [1] V.L. Granatstein, et al., Proc. of 9th Int'l FEL Conf., (Williamsburg, VA, 1987), to be published in *Nucl. Instr. and Meth. in Phys.*, 1988.
- [2] A. Serbeto, B. Levush, and T.M. Antonsen, Jr., submitted to *Phys. Fluids*, 1988.
- [3] B. Levush and T.M. Antonsen, Jr., to be published in *Nucl. Instr. and Meth. in Phys.*, 1988.
- [4] T.M. Antonsen, Jr. and B. Levush, submitted to *Phys. of Fluids*, 1988.
- [5] T.M. Antonsen, Jr. and B. Levush, submitted to *Phys. Rev. Lett.*, 1988.
- [6] J.H. Booske, A. Serbeto, B. Levush, and T.M. Antonsen,

Jr., submitted to *J. Appl. Phys.*, 1988.

- [7] P.E. Latham and T. M. Antonsen, Jr., *Bull. Amer. Phys. Soc.*, 1987, vol. 32, p. 1827.
- [8] P.E. Latham, submitted to *Phys. Fluids*, 1988.
- [9] J.H. Booske, et al., *J. Appl. Phys.*, 1987, vol. 64, p. 6.
- [10] W.B. Herrmannsfeldt, Electron trajectory program, SLAC Report-226, 1979.

Table 1  
Design Parameters for Short Period Wiggler FELs

Beam Voltage (kV)	500	500	410
Beam Current (A)	60	34	20
Waveguide Gap (cm)	0.22	0.22	0.4
Waveguide Width (cm)	5.0	5.0	4.0
Effective Cavity			
Transmissivity (%)	5.5	9.0	10-20
Wiggler Period (cm)	0.54	0.54	1.0
No. of Periods	20	111	25
Peak Wiggler Field (kG)	2.0	2.0	1.5
Intrinsic Efficiency (%)	4.0	13.0	3.6
Thermal Wall Load (kW/cm <sup>2</sup> )	2.0	2.0	0.09
Cavity Power (MW)	22	22	1.3
Taper	no	yes	no
Saturation Time ( $\mu$ s)	0.3	?	0.35
Allowable Axial Energy Spread	$\pm 2\%$	?	$\pm 2\%$
Frequency (GHz)	298	298	120
Output Power (MW)	1.0	1.0	0.280

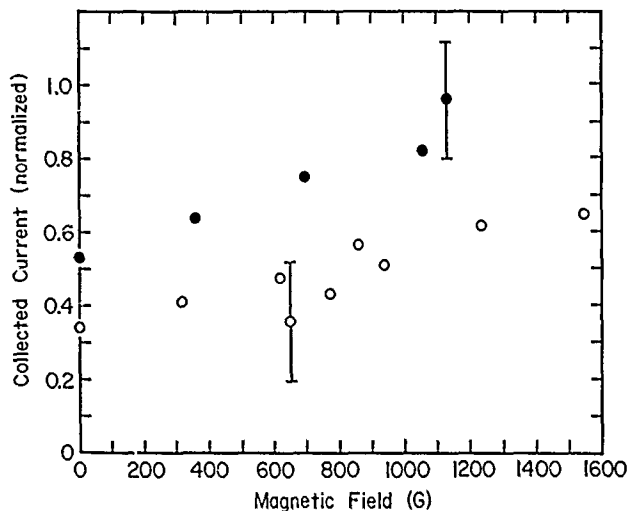


Figure 1

Ratio of transported current to injected current in wiggler-focused sheet beam propagation experiments. Data includes both initial, five-period wiggler experiments (open circles), as well as more recent ten-period wiggler measurements (closed circles).



## TUNABLE MICRO-UNDULATORS FOR FREE ELECTRON LASERS

S.C. Chen, G. Bekefi, S. DiCecca, and R. Temkin  
Department of Physics and Plasma Fusion Center  
MIT, Cambridge, MA 02139

### ABSTRACT

We present the test results of a novel microwiggler structure [1] for free-electron lasers, in which, each 2.4 mm period consists of two channels of miniature electro magnets energized by current with opposite polarities. The magnetic field in each half-period is independently controllable and the tunability is demonstrated experimentally which may provide means for reducing random field errors; for field tapering; for optical klystron configurations; and for electron beam injection.

### INTRODUCTION

Short period (1–10 mm) undulator for free-electron laser (FEL) applications has been a subject of considerable interest [1,2,3,4]. Besides its compactness, such system has the advantage of producing higher frequency radiation with a given electron energy, or conversely, it reduces the electron energy required to access a given wavelength. The magnetic structure is similar to a multi-channel magnetic recording head [5] in which each period consists of two channels of electromagnets excited with current of opposite polarities (Figure 1), hence the magnetic field in each half period is independently controllable. The unique flexibility of this configuration, in principle, allows one to: tune out random errors associated with field variations in individual channels; taper field profile for efficiency enhancement; tailor fields in the entrance introduction and exit region; and construct optical klystron configuration. In this paper, we outline the crucial criteria of the microwiggler design and describe the construction procedure. The test results of a 30 periods, 2.4 mm wavelength prototype is presented, which demonstrated the tunability of the field amplitude. We also discuss cooling requirements to achieve longer pulse or DC operations.

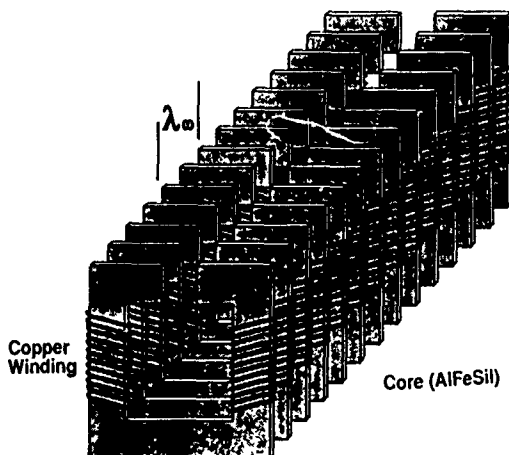


Figure 1. Construction of a micro-undulator

### DESIGN OF MICROWIGGLERS

An outline of the design procedure is presented here, detail formulation of the design can be found in our previous paper [1]. For a given wiggler wavelength  $\lambda_w$ , the relevant parameters of the geometry are gap spacing, core thickness, gap width, winding length, and wire size.

Core thickness governs the longitudinal field profile and is the most important parameter in the design process. Since the cores are excited in an alternating way, the cancellation effect from the adjacent channels tends to reduce the attainable field on axis. Thinner core has smaller crosstalk effect and thus should yield higher field per unit excitation. However, below certain critical core thickness, the harmonic content of the field rises sharply because of the non-cancelling spiky field characteristics.

Gap spacing determines the transverse field profile. To minimize the inhomogeneity and to reduce the field fall-off from the pole face to the beam location (magnet axis), it is desirable to use a gap less than  $\lambda_w/3$ . However, practical concerns like electron beam propagation and optical beam diffraction set the lower limit for the gap spacing. For microwigglers, the choice of gap spacing is uniquely challenging.

These two thin-dimensions, core thickness and gap spacing, also govern the behavior of the magnetic material when the system approaches saturation. In addition, the energetics and the circuit response are analyzed in a parametric way. The number of turns in a fixed winding volume is determined by the wire size, and is treated as a dependent variable. In each half-period core element, the resistance and the inductance are calculated, the ratio  $L/R$  then gives the rise time of winding/core assembly. Interestingly, the rise time depends mainly on core thickness and gap width. The current required to generate a particular average magnetic field across the gap is calculated from Ampere's law. Then the Ohmic heating power in the coil and the total energy dissipated during the pulse can be found. From these simple scalings, one finds that to achieve a certain field in the gap, a long winding length reduces the current, power, and energy required. The wire diameter plays the role of impedance matching between the magnet and the power supply, e.g., thinner wire needs more current at a correspondingly lower voltage.

### MAGNET CONSTRUCTION

We have constructed and tested a 30-period flat pole face prototype with a wiggler period of 2.4 mm. It is assembled in two half brackets, each with 60 precision-cut slots, held together with epoxy and bolts. AlFeSi cores, wound with 160 turns of 40 gauge wire, are sliced to gen-

erate the 3 mm airgap and form the beam channel in the microwiggler. These cores are loaded into the slots in the half-brackets and potted. Terminal boards (electrical interfaces) are connected to the core windings and inserted into the half-brackets. The whole assembly is then lapped and gapped to the final configuration. All mechanical tolerances are held to within 0.3 mil. such that an undulator period error of less than 0.3% is achieved. The error due to machining is controlled in a non-accumulative fashion to help sustaining the phase synchronism in the interaction.

## FIELD MEASUREMENTS

In all the measurements, the microwiggler was driven by one single power source with all the electromagnet channels being excited in parallel. The magnetic field in each half period was independently controlled by varying the current using a series potentiometer. Both DC and 60 Hz AC power supplies were used in the low field CW tests to single out AC effects. For high field tests, a special pulser circuit was constructed. Upon triggering, the low level electronics in the circuit fires the high power SCRs and switches a clean half-period sine wave from the 60 Hz power line into the microwiggler. The magnetic field measurements were made with a motorized miniature Hall probe having an active area of  $0.045 \text{ mm}^2$ . The experiment was conducted at room temperature with no active cooling system in the magnet structure.

In the linear regime of the magnet, we obtained a calibration factor of 110 Gauss/Amp on axis, this is predicted quite well by the analysis described in the last section. With a core thickness of  $\lambda_w/4$ , the partial cancellation between channels generated a nearly perfect sinusoidal field pattern, the third harmonics on axis measured is less than 0.5%. The tunability of the field amplitudes is demonstrated as follows: with equal settings on the tuning potentiometers, the measured field showed a 15% variation in peak field amplitudes (Figure 2). The distinctive field spikes at the entrance and the exit are present as expected.

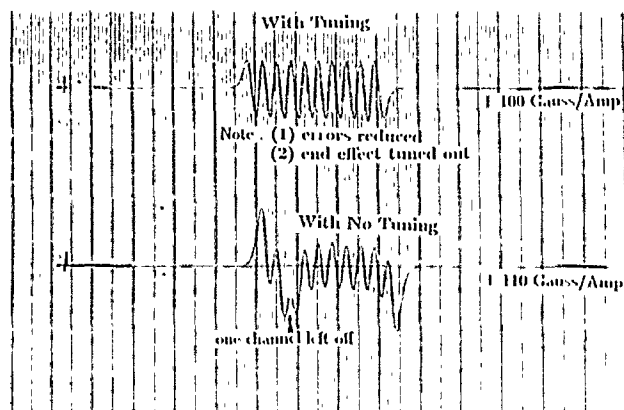


Figure 2. Hall probe measurement of on axis wiggler field before (lower trace) and after (upper trace) tuning.

After carefully tuning up the circuit, the peak field variation can be kept well below 1%, and the wiggler end effects can be adjusted for optimal beam injection.

In addition, we have constructed many single-channel test pieces with various dimensions to verify the fundamental scaling laws discussed in the previous section. More importantly, the behavior of the core array approaching saturation can be examined in detail.

## COOLING

The maximum current that can be pulsed into each channel for 8 ms duration - without causing thermal breakdown - was measured under two conditions: 10 Amperes in microwiggler (with all the channels tightly seated in the slot structure) versus 50 Amperes in air (single core piece excited in room temperature air). The comparison indicates the possibility of higher current operations with further cooling arrangements. In short pulse magnets, the temperature rise is dominated by the thermal mass of the coils, hence precooling of the magnet structure should be effective. For example, precool the copper coil magnet down to nitrogen temperature ( $77^\circ \text{K}$ ) increases the maximum current from 10 A to 30 A. Precooling copper further down is neither economical nor effective because of the temperature dependence of copper resistivity and heat capacity. Longer pulse (100 ms) operation of microwigglers can be achieved through better designs of the magnet core structure to obtain more gauss per ampere. For DC operation, it is imperative to use superconducting coils. For example, using 32 gauge NbSn wire and the same prototype parameters, and assuming the permeability stays high enough at helium temperature, the critical current is estimated to be 20 A.

## CONCLUSIONS

We have designed, constructed and tested a 30 period microwiggler prototype with a 2.4 mm wavelength. The tunability of the longitudinal field profile is demonstrated. The operation characteristics of the magnet in the linear regime agrees well with calculations. With precooling and the use of high saturation core materials, the pulse length and the field intensity will be further improved.

## ACKNOWLEDGEMENT

This work was supported by the Air Force Office of Scientific Research.

## REFERENCES

- [1] S.C. Chen, G. Bekefi, S. DiCecca and A.C. Wang in Tenth International Conference on FEL, Jerusalem, Israel, 1988.
- [2] W.W. Destler, V.L. Granatstein, I.D. Mayergoyz, and Z. Segalov, *J. Appl. Phys.* 60,521 (1986)
- [3] R.M. White, *Appl. Phys. Lett.*, 46, 194 (1985)
- [4] G. Ramian, L. Elias and I. Kimel, *Nuclear Instruments and Methods in Physics Research*, A250, 125 (1986)
- [5] J.L. Dimmers, *J. British Kinematography Sound and Television Soc.*, 54, 234 (1982)

## COLLECTIVE INSTABILITY IN CIRCULAR FREE ELECTRON LASER

Yasushi Kawai, Hirobumi Saito

Institute of Space and Astronautical Science  
Sagamihara, Kanagawa, Japan

Jonathan S. Wurtele

Plasma Fusion Center  
Massachusetts Institute of Technology  
Cambridge, Massachusetts, 02139, U.S.A.

## Abstract

An analytical fluid theory is developed for a circular free electron laser, including the effect of the space charge wave. The dispersion relation of the FEL radiation and the space charge wave is analytically obtained. It is found that the space charge wave gives strong effect on the performance of a circular FEL.

## 1. Introduction

In the circular free electron laser (circular FEL), electrons circulate in a coaxial waveguide, being subject to a uniform axial magnetic field and an azimuthally periodic wiggler magnetic field (see Fig.1). In the previous experimental researches [1-2], millimeter wave radiation has been observed in this device. Also, some theoretical models have been proposed [3-4], but no fluid model that includes the effect of the space charge wave has been discussed. We believe that this paper presents the first fluid theory that accounts for the effect of the space charge wave adequately. Throughout this paper, we use Eulerian description.

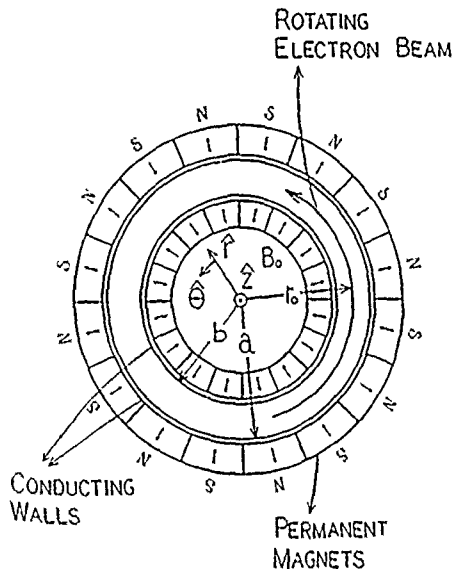


Fig.1 Configuration of Circular Free Electron Laser

## 2. Particle Motion

## 2.1 Equilibrium Motion

Electrons are subject to cyclotron motion in an axially uniform magnetic field  $B_z$ . We assume that there is no axial streaming velocity. Furthermore, azimuthally periodic wiggler field  $B_w = B_w(r_0/r) \sin N\theta$  is imposed (see Fig.1), where  $r_0$  and  $N$  are the Larmor radius given by  $c\beta_0/\omega_0$  and the periodicity of the wiggler field. Here  $\beta_0 = v_0/c$  and  $\omega_0 = eB_z/m\gamma$ , and  $\gamma$  is the familiar Lorentz factor. Therefore the motion of the electrons will be slightly perturbed from cyclotron motion.

The axial component of the velocity is obtained from the Lagrangean equation using the conservation of the canonical momentum. The radial and the azimuthal component of the velocity are obtained, assuming that the parameter  $a_w$  is small, where  $a_w = e r_0 B_w / \sqrt{2} m c N$ . Taking the first order terms of  $a_w$ , we obtain

$$\begin{aligned} v_r &= 0, \\ v_\theta &= r_0 \omega_0, \\ v_z &= v_0 \cos N\theta. \end{aligned} \quad (1)$$

where  $v_0 = \sqrt{2} a_w c / \gamma$ .

## 2.2 Perturbed Motion

The orbit of the beam particle will depart from equilibrium, due to the presence of the electromagnetic fields. In order to express the perturbed velocity in terms of the perturbed fields, linearized relativistic perturbation equation of motion is made of use. All the perturbed quantities are expressed by means of Fourier decomposition with respect to the azimuthal direction

$$\delta F(r, \theta, t) = \sum_n \delta F_n(r) \exp(i\omega t - in\theta). \quad (2)$$

Solving them we obtain

$$\begin{pmatrix} \delta v_{r,n} \\ \delta v_{\theta,n} \\ \delta v_{z,n} \end{pmatrix} = \begin{pmatrix} \frac{\Omega}{\omega(\omega^2 - \omega_0^2)}, & -\frac{\omega}{\omega^2 - \omega_0^2}, & -\frac{N\omega_0(\omega_0 - \Lambda_1\omega_0^2)}{\omega^2(\omega^2 - \omega_0^2)} \\ \frac{\omega}{\omega(\omega^2 - \omega_0^2)}, & \frac{\Omega}{\omega(\omega^2 - \omega_0^2)}, & \frac{N\Omega\omega_0}{\omega^2(\omega^2 - \omega_0^2)} + \frac{\Lambda_1(\omega_0^2 - \Omega\omega)}{\omega^2(\omega^2 - \omega_0^2)} \\ -\frac{N\omega_0\omega_0\Lambda_1}{\omega^2(\omega^2 - \omega_0^2)}, & -\frac{N\omega_0\Omega\Lambda_1}{\omega^2(\omega^2 - \omega_0^2)} - \frac{\Lambda_2}{\omega^2}, & \frac{\Lambda_2}{\omega^2} \end{pmatrix} \begin{pmatrix} \Sigma_1 \\ \Sigma_2 \\ \Sigma_3 \end{pmatrix} \quad (3)$$

where  $\omega_0 = v_0/r$ ,  $\omega_2 = v_0/2r$ ,  $\Lambda_1 = v_0^2/c^2$ ,  $\Lambda_2 = v_0 v_w/2c^2$ ,  $\Omega = \omega - (p+N)\omega_0$ ,  $\omega' = \omega - p\omega_0$ . The quantities  $\Sigma_1$ ,  $\Sigma_2$  and  $\Sigma_3$  are three components of the Lorentz force divided by  $r$ , namely  $\Sigma_1 = -e(\delta E_{r,p+N} - v_z \delta B_{\theta,p+N} + v_\theta \delta B_{z,p+N})/m\gamma$ ,  $\Sigma_2 = -e(\delta E_{\theta,p+N} + v_z \delta B_{r,p})/m\gamma$ , and  $\Sigma_3 = -e(\delta E_{z,p} - v_\theta \delta B_{r,p})/m\gamma$ .

### 3. Field Equations

The field in the circular FEL is assumed to be cut off in the axial direction. This means that the field is divided into two waves, namely TM wave and TE wave. The former, with azimuthal mode number  $p$ , is the FEL radiation field excited by the perturbed axial current  $\delta J_{z,p}$ . The latter, with azimuthal mode number  $p+N$ , is the space charge wave excited mainly by the perturbed azimuthal current  $\delta J_{\theta,p+N}$ , and both of these two waves are excited simultaneously.

#### 3.1 Radiation Field

The radiation field may be very close to a vacuum TM mode in a coaxial waveguide. Here we introduce a quantity  $\delta a = \delta E_{z,p}/\omega$ .

By integrating the Maxwell's equations, we obtain a relation between  $\delta a$  and the perturbed current

$$\delta a = 2\mu_0 f_2 \{(\omega/c)^2 - k_{pq}^2\}^{-1} (a^2 - b^2)^{-1} \int_{r_1}^{r_2} r \delta J_{z,p} dr, \quad (4)$$

where

$$f_2 = (a^2 - b^2) \chi_p^2 (kr_0)^2 / \{a^2 \chi_p' (ka)^2 - b^2 \chi_p' (kb)^2\}. \quad (5)$$

Here  $k$ ,  $f_2$ ,  $\chi_p$ ,  $b$ ,  $a$ ,  $r_1$ ,  $r_2$  are the radial wave number of the vacuum TM mode, the coupling factor of a coaxial waveguide, the eigen function of a coaxial waveguide, the radius of the inner and the outer boundary of the coaxial waveguide, the beam radius of the inner and the outer boundary, respectively.

#### 3.2 Space Charge Wave

While the radiation field is very close to a vacuum TM mode of a coaxial waveguide, the space charge wave is not necessarily close to a vacuum TE mode. We now carry out the analysis by means of the wave admittance after the previous works [5-6] of negative mass instability. Here another quantity  $\delta\phi = -ir\delta E_{\theta,p+N}/(p+N)$  is introduced. We obtain a compact formula for the space charge wave by integrating the Maxwell's equations.

$$\delta\phi = g(c^2\mu_0/2\omega) \int_{r_1}^{r_2} r \delta J_{\theta,p+N} dr, \quad (6)$$

where

$$g = \{(b_+ + b_-) + (p+N)\Delta r/r_0\}^{-1}. \quad (7)$$

Here  $b_+$  and  $b_-$  are the outer and the inner wave admittance, and  $\Delta r = r_2 - r_1$ .

### 4. Dispersion Equation

#### 4.1. Perturbed Current

In order to obtain the dispersion equation we only need to calculate  $\int_{r_1}^{r_2} r \delta J_{z,p} dr$  and  $\int_{r_1}^{r_2} r \delta J_{\theta,p+N} dr$ .

We assume here that the electron number density distribution is almost step function. Considering that the FEL interaction occurs when the vacuum TM mode and the beam mode synchronize, we obtain the first order current density represented by the perturbing field after Lau's method [7].

#### 4.2 Dispersion Equation

Since the FEL radiation occurs at the interaction between a vacuum TM mode and the beam mode  $\omega = (p+N)\omega_0$ , we can put the frequency as  $\omega = ck_{pq} - \Gamma = (p+N)\omega_0 - (\Delta\omega + i\Gamma)$ , where  $\Delta\omega$  is the detuning parameter between the vacuum TM mode and the beam mode, and  $-i\Gamma$  is the growth rate. Substituting the perturbed current density into equations (4) and (6), we finally obtain the dispersion equation in the matrix form as

$$\begin{pmatrix} f_1 \omega_0^2 \frac{a^2 c}{f_2} \frac{1}{(\Delta\omega + i\Gamma)^2} & 1 + f_1 \omega_0^2 \frac{f_2}{f_1} \frac{1}{(\Delta\omega + i\Gamma)^2} \\ 1 - f_1 \omega_0^2 \frac{a^2 c}{f_2} \frac{1}{(\Delta\omega + i\Gamma)^2} & -f_1 \omega_0^2 \frac{a^2 c}{2f_2^2 c} \frac{1}{(\Delta\omega + i\Gamma)^2} \end{pmatrix} \begin{pmatrix} \delta a \\ \delta\phi \end{pmatrix} = \begin{pmatrix} 0 \\ 0 \end{pmatrix}, \quad (8)$$

where  $f_1 = g(p+N)(a^2 - b^2)/2r_2^2 \omega_0^2$  is the plasma frequency defined by  $\omega_p^2 = 2\mu_0 e^2 \sigma_e^2 / m(a^2 - b^2)$  and  $\sigma_e$  is the electron surface density.

The dispersion relation is obtained by setting the determinant of the matrix to zero.

$$\Gamma^2 + 2\Delta\omega\Gamma + (\Delta\omega^2 + f_1 \omega_0^2 \frac{f_2^2}{f_1})\Gamma = \frac{f_2 a^2 \omega_0^2 \omega}{4f_1^2}. \quad (9)$$

In the absence of the wiggler field, the dispersion relation corresponds to that of cyclotron maser instability. Equation (8) and (9) show that space charge wave in circular FEL is itself unstable due to negative mass effect. It makes a good contrast to the linear FEL, in which it is stable.

### 5. Conclusion

This paper presents a fluid theory of circular FEL, including the effect of space charge wave. By analyzing the particle motion of a thin electron beam, it is shown that the two waves, TM mode of the FEL radiation and TE mode of the space charge wave, couple with each other through the electron motion. Combining the results of the particle dynamics and the field structure, the dispersion relation is obtained. The space charge wave itself in the circular FEL is found to be unstable due to the negative mass effect.

- [1] G. Bekefi, R.E. Shefer, and W.W. Destler, Appl. Phys. Letts., **44**, 280(1984).
- [2] W.W. Destler, et al., Phys. Fluids, **28**, 1962(1985).
- [3] Y.Z. Yin, and G. Bekefi, Phys. Fluids, **28**, 1186(1985).
- [4] H. Saito and J.S. Wurtele, Phys. Fluids **30**, 2209(1987).
- [5] R. J. Briggs, and V. K. Neil, Plasma Phys., **9**, 209(1967).
- [6] H. S. Uhm, and R. C. Davidson, Phys. Fluids, **20**, 771(1977).
- [7] Y.Y. Lau, IEEE Trans. Elec. Dev., **ED29-2**, 320(1982).

## SUPPRESSION OF SIDEBANDS BY DIFFRACTION IN A FREE-ELECTRON LASER

T. M. Antonsen, Jr.\* and G. Laval\*\*  
 Laboratory for Plasma Research  
 University of Maryland  
 College Park, Maryland 20742

## ABSTRACT

The stability of sidebands in a free electron laser is determined in the regime in which the three-dimensional structure of the modes is important. It is found that the growth rate of the sidebands in the presence of a fundamental mode which is weakly guided by the beam is reduced. The indications are that for some parameters the spatial growth rate of the sidebands can be made less than that of the fundamental.

## INTRODUCTION

The operation of free electron lasers with tapered wiggler parameters to enhance efficiency requires that the radiation field be nearly monochromatic for optimum performance. However, single frequency equilibria are unstable to the growth of parasitic modes known as sidebands.<sup>1</sup> The most dangerous instability occurs for a wave with a frequency shifted from the fundamental by an amount sufficient to resonate with the synchrotron oscillation of the particles in the ponderomotive well of the fundamental. As was originally shown,<sup>1</sup> in a long device the local gain for the sideband exceeds the gain for the fundamental. Thus, a tapered oscillator would be expected to be unstable in the absence of frequency discriminating feedback.

In this paper we will investigate the effect of the three-dimensional mode structure on the sideband instability. In particular, we will examine the stability of single frequency equilibria in which the radiation is optically guided<sup>2</sup> by its interaction with the electron beam.

The basic effect that we consider relates to the "filling factor" for the beam to the radiation. In general, this filling factor is different for the fundamental and the sidebands and thus the results of one-dimensional theory where all excitations are assumed to have the same filling factor are modified. An additional effect that we consider is the radiation damping that occurs for waves with axial phase velocities greater than the speed of light.

Our main results are as follows. We find that for situations where the fundamental is strongly guided (the radiation and beam waists are comparable) the gain of the sidebands is not significantly modified from the one-dimensional result except for the appearance of a high frequency "tail" for the growth rate due to radiation damping. On the other hand, if the fundamental is weakly guided (radiation waist much larger than the beam waist) the sideband growth rates are suppressed to the extent that their gain

can become less than the gain of the fundamental. This latter result is based on estimates made in the weak taper regime and will require numerical verification in the regime of strong taper.

## SEPARABLE BEAM MODEL

To study the effects of diffraction on the sideband instability in free electron lasers we adopt the separable beam model introduced in Ref. 3. In this model the current source term in the wave equation is assumed to have a separable dependence on the axial distance and radius. This leads to a situation where the particle motion is one dimensional

$$\frac{\partial \psi}{\partial \xi} = p,$$

$$\frac{\partial p}{\partial \xi} = -\frac{\partial}{\partial \psi} \frac{1}{2} (\bar{a} e^{i\psi} + a^* e^{-i\psi}) - \alpha,$$

where  $\psi$  is the particle phase,  $p$  is the detuning,  $\xi = z/L$  measures axial distance where  $L = r_{b0}^2 \omega_0 / c$  is the Rayleigh length based on the electron beam radius,  $\bar{a}(\xi, \tau)$  is the effective radiation field experienced by the particles and  $\alpha$  represents the fictitious acceleration due to tapering.

In the separable beam model the effective field is determined by the following convolution integral

$$\bar{a}(\xi, \tau) = \frac{\hat{I}}{4\pi i} \int_{-\infty}^{\xi} d\xi' \frac{\langle \exp[-i\psi(\xi', \tau - \varepsilon(\xi - \xi'))] \rangle}{1 + i(\xi - \xi')},$$

where  $\hat{I}$  is a normalized current,  $\varepsilon = c/v_b - 1$  is the slippage parameter, and the factor  $i(\xi - \xi')$  in the kernel describes the effects of diffraction.

This system can be linearized about an equilibrium in which all particles are trapped in the bottom of a ponderomotive well. This result is a dispersion relation for the complex wave number  $k(\omega)$  as a function of frequency  $\omega$  of the sideband,

$$\frac{a_0 - k^2}{a_0} = \frac{E(k + \omega\varepsilon + \nu) - E_*(k + \omega\varepsilon - \nu)}{2E(\nu)},$$

where  $a_0$  and  $\nu$  are the amplitude and wavenumber of the equilibrium wave,

$$\bar{a}(\xi) = a_0 e^{i\nu\xi}$$

and

$$E(\zeta) = -E_*^*(-\zeta^*) = -(4\pi)^{-1} e^{\zeta} E_1(\zeta)$$

\*Depts. of Electrical Engineering and Physics and Astronomy.

\*\*Ecole Polytechnique, Centre de Physique Theorique, 91128 Palaiseau, France.

with  $E_1(\xi)$  the exponential integral.

A sample solution for spatial growth rate versus frequency for  $\nu = 1$  and various values of  $k_0 = a_0/\nu^2$  is shown in Fig. (1). Similar plots apply for other values of  $\nu$  with the maximum growth rate normalized to the synchrotron frequency being relatively insensitive to  $\nu$ . As  $\nu$  is increased the growth rate curves approach those of the one dimensional model ( $\nu = \infty$ ). In this case the growth rate vanishes for sufficiently high frequency. In the presence of diffraction growth is present for all frequencies.

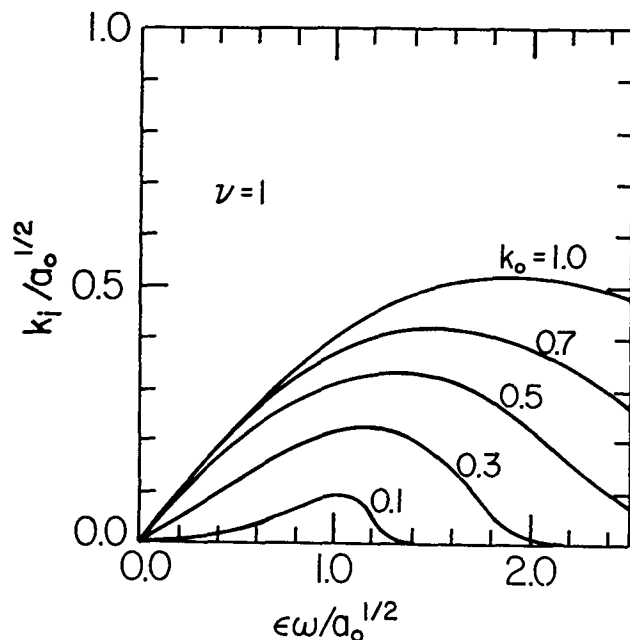


Figure 1

Spatial growth rate of sidebands normalized to synchrotron frequency versus frequency of sidebands normalized to synchrotron frequency for the case  $\nu = 1$  and several values of  $k_0$ .

Figure 2 shows a plot of the ratio of the maximum sideband growth rate to the maximum achievable fundamental growth rate versus  $k_0$  for different values of  $\nu$ . When this number is less than unity one should be able to totally suppress sidebands. This estimate is made in the limit of weak taper ( $\alpha \ll 1$ ) and requires numerical verification.

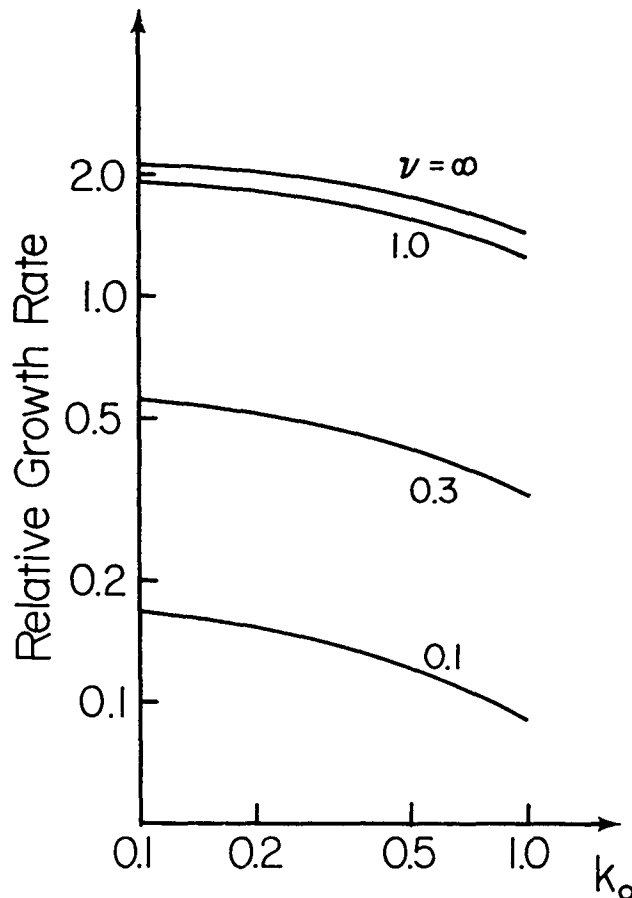


Figure 2

Maximum spatial growth rate of sidebands normalized to the maximum spatial growth rate of the fundamental versus  $k_0$  for different values of the mismatch,  $\nu$ .

#### ACKNOWLEDGEMENT

This work was supported by the U.S. Department of Energy and the Office of Naval Research.

#### REFERENCES

- (1) N. M. Kroll, P. L. Morton, and M. N. Rosenbluth, IEEE J. Quantum Electron., 1981, vol. QE-17, p. 2436.
- (2) P. Sprangle, Cha-Mei Tang, and W. M. Manheimer, Phys. Rev. Lett., 1979, vol. 43, p. 1932 and Phys. Rev. A, 1980, vol. 21, p. 302.
- (3) T. M. Antonsen and B. Levush, Nucl. Instr. Meth., 1988, vol. 000, p. xxx.

# Analysis and Nonlinear Simulation of Quadrupole and Dipole Wiggler FELs for Millimeter Waves\*

J.E. SCHARER, S.F. CHANG, and O.C. ELDRIDGE,

University of Wisconsin-Madison

## ABSTRACT

An FEL amplifier with a helical quadrupole wiggler is investigated analytically and numerically. A 3-D simulation code is utilized to examine the nonlinear evolution of circular waveguide modes as well as the characteristics of relativistic particle motion, which illustrate a strong focussing effect. The simulation predicts a 0.55 dB/cm gain, 2% efficiency, and 8% bandwidth for the optimum TE<sub>21</sub> mode at 300 GHz for an untapered wiggler. Mode competition for an overmoded waveguide and a nonlinear wiggler taper for efficiency enhancement are examined for a linear dipole wiggler in a rectangular guide. It is found that the maximum TE<sub>01</sub> mode efficiency is 53% at 280 GHz and that the TM<sub>21</sub> mode power can be as high as 28% in the uniform wiggler region.

## INTRODUCTION

We consider a free electron laser (FEL) with helical quadrupole or linear dipole magnetic wigglers field inside circular or rectangular guides in the millimeter-wave range. The quadrupole was chosen because its known focussing and stability properties for accelerators might provide improvements at high power and beam density where space charge effects and particle orbit trajectories could be stabilized. A tuneable FEL in the millimeter-wave range has important applications in the areas of communications, high resolution radar, semi-conductor and solid state material properties measurements and as a source for heating fusion plasmas. Work by Ganguly and Freund [1] developed a 3-D nonlinear simulation code for a helical dipole wiggler FEL to examine optimized circular waveguide mode, particle orbits, gain and efficiency. We have modified this code to examine the properties of a helical quadrupole wiggler. Our work on the quadrupole FEL [2, 3] at 300 GHz has shown high gain, broad bandwidth and moderate efficiency for an untapered wiggler. In this work we examine the quadrupole focussing properties, optimized gain, efficiency and bandwidth at 300 GHz. We also examine mode competition and a nonlinear taper for the linear dipole case at 280 GHz.

## ANALYSIS OF THE HELICAL QUADRUPOLE FEL

We analyze the helical quadrupole FEL to compare this configuration to alternative configurations, determine the influence of design parameters on FEL performance, and establish benchmarks for checking the nonlinear computer simulation. We can predict the frequency for the peak of the gain and efficiency curves from the simulation of

A magnetic field solution of the static Maxwell equations in vacuum for a helical quadrupole wiggler field and a uniform guide field is

$$B_r = 2 B_w I_2' (2\lambda) \cos(2\chi),$$

$$B_\theta = -(2B_w / \lambda) I_2(2\lambda) \sin(2\chi),$$

$$\text{and } B_z = B_0 + 2B_w I_2(2\lambda) \sin(2\chi). \quad (1)$$

Where cylindrical coordinates (r, q, z) are used, with

$$\chi = \theta - k_w z, \quad \lambda = k_w r, \quad \text{and } k_w = 2\pi/\lambda_w.$$

We find in our simulations that the TE<sub>21</sub> mode is amplified preferentially, since the electric fields of this mode match the quadrupole structure of the wiggler fields, which means that the field structure matches the lowest order pattern of the perturbed velocity of the electrons in the wiggler field.

We find there is a class of solutions where the phase difference between the electrons and the mode signal field is

stationary, so that the condition that the two curves are tangent yields  $\gamma = (1 - \beta^2)^{-1/2} = [1 + (k_{2n}/2k_w)^2]^{1/2}$  and the frequency  $\omega = k_{2n}c[1 + (k_{2n}/2k_w)^2]^{1/2}$ . This equation predicts the frequency of maximum gain obtained from the computer simulation rather accurately.

## SIMULATION OF FEL GAIN FOR WIGGLERS IN THE 300 GHZ RANGE

We have carried out simulations of the gain, efficiency, and bandwidth for 300 FEL's with a quadrupole wiggler. We have modified a Compton helical dipole code to treat quadrupole or linear dipole wiggler fields through changes in the wiggler field expression, adiabatic entries and consequent modification of the relativistic equations of motion.

For a FEL with a quadrupole wiggler and an axial guide field, the total magnetic field components of Eqn. (1) are used for the nonlinear simulation. The derivation [3] of the dynamic equations for both the TE and TM modes is formally similar to that by Ganguly and Freund [1] except the appropriate choice of the rotating coordinate system which rotates at the same pace as the helical quadrupole wiggler fields, i.e.,  $\hat{e}_1 = \hat{x} \cos(2k_w z) + \hat{y} \sin(2k_w z)$  and  $\hat{e}_2 = -\hat{x} \sin(2k_w z) + \hat{y} \cos(2k_w z)$ .

## RESULTS OF NONLINEAR SIMULATION

We have simulated the operation of the quadrupole FEL configuration near 300 GHz. In these cases we have held the wiggler period fixed at 3 cm, and have varied the beam voltage, beam current, the waveguide radius, and the wiggler field intensity to optimize the FEL performance.

For the 300 GHz range, the beam voltage is 1.6 MeV and the waveguide radius is 0.2 cm to satisfy the tangential intersection conditions. Also, this FEL has a moderate efficiency (5%), broad spectral response (50%), and the spatial gain is 0.47 dB/cm. However, this extremely small waveguide size is difficult to realize. We allow the beam resonance curve to intersect the waveguide dispersion curve at two frequencies with the upper one corresponding to the desired frequency. We increase the waveguide radius to 0.659 cm, which requires a larger beam voltage and beam current, and a stronger wiggler intensity. The simulation results in Fig. 1 show that the efficiency drops to 2% and the bandwidth decreases to 8%, but the spatial gain increases to 0.55 dB/cm, which is due to the larger beam current employed. Orbit trajectories show the quadrupole focussing electron betatron orbits.

We have also carried out a nonlinear simulation for a linear dipole array in a rectangular waveguide near 280 GHz. We modified the code to analyze the rectangular guide modes, relativistic particle orbits and gain in a parallel method to the helical case. Figure 2 illustrates the case of a uniform wiggler for a 280 GHz signal with the following characteristics:  $V_0 = 10$  MeV,  $I_b = 3000$  A,  $r_b = 0.4442$  cm  $\delta\gamma_z / \gamma_0 = 1.5\%$ ,  $\epsilon = 42.8$  mrad - mm,  $B_N = 5 \times 10^4$  A/(rad-cm)<sup>2</sup> with  $B_0 = 4.09$  kG,  $\lambda_w = 10$  cm and a guide which is 3.10 cm square. The TE<sub>01</sub> mode is injected at 500 W with residual TM<sub>21</sub>, TE<sub>03</sub> and TE<sub>21</sub> mode excited at 70  $\mu$ W levels. The TM<sub>21</sub> mode is shown to compete substantially with the TE<sub>01</sub> mode reaching 28% of the wave power near  $k_w z = 70$ . We then add a nonlinear taper section near  $k_w z = 141$  to enhance the efficiency. The taper rate satisfies the KMR equation

$da_w(z)/dz = -2k_w \delta a_{jn}(z) \sin \chi_{res}$ . Figure 3 illustrates the result of the taper which starts at  $k_w z = 142$  and enhances the efficiency to 53% with a suppression of the higher-order modes considered reduced to less than 5% of the total power at  $k_w z = 250$ . In addition we find that the tapered wiggler has a 36% bandwidth about 280 GHz.

We find that the quadrupole and dipole wigglers offer attractive performance in the mm range. We will examine methods for minimizing the mode competition, optimal tapers and the effects of space charge on the performance in future work.

Acknowledgements--This research was supported by the Univ. of Wisconsin Research Committee and in part by NSF Grant ECS-85-14978.

#### REFERENCES

1. A.K. Ganguly and H.P. Freund, "Nonlinear Analysis of Free-Electron-Laser Amplifiers in Three Dimensions," Phys. Rev. A32 4, 2275 (1985).
2. J. Scharer, O. Eldridge, S.F. Chang and N. Lam, "Nonlinear Analysis and Simulation of a Millimeter Range Free Electron Laser with Helical Quadrupole Wiggler." Paper to be published in the proceedings of the 9th International Free electron Laser conference, Sept. 14-18, 1987, Williamsburg, VA., to appear in Journal of Nuclear Instruments and Methods in Physics Research (1988).
3. S.F. Chang, O.C. Eldridge and J.E. Scharer, "Analysis and Nonlinear simulation of a Quadrupole Wiggler FEL at Millimeter Wavelengths," to appear in IEEE Journal of Quantum Electronics, Nov., 1988.

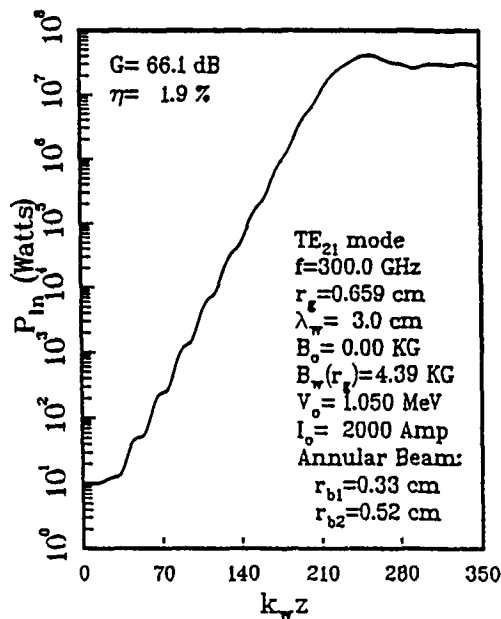


Fig. 1 Spatial evolution of circular TE<sub>21</sub> mode for the FEL with a quadrupole wiggler at 300 GHz

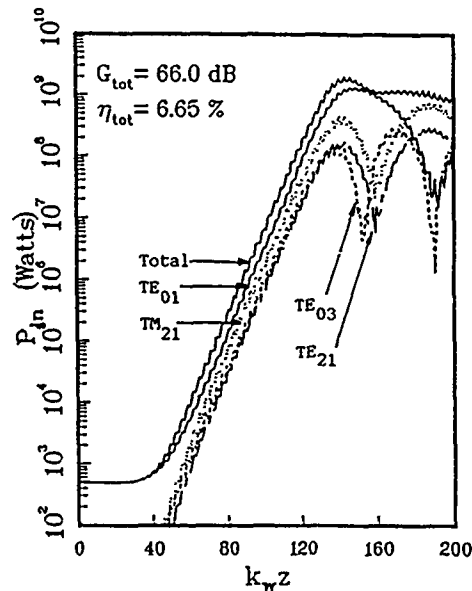


Fig. 2 280 GHz power evolution for rectangular modes with a uniform linear wiggler

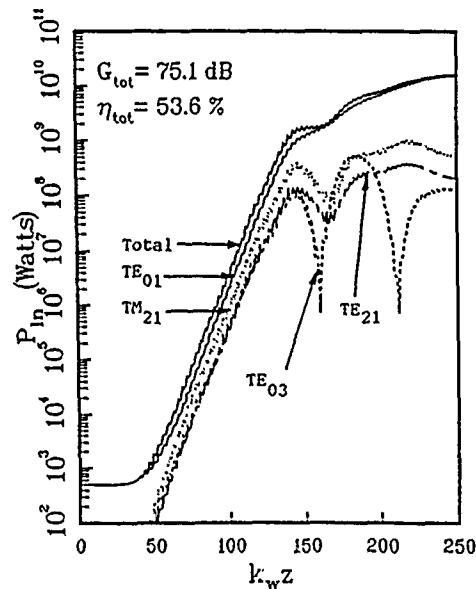


Fig. 3 280 GHz power evolution for rectangular modes with a nonlinear taper



# DEVELOPMENT OF HIGH EFFICIENCY FREQUENCY MULTIPLIERS FOR 130-350 GHz

Timo Tolmunen, Antti Räisänen and Mikko Sironen  
Radio Laboratory  
Helsinki University of Technology  
Otakaari 5 A, SF-02150 Espoo, Finland

## ABSTRACT

In this research the feasibility of developing high efficiency mm-wave multipliers in the frequency range of 130-350 GHz has been studied. A frequency quadrupler for 140 GHz, frequency doublers for 183 GHz and 230 GHz and a frequency tripler for 345 GHz have been analyzed and optimized. The development of high efficiency frequency multipliers is especially important for the spaceborne mm-wave and submm-wave heterodyne receivers used for radio astronomy and remote sensing of the atmosphere.

## INTRODUCTION

Recently we designed, constructed and tested a frequency doubler and a frequency tripler for 80-120 GHz range with very high efficiencies (highest efficiency 45 % and 28 %, respectively) [1,2]. The optimization was based on extensive computer analyses and scaled model measurements.

In this paper we report our continuing effort on developing high efficiency mm-wave multipliers, now for 130-350 GHz range. Computer simulations [3] and scaled model measurements were used for optimization of doublers for 183 GHz and 230 GHz. Preliminary measurements of the doubler for 183 GHz were carried out.

Extensive computer simulations were also made to thoroughly analyze a frequency quadrupler for 140 GHz and a tripler for 345 GHz. In the case of the quadrupler emphasis was placed on the study of optimum idlers at the 2nd and 3rd harmonics. While the highest efficiency ever obtained experimentally from quadruplers at mm-waves is only a few percent [4], our analyses show that theoretically over 50 % efficiency is obtainable when a commercially available varactor is used. These results are now being used in the design of an experimental quadrupler for 140 GHz.

## DOUBLER

An effective doubler requires an optimum matched termination at the 1st and 2nd harmonics and an open circuit for the higher harmonics. Theoretical calculations were carried out for a doubler from 115 to 230 GHz. The analyses showed that in a lossless waveguide mount the efficiency can rise over 50 % [5] in the region of purely reactive multiplication i.e. the diode absorbed power ( $P_{abs}$ ) is about 10 mW and the reverse bias voltage over 6 V. With high input power levels the varactor is driven into conduction which decreases this efficiency. If the multiplication is partly resistive the theoretical efficiency is typically 20-30 % with  $P_{abs} > 30$  mW and reverse bias voltage below 4 V. The diode parameters used in these analyses were:  $C_0 = 10$  fF,  $R_s = 14 \Omega$ ,  $\eta = 1.15$  and  $\gamma = 0.45$ , which are typical for varactors commonly used in this frequency range, e.g. VD012 of Farran Technology.

Using these results and observations from the theoretical and

experimental study of a frequency doubler for 100 GHz [1] a crossed waveguide doubler for 230 GHz and a scaled version for 183 GHz were designed and constructed. Preliminary tests of a doubler for 183 GHz were carried out. In this doubler a VD011-varactor ( $C_0 = 12.5$  fF and  $R_s = 12 \Omega$ ) was used. According to the measurements the highest efficiency obtained was slightly over 20 % and typically 10...20 % in an output frequency range of 160-190 GHz with input power levels below 20 mW (Gunn). With high input power levels 30-100 mW (klystron) the output power of the experimental doubler was 5-10 mW in the range of 170-185 GHz.

The theoretical calculations carried out for VD012 at 230 GHz are approximatively valid also for VD011 at 180 GHz range. The high difference between theoretical and experimental data can partly be explained with high losses of the multiplier structure. Furthermore especially the diode  $\gamma$  might be smaller than the value ( $\gamma = 0.45$ ) used in the calculations. This decreases the efficiency especially at the reactive region. However, it is probably possible to further increase the efficiency of the experimental doubler by careful optimization of whisker shape and length.

## TRIPLER

A frequency tripler requires matched terminations at the input and output frequencies, an optimum idler termination at the 2nd harmonic and an open circuit for the 4th and higher order harmonic frequencies. Computer simulations were carried out for a submm-wave tripler from 115 GHz to 345 GHz using the parameters of VD012-varactor.

The intrinsic efficiency and output power of this tripler is shown in Figure 1. The operation of the tripler is restricted by the diode breakdown voltage ( $V_{BR} \approx -14$  V for VD012) and maximum rectified current for safe operation. This current is typically 10 mA for mm-wave Schottky varactors available today. The instantaneous peak voltage across the diode junction and the rectified current are functions of absorbed power, bias voltage and embedding impedances seen by the varactor at the various harmonics. The dashed lines marked by 10 (mA) and 14 (V) represents the situation when in the case of optimum embedding impedances these limiting current and voltage values are exceeded. An unoptimized termination especially at the 3rd and 4th harmonic changes the voltage (or current) waveform and increases the instantaneous peak voltage considerably. In some cases especially if the input power is high it is possible to burn out the varactor by moving the output backshort.

Reactive multiplication turns partly to resistive when rectified current starts to flow. This is clearly seen in Figure 1: the region of purely reactive multiplication is slightly below the dashed line marked by 0.1 mA. The highest efficiency is obtained in this reactive region. However, it cannot rise over 30 % if safe operation is required.

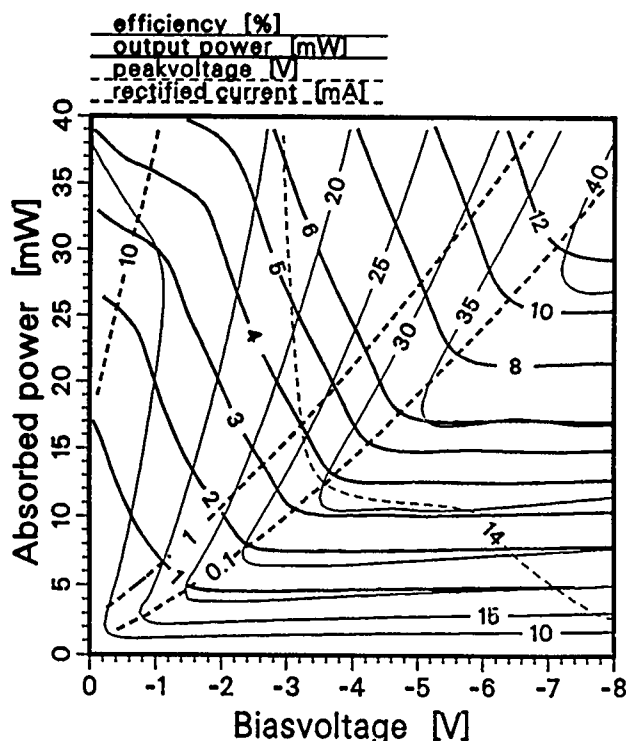


Figure 1. Intrinsic efficiency and output power of a frequency tripler for 345 GHz. On the left side of the thick dashed line marked by 10 (mA) the rectified current exceeds 10 mA. Similarly on the right side of the thin dashed line the instantaneous reverse peak voltage across the diode junction exceeds 14 V. These lines determine the safe operation region of the varactor multiplier.

### QUADRUPLER

A quadrupler is most efficient when it has an idler circuit both at the 2nd and 3rd harmonic frequencies. The simulations showed that with the optimum terminations at both idler frequencies it is possible to obtain quadrupling efficiencies as high as 50–55 % in a reactive region by using commercially available Schottky-varactors (e.g. VD010, having  $C_0 = 19$  fF and  $R_s = 10 \Omega$ ) at the 140 GHz output frequency range. In a quadrupler having only an idler at the 2nd harmonic and a highly inductive termination or an open circuit at the 3rd harmonic the highest efficiency decreases down to about 40 %. The degradation of the efficiency was found to be even more severe if the 3rd harmonic idler termination is slightly capacitive. If the multiplication is partly resistive typical efficiencies are 15...30 % and 5...15 %, respectively.

In a quadrupler perfect idler terminations are of great importance. In a practical design it is necessary to produce a good idler termination at least for the 2nd harmonic although the exact value of this inductive reactance is not critical. This idler termination is essential because the nonlinearity of the C-V-curve of an abrupt-junction varactor is not strong enough to produce higher order harmonics effectively. If the current flow at the 2nd harmonic is permitted the input power is converted first to the 2nd harmonic (doubling) and further to the 4th harmonic (doubling). By permitting the current flow also at the 3rd harmonic it is possible to further increase the quadrupling efficiency. In this case the varactor operates also as an up-converter by mixing the fundamental frequency with the 3rd harmonic.

In a crossed waveguide structure commonly used at the mm-waves it is extremely difficult to provide more than one optimum idler. It is also almost impossible to realize idler terminations which are tunable. Due to this the useable bandwidth of the quadrupler becomes narrower. Both of these facts complicate the practical design.

An experimental quadrupler based on fixed idler terminations is under construction and will be ready for experimental tests at the end of this year. At the diode plane the output waveguide is cutoff at the fundamental and 2nd harmonic. Further away from the diode the waveguide size reduces by a step so that it is cut-off at the 3rd harmonic. At this frequency the high inductance due to the step discontinuity of the waveguide at a distance of  $\lambda_g/4 \dots \lambda_g/3$  is transferred to a short circuit at the diode plane. Due to this effect the total 3rd harmonic idler reactance consists only of the whisker inductance in series with the reactance of a coaxial resonator. This coaxial resonator is used to increase the inductance seen by the varactor at the fundamental frequency [2]. At the 2nd harmonic the reactance of this resonator slightly decreases the total inductance formed by the whisker in series with the high inductance of the cut-off output waveguide.

### CONCLUSIONS

Using commercially available varactors as a frequency doubler from 115 GHz to 230 GHz it is possible to obtain efficiencies up to 50 % in a lossless optimized waveguide mount. If this same varactor is working as a frequency tripler from 115 GHz to 345 GHz the highest efficiency available is only slightly over 30 %. The highest efficiency obtained from an experimental doubler for 183 GHz was 20...22 % when a VD011-varactor was used.

In a quadrupler perfect idler terminations are of great importance. In a practical design it is necessary to produce a good idler termination at least for the 2nd harmonic although the exact value of this inductive reactance is not critical. A perfect termination at the 3rd harmonic further increases the quadrupling efficiency but is usually difficult to realize. Theoretically, a highly inductive termination at the 3rd harmonic works better than slightly capacitive or short circuited termination. If it is possible to fully realize optimum terminations for every harmonic the quadrupling efficiency can rise over 50 % in a lossless waveguide mount.

### REFERENCES

- [1] T.J. Tolmunen and A.V. Räisänen, "An efficient Schottky-varactor frequency multiplier at millimeter waves. Part I: Doubler," *Int. J. of Infrared and Millimeter Waves*, vol. 8, 1313–1336, (1987).
- [2] As above. Part II: Tripler. 1337–1353.
- [3] P.H. Siegel, A.R. Kerr, and W. Hwang, "Topics in the optimization of millimeter-wave mixers," NASA Technical Paper 2287, 512 p., 1984.
- [4] N.R. Erickson, Millitech Corp., South Deerfield, Mass., private communication.
- [5] T. Tolmunen and A. Räisänen, "Analysis and design of 130–250 GHz multipliers," 18th European Microwave Conference Proceedings, Microwave Exhibition and Publishers Ltd., Kent, England, 1988.

## Periodic Monolithic Millimeter-Wave Quantum Well Oscillator

A. Mortazawi, V.P. Kesan, D.P. Neikirk, and T. Itoh  
Department of Electrical and Computer Engineering  
The University of Texas at Austin, Austin, Texas 78712

### Abstract:

A small-signal and large-signal analysis of a traveling wave structure implemented by periodically loading a parallel-plate waveguide with QWITT diodes is presented. The analysis starts with a self-consistent, large-signal model for the diode. The diode model is then coupled to a model for the waveguide circuit and solved using the harmonic balance technique. The output power as a function of frequency for three harmonics for a QWITT oscillator is determined. Our results emphasize the importance of obtaining the ac voltage modulation self-consistently from the circuit when calculating the output power obtained from a QWITT oscillator. The oscillation frequency of the multiple-diode circuit is determined primarily by the periodicity of the structure. The physical dimensions of the waveguide facilitate monolithic fabrication of the oscillator circuit.

### Introduction:

Quantum well oscillators are being considered as potential sources for the millimeter wave spectrum. This is because the resonant tunneling through quantum wells is an inherently rapid transport mechanism, so that the intrinsic cut-off frequency of the device is very high. Even though the quantum well devices are capable of operation at high millimeter wave frequencies [1], their output power is very low. We have recently proposed an improved quantum well structure, the QWITT (quantum well injection and transit time) diode [2]. In the QWITT structure transit time effects are employed to increase the output power of the diode [3, 4]. One way of realizing an oscillator using the QWITT diode is to mount the diode using a metallic post in a parallel-plate waveguide. In order to further increase the output power, a power combiner consisting of a parallel-plate waveguide loaded periodically with QWITT diodes can be realized [5].

### Analysis:

A parallel-plate waveguide loaded periodically with QWITT diodes is shown in Fig. 1. The waveguide is modeled by an equivalent transmission line loaded with an impedance  $Z_p$ . The impedance  $Z_p$  is the sum of the diode impedance and the metal post reactance. A small-signal equivalent circuit model for the QWITT diode [3] is used to obtain the diode impedance as a function of frequency. The metal post inductance,  $X_0$ , to first order is calculated using a conventional mode-matching technique [6]. The impedance  $Z_p = R_d + j(X_d + X_0)$  is then normalized to the characteristic impedance of the parallel-plate waveguide. Once the impedance  $Z_p$  is known, admittance transformations are used to analyze the periodic structure. The oscillation frequency for the circuit is where the imaginary part of the total admittance goes to zero. Using this small-signal analysis the oscillation frequency of the circuit as a function of (a) the distance between the posts, (b) the characteristic impedance of the waveguide, and (c) the impedance of the load, can be determined.

In order to predict the power and efficiency of the QWITT oscillator a self-consistent large-signal circuit model is developed. The large-signal diode model [4] uses a piecewise linearized fit to an experimental dc IV characteristic of the quantum well to describe current injection. Using the Ramo-Shockley theorem for transit time effects, a numerical integration of the injected charge pulse over the entire rf cycle is performed to obtain the device current. The electric field and carrier velocity in the drift region

are assumed to be constant. The large-signal diode model provides the current density through the diode as a function of bias up to three harmonics. For the large-signal analysis of the oscillator circuit a harmonic balance scheme is used [7]. In this method the circuit is divided into two parts, the linear circuit region and the nonlinear diode region. A voltage waveform is applied to both linear and nonlinear circuits, and the current waveform obtained from both the linear and nonlinear parts of the circuit is matched.

### Results and Discussions:

Fig. 2 shows the large-signal conductance and susceptance as a function of oscillation frequency for a QWITT diode (10  $\mu\text{m}$  diameter) operating in the  $3\pi/2$  injection mode. The output power at the fundamental frequency for a single QWITT diode using this large-signal model is shown in Fig. 3. The output power for the higher order harmonics is considerably lower than at the fundamental frequency. The fundamental output power of the QWITT diode as predicted by this model is lower than other large-signal models for the QWITT diode [8] that assume perfect impedance matching by the circuit and large ac circuit modulation ( $\approx 50\%$ ). Fig. 4 shows the dependence of the output power at 94 GHz on  $\Gamma$ , the ratio of the amplitude of the ac voltage to the dc bias across the diode. At any desired oscillation frequency to maximize the output power, the circuit is designed to provide optimum ac modulation,  $\Gamma$ . Table I shows the physical parameters of the QWITT oscillator circuit designed to operate at 94 GHz. The physical dimensions of the waveguide facilitate monolithic fabrication of the oscillator circuit.

### Conclusion:

We have presented a large-signal analysis of a QWITT oscillator implemented by loading a parallel-plate waveguide with QWITT diodes. The analysis uses a large-signal model for the diode which is then coupled to a model for the waveguide circuit and solved self-consistently using the harmonic balance technique. The output power as a function of frequency for the fundamental and three harmonics for a QWITT oscillator is determined using this model. Our results emphasize the importance of obtaining the ac voltage modulation self-consistently from the circuit when calculating the output power obtained from a QWITT oscillator. The oscillation frequency of the multiple-diode circuit is determined primarily by the periodicity of the structure. The physical dimensions of the waveguide facilitate monolithic fabrication of the oscillator circuit.

### References:

1. E.R. Brown, T.C.L.G. Sollner, W.D. Goodhue, and C.D. Parker, IEEE Dev. Res. Conf., VIA-2, Santa Barbara, Calif., June 1987.
2. V.P. Kesan, D.P. Neikirk, B.G. Streetman, and P.A. Blakey, IEEE Elect. Dev. Lett., EDL-8, pp. 129-131, April 1987.
3. V.P. Kesan, D.P. Neikirk, P.A. Blakey, and B.G. Streetman, and T.D. Linton, IEEE Trans. on Elect. Dev., pp. 405-413, April 1988.
4. V.P. Kesan, T.D. Linton, C.M. Maziar, D.P. Neikirk, P.A. Blakey, and B.G. Streetman, 1987 IEEE International Elect. Dev. Meeting Tech. Dig., pp. 62-65, Dec. 6-9, 1987.

5. V.P. Kesan, A. Mortazawi, D.P. Neikirk, and T. Itoh, *Elect. Lett.*, 24, pp. 666-667, 26 May 1988.
6. L. Lewin, "Theory of Waveguides," Halsted Press, New York, 1975.
7. M.S. Nakhla and J. Vlach, *IEEE Trans. on Circuits and Systems*, CAS-23, p. 85, Feb. 1976.
8. I. Song and D.S. Pan, *IEEE Elect. Dev. Lett.*, EDL-8, pp. 560-562, Dec. 1987.

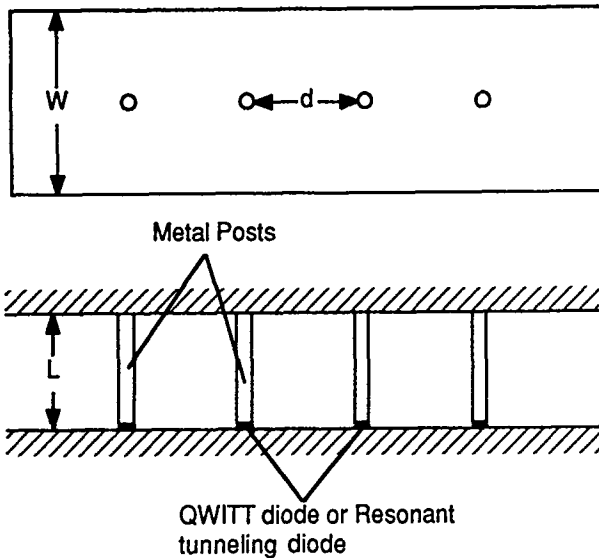


Fig. 1: Schematic representation showing top and side views of parallel plate waveguide circuit periodically loaded by QWITT diodes or resonant tunneling diodes.

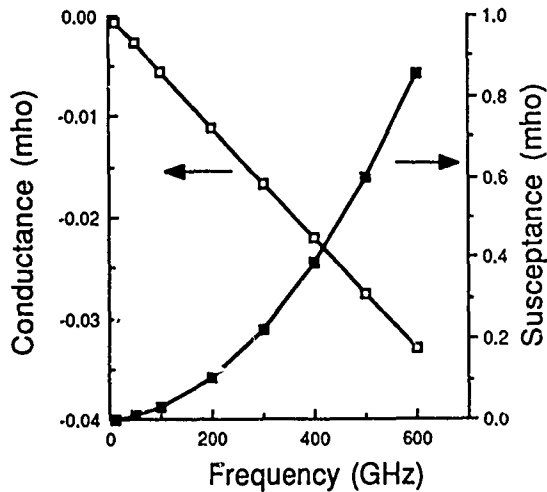


Fig. 2: Large-signal conductance and susceptance as a function of frequency for a QWITT diode ( $10\ \mu\text{m}$  diameter) operating in the  $3\pi/2$  mode.

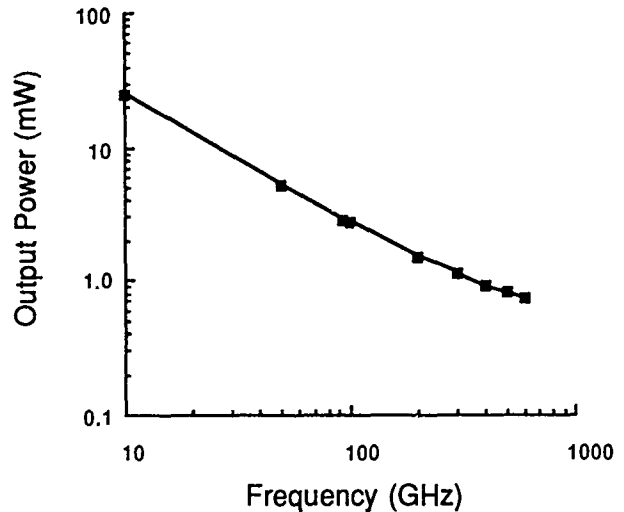


Fig. 3: Output power as a function of frequency for a single QWITT diode oscillator obtained using a large-signal harmonic balance circuit model.

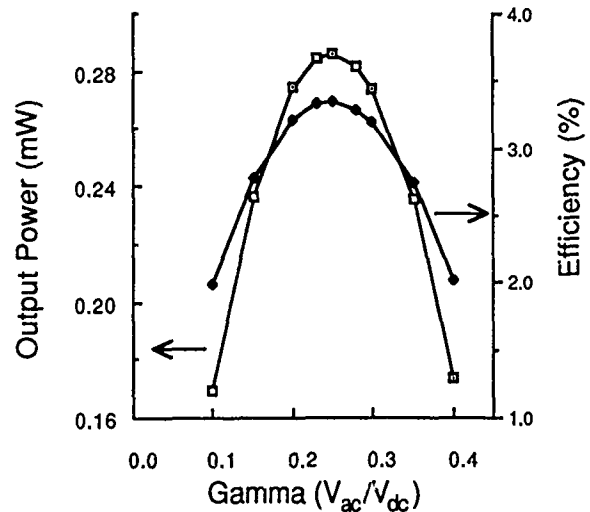


Fig. 4: Output power and efficiency as a function of gamma, the ratio of the ac amplitude and dc bias for a QWITT oscillator, showing the optimum loading condition at 94 GHz.

**Table I: Physical Parameters for a QWITT Oscillator designed to operate at 94 GHz**

Width of the parallel-plate waveguide,  $W = 254\ \mu\text{m}$

Thickness of the parallel-plate waveguide,  $L = 62\ \mu\text{m}$

Diameter of the metal post and diode =  $10\ \mu\text{m}$

Distance between post and load =  $561\ \mu\text{m}$

Load Resistance = 16 ohms

# RIGOROUS FIELD ANALYSIS OF IMPEDANCES OF SOME MILLIMETER WAVE OSCILLATOR CAVITIES

WEI HONG and SIFAN LI

Southeast University  
Nanjing, P.R. China

**ABSTRACT:** This paper presents a generalized field analysis method for calculating the external circuit impedances looking outside from the active devices of some millimeter wave oscillators. For a simple oscillator model with a radial disc and a diode existing in a rectangular waveguide, the numerical results are in agreement with the experimental data. Impedance characteristics for several different oscillator configurations are given, and some useful conclusions for oscillator design are derived.

## 1. INTRODUCTION

It is well known that there are two difficulties existing in accurate computer-aided design of millimeter wave oscillators. The first one is the accurate description of large-signal characteristics of active devices. The second one is the calculation of external circuit impedance looking outside from the devices. Most work on the first one has been done, but so far people still have not achieved very satisfactory results. Generally, the second one is a very complicated electromagnetic field boundary value problem. Up to now only a few work on it has been done. Theoretical study by [1] and experimental investigations by [2] on the radial line transformer in a rectangular waveguide gave some useful conclusions for oscillator design, but the configuration they studied is quite different from that used in practice. This paper presents a generalized field analysis method for calculating the external circuit impedance looking outside from the active device of some millimeter wave oscillators that are often used in engineering. The numerical results for radial line transformer are in good agreement with that in [1] and [2]. Impedance characteristics for several different oscillator configurations are given, and some useful conclusions for oscillator design are derived.

## II. THEORY

A common millimeter wave oscillator configuration is shown in Fig.1, where  $a$ ,  $x$  and  $b$ ,  $y$  are waveguide dimensions,  $d$  and  $d_0$  are the diameters of the radial line and the active device respectively. The thickness of the radial disc is neglected, and generally  $h, b_0 - h < \lambda/2$ . Assuming only  $TM_{00}$  mode in the radial line has been excited by the active device, then only  $TM_{00}$  modes are excited in the cavity. Divide the whole cavity into five regions, then the field components in each region are as follows

In Region I

$$E_y(R, \varphi) = \sum_{m=0}^{\infty} A_m Z_m(kR) \cos(m\varphi) \quad (1)$$

$$H_\varphi(R, \varphi) = \sum_{m=0}^{\infty} A_m Z'_m(kR) \cos(m\varphi) \quad (2)$$

$$Z_m(kR) = J_m(kR) N_m(ka) - N_m(kR) J_m(ka) \quad (3)$$

$$Z'_m(kR) = J'_m(kR) N_m(ka) - N'_m(kR) J_m(ka) \quad (4)$$

$$\beta = -j\omega\epsilon/k, \quad k = 2\pi/\lambda$$

In Region II

$$E_y(R, \varphi) = \sum_{m=0}^{\infty} [B_m J_m(kR) + C_m N_m(kR)] \cos(m\varphi) \quad (5)$$

$$H_\varphi(R, \varphi) = \sum_{m=0}^{\infty} [B_m J'_m(kR) + C_m N'_m(kR)] \cos(m\varphi) \quad (6)$$

In Region III

$$E_y(R, \varphi) = \sum_{m=0}^{\infty} D_m \cos[\pi R(2m+1)\sin\varphi/a_0] \exp(jmR\cos\varphi) \quad (7)$$

$$H_\varphi(R, \varphi) = \sum_{m=0}^{\infty} D_m [jm \cos\varphi \cos[\pi R(2m+1)\sin\varphi/a_0] + \\ - \pi(2m+1)\sin\varphi \sin[\pi R(2m+1)\sin\varphi/a_0]/a_0 \exp(jmR\cos\varphi)] \quad (8)$$

$$j_m^2 = [\pi(2m+1)/a_0]^2 - k^2 \quad (9)$$

In Region IV

$$E_y(R, \varphi) = \sum_{m=0}^{\infty} F_m \cos[\pi R(2m+1)\sin\varphi/a_0] \exp(-jmR\cos\varphi) \quad (10)$$

$$H_\varphi(R, \varphi) = \sum_{m=0}^{\infty} F_m [jm \cos\varphi \cos[\pi R(2m+1)\sin\varphi/a_0] + \\ + \pi(2m+1)\sin\varphi \sin[\pi R(2m+1)\sin\varphi/a_0]/a_0 \exp(-jmR\cos\varphi)] \quad (11)$$

In Region V

$$E_y(R, \varphi) = \sum_{m=0}^{\infty} L_m H_m^{(1)}(kR) \cos(m\varphi) + H_0^{(1)}(kR) \quad (12)$$

$$H_\varphi(R, \varphi) = \sum_{m=0}^{\infty} L_m H_m^{(1)'}(kR) \cos(m\varphi) - H_1^{(1)'}(kR) \quad (14)$$

where  $J_m(\cdot)$ ,  $N_m(\cdot)$  and  $H_m(\cdot)$  are Bessel, Neumann and Hankel functions respectively.

Substitute these field components into following boundary conditions on the interfaces

$$H_\varphi^I = \begin{cases} H_\varphi^{\text{II}}, & h < y < b_0, \\ H_\varphi^{\text{IV}}, & 0 < y < h, \end{cases} \quad 0 < \varphi < 2\pi, R = d \quad (15)$$

$$H_\varphi^{\text{II}} = \begin{cases} H_\varphi^{\text{I}}, & \frac{\pi}{2} < \varphi < \frac{3\pi}{2}, \\ H_\varphi^{\text{IV}}, & -\frac{\pi}{2} < \varphi < \frac{\pi}{2}, \end{cases} \quad 0 < y < b_0, R = a_0/2 \quad (16)$$

$$E_y^{\text{II}} = \begin{cases} E_y^{\text{I}}, & h < y < b_0, \\ E_y^{\text{IV}}, & 0 < y < h, \end{cases} \quad 0 < \varphi < 2\pi, R = d \quad (17)$$

$$E_y^x = \begin{cases} E_y^I, & \frac{\pi}{2} < \varphi < \frac{3\pi}{2}, \\ E_y^{IV}, & -\frac{\pi}{2} < \varphi < \frac{\pi}{2}, \end{cases} \quad 0 < y < b_0, \quad R = a_0/2 \quad (17)$$

and apply a combined technique of Galerkin method and Collocation method to the equations, the following matrix equations can be obtained immediately.

$$[U]_1 \bar{B} + [U]_2 \bar{C} = [U]_3 \bar{A} \quad (18)$$

$$[U]_4 \bar{B} + [U]_5 \bar{C} = [U]_6 \bar{L} + \bar{C} \quad (19)$$

$$[T]_1 \bar{B} + [T]_2 \bar{C} = [T]_3 \bar{D} \quad (20)$$

$$[T]_4 \bar{B} + [T]_5 \bar{C} = [T]_6 \bar{F} \quad (21)$$

$$[U]_7 \bar{B} + [U]_8 \bar{C} = [U]_9 \bar{A} + [U]_{10} \bar{L} + \bar{C} \quad (22)$$

$$[U]_{11} \bar{B} + [U]_{12} \bar{C} = [T]_7 \bar{D} + [T]_8 \bar{F} \quad (23)$$

where  $\bar{A} = (A_0, A_1, \dots, A_n)$  etc. are coefficient vectors. Eliminate the vectors  $\bar{A}, \bar{B}, \bar{C}, \bar{D}$  and  $\bar{F}$  from the matrix equations above, yields

$$[Q] \bar{L} = \bar{V} \quad (24)$$

The coefficient vector  $\bar{L}$  is then obtained immediately from the equation. The external circuit in impedance looking outside from the diode is defined as

$$Z_e = 2P / |I|^2 \quad (25)$$

where

$$P = -j \frac{h d_0}{20} [ |L_0|^2 H_0^{(0)}(k d_0) \bar{H}_1^{(0)}(k d_0) + H_0^{(2)}(k d_0) \bar{H}_1^{(2)}(k d_0) + L_0 H_0^{(2)}(k d_0) \bar{H}_1^{(0)}(k d_0) + L_0 H_0^{(0)}(k d_0) \bar{H}_1^{(2)}(k d_0) ] \quad (26)$$

$$I = j d_0 [ H_1^{(2)}(k d_0) + L_0 H_1^{(0)}(k d_0) ] / 60 \quad (27)$$

### III. NUMERICAL RESULTS

Typical numerical results of several oscillator configurations are shown in Fig.2-5. Following conclusions are then derived.

1. External circuit impedance equal to or less than  $1\Omega$  can easily be achieved by adjusting the height  $h$  of the radial line, that is necessary for matching the diode to output waveguide.

2. In region  $0 < \lambda/4$ , the real part of the impedance  $Z_e$  is inverse proportional to the radius  $d$  of the radial disc, and the imaginary part is proportional to  $d$ . Then, decreasing  $d$  is effective for increasing resonant frequency and increasing  $d$  is useful for matching the diode to the output waveguide.

3. The real part of the external circuit impedance is not sensitive to the position of short circuit when the height  $h$  of the radial disc is less, that is available to extend frequency bandwidth.

### REFERENCES

- [1] K.H. Doring : High transformation ratio for impedance matching with a radial line, *Electro. Lett.* Vol.16 No.2 Januray 1980.
- [2] Zhende Wu : Theoretical study on the radial line transformer in a rectangular waveguide, *Electron. Lett.* Vol.20 No.6 March 1984.

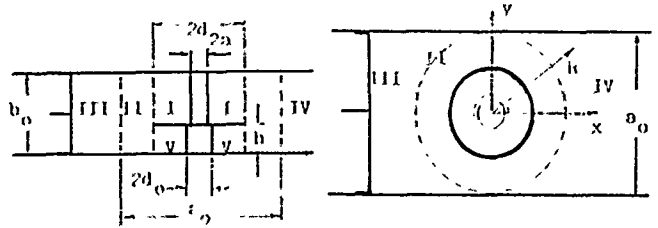


Fig.1 A common millimeter wave oscillator model

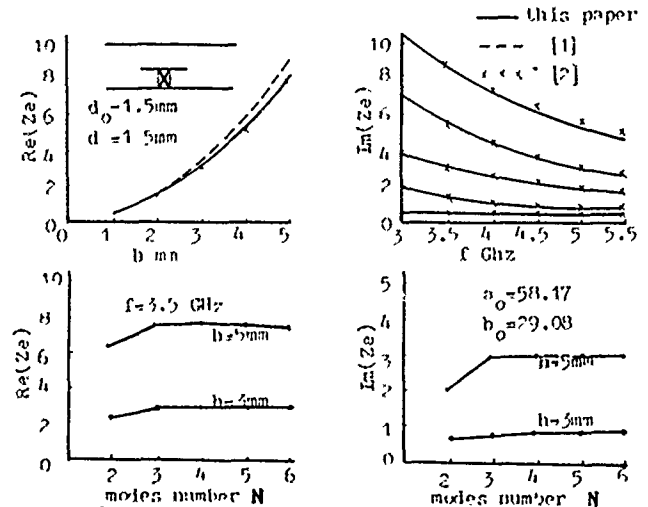


Fig.2 Results for mm-wave oscillator model I

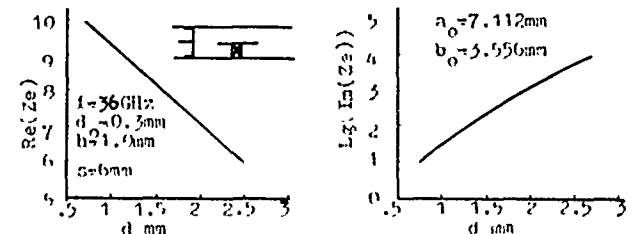


Fig.3 Results for mm-wave oscillator model II

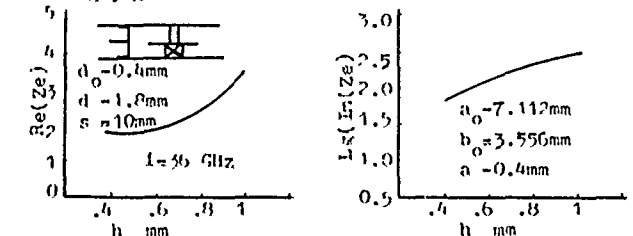


Fig.4 Results for mm-wave oscillator model III

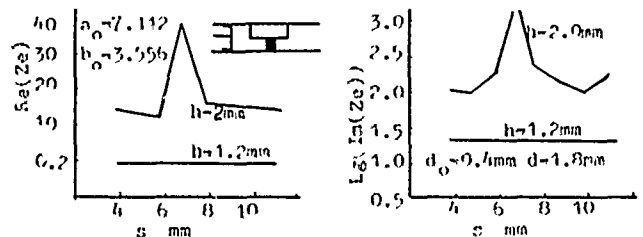


Fig.5 Results for mm-wave oscillator model IV

Han S. Uhm and H. C. Chen  
Naval Surface Warfare Center  
White Oak, Silver Spring, MD 20903-5000

Howard E. Brandt  
Harry Diamond Laboratory  
Adelphi, MD 20783-1197

### ABSTRACT

Diocotron stability properties in a relativistic electron flow generated inside high power magnetrons are investigated within the framework of a linearized macroscopic cold fluid model. A massless guiding-center approximation has been made in this theoretical calculation to be analytically tractable. Closed algebraic dispersion relations obtained in this article are fully relativistic and fully electro-magnetic. Influence of the anode resonator effects are also fully incorporated. Numerical investigation of the dispersion relation is carried out for a broad range of system parameters and results will be presented.

### INTRODUCTION

Although a magnetron is essentially a cylindrical diode with a magnetic field parallel to its axis which provides the magnetic insulation, it is very instructive to study a planar magnetron because of its simplicity. In order to have an efficient mode coupling between the vacuum waveguide mode and the beam mode, the anode includes various kinds of anode resonators. Although there are very successful developments of the magnetron microwave devices, including the microwave oven, theory of the magnetron is very primitive and ad hoc. A self-consistent theory of the magnetron is essential for the development of a high power (>GW) high efficiency magnetron. The major difficulties in developing the self-consistent magnetron theory are the presence of the anode resonators and of the intense electron flow at the cathode.

In recent literature, we have proposed a new microwave tube device called "cusptron", which has a very similar physical configuration to the magnetron with the anode resonators. The cusptron theory also includes a high intensity electron flow. Thus, making use of the mathematical tools developed in the cusptron theory. We derive a self-consistent dispersion relation for both the planar and cylindrical magnetrons. However, the derivation of the final dispersion relation is restricted to a relatively tenuous electron layer satisfying,

$$\omega_{pb}^2(x) \ll \omega_c^2, \quad (1)$$

where  $\omega_{pb}^2(x)$  is the relativistic plasma frequency-squared and  $\omega_c$  is the relativistic cyclotron frequency. In this regard, the dispersion relations obtained in this article will be very useful to investigate the diocotron stability properties in relativistic magnetrons.

### THEORETICAL MODEL

In a planar magnetron, the electrons emitted at the cathode move in the y-direction ExB drift motion. The applied magnetic field  $B_0 = B_e \hat{z}$  in the z-direction and provides the magnetic insulation. The anode resonators are basically a slow wave structure commonly used in various microwave devices. Thus, the phase velocity of the vacuum waveguide mode can be less than the speed of light. Of course, the typical

flow mode is  $\omega = kV_y^0(x)$  where  $\omega$  and  $k$  are the angular frequency and the wavevector of the perturbations, and

$V_y$  is the electron flow velocity in y-direction. This beam mode intersects the vacuum waveguide mode in the  $(\omega, k)$  parameter space, thereby ensuring that the electron kinetic energy is transferred into the electromagnetic energy.

For the present purposes, we specialize to the class of equilibrium profiles in which  $n_b(x)/\gamma_b(x) = \text{const.}$  over the layer cross section, and the linearized Maxwell equations are assumed to be extraordinary-mode eigenvalue equation. Assuming a low frequency perturbation, the eigenvalue equation is express as

$$\begin{aligned} \frac{\partial^2}{\partial x^2} \phi(x) - k^2 \left[ 1 - \frac{\omega^2}{c^2 k^2} + \frac{\omega_{pb}^2(x)}{c^2 k^2} \right] \phi(x) \\ = - \frac{k \phi}{\omega - kV_y(x)} \left[ 1 - \frac{V_y(x)}{c} \frac{\omega}{ck} \right] \frac{\partial}{\partial x} \left[ \frac{\omega_{pb}^2(x)}{\omega_c} \right], \end{aligned} \quad (2)$$

in the limit of a massless, guiding-center fluid. Here, the effective potential  $\phi(x)$  is defined by  $\phi(x) = i \mathcal{E}_y(x)/k$  and  $\omega_{pb}(x)$  is the diocotron frequency.

In solving the eigenvalue equation (2), the boundary conditions must be correctly determined, including the important influence of the anode resonators. Selecting a proper boundary condition, and defining the parameters by  $q^2 = (\omega^2/c^2) - k^2 - \omega_{pb}^2/c^2$ ,  $p^2 = (\omega^2/c^2) - k^2$ ,  $\lambda = qx_b$ , and  $\xi = px_b$ , we eventually obtain the dispersion relation of the diocotron instability in a planar magnetron. That is

$$\frac{\hat{\omega}_{pb}}{\omega - kV_d} \left( 1 - \frac{V_d}{c} \frac{\omega}{ck} \right) = \frac{p}{k} \frac{\cos \xi + G \sin \xi}{\sin \xi - G \cos \xi} - \frac{q}{k} \cot \lambda, \quad (3)$$

for the extraordinary-mode perturbations in an electron layer. Equation (3) determines the complex scillation frequency  $\omega$  in terms of the wavenumber  $k$  and layer parameters  $\hat{\omega}_{pb}$ ,  $V_d$ ,  $x_c - x_a$ , etc. In the

dispersion relation in Eq. (3), we note that perturbations on the outer surface of the electron layer (the left-hand side) are coupled to electromagnetic waves whose phase velocity is slowed down by the anode resonator structure. The dispersion relation of Eq. (3) is fully electromagnetic and valid for relativistic electron flow in the limit where the electrons are treated as a massless, guiding-center fluid.

Shown in Fig. 1 is the normalized growth rate  $\omega_i x_c / c$  and real oscillation frequency  $\omega_r x_c / c$  numerically obtained from Eq. (3) for the parameters  $x_c / x_b = 9$ ,  $L = 2.5 \text{ cm}$ ,  $x_c / x_a = 2.25$ ,  $x_c = 4.5 \text{ cm}$ ,  $V_d / c = 0.1$ ,  $\omega_b x_c / c = 0.9$ , and  $\ell = 1$ . Obviously, a significant growth rate of instability occurs at  $k \approx 0$ , which means the space wave number  $k_s = 2\pi/L$  from  $2\pi\ell = (k - k_s)L$ . Here  $L$  is the periodic length of the anode resonators. The space wavenumber  $k_s = 2\pi/L$  is identified by the well known  $2\pi$  mode perturbation where the phase shift between two adjacent anode resonators is  $2\pi$ . The growth rate of this  $2\pi$  mode perturbation is significant enough so that an intense microwave radiation can be obtained from this instability mechanism. A similar analysis has been also carried out for a cylindrical magnetron. However, we note from Fig. 1 that there are two branches of unstable modes. One is the low frequency mode represented by  $\omega_r^l$  and  $\omega_i^l$  which is the usual diocotron instability. The other one is the high frequency mode represented by  $\omega_r^h$  and  $\omega_i^h$  which is a high radial mode instability. Obviously, the diocotron instability is the dominant unstable mode.

**ACKNOWLEDGEMENT:** This work has been supported in part by the Independent Research Fund at the Naval Surface Warfare Center and in part by the Office of Innovative Science and Technology, the Strategic Defense Initiative Organization, managed by the Harry Diamond Laboratories.

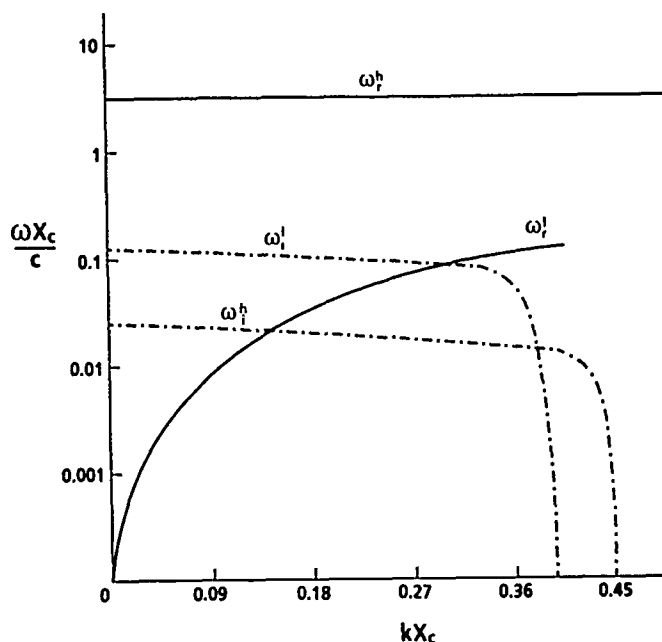


Fig. 1. Growth rate and real frequency obtained from Eq. (3).



# POWER COMBINING SYSTEM USING TWO PUSH PULL POWER AMPLIFIERS

Sachihiro Toyoda

Department of Electrical Engineering

Osaka Institute of Technology

5-16-1 Omiya Asahi-Ku Osaka 535 JAPAN

## Abstract

This paper describes a power combining system using two push-pull power amplifiers. Power amplifiers using two different type phase inverter were proposed and tested at 5-GHz band. Bandwidth of these power combining systems were 1.65 GHz and 1.8 GHz, respectively, and either of their output power were 14.5 W.

## I. Introduction

The development of the solid-state high power amplifiers becomes active. Aiming at the improvement of the output power of the amplifiers, several papers concerning the power combining amplifier structured by mounting multiple number of IMPATT's in a rectangular waveguide cavity or in a circular cavity have already been published 1),2). They used cavities, and hence the combining efficiency was superior. But, because of their low handling power of IMPATT's the combined output remained at low levels. Also, broadband characteristic could not be obtained because of their cavity structures.

After GaAs FET's became available in microwave region, GaAs FET's became to be used to build power combining amplifiers, wherein they are connected through a power divider or a 3 dB directional coupler. The combined power amplifier is further combined to get still higher power levels.

This power combining system gives no additional distortion on its signal because the amplifiers are working in class "A".

The power combining using two push-pull power amplifiers 4) had been reported already. J. R. Lane and R. G. Freitag 4) tried to power combining two class "B" push-pull power amplifiers. They reported that the bandwidth of the power combining was 1 GHz and the maximum output power obtained was 4 W.

The present author also proposed a power combining system using push-pull power amplifiers 5).

The bandwidth and the combining output power of this two class "AB<sub>2</sub>" push pull amplifiers 6) are 1.7 GHz and 14.5 W.

The bandwidth of the power combining amplifier of this experiment is wider by 0.7 GHz than that of the amplifier by J.R. Lane, and the combining power is large by 10.5 W.

## 2. Structure of the power combining amplifiers

The power combining amplifier was constructed by connecting two class "AB<sub>2</sub>" push pull power amplifiers of the frequency range 4.6 - 6.3 GHz bands to a coaxial power divider. The circuit diagram of this power combining amplifier is shown in Fig. 1. As shown in Fig. 1, the frequency bandwidth of a pre-amplifier (HP 8349) was 2 - 20 GHz and the output power was 20 dBm. Two amplifiers were connected in cascade. The output of the cascade amplifiers was supplied to the input of the exciter amplifier. The exciter amplifier was a balanced amplifier. The output power of this balanced amplifier is fed to the input of two push-pull amplifier.

FET's used in those two push-pull amplifiers and the exciter amplifier were internally matched Avantek IM-5459-3. The frequency characteristic of each power amplifier was flat from 4.3 to 6 GHz. The bandwidth was 2.05 GHz, and the output power was 34.5 dBm 5).

These power amplifiers were used for the exciter amplifier and two push-pull power amplifiers.

As shown Fig. 1, as the phase inverter connected to the input and the output sides of the push pull amplifier two different kinds were used thing (see Figs. 2 and 3).

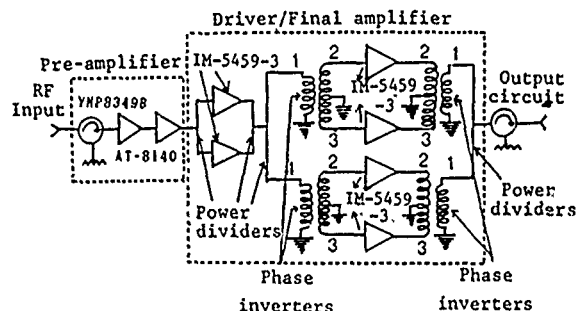


Fig. 1 Block diagram of the power combining system using two push pull power amplifiers

## 3. Experimental result of the power combining amplifier

The photograph of the power combining amplifier is shown in Fig. 2. As shown in Fig. 2, the frequency range of the class "A" power amplifier using the push-pull amplifier is 4 - 6.4 GHz. The bandwidth is 2.05 GHz, and the output power is 3 W. The four power amplifiers with the same characteristic were used. Using the push-pull amplifier for this power amplifier, the drain voltage is constant. It was confirmed from the observation used a network analyzer that the input and output matching had no problem when voltage between gate and source was varied from class "A" to "AB<sub>2</sub>".

In the power combining amplifier shown in 4).

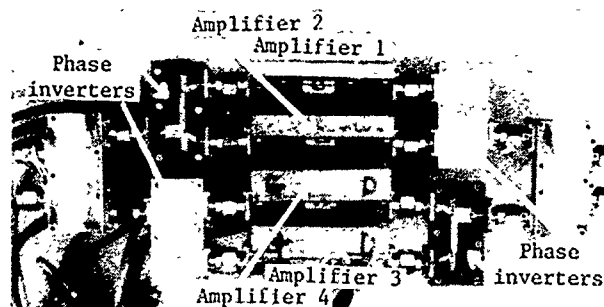


Fig. 2 Photograph of the power combining amplifier

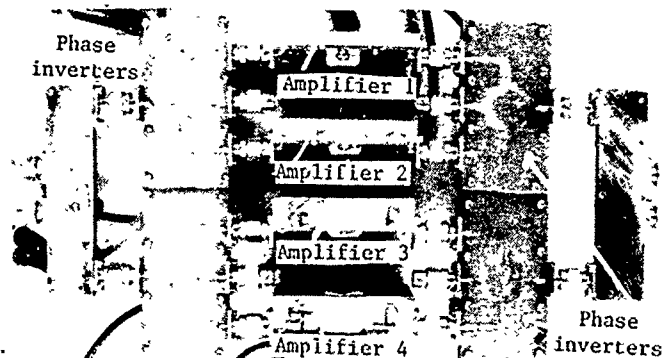


Fig. 3 Photograph of the power combining amplifier  
two class "B" push-pull power amplifiers were used. The maximum power efficiency of the class "B" push pull power amplifier is theoretically 78.5%. But since the transfer characteristic of the FET's is nonlinear in the vicinity of the cutoff point, the cross-over distortion occurs in the operation of class "B" amplification. In order to avoid this cross-over distortion, the bias voltage must be shifted from class "B" to class "AB".

Because of the reason mentioned above, the bias voltages of the amplifiers tested here were shifted to that of the class "AB<sub>2</sub>" operation.

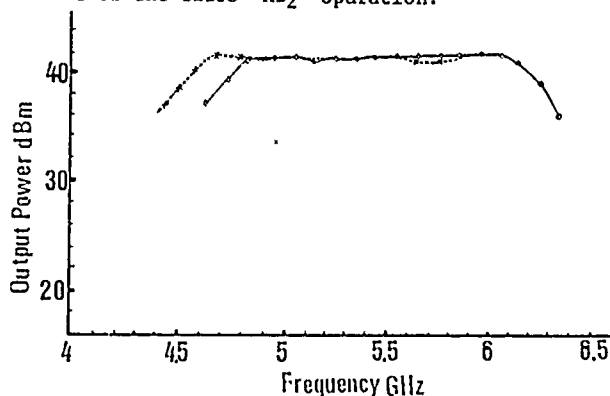


Fig. 4 Frequency characteristic of the push pull power combining amplifier shown in Fig. 2 (A dotted line represents the frequency characteristic of the push pull power combining amplifier shown in Fig. 3)

The push-pull power combining amplifier shown in Figs 2 or 3 was connected in cascade with the pre-amplifier and exciter amplifier shown in Fig. 1. Experiments were carried out at the 5 GHz band. The output frequency characteristics of two different type push-pull power combining amplifiers are shown in Fig. 4. The solid line shown Fig. 4 indicates the frequency characteristic of the push-pull power

combining amplifier shown in Fig. 2. The output power and the bandwidth obtained of the push pull power combining amplifier are 14.5 W (41.6 dBm) and 1.65 GHz. A dotted line shown in Fig. 4 indicates the frequency characteristic of the push-pull power combining amplifier shown in Fig. 3. The output power is the same with that of Fig. 2. The obtained bandwidth is 1.8 GHz, which is better by 0.15 GHz than that of Fig. 2. This slight improvement in the bandwidth is thought to be brought about by a better frequency characteristic of the phase inverter used in Fig. 3. The bandwidth of the class "A" single power amplifier is 2.05 GHz.

Comparison of the result in the bandwidth of the class "A" single power amplifier and the bandwidth of two different power combining amplifiers shows that the bandwidth of the power combining amplifier shown in Figs. 2 and 3 are narrower by 0.4 GHz and 0.25 GHz, respectively, than that of the class "A" amplifier.

Since the bandwidth of the phase inverter used in the push-pull power combining amplifier shown in Fig. 2 was only 2.3 GHz at a center frequency of 5.65 GHz, the obtained bandwidth of the amplifier was 1.65 GHz.

The frequency characteristic of the phase inverter used in the push-pull power amplifier shown in Fig. 3 is superior to that used in Fig. 2. Since the phase angle of S-parameter  $S_{21}$  of four power FET's were not uniform of frequencies below 4.65 GHz, the power output of the amplifier dropped below those frequencies.

When those four FET's (IM-5459-3) used in the present amplifiers are operated in the balanced-type operation, the output power is expected to be 12 W with assuming a 100% efficiency. In the present experiment, where the same FET's are used in two push-pull power amplifiers, obtained output power was 14.5 W.

The measurement of the input-output characteristics and third-order intermodulation distortion of the power combining amplifier shown in Figs. 2 and 3 done using a spectrum analyzer with two signal having equal amplitude at frequencies 5.5 GHz and 5.502 GHz. The intercept point was 57.8 dBm.

## REFERENCES

- 1) S. Toyoda "Waveguide Type Power Combining Amplifiers" Trans. IEICEJ, Vol. J 68-B No. 6 PP. 707-713 June 1985 (in Japanese).
- 2) S. Toyoda "Multiple-Diode Reflection-Type Amplifiers Using IMPATT-Diode" Trans. IEICEJ, Vol. J68-B No. 9 PP. 1029-1035 September 1985 (in Japan)
- 3) P.M. Chirlian "Electronic Circuits: Physical Principles, Analysis and Design", McGraw-Hill.
- 4) J. R. Lane et al. "High-Efficiency 1-, 2-, and 4-W class "B" FET power Amplifiers", IEEE Trans., Microwave Theory and Technology, Vol., MTT-34, No. 12 December 1986.
- 5) S. Toyoda "Push-pull Amplifier Using GaAs FET" Tech. Rep. IEICE, Japan, MW87-67 November 1987.
- 6) S. Toyoda "Power Combining System Using Two Push pull Power Amplifiers", Nat. Conv. IECE, Japan C-666 (1988).

# Quasi-Optical Resonator for Millimeter and Submillimeter Wave Solid-State Sources

Morishige HIEDA, Masatoshi NAKAYAMA, Koji MIZUNO  
Toshihiro AJIKATA and David B. RUTLEDGE\*)

Research Institute of Electrical Communication  
Tohoku University, Sendai 980, Japan

\*)California Institute of Technology Pasadena, CA 91125, U.S.A.

## ABSTRACT

A new cavity for millimeter and submillimeter wave solid-state oscillators is demonstrated. The resonator consists of a Fabry-Perot resonator with a grooved mirror. It has a capability for power combining. Experimental results from X-band models of the resonator are presented. Frequency-locking and power-combining with six Gunn diodes are demonstrated.

## INTRODUCTION

Recently many kinds of oscillators are developed in the millimeter and submillimeter wave region. Solid-state devices have many advantages: small size, low weight, and low-voltage power supplies. As the frequency increases, however, output power becomes smaller and the dimensions of conventional waveguide cavities become very small. Young and Stephan demonstrated power-combining in a quasi-optical resonator of two devices[1]. Popović et al. proposed and demonstrated power-combining using grid oscillators with FET's at 10GHz[2]. Mink gave a theoretical analysis[3]. We have proposed a Fabry-Perot resonator with a grooved mirror for solid-state oscillators[4]. We report here X-band model experiments on up to six Gunn diodes using this cavity.

## CONFIGURATION

The configuration of the model resonator is shown in Figure 1. It consists of a grooved mirror and a concave spherical mirror facing each other. Figure 2 shows the structure of the grooved mirror. The groove pitch must be less than half of oscillator wavelength to avoid diffraction losses[5]. We have chosen  $0.28\lambda$  ( $\lambda$ =wavelength) at 10GHz for groove pitch  $D$  in this experiment. The width of the groove pitch  $d$  is  $0.08\lambda$ , it is equal to Gunn diodes height. The Gunn diodes are mounted in grooves and biased by the top and the bottom plate of each groove. These plates are insulated by thin teflon tape. The Gunn diodes are JRC NJX4410 and typically produce 8mW in a waveguide cavity. The groove depth  $t$  can be continuously adjusted. The size of the grooved mirror is  $5.0\lambda \times 5.0\lambda$ . This is large enough for the beam waist size ( $2.5\lambda\phi$ ) on the mirror surface. Output power is taken out by a coupling hole at the center of the spherical mirror.

The resonator proposed has the following advantages: it has a large heat dissipation capacity, can mount large number of devices, is large enough than wavelength, and can be used with a single bias source.

## EXPERIMENTS

Figure 3(a) shows the oscillation spectrum for a single Gunn diode mounted at the center of the grooved mirror. Figure 3(b) shows the spectrum for six diodes (three-by-two grid). We have succeeded in frequency locking and power combining for the six diodes. It can be seen that the spectrum for six diodes is much narrower than that for a single diode. We supplied the same bias voltage to six diodes and adjusted each groove depth to lock together. The depth of each groove was about  $\lambda/2$ . The spacing between diodes in a groove have been chosen experimentally. We had good results with the spacing of  $\lambda/2$ .

Figure 4 shows how the oscillation frequency varies with the length of the resonator with six diodes. We can identify the modes (TEM<sub>00</sub>, TEM<sub>20</sub>) by measuring field distribution through moving a small piece of absorber around in the resonator. The mechanical tuning range is about 8% for the fundamental (TEM<sub>00</sub>) mode.

## CONCLUSION

We have demonstrated a new resonator for solid-state sources and succeeded in locking and power-combining for six Gunn diodes at X-band.

## ACKNOWLEDGMENTS

We thank Dr. C. Kimura of New Japan Radio Co., Ltd. for providing the Gunn diodes used in this work.

## REFERENCE

- [1] S. Young and K. D. Stephan, 'Stabilization and power combining of planar microwave oscillator', IEEE Microwave Symposium 1987, MTT-S Digest, pp185-188, 1987
- [2] Z. B. Popović, M. Kim and D. B. Rutledge, 'Grid Oscillators', submitted to the International Journal of Infrared and Millimeter Waves
- [3] J. W. Mink, 'Quasi-Optical Power Combining of Solid-State Millimeter wave Sources', IEEE Transactions on Microwave Theory and Techniques, Vol. MTT-34, pp.1017-1025, February 1986.

[4] K. MIZUNO, T. AJIKATA, M. HIEDA, and M. NAKAYAMA, 'Quasi-Optical Resonator for Millimeter and Submillimeter Wave Solid-state Sources', *Electronics Letters*, Vol.24, pp.792-793, June 1988

(5) K. MIZUNO and S. ONO, 'The ledatron', in K. J. BUTTON (Ed.), *Infrared and millimeter waves* (Academic Press, 1979), 1, pp213-232

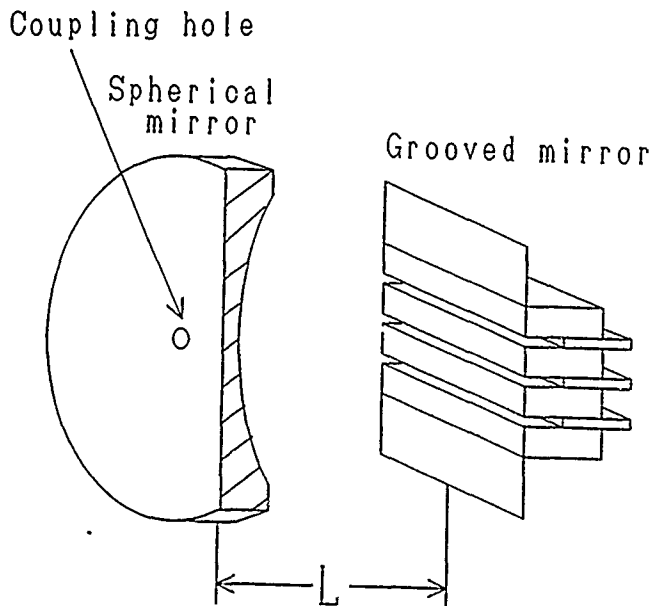


Fig. 1 Resonator configuration

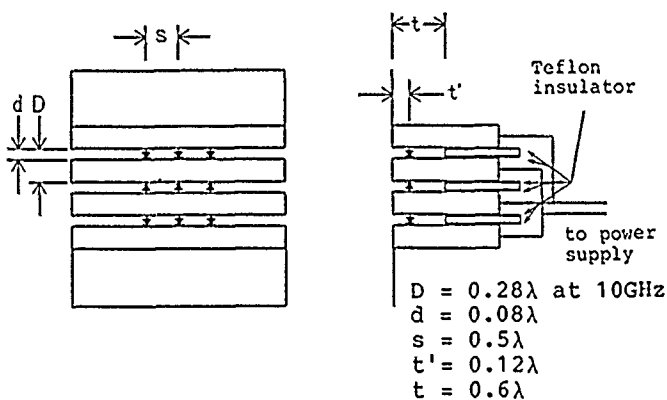


Fig. 2 Grooved mirror configuration

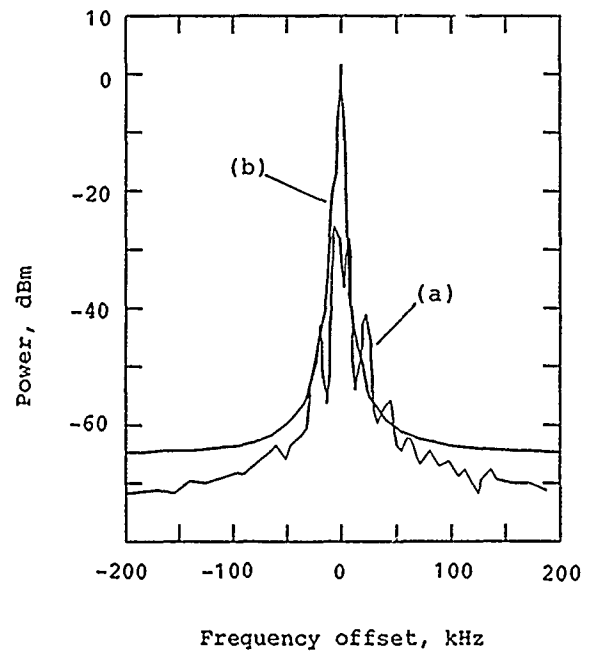


Fig. 3 Spectra of Gunn diode oscillator with the resonator. (a) Single diode mounted at the center of groove mirror. ( $f_c=10.0336$ GHz,  $l=107.2$ mm) (b) Locked six diodes. The C-N ratio is -50dB at a 17kHz offset. ( $f_c=10.1458$ GHz,  $l=107.5$ mm)

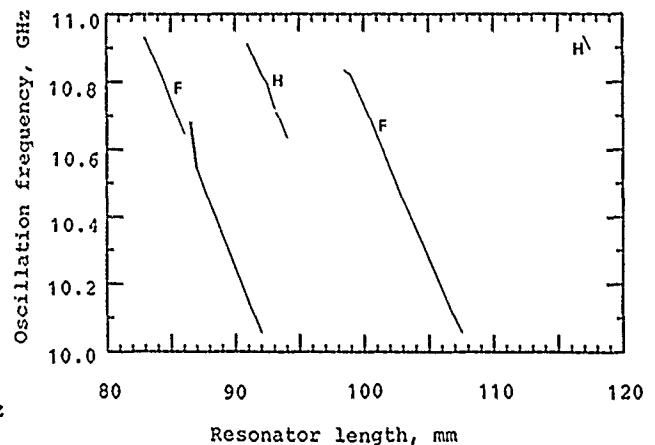


Fig. 4 Measured oscillation frequency of six diodes oscillator versus resonator length  $L$ . F and H represent the fundamental mode (TEM00) and the higher-order mode (TEM20), respectively.

# Numerical Simulation of the Diocotron Instability in Planar Diode Geometry

H. C. Chen and H. S. Uhm  
Naval Surface Warfare Center  
White Oak, Silver Spring, MD 20903-5000

## ABSTRACT

The diocotron instability for sheared, relativistic electron flow in a planar diode geometry with major fields  $E_x(x)$ ,  $B_z(x)$ , and  $V_y(x)$  has been studied numerically by using a two-dimensional electromagnetic relativistic particle-in-cell code. The growth rate and real oscillation frequency are obtained and compared to the analytical results for a tenuous electron flow.

## INTRODUCTION

The diocotron instability is one of the most common instability in any of the cross field devices which has been studied extensively by many authors in the past few decades. However, we are more interested in the case of relativistic electron flow, including the important influence of electromagnetic effects. Recently detailed properties of the diocotron instability for sheared, relativistic electron flow in a planar diode geometry with major field  $E_x(x)$ ,  $B_z(x)$  and  $V_y(x)$  have been studied<sup>1</sup> analytically by using the linearized cold-fluid-Maxwell equations. The theory indicated that relativistic and electromagnetic effects which have been taken into account in the analysis can have a strong stabilizing influence on the diocotron instability. Due to the limitation of the steady-state and linear analytical stability analysis, an attempt is made to simulate the instability numerically by using a two-dimensional electromagnetic relativistic particle-in-cell code. The code has a nice feature for fully relativistic charged particles with self-consistent electric and magnetic field. Furthermore, it is capable of modeling the transient behavior and not just steady state operation. For the proof of principle experiment, we have chosen to simulate the linear stability of diocotron instability in planar diode geometry. Particularly, low-frequency perturbations about a tenuous electron layer is considered where the analytical results are readily available for comparison. The relativistic flow parameter and geometric configuration are to be varied to simulate the instability.

## EQUILIBRIUM MODEL

For a sheared, relativistic electron flow in a planar diode, we simulate the low-frequency flute perturbations about a tenuous electron layer satisfying

$$\omega_{pb}^2(x) \ll \omega_c^2 \quad (1)$$

$$|\omega - kV_y(x)|^2 \ll \omega_c^2$$

where  $\omega_{pb}$  and  $\omega_c$  are plasma and cyclotron frequencies

respectively and  $V_y$  is the  $E \times B$  electron drift velocity. For the class of self-consistent equilibria where  $n_b(x)/\gamma_b(x) = \text{const.}$  the electron layer ( $x_b^- < x < x_b^+$ ) has the equilibrium density profile

$$n_b(x) = \hat{n}_b \cosh [\hat{k}(x - x_b^-)] / \cosh [\hat{k}(x_b^+ - x_b^-)] \quad (2)$$

$$\gamma_b(x) = \cosh [\hat{k}(x - x_b^-)] \quad (3)$$

For the initial conditions, the particles are loaded according to the nonuniform distribution of density specified in (2). The particles pick up their kinetic energy with the expression of (3). Space-charge-limited flow with zero tangential electric field at the cathode and certain electrostatic potential at the anode are assumed. Then the particles are all set to evolve under the influence of external applied voltage and magnetic field. The electric field and the axial magnetic field are determined self-consistently from the Maxwell equation as the simulation continues.

## SIMULATION RESULTS

For the beam parameters chosen, we set  $\omega_{pb}^2 = 0.1 \omega_c^2$  which satisfies condition (1) for tenuous beam. The inner and outer beam layers are located initially in  $\Delta_i = 0.5$  and  $\Delta_o = 0.3$  respectively where  $\Delta_i \equiv x_b^-/d$  and  $\Delta_o \equiv (d - x_b^+)/d$ . For the configuration with axial length ( $L = 16\text{cm}$ ) and gap distance ( $d = 12\text{cm}$ ), the electron particles are loaded initially according to (2) and (3). Note that the equilibrium  $E \times B$  flow velocity of the electron layer is maximum at the outer surface and zero at the inner surface. The perturbation on the outer surface of the electron layer are coupled to perturbations on the inner surface of the layer through the body wave perturbations within the layer. As a result, the electron layer evolves to that shown in Fig. 1 after 2.56nsec. It is believed that the diocotron instability has grown unstable with the wavenumber satisfying  $k = 2\pi N/L$  where  $N$  is any integer. The time evolution of total field energy and particle kinetic energy are shown in Fig. 2 and Fig. 3 respectively. We can see clearly two different frequencies of oscillation. The one with fast oscillation has been identified as cyclotron wave. The other beat wave type oscillation with longer wavelength is due to the natural wave oscillation.

It is intended to simulate the linear instability properly with single wave ( $\omega, k$ ) satisfying the linear dispersion relation, so that we can compare our results to the analytical solution. As we normally do in the linear analysis, we could fix  $k$  and try to find

the growth rate and real oscillation frequency. Here we adapt the technique of small number density perturbation, i.e.,  $n(t=0) = n_0 + \delta n \cos(kx)$ , where  $k = 2\pi/L$ ,  $d = 18\text{cm}$ ,  $L = 22.6\text{cm}$ ,  $A_1 = 0.3$ ,  $A_0 = 0.6$  so that  $kd = 5$  and  $\theta = 0.42$ . This set of parameters allows us to compare our results directly to the analytical results of Fig. 7 in reference 1. The electron layer has been perturbed with fixed  $k$  and evolved to that shown in Fig. 4 after 1.28 nsec. If we examine carefully the phase velocity of the wave motion, the normalized real frequency  $\text{Re}\omega/\text{ck} = 0.24$  is obtained. For the growth rate, we plot the total energy of axial electric field versus time in Fig. 5, the normalized growth rate  $\text{Im}\omega/\text{ck} = 0.15$  is calculated. The simulation results agree extremely well with the analytical results. Again, this is just a proof of principle experiment. The code will be used to study nonlinear problems of beam dynamics especially in complex geometries where analytical work or simple modeling is difficult.

<sup>1</sup>Diocotron instability for intense relativistic nonneutral electron flow in planar diode geometry, R. D. Davidson, et al, Phys. Fluids, 1988.

\*This work is supported by IR at NSWC and by SDIO/IST.

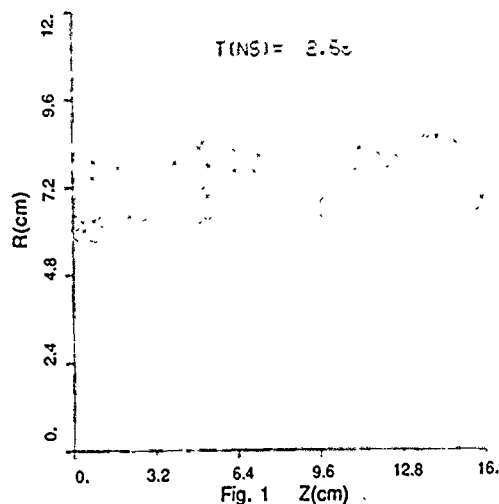


Fig. 1

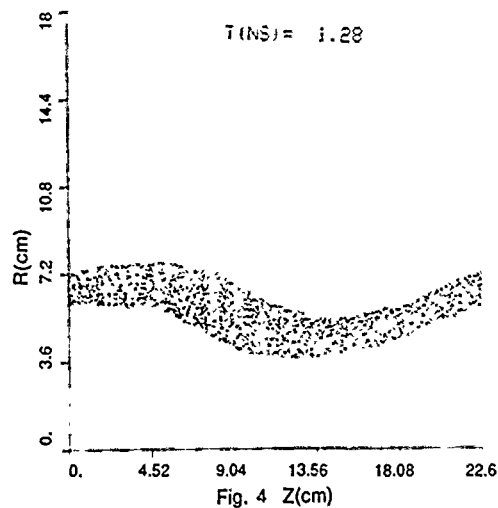


Fig. 4

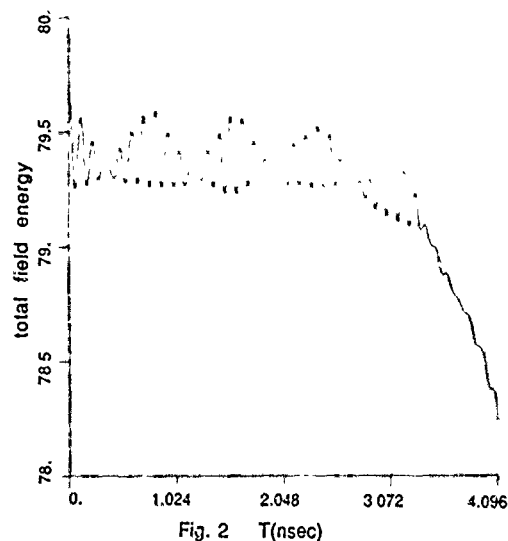


Fig. 2

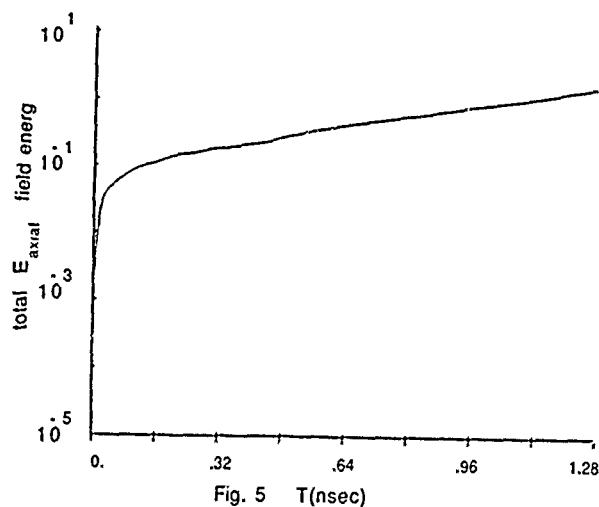


Fig. 5

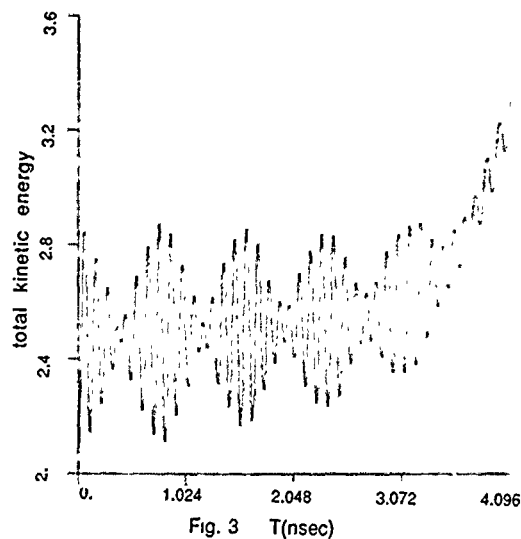


Fig. 3

## PARAMETRIC AMPLIFICATION USING SUPERCONDUCTING TUNNEL JUNCTIONS.

H.K.Olsson and T.Claeson

Chalmers University of Technology, Physics Department  
S-412 96 Göteborg, Sweden,  
Phone: (31)723318, Fax: (31)165176

## ABSTRACT

Stable and low noise operation of a Josephson parametric amplifier has been obtained at 9GHz. Best performance was achieved in the externally pumped modes giving a double side-band noise temperature of  $3\pm 4\text{K}$ , a gain of 13B, and an instantaneous bandwidth of 310MHz. An operation mode that uses the internally generated Josephson oscillation as the pump source gave higher noise ( $\sim 50\text{K}$ ) due to the broad width of the pump.

## INTRODUCTION

The non-linear inductive response of a Josephson junction is suitable for parametric amplification. A negative effective resistance cancels the load resistance at the signal frequency ( $f_s$ ) giving rise to a substantial signal gain transferring power from a pump (p).

We have recently reported [1], very low noise at 9 GHz for a four photon, externally pumped amplifier using shunted tunnel junctions, see Fig.1. The circuit is stabilized by a low  $\beta_L$  Q-value. ( $\beta_L = 2eI_0 L/\hbar$ ,  $I_0$  is the critical current of the tunnel junction,  $L$  the shunt inductance. The Q-value of the LC resonance,  $\omega^2 = 1/LC$ , is given by  $Q = \omega Z_L C$  if circuit losses are assumed negligible,  $C$  is the tunnel junction resistance and  $Z_L$  the load resistance at the resonance frequency  $\omega/2\pi$ ). In particular, a novel transformer, that is used to match the low impedance ( $\sim 0.5\Omega$ ), shunted junction to the external world, allows the use of a sufficiently high  $I_0$  ( $\sim 50\mu\text{A}$ ) to avoid thermally induced instabilities. A choice of  $\beta_L Q$  below but close to 1 is essential. Such parameters will not only give stable but also high gain since the Josephson negative resistance will be close to  $Z_L$ .

This report will touch upon some of the aspects of the low noise amplifier, describe its operation in the three photon externally and the four photon internally pumped modes, and give an improved value of  $T_{dsb} = 3\pm 4\text{K}$  for the externally pumped, four photon mode.

## FABRICATION AND MEASUREMENTS

Nb/oxide/PbBi (or Pb) tunnel junctions were fabricated by evaporating PbBi strips across ion beam oxidized Nb films via holes in SiO. The junction size was  $30\times 19\mu\text{m}$ . The shunt was a series combination of a Pb inductor and a CrAu resistor. The circuit layout and fabrication is described elsewhere [2].

**Josephson Oscillations:** The Josephson oscillations that occur at finite bias voltage can be used as a diagnostic tool, e.g., to determine the resonance frequency, the bandwidth of the transformer, and the stability of the oscillations. The oscillation linewidth results from thermal voltage noise in the shunt resistor. It was determined to be 830 kHz for  $R_s = 17.5\text{m}\Omega$  and  $T = 1.22\text{K}$ . This is close to the calculated value, 890 kHz. The linewidth did not change appreciably with bias voltage or critical current ( $I_0 < 65\mu\text{A}$ ).

**Externally Pumped Modes:** The three photon amplifier ( $f_s + f_i = f_p$ ,  $i = \text{idler}$ ) has to be current biased at zero voltage. An example is given in Fig. 2a where a Josephson current of  $39\mu\text{A}$

(tuned by a magnet) is suppressed to  $14.5\mu\text{A}$  by the pump power and biased at  $10\mu\text{A}$ . By comparing the reflected signal from the amplifier (biased as described) with the one from the same junction with no bias, pump, or magnetic field, a signal gain of 11.6 dB is calculated.

The externally pumped four photon mode ( $f_s + f_i = 2f_p$ ) performs similarly. It is unbiased and has an  $I_0$  of  $49\mu\text{A}$  without pump power. At 9.00 GHz, a signal gain of 11.8 dB is evaluated and it varies smoothly over the pass band. Essentially no extra noise is added in the amplifying state, see Fig. 2b.

**Hot/Cold Noise Measurements:** The noise temperature estimate of the last section ( $T_n = 0\text{K}$  for both modes) has a limited accuracy. A better way is to use the hot/cold method. Here, the signal is a broad band noise source and its temperature,  $T_{in}$ , is varied. The output noise power is related to  $T_{in}$  by  $P_n = k_B \Delta f G_{dsb} (T_{dsb} + T_{in})$  where  $\Delta f$  is the bandwidth of the measurement and  $G_{dsb}$  and  $T_{dsb}$  the double side band gain and noise temperature. (The linear relationship is valid if  $T_{in} \gg \hbar f/k_B$ , which is about 0.5K in the X-band). As we use a cold attenuator and circulator,  $T_{in}$  can be varied from 5 to 13K and an accurate estimate of a small  $T_{dsb}$  can be made.

Fig. 3 shows the linear relation between  $P_n$  and  $T_{in}$  for the four photon amplifier. A least square fit gives  $G_{dsb} = 12.9\text{ dB}$  and  $T_{dsb} = 3\pm 4\text{K}$  at 9.00 GHz. The relationships for two other frequencies within the instantaneous bandwidth of 310 MHz are also shown in the figure. A plot of the gain and the noise temperature as a function of frequency is shown in Fig. 4. The values are less accurate for frequencies outside the calibration frequency (9.0 GHz).

**Internal Pump:** The Josephson oscillation, at finite bias voltage, was used as an internal pump in the four photon mode. A critical current of  $60\mu\text{A}$  gave stable Josephson oscillations with an output power of -73 dBm at 9.07 GHz. The signal gain was 10 dB as compared with the shorted junction. The disadvantage of this mode comes from the broad width of the oscillations that adds noise to the signal. At a signal-to-pump separation of 70 MHz, this corresponded to a noise temperature of about 50K. The noise adds non-linearly with frequency separation in the limited bandwidth.

We conclude that the externally pumped amplifier has a very low noise. For successful operation, it is desirable to use a low impedance external load at the resonance frequency and important that the Josephson oscillations are stable. The low impedance requirement can be fulfilled using a microstrip transformer. Our design calculations gave a  $Z_L$  of  $0.5\Omega$  and this value was verified both by measuring the output oscillator power and from the amplifier parameters giving high gain.

The tuning ability given by the magnetic field dependence of the critical current is very useful. Stable oscillations and a control of the effective negative resistance can be realized.

The disadvantage of our amplifier is that there exist low noise semiconductor transistors in the X-band. At higher frequencies, say 70 GHz, there are no competitors. In principle, there seems to be no obstacles in extending the Josephson amplifier to that region. A higher frequency would permit a higher critical current, a larger range of stable operation, and a higher saturation level. Smaller junctions and higher current densities can be obtained with modern technology. The present problem is to find a cooled circulator at this frequency.

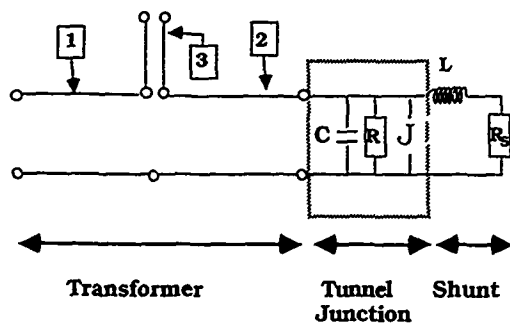


Fig. 1. The resistive rf-SQUID consists of a tunnel junction with a microstrip inductor and resistor as shunt. It is connected to a 50Ω coaxial cable via a quarter wave transformer. The transformer sections 1, 2, and 3 typically have impedances of 20, 2, and 20 Ω, respectively.

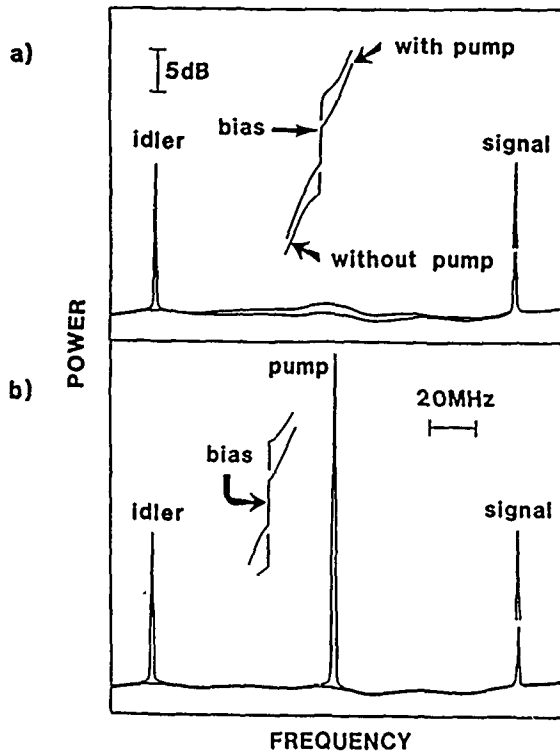


Fig. 2. Externally pumped amplifiers. Reflected signals from a short circuited junction and amplified signals and idlers are shown. The scales are the same in both plots.

(a) The 3 photon amplifier with  $f_s=9.00$  GHz,  $f_p=18.176$  GHz, and  $T=1.25$  K. The inset shows IV-curves with and without pump power.  $I_0=38$  μA.

(b) The 4 photon amplifier with  $f_s=9.00$  GHz,  $f_p=9.07$  GHz,  $P_p=-60$  dBm, and  $T=1.25$  K. The pumped and unpumped IV curves are shown in the inset,  $I_0=49$  μA.

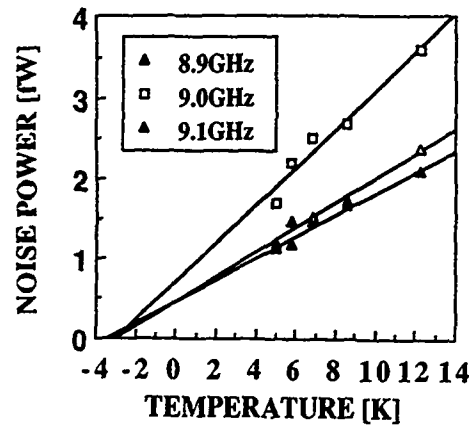


Fig. 3. The noise power output from a 4 photon, externally pumped Josephson amplifier as a function of input temperature. At 9.00 GHz, the plot gives  $G_{dsb}=12.9$  dB,  $T_{dsb}=3\pm 4$  K.  $I_0=48$  μA,  $T=1.27$  K.

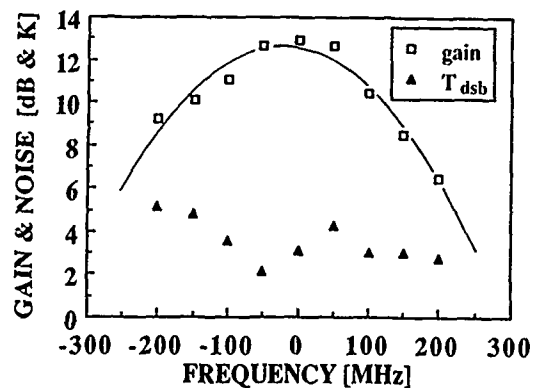


Fig. 4. The frequency dependence of  $G_{dsb}$  and  $T_{dsb}$  of the 4 photon, externally pumped amplifier. The zero of the frequency scale is set to the pump frequency,  $f_p=9.00$  GHz.  $I_0=48$  μA,  $P_p=-59.1$  dBm,  $T=1.27$  K.

## ACKNOWLEDGEMENTS

The work was supported by the Swedish Natural Science Research Council and the Board of Technical Development.

## REFERENCES

1. H.K. Olsson and T. Claeson, Jpn. J. Appl. Phys. **26**, 1547 (1987).
2. H.K. Olsson and T. Claeson, J. Appl. Phys, in print, and H.K. Olsson, PhD thesis, Chalmers Univ. of Tech., Göteborg, 1988.



# PICOSECOND OPTOELECTRONICS AND MILLIMETER-WAVE TECHNOLOGY

Chi H. Lee

Department of Electrical Engineering  
University of Maryland  
College Park, MD 20742

## ABSTRACT

Recent progress on the application of picosecond optoelectronics to microwave and millimeter-wave technology will be reviewed. Generation, control and characterization of pulsed and continuous-wave millimeter-waves will be discussed. A novel network analyzing technique for a 30 GHz monolithic millimeter-wave integrated circuits based on picosecond pulses has been demonstrated.

## INTRODUCTION

I will review recent progress on the application of picosecond optoelectronic technique to millimeter-wave technology. 1988 is a year that we see many exciting developments in the application of ultrafast optics to microwave and millimeter-wave. Through the use of picosecond photoconductor [1] and other phase-locking techniques [2] it is now possible to generate time synchronized pulsed or CW microwave and optical events. This capability leads to the generation, control and characterization of microwaves and millimeter-waves by picosecond or femtosecond optical techniques.

## DISCUSSION

Picosecond optical pulse interaction with the microwave devices and circuits provides a non-invasive probing of these devices. The characterization of microwave and millimeter wave monolithic integrated circuits (MMICs) using picosecond pulse sampling techniques has been demonstrated by a team from the University of Maryland and COMSAT [3]. Picosecond photoconductors are used for signal generation and sampling operations. The measured time domain response allows the spectral transfer function of the MMIC to be obtained. This measurement technique is verified by characterization of the frequency response (magnitude and phase) of a reference 50 $\Omega$  microstrip line and a two-stage  $K_a$ -band MMIC amplifier. For the first time, the direct comparison between the results obtained by the broadband time domain optical measurement and those obtained from conventional frequency domain measurements using a network analyzer has been made. The agreement is quite good. Looking into the future, this may lead to low-cost testing which allows on-wafer characterization of MMICs before dicing the wafer into individual chips. The only electrical connection to the wafer under test is dc bias. This eliminates the need for the use of expansive probe station used for the launching of millimeter-wave signal into the device on wafer from an external source.

A CW measurement technique using picosecond optical sampling of GaAs integrated circuits has been reported by the Stanford University group [4]. The laser pulse timing with respect to the CW microwave is provided by a phase-lock-loop feedback system which synchronizes and stabilizes the laser pulse timing with respect to the microwave synthesizer. This

microwave synthesizer generates reference signal that phase-locks another RF synthesizer which drives the acoustooptic mode-locker and also provides microwave signal launched into the circuit under test. The pulse timing accuracy of 0.3 picoseconds has been achieved. This technique also has 2 ps time resolution, a working sensitivity of 70  $\mu V/\sqrt{Hz}$  and a spatial resolution of 3  $\mu m$ . This technique has been applied to test a number of high speed digital and analog circuit and to probe internal-node of some traveling-wave amplifier.

Electrooptic sampling technique has also been applied for high frequency characterization of thin-film high temperature superconducting transmission lines [5]. Distortion-free propagation of high current density transient has been demonstrated. The high frequency properties can be analyzed by careful study of the relative phase delays of the electrical transients as the temperature of the sample is varied to cover wide temperature range, from 1.8°K to  $T_c$ .

DC to pulsed or CW RF conversion can also be achieved with picosecond photoconductors. Electrical transient of ultrafast risetime and large amplitude can now be generated. Picosecond and subpicosecond photoconducting dipole antennas have been demonstrated which are capable of generating and coherently detecting picosecond [6] and subpicosecond [7] electric pulses. These antennas, when illuminated with femtosecond optical pulses, radiate electrical pulses with frequency spectra extending from dc-to-THz. These microscopic diode antennas have been fabricated on radiation damaged silicon-on-sapphire substrate for both transmitting and receiving. Direct dc to rf conversion using a single lateral PIN diode as an optoelectronic switch and a coaxial structure as a resonant cavity has been reported [8]. The electrical impulse generated by the PIN diode switch is coupled into the cavity via a loop antenna. The resulting magnetic field induces current in the center conductor of a voltage probe which is used to couple the rf signal out of the cavity. A monolithic dc-to-rf converter has also been demonstrated [8]. If the cavity resonator is replaced by a high  $Q$  cavity filter, a complete CW microwave can be generated. This has been demonstrated for the generation of an optically synchronized CW 20 GHz wave [9]. For a multiple element antenna, this technique can be used to generate phase-arrayed radiation since the rf signals are completely in time synchronized with the ps optical pulses.

Looking back into 1988, we see more application of ps optical technique to microwave and millimeter-wave generation and characterization. In the future, as the technique is perfected and technology matured, we can foresee some merging of optics and microwaves.

## REFERENCES

- (1) For a general review in picosecond photoconductor and general ps optical electronic technique, see (a) "Picosecond

- Optoelectronic Devices," Chi H. Lee, edited, Academic Press, Orlando, 1984, (b) "Picosecond Electronics and Optoelectronics," editors, G.A. Mourou, D.M. Bloom and Chi H. Lee, Springer-Verlag, Berlin, 1985, and (c) "Picosecond Electronics and Optoelectronics II," editors: F.J. Leonberger, Chi. H. Lee, F. Capasso and H. Morkoc, Springer-Verlag, 1987.
- (2) B.H. Kolner and D.M. Bloom, "Electro-optic Sampling in GaAs Integrated Circuit," IEEE J. Quantum Electron. Vol. QE-22, pp. 79-93, 1986.
  - (3) P. Polak-Dingels, H.-L.A. Hung, T. Smith, H.C. Huang, K.J. Webb, and Chi H. Lee, "On-Wafer Characterization of Monolithic Millimeter-Wave Integrated Circuit by a Picosecond Optical Electronic Technique," in IEEE MTT-S Int. Microwave Symp. Dig. (New York, NY) pp. 237-240, May 1988.
  - (4) K.L. Weingarten, M.J.W. Rodwell, and D.M. Bloom, "Picosecond Optical Sampling of GaAs Integrated Circuits," IEEE J. Quantum Electron. QE-24, pp. 198-220, 1988.
  - (5) D.R. Dykar, R. Sobolewski, J.C. Chwalek, J.F. Whitaker, T.Y. Hsiang, G.A. Mourou, D.K. Lathrop, S.E. Russek, and R.A. Buhrman, "High-Frequency Characterization of Thin-Film Y-Ba-Cu Oxide Superconducting Transmission Lines," Appl. Phys. Lett. pp. 1444-1446, 1988.
  - (6) A.P. DeFonzo and C.R. Lutz, "Optoelectronic Transmission and Reception of Ultrashort Electrical Pulses," Appl. Phys. Lett. pp. 212-214, 1987.
  - (7) P.R. Smith, D.H. Auston and M.C. Nuss, "Subpicosecond Photoconductive Dipole Antennas," IEEE J. Quantum Electron, QE-24, pp. 255-260, 1988.
  - (8) A. Rosen, P.J. Stabile, A.K. Sharma, Chi H. Lee and P. Polak-Dingels, "Direct DC-to-RF Conversion by Impulse Excitation Utilizing a Lateral PIN Diode as a Switch," Microwave and Optical Technology Letters, Vol. 1, 106-110, 1988.
  - (9) D. Butler, E.A. Chauchard, K.J. Webb, K.A. Zaki, Chi H. Lee, P. Polak-Dingels, H.L.A. Hung and H.C. Huang, "A CW 20-GHz Optoelectronic Source with Phase-Array Applications," Microwave and Optical Technology Lett. Vol. 1, pp. 119-123, 1988.

# Experimental Performance of an Optically Controlled Coplanar Waveguide Phase Shifter with a Thick GaAs Buried Layer. P. Cheung, D. P. Neikirk and T. Itoh.

## Abstract

The experimental performance of an optically-controlled coplanar waveguide phase-shifter fabricated on a heterojunction substrate containing a thick GaAs layer buried between two AlGaAs layers is presented. The measured performance shows that relative phase-shifts of  $100^\circ$  can be obtained even for optical input powers in the  $\mu\text{W}$  range.

## Introduction

Studies of coplanar waveguides (CPW) on semiconductor multi-layered substrates have shown, that within that the range of resistivities covered by most semiconductor substrates and the frequency spectrum of interest for microwave and millimeter wave applications, a slow wave (SW) mode of propagation can exist [1]. A typical structure consist of a thin lossless layer immediately below the CPW, followed by a thicker lossy layer and a third lossless layer. The slow wave factor (SWF), which is the ratio of the effective guide wavelength to the free space wavelength, is a measure of the change of the effective refractive index of the substrate. The magnitude of the SWF is a function of both the resistivity of the buried lossy layer and the thickness of the first layer. Because of the dependence of the SWF on the properties of the underlying substrate, a CPW on a multi-layered substrate can be used as a variable phase-shifter if either the conductivity or layer thicknesses can be actively controlled.

At the 10<sup>th</sup> IR & MMW conference [2], a method of optically controlling a coplanar-waveguide (CPW) phase-shifter was proposed. By the appropriate selection of semiconductor heterojunction substrate materials ( $\text{Al}_{0.4}\text{Ga}_{0.6}\text{As}$  / GaAs /  $\text{Al}_{0.4}\text{Ga}_{0.6}\text{As}$ ) and the corresponding selection of an illuminating source of the correct wavelength (wavelengths longer than 600 nm, but shorter than 860 nm), the conductivity of the buried GaAs layer can be controlled by the intensity of the optical source. The phase shift is then controlled directly by varying the intensity of the illuminator. At last year's IR & MMW conference [3] preliminary measurements of a prototype device were reported. The results indicated that relative phase shift can be obtained even at relatively low levels of intensity. Recently Kwon, et al [4] showed that the slow-wave mode propagating on the CPW can be modeled by a quasi-TEM circuit model. Using this approach we have developed an equivalent circuit model for an ideal optically controlled CPW phase-shifter [5]. The analysis showed that when a large percent of the total "equivalent thickness" of the substrate is lossy, large relative phase-shifts can be obtained. By conformal mapping this translates into a thick second lossy layer for a typical structure. To test this prediction, a device was fabricated on a substrate with a thick GaAs (7 $\mu\text{m}$ ) layer.

## Device Fabrication

The device was fabricated with a lift-off technique using a chlorobenzene soak process. A metal scheme of gold / silver / chrome with a total thickness of  $\sim 1\mu\text{m}$  was deposited to form the conductors. The measured D.C. resistance of the central conductor is  $\sim 8.0\Omega$ . A cross section of the device is shown in Fig. 1. The heterojunction substrate was grown by MBE on an S.I. GaAs substrate with a  $1\mu\text{m}$  buffer layer. All the grown layers are unintentionally doped (approximately  $10^{14}/\text{cm}^3$ , p-type). The device is mounted on a high dielectric low loss printed circuit board (RT-Duroid 6010.5) that also has a CPW fabricated on it. The CPW on the PCB is accessed at both ends by SMA launchers and electrical connections between the CPW on the PCB and the device is made using bonds wires; the microwave package used for testing is shown in Fig. 2.

## Experimental Results

Measurements on the device were performed using an HP 8510B automatic network analyzer. The illuminating source was a microscope illuminator fitted with a red filter. The measured spectrum of the filtered light showed negligible intensity for wavelengths below 704nm, so no light is absorbed in the  $\text{Al}_{0.4}\text{Ga}_{0.6}\text{As}$  (650nm cutoff) layer. The measurements were done at three illuminating intensities of  $3.2\text{mW}/\text{cm}^2$ ,  $32.0\text{mW}/\text{cm}^2$  and  $63.7\text{mW}/\text{cm}^2$ . Since the actual area of the device expose to the illumination is  $1.4 \times 10^{-3}\text{cm}^2$ , the intensities correspond to optical input powers of  $4.5\mu\text{W}$ ,  $45\mu\text{W}$  and  $89\mu\text{W}$ . The measured results are shown in Fig. 3 and 4. Figure 3 shows the insertion loss as a function of varying illuminating intensity over a frequency range of 0.08GHz to 18.0GHz. Structural effects such as bonds wires and SMA launchers obscure the interpretation of the data beyond 10GHz. The insertion loss of a CPW on semi-insulating (S. I.) GaAs substrate is also plotted on the same graph for comparison.

The insertion loss of the device shows an average change in loss of 2dB/GHz over the range of 1.0 - 10.0 GHz. In comparison, the S. I. sample showed an average insertion loss change of 0.5dB/GHz over the same frequency range. The higher insertion loss of the device is attributed to the unintentionally p-type background doping of the heterojunction sample. Simple modelling indicates a background of only  $1 \times 10^{14}\text{cm}^{-3}$  could account for this loss. At the first illumination intensity ( $3.2\text{mW}/\text{cm}^2$ ) the insertion loss change increases to 2.6dB/GHz. For the next two intensities the loss increases from 3.7dB/GHz (for  $32.0\text{mW}/\text{cm}^2$ ) to 4.0dB/GHz (for  $63.7\text{mW}/\text{cm}^2$ ). The maximum insertion loss for the unilluminated device is -23dB at 10GHz; in comparison, the S. I. sample showed a maximum loss of 5dB at 10.0 GHz. The maximum loss for the illuminating intensities are:

illuminating intensity	maximum insertion loss
$3.2\text{mW}/\text{cm}^2$	- 25.0dB at 10.0 GHz
$32.0\text{mW}/\text{cm}^2$	- 29.0dB at 7.7 GHz
$63.7\text{mW}/\text{cm}^2$	- 32.0dB at 7.7 GHz

Figure 4 shows the measured relative phase shift induced by the optical illumination. An intensity of  $3.2\text{mW}/\text{cm}^2$  yields an average phase-shift of  $5.3^\circ/\text{GHz}$ . A maximum relative phase-shift of  $60^\circ$  at 9.5GHz is obtained, even at this very low intensity. This is equivalent to a change in electrical length of 1/6 of a wavelength (i.e., at 10GHz, from 3.0cm to 2.5cm). The maximum relative phase-shift was  $120^\circ$  at 9.5GHz for an intensity of  $63.7\text{mW}/\text{cm}^2$ , corresponding to a length reduction of a factor of one third (i.e. from 3.0cm to 2.0cm).

To calculate the relative change in the 'effective guide index' we use the following equation:

$$\Delta n_{\text{eff}}(I) = n_{\text{eff}}(I_1) - n_{\text{eff}}(I_0) = -\frac{\lambda_0}{2\pi l} (\theta(I_0, f) - \theta(I_1, f))$$

where  $I_0$  indicates zero illumination,  $l$  is the physical length of the CPW,  $\lambda_0$  the free space wavelength at the operating frequency, and  $\theta(I_1, f)$  the measured phase at the frequency  $f$  and illumination intensity  $I_1$ . Figure 5 shows this calculated change in the 'effective guide index'. At the lowest intensity level the speed of the wave is one tenth of its original speed at 0.1 GHz. At same frequency for the highest intensity level the speed is reduced by thirty times its original speed. At a higher frequency, for example at 10GHz, the

lowest intensity shows a reduction in speed by a factor of three from its original speed, while at the highest intensity level the average reduction is a factor of five.

### Conclusion

We have demonstrated that large relative phase-shifts can be achieved with very small optical input powers. The data is consistent with a simple quasi-TEM circuit model, is primarily due to the high sensitivity of the propagation constant to the conductivity of the buried GaAs layer. These results are very promising, indicating that significant phase shift can be obtained from an electrically short structure using very low levels of total optical power. Further optimization of the heterostructure substrate and CPW dimensions is now underway.

### References

- [1] Y. Fukuoka, Yi-Chi Shih and T. Itoh, "Analysis of Slow-Wave Coplanar Waveguide for Monolithic Integrated Circuits," *IEEE Trans. Microwave Theory Tech.*, vol. MTT-31, pp. 567-573, July, 1983.
- [2] P. Cheung, D. Fun, D. Miller, C-K. Tzuang, D. P. Neikirk and T. Itoh, "Optically controlled Coplanar Waveguide Millimeter Wave Phase-Shifter," *Proceeding of the 10th International Conference on Infrared and Millimeter Waves*, 1985.
- [3] P. Cheung, D. P. Neikirk and T. Itoh, "Experimental Performance of an Optically Controlled Coplanar Waveguide Phase Shifter," *Proceedings of the 11th International Conference on Infrared and Millimeter Waves*, 1987.
- [4] Y. R. Kwon, V. M. Hietala, and K. S. Champlin, "Quasi-TEM Analysis of "Slow - Wave" Mode Propagation on Coplanar Microstructure MIS Transmission Lines," *IEEE Trans. Microwave Theory Tech.*, vol. MTT-36, pp. 545-551, June 1987.
- [5] P. Cheung, "A Preliminary Study of an Optically Controlled Coplanar Waveguide Phase-Shifter," Master thesis, Dec. 1987, The University of Texas at Austin, Texas.

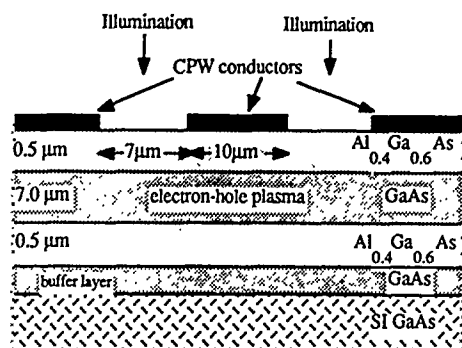


Fig. 1: Cross-section view of device

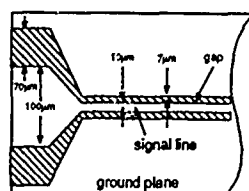


Fig. 2 (a) Schematic of device dimensions.

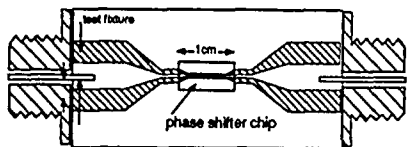


Fig. 2 (b) Schematic of device mounted in the test package.

Fig. 3. Insertion Loss Vs. Freq.

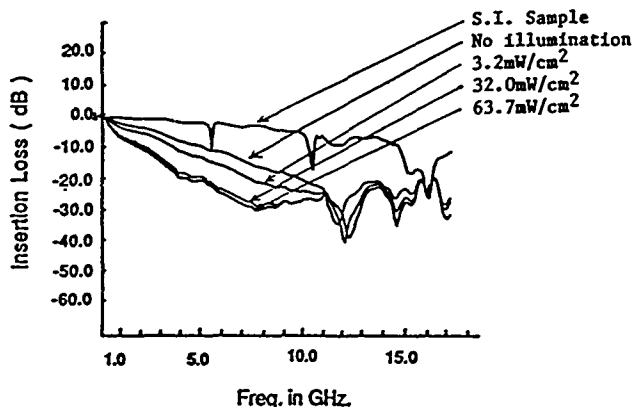


Fig. 4. Relative Phase-Shift Vs. Freq.

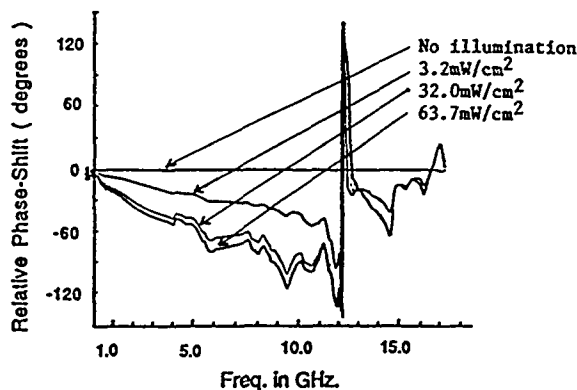
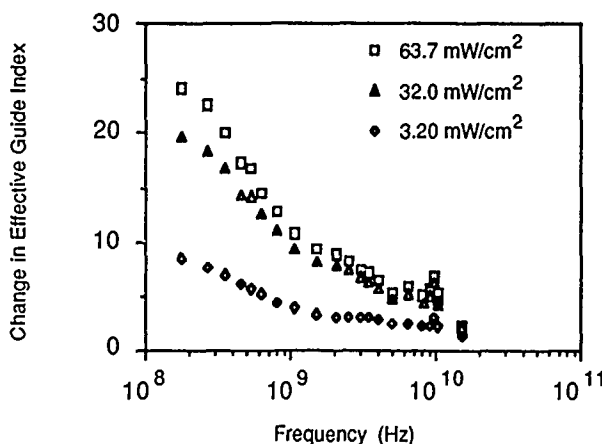


Fig. 5. Change in Effective Guide Index Vs Freq.



This work was sponsored in part by the United States Air Force Office of Sponsored Research, grant number AFSOR 86 0036, and the Texas Advance Research Program.

## STRUCTURAL CONTROL OF MICROSTRIP DISPERSION FOR SHAPING GIGA-HERTZ-BANDWIDTH PULSES

Eikichi Yamashita, Kazuhiko Atsuki, and Yongxi Qian

University of Electro-communications  
Chofu-shi, Tokyo, Japan 182

## ABSTRACT

Recent optical switching devices are using combinations of very short laser pulses, photoconductors, and strip lines. Since laser pulses have gigahertz-bandwidth, signal transmission properties of such strip lines in a wide range of frequencies are decisively important. This paper describes the structural control of the dispersion characteristics of microstrip lines by adding ground conductors on both sides of the strip conductor. Some numerical data are shown.

## INTRODUCTION

Laser pulses with durations of picoseconds have been recently used to make various optical switching devices based on photoconductive effects in semiconductors. As a result of the photoconduction, when shined by laser light, low resistance regions in semiconductors act as switches to produce short electrical pulses.

The configurations of microstrip lines have been often employed in these optical switches, because D.C. bias voltage supplies are connected to the strip conductor on a semiconductor substrate and generated electrical pulses are transmitted through the microstrip lines for various applications such as microwave generation [1], sampling [2], and high-frequency waveform generation [3].

The availability of recent laser pulses with very short rise time enforces us to take into account the wide frequency characteristics of the microstrip lines as gigahertz bandwidth even though very small devices with  $\mu\text{m}$  dimensions can be fabricated.

The microstrip lines are inherently dispersive at high frequencies because of the existence of dielectric substrate materials. Therefore, short electrical pulses are deformed as they propagate along the line. These dispersion effects can also sharpen pulses after propagating some length of a microstrip line due to the fact that high frequency components of the pulses travel with slower speed than the low frequency components and eventually the pulses are compressed.

In this paper, we describe the dispersion properties of general transmission line structures supported by dielectric substrate materials. Some numerical examples are given on microstrip lines and those with additional ground conductors on both sides of the strip conductor. A method for controlling the dispersion effects up to a certain frequency is discussed.

## METHOD OF ANALYSIS

Fig.1 shows a microstrip-like transmission line which contains two dielectric layers, a strip and ground conductor system, and a metallic shield enclosure. The strip conductors are assumed to be negligibly thin and lossless. A hybrid mode analysis is apparently necessary for this inhomogeneous structure.

The propagation constant  $\beta$  is estimated by solving Maxwell's equations. Simultaneous integral equations on some components of electromagnetic fields can be derived, and then these are transformed into a set of linear homogeneous equations by carrying out the non-uniform discretization of the integrals. The determinant of the coefficient matrix for these linear equations should vanish to obtain non-trivial solutions. Then,  $\beta$  is given as solutions of this determinantal equation [4][5].

For a combined structure of a strip and ground conductor system, a supporting dielectric sheet, and a metallic shield enclosure as shown in Fig.1, we can expect the following general features:

- 1) In the quasi-TEM wave approximation which is valid at low frequencies, the existence of the dielectric sheet results in just the increase of line capacitance. When the propagation constant in this approximation is denoted by  $\beta_{\text{TEM}}$  and that in vacuum by  $\beta_0$ , the  $\beta_{\text{TEM}}/\beta_0$  ratio curve against frequency  $f$  is expressed with a horizontal line (curve A in Fig.2).
- 2) When the strip conductor is removed from this structure, the dielectric sheet behaves as an enclosed dielectric slab waveguide with some cutoff frequencies. Hence, the curve of  $\beta/\beta_0$  should indicate usual traits of waveguides (curve B).
- 3) When the electromagnetic fields of the quasi-TEM waves and those of an enclosed dielectric slab waveguide mode resemble each other, the combined structure should couple these fields and new two curves for  $\beta/\beta_0$  appear as the connected lines of the curve A and curve B, at the intersection as shown as the curves,  $C_1$  and  $C_2$ , in Fig.2.
- 4) When such field coupling is tight, the separation between  $C_1$  and  $C_2$  should be large and, therefore, gradual and strong dispersion effects should be observed.
- 5) When coupling is weak, the separation between  $C_1$  and  $C_2$  becomes small and, therefore, the dispersion effects are not appreciable up to the intersection point of A and B where sudden change occurs.

## MICROSTRIP LINES

Fig.3 shows the case of usual microstrip lines. The field coupling is so tight that A, B, and C relations are not clearly observable.

Fig.4 shows some numerical results on an interesting but impracticable case of microstrip lines where the field coupling is weak because the ceiling height is so small that a large amount of energy is distributed into the air region. Expected features of weak coupling are clearly observed in these curves.

MICROSTRIP LINES WITH PARALLEL  
GROUND CONDUCTORS ON BOTH SIDES

Fig.5 shows a case of microstrip lines with parallel ground conductors on both sides where the side ground conductors are so far from the center conductor that the extent of field coupling is tight

as usual microstrip lines. The relations between A, B, and C curves are almost the same as those of microstrip lines.

Fig. 6 shows another case of microstrip lines with parallel ground conductors on both sides where the field coupling is weak because the gaps between the center conductor and ground conductors are so narrow that energy is highly concentrated into the two gap regions. It is another reason of weak coupling that main electric field patterns corresponding to A and B curves are almost orthogonal. Weak coupling relations between A, B, and C curves are clearly observed. When strip transmission lines with least dispersion in a wide range of frequencies are required, structures of this class can be candidates. The dispersion behavior can be thus controlled from

gradual dispersion to sudden dispersion by adjusting the size of the gap width.

#### REFERENCES

- [1] C.J. Clark et al, IEEE Jour. Lightwave Tech., vol. LT-5, pp.388-397, Mar. 1987.
- [2] J.A. Valdmanis et al, Appl. Phys. Lett. vol.41, pp.211-212, Aug. 1982.
- [3] J.M. Proud and S.L. Norman, IEEE Trans. on MTT, vol. MTT-26, pp.137-140, Mar. 1978.
- [4] E. Yamashita and K. Atsuki, IEEE Trans. on MTT, vol. MTT-24, pp.195-200, Apr. 1976.
- [5] E. Yamashita, K. Atsuki, and T. Ueda, IEEE Trans. on MTT, vol. MTT-27, pp.1036-1038, Dec. 1979.

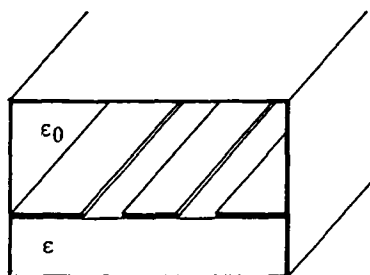


Fig. 1

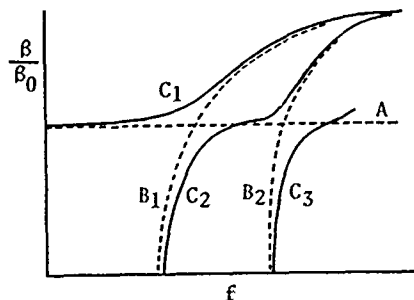


Fig. 2

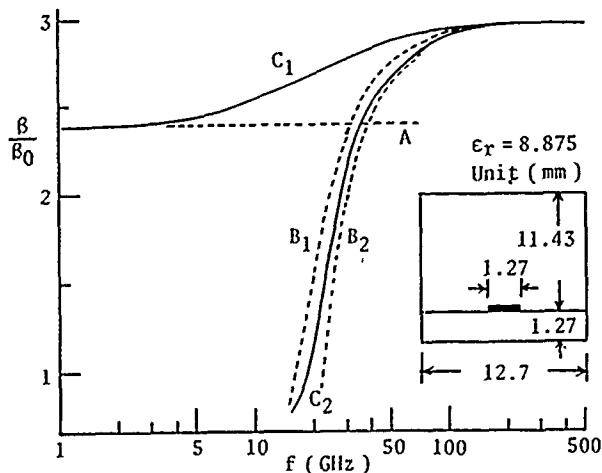


Fig. 3

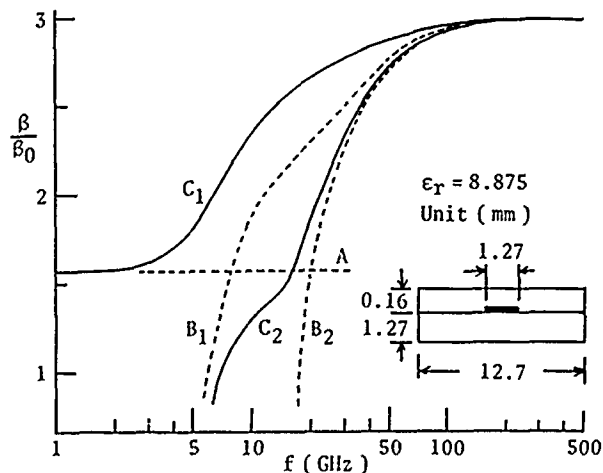


Fig. 4

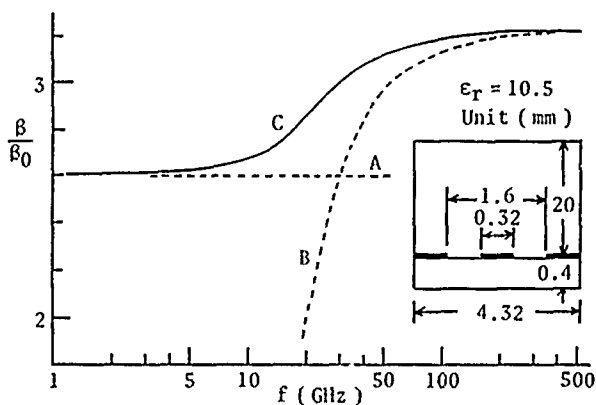


Fig. 5

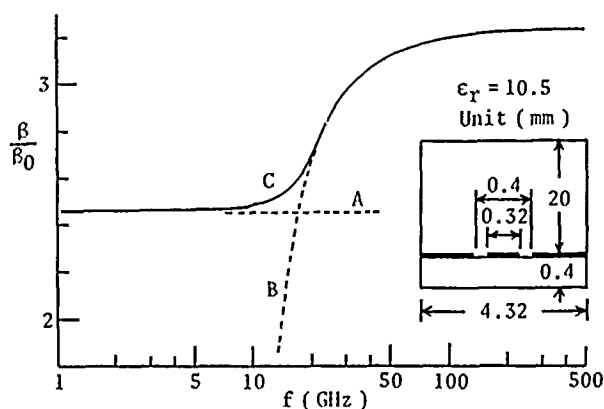


Fig. 6

## INVERTED SLOT LINE FOR MILLIMETER-WAVE OPTICAL MODULATOR

Tsukasa Yoneyama and Tomoaki Kato  
Research Institute of Electrical Communication, Tohoku University  
2-1-1 Katahira, Sendai, 980 Japan

### Abstract

The inverted slot line is proposed with the purpose of applying to optical modulators operating at millimeter-wavelengths. Velocity of millimeter-waves can be matched to that of optical waves in  $\text{LiNbO}_3$  material by simply adjusting the spacing between the slotted surface and the ground plane.

### I. Introduction

Recently, research on high-speed optical modulators[1],[2] has been attracted much attention because of the increasing demand for optical communication systems of very large capacity. A slot line[3] with the  $\text{LiNbO}_3$  substrate is a widely used transmission line for optical modulation up to millimeter-waves, but efficiency of modulation is limited by the large velocity mismatching between the optical waves and millimeter-waves. In order to achieve good velocity matching between the modulated and modulating waves, modified slot lines with the nonsymmetrical electrode structure [4] and with the thin substrate backed by a lower refractive index layer[5] have been studied.

In this paper, the inverted slot line is proposed as a promising transmission medium for optical modulation applications. It is the ordinary slot line placed upside-down over the ground plane with a very small spacing. Though quite simple in structure, the inverted slot line has the possibility that the velocity matching can easily be achieved since the phase velocity of millimeter-waves can widely be adjusted by changing the spacing between the slotted surface and the ground plane. Millimeter-wave transmission characteristics of the inverted slot line have been measured at 50GHz and the results are found to be favorable for the optical modulator construction.

### II. Structure and Principle of Operation

As shown in Fig.1, the inverted slot line is constructed in such a way that the slotted surface faces the conducting ground plane with a very small spacing, say  $50\mu\text{m}$  or less, between each other. Since the electric field of the transmission line is predominantly parallel to the metal plane, the space bounded by the slotted surface and the ground plane is kept below cutoff for transmitted waves and hence the phase velocity becomes infinitely large there. Therefore, the phase velocity of the inverted slot line itself, which can be regarded as being coupled to the below

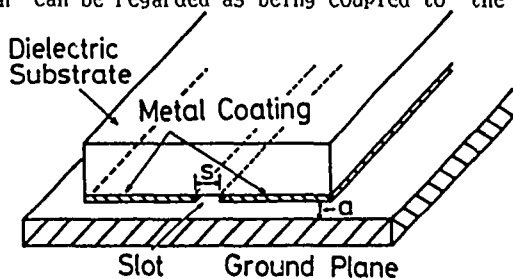


Fig. 1. Structure of the inverted slot line

cutoff parallel plate waveguide through the slot, is considered to be very large and can also be adjusted by varying the spacing between the slotted surface and the ground plane at will. Thus, the inverted slot line is expected to considerably improve the efficiency of optical modulators by facilitating to realize the velocity matching condition.

### III. Measurements

#### 3.1 Effective Refractive Index

In order to confirm the qualitative prediction stated in the previous section, transmission characteristics of the inverted slot line were measured at 50GHz. Though the  $\text{LiNbO}_3$  substrate has to be used for practical optical modulators, the Duroid substrate  $0.254\text{mm}$  in thickness with dielectric constant 10.5 and loss tangent  $3 \times 10^{-3}$  was chosen for fabrication convenience in the present preliminary experiment. Three type of slot lines having different slot widths  $100\mu\text{m}$ ,  $150\mu\text{m}$  and  $200\mu\text{m}$  and the same slot length  $50\text{mm}$  were prepared. The effective refractive index was measured at first by detecting standing wave patterns on the slot lines. The results are presented in Fig.2 with solid curves. It is seen that the effective refractive index decreases with the decreasing spacing between slotted surface and the ground plane as expected. This fact implies that the velocity matching between optical waves and millimeter-waves can actually be achieved by simply adjusting the spacing.

Dispersion characteristics of the inverted slot line  $100\mu\text{m}$  in slot width were also measured over the 48 to 52GHz frequency range. The results are plotted in Fig.3. Dependence of the effective refractive index on frequency is quite small over the measured frequency range at least and hence broadband optical modulators are expected to be realized.

#### 3.2 Attenuation Constant

Measured attenuation constants of the inverted slot lines are shown in Fig.2 with dotted curves. The attenuation constant increases with the decreasing spacing between the slotted surface and the ground plane as predicted, and becomes larger by about 50% for the spacing of  $63\mu\text{m}$  than for the spacing of  $252\mu\text{m}$ . Though the increase in attenuation constant is by no means favorable for the optical modulator, this drawback can be compensated if the velocity matching is really achieved. In this connection, it should be mentioned that the measured attenuation constant can be reduced if both the metal surfaces of the slot line and the ground plane are more carefully finished.

#### 3.3 Field Distributions

Transverse electric field distributions measured over the substrate are shown in Fig.4. Both the horizontal and vertical components are compared to those for the ordinary slot line without the ground plane. Though the fields, especially the vertical components, are spreaded in the inverted slot line, this does not cause any serious trouble in the optical modulation applications since the field spreading of the working horizontal component is only slight.

#### IV. Transitions

The coaxial cables are often used for millimeter-wave excitation in the optical modulators because of their broadband characteristics. In the inverted slot line, however, such an arrangement is not possible since the spacing between the slotted surface and the ground plane is too small to install the coaxial line. In order to overcome such difficulty, a microstrip line is introduced transversely on the opposite side of the substrate as shown in Fig.5[6], and the slot line is excited by the coaxial cable through the microstrip line. Transition between the coaxial line and the microstrip line is achieved by simply connecting them by mechanical pressure. Measured overall conversion loss of the inverted slot line is shown in Fig.6 with solid curve as a function of frequency. The back-to-back technique was used in measurement and transmission losses of the three transmission media, slot line, microstrip line and coaxial line, are all subtracted from the measured loss values. It should be noted that the conversion loss shown in Fig.6 includes not only transition loss between the microstrip line and slot line but also transition losses between the coaxial cable and microstrip line and between the waveguide and the coaxial cable, the waveguide being needed for experimental convenience.

Since the inverted slot line is an open structure, losses are also generated at transition in the form of space waves and surface waves. In order to suppress such additional loss, metal walls are provided around

the slot line. The conversion loss for this case is also shown with dotted curve in Fig.6. Improvement is apparent and the conversion loss is found to be below 1.1dB over the measured frequency range at least.

#### V. Conclusions

The inverted slot line has been proposed as a simple and practical transmission medium for optical modulators operating at millimeter-wavelengths, and its transmission and transition characteristics have been measured at 50GHz. As a result, possibility of velocity matching, small dispersion property and good transition efficiency have been demonstrated. The optical modulator is being designed and fabricated to confirm its potential performance.

#### References

- [1] R.C.Alferness, *IEEE Trans. Microwave Theory Tech.*, vol. MTT-30, pp.1121-1137, 1982.
- [2] F.J.Leonberger, *Opt. Lett.*, vol. 5, pp.312-314, 1980.
- [3] S.B.Cohn, *IEEE Trans. Microwave Theory Tech.*, vol. MTT-17, pp.768-778, Oct. 1969.
- [4] M.Izutsu, T.Sueta, *IEEE J. Quantum Electron.*, vol. QE-14, pp.394-395, Jun. 1978.
- [5] K.Atsuki, E.Yamashita, *IEEE J. Light Tech.*, vol. LT-5, pp.316-319, Mar. 1987.
- [6] G.H.Robinson, J.L.Allen, *IEEE Trans. Microwave Theory Tech.*, vol. MTT-17, pp.1097-1101, Dec. 1960

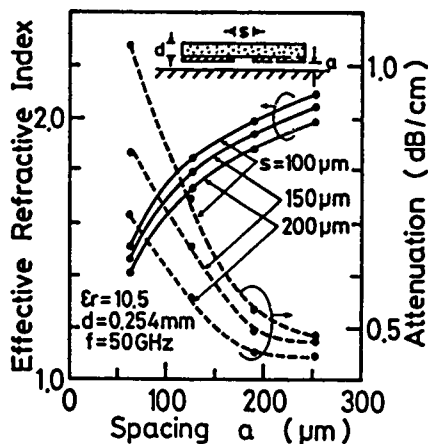


Fig. 2. Effective refractive index and attenuation constant versus spacing between the slotted surface and the ground plane

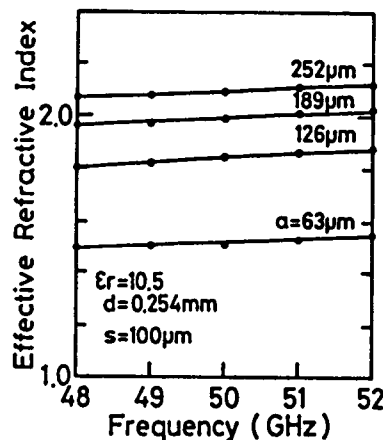


Fig. 3. Dispersion characteristics of the inverted slot line

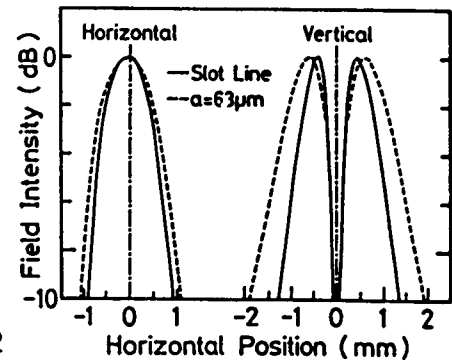


Fig. 4. Transverse electric field distributions of the horizontal and vertical components

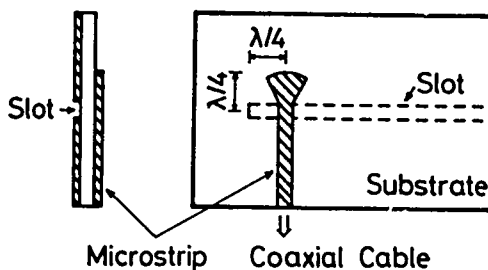


Fig. 5. Transition between the microstrip line and the inverted slot line

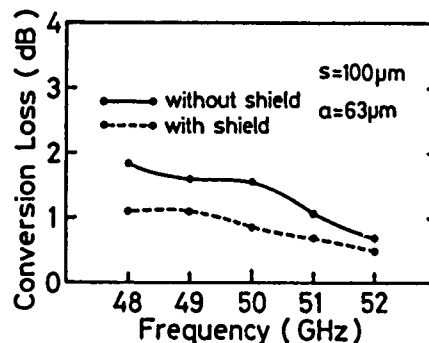


Fig. 6. Frequency characteristics of overall conversion loss for the waveguide-coaxial, coaxial-microstrip and microstrip-inverted slot line transition



# AN OPTOELECTRONIC TECHNIQUE FOR S-PARAMETER MEASUREMENTS OF GaAs MONOLITHIC INTEGRATED CIRCUITS

P. Polak-Dingels,\* H-L. A. Hung,† K. J. Webb,‡  
T. T. Lee,† T. Smith,† and C. H. Lee‡

\*The Laboratory for Physical Sciences, College Park, MD 20740

†COMSAT Laboratories, Clarksburg, MD 20871

‡University of Maryland, College Park, MD 20742

## ABSTRACT

An optical technique using picosecond pulses has been developed to characterize the magnitude and phase of the frequency response of a gallium arsenide (GaAs) monolithic integrated circuit in the millimeter-wave frequency range. The results of the complex S-parameters of an amplifier obtained using this technique were compared with those obtained using the network analyzer method.

## INTRODUCTION

Advances in GaAs microwave and millimeter-wave monolithic integrated circuits (MIMICs) have led to the development of these circuits for various high-volume system applications requiring affordable and highly reliable components. The existing frequency domain approach for RF testing of MIMICs constitutes a significant manufacturing cost. Therefore, a measurement system which can perform on-wafer RF characterization of MIMICs at low cost, and can be commercially manufactured, is highly desirable.

Conventional waveguide measurement systems are limited by the waveguide bandwidth, high fabrication cost for precision fixturing, and oscillations during active device characterization. Present on-wafer RF characterization systems that employ contacting coplanar waveguide (CPW) probes have several limitations in achieving a low-loss, impedance-matched characteristic at millimeter-wave frequencies, and a customized probe card is needed for each set on the wafer.

Recently, optical techniques have been studied for use in characterizing microwave devices and circuits. One approach is to introduce a microwave signal to the circuit through contacting CPW probes, and to use electro-optic sampling of time-domain waveforms (1). Another approach, employing a photoconductive switch for signal generation and sampling, has been used to measure the magnitude of the gain response of an MIMIC (2),(3).

This paper describes refined measurement techniques and presents new results for the optoelectronic characterization of a  $K_a$ -band monolithic amplifier, including both magnitude and phase. Thus, the technique has been extended to perform complex S-parameter measurements. Mechanical contact is not required between the measurement system and the wafer in order to generate waveforms containing the millimeter-wave frequency spectrum. The same measurement system can allow broadband operation from DC to several hundred gigahertz. Emphasis was placed on systematic validation of the optoelectronic approach to S-parameter measurement.

## THE OPTICAL MEASUREMENT SYSTEM

Figure 1 is a schematic diagram of the optoelectronic characterization system, including a 50- $\Omega$  reference line or an MIMIC. The optical source is

provided by a continuous-wave, mode-locked, Nd:YAG laser whose output is compressed and frequency-doubled through a KTP crystal. The 532-nm optical pulses have a repetition rate of 100 MHz and a duration of 5 ps. A short electrical pulse is generated by a DC-biased photoconductive switch at Port a and propagates down the input transmission line toward the circuit. The pulse traveling in the opposite direction is absorbed by a matched termination, which can readily be implemented as an monolithic broadband distributed resistor (4). The pulse approximates a delta function in the time domain, resulting in a very broadband frequency spectrum. Since the input electrical pulse generated is in complete time synchronization with the optical pulse, the electrical pulse can be precisely sampled at Port b by a time-delayed laser pulse illuminating a second picosecond photoconductive switch on the input side of the circuit.

The output of the circuit can be sampled using the same procedure, with a photoconductive switch at the output (Port c or d). By comparing the Fourier transforms of the reflected and transmitted waveform to those of the incident waveform at the input, the two-port forward complex scattering parameters ( $S_{11}$  and  $S_{21}$ ) can be determined without using CPW contacting probes. The magnitude and phase of  $S_{22}$  and  $S_{12}$  can also be measured in a similar manner by simply redirecting the laser pulse to the corresponding locations on the circuit. A minicomputer is used to control the experiment and to perform the fast Fourier transform (FFT), so that frequency domain response can be observed immediately after the measurement.

## MEASURED RESULTS

A reference 50- $\Omega$  microstripline of the same physical length as the MIMIC to be tested was fabricated and used for system calibration. The MIMIC was a two-stage power amplifier with a nominal gain of 4 dB per stage and output power close to 0.5 W at 28 GHz (5). An output power of 1 W has been achieved with these MIMICs in a balanced configuration. The MIMIC was mounted between two pairs of GaAs photoconductive switches which were biased at 20 V. Since the sampled signals are at the 200-Hz chopper frequency, coaxial low-frequency probes (LFPS) such as those employed in existing automated on-wafer DC measurement systems can be used to detect the sampled signal.

Figure 2 depicts the magnitude and phase of the transfer function,  $S_{21}$ , as determined by an FFT of the data obtained from the optical technique. Note that the gain peaks at 28 GHz, as expected. These results can be compared with those in Figure 3, which shows the transfer function measured using the conventional network analyzer technique. Good agreement was obtained in both the magnitude and phase of the broadband response. The frequency

domain data obtained with the optical technique show smoother response than those obtained with the network analyzer, indicating that impedance mismatches were encountered across the frequency band during the network analyzer measurements. Abrupt variations in both magnitude and phase centered at around 10 GHz appeared in the results for both measurement techniques.  $S_{11}$  can be determined by analyzing the reflected wave, which is separated from the incident wave by proper gating of the signals detected at the input.

#### CONCLUSIONS

An optoelectronic characterization technique has been demonstrated to achieve a broadband frequency response for both the magnitude and phase of a  $K_a$ -band MIMIC. The measured scattering parameters show close agreement with data obtained from network analyzer measurements on the MIMIC amplifier. This technique offers significant potential for on-wafer characterization of both high-speed devices and microwave/millimeter-wave circuits. Future development of the optoelectronic technique may lead to characterizations of nonlinear circuits and multiport devices.

#### ACKNOWLEDGMENTS

The authors would like to thank H. Huang, F. Phelepps, A. Meulenberg, D. Mullinix, and J. Chen of COMSAT Laboratories for their technical support.

#### REFERENCES

- (1) K. J. Weingarten, M. J. W. Rodwell, and D. M. Bloom, "Picosecond Optical Sampling of GaAs Integrated Circuit," *IEEE J. Quantum Electron.*, vol. QE-24, pp. 198-200, February 1988.
- (2) H-L. A. Hung, T. Smith, H. C. Huang, P. Polak-Dingels, K. J. Webb, and C. H. Lee, "Optical Electronic Characterization of Monolithic Millimeter-Wave Integrated Circuits," in *12th Int. Conf. on Infrared and Millimeter Waves Conf. Dig.* (Orlando, FL), pp. 87-88, December 1987.
- (3) P. Polak-Dingels, H-L. A. Hung, T. Smith, H. C. Huang, K. J. Webb, and C. H. Lee, "On-Wafer Characterization of Monolithic Millimeter-Wave Integrated Circuit by a Picosecond Optical Electronic Technique," in *IEEE MTT-S Int. Microwave Symp. Dig.* (New York, NY), pp. 237-240, May 1988.
- (4) A. Ezzeddine and H-L. A. Hung, "A  $K$ -band Distributed Microstrip Termination," *Comsat Technical Review*, vol. 14, no. 2, pp. 467-480, Fall 1984.
- (5) H-L. A. Hung, A. Ezzeddine, L. B. Holdeman, F. R. Phelepps, J. F. Allison, A. B. Cornfeld, T. Smith, and H. C. Huang, " $K_a$ -Band Monolithic Power Amplifiers," in *IEEE Microwave and Millimeter-Wave Circuit Symp. Dig.*, (Las Vegas, NV), pp. 97-100, June 1987.

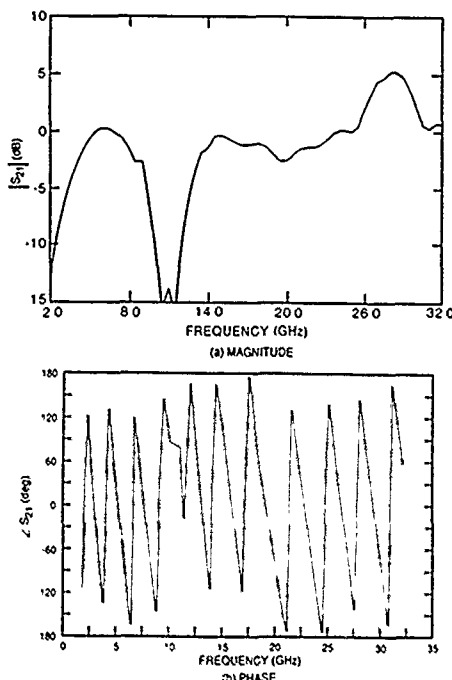


Figure 2. Frequency Response of a MIMIC Amplifier From the Optical Measurement Technique

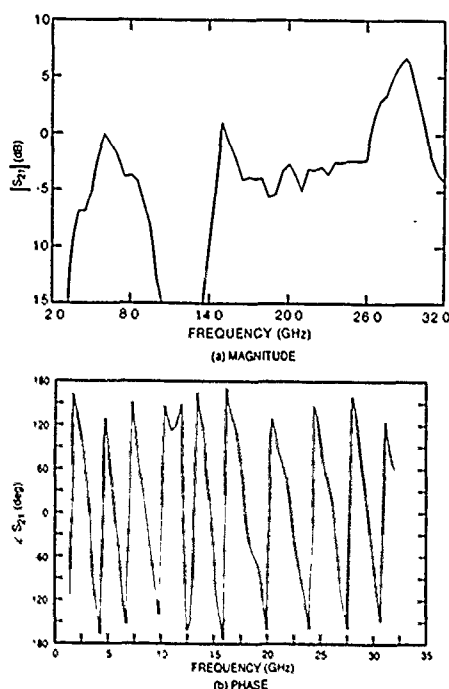


Figure 3. Frequency Response of a MIMIC Amplifier From the Network Analyzer Measurement Technique

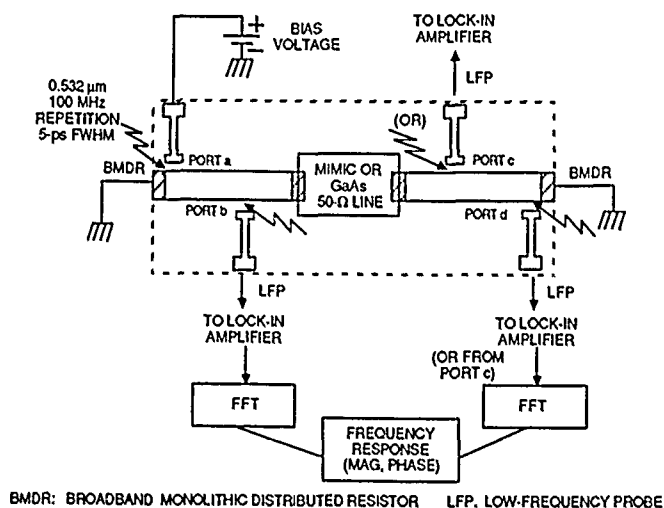


Figure 1. Schematic of the Optoelectronic Characterization System

# EFFECT OF THE LIGHT ON THE ELEMENTS OF THE ELECTRIC SCHEME OF A HEMT

D.Pasquet, B.Zemour, J.L.Gautier, P.Pouvil

E.N.S.E.A  
Les Chênes Pourpres  
95000 CERGY, FRANCE

## ABSTRACT

An optical fiber has been used to illuminate a HEMT. This causes modifications of the static and dynamic characteristics of this component. A home made sophisticated software extracts the elements of the classical electric scheme of microwave FETs from their "S" matrix.

The effect of the light on the major elements are described and compared with the results for MESFETs.

## EXTRACTION OF THE ELECTRIC SCHEME

The usual electric scheme is composed of 13 elements as shown in Fig.1.

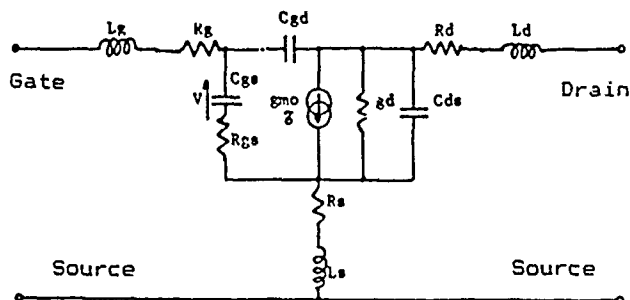


Figure 1  
Electric scheme for microwave FETs

The software which has been used extracts in a first step a few number of elements from the lower frequency measurements. The found values are then introduced into a classical optimization software. The sensitivity to the accuracy of the measurements of matrix "S" is less important than for usual softwares and the optimization lasts a 2 to 5 less long time. [1,2]

## EFFECT OF THE LIGHT ON "S" PARAMETERS

The "S" parameters are measured with a network analyzer the transistor being included in a microstrip fixture. The component is illuminated by a fiber at the output of a laser diode ( $\lambda=845\text{nm}$ ) as shown in Fig.2. The diode delivers 1.3mW but we can roughly consider that only 16 $\mu\text{W}$  enters the semiconductor.

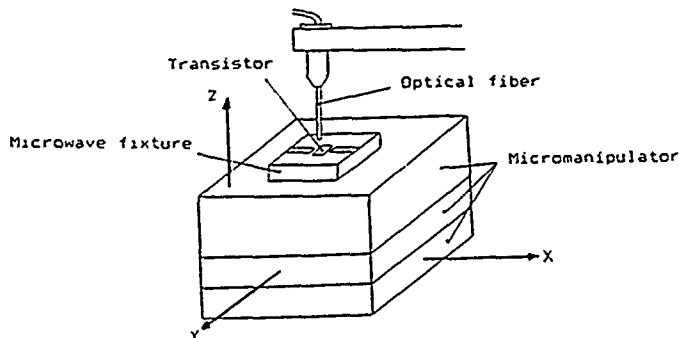


Figure 2  
Experimental set up

It appears a shift of the phase of  $S_{11}$  and an increase of the amplitude of  $S_{21}$ . (Fig.3 and 4). The effect on  $S_{12}$  and  $S_{22}$  are less significant.

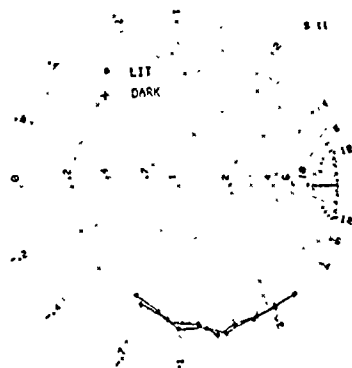


Figure 3  
Variation of  $S_{11}$  with the IR light.

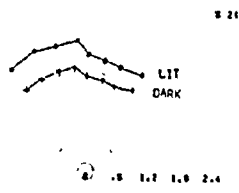


Figure 4  
Variation of  $S_{21}$  with the IR light

# EFFECT OF THE LIGHT ON THE ELEMENTS OF THE ELECTRIC SCHEME

As it can be felt  $g_{mo}$  and  $C_{gs}$  are the more sensitive elements as we can see in Fig.5 and 6

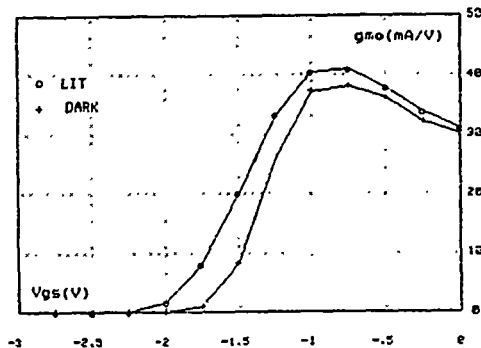


Figure 5  
Effect of the IR light on  $g_{mo}$

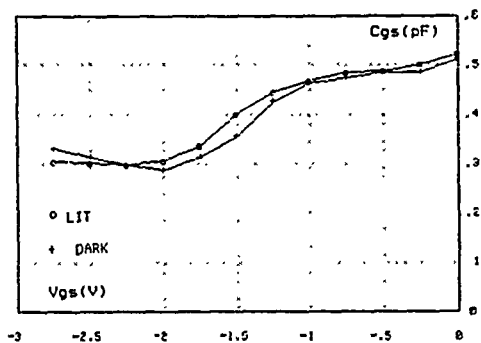


Figure 6  
Effect of the IR light on  $C_{gs}$

It is important to notice that the effect is sensitive on  $g_{mo}$  even when its value is large. In the contrary,  $C_{gs}$  does not change very much.

Some experiments have been made with a HeNe laser ( $\lambda=648\text{nm}$ ). Fig.7 shows that the effect on  $g_{mo}$  is far less sensitive and its increase does not depend on the bias. The other elements are not affected.

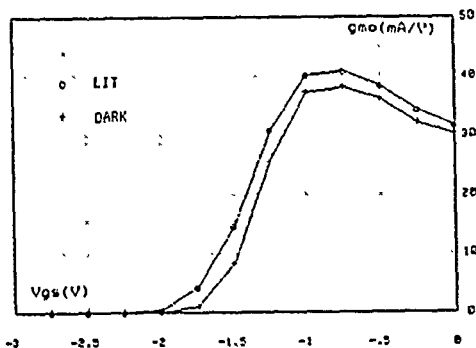


Figure 7  
Effect of the red light on  $g_{mo}$

## CONCLUSION

The effect of the light is more sensitive on  $g_{mo}$  than it is for MESFETs [3] and it appears for large values. By another hand, the sensitivity of  $C_{gs}$  which is significant for MESFETs disappears for HEMTs.

For the applications of light controlled devices, HEMTs seem not to fit for the design of oscillators. In the contrary they would be useful for the performance of light controlled amplifiers which could be simultaneously fast and sensitive.

## REFERENCES

- [1] J.L.Gautier Thèse d'Etat Orsay (France) 1987
- [2] J.L.Gautier D.Pasquet P.Pouvil 5<sup>e</sup> Journées Nationales Microondes Nice 22-24 June 1987 391-393
- [3] J.L.Gautier D.Pasquet P.Pouvil IEEE Transactions on MTT vol MTT23(1985) 819-822

## JOSEPHSON LOCAL OSCILLATOR FOR INTEGRATED RADIOASTRONOMICAL RECEIVERS

R. Monaco, S. Pagano

Istituto di Cibernetica del Consiglio Nazionale delle Ricerche  
I-80072 Arco Felice - Italy

G. Costabile

Dipartimento di Fisica - Università di Salerno  
I-84100 Salerno - Italy

## ABSTRACT

We developed a microwave oscillator based on a series array of 100 long Josephson tunnel junctions coherently working in the fluxon resonating mode. This prototype has satisfied all the requirements (output power, frequency, signal stability and purity) for local oscillator in integrated superconducting millimeter receivers.

## INTRODUCTION

It is well known that mixers based on superconducting tunnel device (SIS mixer) have reached performances well above any other competitive device in the field of mm-wave heterodyne detection. In fact, the very sharp non-linearity of the current versus voltage curve of an SIS tunnel device can be used for quantum limited detection, i.e. for each photon incident on the mixer, one electron is produced in the embedding circuit (1). Besides its frequency broadband response, another major advantage of SIS mixers over Schottky mixers is the low pumping power requirement that is always less than  $1 \mu W$ .

Hitherto the local oscillator required for the operation of SIS mixers has always formed a separate device; the integration on the same chip of both the mixer and the local oscillator would give obvious advantages in terms of economy and simplicity of operation, especially in space born environments (satellites, balloons, etc.) where lightweight, low volume and low consumption devices are strongly recommended.

A Long Josephson Tunnel Junction (LJTJ) is a natural candidate for the realization of mm-wave sources (2): in fact it is well known that such superconducting device, made by two thin film superconducting electrodes separated by an extremely thin oxide tunnel barrier, exhibits current steps in the I-V characteristic (the so-called Zero Field Steps), which correspond to the resonant propagation of one or more magnetic flux quanta (fluxons). When the fluxon is reflected at the junction edge (because of impedance mismatch) an electromagnetic radiation is emitted, the direction of motion reverses and eventually the fluxon reaches the opposite edge of the LJTJ where it undergoes another reflection with associated emission of radiation. This process repeats itself originating a periodic steady state in which the power supplied by the driving dc external bias is balanced by the losses due to both viscous dissipation and radiation emission. As the fluxon can be considered as a relativistic particle in a reflecting edge cavity, the resulting electromagnetic emission has a frequency given by  $f = u/2L$ , where  $u$  is the average fluxon speed and  $L$  is the LJTJ's length: typical values for the fluxon speed  $u$  ( $10^7 m/s$ ) and for the length  $L$  ( $50 \mu m$ ) give  $f = 100 GHz$ . The radiation has a very narrow linewidth (few KHz) because the LJTJ acts as a non-linear tunable high-Q resonant

cavity (3). These simple considerations make very attractive the use of a LJTJ as local oscillator for an SIS mixer because of their complete technological compatibility.

Undoubtedly, the main drawback of the use of an LJTJ as local oscillator for SIS mixers is the small amount of power radiated by a single device (about 10-100 pW) compared to the pumping level for SIS mixers (about 10-100 nW). Nevertheless, to obtain the necessary performance one approach is to put together a large number of LJTJs all operating in the resonating fluxon regime at the same frequency in a phase locked state; such state of coherent fluxon oscillations is often called superradiance because the total emitted power builds up as  $N^2$  while the signal linewidth decreases as  $1/N$ ,  $N$  being the number of LJTJs in the array: this behavior easily produces a considerable power increase using arrays consisting of a limited number of LJTJs.

## LJTJ ARRAYS

We have realized a number of series biased arrays of many LJTJs (up to 100): our preliminary devices were designed to operate at only 10 GHz in order to be able to display the detected signal directly on a X-band spectrum analyzer. All of our samples consist of arrays of highly hysteretic Nb-Nb oxide-Pb LJTJs, 0.5 mm long, dc series biased, having overlap geometry. The measurements were performed in a standard cryogenic equipment at 4.2 K

Fig. 1 shows an enlarged view of an 8-LJTJ device: each LJTJ (shaded area in the lower part of the figure) base electrode has a stub protruding into a  $50 \Omega$  microstrip line which brings the detected radiation from the cryogenic bath to the X-band low noise preamplifier at room temperature. This sort of comb technique provides both the coupling of the fluxon oscillation in each LJTJ with the microstrip line and the coupling among the LJTJs themselves that is necessary to obtain a phase locked state.

Considering that the impedance of an array is usually less than  $1 \Omega$ , it is clear that the power transferred into a  $50 \Omega$  load is very low due to the large impedance mismatch; it should be noted, however, that such mismatch is needed to avoid a severe loading of the oscillators that would lower their quality factor and broaden the linewidth of the emitted signal beyond tolerable values. We have realized two different microwave circuits in which both the broadband and narrowband couplings were achieved. In the case of broadband coupling generally a complex emitted spectrum is displayed on the spectrum analyzer; in fact, as the LJTJs are not identical, the fluxon oscillations in each LJTJ occur at slightly different frequencies and, hence, in general they emit radiation independently. However, if the number of LJTJs in the array is large, they group together in clusters made of several mutually locked LJTJs. The frequency of the emitted lines can be tuned varying either the dc bias or the external dc magnetic field: doing so we were able

to tune the emitted signal over a rather wide frequency range ( 10% of the fundamental frequency). While for the 8-junction array we succeeded in the aim of grouping all the junctions, we were not able to achieve the same result for the 100-junction array. Improving the LJTTs uniformity would make the operation of the device more reliable; however we could measure often a power larger than 100 nW into a 50  $\Omega$  load at room temperature. Details can be found in ref.(4). In the case of narrowband coupling ( 20-junction array), only the emission in the coherent state could be detected. It appeared as a single line in the microwave spectrum, tunable in a range of 50 MHz at the center frequency of 10.0 GHz, very insensitive to thermal and electromagnetic noise if compared with the radiation emitted by a single LJTT. Both the linewidth of the signal and the long term drift of the signal frequency were better than those of the spectrum analyzer, that is less than 10 kHz and  $\pm 25$  kHz/10 min respectively (without any feedback loop to the dc bias current). Further details of the results so far described can be found in ref.(5).

### CONCLUSIONS

The results we have reported show that arrays of LJTTs operated in the resonant fluxon regime are suitable for local oscillator in superconducting microwave devices such as SIS mixers, parametric amplifiers and voltage standard chips. In fact, in our devices a special microwave circuit allows electromagnetic interaction among all the LJTTs which generates phase locked fluxon oscillations with a consequent increase of the radiated power. However, further experimental work is needed, supported by theoretical and numerical studies, to investigate the interaction mechanisms among the junctions and to design a better microwave coupling circuit.

To conclude, although the amount of power detected is already enough for pumping SIS mixers, the operating frequency of the present devices is of limited practical interest for radioastronomical receivers; we believe that in the future, with a proper design of the devices under study, a reliable operation of the local oscillator can be obtained at frequency up to few hundredths of GHz. In this light, the results shown above represent an important step in the realization of an integrated fully superconducting mm-wave receiver.

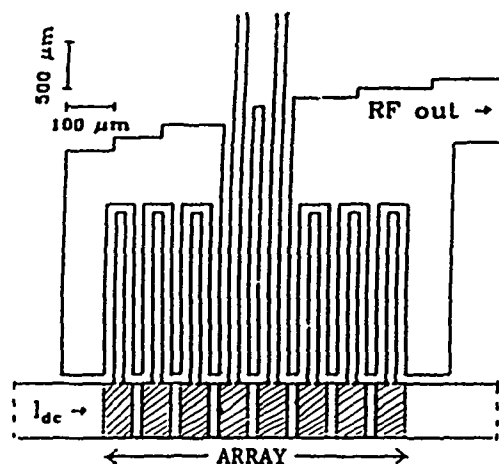


Figure 1  
Sample geometry of the 8-LJTT. The LJTTs are represented by the shaded area.

### REFERENCES

- (1) J.R. Tucker, IEEE J. Quantum Electron (1979), vol.15, pp 1234-1258.
- (2) N.F. Pedersen, in SQUID 80, pp. 739-762. Eds. H.D. Halbohm and H. Lubbig (De Gruiter, Berlin, 1980).
- (3) E. Jorgensen, V.P. Koshelets, R. Monaco, J. Mygind, M.R. Samuelsen and M. Salerno, Phys. Rev. Lett. (1982), vol. 49, pp 1093-1099.
- (4) R. Monaco, S. Pagano and G. Costabile, Phys. Lett. A (1988), vol.131, pp. 122-124
- (5) S. Pagano, R. Monaco and G. Costabile, Proceedings of Appl. Superconducting Conf. (1988). In press.

## BALLOON-BORNE OBSERVATIONS OF THE CYGNUS REGION IN THE FAR INFRARED

C.G. Degiacomi, A. Holenstein, F.K. Kneubühl  
Infrared Physics Laboratory  
ETH (Swiss Federal Institute of Technology)  
CH-8093 Zurich, Switzerland

D. Huguenin  
Geneva Observatory (Geneva University)  
CH-1290 Sauverny, Switzerland

### ABSTRACT

A balloon-borne far-infrared telescope has been designed and built to observe the infrared emission from the Cygnus region in the galactic plane between 120  $\mu\text{m}$  and 300  $\mu\text{m}$  wavelength. The system performance, objects as well as results of the first flight in September 1988 will be discussed.

### INTRODUCTION

Far-infrared and submillimeter-wave astronomy are relatively new branches of astronomical research. This is due to the poor transmission of the terrestrial atmosphere in this spectral range. A restricted number of narrow spectral windows allow the observation of astronomical objects directly from the ground. Reliable observations have therefore to be performed from satellites, stratospheric balloon gondolas or aircraft. Far-infrared astronomy provides important information on gas clouds. It allows the determination of their physical parameters such as temperature, pressure and velocity, as well as of the chemical species and their states of ionization. Radiative cooling of gas clouds may occur by collisional excitation of small molecules, e.g. OH, CO, CH or H<sub>2</sub>O, into higher rotational levels. If high J-levels are excited radiation is emitted in the far infrared. This radiation process dominates hot shocked molecular regions which are related to collapses of cold clouds of a few Kelvin heated to stellar temperatures of a few thousand Kelvin. In these molecular clouds compressed by shocks new stars can form.

Observation of these poorly known collapse processes have become possible in recent years by the application of balloon-borne [1] and airborne [2] instruments. In this context, far-infrared telescopes have been equipped with grating spectrometers or Fabry-Perot interferometers. At stratospheric altitudes the astrophysical instrumentation has the advantage of a highly transparent atmosphere. At the altitudes reached by balloons (30 to 40 km) the atmospheric emissivity and its fluctuations are also considerably lower than at aircraft altitudes (10 to

20 km). The best performance is attained with observations from satellites, e.g. the excellent survey mission performed by the Infrared Astronomical Satellite IRAS [3].

### ASTRONOMICAL OBJECTS

Many regions of molecular gas clouds exist in our galaxy. Some of them show active star formation processes with strong emission of infrared radiation due to shock excited gas. One of the best studied region of star formation is the Orion molecular cloud [4]. In order to obtain further information on formation and evolution of stars the study of other regions of dense interstellar molecular clouds is required.

The survey of the galactic infrared radiation as performed by IRAS [3] shows regions of strong emission at wavelengths between 12  $\mu\text{m}$  and 100  $\mu\text{m}$ , e.g. the Cygnus region in the galactic plane. It is expected that star formation processes also takes place in this region. Fig. 1 reproduces its intensity contourline representation of the 100  $\mu\text{m}$  emission evaluated from the IRAS data in cooperation with the Laboratory for Space Research and the University of Groningen, NL. The IRAS survey was restricted to wavelengths less than 100  $\mu\text{m}$ . The aim of our investigation is to extend this spectral range to longer wavelengths and subsequently to measure detailed spectra of selected objects. First, we intend to fly a balloon-borne infrared telescope to make photometric surveys of the Cygnus region with a 2.5 arcmin spatial resolution at the wavelengths 80  $\mu\text{m}$ , 125  $\mu\text{m}$  and 330  $\mu\text{m}$ . In a second flight we intend to measure spectra of selected objects in the same spectral range with a high-resolution Fabry-Perot interferometer.

### INSTRUMENTATION

We have designed and built a 60 cm far-infrared balloon-borne telescope with attached photometer. A schematic of the complete system is shown in Fig. 2. The Cassegrain-type telescope with a diffraction-limited field of view was previously used for the determination of temperature increases over active regions on the solar disk [5]. For the observation of molecular

clouds in the galactic plane, we have constructed a completely new instrument because of the higher sensitivity required. We have applied a lightweight telescope frame with a honeycomb instrumental platform and a carbon fibre reinforced plastic telescope tube to reduce the weight of the instrument as far as possible without loss of mechanical stiffness. A pointing accuracy of about 20 arcsec for any selected point in the Cygnus region can be attained.

Beside the telescope, our optical system comprises helium-cooled bandpass filters and a cooled detector. Three mesh interference bandpass filters at 80  $\mu\text{m}$ , 125  $\mu\text{m}$  and 330  $\mu\text{m}$  wavelength are used alternatively. As detector we selected a composite silicon bolometer cooled to about 2 K. The detector NEP is  $1.3 \cdot 10^{-14} \text{ W/Hz}^{1/2}$ . It is followed by a cooled preamplifier and a phase sensitive amplifier outside the cryostat. The digitized detector signal together with housekeeping data are transmitted by telemetry to the ground station.

#### FIRST FLIGHT

The first flight of our balloon-borne telescope is planned to take place at the French balloon facility of CNES in September 1988. The gondola weighs slightly below

500 kg, the balloon volume is 380.000  $\text{m}^3$  and the expected observation altitude is 39 km.

#### Acknowledgement:

This study is supported by the Swiss National Science Foundation (SNF), ETH Zurich and Geneva Observatory.

#### REFERENCES:

- [1] Fazio, G.G.:  
Proceedings CIRP 3, eds. Rügsegger, W. and Kneubühl, F.K., 17 (1984)
- [2] Harwit, M.:  
Proceedings CIRP 3, eds. Rügsegger, W. and Kneubühl, F.K., 53 (1984)
- [3] Neugebauer, G., Habing, R.,  
van Duinen, R. et. al.:  
Astrophys. Journal 278, L1 (1984)
- [4] Drapatz, S., Haser, L., Hofmann, R.,  
Oda, N., Iyengar, K.V.K.:  
Astron. Astrophys 128, 207 (1983)
- [5] Degiacomi, C.G., Kneubühl, F.K. and  
Huguenin, D.:  
Astrophys. Journal 298, 918 (1985)

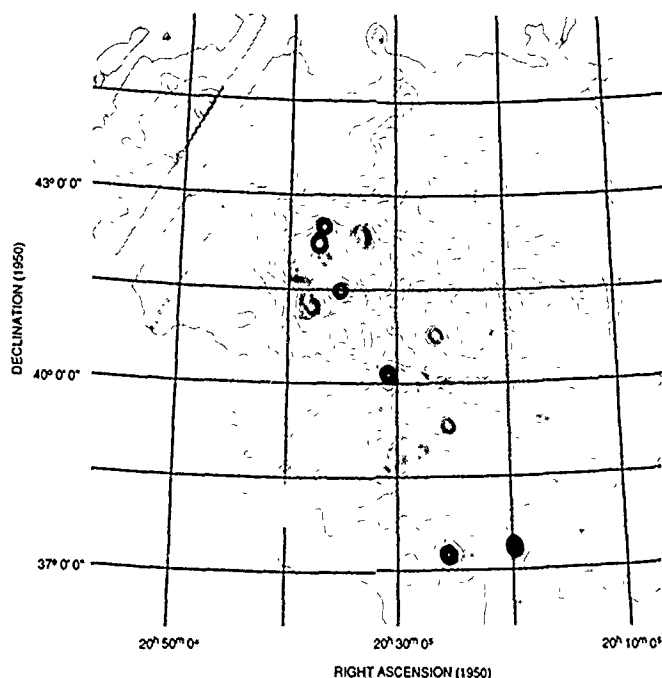


Fig. 1:  
100  $\mu\text{m}$  image of Cygnus region

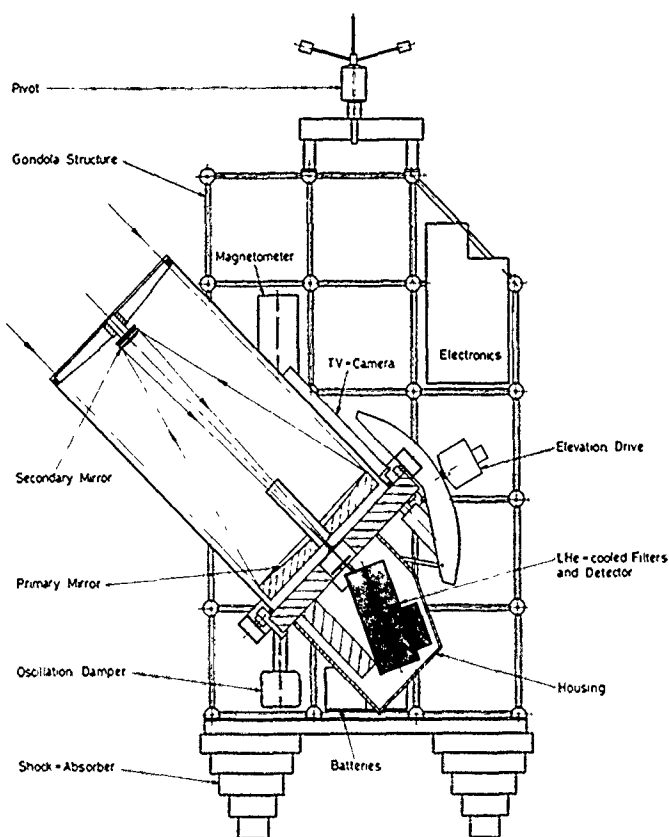


Fig. 2:  
Stratospheric gondola



# 490 GHz SOLID STATE SOURCE WITH VARACTOR QUINTUPLER

RALPH, RÜDIGER AND PETER ZIMMERMANN  
Radiometer-physics  
5309 Meckenheim  
West germany

## ABSTRACT

This report is about a mechanically tunable solid state source with a varactor quintupler in waveguide technique. Its main purpose was to provide output power at 490 GHz for use in a radioastronomy receiver (1). The device has been tested between 470 and 550GHz. Results are presented as increase in rectified current in a dc-biased Schottky-Detector.

## INTRODUCTION

The power requirements of a SIS-heterodyne receiver are  $\sim (h\nu/e)^2/R_N$  which at 490 GHz results in 80 nW with  $R_N=50\Omega$ . However due to circuit and coupling losses in the local oscillator chain typically 3-6 dB more are needed. This can be achieved through a fully solid-state source as now (a) varactor diodes with sufficiently high cut-off frequencies and high breakdown voltages and (b) Gunn oscillators with output power up to 50 mW at 115 GHz are available. Though a tandem-source, for example a tripler-doubler combination with varactor and varistor-diode resp. may be made with a wider tuning range, the one diode with immediate high order multiplication has the advantage of higher reliability. A disadvantage is that it needs reactive terminations at various harmonics (idlers), which makes its manufacturing more difficult. The varactor available, was a 6P2 from the Semiconductor Device Lab, University of Virginia. Its capacitance-voltage dependence is theoretically given by

$$C_j(V) = C_j(0) \left( \frac{\phi}{\phi - V} \right)^{1/2}$$

$C_j(0)$ =capacitance at OV,  $\phi$ =contact potential. The actual device followed this law approx. up to 6V, where the capacitance was a minimum of 6.0 fF. A figure of merit for the multiplier is the dynamic cutoff frequency

$$f_c = \frac{S_{\max} - S_{\min}}{2\pi R_S}$$

$S_{\max}=1/C_{\min}$ ,  $S_{\min}=1/C_{\max}$   
with  $C_{\max}=20$  fF,  $C_{\min}=6.6$  fF and  $R_S=12\Omega$   
this cutoff frequency is 1550GHz. The theory of varactor multipliers as given by Penfield and Rafuse (2) shows the maximum efficiency of a 1-2-4-5 quintupler for an input frequency  $f_0=0.06 f_c$  (in our case  $f_0=98$  GHz) to be about 0.5%. It means that with 50 mW input power, 250  $\mu$ W of output power should be available (ideal case with lossless idler terminations). In practice this cannot be achieved, but allowing 20 dB excessive loss for a worst case, would still result in 2.5  $\mu$ W. In (2) it is also shown that with a

1-2-3-5 Quintupler in the high frequency limit the output power is by a factor of 7 higher than with the 1-2-4-5 Quintupler. To obtain maximum output power the following requirements have to be fulfilled.

- 1.) The input and output circuits should be well matched to the diode.
- 2.) The circuits should completely decoupled
- 3.) The idler frequencies should (a) be tunable, (b) experience no other resistive loss than the unavoidable series resistance of the diode.

## MOUNT DESCRIPTION

The quintupler mount consists of several blocks (see Fig. 1). The central piece, the varactor diode, is soldered to the end of a five-section Tchebycheff filter in coaxial technique and forms part of the first filter section (see Fig. 2). The filter is held isolated in the middle block by a macor bushing. It acts as a low pass for the fundamental and offers high rejection at the idlers and output frequency. Several filters had to build before optimum performance could be achieved, though low frequency modeling was used to verify theoretical design. Input power is coupled through a probe from WR-8 waveguide which was reduced to 1/2 height and terminated by a contacting back-short. The diode surface is flush with the broad-wall of a complex waveguide section in the lower block. This section is beyond cutoff ( $a \times b = 1 \times 0.2$  mm) for the input frequency. Three stub lines in the H-plane allow tuning of the second, third and fourth harmonic. A bottleneck section towards the output (cutoff 430 GHz) allowed propagation from the fifth harmonic upward only. Its length was determined by frequency modeling to achieve low reflection loss. The output waveguide was slightly overmoded to adapt it to the dimensions of a modified potterhorn. The diode was contacted by a whisker of 5  $\mu$ m diameter, mounted on a post of 0.25mm width. The optimum whisker length was 70  $\mu$ m, the post protruded 130  $\mu$ m into the waveguide. DC-connection to the diode was provided through a rejection filter for the fundamental frequency contacting the waveguide probe.

## RESULTS

As there was no adequate power-meter at 490 GHz available, a Schottky-diode detector with circular feedhorn was used. The Schottky-diode has a much less steep DC-characteristic than a SIS-junction, there-

for a rectified current of several  $\mu$ Amps at the diode was regarded as sufficient to drive a SIS-junctions. A circular feedhorn mounted to the multiplier was used to couple its output power to the detector (see fig.3). The mismatch at the feedhorn apertures was used to determine the output frequency by moving the horn and measuring the distances of maxima.

Input power was provided by one gunn oscillator tunable from 94-98 GHz with approx. 50 mW and another gunn oscillator at 110 GHz with 30 mW. The table gives the results as rectified current at the detector after it was biased to 10 A initially. There are no corrections for mismatch between multiplier and detector or loss in the filter.

MULTIPLIER			DETECTOR	
Output frequency GHz	Voltage (V)	current (mA)	current ( A)	
470 (94x5)	6.0	-.45	80	
480 (96x5)	4.8	.00	60	
490 (98x5)	5.6	0.35	50	
440 (110x4)	1.7	1.0	130	
550 (110x5)	1.7	1.0	14	

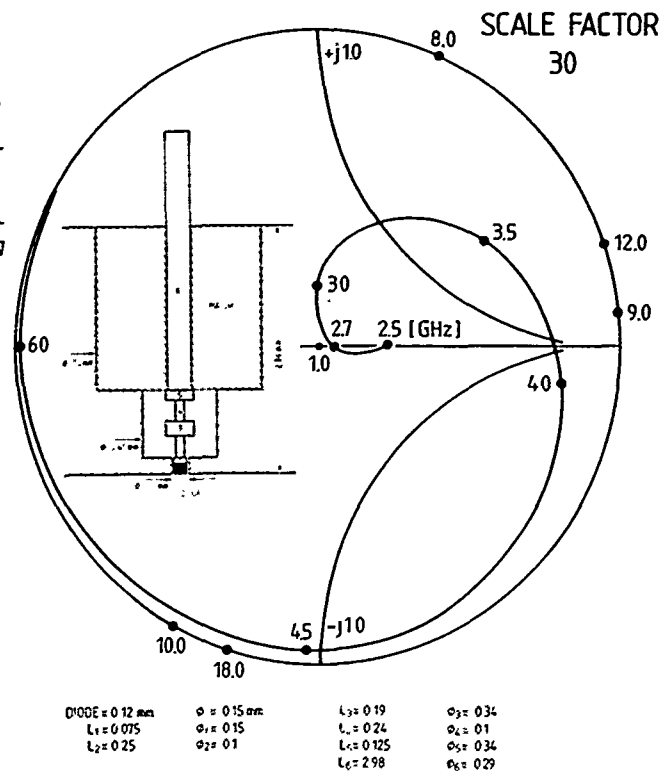


Figure 2

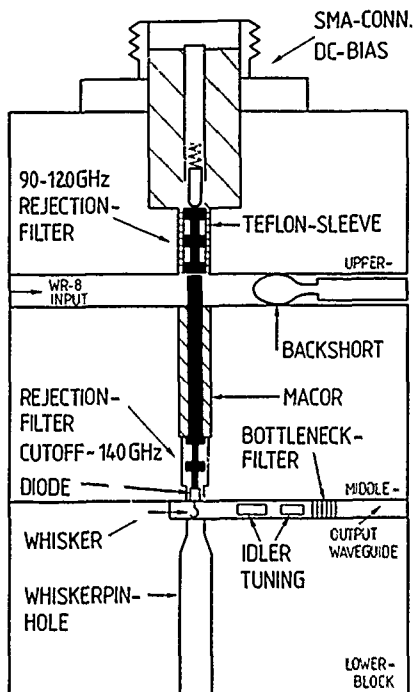


Figure 1



Figure 3

#### REFERENCES

- (1) A broadband Low Noise SIS-Receiver For Submm-Astronomy. - Bütgenbach et al this conference
- (2) Varactor Applications, Penfield and Rafuse MIT-Press 1962

## INDUCTION-LINAC BASED FREE-ELECTRON LASER AMPLIFIERS FOR PLASMA HEATING \*

R.A. Jong

Lawrence Livermore National Laboratory  
University of California, Livermore, California 94550

### ABSTRACT

We describe an induction-linac based free-electron laser amplifier that is presently under construction at the Lawrence Livermore National Laboratory. It is designed to produce up to 2 MW of average power at a frequency of 250 GHz for plasma heating experiments in the Microwave Tokamak Experiment. In addition, we shall describe a FEL amplifier design for plasma heating of advanced tokamak fusion devices. This system is designed to produce average power levels of about 10 MW at frequencies ranging from 280 to 560 GHz.

### INTRODUCTION

Induction-linac driven free-electron laser (IFEL) amplifier experiments in the Electron Laser Facility (ELF) at the Lawrence Livermore National Laboratory (LLNL), have demonstrated high gain and efficiency at microwave frequencies ranging from 34.6 to 140 GHz [1,2]. At 34.6 GHz, exponential gains of 34 dB/m were observed, and overall gains of 43 dB were achieved [1]. Peak power levels of 1 GW were achieved with an overall extraction efficiency of 34%. At 140 GHz, exponential gains of 22 dB/m were demonstrated, along with peak powers exceeding 50 MW and overall gains of 65 dB [2]. These successes have encouraged the development of an IFEL amplifier named the Intense Microwave Prototype (IMP) that will provide high-average-power (about 2 MW) microwaves at 250 GHz for electron cyclotron resonance heating (ECRH) of the plasma in the Microwave Tokamak Experiment (MTX). In addition, we have examined some of the physics and technology issues necessary to extend the IMP design to higher average power levels of up to 10 MW per unit.

We first briefly summarize the physics design of IMP and its expected performance. Next we shall describe the experiment. Then we will discuss the design of an IFEL system for ECRH in advanced tokamak fusion devices such as the Compact Ignition Tokamak or the International Thermonuclear Experimental Reactor. This design will consider two operating frequencies, 280 GHz, suitable for fundamental heating at a 10 T magnetic field, and 560 GHz, suitable for second harmonic heating at 10 T. A summary concludes the report.

### FEL PHYSICS DESIGN AND PERFORMANCE FOR IMP

The design calculations for IMP are detailed in Ref. 3. We used the two-dimensional version of the LLNL free-electron laser simulation code, FRED [4], the simulation code for sideband calculations, GINGER, and the methodology of the wiggler optimization [3] developed for the design of FEL systems, where moderate space-charge effects are important.

Engineering and physics constraints place limits on the waveguide dimensions, the optimum wiggler period, the peak wiggler magnetic flux density, and the maximum electron beam energy that can be used in the FEL system. The engineering constraints are the rf wall loading and the beam linear fill factor (defined as the ratio of the beam linear dimension to the waveguide linear dimension in the same plane). To satisfy these constraints we require a rectangular (or elliptical) waveguide with dimensions 3.5 by 3.0 cm, a wiggler with a 4-cm gap spacing and a 10-cm period, and a maximum peak magnetic field of about 5 kG. With these limits on the wiggler, the physics constraints (i.e. FEL synchronism) set the maximum beam energy at about 11 MeV. Our choice of a 10 MeV beam energy as the operating energy means that we choose to operate with a peak magnetic flux density of about 4.5 kG.

The calculations assumed an electron beam current of 3 kA, a beam energy of 10 MeV, a beam brightness of  $10^8$  A/(m-rad)<sup>2</sup>, and an input laser power of 500 W at 250 GHz. We predict that the peak TE<sub>01</sub> power

will be 12.9 GW (out of a total of 13.2 GW), giving a modal purity of 98% and an energy extraction efficiency of about 44%. The overall gain is about 74 dB with an incremental gain of about 31 dB/m in the exponential gain region. Approximately 70% of the beam particles are trapped in the ponderomotive well.

The FEL performance described above assumes that the FEL parameters are all at their optimum values, with no alignment or wiggler errors, no beam displacements, no energy sweep, and the full rated beam current and input laser power. Such a situation is highly unlikely in the experiment. Calculations were performed to determine the acceptable ranges in the errors when they were applied individually and then when they were combined, i.e., when all the errors are applied simultaneously.

We found that a 10% decrease in the current produces a 20% drop in the output TE<sub>01</sub> power. The dependence of the output TE<sub>01</sub> power on the input laser power is quite weak. Input powers ranging from 200 W to 1 kW are acceptable. The allowed combined error limits for the other listed parameters are  $\pm 1\%$  beam energy sweep, 1 mm beam offset, and 0.1% rms wiggler error. With these combined errors, using a 3 kA beam with 500 W input power, the output TE<sub>01</sub> power decreases from the "no error" value of 12.9 GW to about 11.5 GW. The extraction efficiency drops from 44% to 39%. Variations in beam current of about  $\pm 4\%$  during the pulse may be required to achieve the desired energy regulation. A 4% average sag in the current during a pulse would reduce the output power to about 10 GW (36% extraction efficiency). The beam linear fill factor grows from the no-error value of 50% to about 60% with the combined errors.

### DESCRIPTION OF THE EXPERIMENT

The overall experiment consists of several major segments that are complete experiments in their own right. The Electron Test Accelerator-II (ETA-II) [5] was designed as a high-average-power induction accelerator, expected to produce an electron beam with a current of 3 kA at an energy of up to 10 MeV and a brightness of over  $10^8$  A/(m-rad)<sup>2</sup>. In addition, it was designed to produce 50-ns-wide pulses at a repetition rate (PRF) of 5 kHz for up to 30 s. It is currently being tested at an energy, current, brightness, and PRF of 5.5 MeV, 1 kA,  $6 \times 10^8$  A/(m-rad)<sup>2</sup>, and 1 Hz. In this paper, we assume that the accelerator will successfully provide the 3-kA current at an energy of 10 MeV and a brightness of  $10^8$  A/(m-rad)<sup>2</sup>.

The IMP FEL itself consists of several major subsystems. There is a beam transport system with emittance filter and achromatic jog to transport the beam from the end of the accelerator to the wiggler, a rf coupling and beam matching section to bring the electron beam and input signal together at the entrance to the wiggler, the wiggler itself, and a microwave transport system that transmits the output power to the tokamak. We shall now briefly describe each subsystem.

#### Electron Beam Transport System

The electron beam transport system transports, diagnoses, and conditions the high-average-power electron beam prior to injecting it into the wiggler. It uses a series of solenoid and quadrupole magnets to transport the beam from the exit of the accelerator to the wiggler entrance. Diagnostics are provided in the beamline to measure beam current, energy, position, spatial shape, energy, and brightness. An emittance filter consisting of a series of range-thin graphite apertures in the beamline is used to scatter any low-density halo electrons to the wall over a distributed

\* Work performed under the auspices of the US Department of Energy by the Lawrence Livermore National Laboratory under W-7405-ENG-48

area. At the exit of the wiggler, an Enge magnet is used to magnetically "reimage" the beam from the FEL into a simple graphite beam absorber.

### RF Coupling and Beam Matching Section

Two pairs of quadrupole doublets located immediately in front of the wiggler form the beam matching section, which properly focuses the electron beam into the wiggler to minimize any betatron motion that would otherwise degrade the FEL performance.

The rf coupling section, located near the beam matching section, injects the input microwave signal collinearly with the electron beam. For operation at high average power, a method of coupling the input microwave signal that does not intercept the electron beam is required. The baseline design uses an achromatic jog to offset the axis of the accelerator from that of the wiggler, thereby allowing the microwave signal to be injected straight through the beam matching section into the wiggler. An alternative method that does not require an achromatic jog is desired to minimize costs, and several methods are being studied. In general, these methods involve an apertured reflector that is located within the beamline and injects the microwave signal into the waveguide at an oblique angle.

### Wiggler Design

The wiggler being designed for IMP will have a 3.8-m long high-field section tunable from 4.7 to approximately 2.5 kG, and a second, lower field section tunable from approximately 3.5 to 0.5 kG. It will have a 10-cm period and a gap of about 3.7 cm. In addition, to meet the random wiggler error tolerances determined in the simulations, the pole-to-pole random errors ( $\Delta B/B$ ) must be less than 0.1% rms. We are designing a permanent-magnet laced electromagnetic wiggler for this application [6].

In the laced wiggler concept, permanent magnets are employed to suppress magnetic saturation in the poles of a dc iron-core electromagnetic wiggler; the laced geometry features permanent magnet blocks located between poles (just as in a permanent-magnet hybrid wiggler) actually interspersed in the coils. This configuration allows a higher maximum field to be attained, although the tuning range (within which the random field errors are acceptably small) is somewhat reduced.

### Microwave Transport System

A quasi-optical microwave transmission system has been designed to transport the high power microwave radiation generated within the FEL from the wiggler to the tokamak, a distance of over 30 m. The system uses four copper mirrors, each about 17 by 23 in. in diameter, and whose surface is an elliptic paraboloid. The system has been designed to preserve horizontal polarization, to keep the microwave power density well below mirror surface-heating damage thresholds, and to maintain acceptable transmission losses. Microwave transport codes predict that the total transmission loss from the wiggler through the 4- by 30-cm MTX port is less than 8%, with only half of that occurring after the first mirror. The dominant losses at the first optic arise from loss of power in the side lobes in the far-field radiation pattern of the waveguide aperture. The transmission system is windowless, with the vacuum maintained by two turbopumps and the differential pumping between the FEL and tokamak systems that occurs naturally because of the long vacuum path.

## IFEL DESIGN FOR CIT AND ITER APPLICATIONS

While wall loading was not a problem with the 2-MW average power and the short pulse length of 0.5 s in IMP, the higher average power levels and longer pulse lengths (5 to 10 s) required for the 10-MW designs would make the expected life of a smooth-walled copper waveguide much too short to be considered practical. By considering the low dissipation of the  $HE_{11}$  mode and propagation in a circular, corrugated waveguide, we calculate a temperature rise that is lower by two orders of magnitude (compared to the smooth-walled case), and consequently, the fatigue life of the waveguide is no longer an issue. However, the beam linear fill factor in the waveguide is still important and it determines the required waveguide size and the wiggler gap spacing. We require waveguides with an inner diameter of about 3.5 cm and thus need wiggler parameters that are identical to those of IMP, namely a 4 cm gap, a 10 cm wiggler period, and a limit of 5 kG on the flux density. Moreover, FEL synchronism considerations again put an upper limit on the usable electron beam energy of about 11.5 MeV at 280 GHz and 16 MeV at 560 GHz.

The FEL optimization and error considerations are similar to those for the IMP design. We again have a 3 kA beam with a brightness of  $10^8$  A/(m-rad)<sup>2</sup>. The master oscillator input power to the wiggler is 500 W. A summary of typical parameters is given in Table 1.

To examine the physics and technology advances needed to produce an economical IFEL system for heating CIT or ITER, we have undertaken a systems study [7] to examine the effects of higher magnetic fields and beam energies, changes in the PRF and pulse width, advances in the pulse power drivers, and improvements in ferrite material and cooling. The studies show that costs can be decreased if we do not have to multiplex two pulse power chains in each cell. The most efficient method of obtaining increased peak power in the FEL is to increase the initial electron beam energy. This increase will cause the accelerator costs to go up; however, if the gain increases sufficiently, only one pulsed power chain per cell is required and the costs would decrease. The cost and risk factors are folded into our design strategy to produce a system with minimum cost and reduced risks. For the basic configuration for the 280-GHz, 10-MW FEL, the accelerator has four pulse power chains, no multiplexing, a pulse width of 70 ns, and a PRF of 10 kHz.

## SUMMARY

We have described the IMP FEL presently being built at LLNL for plasma heating experiments in MTX. We expect to produce 2 MW of average power at 250 GHz for periods up to 0.5 s using a 3-kA beam at an energy of 10 MeV and a brightness of  $10^8$  A/(m-rad)<sup>2</sup>. Even with realistic limits on the electron beam offset, beam energy sweep, and random wiggler errors, the calculations indicate that the desired power levels can be achieved.

We have also shown that IFEL technology can be used for plasma heating in an advanced tokamak fusion device, providing average power levels in the 10-MW range at frequencies of 280 and 560 GHz with basically the same machine. The design uses a corrugated waveguide to propagate the  $HE_{11}$  mode and appears to alleviate possible microwave loading problems on the waveguide walls. At 280 GHz, we have chosen as our baseline a 10-kHz design that minimizes the total system costs, since only one pulsed power chain is required per cell. We achieve the required duty factor by using a 70-ns pulse width and by increasing the electron beam energy to 13 MeV, thereby improving the extraction efficiency. We must use vanadium-permendur as the wiggler pole material to achieve the higher magnetic fields required at this higher beam energy.

## REFERENCES

- [1] T.J. Orzechowski, et al., *Phys. Rev. Lett.* **57**, 2172 (1986).
- [2] A.L. Throop, et al., Lawrence Livermore National Laboratory, Livermore, Calif., UCRL-95670, June 1987.
- [3] R.A. Jong, A.L. Throop, and E.T. Scharlemann, Lawrence Livermore National Laboratory, Livermore, Calif., UCRL-98214, April, 1988.
- [4] E.T. Scharlemann, et al., *Nucl. Instr. Methods* **A250**, 150 (1986).
- [5] D.S. Prono, et al., Lawrence Livermore National Laboratory, Livermore, Calif., UCRL-97850, July 1988.
- [6] T.C. Christensen, et al., *IEEE Trans. Mag.* **24**, 1094 (1988).
- [7] R.A. Jong and R.R. Stone, Lawrence Livermore National Laboratory, Livermore, Calif., UCRL-98675, August 1988.

Table 1.

CIT/ITER FEL design summary. Values in parentheses show performance with combined standard errors.

Parameter	560 GHz	280 GHz
Beam energy (MeV)	14	10
Wiggler length (m)	4.0	3.0
Constant magnetic field (kG)	4.0	4.1
Minimum magnetic field (kG)	1.6	1.4
$HE_{11}$ output power (GW)	15 (13)	12 (10)
Extraction efficiency (%)	37 (32)	43 (34)
Trapping efficiency (%)	69 (55)	74 (55)
Linear beam fill factor (%)	50 (60)	50 (60)

## CURRENT THEORETICAL AND EXPERIMENTAL ISSUES ON FREE-ELECTRON LASERS

*F. Hartemann, J.M. Buzzi, G. Mourier and G. Faillon*

Thomson-CSF/DTE, 78140 Vélizy-Villacoublay, FRANCE

### ABSTRACT

*After a brief review of the basic free-electron laser (FEL) physics, we will discuss the following topics : efficiency optimization of a millimeter-wave FEL, optical guiding experiments in a microwave FEL and pulse shaping and compression in a FEL amplifier.*

### EFFICIENCY OPTIMIZATION

It has now long been recognized that the efficiency of FELs depends critically on the quality of the electron beam (axial energy spread  $\Delta\gamma_{\parallel}/\gamma_{\parallel}$ ) and the stability of the electron trajectories in the wiggler field. This last requirement implies that the electrons must be launched adiabatically into the wiggler interaction region and that the beam radius  $r_b$  should be kept small ( $k_w r_b \ll 1$ ). For a constant current density  $j$ , decreasing the beam radius also results in a reduction of the beam current  $i_b = j\pi r_b^2$  and of the space-charge potential drop across the electron beam  $\Delta V \simeq i_b/4\pi\epsilon_0\beta c$ , thus improving the beam quality by reducing the space-charge contribution to the axial energy spread. In addition, in reducing the beam radius, we scrape off the "hot" outer electrons, thus decreasing the thermal contribution to  $\Delta\gamma_{\parallel}/\gamma_{\parallel}$ .

It is equally important to note that FEL operation in the collective regime is characterized by the large separation of the fast and slow space-charge waves supported by the modulated electron beam (as opposed to their degenerate state in the single-particle, Compton, regime). This implies that the electron beam must be intense and cold (the axial velocity spread must be small compared to the phase velocity difference between the fast and slow space-charge waves). As a result, the FEL interaction can be described, in the Raman regime, by a two-wave coupling process, yielding larger gains and higher efficiencies than in the single-particle regime (three-wave coupling).

Based on these simple considerations, we have performed a FEL experiment to demonstrate high-gain, high-efficiency operation of a millimeter-wave FEL in the Raman regime, and to study the saturated efficiency as a function of the beam current and radius. We have operated our millimeter-wave FEL with a number of beam radii and currents, while keeping all other parameters constant : beam

energy 700 keV, axial guide magnetic field  $B_{\parallel} = 9.6$  kG, wiggler amplitude  $B_w = 300$  G, wiggler periodicity  $\ell_w = 20$  mm and output frequency  $\omega^+ / 2\pi \simeq 120$  GHz. The results, shown in Fig. 1, clearly indicate that the saturated efficiency increases with decreasing beam radius and current, as expected from the considerations discussed above. A peak efficiency of about 18 % is obtained for  $r_b = 1$  mm and  $i_b = 30$  A. At radii above the optimum, the electron beam axial energy spread increases, while the quality of the electron trajectories in the wiggler field degrades, yielding lower efficiencies. At lower beam radii, for optically guided modes, the beam diameter becomes smaller than the radiation wavelength ( $2r_b < \lambda$ ) and diffraction can no longer be balanced by refractive guiding.

### OPTICAL GUIDING

One of the remarkable properties of the FEL, apart from its wavelength tunability and high efficiency, is the large phase shift which the resonant interaction induces in the amplified electromagnetic wave. Under proper circumstances, this phase shift can have a sign such that the electromagnetic wave is refracted towards the axis of the electron beam, in a manner somewhat akin to the guiding properties of an optical fiber, and which is now referred to as "refractive guiding" (as opposed to the so-called "gain guiding", which is actually an artifact, where photon depletion due to diffraction is compensated by the large FEL gain inside the electron beam). Refractive optical guiding can balance the effects of diffraction and thereby allow the length of FEL wigglers to exceed the Rayleigh range. Modification of the transverse intensity profile of a single electromagnetic waveguide mode during the FEL interaction has been measured<sup>[1]</sup> (see Fig. 2). This effect is the waveguide analog to free-space optical guiding. The studies were carried out at microwave frequencies (8–12 GHz) in a FEL using a mildly relativistic electron beam of  $\simeq 200$  keV energy and  $\simeq 1.0$  A current. The probing of the RF fields was accomplished by small electric dipole antennas inserted in the interaction region. On Fig. 3, the observed intensity profile modifications are seen to follow the measured FEL-induced phase shifts (wave refracting index), thus clearly demonstrating refractive optical guiding in a FEL.

## PULSE COMPRESSION

The generation of short pulses of coherent electromagnetic radiation is a subject of considerable interest. Such pulses are needed in many diverse areas of physics, such as nonlinear spectroscopy, studies of transient phenomena, surface physics, accelerator physics and optical communications. In addition, the generation of short pulses in an active medium can lead to extremely high instantaneous powers. At high power levels, nonlinear effects such as self-focusing (optical guiding), saturation and sideband instabilities are observed in FEL generators. These properties of FELs make them particularly attractive for the generation of short pulses of coherent electromagnetic radiation.

The pulse compression scheme studied here is the following. A frequency-chirped pulse is injected into the FEL interaction region. Because of the high gain and narrow bandwidth of the FEL interaction, only the resonant frequency band of the pulse is actively amplified. This results in a high-power short pulse of coherent electromagnetic radiation at the output of the laser. For our experimental parameters<sup>[2]</sup> (beam voltage  $V \approx 150$  kV, wiggler periodicity  $\ell_w = 3.5$  cm, gain  $\sim 10$  dB), pulses of a few nanoseconds at a frequency of 10 GHz ( $\Delta\omega/\omega \sim 1\%$ ) were obtained after an interaction length of 2.3 m (see Fig. 4), in good agreement with theoretical expectations<sup>[2]</sup>. For the same input pulses (width  $\Delta t > 100$  ns, frequency chirp  $\alpha/2\pi \sim 5$  MHz/ns), such compression ratios would require hundreds of meters of conventional passive dispersive medium (waveguide, for example), with prohibitively high attenuation.

Finally, it is interesting to note the possibility of self-phase modulation in the FEL at high electromagnetic intensities, via nonlinear effects, yielding chirped pulses that can subsequently compress as they propagate further into the interaction region and eventually reach a soliton-like equilibrium.

## REFERENCES

- [1] F. Hartemann, K. Xu, G. Bekefi, J.S. Wurtele and J. Fa-jans, Phys. Rev. Lett. 59, 1177 (1987).
- [2] F. Hartemann, K. Xu and G. Bekefi, IEEE J. Q. El. QE24, 105 (1988).

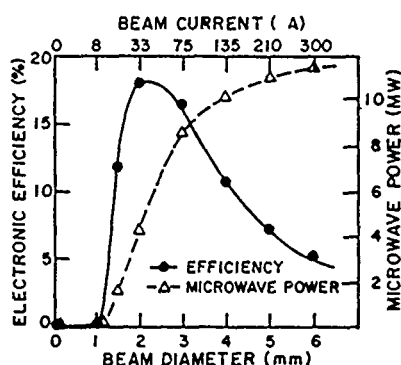


Fig. 1 Microwave power and saturated efficiencies as functions of the beam radius and current.

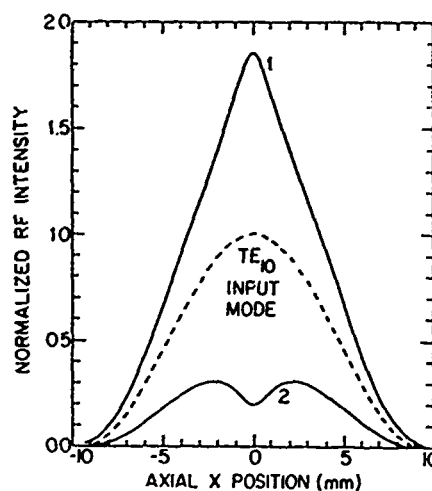


Fig. 2 Wave profile modification induced by the FEL interaction (1) guiding, (2) anti-guiding.

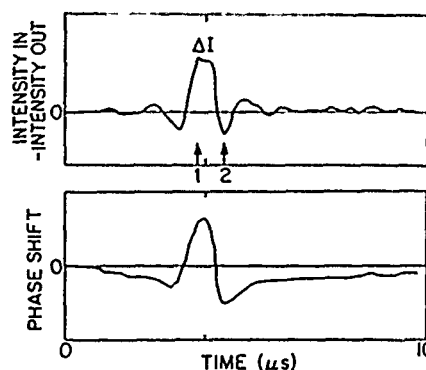


Fig. 3 RF field modification and FEL-induced phase shift as functions of detuning.

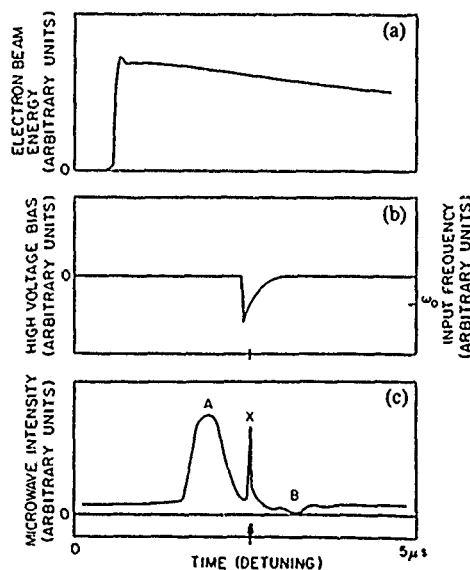


Fig. 4 (a) Time history of the diode voltage (b) Instantaneous frequency of the input chirped pulse (c) Microwave intensity at the FEL output.

## MODE COMPETITION, SUPPRESSION AND CONTROL IN FEL OSCILLATORS\*

Baruch Levush and Thomas M. Antonsen, Jr.  
Laboratory for Plasma Research  
University of Maryland  
College Park, Maryland 20742

## ABSTRACT

The effect of multimode interaction on the efficiency of a low gain FEL oscillator fed by a continuous beam is investigated. Calculations that enable one to design a device in such a way that it will operate at a single frequency with maximum efficiency will be presented.

The model we consider is the one dimensional, low gain oscillator. In a low gain oscillator the frequency and wave number must correspond approximately to a cavity mode. These are determined by quantizing the axial wave number  $k_n = k_0 + n\pi/L$  and  $\omega_n = \omega_0 + n\pi v/L$  where  $n = 0, \pm 1, \pm 2$  labels the mode,  $\omega_0$  and  $k_0$  are the frequency and wave number of some arbitrarily chosen reference mode, and  $v$  is the axial group velocity of the radiation,  $L$  is the interaction length (the same as cavity length). We assumed that the spacing in frequency between adjacent modes is independent of mode number in the range of interest. Thus, for a given injection velocity,  $v_{inj}$ , each mode has its own detuning parameter  $p_n = p_{inj,0} - \epsilon n\pi$ , where  $\epsilon = (v/v_{inj} - 1)$  is the slippage parameter and  $p_{inj,0} = [(k_w + k_0)v_{inj} - \omega_0]/(L/v_{inj})$  is the detuning for  $n=0$  mode, with  $k_w$  the wiggler wave number. The number of modes which will compete for the beam's energy can be estimated by determining the number of modes with detunings under the positive portion of the gain function,  $N \sim \epsilon^{-1}$ . Due to low gain, the radiation field in the resonator can be expressed as a superposition of empty cavity modes whose amplitudes and phases change slowly in time (compared with the transit time of the electrons through the interaction region) due to their interaction with the beam. The field at any point will be nearly periodic in time with a period equal to the round trip travel time of radiation in the cavity, which we assume to be much smaller than the time scale over which the amplitudes change. We may then numerically integrate the following set of equations

$$\frac{d\psi}{d\xi} = p, \quad (1)$$

$$\frac{dp}{d\xi} = \text{Im} \left[ \sum_n a_n e^{i(\psi - n\pi(\epsilon\xi + t_0))} \right], \quad (2)$$

where  $\xi = z/L$ ,  $\psi = (k_w + k_0)z - \omega_0 t$  is the particle's phase in the beat wave potential,  $p$  is proportional to energy deviation defined in the same way as the detuning such that  $p(\xi=0) = p_{inj,0}$ . The quantity  $a_n$  is the complex amplitude of the  $n$ th mode ( $a_n = \omega_n(L/v_{inj})^2$ , where  $\omega_n$  is the synchrotron frequency for a particle at the bottom of the ponderomotive potential well) and it depends on a slow time variable  $\tau_s$  normalized to

the decay time of radiation in the empty cavity.

The evolution of  $a_n$  is described by the equation

$$\left( \frac{d}{d\tau_s} + \frac{1}{2} \right) a_n(\tau_s) = -\frac{i\hat{I}}{4v} \left[ \int_0^2 \frac{dt_0}{2} \right. \\ \left. \int_0^1 d\xi e^{-i[\psi - n\pi(\xi + t_0)]} \right] + S_n(\tau_s) \quad (3)$$

where  $\hat{I}$  is a normalized current,  $2v$  is the fraction of radiation power extracted per pass. The integration is performed for an ensemble of particles with initial phase  $\psi$  and entrance time,  $t_0$ , uniformly distributed over the intervals  $[0, 2\pi]$  and  $[0, 2]$ , respectively. We normalized  $t_0$  such that the radiation travels the length of the resonator in one unit of time. The angular average is over initial entrance phases of the particles. We assumed that all cavity modes have the same damping rate which in normalized units is  $1/2$ . To account for noise a source term,  $S_n$ , proportional to  $N_*^{-1/2} |1 - \cos p_n|^{1/2}$  is added to the mode equation, where  $N_*$  is the number of particles which pass through the system during a cavity decay time.

Single mode theory is obtained from this model by including only the  $n=0$  mode. One then obtains from Eqs. (1)-(2) the average energy extraction  $\Delta p = p_{inj,0} - \langle p(\xi=1) \rangle$  and from the Eq. (3) the value of the current needed to maintain the mode in steady state. This information is displayed in Fig. 1 where level curves of energy extraction and current are plotted in the  $a_0, p_{inj}$  plane. In the plot, current is normalized to minimum value required to start the oscillations in the cavity,  $\chi = 1/I_{start}$ , where  $I_{start} = 29 v$ . Also shown in Fig. 1 is a triangular-shaped region inside of which the single frequency equilibria are stable with respect to the growth of sidebands. Examining Fig. 1 we learn that the single mode equilibrium with maximum efficiency occurring for  $p_{inj} = 5.14$  and  $a_0 = 18$  is not stable. The maximum efficiency stable single mode equilibria is achieved with  $p_{inj} = 5$ ,  $a_0 = 15.2$ , and  $\chi = 3$ . However, if  $\epsilon$  is small, at this current there are many different stable single mode equilibria corresponding to the different detunings of many possible cavity modes, while only one mode corresponding to a detuning  $p_{inj} = 5$  will give the maximum efficiency. Therefore, the question arises as to which single mode equilibrium state the system will evolve.

To answer this question we solved the Eqs. (1)-(3) numerically. For our simulations we chose  $\epsilon = 0.2$ ,  $\chi = 3$ , the number of modes is 21 and  $N_* = 10$ . First, we show the results of a calculation with  $p_{inj,0}$  constant, ( $p_{inj,0} = 2.606$ ), which corresponds to a very sharp rise of the voltage in time after which it remains flat. The time history of the efficiency  $\Delta p$ , the amplitudes of the central mode  $|a_0|$  and neighboring sidebands  $|a_1|$  and  $|a_{-1}|$  are plotted in Fig. 2. The

important result of this calculation is apparent by examining Fig. 2; the dominant mode is the mode with the maximum linear growth rate, while it has a saturated value of  $\Delta p$  which is not the maximum efficiency. Thus, we are to search for ways by which we can control the final state at saturation. We could raise the cavity Q for the desired mode, and not for the others<sup>4</sup> or we could apply mode locking technique either by direct injection<sup>4</sup> or by prebunching of the beam. The solution that we consider here is programming of the rise time of the voltage pulse. To simulate the effect of the time dependence of the voltage pulse in our model we allow for  $p_{inj,0}$  to become a function of slow time,  $\tau_s$ . Only the last few percent of the voltage rise corresponding to values of  $p_{inj}$  of order  $\pi$  will affect the final mode. We choose a model  $p_{inj,0}(\tau_s)$  with the asymptotic behavior being  $p_{inj,0} \sim p_f - t_*/\tau_s$ , where  $t_*$  characterizes how slowly  $p_{inj,0}$  approaches the final value,  $p_f$ .

In Fig. 3a we display the trajectory in the  $p_{inj}$  vs  $a_0$  plane of the dominant mode obtained from a simulation for different values of  $t_*$ . Also shown is the "instant turn on" case where  $p_{inj,0}(\tau_s) = 2.606$ . The final states are different because different modes with different detunings have become dominant depending on the time history of the voltage rise. If the rate of approach to the final voltage is too slow, Fig. 3b, the dominant mode is carried to values of  $p_{inj}$  outside the triangle of stable operation. Then a lower frequency satellite of this mode becomes unstable and grows, eventually becoming the dominant mode. The final state is just inside the stability region with quite high efficiency,  $\Delta p = 5.0$  compared with the maximum for  $\chi = 3$  of  $\Delta p = 5.4$ .

In conclusion, we have demonstrated that two rules should be applied to design a CW, low gain FEL oscillator operating at single frequency at the maximum efficiency. First, the electron beam current should be roughly three times the minimum start-oscillation current. Second, the last few percent of the voltage pulse should approach the designed value sufficiently slowly in time.

#### REFERENCES

1. Ya. L. Bogomolov, V. L. Bratman, N. S. Ginzburg, M. I. Petelin, and A. D. Yanakovskiy, Opt. Comm. **36**, 109 (1981).
2. P. Sprangle, C. M. Tang, and I. Bernstein, Phys. Rev. Lett. **50**, 1775 (1983).
3. T. M. Antonsen and B. Levush, submitted to Phys. Fluids; T. M. Antonsen and B. Levush, submitted to Phys. Rev. Lett.
4. R. J. Harvey and F. A. Dolezal, Appl. Phys. Lett., September 1988.

\*This work was supported by NRL and DOE.

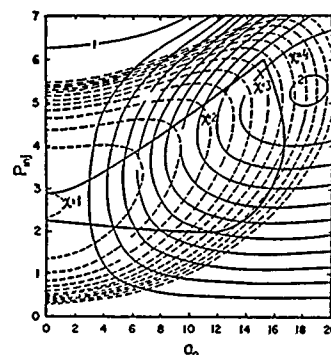


Fig. 1. Solid lines are the equal energy extraction ( $\Delta p$ ) curves in the  $p_{inj}, a_0$  plane. The curve labeled 1 corresponds to  $\Delta p = 0$ , the curve labeled 2 corresponds to  $\Delta p = 5.5$ . The difference between the neighboring level curves is 0.5. The dashed lines are the level curves of  $(I/v)$  which is obtained from the energy balance at a particular value of  $a_0$  and  $p_{inj}$ . The numbers on the curve indicate the values of  $\chi$ . Only inside of the triangular-shaped region single mode operation is possible.

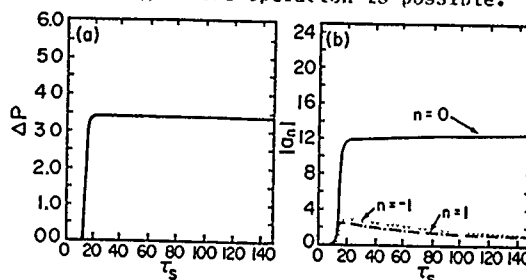


Fig. 2. The time history of (a)  $\Delta p$ ; (b) the amplitude magnitude of  $|a_0|$ ,  $|a_{\pm 1}|$ .

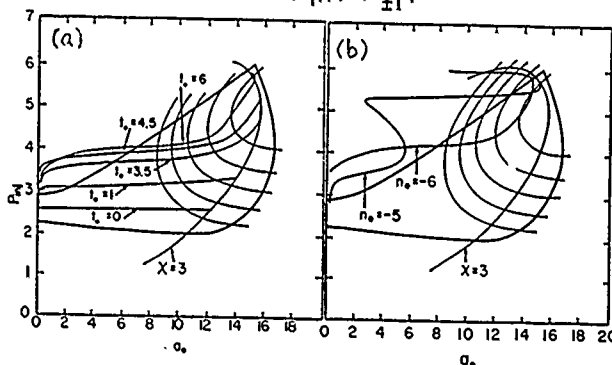


Fig. 3. The trajectories of the amplitude value of the dominant mode in the  $p_{inj}, a_0$  plane together with the stability region, the efficiency level curves and the equilibrium states curve corresponding to  $\chi = 3$  are shown. The voltage tapering parameter  $t_*$  has values (a) 0, 1, 3.5, 4.5 and 6; (b) 7.



# HIGHER HARMONIC EMISSION IN THE UNIFORM MAGNETIC FIELD FREE-ELECTRON LASER

Josip Šoln

Harry Diamond Laboratories, Adelphi, MD 20783-1197

## ABSTRACT

With the help of the unitary  $S$  matrix in the linear recoil approximation, the study of the spontaneous and the stimulated emission and absorption of higher harmonics in the uniform magnetic field free-electron laser is being pursued. The stimulated emission of single-mode photons, being due to just one harmonic, can be tuned to cover a rather limited frequency range, particularly the far-infrared/microwave spectral region. The spontaneous emission, because it is due to all the harmonics, covers a wide spectral region; consequently, at least in principle, it should be able to stimulate at least some higher harmonic radiation. Here, for theoretical and practical reasons, we limit our study largely to harmonics whose emission (absorption) occurs at angles that are "slightly" different from zero with respect to the uniform magnetic field.

## INTRODUCTION

One of the more interesting wiggler-free free-electron lasers (FEL's) is the uniform magnetic field FEL whose on-axis radiation (where the axis direction coincides with the direction of the magnetic field) has essentially Doppler-shifted cyclotron frequencies [1,2]. Stimulated and (to some extent) spontaneous on-axis emission for this FEL has been studied both classically [1] and with the quantum multiphoton formalism [2]. However, as is the case with the usual FEL with a helical wiggler magnetic field, the uniform magnetic field FEL has no on-axis higher harmonic emission. Nevertheless, the

multiphoton formalism predicted that the on-axis gain is easily 20 percent for plane-wave-like 100-GHz radiation with an interaction length ( $L$ ) of 75 cm, magnetic field ( $B$ ) of 0.75 T, total beam energy ( $E$ ) of 1.2 MeV, and beam density of  $10^8 \text{ cm}^{-3}$  [2]. In this example, the gain turned out to be numerically so good mainly because within the multiphoton formalism the gain expression is in the familiar Colson's form [3]; i.e., it scales as  $L^3$ . This should be compared with the classically derived gain [1] which scales only as  $L^2$ ; now a numerical prediction for the gain cannot be expected to be as favorable as when calculated within the multiphoton formalism.

Now, a device is considered to be an FEL if the radiation is Doppler shifted [4]. Consequently, in the uniform magnetic field FEL,  $v_3$ , which enters into the expression of Doppler-shifted relativistic cyclotron frequencies, should be much larger than  $v_\perp$  [2,5]; reasonably, one would expect  $v_\perp$  to be 20 percent or less of  $v_3$ . Here, the parallel and perpendicular components of the electron velocity with respect to the uniform magnetic field are denoted by  $v_3$  and  $v_\perp$ , respectively. (A device which also uses the magnetic field and in which the electron velocity satisfies  $v_\perp \gg v_3$  is the well-known electron cyclotron maser or gyrotron [6]. This device is not considered to be an FEL since it does not have a Doppler shift [1,4].) Because of the requirement that  $v_3$  be large, the emission into higher harmonics, occurring only off-axis, should actually be observed (with reasonably Doppler-shifted frequencies) at angles "slightly" different from zero. In other words, from the

practical point of view, interesting higher harmonic radiation should essentially occur in the forward direction.

### HIGHER HARMONICS

The expression for the electron current density that is needed to calculate the average number of spontaneously emitted photons in the uniform magnetic field FEL is essentially given elsewhere [2]. From the Fourier transformed electron current density [2], one can already deduce that the resonance radiation angular frequencies are of the form

$$\omega_e = l \bar{\omega},$$

where  $l = 1$  corresponds to the fundamental frequency, while  $l \geq 2$  corresponds to the higher harmonic frequencies, which, however, occur only in an off-axis emission. The fundamental angular frequency  $\bar{\omega}$  is the Doppler-shifted angular cyclotron frequency; its dependence on the angle at which the radiation occurs is already given in the references [2,5].

Now, making the usual assumption that  $L$  is much larger than any of the radiation wavelengths [2], the total average number of spontaneously emitted or absorbed photons is obtained in the usual way [2]. From here we define the partial: i.e., for a particular harmonic, the average number of spontaneously emitted or absorbed photons; this in turn defines the partial spontaneously radiated or absorbed energy per unit solid angle. Unfortunately, this energy expression is rather complicated as it involves the products of Bessel functions. However, for higher  $l$ , the "approximation by tangents" [7] for the Bessel functions may be used, which in turn should make it easier to estimate an infinite sum when evaluating the total spontaneously radiated or absorbed energy per unit solid angle.

Preliminary investigations seem to indicate that for at least a first few harmonics the

spontaneous emission can occur at rather small angles for sufficiently energetic beams. This means that, from the practical point of view, the radiation kinematics here and for the on-axis radiation are very much alike. With this in mind, we deduce that for the case of far-infrared radiation associated with first few harmonics, we would need a beam energy of up to 10 MeV,  $B \leq 4T$ ,  $L \leq 100$  cm, and as already mentioned,  $v_{\perp} \leq 0.2$ . In any case, it appears that, at least in principle, not only on-axis but also off-axis (higher harmonic) generated radiation could be used to stimulate emission from electrons further along for sufficiently wide electron beams.

### REFERENCES

- (1) S. K. Ride and W. B. Colson, *Appl. Phys.* 20, 47 (1979).
- (2) J. Šoln, *J. Appl. Phys.* 58, 3374 (1985).
- (3) W. B. Colson, *Physics of Quantum Electronics* (Addison-Wesley, Reading, MA 1978), Vol. 5, p. 157.
- (4) T. C. Marshall, *Free-Electron Lasers* (Macmillan, New York, 1984), p. 117.
- (5) J. Šoln, *Int. J. Infrared Mm Waves*, 7, 111 (1986).
- (6) J. L. Hirshfield, *Gyrotrons*, in *Infrared and Millimeter Waves*, edited by K. J. Button (Academic, New York, 1979).
- (7) I. S. Gradshteyn and I. M. Ryzhik, *Table of Integrals, Series, and Products* (Academic Press, New York, 1965), p. 963.

# A HIGH POWER, 600 $\mu\text{m}$ WAVELENGTH FREE ELECTRON LASER\*

D.A. Kirkpatrick<sup>†</sup>, G. Bekefi and A.C. DiRienzo  
Department of Physics and Research Laboratory of Electronics  
Massachusetts Institute of Technology  
Cambridge, Massachusetts 02139

and

H.P. Freund<sup>†</sup> and A.K. Ganguly  
Naval Research Laboratory  
Washington, DC 20375-5000

## ABSTRACT

We report high power emission (18 MW) at a wavelength of  $\lambda = 640 \mu\text{m}$  and a bandwidth  $\Delta\lambda/\lambda < 0.04$  from a superradiant free electron laser (FEL) excited by a 2 MeV, 1 kA electron beam. Comparison of the experiment with a nonlinear simulation yields good agreement. Theoretical extrapolation to a tapered wiggler experiment shows that power levels of  $\sim 140 \text{ MW}$  could be achieved with an efficiency of  $\sim 7\%$ .

## EXPERIMENT

The outstanding capabilities of free electron lasers (FEL) are their high power outputs, reasonable efficiencies and wavelength tunability. In this paper we present what we believe is the highest power output (18 MW) and highest efficiency ( $\sim 1\%$ ) in a wavelength regime<sup>1-3</sup> ( $\sim 600 \mu\text{m}$ ) that has not been studied extensively.

The experimental arrangement is shown in Fig. 1. The Pulserad 110A accelerator ( $V = 2 \text{ MV}$ ,  $\tau \approx 30 \text{ ns}$ ) energizes a multielectrode field emission electron gun<sup>4</sup> which produces a high current, low emittance electron beam ( $I \sim 900 \text{ A}$ ,  $\Delta V/V < 0.005$ ). A thin solenoid lens focusses the electron beam into a 0.79 cm radius stainless steel evacuated drift tube which also acts as an overmoded circular waveguide for the radiation. A bifilar helical wiggler magnet (with periodicity  $\lambda_w = 3.14 \text{ cm}$ ) is wound onto the outside of the stainless steel drift tube. An adiabatic entrance taper is provided by a series of resistive termination loops<sup>5</sup> which gradually tap current from one winding to the other. A second thin solenoid lens focusses the electron beam entering the drift tube to a beam waist such that the electron beam is matched into the helical wiggler field. The electron beam is then transported and focussed through the wiggler interaction region by means of the focussing provided by the strong helical wiggler magnetic field. In contrast to many previous FELs operated at relatively low beam energies and high currents,<sup>1,2,5,7</sup> there is no applied axial guiding magnetic field in the wiggler interaction region.<sup>8</sup>

The growth rate  $\Gamma = (1/P)dP/dz$  of the electromagnetic wave is obtained<sup>6</sup> by measuring the output power as a function of the wiggler interaction length  $z$ . This length is varied by moving a transverse kicker magnet along the length of the wiggler, thereby turning the electron beam into the drift tube wall and terminating the interaction. The observations are compared with a theoretical analysis of the experimental configuration based on the nonlinear simulation code ARACHNE<sup>10</sup>. This simulation numerically integrates a set of coupled nonlinear differential equations which govern the evolution of an arbitrary number of transverse electric (TE) and/or transverse magnetic (TM) waveguide modes as well as an ensemble of electrons. The analysis is fully three-dimensional and self-consistently includes the overlap of the electron beam and the radiation field of each mode. The electron trajectories are integrated using the complete Lorentz force equations in the presence of a three-dimensional representation of the helical wiggler field, and

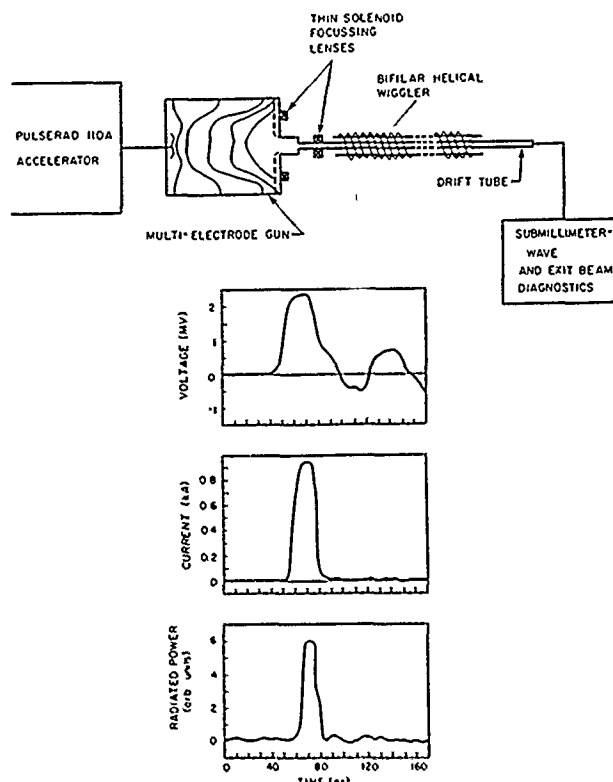


Figure 1: The schematic layout of this experiment, and typical voltage, beam current, and microwave output waveforms.

includes the effects of betatron oscillations and velocity shear on the interaction. Neither self-field nor space-charge effects are included in the simulation, which is valid in the strong-pump Compton regime of operation. The collective dielectric effect of the beam upon the waveguide modes is included self-consistently in the analysis. For a 2.0 MV, 780 A electron beam, the measured power gains of  $56 \pm 3 \text{ dB/m}$  for  $B_w = 1275 \text{ G}$  and  $70 \pm 6 \text{ dB/m}$  for  $B_w = 1510 \text{ G}$  are consistent with the results of the ARACHNE code for a beam temperature of  $\Delta p_{\parallel}/p_{\parallel} \sim 0.0025$ . This is the effective temperature at full width (and  $1/e$  point) due to nonzero beam emittance, and is in good agreement with the measured beam emittance which gives  $0.0022 < \Delta p_{\parallel}/p_{\parallel} < 0.004$ .

The spectrum of the output radiation is measured with a grating spectrometer<sup>11</sup>. The measured spectrum for a 2.3 MV, 930 A electron beam, at a wiggler field strength of 1275 G is shown in Fig. 3, along with the calculated spectrum from ARACHNE. The measured spectral width is approximately  $\Delta\lambda/\lambda \sim 0.04$ . The observed wavelength corresponds predominantly to the excitation of the lowest (TE<sub>11</sub>) mode of the circular waveguide, with a small TM<sub>11</sub> component ( $< 5\%$ ).

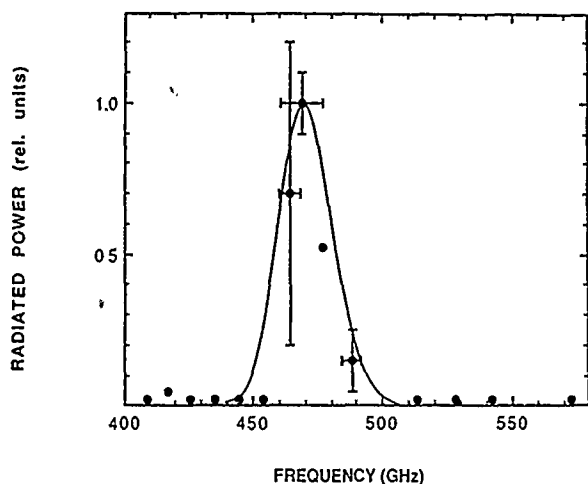


Figure 2: The measured output spectrum for a 2.3 MV, 930 A electron beam; wiggler pump strength  $B_w = 1275$  G. The measured output power is  $P_{out} = 18$  MW.

In conclusion, the measured output power of 18 MW at the measured frequency of 470 GHz represents an order of magnitude increase in the available power for any FEL source operating in the  $\sim 600 \mu\text{m}$  wavelength regime. The corresponding efficiency of 0.8% represents a two order of magnitude increase in efficiency for an FEL operating in this wavelength regime.<sup>1-3</sup>

Previous experiments have noted substantial increases in efficiency when the wiggler field amplitude is tapered<sup>12,13</sup>. An example of the possible effect of tapering the wiggler field amplitude in this experiment is shown in Fig. 4, where the ARACHNE simulation is extended in the axial direction, for both a tapered and an untapered wiggler. The parameters for the simulation shown in Fig. 3 are identical to those in Fig. 2 used in comparison with our experiments. As can be seen in the figure, for the case of the tapered amplitude wiggler, the output power reaches a maximum of 142 MW, corresponding to a 6.6% efficiency. Maintaining the parameters of the electron beam constant, but changing the wiggler period to  $\lambda_w = 2.2$  cm and the initial wiggler field amplitude to  $B_w = 3100$  G (to provide more latitude in the tapering process), results in a maximum possible output power of 263 MW at a frequency of 498 GHz.

#### References

- (1) V.L. Granatstein, S.P. Schlesinger, M. Herndon, and R.K. Parker, *Appl. Phys. Lett.* **30**, 384 (1977).
- (2) D.B. McDermott, T.C. Marshall, S.P. Schlesinger, R.K. Parker, and V.L. Granatstein, *Phys. Rev. Lett.* **41**, 1368 (1978).
- (3) L.R. Elias, R.J. Hu, and G.J. Ramian, *Nucl. Instrum. Methods Phys. Res. A* **237**, 203 (1985).
- (4) D.A. Kirkpatrick, R.E. Shefer, and G. Bekefi, *J. Appl. Phys.* **57**, 5011 (1985).
- (5) J. Fajans, *J. Appl. Phys.* **55**, 43 (1984).
- (6) J. Fajans and G. Bekefi, *Phys. Fluids* **29**, 3461 (1986).
- (7) S.H. Gold, D.L. Hardesty, A.K. Kinkead, L.R. Barnett and V.L. Granatstein, *Phys. Rev. Lett.* **52**, 1218 (1984).

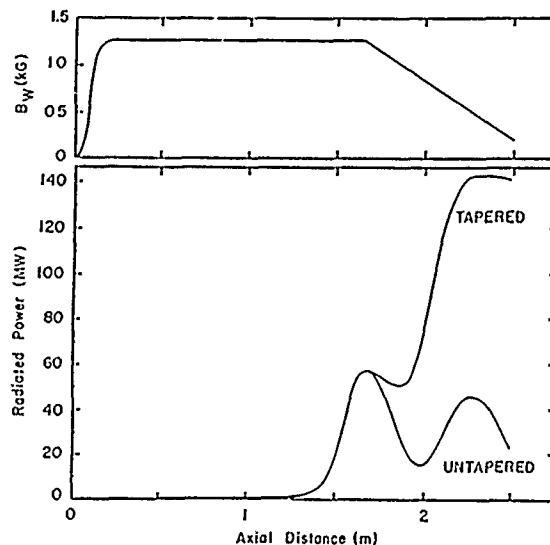


Figure 3: The output power as a function of wiggler length for a tapered and untapered wiggler as calculated with ARACHNE. The parameters of the simulation are:  $V = 2.3$  MV,  $\Delta V/V = 0.25\%$ ,  $I_b = 930$  A,  $B_w = 1275$  G,  $\lambda_w = 3.14$  cm, beam radius = 0.4 cm. The output frequency is 470 GHz. The on-axis amplitude of the wiggler field used in the simulation is shown at the top of the figure.

- (8) To our knowledge, the only other experiment to operate without an axial guide field is J.A. Pasour, R.F. Lucey, and C.A. Kapetanakis, *Phys. Rev. Lett.* **53**, 1728 (1984).
- (9) J. Fajans, J.S. Wurtele, G. Bekefi, D.S. Knowles, and K. Xu, *Phys. Rev. Lett.* **57**, 579 (1986).
- (10) A.K. Ganguly and H.P. Freund, *Phys. Rev. A* **32**, 2275 (1985).
- (11) D.A. Boyd (private communication).
- (12) T. J. Orzechowski, B. Anderson, J.C. Clark, W. M. Fawley, A.C. Paul, D. Prosnitz, E. T. Scharlemann, S.M. Yarema, D. Hopkins, A. M. Sessler and J. Wurtele, *Phys. Rev. Lett.* **57**, 2172 (1986).
- (13) H. Boehmer, M. Z. Caponi, J. Edighoffer, S. Fornaca, J. Munch, G. R. Neil, B. Saur and C. Shih, *Phys. Rev. Lett.* **48**, 141 (1982).

\*Work supported by the Air Force Office of Scientific Research and the National Science Foundation.

<sup>†</sup>Present address: Science Applications International Corporation, McLean, VA 22102.

## BETATRON-SYNCHROTRON RESONANCES IN FREE ELECTRON LASER

Yi-jin Shi

Institute of Atomic Energy,  
P.O. Box 275(18), Beijing, China

Abstract: In terms of Bogoliubov's nonlinear oscillation theory, the first five betatron-synchrotron resonances of  $\Omega_s = (p/q)2k_p$ ,  $p/q = 1/2, 1, 3/2, 1/3, 2/3$  which may occur during laser saturation establishing process have been generally examined. Contrast to previous studies it is found that the most dangerous resonance does not take place in the vicinity of  $\Omega_s = 2k_p$ , but in that of  $\Omega_s = k_p$ . The width of region of  $\Omega_s = k_p$  is proportional to  $\varepsilon$  with  $\varepsilon \propto (k_y^2/k_p^2) \times$  emittance, the passing 'time' over the region due to the laser field being amplified is only one pass over the undulator at most and depends on the gain, and the increment of synchrotron amplitude in passing time is proportional to  $\varepsilon$ .

In summary we conclude that the betatron-synchrotron resonances does not have any significant effect for detaching off-axis electrons in a practical case.

## 1 INTRODUCTION

The betatron-Synchrotron resonance (B-S resonance) is one of free electron laser instabilities besides the side-band instability and first pointed out by Rosenbluth in 1983 [1].

Whether is the betatron-synchrotron resonance a serious obstacle for development of high extraction-gain FEL? Should more attention be paid to overcoming this potential threat in FEL design? These all questions are still interesting in FEL theoretical study. In terms of asymptotic method in nonlinear oscillation theory by Bogoliubov we reached this objective.

Contrast to the previous studies [2], we found that the most dangerous resonant coupling is not the one taking place in the vicinity of  $\Omega_s = 2k_p$  as mentioned by them, but occurs at about  $\Omega_s = k_p$ .

## 2. THE MODEL FOR B-S RESONANCES

The 3-D undulator paraxial field is approximately described by magnetic scalar potential [3]

$$\chi_m = -\frac{B(z)}{k_y} \cosh(k_{yx}x) \sinh(k_{yy}y) \sin\left(\int k_z(z) dz\right) \quad (2.1)$$

with  $k_y(z) = k_{yx}^2 + k_{zy}^2$ , the wavenumber of undulator in  $z$ ,  $x$ , and  $y$  direction respectively. The dimensionless vector potential of the undulator felt by the electron on the betatron trajectories is

$$a_w(x, y, z) = a_w(z) \cosh(k_{yx}x) \cosh(k_{yy}y) \quad (2.2)$$

where  $a_w(z) = eB(z)/mc^2 k_y(z)$ , the value on axis.

In terms of the paraxial approximation,  $x \approx 0$  and  $y \approx 0$  and following the Colson's standard procedure [4], the pendulum equation was written as

$$\frac{d^2\zeta}{dz^2} + \Omega_s^2 (\sin\zeta - \sin\zeta_r) = \varepsilon \Omega_s^2 \sin(2k_p z + \theta_0) (\sin\zeta - \sin\zeta_r) \quad (2.3)$$

with

$$\Omega_s^2 = \Omega_{sy}^2 \left[ 1 + \frac{k_y^2}{k_p^2} (x_0^2 + y_0^2 + \frac{1}{k_p^2} (\theta_{x0}^2 + \theta_{y0}^2)) \right] \quad (2.4)$$

$$\Omega_{sy}^2 = k_y k_p(z) a_w(z) / \gamma^2 \quad (2.5)$$

$$\varepsilon = \frac{k_y^2}{k_p^2} (\beta_c^2 + \beta_s^2)^{1/2} \left[ 1 + \frac{k_y^2}{k_p^2} (x_0^2 + y_0^2 + \frac{1}{k_p^2} (\theta_{x0}^2 + \theta_{y0}^2)) \right]^{-1} \quad (2.6)$$

$$\theta_0 = \arcsin(\beta_c / [\beta_c^2 + \beta_s^2]^{1/2}) + \pi \quad (2.7)$$

$$\beta_c = k_p [(x_0^2 + y_0^2) - \frac{1}{k_p^2} (\theta_{x0}^2 + \theta_{y0}^2)] \quad (2.8)$$

$$\beta_s = x_0 \theta_{x0} + y_0 \theta_{y0} \quad (2.9)$$

where  $x_0, y_0$  is the initial position of betatron orbit,  $\theta_{x0}, \theta_{y0}$  its initial angle with respect to the undulator axis respectively. The betatron frequencies  $k_{px} = k_{py} = k_p$  has been taken for simplicity. This version of the pendulum equation eventually shows that the betatron oscillation leads to an external periodic driving force exerting on a system with the synchrotron oscillation as intrinsic motion.

From eq (2.6)-(2.9) it is obvious that  $(\beta_c^2 + \beta_s^2)^{1/2}$ , thereby  $\varepsilon$  is bounded by the transverse emittance  $\varepsilon_{\perp}$ .

It should be pointed here that although the resonant phase  $\zeta_r$  is dependent on the second derivative of the optical phase with respect to  $z$  as taken into account in previous works [2], we think it has a smaller contribution to the B-S resonances compared with that from transverse dependence of the synchrotron frequency.

## 3. B-S RESONANCE EFFECT ON THE NEAR-RESONANT PHASE ELECTRONS

For the near-resonant phase electrons nonlinear pendulum equation is simplified as Mathieu-like equation

$$\frac{d^2\Delta\zeta}{dz^2} + \Omega_s^2 \Delta\zeta = \varepsilon \Omega_s^2 \sin(2k_p z + \theta_0) \Delta\zeta \quad (3.1)$$

with  $\Delta\zeta = \zeta - \zeta_r$  and  $\Omega_s^2 = \Omega_{s0}^2 \cos\zeta_r$ .

Due to the existence of external periodic force with 'frequency'  $2k_p$  in a system with intrinsic one  $\Omega_s$ , the resonances will take place in the vicinity of  $\Omega_s = (p/q)2k_p$  where  $p$  and  $q$  is to be a couple of mutual prime number and not to be large.

In terms of Bogoliubov's asymptotic method [5], formal solution of eq.(3.1) near resonance is assumed as

$$\Delta\zeta = a \cos\psi + \varepsilon u_1(a, 2k_p z, \psi) + \varepsilon^2 u_2(a, 2k_p z, \psi) + \dots \quad (3.2)$$

with  $\psi = (p/q)2k_p z + \theta$  and  $u_1, u_2, \dots$  being the periodic function of  $2k_p z$  and  $\psi$  with period of  $2\pi$ .

The first term in (3.2) is the fundamental wave and the amplitude  $a(z)$  and phase difference  $\theta(z)$  are assumed as slowly varying functions of  $z$  which are governed by following set of equations

$$\frac{da}{dz} = \varepsilon A_1(a, \theta) + \varepsilon^2 A_2(a, \theta) + \dots \quad (3.3)$$

$$\frac{d\theta}{dz} = \Omega_s - \left(\frac{p}{q}\right)2k_p + \varepsilon B_1(a, \theta) + \varepsilon^2 B_2(a, \theta) + \dots \quad (3.4)$$

the nonlinear functions  $A_1(a, \theta), A_2(a, \theta), B_1(a, \theta), B_2(a, \theta), \dots$  and  $u_1, u_2, \dots$  are determined by harmonic balance principle with respect to the order of small parameter  $\varepsilon$  and assumption that  $u_i$  is orthogonal to the fundamental,  $\cos\psi$  and  $\sin\psi$ .

## 4. THE MAIN RESONANCE

At the first approximation stage the set of equations for  $A_1$  and  $B_1$  is

$$\begin{cases} (\Omega_s - \frac{3}{2}k_p) \frac{\partial A_1}{\partial \theta} - 2A_1 B_1 = -\frac{\Omega_s^2}{2} \sin(\frac{3}{2}\theta - \theta_0) \delta(\frac{1}{2} - z) \\ (\Omega_s - \frac{3}{2}k_p) \frac{\partial B_1}{\partial \theta} + 2A_1 B_1 = -\frac{\Omega_s^2}{2} \cos(\frac{3}{2}\theta - \theta_0) \delta(\frac{1}{2} - z) \end{cases} \quad (4.1)$$

it is easy to solve and obtain

$$\begin{cases} A_1 = -\frac{\Omega_s^2}{4k_p} \cos(2\theta - \theta_0) \\ B_1 = \frac{\Omega_s^2}{4k_p} \sin(2\theta - \theta_0) \end{cases} \quad (4.2)$$

It is obvious that the  $p/q=1/2$  is the only resonance which can occur in the system under the first approximation. The amplitude and phase difference of the first approximation are obtained

$$a^2 = w^2 + v^2, \quad \theta = \arctan(\frac{v}{w}) \quad (4.3)$$

where

$$\begin{cases} w = c_1 e^{\lambda z} + c_2 e^{-\lambda z} \\ v = \frac{[\frac{\Omega_s^2}{4k_p} \sin \theta_0 - (\Omega_s - k_p)]}{\lambda - \frac{\Omega_s^2}{4k_p} \cos \theta_0} c_1 e^{\lambda z} + \frac{[\frac{\Omega_s^2}{4k_p} \sin \theta_0 - (\Omega_s - k_p)]}{\lambda + \frac{\Omega_s^2}{4k_p} \cos \theta_0} c_2 e^{-\lambda z} \end{cases} \quad (4.4)$$

with  $\lambda = \sqrt{(\frac{\Omega_s^2}{4k_p} - (\Omega_s - k_p)^2)}$  and  $c_1, c_2$  being initial constant. It is evident that when the following condition is hold

$$\frac{\Omega_s^2}{4k_p} > |\Omega_s - k_p| \quad (4.5)$$

the  $\lambda$  is real and the amplitude  $a(z)$  will be divergent with  $z$  approaching to infinite. In the same order of approximation, we can rewrite the nonstable condition as

$$|1 - \omega| < \varepsilon/4 \quad (4.6)$$

with  $\omega = k_p/\Omega_s$  and  $\varepsilon = (k_p^2/8k_s)(\beta_c^2 + \beta_s^2)^{1/2}$ .

As mentioned in sec.2,  $(\beta_c^2 + \beta_s^2)^{1/2}$  is bounded by emittance. Therefore even in the worst case that the electron under consideration is initially at the boundary of phase ellipse, the dangerous region leading it's synchrotron oscillation divergent is still very limited and is proportional to emittance, out of it the B-S coupling does not enhance the amplitude of synchrotron oscillation and not detrap the off-axis electrons.

Not losing the generality, we can assume that laser field evolves in the undulator with gain  $\Gamma$  as  $a_s(z) = a_s(0) \exp(\Gamma z)$  then the 'time' to pass over dangerous region of resonance  $p/q=1/2$  is approximately

$$\Delta z/L \approx -\frac{\Gamma}{\Omega_s} \ln(1 - \frac{\varepsilon}{4}) \approx \varepsilon/\Gamma \quad (4.7)$$

where  $G$  is total gain per pass over the undulator with length  $L$ . It shows the passing time  $\Delta z/L$  is related to  $G$ . Even when laser field has reached the saturation,  $G$  is small but still in order of 0.21 or more. So the passing 'time' is not longer than  $\frac{1}{0.21}$  over the undulator at most. Now we estimate the growth of amplitude  $a(z)$  during passing time

$$\Delta a/a = e^{\Delta z \Gamma} - 1 \approx \Delta z \Gamma \approx \frac{\Gamma}{\Omega_s} L \approx \frac{1}{4} \quad (4.8)$$

even in the case of  $\Gamma \sim 1$  and  $L \sim 1$  order of 10, we have

$$\Delta a/a \sim \frac{1}{4} \frac{\Omega_s^2}{k_p^2} \approx 1 \quad (4.9)$$

To confirm the result mentioned above, we recheck it under the second approximation.

A simple calculation yields

$$\frac{\Omega_s \varepsilon}{4k_p} > \left| \Omega_s + \frac{3}{32} \frac{\Omega_s^2 (\Omega_s + k_p)}{k_p^2 (\Omega_s + k_p)} \varepsilon^2 - k_p \right| \quad (4.10)$$

It is obvious that the second order approximation does not result in any substantive effect on  $a(z)$  and  $\theta(z)$ , but shift the resonance frequency  $\Omega_s = k_p$  to  $\Omega_s(1 + 9/64 \varepsilon^2) = k_p$ .

## 5. RESONANCES OF $p/q=1, 3/2, 1/3, 2/3$

Because the driving force under the first approximation only involve one term of  $p/q=1/2$ , higher order approximation is necessary for  $p/q \neq 1/2$  resonances. We carried out the calculation near  $p/q=1, 3/2, 1/3, 2/3$  resonances. The resulting nonstable conditions for them are listed in following

(1)  $p/q=1$

$$\left| \Omega_s - \frac{\Omega_s^2}{16(\Omega_s^2 - k_p^2)} \varepsilon^2 - 2k_p \right| < \frac{\Omega_s^2}{128k_p^2} \varepsilon^2 \quad (5.1)$$

or in the sense of same order of approximation with  $\omega = 2k_p/\Omega_s$

$$|1 - \omega - \frac{\varepsilon^2}{12}| < \frac{\varepsilon^2}{8} \quad (5.2)$$

(2)  $p/q=3/2$

$$|1 - \omega - \frac{9}{128} \varepsilon^2| < \frac{81}{1024} \varepsilon^2, \text{ with } \omega = 3k_p/\Omega_s \quad (5.3)$$

(3)  $p/q=1/3, 2/3$

Up to the third order approximation, we did not get the nonstable condition, that means the resonant coupling of  $p/q=1/3, 2/3$  is the fourth order of  $\varepsilon$  at least.

## 6. THE EFFECT OF B-S RESONANCE ON THE ELECTRON WITH FINITE AMPLITUDE OF SYNCHRONOUS PHASE OSCILLATION

Now we pay some attention to the electrons which is trapped in the bucket and undergoing synchronous phase oscillation with finite amplitude. In this case  $\sin \zeta$  in pendulum eq. (2.3) can be expanded in terms of power series of  $\zeta$  up to some lower order since the synchronous phase is restricted in  $\pm \pi$ .

Following the same procedure as described above, the nonstable condition in the first approximation for  $p/q=1/2$  resonance is obtained

$$|\Omega_{se}(a) - k_p| < \frac{\Omega_s^2}{4k_p} \varepsilon \quad \text{with } \Omega_{se}(a) = \Omega_s \left[ 1 - \frac{a^2}{48} \left( 1 - \frac{a^2}{8} + \frac{a^4}{384} - \frac{a^6}{20736} \right) \right]$$

which is almost the same as (4.5) but with  $\Omega_s \varepsilon(a)$  replacing  $\Omega_s$ .

## REFERENCES

- [1] M.N. Rosenbluth, Appendix, Austin Research Associates Report I-ARA-83-U-62 (1983). See also, M.N. Rosenbluth, IEEE J. Quantum Electron. QE-21 (1985)966
- [2] W.M. Fawley, D. Prosnitz and E.T. Scharlemann, Phys. Rev. A30(1984)2472
- [3] Q.C. Quimby, Nucl. Instr. Methods in Phys. Res. A250 (1986)456.
- [4] E.T. Scharlemann, Lawrence National Laboratory Report No UCRL-92429(1985)
- [5] for example, W.B. Colson, Phys. Quant. Elect. 5(1977)152. (Jacobs et al., editors, published by Addison-Wesley).
- [6] Н.Н. БОГОЛЮБОВ, Ю.А. МИТРОПОЛЬСКИЙ, Асимптотические Методы в Теории Нелинейных Колебаний, Физматгиз (USSR).

## THE EFFICIENCY IMPROVEMENT OF A RAMAN FREE ELECTRON LASER (FEL)

Zhijiang Wang, Zaitong Lu,

Lifen Zhang, Jizhong Chen

Shanghai Institute of Optics and Fine Mechanics,  
Academia Sinica, Shanghai, P.R.China

We have developed a first Raman FEL in China [1]. A recent experiment for improving the efficiency is reported. The wiggler length has been enlarged from 79 cm to 119cm, the efficiency of 3.7% was obtained.

A relativistic electron beam 800A is accelerated across a diode potential of 400 KV and guided through a cylindrical waveguide by an axial magnetic field of 10-12 KG. Peak microwave power of 12 MW has been observed at the wavelength of 8 mm. The experimental results show us that we work at a small single gain region.

The new wiggler with a period of 212 cm is adjustable from 0 to 2 KG. The dependence of wiggler field on microwave output power for different lengths is given

## REFERENCE

- [1] Chen Chu, Zhijiang Wang, et al.,  
Chinese Science, No.11 (1987), 1211.

M.G. Niimura and R.J. Churchill

American Research Corporation of Virginia, Radford, VA.\*

and

I. Alexeff, F. Dyer, and M. Rader

University of Tennessee, Knoxville, TN.\*\*

## ABSTRACT

A rugged, compact, battery-powered millimeterwave (mm-wave) radar has been developed by using a prototype orbitron maser as the source. The orbitron maser was found suitable for such an application since it is high power, wideband (thus multi-channel) and frequency tunable. The radiation emanating directly from the tube was fairly uniform and the divergence angle ( $10^\circ$ ) was diffraction-limited. The orbitron pulse had a fast risetime (100ns), short pulsewidth (500ns) and no spurious oscillations. The orbitron output power was 6.7W minimum (possibly ~6.7kW due to the detector saturation and 400kW input power) at the V-band (50-75GHz). The power levels were similar at lower bands and constant up to 10Hz of repetition frequency. An innovative DC-DC converter was used to amplify 24V of battery potential up to 1000 times. The orbitron maser was characterized by simultaneous measurements of the applied voltage, discharge current (thus input-power and plasma-resistance), luminosity and wave signal. A linear scaling law was found for the mm-wave power to increase with the discharge current. Output power with hydrogen was twice to that observed with air or nitrogen working gases.

## INTRODUCTION

Since the invention of a practical radar source (cavity magnetron) in 1940, research efforts have been concentrated on producing shorter wavelengths as well as higher power. Higher frequencies naturally increase the bandwidth and angular resolution, while reducing the size, of radar. However, the ability to tune the radar frequency over a wide range is often more important for various applications. The orbitron maser [1] is a wideband (1GHz~1THz) source able to scan the fundamental frequency ( $f_0$ ) by changing the applied voltage ( $V_0$ ):

$$f_0 = \frac{6.67 \times 10^4}{r(m)} \left( V_0(V) / \ln\left(\frac{r_2}{r_1}\right) \right)^{1/2} \approx 1.5 \sqrt{V_0(V)} \quad [\text{GHz}]$$

Here,  $r_2/r_1$  (typically 500) is the ratio of tube radius to the radius of the center conductor and the last term is the case  $r=r_1=1.5$  mil tungsten wire. Orbitron is a broadband oscillator even with fixed  $V_0$  because the radius,  $r$ , of the rotating electron beam is continuous in the interval  $r_1 \leq r \leq r_2$ . Therefore, a multichannel radar may be constructed as shown in Fig.1. Alternatively, one can use multiple orbitrons, since the tube can be fabricated inexpensively. Upper and lower frequencies of the each tube may be varied by using wire of different radii and radial plungers of different depths, respectively. Large power handling capability of orbitron is also a great advantage which is not available in solid-state sources, although both are compact. Being free from the dissipation/isolation problems, significantly higher input current/voltage is permissible in orbitrons, indicating feasibility of constructing a high power/frequency radar in a compact dimension. Sealed-off orbitron tubes and a portable power supply have been developed for the field-use of orbitron maser radar. Figure 2 shows the battery-powered high-voltage DC source able to apply max. 24kV-DC pulses on the orbitron tube (located in the right hand side of figure).

## EXPERIMENTAL RESULTS

The potential across the orbitron ( $V_{OB}$  in Fig.2) changes as shown in the upper traces of Figure 3, when the tube is at (a) vacuum, (b) low pressure, and (c) high pressure. The lower traces are mm-wave signals. The voltage drop is due to a rise of the discharge current as becomes clear in Figure 4, where the wave forms of (a) applied voltage, (b) mm-wave signal, and (c) plasma luminosity are shown in reference to that of current (measured by C.T. in Fig.2). Obviously, the mm-wave emission results during the glow-to-arc transition, when the plasma luminosity enhances as shown in Fig.4-c. The risetime of mm-wave signal is the fastest of all. There seems to exist a current threshold for the emission of radiation as is evidenced in the expanded (lower) oscillogram in Figure 5 (the upper traces: mm-wave and lower traces: current). According to Figure 6, the hydrogen gives the maximum output at higher pressures (which is twice higher) than the case of the other gases. Thus, hydrogen is favorable for long-useful-life sealed-off orbitrons. Next, the mm-wave power was plotted with respect to the discharge current in Figure 7. Here, encouraging linear scaling is evident until a saturation occurs with large currents. Simultaneous voltage and current measurements can give information on input power and plasma resistivity as computed for 60mT in Figure 8. At the peak time (100ns) of mm-wave, the input power is ~400kW and the resistivity is ~200Ω. The resistivity decays exponentially as confirmed in Figure 9, more rapidly at 60mT than 30mT. The directionality was measured by a detector translating orthogonally to the orbitron axis. The angle of emission was  $11^\circ$  (with & without a horn antenna) as seen in Figure 10, which is close to the diffraction limited angle,  $\theta = 1.22\lambda/D = 10^\circ$ , since  $\lambda = 4.28$ mm and  $D = 30$ mm. Figure 11 shows typical radar pulses indicating a good reproducibility of  $\pm 16\%$  and the average pulse height of 1V. This measurement was made by a crystal detector with sensitivity of 25V/W (or 40mW/V) and aperture of 6.7cm<sup>2</sup>. The detector was located 1" away from the orbitron of 14cm long so that the power radiated for  $4\pi$  angle would be 6.7W and that for  $11^\circ$  solid-angle be 100mW. These are the most conservative estimation (by 1000 times at least), since the detector was calibrated in 10mV range and is well-known to be saturated above 100mV. Figure 12 is a prototype, hand-held mm-wave radar equipped with an orbitron maser. Figure 13 shows results of a preliminary radar experiment, where transmission and reflection of mm-waves were measured through a water-vapor channel of 47cm long. Figure 14 shows effects of the pure axial magnetic field externally applied; (a) without and (b) with field. With field, the discharge starts earlier as in high pressure tube and no deterioration in signal. This is encouraging since the tapered magnetic field may be applied for future orbitrons in order to increase the energy conversion efficiency.

## Acknowledgements

\* Work supported in part by the US Army under contracts DAAD09-87-C-0029 and DAAH01-87-C-0923.

\*\* Work supported by the Air Force Office of Scientific Research under contract 86-0100.

## REFERENCES

- (1) I. Alexeff, "The orbitron microwave maser", *High Power Microwave Source*, ed. by V.L. Granatstein and I. Alexeff, Artech House, Inc., Norwood, MA (1987), pp. 293-305.





## A LOW-LOSS HIGH-POWER FILTER FOR DIRECT BROADCAST SATELLITE TRANSPONDERS

Toshihiro Nomoto

NHK Science and Technical Research Laboratories  
Setagaya, Tokyo 157, Japan

## ABSTRACT

In designing broadcast satellite transponders, it is required for the filters handling high-power RF signals to have not only low-loss characteristics but also good thermal stability. In order to realize such filter performance, we proposed a 6-pole canonical  $TE_{113}$  dual-mode filter which is formed of silver-plated Super Invar cavities with copper iris plates. The insertion loss and thermal stability of the experimental filter were 0.3dB and 1.5ppm/°C, respectively. Also, no significant deterioration on the filter performance was observed even at the RF input power of around 400W. As a result, it was found that this type of filter was most suitable for the high-power satellite transponders in view of insertion loss, thermal design, volume and weight.

## INTRODUCTION

The transmission power for satellite broadcasts is needed to be hundreds of watts because the desirable broadcasting system is based on direct home reception by low-cost receivers. At present, the transmission power is mainly around 100W. In future, however, higher transmitting power will be required in order to further simplify the receiving terminals. At the transmitter of broadcast satellite transponders, in general, the system in which each channel signal is separately amplified is adopted for the necessity of improving the power efficiency of the TWT's; therefore the input/output multiplexers are used for the channelization. However, the input/output multiplexers directly affect the transmission characteristics of the transponders such as attenuation and group-delay because of consisting of narrow passband filters. In addition, the output multiplexers must handle high-power RF signals. Thus, the multiplexers are very important components in satellite transponders.

The most indispensable performance for high-power filters is that the insertion loss is as low as possible and the heat generated inside the filters, especially at irises, can be easily and efficiently transported to the satellite base plate or to free space, in order to keep their own thermal stability. In order to design a low-loss filter, first of all, resonators with high unloaded  $Q$  ( $Q_0$ )

must be applied. Secondly, the number of resonators should be minimized under the condition of satisfying the necessary attenuation characteristics. However, the increase of resonators is often preferable to the thermal design because the surface area becomes larger.

The developments of high-power filters or multiplexers using oversized cavities have been made by D. J. Rosowsky et al.[1] and A. E. Williams et al.[2]. However, because the regulations such as channel assignments and technical standards decided at WARC-BS are different in each Region (this means that the requirements to the attenuation characteristics of the multiplexers are also different in each Region), the design feature of these multiplexers has not always applied to the broadcast satellites in other regions.

We have been investigating an optimum filter for high-power broadcast satellites in Region 3, and proposed a 6-pole canonical dual-mode filter consisting of  $TE_{113}$  cylindrical cavities which utilized silver-plated Super Invar waveguides and copper irises.

## DESIGN FEATURE

Channel bandwidth and separation for satellite broadcasts assigned to Japan, are 27MHz and 38.36MHz, respectively; therefore rejection band is defined as frequency ranges separated by more than  $\pm 24.86$ MHz from the center frequency of each channel. To satisfy the necessary attenuation characteristics of the filter for output multiplexers in rejection bands [3](see Table 1), we considered that 4-pole and 6-pole elliptic function filters were suitable for realizing low-loss characteristics. A comparison between the two types of filters was made on insertion loss at the center frequency, group delay within the 27MHz-band, and filter bandwidth as a function of minimum out-of-band rejection. It is found that the 6-pole filter may realize the satisfactory electrical performance, compared with the 4-pole filter. The former is also advantageous for heat radiation.

Different types of oversized cavities are evaluated in order to obtain high  $Q_0$  (more than to 12,000).  $TE_{011}$  cylindrical cavities have been able to obtain the  $Q_0$  of about 20,000 [4]. However, it may be difficult to sufficiently separate degenerate  $TE_{011}$  and  $TM_{111}$  resonant modes and to design waveguide manifold multiplexers. In addition, the use of  $TE_{011}$  mode is disadvantageous in volume and weight. From such reasons, cylindrical  $TE_{011}$  mode has not been used, but cylindrical  $TE_{113}$  or  $TE_{114}$  mode has been used for satellite application. The use of these modes makes it possible to utilize dual-mode, so that cross-couplings required to realize elliptic function responses are easily achieved and volume and weight are saved. We decided to select  $TE_{113}$  dual-mode cavities by the tradeoff between the  $Q_0$  and the volume and weight of 6-resonator filters using  $TE_{113}$  or  $TE_{114}$  mode.

Fig.1 shows the geometry of a 6-pole canonical  $TE_{113}$  dual-mode filter with an orthomode T-shaped junction, which can achieve the isolation of more than 55dB between the input and output signals and acts a waveguide manifold

Table 1 Specifications for filters

Items	Requirements
Insertion loss at $f_0$	$\leq 0.4$ dB
Return loss	$\geq 20$ dB
Bandwidth	$\geq 27$ MHz
Input power	400W
Attenuation	
at $f_0 \pm 24.86$ MHz	$\geq 15$ dB
14.0-14.31GHz	$\geq 40$ dB

 $f_0$ : channel center frequency

for multiplexers. It is known that reduction of the  $Q_0$  of a coupled-cavity filter is caused by surface roughness, coupling apertures, and tuning screws. The insertion loss is, therefore, minimized by keeping the surface roughness of less than  $0.2\mu\text{m}$ , optimizing the thickness of iris plates and shape of coupling apertures (using thin iris plates and circular apertures), and carefully choosing the material of tuning screws (using low-loss dielectric screws)[3].

Super Invar may be the most suitable material for obtaining the high thermal stability of a filter assembly, while it is too difficult to remove the heat generated at the irises due to the very poor thermal conductivity, which is below 1/30 of that of silver. It will be very important to use material with a good thermal conductivity such as silver or copper for the iris plates instead of Super Invar. But, the connection between two materials with the different thermal expansion coefficients produces the considerable problems. For instance, a warp of the iris plates and a change in dimensions of the coupling apertures would be observed. The experimental filter was, therefore, formed of silver-plated Super Invar waveguides and copper thin iris plates ( $0.3\text{mm}$ ), and the cavity seams were laser-welded under the condition of keeping the temperature of the entire assembly around  $150^\circ\text{C}$  (much lower than that of brazing) so as not to produce the warp of the iris plates and not to need to modify the coupling aperture dimensions. The generated heat can be transported only through the brackets which is directly attached to the iris plates.

### EXPERIMENTAL RESULTS

Fig.2 shows the attenuation and return loss characteristics measured within the temperature range of  $25^\circ\text{C}$  to  $95^\circ\text{C}$ . The frequency shift is  $1.3\text{MHz}$ , or the thermal stability is about  $1.5\text{ppm}/^\circ\text{C}$ . The insertion loss at the center frequency is  $0.3\text{dB}$  at  $25^\circ\text{C}$ . The averaged  $Q_0$  is estimated to be over 15,000, or the  $Q_0$  efficiency is approximately 75% which has never achieved yet. This result proves that the optimization techniques have been greatly effective for realizing a low-loss filter.

The high-power tests were carried out at the input power of 200W, 290W and 380W in a vacuum chamber. Fig.3 shows the temperature on the filter surface. No deterioration in the electrical performance including multiplications was observed during the tests. The measured temperature is in good agreement with the result of the thermal analysis. Judging from the results of such thermal and high power tests, a stable operation can also be expected at around 400W input power in space environment.

### CONCLUSIONS

A low-loss high-power 6-pole canonical  $\text{TE}_{113}$  dual-mode filter for direct broadcast satellite transponders has been designed and developed. The measured results show that the experimental filter has the satisfactory electrical and thermal performance, and that the optimization techniques applied to this filter design are greatly effective for realizing a low-loss high-power filter.

### REFERENCES

- (1) D.J.Rosowsky and D.Wolk, IEEE Trans. Vol.MTT-30, 1982, pp.1317-1323.
- (2) A.E.Williams, W.C.Tang, and C.Inker, 15th European Microwave Conference, 1985, pp.355-363.
- (3) T.Nomoto, Trans.IECE Japan, Vol.J67-B, 1984, pp.916-923.
- (4) H.L.Thal, Jr., IEEE Trans. Vol.MTT-27, 1979, pp.982-986.

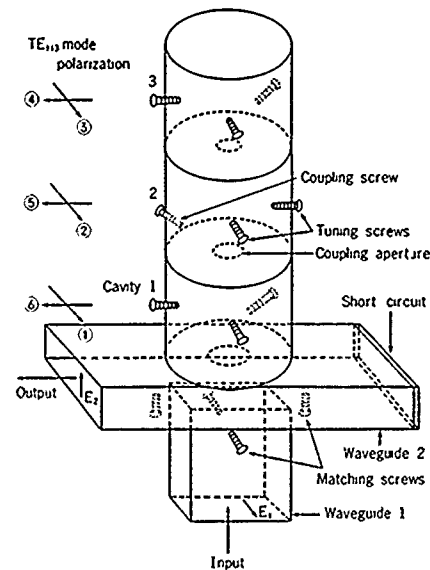


Fig.1 Geometry of a 6-pole canonical dual-mode filter

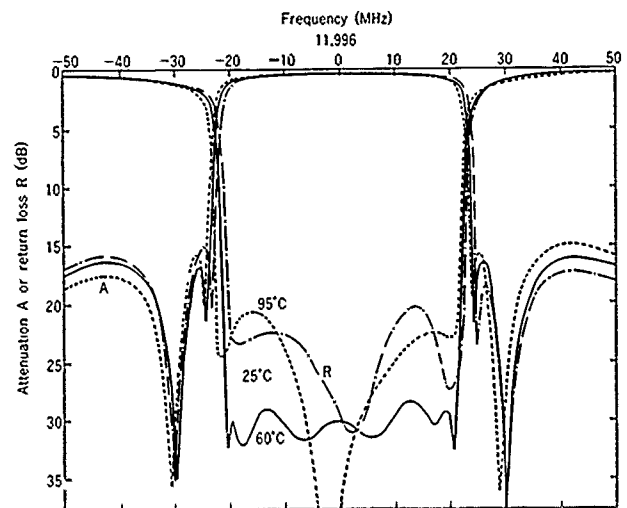


Fig.2 Attenuation and return loss of the filter

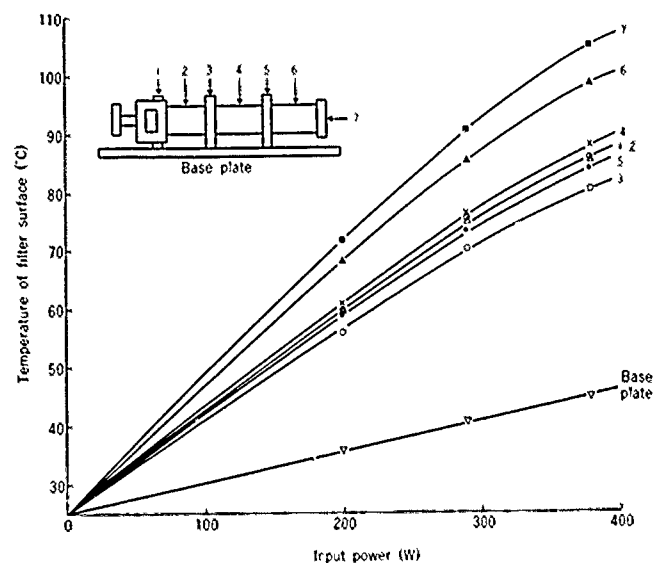


Fig.3 Temperature on the filter surface

# A MODEL BASED TECHNIQUE FOR MILLIMETER WAVE RADAR TARGET RECOGNITION

Firooz A. Sadjadi

Honeywell Systems and Research Center MN65-2300  
3660 Technology Drive  
Minneapolis, MN 55418

## ABSTRACT

A technique for recognizing real targets by millimeter wave (MMW) radar at 35 GHz and 94 GHz is presented. The recognition is performed by a model based technique in which real targets are represented by their high range resolution (HRR) profiles in a hierarchical fashion.

The unknown signal is classified by a model matching method and a coarse-fine searching technique. The advantages of this model based method are in low storage capacity, fast processing time and high recognition performance. Moreover this technique is very easily modifiable to incorporate infrared sensor processing.

We will present the results of the several experiments that we have conducted.

## INTRODUCTION

Automatic Recognition of targets (ATR) has been in the process of development during the last decade<sup>1</sup>. The goal of such a system is to either provide timely and accurate assistance to a human operator who is the ultimate decision maker or to be totally autonomous in extraction of necessary information, its processing and final decision making.

A large portion of the technical work in ATR has been, up to very recently, limited to the use of imaging sensors such as infrared (IR), visible or radar. The widespread use of millimeter wave radar (MMW) has become only very recently feasible due to the rapid progress in the MMW radar hardware developments<sup>2</sup>. High range resolution (HRR) radar signatures at 35 GHz and 94 GHz do provide a wealth of information about the different target attributes. It is the exploitation of these attributes that is addressed in this paper.

In the work summarized in this paper we present a novel model based technique for recognizing tactical military targets by means of high range resolution millimeter wave (HRRMMW) radar signatures. We examine this technique and provide the results of several experiments that we have conducted.

## MODEL BASED APPROACH

A traditional approach to target recognition by MMW radar in the past has been by using statistical pattern recognition techniques. In this approach for each target various radar signatures corresponding to different viewing angles are used to train a statistical classifier which is used to classify the radar signature of an unknown target. The techniques employing this approach has shown severe limitations in their recognition performance largely due to the large variations of the MMW radar signatures with the changes in the viewing angles.

Another approach which is detailed here is to employ model matching techniques. In this approach a model or models for each target is created in terms of the discriminatory attributes of every viewing angle signature. Since the MMW radar signatures vary from angle to angle for every target, the model-driven technique has the potential of exploiting these variations better than the traditional approach. Moreover, this approach has the generality of concept to include in its model not only physical feature values but also symbolic relations and this could improve the recognition performance and increase the robustness. Last, but not least, the presence of clutter and/or countermeasures have devastating effects on the performance of traditional techniques and the best hope for dealing with these problems seems to be with model based recognition methods<sup>3,4</sup>.

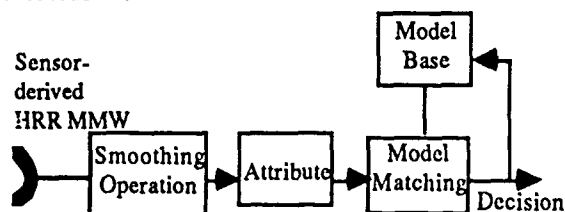


Figure 1. Model-Driven HRRMMW Target Recognition

Figure 1 shows a schematic diagram of our model-based approach. It consists of the following steps:

- 1) Creating models of the targets of interest - Each model consists of the high range resolution (HRR) millimeter wave (MMW) radar signature of the target obtained from every aspect angle. Another way of creating this model

is to use the 3D scatterer's model of each target and to obtain the HRR profiles from it.

- 2) Extraction of attributes - This step can be as general in using the whole HRR signature or it can consist of extracting a set of features from each HRR corresponding to every angle, or it can consist of a set of relational trees obtained for each signature.
- 3) Matching - This process consists of two substeps: search strategy to speed up storage processing time and decision function or matching function operation for the selection of appropriate classifiers. In our approach we have a novel coarse to fine search technique that can reduce the search space by large amounts.

## EXPERIMENTS

In one experiment conducted during 83-84 we used 3D scatterer data that is available from ERIM<sup>5</sup> to generate 1-D radar signatures of targets. These 'model signatures' were used in a matching scheme against real radar signatures of the same targets that has been acquired by radars. The targets used were tanks and APC's.

AZIM ELEV	180°	210°	300°	330°
32°	.59	.24	.44	.47
6° + Δ	.62	.36	.54	.56

Table 1. Matching Results in the Experiment-I

Table 1 shows a typical normalized correlation results of blue tank (180° az and 6° elev.) MMW radar signature with the model derived signatures (derived from 3-D ERIM data base) of an blue tank at various azimuth & elevation angles. As can be seen, the highest value, .62, is obtained from the correct value of Az & El. for the blue tank.

In the second study using High Range Resolution Signatures available from the government's TABILS 12 data base and ERIM 3-D data base, and using features extracted from these signatures, it was shown that in all of the cases, no matter what the azimuth angles of the targets were, the two tanks were classified correctly. A moderate amount of noise and clutter was involved that we dealt with by noise smoothing and threshold selecting.

Typical results are tabulated below:

$$d(x,y) = ||F_x - F_y||$$

is the distance between the feature vectors of the target and the stored model. The smallest distances signify the decision parameters.

AZIM DISTANCE	0°	90°	150°	180°	210°
d(red_target_210° blue model)	72.4	129.7	126.4	149.7	113.7
d(red_target_210° blue model)	189.1	132.6	196.4	157.5	174.4

AZIM DISTANCE	240°	270°	300°	360°
d(red_target_210° blue model)	183.5	128.5	208.3	172.7
d(red_target_210° blue model)	207.5	135.6	208.0	166.0

Table 2. Matching Results in the Experiment-II

The red target at 210° azimuth obtained from ERIM 3-D data base has been correctly classified as a red target from the stored model obtained from HRR Signatures of TABILS 12 data base. In this case the angle also is correctly identified. In 90 different tests using a red target at different angles from an ERIM data based and stored models of blue and red targets at various angles from TABILS 12, the red target was always classified correctly.

## SUMMARY

A model based technique for recognizing tactical military targets by HRRMMW radar was presented. The technique was shown to have high recognition performance and robust in terms of viewing angle changes. Its effectiveness in presence of high clutter and countermeasure remains to be studied.

## REFERENCES

- (1) F. Sadjadi, H. Nasr, *Intelligent Automatic Target Recognition Systems*, SPIE Tutorial Course Notes, August 1988.
- (2) S. Johnson, *Millimeter Wave Radar*, ARTECH HOUSE, Dedham, MA. 1980.
- (3) F. Sadjadi, "A Model Based Technique for Using MMW High Range Resolution Radar for Target Recognition," *Honeywell Interoffice Correspondence*, February 1985.
- (4) F. Sadjadi, "3-D Target Recognition Using Infrared (IR) and Millimeter Wave (MMW) Radar Sensors," *Honeywell Interoffice Correspondence*, August 1984.
- (5) E. Johnson, A. Maffett, "35 GHz Active Signature Measurements," AFATL-TR-79-3, ERIM, January 1979.

## RECENT ADVANCES IN MILLIMETER WAVE UP AND DOWN CONVERTERS

Charles Oleson, Arthur Larsen  
Richard Chew and Walter Day

Varian Solid State Microwave Division  
Santa Clara, California

## ABSTRACT

A 26 to 40 GHz block converter for receiver frequency extension will be described. The converter has a 15 dB NF, 10 dB conversion gain, >50 dB spurious-free dynamic range, built in BITE, 44 GHz L.O. and measures 3x3x1 inches. A 33 to 36 GHz up/down converter for an airborne jammer pod will also be described.

## 26 TO 40 GHz BLOCK CONVERTER

A 26 to 40 GHz block converter has been developed to extend the frequency range of existing microwave receiving systems. This converter design makes use of state-of-the-art MMIC devices in order to achieve a highly compact package size of 3x3x1 inches. Figure 1 shows the block diagram of the converter. A dielectric resonator oscillator (DRO), which utilizes a GaAs FET for the oscillator and GaAs MMIC's for the buffer amplifier stages, is employed as the local oscillator at 14.67 GHz. The DRO output is used to drive a tripler which provides the 44 GHz, high side L.O. signal for the mixer. The DRO output is also applied to a doubler, on command, which provides an in-band BITE signal at 29.33 GHz. Phase noise of the DRO is typically -80 dBc/Hz at 10 KHz offset and the temperature stability is better than 4 ppm/°C.

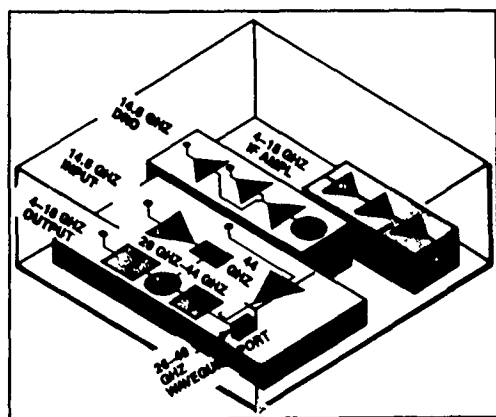


Figure 1  
26 to 40 GHz Block Converter Diagram

The mixer block, shown in Figure 1, utilizes suspended substrate construction and contains the mixer, multipliers, an L.O. band-pass filter, a 20 GHz low-pass filter and a 44 GHz band-rejection filter to minimize L.O. re-radiation. The converter's noise figure of 15 dB results from a mixer conversion loss of 8.0 dB and an IF amplifier having a noise figure of 7 dB. The IF amplifier utilizes all MMIC construction and provides 18 dB gain. The mixer circuit has a 1 dB compression point of 0 dBm. It utilizes beam lead diodes in a balanced design.

Both the DRO and the IF amplifier utilize internal monolithic voltage regulators and reverse protection diodes. They are packaged in hermetic, laser welded aluminum housings and are subjected to MIL-STD-883 reliability screening. Figure 2 shows a photograph of the 26-40 GHz converter with a waveguide input.

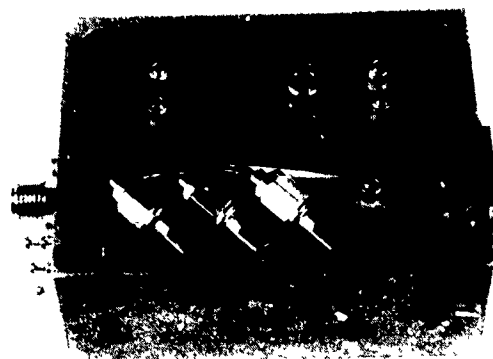


Figure 2  
26 to 40 GHz Block Converter

Typical performance specifications are:

Frequency Range	26-40 GHz
IF Frequency	4-18 GHz
L.O. Frequency	44 GHz
Converter Noise Figure	15 dB
Conversion Gain	10 dB $\pm$ 3 dB
Gain Linearity	$\pm$ 2 dB
Input Power @ 1 dB Compression	0 dB
Spurious Free Dynamic Range	$\geq$ 50 dB
Operating Temperature	-20 to +65°C
Input Power	+15 Vdc @ 0.7A

### 33 TO 36 GHz UP/DOWN CONVERTER

A 33 to 36 GHz up/down converter has been developed for frequency extension of an airborne jammer pod. The basic architecture of the up/down converter is shown in Figure 3. A phase-locked DRO, referenced to a 100 MHz crystal oscillator, is used to provide a high stability, low phase noise signal at 12.5 GHz. This signal is doubled and amplified to provide the L.O. signal for both the up and down converters. The L.O. power divider/filter and the converter/filter assemblies are suspended substrate structures. The mixers utilize beam lead diodes and exhibit excellent performance in an airborne temperature and vibration environment.

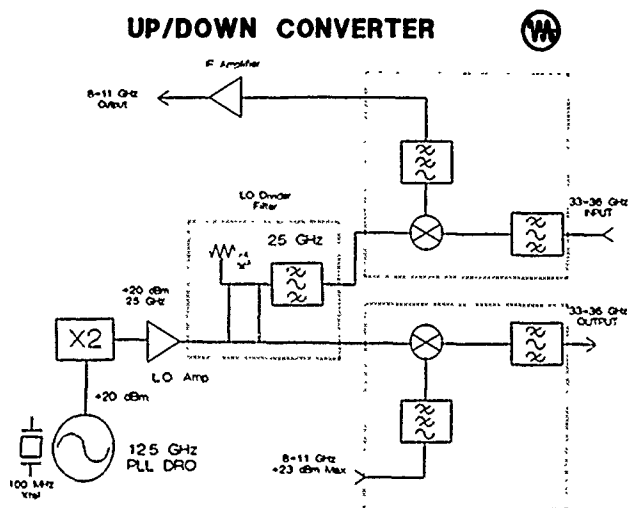


Figure 3  
33 to 36 GHz Up/Down Converter Diagram

Figure 4 is a photograph of the VZA-3301 AA, 33 to 36 GHz up/down converter. The suspended substrate mixer/filter/divider structures may be seen in the left center of the converter assembly.

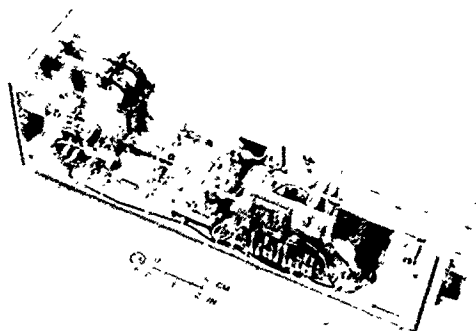


Figure 4  
VZA-3301 AA, 33 to 36 GHz Up/Down Converter

Typical performance specifications for the up/down converter are:

RF Frequency	33 to 36 GHz
IF Frequency	8 to 11 GHz
Down Conversion:	
RF Power	+13 dBm max.
Loss	13 dB max.
Up Conversion:	
IF Power	+23 dBm max.
Loss	23 dB max.
L.O. Feedthrough	-30 dBm typ.
L.O. Accuracy	+200 KHz
L.O. Stability	20 Hz in 75 ns
Temperature Range	-40 to +60°C

## 205 GHZ SIS RECEIVER DEVELOPMENT FOR REMOTE SENSING APPLICATIONS

W. R. McGrath,<sup>1</sup> C. N. Byrom,<sup>1</sup> B. N. Ellison,<sup>2</sup>

M. A. Frerking,<sup>1</sup> and R. E. Miller<sup>3</sup>

1: Jet Propulsion Laboratory, Pasadena, California

2: California Institute of Technology, Pasadena, California

3: AT&T Bell Laboratories, Murray Hill, New Jersey

### INTRODUCTION

There are many applications of remote sensing in the frequency range near 200 GHz. The determination of the role of man-made chlorine compounds in the destruction of the ozone layer observed through the emission from ClO near 200 GHz is one example. Another example is the observation of CO at 230 GHz as a tracer of matter in the interstellar medium. Heterodyne receivers are the instrument of choice to perform these observations due to their high sensitivity and spectral resolving power. The nonlinear tunneling currents in a superconductor-insulator-superconductor (SIS) tunnel junction have been shown both theoretically and experimentally [1] to provide the lowest noise mixing element at millimeter wavelengths in these receivers. When properly optimized, an SIS mixer displays the important properties of conversion efficiency greater than unity and noise temperature approaching the quantum limit.

SIS receivers intended for radio astronomy applications near 230 GHz have been reported [2,3]. These receivers show excellent performance compared to competing Schottky-diode based receivers. This report describes preliminary tests of a 205 GHz SIS receiver which employs a Pb-alloy tunnel junction in a waveguide mixer mount. Double sideband receiver noise temperatures as low as 113 K have been measured. This receiver development serves as an initial step toward development of a 600-700 GHz SIS receiver for use on the California Institute of Technology Submillimeter Observatory, Mauna Kea, Hawaii.

### RECEIVER DESIGN

The tunnel junctions are fabricated on 0.1 mm thick  $\times$  0.18 mm wide  $\times$  3.6 mm long fused quartz substrates using a tri-layer photoresist bridge technique similar to that described by Dolan [4]. The base electrode of PbInAu is 200 nm thick, and the counter electrode of PbAu is 300 nm thick. The tunnel barrier is formed by thermal oxidation. The mixing results given in Table I were obtained for a junction with a normal state resistance  $R_n = 21 \Omega$ , a critical current density  $J_c = 1.7 \times 10^4 \text{ A/cm}^2$  and an area of approximately  $0.7 \mu\text{m}^2$ . The gap voltage is  $V_g = 2.5 \text{ mV}$  at 4.2 K, and the width of the quasiparticle current rise at  $V_g$  is estimated to be  $\Delta V_g = 0.6 \text{ mV}$ . This is less than the characteristic photon voltage  $hf/e = 0.85 \text{ mV}$  at 205 GHz. Using the value of  $J_c$ , the junction area, and data published by Magerlein [5], the junction capacitance is estimated to be  $C = 36 \text{ fF}$ . This implies a value of about 1 for the junction relaxation parameter  $\omega R_n C$ , where  $\omega = 2\pi f$  and  $f = 205 \text{ GHz}$ .

Figure 1 shows a block diagram of the receiver which is mounted in a commercial vacuum cryostat. The mixer is a full height waveguide mount similar in design to that described in ref. 2 employing a noncontacting backshort and E-plane tuner located  $\lambda_g/2$  in front of the junction. The junctions are mounted at the edge of the waveguide broad wall with one lead grounded at the opposite wall. The other lead containing an rf choke filter is connected to an SMA connector to provide the mixer IF output. Measurements on a 48 $\times$ -scale model of the mixer block indicated that this mount arrangement can properly match junctions with rf impedance 10-200  $\Omega$  and with  $\omega R_n C$  values up to about 3.

The mixer block is integrated with a dual-mode conical horn whose properties have been previously reported [6]. The far-field pattern has a 3 dB half angle of  $6^\circ$ . A spherical,  $f/1.25$  teflon lens provides an input beam waist located at the entrance aperture to the dewar. This arrangement minimizes aperture diameter and, hence, the heat load on the dewar.

Due to the low local oscillator (LO) power requirements of SIS mixers, a simple room temperature mylar beam splitter is used to reflect about 2% of the incident LO power into the dewar. The LO source consists of a 68.3 GHz Gunn oscillator driving a  $\times 3$  frequency multiplier which employs a whisker-contacted Schottky barrier diode. A similar arrangement is used to provide monochromatic signals for single sideband (SSB) tuning of the mixer.

Power from the mixer is coupled to the L-band IF system through a microstrip matching circuit similar to one previously reported [2]. A 20 dB bidirectional coupler allows test signals to be injected for evaluating the mixer IF mismatch and the IF system gain. A commercial [7] low-noise HEMT amplifier provides the first gain stage. Room temperature bandpass filters with a center frequency  $f_0 = 1.4 \text{ GHz}$  and bandwidth  $BW = 100 \text{ MHz}$  or with  $f_0 = 1.589 \text{ GHz}$  and  $BW = 200 \text{ MHz}$  were used for the receiver noise measurements.

Receiver noise temperature  $T_R$  was measured using the conventional Y-factor method by placing hot and cold loads in the signal beam path as shown in Fig. 1 and measuring the total IF output power. The hot load is a room temperature piece of Eccosorb AN-72 absorber, and the cold load is a liquid-nitrogen-cooled, pyramidal cone of Eccosorb sufficiently large to completely fill the input beam. However, some of the early double sideband (DSB) measurements used a flat Eccosorb load which gave less stable results due to standing waves. For DSB measurements, the backshort, E-plane tuner, LO power, and bias



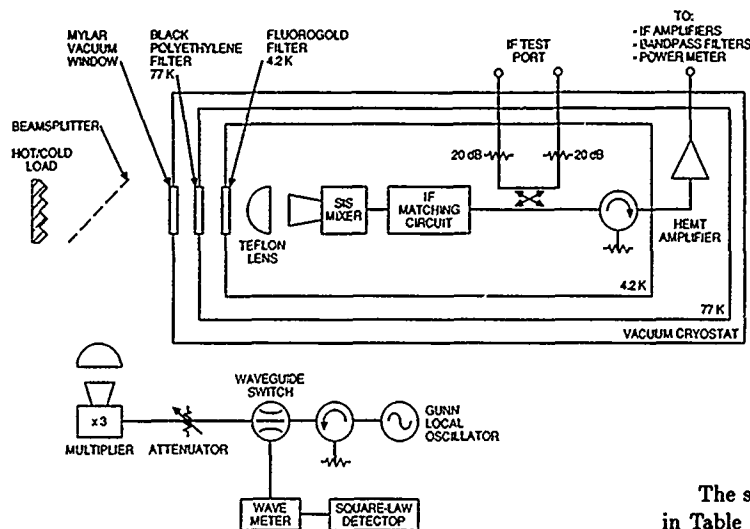


Fig. 1 Block diagram of SIS receiver

voltage were iteratively adjusted to maximize the total IF output power with the hot load in place. For single sideband measurements, a monochromatic signal at either the upper sideband (USB) or lower sideband (LSB) was injected into the receiver, and the IF output power was maximized. While this procedure gave good results, it does not necessarily minimize the receiver noise since optimal tuning conditions may be missed[8]. No sideband ratios were measured for SSB measurements.

## RESULTS AND DISCUSSION

The double sideband receiver noise measurements are listed in Table I. All data were taken on the first photon step below the gap and the junction temperature was estimated at slightly above 4.2 K. Good performance was obtained over the frequency range from 200 to 211 GHz. The large uncertainty in the 211.2 GHz measurement is due to the use of a flat piece of Eccosorb for the cold load. Reflections at the LO frequency presumably between the load and feed horn lens caused some variations in the IF output power. The pyramidal cold load eliminated these problems. At 205 GHz, a value  $T_R = 113$  K was obtained with the backshort position optimized close to the junction. Retuning with the backshort  $\lambda_g/2$  farther from the junction usually produced noise temperatures closer to 200 K. This is most probably due to the sensitivity of the mixer tuning to backshort position. This sensitivity was also seen in the large-scale model and in other similar mixer mounts[8]. In general, all the measurements required careful adjustment of the backshort. These results are comparable to previous receiver measurements made at a reduced cryostat temperature of 2.4 K.

A rise in  $T_R$  below 200 GHz is expected since model measurements indicate that the transmission of the rf choke filter on the substrate begins to increase in this region. In addition, Josephson effects made tuning difficult, and the mixer may not have been fully optimized. The high drop back voltage of 1.6 mV generally made tuning the receiver difficult. A magnetic field from a superconducting magnet close to the mixer reduced the interference from Josephson effects with no adverse effect to the receiver noise temperature.

Table I. Double Sideband Receiver Noise Measurements

LO Frequency [GHz]	$T_R$ (DSB) [K]
198.4	$249 \pm 12$
205	$113 \pm 11$
211.2	$131 \pm 38$

Table II. Single Sideband Receiver Noise Measurements

Signal Frequency [GHz]	$T_R$ (SSB) [K]
203.3 (LSB)	$170 \pm 11$
206.5 (USB)	$247 \pm 13$
207 (LSB)	$178 \pm 11$
210 (USB)	$194 \pm 22$

The single sideband receiver noise measurements are listed in Table II. The SIS receiver showed slightly improved performance as a SSB receiver since the lowest values are less than twice the DSB measurements. The best value  $T_R = 170$  K was obtained at 203 GHz. There is a large spread in these measurements, particularly near 206 GHz - 207 GHz. This is probably again a result of the sensitive tuning of the mixer.

In all the measurements reported above, the mixer was well matched at the IF with a return loss typically of -6 dB to -10 dB. Values as high as -5 dB and as low as -15 dB were also observed.

## SUMMARY

We have built and tested a prototype 205 GHz SIS receiver for remote sensing applications. Double sideband receiver noise temperatures as low as 113 K and single sideband values of 170 K were obtained with a Pb-alloy junction at an ambient temperature close to 4.2 K. Measurements on junctions with improved rf filters and on NbN junctions are currently in progress.

## ACKNOWLEDGEMENTS

This work was supported in part by the Jet Propulsion Laboratory, California Institute of Technology, under contract with the National Aeronautics and Space Administration.

## REFERENCES

- (1) J.R. Tucker and M.J. Feldman, *Rev. Mod. Phys.* **57**, 1055 (1985).
- (2) B.N. Ellison and R.E. Miller, *Int. J. IR and mm Waves* **8** (1987).
- (3) R. Blundell, M. Carter and K.H. Gundlach, *Int. J. IR and mm Waves* **9**, 361 (1988).
- (4) G.J. Dolan, *Appl. Phys. Lett.* **31**, 337 (1977).
- (5) J.H. Magerlein, *IEEE Trans. Magn.* **MAG-17**, 286 (1981).
- (6) H.M. Pickett, J.C. Hardy, J. Farhoomard, *IEEE Trans. Microwave Theory Tech.* **MTT-32**, 936 (1984).
- (7) Berkshire Technologies, Inc., Oakland, CA.
- (8) W.R. McGrath, P.C. Richards, D.W. Face, D.E. Prober, F.L. Lloyd, *J. Appl. Phys.* **63**, 2479 (1988).

# LIGHT-CONTROLLED MICROSTRIP LINE COUPLER

Hitoshi SHIMASAKI  
Faculty of Engineering  
Osaka University  
Osaka 565, Japan

Makoto TSUTSUMI  
Faculty of Engineering and Design  
Kyoto Institute of Technology  
Kyoto 606, Japan

## ABSTRACT

An optically-controlled microstrip line coupler is analysed based on Galerkin's method in the spectral domain. The scattering parameters of ports are derived as a function of plasma density in semiconductor substrate. Results are confirmed by experiments in the frequency band from 1 to 15 GHz.

## INTRODUCTION

Recently semiconductor waveguides with high resistivity have been studied extensively in the millimeter wave integrated circuit. One interesting aspect of waveguides is the optical control of phase and amplitude of wave propagation. [1] The principle is to use optical injection of plasma by illuminating the waveguide with above bandgap radiation thereby changing the dielectric constant and conductivity of semiconductor.

This paper discusses about an optically-controlled microstrip line coupler. Theory is based on Galerkin's method in the spectral domain [2] and experiments are carried out using high resistivity silicon substrate and Light-Emitting Diode (LED) arrays.

## THEORY

Figure 1 shows the cross section of the microstrip line coupler. Two microstrips having width  $2w$  are separated by distance  $2c$ . The semiconductor substrate consists of two layers. When its surface is illuminated with light, the upper layer of the substrate is assumed to be covered with plasma. It is also assumed that the depth of injected plasma layer  $t_p$  is uniform extent in the  $x$  and  $z$  directions.

The permittivity of the plasma layer is given by [1]

$$\epsilon_p = \epsilon_s - \sum_{i=e,h} \frac{\omega_{pi}^2}{\omega^2 + \nu_i^2} \left( 1 + j \frac{\nu_i}{\omega} \right) \quad (1)$$

$$\omega_{pi}^2 = n_p e^2 / \epsilon_0 m_i^*$$

where  $\omega_{pi}$  is plasma frequency and  $\nu_i$  is collision frequency.

The Fourier transform of vector potentials of magnetic and electric type is defined by

$$\tilde{\Phi}(n, y) = \int_{-a}^a \phi(x, y) \exp(j k_n x) dx \quad (2)$$

Eliminating unknown amplitude coefficients of fields with boundary conditions, we obtain

$$\begin{aligned} \tilde{G}_{11} \tilde{J}_z(n) + \tilde{G}_{12} \tilde{J}_x(n) &= \tilde{E}_z(n, y=d) \\ \tilde{G}_{21} \tilde{J}_z(n) + \tilde{G}_{22} \tilde{J}_x(n) &= \tilde{E}_x(n, y=d) \end{aligned} \quad (3)$$

where  $\tilde{J}_z$  and  $\tilde{J}_x$  are the Fourier transform of the current components on two strips.  $\tilde{G}$  is the Fourier transform of Green's functions. Galerkin's procedure is applied in (3) in order to obtain the determinantal equation.  $J_x$  and  $J_z$  are expanded in terms of basic functions as

$$J_z(x) = \sum c_m J_{z,m}(x), \quad J_x(x) = \sum d_\mu J_{x,\mu}(x) \quad (4)$$

where  $c_m$  and  $d_\mu$  are unknown coefficients. Chebyshev's polynomials should be chosen as basic functions  $J_{z,m}(x)$  and  $J_{x,\mu}(x)$ . After substituting (4) into (3) we take the inner products with the basic functions. This yields the dispersion relation.

Scattering parameters including loss may be defined as

$$\begin{aligned} |S_{31}| &= \exp(-\bar{\alpha} l_T) \left| \cos \frac{\Delta\beta}{2} l_T \right| \\ |S_{41}| &= \exp(-\bar{\alpha} l_T) \left| \sin \frac{\Delta\beta}{2} l_T \right| \end{aligned} \quad (5)$$

$$\bar{\alpha} = \frac{1}{2} (\alpha_e + \alpha_o), \quad \Delta\beta = (\beta_{re} - \beta_{ro}) - j(\alpha_e - \alpha_o)$$

where suffixes  $e$  and  $o$  show the even and odd modes respectively, and  $l_T$  is the coupling length.

For the numerical evaluation, we have assumed that the thickness of the substrate is 0.2mm with dielectric constant 11.8 and the plasma thickness  $t_p$  is 0.02mm. Plasma density, the density per unit area, is defined by the product of  $n_p$  and  $t_p$ . The number of expansion functions of currents is two for  $J_z(x)$  and one for  $J_x(x)$ . The convergence of the solution is confirmed by increasing matrix size up to  $6 \times 6$ . The matrix size of  $3 \times 3$  is used in the following calculations.

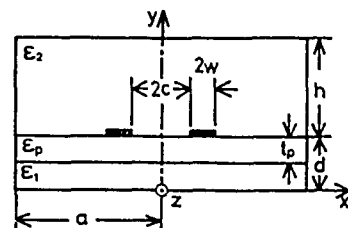


Fig.1 Cross section of coupled microstrip lines.

In Fig.2 scattering parameters of S31 and S41 are plotted versus plasma density  $n_p \cdot t_p$  for two coupling lengths  $l_T$ . It is clear that S41 can be tuned from -30 to -11dB by changing plasma density over  $10^{14}/\text{cm}^2$ , whereas S31 changes from 0 to -10dB with increasing small loss. This phenomenon is useful for optically-controlled coupler application.

### EXPERIMENTS

Figure 3 shows an experimental setup of the optically-controlled microstrip line coupler. The substrate in the coupling region consists of a layered structure with the high resistivity 2000-5000 $\Omega\text{cm}$  Silicon and Teflon. In the output and input ports the substrate consists of thick Teflon slab of thickness 0.4mm. The strip widths in coupling and port regions are 0.7mm and 1.3mm respectively.

Optical control is realized when coupling region between two strips is illuminated with 7 LED's. The maximum light power is 30mW for the current of 200mA.

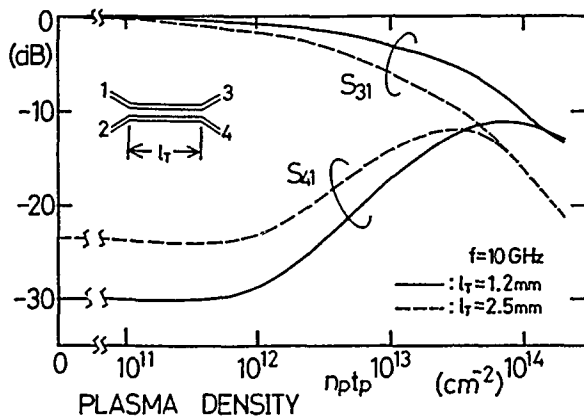


Fig.2 Variation of scattering parameters as a function of plasma density.

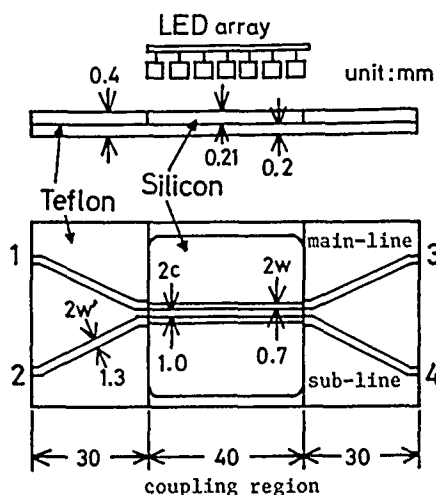


Fig.3 The optically-controlled microstrip line coupler.

Effects of light intensity on scattering parameters S31 and S41 are measured for the frequency band from 1 to 15 GHz as shown in Fig.4. Theoretical results are also shown in the figure with dashed lines. The amplitude of S41 increases with decreasing frequency, but abrupt changes of amplitude of S41 are observed. This may be attributed to the standing wave behaviour due to finite length of the mount structure. In the figure 0dB line in abscissa means the reference line without emitting the light. The overall agreement between experimental data and theory is observed.

From the experiment the plasma density induced by the LED is evaluated to be about  $3 \times 10^{11}/\text{cm}^2$  which is one-third as large as the theoretically estimated value.

### CONCLUSIONS

We have analysed coupling properties of two microstrip lines that contain a plasma dominated region by making use of the spectral domain method. Scattering parameters in each ports have been evaluated numerically as a function of plasma density. Experiments were carried out using high resistivity silicon and LED. The agreement of theoretical and experimental results was satisfactory. The plasma density observed from the experiments is one-third as large as the theoretically estimated value.

### REFERENCES

- (1) C.H.Lee, P.S.Mak and A.P.DeFonzo: "Optical Control of Millimeter-Wave Propagation in Dielectric Waveguides", IEEE Journal of Quantum Electronics, Vol.QE-16, No.3, pp.277-288 (March 1980).
- (2) T.Itoh and R.Mitra: "Spectral-Domain Approach for Calculating the Dispersion Characteristics of Microstrip Lines", IEEE Trans. on Microwave Theory & Tech. Vol.MTT-21, pp.496-499 (July 1973).

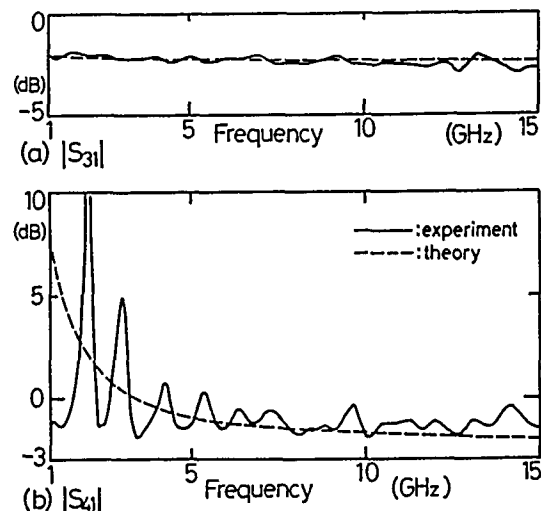


Fig.4 Experimental result of frequency dependence of scattering parameters.

## OPTICAL GENERATION AND DISTRIBUTION OF MICROWAVE SIGNALS

George J. Simonis and Kenneth G. Purchase

LABCOM, Harry Diamond Laboratories  
2800 Powder Mill Road  
Adelphi, MD 20783-1197

## ABSTRACT

We report the results of the optical generation of microwave signals superimposed as a modulation on an optical carrier by means of laser heterodyning. The modulated optical carrier can be easily distributed with fiber-optic cables. This approach offers microwave distribution advantages in size, weight, cost, and frequency diversity, which are desirable in important applications such as phased antenna control.

The technical area of the optical generation and distribution of microwave signals is undergoing very rapid growth in recent years as supporting technologies such as integrated optics, fiber-optic communications, and microwave and millimeter-wave monolithic integrated circuits (MIMIC) mature and find practical applications. Many researchers have contributed to this growth, but since space limitations do not allow a recounting here, note that reviews on this subject are available [1,2]. Our work involves the use of a relatively recent development, the diode-laser-pumped 1.06  $\mu\text{m}$  wavelength Nd:YAG ring laser [3]. This laser has inherent in its design a very pure single-mode (less than 5-kHz linewidth over 1 ms), a potential for tuning over as much as 100 GHz, good frequency stability (a few megahertz over minutes), high power efficiency, compact dimensions and isolation from optical feedback.

Fig. 1 presents the experimental configuration and our approach to the generation of microwave signals (solid lines). Fig. 1 also shows (with dotted lines and det .3 removed) how this approach could control a multi-channel phased-array antenna. Fiber-optic lines would run from the controller to optical detectors feeding MIMIC power amplifiers behind the radiating elements. The actual microwave power would come from the MIMIC power amplifiers. At this time, the two lasers being mixed are free-running and not intentionally coupled to each other in any way. The locking together of these lasers at the desired offset frequency can be expected to improve the microwave linewidth by orders of magnitude over the results reported here. Such an effort is under way. In a much more complicated configuration using less-ideal semiconductor diode lasers, a linewidth of less than 10 Hz has been reported at 35 GHz by other researchers using laser injection locking to enhance the coherence between the optical signals being heterodyned [4]. That configuration could not be easily tuned over large frequency ranges.

The principle employed for phase control in our work is to phase shift one of the optical carriers in one of the channels relative to other before the lasers are mixed in order to achieve a corresponding phase shift in the microwave heterodyne signal for that channel. Although mirror translation was used

to introduce the phase shift for the results reported here, integrated optical phase shifters are being incorporated and will be reported in the future. Optical beam steering techniques could also be considered for relative phase shift control between channels, as has been demonstrated by other researchers [5].

The optical heterodyne signal observed at 10 GHz is presented in Fig. 2. A Hewlett Packard 8566B spectrum analyzer was used to record these signals. Excellent signal-to-noise ratio and single-mode performance are observed on this scale. Microwave amplifiers were inserted between the detector and the spectrum analyzer for this measurement. Fig. 3 shows similar performance on an expanded frequency scale. On this scale, double peaks are apparent in the heterodyne signal about 50 dB below the main peak and between 200 and 300 kHz offset from the main peak. These peaks are due to relaxation oscillations in the individual lasers. Such amplitude instabilities are common in lasers and have a frequency determined by laser parameters such as gain, output coupling, and cavity dimensions. Laser power-leveling circuitry coupled to the pump diode laser has been shown to reduce this instability in these Nd:YAG ring lasers [6].

Fig. 4 is a partial display of the effortless microwave tuning range of this approach. Frequencies above 24 GHz require an external mixer on the spectrum analyzer. Frequency differences as large as 100 GHz should be achievable. Tuning down to dc was straightforward but appeared on a separate display range. The data in Fig. 4 were taken with no amplifiers attached to the detector.

Fig. 5 shows the output signal on an oscilloscope for three detectors and three output channels. The difference frequency was about 100 MHz here. In the figure, phase shifts of a fraction of  $2\pi$  were achieved by moving a mirror in one channel by fractions of the 1- $\mu\text{m}$  optical wavelength. Shifts of many multiples of  $2\pi$  were also easily demonstrated. In a practical application, integrated optical means would be used for optical amplitude and phase control. Thus, the same microwave phase shift could be achieved across a very broad microwave frequency range (perhaps as large as dc to 100 GHz) without need of a microwave phase shifter or change in much of the generating, controlling or distributing hardware. A bandwidth of 100 GHz amounts to only 0.03% of the carrier frequency for these 282-THz lasers. This offers some exciting possibilities in other broad-band microwave applications. The use of these signals as local oscillators for mixers at each of the receiving apertures would allow control of receive antenna beams as well. MIMIC technology, which is under development in a number of laboratories, would allow common apertures for the transmit and receive functions to be combined with this electro optical approach.

## REFERENCES

- (1) H. F. Taylor, *Optics News*, 22-25, (Jan 1988).
- (2) J. J. Pan, *Microwave Syst. News and Comm. Tech.*, 17, 30-43 (Oct 1987).
- (3) T. J. Kane and Robert L. Byer, *Opt. Lett.* 10, 65-67 (1985).
- (4) L. Goldberg, A. M. Yurek, H. F. Taylor, and J. F. Weller, *Electronics Letters* 21, 814-815 (1985).
- (5) M. Tainburrini, M. Parent, L. Goldberg and D. Stillwell, *Electronics Letters* 23, 680-681 (1987).
- (6) Lightwave Electronics, Mountain View, CA, private communications.

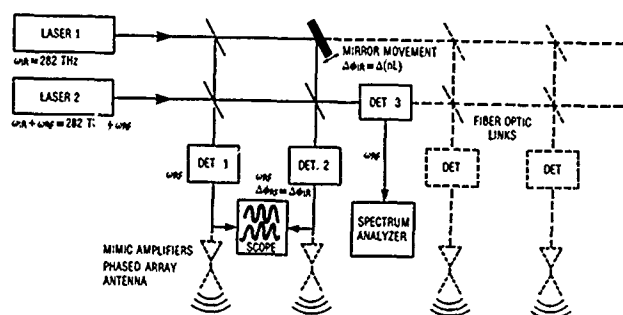


Fig. 1 Experimental configuration

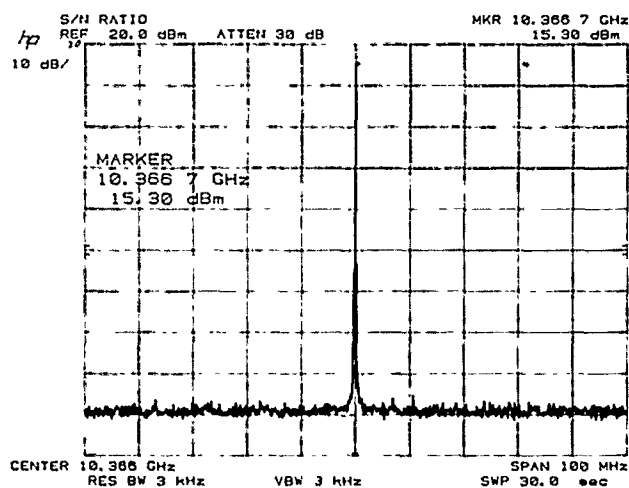


Fig. 2 Optical heterodyne signals at 10 GHz, 10 MHz/div, 10 dB/div.

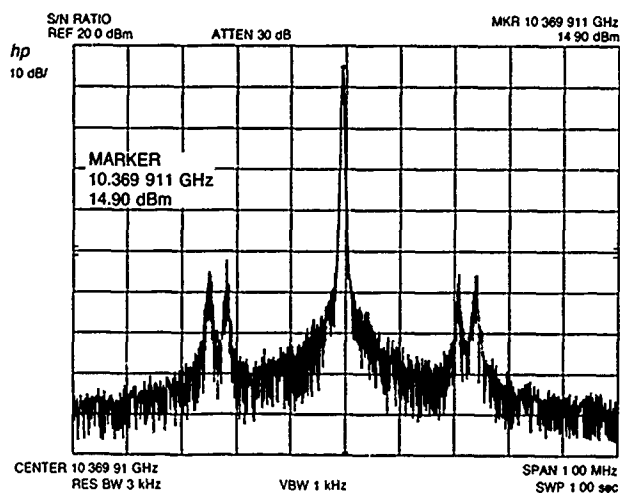


Fig. 3 Optical heterodyne signals at 10 GHz, 100 kHz/div, 10 dB/div.

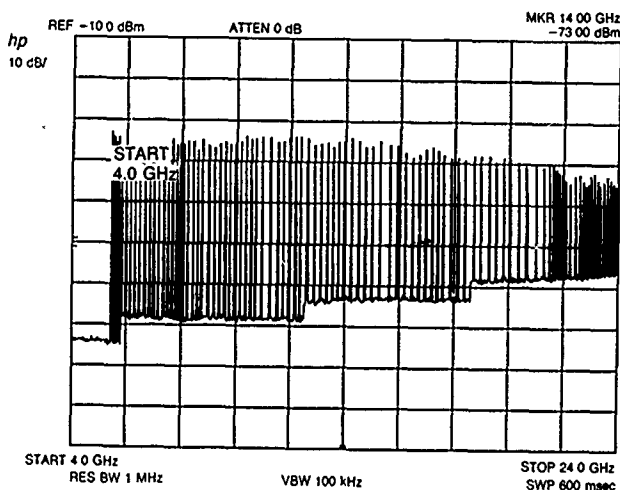


Fig. 4 Partial display of heterodyne tuning, 2 GHz/div.

Fig. 5 3-channel output of system. Middle channel was phase-shifted by mirror movement, 2 ns/div.

# INFLUENCE OF WAVELENGTH ON THE PERFORMANCE OF COLLECTIVE THOMSON SCATTERING FOR ALPHA-PARTICLE DIAGNOSTICS

P. P. Woskov, D. R. Cohn, J. S. Machuzak, and D. Y. Rhee

Plasma Fusion Center  
Massachusetts Institute of Technology  
Cambridge, MA

## ABSTRACT

The 10  $\mu\text{m}$  CO<sub>2</sub> laser, submillimeter-wave FELs, and millimeter-wave gyrotrons are all being proposed for collective Thomson scattering alpha-particle diagnostics. We will assess the relative advantages and disadvantages with wavelength scaling in the 5 mm to 10  $\mu\text{m}$  range for this diagnostic.

## INTRODUCTION

There has been considerable interest recently in the development of collective Thomson scattering as a diagnostic of confined alpha-particles in DT burning tokamaks (1,2). The implementation of this diagnostic has been proposed at wavelengths where high-power resources are presently available, namely the 10  $\mu\text{m}$  CO<sub>2</sub> laser (3) and the millimeter-wave gyrotron (4), at the extremes of the necessary wavelength range. It has also been claimed that the middle of this wavelength range is the optimum and the development of a  $\sim 100\mu\text{m}$  free electron laser (FEL) has been proposed (5). Also, CO<sub>2</sub> laser pumped molecular far infrared lasers (FIR) have a number of strong transitions and have been used for thermal ion collective Thomson scattering in tokamaks (6,7). With the choice of available wavelengths and source technologies increasing, an assessment is needed on the influence of wavelength on the performance of this diagnostic.

## ALPHA-PARTICLE COLLECTIVE THOMSON SCATTERING CONDITION

The first consideration in the choice of wavelength is the need to satisfy the condition for scattering from collective electron fluctuations. It should be satisfied with sufficient margin so that the fast alpha-particle component of the spectrum, for fractions as low as  $n_\alpha/n_e \approx 0.1\%$ , exceeds the thermal electron component. This condition can be defined in terms of the Salpeter parameter

$$\alpha = (|\mathbf{k}| \lambda_D)^{-1} \geq 3 \quad (1)$$

where  $|\mathbf{k}| = |\mathbf{k}_0 - \mathbf{k}_s| = (4\pi \sin \theta/2)/\lambda_0$  is the fluctuation wavenumber as determined by the scattering angle,  $\theta$ , and source wavelength,  $\lambda_0$ , and  $\lambda_D[\text{m}] = 7.43 \times 10^3 (T_e[\text{eV}]/n_e[\text{m}^{-3}])^{1/2}$  is the electron Debye length. The one exception to the above condition is when the  $\mathbf{k}$  to  $\mathbf{B}$  angle is near  $90^\circ$  (8). However, even in that case large  $\alpha$  is important to keep the signal strength up.

Figure 1 shows the tradeoff between scattering angle and wavelength in meeting this condition for a range of Debye lengths typical of tokamak plasmas. The longer the wavelength the larger the scattering angle, which would facilitate rejection of stray source radiation, improve spacial resolution, and improve the flexibility in adapting to a given port access on a tokamak. In addition, at a given scattering angle, longer wavelengths would increase the range of validity of the scattering condition to plasmas of higher temperatures and lower densities.

## SIGNAL TO NOISE

The scattered signal,  $P_S$ , is noiselike as well as the total background,  $P_N$ , due to plasma emission and receiver noise temperature. When  $P_S/P_N \ll 1$  and  $(\Delta f \tau) \gg 1$  then the signal to noise ratio is given by

$$S/N = \frac{P_S}{P_N} \sqrt{\Delta f \tau} \quad (2)$$

where  $\Delta f$  is a receiver frequency channel width and  $\tau$  is the integration time. Eq. 2 assumes signal modulation and lock-in detection are used if necessary.

The scattered signal is given by

$$P_S = P_0 n_e r_e^2 L \Omega \Gamma S(k, \omega) \quad (3)$$

where  $P_0$  is incident power,  $r_e = 2.82 \times 10^{-13}$  cm the classical electron radius,  $L \Omega \approx \lambda_0/(F\# \sin \Theta)$  from the antenna theorem where  $F\#$  is the receiver optics f-number,  $\Gamma(\Theta)$  is a geometrical form factor, and  $S(k, \omega)$  is a frequency form factor. Hutchinson (10) has shown that the mean of the frequency form factor for alpha-particles is

$$S_\alpha(k, \omega) = \frac{\lambda_0 n_\alpha}{2\pi v_\alpha n_e \sin \Theta/2} \quad (4)$$

when the distribution function is limited between  $-v_\alpha$  and  $+v_\alpha$  ( $v_\alpha = 1.3 \times 10^7$  m/s, 3.5 MeV alpha velocity) and there are no plasma resonances.

It can therefore be shown that the signal to noise ratio scales as

$$S/N \propto \frac{\lambda_0^{3/2}}{P_N \sin \Theta (\sin \Theta/2)^{1/2}} \quad (5)$$

Table 1

Comparison of Possible Sources for  
Collective Thomson Scattering Alpha-  
Particle Diagnostics

Source	$\lambda$ (mm)	Peak Power (MW)	Av. Power (W)
Gyrotron	10-1	1	$\geq 10^5$
FEL	10-0.01	$10^2$	$\geq 10$
Molecular FIR	0.152, 0.114, 0.090, etc.	2	$< 1$
CO <sub>2</sub>	0.01	$10^2$	$> 1$

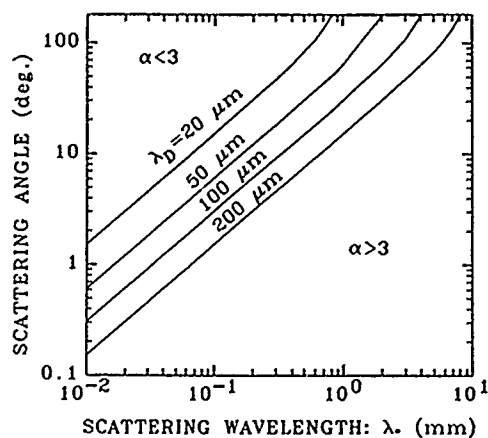


Figure 1  
Collective Thomson scattering condition for  
alpha-particle diagnostics except for  $\mathbf{k}$  near  
perpendicular to  $\mathbf{B}$

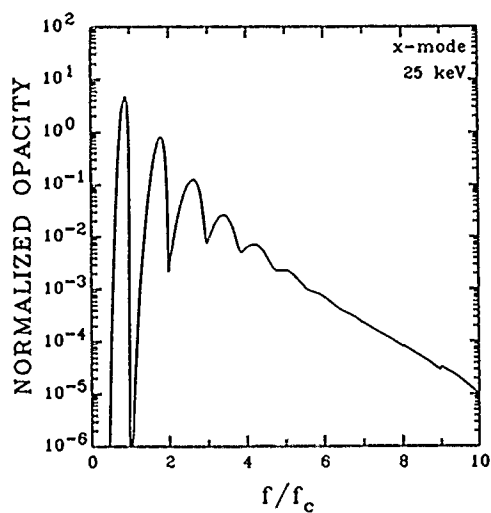


Figure 2  
Electron cyclotron emission/absorption for  
propagation perpendicular to the  
magnetic field

where we have taken into account that  $\Delta f \propto (\sin \Theta/2)/\lambda_0$ . The  $\lambda^3$  scaling given in (10), Eq. 20 is misleading because the receiver spot size,  $D$ , in the denominator is a function of  $\lambda$ . However, wavelength scaling stronger than  $\lambda^{3/2}$  is possible through  $P_N$ , if receiver temperature limited, since the quantum noise limit is proportional to  $1/\lambda$  and more sensitive receivers are in general available at longer wavelengths.

### PLASMA ACCESSIBILITY

The plasma medium will restrict the usable wavelengths. The absolute long wavelength limit will be the lower extraordinary mode (X-mode) cutoff frequency.

$$f_1 = [(f_c/2)^2 + f_p^2]^{1/2} - f_c/2 \quad (6)$$

Where  $f_c = 28$  GHz/Tesla, the electron cyclotron resonance and  $f_p = 8.97 \sqrt{n_e [m^{-3}]}$  Hz the electron plasma frequency. Refraction, however, will effectively limit the maximum wavelength to about twice the cutoff frequency.

Electron cyclotron emission/absorption (ECE) will be the next major restriction. Figure 2 shows a plot of normalized opacity versus frequency for X-mode propagation perpendicular to the magnetic field in a  $T_e = 25$  KeV plasma (11), Er. 14. This is the worse case for opacity when  $T_e < 50$  KeV, and there are no runaway electrons. The optical depth is obtained by multiplying the normalized opacity by the factor  $2\pi f_p^2 R / cf_c \approx 10^3$  where  $R$  is the tokamak major radius. For practical purposes the optical depth should be less than 0.01. Without a viewing dump, because of wall reflections, Figure 2 would also be valid for other propagation directions and for the O-mode.

The wavelengths that could be used for collective Thomson scattering are therefore: 1) between the fundamental electron cyclotron resonance and the X-mode cutoff, 2) between  $f/f_c = 1$  and 2 in O-mode to avoid the upper X-mode cutoff, or 3) above the 10th harmonic. For example, in a 10 Tesla compact ignition tokamak (CIT), these wavelengths would correspond to 2-1, 0.75, or  $\leq 0.1$  mm, respectively. To use the middle wavelength would require a vertically oriented scattering geometry with a viewing dump to avoid spacial overlap of the ECE due to the  $1/R$  magnetic field dependence not shown in Figure 2. Also, with higher electron temperatures,  $T_e > 25$  KeV, the lower two diagnostic wavelengths would become increasingly more difficult to use.

### TECHNOLOGY LIMITS

Table 1 lists possible source technologies for this diagnostic that are or expected to be available. High average power is just as important as high peak power because of the dependence of signal to noise ratio on integration time, Eq. 2. The gyrotron and expected performance of FELs have an advantage in this respect. The very low average power of molecular FIR lasers combined with their relatively low peak power would make this source technology a marginal candidate unless additional development is undertaken.

Low noise receiver bandwidth capability is another consideration. Schottky diode mixers available in the 10-0.1 mm wavelength range have bandwidths on

the order of 10 GHz, sufficient to detect all or a large part of the alpha-particle spectrum. In the 0.10-0.010 mm range, low noise wide bandwidth mixers are not available. At 0.010 mm cooled low noise HgCdTe mixers with bandwidths of a few GHz are possible, but because the alpha spectrum would be over 20 GHz wide at this wavelength, more than one receiver would be needed.

### CONCLUSIONS

The wavelength for collective Thomson scattering diagnostics of alpha-particles should be chosen as long as possible, consistent with plasma accessibility. The ease of meeting the collective Thomson scattering condition and signal to noise ratio are improved with wavelength. Also, the availability of high average power sources and low noise, wide bandwidth receivers is improved. The longest wavelength accessible to the plasma is therefore the optimum. Spacial resolution will not be an important wavelength limit because even with  $\lambda = 5$  mm the 3 dB Gaussian beam resolution is 4 cm with F#11 optics, quite suitable in large DT burning tokamaks. The use of shorter wavelengths is only justified if plasma emission/absorption or refraction are too severe at longer wavelengths.

### REFERENCES

- (1) L. Vahala, G. Vahala, and D. J. Sigmar, *Nucl. Fusion*, 1986, vol. 26, pp. 51-60 and MIT Plasma Fusion Center PFC/JA-88-4, submitted to *Nucl. Fusion*, 1988.
- (2) T. P. Hughes and S. R. P. Smith, *Joint European Torus*, JET-P(87)46, 1987, 17 pages.
- (3) R. K. Richards, C. A. Bennett, L. K. Fletcher, H. T. Hunter, and D. P. Hutchinson, this conference.
- (4) P. P. Woskov, *MIT Plasma Fusion Center*, PFC/RR- 87-16, 1987, 30 pages.
- (5) R. E. Shefer, R. L. Watterson, R. E. Klinkowstein, and J. S. Wurtele, *Bull. Amer. Physical Soc.*, 1988, vol. 33, abstract, Oct.
- (6) P. Woskoboynikow, W. J. Mulligan, J. Machuzak, D. R. Cohn, R. J. Temkin, T. C. L. G. Sollner, and B. Lax, *Europhysics Conference Abstracts*, 1983, vol. 7D, part II, pp. 81-84.
- (7) R. Behn, D. Dicken, J. Hackmann, S. A. Salito, and M. R. Siegreist, this conference.
- (8) R. E. Aamodt, Lodestar Research Corp., DOE/ER/53261-T2, 1988.
- (9) N. Bretz, *Princeton Plasma Physics Laboratory*, PPPL-2396, 1986, 14 pages.
- (10) I. H. Hutchinson, *Joint European Torus*, JET-R(87)07, 1987, 24 pages.
- (11) A. Nassri and M. Heindler, *Phys. Fluids*, 1986, vol. 29, pp. 3275-3280; note Eq. 22 is in error by a factor of  $\pi$  too large.



# A CO<sub>2</sub> LASER THOMSON SCATTERING DIAGNOSTIC FOR THE MEASUREMENT OF FUSION PRODUCT ALPHA PARTICLES\*

R. K. Richards, C. A. Bennett,<sup>†</sup> L. K. Fletcher,<sup>§</sup> H. T. Hunter, and D. P. Hutchinson

Oak Ridge National Laboratory  
Oak Ridge, TN 37831

## ABSTRACT

A Thomson scattering diagnostic for measuring the alpha particle velocity distribution is described. Calculations of scattering are made for a CIT type plasma using available CO<sub>2</sub> laser and heterodyne technology. Tests of a long pulse CO<sub>2</sub> laser, multichannel heterodyne detector, and an absorption cell for stray laser radiation are presented.

## INTRODUCTION

The next generation of fusion reactors has as its main physics goal the study of alpha-particle heating (1). To study these alpha particles we have examined the feasibility of a Thomson scattering diagnostic based on a high power CO<sub>2</sub> laser (2). The scattering geometry for this diagnostic is depicted in Fig. 1. The scattered power,  $P_s$ , into the solid angle  $d\Omega$  and over the frequency interval  $d\omega$  is given by (3)

$$P_s d\Omega d\omega = P_I r_0^2 n_e L d\Omega \frac{d\omega}{2\pi} S(\vec{k}, \omega) \quad (1)$$

where  $P_I$  is the incident laser power,  $r_0$  is the electron radius,  $n_e$  is the electron density,  $L$  is the scattering length, and  $S(\vec{k}, \omega)$  is the spectral density function which can be separated into contributions from the individual species in the plasma (4).

$$S(\vec{k}, \omega) = S_e(\vec{k}, \omega) + S_D(\vec{k}, \omega) + S_T(\vec{k}, \omega) + S_\alpha(\vec{k}, \omega) \quad (2)$$

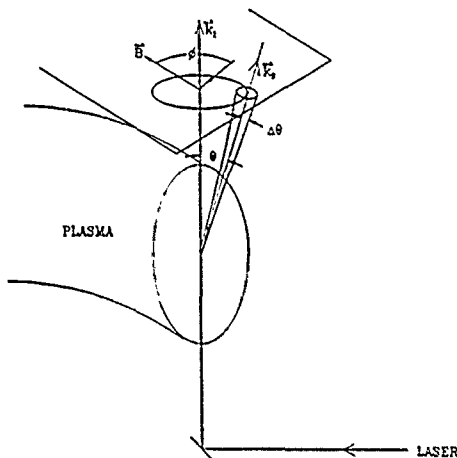


Figure 1.  
The scattering geometry.

The measurement of the alpha particles requires that  $S_\alpha$  form a substantial portion of  $S(\vec{k}, \omega)$ ; this permits the spectrum of the scattered power to be used in a measurement of the alpha particle velocity distribution. To achieve this, past studies have shown that detection of scattered radiation must be performed at small angles (2,4). For a 1° scattering angle and the plasma parameter expected in the Compact Ignition Tokamak (CIT) (1), a plot of the scattered power spectrum is given in Fig. 2.

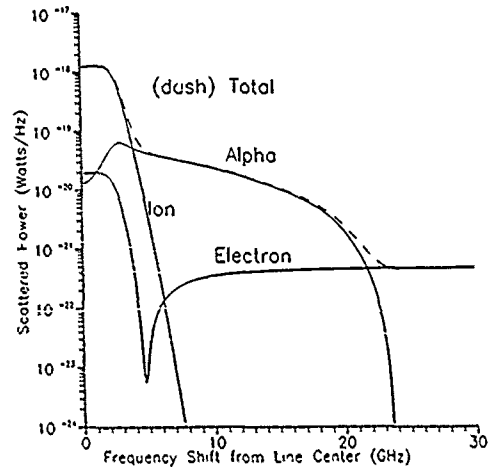


Figure 2.  
The scattered power spectrum for a CIT type plasma for  $P_I = 2$  MW and a 1° scattering angle.

Because of the small signal levels expected in the presence of a large incident laser beam, care must be taken to reduce any stray laser radiation to a minimum. The use of unstable resonator optics helps maintain a low divergent laser beam and heterodyne detection (5) rejects the collected stray laser power provided the stray power remains well below the 1 mW power level of the detectors local oscillator. To achieve this a resonant absorption cell has been investigated which acts as a notch filter at the CO<sub>2</sub> laser lines. This is similar to a previously proposed filter for use in the measurement of keV ions (6).

## RESULTS

Component tests of the pulsed laser, heterodyne detectors, and notch filter have proven successful. A complete systems test on a nonburning plasma is being developed which is to observe the Thomson scattering from the electrons.

## REFERENCES

\*This work was sponsored by the Office of Fusion Energy, U.S. Department of Energy, under Contract No. DE-AC05-84OR21400 with Martin Marietta Energy Systems, Inc.

†On sabbatical leave from the University of North Carolina at Asheville.

‡Tennessee Technological University, Cookeville, TN.

- (1) D. Post et al., PPPL-2389 (1986).
- (2) R. K. Richards, K. L. Vander Sluis, and D. P. Hutchinson, Feasibility of Alpha Particle Measurement in a Magnetically Confined Plasma by CO<sub>2</sub> Laser Thomson Scattering, ORNL/TM-10363, Martin Marietta Energy Systems, Inc., Oak Ridge Natl. Lab., August 1987.
- (3) J. Sheffield, Plasma Scattering of Electromagnetic Radiation (Academic, New York, 1975).
- (4) L. Vahala, G. Vahala, and D. J. Sigmar, Nucl. Fusion 25, 51 (1986).
- (5) C. A. Bennett, "Design and Calibration of a Two-Channel Low Noise Heterodyne Receiver at 10.6 Microns," 13th Intl. Conf. on Infrared and Millimeter Waves, Honolulu, Hawaii, Dec. 5-9, 1988.
- (6) N. Bretz and G. Taylor, PPPL Report #47 (1982).

# ECRH of Trapped Electrons in Tokamaks

S. P. Kuo  
Polytechnic University  
Farminale, NY 11735

M. C. Lee  
Massachusetts Institute of Technology  
Cambridge, MA 02139

## Abstract

Heating of plasma electrons by high power millimeter wave fields at the electron cyclotron harmonic resonance is studied. A mirror magnetic field is modelled for investigating the local trapping of electrons. Then, the suprathermal electrons generated by the ECRH of trapped electrons is analyzed. It is generally believed that these hot electrons can be used to produce the average minimum  $\bar{B}$  field configuration for stabilizing the interchange mode.

## 1. Introduction

Considerable interest in electron cyclotron resonance heating by high power *rf* waves is stimulated by the availability of gyrotrons<sup>1</sup> and the successful demonstration of ECRH in fusion research devices<sup>2,3</sup>. The high power level of the heating sources and the effectiveness of the ECRH heating schemes<sup>4,5,6</sup> suggest the possibility of generating energetic electrons. It has been seen experimentally that the created annuli of hot electrons provide stability on Elmo Bumpy Torus<sup>2</sup>.

The efficiency of electron heating depends on the rate of net energy gain throughout the entire period of the wave-particle interactions. Hence, a resonance condition assures the effectiveness of the ECRH process. However, an exact resonance condition is hard to achieve. A small mismatch from the resonance condition causes deterioration in the "effective" heating efficiency. This is the detuning effect introduced by, for instance, the inhomogeneity of the background magnetic field and the motion of the electron guiding center.

As shown in the previous work<sup>5</sup>, the detuning effect can be removed when a bounce motion is introduced to the guiding center motion of electrons. The bounce motion results from a simple harmonic oscillation of electrons along the uniform background magnetic field, which is imposed by an externally applied field. In the present work, the previous theory is extended by considering the trapped electrons in the local mirror field of a general magnetic field configuration. The proposed process is applicable to the heating and generating energetic electrons in the Tokamak type of fusion devices.

## 2. Formulation of the Theory

The equation of motion of an electron in the micro-wave fields and the background mirror magnetic field can be written as

$$\frac{d\vec{v}}{dt} = -\left(\frac{e}{m}\right)\{\vec{E}_1(\vec{r}, t) + \frac{1}{c}\vec{v} \times \vec{B}_1(\vec{r}, t) + \frac{1}{c}\vec{v} \times \vec{B}\} \quad (1)$$

where  $\vec{r} = (\vec{r}_\perp, z)$ ,  $\vec{r}_\perp$  and  $\vec{v}_\perp$  are related through the guiding center position  $\vec{R}_\perp$  as

$$\vec{r}_\perp = \vec{R}_\perp - \frac{1}{\Omega} \hat{z} \times \vec{v}_\perp(t) \quad (2)$$

the mirror magnetic field is given by

$$\begin{aligned} \vec{B} = & B_0[1 + (1/L^2)(z^2 - R_\perp^2/2) \\ & - (1/2L^2)(v_\perp^2/\Omega^2)]\hat{z} \\ & + (B_0/L^2\Omega)\vec{R}_\perp \cdot \hat{z} \times \vec{v}_\perp \hat{z} - (B_0/L)z \\ & \cdot [\vec{R}_\perp - (1/\Omega)\hat{z} \times \vec{v}_\perp(t)] \end{aligned} \quad (3)$$

where  $L$  is the scale length of the mirror field. It is convenient to introduce a drift velocity  $\vec{v}_D = -\langle \vec{F}_\perp \rangle \times \hat{z}/eB = -(\Omega_0/2\Omega^2)(v/L)^2\vec{R}_\perp \times \hat{z}$  and let  $\vec{v} = \vec{u} + \vec{v}_D$  where  $\vec{F}_\perp = (m\Omega_0/L^2\Omega)\vec{R}_\perp \cdot (\hat{z} \times \vec{v}_\perp)(\hat{z} \times \vec{v}_\perp)$ .

Consider an ordinary polarized heater wave propagating on the  $x-z$  plane with  $\vec{k} = \hat{x}k_\perp + \hat{z}k_\parallel$ . The wave fields can be then expressed as  $\vec{E}_1(\vec{r}, t) = (\hat{z}k_\perp/k - \hat{x}k_\parallel/k)E_1 \cos(k_\perp x + k_\parallel z - \omega t)$  and  $\vec{B}_1(\vec{r}, t) = -\hat{y}B_1 \cos(k_\perp x + k_\parallel z - \omega t)$  where  $cE_1/B_1 = \omega/k$ . It is found that

$$\begin{aligned} \frac{du_z}{dt} = & \Omega_0 \frac{B_1}{B_0} (u_z - (k_\perp/k) \frac{\omega}{k}) \\ & \cdot \cos(k_\perp x + k_\parallel z - \omega t) + \frac{F_\parallel}{m} \end{aligned} \quad (4)$$

and

$$\begin{aligned} u = & u_z - iu_y \\ = & \exp \left[ -i(\theta_0 + \int_0^t dt'(\Omega - \omega_D)) \right] \{u_{10} + \\ & \int_0^t dt' \exp \left[ i(\theta_0 + \int_0^{t'} ds(\Omega - \omega_D)) \right] \\ & \cdot (\Omega_0 B_1/B_0)(k_\parallel \omega/k^2 - u_z) \\ & \cdot \cos(k_\perp x + k_\parallel z - \omega t') \} \end{aligned} \quad (5)$$

where  $F_\parallel = -(m\Omega_0/L^2\Omega)v_\perp^2$ ,  $\omega_D = (\Omega_0/2\Omega^2)(v_\perp^2/L^2)$  and  $\Omega = \Omega_0[1 + (1/L^2)(z^2 - R_\perp^2/2)]$ .

Assuming that the guiding centers of the trapped electrons are distant from the central axis, viz.,  $|R_\perp(0)| \gg |z|$ , then  $\Omega \approx \Omega_0(1 - R_\perp^2(0)/2L^2) = \text{constant}$ . At resonances,  $\omega = n\Omega$ , equation

(4) becomes

$$\left(\frac{d^2}{dt^2} + \omega_B^2\right) = -2a(t) \sin(\Phi + \int_0^t \omega_B dt') \quad (6)$$

where  $\omega_B = (\omega_0/\omega)(v_z^2/L^2)$  is the bounce frequency,

$$a(t) = (\omega/k_\perp)(k_\parallel^2/k^2)\Omega(B_1/B_0) \cdot J_n(k_\perp R_{\perp 0})J_n(W)J_1(X) \sin n(\pi/2 + \theta_0 + \psi + \phi_0)$$

, where  $\theta_0 = \tan^{-1}(v_{y0}/v_{x0})$ ,  $\phi_0 = \tan^{-1}(R_{\perp y}(0)/R_{\perp z}(0))$ ,  $\psi = \tan^{-1}(u_y/u_x) - \tan^{-1}(v_{y0}/v_{x0}) - \Omega t + \int_0^t \omega_D dt'$ .

From equation (6), one can obtain

$$\begin{aligned} & |\cos[n(\psi + \theta_0 + \phi_0 + \pi/2)]| \\ &= 1 - \frac{J_n^2(W_0)}{J_n^2(W)} \sin^2[n(\theta_0 + \phi_0 + \pi/2)]^{1/2} \end{aligned} \quad (7)$$

and

$$\begin{aligned} \frac{d}{dt} W^2 &= \pm \frac{2neE_1}{m\Omega} \frac{k_\perp k_\parallel}{k} J_n(k_\perp R_{\perp 0}) J_0(X) \\ &\cdot [J_n^2(W) - J_n^2(W_0) \sin^2(n(\theta_0 + \phi_0 + \pi/2))]^{1/2} \end{aligned} \quad (8)$$

where  $W = k_\perp u_\perp/\Omega$  and  $\psi = \tan^{-1}(u_y/u_x) - \tan^{-1}(v_{y0}/v_{x0}) - \Omega t + \int_0^t \omega_D dt'$ . Equation (8) defines the heating rate of a single electron. Its analysis is given as follows.

### 3. Analysis

Only electrons outside the loss cone with  $(v_{z0}/v_{\perp 0}) < (1 - B_0/B_m)^{1/2}/(B_0/B_m)^{1/2}$  can be trapped locally and heated resonantly in a long enough period. Therefore, attention will be focussed on these electrons with  $|X| \leq |k_\parallel v_{z0}/\omega_{B0}| < (B_m/B_0 - 1)^{1/2} k_\parallel L(1 - R_{\perp 1}^2(0)/2L^2)^{1/2}$ .

The following relation can be derived from (8)

$$\begin{aligned} & \frac{dW^2}{[J_n^2(W) - J_n^2(W_0) \sin^2 n(\theta_0 + \phi_0 + \pi/2)]^{1/2}} \\ &= \frac{2neE_1}{m\Omega} \frac{k_\perp k_\parallel}{k} J_n(k_\perp R_{\perp 0}) dt \end{aligned} \quad (9)$$

Two cases, the fundamental ( $n = 1$ ) and the second harmonic resonance ( $n = 2$ ) heating of electrons, are considered.

For case 1:  $n = 1$

Integrating (12) yields

$$\begin{aligned} v_\parallel^2 &= v_{\perp 0}^2 + v_{\perp 0}(eE_1/m)(k_\parallel/k) \\ &\cdot J_1(k_\perp R_{\perp 0})t \cos(\theta_0 + \phi_0 + \pi/2) \\ &+ (e^2 E_1^2/4m^2)(k_\parallel/k)^2 J_1(k_\perp R_{\perp 0})t^2 \end{aligned}$$

and

$$T_\perp = T_{\perp 0} + (e^2 E_1^2/8m)(k_\parallel/k)^2 J_1^2(k_\perp R_{\perp 0})t^2$$

For case 2:  $n = 2$

$$\begin{aligned} v_\perp^2 &= v_{\perp 0}^2 [\cosh at \\ &+ \cos 2(\theta_0 + \phi_0 + \pi/2) \sinh at] \end{aligned}$$

and

$$T_\perp \simeq T_{\perp 0} \cosh <a> t$$

where  $<a> = a_1 <X>$ ,  $a_1 = \frac{\sqrt{6}\Omega_0\omega}{16} \frac{k_\parallel^2}{k_\perp^2} B_1/B_0 J_2(k_\perp R_{\perp 0})(k_\perp^2 T_{\perp 0}/m\Omega^2)^{1/2}$ ,  $<X> = (k_\parallel v_{z0}/<\omega_B>) \cos(a_1 k_\parallel \int_0^t dt'/<\omega_B>)$  and  $<\omega_B> = (\Omega_0 T_{\perp 0}/m\Omega L^2)^{1/2} [\cosh <a> t]^{1/2}$ .

### 4. Summary

The theory of electron heating via the cyclotron resonance mechanism has been formulated. The process under consideration is the interaction between electrons and the obliquely incident pump wave with ordinary polarization in a mirror magnetic field. The mismatched resonance condition in inhomogeneous plasmas, known as the detuning effect in the resonance heating of electrons by the obliquely incident waves, can be removed provided that the bounce motion of electrons occurs. The rates of electron heating for the fundamental and the second harmonic cyclotron resonances are derived in the previous sections. They will be used to evaluate the heating of trapped electrons in Tokamak devices. The numerical results will be presented and discussed in the meeting.

Acknowledgements. This research was sponsored jointly by the Air Force Office of Scientific Research, grant number AFOSR-85-0316 and the NASA grant NAG 5-1051 at the Polytechnic University, and by the NASA contract NAG 5-1055 at the Massachusetts Institute of Technology.

### References

1. K. E. Kreischer and R. J. Temkin, *Phys. Rev. Lett.*, **59**, 547 (1987).
2. R. A. Dandl et al., *Plasma Phys. Controlled Nucl. Fusion Res.*, vol. 2, IAEA-CN-3712-4, 365 (1979).
3. R. M. Gilgenbach et al., *Phys. Rev. Lett.*, **44**, 647 (1980).
4. S. P. Kuo and B. R. Cheo, *Phys. Fluids*, **24**, 784 (1981).
5. S. P. Kuo and B. R. Cheo, *Phys. Fluids*, **26**, 3018 (1983).
6. S. P. Kuo and B. R. Cheo, *Phys. Lett.*, **109A**, 39 (1985).

## MEGAWATT CW MILLIMETER WAVE TRANSMISSION SYSTEMS

M. Thumm, H.J. Barkley, W. Kasperek, G.A. Müller, P.G. Schüller

Institut für Plasmaforschung, Universität Stuttgart  
D-7000 Stuttgart 80, Fed. Rep. of Germany

## ABSTRACT

The properties of highly oversized tubular  $HE_{11}$  waveguide (circumferentially corrugated or dielectrically lined metal guide) and of quasi-optical Gaussian beam waveguide (using focusing metallic mirrors) are reviewed and compared in order to extract the specific advantages and disadvantages of these two approaches for use in low-loss megawatt CW millimeter-wave transmission systems. Manufacturing imperfections may limit the application of the convenient  $HE_{11}$  waveguide to the 1 MW / 100 to 140 GHz range. Quasi-optical transmission is ideal for multi-megawatt millimeter- and submillimeter-wave systems using beam combination. Depending on the power and frequency requirements and on the accessibility constraints, combined systems may be realized.

## INTRODUCTION

The efficient generation and transportation of high power radiation in the millimeter and submillimeter regions has received considerable attention for RF heating of plasmas in reactor-type thermonuclear fusion experiments. In magnetic-confinement devices as steady-state tokamaks and stellarators four tasks for this electron cyclotron resonance heating (ECRH) systems were identified [1]: plasma start-up (pre-ionization), bulk plasma heating (at fundamental or 2nd harmonic ECR frequency  $f_{ce}$ ), profile control and plasma current drive at upshifted ( $1.3 f_{ce} < f < 1.5 f_{ce}$ ) frequency. Depending on the desired heating scenario and on the magnitude of the confining magnetic field, powers between 10 MW and approximately 100 MW and frequencies from 100 GHz to almost 600 GHz are needed. Efficient application of ECR-waves requires the launching of an axisymmetric, pencil-like millimeter-wave beam into the plasma, with well-defined direction and with a specific, controllable polarization state. Tunable (or step-tunable) single-mode sources capable of high average power ( $\geq 1$  MW/unit) continuous operation in the frequency range increasing from 100 GHz to 600 GHz are currently under development. These investigations include circular-cavity gyrotrons, quasi-optical gyrotrons, cyclotron autoresonance masers (CARMs) and free-electron masers (FEMs) [see this Conf. Digest].

The down conversion of the complicated higher-order modes (e.g. rotating whispering gallery modes (WGMs)) of the future WGM gyrotrons and CARMs utilizing conventional in-waveguide mode transformers [2] with highly oversized waveguide diameter is practically impossible. At reduced diameters, the possibility of RF breakdown in the waveguide may be inevitable. Thus, present day solutions of microwave power transmission (oversized  $TE_{01}$  waveguide [2]) appear to be inadequate to satisfy future requirements. The improvement of the conversion efficiency of quasi-optical mode transducing antennas ( $\eta \approx 80\%$ ) [3] which are installed inside the source and directly convert rotating asymmetric higher-order modes into a linearly polarized, collimated free-space Gaussian beam is of particular importance for the

future prospects of ECRH. Since quasi-optical gyrotrons and FEMs may also emit a linearly polarized fundamental mode, there are two major concepts for low-loss high-power millimeter-wave transmission:

- (1) closed, highly oversized tubular  $HE_{11}$ -mode waveguide. The perfectly linearly polarized  $HE_{11}$  hybrid mode couples by 98 to 99 % to the free-space  $TEM_{00}$  mode.
- (2) quasi-optical  $TEM_{00}$  transmission through a Gaussian beam waveguide using focusing reflectors as phase correcting elements [4].

This paper compares these two approaches and discusses their specific advantages, disadvantages and limits. Both systems may be designed without vacuum windows at the output of the sources and at the input ports of the plasma vessel. However, if ceramic MW/CW millimeter wave windows (e.g. cryogenic sapphire windows) would be available, this would simplify the handling of the ECRH system since then the problem of tritium contamination must not be faced.

HIGHLY OVERSIZED TUBULAR  $HE_{11}$  WAVEGUIDE1. Properties of Overmoded Circular  $HE_{11}$  Waveguide

Two major possibilities for a closed waveguide propagating the  $HE_{11}$  hybrid mode at CW powers around 1 MW (I.D. = 70 - 90 mm) and frequencies up to approximately 140 GHz have been considered:

- corrugated circular metal waveguide [2]
  - dielectrically coated circular metal guide [5].
- At  $f = 140$  GHz and I.D. = 88.9 mm the  $HE_{11}$  hybrid mode exhibits the following features:

- (a) ohmic attenuation:
  - corrugated Cu-waveguide (slot depth  $d = \lambda/4$ ):  
 $\alpha = 5 \cdot 10^{-5}$  dB/m,
  - dielectrically lined ( $Al_2O_3$ ) Cu-waveguide [5]  
 $(\tan \delta = 1.14 \cdot 10^{-3}, \epsilon_r = 8.8, d = 0.095 \text{ mm})$ :  
 $\alpha = 3 \cdot 10^{-4}$  dB/m,
- (b) maximum electric field on axis at 1 MW power:  
 $E_{\max}(0) = 7$  kV/cm,
- (c) maximum electric field at the waveguide surface:  
 $E_{\max}(a) = 70$  V/cm,
- (d) broadband characteristics from 80 - 170 GHz.

By reducing the slot depth to  $d = 0.3 \lambda/4$  and choosing a lower conductivity material for the waveguide (e.g. stainless steel), the guide acts as a mode filter for higher order spurious modes, while the attenuation of the  $HE_{11}$  mode remains negligible. Several possibilities to manufacture corrugated or dielectrically lined waveguide are being investigated.

## 2. Quasi-Optical Waveguide Bends

The highly oversized dimension of the waveguide makes it possible to use quasi-optical (mirror) bends. The main advantages of such  $HE_{11}$  mitre bends are the compactness (flexible geometry) and large bandwidth. The theoretical mode conversion loss for a plane  $HE_{11}$  mitre bend is given by the following asymptotic formula (H- and E-plane) [6]:

$$P_c(\text{dB}) = [\lambda/(a \cdot \sin \phi)]^{3/2}, \quad (1)$$

where  $\phi$  is the bend angle and  $a$  the waveguide ra-

dus. Our measurements are in good agreement with this expectations. The ohmic attenuation at the plane Cu-mirror of the bend is described by:

$$H\text{-plane bend: } P_H(\%) = 0.37 \cdot S \cdot (1/3\lambda)^{1/2} \cdot \cos \phi \quad (2)$$

$$E\text{-plane bend: } P_E(\%) = 0.37 \cdot S \cdot (1/3\lambda)^{1/2} / \cos \phi \quad (3)$$

where the factor  $S = 1.5-2$  refers to the non-ideal conductivity (surface roughness). The expected total losses for a  $90^\circ$  HE<sub>11</sub> mitre bend in a I.D. = 88.9 mm waveguide at 140 GHz are:

$$H\text{-plane bend: } P_L^H = 0.4 \% \quad (0.15 \% \text{ ohmic losses})$$

$$E\text{-plane bend: } P_L^E = 0.55 \% \quad (0.3 \% \text{ ohmic losses}).$$

The conversion losses (0.25 %) can be reduced by using phase corrected (curved) mirrors [6].

### 3. Influence of Imperfections

Conversion losses to spurious modes at junctions between different waveguide sections and mitre bends (abrupt tilts) scale with  $a/\lambda$ . Due to this scaling, the open quasi-optical beam waveguide becomes superior to the closed circular waveguide for frequencies above approx. 140 GHz and at powers in the multi-megawatt range (radius  $a$  must be larger).

## QUASI OPTICAL BEAM TRANSMISSION SYSTEM

### 1. Properties of Quasi-Optical Mirror Waveguide

The propagation of Gaussian beams has been treated extensively [7]. The maximum electric field strength  $E_0$  exists in the center of the reference plane (beam waist with radius  $w_0$ ). For  $w_0 = 0.1$  m and  $E_0 = 10^6$  V/m we have a peak power carrying capability of  $P_T(\text{peak}) = 42$  MW. The power density on the focusing metallic mirrors is much lower, so that reflector beam waveguides with very high power carrying capability can be set up. The losses of a beam waveguide arise from several contributions:

- The finite size of the reflectors (effective radius  $a$ ) leads to inevitable diffraction losses  $\Delta P/P > \exp(-2a^2/w^2)$  due to truncation of the beam (spillover) and due to the related change in the beam parameters ( $\approx 0.1$  % per reflector). Properly treated, the diffraction losses do no harm and, moreover, provide mode filtration.
- The ohmic losses are the same as in the case of the HE<sub>11</sub> mitre bend (see the preceding chapter)
- Phase errors due to the non-ideal shape of the quadratically corrected reflectors and due to misalignment of the guide lead to conversion of the TEM<sub>00</sub> mode into higher-order modes, which are strongly attenuated by diffraction ( $\approx 0.2$  % per reflector)

The feasibility of reflector beam waveguides for millimeter-wave power transmission was demonstrated experimentally at 140 GHz [4]. The measured total transmission losses including the coupling losses from HE<sub>11</sub> waveguide launchers are in good agreement with the theoretical values.

### 2. Universal Polarizer

A quasi-optical approach to obtain any desired polarization state (rotated linear, elliptical or circular) from the linear polarization of the millimeter-wave source output coupler is the use of a corrugated surface reflector having fixed groove depth, combined with a polarization rotator [8]. The rotatable device consists of a smooth roof-top mirror facing a flat corrugated surface (see Fig. 1). A

corrugation period of almost  $0.6 \lambda$  (with equal groove and tooth width) and an electrical slot depth of approximately  $0.2 \lambda$  is chosen. The structure has wide band characteristics ( $\Delta f/f \approx 10 - 15$  %).

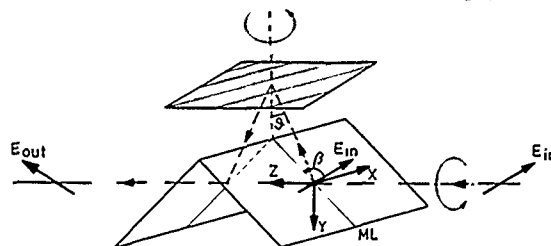


Fig. 1 Schematic of the universal polarizer

## COMPARISON OF THE TWO OPTIONS

Both high-power transmission concepts have similar losses (0.5 - 0.6 % per reflection section), they simply perform bends to overcome obstacles and provide the possibility to use specific mirrors as quasi-optical hybrid couplers [7] for on-line power monitoring purposes. If quasi-optical mode converters are utilized as gyrotron output mode couplers, both approaches include a quasi-optical feeder which forms the Gaussian beam (mode matching mirrors). In most cases both concepts will use the quasi-optical polarizer and quasi-optical wave launching antennas. Depending on the particular accessibility constraints of the plasma experiment, a combined transmission system may be realized.

The advantages of the tubular HE<sub>11</sub> waveguide are:

- very compact and flexible geometry (mitre bends)
- inherent RF shielding
- no need for remotely controlled alignment and adjustment
- broadband characteristics
- mode selective absorbers are feasible, but manufacturing imperfections may limit its usage to the 1 MW / 100 to 140 GHz range.

The quasi-optical reflector beam waveguide exhibits the following advantageous features:

- very high power capability
- inherent mode filtering properties due to out-scattering of unwanted higher order modes
- polarizers and power combiners [9] are feasible
- no need for special waveguide sections for compensation of thermal expansion.

Such systems are ideal for multi-megawatt millimeter and submillimeter-wave transmission with beam combination. A broadband mirror waveguide is not very easy to realize. The only solution is to design a confocal beam waveguide [7] which needs many more mirrors than a quasi-optical waveguide with large mirror distances (higher losses and costs).

## REFERENCES

- [1] W.M. Nevins, ITER CD&H TechMeet, Garching, 1988.
- [2] M. Thumm, Int. J. Electronics, 1986, 6, p. 1135.
- [3] S.N. Vlasov et al., Radio Eng. Elect. Phys., 1975, 20, p.14.
- [4] W. Kasperek et al., Conf. Digest 11th Int. Conf. Infr. and Mill. Waves, Pisa, Italy, 1986, p.212.
- [5] F. Krahn, NTZ Archiv, 1980, 2, p. 7.
- [6] R.B. Vaganov, Radio Eng. Elect. Phys., 1973, 18, p. 137 and p. 170.
- [7] E.C. Okress, ed., Microwave Power Engineering, Vol. 1., Academic Press, 1968.
- [8] L.H. Johnson, Appl. Optics, 1977, 16, p. 1082.
- [9] J.B. Beyer et al., IEEE Trans. PS, 1983, 11, p.255.

## LOW LOSS BROADBAND MULTIMODE CIRCULAR CORRUGATED WAVEGUIDE PERFORMANCE

A. Cavallo, J. Doane\*, R. Cutler, J. Brenner\*\*, Princeton Plasma Physics Laboratory, Princeton, NJ 08540 USA, \*General Atomics, La Jolla, CA. USA  
\*\*Brenner Tool and Die, Croydon, PA. USA

### ABSTRACT

A 30 meter long circular corrugated waveguide run (i.d.=6.35 cm) with a corrugation period and depth of 250 $\mu$  has been fabricated. It is designed for low loss (<0.01 dB/m) multimode operation over the frequency range of 75-575 GHz. It will be installed on TFTR (Tokamak Fusion Test Reactor) for use in electron cyclotron emission measurements. Results will be compared to those obtained using conventional tall rectangular C-band waveguide.

### INTRODUCTION

Electron temperature measurements from blackbody electron cyclotron emission have proven to be very useful for understanding tokamak plasmas. A critical component of the instrumentation necessary for such measurements, especially for those instruments which must be calibrated absolutely, is the light transport system which brings the signal from the plasma to the radiometer. For best results this system must match the source to the instrument and its detector over the frequency range of interest.

The maximum power at the detector is determined by two effects: power coupled to a waveguide mode by a blackbody is  $kT_e$  per unit frequency and the number of modes (N) accepted by the detector is  $N = E/\lambda^2$ . Here  $E$  is the etendue of the detector, in this case about 0.2 cm<sup>2</sup>/str, and  $\lambda$  is the wavelength of interest. For TFTR,  $\lambda \approx 1$  mm (300 GHz), and up to twenty modes could be accepted by a properly designed instrument. The advantages of a multimode low loss broadband transmission line are clear for this case.

Rectangular copper waveguide in the tall mode is used at present on TFTR. Due to mode filtering and mode conversion in the seven miter bends in this waveguide run, it functions as a single mode system. Hollow dielectric waveguides are also limited to single mode operation in this case as well(1). A lens relay system (2), while useful over short distances, would have prohibitive losses for the required 30 meter run.

A solution to this problem was given by Doane (3), who showed theoretically that corrugated cylindrical waveguide could function as a low loss multimode broadband transmission line. For our region of interest, 75 GHz < f < 575 GHz, corrugations with a 0.01 in (250 $\mu$ ) pitch and depth machined inside a 2.5 in. id cylinder were necessary. This turned out to be a very difficult manufacturing problem.

This work was taken on as a challenge by a creative machine shop with state of the art tooling (4). After some unexpected experimentation, it was decided to fabricate the waveguide by machining a screw thread inside ten inch long sections of cylindrical aluminum tubing. Calculations by J. Doane indicated that this was an excellent approximation to the desired structure, and that effects such as polarization rotation would be negligible. Cost of the waveguide, including the end flanges, is about \$450/meter, a very reasonable figure.

### MEASUREMENTS

Single mode insertion loss measurements of the new corrugated waveguide at 60 GHz and 140 GHz have been completed. A gaussian beam (HE11 mode) from a corrugated horn was matched to the waveguide using plano-convex polyethylene lenses. The source was swept over 1 GHz around 60 GHz and over 0.5 GHz around 140 GHz to eliminate standing wave effects. A baseline was obtained by making measurements using two 10 inch sections of corrugated waveguide; sixty feet of corrugated waveguide and six miter bends were then inserted between these two sections and the resulting signal subtracted from the baseline to determine the system loss.

Insertion loss of the corrugated waveguide at 60 GHz, which is outside the range of good performance for the waveguide, was determined to be between 0.07 to 0.14 dB/m. Taking into consideration the decreased conductivity of aluminum at microwave frequencies and the behavior of wall currents in the sides and bottom of the corrugations, this result is in good agreement with theoretical expectations (3).

At 140 GHz a maximum insertion loss of 0.5 dB for 60 feet of corrugated waveguide plus six 90 degree miter bends was determined. This is in good agreement with calculations.

Multimode measurements using the new waveguide are to be undertaken; results will be reported.

### ACKNOWLEDGMENTS

We would like to thank Paul Waskov (MIT) for lending us the 140 GHz scalar horn and John Machuzak (MIT) for substantial help with the 140 GHz measurements. M. Thumm (Stuttgart) suggestion for the flanges for the corrugated waveguide resulted in a substantial saving for the project.

### REFERENCES

1. J.P.Crenn, IEEE Trans. on Microwave Theory and Tech., 27, 573, 1979.
2. F.J.Stauffer, Rev. of Scientific Instruments, to be published, 1988.
3. J.Doane, Infrared and Millimeter Waves, 13, 123, (1985).
4. Brenner Tool and Die, Croydon, PA.



## INITIAL OPERATION OF A POLARIZATION-CONTROLLED BEAMED ECH LAUNCHER\*

T. S. Bigelow, C. R. Schaich, T. L. White

Oak Ridge National Laboratory  
Oak Ridge, TN 37831

### ABSTRACT

A system for launching 53.2-GHz electron cyclotron heating (ECH) power is being installed on the Advanced Toroidal Facility (ATF) fusion experiment at Oak Ridge National Laboratory. The launcher provides a narrow linearly polarized beam. The plane of polarization is easily rotated. Measurements indicate that the launcher will have a -20 dB beam width of 15 cm at the plasma center and polarization purity of >97%.

The ATF (1) requires 53.2-GHz microwave power for ECH plasma ionization and heating; this power is generated by a 200-kW cw gyrotron. Theoretical ray tracing studies have shown almost complete first-pass power absorption is possible if the power is within the saddle point in the proper polarization (2). Therefore, a narrow-beam-width launcher with adjustable polarization is being developed. In ATF the confining magnetic field can operate continuously at 1 T or in long pulses at 2 T. Either second harmonic or fundamental ECH absorption occurs, depending on the field strength, and it is of interest to operate experiments using both values. With perpendicular propagation and low-field-side launch, the ECH power must be in the extraordinary mode (X-mode,  $E_{rf}$  perpendicular to  $B_0$ ) for second harmonic ( $\omega = 2\omega_{ce}$ ) or in the ordinary mode (O-mode,  $E_{rf}$  parallel to  $B_0$ ) for fundamental ( $\omega = \omega_{ce}$ ) operation. The magnetic field in ATF is formed primarily by helical windings, which produce a shear in the plane of the field along a radial chord. This shear may cause polarization rotation of the ECH wave as it travels through the outer plasma regions because of the unequal O- and X-mode phase velocities at higher plasma density (similar to Faraday rotation). The ECH resonance zone is a 10-cm-wide saddle point near the plasma center.

### LAUNCHER DESCRIPTION

Power is available from a Varian gyrotron oscillator in the  $TE_{02}$  mode in 6.35-cm-diam. waveguide. A rippled wall mode converter is used to convert the  $TE_{02}$  mode into the  $TE_{01}$  mode. A Vlasov launcher (3) converts the circular electric mode to a linearly polarized beam as shown in Fig. 1. A parabolic profile downtaper to 3.83 cm allows the Vlasov section to be shorter (45 instead of 150 cm) and reduces the beam waist size for a tighter focus at the

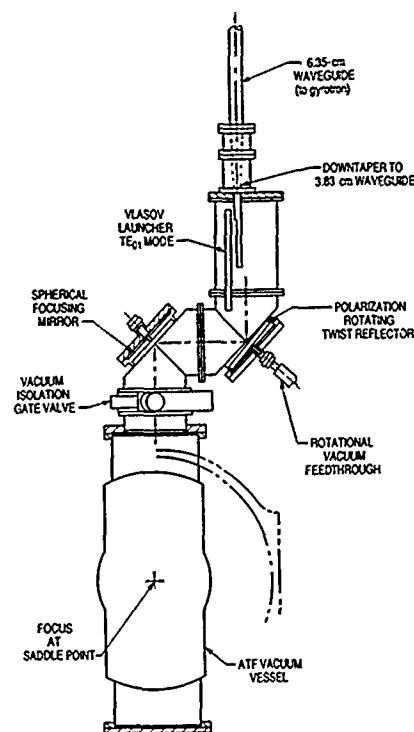


Figure 1  
View of the launcher configuration

plasma. The polarization angle can be set to any orientation by a grating reflector, which can be rotated using a vacuum feedthrough. Two designs for this grating will be tested. The first has a pure Teflon substrate, is inexpensive to build (using printed circuit techniques), and may be adequate for long pulses at high power. The second design is an all-copper machined grating. The polarization plane can be rotated under power during a plasma shot. A spherical reflector focuses the beam from the grating reflector to a spot at the ECH resonance point in the ATF vessel. The 160-cm curvature radius of this spherical reflector was determined in the laboratory to give the narrowest beam within the plane that corresponds to the radial direction in ATF, where the saddle point is narrow.

### RESULTS AND CONCLUSIONS

Laboratory measurements indicate the launcher -20 dB spot diameter is 15 cm and that worst-case polarization rotation is 97% as shown in Fig. 2. This plot was generated by scanning a waveguide detector at a distance comparable to the plasma center in two principal planes. Some tuning will be attempted to narrow the beam width by changing the reflector focal length. The initial design radius was determined using a vacuum-deformed

\*Research sponsored by the Office of Fusion Energy, U.S. Department of Energy, under contract DE-AC05-84OR21400 with Martin Marietta Energy Systems, Inc.

(1)Lyon, J. F., et al., Fusion Technol. 10 (8), p. 179 (1986).  
(2)Goldfinger, R. C. and Batchelor, D. B., Nucl. Fusion 27 (1), p. 31 (1987).  
(3)Vlasov, S. N. and Orlova, I. M., Radio Physics and Quantum Electronics 17 (1) p. 115 (1974).

Mylar membrane, which may have a slightly different shape than spherical. A 10-cm beam width (-20 dB) was possible when the membrane deflection was optimized. As shown in Fig. 2, the cross-polarization power measured with the polarization rotated 90°, is less than 2-3%. The launcher will be installed during a scheduled shutdown in September and it is hoped that some preliminary high-power measurements can be made soon after.

A plasma absorption diagnostic will be mounted opposite the launcher to measure the first-pass absorption. Measurements of the power and phase shift of fields in two planes will make it possible to determine the effects of the magnetic shear on the wave polarization and absorption efficiency for different launch polarizations.

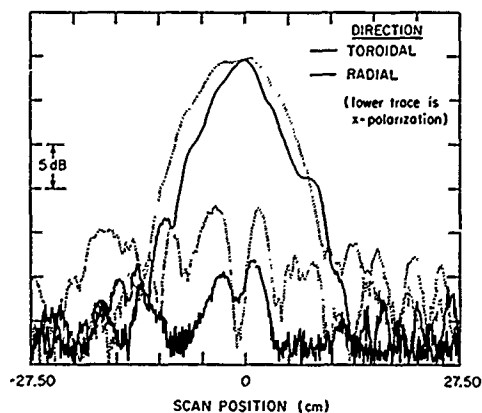


Figure 2  
Measured launcher pattern scan in two planes

# VERY SHORT QUASI-PERIODIC AND APERIODIC MODE CONVERTERS FOR 60 AND 140 GHz GYROTRONS\*

M. J. Buckley, G. H. Luo, and R. J. Vernon

Department of Electrical and Computer Engineering  
University of Wisconsin, Madison, Wisconsin 53706-1691 USA

## ABSTRACT

Very short, broad bandwidth designs will be discussed for varying-radius mode transducers for TE<sub>02</sub>-TE<sub>01</sub> and TE<sub>03</sub>-TE<sub>02</sub> mode conversion in a 2.779 cm diameter circular waveguide at 60 and 140 GHz and for TE<sub>15,2</sub>-TE<sub>15,1</sub> mode conversion in 2.54 cm diameter waveguide at 140 GHz.

## I. INTRODUCTION

Gyrotrons currently in use (and some being developed) for plasma heating have outputs in a TE<sub>0n</sub> mode in a highly overmoded circular waveguide. These modes are not normally suitable for plasma heating. Thus a TE<sub>0n</sub> mode output is commonly converted to the TE<sub>11</sub> mode in a smooth-wall circular waveguide or to the HE<sub>11</sub> mode in a corrugated circular waveguide with a system of waveguide mode converters. A typical TE<sub>0n</sub>-TE<sub>11</sub> waveguide mode converter system is shown in Fig. 1 [1].

In this paper, we present designs for mode transducers for 60 GHz and 140 GHz gyrotrons. The gyrotron's output mode is assumed to be in a 6.35 cm diameter circular waveguide which is commonly tapered to a 2.779 cm diameter. We will present designs for quasi-periodic varying-radius mode transducers to convert the TE<sub>0n</sub> mode into the TE<sub>0n-1</sub> mode and which in some cases include part, but not all, of the taper. The aperiodic mode transducers convert the TE<sub>0n</sub> mode into the TE<sub>0n-1</sub> mode and include all of the 6.35 cm to 2.779 cm taper. Experimental results will be presented.

Some gyrotrons under consideration or development have outputs in high-order rotating TE<sub>m1</sub> or TE<sub>m2</sub> modes. In particular, one 140 GHz gyrotron under development has its output in a rotating TE<sub>15,2</sub> mode. A sequence of waveguide mode converters to obtain the TE<sub>11</sub> mode does not appear to be practical for a gyrotron with a rotating TE<sub>15,2</sub> mode output so a rotating-mode type Vlasov launcher is planned for use with this tube. Although TE<sub>15,2</sub> Vlasov launchers are possible, they appear to produce a double-peaked output which would be undesirable. Thus we are developing a TE<sub>15,2</sub>-TE<sub>15,1</sub> waveguide mode converter for this application.

## II. VARYING-RADIUS MODE CONVERTERS

For varying-radius mode converters, the coupled mode equations for the TE<sub>0n</sub> modes can be written in the form [2]

$$\frac{dA_n}{dz} = -\gamma_n(z)A_n + \sum_{q \neq n} K_{nq}(z)A_q \quad (1)$$

where

$$K_{nq}(z) = \frac{1}{a} \frac{da}{dz} \frac{x'_{0n} x'_{0q}}{(x'_{0n})^2 - (x'_{0q})^2} \left[ \left( \frac{\beta_n}{\beta_q} \right)^2 + \left( \frac{\beta_q}{\beta_n} \right)^2 \right]. \quad (2)$$

\*This work was supported by the U. S. Department of Energy.

Here  $A_n$  is the complex amplitude of the TE<sub>0n</sub> mode, normalized such that  $|A_n|^2$  is the power transported in the z direction,  $a = a(z)$  is the radius of the converter (which is a function of z),  $x'_{0n}$  is the nth zero of  $J'_0(x)$  excluding the one at  $x=0$ , and  $\gamma_n(z) = \alpha_n + j\beta_n$  is the propagation constant of

the TE<sub>0n</sub> mode with  $\beta_n = \beta_n(z) = \sqrt{k^2 - (x'_{0n}/a)^2}$ , k being the free space wavenumber. In the coupled mode equations, modes traveling in the -z direction have been neglected. Backward traveling modes, calculated by an invariant imbedding technique [3], have been shown to be negligible in all the cases considered here except in Sec. IV which has not been checked yet.

## IIA. Quasi-Periodic Varying-Radius Mode Converters

For the quasi-periodic varying-radius mode converters, following Kovalev [4], we used a radial variation of the form

$$a(z) = a_1 \left\{ 1 + \frac{\epsilon_1}{a_1} [1 + C_1 \cos(H_2(z))] [1 \pm \cos(H(z))] \right\} \quad (3)$$

where  $\epsilon_1/a_1$  is the relative perturbation amplitude,  $C_1 \cos(H_2(z))$  is a small term used to suppress coupling to the TE<sub>0n+1</sub> mode, and  $H(z)$  is approximately equal to

$\int_0^z [\beta_{0n-1}(s) - \beta_{0n}(s)] ds$ . For a 1-1/2 period transducer, the plus sign in (2) is used and  $0 \leq H(z) \leq 3\pi$ . For a 2-period transducer, the minus sign in (2) is used and  $0 \leq H(z) \leq 4\pi$ .

Using the method outlined in the previous paragraphs, we have designed 1-1/2 and 2-period 60 GHz mode converters both having a numerically calculated efficiency of 99.6% with losses taken into account. These shorter mode converters also have 90% conversion efficiency bandwidths which are more than twice that of Moeller's pioneering 5-period design [5]. Preliminary measurements have been made on the 2-period converter in the reverse direction using the open-end radiation pattern method [6]. With an approximately 99% pure TE<sub>01</sub> mode input into the TE<sub>01</sub> end, a better than 99% pure TE<sub>02</sub> mode was found at the output (Fig. 2). Measurements taken with a k-spectrometer support these results. A single period TE<sub>02</sub>-TE<sub>01</sub> 60 GHz mode converter with greater than 97% efficiency has also been designed, fabricated, and tested.

## IIB. Aperiodic Tapered TE<sub>0n</sub>-TE<sub>01</sub> Mode Converters

The basis for the aperiodic TE<sub>0n</sub>-TE<sub>01</sub> converter designs can be seen by examining Fig. 3. Figure 3a shows a taper and a 2-cycle mode transducer. Figure 3b shows the diameter variation of a conventional 1-1/2 cycle device "unfolded" with two flat sections one-half beat wavelength long inserted. The aperiodic device is substantially shorter than the combined length of the taper and 2-period mode

transducer. Due to the constraint that the taper go from 6.35 cm to 2.779 cm, the ideal diameter variation of Fig. 3 was altered. Figure 4 shows the diameter variation of a 99.4% efficient 60 GHz  $TE_{02}$ - $TE_{01}$  mode converter-taper which is only about half the length of the separate converter and taper which it replaces. In addition the combined converter-taper has a 30% greater 90%-conversion-efficiency bandwidth. A design for a 140 GHz  $TE_{03}$ - $TE_{01}$  mode converter-taper combination has also been developed.

### III. A VARYING-RADIUS $TE_{15,2}$ - $TE_{15,1}$ MODE CONVERTER

A preliminary design for a 3-period  $TE_{15,1}$  -  $TE_{15,2}$  mode converter has been developed. Its length is less than 9 cm. It takes into account all 11 coupled modes ( $TE_{15,1}$  -  $TE_{15,6}$  and  $TM_{15,1}$  -  $TM_{15,5}$ ). It has a computed efficiency of greater than 91% with losses taken into account. The design procedure is made more difficult by a very strong coupling between the  $TE_{15,2}$  and  $TE_{15,3}$  modes. However, designs with higher conversion efficiency should be obtainable.

#### REFERENCES

- [1] R. J. Vernon and U. Rhee, Tenth International Conference on Infrared and Millimeter Waves, Orlando, FL, pp. 164-165, 1985.
- [2] H. G. Unger, Bell. Syst. Tech. J., Vol. 37, pp. 899-912, 1958.
- [3] R. Bellman and G. M. Wing, An Introduction to Invariant Imbedding, John Wiley and Sons, (New York), pp. 25-28, 1975.
- [4] N. Kovalev, J. Orlova and M. Petelin, Izvestiya VUZ. Radiofizika, vol. 11, pp. 449-450, 1968.
- [5] C. Moeller, Int. J. Electronics, Vol. 53, 587-593 (1982).
- [6] R. J. Vernon, W. R. Pickles, M. J. Buckley, F. Firouzbakht and J. A. Lorbeck, Mode Content Determination in Overmoded Circular Waveguides by Open-End Radiation Pattern Measurement, IEEE Int. Symposium on Antennas and Propagation, Blacksburg, VA, June 1987.

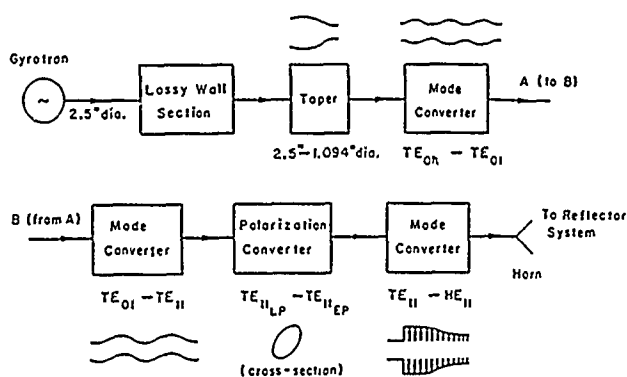


Fig. 1. A  $TE_{0n}$ - $HE_{11}$  mode converter system. The gyrotron output mode could be any  $TE_{0n}$  mode. For a  $TE_{01}$  mode gyrotron output, the first mode converter ( $TE_{0n}$ - $TE_{01}$ ) is omitted. For a  $TE_{0n}$  gyrotron output with  $n > 2$ , the  $TE_{0n}$ - $TE_{01}$  mode converter may have two or more stages. The minimum waveguide diameter after the taper was chosen to be 1.094". Larger minimum waveguide diameters are possible.

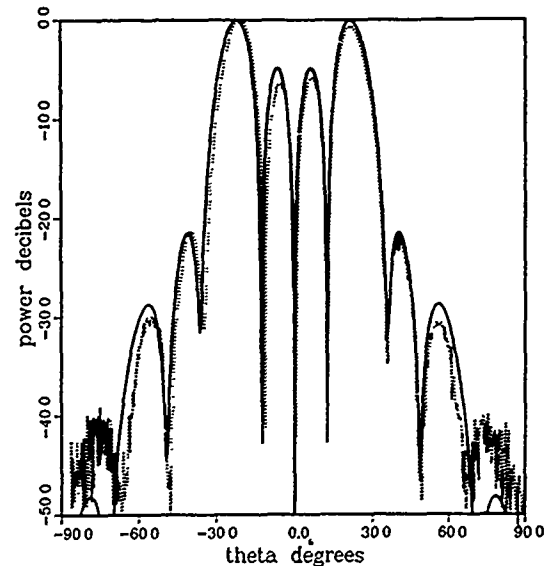


Fig. 2. Low-power open-end output radiation pattern taken at a distance of 1.6 m for the  $TE_{02}$ - $TE_{01}$  converter for a  $TE_{01}$  mode input. This pattern indicates about a 99%  $TE_{02}$  mode output.

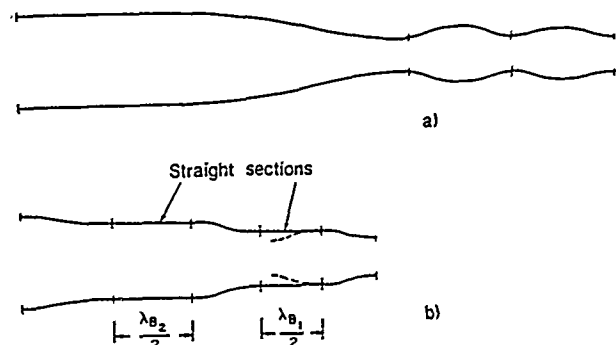


Fig. 3. (a) A downtaper and  $TE_{02}$ - $TE_{01}$  mode converter compared with (b) an unfolded periodic perturbation mode converter combining both of these functions and having a shorter length than a previous downtaper alone.

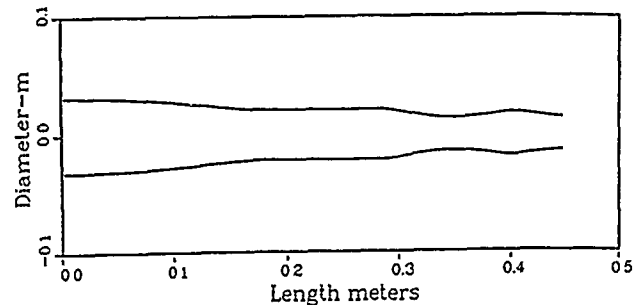


Fig. 4. Cross-sectional view of 60 GHz  $TE_{02}$ - $TE_{01}$  mode converter-taper. The device tapers from a 2.5" diameter waveguide to a 1.094" diameter waveguide. From two mode considerations, it can be shown that the flat section must be exactly one-half of a  $TE_{02}$ - $TE_{01}$  beat wavelength long. The device has an efficiency (including losses) of 99.4% and is 44.75 cm long.

## AN X-BAND VLASOV-TYPE MODE CONVERTOR

B.G. Ruth, C.D. Schlesiger, and R.K. Dahlstrom

Harry Diamond Laboratories  
Adelphi, MD

## ABSTRACT

The far-field radiation patterns from three different circular waveguide antennas are measured with an antenna pattern-mapping system. The radiating ends of the waveguide antennas are each cut at a specific angle relative to the center axis of the waveguide, forming the waveguide launcher component of a Vlasov-type mode convertor. This paper addresses the radiation patterns launched from the waveguide antennas as the first step in the design of a Vlasov-type mode convertor that will function at high power levels in the X-band frequency range (8 to 12 GHz).

## INTRODUCTION

Many of the high-power microwave (HPM) sources in an advanced state of development (e.g., the relativistic backward-wave oscillator (BWO), the magnetron, and the virtual cathode oscillator (vircator)) generate power in cylindrically symmetric TM modes. These modes are not suitable for directly driving antennas because of sidelobe generation, gain reduction, and inefficient power loading on the antenna aperture. One method of optimizing antenna performance in conjunction with these HPM sources is the use of a Vlasov-type mode convertor, which is a quasioptical device that converts circular TM or TE modes to an approximation of a plane-parallel linearly polarized Gaussian-profile beam [1].

Three different waveguide antennas were fabricated as candidates for the radiator component of a Vlasov-type mode convertor, which would ultimately be driven by a circular  $TM_{01}$  wave from an HPM source operating in the X-band frequency range. Each of these antennas consists of a 40-cm section of circular stainless steel pipe (inner diameter = 4.76 cm) with the radiating end sliced at an angle  $\alpha$  relative to the center axis of the pipe, resulting in an elliptical aperture (Figure 1). This aperture configuration is used because it minimizes the length of the aperture perimeter and thus the number of sharp edges, which is important at high power levels, where field intensification at sharp edges can result in arcing. Three slice angles were used in antenna fabrication:  $\alpha = 30^\circ$ ,  $45^\circ$ , and  $60^\circ$ .

## BASIC THEORY

The operating theory of a Vlasov-type mode convertor is derived from geometrical optics and is summarized in the Brillouin concept [2]. According to this theory, the electromagnetic waves within a circular waveguide can be represented as a superposition of plane waves whose wave vectors  $k$  form the angle  $\beta = \sin^{-1}[(\lambda_g p_{mn})/(2\pi r)]$  with respect to the center axis of the waveguide, where  $\lambda_g$  is the waveguide wavelength,  $p_{mn}$  is the root of the Bessel function equation  $J_m(p_{mn}) = 0$  (for  $TM_{mn}$  modes), and  $r$  is the inner waveguide radius. For the case of a  $TM_{01}$  mode of wavelength  $\lambda_g = 4.21$  cm (the output of an 8.6-GHz BWO that will be used to test the mode convertor at high power levels), the propagation angle  $\beta = 42^\circ$ . Ignoring diffraction effects due to the edges of the waveguide, the radiating waves are also launched at the angle  $\beta$  with respect to the center axis. This analysis, however, was originally designed for radiators with much higher frequency output ( $>60$  GHz), and thus should only serve as a guideline for predicting the behavior of the waveguide aperture at X-band frequencies.

## MEASUREMENTS

The radiation patterns launched from the aperture antennas were mapped in an anechoic chamber (in the far-field region) by a setup consisting of a multi-axis pedestal (upon which the waveguide radiators were mounted), an X-band receiving horn, and a computerized data-acquisition system. The pedestal can rotate in both the  $\theta$  and  $\phi$  planes through a complete  $360^\circ$ . A standard gain horn was first used in place of the waveguide radiators to establish the 0-dB isotropic gain level. Then a circular waveguide radiator with a straight-cut aperture ( $\alpha = 90^\circ$ ) was mounted, along with a  $TM_{01}$  mode launcher, upon the multi-axis pedestal. This measurement was to verify that a  $TM_{01}$  wave was actually being launched into the waveguide radiators with slant-cut apertures. Finally, each of these radiators, along with the  $TM_{01}$  mode launcher, was separately mounted upon the multi-axis pedestal, and antenna patterns were mapped (at 8.6 GHz) for each of the three radiators. In addition, patterns were mapped from the  $\alpha = 30^\circ$  radiator (a) at frequencies of 8.3 and 8.9

GHz, and (b) with dielectric windows of teflon and fiberglass inserted into the antenna apertures (at 8.6 GHz).

Figure 2 is a profile of the output (in the  $\theta$ -plane where  $\phi = 0^\circ$ ) from the straight-cut aperture antenna. If  $\theta = \phi = 0^\circ$  is defined to be on the center axis of the waveguide, then only the radiation between  $\theta = -90^\circ$  and  $\theta = +90^\circ$  need be considered, since it is approximately this portion that is launched into the slant-cut aperture radiators by the  $TM_{01}$  mode launcher. Ignoring diffraction effects, the radiation pattern presented in Figure 2 represents a reasonably pure  $TM_{01}$  mode. An example of typical measured patterns is shown in Figures 3(a) and 3(b), which are the radiation profiles from the  $\alpha = 30^\circ$  radiator with the 6-mm-thick fiberglass window in the aperture, swept in the  $\theta$ -plane at  $\phi = 0^\circ$  and  $\phi = 90^\circ$ . The profile in Figure 3(a) indicates a  $TM_{01}$  mode output in the symmetric  $\theta$ -plane at  $\phi = 0^\circ$ ; the two smaller peaks on either end are aperture effects and not higher modes, since the next propagating circular mode ( $TM_{02}$ ) has a waveguide cutoff frequency above 8.6 GHz. In Figure 3(b), the radiation is partially collimated along an axis centered on  $\theta = 35^\circ$ , which is approximately equal to the propagation angle  $\beta$  calculated above; the difference is probably due to the wavelength shift in the transition from waveguide to free space.

#### CONCLUSIONS AND PLANS

From the data taken (which will be presented in full in a later paper), it is evident that the  $\alpha = 30^\circ$  antenna forms the best collimated beam of radiation. There is also evidence that a properly configured dielectric lens mounted in the antenna aperture can enhance the boresight beam and suppress sidelobe gain.

In the next series of measurements, the near field regions of the antenna apertures will be mapped. This is necessary to determine the behavior of the partially collimated beam in the region where a parabolic (or other special contour) reflector will be placed to further collimate and/or mode-convert the radiation. Taken together, the waveguide radiator and reflector form a Vlasov-type mode convertor that will eventually be tested at high power levels.

#### REFERENCES

- 1) S.N. Vlasov and I.M. Orlova, "Quasioptical transformer which transforms the waves in a waveguide having a circular cross section into a highly directional wave beam," *Radiofizika*, Vol. 17, No. 1, pp. 148-154, January, 1974.
- 2) B.Z. Katsenelenbaum, *High-Frequency Electrodynamics*, Nauka, 1966.

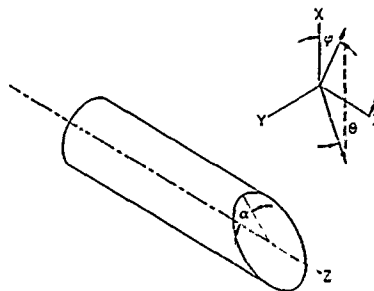


Figure 1. Radiator component of a Vlasov-type mode convertor.

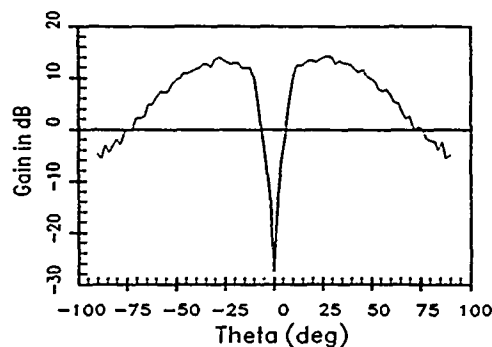


Figure 2. Far-field radiation pattern from a  $TM_{01}$  mode launcher.

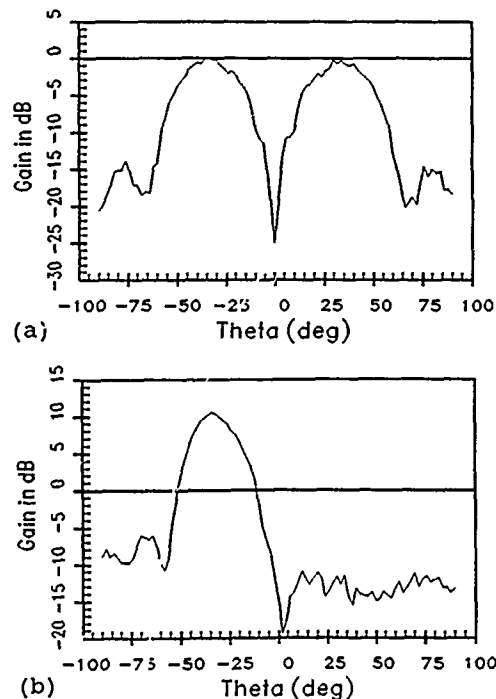


Figure 3. Far-field radiation patterns from a slant-cut antenna aperture ( $\alpha = 30^\circ$ ) with a fiberglass window at (a)  $\phi = 0^\circ$  and (b)  $\phi = 90^\circ$ .

## A Quasi-Optical Converter for Efficient Conversion of Whispering Gallery Modes into Narrow Beam Waves

A. Möbius, K. Kreischer, and R. Temkin  
Plasma Fusion Center  
Massachusetts Institute of Technology  
Cambridge, Ma, 02139

### Abstract

A quasi-optical converter for converting rotating whispering gallery modes into a linearly polarized quasi-Gaussian beam was designed and experimentally tested. The shapes of the launcher and the reflectors were optimized in order to increase the efficiency.

### Introduction

The goal of this work was the design and investigation of a quasi-optical system that would efficiently convert rotating whispering gallery modes produced by a step tunable gyrotron into a quasi-Gaussian beam. One type of converter, known as a Vlasov coupler [1], is shown in Fig. 1 and consists of a helical cut waveguide which serves as a launcher and a parabolic reflector. The radiation field of the launcher has been measured and compared with the theory. Encouragingly, the experimental results agreed well with the theory. To increase the efficiency, reflectors have been designed by means of geometric optics.

### Radiation Field of the Launcher

In order to calculate the radiation field of the launcher, two methods are possible: use of the wall currents of the coupler as the source, or applying the aperture field method. The second method proved to be more efficient, since the problem could be reduced to two dimensions, if the aperture is chosen to be the shaded surface in Fig. 2. Since the radius of the waveguide is not very large compared to the wavelength, the radiation field had to be calculated by vector diffraction theory. The formula used to calculate the field distribution was the Stratton-Chu formula [2]. For the far-field the Franz formula was more convenient [2].

Figure 3 shows plots of the equi-power lines of the far field of the  $E_\phi$  component, which contributes mainly to the radiation field, for the  $TE_{16,2}$  at 149 GHz and a waveguide radius  $R_w$  of 17 mm. It was found that the more oversized the waveguide, the higher becomes the ratio of the power of the  $E_\theta$  component to that of the  $E_\phi$  component. To achieve a highly polarized beam and to keep the converter dimensions to a reasonable size the output waveguide diameter should be only big enough that its wave-impedance comes close to that of the free-space impedance, which then reduces the reflection back into the waveguide.

### Measurements

Measurements were made using the rotating whispering gallery modes generated by the MIT megawatt gyrotron, which produced 600 kW during 3  $\mu$ sec. The frequency was step tunable from 126 to 149 GHz, which corresponds to the  $TE_{12,2}$  through the  $TE_{16,2}$  modes.

A straight pipe was attached to the window and the rotatable launcher was attached behind it. The window gap unfortunately created spurious modes which could be observed by far field scans or the evaluation of liquid crystal patterns. To keep the effect of spurious modes low the measurements were performed with the diode centered on the main lobe of the launcher. This was done by placing the diode at a fixed angle with respect to the launcher axis and rotating the converter. This angle is the same as the angle of the main lobe in the far field of a circular waveguide.

The circles in Fig 4 show an azimuthal scan of the  $E_\phi$  component of the  $TE_{16,2}$  mode, while the solid lines show the theoretically predicted results. The good agreement between theory and experiment indicated that the assumptions connected with the aperture field method are valid.

Because the angle  $\gamma$  the launcher has to be cut, see Fig 1, is independent of the mode as long as the gyrotron is operated near cutoff, the launcher is applicable for a variety of modes. We have confirmed this experimentally by step tuning from the  $TE_{12,2}$  mode at 126 GHz through the  $TE_{16,2}$  mode at 148.6 GHz. This means the launcher can be incorporated into the gyrotron vacuum system and the gyrotron can still be operated over a range of frequencies.

### Design of the Reflectors

As the radial index of the waveguide mode increases the RF field is no longer concentrated at the waveguide wall, and the line source assumption for  $TE_{m1}$  modes, which leads to a parabolic reflector, is no longer valid. To design a reflector for  $TE_{mn}$  modes, advantage was taken of the fact that rotating modes can be expanded in plane waves that propagate at the angle  $\gamma = \arctan(k_\parallel/k_\perp)$  to the waveguide axis, where  $k_\parallel$  and  $k_\perp$  are the wave propagation vectors in the axial and the perpendicular direction, and form a circular caustic at the radius  $R_c = R_w * m/X_{mp}$ , where  $R_c$  is the radius of the caustic, and  $X_{mp}$  is the  $p^{\text{th}}$  zero of the derivative of the Bessel function of the  $m^{\text{th}}$  order [3].

By the plane wave representation, it can be further shown that the phase varies linearly on the caustic. That part of the caustic which is bordered by the first ray no longer reflected by the waveguide wall and the last ray reflected by the edge is called the 'radiating caustic.' The phase front (dashed line in Fig 5), of the radiating caustic (solid line) can now be calculated and by means of geometric optics the reflector shape can be designed such that the output rays are parallel lines which have an approximately Gaussian transverse distribution.

Since the axial distribution of the aperture is uniform with a linear phase variation, the far field has several maxima in the lateral direction. The efficiency is reduced because the energy in the side lobes is lost. To increase the efficiency, a combination of mainly two ideas has been investigated. The first idea was to spread the  $k$ -vectors and the aperture field distribution by slightly tapering the launcher. A reflector then has to be designed such that the transverse energy distribution comes close to a Gaussian. Parameter variations show that this can be achieved by nonlinear tapering, where tolerances have to be kept extremely narrow. To reduce the energy in the remaining sidelobes the beam was spread out by using two reflectors.

### References

- [1] S. N. Vlasov et al, Radio Eng, Vol. 20, No 10, pp 14-17, October 1975
- [2] Jin Au Kong, Electromagnetic Wave Theory, pp 381 John Wiley & Sons, 1986
- [3] L. A. Weinstein, Open Waveguides and Open Resonators, pp 139, The Golem Press, Boulder, Colorado 1969

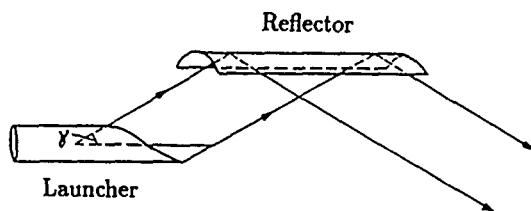


Fig 1: Vlasov Converter

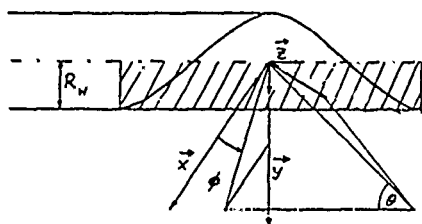


Fig 2: Launcher Aperture

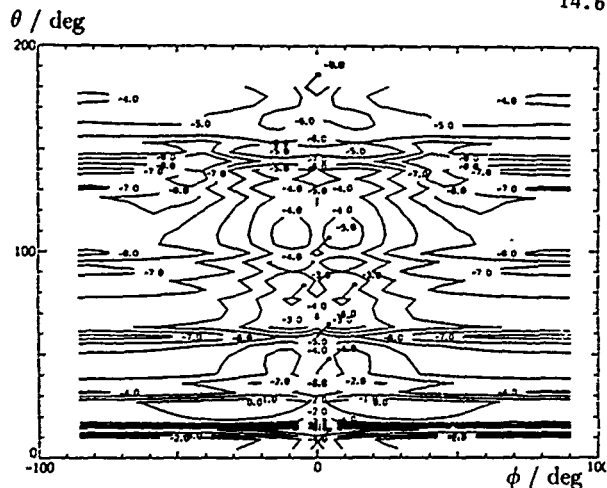


Fig 3: Equi-Power Lines of the  $E_{\phi i}$  Component of the Launcher (Counter Levels -10 dB)

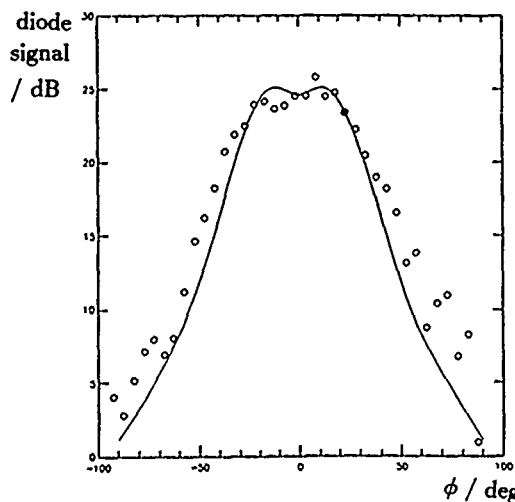


Fig 4: Calculated and Measured Dependence of the  $E_{\phi i}$  Component on the Azimuth

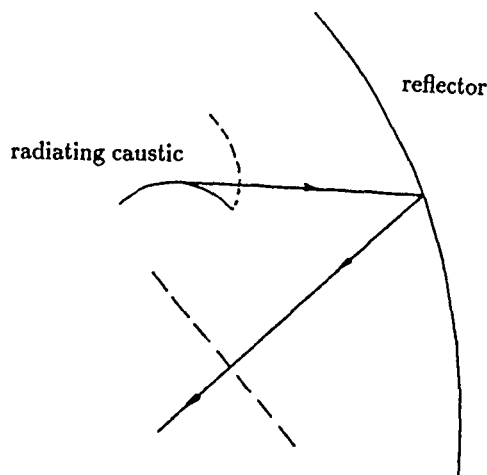


Fig 5: Radiating Caustic, Reflector (solid lines) and phase fronts (dashed lines)



## Design of the CIT Gyrotron ECRH Transmission System

J.A. Casey, P. Woskov, D. Cohn, R. Temkin

M.I.T. Plasma Fusion Center, NW16 167 Albany St., Cambridge, MA 02139

### Abstract

Plans for Electron Cyclotron Resonant Heating in the Compact Ignition Tokamak call for at least 10 MW at fields from 7T to 10T with extension to 40 MW possible. 1 MW CW Gyrotron sources for fundamental heating are currently in the design phase. The transmission system must accommodate these high powers in addition to the constraints of small space and access in a tritium environment. Quasi-optical and corrugated guide systems are under consideration, as well as hybrid designs. A preliminary design is presented, and options for alternatives are discussed.

### Introduction

Auxiliary heating will be required as a supplement to ohmic heating for ignition experiments in the Compact Ignition Tokamak (CIT). Calculations show that a minimum of 10–15 MW auxiliary heating (depending on the energy confinement scaling assumptions) will be required to heat to ignition (where the alpha heating power is equal to the plasma energy loss rate) with possibly 30–40 MW required. Baseline plans for CIT require 10 MW of ion cyclotron heating. Upgrade plans for increased ion cyclotron heating power, and/or for electron cyclotron resonance heating (ECRH) require up to 30–40 MW effective in magnetic fields from 7 to 10 T, with at least 10 MW introduced per  $35 \times 100$  cm port.

It has been proposed<sup>1</sup> that an ECRH system be developed for CIT based on 280 GHz, 1 MW, CW gyrotrons<sup>2,3</sup>. This gyrotron design incorporates a large cavity radius to reduce wall loading, and high ( $m \approx 70 - 80$ ) azimuthal and low ( $n \approx 4$ ) radial mode numbers to minimize mode competition. A helical Vlasov launcher<sup>4</sup> will be used to separate the radiation from the electron beam, generating a nearly-Gaussian beam (linearly polarized, peaked on axis). Frequency adjustment over the 7 to 10 T range may be possible using step-tuning<sup>5</sup>.

This power must be transmitted effectively from the gyrotrons to the tokamak. Due to neutron irradiation considerations, the gyrotron sources must be located a distance ( $\approx 17$  meters

lateral and  $\approx 10$  meters vertical) from the tokamak. The transmission line components must be compatible with operation in a neutron environment, and serviceable using proposed remote maintenance equipment. Frequency tuning and heating profile width adjustments are desirable, and may be required for effective heating, profile control, and plasma stability control.

### Techniques

Several transmission techniques are under consideration. These are: an optical mirror relay line propagating a linearly polarized gaussian beam, an overmoded corrugated metal or hollow dielectric guide propagating an  $HE_{11}$  mode, and an overmoded smooth wall metal guide propagating the circular  $TE_{01}$  mode. Output coupling via the quasi-optical helical Vlasov launcher favors the first two approaches. Hybrid systems are also possible, combining two or more of the above techniques.

Corrugated metal waveguide has been shown to be effective<sup>6</sup> in transmitting millimeter wavelengths with low loss over a long ( $\approx 10$  meter) path including mitre bends. The low-loss characteristics of corrugated guide are calculated to extend over a suitably wide bandwidth to apply to the CIT tuning requirements. The quasi-Gaussian radiation pattern produced by the Vlasov launcher should couple efficiently into the  $HE_{11}$  mode, however further R&D efforts will be necessary to optimize this. The narrow divergence ( $< 2^\circ$  for 3dB divergence of 280 GHz  $HE_{11}$  mode in a 2.5 inch guide) allows simple termination of the guide at the tokamak port as a launching antenna. Other advantages of corrugated guide are the compact size of the components, and the inherent self-alignment and beam enclosure for safety. Disadvantages include the large number of components at the tokamak port (where maintenance must be remotely accessible), and the inability to change the focussing of the launched beam.

A quasi-optical propagation scheme would use mirror relay lines to transmit power from the gyrotrons to the tokamak. Since the radiation is

ultimately launched from a final focussing mirror, the beam convergence at the plasma surface can be adjusted for an optimum heating profile. The major difficulty with quasi-optical propagation is the inherently larger system size, since the required diameter of mirrors increases with mirror separation due to diffraction. For 1 mm wavelengths and an 8 meter mirror to mirror separation, about six 22 cm diameter mirrors will be necessary for each transmission line. Although possible for a 10 MW system, the maintenance and alignment requirements of such a large system become formidable at 30–40 MW.

We present in figure 1 a preliminary design for a hybrid transmission system with the following features. Corrugated waveguide will be used between the gyrotrons and the beam-combiner, (discussed below). This optimizes space utilization in the gyrotron room of the CIT facility, and allows longer straight runs of waveguide than a quasi-optical system would allow. In the basement below the CIT cell, we launch from corrugated guide into a quasi-optical relay mirror system, combining beams from six gyrotrons into a single optical system. This has the advantage of reducing the number of components in the CIT cell to a single large ellipsoidal mirror (plus cooling and alignment hardware) for each transmission line. A 10 MW system could be built with two such sub-systems

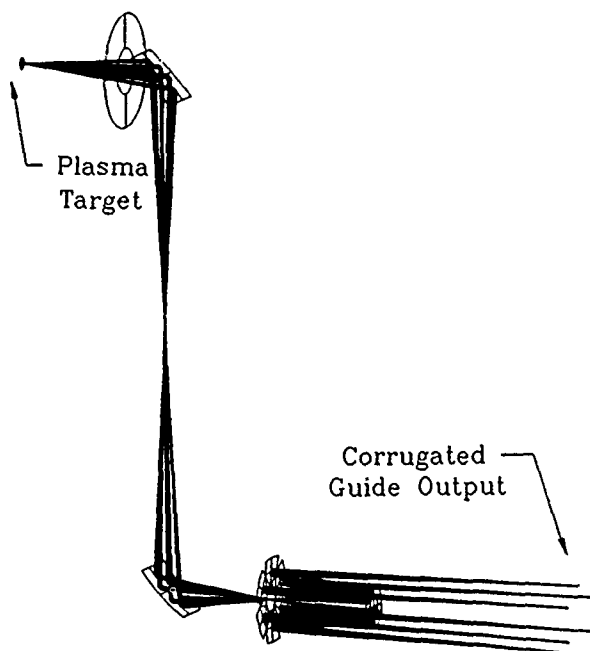


Figure 1. Preliminary design for a hybrid transmission system utilizing corrugated waveguide transmission into a beam combining assembly. The rays shown bound the 3dB pattern for 280 GHz.

launching into a single port.

It is important to note that the beams are not truly combined in this geometry, they merely share the same optical elements over the transmission path. It is also assumed that all the gyrotrons combined in one system will be independent oscillators, with frequency differences greater than the characteristic heating times of the mirror surfaces, so that interference patterns will not generate hot spots. Note that the 3dB beams shown are somewhat filamented at the mirrors, showing the discrete beam propagation paths. The 20dB patterns at lower frequency fill the mirrors and overlap considerably more. In this preliminary design, the two relay mirrors are ellipsoidal, as are the six independent collector mirrors. A plane mirror is used at the focus. Power densities are kept below 20 kW/cm<sup>2</sup>, and 99% efficiency is kept for  $f > 196$  GHz. (The ray tracing in this example accounts only for geometric optics; once a preliminary design is selected, the component parameters will be trimmed using more exact techniques.)

The choice of transmission line technology for the CIT ECRH system will ultimately depend on a number of factors, including output coupler beam quality, gyrotron unit size (output power), required total system power (total number of gyrotrons), and requirements for launching flexibility at the plasma. We believe that the above-mentioned options (corrugated waveguide, quasi-optical relay line, hybrid system, optical beam combiner) are valid designs at this stage, warranting further investigation.

## References

- <sup>1</sup>J.A. Casey, R.S. Post, R. Temkin, M. Afsar, D. Cohn, K. Kreischer, R. Myer, M. Porkolab, P. Woskov, and H. Jory. M.I.T. PFC/IR-88-2.
- <sup>2</sup>K.E. Kreischer, and R.J. Temkin. IEDM Tech. Digest, IEEE Cat. No. 87 CH2515-5 p804 (1987).
- <sup>3</sup>L. Ives, K. Felch, and H. Jory. Proc. Twelfth Int. Conf. Inf. and Millimeter Waves, Orlando, Fla. p196 (1987).
- <sup>4</sup>A. Mobius, *et al*, these proceedings.
- <sup>5</sup>K.E. Kreischer, R.J. Temkin. Phys. Rev. Lett. 59, 547, (1987).
- <sup>6</sup>J. Doane, *et al*, these proceedings.

# PRELIMINARY LOW-POWER INVESTIGATION OF TE<sub>0n</sub> MODE VLASOV LAUNCHERS\*

P. J. Sealy and R. J. Vernon

Department of Electrical and Computer Engineering  
University of Wisconsin, Madison, Wisconsin 53706-1691, USA

## ABSTRACT

Preliminary results for an experimental and theoretical investigation of TE<sub>0n</sub> mode Vlasov launchers which might be used in conjunction with some gyrotrons will be discussed. We will present experimental radiation patterns taken directly from the half-cylinder baffle and also from the parabolic-cylinder reflector that it feeds. Variations of the half-cylinder baffle and orientation position of the parabolic reflector will be considered.

## I. INTRODUCTION

Gyrotrons currently in use for plasma heating and some under development have outputs in a TE<sub>0n</sub> mode. TE<sub>0n</sub> modes are not suitable for direct plasma heating or launching from a conventional horn. Each has a null in its radiation pattern on the waveguide axis, an azimuthally polarized radiation electric field, and relatively low maximum gain. Thus these modes are commonly converted to the TE<sub>11</sub> mode in a smooth-wall circular waveguide or the HE<sub>11</sub> mode in a corrugated circular waveguide by a system of mode converters. An alternative to such a system is a TE<sub>0n</sub> mode Vlasov launcher [1], shown in Fig. 1. Here the circular waveguide ends in a half-cylinder "baffle" which directs the wave into a collimating parabolic-cylinder reflector. Such a device can launch a TE<sub>0n</sub> mode directly into a linearly polarized beam. It can also be used with TM<sub>0n</sub> modes such as are commonly produced by high-power virtual-cathode oscillators and certain relativistic BWO's and magnetrons. Another major goal of this work is to apply the results obtained to TE<sub>m1</sub> and TE<sub>m2</sub> rotating mode type Vlasov launchers which will have important application with new gyrotrons currently under development.

## II. SIMPLE THEORETICAL ANALYSIS

The structure of the baffle may be determined approximately from a simple geometrical picture of cylindrical waves reflecting from the inner guide surface. This is an extension of the concept of decomposition of a mode in a rectangular waveguide into plane wave components. The longitudinal field components in a circular waveguide are of the form

$$\Psi = C J_m(k_p \rho) \cos m\phi e^{-j\beta z}. \quad (1)$$

Here C is an amplitude constant, J<sub>m</sub> is the mth order Bessel function of the first kind, and  $\beta^2 = k^2 - k_p^2$ . For TE<sub>mn</sub> modes,  $\Psi = H_z$  and  $k_p = x'_{mn}/a$ , while for TM<sub>mn</sub> modes,  $\Psi = E_z$  and  $k_p = x_{mn}/a$ , where  $x_{mn}$  and  $x'_{mn}$  is the nth zero of J<sub>m</sub>,  $x'_{mn}$  is the nth zero of J'\_m, and a is the guide radius.

J<sub>m</sub> in Eq. (1) can be expressed in terms of Hankel functions of the first and second kind,

$$\Psi = \frac{C}{2} [H_m^{(1)}(k_p \rho) + H_m^{(2)}(k_p \rho)] \cos m\phi e^{-j\beta z} \quad (2)$$

where

$$H_m^{(1,2)} = J_m \pm jN_m, \quad (3)$$

N<sub>m</sub> being the Bessel function of the second kind. For e<sup>jωt</sup> time dependence, H<sub>m</sub><sup>(1)</sup> and H<sub>m</sub><sup>(2)</sup> may be considered as incoming and outgoing cylindrical waves respectively. In a simple geometric picture, these waves can be represented by rays making an angle with the guide axis given approximately by  $\alpha = \sin^{-1}(k_p/k)$  and reflecting multiply from the waveguide walls. This expression for α becomes more accurate for larger ρ, near the waveguide wall.

From this simplistic bouncing ray picture, we see that if we cut a half cylinder with a length of approximately  $l = 2a/\tan \alpha$  from the end of the waveguide, all the rays will exit from the cut at the angle α to the waveguide axis over the range of φ for which the guide wall has been removed. If a parabolic-cylinder reflector is placed with its focal line along the guide axis, the emerging wave will be redirected and collimated into a linearly polarized beam. Of course, the simple geometrical picture is inaccurate and needs refinement. Our next step in this refinement was determining the fields radiated from the baffle and waveguide using equivalent waveguide wall currents for  $-\alpha \leq z \leq \alpha$  and  $\pi/2 \leq \phi \leq 3\pi/2$ . The unperturbed waveguide fields were used to obtain the first approximation to these currents. Using the coordinate system shown in Fig. 2 for a TE<sub>0n</sub> mode, we write

$$\vec{A} = \iint_{S'} \vec{J}_s \frac{e^{-jkR}}{4\pi R} ds' \quad (4)$$

$$\hat{a}_\phi = \frac{C J_0(x'_{0n})}{4\pi r} \int_{-\alpha}^{\alpha} e^{-j\beta z'} \int_{\pi/2}^{3\pi/2} e^{-jkR} \hat{a}_\phi' dz' d\phi'. \quad (5)$$

In the far field, this can be solved for φ=0 giving

$$A_\phi(\phi=0) = \frac{C J_0(x'_{0n})}{4\pi r} e^{-jkr} 2\alpha \frac{\sin[(k\cos\theta-\beta)l]}{[(k\cos\theta-\beta)l]} \cdot \pi [J_0(k\sin\theta) - jH_0(k\sin\theta)] \quad (6)$$

where H<sub>0</sub>(x) is a Struve function and

$$E_\phi = -j\omega A_\phi. \quad (7)$$

## III. MEASUREMENTS

Measurements were made for a TE<sub>01</sub> mode in a 2.779 cm diameter waveguide operated at 60 GHz. Figure 3 shows a measured near-field radiation pattern from the baffle in the plane φ = 0, and so can be compared to the electric field obtained from Eq. (6), also shown in Fig. 3. A TE<sub>01</sub> launcher was

\*This work supported by the U.S. Dept. of Energy.

also constructed using a parabolic cylinder of focal length  $p = 2.54$  cm. This value was chosen to make the main beam  $\theta$  and  $\phi$  beamwidths as nearly equal as possible. Experimental results show that the full 10 dB beamwidths are  $\Delta\theta = 7.36^\circ$  and  $\Delta\phi = 7.2^\circ$ . Figure 4 is a near-field measurement of  $E_\phi$  radiated from the launcher (Fig. 1a) for  $\phi = \pi$ .

Measurements were made for several values of reflector polar tilt angle,  $\Omega$ , the angle between the focal line and the guide axis in an experimental investigation of beam steering. The shape of the radiation pattern changed little from Fig. 4. However, the peak level and beamwidth did change somewhat, as well as did the position of the maximum as shown in Fig. 5.

#### REFERENCES

- [1] S. N. Vlasov and I. M. Orlova, "Quasioptical Transformer which Transforms the Waves in a Waveguide Having Circular Cross Section into a Highly Directional Wave Beam," *Radiophysics Quantum Electron.*, Vol. 17, p. 148, 1974.

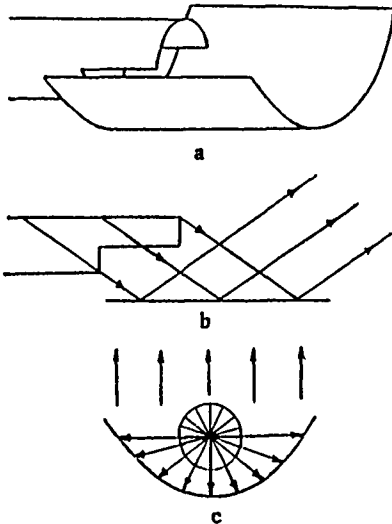


Fig. 1. a)  $TE_{0n}$  or  $TM_{0n}$  Vlasov launcher showing the half-cylinder baffle and parabolic-cylinder reflector. b) and c) Cross sectional views of a) showing geometrical ray directions.

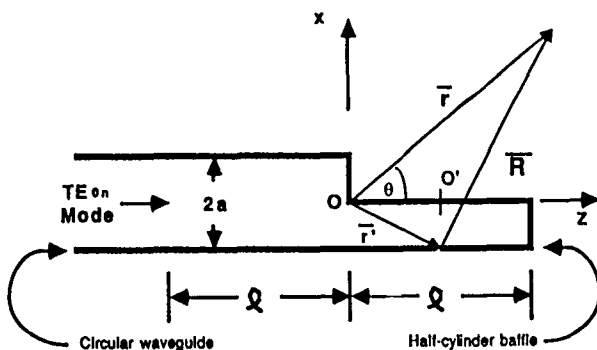


Fig. 2. Side view of the half-cylinder baffle with the coordinate system used.

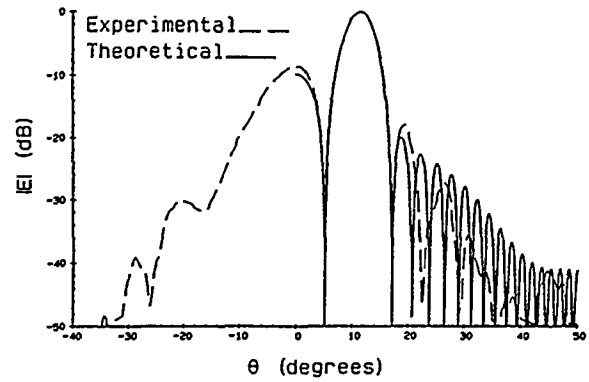


Fig. 3. Comparison of the theoretical and measured near-field radiation pattern from the half-cylinder baffle. The theoretical calculation uses the origin  $O$  from Fig. 2 and the experimental results use the origin  $O'$  from Fig. 2.

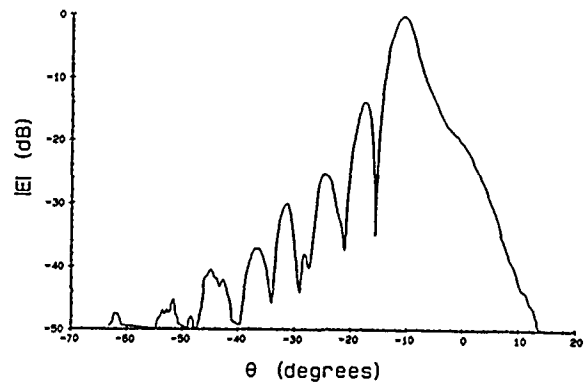


Fig. 4. Measured near-field radiation pattern of the  $TE_{01}$  Vlasov launcher. The origin  $O$  from Fig. 2 is used.

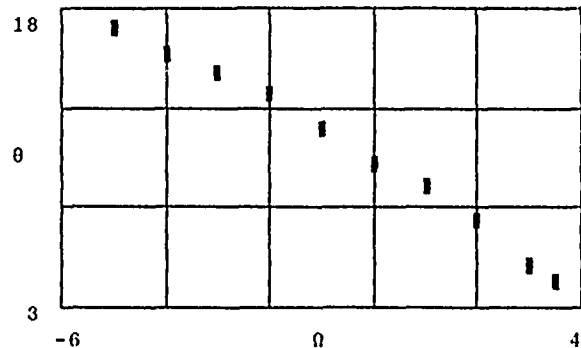


Fig. 5. The location of the maximum of  $|E|$  vs  $\Omega$  showing the beam steerability. The origin  $O$  is used.  $\Omega$  is the polar tilt angle of the reflector.

## OBSERVATION OF UBITRON FUNDAMENTAL MODE AMPLIFICATION

Robert H. Jackson, Dean E. Pershing\*, Hans Bluem†

Naval Research Laboratory, Vacuum Electronics Branch  
Washington, D.C. 20375-5000

## ABSTRACT

Operation of a ubitron/FEL amplifier is reported. The experiment has been operated using the fundamental wiggler harmonic interaction with the  $TE_{11}$  circular waveguide mode. Small signal gains as high as 12dB have been observed at a voltage 15% below design level with a minimum instantaneous bandwidth exceeding 25%. A gain per free-space wavelength approaching  $0.9\text{dB}/\lambda$  has been achieved. Experimental results are compared with small signal calculations and future plans are discussed.

## INTRODUCTION

The Naval Research Laboratory has instituted a program to investigate the ubitron/FEL interaction [1]-[3] as the basis for a new class of high-power, broadband micro- and millimeter-wave amplifiers. Attractive features of the ubitron include high power (due to the fast-wave nature of the interaction), high gain, relatively broad instantaneous bandwidth, high frequency operation, and compatibility with space-charge limited, laminar-flow electron gun configurations. The NRL program consists of both theoretical and experimental efforts to explore ubitron performance and identify critical technology issues. The performance goals for the amplifier are 30dB large signal gain ( $2-3\text{dB}/\lambda$ ), saturated instantaneous bandwidth  $\geq 20\%$  and an efficiency  $\geq 15\%$  (without enhancement techniques). These values are considered sufficient to demonstrate the potential of the ubitron as a practical alternative for high-power, high-frequency RF generation.

 $K_u$ -BAND UBITRON AMPLIFIER

The experimental configuration consists of a modified SLAC klystron electron gun, injected-current monitor, modified turnstile RF input coupler, double tapered bifilar helix wiggler and solenoid magnets, transmitted-current monitor, RF output monitors and a water calorimeter/load. Details of component designs and performance have been reported elsewhere, see [4]-[5]. Operation in  $K_u$ -band as a single stage amplifier was chosen because of equipment and diagnostic availability, and reduced constraints on beam quality and fabrication tolerances.

Several modifications have recently been made to the experiment to correct problems and improve performance. A modified solenoid pole piece has resulted in up to two orders of magnitude reduction in the beam axial velocity spread ( $0.26\% \geq \Delta v_z/v_z \geq 0.023\%$  depending on trim coil setting). The wiggler has been rewound to repair damage resulting from a coolant flow failure. Although the present wiggler differs in several minor geometrical respects from the old (round instead of rectangular wire, new end pieces, etc.), a reduction in the number of turns has resulted in a significantly reduced wiggler strength (gauss per ampere). This has necessitated a shift from dc to pulsed wiggler operation.

The present (and design) operating parameters for the experiment are given in Table I. The modulator voltage and repetition rate are tunable over a wide range, but the pulse width is fixed. Beam current is tunable from a few amperes to  $\sim 30$  amperes by adjustment of a trim coil located over the cathode. The wiggler has adiabatic entrance and exit profiles and is driven by a pulsed current supply at the modulator frequency. The solenoid is operated dc with a flat field profile for all results reported here. The frequency range of the experiment is presently limited by the RF driver amplifier on the low side and RF input coupler fall-off on the high side.

In order to achieve high gain, efficiency and bandwidth simultaneously, operating parameters have been chosen to produce a grazing intersection of the wiggler-shifted negative energy space-charge wave with the  $TE_{11}$  circular waveguide mode. Figure 1 shows the curves for one set of parameters for the ubitron and for the first two gyrotron harmonics. Note that a broad intersection is achieved for the ubitron line and that possible gyrotron interactions are well separated and would be identifiable by both frequency and mode. Operation near grazing intersection should have a beneficial effect on issues such as phase sensitivity to voltage and wiggler variations.

Figure 2 shows typical voltage and RF monitor traces. Two traces are shown for the RF, the transmitted RF-driver signal without the wiggler (lower) and an amplified signal with wiggler turned on. The width of the RF driver pulse and the overlap with the voltage pulse can be adjusted as desired. Although the portion of the RF driver pulse before the voltage flat top could be used to determine gain, this does not account for several factors such as beam loading of the input coupler (see Fig. 2). Hence, gain is determined from the output power measured with the wiggler turned off and the output power measured with the wiggler turned on, all other factors being held constant. Both a digital oscilloscope and a peak power meter are used for these measurements. Other factors monitored on each pulse are diode current, injected current, transmitted current, wiggler current and calorimeter temperature.

RF performance has been observed as a function of input signal polarization, RF-drive power, wiggler field, injected current and frequency. One of the unique features of this experiment is a flexible input coupling scheme providing the ability to launch circularly and linearly polarized waves, as well as selected waveguide modes. The RF results presented below were measured using a left circularly polarized input wave. As predicted by theory, very little or no gain was observed using right circular polarization. Theory also indicates that the combination of a helical wiggler field and a circularly polarized wave will yield the highest gain for a given input power and wiggle velocity.

All measurements are in the small signal range, and the power out is directly proportional to power in. In the collective mode of operation, the gain is proportional to  $\alpha$ , the ratio of  $v_{\perp}/v_{\parallel}$ , which is approximately linearly proportional to the wiggler field. Measurements of gain versus wiggler field show this type of linear behavior initially, but then the gain rolls over and begins to drop with increasing wiggler field as the ubitron line decouples from the waveguide mode.

In the collective mode, gain is proportional to the square root of the injected current. The measured gain appears to be consistent with this dependence, but the range of currents tested is not sufficient to discriminate between a  $I^{1/2}$  (collective) or  $I^{2/3}$  (strong-pump) dependence.

The measured gain versus frequency is shown in Figure 3 (dots) along with a small signal calculation (curve)[6]. The measured values show a double-peak profile over the 13.5-17.2GHz band with a peak gain of 12.2dB at 13.5GHz. Assuming that gain occurs mainly over the 12 uniform periods in the wiggler, this translates into  $\sim 0.9\text{dB}$  per free space wavelength. This value, achieved at less than optimum operational parameters, is an improvement over the 0.5-0.7dB per free space wavelength achieved in Phillips' experiments [1]-[3]. Small signal calculations use the measured experimental parameters, with the exception of beam current, which is reduced to 10 A in order to match the experimental gain profile. This reduction is necessary due to the thin-beam approximation used in the gain equations which results in a beam plasma frequency substantially higher than actual, by approximately a factor of six in this case [7]. The higher plasma frequency in the calculations causes the dispersion curves to decouple at low current values. If the calculated gain is multiplied by the square root of the current ratio (30A/10A) a peak small signal gain of

\* Mission Research Corporation, Newington, VA 22122

† University of Maryland, EE Department, College Park, MD 20742

$\approx 17\text{dB}$  is obtained for 12 wiggler periods. When launching losses are taken into account this is in reasonable agreement with measurements.

### CONCLUSIONS

Amplifier operation of the NRL ubitron experiment has been achieved with a peak gain of 12.2dB and a bandwidth exceeding 25%. The interaction has been identified by frequency, waveguide mode and amplification characteristics to be a fundamental wiggler harmonic ubitron/FEL interaction with the  $\text{TE}_{11}$  waveguide mode. Reasonable agreement has been obtained between measurements and theory concerning gain, bandwidth and general performance characteristics. In particular, higher values of gain per free-space wavelength have been achieved due to the combination of helical wiggler and circularly polarized waveguide mode. These growth rates are especially impressive given the low value of beam  $\alpha$ ,  $\approx 0.16$ . Gain per free-space wavelength is an important parameter to optimize for future ubitron applications.

Immediate plans include improvements in the small signal calculations to correct the handling of space charge and nonlinear calculations for both present and design experimental parameters. Additional measurements such as calorimetric efficiency, enhancement by axial field tapering and phase sensitivity are also planned. Operation of the experiment at the design voltage will begin shortly.

The authors would like to acknowledge useful discussions with Drs. A. K. Ganguly and H. P. Freund. This work was supported by the Office of Naval Technology and the Office of Naval Research.

### REFERENCES

- (1) R. M. Phillips, *IRE ED-7* (1960) p. 231.
- (2) R. M. Phillips, *Proc. 4th Int. Congress on Microwave Tubes*, Scheveingen (1962) Centrex Pub. Co., Eindhoven, p. 371.
- (3) C. E. Enderby and R. M. Phillips, *IEEE Proc.* 53 (1965) p. 1648.
- (4) R. H. Jackson and D. E. Pershing, *Technical Digest Int. Electron Devices Meeting* (1986) 342.
- (5) R. H. Jackson, D. E. Pershing and F. Wood, *Proc. 8th Int. Free Electron Laser Conf., Nucl. Instrum. Meth.* A259, 99(1987).
- (6) H. P. Freund and A. K. Ganguly, *Phys. Rev.* A28 (1983) p. 3438.
- (7) A. K. Ganguly, private communications.

Table I  
Ubitron Experimental Parameters

	Present	Design
Voltage (kV)	190-216	250
Current (A)	0-30	30-100
Beam Radius (cm)	0.4	0.4
Pulse Length ( $\mu\text{Sec}$ )	1	1
Repetition Rate (Hz)	3-30	1-100
Wiggler:		
Period (cm)	2.54	2.54
Entrance (periods)	5	5
Uniform (periods)	12	12
Exit (periods)	3	3
Field (gauss)	270	500
Solenoid (kilogauss)	2.5	1-3.2
Frequency (GHz)	13.5-17.2	12.4-18

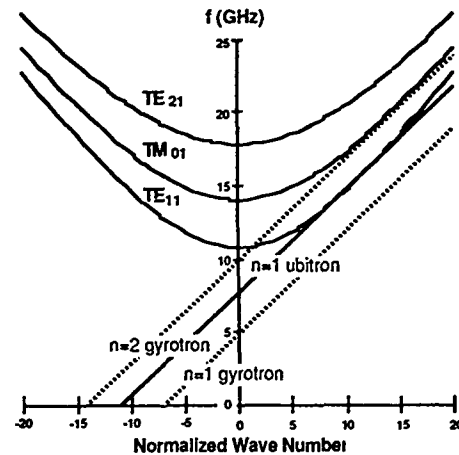


Figure 1

Uncoupled dispersion curves for operation at 216kV, 2.5kG solenoid field, 30A beam current and 270G wiggler field ( $v_{\perp}/v_{\parallel} \approx 0.16$ ).

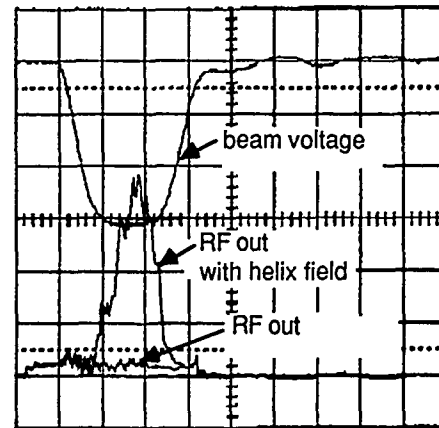


Figure 2

Example of typical RF data with and without the wiggler field. Scales are 1  $\mu\text{Sec}/\text{div}$  and 70.9kV/div for beam voltage.

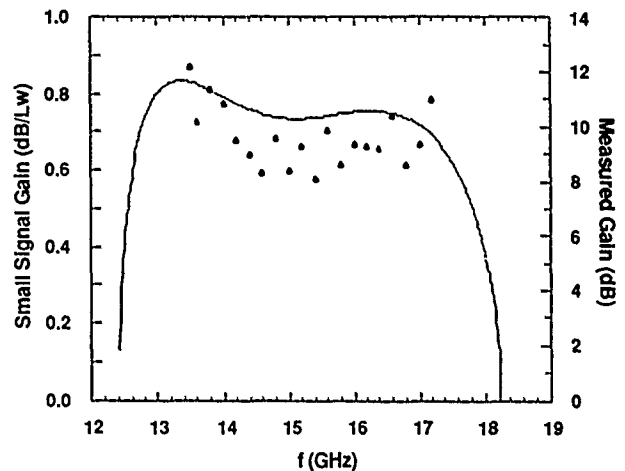


Figure 3

Comparison of calculated (curve) and observed (dots) small signal gain. The calculated values are based on the equations in [4] and are given in dB per wiggler period. Note that the measurements are for a beam current of 30A and the theoretical values are for 10A (see discussion in text.)

# OPTIMIZATION OF A PLANAR OROTRON

*J. E. Walsh, J. A. Jackson, and E. M. Marshall*

*Department of Physics and Astronomy  
Dartmouth College  
Hanover, N.H. 03755*

## ABSTRACT INTRODUCTION

The Planar Orotron has traditionally consisted of a uniform, rectangular metal grating opposed by a planar conductor (Fig. 1a). Unbounded at the sides, this open resonator supports travelling waves with frequencies which are determined by the grating dimensions. The dispersion and gain characteristics for this device have been documented theoretically and experimentally in the low beam voltage (5 - 20 kV) regime,<sup>1</sup> where powers of up to 2 kW and efficiencies of a few percent at 35 GHz have been recorded. In the frequency range of 150 to 175 GHz, output powers are typically less than 1 W, and efficiencies less than 0.5%. Attempts to improve the output power and efficiency by modifying the resonator design are currently underway in the 30 - 40 GHz range. The new designs are the following, which appear in Figures 1 and 2:

- 1) A uniform grating is opposed by an identical uniform grating, with a symmetric orientation in the resonator. (Fig. 1b)
- 2) A uniform grating is opposed by an identical uniform grating, with an antisymmetric orientation in the resonator. (Fig. 1c)
- 3) The uniform grating is replaced by a grating with a slight taper (< 10%) and opposed by a conducting plane. (Fig. 2a)
- 4) The tapered grating is opposed by an identical tapered grating with a symmetric orientation in the resonator. (Fig. 2b)

The grating and resonator parameters of interest are shown in the Figures. They are the period,  $l$ , and the ratios of groove depth to grating period,  $d/l$ , groove width to grating period,  $s/l$ , and the ratio of inner resonator height to grating period,  $(b-d)/l$ . In Fig. 2, the groove depth,  $d$ , and the distance from the base of the slot to the surface of the opposing component,  $b$ , are both functions of the axial position,  $z$ .

## THEORY

The theory outlined in Reference 1 has been modified to accommodate the new uniform grating resonators. For the traditional planar orotron, the simplest dispersion relation results from the assumption of TM modes in the resonator. The z-component of the electric field to which the beam couples has a sinh dependence normal to the grating surface as is shown in Fig. 1a. When the grating is symmetrically opposed by a uniform grating, the  $E_z$  field may be either antisymmetric or symmetric in the resonator, described by a sinh or a cosh function, respectively, as is shown in Fig. 1b. In the antisymmetric resonator, the fields are described by a linear combination of sinh and cosh functions. As a result of these modifications, the tuning curves for the antisymmetric mode in the symmetric resonator are virtually unchanged from those of the traditional planar orotron, while

those of the symmetric mode in the symmetric resonator differ in that low frequency cut-offs occur. For the antisymmetric resonator with a given grating design, considerably higher frequencies are predicted than those for the traditional model.

The gain may be found in the usual manner, in terms of the inverse quality factor of the beam:

$$\frac{1}{Q_b} = - \frac{d\mathcal{E}/dt}{\omega \mathcal{E}_T}$$

where  $d\mathcal{E}/dt$  is the energy given up by the beam to the z-component of the field, and  $\mathcal{E}_T$  is the total energy stored in the resonator. The frequency of the mode is given by  $\omega$ . Thus for modified forms of the fields inside the various resonators, the gain and subsequently the start current may be calculated.

For the tapered grating resonators, a corrected expression for the dispersion has yet to be developed, but progress has been made on a technique for optimizing the gain. In this model, particles move in the frame of a wave which has a changing wavelength, and the resulting change in the particle energy may be found. Phase space and gain surface plots are then used to compare gratings of various tapers, to determine which taper yields the maximum decrease in particle energy, or increase in field energy, for a given beam.

## EXPERIMENTAL RESULTS

To date, a number of resonator designs have been tested and compared in the low voltage (5 - 20 kV) regime. All have used a grating design with  $l = 0.155$  cm,  $d/l = 1.0$ ,  $s/l = 0.5$ , and  $(b-d)/l = 2.3$ . In the traditional planar orotron design, this grating produces frequencies of 30 - 40 GHz in the 5 - 20 kV regime. The gratings are 2 cm wide, and 15 cm long. For the tapered gratings, the  $d/l$  value is 1.0 at the beam entry end, and reduces by the taper percentage at the beam exit end. To make comparisons between the resonators, frequency, start current, and power and efficiency have been systematically measured, and compared with theory whenever possible. It should also be noted that the machine alignment, unaltered during the comparisons, is not necessarily optimized for maximum output power. Frequency data is compared to tuning curves resulting from the primary and one or two upper branches of the dispersion relations for each case. In Fig. 3, for example, data from a single-sided, 8% tapered grating resonator is displayed against the standard theory. The discrepancy shown is typical of all of the resonator designs studied, and may be due to the fact that the theory assumes the gratings to be infinitely wide, an inaccurate assumption for the wavelength range in question. While in some cases the data suggest that coupling is to one of the upper branches, this does not appear to be the case for the tapered design of Fig. 3.

Data for power and efficiency as functions of guide current are the best yardstick for comparing the various resonator designs. For the range of  $I = 1.4$  A, for example, the double-sided 8%

tapered design produces powers of up to 315 W and efficiencies of up to 3%, compared to the single sided 8% tapered design which produces powers of up to 180 W and efficiencies of up to 1.7%. The symmetric and antisymmetric designs are the next best performers, followed by the traditional design which produces powers of up to 70 W and efficiencies of up to 0.2%. Tapers in excess of 10% do not perform as well as those which are less than 10%.

Other results which will be covered include start current data and comparisons with theory, and high voltage (< 150 kV) behavior, which is currently under study. In addition, the most promising designs are to be tested using high frequency gratings, and these results will also be discussed.

### ACKNOWLEDGMENT

Support of Naval Research Laboratory Contract N00014-87-K-2027 is gratefully acknowledged.

### REFERENCE

<sup>1</sup>Marshall, E. M., P. M. Phillips, and J. E. Walsh, IEEE 16, No. 2, 199-205, Apr. 1988.

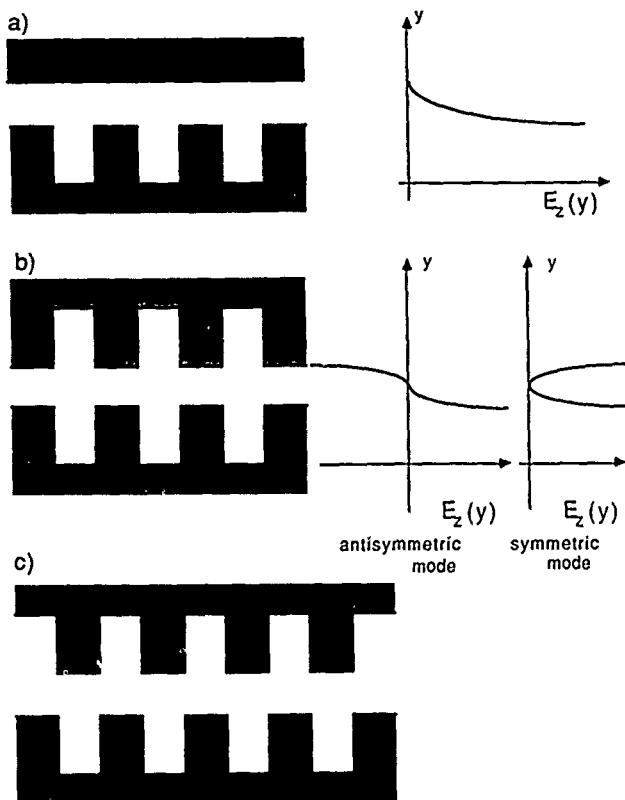


Figure 1: Uniform Grating Resonators

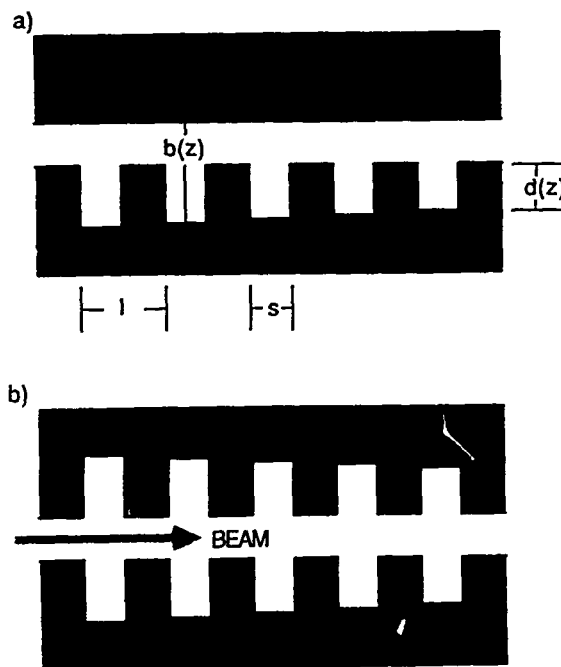


Figure 2: Tapered Grating Resonators  
(Shown with exaggerated tapers)

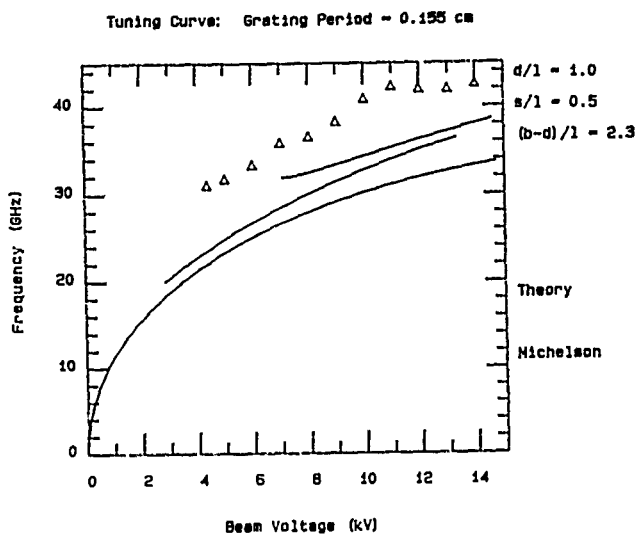


Figure 3: Tuning Curve



# THE CIRCULAR ORBIT LINEAR THEORY OF AXIAL INJECTION ORBITRON MASER OSCILLATORS

John M. Burke

Burke Technologies, Inc.  
San Diego, California 92111-1316

## ABSTRACT

A fully relativistic theory of axial injection orbitron maser (AXIOM) oscillators has been completed. The theory models the interaction of axially injected electrons in helical trajectories with the fields of a coaxial cavity resonator. The theory treats TE or TM modes with sinusoidal axial field profiles. The power transferred from the electron beam to the cavity fields is calculated in terms of a general distribution function and the cavity parameters. A cold beam distribution function is used to evaluate the theory. The results of the theory are presented in terms of the threshold value of the cavity  $Q$  times the electron beam current  $I_{Beam}$  required for self-oscillation.

## INTRODUCTION

The development of fast-wave devices, principally the Electron Cyclotron Maser (ECM) or gyrotron has made possible the efficient generation of high power millimeter wavelength electromagnetic waves. One drawback to these devices with respect to size, weight, and cost is that they require large magnetic fields. Thus, there is current interest in developing a high power millimeter wave source that does not require the use of a large magnetic field. The device that we are studying is called the *Axial Injection Orbitron Maser* or AXIOM [1,2], and is a combination of the basic orbitron maser concept [3] and the standard ECM configuration. A conceptual design of an AXIOM oscillator is shown in Figure 1. The interaction region of an AXIOM employs a coaxial cylindrical geometry with the inner conductor held at a positive potential with respect to the outer conductor. Electrons are radially confined by the positive potential of the inner conductor and can travel around it in circular orbits or in noncircular, low angular momentum orbits.

We believe that a high frequency, high efficiency maser that operates at high power levels can be realized by using the AXIOM concept. Electrons would be injected with a large value of axial momentum in a region with a low radial electric field. The electrons would then be adiabatically compressed into the interaction region where the radial electric field is large. The adiabatic compression process has the advantage that it increases the electron density as well as the ratio of their perpendicular to parallel energy. The electrons would not be axially trapped in the interaction region as in the early orbitron experiments, but would rapidly transit the interaction region where they would resonantly transfer their energy to the radiation fields. This injection scheme is very similar to the one used in most ECM devices which have been shown to operate at high powers with high efficiencies. The AXIOM would also operate in ultra-high vacuum, as is the case with most ECM devices. Most importantly, axial injection allows one to maximize the efficiency of the maser interaction by providing a means to produce an electron beam whose distribution function is optimized for the power level requirements of the device. It also provides a means of optimally positioning the electron beam to interact with a given waveguide or cavity mode.

## LINEAR THEORY

The circular orbit linear theory of AXIOM oscillators assumes a TE or TM mode with a sinusoidal axial field profile is present in the cavity. The perturbed beam current density due to these fields is computed by integrating the linearized Vlasov equation over unperturbed orbits. This integration is particularly simple due to the symmetry of the circular orbits and is valid for any electron energy. The perturbed beam current is then used to calculate the power transferred from the electron beam to the cavity fields as a function of the beam and cavity parameters. The beam current required for the cavity to self-oscillate can then be obtained from the definition of the cavity

$Q$  and the requirement that the power transferred from the electron beam to the cavity fields has to be greater than the power lost from the cavity due to diffractive and dissipative losses.

## RESULTS

We use a cold beam distribution function to evaluate the theory in which the electrons are all assumed to have the same radius from the inner conductor and the same ratio of perpendicular to parallel velocity. This has the advantage that it allows for simple evaluation of the theory and yields results that are easily interpretable.

We compute the beam current required for the cavity to self-oscillate versus the voltage on the inner conductor for various modes to investigate the mode competition problems associated with a given cavity design. The threshold current for self-oscillation can also be plotted as a function of electron beam radius to find the beam position required to maximize or minimize the interaction with a given mode.

## REFERENCES

- [1] J. M. Burke, W. M. Manheimer, and E. Ott, in *High Power Microwave Sources*, edited by Victor L. Granatstein and Igor Alexeff (Artech House, Norwood, MA, 1987), Chapter 7.
- [2] J. M. Burke and W. M. Manheimer, US Patent Number 4,754,196, June 28, 1988.
- [3] I. Alexeff and F. Dyer, *Phys. Rev. Lett.* **45**, 351-354 (1980).

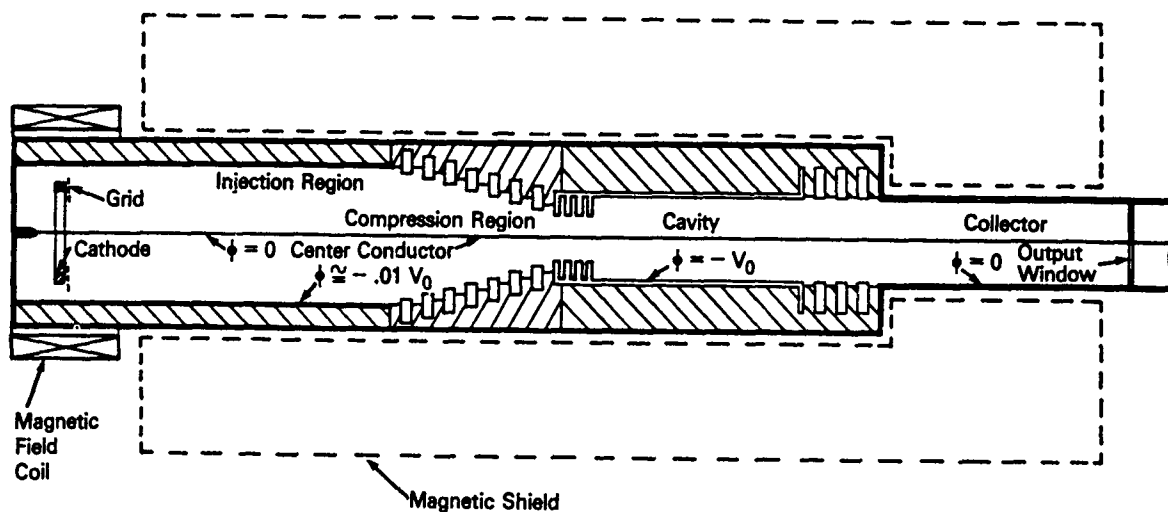


Figure 1  
Conceptual Design of an AXIOM Oscillator

# Pulsed and Steady-State Multianode Orbitron MASERs\*

I. Alexeff, F. Dyer, and M. Rader

University of Tennessee

Knoxville TN, 37996-2100

## Abstract

We have designed, built and tested several steady-state Orbitron MASERs, which have the unique property of having multiple anode wires. We have found that the multiwire structure increased the output power, efficiency, and reduced the heat loading of individual anode wires. We have also experimented with these devices in a pulsed mode and found similar results.

## Introduction to the Orbitron MASER

The Orbitron MASER is a device, which can be used as a source of high frequency radiation. In its most basic physical form, it consists of a metal outer shell, which is cylindrical in form, and a thin metal wire, which is positioned along the axis of the metal shell. This basic device is shown in figure 1. This basic device can be described by an inner radius ( $r_0$ ), which is the radius of the inner wire, and an outer radius ( $r_1$ ), which is the radius of the outer shell.

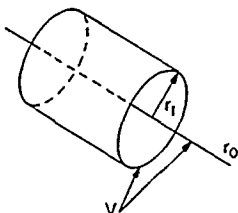


Figure 1

It is possible to produce high frequency rf radiation from such a simple device by applying a high potential between the inner wire, and outer shell. This must be done in such a way that the wire is biased positive with respect to the outer shell. The potential applied between the two surfaces creates a strong radial electric field, which will trap negatively charged particles in orbit around the positively biased wire. In this device the outer shell acts as a microwave cavity and the entire device resembles a coaxial line. These orbiting particles are negative mass unstable and couple to cavity modes within the shell-wire system. The frequency of this radiation ( $\Omega$ ) is proportional to the radius of the particle orbit, and the highest frequency at any particular voltage is proportional to the radius of the central wire. From solving the appropriate force balance equations we find that

$$\Omega = 1/r (ZeV / m_e \ln(r_1/r_0))^{1/2}$$

where  $V$  is the potential between the wire and shell,  $m_e$  is the electron mass, and  $Ze$  is the sign and charge of an electron<sup>1</sup>

The electron feed for the Orbitron MASER can be accomplished in one of two ways. Either by electrons sucked from a cold cathode discharge or a hot electron emitter, in a high vacuum. The first can be accomplished with relative ease since, for high wire potentials, the device operates on a short pulse basis and none of the interior parts experiences a large rise in temperature. However the hot cathode device, especially in the steady-state, often experiences a sharp increase in anode temperature. It has been theorized that a multiple wire anode structure should decrease the heat loading for each individual wire. If these wires are very closely spaced they should constructively couple and increase the output power for any given current. This is analogous to multiple atoms in a LASER.

## Experimental Data From Multiwire Orbitrons.

In the first group of experiments involving a single wire Orbitron with a hot filament, open cavities between 5 and 10 cm in length were used with a diameter of between 1 and 2 cm. These cavities generated a series of harmonics for which the fundamental was determined by an external cavity cable resonance. We next increased the number of anode wires from one to two. This was done in the belief that this would increase the power output and the frequency range, which was indeed the case. Fig. 2 is a comparison between the spectral emission of one and two center wires. The pressure was at  $5 \times 10^{-6}$  torr and the voltage in the top spectral pictures was 1.2 kV, while at the bottom it was 800 V. Both had a current of about 34 mA on the center wire. Some nonharmonic frequencies can be seen in the two-wire spectral picture, as well as a series of harmonically related spectral lines. These nonharmonic emission lines disappear as the current or the voltage is increased, and so what appears to be phase locking occurs between the wires. The harmonic lines stay constant in frequency in both pictures, but change in amplitude.

The number of center wires was increased to four, arranged in a planar array, and the power and the apparent phase locking increased significantly, but more importantly, the upper limit of frequency emission went up sharply. Fig. 3 is an example of this. The input operating voltage to this device was 500 V, and the radius of the central wire was 3 mils or 0.075 mm. Under these operating conditions the highest circular frequency is 8.3 GHz, and so this is within a factor of 1.5 of the smallest computed orbit frequency for circular orbits.<sup>2,3</sup>

We next added water cooling to the outer cavity of the device, to reduce wall heating and arranging the central wires in a circular array. This had the same effect of reducing the wire heat load, but it also created a peculiar resonance in the system, as shown in figure 4. This resonance caused high frequency lines to appear at low voltages, but disappear at higher voltages. This resonance, we believe, is the result of a stabilization of the device caused by the introduction of a positive mass drift region. This region, located in the hollow anode structure, is caused by axisymetry of the anode structure.

During this experiment, we also tried pulsing the device to a high voltage, using a delay line to reduce spark gap noise and shape the pulse. This allowed us to produce x band radiation, as shown in figure 5, on an extended pulse basis from the device, yet have no visible heating of the central wires even at high repetition rates.

#### Conclusion

We have successfully demonstrated that the Orbitron can operate in a multiwire configuration. This multiwire configuration helps reduce heat load on the individual wires, improves the output frequency, and boosts the output power. A high frequency resonance can be achieved through the proper anode configuration. The Orbitron MASER can operate in a high vacuum and at the frequency range of its plasma filled counterparts.

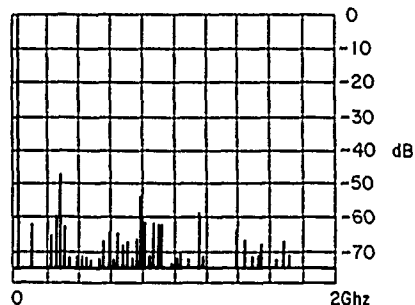
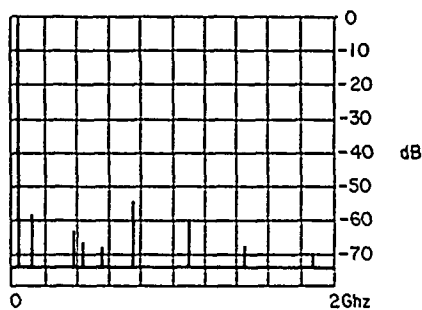


Figure 2

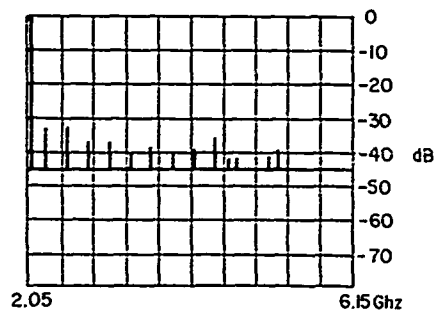


Figure 3

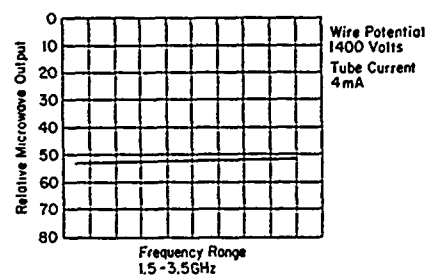
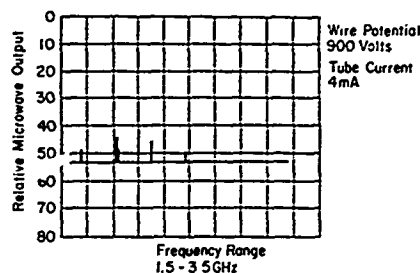


Figure 4

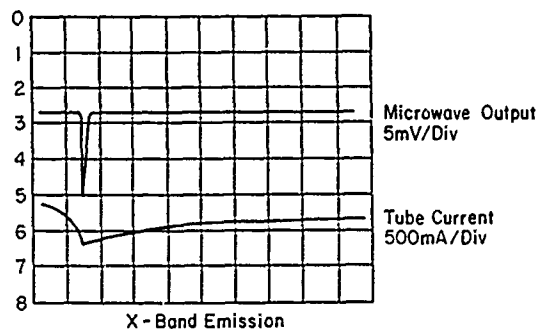


Figure 5

#### References

1. I. Alexeff and F. Dyer, *Phys. Rev. Lett.*, vol 45, p. 351, 1980  
I. Alexeff, *IEEE Trans. Plasma Sci.*, vol PS-12, p 2880, 1984  
I. Alexeff, *Phys. Fluids*, vol 28, p. 1990, June 1985
2. J. M. Burke, W. M. Manheimer, and E. Ott, *Phys. Rev. Lett.*, 56, p. 2652, 1986  
A. K. Ganguly, H. P. Freund, and S. Ahn, *Phys. Rev.* 56, p. 2199, 1987
3. M. Rader, F. Dyer, and I. Alexeff, *IEEE Trans. Plasma Sci.*, vol PS-15, p 56, 1987

# HIGH EFFICIENCY OPERATION OF THE MODIFIED PENIOTRON USING $TE_{11}$ RECTANGULAR WAVEGUIDE CAVITY

K.Yokoo, M.Razeghi, N.Sato and S.Ono

Research Institute of Electrical Communication  
Tohoku University  
Sendai 980, Japan

## ABSTRACT

The modified peniotron oscillator proposed by the authors has been experimentally studied and a fairly high electronic efficiency of 50% and 62% of the efficiency by the use of a potential-depressed collector were obtained. This paper describes the operation characteristics of the modified peniotron and point out that the alignment of the respective axes of the tube and the magnetic circuits is very important in a peniotron tube.

## INTRODUCTION

The modified peniotron proposed by the authors in 1985 has been expected to have a very high transverse efficiency of nearly 100% for rotational electron beam energy and also nearly same conversion efficiency for total electron beam energy by the use of a potential-depressed collector due to the ideal peniotron interaction in a  $TE_{11}$  rectangular waveguide cavity[1]. We have reported the preliminary experimental results of the modified peniotron at 10 GHz[2], in which we described the design considerations of the test tube, the formation of a hollow rotating electron beam and were the first to demonstrate the peniotron interaction in a ridgeless waveguide cavity. But, the output powers were several hundred watts and the conversion efficiencies were a few percents. These low values of the experimental results were estimated to be due to the misalignment of the respective axes of the tube and the magnetic circuits.

We have tried to adjust the concentricity of those axes by using an optical microscope and a laser beam and obtained the output power of 10KW with the electronic efficiency of 50% by using the same test tube. The efficiency was improved to 62% by applying a depression potential to the collector.

This paper describes the experimental results obtained from the test tube and discuss the operation characteristics.

## EXPERIMENTAL SET UP

Details of the configuration of the test tube and the experimental set up were described in the previous paper[2], as the scheme of the experimental set up is shown in Figure 1. As shown in the figure, the test tube is a demountable one. All of the subassemblies of the electron gun to the RF circuits were aligned and constructed to the final tube with an acceptable axial offset of 50 $\mu$ m by using an optical microscope on an optical bench. The concentricity of the tube axis and the magnetic circuit axes was adjusted by measuring the intensity of a laser beam passing through the small holes drilled at the same axial offset on the tube and the magnetic circuits. This alignment technique allowed to pass

Table 1

Parameters of the designed values and the experimental results.

	Designed values	Experimental values
Operation frequency(GHz)	10	10.03
Output power(KW)	10	10
Electronic efficiency(%)	80	50
Beam current(A)	0.42	0.92
Accelerating voltage(KV)	30	30
Loaded Q of cavity	2000	2000
Pulse width( $\mu$ sec)	20	20
Duty ratio	1/5000	1/5000
Velocity ratio	2	$\approx$ 3

all of beam current to the collector and to obtain the maximum output power without applying the deflection potential on two pairs of the deflection plates position in the beam tunnel between the electron gun and the RF circuit, which was essential to increase a transmittance of the beam current and to get higher output power at the previous experiments. These experimental results showed that the gun-tube and the magnetic circuit alignments were successfully accomplished.

## RESULTS AND DISCUSSIONS

Experiments of the test tube were carried by the pulse conditions listed in Table 1.

Figure 2 shows the output power and the energy conversion efficiency as a function of the beam current at the accelerating voltage of 30KV. The beam current was changed by controlling the cathode temperature and the DC magnetic field intensity was adjusted to produce the highest output power at each beam current. The output power and the conversion efficiency increased with increase of the beam current and reached to the highest output power of 10KW and the conversion efficiency of 36%, respectively, at the beam current of 0.92A. The conversion efficiency includes the loss in the cavity, and, then, 36% of this value corresponds to the electronic efficiency of nearly 50%, considering the unloaded cavity Q value of 8,000 and the loaded Q of 2,000 in the test tube. This value is still lower comparing with the maximum efficiency of 80% for the ideal interaction of this test tube. The conversion efficiency is probably limited by the distributions of the beam centre and the velocity ratio of the rotating electron beam.

The conversion efficiency in the modified peniotron with the ideal electron beam should be substantially improved by applying a depression potential to the collector, because the electrons have an unique axial energy after interaction. Figure 3 shows the collector current and the output

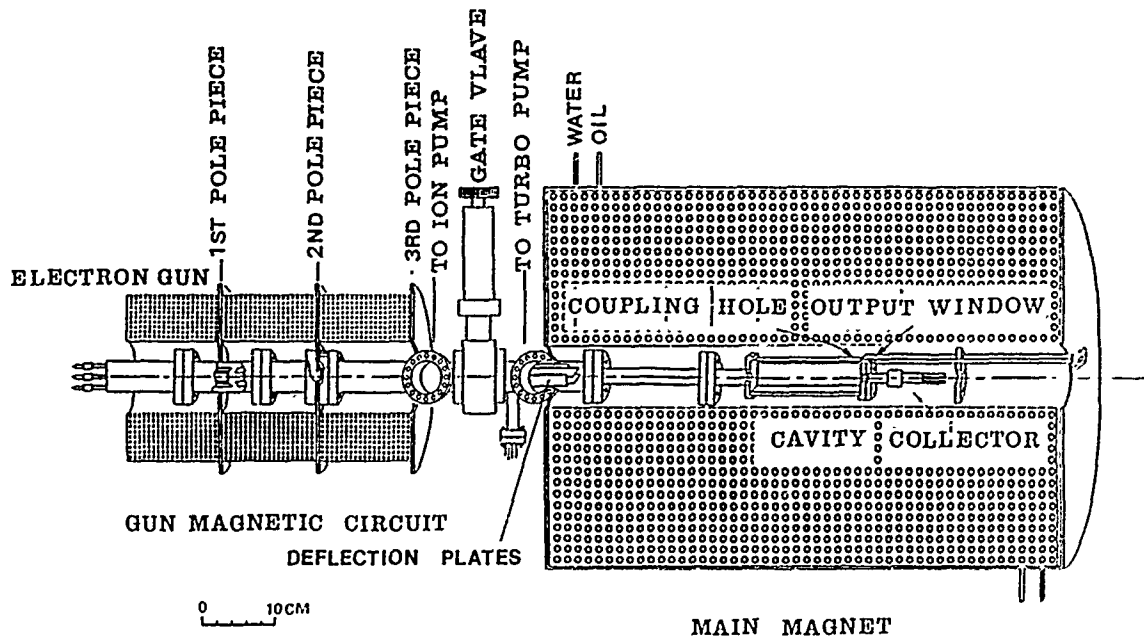


Fig. 1 Schematics of the modified peniotron.

power as a function of the collector depression potential at the accelerating voltage of 30KV. The figure shows that the output power reaches the peak value at the depression potential of about 2.5KV probably due to the decrease of the longitudinal velocity of electrons, that is, the increase of the value of velocity ratio in the interaction cavity. If we assume that the beam current of 0.82A without the depression potential is not changed by the applied potential, the peak output power corresponds to the conversion efficiency of 44% and the electronic efficiency of 62%, respectively. Differentiation of the corrector current distribution with respect to the potential gives the information of the velocity ratio of the electron beam. This experiment showed that the velocity ratio of the electrons were distributed around the value of 3 and these electron beam should enable the electronic efficiency to be little bit higher in the operation of the modified peniotron than that of the designed value. The fact reducing the efficiency suggests that the electrons were not completely rotating about the axis of symmetry of the tube and the alignments of the gun-tube and the magnetic circuits were not sufficient.

Therefore, it can be seen that more precise designs of the electron gun and the cusped magnetic circuit and alignments of the tube and the magnetic circuits to form an axially symmetric hollow rotating electron beam with small dispersion of the velocity ratio have a potential to increase the electronic efficiency of the modified peniotron.

Finally, we summarized the experimental results comparing with the design values in Table 1.

This work was partially supported by a Grant-in-Aid for Scientific Research from Ministry of Education, Science and Culture in Japan.

#### REFERENCES

- [1] M.Razeghi, N.Sato, T.Suzuki, K.Yokoo and S.Ono: Int. J. Electronics 59 (1985) 533.
- [2] K.Yokoo, T.Suzuki, M.Razeghi, N.Sato and S.Ono: Int. J. Electronics 64 (1988) (to be published)

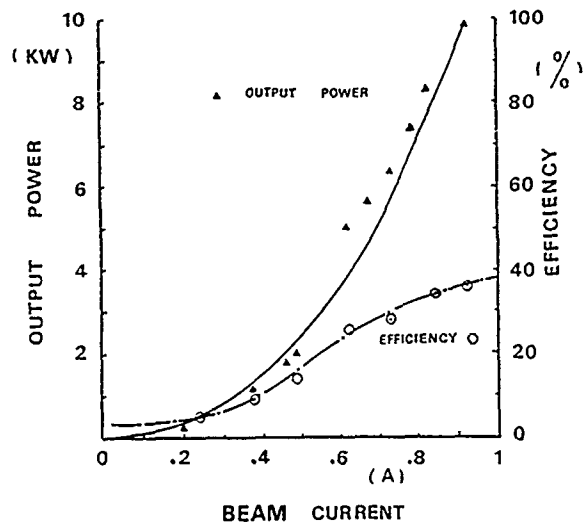


Fig. 2 Output power and efficiency as a function of beam current.

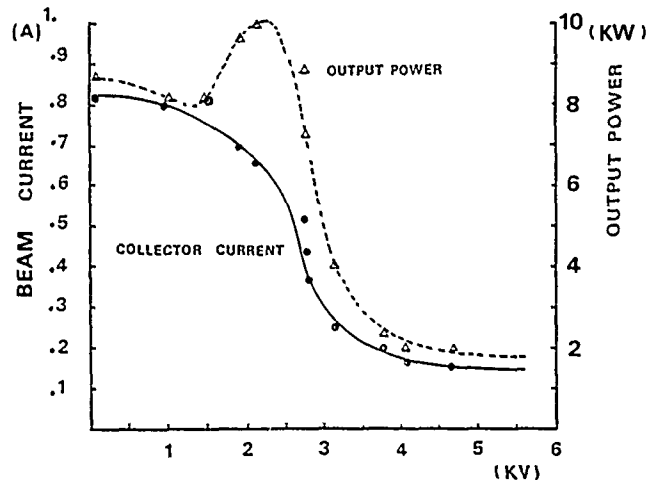


Fig. 3 Collector current and output power as a function of collector depression potential.

# AUTO-RESONANT PENIOTRON FOR HIGH POWER MILLIMETRE WAVE GENERATION WITH AN EXTREMELY HIGH EFFICIENCY

K.Yokoo, S. Ono and N.Sato

Research Institute of Electrical Communication  
Tohoku University  
Sendai 980, Japan

## ABSTRACT

We propose a new configuration of the auto-resonant peniotron oscillator (ARPO) consisting of an oscillator part with a low output power and an amplifier part and report the analytical results of its operational characteristics. The results show that a multi megawatts oscillator tube with an extremely high conversion efficiency should be possible to develop even in the millimetre and the submillimetre wave regions.

## INTRODUCTION

Recently, electron tubes used for electron cyclotron resonance heating (ECRH) of magnetically confined plasmas have required to have multi megawatts of output power in the millimetre wave region. One of candidates for such a tube would be the auto-resonant peniotron amplifier (ARPA), reported by Baird et al. [1]. In the ARPA operation, both of the transverse and the longitudinal velocities of injected electrons change together, so that the resonant condition between all of electrons and a propagating electromagnetic wave is kept until most of kinetic energies of electrons have extracted by the wave. In the ARPA, therefore, operation with an extremely high conversion efficiency should be expected to take place. The ARPA is also expected to have other two advantages for generation of high power and high frequency electromagnetic waves comparing with usual gyrotrons and peniotrons, that is, its required DC magnetic field intensity can be substantially reduced even in a cyclotron fundamental operation due to the Doppler effect and, also, allowed power dissipation in a used interaction circuit becomes higher, because the circuit has a larger radius compared with those of usual gyrotrons and peniotrons. However, if we consider about the auto-resonant peniotron oscillator (ARPO), we will not expect such a high conversion efficiency as that of the ARPA, because the resonant condition between an electron beam and a reflected electromagnetic wave existing in an interaction cavity is not satisfied. For the sake, we propose the configuration of the ARPO consisting of an oscillator part with a considerably low power and an amplifier, which enable to generate a very high power with a comparably high conversion efficiency to that of the ARPA in the millimetre and the submillimetre wave regions.

## HIGH EFFICIENT ARPO

It has been well known that the peniotron interaction was highly efficient [2], [3]. Especially, the ideal peniotron interaction which can take place in the gyro-peniotron proposed by Vitello [4] and, also, in the modified peniotron proposed by the authors [5], is extremely efficient, because almost all of the transverse energy of the electron beam can be given to the wave. Therefore, if the auto-resonant mechanism can be confined in the ideal peniotron interaction, almost

all of the total kinetic energy of an injected electron beam will be transferred to an electromagnetic wave and an extremely high conversion efficiency will be achieved. Baird et al. showed first this possibility by their proposal of the ARPA [1]. We have also carried computer simulations to study the features for both of the ARPA and the ARPO.

Figure 1 shows one of the simulation results of the ARPA characteristics, in which the RF power level and the relative electron energies of all of the sample electrons used for the simulation are shown as a function of the position along the waveguide axis for the input power of 10kW and the beam current of 13.5A. The parameters used for the simulations are same for both of the ARPA and the ARPO and are summarized in Table 1. In the simulation, twenty-four sample electrons are used, but their relative

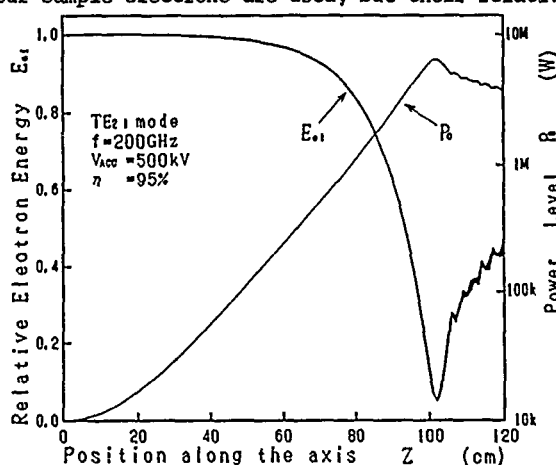


Fig. 1 Relative electron energies and power level as a function of amplifier axis in ARPA.

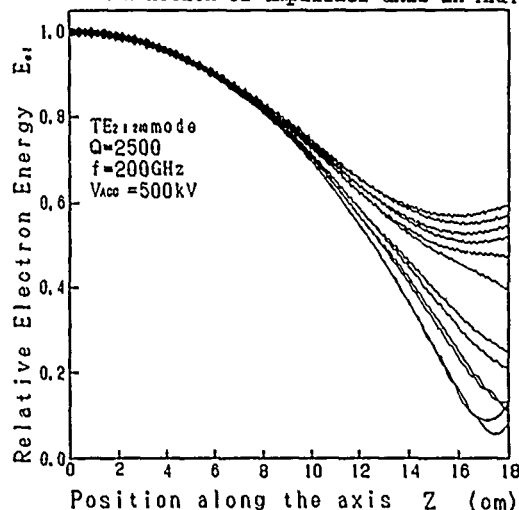


Fig. 2 Relative electron energies as a function of cavity axis in ARPO.

kinetic energies are well expressed by only one curve as shown in Fig. 1, which means that they have about the same experiences throughout the interaction region and the ideal peniotron interaction take place in this interaction. As shown in Fig.1, the relative energies of all the sample electrons become simultaneously the minimum value at  $Z=100\text{cm}$ . This value corresponds to the conversion efficiency of 94.9% and to the highest RF power of 6.42MW which are in a good agreement with expected values for the assumed operation parameters( The conversion efficiency of 100% is theoretically possible by choosing the parameters).

Figure 2 shows the relative electron energies of the sample electrons as a function of the axial position in the cavity at the beam current of 13.5A, as one of the operational characteristics of the ARPO. The relative energies of the respective electrons at the exit of the cavity correspond to the maximum conversion efficiency of 66.6% at the output power of 4.5MW and they become dispersive, which means that the electrons have different experiences with one another in the interaction region due to the existence of a reflected wave. That is the reason why the maximum conversion efficiency is limited at the lower value than that in the operation of the ARPA. However, we noticed that the energy dispersion becomes remarkable in the latter half of the cavity length but it is very small throughout the first half where each electron still has an enough energy. From this fact, we propose the new configuration of the ARPO which enable to generate a very high power with an extremely high conversion efficiency, as its schematic diagram is shown in Figure 3. As shown in the figure, it is consisting of two interaction regions. The first region works as an oscillator with a rather small output power( we will write its output power as the oscillator power in the following), so that the energy dispersion of an electron beam is still very small at the exit of this region. The second region works as an amplifier of the oscillator power. In this region, we will be able to expect to take place the operation of the ARPA and to be attained an extremely high conversion efficiency, because there is no reflected wave. We carried the computer simulations in order to confirm our expectation. For the simulations, the same parameters listed in Table 1 were also assumed.

Figure 4 shows the overall conversion efficiency and the required beam current as a function of the oscillator power. As shown in the figure, the conversion efficiency decreases from nearly 95% to 66% with increase of the oscillator power. As one can see easily, its upper value is nearly equal to that obtained in the operation of the ARPA and the lower value is similar to the maximum efficiency in the previously mentioned operation of the ARPO.

Figure 5 shows the power level as a function of the axial position in the amplifier region for several values of the oscillator power. The highest amplified power increases slightly with the decrease of the oscillator power, but, of course, the lower the oscillator power becomes, the longer the length of the amplifier region is required.

By these simulation results, we could confirm our expectations and see that the ARPO with this new configuration had definitely promising operation characteristics for generation of an intense power in the millimetre and the submillimetre wave regions.

This work was supported by a Grant-Aid for Scientific Research from Ministry of Education, Science and Culture.

Table 1  
Simulation parameters

Operation frequency	: 200 GHz
Accelerating voltage	: 500 kV
Initial velocity ratio	: 0.936
DC magnetic field intensity	: 5.23 T
Radius of waveguide	: 2.28 mm
Cavity mode	: $TE_{21240}$
Cavity length	: 18 cm
Loaded Q	: 2,500

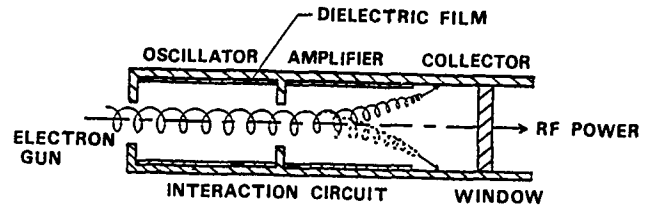


Fig. 3 Schematic diagram of the ARPO configuration.

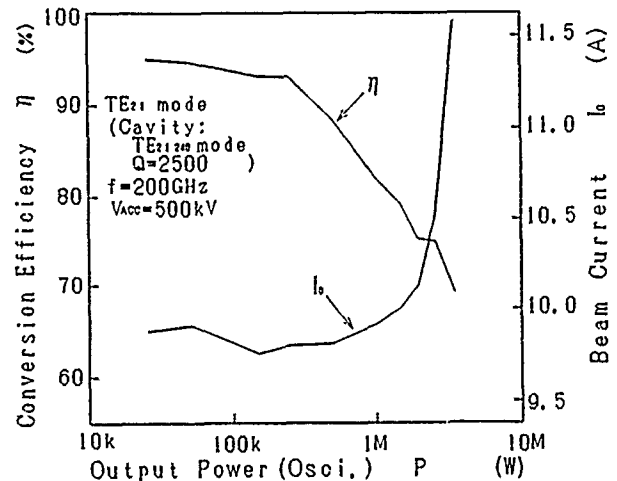


Fig. 4 Efficiency and beam current versus output power of the oscillator in the ARPO.

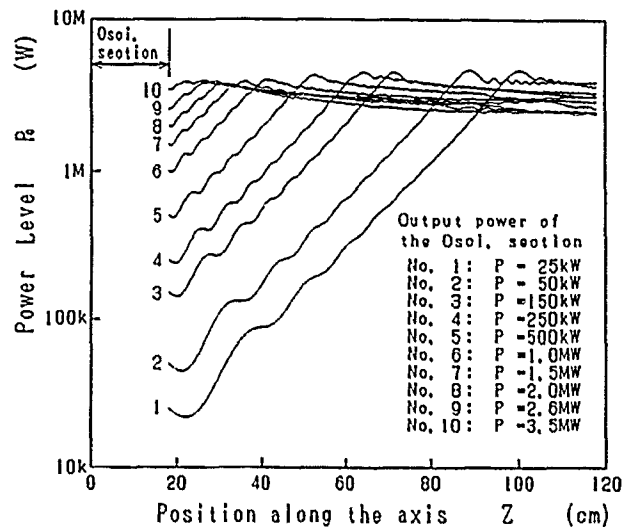


Fig. 5 Power level versus amplifier axis in the ARPO for several output power.

[1] Baird, et al.: Tech Digest IEDM(1987) 913.

[2] Yamanouchi, et al.: Proc.5th Int. Cong. on Microwave Tubes(1964).

[3] Dohler, et al.: Tech. Digest IEDM(1987) 400.

[4] Vitello : Proc. 9th Conf. on IR & MM waves(1984)

[5] Razeghi, et al.: Int. J. Elect. 59(1985) 533.



# A NEW FUNDAMENTALLY PUMPED BALANCED MIXER FOR G-BAND (140-220 GHz)

I. Galin  
Aerojet ElectroSystems Company  
Azusa, California 91702

## ABSTRACT

This paper presents a structure for a fundamentally pumped balanced mixer with whisker contacted diodes. The structure suggests compact and unique solutions for placing two connected diodes in an extremely small hybrid T, and for a low loss adjusted waveguide short.

At 183 GHz this mixer's noise temperature was under 600 K double-sideband measured at room temperature, a figure achieved until now only with single-ended mixers.

## INTRODUCTION

The fundamentally-pumped balanced mixer (FPBM) described in this paper is derived from the single-ended mixers as shown in Figure 1. Their respective LO and IF ports are connected in parallel, and their signal ports are connected in series. The LO drives the two mixer diodes 180° out of phase. This FPBM configuration, shown in Figure 2, has well known features [1], attractive enough to establish its dominance at microwave and at millimeter-wave frequencies up to 100 GHz. [2]

FPBMs have been reported above 100 GHz, but not above 170 GHz [3], [4]. Furthermore, their electrical performance has been inferior to single-ended mixers because of parasitic elements associated with their packaged mixer diodes.

This paper describes an FPBM structure for higher millimeter-wave frequencies, with electrical performance comparable to single-ended mixers.

## DESCRIPTION OF CONSTRUCTION

Figure 3 shows the FPBM structure developed at Aerojet ElectroSystems Company. This structure consists of an IF connector, two waveguide sections, one for the signal and the other for the LO. A printed circuit network interconnects these parts, and hosts two whisker contacted diodes.

The two full height waveguide sections are constructed as split-blocks, split along the middle of their broadwalls. The printed circuit is configured as a suspended stripline on a dielectric substrate. This substrate is colinear with the signal waveguide, across the LO waveguide, and connected to the IF connector. The suspended stripline network consists of the TEM-mode portion of the LO transition from waveguide  $TE_{01}$ -mode to the TEM-mode on the suspended stripline, and also includes a low pass filter for the IF. The two whisker contacted diodes are mounted as shown in Figure 4, and bridge the suspended stripline to the broadwalls of the signal waveguide.

## HYBRID T AND ADJUSTABLE WAVEGUIDE SHORT

The junction between the colinear cascade of the signal waveguide and the suspended stripline constitute a simple and compact hybrid T. The suspended stripline substrate bifurcates the signal

waveguide along the plane of maximum E-field. This substrate provides a convenient location for mounting whisker contacted diodes, necessary for high quality FPBMs at high millimeter-wave frequencies.

The main portion of the suspended stripline substrate rests in a mechanical enclosure with dimensions designed to limit the signal to propagate only in the waveguide. At the plane bordering the signal waveguide this mechanical enclosure constitutes a fixed waveguide short for the signal. The rest of the suspended stripline substrate with the contacted diodes rests beyond this fixed short, in the signal waveguide. The length of this portion of the suspended stripline is varied by sliding the substrate. This adjustment provides simple and low-loss tuning to the length of the shorted waveguide stub terminating the diodes in the signal waveguide. In the LO waveguide, a conventional sliding short tunes the LO coupling to the diodes.

## 183-GHz PROTOTYPE

The FPBM prototype was constructed and designed to operate at G-band (140-220 GHz). The signal and LO waveguide are WR-5 (0.051 in. x 0.0255 in.), and the suspended stripline substrate is fused quartz 0.003 in. thick and 0.030 in. wide. The mixer diodes are from the University of Virginia ( $R_s = 4\Omega$ ,  $C_{10} = 7fF$ ,  $V = 68$  mV,  $V_{br} = 5V$ ) contacted with 0.0005-in. diameter Ni-Au wire.

A 183-GHz, 20-mW oscillator was used to measure conversion loss and noise figure at room temperature for IF frequencies up to 4 GHz. The best results were:

- Mixer noise figure 4.8 dB double sideband
- Conversion loss 7 dB.

## CONCLUSION

FPBMs and single-ended mixers yield theoretically identical mixer conversion loss and mixer noise figure. The parity of these essential mixer properties, certainly, cannot explain the dominance of FPBMs at frequencies up to 100 GHz. FPBMs are superior relative to properties like: LO AM-noise suppression, operation bandwidth, and isolation between the LO and signal inputs. These mixer properties are generally secondary in importance, but they gain relative importance in frequency bands that have many applications and activities. Thus, the availability of FPBM is not only indicative for maturing mixer technology at any frequency band, but also a key to such state of technology. The FPBM presented in this paper may very well indicate the way to maturity, for the technology of millimeter-wave mixers at 200 GHz and beyond.

- [1] A.R. Kerr, "Noise and Loss in Balanced and Subharmonically Pumped Mixers: Part I - Theory," IEEE Trans MTT, 27, pp 938-943, Dec. 1979.
- [2] G. Spacek, "Stripguide Balanced Mixer," U.S. Patent 3,584,308 (1970).
- [3] C. Gupta, T. Del-Conte, "Trends in MM-wave Mixer Designs," Microwave Journal, Vol. 27, Apr 1984.
- [4] L.Q. Bui, N. Ton and D. Ball, "A D-Band Millimeter-Wave Crossbar Mixer," IEEE MTTTS Digest, 1984.

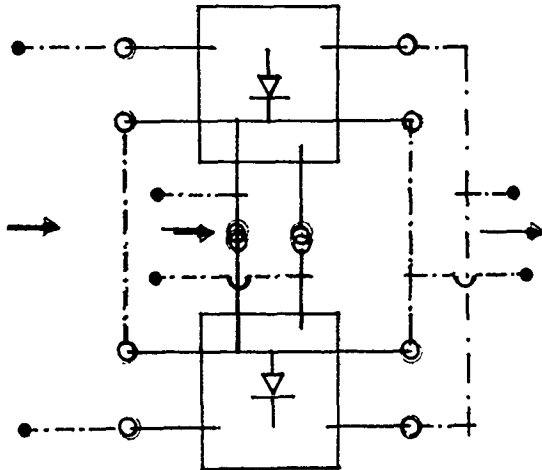


Figure 1: Two Single-Ended Mixers Connected.

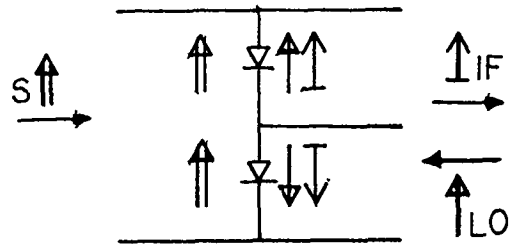


Figure 2: Fundamentally Pumped Balanced Mixer.



Figure 4:  
Whisker Contacted Diodes In A Hybrid T Structure.

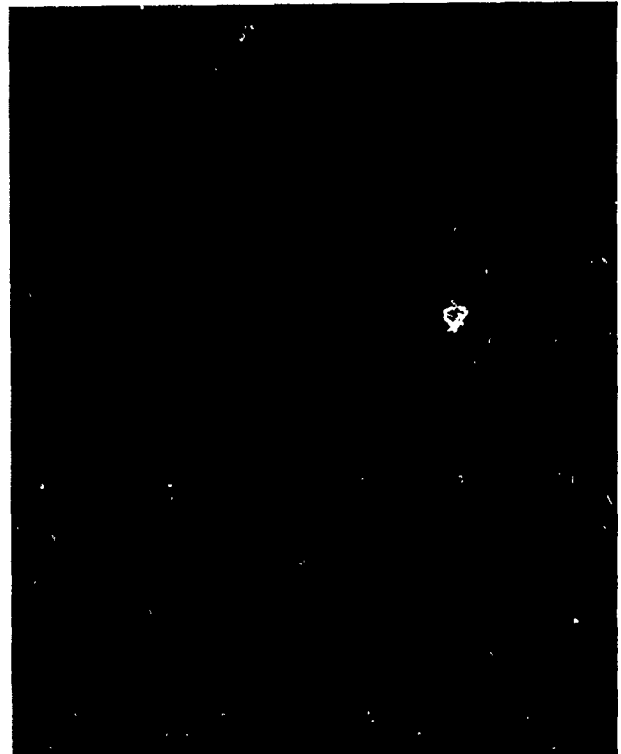


Figure 3: A Millimeter-Wave Fundamentally Pumped  
Balanced Mixer Structure.

## LARGE-AREA BOLOMETERS FOR MILLIMETER-WAVE POWER CALIBRATION

Gabriel M. Rebeiz, Curtis C. Ling

Electrical Engineering and Computer Science Department  
The University of Michigan, Ann Arbor, MI 48109-2122

and David B. Rutledge

Division of Engineering and Applied Science  
California Institute of Technology, Pasadena, CA 91125

### ABSTRACT

An accurate monolithic power meter has been developed for millimeter-wave applications. The detector is a large-area Bismuth bolometer, integrated on a fused-Quartz substrate. It simply measures the temperature change caused by the absorption of millimeter-wave radiation. The power meter is easy to fabricate, and can be calibrated using a low-frequency network. The measured responsivity for a 1x1cm bolometer is about 1mV/W, at a bias of 1V, and a video modulation of 100Hz. The noise spectrum exhibits a 1/f rolloff below 1KHz, and is limited by the Johnson noise for higher frequencies. The NEP of the detector is  $3 \times 10^{-6} \text{ W Hz}^{-1/2}$  at a video modulation of 1KHz. It is possible to decrease the current NEP by fabricating bolometers with higher responsivities. Possible application areas are absolute power calibration and localized power-density measurements for millimeter and submillimeter wavelengths.

### INTRODUCTION

Power measurements at millimeter-wave frequencies is conventionally done using waveguide power meters. However, these become very expensive in the millimeter-wave bands, and are simply not available for frequencies higher than 200GHz. Bloch and Gaddy [1] integrated a  $0.5 \text{ mm}^2$  Bismuth bolometer for infrared detection. The measured responsivities were low because the device was optimized for wide bandwidth. We have developed a large-area bolometer optimized for millimeter-wave power detection. The bolometer is much thinner than a wavelength, and therefore presents a millimeter-wave surface impedance equal to its DC resistance per unit

square. This fact, in conjunction with the bolometer large size, allows the use of a transmission-line equivalent circuit to determine accurately the mismatch between the bolometer and an incident plane-wave. This gives the fraction of the incident power absorbed by the bolometer. If the bolometer responsivity is known using, for example, a LF calibration network, an accurate power-density measurement is then made at millimeter wavelengths.

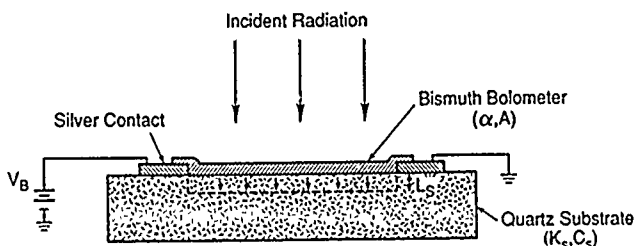


Fig. 1. A monolithic large-area bolometer (LAB).

### THEORY

The bolometer is a heat sensitive device, and will respond to the average power of an amplitude modulated signal. The bolometer will then heat up and cool down at the modulation frequency. This will generate a heat wave that will propagate a distance  $L_S$  (thermal diffusion length) into the substrate. Assuming a one-dimensional heat flow model, and neglecting the thermal conductance of air and the silver contacts,  $L_S$  is then given by [2]

$$L_S = (K_S / (2\pi f C_S))^{1/2}$$

where  $K_S$  and  $C_S$  are the thermal conductivity and capacity of the substrate, respectively, and  $f$  is the modulation frequency. The thermal diffusion length is very short in a fused-Quartz substrate,

being less than 400mm for a modulation frequency of 1Hz. This means that, for all practical purposes, the heat wave never reaches the back of the substrate. The bolometer responsivity is then given by [2]

$$\text{Resp} = \alpha V_B L_S / (A K_S)$$

where  $\alpha$  is the temperature coefficient of resistivity of Bismuth,  $A$  is the area of the bolometer, and  $V_B$  is the bias voltage. For a fused-Quartz substrate with  $K_S = 1.6 \text{ Wm}^{-1} \text{ K}^{-1}$  and  $C_S = 2.36 \times 10^6 \text{ Jm}^{-3} \text{ K}^{-1}$ , and with  $\alpha = 0.003 \text{ K}^{-1}$  for a 1000Å Bismuth layer, the theoretical responsivity for a bolometer with the same specifications given above, is equal to 0.65mV/W.

### MEASUREMENTS

The frequency response of the bolometer is measured using the LF network shown in Fig. 2. An amplitude modulated 4.3MHz signal is applied to the bolometer. The bolometer is too slow to follow the 4.3MHz signal, and responds to the average power of the input signal. The frequency response is found by varying the modulation frequency and measuring the output signal from the bolometer. The output signal drops as  $f^{-1/2}$ , in agreement with the theoretical model. In order to calibrate the bolometer, the RF power absorbed must be known. This is done by monitoring the instantaneous applied voltage across the bolometer. An absolute responsivity of 0.85mV/W is found for a 35Ω bolometer, at a bias of 1V, and a modulation frequency of 100Hz. The discrepancy with the theoretical responsivity arise because of uncertainties in the values of  $\alpha$  and  $K_S$ .

The frequency response can also be found using the millimeter-wave system shown in Fig. 3. In this case, the source is amplitude modulated, and the output signal from the bolometer is detected using a lock-in amplifier. The measured frequency response drops as  $f^{-1/2}$ . The absolute responsivity is found by measuring the source power with an accurate waveguide power meter, and by using a calibrated horn antenna. A transmission-line equivalent circuit is used to calculate the power absorbed by the bolometer. The absolute responsivities measured with an 80.7GHz system (and a 93.2GHz system) were within 10% of the measured responsivities using the LF system.

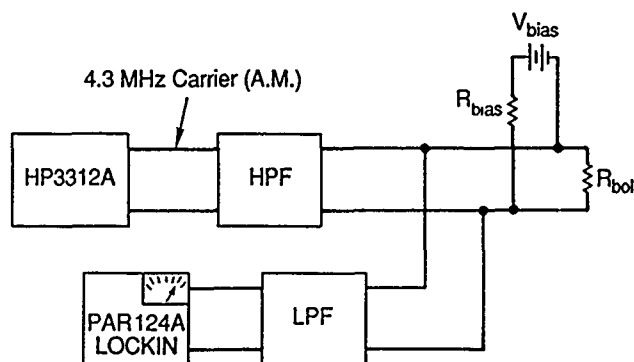


Fig. 2. The LF calibration network.

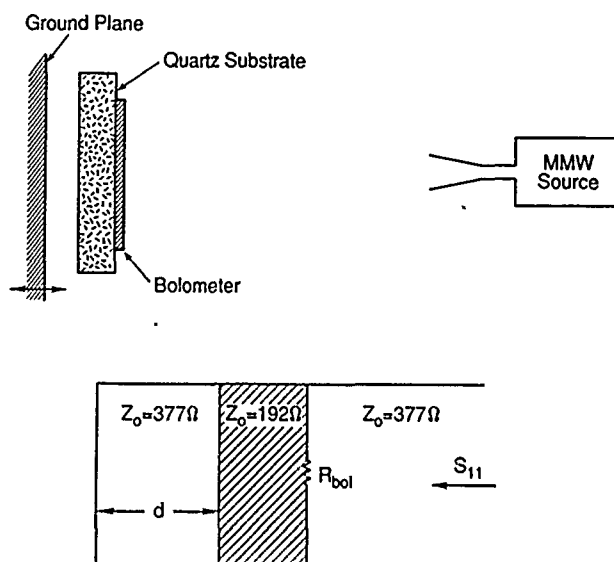


Fig. 3. The transmission-line equivalent circuit.

### ACKNOWLEDGEMENTS

This work was supported by the Innovative Space Technology Center at the Jet Propulsion Laboratory, and is now supported by the Center of Space Terahertz Technology at the University of Michigan, Ann Arbor.

### REFERENCES

- [1] W. H. Block and O. L. Gaddy, "Thin metal film room-temperature IR bolometers with nanosecond response times," IEEE Journal Quantum Electronics, vol. QE-9, No. 11, November 1973.
- [2] E. Holman, "Heat Transfer," First Edition, McGraw Hill Book Company, New York, 1963.

# Series-Connected Josephson-Effect Mixers for Millimeter-Wave Radiation

Hiroshi Ohta, Toshiaki Matsui\* and Bokuji Komiyama\*

The Institute of Physical and Chemical Research,  
Hirosawa 2-1, Wako-shi, Saitama 351-01, Japan;

\*Communication Research Laboratory, Ministry of Posts and Telecommunications,  
Nukukitamaichi 4-2-1, Koganeishi, Tokyo 184, Japan

## Abstract

Millimeterwave detectors have been made of a series-connected array of Josephson junctions. Each junction of the array responds in phase to radiation and therefore the series-connected array as a whole behaves as if it were a single Josephson junction. When the Josephson junctions have a high critical current density, the IF outputs have sharp peaks at the voltages  $V = 2N\Delta/ne$  where  $N$  is the number of the Josephson junctions in series connection and  $n$  is an integer. The subharmonic energy gap structures in voltage-current curves of Josephson junctions come from the Andreev-reflection-assisted-tunneling according to the recent Arnold theories.

## Introduction

Josephson junctions for millimeter-wave mixers have a small junction-area with a small capacitance. Their critical currents cannot be very small because of noise roundings in the voltage-current curves. Therefore Josephson junctions for millimeter-wave mixers inevitably have a high critical-current density. Recent lithographic techniques can make good Josephson junctions of high critical-current density. The recent Arnold theory explains very well behaviors of Josephson junctions with a larger critical-current density than  $10^4 \text{ A/cm}^2$ .

## Fabrication of Quasi-Planar Junctions

Our mixers are made of short weak links named Quasi-Planar junction as shown in Fig.1. Fabrication techniques of Quasi-Planar junction are described in details in References [9] and [8]. QP junctions are made only of niobium on 0.5 mm thick fused quartz substrates.<sup>7</sup> Niobium thin films are prepared by a 4 inch magnetron-type rf sputtering system. Both of the niobium electrodes are made by lift-off. The weak links of niobium are prepared by electron beam lithography and dry etching.

## The Arnold Theory

The typical temperature dependence of the critical current of QP junctions is that of short weak links in the clean limit.<sup>2</sup> Heavy anodization of the weak link portion of QP junctions can change the temperature dependence of the critical current from that of a short weak link to that of a tunnel Josephson junction.<sup>1</sup> These observations agree with the recent general theory presented by D.B. Arnold which explains the temperature dependence of the critical currents both of metallic weak links and tunnel Josephson junctions consistently.<sup>3,5</sup> Before anodization of weak links, the critical current density of QP junctions are around  $10^4 \text{ A/cm}^2$ . Since the weak link portion of QP junctions is three-dimensionally constricted, nonequilibrium effects are minimized. Unless the transmission coefficient between the superconducting electrodes  $|T|^2$  is much smaller than unity, higher order terms  $|T|^4$ ,  $|T|^6$ ,  $|T|^8$ , ... must be taken into account according to the Arnold theory.<sup>4</sup> The total current is not a sum of the pair current and the quasi-particle current anymore. The Andreev reflection assisted tunnel currents flow at finite voltages below the energy gap voltage  $2\Delta/e$ . Any Josephson junctions of high critical current densities must have subharmonic energy-gap structures or subgap currents including tunnel junctions. Millimeter or Submillimeter wave detectors must have high critical current densities.



Fig.1 Electron microscope picture of a Quasi-Planar junction. The line of electron beam resist is  $0.17 \mu\text{m}$  wide and  $0.4 \mu\text{m}$  high where a  $0.17 \mu\text{m}$  wide and  $0.013 \mu\text{m}$  thick niobium weak link lies underneath.

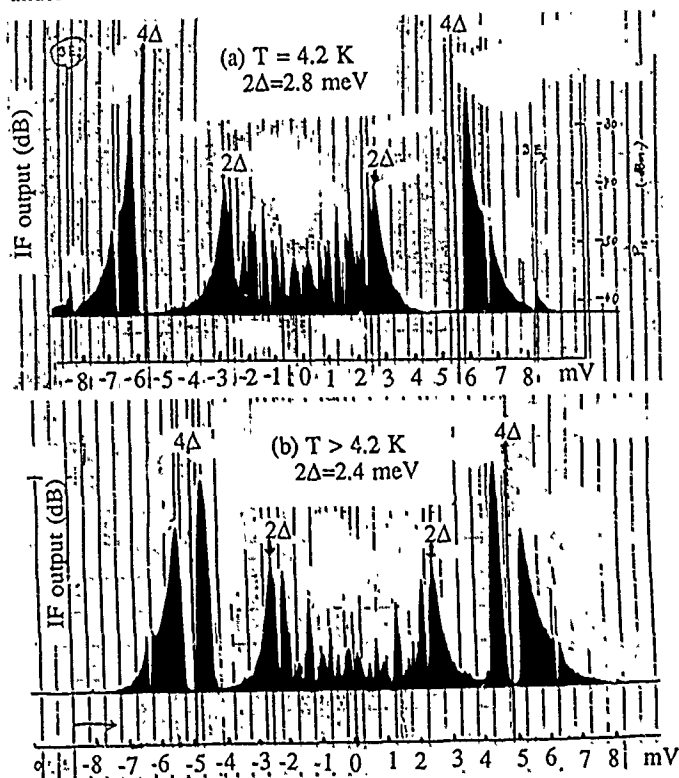


Fig.2 IF output from a 100 GHz mixer of a series-connected array of eleven Quasi-Planar junctions in different temperatures (a) & (b). The IF output peaks at the voltages  $2N\Delta/ne$  where  $N=11$  and  $n$  is an integer.

### Millimeter-wave Mixers

We have observed subharmonic energy-gap structures in the IF output from 100 GHz mixers of a series-connected array of eleven QP junctions as shown in Figs.2 (a) and (b) in different ambient temperatures. The IF outputs from a Josephson mixer is proportional to the dynamic resistance of the Josephson junction. <sup>11</sup> The IF output peaks at the voltages

$$V = 2N\Delta/ne \quad (1)$$

where  $N=11$  and  $n$  is an integer. <sup>7</sup> Note that no IF peaks are observed at  $4\Delta/e$  because  $11/n$  is never 2 for any integer  $n$ . Figure 3 shows that the electron gets enough energy to get into the superconductor S in the right hand side after  $n = 2\Delta/(eV/N)$  times Andreev reflections. It has been assumed that each junction of the array responds in phase to radiation and therefore shares the applied voltage  $V$  evenly. It should be noted that in Fig.3 one electron and  $n = \Delta/(eV/N)$  pairs have been transferred across the barrier at the same time to conserve the energy. When a large power from a local oscillator is applied to the mixer, pairs are transferred across the barrier in the reverse direction absorbing photons of local oscillator frequency  $\omega$  in Fig.3. Namely the ac Josephson effect dominates the Andreev reflection assisted tunneling when

$$\omega_J = 2eV/\hbar N = l\omega \quad (2)$$

where  $l$  is an integer. The observed patterns of IF outputs are similar to those of the dynamical resistance vs. bias voltage calculated numerically by G.B.Arnold as shown in Fig.6. For better comparison between experiment and theory we must measure both the transmission coefficient  $17^{12}$  and the energy-gap ratio  $\Delta_1/\Delta_2$  exactly. In this mode of mixing the Andreev reflection assisted tunneling plays an important role directly or indirectly. For further understandings of this mixing, the Arnold theory must be extended to include the effect of applied microwave radiation like the Werthamer theory.

### Harmonic Mixing

Harmonic mixers for millimeter and far-infrared waves are important because of lack of high-power local oscillators. <sup>10</sup> We have done preliminary experiments of harmonic mixing using a series-connected array of eleven QP junctions as shown Figs.4 and 5. The signal frequency is 105.9 GHz and the local oscillator frequency is 9.58 GHz. The IF peaks appear at the voltages  $V = 2N\Delta/ne$  again. Harmonic mixings are very effective in Josephson mixers because of their strong nonlinearities. We are preparing harmonic mixing experiment in far-infrared regions.

### References

- [1] H.Ohta, M.Takahata, Y.Yamada and Y.Takahashi, Japan. J. Appl. Phys. vol.26 Supplement 26-3 (1987)p.1613.
- [2] K.K.Likharev, Rev. Mod. Phys. 51(1979) p.101.
- [3] G.B.Arnold, J.of Low Temp. Phys. 59 (1985) p.143.
- [4] G.B.Arnold, J.of Low Temp. Phys. 68 (1987) p.1.
- [5] T.M.Klapwijk, *SQUID'85-Superconducting Interference Devices and their Applications* 1985 Walter de Gruyter & Co., Berlin, New York, p.1.
- [6] M.A.Peshkin and R.A.Burman, Phys.Rev.B, vol.28 (1983) p.161
- [7] H.Ohta, T.Matsui, T.Igarashi, S.Kodaira, Y.Yamada and Y.Takahashi, IEEE Trans. on Magnetics MAG-19 (1983) 601. H.Ohta and Y.Yamada, IEEE Trans.on Magnetics MAG-21(1985)p.951.
- [8] H.Ohta, §III • 1 • 4 • 4[3] Superconducting Weak Link in pp. 699-703 of *THIN FILM HANDBOOK* edited by Japan Society for the Promotion of Science 131st Committee, 1983, Ohmsha, Co., Tokyo (in Japanese).
- [9] H.Ohta, M.Takahata, Y.Takahashi, K.Shinada, Y.Yamada, T.Hanasaka, Y.Uchikawa, M.Kotani, T.Matsui and Bokuji Komiyama, to be published in IEEE Trans. on Magnetics MAG-25(1989).

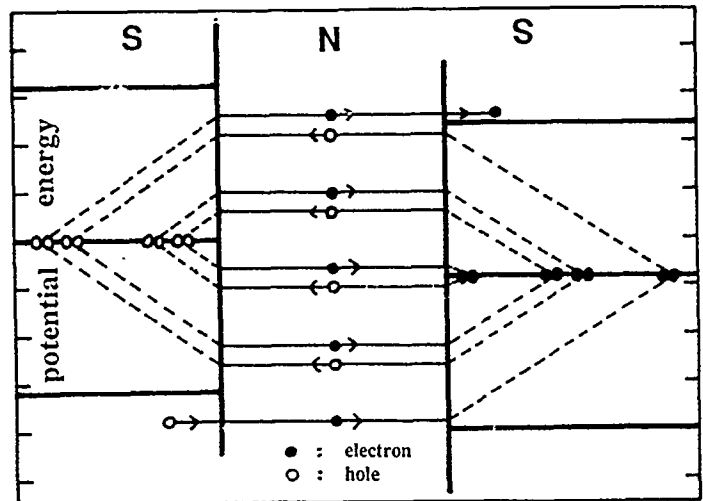


Fig.3 Andreev Reflection Assisted Tunneling. One electron and  $n = \Delta/(eV/N)$  pairs transfer across the barrier conserving the energy.

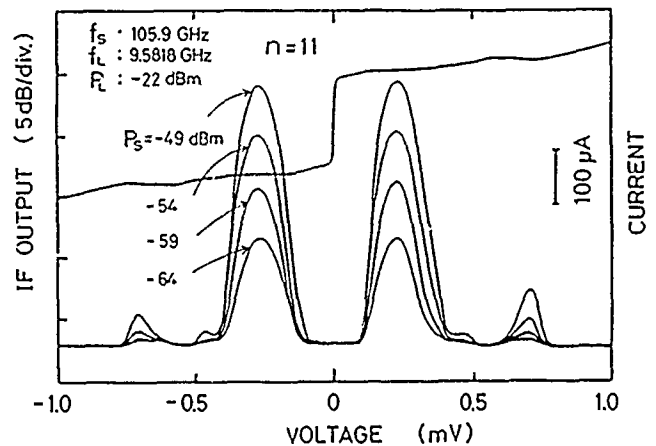


Fig.4 I-V and IF signal vs. V with a low local oscillator power. The number of junctions in series connection is eleven.

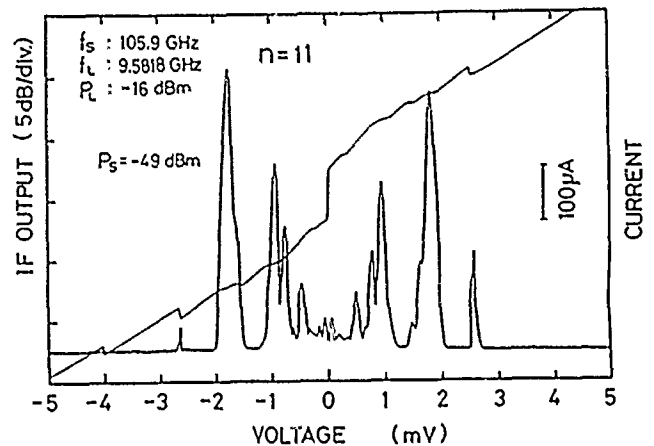


Fig.5 I-V and IF signal vs. V with a medium local oscillator power. The number of junctions in series connection is eleven.

- [10] T.Matsui, B.Komiyama and H.Ohta, to be published in IEEE Trans. on Magnetics MAG-25(1989).
- [11] A.N.Vystavkin, V.N.Gubankov, L.S.Kuzumin, K.K.Likharev, V.V.Migulin and V.K.Semenov, Rev.Phys.Appl., 9(1974)p.79.

## A MULTICHANNEL SUBMILLIMETER WAVE INTERFEROMETER SYSTEM ON ATF

D. P. Hutchinson, C. H. Ma, K. L. Vander Sluis, C. A. Bennett,<sup>†</sup> and J. Lee,<sup>§</sup>Oak Ridge National Laboratory  
Oak Ridge, TN 37831

## ABSTRACT

A high resolution multichannel far-infrared interferometer has been constructed for the ATF experiment at Oak Ridge. The system consists of a pair of cw 119- $\mu\text{m}$  methanol lasers, optically pumped by separate CO<sub>2</sub> lasers. An external Stark-cell modulation scheme is used to stabilize the frequencies of the CO<sub>2</sub> lasers. The system is designed to be operated, monitored, and stabilized by a PC computer.

## INTERFEROMETER

A 15-channel interferometer operating at a wavelength of 119  $\mu\text{m}$  has been developed for the ATF experiment at the Oak Ridge National Laboratory. A schematic diagram of the interferometer is shown in Fig. 1. The large number of channels is achieved by the use of reflective beam expansion optics to create a beam 2 cm  $\times$  45 cm [1]. After passing through the plasma discharge, the elongated beam produced by the cylindrical mirrors is dissected at the focal plane of the optics system by an array of 15 off-axis paraboloid reflectors, each of which illuminates a single Schottky-diode detector. The use of the beam expanding optics system reduces the number of optical elements required for the interferometer to approximately 2-3 per channel. The FIR light beams are transported from the laser room to the experimental area by 25 mm i.d. dielectric waveguides purged with dry nitrogen.

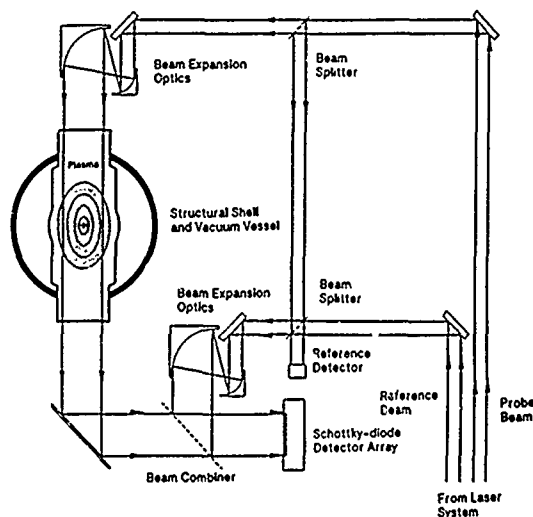


Figure 1.  
Schematic diagram of interferometer

## REFERENCES

\*Research sponsored by the Office of Fusion Energy, U.S. Department of Energy, under Contract No. DE-AC05-84OR21400 with Martin Marietta Energy Systems, Inc.

<sup>†</sup>On sabbatical leave from the University of North Carolina at Asheville.

<sup>§</sup>University of Tennessee, Knoxville.

[1] C.A.J. Hugenholtz and B.J.H. Meddens, Rev. Sci. Instrum. **53**, 171 (1982).

# FIR Polarimeter/Interferometer for JIPP T-II U

A. Yasuda

Tokyo University of Mercantile Marine, Koto-ku, Tokyo 135, Japan

K. Kawahata and J. Fujita

Institute of Plasma Physics, Nagoya University, Nagoya 464-01, Japan

S. Okajima

Faculty of Engineering, Chubu University, Kasugai 487, Japan

Y. Nagayama

Faculty of Science, The University of Tokyo, Bunkyo-ku 133, Tokyo, Japan

## ABSTRACT

A one channel FIR polarimeter/interferometer, with HCN laser of 0.337 mm is designed for JIPP T-II U Tokamak, in order to prove the possibility of the inference of current density distribution. The measurement itself is successful, of the distributions of the line density and Faraday rotation angle with the accuracy of 0.1 fringe and 0.1 degree respectively.

## INTRODUCTION

For the study of the fundamental behavior, such as transport phenomena and plasma stability, of tokamak plasmas, it is important to measure the electron density distribution and the current density profile. A one channel FIR polarimeter/interferometer, with HCN laser of 0.337 mm is designed for JIPP T-II U Tokamak<sup>1</sup>, with reference to the system in TEXTOR<sup>2</sup>, in order to prove the possibility of the inference of current density distribution.

## EXPERIMENTAL SETUP AND RESULT

The schematic diagram is shown in Fig.1. A high power HCN laser<sup>3</sup>, of which laser cavity is 5 m and maximum output power is 500 mW, is installed in the diagnostic room 8 m apart from the tokamak. The laser beam is introduced to the meter through a 6 m dielectric waveguide of 59 mm in diameter. All the optical components of the meter are fixed to a C-shaped framework, which is mounted on a truck movable radially to the major radius and isolated from the plasma vessel and the magnetic coils. The reference beam of a Mach-Zehnder type interferometer is modulated by the rotating grating and suffers the frequency shift. Ga-As Schottky barrier diode mixers with corner cube mount<sup>4</sup> are used as detectors to obtain high temporal resolution with good signal-to-noise ratio. Although the beat frequency  $\Delta f$  is 10 kHz in the present experiment, it goes up to 50 kHz recently.

The interferometric signal  $S_I$  is given by

$$S_I \propto \cos \Omega \cos(2\pi\Delta f t + \Delta\phi),$$

where  $\Delta\phi$  is the phase shift caused by the electron line density,  $n_e\lambda$ , and  $\Omega$  is the Faraday rotation angle proportional to the poloidal magnetic field  $B_{p//}$  and  $n_e\lambda$  along the probing beam path. It is detected in reference to the unmodulated reference signal  $S_R$  ( $\propto \cos(2\pi\Delta f t)$ ).

The polarimetric signal  $S_F$  is given by

$$S_F \propto \sin \Omega \cos(2\pi\Delta f t + \Delta\phi).$$

It is detected as an amplitude increment which is proportional to the reflected one, produced by Faraday rotation of the probing beam, at the wire grid beam recombiner. In the present experiment, only the amplitude variation is detected. The direction of the  $B_{p//}$  can be detected by using a phase sensitive detector, which is controlled by the  $S_I$ , in our recent system.

By shifting the observation points shot by shot in radial direction, temporal variations of the fringeshift (upper trace) and Faraday rotation angle (lower trace) are observed as shown in Fig.2. One vertical division is 0.5 V for both traces in each pattern. It corresponds to 0.8 fringe or  $5.2 \times 10^{20} \text{ m}^{-2}$  of  $n_e\lambda$  and 2 degree. The minimum detections of both measurements are about 0.1 fringe and 0.1 degree, respectively. The calibration of the amplitude of the  $S_F$  is executed by rotating the half-wavelength quartz plate in the probing beam path.

This laser wavelength of 0.337 mm, used here, is appropriate for the measurement of JIPP T-II U in considering that the fringeshift and the rotation angle are moderate and the refraction effect is negligibly small. The elliptical polarization<sup>5</sup> due to the toroidal B field, 2.9 T in the experiment, however can not always be neglected.

## RESULT OF THE RECENT EXPERIMENT

Figure 3 (a) and (b) show the temporal variations of the fringeshift and Faraday rotation angle observed in the recent experiment. They are acquired and displayed by the super mini-computer data acquisition system<sup>6</sup>. The discharge lasts about 400 ms in the normal operation. However it disrupts abruptly after about 200 ms often in the experiment.

Figure 4 (a) and (b) are radial profiles of the fringeshift and Faraday rotation angle at 100, 200 and 300 ms, deduced from the observed patterns, such as Fig.3, at different radial positions under the same discharge condition. The center of the vacuum chamber locates 930 mm from the Tokamak center. The radius of the chamber is 245 mm. The outer wall of the chamber locates at 1175 mm from Tokamak center. The profiles at 100 and 200 ms are rather smooth before the disruption.

We are preparing a 6-channel meter with reference to the present experiment.



## REFERENCES

- 1) K. Toi et al., in Plasma Physics and Controlled Nuclear Fusion Research (Proc. 10th Int. Conf., London, 1984) Vol.3, IAEA, Vienna (1985) 353.
- 2) H. Soltwisch, Rev.Sci.Instrum., 57 (1986) 1939.
- 3) S. Okajima, K. Kawahata, T. Tetsuka, S. Kubo and J. Fujita, 11th Int. Conf. on IR and MM Waves, Pisa, 1986, Conference Digest, p.249.
- 4) T. Tetsuka, K. Kawahata, A. Nishizawa, J. Fujita and S. Okajima, Int. J. Infrared Millim. waves 6 (1985) 729.
- 5) F. De Marco and S. E. Serge, Plasma Physics 14 (1972) 245.
- 6) S. Hidekuma et al., Ann. Rev. IPPJ (Apr.1986-Mar.1987), p.32

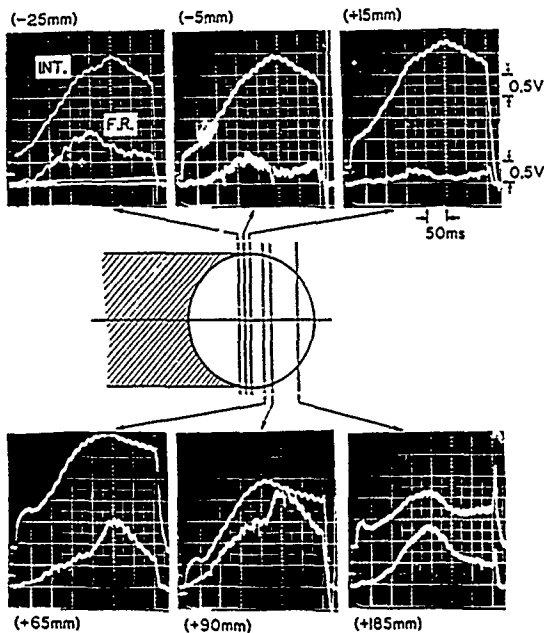


Fig.2 Temporal variations of fringes shift (upper trace) and Faraday rotation angle (lower trace) at different positions of JIPP T-II U.

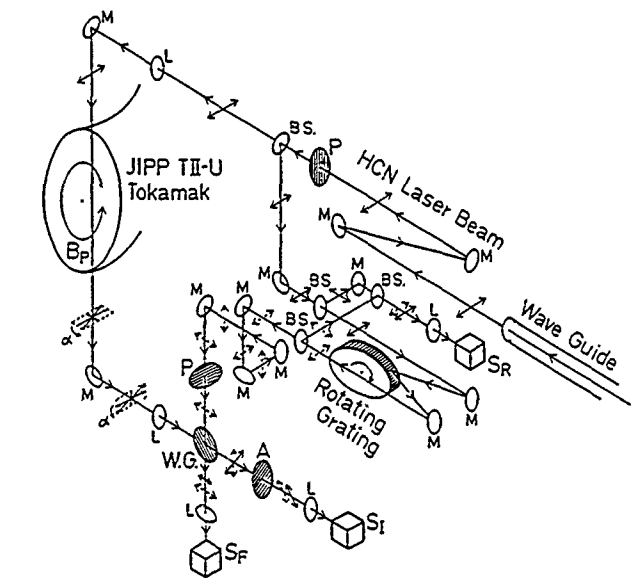
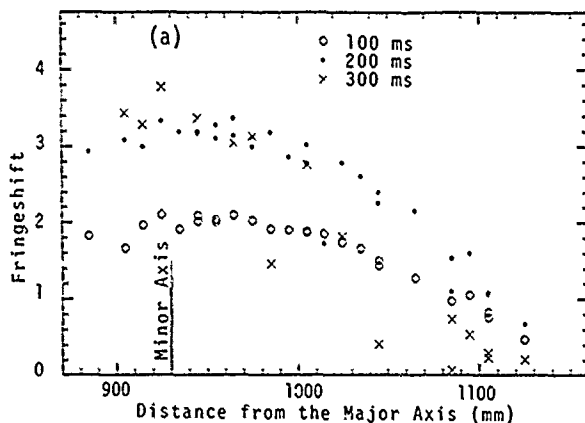


Fig.1 Schematic diagram of the experimental setup.

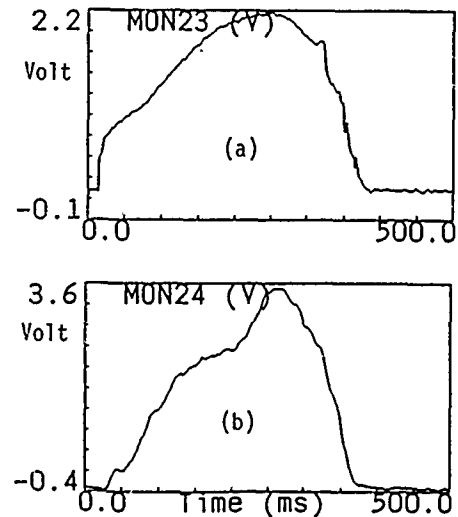


Fig.3 Temporal variations of (a) fringe shift and (b) Faraday rotation angle at  $R = 1005$  mm in the recent experiment.

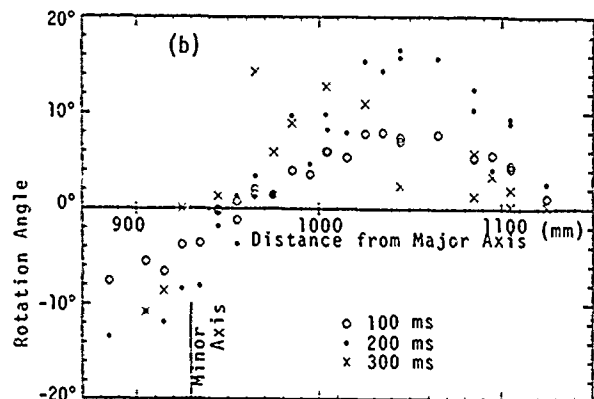


Fig.4 Radial profiles of (a) fringes shift and (b) rotation angle at 100, 200 and 300 ms.

# A Multichannel HCN Laser Interferometer for Electron Density Measurements on the JIPP T-IIU Tokamak

K. Kawahata and J. Fujita

Institute of Plasma Physics, Nagoya University, Nagoya 464-01, Japan

A. Yasuda

Tokyo University of Mercantile Marine, Koto-ku, Tokyo 135, Japan

S. Okajima

Faculty of Engineering, Chubu University, Kasugai 487, Japan

## Abstract

A six-channel HCN laser interferometer system has been developed for the measurement of the electron density profile in the JIPP T-IIU tokamak. The optical configuration is of the Michelson interferometer type, of which reflecting mirrors are directly attached on the wall of the vacuum vessel. This optical configuration enables the density profile measurements by the multichannel laser interferometer with a small optical window.

## 1. Introduction

In recent years the high density plasmas in the range of  $10^{20} \text{ m}^{-3}$  have been achieved in tokamak devices and helical devices. For the measurements of such high electron density, Infrared laser and Far-Infrared laser interferometers have widely been used. In the JIPP T-IIU tokamak<sup>1)</sup>, the maximum electron density is about  $10^{20} \text{ m}^{-3}$  and the plasma size of  $a_p = 23 \text{ cm}$ . An HCN laser source is considered to be appropriate for the probe beam of the interferometer from the view points of mechanical stability and diffraction effects caused by the plasma.

For the measurement of the density profile it is necessary to construct a multichannel interferometer system. Usually, to construct a multichannel assembly it is necessary to equip with a large sized window or a large number of windows<sup>2)</sup>. However, this requirement is not always satisfied in toroidal devices. In the JIPP T-IIU device, there are no windows that satisfy such requirements. Then we have developed a Michelson type interferometer which enables us to measure the full density profile through single small window.

## 2. Experimental arrangement and results

Figure 1 shows a schematic drawing of the optical configuration of a 6-channel HCN laser interferometer. A high power HCN laser<sup>3)</sup>, which has a cavity length of 5 m and the maximum output power of 0.5 W, is installed in the diagnostic room 8 m apart from the tokamak. The laser beam propagates 6 m to reach the interferometer through a dielectric waveguide of  $\phi 59 \text{ mm}$  (Pyrex glass). The laser beam is divided into 6 probe beams and a reference beam by the beam splitters (B.S.1-6) made of quartz. Each probe beam split off at B.S.1-6 enters into the vacuum chamber through a quartz window, and reflected by the concave mirrors made of stainless steel which are directly

attached on the wall. In order to read the phase shift directly, a frequency of the reference beam is Doppler shifted by means of the rotating grating ( $\Delta f = 50 \text{ kHz}$ ). The reference beam is matched with the probe beams at B.S.14-19 by the TPX lens L5.

For the detection of the interference signals and the reference signal, compact sized Schottky barrier diode mixers with corner cube mount<sup>4)</sup> are used, which give higher frequency response with good signal to noise ratio. The phase difference between probe and reference signals is directly read out by a digital counter, which enables us to measure the phase shift within a dynamic range of  $16 \times 2\pi$  with an accuracy of  $1/16 \times 2\pi$ . As is seen in Fig.1, this interferometer system is composed of 2 interferometers, 3 chords (including midplane chord) interferometer in the upper side of the plasma column and 4 chords interferometer in the lower side. Therefore, it is possible to examine up-down asymmetry of the plasma density profile. In the usual operation regime of the tokamak plasma, it is considered that the plasma has up down symmetry. In this case this interferometer system can be operated as 6-channel interferometer in a half plasma radius.

Figure 2 shows the effects of the change of the toroidal magnetic field and equilibrium field on the interferometry signals. When the toroidal field ( $B_t = 2.9 \text{ T}$ ) is excited, the phase of the interferometer gradually shifts and becomes a constant value during flat top of the field, where the plasma discharge occurs ( $t = 2.5 \text{ s}$ ). After the plasma discharge, low frequency oscillations appear due to the mechanical vibration. The amplitude of the vibration is about  $13 \mu\text{m}$  which corresponds to the fringe shift of  $1/13$  fringe. At the present system, there is no installation of visible wavelength interferometer for the correction of the vibration, so that the noise equivalent average density is about  $6 \times 10^{17} \text{ m}^{-3}$ .

Figure 3 shows the temporal variations of the line integrated density for 6 different chords. The plasma discharge starts at 17 ms. The base lines before  $t = 17 \text{ ms}$  contain the noise signals from the vibration of the vacuum vessel caused by energizing the toroidal coil. It is found that a vibration-compensating interferometer is not necessary. The Abel-inverted profile is shown in Fig.3(b). The measured density profile is relatively uniform at the start-up phase of the discharge and well fitted by  $n_e(r) = n_e(0) [1 - (r/a)^2]^m$  at the flat-top phase, where the index  $m$  is between 1.0 and 1.2.

#### 4. Conclusion

We have developed 6-channel HCN laser interferometer for the density profile measurement on the JIPP T-IIU tokamak. The optical configuration is of the Michelson interferometer type, of which reflecting mirrors are directly attached on the wall of the vacuum vessel. It is found that this optical configuration enables us the density profile measurements by the multichannel laser interferometer with a small optical window.

#### References

- [1] K. Toi et al., in Plasma Physics and Controlled Nuclear Fusion Research (Proc. 10th Int. Conf., London, 1984) Vol.3, IAEA, Vienna (1985) 353.
- [2] D.K. Mansfield, H.K. Park, L.C. Johnson, H.M. Anderson, R. Chouinard, V.S. Foote, C.H. Ma and B.J. Clifton, PPPL 2450.
- [3] S. Okajima, K. Kawahata, T. Tetsuka, S. Kubo and J. Fujita, 11th Int. Conf. on IR and MM Waves, Pisa, 1986, Conference digest, p.249.
- [4] T. Tetsuka, K. Kawahata, A. Nishizawa, J. Fujita and S. Okajima, Int. J. Infrared Millim. Waves 6 (1985) 729.

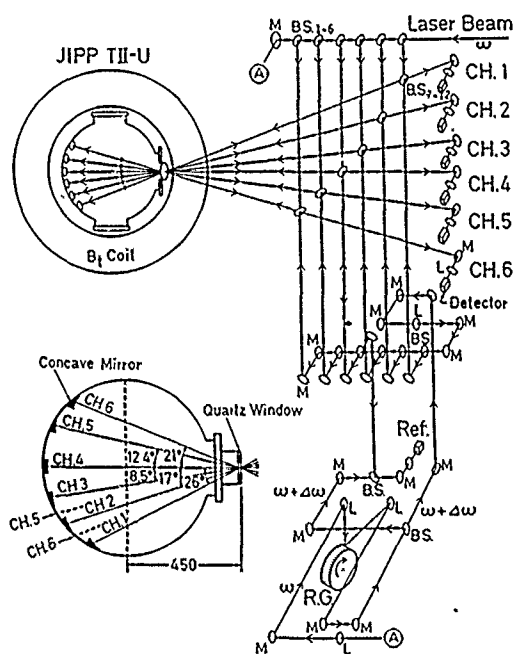


Fig.1 Schematic drawing of 6-channel HCN laser interferometer.

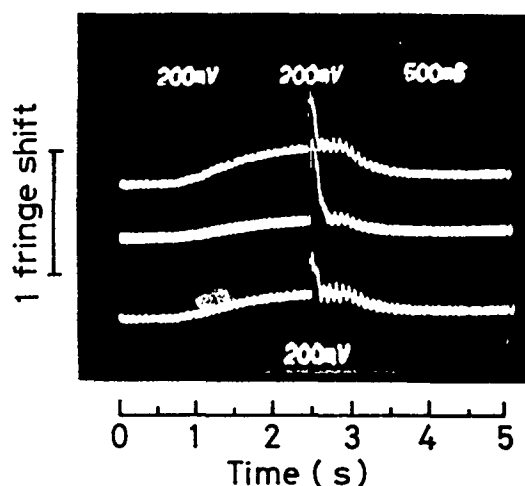


Fig.2 Time behaviours of line integrated densities for 3 different chords.

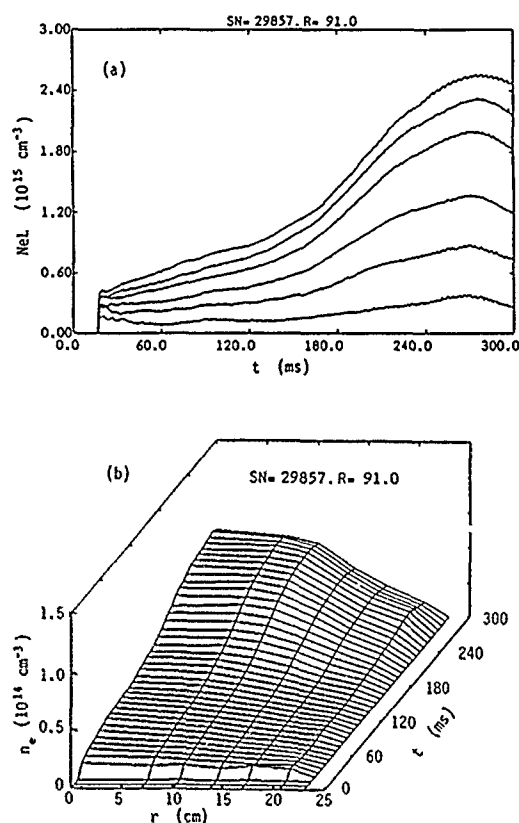


Fig.3 (a) Line integrated densities for 6 different chords.  
(b) Time evolutions of the density profile.

# SCATTERING OF MILLIMETER-SUBMILLIMETER RADIATION FROM THE TORTUS TOKAMAK PLASMA

M.D. Bowden, P.W. Fekete, M.J. Ballico, G.F. Brand, I.S. Falconer,  
B.W. James & K.J. Moore

School of Physics, University of Sydney  
NSW 2006, AUSTRALIA

T. Idehara

Faculty of Engineering, Fukui University  
Fukui 910, JAPAN

## ABSTRACT

A formic acid laser operating at  $433\ \mu\text{m}$  and a gyrotron which is step-tunable in the range 75–330 GHz are being used to study density fluctuations in a small tokamak during Alfvén wave heating. The scattering systems and recent results will be discussed.

## INTRODUCTION

TORTUS, a small tokamak ( $R = 0.44\text{m}$ ,  $a = 0.10\text{m}$ ) which produces a 30 ms long plasma with  $T_e \sim 100\text{ eV}$ , is being used to study Alfvén wave heating. A 60 kW RF pulse is applied during a 10 ms interval to three pairs of antennas located at different toroidal positions. A fast Alfvén wave is excited in the plasma and according to theory [1] mode conversion to a kinetic Alfvén wave (which is strongly damped) occurs at a resonance surface where the toroidal propagation velocity coincides with the local Alfvén velocity. A scattering system employing millimeter and submillimeter waves is being used to investigate electron density perturbations associated with these waves.

## SCATTERING DIAGNOSTICS

Two sources are being used. A 10W gyrotron which can be step-tuned over the frequency range 75 GHz – 330 GHz ( $0.9\text{ mm} - 4\text{ mm}$ ) is used in conjunctions with a quasi-optical antenna to produce a plane polarized beam as shown in Fig. 1 [2]. The other source is a 10 mW optically pumped formic acid vapour laser operating at  $433\ \mu\text{m}$  [3]. Both sources can be used in a far forward scattering arrangement [4] which is suitable for detecting perturbations with wavelengths greater than  $\pi w_0$  where  $w_0$  is the beam waist radius. The laser can also be used for conventional finite angle scattering which allows detection of perturbations with wavelengths  $\sim \lambda/(2\sin\theta)$  where  $\lambda$  is the laser wave length and  $\theta$  is the scattering angle [5]. The detection system, which employs quadrature RF mixing techniques, is shown in Fig. 2. The amplitude  $A$  and phase  $\theta$  of the signal at the wave frequency (5MHz) from the detector are

calculated from the outputs of the detection system which give  $A\sin\theta$  and  $A\cos\theta$ .

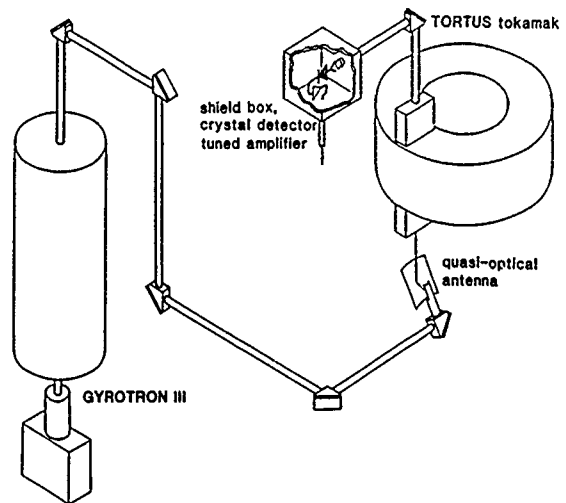


Figure 1

The gyrotron far forward scattering system on TORTUS

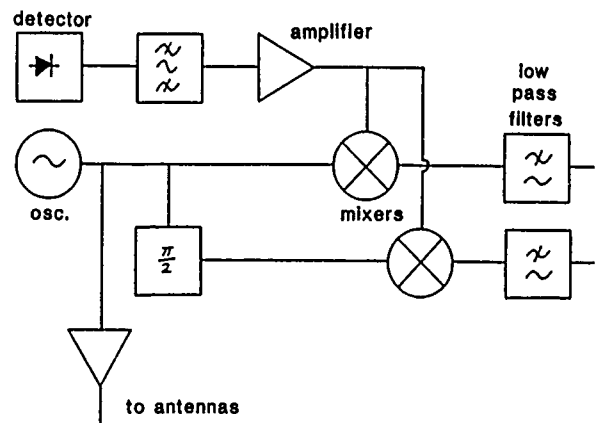


Figure 2

The detection system for scattering experiments on TORTUS.

## RESULTS

The first results from the far forward scattering system with the laser as source are shown in Fig. 3. Similar results have been obtained with the gyrotron as the source. So far, no evidence of a resonance layer has been found; it seems likely that the present results can be explained in terms of refraction of radiation by density perturbations associated with the fast Alfvén wave.

## ACKNOWLEDGEMENTS

This work has been supported by the Australian Research Council, the University of Sydney, the Australian Institute of Nuclear Science and Engineering and the Science Foundation for Physics within the University of Sydney. The authors are grateful to V. Buriak, P. Denniss, N.A. Lowe, G.T. Marlin J.R. Piggott and K. Weigert for technical assistance.

## REFERENCES

- (1) D.W. Ross, G.L. Chen and S.M. Mahajan, *Phys. Fluids*, 25, 652 (1982).
- (2) G.F. Brand, P.W. Fekete and K.J. Moore  
12th Int. Conf. Infrared and Millimeter Waves, Orlando, Florida, 1987 p356
- (3) P.A. Krug, P.A. Stimson and I.S. Falconer, *J. Phys. E (Sci. Instrum.)*, 19, 960 (1986).
- (4) D.E. Evans, M. von Hellerman and E. Holzhauer, *Plasma Physics*, 24, 819 (1982).
- (5) H. Park, W.A. Peebles, A. Mase and N.C. Luhmann, Jr., *Appl. Phys. Lett.*, 37, 279 (1980).

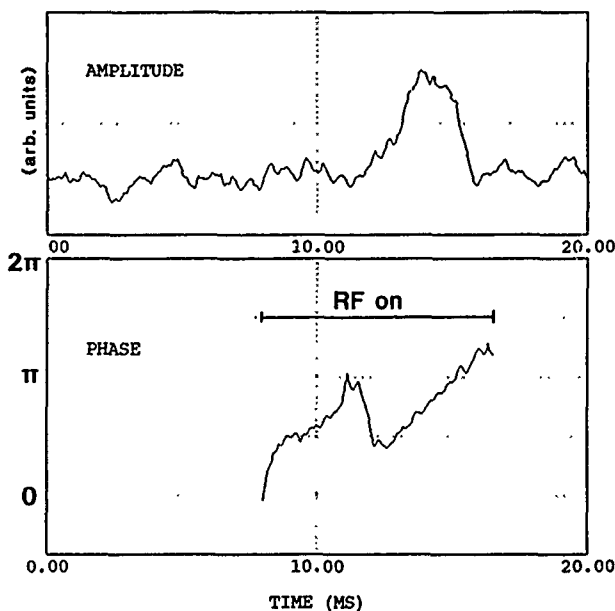


Figure 3

Amplitude and phase of signal from the Schottky diode detector used in the laser far forward scattering system for the laser beam passing along a diameter of the plasma (average of five shots).

A HIGH POWER CH<sub>3</sub>OH LASER SYSTEM USING STARK STABILIZED CO<sub>2</sub> PUMP LASERS\*D. P. Hutchinson, C. A. Bennett,<sup>†</sup> J. Lee,<sup>§</sup> L. K. Fletcher,<sup>#</sup> C. H. Ma, and K. L. Vander SluisOak Ridge National Laboratory  
Oak Ridge, TN 37831

## ABSTRACT

A dual channel, 119- $\mu$ m wavelength laser system has been constructed for the ATF experiment at Oak Ridge. The pump lasers utilize external Stark cells for locking the CO<sub>2</sub> laser to the absorption frequency of the CH<sub>3</sub>OH lasers. Stark plates have also been attached to the dielectric waveguide resonators of the FIR lasers to affect precise tuning of the 119  $\mu$ m lasers.

## SYSTEM DESIGN

A 119- $\mu$ m wavelength multichannel interferometer has been constructed for the Advanced Toroidal Facility (ATF) at the Oak Ridge National Laboratory. Two CH<sub>3</sub>OH dielectric waveguide lasers with 23-mm-i.d.  $\times$  240-cm-long resonator are optically pumped by separate CO<sub>2</sub> lasers. Each CO<sub>2</sub> pump laser utilizes a curved 15-meter radius grating with a flat 85% reflective output coupler. The zero order radiation from the gratings are directed into separate Stark cells used to lock the pump lasers on the CH<sub>3</sub>OH absorption peaks [1]. The CO<sub>2</sub> laser produces approximately 160 W of single mode power on the 9P36

line used to pump the alcohol lasers. The prototype FIR laser developed for this system has produced 1.2 W of power at 119  $\mu$ m.

In order to improve the stability and tuning of the FIR lasers, Stark plates have been added to the FIR resonator tubes. By applying a d.c. voltage to these plates, the FIR frequency may be adjusted with greater precision than with a mechanical translation stage.

## REFERENCES

- \*Research sponsored by the Office of Fusion Energy, U.S. Department of Energy, under Contract No. DE-AC05-84OR21400 with Martin Marietta Energy Systems, Inc.
- <sup>†</sup>On sabbatical leave from the University of North Carolina at Asheville.
- <sup>§</sup>University of Tennessee, Knoxville.
- <sup>#</sup>Tennessee Technological University, Cookeville.
- [1] S. Okajima, M. Yamanaka, A. Nishizawa, S. Makino, M. Kondo, S. Kon, and J. Fujita, *Infrared Phys.* 25, 569 (1985).

# SIMULTANEOUS MULTILINE OPERATION OF A FORMIC ACID LASER AND APPLICATIONS

M.D. Bowden, I.S. Falconer, B.W. James

School of Physics, University of Sydney  
NSW 2006, AUSTRALIA

L.B. Whitbourn

CSIRO Division of Exploration Geoscience  
Lindfield, NSW 2070, AUSTRALIA

J.C. Macfarlane

CSIRO Division of Applied Physics  
Lindfield, NSW 2070, AUSTRALIA

## ABSTRACT

A formic acid laser has been operated simultaneously on three lines of a cascade sequence by suitable choice of the resonator length, resulting in enhanced power on all three lines. The phenomenon can be used to construct a phase-modulated interferometer. For the output coupler used which exhibits phase anisotropy, simultaneous output on two orthogonally polarized lines of a cascade sequence has also been obtained.

## INTRODUCTION

In an optically pumped submillimeter (SMM) laser rotational relaxation can lead to an inverted population for cascade transitions of the directly pumped rotational transition as shown in Fig. 1. Thus, if the resonator length is adjusted to an appropriate value, laser output can be achieved simultaneously on two or more members of a rotational cascade sequence. Such a mode of operation of a HCOOH laser on three different cascade sequences, each consisting of three transitions, has been reported previously [1]. Under such conditions the power of each lasing transition is enhanced above the power each would produce when lasing by itself.

## THE LASER

The HCOOH laser used for this study is pumped by a 50 W beam from a grating tuned CO<sub>2</sub> laser focused through a small hole in one of the SMM resonator reflectors, a polished, gold-plated copper mirror. The other reflector, the output coupler, is an aluminum strip grating deposited on a fused quartz substrate, the rear surface of which is coated with a layer of Teflon approximately one-quarter-wavelength thick to minimize the effect of multiple reflections of the SMM beam within the substrate. A Pyrex waveguide of length 1.5m and internal diameter 48 mm was used in these

studies. A detailed account of the performance of this laser is available elsewhere [2].

## APPLICATIONS

A phase-modulated interferometer, constructed using a HCOOH laser operating simultaneously on three different wavelengths ( $\lambda_1 > \lambda_2 > \lambda_3$ ) as shown in Fig. 2, has been described previously [3]. Fabry-Perot etalons with metal mesh mirrors are used as filters so that one of the wavelengths  $\lambda_2$  propagates along the probing arm while the other two propagate along the reference arm. Each detector produces a beat frequency output at  $f_1 - 2f_2 + f_3$  where  $f_1 = c/\lambda_1$ , etc. For all three cascade sequences studied the beat frequency is

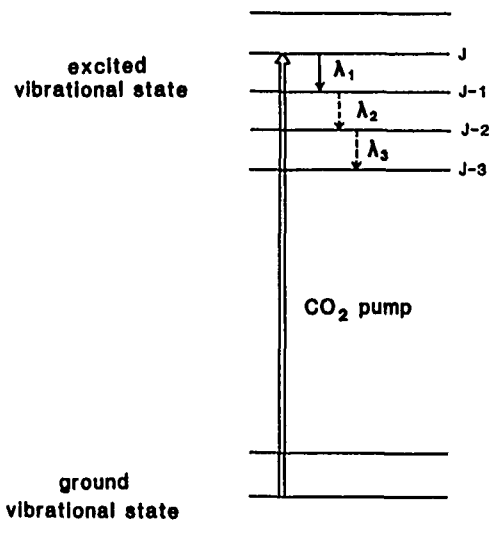


Figure 1

Energy levels for an optically pumped submillimeter laser.

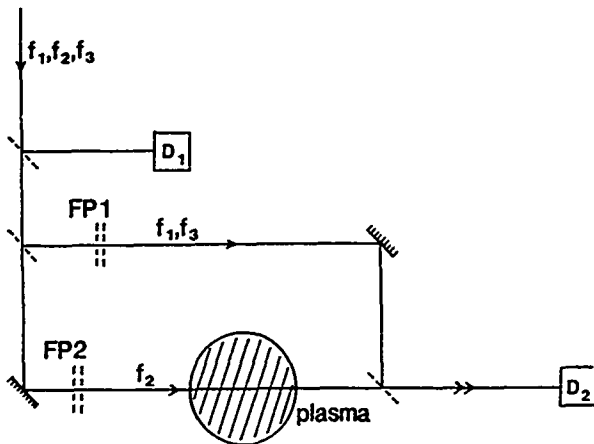


Figure 2

A phase-modulated interferometer employing a HCOOH laser operating simultaneously on three different cascade lines.

near 1 MHz. A change in optical path length in the probing arm of the interferometer will produce a corresponding change in phase between the radiofrequency signals from the detector D1, which monitors the beat frequency, and the detector D2 which records the output of the interferometer.

Even when only a single wavelength output is needed, simultaneous multiline operation can provide a means of significantly increasing the output power at the desired wavelength [1] provided the desired line can be efficiently separated from the other lines. The strip grating output coupler [4] used in this laser exhibits phase anisotropy. Thus the polarization of the output can be switch from being parallel to the strips of the output coupler to being perpendicular by a small change in resonator length [5]. It has been found possible to operate the laser such that it simultaneously produces orthogonally polarized output in the same transverse mode on two lines of a cascade sequence [6]. This provides submillimeter laser operating at two wavelengths which can be readily separated.

#### ACKNOWLEDGEMENTS

The authors acknowledge support from the CSIRO/University of Sydney Collaborative Research Fund and the University of Sydney Science Foundation for Physics. We are grateful to Dick Phillips, Peter Dencher and Rex Binks for excellent technical assistance.

#### REFERENCES

- (1) P.A. Stimson, B.W. James, I.S. Falconer, L.B. Whitbourn and J.C. Macfarlane, *Appl. Phys. Lett.* 50, 786 (1987).
- (2) L.B. Whitbourn, J.C. Macfarlane, P.A. Stimson, B.W. James and I.S. Falconer, *Infrared Phys.* 28, 7 (1988).
- (3) B.W. James, I.S. Falconer, M.D. Bowden, L.B. Whitbourn, P.A. Stimson and J.C. Macfarlane, *12th Int. Conf. Infrared and Millimeter Waves*, Orlanda, Florida, 1987 p379
- (4) D. Véron and L.B. Whitbourn, *Appl. Opt.* 25, 619 (1986).
- (5) L.B. Whitbourn, J.C. Macfarlane, I.S. Falconer, B.W. James and P.A. Stimson, *Appl. Phys. Lett.* 48, 957 (1986).
- (6) M.D. Bowden, B.W. James, I.S. Falconer, P.A. Stimson, J.C. Macfarlane and L.B. Whitbourn, To be published in *Int. J. Infrared Millimeter Waves*.



# ION TEMPERATURE MEASUREMENTS IN A TOKAMAK BY COLLECTIVE THOMSON SCATTERING OF FIR LASER RADIATION

R. Behn, D. Dicken\*, J. Hackmann\*, S.A. Salito and M.R. Siegrist  
 Centre de Recherches en Physique des Plasmas  
 Association Euratom - Confédération Suisse  
 Ecole Polytechnique Fédérale de Lausanne  
 21, Av. des Bains, CH-1007 Lausanne - Switzerland

\*) Permanent address: Institut für Laser- u. Plasmaphysik, Universität Düsseldorf F.R.G.

## INTRODUCTION

As a result of steady progress in high power FIR lasers and sensitive, low-noise detection systems, the equipment is now available to measure the ion temperature ( $T_i$ ) of tokamak plasmas by Thomson scattering from thermal density fluctuations. Using a laser in the far-infrared wavelength range permits scattering angles as large as  $90^\circ$  which results in excellent spatial resolution of the measurement. Heterodyne receivers built around Schottky barrier diode mixers combine high sensitivity with large electrical bandwidth to cover the frequency spread of the scattered radiation. After a first demonstration of feasibility was reported by Woskoboinikow et al (1), recent improvements on our system made it possible for the first time to measure  $T_i$  in a single laser shot.

## DESCRIPTION OF THE EXPERIMENT

For our experiment on the TCA tokamak we have chosen the optically pumped  $D_2O$  laser which emits on a Raman transition at  $385\mu m$  (778.6 GHz) when pumped by a single mode  $CO_2$  laser tuned to the 9R(22) line. The  $D_2O$  laser has an unstable resonator in an L-shaped configuration with a total length of 4m. A free standing wire grid at the vertex allows efficient coupling of the pump beam into the cavity. The pump energy of 600J in a single mode pulse of 1.4 $\mu s$  duration is supplied by a  $CO_2$  laser system comprising a hybrid-TEA laser oscillator and an e-beam preionized power amplifier. At a filling pressure of 6.5mbar of  $D_2O$  the FIR laser produces 0.5J in 1.4 $\mu s$ .

The optical system installed on TCA has been designed to focus the  $D_2O$  laser beam to a waist of 3mm at the plasma centre and to observe the scattered radiation at  $90^\circ$  within a solid angle of  $4.3 \cdot 10^{-3}$  sterad. A beam dump made of a PYREX-cone and a viewing dump made of MACOR ceramic have been installed in the tokamak vessel to reduce stray light.

A heterodyne receiver comprising 20 channels (bandwidth 80MHz) is used to analyze the part of the spectrum that is shifted from the laser line towards higher frequencies. The local oscillator is provided by a c.w. FIR laser ( $CD_3Cl$ ) emitting at 782.2 GHz at a frequency offset by 3.6 GHz from the  $D_2O$  laser. Scattered radiation and local oscillator are combined in a quasi-optical diplexer and focused onto the Schottky diode mixer (supplied by MPI für Radioastronomie, Bonn, FRG). The signals from the receiver output are fed into a CAMAC-ADC (LeCroy 2250L), which includes a gated integrator and a buffer memory. After each shot the data from 12 channels are transferred to the main computer for further analysis.

Calibration of the receiver system using black-body sources yielded a noise temperature of 8000 °K (DSB). A beam duct filled with pure nitrogen had to be installed to avoid absorption losses due to humidity in the air along the 10m path from the tokamak to the receiver input.

## RESULTS

Several series of experiments have been carried out to measure the ion temperatures of plasmas with different majority ions ( $H^+$ ,  $D^+$ , and  $He^{++}$ ). Within each series several shots with identical plasma parameters ( $N_e$  and  $T_e$ ) were obtained such that the data could be averaged to improve the signal-to-noise ratio of the  $T_i$  measurement. The results are presented in fig. 1 where 3 spectra corresponding to H-, D-, and He-plasmas are superposed. The amplitudes have been scaled to allow a direct comparison of the halfwidth of the spectra. The decrease in the halfwidth with increasing ion mass is clearly observed.

At high plasma densities the signal-to-noise ratio was sufficient for  $T_i$  measurements in a single shot. A typical result for a H-plasma is shown in fig. 2. The solid curve gives the shape of the spectrum obtained from the fitting routine. For the given plasma parameters a  $T_i$  value of 330 eV was found. A summary of single shot measurements for H-, D-, and He-plasmas is presented in table 1. Since the other plasma parameters were constant within each series, the fluctuations in the  $T_i$  values are interpreted as the uncertainties of the measurement. The relative error is in the range of 20 to 30%

The influence of the impurity ions and the magnetic field on the shape of the spectrum is demonstrated by fig. 3 which shows calculated spectra for a H-plasma. It can be seen that the contribution from impurities (C, O, Fe) in concentrations typical for tokamak plasmas is restricted to the central part of the spectrum. However, the existence of a magnetic field almost perpendicular to the difference k-vector leads to a noticeable deformation also at larger frequency shifts. For the series of measurements reported here, a 300MHz band starting from the centre of the spectrum has been excluded. The reason is that apart from the influence of the impurities, whose concentrations are not precisely known, this band is also affected by stray light making a quantitative analysis uncertain. The influence of the magnetic field becomes negligible when a scattering geometry is chosen that avoids the perpendicular orientation of the k-vector to the

B-field. For future experiments we will change this angle to  $85^\circ$  which should make the interpretation of the spectra easier.

### SUMMARY

A  $D_2O$  FIR laser emitting  $0.5J$  in  $1.4\mu s$  at  $385\mu m$  and a heterodyne receiver with a noise temperature of  $8000^\circ K$  (DSB) were used in a Thomson scattering experiment to measure the ion temperature of a tokamak plasma during a single laser shot. Series of measurements under reproducible plasma conditions have been carried out in H-, D-, and He-plasmas. Their statistical analysis yielded a typical relative error of 25% for a single shot measurement.

- (1) P. Woskoboinikow, W.J. Mulligan, J. Machuzak, D.R. Cohn, R.J. Temkin, T.C.L.G. Sollner, and B. Lax, "385 $\mu m$   $D_2O$  Laser Collective Thomson Scattering Ion Temperature Diagnostic", 11th European Conf. on Contr. Fusion and Plasma Physics, Aachen, FRG, 5-9 September 1983

### Figure Captions :

Fig.1 Spectra of scattered radiation obtained for different ion species  
H : hydrogen plasma  
D : deuterium plasma  
He: helium plasma

Fig. 2 Thomson scattering from a H-plasma  
The spectrum has been recorded in a single laser shot.

Fig. 3 Calculated spectra for a H-plasma  
(1) no impurities; no magnetic field  
(2) impurities included (C, O, Fe;  $Z_{eff}=2.5$ ); no magnetic field  
(3) no impurities; magnetic field at  $89^\circ$   
(4) impurities included; magnetic field at  $89^\circ$

Table 1 Summary of  $T_i$  measurements

	H-Plasma	D-Plasma	He-Plasma
$N_e$	$5.5 \cdot 10^{19} m^{-3}$	$5.3 \cdot 10^{19} m^{-3}$	$5.0 \cdot 10^{19} m^{-3}$
$T_e$	680 eV	830 eV	600 eV
$Z_{eff}$	2.5	2.5	2.7
$T_i(\text{fit})$	250 eV	310 eV	380 eV
	320	450	430
	440	320	370
	230	460	410
	260	220	470
	370	300	260
	460	480	470
	300	490	270
	320	450	400
mean	330 (+30) eV	390 (+30) eV	390 (+25) eV
stand.dev.	80 eV	100 eV	80 eV
rel.error	25%	26%	20%

Fig.1

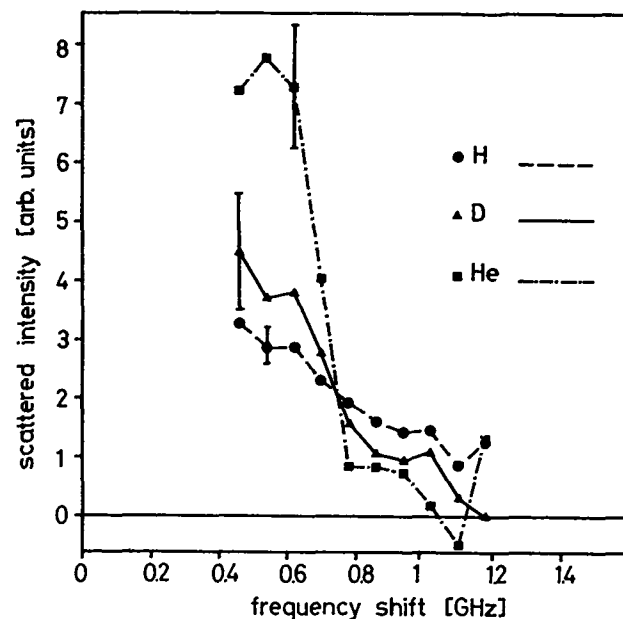


Fig. 2

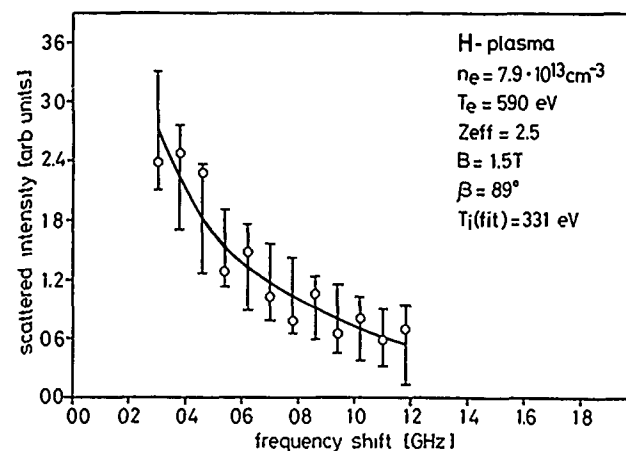
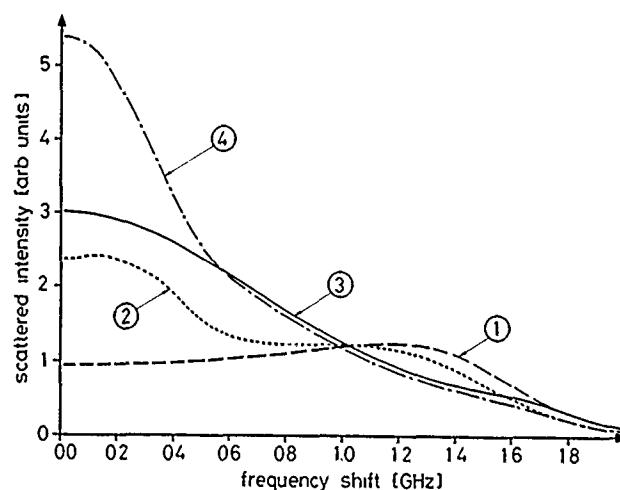


Fig. 3



## DESIGN AND CALIBRATION OF A TWO-CHANNEL LOW NOISE HETERODYNE RECEIVER AT 10.6 MICRONS\*

C. A. Bennett,<sup>†</sup> R. K. Richards, and D. P. HutchinsonOak Ridge National Laboratory  
Oak Ridge, TN 37831

## ABSTRACT

A dual channel, low noise heterodyne receiver has been constructed for Thomson scattering from alpha particles in a burning plasma experiment. A real time calibration method has been devised which references the integrated system noise to a blackbody source. Two wideband (>1GHz) HgCdTe photovoltaic mixers yield a double sideband system noise equivalent power of less than  $1.5 \times 10^{-20}$  W/Hz.

## INTRODUCTION

It has been established that heterodyne spectroscopy of Doppler shifted Thomson scattered CO<sub>2</sub> laser radiation can provide a method for determining the kinetics of fusion produced alpha particles [1]. Signal levels expected for this experiment require that the sensitivity of the receiver system be monitored constantly for neutron induced transmission changes in the optical train as well as for alignment perturbations due to movement of the reactor vessel. We describe a simple method for producing an absolute broadband sensitivity calibration by referencing the output of the receiver to a blackbody standard; this technique will provide any receiver system with an accurate measure of system noise and is routine enough to be used as a real time check for receiver sensitivity changes.

For a reversed bias photovoltaic photomixer, the optimum noise equivalent power per unit frequency interval (NEP) [2] has contributions from both shot noise and from thermal noise. Contributions from the signal power and from the noise power appear at the output of the preamplifier; this signal is subsequently rectified, averaged, and amplified to give a d.c. output linearly proportional to the signal power. The post detection signal to noise ratio accounts for this signal averaging, and is given by [3]

$$\text{SNR}_{\text{pd}} = \frac{P_s}{P_s + P_N} \sqrt{B\tau + 1} \quad (1)$$

where  $B$  = IF bandwidth,  $\tau$  = signal integration time,  $P_s$  = signal power and  $P_N$  = noise power.

Figure 1 shows the calibration setup. Each diode had a bandwidth in excess of 1 GHz. The chopper wheel was covered with an absorbing layer of high emissivity material and was maintained at room temperature while a variable temperature blackbody source produced the signal power. An objective ZnSe lens forms a reverse projection of the LO beam which fits entirely within the aperture of the blackbody source. Each amplifier had 33 dB of gain, a noise figure of 1.3 and a 1 GHz bandwidth. An RF diode rectified the amplified signal and this voltage was

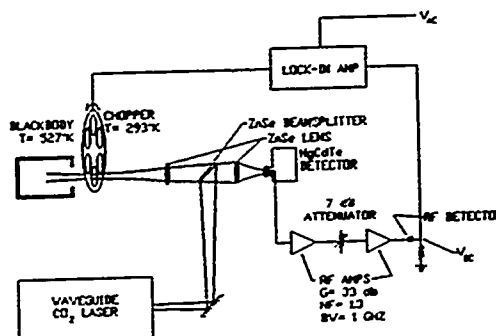


Figure 1.  
Calibration setup

measured with a digital voltmeter. The a.c. component of the rectified signal was analyzed by a lock in amplifier referenced by the chopper.

Figure 2 illustrates the signal at the input of the lock in amplifier. The rectified IF signal is modulated beneath an approximately square wave envelope at the chopping frequency. Since the heterodyne signal is generated over a double side band, we obtain [4]

$$\text{NEP} = 2 V_{\text{dc}} / \alpha V_{\text{ac}} - \frac{1}{2} (P_B - P_R) - 2P_R \quad (2)$$

where  $\alpha$  accounts for the fact that the lock in amplifier measures only the fundamental component of the modulating envelope; our chopper wheel aperture and LO beam shape gave  $\alpha = 2.26$ .

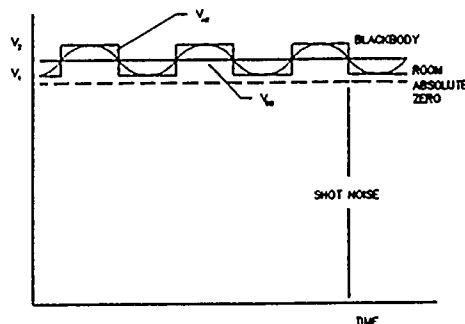


Figure 2.  
Signals used for calibration

## RESULTS

Under broadband conditions, our wide bandwidth mixers gave voltage levels consisting of an a.c. component of around 0.5 mv and a d.c. component of about 10-20 mv; these voltages were conveniently monitored on an oscilloscope placed across the RF diode as the system alignment and LO power were adjusted for optimum receiver performance. The system noise levels and quantum efficiencies were easily optimized to values close to the performance parameters of the individual photomixers.

## REFERENCES

\*Research sponsored by the Office of Fusion Energy, U.S. Department of Energy, under Contract No. DE-AC05-84OR21400 with Martin Marietta Energy Systems, Inc.

†On sabbatical leave from the University of North Carolina at Asheville.

- [1] R. K. Richards, K. L. Vander Sluis, and D. P. Hutchinson, ORNL/TM-10363, Martin Marietta Energy Systems, Inc., Oak Ridge Natl. Lab., March 1987.
- [2] B. J. Peyton, A. J. DiNardo, G. M. Kanishak, F. R. Arams, R. M. Lange, and E. W. Sard, IEEE J. Quan. Elec. QE-8, 252 (1972).
- [3] E. Holzhauer and J. H. Massig, Plasma Phys. 20, 867 (1978).
- [4] C. A. Bennett, R. K. Richards, and D. P. Hutchinson, ORNL/TM- 10419, Martin Marietta Energy Systems, Inc., Oak Ridge Natl. Lab., March 1988.

## Calibration of 10-Channel Grating Polychromator

K. Kawahata, M. Sakamoto, J. Fujita

Institute of Plasma Physics, Nagoya University, Nagoya 464-01, Japan

H. Matsuo

Department of Astrophysics, Nagoya University, Nagoya 464-01, Japan

K. Sakai

Department of Applied Physics, Osaka University, Osaka 565, Japan

### Abstract

A high temperature ( $T = 500^\circ\text{C}$ ) radiation source has been developed for the calibration of electron cyclotron emission measuring system on the JIPP T-IIU tokamak. The source has a heated area of  $\phi 150$  mm, and has the same emissivity as that of the microwave absorber Eccosorbe. The grating polychromator has been calibrated using the radiation source developed. The obtained electron temperatures agree with those by Thomson scattering within 10 %.

### 1. Introduction

The measurement of electron cyclotron emission (ECE) is powerful diagnostics<sup>1-3</sup> for high temperature plasmas. When the plasma emits and absorbs the radiation as a black body, it is possible to determine the electron temperature profile simply from the measured spectrum of ECE. In order to determine the absolute value of the electron temperature from the ECE measurements, the normalization of the spectrum to the Thomson scattering values has widely been used. When the ECE diagnostics can be calibrated absolutely without helps of any other plasma diagnostics, they would be more useful for measuring electron temperature. However, there exist no suitable radiation sources in the region of sub-millimeter and millimeter waves. Then, a new high temperature ( $T \approx 500^\circ\text{C}$ ) radiation source has been developed for the calibration of ECE measurements in the JIPP T-IIU tokamak<sup>4</sup>).

### 2. High Temperature Radiation Source

The radiation source is composed of a heater plate (Cu,  $\phi 190$  mm  $\times$  t 40 mm) and a radiation plate (Macor,  $\phi 150$  mm  $\times$  t 30 mm). The size of the radiation source is determined from the following considerations; (1) it has wide aperture which is larger than the main lobe of the antenna pattern, (2) it has a large heat capacity to give good temperature stability and (3) it can be heated up to the temperature of  $500^\circ\text{C}$  with good temperature uniformity across the radiation surface. We have adopted the Macor as a radiation material from the view points of its high absorption coefficient compared with common ceramics and fused silica and its excellent machinability. The complex optical and dielectric parameters of Corning Macor has been measured by M. N. Afsar and Kenneth J. Button<sup>5</sup>). The absorption coefficient increases monotonically with increasing frequency. For the wavelength of  $1/\lambda = 5 - 7\text{ cm}^{-1}$  where the second harmonic ECE appears in JIPP T-IIU, the absorption coefficient is in the region of 2 - 3 Neper/cm.

The temperature of the source is measured by the use of thermocouples and a thermoviewer (JTG-IBL, JEOL LTD., Japan) which operates in the wavelength region of 8 - 13  $\mu\text{m}$ . Figure 1 shows the thermogram of the radiation source measured by the thermoviewer. The temperature distributions along the crossed hair are shown on the left side and lower side in the figure. The temperature scale is  $3^\circ\text{C}/\text{div}$ . It is found that the temperature variation across the source surface is less than  $\pm 5$  K at the temperature of  $369^\circ\text{C}$ .

The radiation spectrum emitted from the source was measured using a Martin-Pulley Fourier transform spectrometer. Figure 2 shows the normalized spectrum of the radiation from the Macor to that from a microwave absorber (Eccosorbe). The emissivity of the Macor is found to be the same value as the Eccosorbe in the frequency range of 100-500 GHz. The microwave absorber at the Liq.  $\text{N}_2$  temperature has been used for the calibration of ECE<sup>1, 3</sup>), because it has a high emissivity at the millimeter wavelengths. The effective temperature difference from the room temperature is low ( $T_B \approx 216^\circ\text{K}$ ), so that it is necessary to accumulate the output signals for a long time to achieve enough signal to noise ratio. On the other hand, in the case of the Macor we can get about two times effective temperature difference compared with the Eccosorbe, which results in not only a reduction of the calibration time but also an improvement of an accuracy of the calibration data.

### 3. Calibration of the Grating Polychromator

The calibration measurements using the developed source have been carried out for a 10 channel grating polychromator<sup>6</sup>). The radiation from the source is chopped at the frequency of 38 Hz and detected by Liq. He cooled indium antimonide hot electron bolometers. In order to increase the signal to noise ratio, the output signal is amplified with a lock-in mode at the time constant of 128 s. Figure 2 shows the relation between the CH5 output signal of the polychromator and the surface temperature of the Macor. The calibrated responsivity is found to be about 690 eV/V which is within 10 % of those with Thomson scattering.

### 4. Conclusion

A new high temperature radiation source has been developed for the calibration of ECE in the JIPP T-IIU tokamak. It has an emissivity of 0.95-1.0 in the frequency range of 100 - 500 GHz. The temperature stability is about 0.5%/hour at the temperature of  $\sim 400^\circ\text{C}$ , and the temperature nonuni-

formity across the surface is less than 2 %. It is found that the absolutely calibrated temperatures are consistent with those measured by the Thomson scattering.

### References

- [1] K. Kawahata, M. Sato, T. Tetsuka, N. Noda and K. Sakai, Jpn. J. Appl. Phys. 21 (1982) 1633.
- [2] A.E. Costley, E.A.M. Baker, D.V. Bartlett, D.J. Cambell, M.G. Kiff and G.F. Neill, "First measurements of ECE from JET", Paper presented at 4th Int. Workshop on ECE and ECH, Frascati, (1984) 1.
- [3] F.J. Stauffer, D.A. Boyd, R.C. Cutler and M.P. McCarthy, Rev. Sci. Instrum. 56 (1985) 353.
- [4] K. Toi et al., in Plasma Physics and Controlled Nuclear Fusion Research (Proc. 10th Int. Conf., London, 1984) Vol.3, IAEA, Vienna (1985) 353.
- [5] M.N. Afsar and K.J. Button, Int'l. J. IR & MM Waves 3 (1982) 319.
- [6] K. Kawahata, R. Ando, J. Fujita and K. Sakai, 11th Int. Conf. on IR and MM Waves, Pisa, 1986, Conference digest, p.414.

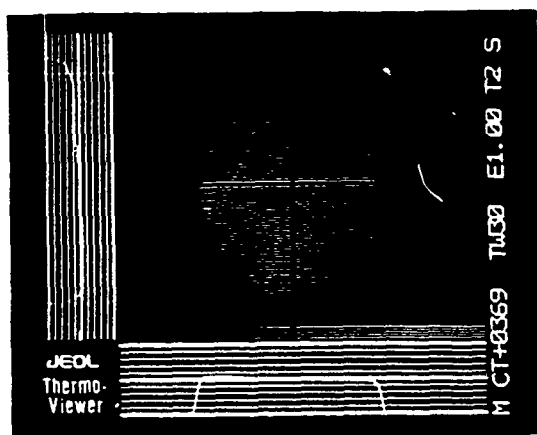


Fig.1 Two-dimensional distribution of the surface temperature measured by the Thermoviewer.

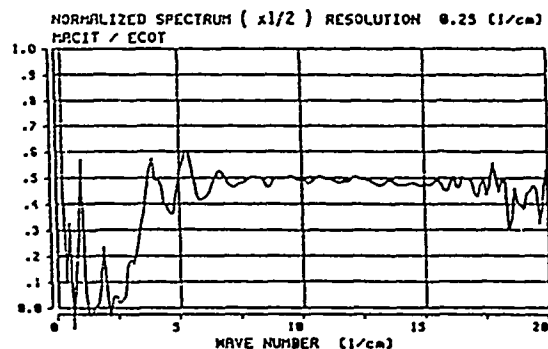


Fig.2 Normalized spectrum of the radiation from the Macor to that from the Eccosorbe.

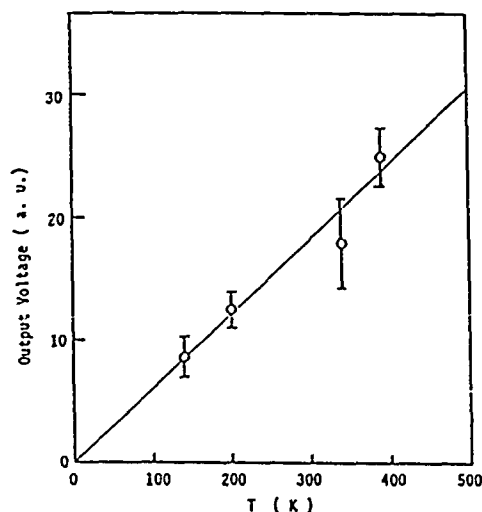


Fig.3 Dependence of the CH5 ECE intensity on the surface temperature of the Macor.

# A STARK-TUNED $\text{CH}_3\text{OH}$ LASER FOR USE IN HIGH FREQUENCY MODULATED INTERFEROMETRY

D.K. Mansfield, M. Vocaturo, L. Guttadora

Princeton University Plasma Physics Laboratory  
Princeton, New Jersey 08543 USA

## ABSTRACT

A Stark-tuned laser operating on the 119 micron line of  $\text{CH}_3\text{OH}$  has delivered reasonably high power (several tens of milliwatts at 30 Watts of pump power) while simultaneously exhibiting a doublet splitting of about 10 MHz, which is an order of magnitude larger than the modulation frequencies currently being used in plasma interferometers. Because the resonator design has allowed the attainment of both high power and high doublet splitting, this type of laser would be usable in the type of multi-channel interferometers currently employed on the large-scale plasma devices being used in magnetic fusion research.

## INTRODUCTION

Interferometric measurements of the plasma electron density on the present generation of large magnetic fusion experiments is being carried out with the use of modulated far-infrared (FIR) lasers. In the majority of existing systems the modulation of the laser beam is accomplished either by mechanical means - for instance by a rotating grating- or by optical means involving the beating together of two frequency-shifted FIR lasers. In the former case, modulation frequencies are limited by mechanical considerations to  $10^4$  -  $10^5$  Hz while in the latter case modulation is limited to about 1 MHz because of the very narrow gain bandwidth exhibited by submillimeter lasers. In practice, because the modulation frequency is so low, the most nagging problem remaining with these interferometric systems is the loss of fringe count due to the rapid changes of density in the plasma device. The rapid density changes are caused by the injection of solid pellets into the plasma core, by sudden loss of confinement due a major plasma disruption, or by fast MHD activity excited in the plasma core. Each of these phenomena have been the cause of density changes which were rapid enough to cause fringe loss in the TFR interferometer system, which employs two  $\text{CH}_3\text{OH}$  lasers operating at 119 microns and has a modulation frequency of 1 MHz (1).

Interferometric systems on future pellet-fueled plasma devices, such as CIT, should be hardened against fringe loss if they are to be used as critical diagnostics. A way of hardening against fringe loss is to increase the modulation frequency above the 1 MHz region. However, to be of use in a practical multi-channel interferometer, the output power of any frequency-shifted laser must be in the range of 10 - 100 mW or higher.

## LASER DESIGN AND RESULTS

Bionducci has demonstrated that the gain curve of the 119 micron line of  $\text{CH}_3\text{OH}$  breaks into two distinct gain curves under the influence of an externally applied electric field and that the frequency difference between this doublet is linearly proportional to the electric field strength (2). In order to exploit

this fact for the purposes outlined above, a Stark-tuned  $\text{CH}_3\text{OH}$  laser was constructed which, when operating on the 119 micron line, can not only achieve doublet-splitting frequencies (and therefore modulation frequencies in a dual laser system) much higher than 1 MHz, but also can deliver power levels that are high enough for multi-channel interferometric operation.

The 1 meter long FIR resonator tube consists of a 2 mm thick rectangular pyrex tube with inside dimensions of 22 mm x 9.5 mm. Polished brass electrodes were epoxied to the larger inside faces of the tube and the entire waveguide assembly was placed inside a cylindrical water jacket. A flat copper mirror with a 4 mm hole is used as the input coupler while a standard silicon hybrid coupler with a 6 mm aperture is employed to couple out the FIR power. Because the electrodes are located inside the rectangular pyrex tube, the walls of the FIR resonator can be cooled without concern about electrical breakdown in the cooling liquid during the application of the Stark field. Wall cooling, in turn, allows the attainment of enhanced FIR powers (3).

Using the resonator herein described, FIR output powers of several tens of milliwatts have been achieved at a pump power of 30 Watts. Simultaneously, doublet splitting of about 10 MHz have been observed with the application of a Stark field of only about 500 volts/cm. In addition, the familiar non-linear Hanle effect has been observed with this resonator (1).

Because the efficiency of this laser compares reasonably well with that observed in the standard hollow-dielectric type of FIR resonator, and because the achievable modulation frequency is an order of magnitude higher, the Stark-tuned laser may find use in the next generation of FIR interferometers on large-scale magnetic fusion devices such as CIT.

This work supported by US DOE Contract No. DE-AC02-76-CHO-3073.

## REFERENCES

- (1) D.K. Mansfield, H.K. Park, L.C. Johnson, H.M. Anderson, R. Chouinard, V.S. Foote, C.H. Ma, and B.J. Clifton, Appl. Opt. 26, (1987) 4469.
- (2) G. Bionducci, M. Inguscio, A. Moretti, and F. Strumia, Infrared Phys. 19, (1979) 297.
- (3) D.K. Mansfield, E. Horlbeck, C.L. Bennett, and R. Chouinard, Int. J. of Infrared and Millimeter Waves 6, (1985) 867.

# THE EFFECTS OF TURBULENCE IN CLEAR AND TURBID ATMOSPHERES ON MILLIMETER WAVE PROPAGATION

R. W. McMillan and R. A. Bohlander  
Georgia Institute of Technology  
Atlanta, Georgia 30332

R. J. Hill and S. F. Clifford  
National Oceanic And Atmospheric Administration  
Boulder, Colorado 80303

## ABSTRACT

Atmospheric turbulence, which is a readily observed phenomenon at visible wavelengths, also causes fluctuations in intensity and phase at millimeter wavelengths. This paper describes a series of experiments conducted at a site near Flatville, IL which measured these effects at a broad range of MMW frequencies in clear air, rain, fog, and snow. It was found that the maximum rms intensity fluctuations observed were 14% of the mean, while the largest rms angle-of-arrival fluctuations were 36 microradians. Discussions of the experimental arrangement, as well as results obtained in measuring the probability distribution functions of fluctuations, the mutual coherence function, spectral densities, and pertinent atmospheric parameters will be presented.

## 1. INTRODUCTION

The major effect of the atmosphere on MMW propagation is attenuation, but a series of experiments conducted by personnel from Georgia Tech, NOAA, and the U.S. Army Atmospheric Sciences Laboratory during 1983-85 have shown that atmospheric turbulence may also cause marginal degradation of MMW systems. As in the propagation of visible and near-infrared radiation, the effects of turbulence may be measured by the magnitude of the index of refraction structure parameter  $C_n^2$ , but unlike these other wavelength ranges,  $C_n^2$  comprises contributions from the humidity and temperature-humidity cross-structure parameters  $C_Q^2$  and  $C_{TQ}$ , as well as the temperature structure parameter  $C_T^2$  [1,2,3]. The next section discusses the experimental configuration used to measure atmospheric fluctuations and the metrological instrumentation used to characterize the atmosphere during these experiments. Section 3 gives some selected results, followed by conclusions in Section 4.

## 2. EXPERIMENT

The MMW turbulence experiments were conducted at a site near Champaign-Urbana, Illinois, at the town of Flatville, a site chosen for its exceptional flatness and fetch. These characteristics are desirable for atmospheric experiments because the atmosphere is considered to be homogeneous under these conditions. Figure 1 is a photograph of the transmission range viewed from the transmitter site to the receiver site, South to North. The transmitter was mounted in a small step-van truck placed upon a mound of earth so that the transmitter and receiver apertures were at the same height. The receiver, located at a range of 1374 m, comprised four apertures spaced up to 10m apart, so that phase relationships for the six different aperture spacings could be measured. The atmosphere was characterized by two meteorological instrumentation stations, two propagation paths for determination of visible  $C_n^2$ , two optical rain gauge paths, particle size spectrometers, and several weighing-bucket rain gauges. Figure 2 is a diagram of the propagation path showing the range and the relationships of the instrumentation to it.

Measurements were made at 116, 142, 173, and 230 GHz. It has been shown that the clear-air results obtained at these frequencies may be readily scaled to other frequencies of interest [4]. The transmitter used CW phase-locked klystron oscillators feeding an off-set paraboloid antenna. The receiver antennas were polyethylene lenses fed by corrugated horns, and local oscillator distribution to the four receivers was effected by an optical beam waveguide system. The receiver local oscillator was also a phase-locked klystron, and was operated nominally at one-half the transmitter frequency, so that harmonic mixers were required. The first intermediate frequency was 930 MHz, and a second conversion gave an IF of 30 MHz so that the phase-shifting operations and calibration necessary for determination of the mutual coherence function could be conveniently effected.

## 3. RESULTS

It was found during this series of measurements that the magnitudes of intensity and phase fluctuations are such as to cause marginal degradation of MMW systems performance. One of the largest rms intensity fluctuations observed on a hot, humid summer day was 14% of the mean intensity, and a comparable rms angle-of-arrival (AOA) fluctuation was 36 microradians. Fluctuation levels observed in inclement weather were generally smaller than those observed in clear air. Figure 3 shows a probability distribution function of intensity observed at 230 GHz in light rain. The different peaks in this distribution probably correspond to different rain rates. The corresponding phase PDF is shown in Figure 4, and



appears to be Gaussian, as one would expect for clear air, indicating that varying rain rates have little effect on the phase PDF, even though the intensity PDF is significantly affected. The rms values for the corresponding PDFs observed in clear air are significantly larger.

#### 4. CONCLUSIONS

The results of the series of MMW turbulence measurements made at Flatville indicate that there is some cause for concern for the MMW systems designer, especially in considering the AOA fluctuation levels. Also of concern is the fact that these levels may be higher for propagation paths over water or under high humidity conditions, such as in the tropics. The fabrication of a MMW  $C_n^2$  meter similar to those used for characterization of turbulence at visible wavelengths would be useful for evaluation of turbulence effects under these conditions. This work was sponsored by the U.S. Army Research Office, Contract No. DAAG29-81-K-0173.

#### REFERENCES

1. R. J. Hill, S. F. Clifford, and R. S. Lawrence, J. Opt. Soc. Amer., Vol. 70, pp. 1192-1205, 1980.
2. R. J. Hill, R. A. Bohlander, S. F. Clifford, R. W. McMillan, J. T. Priestley, and W. P. Schoenfeld, IEEE Trans. Geoscience and Remote Sensing, Vol. 26, No. 3, pp. 330-342, 1988.
3. R. A. Bohlander, R. W. McMillan, E. M. Patterson, S. F. Clifford, R. J. Hill, J. T. Priestley, and W. P. Schoenfeld, *ibid.*, pp. 343-354.
4. R. W. McMillan, R. A. Bohlander, G. R. Ochs, R. J. Hill, and S. F. Clifford, Opt. Eng., Vol. 22, pp. 32-39, 1983.



Figure 1. Photograph of propagation range viewed from transmitter to receiver.

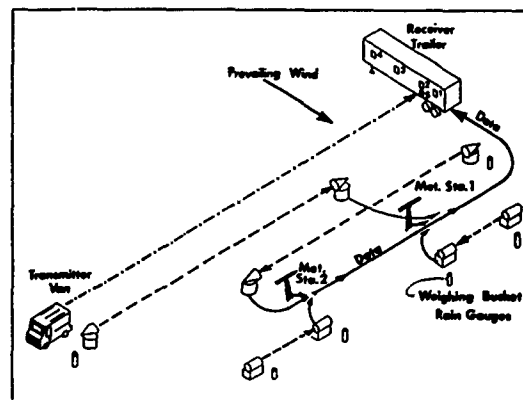


Figure 2. Diagram of experiment showing relationship of transmitter and receiver to meteorological instrumentation.

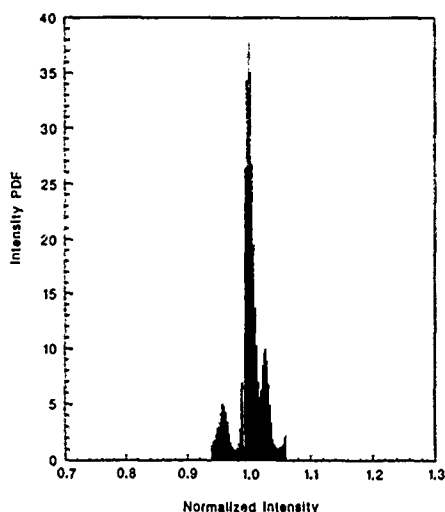


Figure 4. Intensity probability distribution function measured in light rain at 230 GHz.

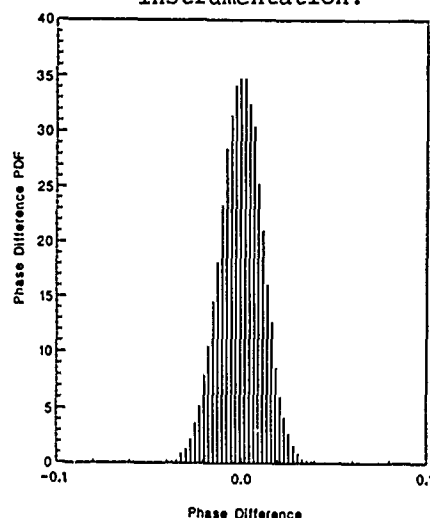


Figure 5. Phase PDF corresponding to Figure 4.

## ATMOSPHERIC ATTENUATION AND DELAY RATES BETWEEN 1 GHz AND 1 THz

Hans J. Liebe

National Telecommunications and Information Administration  
Institute for Telecommunication Sciences  
325 Broadway  
Boulder, CO 80303-3328

Abstract

A practical, PC-operated atmospheric propagation model (MPM) was developed by ITS that predicts attenuation (dB/km) and delay (ps/km) rates for frequencies between 1 GHz and 1 THz. Input variables are barometric pressure, ambient temperature, relative humidity, hygroscopic aerosol concentration, suspended water or ice droplet concentration, and rain rate. Details of the MPM code are discussed briefly, model predictions are presented, and comparisons with data from propagation experiments studying water vapor and fog effects (50 to 430 GHz) are shown.

## AN ALGORITHM FOR ESTIMATING CLOUD ATTENUATION AT MILLIMETER WAVELENGTHS

Edward E. Altshuler and Richard A. Marr

Rome Air Development Center  
Electromagnetics Directorate  
Hanscom AFB, MA 01731-5000

## ABSTRACT

Total atmospheric attenuation under conditions of cloud cover was measured at frequencies of 15 and 35 GHz using the sun as a source. Over 300 sets of data were collected at each frequency. An algorithm for estimating the slant path attenuation under conditions of cloud cover as a function of elevation angle, frequency and surface absolute humidity was derived.

## INTRODUCTION

In this paper, cloud attenuations were inferred from extinction measurements using the sun as a source. Measurements were made at frequencies of 15 and 35 GHz during sunrise and sunset at elevation angles from near the horizon up to 20°. Preliminary results obtained from these data were reported [1]. Of these data, 58 sets were designated "clear sky"; these results have been compared with theoretical values and have been published [2]. The remaining data were divided into two categories: if there was total cloud cover during the course of the measurements, such that the sun was not visible, then these data were designated "cloud"; if conditions were those of partial cloud cover, the data were designated "mixed cloud".

## THEORETICAL CONSIDERATIONS

Attenuation by cloud is a complex function of the particle size distribution, density, temperature, index of refraction, wavelength and cloud extent. The attenuation is primarily due to absorption by the cloud droplets; scattering losses are secondary. For uniform cloud cover it is reasonable to assume that the attenuation is proportional to the distance through the cloud. Thus the total attenuation should be proportional to the cosecant of the elevation angle. For low elevation angles the following distance expression for a curved earth has been derived using the law of cosines [2].

$$D(\theta) = [(a_e + h_e)^2 - a_e^2 \cos 2\theta]^{1/2} - a_e \sin \theta \quad (1)$$

$\theta$  = elevation angle

$D(\theta)$  = distance through the attenuating layer

$a_e$  = effective earth radius (Km)

$h_e$  = effective height of the attenuating layer (Km)

The effective height  $h_e$  of the attenuating atmosphere is defined as follows. If all of the oxygen, water vapor and cloud liquid water in the atmosphere were compressed into a uniform layer having a weighted density equal to that of the oxygen, water vapor and cloud liquid water at the earth's surface, then the height of that layer is designated as the effective height of the attenuating medium. We have assumed

that the attenuation  $A(\theta)$  is proportional to the distance through the lower atmosphere  $D(\theta)$ .

$$A(\theta) = a_0 + a_1 D(\theta) \quad (2)$$

But as the distance  $D(\theta)$  approaches zero, the attenuation  $A(\theta)$  also approaches zero. Thus for  $a_0 = 0$  we would like to determine a value for  $a_1$  which produces a best fit for the regression line.

## RESULTS

The surface absolute humidity and surface refractivity were computed from the surface temperature, dew point and pressure. The effective earth radius was then computed from the surface refractivity. A linear regression of attenuation vs distance through the attenuating layer was conducted for a set of effective heights of the atmosphere ranging from .1 to 8 km in .1 km intervals. For each set of data the standard error was calculated and plotted as a function of effective height; the effective height which produced the minimum standard error was selected as the effective height of the atmosphere. With  $a_e$  and  $h_e$  determined,  $A(\theta)$  was then plotted as a function of  $D(\theta)$ . With (2), a regression line with slope  $a_1$  was computed. The corresponding set of zenith attenuations was then computed by multiplying the attenuation coefficients by the effective heights.

For cloud conditions that were designated uniform, the angle dependence of the attenuation was comparable to that for clear sky conditions [1]. Typical attenuations are shown in Fig. 1. For comparison, clear sky attenuations for approximately the same surface absolute humidity and effective height are also shown. Note the high correlation of attenuation with the distance through the attenuating atmosphere. As expected, the attenuation produced by complete cloud cover is higher than that for clear sky.

A zenith attenuation was extrapolated from each set of data which was considered representative of uniform cloud cover; that is the attenuation had a linear dependence on the distance through this atmosphere. The zenith attenuations were then plotted as a function of the surface absolute humidity and a regression analysis was done on these data. In Fig. 2 123 zenith attenuations for cloud conditions are plotted as a function of surface absolute humidity for frequencies of 15 and 35 GHz. Regression lines were derived where  $a_p$  is the dry term coefficient corresponding to the oxygen attenuation and  $a_w$  is the wet term coefficient which corresponds to the water vapor and liquid water attenuations. For complete cloud cover,

$$A_{15 \text{ GHz}} = .051 + .0047\rho \quad (3)$$

$$A_{35 \text{ GHz}} = .182 + .0161\rho \quad (4)$$

where  $\rho$  is in  $\text{gm/m}^3$ .

The regression line statistics are summarized in Table 1.

In this paper we assume that cloud attenuation has a frequency dependence similar to that of fog Altshuler [3]. Since it is not practical to obtain the temperature of the liquid water content of the cloud, a nominal value of 10°C was assumed. The resulting expression for the zenith attenuation for complete cloud cover is

$$A_z(\lambda, \rho) = \left( -0.0242 + \frac{0.00075\lambda + .403}{1.15} \right) (11.3 + \rho) \quad (5)$$

where  $A_z$  is in dB and  $\lambda$  is in millimeters. This is believed valid for the window regions from 15 to 100 GHz.

#### AN ALGORITHM FOR CLOUD ATTENUATION

We have examined the angle, humidity and frequency dependence of cloud attenuation. Equation (5) provides an expression for the zenith attenuation as a function of the surface absolute humidity and wavelength. For elevation angles above about 8°, we simply multiply (5) by  $\csc \theta$ ; for angles below about 8° we multiply (5) by the distance obtained from (1). For complete cloud cover the total atmospheric attenuation is

(6)

$$A(\theta, \lambda, \rho)_{\text{cloud}} = \left( -0.0242 + \frac{0.00075\lambda + .403}{1.15} \right) (11.3 + \rho) D(\theta)$$

$$D(\theta) = \csc \theta \quad \theta > 8^\circ$$

$$= [(a_e + h_e)^2 - a_e^2 \cos^2 \theta]^{1/2} - a_e \sin \theta \quad \theta < 8^\circ$$

where  $a_e$  is the effective earth radius = 8497 Km  
 $h_e$  is the effective height of attenuating atmosphere  
 = 6.35 - .302 $\rho$  (Km)

#### CONCLUSIONS

We have analyzed 341 sets of cloud attenuation data measured simultaneously at frequencies of 15 and 35 GHz in the Boston area. Regression lines for estimating the zenith attenuation at 15 and 35 GHz, both for cloud and mixed cloud conditions, have been derived for climates similar to the Boston area. Its applicability to other regions of the world would depend on their respective climatic conditions.

#### REFERENCES

1. Altshuler, E. E., M. A. Gallop, Jr., and L. E. Telford (1978) Atmospheric attenuation statistics at 15 and 35 GHz for very low elevation angles, Radio Sci., 13(5), 839-852.
2. Altshuler, E. E. and R. A. Marr (1988), A comparison of experimental and theoretical values of atmospheric absorption at the longer millimeter wavelengths, IEEE Trans. Antennas Propag. to be published.
3. Altshuler, E. E. (1984), A simple expression for estimating attenuation by fog at millimeter wavelengths, IEEE Trans. Antennas Propag. AP-32 (7), 757-758.

TABLE 1

#### SUMMARY OF REGRESSION LINE PARAMETERS

Type of Day	n	$A_D$	$S_D$	$A_W$	$S_W$	r
Uniform Cloud	123					
15 GHz		.051	.0030	.0047	.00032	.80
35 GHz		.182	.0095	.0161	.00100	.82
Uniform Mixed Cloud	112					
15 GHz		.048	.0029	.0036	.00034	.71
35 GHz		.176	.0070	.0115	.00084	.79
Clear	58					
15 GHz		.048	.0025	.0035	.00045	.72
35 GHz		.177	.0052	.0093	.00095	.79

n = number of sets of data  
 $A_D$  = dry term regression coefficient  
 $S_D$  = dry term standard error  
 $A_W$  = wet term regression coefficient  
 $S_W$  = wet term standard error  
 r = correlation coefficient

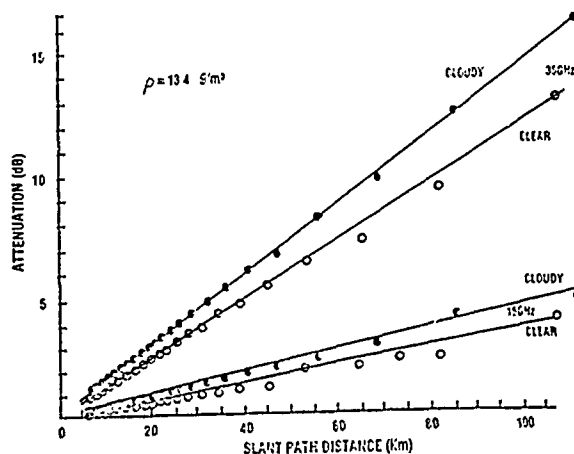


Fig. 1. Attenuation dependence on distance for uniform cloud and clear sky conditions.

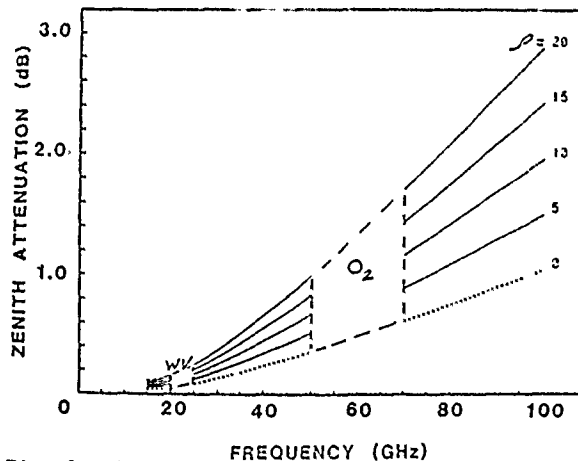


Fig. 2. Zenith attenuation vs. frequency for cloud conditions.

## MILLIMETER WAVE ATMOSPHERIC PROPAGATION STUDY AT CRL

T.Ihara\*, T.Manabe\*\*<sup>1</sup>, J.Awaka\*\*, and Y.Furuhashi\*\*\*\* Kashima Space Research Center, Communications Research Laboratory  
Kashima, Ibaraki, Japan

\*\* Communications Research Laboratory, Koganei, Tokyo, Japan

\*\*\* ATR Optical and Radio Communications Research Laboratories  
Higashi-ku, Osaka, Japan

## ABSTRACT

Communications Research Laboratory conducted millimeter wave propagation experiments at radio window frequencies 1.7, 11.5, 34.5, 50.4, 81.8, 140.7, 245.5 GHz and at 350 THz on short terrestrial paths in a suburb of Tokyo during 1979 - 1986. Main results of these experiments will be presented.

## INTRODUCTION

To promote the utilization of millimeter waves, it is necessary to clarify the atmospheric propagation characteristics. Communications Research Laboratory (formerly Radio Research Laboratory) conducted millimeter wave propagation experiments at radio window frequencies 1.7, 11.5, 34.5, 81.8 GHz on a 1.3 km path, and at 50.4, 81.8, 140.7, and 245.5 GHz and 350 THz on a 0.81 km path in a suburb of Tokyo during 1979 - 1986. In addition to propagation data, various meteorological parameters were also measured. In the following, main results of these experiments will be presented. Details of the experimental system were reported elsewhere [1], [2].

## EFFECTS OF HYDROMETEORS

Effects of rain

At millimeter wavelengths, the relationship between rain attenuation and rain rate appreciably changes depending on raindrop size distribution [3]. Therefore, a prime objective of our experiment was to clarify the characteristics of raindrop size distribution on an actual propagation path.

For this purpose, we examined a technique to infer a path-averaged raindrop size distribution  $\bar{N}(D)$  ( $\text{mm}^{-1} \text{m}^{-3}$ ) from multifrequency attenuation measurements [1]. The examined method assumes a trial function of  $\bar{N}(D) = N_0 \exp(-\lambda D)$  where  $D$  is the drop diameter (mm). Parameters  $N_0$  and  $\lambda$  are so determined as to best fit the measured attenuations. This method was applied to attenuation data at 11.5, 34.5, and 81.8 GHz and differential phase data between 11.5 and 34.5 GHz observed for a heavy rain event.  $\bar{N}(D)$  thus inferred was in good agreement with raindrop size distribution directly measured by disdrometer at the receiver site of propagation path. Hence, a feasibility of the examined inference method of  $\bar{N}(D)$  was demonstrated [1]. Once  $\bar{N}(D)$  is inferred, rain attenuations at arbitrary frequencies and other  $\bar{N}(D)$ -related quantities such as a path-averaged rain rate  $\bar{R}$  (mm/h) can be calculated from the inferred  $\bar{N}(D)$  [4].

Statistical estimation of rain attenuations is indispensable in the design of millimeter wave

<sup>\*\*1</sup> on assignment at ATR Optical and Radio Communications Research Laboratories

communication links. This requires a knowledge of the average relationship between rain attenuation coefficient and rain rate. This relationship is derived from the average raindrop size distribution. In order to obtain such  $\bar{N}(D)$  averaged over long time period, the trial function method was applied to equiprobable values of attenuations in the cumulative distributions of rain attenuations measured at 11.5, 34.5, and 81.8 GHz for three years [5]. As a result, we obtained

$$\bar{N}(D) = 17300 \bar{R}^{-0.16} \exp(-5.11 \bar{R}^{-0.253} D) \quad (1)$$

Rain attenuation coefficients between 10 to 300 GHz, based on Eq. (1), are shown in Fig. 1, along with those for Laws and Parsons (L-P) distribution and for Marshall and Palmer (M-P) distribution [5]. Drop size distribution of Eq. (1) gives a larger number of small drops than the Laws and Parsons drop size distribution which is most widely used in the theoretical estimation of rain attenuations. Since small raindrops can produce significant attenuation at millimeter wavelengths, attenuation coefficients based on Eq. (1) are greater than those for Laws and Parsons drop size distribution at frequencies above about 80 GHz.

Our results shown in Fig. 1 are estimates based on the attenuation data measured at 11.5, 34.5, and 81.8 GHz. However, it is noteworthy that this estimate explains well rain attenuation data measured at 50.4, 81.8, 140.7, and 245.5 GHz on a 0.81 km path [6]. This fact suggests that the drop size distribution given by Eq. (1) is applicable to whole the millimeter wave region under the Japanese rain climate.

Effect of other hydrometeors

Effect of fog was examined at 50 GHz and 350 THz [7]. Attenuation due to fog observed at 50 GHz was negligibly small, while a dominant part of high attenuation data at 350 THz was caused by fog. Duration time of attenuation for 10 dB level was less than 10 minutes at 50 GHz because of localized intense rain, while it reached a few 100 minutes at 350 THz in some fog event.

Depolarization due to wet snow was observed at 34.5 GHz with circularly polarized wave [8]. Theoretical estimation of depolarization assuming an oblate spheroidal snowflake model was made. It was found that the theoretical estimate obtained assuming a snowflake shape with an axial ratio of about 0.6 explained the trend of measured data.

## EFFECTS OF WATER VAPOR

Effects of water vapor in the millimeter wave window regions were examined by using an experimental system at 81.8 and 245.5 GHz on a 0.81 km path [9].

This experimental system was capable of measuring not only the amplitude at each frequency but also the differential phase delay between the two frequencies [2].

As can be seen in Fig. 2, measured attenuation showed a quadratic dependence on water vapor density. Attenuations in excess of theoretical predictions derived by the line-by-line calculations were observed at both frequencies (only the case of 245.5 GHz is shown in Fig. 2). The quadratic dependences of these excess absorption on water vapor density imply that either the absorption due to far-wing contributions from self-broadened infrared absorption lines or the absorption due to water dimer may play some important roll in the millimeter wave window region. Although the mechanism of excess absorption still remains to be solved, it is noteworthy that, as seen in Fig. 2, our experimental data at 81.8 and 245.5 GHz were in good agreement with estimates based on Liebe's semi-theoretical and semi-empirical model [10].

Contrary to the case of attenuation, the measured refractive dispersion (proportional to differential phase delay) between 245.5 and 81.8 GHz were in fairly good agreements with the exact line-by-line calculations, and "excess dispersion" corresponding to the excess absorption was not appreciable.

#### SCINTILLATION DUE TO ATMOSPHERIC TURBULENCE

Characteristics of scintillation due to atmospheric turbulence were examined at 81.8 GHz and 245.5 GHz where water vapor absorptions are not negligible [11]. At both frequencies examined, it was found that the scintillation spectrum of logarithmic amplitude was affected by the existence of gaseous absorption as theoretically predicted by Ott [12]: that is, the low frequency components of scintillation spectrum were enhanced. Similar enhancement was also observed for scintillation spectrum of differential phase delay between 81.8 and 245.5 GHz.

#### CONCLUSION

Main results of terrestrial millimeter wave propagation experiment made by CRL in a suburb of Tokyo were briefly introduced. More detailed information on each experimental result is available from the listed references.

#### REFERENCES

- [1] Y.Furuhashi and T.Ihara, IEEE Trans. Ant. Prop., 1981, Vol. AP-29, pp. 275-281.
- [2] Y.Furuhashi, T.Manabe, T.Ihara, K.Tohma, K.Kitamura, and Y.Imai, Proc. URSI-F Symp., 1983, ESA SP-194, pp.165-171.
- [3] R.Olsen, D.V.Rogers, and D.B.Hodge, IEEE Trans. Ant. Prop., 1978, Vol. AP-26, pp.318-329.
- [4] T.Ihara and Y.Furuhashi, Radio Sci., 1981, Vol. 16, pp. 1365-1372.
- [5] T.Ihara, Y.Furuhashi, and T.Manabe, Trans. IECE Japan, 1984, Vol. E67, pp. 211-217.
- [6] T.Manabe, T.Ihara, J.Awaka, and Y.Furuhashi, IEEE Trans. Ant. Prop., 1987, Vol. AP-35, 1326-1330.
- [7] T.Manabe, T.Ihara, J.Awaka, K.Kitamura, K.Okamoto, and K.Araki, Nat. Conv. Record of IEICE (in Japanese), 1987, p.3-3.
- [8] T.Ihara, Y.Furuhashi, and K.Tohma, Trans. IECE Japan, 1982, E65, pp.16-22.

- [9] T.Manabe, Y.Furuhashi, T.Ihara, S.Saito, H.Tanaka, and A.Ono, Int. J. Infrared and Millimeter Waves, 1985, Vol. 6, pp. 313-322.
- [10] H.J.Liebe, NTIA Rep., 1983, pp. 83-137.
- [11] T.Manabe and Y.Furuhashi, Proc. 1985 Int. Sym. on Ant. and EM Theory, Beijing, 1985, pp. 285-288.
- [12] R.T.Ott, IEEE Trans. Ant. Prop., 1977, AP-25, pp. 254-260.

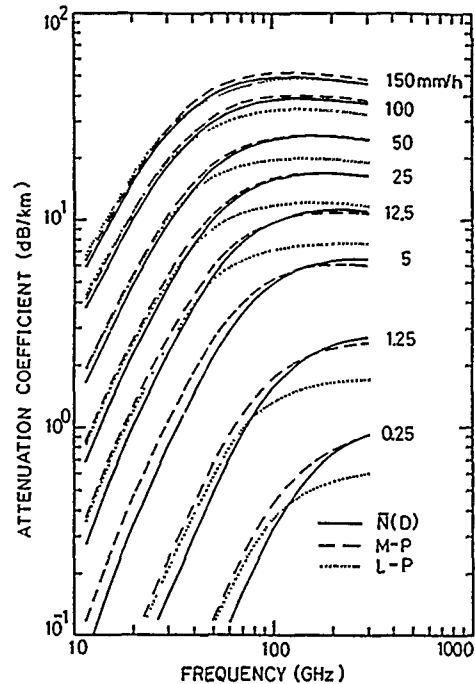


Fig. 1 Attenuation coefficients due to rain. (10-300 GHz)

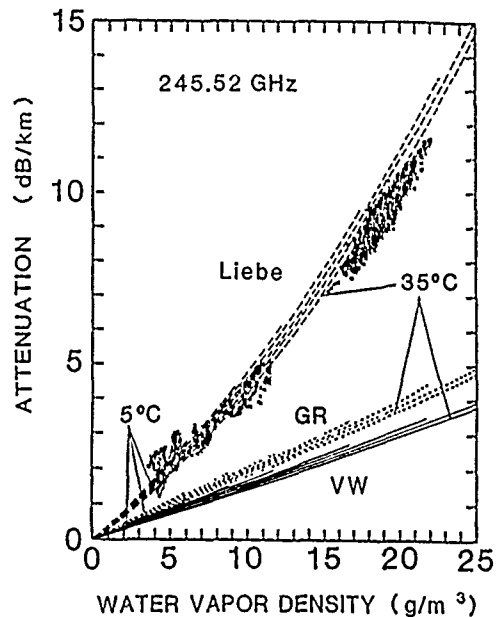


Fig. 2 Attenuation coefficient due to water vapor at 245.5 GHz.  
measured: x. line-by-line calculations:  
Van Vleck-Weisskopf —, Gross .....  
Liebe's model: — .

## FOR FUTURE METEOROLOGICAL MILLIMETER-WAVES SATELLITE MISSIONS:

## A RADIATIVE TRANSFER MODEL AND AN AIRBORNE CAMPAIGN.

C. Prigent

Laboratoire de Radioastronomie Millimétrique  
Observatoire de Meudon - 92190 Meudon - FRANCE

P. Abba

Alcatel-Espace  
26 av. J.F.Champollion - 31037 Toulouse - FRANCE

N.A. Scott

Laboratoire de Météorologie Dynamique  
Centre National de la Recherche Scientifique  
Ecole Polytechnique - 91128 Palaiseau Cedex - FRANCE

## ABSTRACT

To prepare the future meteorological radiometric satellite missions, we developed a synthetic atmospheric millimeter-waves radiative transfer model including the roughened sea surface emissivity and all-weather conditions. It is to be confronted with measurements of an airborne campaign in window regions of the atmospheric spectrum.

## INTRODUCTION

The data interpretation of the future meteorological millimeter-waves missions aboard satellites (METEOSAT 2nd Generation, AMSU) is highly dependent on the validity of the radiative transfer model in the atmosphere (1). Above 60 GHz, very few complete models have been developed and the in situ observations are sparse. The approach we propose benefits from the last progress in spectroscopic data, includes all-weather conditions and presents an original treatment of the roughened sea surface emissivity. It will soon be confronted with the results of an English-French measurement campaign in window regions of the atmospheric spectrum: the MARSS (Microwave Airborne Radiometer Scanning System) experiment.

## A SYNTHETIC RADIATIVE TRANSFER MODEL

For computation purposes, our model, derived from the Stransac code (2), considers 40 pressure levels dividing the atmosphere up to 70 km.

The absorption coefficient of each layer accounts for:

- the line-by-line summation of the atmospheric constituents absorption based on the spectral line data bank GEISA from the Laboratoire de Météorologie Dynamique (3). The line shape problem has been envisaged on the basis of the last enhancements of Rosenkranz treatment of the Van Vleck-Weisskopf theory;
- the continuum spectra for dry air and water vapour (4);
- the absorption and scattering by hydrometeors (rain, clouds, fog...) according to Mie diffusion theory (as expressed by (5)). The individual particle contributions are integrated over the drops radius distribution in the cloud or rain.

The upwelling microwave radiation measured by a radiometer is the sum of 1) the direct contribution of each layer, 2) the thermal emission from the earth surface attenuated by the atmosphere, 3) the downwelling radiation reflected by the surface and then attenuated by the atmosphere.

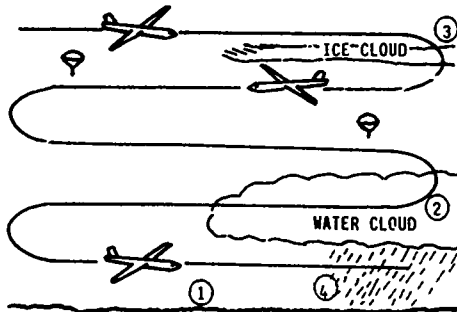
In the atmospheric windows, the surface emissivity is the dominant feature of the radiative transfer. For the soil and for the calm ocean, this parameter is well-established. But uncertainties arise from the variation of roughened sea surface emissivity with wind direction and speed and foam coverage. In the millimeter-waves region, it is relevant to describe the ocean surface as a set of flat facets (6) with a two-dimensional slope distribution (photometrically evaluated (7)). Assuming a fixed view angle, we calculate, for each facet, the direction and corresponding brightness temperature of the downwelling radiation which, specularly reflected on the facet, impinges on the receiver; the elementary contribution to the upwelling brightness temperature is computed using a reflection coefficient calculated from the Fresnel relations. Then, all the contributions are added up, weighted by the probability density of the surface slope distribution. This computation accounts for polarization. A partial foam coverage is considered.

The hydrometeors scattering is iteratively accounted for in the radiative transfer treatment. First, the up- and down-welling radiations are computed for each atmospheric layer, ignoring the scatter, in order to obtain the brightness temperatures for several directions independently. Then, until convergence, the brightness temperatures are recomputed iteratively using, for the scattered radiations, the brightness temperatures calculated in the previous iteration. At each iteration, an individual particle rescatters the radiation of the previous iteration, thus providing a full multiple scattering treatment.

The synthetic radiative transfer model we are developing is implemented in Fortran, on PC-AT and on VAX 8600. It offers an interactive relationship with the user, proposing multiple possibilities for each atmospheric and surface parameters. This synthetic model and the systematic sensitivity analyses we have performed for a large number of its parameters, prepare us to the data treatment of the MARSS experiment.

## THE MARSS EXPERIMENT

An airborne millimeter-waves sounder operating in the 89 and 157 GHz channels -MARSS (Microwave Airborne Radiometer Scanning System)- is jointly developed by the British Meteorological Office and the Laboratoire de Météorologie Dynamique (France). The receiver system, produced by Marconi Space System, is sensitive to 0.5K in both channels. This instrument will fly on the Hercules C-130 dedicated aircraft of the Met Office. It provides up- and down-looking with  $\pm 45^\circ$  angle along track scanning. Observations are planned on spiral ascents and on race track flight paths at selected altitudes from sea level to above ice clouds.



### Objectives of MARSS flights:

- 1° - sea surface emissivity measurements
- 2° - attenuation of liquid water clouds
- 3° - impact of ice clouds
- 4° - precipitation monitoring

## FUTURE PLANS

In a next step, a complete breadboard of the METEOSAT 2nd Generation millimeter-waves project will be flown. The instrument is presently assembled at Paris-Meudon Observatory, with a technological support from Matra and under the responsibility of the french Centre National d'Etudes Spatiales.

## ACKNOWLEDGEMENTS

The authors wish to express their thanks to A. Chédin and N. Scott (Laboratoire de Météorologie Dynamique) and D. Pick (British Meteorological Office) for their valuable advices. This study has been partially financially supported by the Centre National d'Etudes Spatiales and by Alcatel Espace.

## REFERENCES

- (1) A. Chédin, N. Scott, C. Wahiche and P. Moulinier, *J. Climate Appl. Meteorol.*, 1985, vol.24, pp. 128-143.
- (2) N. Scott, *J. Quant. Spectrosc. Radiat. Transfer*, 1974, vol. 14, pp. 691-704.
- (3) N. Husson et al, *Annales Geophysicae*, 1986, vol. 4 2, pp. 185-190.
- (4) H. J. Liebe, NTIA report 87-224, US Department of Commerce, 1987.
- (5) D. Deirmendjian, "Electromagnetic scattering on spherical polydispersions", 1969, Elsevier.
- (6) T. T. Wilheit, *IEEE Trans. Geo. Electr.*, 1979, vol. GE-17(4), pp. 244-249.
- (7) C. Cox and W. Munk, *J. Opt. Soc. Am.*, 1954, vol. 44(11), pp. 838-850.
- (8) J. M. Millet, "Détermination du contenu en eau de l'atmosphère par radiométrie hyperfréquence spatiale, Ph.D. Thesis, Paris 7 University, 1984.



# MESOSPHERIC RADIOWAVE PROPAGATION IN THE 60 GHz BAND AFFECTED BY ZEEMAN-SPLIT OXYGEN LINES

H.J. Liebe, G.A. Hufford, and A.S. Katz

National Telecommunications and Information Administration  
Institute for Telecommunication Sciences  
Boulder, CO.

## ABSTRACT

A model was developed to analyze anisotropic propagation of plane, polarized radiowaves in the mesosphere as influenced by the geomagnetic Zeeman effect displayed by  $O_2$  spectral lines positioned in the 60 GHz band. To provide an example here, the  $5+$  line, centered at the frequency  $f_0 = 59.59058$  GHz, has been chosen and two cases are discussed: from a location known by latitude and longitude, a radiowave (a) propagates north in an altitude of 75 km at the frequency  $f_0 + 1$  MHz covering a distance of up to 1000 km; and (b) enters the atmosphere at 100 km altitude, heads in either N, E, S, or W directions, descends to the 75 km level, and then exits again. In the first case, attenuation and polarization state are followed along the path; in the second case, total path attenuations as a function of frequency deviation ( $f_0 \pm 4$  MHz), initial polarization, and direction are given.

## INTRODUCTION

About 40 spectral lines of the molecule  $O_2$  are found between 50 and 70 GHz. At high-altitude pressures ( $1.2$  to  $3 \cdot 10^{-5}$  kPa), these lines appear as isolated features and their spectral signature is governed by the Zeeman effect due to the geomagnetic field  $B$  whose strength varies from about 23 to 65  $\mu$ Tesla depending on location and height ( $h = 30 - 100$  km). Each line splits into three groups of Zeeman components which are spread, proportional to  $B$ , over a range of a few megahertz and which react anisotropically with the electromagnetic field of a radiowave [1],[2].

Magnitude and direction of the vector  $B$  are calculated with the geocentric model MAGFIN, updated with 1985 coefficients [3]. To allow for geodetic input coordinates (i.e., LATitude, LONgitude, and  $h$  = height above sea level), a correction to latitude and height is applied to account for the flattening ( $1/298.25$ ) of the earth ( $r_E = 6371.2$  km).

## REFRACTIVITY MATRIX

In a Cartesian coordinate system having the  $z$ -axis pointing in direction of the geomagnetic vector  $B$ , the anisotropic medium can be represented by a refractivity matrix [4]

$$N = \begin{vmatrix} N_+ + N_- & -i(N_+ - N_-) & 0 \\ i(N_+ - N_-) & N_+ + N_- & 0 \\ 0 & 0 & N_0 \end{vmatrix},$$

where  $N_0$ ,  $N_+$ ,  $N_-$  are complex-valued functions of frequency and comprise the three groups mentioned above. The shape of these functions is illustrated for an example in Fig.1.

To study how a radiowave behaves as it propagates through this medium, the coordinate system must be rotated so that the  $z$ -axis points in the direction of propagation. Thus the angle  $\phi$  between the vector  $B$  and the propagation vector is important. It determines a 2-dimensional matrix which describes how the radiowave field components change within the plane of polarization. This  $2 \times 2$  matrix has two eigenvalues  $v_1, v_2$  with corresponding eigenvectors,

each defining a characteristic wave that retains its original polarization as it propagates through the medium. The polarization state can be expressed by four real-valued Stokes parameters. When  $\phi = 0$  or  $180^\circ$ , these characteristic waves are left- and right-circularly polarized; when  $\phi = 90^\circ$  or  $270^\circ$ , they are linearly polarized. Examples for frequency and  $\phi$  dependences of  $v_1, v_2$  are displayed in Fig. 2.

## RADIOWAVE PROPAGATION

Generally, a radiowave is defined as linear combination of the two characteristic waves. Horizontal and vertical field components (HZE, VTE) plus a phase angle (POL) or a matching set of Stokes parameters ( $g_{1,2,3}$  normalized to  $g_0=1$ ) describe the polarization state. Typically, the imaginary parts (expressed in dB/km) of  $v_1$  and  $v_2$  differ (see Fig. 2), favoring after some propagation distance the characteristic wave with the lower value; simultaneously, different real parts (in deg/km) affect the phase angle POL. As a consequence, the polarization ellipse changes its axial ratio and rotates (as in Faraday-rotation) approaching the polarization state of the dominant characteristic wave.

Propagation effects are shown in Fig. 3 for a case where  $h, B$ , and  $\phi$  are given ( $v_1, v_2$ ) and distance  $S$  varies. A radiowave at the frequency  $f_0 + 1$  MHz with two initial polarizations propagates a path extending at  $h = 75$  km to a length of up to 1000 km.

Computations are more complicated for the example of a tangential path from outer space through the mesosphere (U.S. Std. Atm. 76) reaching a minimum height,  $h_t = 75$  km. A point on a straight line through a homogeneous path cell, starting at  $h = 100$  km in a given direction (AZI\_muth) under a negative elevation angle (ELV =  $-5.1^\circ$ ), was traced via the coordinates LAT, LON, and  $h$ . Geodetic locations were transformed into geocentric coordinates to compute  $B, \phi$ , and path increments  $\Delta S$  for 1-km height intervals; then a numerical integration was performed whereby the anisotropic behavior of each cell was evaluated analogously to the case exemplified in Fig. 3. The final polarization after traversing one cell served as starting polarization for the next. Resultant path attenuations for three different initial polarizations and four propagation directions are plotted in Fig. 4 as a function of frequency deviation. Each curve represents the integration over fifty ( $100 - 75 - 100$  km) 1-km height cells performed at 100 frequencies between  $f_0 \pm 4$  MHz.

## REFERENCES

- [1] W.B. Lenoir, *J. Geophys. Res.*, 1968, vol. 73, pp. 361 - 376.
- [2] H.J. Liebe, *Radio Sci.*, 1981, vol. 16(6), pp. 1183 - 1199.
- [3] D.R. Barraclough, *PAGEOPH*, 1985, vol. 123, pp. 641 - 645.
- [4] P.W. Rosenkranz and D.H. Staelin, *Radio Sci.*, 1988, vol. 23(5), in press.

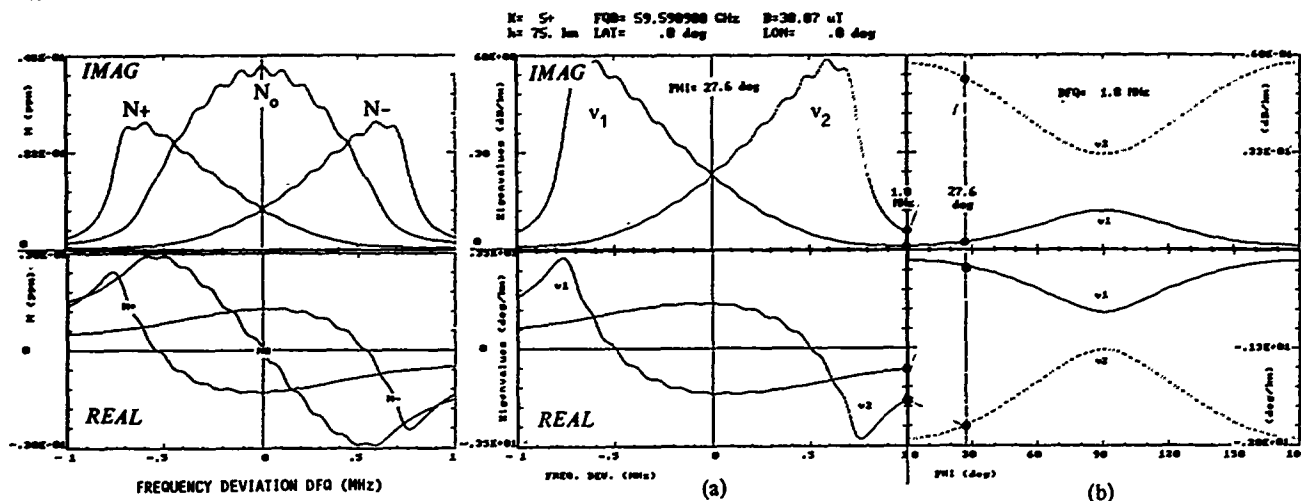


Figure 1

Figure 2

Complex refractivity components  $N_0$ ,  $N_+$ , and  $N_-$  (ppm) in the vicinity ( $DFQ = \pm 1$  MHz) of the  $5+ O_2$  line center at 75 km altitude for a magnetic field strength of 30.07  $\mu T$ .

Complex eigenvalues  $v_1$  and  $v_2$  for the  $5+$  line (IMAG in dB/km, REAL in deg/km): (a) around the line center ( $DFQ = \pm 1$  MHz) at an orientation angle  $\Phi = 27.6^\circ$  and (b) for all orientation angles ( $\Phi = 0$  to  $180^\circ$ ) at a frequency deviation  $DFQ = +1$  MHz. Altitude above sea level is  $h = 75$  km and geographic coordinates are  $LAT = 0^\circ$  (equator) and  $LON = 0^\circ$  (Greenwich).

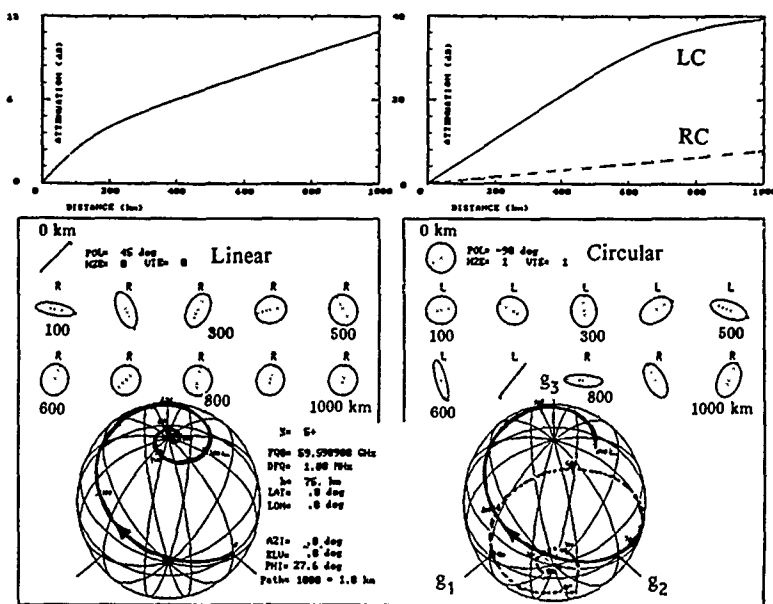


Figure 3

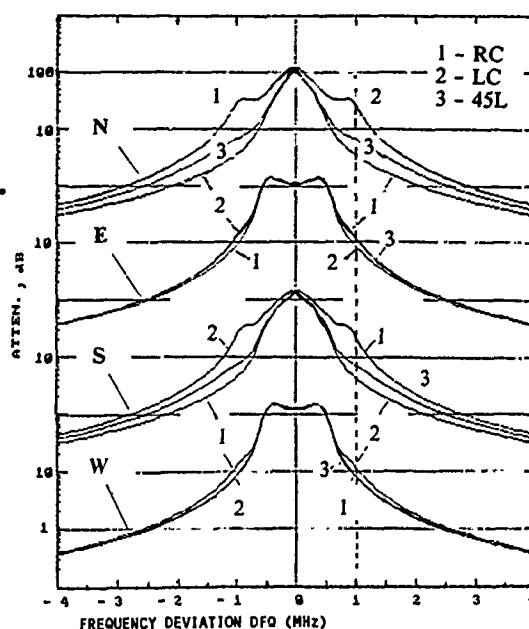


Figure 4

Attenuation, Faraday rotation, and polarization state (Stokes parameters  $g_1, g_2, g_3$  on Poincaré sphere) for initially linear (45L) and left-circular (LC) polarized radiowaves propagating a distance of 1000 km at  $h = 75$  km horizontally ( $ELV = 0^\circ$ ) in the N direction ( $AZI = 0^\circ$ ) under the computed orientation angle  $\Phi = 27.6^\circ$  at a frequency deviation  $DFQ = +1$  MHz from the  $5+$  line center. The results at 1000 km are:

	A, dB	HZE	VTE	POL, deg
*RC	8.0	1	1.04	88.0
*VL	10.8	1	1.05	87.8
45L	10.9	1	1.04	87.4
*HL	11.2	1	1.03	88.2
LC	39.5	1	1.37	70.0

\* (RC = right-circular, VL = vertical linear, and HL = horizontal linear initial polarizations, not shown). HZE and VTE are the horizontal and vertical electric field components and POL is the phase angle ( $VTE = |VTE| \exp(i \text{ POL})$ ).

Attenuation for tangential paths through U.S. Std. Atm. 76 in the vicinity ( $DFQ = \pm 4$  MHz) of the  $5+$  oxygen line. The radiowave enters the atmosphere at  $LAT = 0^\circ$ ,  $LON = 0^\circ$ , and  $h = 100$  km with an elevation angle  $ELV = -5.1^\circ$ , propagates in either N, E, S, or W directions ( $AZI = 0^\circ, 90^\circ, 180^\circ$  and  $270^\circ$ ), approaches a tangential height of 75 km, and leaves the atmosphere at  $h = 100$  km. Path lengths:  $S_{path} = 1129$  km for N,S and 1140 km for E,W; initial polarizations: RC, LC, and 45L. Path attenuations  $A$  (dB) at  $DFQ = +1$  MHz are:

AZI	HL	VL	Ratio	RC	LC	Ratio
$0^\circ$ N	6.4	6.7	1.05	3.5	27.6	7.89
$90^\circ$ E	13.5	8.7	1.55	12.6	9.1	1.39
$180^\circ$ S	7.1	7.6	1.07	22.7	4.4	5.16
$270^\circ$ W	11.9	8.5	1.40	8.5	12.3	1.45

## STATUS AND FUTURE PLANS OF HIGH POWER SOURCES

## FOR PLASMA HEATING

T. V. George  
Office of Fusion Energy  
Department of Energy  
Washington, D. C.

## ABSTRACT

The presentation will address the motivation, the strategy and the plan for developing high average power millimeter wave sources under the sponsorship of the Office of Fusion Energy, Department of Energy. Ongoing efforts and expected trends in line with the recent recommendations of a number of review panels will be discussed. The presentation will also highlight some of the fusion experimental applications.

## MOTIVATION

Application of high power electromagnetic waves in the frequency range up to several hundred gigahertz for heating plasmas in thermonuclear fusion devices by electron cyclotron resonance techniques has been the prime motivation behind the development of various types of millimeter wave sources under the sponsorship of the Office of Fusion Energy (OFE), U.S. Department of Energy. The program strategy has been to promote fundamental research on promising concepts at Universities and National laboratories leading to the establishment of an industrial base to supply reasonably priced devices to the various fusion laboratories around the world.

## HISTORY

Since 1976, the OFE has supported the development of both pulsed and steady-state (cw) gyrotrons operable at several fixed frequencies in the 28 GHz to 140 GHz range (corresponding to the fundamental resonance at plasma confining magnetic fields ranging from 1T to 5T) and with average power in excess of 200 kW. From the seventies, the program directly led to establishing a strong industrial capability at Varian Associates. Under a contract placed in 1976, Varian succeeded in developing a 200 kW 28 GHz gyrotron which was tested satisfactorily to a power level well over 300 kW in the cw mode. A follow-on contract covering a period from 1980 to 1984 resulted in 200 kW cw and pulsed 60 GHz gyrotrons as well as a number of scale variations covering the entire frequency range up to 70 GHz. During the next two years Varian established the capability to provide 200 kW, pulsed and 100 kW cw 140 GHz gyrotrons. So far, Varian has sold over one hundred gyrotrons to various fusion laboratories around the world. The objective of the current program at Varian is to develop a 1 MW 140 GHz gyrotron with a follow on objective of developing 1 MW 280 GHz gyrotrons for use on the next major U.S. fusion device called Compact Ignition Tokamak (CIT) which is expected to produce first plasma in 1996.

## STRATEGY

The program emphasizes pioneering research at several laboratories. Since the OFE's funding limitations do not permit supporting research on all known concepts and since other funding agencies are also involved in developing devices which could ultimately be of value to the fusion program, it has been necessary for the OFE program to continuously evaluate the status and make use of results from all leading research activities around the nation. For example, the Free Electron Laser system, under development at the Lawrence Livermore Laboratory, supported by the Strategic Defense Initiative Office is being used for tokamak heating studies. The large number of papers which are presented at this conference is indicative of the importance of this field in terms of the interest demonstrated by the technical community as well as the applications envisaged by the funding agencies.

## PLANS

The major basic research activities supported by OFE are: volume mode and whispering gallery mode gyrotrons at the Massachusetts Institute of Technology under Dr. Richard Temkin, the Quasi-Optical gyrotron concept at the Naval Research Laboratory under Dr. Wallace Manheimer, and the Small Periodic Wiggler Free FEM at the University of Maryland under Dr. Victor Granatstein. The University of Wisconsin, Madison, also has a program to develop transmission system components under Dr. R. Vernon and Dr. S. Seshadri. A number of worthy tasks such as the investigation of Cyclotron Auto-Resonance Maser (CARM) at UCLA, NRL or MIT, as well as the Ubitron and Backward Wave Oscillator (BWO) studies at NRL have not been funded by the OFE program. But it should be emphasized that the value of all such research activities in serving the fusion program needs is well recognized by the OFE program. Hence, the overall strategy has been to identify concepts which need to be further developed to meet the specific needs of the fusion program through periodical reviews and strengthen the efforts to establish an adequate data base necessary for initiating industrial projects. During 1987 and 1988 there were three such major reviews: a DOE special panel chaired by Dr. Thomas Marshall, Columbia University, a JASON committee chaired by Dr. Francis Perkins, Princeton University and a Magnetic Fusion Advisory Committee panel chaired by Dr. Lee Berry, Oak Ridge National Laboratory. This presentation will summarize the panel findings and highlight the features of the major devices currently under investigation.

Presently, the MIT program on whispering gallery mode has been given the highest priority; the goal of which is to demonstrate a 280 GHz 1 MW short pulsed gyrotron within a year. The plan is to initiate the industrial development program following the concept demonstration at MIT. Studies on separating the spent electron beam from the electromagnetic wave as they emerge from the gyrotron cavity are also being undertaken to facilitate energy recovery from the spent beam.

Recent plasma heating experiments conducted on tokamak devices such as D-III located at San Diego, California, using a total of ten 200 kW, long pulsed 60 GHz gyrotrons have clearly established the continued need for such sources. The presentation will also highlight the experimental applications.

## MEGAWATT GYROTRONS FOR ECR HEATING\*

K. Felch, C. Hess, H. Huey, E. Jongewaard, H. Jory, and R. Pendleton

Varian Associates, Inc.  
Palo Alto, CA

### ABSTRACT

Varian is in the process of developing gyrotrons capable of generating power levels of 1 MW CW at a frequency of 140 GHz. The first experimental gyrotron in this program has been designed to generate short-pulse power levels of 1 MW and up to 400 kW CW. In recent tests on this gyrotron, a short-pulse power level of 820 kW was obtained at 21% efficiency. While operating at peak power levels of 350-400 kW, the duty factor was raised to 10% (30 pps, 3.33 ms-pulse duration). Power losses in various parts of the tube have been measured and are in agreement with theoretical predictions. Tests at higher average powers, up to the 400 kW CW goal for the tube, are underway. Design efforts aimed at increasing the average power capabilities of the gyrotron up to 1 MW are in progress.

### INTRODUCTION

Gyrotron oscillators have been effectively employed in heating magnetically-confined plasmas, at the electron cyclotron resonance (ECR) frequency, in a variety of fusion experiments(1). In these experiments, gyrotrons with long-pulse or CW output powers of a few hundred kilowatts have been utilized at frequencies up to about 100 GHz. However, ECR heating in large, reactor-size fusion experiments, will require input microwave power levels of 10-100 MW at frequencies ranging from 100 GHz to 300 GHz(2).

To address this need, Varian has begun the development of gyrotrons capable of generating power levels of 1 MW CW at a frequency of 140 GHz. The basic design approach followed in the current gyrotron development program is significantly different than that of earlier efforts at lower frequencies and power levels. While most previous tubes were designed to generate output power in the  $TE_{0n}$  or circular-electric class of waveguide mode(3), the current work utilizes  $TE_{mn}$  whispering-gallery modes where  $m \gg n$ . In contrast to circular-electric modes, energy stored in a whispering-gallery-mode cavity is concentrated near the walls of the cavity, thereby requiring a relatively large-diameter electron beam for efficient interaction. The choice of whispering-gallery modes over other classes of interaction circuits is based on an intricate set of design trade-offs that include considerations of mode competition, ohmic losses in the cavity, efficiency, potential depression of the electron beam, and electron gun design(4). Experimental research with whispering-gallery-mode gyrotrons is also being carried out at MIT, where short-pulse power levels of 750 kW have been obtained at a frequency of 148 GHz(2), and in the Soviet Union(5).

In working toward the 1 MW CW goal at 140 GHz, several experimental vehicles will be constructed and tested to verify the design of the important elements of the gyrotron. The first tube in the program has been designed to generate short-pulse power levels of 1 MW and CW power levels up to 400 kW. Testing of this tube will serve to validate the basic design of the electron gun and interaction circuit. In addition, operation at CW powers up to 400 kW will provide useful information concerning whispering-gallery-mode operation at high average power levels.

Thus far, the first experimental tube has been constructed, tested, rebuilt, and partially tested a second time. In

the following we summarize the important design features of the tube, review the results of the first tube tests, and discuss the tests carried out thus far on the rebuilt version of the tube.

### DESIGN OF FIRST EXPERIMENTAL 1 MW GYROTRON

The design of the first experimental 140 GHz, 1 MW gyrotron is based on the interaction between a hollow electron beam provided by a magnetron injection electron gun and a simple, tapered cavity designed to generate power in the  $TE_{15,2}$  mode at 140 GHz. The nominal beam voltage and current for the gun are 80 kV and 35 A, respectively. The magnetic field in the cavity and gun regions is provided by a superconducting magnet. For operation at 140 GHz, a magnetic field of 56 kG is required in the interaction region.

Output power from the cavity travels through the collector and out of the tube through a double-disc, face-cooled window. The up and down tapers in the tube are designed to preserve the purity of the generated  $TE_{15,2}$  mode. The spent electron beam follows the diverging magnetic field lines out of the cavity and is deposited on the walls of the collector.

All elements of the tube are designed for operation up to power levels of 400 kW CW and 1 MW for pulse durations of less than 20 ms. Further details of the design of the first experimental 140 GHz, 1 MW gyrotron have been published elsewhere(6).

### TEST RESULTS

#### First Test

During the first tests of the tube, peak output powers up to 300 kW at 18% efficiency were produced with pulse durations of less than 1 ms. Operation at longer pulse durations or higher peak powers was prevented by spurious oscillations in the beam tunnel between the electron gun and the interaction cavity. At high peak power or long pulse duration, the spurious oscillations activated protective circuitry and turned off the gyrotron.

Measurements of the microwave losses in various portions of the tube were made with pulse repetition rates that produced 15 kW average output power. Power losses were measured in the beam tunnel, interaction cavity, output taper, collector insulator, and output window. The results agreed well with calculated values except in the beam tunnel.

Following tests on the tube, the tube was disassembled and examined for possible damage. All portions of the tube were undamaged with the exception of the beam tunnel. A portion of the beam tunnel adjacent to the cavity was significantly damaged. The damage pattern was consistent with the presence of spurious oscillations in that region.

To eliminate the beam tunnel oscillations that served to limit tube performance during the first series of tests, a new beam tunnel was designed and constructed. In the new beam tunnel, geometry changes were incorporated to minimize the amount of stored energy in the critical portion of the beam tunnel near the cavity to prevent oscillations. In addition, the cooling design for the beam tunnel was improved.

#### Second Test

Following the reassembly of the tube with the new beam tunnel, a second set of tests were begun. In these tests, an output power of 655 kW was obtained with 26% efficiency during

\*The 140 GHz gyrotron oscillator is being developed under contract with Lawrence Livermore National Laboratory, operated by the University of California for the U. S. Department of Energy, under Prime Contract W-7405-eng-48.

operation at the nominal beam voltage of 80 kV. A plot of output power and efficiency versus beam current is shown in Figure 1. In carrying out the measurements shown in Figure 1, cavity magnetic field and gun-anode voltage (which controls the perpendicular to parallel velocity ratio of the electron beam) were optimized. Microwave losses were measured in the beam tunnel, cavity, collector insulator, output taper, and output window. For operation at 655 kW, total measured rf losses were 98 kW. These measurements are in good agreement with theoretically predicted loss calculations. If these power losses are added to the measured output power, the total power generated in the cavity was 753 kW, resulting in an interaction efficiency of 30%. Though not totally eliminated in some regions of parameter space, the beam tunnel oscillations observed during the first series of tests were significantly reduced.

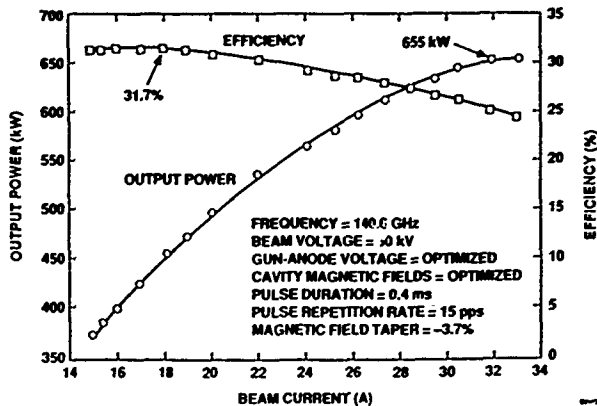


FIGURE 1. OUTPUT POWER AND EFFICIENCY VS BEAM CURRENT FOR BEAM VOLTAGE OF 80 kV

In Figures 2 and 3 the results of increasing the beam voltage to 90 kV and 95 kV, respectively, are plotted. Figure 2 is a plot of output power and efficiency versus beam current at 90 kV beam voltage, and Figure 3 is a plot of output power versus gun-anode voltage for constant beam current at 95 kV. At 90 kV, an output power of 750 kW was obtained at 22% efficiency and at 95 kV an output power of 820 kW was measured at 21% efficiency.

In addition to the short-pulse measurements (< 1 ms pulse duration), tests were carried out at 10 ms pulse duration for output powers of 400 kW. Average powers of 35 kW to 40 kW were obtained when operating at a duty cycle of 10% (30 pps, 3.3 ms pulse duration). Preparations are currently being made to test the tube to higher average power and ultimately to 400 kW CW. In addition, further exploration of tube operating parameters will be made to try to increase the efficiency of the tube and allow peak powers of 1 MW to be obtained.

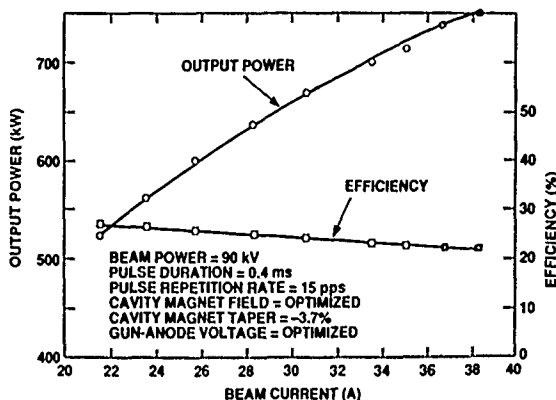


FIGURE 2. OUTPUT POWER AND EFFICIENCY VS BEAM CURRENT FOR BEAM VOLTAGE OF 90 kV

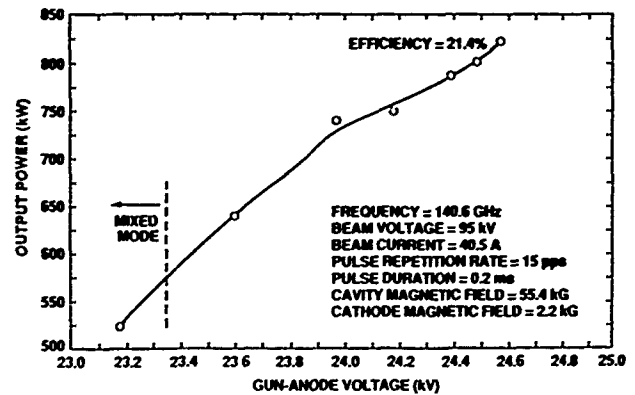


FIGURE 3. OUTPUT POWER VS GUN-ANODE VOLTAGE FOR BEAM VOLTAGE OF 95 kV

### CONCLUSIONS

The results obtained during the second series of tests on the first experimental 140 GHz, 1 MW gyrotron represent an important step in reaching the 1 MW CW goal for the current development program. Additional testing of the tube should further validate the average power capabilities of the tube. Subsequent tubes will serve to address the problems encountered in designing a tube for full 1 MW CW operation. Problem areas include cavity wall losses, thermomechanical stresses in the output window, electron beam collection, and output coupling from the tube. In addition, continued efforts will be made to increase the overall efficiency of the design.

### REFERENCES

- (1) R. Prater, V. S. Chan, and T. C. Simenon, "The Status of Electron Cyclotron Heating and Current Drive and the Role of DIII-D," GA Technologies Report - GA-A18795, May 1987.
- (2) K. Kreischer, T. Grimm, A. Mobius, and R. Temkin, "The Design of Megawatt Gyrotrons for the Compact Ignition Tokamak," 13th Int. Conf. Infrared and Millimeter Waves, Conference Digest, 1988.
- (3) H. Jory, "Status of Gyrotron Development at Varian Associates," Proc. 4th Int. Symp. on Heating in Toroidal Plasmas, 1984, Vol. 2, pp. 1424-1430.
- (4) K. E. Kreischer, B. G. Danly, J. B. Schutkeker, and R. J. Temkin, "The Design of Megawatt Gyrotrons," IEEE Trans. Plasma Science, 1985, Vol. PS-13, No. 6, pp. 364-373.
- (5) V. A. Flyagin and G. S. Nusinovich, "Gyrotron Oscillators," Proc. IEEE, 1988, Vol. 76, No. 6, pp. 644-656.
- (6) K. Felch, L. Ives, E. Jongewaard, H. Jory, and S. Spang, "Initial Operation of a High-Power, Whispering-Gallery-Mode Gyrotron," 12th Int. Conf. Infrared and Millimeter Waves, Conference Digest, 1987, pp. 146-147.

# EXPERIMENTAL STUDIES ON THE 120 GHz GYROTRON OF MITSUBISHI ELECTRIC CORP.

T.Kikunaga, T.Shimozuma, H.Asano, Y.Yasojima,  
Y.Murai, K.Nakashima and T.Tsukamoto

Central Research Laboratory, Mitsubishi Electric Corp.  
Amagasaki, Hyogo, 661 Japan

## ABSTRACT

Design and experimental studies of the 120 GHz,  $TE_{03}$  mode gyrotron of Mitsubishi Electric Corp. are reported. Since the first operation of our 120 GHz,  $TE_{03}$  mode gyrotron<sup>(1)</sup>, our efforts have been aimed at increasing an output power on the second tube. The second tube is a modular type and allows interchange of important parts such as a magnetron injection gun, a cavity and a window. The tube with a non-laminor gun and a simple tapered cavity ( $Q=579$ ) has achieved the maximum output power of 167 kW at 120 GHz in the  $TE_{03}$  mode with short pulse. The efforts for increasing pulse width have been also continued. A 150 kW, 10 msec, sealed type of gyrotron was reported at the 5th Annual Conference of the Japan Society of Plasma Science and Nuclear Fusion Research (March, 1988). In this paper, most part is devoted to descriptions of short pulse operation on the second tube. The rest introduces the design of a complex cavity for high power ( $\sim 200$  kW) and long pulse ( $\sim 100$  ms) gyrotrons.

## INTRODUCTION

In Mitsubishi Electric Corp. a high power ( $>100$  kW) and high frequency ( $>100$  GHz) gyrotron for electron cyclotron heating of fusion plasmas has been developed since 1985. The first tube generated an output power of 20.1 kW at 120.06 GHz with a pulse width of 1 ms in 1986<sup>(1)</sup>. This tube is going to be used for the power source for millimeter wave scattering measurement of tokamak plasmas at Kyoto University. A test of cw operation at low power was carried out and an output power of 150 W high enough for scattering experiments was obtained at 120 GHz.

The second tube was designed and constructed in order to test the important parts of a high power ( $\sim 200$  kW) gyrotron, namely, a magnetron injection gun, a cavity and a window.

This tube is a modular type which can be separated into four parts; the magnetron injection gun, the main body, the collector, and the window. All parts are connected with flanges, and especially, it is possible to make an exchange of the cavity. Therefore, the characteristics of gyrotron oscillation on various profiles of

cavities, including a complex cavity, can be studied. The maximum output power of 167 kW was achieved at a beam voltage of 63.9 kV and a beam current of 10.2 A in the first experiment of this tube with a simple tapered cavity.

## DESIGN OF THE SECOND TUBE

The cavity used in the first experiment of the second tube was a simple tapered cavity. The cavity has a theoretical diffractive  $Q$  of 579. The electron beam interacts with the second radial maximum of the electric field of the  $TE_{03}$  cavity mode. The cathode has half-angle of  $15^\circ$  and the emitted hollow electron beam forms a non-laminor flow. The emission belt which has an area of  $2.5 \text{ cm}^2$  is able to emit a beam current of 10 A. The output taper from one end of the cavity to the beam collector of 28 mm in diameter is a  $2^\circ$  linear taper. The output window consists of a single sapphire disk with edge cooling. Two electrical isolation gaps in the gyrotron enable us to detect each current separately flowing into the main body, the collector and the window.

The main magnetic field is generated by superconducting coils which can produce the maximum magnetic field of 6 T. Two pairs of transverse trim steering coils placed around the main superconducting coils produce the radial magnetic field in the cavity to adjust the electron beam trajectory through the cavity.

A one-hole-coupler for measurement of the oscillation frequency and a water load for output power measurement are set up above the output window.

## EXPERIMENTAL RESULTS

An Oscillation mode map was taken at a beam voltage  $V_b$  of 60 kV and a beam current  $I_b$  of 10 A by changing the gun-anode voltage and the main magnetic field, as shown in Fig.1. The oscillation of 120.18 GHz to 120.19 GHz was identified as the designed  $TE_{03}$  mode. All oscillations of 117.68 GHz to 117.70 GHz, 117.80 GHz and 117.85 GHz are the  $TE_{23}$  mode. The oscillation of 124.2 GHz was observed at the main magnetic field above 4.7 T and

identified as the  $TE_{52}$  mode. The  $TE_{23}$  mode and the  $TE_{52}$  mode are competing modes with the  $TE_{03}$  mode. In this experiment, the  $TE_{03}$  mode competed with the  $TE_{52}$  mode at the high field side in the region of the  $TE_{03}$  mode oscillation, but not with the  $TE_{23}$  mode.

Figure 2 shows a plot of the measured output power as a function of the beam current at a beam voltage  $V_b$  of 63.9 kV and a gun-anode voltage  $V_a$  of 23 kV. The main magnetic field was optimized to obtain the highest output power at each beam current. The maximum output power of 167 kW was achieved at  $I_b=10.2$  A with an efficiency of 25.8%, and the  $TE_{03}$  mode was surely excited from the measured frequency. Longer pulse operation was also tested, and a pulse with of 1.1 ms was achieved at an output power of 80 kW.

### DESIGN OF A COMPLEX CAVITY

Our next program is to develop a 120 GHz, 200 kW, 100 ms gyrotron. On the  $TE_{0n}$  mode gyrotron with a simple cavity, the mode competition will become an important problem. We have started the design studies of a complex cavity. Figure 3 shows an example of a  $TE_{02}/TE_{03}$  complex cavity.

### CONCLUSIONS

The second modular gyrotron tube developed at Mitsubishi Electric Corp. has achieved an output power of 167 kW with an efficiency of 25.8%. The excitation of the  $TE_{03}$  mode was verified from the measured frequency of 120.18 GHz to 120.19 GHz.

On the basis of the experimental results of the second tube, the third gyrotron of the sealed tube was designed and constructed. The magnetron injection gun and the cavity of the third gyrotron had the same profiles as those of the second tube except the down taper angle of the cavity. The third tube has generated the maximum output power of 152 kW with the frequency of 120.1 GHz,  $TE_{03}$  mode and a pulse width of 10.2 ms<sup>(2)</sup>.

The complex cavity with a diffractive Q value of 534 is being constructed now, and its experimental test will be carried out soon, using the second tube.

### ACKNOWLEDGEMENT

The authors wish to acknowledge Prof. S.Tanaka and Associate Prof. Y.Terumichi of Kyoto University for their helpful discussions on this work.

### REFERENCES

- (1) T.Simozuma, T.Kikunaga, Y.Yasojima, Y.Murai, M.Iwamoto and K.Nakashima, Proc. of 6th Int. Conf. High-Power Particle Beams, 1986, pp.527-530.

- (2) T.Kikunaga, T.Shimozuma, H.Asano, Y.Yasojima, Y.Murai, Y.Ieki, T.Tsukamoto, T.Nagashima, K.Sakamoto and M. Shiho, 5th Annual Conf. of the Japan Society of Plasma Science and Nuclear Fusion Research, March 1988, p.213

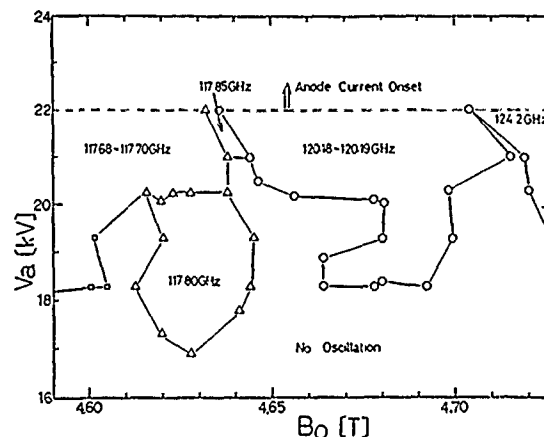


Fig.1 Oscillation mode map at  $V_b=60$  kV and  $I_b=10$  A

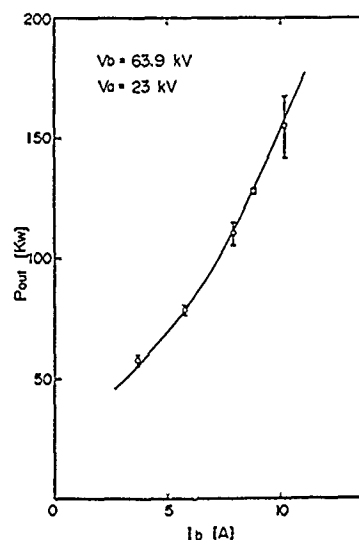


Fig.2 The measured output power as a function of the beam current at  $V_b=63.9$  kV and  $V_a=23$  kV



Fig.3 An example of a  $TE_{02}/TE_{03}$  complex cavity



# THE DESIGN OF MEGAWATT GYROTRONS FOR THE COMPACT IGNITION TOKAMAK

K.E. Kreischer, T.L. Grimm, A.W. Mobius and R.J. Temkin

Plasma Fusion Center  
Massachusetts Institute of Technology  
Cambridge, Ma.

## ABSTRACT

A 1 MW, 280 GHz gyrotron oscillator suitable for ECR heating of the Compact Ignition Tokamak (CIT) is presently being designed. The design is based on successful features of our present experiment, which has generated powers up to 765 kW in the  $TE_{16,2,1}$  mode at 148 GHz. In the 280 GHz gyrotron, an 80 kV, 50 A annular beam will interact with a high order whispering gallery mode. Parametric studies indicate that a cavity with a diameter of at least  $20\lambda$  is required to keep wall losses low. Detailed studies of the electron gun and 12 T magnet indicate both are feasible. Initial experiments are planned for late next year.

## INTRODUCTION

Rapid advances in the development of high power gyrotron oscillators have greatly improved prospects of using such sources for ECR heating of fusion plasmas. Gyrotrons are particularly attractive sources for ECRH because they can operate continuously at low voltages ( $<100$  kV). One major obstacle to generating megawatt powers at frequencies above 100 GHz is the need to operate in large cavities with closely spaced modes. At M.I.T., recent oscillator experiments [1] with a single tapered cavity indicate that mode stability and suppression of nearby competing modes prevail even when operating in very high order modes. We observed single mode emission at 243 GHz with output powers of 470 kW from a cavity with a diameter of  $12\lambda$ .

Gyrotrons are also attractive because of their high efficiency ( $\eta$ ). Nonlinear theory indicates that an  $\eta$  of 50% can be achieved with a single cavity, with the possibility of using depressed collectors to provide further improvements. At MIT, our goal over the past year has been to increase the output power and efficiency of our 140 GHz gyrotron. Initial experiments with a long cavity having a  $6\lambda$  interaction length ( $L$ ) generated 765 kW at 96 kV and 36 A. A peak  $\eta$  of 30% occurred at 20 A, but a drop in  $\eta$  was measured at higher currents (see Figure 1). One possible explanation is a diffractive  $Q$ ,  $Q_D$ , that is higher than expected, which would shift the peak efficiency to lower currents, and cause overbunching at higher currents. The higher  $Q_D$  could be the result of mismatches in the output section of the gyrotron, in particular at the window. A shorter cavity with  $L = 4.2\lambda$  and lower  $Q_D$  of 300 is presently being tested. Self-consistent nonlinear theory indicates that this cavity can achieve peak powers and efficiencies similar to those of the long cavity. This cavity also has a high starting current of 6.4 A, and should therefore experience less mode

competition when operating at 80 kV and 35 A.

## PARAMETRIC ANALYSIS

A parametric analysis of a 280 GHz gyrotron indicates that megawatt powers can be generated efficiently if limitations due to mode competition can be overcome. Because of the high ohmic cavity losses, it is necessary to operate in a very high order mode. The index  $\nu_{mp}$  of the lowest order  $TE_{m,p,1}$  mode that one can utilize can be calculated from the following equation [2]:

$$(\nu_{mp}^2 - m^2) = \frac{2470\mu\beta_{||}P(MW)\nu^{2.5}(GHz)}{\beta_{\perp}^2\rho_{ohm}(W/m^2)}$$

where  $\rho_{ohm}$  is the average cavity wall losses, and a  $\mu$  of about 20 is required for 280 GHz operation. This equation indicates the strong dependence of  $\nu_{mp}$  on frequency. The dependence of the minimum cavity diameter, which occurs for  $TE_{0,p,1}$  modes, on output power and cavity ohmic losses is shown in Fig. 2. For a 1 MW gyrotron with a conservative wall loss of  $2$  kW/cm<sup>2</sup>, a minimum diameter of  $20\lambda$  is required. Operating in  $m \neq 0$  modes requires even larger diameters.

Based on our past experimental results, asymmetric surface modes are the most attractive. Not only do these modes experience less mode competition, but the beam can be placed near the cavity wall to reduce voltage depression. The parameters of a potential 280 GHz design based on the  $TE_{80,4,1}$  are given in Table 1. A modest  $\eta$  of 25% is assumed although higher values are likely. The major difference with the 140 GHz gyrotron is the increase in the radial dimensions of the beam and cavity. The beam will also couple strongly to all nearby  $TE_{m,4,1}$  modes, resulting in step tuning with approximately 3 GHz steps. An internal, quasi-optical converter could be used to transform the output radiation of these modes into a linearly polarized, Gaussian beam, and separate the rf power from the electron beam. This would simplify the design of the collector, and allow the possibility of depressed operation in order to enhance the overall efficiency. Such a design would also simplify the output window, which could be made larger to reduce the power density and positioned at the Brewster angle to minimize reflections back into the cavity.

## GUN DESIGN

An adiabatic model [3] has been used to select the main parameters of an 80 kV, 50 A electron gun. Constraints on the beam radius, thickness and density in the cavity,

as well as the maximum electric field between the cathode and first anode ( $E_c$ ), have been taken into account. Figure 3 shows the effect of varying  $E_c$  on magnetic compression and cathode radius, with the dashed lines indicating our design values. This design has a cathode angle of  $35^\circ$  and an emitter current density of  $5.8 \text{ A/cm}^2$ . The gun operates at 6.5% of the Langmuir current, consistent with present gyrotron guns. The electrode shapes have been optimized using the Herrmannsfeldt code. The design presently produces an annular beam with  $v_\perp/v_\parallel = 2$  and  $\Delta v_\perp/v_\perp = 4.6\%$  in the cavity.

This research is supported by the Department of Energy under Contract DE-AC02-78ET51013.

### REFERENCES

- [1] K.E. Kreischer and R.J. Temkin, Phys. Rev. Lett. **59**, 547 (1987).
- [2] K.E. Kreischer, B.G. Danly, J.B. Schutkeker, and R.J. Temkin, IEEE Trans. Plasma Science **PS-13**, 364 (1985).
- [3] J.M. Baird and W. Lawson, Int. J. Electron. **61**, 953 (1986).

TABLE 1                      140 GHz      280 GHz

Current(A)	35	50
Voltage(kV)	80	80
$\eta_T(\%)$	36	25
Velocity ratio	1.93	2.0
Beam radius(cm)	0.53	1.4
Cavity radius(cm)	0.75	1.7
Cavity length(L/ $\lambda$ )	6.0	7.1
Diffraction Q	450	630
Magnetic compression	30	40
Cavity current density(A/cm <sup>2</sup> )	384	510
Beam thickness( $r_L$ )	3.85	3.2
Voltage depression(%)	4.0	2.6
Emitter radius(cm)	2.89	8.9

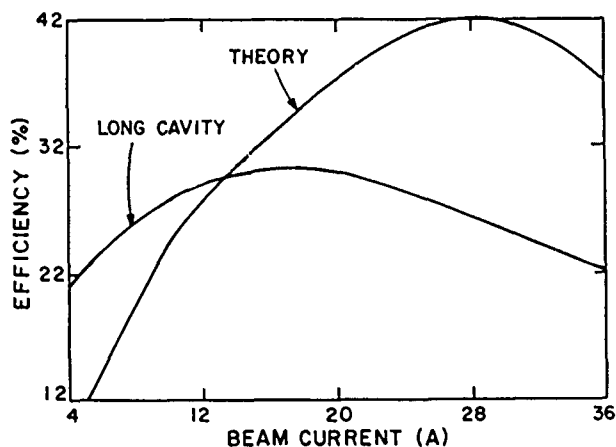


Figure 1  
Optimum theoretical and experimental  
efficiency for the  $TE_{16,2,1}$  mode

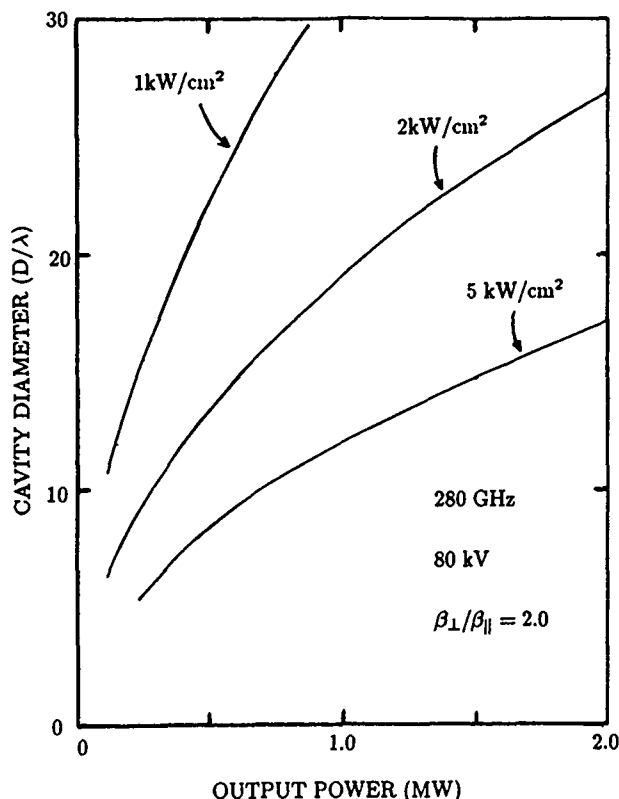


Figure 2  
Minimum cavity diameter as a function  
of average ohmic wall losses.

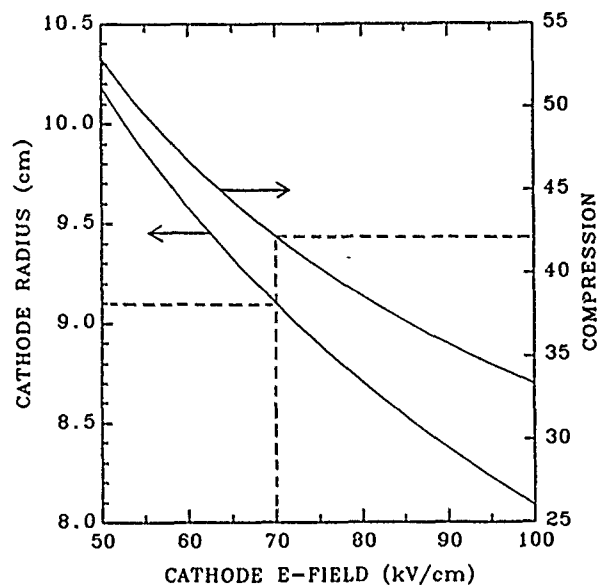


Figure 3  
Cathode radius and magnetic compression  
as a function of the electric field between  
the cathode and first anode.

## DEPRESSED COLLECTORS FOR GYROTRONS

M.E. Read and A.J. Dudas  
Physical Sciences, Inc., Alexandria, VA 22314

W. Lawson and A. Singh  
Laboratory for Plasma Research, University of Maryland  
College Park, MD 20742

### INTRODUCTION

The gyrokylystron is a potential source for driving advanced accelerators, such as the proposed 300-500 GeV electron-positron collider. Sources with frequencies higher than those commonly used in accelerators (e.g. 2.9 GHz) are desired because higher accelerating gradients can be created, thus reducing the length and cost of the device. Because of the inherent advantages of gyrotrons, such a source is expected to be able to produce significantly higher power at high frequencies than that possible with a linear beam tube. A 10 GHz, 30 MW gyrokylystron is being developed at the University of Maryland to demonstrate this potential.[1]

However, it is recognized that the gyrokylystron's efficiency is inferior to its linear beam counterpart because gyrotrons extract energy primarily from only beam rotational motion. Thus, for high average power systems, as a large accelerator clearly is, a method for enhancing the efficiency is important.

For example, a scaling study relevant to the electron-positron collider predicts a required average RF system power of 100-200 MW. If the capital costs of the input power supply and regulator and cooling system are \$0.40 per Watt,[2] then an increase in the efficiency from 30% to 63% would result in a \$140 million saving in a 200 MW system. Coupled with expected savings in operating costs, this clearly points out the importance of efficiency enhancement.

Depressed collectors are commonly used in linear beam tubes. The total efficiency,  $\eta_t$ , of a tube with a depressed collector is given by  $\eta_t = \eta_e / (1 - \eta_r(1 - \eta_e))$ , where  $\eta_e$  and  $\eta_r$  are the electronic and collection efficiencies, respectively. This relationship is plotted in Figure 1, which shows that substantial increases in the total efficiency can be obtained with collection efficiencies over 60%.

### DESIGN ISSUES

#### Conversion of Rotational to Axial Motion

A depressed collector can recover only that energy which is associated with axial motion. The beam in a gyrotron has most of its energy in rotational motion, which then must be converted for efficient collection. Some of the conversion can be accomplished through an adiabatic reduction of the magnetic field. Initial simulations (using EGUN, by W. Herrmannsfeldt) indicate that the velocity ratio,  $a$ , can be reduced from  $\sim 1.5$  to  $\sim 0.2$  in this manner. At this point the scale length of the Larmor orbit in the axial direction becomes very large, and further adiabatic decompression would require a prohibitively long and large diameter system. To further reduce the field in a reasonable length and without too much heating of the beam, a cusp has been found to be effective.

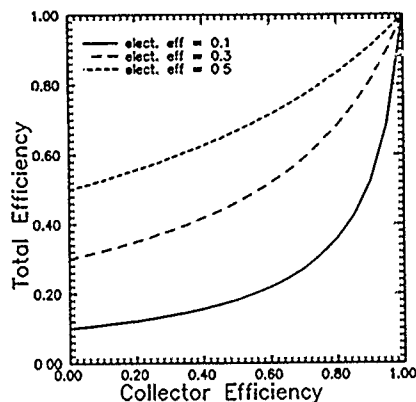


Figure 1. Total Efficiency of a microwave tube with a depressed collector, as a function of the collector and electronic efficiencies.

#### Number of Electrodes

Because the electronic efficiency of the gyrotron is predicted to be moderately high, the beam exiting from the cavity will have a significant energy spread. The electron spectra calculated for the 30 MW gyrokylystron are shown in Figure 2. As can be seen, while there is a peak at roughly half the initial energy of 500 kV, a significant fraction of the beam electrons will have energies elsewhere in the spectrum. To efficiently collect a beam with such a spectrum, multiple collection electrodes are required. The efficiency for 2, 3 and 4 element collectors, assuming roughly optimized electrode voltages and perfect collection on each electrode (no reflections or secondaries), has been calculated as given in Table 1. A 3 element collector appears most reasonable.

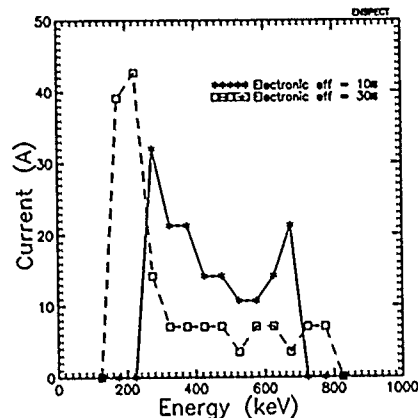


Figure 2. Energy spectrum of spent beam from 30 MW gyrokylystron. The initial energy is 500 keV, the current, 150 A. Spectra for electronic efficiencies of 10% and 30% are given.

**Table 1. Collection and total efficiencies.**

Electronic Efficiency	Number of Electrodes	Collector Efficiency	Total Efficiency
10	2	79	35
10	3	84	41
10	4	86	45
30	2	71	59
30	3	77	65
30	4	80	69

**Backscattered Electrons**

At the voltages of interest, both true secondaries and reflected primaries will be encountered. Data in the literature indicate that the total backscatter coefficient over the range 100 kV - 300 kV is on the order of 0.3 for copper, and approximately 0.05 for graphite. (The graphite can be used as the actual electrode material or deposited on the surface of copper.) Even with this relatively modest coefficient, it will be important to avoid producing or reflecting electrons where they can be accelerated to another electrode or back to the cavity, thereby decreasing efficiency. This requires that the electrons impact on the electrodes on the side away from the cathode, i.e., the axial motion must be reversed.

**INITIAL DESIGN**

An initial design for a depressed collector for the University of Maryland gyrokystron is shown in Figure 3. The trajectories shown are from EGUN, with an initial beam energy spectrum for

a gyrokystron efficiency of 10%. In order to focus, then deflect the high energy portion of the beam, a compound cusp in combination with a magnetic field "bump" was required, as shown. The collection efficiency of this design, ignoring effects of secondaries, etc., is 82%. This is close to the value given in Table 1, which was determined using an idealized collection model. Optimization of the electrode potentials may increase this value. Adjustment of the electrode position and potentials should also improve the locations of the electron impact, and could reduce the necessity for some of the complex shaping required to avoid electrons reaching the insulators.

The effect of backscattered electrons will be studied by forming "secondary" cathodes at the electrode surfaces. This will be done via modifications of EGUN.[2]

**CONCLUSIONS**

Initial calculations indicate that a depressed collector for the U.Md. gyrokystron could have a high (80%) collection efficiency. Total efficiencies exceeding 60% should thus be possible.

Research supported by the Department of Energy, Contract #DE-AC05-88ER80646.

**REFERENCES**

- [1] K.R. Chu, et al., Trans. Plasma Sci. PS13, 444 (1985).
- [2] J. Petillo, Personal Communication

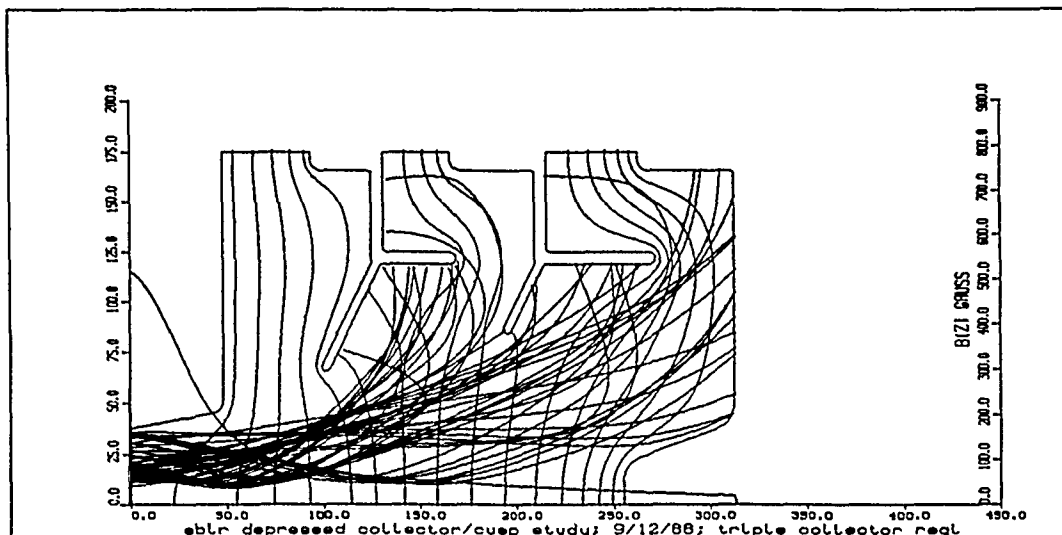


**Figure 3.** Sketch of an initial design for a depressed collector for a 30 MW gyrokystron. Axes scales are in mesh units, with 1 mesh unit = 1.25 mm. The horizontal axis is the z direction, the vertical, r. The largely vertical lines in the plot are equipotential lines, while those starting nearly horizontal on the left are the beam trajectories.

## GYROTRON IV - A NEW TUNABLE GYROTRON

G.F. Brand  
School of Physics, University of Sydney,  
NSW, 2066, AUSTRALIA

## INTRODUCTION

GYROTRON IV is the latest in a series of tunable gyrotrons designed and constructed at the University of Sydney (1). Like GYROTRON III, it is tuned by raising the field of a 12 T superconducting magnet. One cavity resonance after another is excited. It will provide more than 10 W of cw power over the frequency range 75 to 330 GHz. However, a number of design changes have been made to simplify the construction and improve the quality of the output.

## NEW DESIGN

The construction of GYROTRON IV is shown in Fig. 1. The fabrication of most of the components is very straightforward - perhaps this will encourage other groups to construct their own gyrotrons.

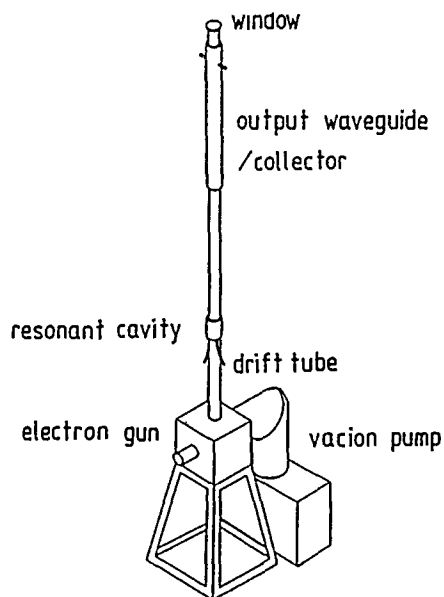


Fig. 1. GYROTRON IV

Its height is 1.87 m. It fits into the 50 mm bore of the superconducting magnet which is lowered onto it from above.

The gyrotron is pumped from the stainless-steel electron gun cube by a 60 l.s<sup>-1</sup> Varian Vacion pump. The entire electron gun structure (Fig. 2) is mounted on a 6-inch conflat blank which is attached to the bottom of the cube. This allows for easier access.

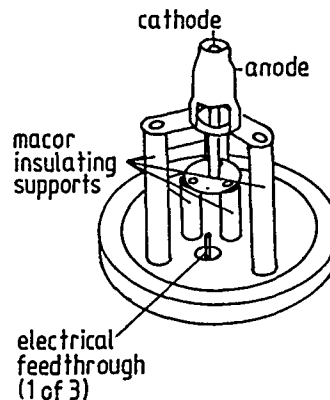


Fig. 2. The electron gun.

The resonant cavity is water-cooled for frequency stability. The stainless steel water jacket provides mechanical support for the profiled copper cavity. The construction of the cavity as a single unit permits easy interchanging so that cavities with other profiles can be tested.

The copper output waveguide which also serves as the collector for the electron beam is water-cooled.

Design changes to improve the quality of the output include:

(1) a step in the cavity profile and sine-squared transitions from the drift tube to the cavity and from the step to the output waveguide (Fig. 3).

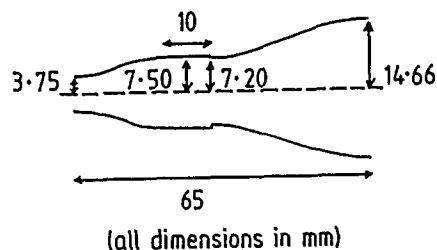


Fig. 3. The profile of the resonant cavity. The electron gun lies to the left.

One important difference between low-power and high-power gyrotrons is the constriction at the output end which prevents the escape of all but a small fraction of the energy in the cavity. This ensures that starting currents are low. Any power that escapes does so by mode conversion from the main cavity mode to an adjacent mode in the vicinity of the constriction.

The step ensures that the location of the mode conversion is precisely known and the sine-squared transitions ensure that mode conversion is minimal elsewhere. Furthermore, calculations of mode conversion for a step are much simpler than those for a waveguide-taper junction.

Calculations of the resonant frequencies of the  $TE_{0m}$  modes are tabulated below.

TABLE 1

Resonant Frequencies and Diffraction Q's  
for  $TE_{0m}$  modes in GYROTRON IV.

TE mode	resonant frequency (GHz)	diffraction Q
0 4	85.32	$8.8 \times 10^3$
0 5	105.27	8.5
0 6	125.24	8.7
0 7	145.20	9.0
0 8	165.17	9.4
0 9	185.14	9.9
0 10	205.11	10.2
0 11	225.08	10.5
0 12	245.06	10.8
0 13	265.04	11.0
0 14	285.01	11.3
0 15	304.99	11.5
0 16	324.97	11.6

These calculations were carried out in the following way. A first estimate of the resonant frequency was obtained by treating the cavity as a cylinder with closed ends. The reflection coefficient for the main cavity mode, taking into account mode conversion to other  $TE_{0m}$  modes at the step, was calculated using this frequency. This reflection coefficient was used as one boundary condition for a new estimate of the resonant frequency which takes into account the slowly-varying profile of the cavity (2) going from the step towards the electron gun. This new frequency is used to obtain a refined estimate of the reflection coefficient, and so on.

There will also be strong  $TE_{1m}$  modes occurring between these  $TE_{0m}$  modes.

(ii) The profiled output window which has been used in our other gyrotrons (3) to provide a non-reflecting transition between the vacuum and the outside will be replaced by a plane window.

While bench tests of the profiled windows with an incident gaussian beam confirm that reflections are indeed small over the frequency range of interest, it does seem likely that the

regular pattern can produce mode conversion to modes of other symmetries. To eliminate this possibility a plane fused silica window will be used.

Calculations for the plane window (diameter 40 mm) show that the reduction in the transmitted power due to reflection back into the waveguide will never be greater than 2.4 dB.

### GYROTRON OPERATION

Like GYROTRON III, the new gyrotron will be operated typically with an accelerating voltage of 10 kV and a beam current of 50 mA. Experience with GYROTRON III has shown that the separate anode-cathode power supply can be replaced by a single 15 M $\Omega$  resistor connected between the anode and the resonator body which is grounded.

The anode finds a suitable potential because some electrons are reflected back to it before reaching the cavity. Negative feedback occurs. If the anode potential is too high, more electrons have a large initial transverse energy and so more electrons are reflected back thereby lowering the anode potential.

A quasi-optical antenna will be mounted at the top of the gyrotron to couple the radiation into a low-order mode in a waveguide. GYROTRON IV will replace GYROTRON III as a source for millimeter-submillimeter wave scattering on the department's TORTUS tokamak plasma (4).

### ACKNOWLEDGEMENTS

This work has been supported by the Australian Research Grants Scheme, the University of Sydney, the Australian Institute of Nuclear Science and Engineering and the Science Foundation for Physics within the University of Sydney.

Special thanks for comments on the design to Dr M. Gross and for technical support to N.A. Lowe, G.T. Marlin and J.R. Piggott.

### REFERENCES

- (1) G.F. Brand 'Tunable Gyrotrons' in INFRARED AND MILLIMETER WAVES (ed. K.J. Button, Academic Press) Vol. 14, pp 371-408 (1985).
- (2) S.N. Vlasov, G.M. Zhislin, I.M. Orlova, M.I. Petelin and G.G. Rogacheva Radiophys. Quantum Electron. 12, 972-978 (1969).
- (3) J.Y.L. Ma and L.C. Robinson Opt. Acta 30, 1685-1696 (1983).
- (4) M.D. Bowden, P.W. Fekete, M.J. Ballico, G.F. Brand, I.S. Falconer, T. Idehara, B.W. James and K.J. Moore. Paper presented at this conference.

# CHARACTERISTICS OF COUPLED PLANAR STRIP-SLOT RESONATORS WITH MULTIPLE-LAYER DIELECTRICS

Aosheng Rong      Sifan Li  
Research Institute of EMF and Microwaves  
Southeast University  
Nanjing, P.R.China

## ABSTRACT

Coupled planar strip-slot resonators with multiple-layer dielectrics are investigated by the reaction theorem in electromagnetic field theory. A variational formula for the resonant frequency is established, which involves only the electric fields on slots and the electric currents on strips. Two coupled suspended rectangular strip-slot resonators are computed. The numerical results agree well with the experimental data.

## INTRODUCTION

Planar resonators are indispensable circuit elements for millimeter wave integrated oscillators, antennas and measurement systems. In the range of millimeter wave frequency, the resonant frequency of these resonators needs accurate calculation based on the rigorous electromagnetic field theory, because of their smaller dimensions compare to the operating wavelength. Some numerical methods such as two-dimensional spectral domain approach have been presented [1,2]. But the characteristic equations involved in these methods usually require high numerical expense. In this paper, the application of the reaction theorem in electromagnetic field theory is presented to coupled planar strip-slot resonators with multiple-layer dielectrics. A recursive relation of electromagnetic fields between adjacent dielectric regions is derived, from which the characteristic equation for the resonant frequency of the resonators is established. This equation is stationary and involves only unknown electric fields on slots and the electric currents on strips. Therefore, it can be calculated with less CPU time.

## PRINCIPLE

Fig.1 shows the coupled planar strip-slot resonator with  $N$ -layer dielectrics. It is assumed that the slots are deposited on the surface between  $k_1$ th and  $k_1+1$ th layer; the metallic strips are between  $k_2$ th and  $k_2+1$ th layer. Because the true field at resonance is a source free field, by the reaction theorem [3,4], the reaction of any field on its own sources is zero, that is,

$$\sum_{k=1}^N \iint_{\tau_k} (\bar{E} \cdot \bar{J} - \bar{H} \cdot \bar{M}) d\tau + \sum_{k=1}^{N-1} \iint_{S_{ik}} (\bar{E} \cdot \bar{J}_{sk} - \bar{H} \cdot \bar{M}_{sk}) ds + \iint_{S_0} (\bar{E} \cdot \bar{J}_s - \bar{H} \cdot \bar{M}_s) ds = 0 \quad (1)$$

Where  $S_0$  refers to outer boundary and  $S_{ik}$  inner sur-  
ner surfaces.  $\bar{J}, \bar{M}; \bar{J}_s, \bar{M}_s$  and  $\bar{J}_{sk}, \bar{M}_{sk}$  are the assumed  
electric and magnetic sources. They are found from

the trial fields according to

$$\begin{aligned} \bar{J} &= -j\omega \epsilon_0 \epsilon_{rk} \bar{E} + \nabla \times \bar{H} \\ \bar{M} &= -j\omega \mu \bar{H} - \nabla \times \bar{E} \\ \bar{J}_s &= \bar{H} \times \bar{n} \\ \bar{M}_s &= \bar{n} \times \bar{E} \\ \bar{J}_{sk} &= (\bar{H}^{(k)} - \bar{H}^{(k+1)}) \times \bar{u}_y \\ \bar{M}_{sk} &= \bar{u}_y \times (\bar{E}^{(k)} - \bar{E}^{(k+1)}) \end{aligned} \quad (2)$$

If the trial fields are so chosen as to satisfy the source free Maxwell's equations in  $\tau_k$  and homogenous conditions on boundary  $S_0$ , then  $\bar{J}, \bar{M}$  and  $\bar{J}_s, \bar{M}_s$  vanish.

Thus, Eq.(1) reduces into

$$\sum_{k=1}^{N-1} \iint_{S_{ik}} (\bar{E} \cdot \bar{J}_{sk} - \bar{H} \cdot \bar{M}_{sk}) ds = 0 \quad (3)$$

The trial fields  $\bar{E}^{(k)}, \bar{H}^{(k)}$  in the region  $\tau_k$  are expanded in terms of TE' and TM modes in the rectangular waveguide with inner dimension  $a \times c$ . Let the trial fields be continuous on the surfaces  $y=y_k$  ( $k=k_1, k_2$ )

$$\begin{aligned} \bar{E}_t^{(k)} &= \bar{E}_t^{(k+1)} \\ \bar{H}_t^{(k)} &= \bar{H}_t^{(k+1)} \end{aligned} \quad (4)$$

A recursive relation of the trial fields between adjacent dielectric regions can be derived. And then, suppose the trial electric fields on the slots to be

$$\bar{E}_t^{(k_1)} = \bar{E}_t^{(k_1+1)} = \bar{E}_{to} \quad (5)$$

Generally,  $\bar{H}_t^{(k_1)}$  does not equal to  $\bar{H}_t^{(k_1+1)}$ , so a surface electric current  $\bar{J}_s$  will exist on the surface  $y=y_{k_1}$

$$\bar{J}_s = \bar{u}_y \times (\bar{H}_t^{(k_1)} - \bar{H}_t^{(k_1+1)}) \quad (6)$$

Impose the trial fields on the surface  $y=y_{k_2}$  to satisfy the condition as follows

$$\begin{aligned} \bar{E}_t^{(k_2)} - \bar{E}_t^{(k_2+1)} &= 0 \\ \bar{u}_y \times (\bar{H}_t^{(k_2)} - \bar{H}_t^{(k_2+1)}) &= \begin{cases} \bar{J}_s, & \text{on strip } S_w \\ 0, & \text{on } S_{ik_2} - S_w \end{cases} \end{aligned} \quad (7)$$

From above recursive relation and Eq.(3)-(7), a

stationary characteristic equation for the resonant frequency can be established.

$$\det \begin{bmatrix} A_{11} & A_{12} \\ A_{21} & A_{22} \end{bmatrix} = 0 \quad (8)$$

Where the submatrices  $A_{pq}$  ( $p, q=1, 2$ ) depend on the shape and the dimensions of the resonator. They imply only the electric fields on the slots and the electric currents on the strips.

#### NUMERICAL EXAMPLES

Coupled suspended rectangular strip-slot resonators shown in Fig.2(a) and (b) are computed. Fig.3(a) and (b) show the resonant frequencies  $f_0$  versus the strip length  $l_s$ . As seen in the figures, the present results agree well with the experimental data [1].

#### REFERENCES

- [1] K.Kawano, IEEE Trans. MIT, 33(1985), 38-43
- [2] R.Kanna et al, Electronic Letter, 22(1986), 376-377
- [3] R.F.Harrington, Time-Harmonic Electromagnetic fields New York; McGraw-Hill, 1961
- [4] V.H.Runsey, Phys.Rev., Ser.2, 94(1954), 1483-1491

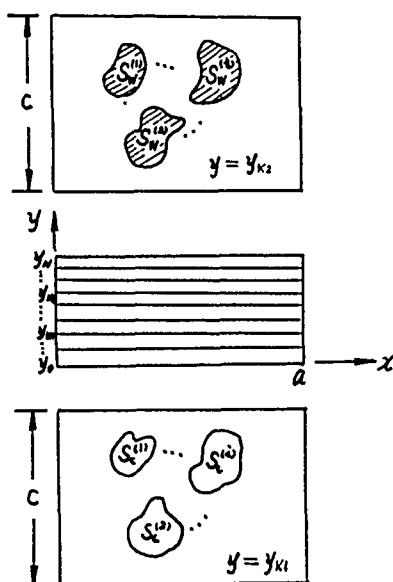


Fig. 1

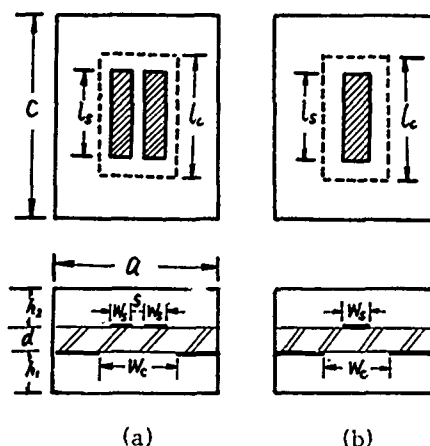


Fig. 2

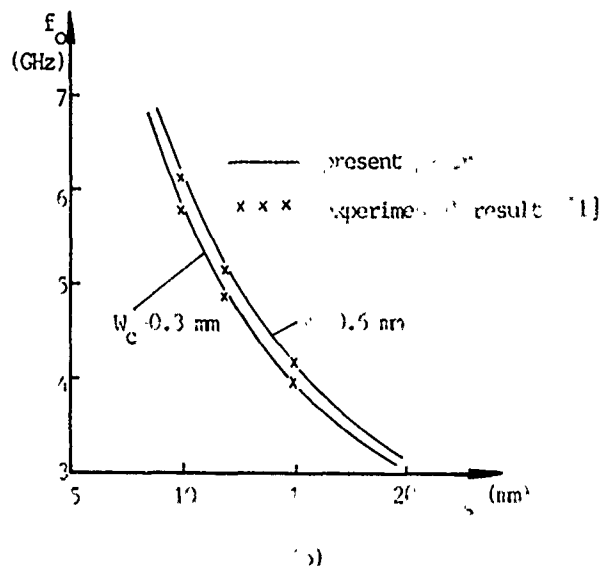
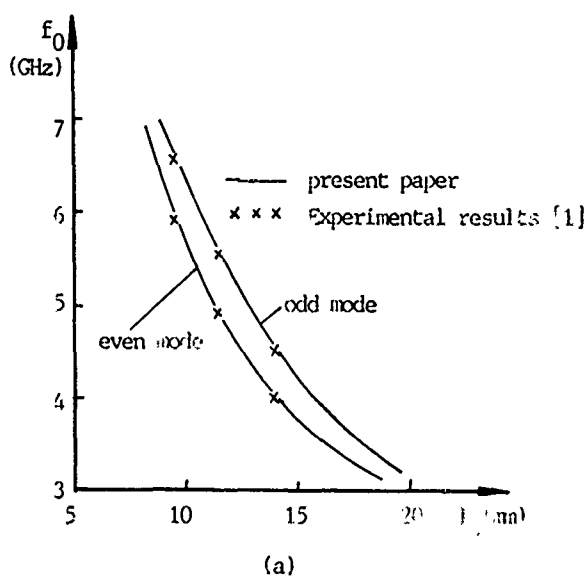


Fig. 3



# EXCITATION AND TRANSMISSION MEASUREMENTS OF DIELECTRIC ROD WAVEGUIDE HE<sub>11</sub> MODE IN THE 50-150 GHz RANGE

Y. Yamamoto and K. Fujisawa

Department of Electrical and Electronic Engineering,  
Faculty of Engineering, Osaka Sangyo University  
Daito, Osaka 574, JAPAN

## ABSTRACT

The sole excitation of the HE<sub>11</sub> mode along the dielectric rod waveguide up to the 150 GHz band has been studied. Measurements have been done on the guide-wavelengths along the TPX rod waveguide with diameters 3.1, 2.0, 1.5 and 1.0 mm in the 150 GHz band. It has been shown that the TPX rod waveguide with a diameter less than or equal to 1.5 mm can transmit only the HE<sub>11</sub> mode in the 150 GHz band.

## INTRODUCTION

The HE<sub>11</sub> mode of a dielectric rod waveguide is very suited to transmit both the signal and LO waves in a Josephson harmonic mixer, because it has no cutoff frequency and has very low loss. In the previous paper[1], we proposed a composite waveguide which consisted of a TPX (polymethylpentene) rod waveguide with a diameter 3.1 mm coupled to metal rectangular waveguides WRJ740 at both ends. The sole excitation of the HE<sub>11</sub> mode was confirmed in the frequency range of 52-104 GHz. It was concluded that to secure the sole excitation of the HE<sub>11</sub> mode up to 150 GHz, the diameter of the rod waveguide must be reduced smaller than 3.1 mm.

In this report, measurements have been done in the 150 GHz band on the guide-wavelengths along the TPX rod waveguides with various diameter smaller than 3.1 mm.

## EXPERIMENTAL RESULTS

The guide-wavelength along the dielectric rod waveguide with diameters 3.1, 2.0, 1.5, 1.0 mm have been measured. The dielectric material is TPX ( $\epsilon_r=2.12$ ) and the methods of excitation and measurement are the same as the previous one[1]. The phase constants  $\beta$ 's obtained from the measurements have been compared to the well-known dispersion equation[2];

$$\left\{ \frac{1}{p} \frac{J_m'(p)}{J_m(p)} + \frac{1}{q} \frac{K_m'(q)}{K_m(q)} \right\} \left\{ \frac{\epsilon_r J_m'(p)}{p J_m(p)} + \frac{1}{q} \frac{K_m'(q)}{K_m(q)} \right\} = m^2 \left( \frac{1}{p^2} + \frac{1}{q^2} \right) \left( \frac{\epsilon_r}{p^2} + \frac{1}{q^2} \right), \quad (1)$$

$$\left( \frac{p}{a} \right)^2 = \omega^2 \epsilon_r \epsilon_0 \mu_0 - \gamma^2,$$

$$\left( \frac{q}{a} \right)^2 = -\omega^2 \epsilon_0 \mu_0 - \gamma^2,$$

$$\gamma = \alpha + j\beta,$$

where  $a$  is the radius of the rod.

In Fig. 1, measured phase constants  $\beta$ 's on the dielectric rod waveguide with a diameter 3.1 mm are plotted versus the frequency  $f$ , together with the theoretical curves from Eq.1. The experimental data lie very close to the theoretical dispersion curve of the HE<sub>11</sub> mode except in the 150 GHz band. In the 150 GHz band, it seems that other higher modes are excited.

To suppress the excitation of higher modes and to secure the sole excitation of the HE<sub>11</sub> mode up to the 150 GHz band, we made various TPX rod waveguides with diameters smaller than 3.1 mm, and measured the dispersion relations. The experimental dispersion data in the 150 GHz band and the theoretical curves are

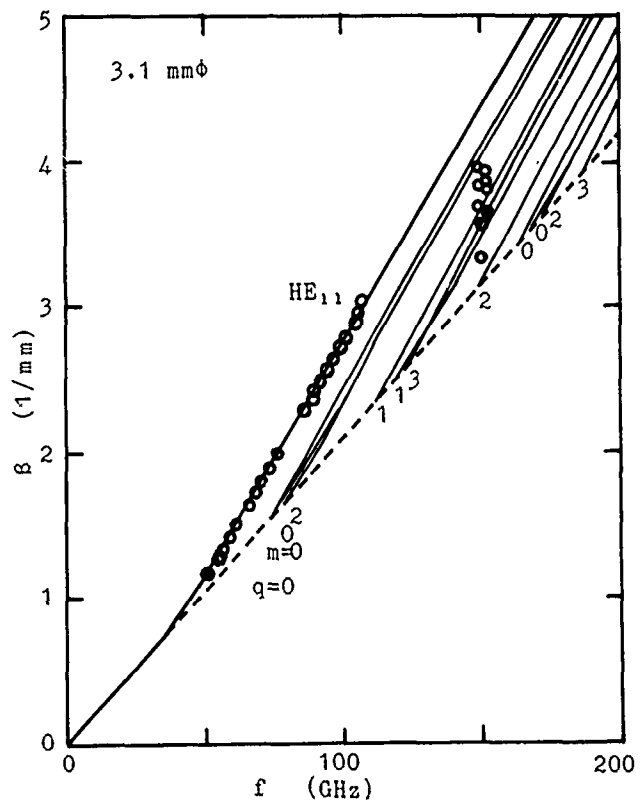


Figure 1  
Measured and theoretical dispersion relations on the TPX rod waveguide with a diameter 3.1 mm.

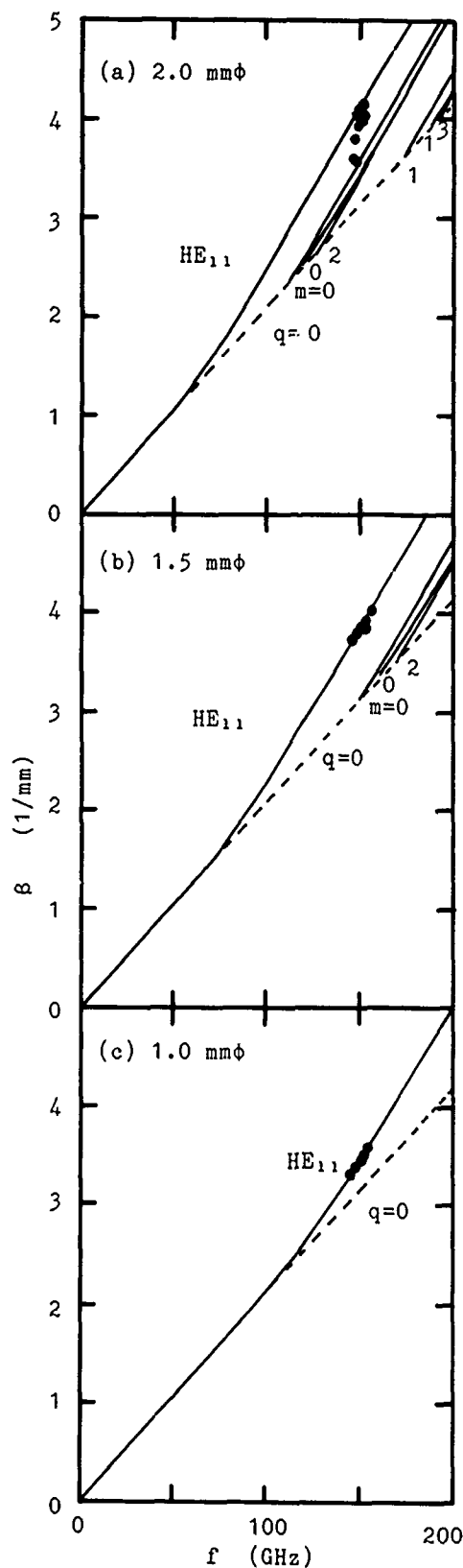


Figure 2  
Measured and theoretical dispersion relations on the TPX rod waveguide with diameters (a) 2.0mm, (b) 1.5mm and (c) 1.0mm.

shown in Fig. 2 (a), (b) and (c), for rod diameters 2.0 mm, 1.5 mm and 1.0 mm, respectively. For a rod diameter 2.0 mm, the plots of the data distribute both on the  $HE_{11}$  mode curve and on the higher mode curves. This suggests the excitation of spurious modes besides the  $HE_{11}$  mode, but the  $HE_{11}$  mode is dominantly excited for a rod diameter 2.0 mm. This is different from the case of a diameter 3.1 mm. In Fig. 2(b), it is shown that the sole excitation of the  $HE_{11}$  mode has been observed on the rod with a diameter 1.5 mm in the 150 GHz band. In Fig. 2(c), we observe the sole excitation of the  $HE_{11}$  mode on the TPX rod waveguide with a diameter 1.0 mm in the 150 GHz band. Theoretically also, no other higher modes exist.

#### DISCUSSIONS AND CONCLUSIONS

As state above, it is observed that the TPX rod waveguide with a diameter smaller than 1.5 mm transmit the  $HE_{11}$  mode solely in the 150 GHz band.

Theoretically, the  $TE_{01}$  and  $TM_{01}$  modes can be excited on the TPX rod waveguide with a diameter 1.5 mm, but they have not been observed experimentally. The suppression of these modes is supposed to be due to the exciting method[1] which uses the coupling between the rectangular waveguide  $TE_{10}$  mode and the dielectric rod waveguide mode.

#### REFERENCES

- (1) Y.Yamamoto, K.Fujisawa, T.Takemura and S.Kita, Int. J. Infrared Millimeter Waves, 1988, vol.9, pp.29-40.
- (2) E.Snitzer, J. Opt. Soc. America, 1961, vol.51, pp.491-498.

# A NEW APPROACH FOR THE ANALYSIS OF WAVEGUIDES WITH MULTIPLY CONNECTED CROSS SECTION

A.S. Omar and K. Schünemann

Technische Universität Hamburg-Harburg  
Arbeitsbereich Hochfrequenztechnik  
Postfach 90 14 03, D-2100 Hamburg 90  
West-Germany

## ABSTRACT

An approach for the analysis of waveguides with multiply connected cross section is presented. It is based on a field expansion with respect to the normal modes of the corresponding hollow waveguide with the same outer conductor. This is in particular useful if the outer conductor has a rectangular or circular cross section. The method can be applied to a large number of guiding structures with both touching and non touching inner conductors. This includes e.g. ridged waveguides, finned waveguides, strip lines, and two wire transmission lines. Here the validity of the method is checked by analyzing a coaxial line.

## INTRODUCTION

Except for waveguides whose cross sections coincide with the surfaces of one of the orthogonal coordinate systems, a systematic analysis of the eigenmodes is not available. Many guiding structures have a rectangular or circular outer boundary and touching or non touching metal inserts. Examples are strip lines, finned waveguides, ridged waveguides, and two wire transmission lines. These structures can systematically be analyzed by expanding their electromagnetic field with respect to the eigenmodes of the corresponding hollow rectangular or circular waveguide. This method principally is a continuation of that presented in [1] for the analysis of inhomogeneously and anisotropically filled waveguides. If both methods are combined, structures with inhomogeneous or anisotropic filling can equally be analyzed.

In this paper, only waveguides with doubly connected cross section are analyzed. The extension to the multiply connected case is straightforward. Although the waveguide with a touching inner conductor has a simply connected cross section, it will be analyzed here as a special case of a doubly connected one.

## MATHEMATICAL FORMULATION

Consider a waveguide with a cross section as shown in Fig. 1. The direction of propagation, in which the structure is uniform, is taken along the z-axis. The corresponding propagation constant is  $\beta$ .

### 1) TE Modes

Let  $\{h_{zn}\}$  be the complete set of axial magnetic fields which characterizes the TE modes in the hollow waveguide with cross section S (i.e. with the metal insert  $S_0$  removed). The different modes are orthogonal according to [2]

$$\int_S h_{zn} h_{zm} dS = P_{nh} \delta_{nm}, \quad (1-a)$$

$$\int_S (\nabla_t h_{zn} \cdot \nabla_t h_{zm}) dS = k_{nh}^2 P_{nh} \delta_{nm}, \quad (1-b)$$

where  $k_{nh}$  is the cutoff wavenumber of the TE mode characterized by  $h_{zn}$ . The field components of a TE mode in the original structure (i.e. with the metal insert  $S_0$  present) fulfill the following equations [3]:

$$\nabla_t \times \underline{e} = -j\omega\mu_0 h_z \hat{k}, \quad (2-a)$$

$$j\beta \underline{e} = j\omega\mu_0 (\underline{h} \times \hat{k}), \quad (2-b)$$

$$\nabla_t \times \underline{h} = 0, \quad (2-c)$$

$$k_c^2 \underline{h} = -j\beta \nabla_t h_z, \quad (2-d)$$

where  $\nabla_t$  is the transverse del operator,  $\underline{e}$  and  $\underline{h}$  are the transverse electric and magnetic fields, respectively, and  $k_c$  is the cutoff wavenumber ( $k_c^2 = k_0^2 - \beta^2$ ).

Our aim now is to find series expansions with respect to  $\{h_{zn}\}$  and  $\{\nabla_t h_{zn}\}$  which identically vanish on  $S_0$  and converge to  $h_z$  and  $\underline{h}$ , respectively, on  $(S-S_0)$ . Because  $h_z$  does not vanish on  $C_0$ , its series expansion has a step discontinuity at  $C_0$ , and hence the series expansion of  $\underline{h}$  cannot be obtained by a term by term differentiation of (2-d). The two series can, however, be written as

$$\sum_n \frac{a_n}{\sqrt{P_{nh}}} h_{zn} = \begin{cases} h_z & \text{on } (S-S_0) \\ 0 & \text{on } S_0 \end{cases}, \quad (3-a)$$

$$\sum_n \frac{b_n}{\sqrt{P_{nh}}} \nabla_t h_{zn} = \begin{cases} \underline{h} & \text{on } (S-S_0) \\ 0 & \text{on } S_0 \end{cases}. \quad (3-b)$$

Substituting (3) into (2) and making use of the orthogonality relation (1), one obtains

$$b_n = \frac{-j\beta}{k_{nh}^2} a_n, \quad (4-a)$$

$$k_{nh}^2 \left( \frac{k_c^2}{j\beta} b_n + a_n \right) = \sum_m C_{nm}^h a_m, \quad (4-b)$$

where

$$C_{nm}^h = \frac{2}{\sqrt{P_{nh} P_{mh}}} \oint_{C_0} h_{zm} (\nabla_t h_{zn} \cdot \hat{n}_0) dt. \quad (4-c)$$

Equation (4) can be written in matrix form

$$([\Lambda^h] - [C^h]) \underline{a} = k_c^2 \underline{a}, \quad (5)$$

where  $[\Lambda^h]$  is a diagonal matrix with elements  $k_{nh}^2$ ,  $[C^h]$  is a square matrix with elements  $C_{nm}^h$ , and  $\underline{a}$  is a column vector with elements  $a_n$ .

## 2) TM Modes

In a similar way, the axial electric field of a TM mode can be expanded as

$$\sum_n \frac{a_n}{\sqrt{P_{nh}}} e_{zn} = \begin{cases} e_z & \text{on } (S-S_0) \\ 0 & \text{on } S_0 \end{cases} \quad (6)$$

The corresponding eigenvalue equation is then given by

$$([\Lambda^e] + [C^e]) \underline{a} = k_c^2 \underline{a}, \quad (7)$$

where all quantities with sub- or superscript "e" have the same meaning with respect to the TM case as the corresponding quantities with sub- or superscript "h" with respect to the TE case.

## NUMERICAL RESULTS

To demonstrate the validity of the method, a coaxial transmission line, for which the eigenmodes are analytically known, has been analyzed. The outer and inner conductors have radii  $a$  and  $b$ , respectively. For rotational symmetric TM modes we can write

$$e_{zn} = J_0(k_{ne} r), \quad (8-a)$$

$$k_{ne} = \frac{p_n}{a}, \quad (8-b)$$

$$P_{ne} = \pi a^2 J_1^2(p_n), \quad (8-c)$$

where  $p_n$  is the  $n$ 'th zero of  $J_0(x)$ .

Fig. 2 shows the electrostatic potential  $\psi$  and the radial electric field  $e_r$  corresponding to the dominant TEM mode of the coaxial line. The TEM mode is, in fact, a TM mode with zero cutoff wavenumber. The vanishing of  $k_c$  leads to a vanishing of  $e_z$ . On the other hand, the quantity  $(-jk_0 e_z / k_c^2)$  is not vanishing and plays the same role as an electrostatic potential  $\psi$ .

## REFERENCES

- [1] A.S. Omar and K. Schünemann, "Complex and backward-wave modes in inhomogeneously- and anisotropically-filled waveguides," IEEE Trans. Microwave Theory Tech., vol. MTT-35, pp. 268-275, 1987.
- [2] R.E. Collin, Field Theory of Guided Waves. New York: Mc Graw-Hill, 1960.
- [3] R.E. Collin, Foundations for Microwave Engineering. New York: Mc Graw-Hill, 1966.

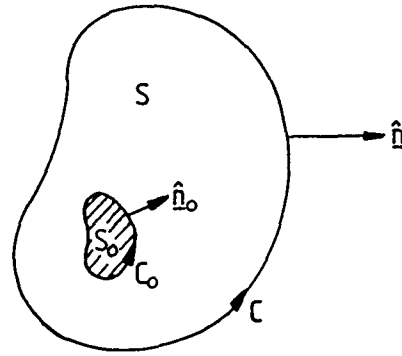


Fig. 1: A doubly connected cross section.

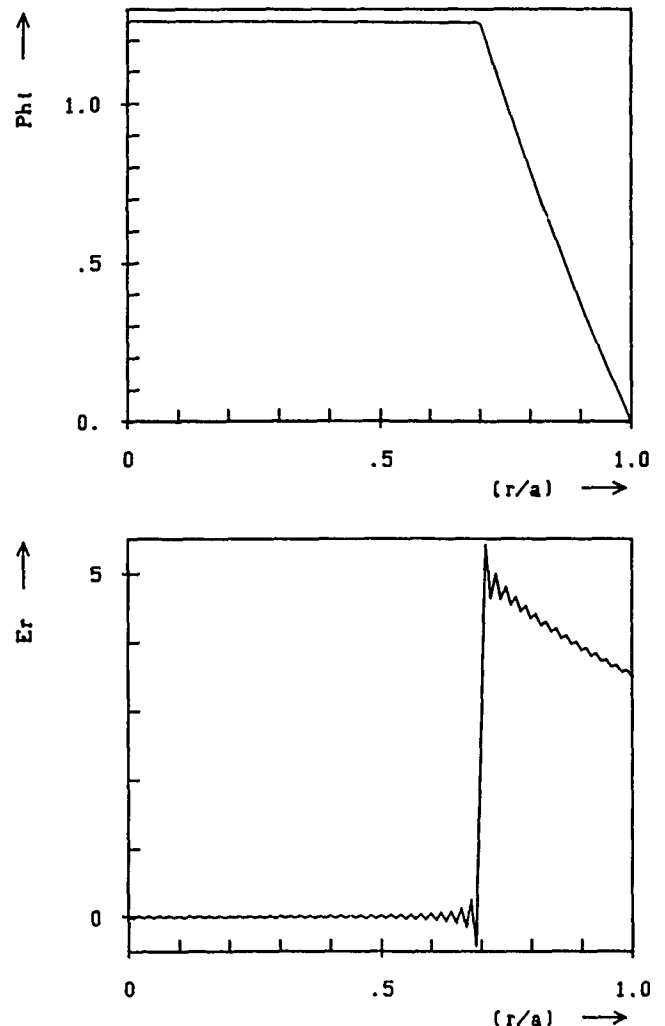


Fig. 2: The electrostatic potential and the radial electric field of the TEM mode on a coaxial transmission line with  $b/a = 0.7$ .

# MODAL ANALYSIS OF A CIRCULAR WAVEGUIDE BIFURCATION FOR CCTWTS

Fujiang Lin and A.S. Omar

Technische Universität Hamburg-Harburg  
Arbeitsbereich Hochfrequenztechnik  
Postfach 90 14 03, D-2100 Hamburg 90  
West Germany

## ABSTRACT

Using modal analysis, an analytical solution to a circular waveguide discontinuity is obtained which is found in a wide class of coupled cavity travelling wave tubes (CCTWTs). The generalized scattering matrix (GSM) of the junction is obtained for both azimuthally dependent and independent excitations. The convergence of the numerical results is investigated by comparing the field distributions at both sides of the junction. The (GSM) of the different junctions can be cascaded in order to characterize a single cavity of the TWT structure.

## INTRODUCTION

Recent interest in computer aided analysis and design of CCTWTs necessitates an exact analysis of both junction and cavity. The waveguide discontinuity under consideration is a junction between a circular waveguide and a composite region comprising a coaxial waveguide with hollow inner conductor (Fig. 1b). A junction of this type is part of a device called the "Marcatili Coupler", which represents the main building block in a wide class of CCTWTs (Fig. 1a).

The abrupt junction described above has been analyzed by using a moment method for an infinitesimally thin inner conductor [1]. The method has been modified in [2] for finite thickness and generalized in [3] by applying the conservation of complex power technique (CCPT). These analyses were only carried out for azimuthally independent  $TE_{0n}$  modes. In conjunction with CCTWT application, the important operation is, however, characterized by a mixed TE-TM excitation. This case is treated here in a similar way as for azimuthally independent excitations by applying the modal analysis method [4].

## THEORY

The structure under consideration is shown in Fig. 1b. It is modelled by a 2-port junction between a large circular waveguide ( $z < 0$ ) and a bifurcation of a coaxial line and a small circular waveguide ( $z > 0$ ). To obtain the GSM, the electromagnetic fields in each waveguide are expanded in terms of the corresponding complete sets of their orthogonal TE and TM modes (the TEM mode of the coaxial line is included in the azimuthally independent TM modes). Using the orthogonality of the eigenmodes and the continuity equations of the transverse electric and magnetic fields at the junction, one obtains a solution for the modal coefficients [4].

Let the  $N_i$ -dimensional column vectors  $\underline{a}^{(i)}$  and  $\underline{b}^{(i)}$  ( $i = 1, 2, 3$ ) be the complex amplitudes of the incident and scattered modes, respectively. The transverse electromagnetic fields at both sides of the junction are then expressed as

$$\begin{bmatrix} \underline{E}_t^{(1)} \\ \underline{H}_t^{(1)} \end{bmatrix} = \sum_{n=1}^{N_1} \begin{bmatrix} a_n^{(1)} e^{-j\beta_n^{(1)} z} & b_n^{(1)} e^{j\beta_n^{(1)} z} \end{bmatrix} \begin{bmatrix} \underline{e}_n^{(1)}(r) \\ \underline{h}_n^{(1)}(r) \end{bmatrix}$$

$$r \leq s_1, z \leq 0,$$

$$\begin{bmatrix} \underline{E}_t^{(2)} \\ \underline{H}_t^{(2)} \end{bmatrix} = \sum_{n=1}^{N_2} \begin{bmatrix} b_n^{(2)} e^{-j\beta_n^{(2)} z} & a_n^{(2)} e^{j\beta_n^{(2)} z} \end{bmatrix} \begin{bmatrix} \underline{e}_n^{(2)}(r) \\ \underline{h}_n^{(2)}(r) \end{bmatrix}$$

$$r \leq s_2, z > 0,$$

$$\begin{bmatrix} \underline{E}_t^{(3)} \\ \underline{H}_t^{(3)} \end{bmatrix} = \sum_{n=1}^{N_3} \begin{bmatrix} b_n^{(3)} e^{-j\beta_n^{(3)} z} & a_n^{(3)} e^{j\beta_n^{(3)} z} \end{bmatrix} \begin{bmatrix} \underline{e}_n^{(3)}(r) \\ \underline{h}_n^{(3)}(r) \end{bmatrix}$$

$$r \leq s_3, z > 0,$$

(1)

where  $\underline{e}_n^{(i)}$  and  $\underline{h}_n^{(i)}$  are the transverse electric and magnetic field vectors of the  $n$ -th modes in waveguide  $i$ . In a similar way as proposed in [4] and [5], the GSM of the junction is obtained:

$$\begin{bmatrix} \underline{b}^{(1)} \\ \underline{b}^{(2)} \\ \underline{b}^{(3)} \end{bmatrix} = \begin{bmatrix} \begin{bmatrix} S_{LL} & S_{LR} \end{bmatrix} \\ \begin{bmatrix} S_{RL} & S_{RR} \end{bmatrix} \end{bmatrix} \begin{bmatrix} \underline{a}^{(1)} \\ \underline{a}^{(2)} \\ \underline{a}^{(3)} \end{bmatrix} \quad (2)$$

The  $(n, m)$  element of  $S_{ij}$  ( $i, j = L, R$ ) is the amplitude of the scattered  $n$ -th mode at port  $i$  which is due to an incident  $m$ -th mode with unit amplitude at port  $j$ . These elements are calculated in a similar way as in [5]. Once the GSM of the bifurcation is obtained, they can be used directly in the ongoing analysis of the element calculation of a CCTWT by cascading the different discontinuities [5].

To examine the convergence of the numerical results, the field distributions at both sides of the discontinuity as given by (1) are calculated and compared. Assuming the incident mode distribution, the scattered modes are obtained from (2).

## RESULTS

- 1.) Azimuthally independent TE mode excitation: In this case only  $TE_{0n}$  modes are taken into account. Only 10 modes in the large circular waveguide were needed in order to obtain convergent results. The agreement with experimental and other published results is excellent. Fig. 2 presents magnitude and phase of the reflection coefficient for  $TE_{01}$  mode excitation. Fig. 3 presents the corresponding field distribution.
- 2.) Azimuthally independent TM mode excitation: In this case only  $TM_{0n}$  and TEM modes are considered. 20 modes in the large waveguide are needed for convergent results. Fig. 4 presents the field distribution for  $TM_{01}$  mode excitation.
- 3.) Mixed TE and TM mode excitations: Now the exciting field is azimuthally dependent and the TM modes of the large circular waveguide are coupled to the TE modes of the composite waveguide and vice versa. The number of modes to be used in the large waveguide is about twice as large as for the azimuthally independent excitation case in order to achieve the same quality of convergence. Fig. 5 presents the field distribution for  $TE_{21}$  mode excitation. As much as 40 modes had to be used.

## REFERENCES

- [1] A.J. Sangster and D.J. McIntosh, "Analysis of an end junction between a coaxial waveguide, with a hollow inner, and a circular cylindrical waveguide," Proc. IEE, vol. 130, Pt. H, pp. 297-303, 1983.
- [2] A.J. Sangster and D.J. McIntosh, "Coaxial waveguide to circular cylindrical waveguide junction," Proc. IEE, vol. 132, Pt. H, pp. 203-205, 1985.
- [3] J.M. Rebollar and J. Esteban, "Application of field theory analysis of multiport-multi-discontinuity structures to circular-electric mode waveguide junction and couplers," Proc. IEEE, AP-S (Syracuse), pp. 564-567, 1988.
- [4] A. Wexler, "Solution of waveguide discontinuities by modal analysis," IEEE Trans. Microwave Theory Tech., vol. MTT-15, pp. 508-517, 1967.
- [5] A.S. Omar and K. Schünemann, "Transmission matrix representation of finline discontinuities," IEEE Trans. Microwave Theory Tech., vol. MTT-33, pp. 765-770, 1985.
- [6] B. Oguchi, "Circular electric mode directional coupler," IRE Trans. Microwave Theory Tech., vol. MTT-8, pp. 660-666, 1960.

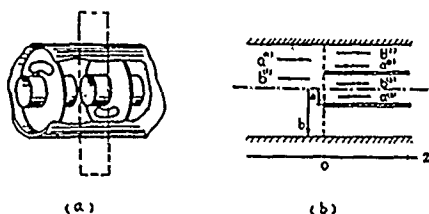


Fig. 1: a) Schematic diagram of a CCTWT, b) A circular waveguide bifurcation.

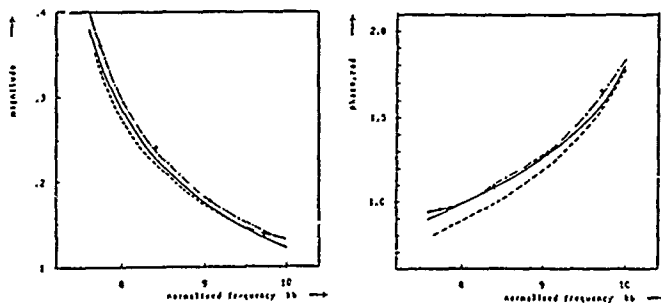


Fig. 2: Reflection coefficient of the  $TE_{01}$  mode, +++ [6], ---- [1], - - - - [3].

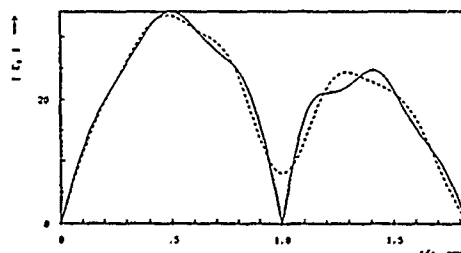


Fig. 3: The aperture electric field for  $TE_{01}$  excitation.

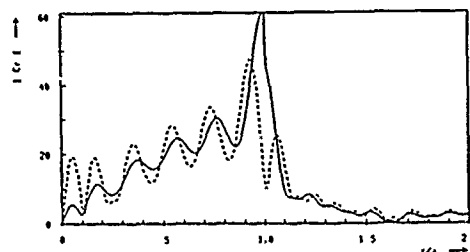


Fig. 4: The aperture electric field for  $TM_{01}$  excitation.

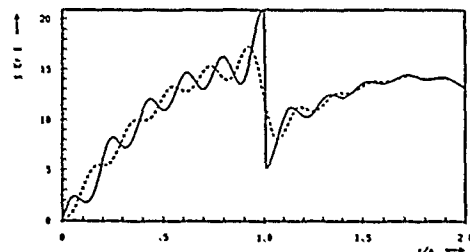
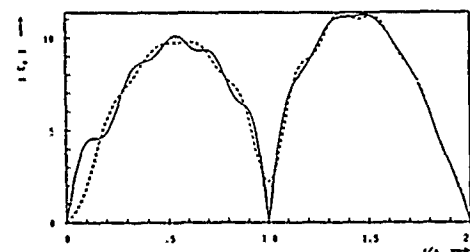


Fig. 5: The aperture electric field for  $TE_{21}$  excitation.

# ANALYSIS OF ECCENTRIC ANNULAR WAVEGUIDES

Yunsheng Xu and A.S. Omar

Technische Universität Hamburg-Harburg  
Arbeitsbereich Hochfrequenztechnik  
Postfach 90 14 03, D-2100 Hamburg 90  
West Germany

## ABSTRACT

Cutoff frequencies and field configurations are calculated for both TE and TM modes of the eccentric annular waveguide. In the analysis the cross section of the waveguide is transformed into a coaxial line by conformal mapping. Then TE and TM modes are expanded in terms of the corresponding coaxial modes. Excellent agreement with results obtained by other published methods is achieved. The advantage of the proposed method is its fast convergence.

## INTRODUCTION

The properties of eccentric annular waveguides have been a subject of certain interest. Some methods have been developed to analyze this structure (e.g. [1] - [3]). It has been proved that orthogonal expansion and conformal mapping are powerful methods for the solution of various waveguide transmission problems. In this paper a combination of both methods is used to solve the problem. By linear conformal mapping, the cross section of the waveguide is transformed into a geometrically simpler region, namely into a coaxial line. The TE and TM modes of the eccentric guide are then expanded in terms of the corresponding coaxial modes.

## THEORETICAL FORMULATION

Consider a waveguide with an eccentric annular cross section as shown in Fig. 1a. A conformal mapping which transforms this eccentric annulus into a concentric one, can be written as follows:

$$w = f(z) = u + iv = (x_1 - x_2) \frac{z - x_1}{z - x_2} \quad (1)$$

where

$$\begin{pmatrix} x_1 \\ x_2 \end{pmatrix} = \frac{1}{2d} \left[ - \left( r_2^2 - r_1^2 - d^2 \right) \pm \sqrt{\left( r_2^2 - r_1^2 - d^2 \right)^2 - 4d^2 r_1^2} \right] \quad (2)$$

Although  $x_2$  becomes infinite if  $d$  tends to zero,  $w$  converges to  $z$ , so that the concentric waveguide can be taken as a special case in our treatment.

In the following analysis TM modes are considered. TE modes can be analyzed similarly. The longitudinal electric field  $E_z$  of TM modes satisfies the following equation in the  $w$ -plane:

$$\nabla_t^2 E_z + k_c^2 \left[ f'(z) \right]^{-2} E_z = 0 \quad (3)$$

where  $k_c$  is the cutoff wave number.

Let  $\{e_{zi}\}$  be the complete set which characterizes the TM modes of the coaxial waveguide in Fig. 1b. Then the following orthogonality relation is satisfied:

$$\int_S e_{zi} e_{zj} ds = \delta_{ij} \quad (4)$$

$E_z$  can be expanded in terms of  $\{e_{zi}\}$  as

$$E_z = \sum_i a_i e_{zi} \quad (5)$$

Using (3) - (5) one can obtain the following matrix eigenvalue problem:

$$\begin{bmatrix} T \end{bmatrix} \begin{bmatrix} A \end{bmatrix} = k_c^{-2} \begin{bmatrix} A \end{bmatrix} \quad (6)$$

where

$$t_{ij} = \frac{1}{k_c^2} \int_S \frac{e_{zi} e_{zj}}{|f'(z)|^2} ds \quad (7)$$

## RESULTS AND COMPARISON

Some numerical results are presented in Table I and Table II and compared with those from [3]. In [3] the lower and upper bounds are given for the exact cut-off frequencies, using the method of intermediate problems and the Ritz-method, respectively.

It can be seen that the lower order cutoff wavenumbers which are calculated by this method lie between the bounds given by [3]. In this case the method here provides a more accurate approximation than the Ritz-method which gives the upper bounds only. Some of the higher order wavenumbers do go beyond the upper bounds given by [3], as the eccentricity increases. This can be explained as being due to using insufficient number of expansion terms in modelling field patterns.

## REFERENCES

- [1] H.Y. Yee and N.F. Audeh, "Cutoff frequencies of eccentric waveguides," IEEE Trans., vol. MTT-14, pp. 487-493, 1966.
- [2] E. Abaka and W. Baier, "TE and TM modes in transmission lines with circular outer conductor and eccentric circular inner conductor," Electron. Lett., vol. 5, pp. 251-252, 1969.
- [3] J. R. Kuttler, "A new method for calculating TE and TM cutoff frequencies of uniform waveguides with lunar or eccentric annular cross section," IEEE Trans., vol. MTT-32, pp. 348-354, 1984.

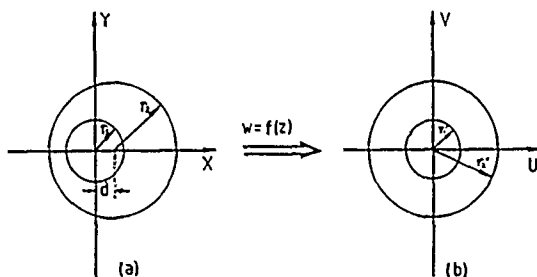


Fig.1: The conformal mapping  $w = f(z)$  transforms the eccentric annulus in the  $z$ -plane into a concentric one in the  $w$ -plane.

D/R1=0.2					D/R1=0.4					D/R1=0.6				
MODE	LOWER	UPPER	SYMM		MODE	LOWER	UPPER	SYMM		MODE	LOWER	UPPER	SYMM	
1	4.4454	5.4411	5.4703	S	1	4.0162	4.8052	4.8111	S	1	4.2012	4.2012	4.2118	S
2	5.4411	5.4411	5.4411	S	2	5.3114	5.3088	5.3122	A	2	5.1225	5.1179	5.1237	A
3	4.4742	4.4742	4.4742	S	3	4.1724	4.1703	4.1725	S	3	5.0907	5.0726	5.0944	S
4	4.2032	4.1932	4.2102	A	4	4.7991	4.7965	4.8002	A	4	4.2718	4.2714	4.2751	A
5	7.20418	7.20327	7.20483	S	5	7.2016	7.2003	7.2027	S	5	7.2322	7.210	7.2525	S
6	7.21233	7.21136	7.21298	A	6	7.2608	7.2559	7.2619	A	6	7.2927	7.276	7.2977	A
7	8.6924	8.6822	8.6962	S	7	8.6977	8.6914	8.6991	S	7	8.201	8.081	8.316	S
8	8.6915	8.6820	8.6932	A	8	9.0094	8.9996	9.0104	A	8	8.650	8.282	8.646	S
9	8.6915	8.6930	8.6972	S	9	9.3419	9.3404	9.3446	S	9	9.208	8.829	9.210	A
10	9.2344	9.2342	9.2372	A	10	9.4744	9.4728	9.4763	S	10	9.204	8.900	9.276	A
11	9.2367	9.2344	9.2372	S	11	9.9545	9.9516	9.9577	A	11	9.92	8.90	9.88	S
12	10.3189	10.3154	10.3199	A	12	10.100	10.000	10.101	A					
13	10.3190	10.3150	10.3199	S	13	10.200	10.200	10.200	S					
14	10.726	10.709	10.744	A	14	10.829	10.648	10.842	S					
15	11.249	11.245	11.254	A	15	10.851	10.775	10.812	S					
16	11.238	11.237	11.240	S	16	10.921	10.821	10.923	S					
17	11.230	11.231	11.240	A	17	11.335	11.220	11.357	A					
18	11.829	11.742	11.845	A	18	11.778	11.524	11.777	S					
19	12.340	12.309	12.345	S	19	11.778	11.548	11.745	A					
20	12.341	12.345	12.345	S	20	12.27	11.78	12.26	S					
21	12.341	12.379	12.399	A	21	12.75	12.00	12.74	S					
22	12.340	12.399	12.345	S	22	12.79	12.27	12.74	A					
23	12.340	12.345	12.345	A	23	12.95	12.34	12.95	A					
24	12.444	12.383	12.448	S										
25	12.444	12.426	12.444	A										
26	12.444	12.426	12.444	S										
27	12.444	12.426	12.444	A										
28	12.444	12.426	12.444	S										

Table I: TM cutoff wavenumbers for eccentric annular waveguides with  $r_2/r_1 = 2.0$ ,  $d/r_1 = 0.2, 0.4$  and  $0.6$ .

Number of expansion terms = 40, lower and upper bounds from [3] correspond to 70 term expansions.

D/R1=0.2					D/R1=0.4					D/R1=0.6				
MODE	LOWER	UPPER	SYMM		MODE	LOWER	UPPER	SYMM		MODE	LOWER	UPPER	SYMM	
1	1.19123	1.19001	1.19175	A	1	1.25218	1.25114	1.25218	A	1	1.40792	1.40694	1.40793	S
2	1.31202	1.31002	1.31202	S	2	1.40792	1.40694	1.40793	S	2	1.40792	1.40694	1.40793	S
3	2.4204	2.4267	2.4203	A	3	2.4829	2.4815	2.4840	A	3	2.4829	2.4815	2.4840	A
4	2.4443	2.4408	2.4444	S	4	2.4841	2.4827	2.4862	S	4	2.4841	2.4827	2.4862	S
5	3.4203	3.4142	3.4203	A	5	3.5276	3.5247	3.5298	A	5	3.5276	3.5247	3.5298	A
6	3.4218	3.4157	3.4218	S	6	3.5276	3.5247	3.5298	A	6	3.5276	3.5247	3.5298	A
7	4.7894	4.7804	4.7899	A	7	4.8174	4.8127	4.8192	S	7	4.8174	4.8127	4.8192	S
8	4.7900	4.7804	4.7901	S	8	5.1132	5.1036	5.1138	A	8	5.1132	5.1036	5.1138	A
9	5.9281	5.9218	5.9285	S	9	5.1134	5.1031	5.1129	S	9	5.1134	5.1031	5.1129	S
10	5.9281	5.9231	5.9285	A	10	5.822	5.792	5.834	A	10	5.822	5.792	5.834	A
11	6.2534	6.2321	6.2499	S	11	6.240	6.226	6.241	A	11	6.240	6.226	6.241	A
12	7.01	7.027	7.048	S	12	6.259	6.240	6.262	S	12	6.259	6.240	6.262	S
13	7.075	7.035	7.067	A	13	6.597	6.542	6.599	S	13	6.597	6.542	6.599	S
14	7.144	7.111	7.129	A	14	7.308	7.236	7.311	A	14	7.308	7.236	7.311	A
15	7.929	7.867	7.911	S	15	7.381	7.302	7.385	S	15	7.381	7.302	7.385	S
16	8.075	8.075	8.084	S	16	7.389	7.324	7.392	A	16	7.389	7.324	7.392	A
17	8.243	8.093	8.182	A	17	7.970	7.881	7.944	S	17	7.970	7.881	7.944	S
18	8.243	8.093	8.182	S	18	8.487	8.304	8.500	S	18	8.487	8.304	8.500	S
19	8.486	8.089	8.232	A	19	8.485	8.323	8.492	A	19	8.485	8.323	8.492	A
20	8.486	8.251	8.412	S	20	8.621	8.463	8.426	A	20	8.621	8.463	8.426	A

Table II: TE cutoff wavenumbers for eccentric annular waveguides with  $r_2/r_1 = 1.5$ ,  $d/r_1 = 0.3$  and  $r_2/r_1 = 2.0$ ,  $d/r_1 = 0.4$ .

Number of expansion terms = 40, lower and upper bounds from [3] correspond to 60 term expansions.



## CHARACTERISTICS OF DOUBLE-GROOVE GUIDE FOR 100 GHz OPERATION

Dr. Yat Man CHOI

Department of Electronic Engineering  
 Hong Kong Polytechnic  
 Hung Hom, Kowloon, Hong Kong.

## ABSTRACT

There are two types of possible transmission modes in double-groove guides:

1. modes with a concentration of energy in the groove regions, and
2. modes with a concentration of energy in the region between the two grooves.

Attention had been concentrated on the first type of modes [1]. This paper gives the theoretical and experimental work on the second type of modes.

## INTRODUCTION

Double-groove guide, as shown in figure 1, could have characteristics of interest. There are two types of possible transmission modes which have been given in the abstract.

During some experimentation of double-groove guide with excitation midway between the grooves, some additional modes were identified. This is the second type of modes, which is the main subject of this paper.

## THEORETICAL AND EXPERIMENTAL CHARACTERISTICS

Both types of modes have power flow in the z-direction only. The first type is characterized by an imaginary wavenumber in the y-direction in regions B and S, and is a low-loss transmission mode.

The second type is characterized by an imaginary wavenumber in the y-direction in region A, and is a high-loss transmission mode. For such type of modes to diverge, the following condition must be satisfied:

$$k_{xS}^2 + k_{yS}^2 - k_{xA}^2 \geq 0 \quad (1)$$

Provided that  $k_{yS}$  is real,  $k_{xS}^2 - k_{xA}^2 \geq 0$ ,

or  $\frac{r\pi}{2c} \geq \frac{p\pi}{2b}$ , where  $p \geq r$ . Therefore, if

$$2c \geq \frac{r}{p} (2b), \quad (2)$$

the modes are not diverged and are confined transmission modes. If  $p = r$ , it is not possible for condition (2) to be satisfied, and the mode is unconfined. However, if  $p > r$  it is possible that condition (2) is satisfied. The modes in this case are denoted by  $TE_{rn}(S)-TE_{pn}(A)$  and  $TM_{rn}(S)-TM_{pn}(A)$  mode-pairs where  $r$  and  $p$  are integers denoting the number of half sinusoidal field variations in the x-direction in region S and A respectively. It is noteworthy that condition (2) has the same expression as equation (13) of reference [1], which means that all the diverged higher-order modes could be confined in region S and become transmission modes. To confirm such moding characteristic,

a resonance technique was used. Figure 2 shows the resonance spectra obtained when the resonator was excited by an aperture centred on  $y = 0$  (centre of region S). The two spectra correspond to detection at the centre of region S and at one of the groove centres (groove 1) at the other end of the resonator. One or more set(s) of  $TE_{rn}(S)-TE_{pn}(A)$  mode-pair resonances were contained within each spectrum, which were identified by the perturbation technique. The field distribution of the  $TE_{11}(S)-TE_{31}(A)$  mode-pair is shown in figure 3. The experimental guide attenuation constant of this mode is approximately 2 dB/m at 100 GHz for a groove separation of 5 mm. In general, the  $TE_{rn}(S)-TE_{pn}(A)$  mode-pairs are high loss modes. It is expected that this mode will disappear when the guide is made longer. The attenuation of this mode decreases as the groove separation  $2s$  or the guide width  $2a$  increases. This mode is easily excited at the centre between the two grooves. It can also be excited from one of the grooves. As an example, figure 4 shows that, in addition to the  $TE_{11}$  and  $TE_{12}$  modes of the first type, other modes which could possibly be of the second type were detected with excitation at the centre of the groove. It had been shown experimentally that when excitation was at the centre between the two grooves, the number of mode-pairs excited increase as the groove separation  $2s$  increases. When excited at the centre of the groove, the number of mode-pairs excited decrease as the groove separation  $2s$  increases, but increases as the groove width  $2a$  increases. This type of modes may be generated at discontinuities, corners, etc., and may cause energy losses in power transmitted in the fundamental mode, possible interactions between other modes excited by different components, and possible occurrence of trapped-mode resonances.

## CONCLUSION

The two types of transmission modes in double-groove guide had been demonstrated. The first type of modes were documented [1]. The attenuation of the  $TE_{11}$  mode is marginally lower than that for single-groove guide. The second type of modes which have high loss, may also cause higher energy losses in the fundamental mode, mode interactions and trapped-mode resonances. Hence, double-groove guide is not attractive for normal propagation, but the presence of the two modes ( $TE_{11}$  and  $TE_{12}$ ) with a difference in phase constant suggests the possibility that a groove-guide power coupler can be developed [1].

## REFERENCE

[1] Choi, Y.H. and Harris, D.J., "Groove guide for short millimetric waveguide systems", *Infrared and Millimeter Waves*, Volume 11, Chapter 3, pp. 99-104, Dec 1984.

## ACKNOWLEDGEMENT

The support of the Hong Kong Polytechnic, Hong Kong and the University of Wales Institute of Science and Technology, United Kingdom on this work is gladly acknowledged.

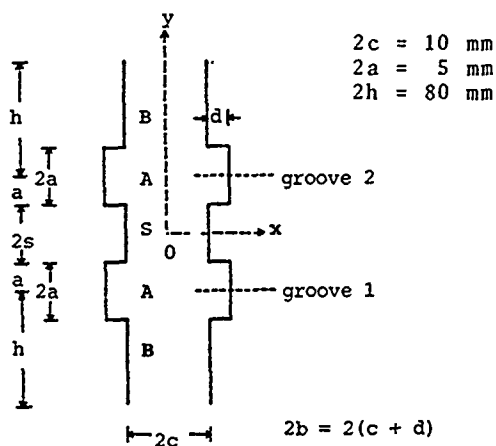


Figure 1

Cross-section of double-groove guide.

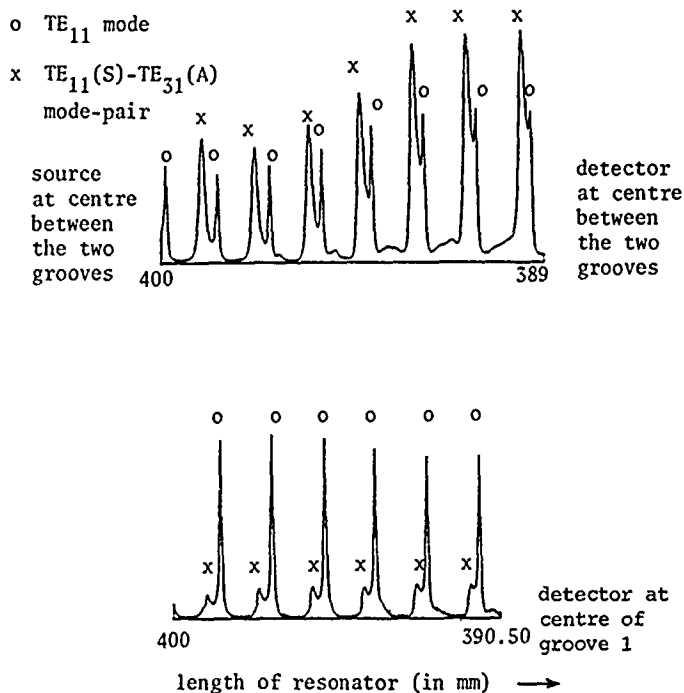


Figure 2

Resonance spectra of double-groove guide:

$2s = 5 \text{ mm}$ ,  $d = 3\frac{1}{3} \text{ mm}$  and  $\lambda_0 = 3 \text{ mm}$ .

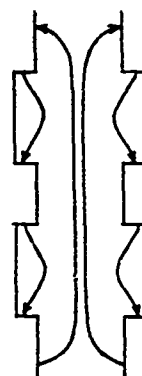


Figure 3

Field pattern of the  $TE_{11}(S)-TE_{31}(A)$  mode-pair in double-groove guide.

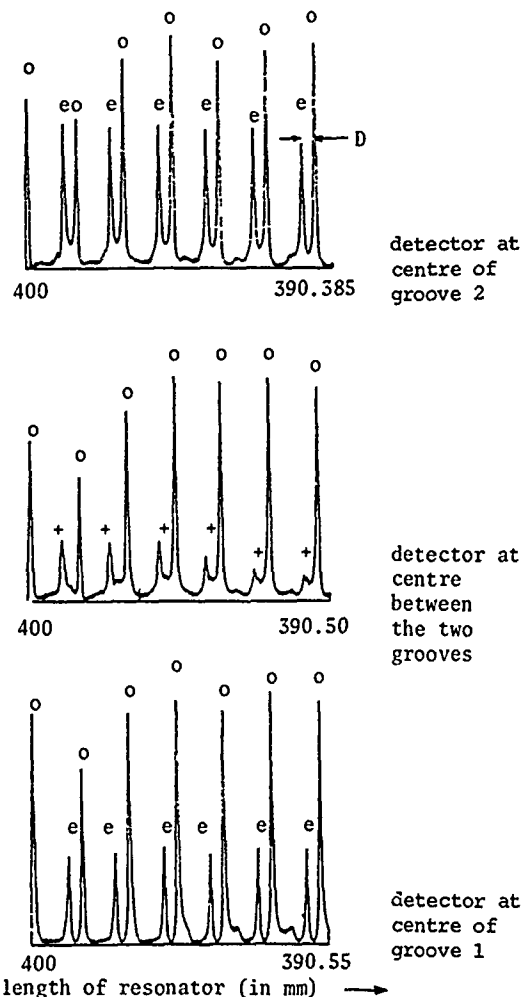


Figure 4

Resonance spectra for double-groove guide:

$2s = 5 \text{ mm}$ ,  $d = 3\frac{1}{3} \text{ mm}$  and  $\lambda_0 = 3 \text{ mm}$ .

+ other modes  
o  $TE_{11}$  mode  
e  $TE_{12}$  mode

PROCESSING AND ELECTRICAL PROPERTIES OF HIGH- $T_c$  SUPERCONDUCTORS

R.B. Poeppel, M.T. Lanagan, J.P. Singh, K.C. Goretta, J.T. Dusek,  
S.E. Dorris, U. Balachandran, C.L. Bohn, and J.R. Delany

Argonne National Laboratory  
Argonne, Illinois 60439

## ABSTRACT

This paper presents an overview of ceramic fabrication techniques and electrical properties of high- $T_c$  superconductors. Fabrication of bulk ceramic and composite, high- $T_c$  superconducting wires and tapes is discussed. Direct-current critical current density data and surface resistance data at rf and microwave frequencies are presented for the  $YBa_2Cu_3O_{7-x}$  and  $Ba_2Sr_2CaCu_2O_{8+y}$  phases.

## PRINCIPLES OF FABRICATION

The most common way to synthesize high- $T_c$  powder is to conduct a reaction between the constituent oxides at high temperature. The Y-Ba-Cu-O (YBCO), Bi-Sr-Ca-Cu-O (BSCCO), and Tl-Ca-Ba-Cu-O (TCBCO) systems have the most promising properties, and the discussion in this paper will be limited to these materials.  $YBa_2Cu_3O_{7-x}$  was synthesized by calcining a mixture of precursor powders of  $BaCO_3$ ,  $Y_2O_3$ , and  $CuO$  at  $890^\circ C$ ;  $Bi_4Sr_3Ca_3Cu_6O_z$  was synthesized by heating a mixture of oxides and carbonates to  $820^\circ C$ . Powder calcination is a complex process owing to residual  $BaCO_3$  and formation of low-melting eutectics, and several heat treatments were needed to produce the proper YBCO and BSCCO phases (1,2). TCBCO powders are also commonly synthesized by mixing constituent oxides and carbonates; and calcining at temperatures that average about  $900^\circ C$  (3). The YBCO, BSCCO, and TCBCO systems are characterized by copper-oxygen sheets in the a-b plane of the crystal lattice. Several superconducting phases are possible for the BSCCO and TCBCO systems, and their formation is sensitive to the preparation conditions (3,4).

Three basic ceramic-forming processes have been employed: extrusion, tape casting, and thick-film technology. The superconducting powder is mixed with a set of organics for each fabrication process. A solvent provides the basic vehicle into which the oxide powder and other organics are loaded. Care must be taken to select a solvent that is compatible with the powder and other organic constituents. Dispersants are used to deflocculate the inorganic particles in the solvent, and to assist in obtaining high green density. Binders impart strength to the green body, and plasticizers allow greater flexibility by reducing the glass transition temperature of the binder. The rheological properties of each formulation must be tailored for a specific fabrication process. For example, tape castings and thick films have typical viscosities on the order of 2000 cps and 20,000 cps, respectively.

After the powder and organic constituents are combined, the mixtures are available for fabrication. The extrusion process consists of placing a large pressure (approximately 20 MPa) on the plastic mass and forcing it through a small aperture. Wires with radii between 0.2 and 1.5 mm have been manufactured in lengths of well over 200 cm. The wires have great flexibility in the unfired state and 3-cm-diameter coils with 5 to 10 turns have been fabricated (5). Tape cast samples of thicknesses from 0.01 to 0.2 mm are made by passing a doctor blade over a plastic mass on a glass plate to form a uniform layer. After removal from the glass plate, the unfired tape is very flexible because of the organics incorporated in the cast material. Thick-film formulations have been used to coat substrates in sheet and wire form. Specific patterns are applied by silk screening on a silver foil, and more complex shapes such as silver wire are coated with a brush.

The heat treatment schedule for fabricated shapes of YBCO or BSCCO is divided into three parts. Initially, a slow increase in temperature up to  $350^\circ C$  is required to remove organics from the green body. Rapid removal of organic material will result in cracked or bloated samples. Sintering a well-calcined powder will induce formation of a liquid phase with an onset temperature between  $930$  and  $1015^\circ C$  for YBCO (1) and about  $900^\circ C$  for BSCCO (2). The onset temperature of the liquid phase is dependent upon the partial pressure of oxygen. The final step is an annealing procedure that incorporates oxygen into the YBCO lattice to form the superconducting orthorhombic phase (6). The BSCCO system does not require the annealing procedure (4).

For many applications, the high- $T_c$  superconductor must be bonded to a normal conductor. If the superconductor should quench, then the current will shunt across the normal conductor. Generated thermal energy can also be removed from the superconductor by a good thermal conductor. Thick films of YBCO and BSCCO have been deposited on silver substrates. Silver is compatible with the superconducting materials at the high processing temperatures. Coprocessing of materials will entail studies of the interface between superconductor and substrate materials. Match of thermal expansion coefficients is another area of concern (7).

## PROPERTIES

Electrical properties must be optimized before these ceramic materials can be converted into actual components. The superconducting transition temperature for YBCO is close to 90 K, although lower transition temperatures may be found for materials with a depleted oxygen content (8). The

BSCCO system has three different phases that have  $T_c$  values of 20, 80, and 110 K; the transition temperature is related to the number of Cu-O planes in the unit cell. Additions of Pb have been found to enhance the transition temperature of BSCCO (9).

A critical current density of  $1270 \text{ A/cm}^2$  has been measured on a YBCO extruded wire (diameter = 0.025 cm). This critical current density is substantially lower than values for epitaxially grown thin films ( $10^6 \text{ A/cm}^2$ ). The exact mechanism for the limitation of critical current in bulk samples has not been determined, and several possible explanations have been suggested (10). BSCCO samples have exhibited critical current densities of about  $150 \text{ A/cm}^2$  (2).

Previous measurements on YBCO bulk samples have shown that a sharp drop occurs in rf surface resistance as temperature is decreased from 100 K to liquid nitrogen temperature (11). The frequency dependence of surface resistance of the YBCO and BSCCO superconductors is shown in Fig. 1. An explanation of the cavity configurations for the measurements may be found in Ref. 12.

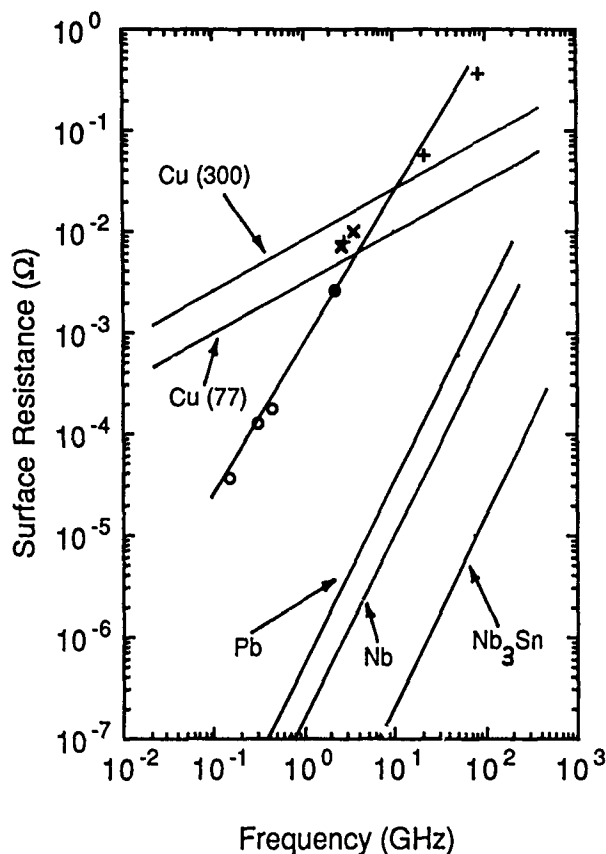


Figure 1

Frequency dependence of surface resistance at low field. "o" denotes YBCO bulk wire at 77 K; "•", YBCO thick film coated on silver wire at 77 K; "x", BSCCO thick film coated on a silver plate at 4.2 K; "+", YBCO bulk samples (13). Data for Pb, Nb, and  $\text{Nb}_3\text{Sn}$  are at 4.2 K.

Although the surface resistance of YBCO is higher than the resistances of other superconductors, it follows a similar frequency dependence to those of Pb, Nb, and  $\text{Nb}_3\text{Sn}$  superconductors. The

high surface resistance of ceramic materials is being studied, and it is hoped that single-crystal measurements will elucidate the loss mechanism. The frequency at which the YBCO superconductor and copper surface resistances are equivalent is approximately 3 GHz, and is an order of magnitude lower than that for copper at 150 MHz.

YBCO thick films coated on silver wire have properties similar to those of the bulk ceramic, and have the advantage of being easily fabricated into samples of large area and complex shape. As an example, the BSCCO samples in Fig. 1 were thick films coated on a 15.3-cm silver plate.

#### ACKNOWLEDGMENTS

This work was supported by the U. S. Department of Energy, BES-Materials Sciences, and the Office of Energy Storage and Distribution, Conservation, and Renewable Energy, under Contract W-31-109-Eng-38. The support of the U. S. Army Strategic Defense Command is also gratefully acknowledged.

#### REFERENCES

- (1) K.C. Goretta et al., to be published in *Mater. Lett.*
- (2) U. Balachandran, unpublished information.
- (3) R.M. Hazen, L.W. Finger, R.J. Angel, C.T. Prewitt, N.L. Ross, C.G. Hadidiacos, P.J. Heaney, D.R. Vebe, Z.Z. Sheng, E. El Ali, and A.M. Hermann, *Phys. Rev. Lett.*, 1988, vol. 60, pp. 1657-1660.
- (4) K. Kitazawa, S. Yaegashi, K. Kishio, T. Hasegawa, N. Kanazawa, K. Park, and K. Fueki, to be published in *Adv. Ceram. Mater.*, 1988.
- (5) K.C. Goretta, J.T. Dusek, J.P. Singh, M.T. Lanagan, U. Balachandran, S.E. Dorris, and R.B. Poeppel, to be published in *Proc. World Congress on Superconductivity*, Houston, TX, 1988.
- (6) D. Shi, K. Zhang, and D.W. Capone II, 1988, *J. Appl. Phys.*, vol. 64, 1995-1998.
- (7) M.T. Lanagan, R.B. Poeppel, J.P. Singh, D.I. Dos Santos, J.K. Lupp, U. Balachandran, J.T. Dusek, and K.C. Goretta, to be published in *Proc. Eighteenth Rare Earth Research Conference*, Lake Geneva, WI, September 12-16, 1988.
- (8) D. Shi, D.W. Capone II, K.C. Goretta, G.T. Goudey, and K. Zhang, 1988, *J. Appl. Phys.*, vol. 63, pp. 5411-5414.
- (9) U. Balachandran, D. Shi, D.I. Dos Santos, S.W. Graham, M.A. Patel, B. Tani, K. Vandervoort, H. Claus, and R.B. Poeppel, unpublished information.
- (10) N. Chen et al., unpublished information.
- (11) J.R. Delany, K.C. Goretta, R.B. Poeppel, and K.W. Shepard, 1988, *Appl. Phys. Lett.*, vol. 52, pp. 930-932.
- (12) C.L. Bohn, J.R. Delany, D.I. Dos Santos, M.T. Lanagan, and K.W. Shepard, to be published in *Applied Superconductivity Conf. Proc.*, San Francisco, CA, August 21-25, 1988.
- (13) G. Muller, D. J. Brauer, R. Eujen, M. Hein, H. Piel, L. Ponco, U. Klein, and M. Peiniger, to be published in *Applied Superconductivity Conf. Proc.*, San Francisco, CA, August 21-25, 1988.

# AN OPEN RESONATOR FOR TESTING SURFACE RESISTIVITY OF \* SUPERCONDUCTOR FILMS & METALLIC SAMPLES AT 100-120 GHz

T. Matsui, M. Kiyokawa and B. Koriyama

Communications Research Laboratory, Ministry of Posts  
& Telecommunications, Koganei, Tokyo 184, JAPAN

## ABSTRACT

A 100-120 GHz open resonator, which has a hemispherical configuration with a plane mirror as the sample itself, is described as a powerful tool for testing mirror samples. Very weak coupling, which is necessary for the high  $Q$  factor, have been achieved without facing with large transmission loss by using a partially-transparent circular aperture which is larger than wavelength. Weak effect on sample surface is sensitively detected by the precise measurement of high quality factor and frequency shift of the open resonator.

## INTRODUCTION

For the application of superconductivity to communication devices, the recent discovery of superconductors with transition temperature above liquid nitrogen has raised the possibility of a new situation. Superconductors are attractive as low loss materials for radio frequency, microwave, millimeter & submillimeter wave frequencies. Gold and aluminum films at room temperature can not be good conductors at short-millimeter & submillimeter wave frequencies. Thin-film technologies for conventional superconductor Nb & NbN have been achieved within the decade. Superconductive devices made of Nb ( or NbN ) high-quality films have successfully been developed and used in the experimental studies.

The surface impedance at microwave & millimeter waves is a basically important characteristic for thin-films of high  $T_c$  superconductors. Experiments on the surface impedance measurements of bulk sample, single crystals and thin-films have been reported by many researchers.<sup>1-3</sup> The rectangular or the cylindrical closed cavities are used in their experiments. While, the most of high-temperature-superconductor samples have shown poor characteristics at microwave frequencies lower than 10 GHz. In case of single crystals, measurements was limited by the copper cavity with low  $Q$ .<sup>1</sup> The more sensitive and precise measurement system is necessary for studying physics and deposition process of high-temperature superconductor films with high quality for applications at high frequencies. This is our main motive of this work.

The sensitivity for loss measurement is increased in proportion to the  $Q$  factor.<sup>4</sup> The surface impedance measurement at the higher frequency is direct and effective to test the potential of the high temperature superconductors for applications at high frequencies. Moreover, the higher current density can be induced on the surface of mirror samples by the resonator with the higher  $Q$  factor, when the almost same efficiencies are reserved in the mode conversions from the excitation beam to the  $TEM_{00q}$  Gaussian mode in the open resonators with different  $Q$  factors. Taking all these things into consideration, a new open resonator system is developed for measurements of extremely low-absorbing materials at short millimeter waves.

## OPEN RESONATOR

At the microwave frequencies, closed cavities of fundamental mode are commonly used for material measurement. The microwave resonant closed cavity becomes too small at millimeter wave frequencies.<sup>5</sup> It is impracticable to make a very small closed-cavity with high  $Q$  factor even if its inside walls are made of an ideal superconductor. A basic type of open resonator uses two plane metal reflectors to form a resonant structure similar to that of a Fabry-Perot "etalon". The plane-parallel resonator requires accurately parallel reflecting surfaces.<sup>4</sup> For the beam of finite diameter,  $Q$  factor is limited by diffraction loss.<sup>4</sup> The high quality factor is easily achieved by using an open resonator with spherical mirrors. Negligible small diffraction loss can be attained by the use of two spherical mirrors with large aperture.<sup>5,6</sup> A further property of the concave spherical resonator is that the optical alignment is not extremely critical.<sup>5,6</sup>

In order to investigate planer samples,<sup>7,8</sup> the hemispherical configuration is convenient, where a plane mirror sample is placed near the center of curvature of the spherical mirror.<sup>9</sup> The normal modes of this class of resonator are well characterized by the scalar Gaussian beam theory.<sup>10</sup> Figure 1 shows a hemispherical configuration with waveguide coupling. At long millimeter wave frequencies, the electromagnetic energy is commonly coupled in and out of the resonator by waveguide. A small coupling hole in each mirror is used to transmit the energy to and from the input and output waveguide. In a resonator of this type, high  $Q > 10^5$  is easily attained with very small coupling hole which is required to minimize coupling perturbation. By the strong diffraction effect at a coupling hole smaller than the wavelength, major part of millimeter wave power coupled through the aperture is diffused outside of the open resonator and do not enter the resonant mode  $TEM_{00q}$ . Within the ordinary coupling method, the achievement of high  $Q$  factors ( $>10^5$ ) entail high resonator insertion-losses,<sup>4</sup> which may be the order of 25-30 dB.

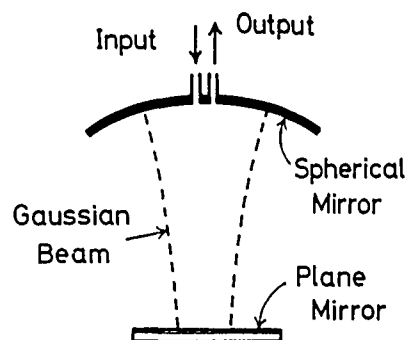


Figure 1  
Hemispherical open resonator  
with waveguide coupling

In designing hemispherical resonators, We adopted a quasi-optical coupling method to minimise coupling perturbation and mode conversion loss from excitation beam to a fundamental Gaussian mode  $TEM_{00q}$ . Spherical mirrors were made of sputtered gold (or Nb) film on an optically polished glass-substrate. Fine gold-film pattern was fabricated on a circular area in the center of the spherical mirror by using photolithographic and dry-etching process. The coupling aperture is designed to be almost same with the size of Gaussian beam on spherical mirror surface. The transmittance of partially transparent circular-area can be selected between orders of  $10^{-3}$  &  $10^{-5}$ . The mode conversion loss was successfully improved by the spherical mirror with the coupling aperture larger than the wavelength. Figure 2 shows a hemispherical open resonator with a quasi-optical coupling aperture. The spherical mirror is 80 mm in diameter & radius of curvature is 200 mm.

In case of conventional hemispherical resonator with high Q factor, power reflection from input coupling is insensitive for resonance, because major part of power coupled through the aperture is diffused outside of the resonator mode, and can not relate to interference at the input coupling, schematically shown in Figure 3-a. Therefore, transmission measurement is usually used for the precise measurement with this type open resonator. On the contrary, in our new open resonator, power reflection from a coupling aperture is sensitive for resonance, schematically shown in Figure 3-b. The reflection type is convenient for precise measurement of mirror samples. It becomes effective due to improvement of mode conversion efficiency that large energy can be stored in high Q cavity by the relatively small power.

#### OPEN RESONATOR SYSTEM

The block diagram of a 100-120 GHz open resonator system is shown in Figure 4. Gunn phase-locked oscillator is tunable electrically over the range +100 MHz. The frequency is stable to 1 in  $10^5$  and can be measured to this accuracy. This system is in principle capable of measuring Q factor of  $10^7$  to better than 1 percent. The experimental Q for gold film at room temperature is higher than 240,000. Sample temperature can be settled from above 4.3K to 200K. This system is suitable for surface measurements of low resistive loss materials at low temperature. Temperature and current-density dependence and detailed comparison of our results will be presented at the conference.

\* supported by Science & Technology Agency, JAPAN

#### REFERENCES

- (1) W.W.Fuller, et al., to be published in IEEE Trans. Magn., 1989.
- (2) G.Muller, et al., ibid.
- (3) M.Kobayashi, et al., ibid.
- (4) R.N.Clarke and C.B.Rosenberg, J. Phys. E: Sci-Instrum., 1982, Vol.15, pp9-24.
- (5) R.J.Cook, R.G.Jones and C.B.Rosenberg, IEEE Trans. Instrum. Meas., 1974, Vol.IM-23, pp438-442.
- (6) G.D.Boyd and J.P.Gordon, Bell Syst.Tech.J., 1962, Vol.40, pp489-508.
- (7) R.G.Jones, Electron.Lett., 1975, Vol.11,pp545-547.
- (8) J.K.Myler, J.R.Samble and J.E.Cousins, J.Phys. E: Sci. Instrum., 1980, Vol.13, pp298-291.
- (9) R.G.Jones, Proc. IEE, 1976, Vol.123, pp285-290.
- (10) H.Kogelnik and T.Li, Proc.IEEE,1966,Vol.54,p1312.

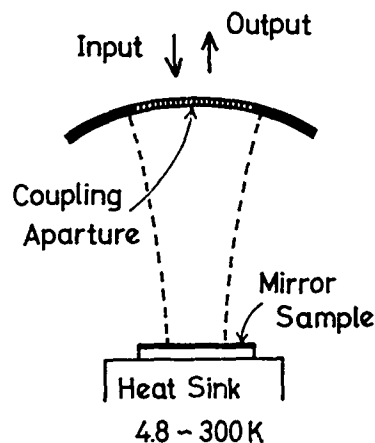


Figure 2  
Hemispherical open resonator  
with quasi-optical coupling

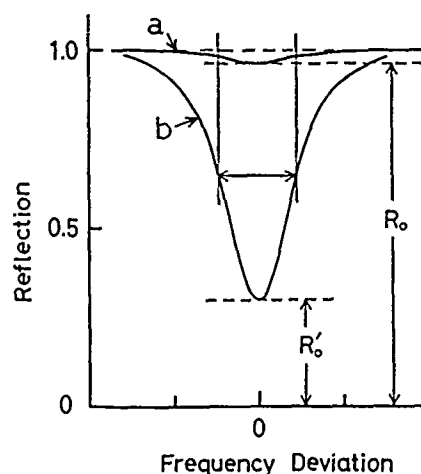


Figure 3  
Reflection around the resonance frequency  
a; waveguide coupling, b; quasi-optical coupling

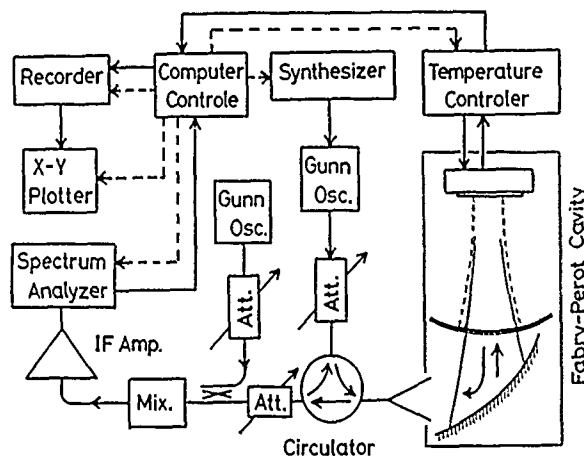


Figure 4  
Block diagram of open resonator system  
( 100-120 GHz )

## ANTIFERROMAGNETIC ORDER IN HIGH Tc SUPERCONDUCTOR OXIDES

S. Yoshimori and M. Kawamura

Department of Physical Electronics  
Tokyo Institute of Technology  
Tokyo 152, Japan

## ABSTRACT

We propose the multi-Cu-O<sub>2</sub>-layer structure model of high Tc superconducting oxides such as Bi<sub>2</sub>Sr<sub>2</sub>Ca<sub>2</sub>Cu<sub>3</sub>O<sub>12</sub>. The 'hole-Cooper pair' formation and the Bose condensation of the pairs are described by the theory of Huang of MIT. The attractive interaction is due to the antiferromagnetic order of Cu-O<sub>2</sub> layer. Dependence of Tc on the number of Cu-O<sub>2</sub> layers is quantitatively analyzed.

Pressure dependence of Tc is also analyzed by use of our model.

## INTRODUCTION

Since discovery of high Tc superconducting oxides, the mechanism of high Tc superconductivity has been actively investigated. The experimental research for investigating the nature of the systematic superconductors such as Bi-Sr-Ca-Cu-O and Tl-Ba-Ca-Cu-O will lead to the true theory.

Observations of the Josephson effect by using the point-contact junction and the flux quantization imply that the charge carriers are the Cooper pairs. The Hall coefficient of high Tc superconducting materials shows that the Cooper pair consists of two electrons. High Tc superconducting materials without hole doping are antiferromagnetic. The isotope effect of oxygen is small. The conduction properties are strongly anisotropic and show the 2D behaviour.

The experimental results mentioned above indicate that the attractive interaction is given rise in Cu-O<sub>2</sub> plane. However, as Hohenberg pointed out in 1967, the superconducting state at finite temperature can occur only in 3D system. The weak but finite interaction between the interlayers is needed for high Tc superconductivity even though the Cooper pairs are bound in the plane.

In this paper, it is assumed that the antiferromagnetic order of spins at Cu sites is the origin of the attractive interaction. We think that the critical temperature Tc depends on the magnitude of the inter-Cu-O<sub>2</sub> layer interaction. We try to represent the interlayer interaction as the tunnel phenomena of the Cooper pairs and we propose the multi-Cu-O<sub>2</sub>-layer structure model of high Tc superconductor to calculate the magnitude of the interaction.

## ATTRACTIVE INTERACTION

In the BCS theory, the 3D-positive-ion configuration is the background to create the attractive interaction. In this paper, the 2D

spin configuration on the Cu-O<sub>2</sub> plane is the background of high Tc superconductivity. Huang and Manousakis described the antiferromagnetic order and high Tc superconductivity. According to their theory, the scenario of the superconductivity can be illustrated as Fig.1. The smallest charge mobiles that have zero momentum and Bose-condensate are the 'hole Cooper pairs'. The holes created on the oxygen sites in Cu-O<sub>2</sub> layer can form the pairs. The attractive interaction between two holes is due to the antiferromagnetic order of the spins on Cu sites.[1]

Huang and Manousakis derived the following expression of Tc.

$$T_c = J \frac{8\pi}{[\zeta(3/2)]^2} r^{\frac{1}{3}} (1 + \frac{r}{2}) x^{\frac{2}{3}} \quad (1)$$

Here J is the energy of the spin-exchange interaction, r the hopping amplitude of the pairs and x is the doping fraction.

MULTI-Cu-O<sub>2</sub>-LAYER STRUCTURE MODEL

Huang used the hopping amplitude of the pairs as the fitting parameter. On the other hand, we assume that the interlayer hopping amplitude can be replaced with the tunneling probability of the pairs. The hole Cooper pairs with mass of 2m tunnel between the inter-Cu-O<sub>2</sub>-layers. We propose the multi-Cu-O<sub>2</sub>-layer structure model of high Tc superconductor in order to calculate the tunneling probability.

Figure 2 is the schematic of the multi-Cu-O<sub>2</sub>-layer structure of Bi<sub>2</sub>Sr<sub>2</sub>Ca<sub>0</sub>Cu<sub>1</sub>O<sub>6</sub> and Bi<sub>2</sub>Sr<sub>2</sub>Ca<sub>1</sub>Cu<sub>2</sub>O<sub>8</sub>. The periodic potential structures corresponding to Fig. 2 are shown in Fig.3. The models illustrated in Fig. 2 and 3 are called the multi-Cu-O<sub>2</sub>-layer structure models of high Tc superconducting oxides. We liken the Cu-O<sub>2</sub> layer to the conduction layer. The Cu-O<sub>2</sub> layer is the potential well. The interlayer portions are likened to the barriers with effective heights.

By applying the 1D Schrodinger wave equation to the potential structures, the determination equations which give the energy wave number(E-k) relations are derived. The energy of the pair in the potential well is obtained by numerically solving the determination equation and the tunneling probability can be calculated by use of the well-known formula.

Tc VS NUMBER OF Cu-O<sub>2</sub> LAYERS

The relationship between Tc and number of Cu-O<sub>2</sub> layers, n, for Bi<sub>2</sub>Sr<sub>2</sub>Ca<sub>n-1</sub>Cu<sub>n</sub>O<sub>2n+6</sub>

can be analyzed by using the barrier heights and lengths shown in Table I.

The calculated results are shown in Fig. 4. If  $T_c$  of  $n=1$  and 2 are assumed to be 10K and 80K, respectively,  $T_c$  of  $n=3$  becomes 105 K. This value agrees with the experimental  $T_c$ .

$T_c$  of  $n=4$  and 5 which are not experimentally investigated are also calculated and shown in Fig. 4. These results are the predictions.

#### ANISOTROPY OF NORMAL CONDUCTANCE

Anisotropy of normal conductance of the oxide can be also calculated by use of our model. Anisotropy of normal conductance is represented by  $\sigma(ab)/\sigma(c)$ , where  $\sigma(ab)$  and  $\sigma(c)$  are the conductance of a-b plane and of the c-axis direction, respectively.

If  $\sigma(ab)/\sigma(c)$  of  $\text{La}_{1.85}\text{Sr}_{0.15}\text{CuO}_4$  is assumed to be 30, the anisotropies of Bi-Sr-Ca-Cu-O system are as shown in Table II. The higher  $T_c$  increases, the less the anisotropy decreases.

#### PRESSURE DEPENDENCE OF $T_c$

The multi-layer structure model adopts the crystal structure along c-axis. Therefore, the pressure dependence of  $T_c$ ,  $dT_c/dP$  can be analyzed by use of our model. No theory which can explain  $dT_c/dP$  of high  $T_c$  superconducting oxides has been known.

Fueki group of Tokyo University systematically investigated  $dT_c/dP$  and  $dT_c/dx$  of  $\text{La}_{1.85}\text{Sr}_{0.15}\text{CuO}_4$ . So we calculated its  $dT_c/dP$ . The results are shown in Fig. 5. [2]

#### CONCLUSIONS

The multi-Cu-O<sub>2</sub>-layer structure model of high  $T_c$  superconductor was proposed to describe the relationship between  $T_c$  and number of Cu-O<sub>2</sub> layers. Anisotropy of normal conductance was analyzed in the frame of our theory. The pressure dependence of  $T_c$  was calculated.

#### REFERENCES

- (1) Huang and E. Manousakis, Phys. Rev. B, 1987 vol. 36, p. 8302
- (2) S. Yomo, K. Kitazawa, K. Fueki, Jpn. J. Appl. 1987, vol. 26, p. L603

Table I. Structure and barrier height parameters of typical high  $T_c$  superconductors

High $T_c$ superconductors	$L_{\text{Ox}}(\text{\AA})$	$L_{\text{bar}}(\text{\AA})$	$L_{\text{CuO}_2}(\text{\AA})$	$V_1(\text{eV})$	$V_0(\text{eV})$	$T_c(\text{K})$
$\text{La}_{1.85}\text{Sr}_{0.15}\text{CuO}_{4-x}$	2.0	11.24		2.655		37.0
				2.61		40.0
$\text{YBa}_2\text{Cu}_3\text{O}_{7-x}$	2.0	5.67	3.0	3.0	15.5	94.5
$\text{Bi}_2\text{Sr}_2\text{CuO}_8$	2.0	10.3		3.9		10.0
$\text{Bi}_2\text{Sr}_2\text{Ca}_1\text{Cu}_2\text{O}_8$	2.0	10.3	3.0	3.9	15.6	80.0

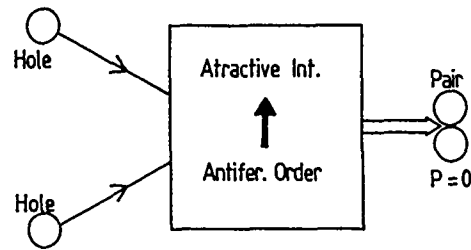


Fig. 1.

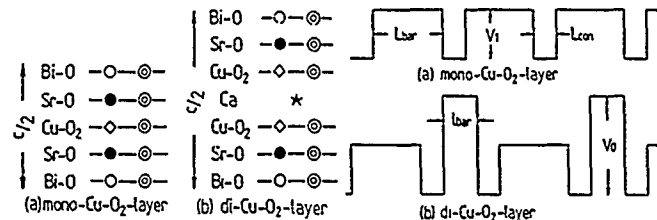


Fig. 2.

Fig. 3.

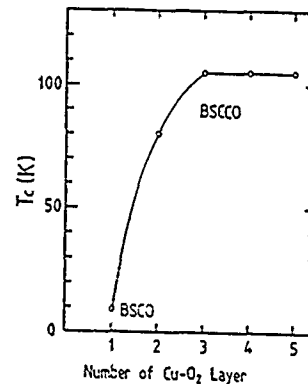


Fig. 4.

Table II. Anisotropy of normal conductance

Material	$T_c(\text{K})$	$\sigma(ab)/\sigma(c)$
$\text{La}_{1.85}\text{Sr}_{0.15}\text{CuO}_4$	40	30
$\text{Bi}_2\text{Sr}_2\text{CuO}_8$	10	2000
$\text{Bi}_2\text{Sr}_2\text{CaCu}_2\text{O}_8$	80	45
$\text{Bi}_2\text{Sr}_2\text{Ca}_2\text{Cu}_2\text{O}_{10}$	105	20

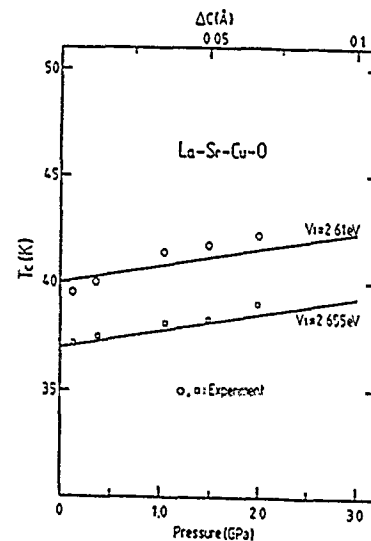


Fig. 5.



# MEASUREMENT OF SUPERCONDUCTOR SURFACE IMPEDANCE BY USING A PARALLEL PLATES OPEN RESONATOR EXCITED BY DIELECTRIC ROD $HE_{11}$ MODE

K.Fujisawa, Y.Yamamoto and F.Okuda

Department of Electrical and Electronic Engineering,  
Faculty of Engineering, Osaka Sangyo University  
Daito, Osaka 574, JAPAN

## ABSTRACT

The principle and experimental setup to measure the superconductor surface impedance is described, which characterizes in using an open resonator. The open resonator comprises a couple of parallel conducting plates penetrated perpendicularly by a thin dielectric rod. Along the dielectric rod, the  $HE_{11}$  mode is excited and its resonance between the parallel plates is exploited for finding the surface impedance of the superconducting plate.

## INTRODUCTION

Recent remarkable developments in fabrication technologies of high- $T_c$  superconducting thin-films give prospects of making various new devices utilizing them. In this respect, it is important to measure the temperature and frequency dependences of superconducting thin-film surface impedance, because they give valuable informations on the gap energy and the magnetic field penetration depth of superconducting thin-films. Also, they clarify the availabilities of superconducting thin-films to rf devices.

We present a measuring method, which uses an open resonator composed of two parallel conducting plates. These plates are superconducting or normal conducting thin-film deposited substrates. To confine the electromagnetic fields in between the plates and to avoid radiation losses, a thin dielectric rod is arranged to penetrate the plates perpendicularly and to guide the  $HE_{11}$  mode. By using this resonator, the superconducting thin-film surface impedance can be accurately obtained from measured data on the  $Q$  and the resonant frequency. As the  $HE_{11}$  mode has no cutoff frequency, this resonator can be used for wide frequency ranges. The basic principle and experimental setup are described below.

## CONSTRUCTION OF THE OPEN RESONATOR AND ITS RESONANCE PROPERTIES

The construction of the resonator is shown schematically in Fig.1.

On a copper block, two plate holders are placed in parallel. The plate holder 1 is fixed to the copper block, and the other plate holder 2 is movable, thus making the distance  $l$  between the plates variable. On the plate holders and on the conducting plates, small holes with diameter  $2a$  (in this case,  $2a=1.6\text{mm}$ ) are opened and a thin dielectric rod (in this case, TPX rod with  $\epsilon_r=2.12$ ) with the same diameter  $2a$  runs

through them, thus constructing an open resonator. The thin dielectric rod is connected to dielectric cylinders at both ends. These two dielectric cylinders constitute the input and output waveguides to the resonator and transmit the  $HE_{11}$  mode.

At resonance, two oppositely traveling  $HE_{11}$  modes are excited between the plates, and produce a standing wave. Here, we use the following notations.

- $W$ : stored energy per unit length for each traveling wave
- $P_d$ : dielectric rod loss per unit length for each traveling wave
- $P_c$ : surface loss of a conducting plate for the standing wave
- $P_r$ : radiation loss through two coupling holes for the standing wave

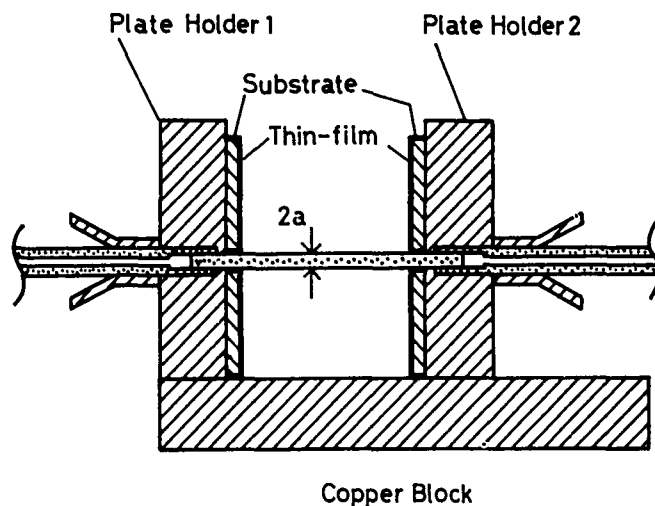


Figure 1  
Schematic construction of the open resonator.

$Z_s^{(n)} = R_s^{(n)} + jX_s^{(n)}$  : surface impedance of a normal conductor  
 $R_s^{(s)} = R_s^{(s)} + jX_s^{(s)}$  : surface impedance of a superconductor  
 $\sigma_n$  : normal metal conductivity  
 $\sigma_1 - j\sigma_2$  : superconductor complex conductivity  
 $\lambda^{(n)} = (\omega\mu_0\sigma_n/2)^{-1/2} = \delta$  : normal metal field penetration depth  
 $\lambda^{(s)} = (\omega\mu_0\sigma_2)^{-1/2}$  : superconductor field penetration depth

Assuming the film thickness is sufficiently larger than the field penetration depth, following relations are obtained,

$$\begin{aligned}
 Z_s^{(n)} &= \frac{1}{\sigma_n \delta} (1+j) = \frac{1}{2\omega\mu_0\lambda^{(n)}} (1+j) \\
 Z_s^{(s)} &= \omega\mu_0\lambda^{(s)} \left( \frac{\sigma_1}{2\sigma_2} + j \right)
 \end{aligned} \quad (1)$$

The effect of the surface reactance  $X_s$  to the standing wave has been analyzed by using a transmission line analogue for the  $HE_{11}$  mode. In this treatment, we have used the TE-wave impedance  $Z_{TE} = \omega\mu_0/\beta$  for the  $HE_{11}$  mode wave impedance and have used it as the characteristic impedance of the analogue line. This approximation is reasonable, because the TE-wave component is more dominant than the TM-wave component in the  $HE_{11}$  mode. By this approximate analysis, we have obtained the conclusion that the existence of  $X_s$  is replaced by a small backward displacement of the conducting plate wall, where

$$\begin{aligned}
 \Delta l^{(n)} &\approx \frac{1}{2}\delta = \frac{1}{2}\lambda^{(n)} \\
 \Delta l^{(s)} &\approx \lambda^{(s)}
 \end{aligned} \quad (2)$$

The resonance condition is given by

$$1 + \Delta l_1 + \Delta l_2 + \Delta l_0 = N\lambda_g/2, \quad N: \text{integer} \quad (3)$$

where  $\Delta l_0$  is brought by the coupling holes. At resonance, we have

$$\Delta\omega = \frac{\omega_0}{Q_L} = \frac{P_d}{W} + \frac{P_{c1} + P_{c2} + P_r}{2W} \quad (4)$$

where  $\Delta\omega$  is the half power width of the resonant transmission curve of resonator, and  $Q_L$  is the loaded Q.

#### MEASUREMENT OF SURFACE IMPEDANCE

First, we use two equal normal conducting plates in the resonator and excite resonances for two resonator lengths  $l_1$  and  $l_2$  at almost equal frequencies (the difference between the two resonant frequencies  $\omega_1$  and  $\omega_2$  are kept as small as possible). Using Eqs.(3) and (4), we have

$$\begin{aligned}
 l_1 + \lambda^{(n)} + \Delta l_0 &= \frac{1}{2}N_1\lambda_g1 \\
 l_2 + \lambda^{(n)} + \Delta l_0 &= \frac{1}{2}N_2\lambda_g2
 \end{aligned} \quad (5)$$

$$\frac{P_c^{(n)}}{W} = \frac{l_1 l_2}{l_2 - l_1} (\Delta\omega_1 - \Delta\omega_2) - \frac{P_r}{2W} \quad (6)$$

$P_r/W$  can be obtained from calculation or

preliminary experiment. Therefore,  $P_c^{(n)}/W$  is determined from Eq.(6). The theoretical expression for  $P_c^{(n)}/W$  has been obtained including  $\sigma_n$  or  $R_s$ . Then,  $\sigma_n$  or  $R_s$  can be obtained from the measured value of  $P_c^{(n)}/W$ .

Secondly, we replace a superconducting plate for one of the normal conducting plates used in the above experiment, and conduct similar experiment. In this experiment, two resonator lengths  $l_1'$  and  $l_2'$  are set almost equal to  $l_1$  and  $l_2$  respectively. Also, the two resonant frequencies  $\omega_1'$  and  $\omega_2'$  are kept almost equal to each other, and to  $\omega_1$  and  $\omega_2$ . Then, we have

$$\begin{aligned}
 l_1' + \lambda^{(s)} + \frac{1}{2}\lambda^{(n)} + \Delta l_0 &= \frac{1}{2}N_1\lambda_g1' \\
 l_2' + \lambda^{(s)} + \frac{1}{2}\lambda^{(n)} + \Delta l_0 &= \frac{1}{2}N_2\lambda_g2'
 \end{aligned} \quad (7)$$

$$\frac{P_c^{(s)} + P_c^{(n)}}{2W} = \frac{l_1' l_2'}{l_2' - l_1'} (\Delta\omega_1' - \Delta\omega_2') - \frac{P_r}{2W} \quad (8)$$

From Eqs.(5) and (7), we have

$$\begin{aligned}
 \lambda^{(s)} - \frac{1}{2}\lambda^{(n)} &= \frac{1}{2}N_1(\lambda_g1' - \lambda_g1) + l_1 - l_1' \\
 &\approx \frac{1}{2} \frac{\partial \lambda_g}{\partial \omega} \Big|_{\omega_1} N_1(\omega_1' - \omega_1) + l_1 - l_1'
 \end{aligned} \quad (9)$$

$\sigma_n$  has been determined by the former experiment, and so  $\lambda^{(n)}$  is obtained from calculation. In Eq.(9),  $\partial \lambda_g / \partial \omega|_{\omega_1}$  is calculable from the dispersion equation. Then,  $\lambda^{(s)}$  can be obtained from Eq.(1). From Eqs.(6) and (8), we have

$$\frac{P_c^{(s)} - P_c^{(n)}}{2W} = \frac{l_1' l_2'}{l_2' - l_1'} \{ (\Delta\omega_1' - \Delta\omega_2') - (\Delta\omega_1 - \Delta\omega_2) \} \quad (10)$$

By using  $P_c^{(n)}/W$  obtained from the former experiment,  $P_c^{(s)}/W$  is determined from Eq.(10). From this,  $R_s^{(s)}$  can be calculated.

#### EXPERIMENTAL SETUP

The open cavity block is fixed on the 4K stage in the cold box of SUMITOMO's Refrigerator SRJ803. To lower the stage temperature to 4.3K from room temperature, it takes about 6 hours. Accordingly, it is possible to conduct the measurements at various intermediate temperatures. This is particularly suited to obtain the temperature dependence of high- $T_c$  superconducting thin-film surface impedance. To conduct the experiments speedily, we are using U-band sweep generator (WILTRON 6672A) and scalar network analyser (WILTRON 560A).

The experimental data will be presented at the Conference.

# OPEN TUBE RESONATORS FOR MILLIMETER/SUBMILLIMETER-WAVE SURFACE RESISTIVITY MEASUREMENTS

P. P. Woskov, D. Y. Rhee, and D. R. Cohn

Plasma Fusion Center  
Massachusetts Institute of Technology  
Cambridge, MA

## ABSTRACT

We present a novel technique for the measurement of surface resistivity using whispering gallery modes in an open cylindrical resonator. Preliminary results for copper at 140 GHz and application to high  $T_c$  superconductors will be presented.

## INTRODUCTION

Ohmic loss at millimeter/submillimeter-wave frequencies is an important parameter for the development of resonators, high-power sources, and transmission lines. In many cases it is the limiting factor in power capability and efficiency. However, the frequency dependence of copper resistivity is not adequately characterized (1,2). Moreover, high temperature superconductors have the potential of low resistivity at millimeter/submillimeter wavelengths, but more study is needed to improve understanding and material development (3). Measurements of low temperature superconductors at high frequency would also be of interest.

Conductivity measurements at frequencies up to 70 GHz are typically made by constructing a closed resonator and measuring its  $Q$  in the fundamental mode. This technique becomes increasingly difficult at higher frequencies because of shrinking dimensions. Furthermore, the use of a Fabry-Perot open resonator at frequencies >70 GHz requires very high  $Q$  operation, critical alignment, and has input/output coupling uncertainties.

In this presentation we describe a novel new resonator technique that can be readily extended into the Terahertz frequency range without the disadvantages of the closed resonator or Fabry-Perot. It is based on the use of surface modes in an open cylindrical tube resonator. It is an extension of previous work with cold cavity gyrotron  $Q$  measurements (4). The major advantages of this type of open resonator are: 1) the  $Q$  factor can be minimized for more sensitivity, 2) it is applicable to very high frequency measurements, 3) input/output coupling does not require special design, and 4) the  $Q$  factor does not depend on a critical alignment.

## THE OPEN TUBE RESONATOR

The open tube resonator(5) is a straight section of waveguide open at its ends. Near the cutoff frequency of a given guide mode, diffraction at the open ends provides the feedback to establish resonances. In a cylindrical guide, when the guide length  $L \gg \lambda$ , the

TE<sub>mp</sub> resonances are given by

$$f_{mp} \approx \frac{v_{mp}c}{2\pi r}$$

where  $v_{mp}$  is the  $p$ th zero of the  $J'_m$  Bessel function, and  $r$  is the guide radius.

If the internal dielectric is lossless, the total  $Q$  depends only on the diffraction losses at the open ends and on the wall losses due to the surface resistivity

$$Q_T = (Q_D^{-1} + Q_\Omega^{-1})^{-1} \quad (1)$$

where  $Q_D$  is the diffractive  $Q$  and  $Q_\Omega$  is the ohmic  $Q$ . Input and output coupling is achieved through  $Q_D$ . The diffractive  $Q$  is given by

$$Q_D = \frac{4\pi}{(1-R_1R_2)} \left(\frac{L}{\lambda}\right)^2 \quad (2)$$

where  $R_1$  and  $R_2$  are the reflectivities at the resonator ends and  $L$  is the length of the stored field. Computer codes exist for evaluating  $Q_D$  (6). The ohmic  $Q$  is given by

$$Q_\Omega = \frac{r}{\delta} \left[1 - \left(\frac{m}{v_{mp}}\right)^2\right] \quad (3)$$

where  $\delta = (\rho/f\mu)^{1/2}$  is the skin depth,  $\rho$  is the surface resistivity, and  $\mu$  is the permeability.

For a given resistivity,  $Q_\Omega$  can be made much lower than in any other resonator by using a surface mode where  $m \gg 1$  and  $p = 1$  (also referred to as whispering gallery modes). Having a  $Q_\Omega$  as low as possible allows a lower  $Q_D$  to be used which reduces the requirement on diagnostic source linewidth and frequency stability and increases the signal levels for measurement. This is an important consideration in a wavelength range where the performance and availability of sources and detectors decreases with frequency. It would also make possible the measurement of much lower resistivities than could be made with other types of resonators.

At the same time using a higher order mode keeps the resonator dimension large relative to the wavelength, making practical measurements well into the Terahertz range. In fact one sample cavity could be used to make measurements at many frequencies by tuning to different modes. An open resonator has an advantage over a closed resonator in going to higher order modes because the mode density is less, and the complication of input/output coupling holes is not necessary. In comparison to the Fabry-Perot open resonator, the open tube can make use of diffractive coupling without ambiguity to the transverse mode, excited, does not need alignment, and can work with a much lower  $Q$ .

## EXPERIMENT

Experiments have been started to demonstrate the feasibility of using the open tube resonator for surface resistivity measurements. The experimental arrangement is illustrated in Figure 1. A cylindrical resonator is placed between two conical up tapers and a Vlasov coupler (7) at one end to facilitate input/output coupling. For these tests the TE<sub>61</sub> mode at 140 GHz has been chosen. An unleveled, swept tunable impatt diode with 3-4 MHz linewidth and up to 10 mW power was used as the diagnostic source. A heterodyne receiver, with a Schottky diode mixer and a tripled Gunn oscillator as the local oscillator, was used as the detector.

The detected signal for a copper resonator at room temperature is shown in Figure 2 with the receiver viewing a peak of the far field pattern at A in Figure 1 and the impatt diode beam is coupled through the Vlasov coupler. The four peaks correspond to 4 longitudinal modes with mode numbers  $\ell = 2, 3, 4$ , and 5. The ability to detect more than one longitudinal mode is good because ohmic  $Q$  is approximately the same for adjacent modes, and diffractive  $Q$  varies in a predictable way as  $\ell^{-2}$ . Therefore both  $Q_{\Omega}$  and  $Q_D$  can be determined from the signal for 2 or more modes without any assumptions. There are no independent parameters.

The  $Q_T$  measured due to the width of the first peak ( $\ell = 2$ ) is approximately 2000 which is an order of magnitude less than the limit due to the impatt diode linewidth and more than two orders of magnitude less than typically required with Fabry-Perot resonators. However, this low a  $Q_T$  is limited by the ohmic losses,  $Q_D$  being approximately 5000 in this case. The measurements are consistent with copper resistivity at 140 GHz but are not yet precise.

Experimentation is underway to improve the resolution of the resonator peaks which tend to overlap as shown in Figure 2. If the impatt diode beam were perfectly matched to the Vlasov coupler, and the coupler were 100% efficient, then the signal should look like a highpass filter response with no resonances. However, the resonator is also acting as a mode converter at the resonances and this appears as peaks in the detected signal. It may be possible to sharpen the

observed resonances by launching the diagnostic beam in the near field from the conical taper end and viewing the signal through the Vlasov coupler. Also, viewing in reflection as in (4) may be another alternative. Results of this experimentation will be presented as well as measurements of different metals and at different temperatures.

High  $T_c$  superconductor measurements could be made by immersing the outside of the resonator in a cryogenic such as liquid N<sub>2</sub> while flowing a dry gas through the test setup. Another cooling method could be to flow a supercooled gas such as N<sub>2</sub> or He through the resonator to cool only the working surface. The cooling gas could then act simultaneously as the lossless dielectric and the coolant. The use of narrow linewidth sources in combination with low  $Q_{\Omega}$  open tube resonator modes could make possible measurements of high frequency resistivity which is many orders of magnitude lower than that of copper. These measurements would be useful in developing improved RF properties of high  $T_c$  superconductors.

## REFERENCES

- (1) F. J. Tischer, *IEEE Trans. Microwave Theory and Tech.*, 1976, MIT-24, pp. 853-858.
- (2) L. W. Hinderks and A. Maione, *The Bell System Tech. J.*, 1980, vol. 59, pp. 43-65.
- (3) D. R. Cohn, L. Bromberg, W. Halverson, B. Lax, and P. P. Woskov, *Int. J. of Infrared and Millimeter Waves*, 1987, vol. 8, pp. 1503-1524.
- (4) P. P. Woskoboinikow and M. J. Mulligan, *IEEE Trans. Microwave Theory and Tech.*, 1987, MIT-35, pp. 96-100.
- (5) L. A. Vainshtein, *Soviet Physics JETP*, 1963, vol. 17, pp. 709-719.
- (6) A. W. Fliflet and M. E. Read, *Int. J. Electron.*, 1981, vol. 51, pp. 475-484.
- (7) S. N. Vlasov, L. I. Zagryadskaya, and M. I. Petelin, *Radio Eng.*, 1978, vol. 20, pp. 14-17.

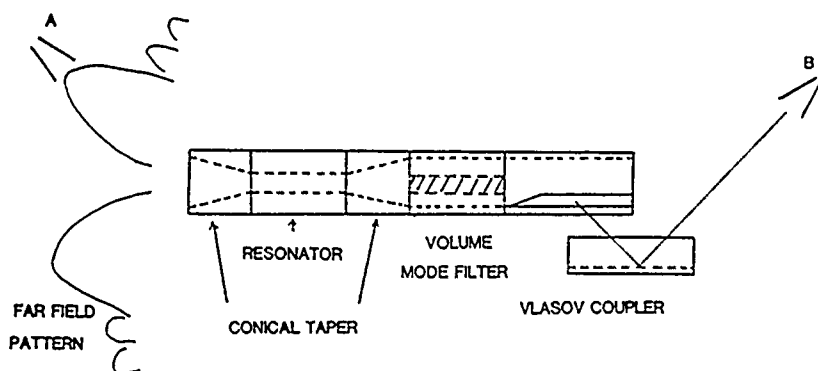


Figure 1  
Experimental setup for measuring the  $Q$  of modes in a cylindrical open resonator

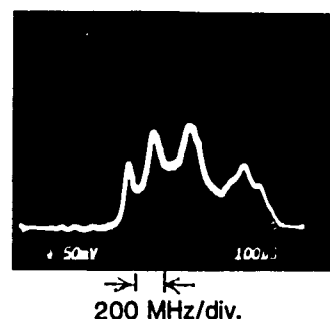


Figure 2  
TE<sub>61</sub> resonances at 140 GHz. The four peaks correspond to the longitudinal modes  $\ell = 2, 3, 4$ , and 5

## A FAST, WIDE-SPECTRAL RANGE PHOTOCONDUCTIVITY FIR-DETECTOR SYSTEM

Michael von Ortenberg and Jürgen Geiger

Physikalisches Institut der Universität Würzburg  
D-8700 Würzburg, F. R. Germany

## ABSTRACT

We present a fast, wide-spectral range photoconductivity FIR-detector system suitable for application in short, pulsed high magnetic fields.

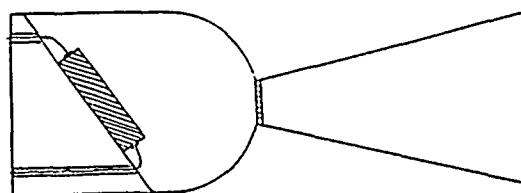
## INTRODUCTION

Submillimeter-Magneto Spectroscopy is one of the most effective tools in the investigation of electronic properties of solids. In the usual experimental arrangement a DC-magnetic field in connection with modulation of the electromagnetic radiation is applied to take advantage of phase-sensitive modulation and thus tremendously enhancing the signal-to-noise ratio of the experiment. The magnetic field range covered by superconducting solenoids is at the moment up to about 15 Tesla, whereas hybrid systems peak up to about 30 Tesla. Higher magnetic field intensities are only available in short-time, pulsed fields with a pulse length to the order of some ten milliseconds.

The essential issue of the present effort is the combination of high-frequency modulation spectroscopy together with pulsed, high magnetic fields. Due to the necessary resolution of the final signal a modulation frequency of some hundred kHz is necessary. The successful application of this concept in "DC"-magneto transport in pulsed magnetic fields has recently been demonstrated and results in a exorbitant increase of the signal-to-noise ratio [1]. The extension of this method to "optical" frequencies is the consequent objective for the future. This implies, however, both a fast modulation of the FIR-radiation as well as a corresponding fast detector-system.

## EXPERIMENTAL ARRANGEMENT

In contrast to the usual bolometers used in submillimeter magneto spectroscopy for a frequency response of some hundred kHz only photoconductive detectors can be applied. To cover the essential part of the submillimeter spectrum we applied three different photoconductive semiconductors, namely n-type InSb, n-type GaAs, and Ge:Ga, and mounted them together in the same integrating sphere, as shown schematically in Fig. 1.



Detector Elements

Cold Window

Cone

Fig. 1

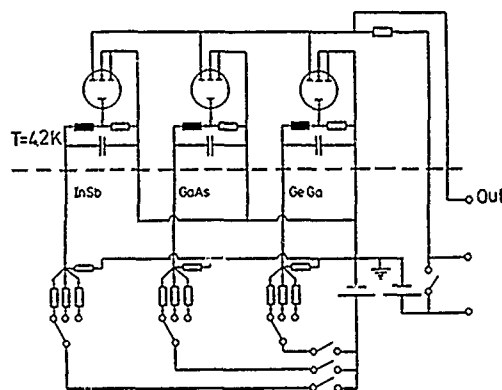


Fig. 2

Black polyethylene at the opening of the integrating sphere was used as cold filter to block of room temperature radiation. To reduce noise we used He-cooled preamplifiers and load resistors mounted in the direct vicinity of the integrating sphere. The diagram of the electrical circuit is given in Fig. 2.

Of special interest are now the three parameters response time, spectral range, and sensitivity. As matter of fact the response time is not limited by the physical mechanism of photo excitation, but by the layout of the amplifiers. As can be seen in Fig.3 the response time is about 2  $\mu$ sec thus resulting in a frequency limit of about 500 kHz sufficiently high for the application in pulsed magnetic fields.

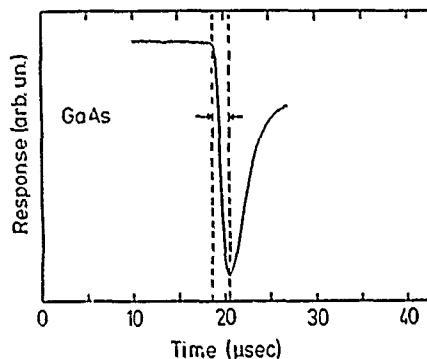


Fig. 3

An interesting feature of the detector is, that all three detector materials exhibit a photoresponse also for such low radiation frequency, that a direct photo-ionisation can be definitely excluded. In Fig. 4 we have plotted as example the normalized response in the range between 80 and 115 GHz. The physical mechanism resulting in the pronounced resonance-like spectrum is not known yet.

No definite numerical value has been obtained yet for the sensitivity nor the NEP. From comparison of the performance with the well known Ge-bolometer of the INFRARED LABORATORIES, Tuscon, our detector has at least comparable parameters. The exact noise investigation is in progress.

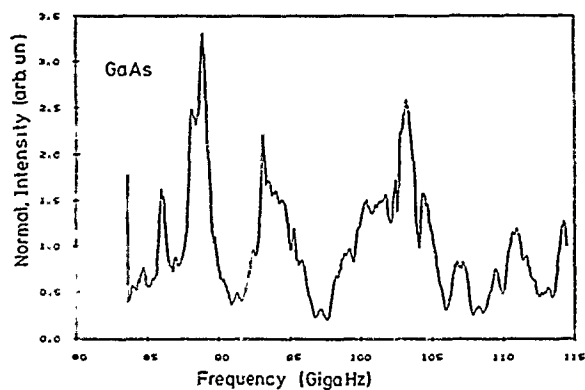


Fig. 4

### SUMMARY

We present a triple-photoconductive detector system with a spectral range between 80 GHz to 5000 GHz and a response time smaller than 2  $\mu$ sec. The design of the system is especially conceived for application pulsed-magnetic-field laser-spectroscopy.

### REFERENCES

- [1] Michael von Ortenberg  
Proc. of "The Intl. Conference on Application  
of High Magnetic Fields in Semiconductor  
Physics", Würzburg 1988, ed. G. Landwehr

## High Dynamic Range Infrared Detectors

A. G. U. Perera, Department of Physics, University of Pittsburgh, Pittsburgh, PA 15260.  
and  
D. D. Coon, Microtronics Associates, 4516 Henry Street, Pittsburgh, PA 15213.

We describe the use of cryogenically cooled, extrinsic silicon  $p^+-n-n^+$  diodes in an unconventional mode of operation as infrared detectors[1], which offer an unusually large dynamic range. The use of these detectors for high dynamic range IR radiometry and IR imaging would require no preamplifiers and could open the way to new means of 3-D processing at or near the focal plane.[2] The detectors perform intensity-to-frequency conversion via circuits with very low power consumption. To our knowledge, these are the only detectors which perform direct IR intensity-to-frequency conversion in the detector itself.

For  $p^+-n-n^+$  diodes, we have observed pulses with energy dissipation down to 4 picojoules/mm<sup>2</sup>/pulse and a quiescent power dissipation of 10 picowatts/mm<sup>2</sup>. Considering the thermodynamic efficiency of cooling, these numbers correspond to 290 picojoules/mm<sup>2</sup>/pulse and 710 picowatts/mm<sup>2</sup> at room temperature. Low power dissipation is useful in terms of cooling requirements. The spectral response of these detectors has been measured[3] with a liquid-helium-cooled monochromator and found to be similar to other extrinsic detectors[4] employing the same impurity.

Many accurate means of measurement are based on the conversion of an analog input signal to a frequency which can be accurately measured. There are many situations in which a high dynamic range is useful simply by the nature of the application. For example, luminosities of astrophysical sources vary over many orders of magnitude.[5] Measurements of high radiometric fidelity are complicated whenever the range of luminosity exceeds the dynamic range of the detector system.

The detectors generate pulses which are nearly uniform in height and the incident IR intensity controls the pulse repetition rate over a pulse rate dynamic range of about  $10^6$ . Pulse heights are typically in the range 1 volt to 50 volts which eliminates the need for preamps. Three neutral density filters with 0.01 transmission were used to measure detector response over a dynamic range of about  $10^6$ . The reflectivity of the filters has been taken into consideration, since with more than one filter in the beam, multiple reflections can increase the beam intensity somewhat. The formula for the transmitted beam after passing through three filters is  $T_1 \times \frac{T_2}{1-R^2} \times \frac{T_3}{1-R^2}$  where  $T_1$ ,  $T_2$  and  $T_3$  are the transmission coefficients of the three filters (0.01 in our case) and  $R$  is the reflection coefficient of the filters, which is 0.3 for our filters because they are made of silicon. This result is used in Figs. 1 and 2.

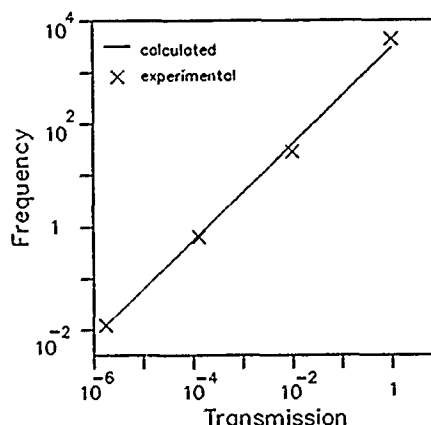


Figure 1: Pulse rate vs incident IR flux (transmission) with unit flux representing the flux incident on the detector without any filters in the IR optical path. The detector bias voltage was 14.6 volts and the dark pulse rate was  $1.9 \times 10^{-3}$  Hz. The 4 displayed data points indicate a dynamic range of nearly  $10^6$ . Including the dark pulse rate brings the dynamic range to about  $2 \times 10^6$ .

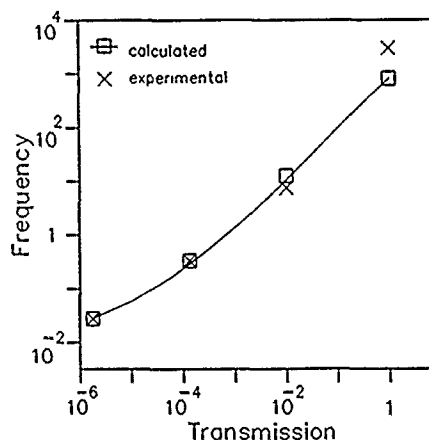


Figure 2: The detector output for an IR source temperature of about 100 K. This data set shows much more curvature than the results in Fig. 1, which agrees with the model. This pronounced curvature can be intuitively understood. As the intensity associated with all four points is reduced, the pulse rate for each point is reduced. The lowest intensity point is the first one to approach a lower bound associated with the dark pulse rate. This results in a flattening on the left hand side of the plot.

From our previous work,[6] the firing rate in terms of the incident intensity  $I$ , dark rate  $f_{dark}$  and a parameter  $I_0$  is given by

$$f = f_{dark} \frac{I/I_0}{\ln(1 + I/I_0)}$$

This model is used to obtain the calculated frequency response for fits shown in Figs. 1 and 2.

The data in Fig. 1 show that the detector is sensitive to IR over a range of intensities of about  $10^6$ . The IR source on-off ratio when all three filters are in the IR path is about 6. That is, the frequency is  $1.9 \times 10^{-3}$  Hz with IR source off and  $1.2 \times 10^{-2}$  Hz with IR source on. This shows that there is measurable response at the low end of the intensity range despite the approximately  $10^6$  attenuation. In other words, there is a pulse rate which is distinguishable from a dark pulse rate. The approximately linear character of the data plotted in Fig. 1 agree with the model given above.[6] Fig. 2 shows the same comparison for a data set obtained with a lower IR source temperature of around 100 K. In this data set, the experimental points show a larger curvature than in the previous two sets. This agrees with the model, for at lower intensities the model tends to show some curvature. For data in Fig. 2,  $f_{dark}$  is  $1.9 \times 10^{-2}$  Hz and  $I/I_0$  is 1.01 for the lowest experimental intensity. The IR source on-off ratio when all three filters are in the IR path is about 1.5. That is, the experimentally observed frequency is  $1.9 \times 10^{-2}$  Hz with the source off (dark rate) and  $2.7 \times 10^{-2}$  Hz with

the source on. Note that the calculated and observed dark rates match very closely. This is equivalent to saying that the model extrapolates well to  $I = 0$ . This is not surprising for low intensity data.

Acknowledgements: This work was supported in part by NASA Goddard Space Flight Center under contract # NAS5-30282.

## References

- [1] D. D. Coon and A. G. U. Perera, *Applied Physics Letters* **51**, 1086 (1987).
- [2] D. D. Coon and A. G. U. Perera, *Int. J. IR and Millimeter Waves* **8**, 1037 (1987).
- [3] D. D. Coon and A. G. U. Perera, *Solid-State Electronics* **29**, 929 (1986).
- [4] D. D. Coon, S. D. Gunapala, R. P. G. Karunasiri and H.-M. Muehlhoff, *Electronics Letters* **19**, 1070 (1983).
- [5] M. Harwit, J. R. Houck, B. T. Soifer and G. G. C. Palumbo, *The Most Luminous Far-Infrared Extragalactic Sources*, Infrared Processing and Analysis Center, IRAS Preprint No. 0023.
- [6] D. D. Coon and A. G. U. Perera, *Applied Physics Letters* **51**, 1711 (1987).



## PYROELECTRIC INFRARED DETECTORS FOR PRECISION EARTH SENSOR

K. Nakamura\* T. Ishigaki\* A. Kaneko\*  
S. Takahashi\* J. Nishida\*

Y. Wakabayashi\*\* H. Nakamura\*\*

\*Matsushita Research Institute Tokyo, Inc.  
3-10-1 Higashimita Tama-ku Kawasaki-Shi, Japan 214

\*\*National Space Development Agency of Japan, Tsukuba Space Center  
2-1-1 Sengen Tsukuba-Shi Ibaraki, Japan 305

## ABSTRACT

New IR detectors with twin elements were developed for precision earth sensors of satellites. Two sorts of pyroelectric elements, ceramics and sputtered films, were studied. Each element is mounted on an immersion lens. Minimum random error of attitude measurement is much smaller ( $0.012^\circ$ ) than that ( $0.06^\circ$ ) of our preceding type.

## INTRODUCTION

Instead of thermopiles or thermistor bolometers, we have been developing earth sensors using pyroelectric IR detectors for Engineering Test Satellites (ETS) of National Space Development Agency of Japan (NASDA) and the sensors were used for ETS-IV<sup>1)</sup> launched in 1981 and ETS-V<sup>2)</sup> in 1987. Precision earth sensors<sup>3)</sup> are in process of development as main attitude sensors for three-axis stabilized satellite under the program of NASDA and it was decided to be adopted into ETS-VI which is a synchronous satellite and is going to be launched in 1992. In order to attain our purpose, it is necessary to develop high sensitive IR detectors that have two channels of the field of view (FOV). So new IR detectors have been researched by Matsushita Research Institute Tokyo, Inc. (MRIT) and NASDA, Tsukuba Space Center.

## PRECISION EARTH SENSOR

The earth sensor consists of four modules from scanning mirror to digital signal processor illustrated in Fig. 1. This is a kind of optical sensors detecting the IR radiation ( $14\sim 16\mu\text{m}$ ) from CO<sub>2</sub> in the atmosphere. The IR telescope consisting of an objective Ge lens and a detector is the most important module dominating the performance of the sensor. The IR detector has a pair of pyroelectric elements and each element is mounted on a single convex lens respectively, so that the earth sensor has two channels of FOV. The FOV is caused to scan through  $24^\circ$  at 8 Hz by means of sinusoidal oscillation of a plane mirror. The cant angles of FOV are  $\pm 3.82^\circ$  respectively.

As the earth is an extended target, earth sensors are designed to locate the earth horizon in order to determine the orientation of a satellite toward the earth. The signal of the sensor is obtained when FOV crosses the horizon as in Fig. 2. The attitude of a satellite to the earth is determined by the error angles of roll and pitch. The angular signals are expressed in values relative to the encoder reference pulse of the scanning mirror system as in Fig. 2.

The pitch angle is given by

$$p = (L_{i1} - L_{i2} - L_{i3} + L_{i4}) / 4 \quad (1)$$

The roll angle is given by

$$r = \sum_{j=1}^4 (L_{2j} - L_{1j}) / (8 \tan \theta) \quad (2)$$

where  $\theta$  is scan latitude ( $27^\circ$ ) and  $L_{ij}$  is the angular signal<sup>3)</sup>.

Features of the IR telescope are as follows<sup>4)</sup>.

## 1) Low Optical Aberration

In order to keep optical aberration low level, an aspher-

ical objective lens and an immersion lens are adopted.

## 2) Low Cross Talk

Electrical and optical separations between two channels of the telescope have been investigated in order to decrease the cross talk which has effects on the performance of earth sensors.

## INFRARED DETECTOR

The construction of the new IR detector is shown in Fig. 3. The main frequency components of output signals shown in Fig. 2 are 60~300Hz. Considering this condition the IR detectors have been designed to fit in with the sensor. Especially, on the development of the high sensitive detectors, the mounting structures of pyroelectric el-

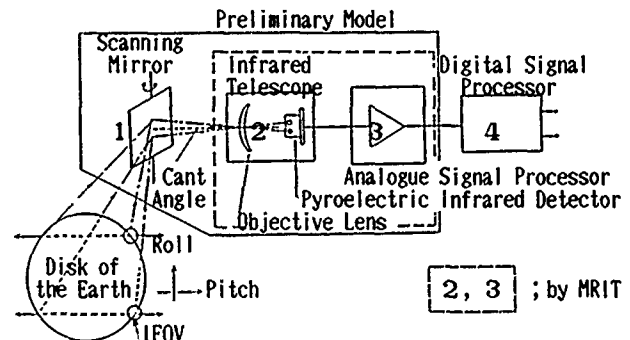


Fig. 1 Construction of the Precision Earth Sensor

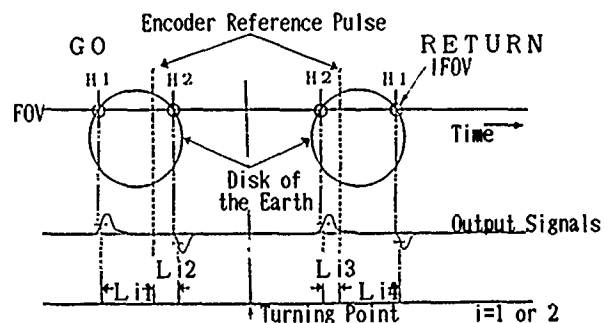


Fig. 2 Pulses Indicating the Horizon and Angular Readout Signals ( $L_{ij}$ )

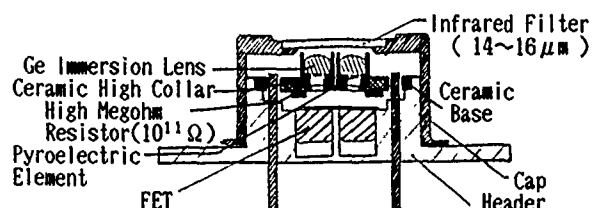


Fig. 3 Construction of the Infrared Detector

elements have been investigated. So thermal time constant ( $\tau_T$ ), determining the frequency characteristics of the IR detectors, may be longer than 3ms which is equivalent to the lower frequency (60Hz) of the earth sensor signals.

Features of the detectors are as follows, compared with preceding detectors. (Table 1)

#### 1) The Element Material and the Thickness

A-type; Lead titanate ceramic flake (PTO;  $10\mu\text{m}$ ), the same material compared with preceding one ( $30\mu\text{m}$ ).

B-type; Sputtered epitaxial film<sup>5)</sup> of calcium-modified lead titanate (PCTO;  $4\mu\text{m}$ ).

#### 2) Sensitive Area

Diameter of sensitive area is small ( $\phi 0.3\text{mm}$ ) in comparison with the preceding type ( $\phi 0.9\text{mm}$ ), so that focus length and F number of lens can be designed smaller than preceding one in the same condition of instantaneous FOV (IFOV  $\sim \phi 1.5^\circ$ ).

#### 3) The Immersion Lens

After the optical design of the immersion lens (small single convex lens), it was decided that the gap between the lens and pyroelectric element is  $5\mu\text{m}$ . The gap prevents  $\tau_T$  from lowering under the minimum limit (3ms).

#### 4) Detector with Twin-Elements

In spite of employing a pair of IR sensing elements, the new detector is designed to be almost equal in size and weight to preceding one which contains only one element without the immersion lens.

Table 1 CHARACTERISTICS OF IR DETECTORS FOR TRIAL

CHARACTERISTIC ITEMS	PRECEDING IR DETECTOR	IR DETECTORS FOR PRECISION EARTH SENSOR	
	FLAKE TYPE	A; FLAKE TYPE	B; SPUT. FILM
PYRO. MATERIAL	PTO CERAMICS	PCTO	
PYRO. COEF.	$2.5 \times 10^{-8} \text{C}/\text{cm}^2\text{K}$	$\sim 6 \times 10^{-8}$	
DIELEC. CONST.	180	$\sim 300$	
Tan $\delta$	0.6 % at 1kHz	1.0%	
ELEMENT SIZE	$\phi 0.9\text{mm}, 30\mu\text{m}$	$\phi 0.3\text{mm}, 10\mu\text{m}$	$\phi 0.3\text{mm}, 4\mu\text{m}$
WINDOW	IR FILTER (Ge; $14\sim 16\mu\text{m}$ )		
MOUNT STRUC.	SINGLE ELEMENT	ELEMENT WITH IMMERSION LENS	
ELEMENT NUMBER	1	2	
DETECTOR SIZE	$\phi 37.0\text{mm} \times 20\text{mm}$	$\phi 40.0\text{mm} \times 18\text{mm}$ height	
WEIGHT	36g	40g	
D at 120Hz	$0.6 \times 10^9 \text{Hz}^{1/2}/\text{V}$	$1.5 \times 10^9 \text{Hz}^{1/2}/\text{V}$	$2.7 \times 10^9 \text{Hz}^{1/2}/\text{V}$
EL. CAPACITY	35pF	13pF	60pF
$\tau_T$	60ms	4ms	$\sim 6\text{ms}$

## EXPERIMENT AND EVALUATION

The IR detectors have been manufactured for trial, using new material (PCTO) and usual one (PTO). Characteristics of the detectors are shown in Table 1. The detectivity (D) is the ratio of the responsivity (Rv) to the noise (N). The frequency characteristics of Rv and N are shown in Fig. 4.

The random errors of the sensor on pitch axis were estimated by using the two sorts of the IR detectors (IFOV  $\sim 1.5^\circ$ ) and the preceding one (IFOV  $\sim 1.9^\circ$ ). The test module consisting of either new type detector and the objective lens ( $\phi 25\text{mm}$ ) was assembled into the preliminary model of the sensor with a forced oscillating mirror<sup>3)</sup> made by NEC and one channel of analogue signal processor. The results of the experiment are illustrated in Fig. 5. The random error of A-type detector (PTO) is  $\sim 0.03^\circ$  and B-type one (PCTO) is  $0.012^\circ \sim 0.015^\circ$ . A-type detector satisfies the specification of the earth sensor for ETS-VI. We are going to investigate B-type in order to confirm the reliability as one of parts for space use.

## ACKNOWLEDGMENT

We wish to thank Professor E. Yamaka of Tsukuba Univ. for his devoting and guidance on the research of PCTO sputtered epitaxial thin film, the members at NEC for the development of the precision earth sensor containing the scanning mirror and our colleagues concerned.

## REFERENCES

- 1) Y. Wakabayashi et al., AIAA Guidance and Control Conference, San Diego, California 1982.
- 2) M. Ikeuchi et al., Electronics and Communication Engineers of Japan, ED 84-163, 1985.
- 3) Y. Wakabayashi et al., Electronics and Communication Engineers of Japan, SANE 86-19, 1986.
- 4) K. Nakamura et al., Electronics and Communication Engineers of Japan, ED 87-173, 1988.
- 5) H. Watanabe and E. Yamaka et al., The Japan Society of Applied Physics and Related Societies, 30p-k-14, 1987.

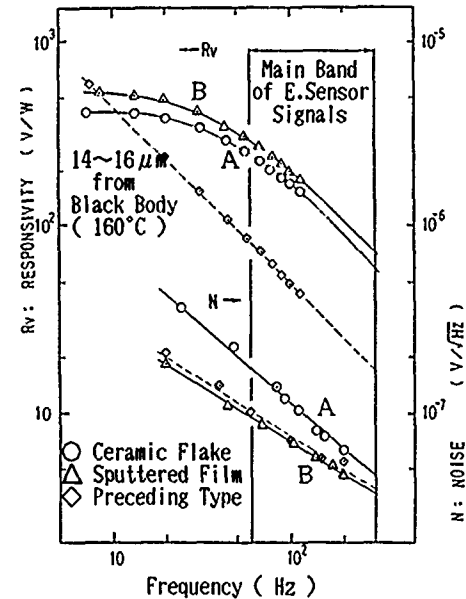


Fig. 4 Frequency Characteristics of IR Detectors for Trial

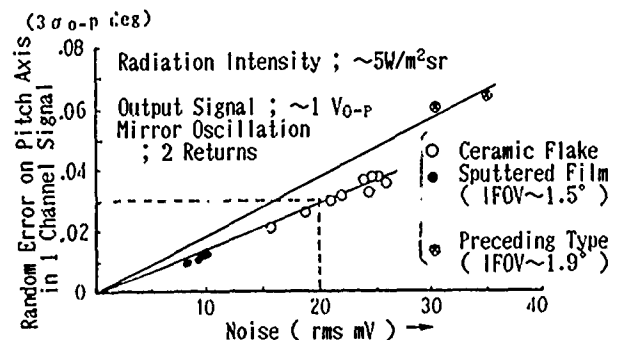


Fig. 5 Random Error on Pitch Axis

# The dependence of GaAs Schottky diode noise on dry etching damage

T. Suzuki, T. Iinuma and K. Mizuno

Research Institute of Electrical Communication  
Tohoku University, Sendai 980 Japan.

## Abstract

The noise of GaAs Schottky diode caused by dry etching damage has been studied. The number of traps near the Pt/GaAs interface increases with the damage, and this greatly increases flicker noise. These experimental results can be explained by a theoretical calculation.

## Introduction

Millimeter wave and submillimeter wave measurements are very useful for plasma diagnostics(1), radio astronomy and molecular spectroscopy. The GaAs Schottky diode has advantages of high sensitivity, high speed responsibility and room temperature operation for those measurements. We have been studying and fabricating GaAs Schottky diodes for submillimeter wave detectors and mixers(2). The noise characteristics of a Schottky diode are important for sensitive detectors and mixers. Here the noise dependence on dry etching damage in fabrication process is reported.

## The dependence of the noise and other characteristics on dry etching

Our GaAs Schottky diode is a honeycomb type for millimeter and submillimeter wave detectors. The contact holes of 1 $\mu$ m diameter are opened by reactive ion etching of C<sub>2</sub>F<sub>6</sub> gas plasma. This dry etching process damages the GaAs surface. Photo.1 shows the



Photo.1. The roughed GaAs surface by the effect of dry etching damage.

effect of the damage. This is the GaAs surface slightly etched by H<sub>2</sub>SO<sub>4</sub>/H<sub>2</sub>O<sub>2</sub>/H<sub>2</sub>O(40:1:2) solution after 3 minutes dry etching. The surface of GaAs is very rough, and the pitch seems to be about 2000Å. However the surface of slightly wet-etched GaAs without dry etching is smooth. This fact indicates that dry etching damages GaAs surface. The depth of the damaged layer is about 900Å. Fig.1 shows the I-V curves with dry etching and without dry etching. No.1 shows the damaged diode's I-V curve. At a low forward bias voltage, the recombination current is very large for the damaged diode. The ideality factor

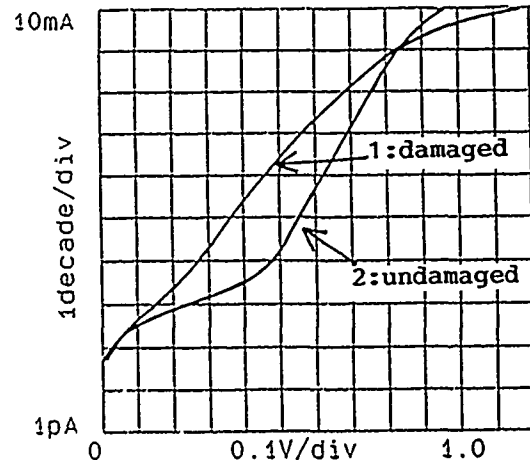


Fig.1. The difference of I-V curves between damaged and undamaged diodes by dry etching process.  
No.1:damaged, $n=1.55$ , $\phi_{bn}=0.68V$ ,  
No.2:undamaged, $n=1.16$ , $\phi_{bn}=0.92V$ .

and barrier height are poor. No.2 shows the undamaged diode's I-V curve. A good ideality factor of 1.16, and a barrier height of 0.92V are obtained. However, even if the damaged layer is not entirely removed, we can often see good I-V curves. For example, when the damaged layer that is left is under 600Å thick, the curves are as good as the undamaged diodes. This means that I-V curve does not give a good indication of the damage.

C-V measurement is often used to detect the damages. Fig.2 shows the  $1/C^2$  versus bias voltage. These capacitance were measured at 10MHz. The diodes of 6 $\mu$ m diameter were used to be measure accurately. The plots of No.1 is the damaged diode's capacitance. The plots of No.2 is the undamaged diode's capacitance. These plots are not so different from each other, and the barrier heights are both about 1.2V. This means ( $\times 10^{27}$ )

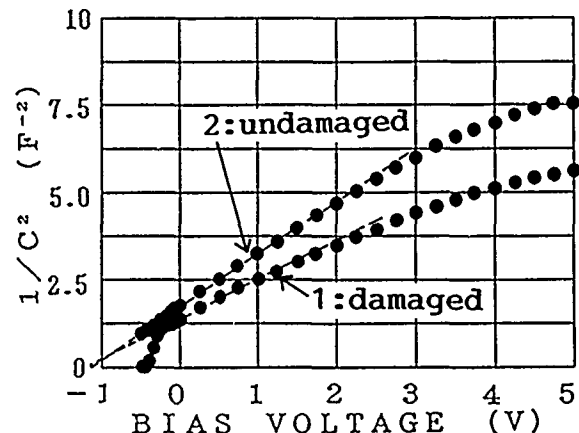


Fig.2. The difference of C-V curves between damaged and undamaged diodes.

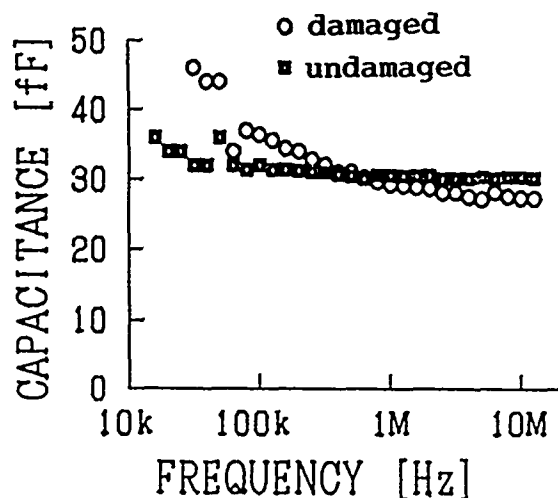


Fig.3. Frequency plots of barrier capacitance.

that the C-V measurement is not very sensitive to detect the damage.

Fig.3 shows the barrier capacitance versus frequency. The circles are the damaged diode's capacitance. This capacitance decreases with frequency. This frequency dispersion indicates that the dry etching process increases the number of traps. The squares are undamaged diode's capacitance. These plots of capacitance are constant above 30KHz. This indicates that the number of traps is much less than that for the damaged diode. A frequency plot of capacitance is a more sensitive indicator of traps than I-V and C-V measurements.

Fig.4 shows the noise characteristics of the diodes. The vertical axis is noise power amplified

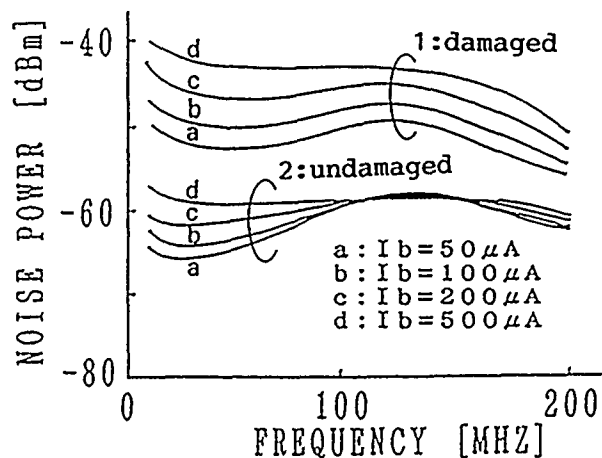


Fig.4. The noise characteristics of damaged and undamaged diodes.

by a pre-amplifier of 60dB gain. Band width is 300KHz. Curves in No.1 are the damaged diode's noise. These noise are not white noise but flicker noise. The curves of No.2 are the undamaged diode's noise. These flicker noise are not often of  $1/f$  slope. The damaged diode's noise reaches to over 200MHz (IF-band), and is about 10dB larger than the undamaged diode's noise. It has been found experimentally the IF-band flicker noise depends sensitively on the number of traps near the metal-semiconductor interface. So the noise measurements must be useful to detect those traps near metal-semiconductor interface.

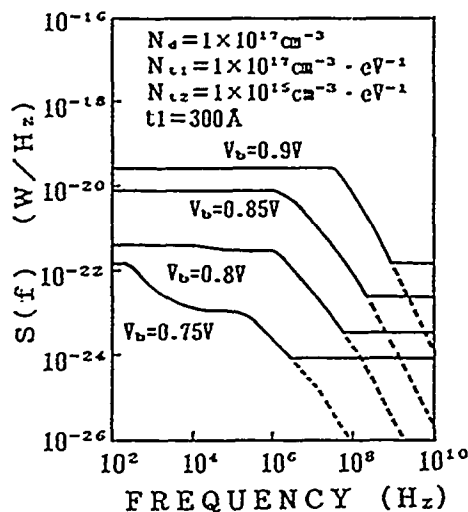


Fig.5. Theoretical calculation of flicker noise.

The flicker noise was calculated theoretically by using a modification of Hsu's method(3). We changed the trap's distribution to a step profile from Hsu's homogeneous distribution. Fig.5 shows a result of this calculation. The trap's distribution was assumed to have a higher concentration near metal-semiconductor interface is  $10^{17} \text{ cm}^{-3} \text{ eV}^{-1}$  and a lower concentration of  $10^{15} \text{ cm}^{-3} \text{ eV}^{-1}$  in the rest of the depletion layer. The thickness of higher concentration was assumed to be 300Å. The vertical axis is spectral intensity. There is a frequency independent region, a  $1/f$  region, transient region, a  $1/f^2$  region and a white noise region. The noise of transient region depends on the higher trap concentration layer near the metal-semiconductor interface. The lower-frequency flicker noise depends on the traps in entire depletion layer. These calculations can explain the experimental results that the flicker noise reaches to above 200MHz and has not often  $1/f$  slope.

#### Conclusion

These experimental and theoretical results conclude as follows,

1. Dry etching damage increases the number of traps in GaAs and degrades the diode characteristics.
2. Frequency plots of barrier capacitance are a more sensitive indicator of traps than I-V and C-V measurements.
3. The flicker noise from the traps often reaches to over 200MHz, and this IF-band flicker noise depends on the traps near the metal-semiconductor interface.
4. It is necessary to remove the damaged layer completely to fabricate a low noise diode.
5. This noise measurement is useful to detect the traps near the metal-semiconductor interface.

#### References

- (1) N.C.Luhmann, Jr.: Infrared and Millimeter Waves, ed. K.J.Button(Academic Press, New York, 1979) Vol.2.
- (2) T.Suzuki and K.Mizuno :Oyo Buturi,(The Japan Society of Applied Physics) 57 (1988) 691.
- (3) S.T.Hsu :IEEE Trans. Electron Devices, ED-18 (1971) 882.

# MINIMIZATION OF HEATING EFFECTS OF A MECHANICALLY STABLE MOM POINT CONTACT DIODE FOR HIGH POWER CO<sub>2</sub> LASER DETECTION

C. Yu, and C. S. Tan

Department of Electrical Engineering  
North Carolina A & T State University  
Greensboro, NC 27411

## ABSTRACT

Diode heat sinking and contact resistance optimization play key roles in MOM point contact diode thermal stability for high power laser detection. Such enhancement is realized by further optimization of the hooking parameters of the etched whisker tip.

## INTRODUCTION

The deliberately hooked, unblunted tungsten whisker tip in contact with a nickel coated quartz post in the metal-oxide-metal diode structure has been repeatedly reported by us to exhibit highly stable detection and mixing characteristics both for microwave and infrared radiation [1-4]. From a structural point of view, hooking should provide some cushioning for mechanical vibrations, a free end for thermal expansion and contraction under intense laser irradiation, and a rounded bend in the oxide layer that is less susceptible to electric charge buildup and eventual puncture of the oxide insulation layer. With proper hook chaping, sharp tip field enhancement in the junction area is not significantly degraded as long as the sharp tip does not deviate too far from that area due to excessive hooking. As a result, the optimally hooked-tip diode is a much more stable diode.

## FURTHER STABILIZATION OF DIODE PARAMETERS

It is quite evident that any hooking will bring about some degree of stability to the MOM diode. The task lies in the definition of the optimum hook desired. It has been reported [5] that oxide layer thickness is a critical parameter in defining the diode conduction mechanism, and hence diode temperature characteristics (see Fig. 1). Furthermore, even for oxide layer thicknesses that favor the tunneling mechanism, the rectified voltage across the diode is very much dependent on oxide thickness (Fig. 2) [5], and hence diode resistance (Fig. 3) [6]. Essentially, both Figs. 2, 3 indicate a flat top or a region of maximum stability of the diode. This region is defined by oxide layer thickness, which can be established by various means.

## UNHOOKED-TIP DIODE DETECTOR OUTPUT UNDER HEATING

Most workers in this field have not accepted the concept of an unblunted hooked tip. Their diodes thus consist of a sharp etched tungsten whisker tip in contact with the nickel oxide layer, the thickness of which is pre-controlled. Under chopped cw CO<sub>2</sub> laser irradiation with lens focusing, the temperature

of the tip is likely to reach a value that often produces a red hot tip, even causing vaporization of the tip. Such a temperature rise will certainly lead to significant expansion and contraction of the whisker tip, changing the contact pressure and oxide layer thickness of the diode. Due to the critical link between detected voltage and oxide layer thickness, diode output will be very sensitive to laser heating, even if the flat top region of oxide thickness is used initially. Such a situation is clearly demonstrated in Fig. (4) [6]. Here, heating of the diode is controlled by varying the chopping speed. A five-fold variation in the diode output is observed at low and high chopper speeds. It is recognized that there is less heating at lower chopper speeds. As speed increases, the heating cycle is much shorter than the cooling cycle of the diode structure, so that there is very little cooling, and the diode is progressively heated. Tip expansion ensues, leading to reduced oxide layer thickness, reduced contact resistance and detected output.

## HOOKED-TIP DIODE DETECTOR OUTPUT UNDER HEATING

A number of hooked-tip diodes are fabricated and optimized in terms of oxide layer thickness by deliberate penetration of the tip into a naturally overgrown oxide layer. These diodes are then irradiated by chopped, focussed cw CO<sub>2</sub> laser radiation at two incident laser power levels. The results are shown in Fig. 5. Within experimental error, there is no noticeable heating effect at the 0.85 W incident laser power level. At the 2.75 W level, the heating effect is only about 20%.

## CONCLUSIONS

We can safely note that preservation of oxide layer thickness under various ambient conditions is the key to stabilization of the MOM point contact diode. It has so far been discovered that controlled hooking of the tip is a very convenient and inexpensive means of accomplishing this goal. This minor modification of the tip has brought about significant improvement to the stability of the diode without severe degradation to diode performance. The resulting diode can be a rugged unit for field and high power applications.

## ACKNOWLEDGMENT

This work was supported by Grant DAAG 29-83-G-0114 and partially by Grant NAAL 03-88-G-0005 from the U.S. Army Research Office, Research Triangle Park, North Carolina, also Grant NAG-1-815 of NASA Langley Research Center, Hampton, Virginia.

## REFERENCES

- (1) C. Yu, and M. A. Hemmatian, Proc. 8th Intern. Conf. on Infrared and MM Waves, Miami, Florida (Dec. 1983) T6.4.
- (2) C. Yu, M. A. Hemmatian, A. Niczad, Y. Taghipour, and S. A. Yekrangian, SPIE Proc. 544, 78 (1985).
- (3) C. Yu, M. A. Hemmatian, and S. A. Yekrangian, Proc. 10th Intern. Conf. on Infrared and MM Waves, Lake Buena Vista, Florida (Dec. 1985) p. 133.
- (4) C. Yu, and A. Niczad, Proc. 10 Intern. Conf. on Infrared and MM Waves, Lake Buena Vista, Florida (Dec. 1985) p. 135.
- (5) Y. Yasuoka, T. Sakurada, and T. Miyata, Jap. J. Appl. Phys. 17, 171 (1978).
- (6) T. Sakurada, Y. Yasuoka, and T. Miyata, Electron. and Commun. in Japan 59-C, 92 (1976).

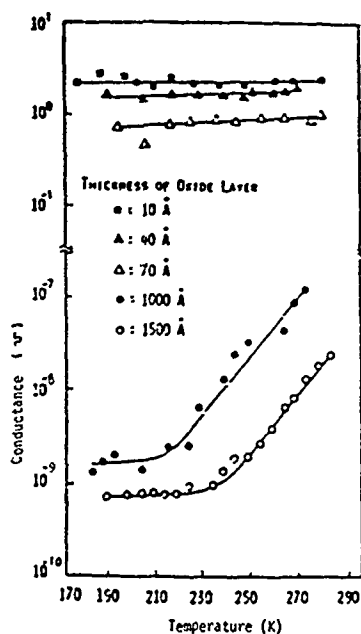


Fig. 1.  
(from Ref. 5)

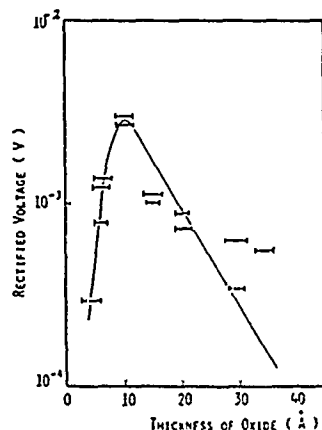


Fig. 2.  
(from Ref. 5)

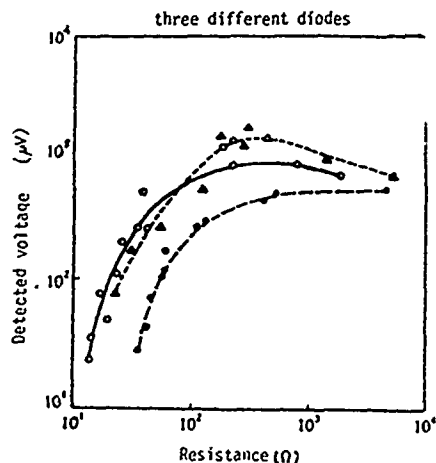


Fig. 3. (from Ref. 6)

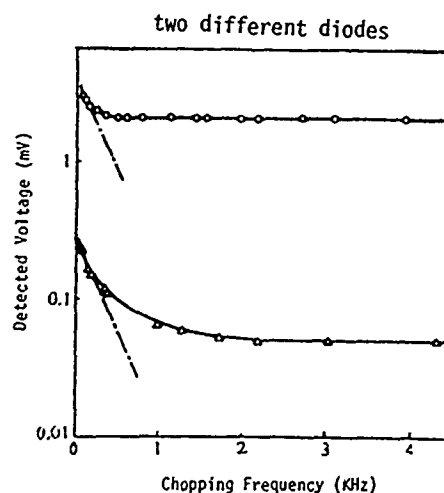


Fig. 4. (from Ref. 6)

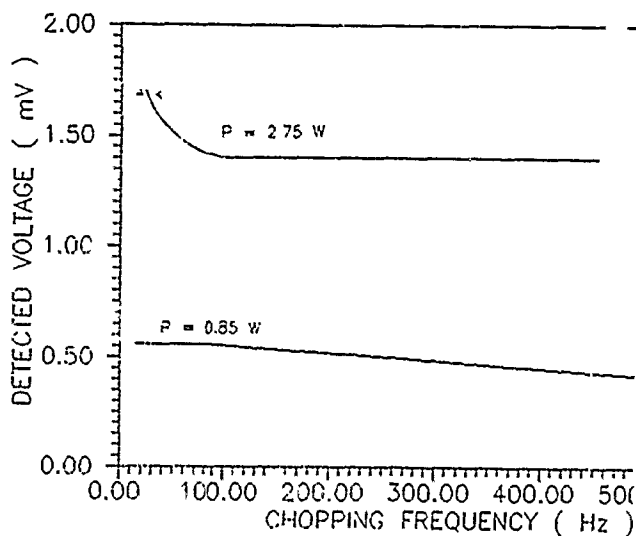


Fig. 5.

# CHARACTERISTICS OF A SCHOTTKY-BARRIER DIODE MIXER WITH CONICAL HORN ANTENNA FOR SUBMILLIMETER WAVELENGTHS

H. Nett

Max-Planck-Institut für Radioastronomie, Auf dem Hügel 69  
5300 Bonn 1, West Germany

B. J. Clifton\*

Massachusetts Institute of Technology, Lincoln Laboratory  
P. O. Box 73 Lexington, Mass. 02173, USA

## ABSTRACT

Antenna characteristics and noise performance of an improved quasi-optical Schottky-barrier diode mixer have been investigated at 800 GHz. Measurements indicate that system noise can be reduced by about 25% by adding a conical horn structure to a corner cube mixer.

## INTRODUCTION

During the past two decades heterodyne techniques using GaAs Schottky-barrier diode mixers have been extended to the short submillimeter wavelength range. A widely used mixer design is the quasi-optical corner cube [1] or corner reflector mount [2], both consisting of a long wire antenna (whisker), which serves to couple the electromagnetic fields to the Schottky diode, combined with a system of two or three orthogonal reflecting planes. Calculations using an extended theoretical model of the current distribution on the radiating elements gave good agreement with antenna patterns measured on a scaled model of the corner cube mixer [3].

Herrmann [4] attached a conical horn antenna to a corner reflector mount and showed that the coupling of a Schottky diode to an incoming focused beam could be improved by about 2 dB at 600 GHz. From beam pattern measurements he concluded that the increase in coupling efficiency could be explained by an improved match between the spatial field distribution and the antenna pattern.

In this paper we will present results of antenna beam measurements for both a conical horn antenna structure and a conventional corner cube antenna. For the corner cube mount in the heterodyne detection mode it is shown that the coupling to a signal source can be increased by about 1.4 dB when a conical horn is attached to the mixer block. Results of noise measurements are presented showing that a system noise temperature of 6,600 K (single sideband) at 803 GHz can be achieved using a conical horn antenna structure.

## CORNER CUBE MIXER MOUNT

The mixer consists of a Schottky-barrier diode chip (from Mattauch, U. Va., type 117) of size  $250 \times 250 \mu\text{m}$  mounted in the ground plane of the mixer block and a  $90^\circ$  rooftop reflector which can be adjusted for optimum spacing from the whisker axis. The whisker consists of  $25\text{-}\mu\text{m}$ -diam. AuNi wire, the tip of

which is sharpened by an electrolytical etching process. The length of the antenna is determined by a  $90^\circ$  bend in the wire towards the apex of the reflector and is chosen to be  $4\lambda$  at an operating frequency of 800 GHz.

After the contact between the whisker and one of the anodes has been established, the reflector is adjusted to a spacing of  $1.23\lambda$  between whisker and the vertex of the reflector. This was found to be optimum for the  $4\lambda$  antenna and the optics used in the laboratory test setup. The conical horn can be mounted to the mixer block without disturbing the mixer adjustment, and is positioned so that the cone axis coincides with the whisker axis.

## ANTENNA PATTERN MEASUREMENTS

The mixer block is mounted on a rotary positioner that allows rotation of the block about two orthogonal axes. The linearly polarized beam of an optically pumped far-infrared laser (803 GHz) is used as a radiation source. The beam is only slightly divergent and has a width of 40 mm at the location of the mixer block so that an approximate plane wave field can be assumed to be incident on the antenna. The maximum video response of the Schottky diode is about 15 mV, which is well within the square law region of the diode detector. For a measurement of a plane section through the antenna pattern the antenna mount is either rotated about a horizontal axis ('elevation section') or about a vertical axis ('azimuth section') while the video response of the diode is recorded simultaneously.

Elevation patterns in the principal E-plane are shown in Fig. 1. The 'box-data' curve represents the measurement with the conventional corner cube antenna while the solid curve shows the result with the horn antenna mounted in the corner cube. In this diagram the curve measured without the conical horn is normalized to the maximum observed in the pattern measured with the horn.

Figure 2 shows azimuth patterns in the quasi-H-plane, a) for the corner cube antenna and b) for the horn antenna, through the main lobe which is located around  $\alpha_0 = 26^\circ$  (case a) and around  $\alpha_0 = 25^\circ$  (case b). In both diagrams the solid lines denote the co-polarized and the 'box-data' the cross-polarized patterns. The cross-polarized patterns are normalized to the respective maxima in the co-polarization patterns.

## BEAM CHARACTERISTICS OF THE RECEIVER

To test the performance of the antenna structures in a heterodyne detection system an

\* Supported by an Alexander von Humboldt Research Award

experimental setup as shown schematically in Fig. 3 was used. The mixer block is mounted in the receiver so that its principal polarization is vertical, i. e., perpendicular to the plane of Fig. 3. The horizontally polarized laser-LO source (803 GHz) and the signal radiation are coupled to the mixer by a Martin-Puplett-type diplexer that is tuned to  $2\Delta = 10.48$  mm. This corresponds to an intermediate frequency of 1.43 GHz, the center frequency of the IF amplifier system connected to the mixer. A mercury-vapor lamp is used as signal source. The emitted FIR radiation is collimated by a TPX-lens and an aperture of 10 mm diameter is placed in front of the lens. For receiver beam measurements the setup can be translated horizontally ('azimuth', x-direction in Fig. 3) or vertically ('elevation') at a distance of 850 mm from the signal port of the diplexer while the IF signal is recorded simultaneously. To measure the response of the mixer in the horizontal polarization ('cross polarization') the diplexer is tuned to zero path difference. In this case the vertically polarized component of the signal as passed by grid 1 is transformed to a horizontally polarized beam at the mixer output port. In Fig. 4 (a) and (b) the azimuth scans for both polarizations are shown.

The peak signal is increased by about 1.4 dB when the horn is attached to the mixer. The cross-polarized component appears about 5.5 dB below the peak value for the horn antenna structure and 7.7 dB below the peak value for the antenna without the horn.

From noise temperature measurements it was found that the system noise temperature (single sideband) is reduced from 8,300 K ( $T_M = 6,700$  K) for the conventional corner cube antenna to 6,600 K ( $T_M = 5,250$  K) for the horn antenna structure. The noise temperature of the IF amplifier was 95 K.

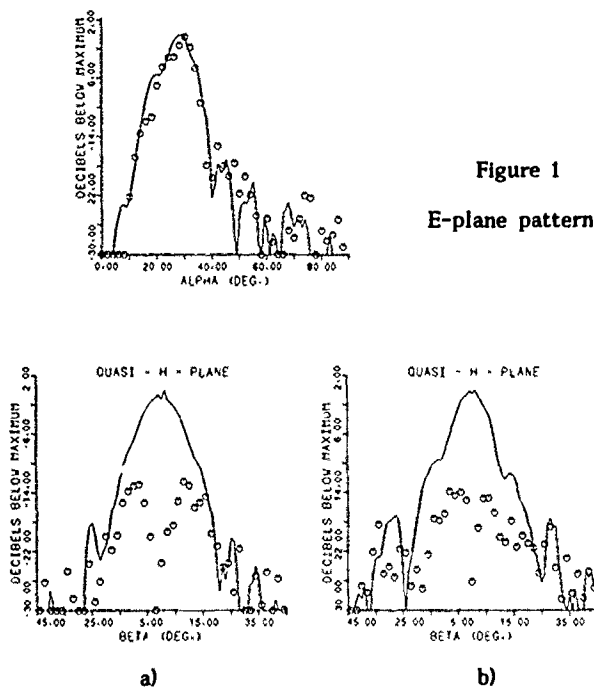


Figure 2 Quasi-H-plane patterns

## CONCLUSIONS

It has been shown experimentally that the performance of a heterodyne receiver for submillimeter wavelengths can be improved by attaching a horn structure to the corner cube mixer. Upon comparing both antenna structures it is seen that although the video response of the mixer is essentially unchanged the heterodyne sensitivity is improved by about 25%. Furthermore it is seen that both antenna structures have strong sidelobes in the cross-polarized field which result from the beam-transforming properties of the optics used in front of the mixer. These sidelobes can be eliminated from the signal path by using polarization selective elements in the optical system between signal source and the mixer.

## REFERENCES

- [1] Fettermann, H. R., Tannenwald, P. E., Clifton, B. J., Parker, C. D., Fitzgerald, W. D., and Erickson, N. R., *Appl. Phys. Lett.*, 1978, vol. 33, pp. 151-154.
- [2] Kräutle, H., Sauter, E. and Schultz, G. V., *Infrared Phys.*, 1977, vol. 17, pp. 477-483.
- [3] Vowinkel, B., *Int. J. Infrared and Millimeter Waves*, 1986, vol. 7, pp. 155-170.
- [4] Herrmann, K., *10th Int. Conference Infrared and Millimeter Waves*, Lake Buena Vista, Florida, 1985

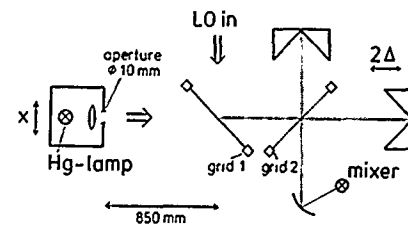


Figure 3 Schematic setup for the beam measurements

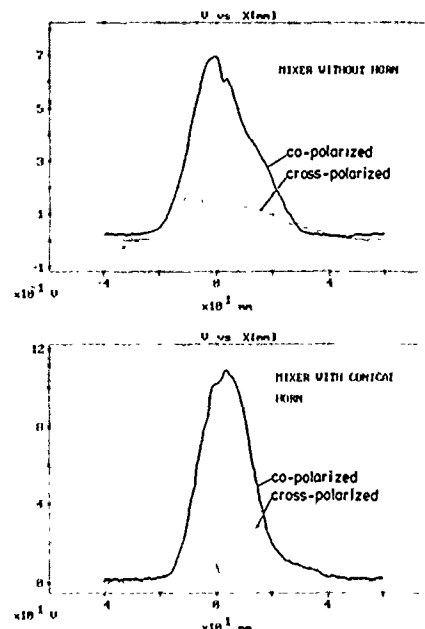


Figure 4 a) System beam scans (corner cube antenna) linear scale

Figure 4 b) System beam scans (horn antenna)



## ADIABATIC DEMAGNETIZATION COOLER FOR FAR INFRARED DETECTOR

Akio Sato, Takashi Yazawa

Toshiba Research and Development Center  
Ukishima, Kawasaki, Japan

Junya Yamamoto

Laboratory for Applied Superconductivity, Osaka University  
Suita, Osaka, Japan

## ABSTRACT

An small adiabatic demagnetization cooler for an astronomical far infrared detector has been built. Single crystals of manganese ammonium sulphate and chromium potassium alum, were prepared as magnetic substances. The superconducting magnet was indirectly cooled and operated by small current up to 13.3 A, the maximum field being 3.5 T. As a preliminary step, adiabatic demagnetization to zero field was implemented. The lowest temperature obtained was 0.5 K, for 5.0 K initial temperature.

## INTRODUCTION

The best performance of a far infrared detector used in space is achieved when operated at the lowest possible temperature. A dilution refrigerator is a very efficient method to achieve a temperature below 0.3K. Under zero gravity circumstances, however, this method would require some means of separating the two phases in the mixing chamber. Another method to achieve a temperature below 0.3K is an adiabatic demagnetization, which works even in space. We have developed a small-sized adiabatic demagnetization cooler based on a feedback controlled demagnetization [3 and 4], foreseeing its use in space. The refrigeration sequence considered here is shown in Fig. 1. First, a magnetic field is applied to a magnetic working substance, decreasing the entropy (AB in Fig. 1). During this process, a heat switch between the magnetic substance and a liquid helium bath is turned on. When the magnetic substance temperature reaches the bath temperature, the heat switch is turned off. The magnetic field is then reduced to a certain field, so that the temperature for the magnetic substance and a detector goes down to a target temperature, below 0.3K (BC), followed by a slow demagnetization with a feed back control, which maintains the temperature (CD).

## APPARATUS

Chromium potassium alum and manganese ammonium sulphate, whose ordering temperatures are 0.01K and 0.17K[5], respectively, are selected as the magnetic working substances. The single crystals has been prepared, which have higher thermal conductivity than pressed powder. These crystals

are 18 mm in diameter and 50 mm in length. Care must be taken, lest decomposition associated with the crystallization water loss should occur. Cooling power is estimated by the heat absorbed in the isothermal demagnetization process at the target final temperature  $T_f$ , following the adiabatic demagnetization from the initial magnetic field. In case of the manganese ammonium crystal, about 0.1 J cooling power is expected for the initial 4.2 K temperature and 3.5T magnetic field and the 0.3 K final temperature. If the heat leak from the bath to the magnetic working substance is less than  $10^{-5}$  W, the final temperature will be maintained for a few hours. The bobbin for the superconducting magnet is made of copper, whose surface is plated with gold. The magnet, placed in vacuum and connected thermally to the bottom of the helium bath, is cooled only by conduction through the gold-plated bobbin, which would ensure the magnet operation under non-gravity circumstances. The 3.5 T magnetic field was obtained at the 13.3 A current. A vacuum vessel was set in the bore of the superconducting magnet and the magnetic working substance was sustained by an FRP rod in the vessel[2]. A charcoal adsorption pump was used as the heat switch, the charcoal being 1 gram. The vessel was outgassed and backfilled with gas helium to atmospheric pressure at room temperature. All the gas would be absorbed by the charcoal adsorption pump and a good vacuum would be obtained after the charcoal was cooled. A carbon glass resistance thermometer and a germanium resistance thermometer were set in the magnetic working substance. Heat leak from the helium bath to the magnetic substance was estimated to be as shown in Table 1. The residual gas conduction would be the main origin for a heat leak under  $10^{-4}$  Pa pressure. In order to lower the heat leak value to less than  $10^{-5}$  W, a vacuum better than  $10^{-5}$  Pa is required. So, effectively using the charcoal adsorption pump is the key technique.

## ADIABATIC DEMAGNETIZATION EXPERIMENT

As a preliminary step, an experiment on complete demagnetization of manganese ammonium sulphate crystal to zero field was carried out at the 4.2 K bath temperature. Figure 2 shows a typical experimental result. A 3.5 T magnetic field was applied to the manganese ammonium sulphate crystal with the heat switch on. The salt temperature first

increased to about 7 K, then began to decrease due to the effect of the heat switch. When the temperature reached 5.0 K, the salt was demagnetized at a constant rate of 0.26 T/min. The salt temperature was then reduced to 0.50 K. The salt temperature rose slowly from 0.50 K to 0.58 K under zero field for about 20 minutes, followed by a steep rise to 4.2 K. Figure 3 shows the trace of this result on the entropy temperature diagram. The demagnetization process from 5.0 K to 1.0 K was nearly adiabatic. The deviation from the adiabatic process was caused by the heat leak to the salt and the thermal capacity of the working substance holder. The heat leak was estimated to be of  $10^{-4}$  W order, which was larger by one order than our design. The charcoal adsorption pump should be improved in order to reduce heat leak to the magnetic working substance due to residual gas conduction. The process below 1 K deviated extremely from the adiabatic and was rather isothermal. The cause for this result is partly explained by a possibility of crystallization water loss which led to increased interactions between manganese ions, and to a rise of the magnetic ordering temperature of the manganese ammonium sulphate crystal up to about 0.5 K. The steep temperature rises, shown in Fig. 2, also seems to support the above deduction.

The means for achieving a thermal link between the working substance and the detector remains unsolved.

#### ACKNOWLEDGMENTS

This work was financially supported by the Institute of Space and Astronautical Science under contract No. D-4-1.

#### REFERENCES

- (1) J. V. Radostitz, T. G. Nolt, P. Kittel and R. J. Donnelly, *Rev. Sci. Instrum.*, 1978, vol.49, pp.86-88.
- (2) J. Yamamoto, A. Sato and M. Sahashi, *Adv. Cryo. Engr.*, 1984, vol.33, pp.879-883.
- (3) P. Kittel, *J. Energy*, 1980, vol.4, pp.266-272.
- (4) R. D. Britt and P. L. Richards, *Int. J. Infrared and Millimeter Waves*, 1981, vol.2, pp.1083.
- (5) G. K. White, 'Experimental techniques in low temperature physics'. third edition, Oxford Science Publication, pp.219-254.

Table 1 Estimated heat leak from helium bath to working substance

Bath temperature	4.2 K	2.2 K
Heat conduction through FRP rod	$7.4 \times 10^{-7}$ W	$5.6 \times 10^{-8}$ W
Heat conduction through wires	$3.0 \times 10^{-6}$ W	$8.2 \times 10^{-7}$ W
Radiation	$5.6 \times 10^{-9}$ W	$4.2 \times 10^{-10}$ W
Residual gas conduction ( $10^{-4}$ Pa)	$3.5 \times 10^{-5}$ W	$2.2 \times 10^{-5}$ W

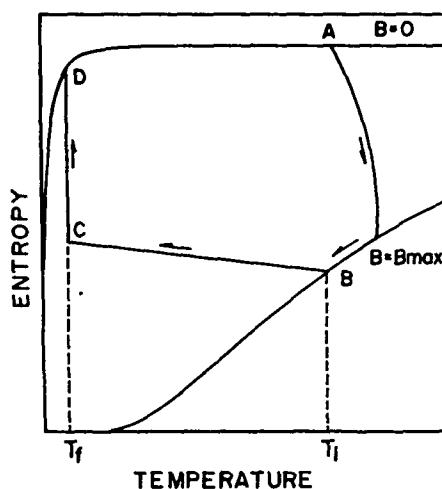


Fig.1 Process for cooling a far infrared detector

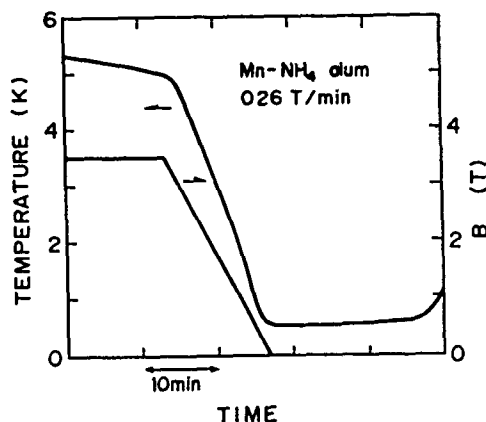


Fig.2 Cooling down hysteresis for complete demagnetization to zero field

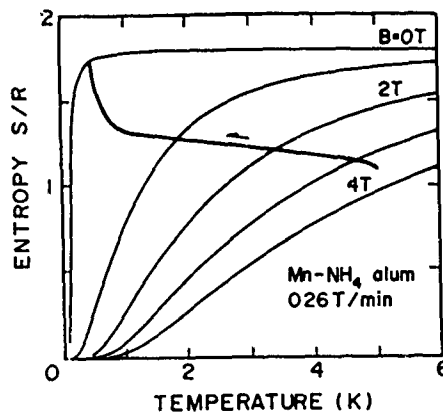


Fig.3 Trace on the entropy temperature diagram

# THE STUDY OF ANTIREFLECTION DIELECTRIC FILM MATERIAL ON MERCURY CADMIUM TELLURIDE INFRARED DETECTOR SURFACE

Luo Yuanhai Shu Yuwen

NORTH CHINA RESEARCH INSTITUTE  
OF ELECTRO-OPTICS IN CHINA

## ABSTRACT

The performance of Mercury Cadmium Telluride (MCT) infrared detector is not only determined by electrical parameters of material, but also by the surface state of sensitive element.

This paper shows that by coating the surface of 8-12μm MCT detector with an antireflecting dielectric material, reflection on the surface of sensitive element is decreased and quantum efficiency is increased therefore detectivity and responsivity are increased, usually by 15-30%.

## INTRODUCTION

The index of 8-12μm MCT is about 3.5. If there is not the antireflection film on a surface it will be about 30% loss in radiation due to reflection and transmission rate is quite low.

An ideal antireflection film should have an index of refraction which is the square root of the multiplication of the indexes of refraction of incident medium and substrate. (1)

$$i.e. \quad n_f = (n_i n_s)^{\frac{1}{2}} \dots (1)$$

where  $n_i$ ,  $n_f$ , and  $n_s$  are indexes of refraction of incident medium, thin film and substrate respectively. The optical thickness of thin film is one fourth of the specified wavelength.

Intrinsic detector materials tend to be highly absorptive and for a good detector only the front surface is significant. If there is not antireflection film, quantum efficiency reduces to

$$\eta = (1-R) \sim 0.65 \dots (2)$$

where  $\eta$  is quantum efficiency,  $R$  is reflectivity of detector surface.

By coating antireflection film, the quantum efficiency would be 0.95. (2). Therefore decreasing reflectivity and increasing quantum efficiency are available. The performance of detector will be improved.

## COATING ANTIREFLECTION FILM

In our experiments, The surface of MCT photoconductor are deposited with ZnS and ZnSe. The index of refraction of ZnS is 2.20 - 2.35 and ZnSe is 2.58. The index of refraction  $Hg_{0.8}Cd_{0.2}Te$  is about 3.35. The indexes of refraction of ZnS and ZnSe are just between that of incident medium and MCT.

increasing rate of detectivity ( $D_{bb}^*$ ) and responsivity ( $R_v$ ) are listed in Table 1 and 2 after coating antireflection film. In common, this agrees with theoretical prediction.

## REFERENCES

- (1) U.K. H.A. Macleod. Technology of Optic Thin Film. P53-92.
- (2) Opt. ENG. Vol.15, No.6, 498 (1976)
- (3) U.S. R.K. Willardson and A.C. Beer (Infrared Detector. 361-407)

Table 1  
Increasing rate of coating ZnSe (%)

No	$D_{bb}^*$ ( $CM \cdot Hz^{\frac{1}{2}} W^{-1}$ )	$R_v$ (V/W)
1	41	21
2	34	39
3	29	11
4	37	17
5	44	11
6	48	25
7	12	16
8	42	25

Table 2  
Increasing rate of coating ZnS (%)

No	$D_{bb}^*$ ( $CM \cdot Hz^{\frac{1}{2}} W^{-1}$ )	$R_v$ (V/W)
1	9.7	6.4
2	-9.4	37.8
3	22.2	35.3
4	15.1	24.6
5	1.6	26.9
6	19.0	9.9
7	19.4	18.2
8	20.2	25.0

## On the work mechanism of MIM point contact diode

N.Ioli, A.Moretti, D.Pereira\*, M.Prevedelli, F.Strumia and G.Carelli  
Department of Physics, University of Pisa-Italy  
and M.Inguscio, University of Napoli-Italy

### INTRODUCTION

Many theoretical and experimental studies have been reported (1,2) on the metal-insulator-metal (MIM) point contact diode as a device to measure infrared optical frequencies.

Electron tunnelling is the most widely accepted explanation for the extremely broadband response of MIM diodes. However, there is evidence for at least one more phenomenon, slower and possibly of thermal origin, occurring in the diode (3); this effect could be responsible of a masking effect particularly important near visible frequencies (2), where the absorption of the metals becomes greater, and tentatively contributes to opposite polarity video detection at visible wavelengths (4).

Purpose of the present work was to perform a systematic investigation on a W-Ni MIM point contact diode at different IR and FIR wavelengths. Results will be discussed which yield the determination of a cutoff for the slow mechanism and clearly demonstrate the suggested thermal origin of the effect.

### EXPERIMENTAL

The sources used in the experiments were: waveguide CO<sub>2</sub> lasers, optically pumped far infrared lasers (5), covering the 40-3000  $\mu$ m region, and a microwave sweeper in the range 0-18 GHz.

The diodes under investigation were W-NiO-Ni point contact type. The base was a polished Ni surface. The whisker was produced by electrically etching a 25  $\mu$ m diameter tungsten wire. The resistance could be adjusted mechanically from a few ten to several thousand ohms.

### RESULTS

Most of the measurements were performed on the beat note from the heterodyning of two or more sources. In particular the signal to noise ratio dependence on the diode impedance was investigated. In fig.1 the results for a second order mixing measurement  $v_{beat} = v_{L1} - v_{L2}$  are shown,  $v_{L1}$  and  $v_{L2}$  were both from a CH<sub>3</sub>OH laser at 119  $\mu$ m. One of them was frequency shifted by Stark effect and a beat note at 17 MHz could be observed on a spectrum analyzer.

A general feature of the measurement is the signal to noise ratio maximum between 300 and 400  $\Omega$  with a gradual decrease at higher resistance and a rapid one at lower resistances. This is similar to the behaviour observed in (3) for 3<sup>rd</sup> or higher order measurements, implying fast response of the diode.

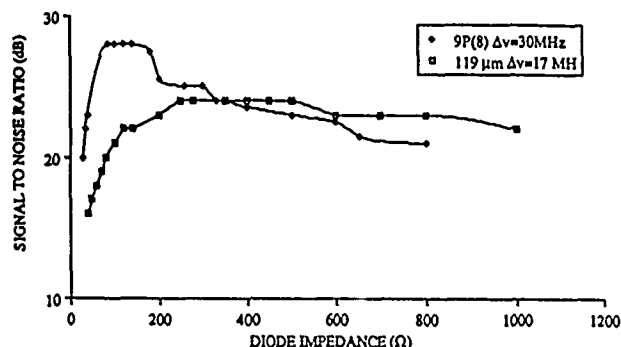


FIG.1 - Signal to noise ratio vs diode impedance for the 119  $\mu$ m of CH<sub>3</sub>OH and for CO<sub>2</sub>

The same 2<sup>nd</sup> order measurement, but performed at 10  $\mu$ m using two CO<sub>2</sub> lasers exhibits the different behaviour shown in fig.1, in agreement with the results of (2). In contrast with the measurement at 119  $\mu$ m and with 3<sup>rd</sup> or higher order measurements with high frequency mixing (>1 THz), the response curve in this case exhibited an increase of the beat note signal to noise ratio at lower resistances. The behaviour was the same when the frequency separation of the two CO<sub>2</sub> laser lines was increased from 30 to 250 MHz.

This suggested that the second mechanism of operation of the diode, causing the response maximum to be at lower resistances, although "slow", had a cut off frequency higher than, at least, 250 MHz. On the other hand, this second mechanism does not show up for measurements implying a cut off higher than 1 THz, so we decided to carefully investigate its frequency cut off.

At this purpose, since the tuning of the CO<sub>2</sub> lasers could not be increased significantly, we performed measurements heterodyning two CO<sub>2</sub> lasers oscillating on the same line and a microwave source. We studied the low-resistance effect as a function of the microwave frequency measuring the 3<sup>rd</sup> order  $v_{beat} = v_{L1} - v_{L2} \pm v_{\mu w}$ . The results are illustrated in fig.2. At the lower value of the frequency the behaviour is pretty similar to that using only two CO<sub>2</sub> lasers. However the low resistance effect gradually decreases increasing the frequency and at 3.5 GHz the response curve is again similar to that of 119  $\mu$ m and to those for very fast response (2). For a better determination of the cut off value we made measurements at fixed resistance and changing the microwave frequency. In fig.3 it is evident that the signal at 75  $\Omega$  has a dramatic cut off between 3 and 4 GHz. On the contrary at 350  $\Omega$ , when the diode is on its maximum response for the "fast" mechanism, we have no evidence of cut off, at least in the range explored.

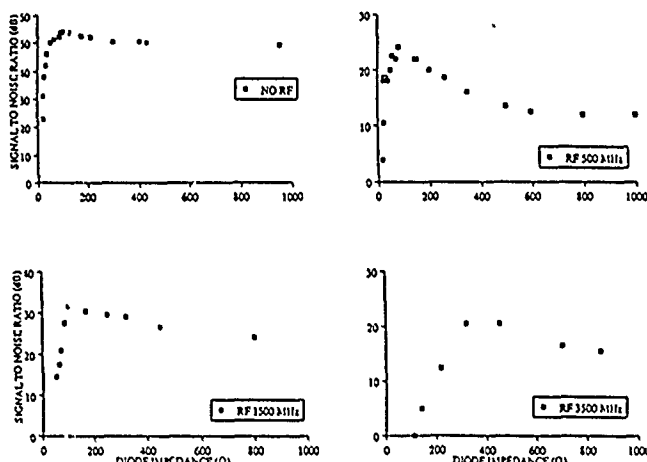


FIG.2 - Signal to noise ratio vs diode impedance for two CO<sub>2</sub> lasers plus microwave

It is suggestive to analyze the situation from the point of view of heating and cooling of the system under the effect of irradiation. When the radiation is focused on the contact, both the metals involved (W and Ni) are heated and their temperature increases depending on the amount of energy absorbed. There are two

mechanism involved: the absorption of radiation from the metal and the current flow through the junction whose effect could take to a change in the ohmic resistance due to the thermal expansion and a variation of the electronic temperature and hence of the tunneling current.

If this were the case, a "thermal detection" mechanism could really arise, with a response bandwidth determined by the thermal relaxation processes, and the signal shouldn't be affected by the microwaves, which absorption is negligible.

It is reasonable to assume two different thermal relaxation times for the whisker and the base, the one for the latter being much faster. We can think the whisker to be a long wire with the ending at fixed temperature; solving the classical heat equation for a long rod (1cm long, 25  $\mu\text{m}$  diameter) it results a typical time of 27 msec.

We assume the base to be a semi-infinite slab with a surface reflectivity  $R$ , a thermal diffusivity  $k$  and an absorption coefficient for unit length  $\alpha$ . Supposing a temporally square laser irradiance with a uniform spatial distribution, the typical time of the system is, according to (6),  $t = (k\alpha^2)^{-1}$ ; for  $\lambda = 10.6 \mu\text{m}$   $t = 0.32 \text{ nsec}$ ; if we consider the temperature decrease, the -3dB point is about 3.5 GHz.

This values are fairly consistent with the data shown in fig.2 and 3. It is worth noting that, should this be the explanation of the cut off of the "low speed" mechanism, the value would depend on the wavelength of the radiation, provided that it is absorbed by the metals. In particular these data could also be related to the measurements performed in (4) with visible laser sources.

We performed measurements at different wavelengths in the range where metals change their reflectivity as suggested from the measurements in fig.1, with the effect present at 10  $\mu\text{m}$  and absent at 119  $\mu\text{m}$ .

The transition between the two behaviours occurs at wavelengths between 30 and 50  $\mu\text{m}$ . In fig.4 it is reported the behaviour at 41.6  $\mu\text{m}$  which in fact is somewhat intermediate between the two extreme cases.

The temperature's rise is proportional to  $(1-R)$  and for Ni we have, from (7):

$\lambda$ ( $\mu\text{m}$ )	$1-R$ (10 <sup>2</sup> )
10	2.47
20	1.60
50	0.95
100	0.75
200	0.58

So the heating is negligible at long wavelength. If the system were sensible enough to reveal such effect for long wavelength, it should be seen again a cutoff but at lower frequencies ( $\nu = k\alpha^2$ ).

The temperature reached by the base, irradiated by a CW CO<sub>2</sub> laser of 10mW/mm<sup>2</sup> of power focused on the base at 5  $\lambda$ , is about 800 C. As the MIM diode is a non-linear device it was impossible to measure the impedance lowering with laser on and off.

On the contrary it's possible to estimate the temperature effect on the current flow  $J(T)$  through the junction (8). Assuming  $T = T_0 + \Delta T_L$ , where  $T_0$  is the metal temperature and  $\Delta T_L$  the temperature increase due to the current at the laser beat frequency, the quadratic term of  $J$ , sensitive to impedance, gives a significant contribution just in the case of "high" temperature of the Ni bulk, roughly estimate about 800K while  $\Delta T_L = 150\text{K}$ .]

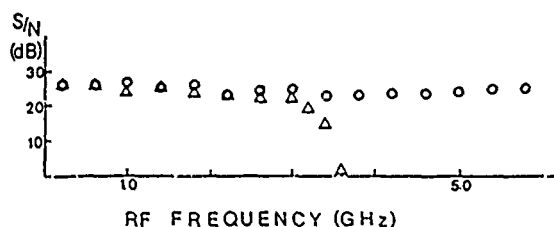


FIG.3 - Signal to noise ratio vs. microwave frequency

When we consider the junction and the microwave at frequency  $\omega_\mu$ , the correction have to be compared with the 3<sup>rd</sup> order tunnelling, responsible of the term  $\cos(\omega_\mu \pm \Delta\omega_L)$ . The temperature of the junction in this case is  $T = T_0 + \Delta T_L + \Delta T_\mu$ . Neglecting the faster terms, the part in  $T^2$  will have a significant term proportional to  $\cos(2\omega_\mu \pm \Delta\omega_L) \text{sgn}(eV)$ , where  $V$  is the potential difference between the metals; for  $eV \gg kT$  and  $|V\omega_\mu(t)| \gg |V\Delta\omega_L(t)|$  it results  $\text{sgn}(eV) \approx \omega_\mu$  and so the complete correction will be proportional to:

$$A(\phi_0)(\Delta T_\mu * \Delta T_L) \cos(\omega_\mu \pm \Delta\omega_L) \text{ or } A(\phi_0)(\Delta T_\mu * \Delta T_L) \cos(3\omega_\mu \pm \Delta\omega_L)$$

where  $A(\Phi)$  is a function of the equilibrium chemical potential of the two metals  $\Phi$ , and is much smaller than in the previous case, but the same is for tunnelling efficiency.

In all these cases the effect is worth noting at low impedance because

1) the dissipated power is greater when the antenna coupling is optimum (for the microwaves at low impedance 50  $\Omega$ )

2) supposing  $V$  constant in the diode mechanism the dissipated power  $P = V^2/R$  is greater for  $1/R$  smaller and the superposition of the thermal and tunnelling effects results the shape of fig.3.

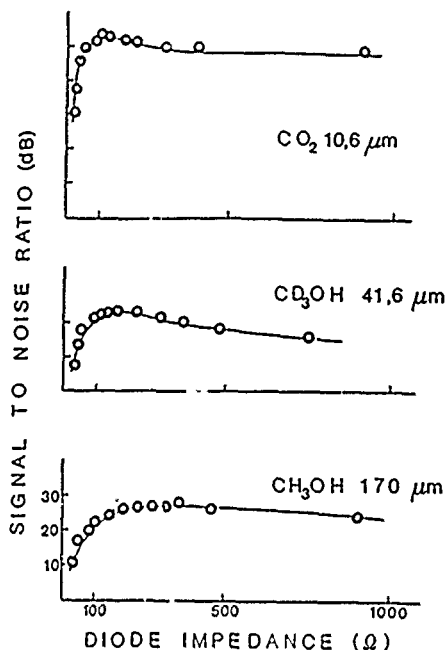


FIG.4 - Signal to noise ratio vs. diode impedance for different wavelengths.

#### REFERENCES

- (1) - K.M. Evenson, D.A. Jennings and F.R. Petersen: J.Phys. (Paris) Vol.42, pp.C8-C47: 1981
- (2) - K.M. Evenson, M. Inguscio and D.A. Jennings: J. Appl. Phys. Vol.57 pp.956-960: 1985
- (3) - A. Sanchez, C.F. Davis, D.C. Liu, and A. Javan: J. Appl. Phys. Vol.49, pp.5270-5277: 1978
- (4) - H.V. Vol.Daniel, M. Steiner and H. Walther: Appl. Phys. Vol.25, pp.7-12: 1981
- (5) - M. Inguscio, N. Ioli, A. Moretti, F. Strumia and F. D'Amato: Appl. Phys. Vol. B 40, pp.165-169: 1986
- (6) - J.H. Bechtel: J. Appl. Phys. Vol.46 pp.1585-1593: 1975
- (7) - M.A. Ordal, R.J. Bell, R.W. Alexander Jr., L.L. Long and M.R. Querry: Appl. Opt. Vol.26, pp.744-752: 1987
- (8) - J.G. Simmons, J. Appl. Phys. Vol.35, pp.2472-2481: 1964

## PRELIMINARY RESULTS FROM THE UNIVERSITY OF MARYLAND X-BAND GYROKLYSTRON\*

W. Lawson, J. Calame, M. Skopec, D. Welsh, B. Hogan, M. Naimann, J. Renbaum, and M.E. Read†  
Laboratory for Plasma Research  
University Maryland, College Park, MD 20742

### INTRODUCTION

The results of scaling studies for the next generation of linear electron-positron colliders have demonstrated a need for high pulse power, high efficiency, high gain microwave (8-30 GHz) amplifiers.<sup>1</sup> As part of our investigation into the suitability of gyrotron amplifiers for this application, we are constructing an X-band gyroklystron which is predicted to achieve a peak power of 30-50 MW.<sup>2</sup> A schematic of the major subsystems of the initial two-cavity gyroklystron is shown in Fig. 1. The modulator supplies a 500 kV, 200 A, 1.5  $\mu$ s pulse with an intermediate voltage to a double-anode Magnetron Injection Gun (MIG). The MIG generates a rotating beam which passes through the circuit after being adiabatically compressed. The beam's phase-space distribution is modulated by a microwave signal which is injected into the first cavity. Energy is extracted axially through a coupling aperture in the second cavity and travels through a nonlinear waveguide to a half-wavelength output window. The beam expands in the decreasing magnetic field and impinges on a 35 cm section of the output waveguide. A directional coupler and water calorimeter (not shown) measure the peak and average microwave power. The nominal parameters of this configuration are listed in Table I and details of these subsystems are discussed below.

### ELECTRON BEAM GENERATION

The 500 kV voltage pulse is generated by a line-type modulator, which is similar in design to those used by the SLAC klystrons.<sup>3</sup> Four pulse-forming networks (PFNs) in parallel are resonantly charged on command to 46 kV and are switched through two thyratrons into a 1:22 pulse transformer which provides the required potential.

The electron gun is in the double anode MIG configuration.<sup>4</sup> Key dimensions of the gun design are listed in Table II and the simulated beam properties at 160 A are listed in Table I. The peak electric field at the cathode tip is less than 90 kV/cm. The stated cathode loading is 40 percent of the space charge limiting current. The axial velocity spread remains below  $\Delta v_z = 10\%$  for a current range from 120 A to 240 A. The gun has been constructed by Varian Associates and has passed its acceptance test. A 1  $\mu$ s, 500 kV pulse was applied to the MIG when the cathode was cold. The voltage pulse and charging current are shown in Fig. 2. Without the axial magnetic field, a 143 kV pulse was applied with the cathode hot ( $\sim 950^\circ\text{C}$ ) and the control anode grounded. The resulting 120 A pulse represents a current density of 4.2 A/cm<sup>2</sup> and is shown in Fig. 3. The current was limited by the impedance of the modulator. Preparations are being made to draw the full power beam.

### MICROWAVE CIRCUIT

The low Q of the input cavity is realized by two thin, carbon-impregnated dielectric annuli located on either cavity

end at the outer radius. We have shown both experimentally and analytically that we can achieve the required frequency and Q with such absorbers. The input power is supplied by a 3 $\mu$ s, 100 kW magnetron and is injected into the cavity through a single aperture on the outer wall ( $r = \text{constant}$ ) of the cavity.

Because of constraints on beam power, the drift tubes are not cutoff to the TE<sub>11</sub>, TE<sub>21</sub> and TM<sub>01</sub> modes at 10 GHz. Theoretical calculations<sup>5</sup> indicated that metal drift tubes will produce spurious oscillations with these modes, so a drift tube consisting of alternate washers of metal and lossy dielectric is being considered. Again, both experimental and analytic results indicate the viability of this technique. Our first tube will utilize six rings of magnesia with a 1% concentration of silicon carbide. The dielectric rings are 22% wider than the alternating metal rings and have a depth of 1.6 cm. The drift tube provides 117 dB isolation for the TE<sub>01</sub> mode and more than 16 dB isolation for the uncutoff modes at 10 GHz.

The output cavity Q is essentially diffractive and is sufficiently larger than the minimum Q so that a simple coupling iris can be used for the endfire system. Cold testing has confirmed both the frequency and Q predicted by an analytic mode expansion code for a variety of configurations.

The vacuum vessel between the output cavity and the output window doubles as the microwave and beam transport system. A nonlinear taper brings the waveguide radius from 2.60 cm to the beam dump radius of 3.57 cm in 19.5 cm. The smaller radius can support only the lowest circular electric mode (TE<sub>01</sub>) at 10 GHz while the larger radius can support the lowest two circular modes. To minimize mode conversion, a raised cosine radius is used. An approximate analytic solution predicts the mode conversion to be less than  $1.1 \times 10^4$  percent in power.

Computer simulations of the beam with and without microwave interaction show that the beam is dumped fairly uniformly by the decaying magnetic field over a 35 cm distance in the beam dump. This keeps the instantaneous temperature rise below 20° and the average temperature rise sufficiently low to allow modest water cooling. A dumping magnet prevents the few high energy electrons from reaching the output window. The vacuum port consists of a stainless steel tube with 150 holes distributed uniformly in angle and axial position to provide sufficient conductance with minimal microwave interference.

A second nonlinear taper is used after the beam dump to bring the radius to 6.35 cm. At that radius, four circular electric modes can propagate, but the ideal mode conversion to all other modes is still less than 0.002 percent in power. A half wavelength BeO window, brazed to a stainless steel flange via a Kovar ring, provides the vacuum-to-air interface.

### DIAGNOSTICS

There will be several standard external current transformers in conjunction with current breaks to measure the instantaneous beam current at several locations along the system. Capacitive probes, which consist of four 90° sections and a sapphire insulator, will be used at several locations in an initial

\*Work supported by U.S. Department of Energy.

† Physical Sciences, Inc., Alexandria, VA.

beam test to measure total beam density and relative location. The two diagnostics jointly will give an estimate of the average axial velocity and (along with the beam voltage) will provide information about the average velocity ratio.

The microwave diagnostics consist of both peak and average power measurements. The peak power measurement involves a mode selective directional coupler combined with a crystal detector. Because the circular guide is highly overmoded and the rectangular guide is not, the phase velocity of the two waves cannot be the same and two sets of coupling holes are required. The 50 dB,  $TE_{01}^0 \rightarrow TE_{10}^0$  coupler is designed to maximize  $TE_{01}^0$  directivity (-83 dB) and minimize  $TE_{11}^0$  coupling (-75 dB). The detector will provide the signal envelope and, with proper calibration, an estimate of the peak power. A non-resonant water calorimeter will provide the average power measurement and a check of the peak power measurement. Water is circulated between two 19.5 cm long stycast cones to maximize sensitivity. The thickness is adjusted to guarantee a minimum attenuation of 28 dB.

### REFERENCES

1. M. Reiser, D. Chernin, W. Lawson, and A. Mondelli, 3rd Workshop of the INFN Eloisatron Project, Erice, Italy, May 1987.
2. K.R. Chu, V.L. Granatstein, P.E. Latham, W. Lawson, and C.D. Striffler, IEEE Trans. Plasma Sci., **PS-13**, pp. 424-434, 1985.
3. *The Stanford Two Mile Accelerator*, edited by R.B. Neal (W.A. Benjamin, Inc., New York, 1968), p. 411.
4. W. Lawson, J. Calame, V.L. Granatstein, G.S. Park, C.D. Striffler, and J. Neilson, Int. J. Electronics, **61**, pp. 969-984, 1986.
5. J. Neilson, P.E. Latham, M. Caplan, W. Lawson, submitted to IEEE Trans. Microwave Theory Tech., August, 1988.

Table 1.  
The Two Cavity Gyrokystron Parameters.

Beam	Power $P_0$	80 MW
	Voltage $V_0$	500 kV
	Velocity ratio $v_{\perp}/v_z$	1.5
	Velocity spread $\Delta v_z$	7.0%
	Larmor radius $r_L$	0.43 cm
	Center radius $r_g$	0.79 cm
	Guiding spread $\Delta r_g$	0.20 cm
	Axial field $B_0$	0.565 T
Circuit	Mode (both cavities)	$TE_{011}$
	Peak Efficiency	33%
	Gain	27 dB
Input Cavity	Radius	4.50 cm
	Length	1.53 cm
	Q	225
Drift Tube	Injected Power	50 kW
	Radius	1.50 cm
	Length	9.00 cm
Output Cavity	Radius	2.11 cm
	Length	2.38 cm
	Q	165
Aperture	Radius	1.50 cm
	Length	0.33 cm
Output Guide	Radius	2.60 cm

Table 2.  
80 MW MIG Electrode Specifications.

Cathode Radius $r_c$	0.0228 m
Emitter Strip Width $\ell_s$	0.020 m
Cathode-Control Anode Gap $d_{ac}$	0.0613 m
Cathode Half Angle $\phi_c$	20°
Compression Ratio $f_m$	12
Control Anode Voltage $V_a$	143 kV
Emission Current Density $J_c$ (Uniform)	5.61 A/cm <sup>2</sup>

### GYROKLYSTRON SCHEMATIC

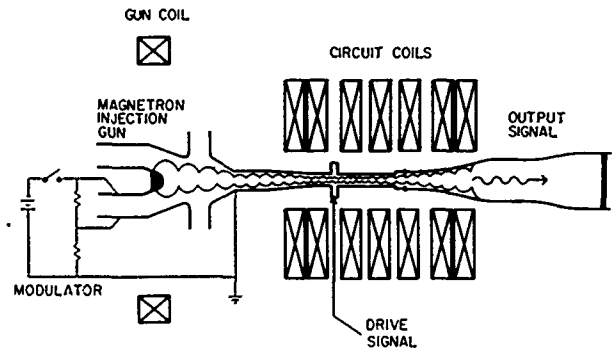


Figure 1.  
The University of Maryland 30 MW Gyrokystron.

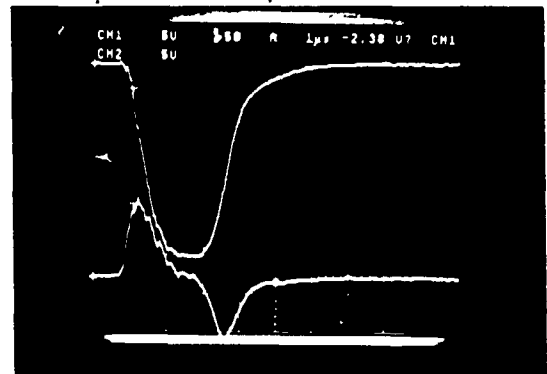


Figure 2.  
A typical modulator pulse. The upper trace shows the voltage pulse with 100 kV/div. The lower trace shows the charging current with 50 A/div. The sweep rate is 1 μs/div.

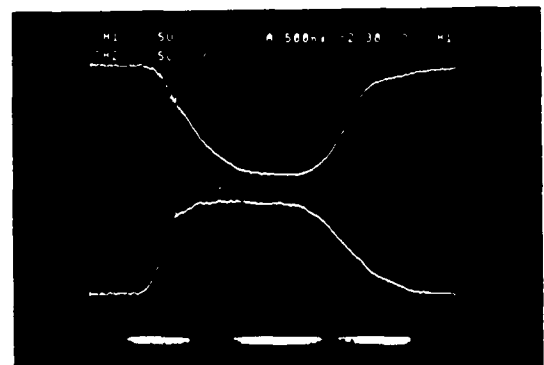


Figure 3.  
The current pulse. The upper trace shows the voltage pulse in 50 kV/div and the lower trace shows the current pulse in 50 A/div. The sweep rate is 500 ns/div.

# Mode Interaction in a Primed Gyrotron

A. H. McCurdy\* and C. M. Armstrong

Electronics Science and Technology Division, Code 6840  
Naval Research Laboratory, Washington, D.C. 20375-5000

## ABSTRACT

Multi-mode operation in an overmoded gyrotron experiment is compared with the predictions of a quasi-linear theory. The different regimes of strong and weak coupling of the  $TE_{111}$  mode to other modes are determined. The effects of transit time broadening and beam perpendicular energy change on mode competition is investigated. The start-up of oscillation is studied in both primed and unprimed conditions. Finally the theory is used to predict the degree of mode control obtained by a driving signal of given amplitude.

## INTRODUCTION

It has been experimentally shown that a priming (injected external) signal can stabilize an overmoded oscillator under certain conditions.<sup>1</sup> Stable, single-mode operation is important because it enables the gyrotron to attain its maximum efficiency.

The priming phenomenon requires only a small, (often on the order of 100 times the noise power level), external signal near the frequency of the desired mode. The signal must be present during the buildup of oscillation and has no effect during the oscillation steady state. The method should be applicable to all cases of strongly coupled modes, since the primed mode has the potential to suppress the others. Weakly coupled modes may not be controlled unless the effective growth rates of the competing modes can be driven negative.

## EXPERIMENTAL

A schematic of the gyrotron oscillator is shown in Fig. 1. The oscillator operated with 4  $\mu$ s pulses at 22 KeV. The operating frequency is near 5.0 GHz and the power levels are typically 100 W. The cavity is a cylindrical waveguide about 10 free space wavelengths in length. The transverse dimension of the cavity is such that only  $TE_{11}$  modes can be supported. Power is coupled out of the cavity by means of the probes in the side walls. There are a total of 16 capacitively coupled probes and two inductively coupled ones (see insert in Fig. 1).

Because the cavity ends are closed and the cavity is long, many axial TE modes may be excited. The axial mode spacing is about .5% of the fundamental resonant frequency. The electron transit time broadening is about three times the modal frequency spacing. The mode in which the gyrotron operates is determined in two ways. One is

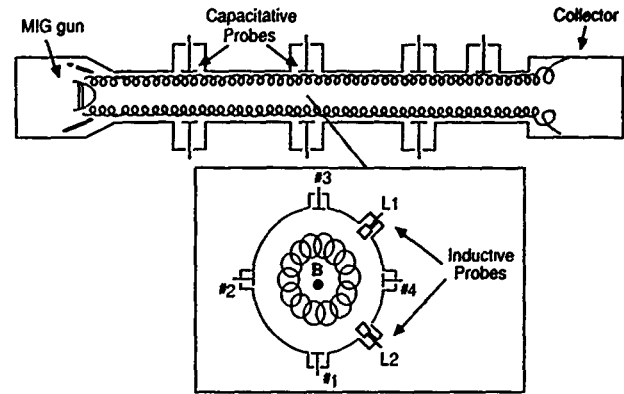


Fig. 1 Configuration of the gyrotron with insert showing midplane probe geometry.

via tunable bandpass filters in the gyrotron output line. In this way the mode is identified by relating the oscillation frequency to cold cavity resonant frequencies. The other way is to spatially resolve the electric field profile of the mode along the cavity axis using the various probes.

It is found that the intensity of mode competition is quite sensitive to changes in the electron axial and perpendicular velocity. Two different effects can be responsible. One is that the gain of the different modes depends on the perpendicular velocity. The other is the dependence of electron transit time on the axial velocity. The transit time sets the gain bandwidth of the electron cyclotron maser mechanism. We have measured the dependence of mode competition on these two sources. The mean axial electron velocity is measured by using the capacitively coupled probes in an electrostatic mode. The perpendicular velocity is changed by varying the voltage split between the mod-anode and cathode of the magnetron injection gun.

The temporal evolution of two competing modes is studied during the early period of oscillation buildup. The modes are separated by passing the gyrotron output rf through tuned bandpass filters. From crystal diode traces of the rf power as a function of time, the mode dynamics can be determined.

The gyrotron is primed by launching an external rf signal through two adjacent probes at the cavity midplane. The phase shift between probes is maintained at ninety degrees so that a pure right-hand circularly polarized wave is excited in the gyrotron cavity. This polarization has been found to couple optimally to the gyrating electrons. The gyrotron output is monitored through another probe. Fig. 2 shows the results of an experiment where a  $TE_{111}$  mode is primed from a pure  $TE_{112}$  mode. It can be seen in this case that virtually



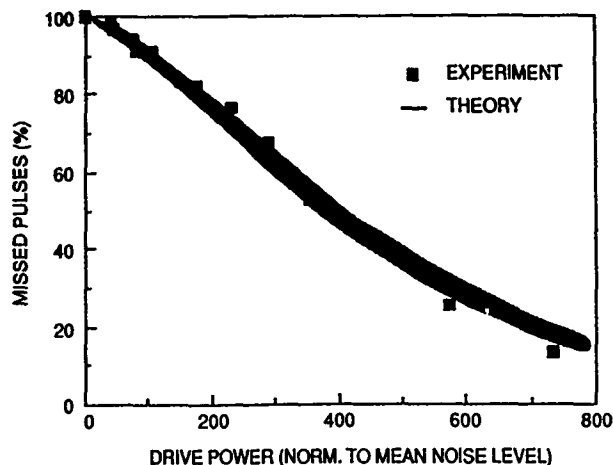


Fig. 2 Degree of mode control achieved with a given drive power. Shading shows standard deviation in predicted control.

pure mode operation can be obtained at a drive-to-noise power ratio of  $\sim 1000$ . (noise power has been determined to be  $\sim .3 \mu W$ ).

### THEORY

The mode evolution is modelled using the quasi-linear theory of Lamb.<sup>2</sup> By averaging over the radiation period and beam transit time, the slowly evolving mode amplitudes and phases can be described. In the case where the modes are not equally spaced in frequency and the cavity resonance widths are much less than the intermode frequency spacing, the mode interaction can be described in terms of equations independent of the phases:

$$\begin{aligned} \frac{dP_1}{dt} &= P_1 (\alpha_1 - \beta_1 P_1 - \theta_{12} P_2) \\ \frac{dP_2}{dt} &= P_2 (\alpha_2 - \beta_2 P_2 - \theta_{21} P_1) \end{aligned} \quad (1)$$

for two modes. Only terms up to second order in the power have been retained on the right hand side of the rate equations. The coefficients have been approximated for the gyrotron in ref [3]. The evolution of two strongly coupled modes using experimentally determined coefficients is shown in Fig. 3. There are stable steady states at  $(P_1=P_1^{sat}, P_2=0)$  and  $(P_1=0, P_2^{sat})$ . Because the linear growth rates are unequal, the separatrix (separating the trajectories approaching  $P_1^{sat}$  and those approaching  $P_2^{sat}$ ) has the equation:

$$P_2 = C P_1^{\alpha_2/\alpha_1}$$

near the origin. Here the constant C is a function of all the coefficients of Eqs. 1. This constant is found by solving Eqs.1 numerically.

To model the priming experiment, the initial condition for Eqs. 1 is modified to include the external signal. Thus the primed mode has an initial condition of drive signal plus noise while the unprimed mode grows from noise only. It has been found that the

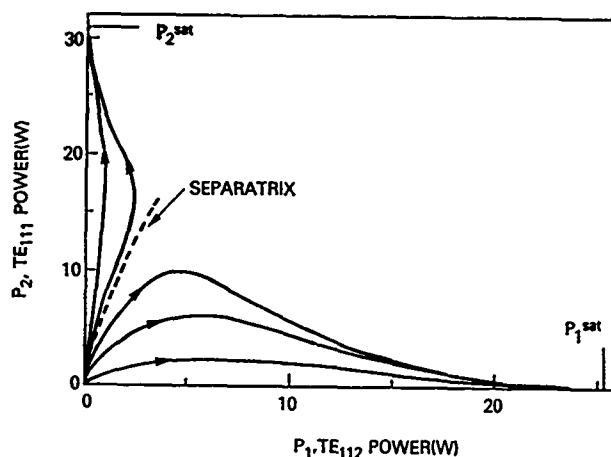


Fig. 3 Mode evolution for competition between  $TE_{112}$  (mode 1) and  $TE_{111}$  (mode 2).

preoscillation noise amplitude in a gyrotron varies from pulse-to-pulse according to a Rayleigh distribution,  $P_R$ .<sup>4</sup> The fraction of missed pulses, (pulses not in the primed mode), can be determined from:

$$F = \int_{x=0}^{\infty} dx P_{RINV}(x) \int_{n=0}^{\infty} dn P_D(n) S(x)$$

where  $P_D$  is the probability distribution of the amplitude of the driven mode<sup>4</sup> and  $S(x)$  is the equation of the separatrix (in terms of amplitude rather than power).  $P_{RINV}$  is the probability of the noise amplitude, A, being between  $x$  and  $x+dx$  where  $x=1/A$ .

The line in Fig. 2 shows the predicted mean missed pulse fraction using the experimental parameters. The shaded region indicates the area within one standard deviation of the mean. It is clear that the experimental points all fall near this region. We thus have confidence that the experiment is correctly modelled.

### CONCLUSION

It is found that the quasi-linear approximation allows accurate prediction of the different regimes of mode interaction and correctly models the phenomenon of mode selection by an external signal. This theory then can be used to evaluate the benefits to be obtained from a priming signal in a given multi-mode oscillator.

Sponsored by the Offices of Naval Technology and Naval Research.

(\*) Omega-P, Inc., 2008 Yale Station, New Haven, CT 06520.

- (1) A.H. McCurdy and C.M. Armstrong, in Conference Digest of the Twelfth International Conference on Infrared and Millimeter Waves, Lake Buena Vista, Florida (1987) p. 202.
- (2) W.E. Lamb, Jr., Phys. Rev. A **134**, 1429 (1964).
- (3) G.S. Nusinovich, Int. J. Electron. **51**, 457 (1981).
- (4) A.H. McCurdy and C.M. Armstrong, IEEE Trans. Microwave Theory Tech. **36**, 891 (1988).

# 85 GHz $TE_{1,3}$ PHASE-LOCKED GYROKLYSTRON OSCILLATOR EXPERIMENT

J. M. Burke\*, M. A. Czarnaski\*\*, R. P. Fischer, M. Giangrave,  
A. W. Fliflet, and W. M. Manheimer

High Power Electromagnetic Radiation Branch, Code 4742  
Plasma Physics Division, Naval Research Laboratory  
Washington, D.C. 20375-5000

## ABSTRACT

We are studying the phase-locking of highly overmoded gyrotrons using a moderate power ( $\sim 50$  kW) 85 GHz two cavity  $TE_{1,3}$  gyrokystron oscillator. The latest experimental and theoretical results will be presented.

## INTRODUCTION

Phase-locked gyrokystron oscillators offer many advantages over conventional gyrotrons including better mode control resulting in higher efficiency operation, narrow band frequency tunability and the possibility of coherently combining many sources for ultra-high power applications. We are studying phase-locking of overmoded gyrotrons at moderate power levels ( $\sim 50$  kW) in an 85 GHz two cavity  $TE_{1,3}$  gyrokystron oscillator configuration as shown in Figure 1. The key issues to be addressed by the experiment are:

- Maximization of the phase-locking bandwidth
- Phase sensitivity to beam parameters
- Stray oscillations in the drift region

The design parameters of the 85 GHz  $TE_{1,3}$  phase-locked gyrokystron oscillator experiment being constructed at the Naval Research Laboratory are given in Table I.

Table I

### Phase-Locked Gyrokystron Oscillator Design Parameters

Frequency	85 GHz
Operating Mode	$TE_{1,3}$
Beam Voltage	70 kV
Beam Current	< 6 Amps
Output Cavity Q	$\sim 2000$
Input Cavity Q	$\sim 500$
Isolation	> 45 dB
Output Power	$\sim 50,000$ Watts
Input Power	< 500 Watts

## DESIGN CONSIDERATIONS

The principal issue to be confronted in the design of a highly overmoded phase-locked gyrokystron oscillator is the maximization of the phase-locking bandwidth. The major design problems that must be considered in maximizing the phase-locking bandwidth are:

- Self-oscillation of the input cavity
- Input cavity minimum length limitations due to mode conversion at cavity tapers
- Input cavity minimum length limitations due to cutoff waveguide diameter

- Isolation of the input and output cavities due to mode conversion at cavity tapers
- Coupling to the proper mode in the input cavity
- Drift length limitation due to beam spread

The design of an experiment has been completed which self-consistently addresses all of the design constraints discussed above.

## EXPERIMENT

We are now performing experiments on the phase-locked gyrokystron oscillator experimental apparatus with the input cavity section removed. The purpose of this experiment is to observe the operation of the tunable output cavity without being concerned about self-oscillation of the input cavity.

Three input cavity designs with different cavity lengths and slot angles have been fabricated. The cavities are being cold tested to determine their exact resonance frequencies and cavity Q's and to optimize the diameter of their coupling apertures.

Upon completion of the tunable oscillator experiment and cold testing of the input cavities the phase-locked gyrokystron oscillator experiment will be assembled and testing will begin.

## CONCLUSIONS

A highly overmoded phase-locked gyrokystron oscillator experiment has been designed and is being built at the Naval Research Laboratory. A preliminary experiment is being performed to investigate the operation of the tunable output cavity without the complications associated with the input cavity. Three different input cavity designs have been fabricated and are being cold tested. Upon completion of the tunable oscillator experiment the phase-locked gyrokystron oscillator experiment will be assembled and tested.

## ACKNOWLEDGMENTS

This work was supported by the Office of Naval Research and by the Office of Innovative Science and Technology, Strategic Defense Initiative Organization under a contract administered by the Harry Diamond Laboratories.

\*) Burke Technologies, Inc., San Diego, CA 92111.

\*\*) JAYCOR, Inc., Vienna, VA 22180.

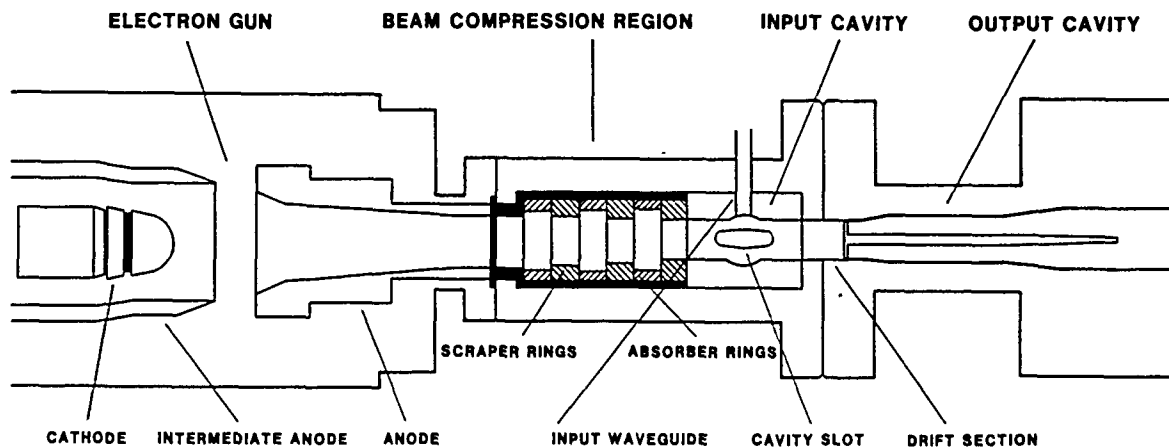


Figure 1  
The NRL 85 GHz  $TE_{1,3}$  Phase-Locked Gyrokystron Oscillator Experiment

# FEASIBILITY OF 30 GHz GYROKLYSTRON AMPLIFIERS FOR DRIVING LINEAR SUPERCOLLIDERS

V.L. Granatstein, W. Lawson, and P.E. Latham  
Laboratory for Plasma Research  
University of Maryland, College Park, MD 20742

## ABSTRACT

Operation of linear supercolliders at a frequency above the 10-17 GHz range which is usually considered would have a number of important advantages including reduced accelerator average power consumption ( $\sim \omega^{-1}$ ), and more compact microwave pulse compression circuits. Frequency scaling of gyroklystrons is especially advantageous since peak power rating of these tubes scales as  $\omega^{-1}$ , while peak power per feed required by the accelerator scales as  $\omega^{-2}$ . Gyroklystron amplifiers which would be suitable for driving linear supercolliders at 30 GHz are being designed.

## INTRODUCTION

Microwave power tube requirements for future rf linear supercolliders depends critically on the rf frequency. A fair comparison of design options at different frequencies may be arrived at by specifying that the accelerating gradient and the luminosity be held fixed.<sup>1</sup> Then, if one assumes that the number of particles per bunch and the group velocity of the microwaves in the accelerating structure are also independent of rf frequency, the following frequency scaling of the accelerator parameters may be deduced<sup>2</sup>:

$$\text{peak power per feed, } P_f \sim \omega^{-2} \quad (1)$$

$$\text{filling time, } T_{\text{fill}} \sim \omega^{-3/2} \quad (2)$$

$$\text{number of feeds, } N_f \sim \omega^{3/2} \quad (3)$$

$$\text{rf pulse repetition frequency, } f_r \sim \omega \quad (4)$$

The average rf power required to drive the accelerator is

$$P_{AV} = P_f T_{\text{fill}} N_f f_r \quad (5)$$

and using the proportionalities in Eqs. (1) - (4), it is seen that

$$P_{AV} \sim \omega^{-1} \quad (6)$$

Thus, considerations of accelerator average power, consumption, favour going to a higher rf frequency with  $\sim 30$  GHz being the upper limit imposed by wake field effects in the accelerator and by manufacturing considerations.

## MICROWAVE TUBE REQUIREMENTS

Accelerator rf parameters have been calculated at an rf frequency of 18.62 GHz for an accelerating gradient of 83 MV/m corresponding to a length of 6 km for a 0.5 TeV accelerator or 12 km for a 0.5 TeV on 0.5 TeV  $e^-e^+$  collider.<sup>1</sup> In Table I, these accelerator parameters are displayed together with parameters at frequencies of 10 GHz and 30 GHz which have been obtained by scaling according to the relationships in eqs. (1) - (6).

To relate the accelerator parameters to required microwave tube specifications, one needs to specify both the number of accelerator feeds which will be driven by a single tube and the characteristics of any rf pulse compression circuit which will be used between each tube and the accelerator. Assuming four feeds per tube, and  $8\times$  pulse compressing with 90% compression efficiency, specifications of microwave tubes required at various frequencies have been calculated and are displayed

in Table II.

Table I. Accelerator Parameters at Various RF Frequencies  
(Accelerating gradient 83 MV/m, luminosity  $10^{33} \text{ cm}^{-2} \text{ sec}^{-1}$ ,  $4.2 \times 10^9$  particles per bunch, 10 bunches per rf pulse,  $P_{AV}$  calculated for  $2 \times 0.5$  TeV)

	10 GHz	18.62 GHz	30 GHz
$P_f (\sim \omega^{-2})$	361 MW	104 MW	56 MW
$T_{\text{fill}} (\sim \omega^{-3/2})$	153 ns	61 ns	30 ns
$N_f (\sim \omega^{3/2})$	2467	5454	11,142
$f_r (\sim \omega)$	81 Hz	150 Hz	242 Hz
$P_{AV} (\sim \omega^{-1})$	186 MW	100 MW	62 MW

Table II. Microwave Tube Parameters

	10 GHz	18.62 GHz	30 GHz
$P_p$	200 MW	58 MW	31 MW
$\tau$	1.23 $\mu\text{s}$	0.49 $\mu\text{s}$	0.24 $\mu\text{s}$
PRF	81 Hz	150 Hz	242 Hz
No. of Tubes	617	1364	2785

There is, of course, interest in making the collider as short as possible which for a fixed final energy requires increasing the accelerating gradient,  $E_a$ . However, it should be noted that peak power per feed depends on  $E_a$  as

$$P_f \sim E_a^2 \lambda^2 \quad (7)$$

Thus, halving the length of a collider would increase the peak power per feed by a factor of 4. Extrapolating from Table II, it is seen that to achieve a 0.5 TeV on 0.5 TeV  $e^-e^+$  collider with an overall length of 6 km would require 10 GHz tubes with peak power of 800 MW or 30 GHz tubes with peak power of 124 MW.

Several development programs are underway on amplifiers in the 7-10 GHz frequency band (nominally in X-band), and with pulse duration near 1  $\mu\text{s}$ . At SLAC, a "conventional" klystron at 8.6 GHz has produced peak output power of 24 MW with 43% efficiency; the tube voltage was 340 kV. The SLAC program plans to proceed to development of a 100 MW X-band klystron at higher voltage; 100 MW was estimated to be the limit possible in a klystron with a 1  $\mu\text{s}$  pulse width.<sup>4</sup>

A second type of microwave amplifier, the gyrocon or rotating beam amplifier<sup>5</sup>, is being developed at the Institute of Nuclear Physics (INP) in Novosibirsk. It was recently reported<sup>6</sup> that a 7 GHz gyrocon is producing an output power of 60 MW with 25% efficiency; tube voltage was at the uncomfortably high level of 1.2 MV. Future development efforts will attempt to develop a gyrocon with similar peak power but with an operating frequency of 14 GHz.

Yet a third approach is the gyroklystron amplifier under development at the University of Maryland. This amplifier is expected to produce 30-50 MW of peak output power at 10

GHz with tube voltage of 500 kV. A design concept for an X-band gyrokystron operating at a peak power of 180 MW with a tube voltage of 800 kV has also been presented.<sup>8</sup>

It appears that in all of these approaches, difficulty will be encountered in producing the levels of peak power specified in the first column of Table II for operation in X-band.

### SCALING LAWS FOR GYROKLYSTRONS

Gyrokystrons employ magnetron injection guns (MIGs) as their source of electrons. The scaling of the power of electron beams produced by MIGs will thus determine the microwave power level produced by the gyrokystron assuming that circuits can be designed which are equally effective in correcting beam energy to microwave energy.

An approximate set of analytic equations describing electron motion in a MIG<sup>9</sup> can be used to describe the scaling of electron beam power,  $P_b$ , with variation in salient beam parameters. A useful approximate relationship is given by

$$P_b \sim \left(\frac{r_{g0}}{r_{L0}}\right) E_c \omega^{-1} V_0^2 \left[1 + \left(1 + \frac{eV_0}{mc^2}\right)^{-1}\right] \quad (8)$$

where the subscript 0 denotes quantities in the gyrokystron circuit region, and  $r_{g0}$  is the electron beam guiding radius,  $r_{L0}$  is the Larmor radius,  $eV_0$  is the electron energy, and  $E_c$  is the electric field at the cathode.

In writing eq. (8), it is assumed that  $V_0$ ,  $\omega$ ,  $E_c$  and  $(r_{g0}/r_{L0})$  are independent quantities. Also, the following quantities are assumed to hold constant: (1) the ratio of perpendicular to parallel velocity ( $v_{\perp 0}/v_{\parallel 0}$ ); (2) the cathode slant angle; (3) the spread in guiding center radius normalized to  $r_{L0}$ ; (4) the cathode current density normalized to the space charge limited current density; and, (5) the spacing between the cathode and final anode normalized to the Larmor radius at the cathode.

A MIG has been designed<sup>8</sup> for a 10 GHz gyrokystron that would operate with a peak output power of 180 MW. Compared with the 40 MW gyrotron currently under development, the higher design value of output power was achieved by increasing tube voltage from 500 kV to 800 kV and by doubling the guiding center radius (see eq. (8)). It was proposed that a  $TE_{01}$  co-axial circuit be used in place of the  $TE_{01}$  hollow cylindrical circuit to accommodate the larger electron beam while avoiding aggravation of the problem of spurious modes. The parameters of the two 10 GHz gyrokystron designs are compared in Table III.

Also in Table III, we present parameters for 500 kV and 800 kV gyrokystrons scaled to operating frequency of 30 GHz. The beam power has been scaled according to the frequency Table III. Estimated Gyrokystron Performance. (Efficiency has been calculated as 45% for the gyrokystron with the 500 kV, 80 MW beam, and is assumed to be at the same value for the other designs.  $P_b$  is electron beam power.  $P_p$  is microwave output power.)

	10 GHz		30 GHz	
	500 kV	800 kV	500 kV	800 kV
Voltage, $V_0$	500 kV	800 kV	500 kV	800 kV
$P_b$	80-100 MW	400 MW	30 MW	133 MW
Efficiency	45%	45%	45%	45%
$P_p$	36-45 MW	180 MW	13 MW	60 MW
Mode	$TE_{01}^+$	$TE_{01}^+$	$TE_{01}^+$	$TE_{01}^+$

dependent in eq. (8). Note especially that for a frequency of 30 GHz and a tube voltage of 800 kV, the achievable peak output power is estimated to be 60 MW, about twice as large as the requirement listed in Table II for achieving an accelerating gradient of 83 MV/m. This added factor of 2 would be used to increase the accelerating gradient to 117 MV/m and decrease the number of tubes required from 2785 to 1975. Alternatively, one would keep the accelerating gradient at 83 MV/m and use one 30 GHz, 60 MW to drive eight ports which would reduce the number of tubes required to 1393.

### SUMMARY

The peak power per feed in a linear collider scales inversely as frequency squared; i.e.,  $P_f \sim \omega^{-2}$ . On the other hand, while the peak power capability of gyrokystrons scales inversely as the first power of frequency; i.e.,  $P_p \sim \omega^{-1}$ . Thus, if gyrokystrons are used to drive a linear collider the number of feeds driven by a single tube,  $n_f$ , will scale as  $n_f \sim \frac{P_p}{P_f} \sim \omega$  and the number of gyrokystron tubes,  $N_t$ , required for a collider of given final energy will scale as  $N_t \sim \frac{N_f}{n_f} \sim \omega^{1/2}$ . This relatively modest increase in the number of tubes (and in the capital costs) as rf frequency is increased may well be an acceptable trade-off to gain the lower value of average power consumption which scales as  $\omega^{-1}$ .

Because of the considerations above, the University of Maryland is beginning to conduct detailed design studies of gyrokystrons at 30 GHz in the  $K_a$ -band pointing to a possible follow-on to their 10 GHz gyrokystron development. It has also been pointed out that the choice of 30 GHz may have other advantages; for example, pulse compression circuitry will be more compact at the higher rf frequency.<sup>10</sup> Finally, we note that short pulse,  $K_a$ -band, gyrotron oscillators have recently been operated with output power of 100 MW for a tube voltage of 600 kV and 200 MW for a tube voltage of 1.2 MV; these results give encouragement that one can successfully develop gyrotron amplifiers (gyrokystrons) with similar output power.

### REFERENCES

1. D. Chernin and A. Mondelli, "Design Constraints for  $e^+e^-$  Linear Supercolliders," Science Applications International Corp. report no. PTN88-002, Aug. 1, 1988.
2. A. Mondelli, private discussions.
3. Z. D. Farkas, IEEE Trans. MTT-34, 1036 (1986).
4. M.A. Allen, "RF Power Sources," SLAC-PUB-4646, May 1988.
5. G. I. Budker, U.S. Patent No. 3,885,193 (1975); also see I.A. Shenhkhtman, Radio Eng. and Elec. Phys. 9, 103 (1983).
6. V.E. Balakin (INP), oral presentation at the Workshop on "Physics of Linear Colliders", Capri, June 13-17, 1988.
7. V.L. Granatstein et al., IEEE Trans. NS-32, 2957 (1985); also, W. Lawson, et al., "Preliminary Results from the University of Maryland X-Band Gyrokystron," in these proceedings.
8. A. Mondelli, et al., "RF frequency scaling and gyrokystron sources for linear supercolliders," Proc. 3rd Workshop of the INFN Eloisatron Project (Erice, May 1987).
9. J.M. Baird and W. Lawson, Int. J. Electron. 61, 953 (1986); also W. Lawson, IEEE PS-16, 290 (1988).
10. Z. D. Farkas, private communication.
11. S. Gold, et al., IEEE Trans. PS-13, 374 (1985); also, S. Gold, private communication.

## AC SPACE CHARGE EFFECTS IN MODERATELY RELATIVISTIC GYROTRONS

P.E. Latham and T.M. Antonsen, Jr.  
Laboratory for Plasma Research  
University of Maryland, College Park, MD 20742

## ABSTRACT

The effects of AC space charge fields are included in the analysis of moderately relativistic gyrotrons. We adopt the slow time scale formalism developed by Antonsen, Manheimer and Levush [1] to describe the transverse self-fields while the electromagnetic fields are given by the cold cavity modes. Using a partially self consistent numerical code [2], simulations of multi-cavity gyrokystron amplifiers were performed. Preliminary studies indicate that there is an increase in *both* gain and efficiency.

We believe that this increase in efficiency can be attributed to the relative weakness of the AC space charge field compared to the electromagnetic field: in high voltage, high current devices the interaction length is short so that the cavities do not self-oscillate. Because of the short interaction length the electromagnetic field must be large, making the AC space charge

field small in comparison. Thus, in relativistic gyrotrons the AC space charge field is not strong enough to significantly disrupt the particle orbits.

A detailed numerical and theoretical study of both gyrotron oscillators and amplifiers is underway, and results will be presented at the conference.

## References

- [1] T.M. Antonsen, Jr., W.M. Manheimer, and B. Levush, "Effects of AC and DC Transverse Self-Fields in Gyrotrons," *Int. J. Electron.* **61**, 823 (1986).
- [2] K.R. Chu, V.L. Granatstein, P.E. Latham, W. Lawson, and C.D. Striffler, "A 30-MW Gyrokystron-Amplifier Design for High-Energy Linear Accelerators," *IEEE Trans. Plasma Sci.*, **PS-13**, 424 (1985).

# Calculation of Limiting Current in Connection with Application to Gyrotron

Han S. Uhm and Celso Grebogi

Naval Surface Warfare Center  
White Oak, Silver Spring, MD 20903-5000

## ABSTRACT

The space charge limiting current in a wave cavity and in presence of electromagnetic fields is calculated in connection with application to high power gyrotrons. It is found that the ponderomotive energy alters radically the build up of beam electrostatic energy. As a consequence, the limiting current can be greatly decreased or enhanced depending on whether the ponderomotive energy is positive or negative, respectively. This effect can be observed experimentally and it has important practical consequences for present high-current particle beam experiments.

## INTRODUCTION

The propagation of high-current particle beams in a wave cavity or drift tube and in presence of electromagnetic fields is a basic theoretical problem in physics. The latest revival in its theoretical interest reflects the recent experimental advances in high-power free-electron lasers, gyrotrons, collective-ion accelerations, and so on. A basic phenomena occurring in these experiments is that as the beam current is increased, an electrostatic potential depression builds up due to the beam's self space charge field and as a result, the beam current cannot be increased beyond a certain amount. This is the limiting current of the cavity and it is a theoretical limit on the current, and hence on the power, in devices like gyrotrons. The problem of limiting current of particle beams in a cavity has been addressed before, but not taking into account the presence of electromagnetic fields in the cavity. However, in the present charged particle beam experiments, the particle beam does propagate in the presence of electromagnetic fields which changes fundamentally the physical situation. The oscillating electromagnetic field creates a quasistatic ponderomotive potential<sup>1</sup> which affects the particle motion, and hence, the limiting current. The static magnetic field, on the other hand, introduces resonances due to the coupling of the gyromotion with the particle motion in the electromagnetic wave field. Again, the limiting current calculations should reflect this occurrence. The inclusion of all these issues results in a more complete and realistic treatment of the limiting current problem applicable to present experimental situations.

The practical consequence of this work is that experimentalists will have at hand the right behaviour and value of the limiting current for their experiments, which, typically, can be considerably different from the value found without considering the electromagnetic fields in the cavity. We find that the combined effects resulting from the oscillating electromagnetic field and the static magnetic field can greatly decrease or enhance the limiting current

depending on whether the ponderomotive energy is positive or negative, respectively. Our calculations show that we can obtain, say, an order of magnitude reduction in the limiting current of a 100kV relativistic electron beam using only modest electromagnetic fields, and consequently, a decrease in power produced by, say, a gyrotron. Physically, this occurs because a positive ponderomotive energy of some appropriate cavity mode enhances the beam space charge electrostatic energy. Alternatively, we can think that the positive ponderomotive energy reduces the potential energy associated with the beam accelerating system. This is reflected as a decrease in the beam kinetic energy with a consequent decrease in the current that is able to propagate through the cavity.

## THEORETICAL MODEL

To derive the limiting current, we impose the following energy conservation condition for the relativistic beam:

$$K \equiv (r - 1) mc^2 + e\phi + K_2 = (r_0 - 1) mc^2 \equiv e\phi_c, \quad (1)$$

where  $\phi_c$  is the potential of the accelerating system and  $K_2$  is the ponderomotive Hamiltonian. The left-hand side of Eq. (1) is the particle guiding center Hamiltonian  $K$  which is the total particle beam energy inside the wave cavity. Here we are using the notation of Refs. 1 and 2. The Hamiltonian  $K(R, \mu, U_\parallel)$  results from an averaging over the

gyromotion and fast oscillations due to the waveguide electromagnetic fields. Both averages were done<sup>1,2</sup> using Lie transforms resulting in a Hamiltonian containing only the slow effects on the guiding center. The averaged dynamical variables have the following meaning: The first variable  $R$  is the radial position of the guiding center, where  $R = 0$  is the center of the waveguide. The next variable  $\mu$  is the magnetic moment and is related to the perpendicular guiding center drift  $U_\perp$  through  $\mu = mU_\perp^2/2B$ , where  $B$  includes the external magnetic field, and the longitudinal and azimuthal self-fields. Finally,  $U_\parallel = v$  is the parallel world velocity of the guiding center, where the relativistic factor is defined as

$$r = \left(1 + \frac{2\mu B}{mc^2} + \frac{U_\parallel^2}{c^2}\right)^{1/2}.$$

In Eq. (1), the term  $(r - 1) mc^2$  is the kinetic energy of the beam particle,  $e\phi(R)$  is the potential energy which, in this case, is the beam space charge electrostatic energy, and  $K_2(R, \mu, U_\parallel)$  is the ponderomotive Hamiltonian, which, being velocity-dependent, is a generalization of the ponderomotive potential. We see from Eq. (1) that a positive ponderomotive energy  $K_2$

enhances the potential energy  $e\phi$  while a negative  $K_2$  counterbalances  $e\phi$ . Alternatively, we can think of  $K_2$  as reducing or enhancing  $e\phi$ , the accelerating potential. It is possible to show that when the ponderomotive energy is included in the calculation of the limiting current, the maximum energy depression of the function  $e\phi(R) + K_2(R, \nu, U)$  still occurs at  $R = 0$  for solid beams and at  $R = R_a$  where  $R_a$  is the inner beam radius, for hollow beams as in the case when  $K_2 = 0$ .

To illustrate how this formalism works, we choose the  $TE_{11}$  mode for the oscillating electromagnetic field, since the maximum electromagnetic field occurs at the center of the beam, for a solid beam, and the  $TE_{01}$  mode, since the maximum electromagnetic field can be set at the inner beam radius, for a hollow beam. These are the beam radial positions where the beam electrostatic energy build up is maximum. The derivation of the expression for the relativistic ponderomotive Hamiltonian for magnetized particles is rather involved. In Ref. 1, a general formula for the ponderomotive Hamiltonian was obtained. In that derivation, it was allowed for arbitrary  $k\rho, E_\perp/E_\parallel, \omega/\Omega, k_\parallel/k, v/c < 1$ , polarization, and for slowly growing and spatially modulated waves, where  $\omega$  and  $k$  are the mode frequency and wavenumber, respectively, and where  $\Omega = eB/mc$ . However, in this work we need particular expressions for the ponderomotive Hamiltonian corresponding to  $k\rho \ll 1$ , and to  $TE_{01}$  and  $TE_{11}$  modes. We know that the parallel components of both fields is zero while the perpendicular component is only azimuthal for the  $TE_{01}$  mode,  $|E_\perp|^2 = |E_\phi|^2$ , but azimuthal and radial for the  $TE_{11}$  mode,  $|E_\perp|^2 = |E_\phi|^2 + |E_R|^2$ . After some algebra we obtain the following expression for the ponderomotive Hamiltonian

$$K_2(R, \nu, V_\parallel) = \frac{e^2 |E_\perp|^2}{4m\omega^2} \frac{(\omega - k_\parallel V_\parallel)^2}{(\omega - k_\parallel V_\parallel)^2 - c^2}, \quad (2)$$

Substituting Eq. (2) into Eq. (1) and carrying out a straightforward calculation with the conservation principle of energy, we get

$$I(r) = I_G (r^2 - 1)^{1/2} \left( \frac{r_0}{r} - 1 + \frac{\kappa}{2 - r^2} \right), \quad (3)$$

where  $\kappa = e^2 |E_\perp|^2 / m^2 c^2 \omega^2$ ,  $\eta = eB/\omega mc$ ,

$r = (1 - U_\parallel^2/c^2)^{1/2}$ , and  $I_G$  is the Alfvén current with the geometric factor. To determine the limiting current, we maximize  $I(r)$  as given by Eq. (3). The maximization condition, for both geometries, is

$$r^3 - r_0 - \frac{\kappa r^3 (\eta^2 + r^2 - 2)}{(\eta^2 - r^2)^2} = 0. \quad (4)$$

The solution of Eq. (4) gives a root  $r = r^*$ , which, when substituted in Eq. (3), yields the limiting current  $I_{lim} = I(r^*)$ . We select the correct root  $r$  by knowing that, when  $\kappa = 0$ ,  $r$  reduces to the well-known standard limiting current calculation

without the rf waveguide mode. For this case, the maximization condition gives  $r^* = r_0^{1/3}$ , which implies, from Eq. (3), that

$$I_{lim}^{\kappa=0} = I_G (r_0^{2/3} - 1)^{3/2}. \quad (5)$$

To realize the extent to which the presence of electromagnetic fields in the wave cavity alters the limiting current, we solve Eqs. (4) and (3) numerically for typical parameters and plot the results in Figs. 1. In Fig. 1, we plot

$I_{lim}/I_{lim}^{\kappa=0}$  versus  $\kappa$ , for various  $\eta$  at fixed  $r_0 = 1.2$  (100kV electron beam). We vary  $\kappa$  between  $\kappa=0$ , when  $I_{lim}/I_{lim}^{\kappa=0} = 1$ , and  $\kappa=0.5$ , which corresponds to an oscillating electric field of amplitude  $E_\perp \approx 120\text{kV/cm}$  if  $\omega \approx 10^{10}$  rad/sec, well below the breakdown field. We observe that the electromagnetic fields in the wave cavity can increase ( $I_{lim}/I_{lim}^{\kappa=0} > 1$ ) or decrease ( $I_{lim}/I_{lim}^{\kappa=0} < 1$ ) the limiting current as compared with a cavity without fields in it. An increase occurs for  $\eta > 1$  (in fact,  $\eta > r$ , equivalently,  $\Omega > \omega$ ), which corresponds to a negative ponderomotive energy, while a positive ponderomotive energy ( $\eta < 1$ ) decreases the limiting current. For example, from the plot, for  $\kappa = 0.2$  and  $\eta = 1.7$  we obtain a 95% enhancement while for the same  $\kappa$  but for any  $\eta < 1$  there is a complete current cut-off in the cavity.

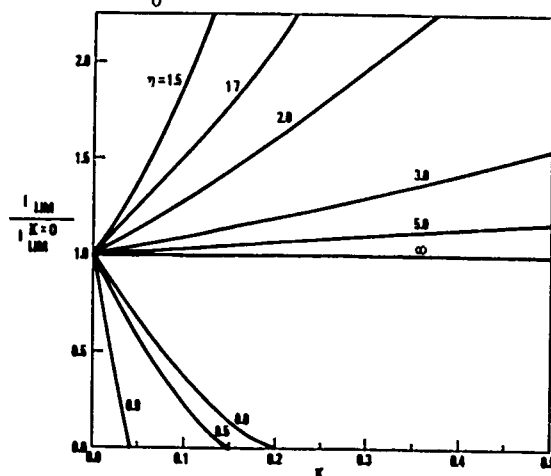
In conclusion, we developed a theory to treat the propagation of a charged particle beam in a wave cavity when electromagnetic fields are present. This physical situation is typical in present experiments. We find that the limiting current problem is modified considerably to account for these fields.

**ACKNOWLEDGEMENT.** This work was supported by the Independent Research Fund at NSWC.

1. C. Grebogi and R. G. Littlejohn, Phys. Fluids 27, 1996 (1984).
2. C. Grebogi and H. S. Uhm, Phys. Rev. A 34, 4083 (1986).

#### Figure Captions

Fig. 1 The ratio  $I_{lim}/I_{lim}^{\kappa=0}$  versus  $\kappa$  for various  $\eta$  and  $r_0 = 1.2$ .





# NONRADIATIVE SYMMETRICAL DIELECTRIC GRATING WAVEGUIDE FOR MMW DBR GUNN OSCILLATORS

Zong-Wen Li

Department of Radio Engineering  
South East University  
Nanjing, Jiangsu.  
The People's Republic of China

## ABSTRACT

In this paper a nonradiative symmetrical dielectric grating waveguide and its application to MMW DBR Gunn oscillator is presented. The width of symmetrical dielectric strips is selected carefully in order to avoid the leakage and resonance effect. A DBR oscillator has been designed and tested, Its power output is 70-100mW and frequency stability is better than  $10^{-6}$  at 40 GHz which is 10 times better than that of MMW DBR oscillator using the inverted strip dielectric waveguide(1).

## INTRODUCTION

The inverted strip dielectric waveguide (ISDG) is very useful for several passive and active integrated components at millimeter wave band.

The advantages of ISDG shown in Fig.1 over other transmission lines at millimeter wave band are: 1) relative large size which is easier to be fabricated, 2) low conductor loss due to less surface current, 3) ground plane serves as heat sink as well as a bias return for the solid-state diode mounted in the ISDG. 4) The bonding material is not required by means of the mechanical pressure, so the bonding loss is avoided. But ISDG as an open dielectric waveguide suffers from radiation especially caused by different discontinuities. The radiation loss is higher than that of image guide since ISDG belongs to a weakly guiding structure.

In order to reduce radiation loss an improved symmetrical structure of ISDG has been tried. It consists of two parallel ground planes, two dielectric strips and one dielectric slab as the guiding layer. It is a semiopen structure named as symmetric ISDG (SISDG) shown in Fig.2. The EMF energy is concentrated in the middle portion of line to propagate along z-axis, since  $\epsilon_2 > \epsilon_1$  and the lens effect of two strips. The fields decay exponentially along x-direction. From the edges of the strips it decays at least 10 dB per wavelength(2).

Furthermore in order to eliminate resonance and leakage effect the width of the strips, the guided wave mode and the separation b between two ground planes should be carefully selected. Then the SISDG may be become a nonradiative dielectric guiding structure. The outer configuration of SISDG is somewhat like H-guide but the inner construction is different from H-guide. So the radiation loss in the nonradiative SISDG is weaker than that in ISDG. The propagation characteristics and Bragg interaction property of a transmission line with symmetrical dielectric

grating structure were analyzed in (5,6).

## DBR OSCILLATOR

In Fig.2(a) if the regions I, II and III are individually infinitely wide in the x-direction each becomes a slab waveguide ( $\partial/\partial x = 0$ ) the propagation characteristics of the uniform SISDG can be computed by means of the transverse resonant principle and the EDC method. The dispersion curves (k- $\beta$  diagram) for the modes of space harmonics in the SISDG with symmetric periodical perturbation are also given (1,2). If the Bragg condition is satisfied

$$\Lambda = p\pi/\beta_s = p\lambda_{gs}/2 \quad (1)$$

in the Bragg reflection region, then the strong mode-coupling will take place due to the distributed interaction between the forward and the backward-wave along the z-direction over a considerable distance  $z=L \gg \lambda$ .

The coupling coefficient of the wave to wave interaction for  $TM_{so}$  mode is derived as

$$K_s = (\omega\mu/2) \int_{-a}^0 \frac{j a_p(x)}{n^2(x)} \left[ \mathcal{H}_y^{(s)}(x) \right]^2 dx$$

$$= \frac{4}{3} \frac{\pi^2 s^2 n_1^4 (n_1^2 - n_0^2)}{\lambda p n_2^3 (n_1^2 + n_0^2)} (a/t)^3 \cdot \left[ 2 - \frac{3\lambda/a}{2\pi(n_2^2 - n_1^2)^{1/2}} + \frac{3(\lambda/a)^2}{4\pi^2(n_2^2 - n_1^2)} \right] \quad (3)$$

By the phenomenon of surface wave stop-band based on the theory of coupled modes the Bragg reflection with both the frequency- and the mode-selectivities occurs and results in the positive feedback to the Gunn diode inserted in the guiding layer of the SISDG with the symmetric grating structure as shown in Fig.3. The oscillation has a spectral purity at millimeter wave band. When the feedback satisfies the oscillation conditions.

A MMW DBR oscillator based on the SISDG has been designed and tested. Its power output is between 70-100 mW at 40GHz as shown in Fig.4. The frequency stability in a period of 15 hours at room temperature is  $10^{-6}$  which is 10 times better than that of MMW DBR oscillator based on the ISDG.

A Gunn diode is mounted vertically in the guiding layer of SISDG. One of the ground planes serves as a heat sink. The vertical location of the diode can be adjusted for

maximum output power and designed frequency. The positive bias is fed to the diode from the top conducting plane through RF choke.

In order to improve the characteristics of DBR oscillator a horn transition between the metal waveguide and the SISDG has been designed and adjusted carefully. The notch depth of grating grooves must be taken as small as  $1/20$  and the width of symmetric dielectric strips must be chosen appropriately to eliminate leakage and resonance effect.

# REFERENCES

- (1) Li Zong-Wen, Zhang Wen-Sun "Design and performance of the millimeter wave DBR Gunn oscillators" IEEE MTT-S 1986 International Microwave Symp. Dig. pp531-534.
- (2) T. Itoh "Inverted strip dielectric waveguide for millimeter-wave integrated circuits" IEEE Trans. Vol. MTT-24 pp821-827 NOV. 1976.
- (3) S.T. Peng and A.A.Oliner "Guidance and leakage Properties of a class of Open Dielectric waveguide". IEEE Trans. Vol. MTT-29 pp843-869 Sep. 1981.
- (4) T. Yoneyama and S. Hishida "Nonradiative Dielectric Waveguide for millimeter wave Integrated Circuits " IEEE Trans Vol. MTT-29 pp1188-1192 Nov. 1981.
- (5) S.T. Peng "Theoretical analysis of dielectric grating for millimeter wave and integrated optics Applications" Microwave Research Institute Polytechnic Institute of New York 1980.
- (6) H. Shigesawa and M. Tsuji "A completely theoretical design method of dielectric image guide grating in the Boragg reflection region "IEEE Trans. Vol. MTT-34 pp420. April. 1986.

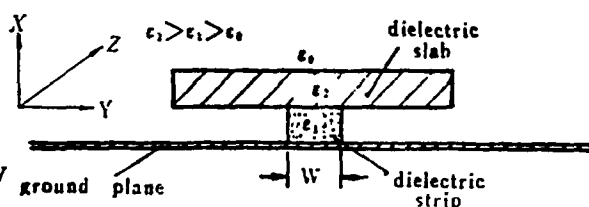
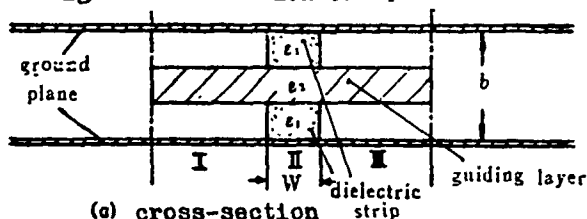
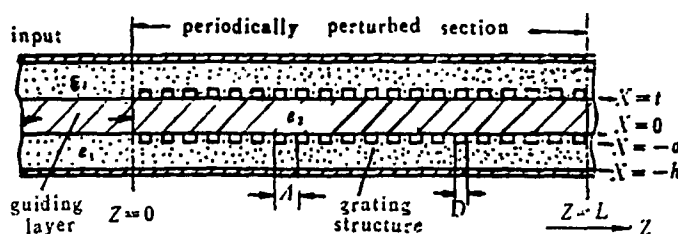


Fig.1 Cross-section of Open ISDG



(a) cross-section



(b) longitudinal section of Region II

Fig.2 Structure of Semiopen SISDG

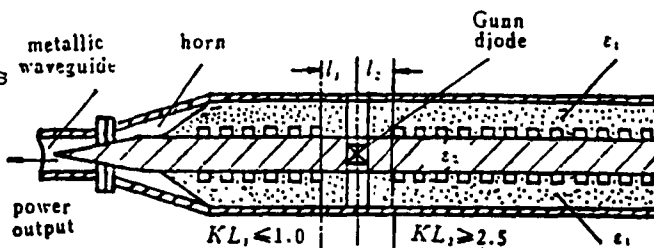


Fig.3. DBR Oscillator

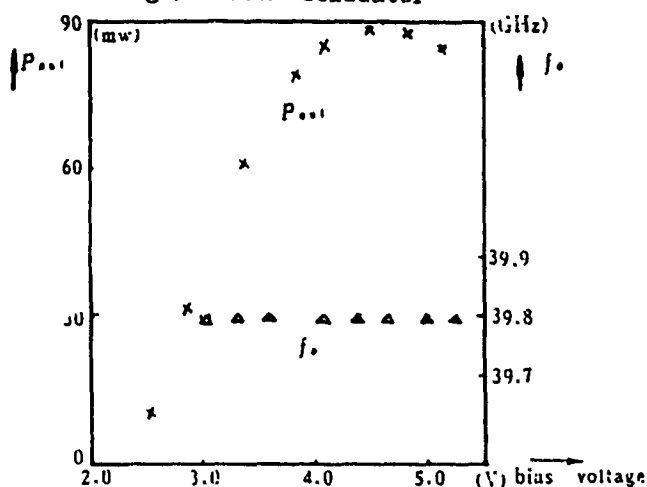


Fig.4 Measured data of DBR oscillator

# NUMERICAL RESULTS ON DIELECTRIC RESONATORS INSIDE WAVEGUIDES

A. Jöstingmeier and A.S. Omar

Technische Universität Hamburg-Harburg

## ABSTRACT

A mode matching method for the analysis of a cylindrical dielectric resonator with arbitrarily shaped cross-section inside a waveguide is presented which allows series expansions of the fields in the region of the dielectric insert and of the waveguide with different numbers of eigenmodes. Furthermore complex modes can simply be taken into account. Resonant frequencies above the cut-off frequency of the dominant mode of the waveguide are complex due to energy radiation. The method is verified for some special cases.

## I. INTRODUCTION

Recently the interest in theory and application of dielectric resonators has been risen. An overview of the state of the art has been well documented in [1]. In [2] - [5] the resonant frequencies, field distributions, and loss mechanisms of the special case of a circular cavity with a coaxial circular dielectric insert were examined. Unfortunately the authors used only the electric and magnetic eigenfunctions of the empty circular waveguide as test-functions which restricts their method to the case of equal numbers of eigenfunctions at both sides of the discontinuity at the end surfaces of the dielectric insert. This must be regarded as a severe handicap keeping in mind the relative convergence phenomenon, which is described in [6]. Moreover the orthogonality relation which is applied in our method uses the cross product of the electric and magnetic eigenfunctions. This is more suitable for taking complex modes into account [7].

The eigenmodes of the dielectric resonator can be divided into two classes. One class contains the eigenmodes with magnetic, the other class the eigenmodes with electric conducting wall symmetry in longitudinal direction. To simplify the calculations, only the magnetic conducting wall type eigenmodes are taken into account because the dominant eigenmode belongs to this class.

## II. METHOD OF ANALYSIS

Consider the structure shown in figure 1. The waveguide is infinitely extended and contains a coaxial dielectric cylinder of relative permittivity  $\epsilon_{r1}$  and length  $2L$  with arbitrarily shaped cross-section. The space between the dielectric insert and the perfectly conducting wall of the waveguide is filled with another dielectric of relative permittivity  $\epsilon_{r2}$ . For the transverse electric and magnetic fields in regions "a" and "b",  $\underline{E}_a$ ,  $\underline{E}_b$ ,  $\underline{H}_a$  and  $\underline{H}_b$ , respectively, we can set up:

$$\underline{E}_a = \lim_{N \rightarrow \infty} \sum_{i=1}^N \left[ a_i^+ \exp(-\gamma_{a,i} z) + a_i^- \exp(\gamma_{a,i} z) \right] \underline{e}_{a,i} \quad (1)$$

$$\underline{H}_a = \lim_{N \rightarrow \infty} \sum_{i=1}^N \left[ a_i^+ \exp(-\gamma_{a,i} z) - a_i^- \exp(\gamma_{a,i} z) \right] \underline{h}_{a,i} \quad (2)$$

$$\underline{E}_b = \lim_{M \rightarrow \infty} \sum_{j=1}^M \left[ b_j^+ \exp(-\gamma_{b,j} z) + b_j^- \exp(\gamma_{b,j} z) \right] \underline{e}_{b,j} \quad (3)$$

$$\underline{H}_b = \lim_{M \rightarrow \infty} \sum_{j=1}^M \left[ b_j^+ \exp(-\gamma_{b,j} z) - b_j^- \exp(\gamma_{b,j} z) \right] \underline{h}_{b,j} \quad (4)$$

$\underline{e}_{a,i}$ ,  $\underline{h}_{a,i}$ ,  $\gamma_{a,i}$ ,  $a_i^+$ ,  $a_i^-$ ,  $\underline{e}_{b,j}$ ,  $\underline{h}_{b,j}$ ,  $\gamma_{b,j}$ ,  $b_j^+$ , and  $b_j^-$  are the

transverse electric and magnetic eigenfields, the propagation constants, and the complex amplitudes of the forward and backward travelling eigenmodes in the regions "a" and "b", respectively. Now the following orthogonality relations are valid:

$$\int_S \left( \underline{e}_{a,i} \times \underline{h}_{a,j} \right) \cdot \underline{u}_z \, dS = \delta_{ij} P_i \quad (5)$$

$$\int_S \left( \underline{e}_{b,i} \times \underline{h}_{b,j} \right) \cdot \underline{u}_z \, dS = \delta_{ij} Q_i \quad (6)$$

$\underline{u}_z$  denotes the unit vector in z-direction,  $\delta_{ij}$  the Kronecker delta and S the common cross-section of regions "a" and "b". As was discussed in [7], the continuity of the transverse electric and magnetic fields across S yields an infinite set of linear equations:

$$[\lambda_p] \left[ \underline{a}^+ + \underline{a}^- \right] = [A] \left[ \underline{b}^+ + \underline{b}^- \right] \quad (7)$$

$$[\lambda_q] \left[ \underline{b}^+ - \underline{b}^- \right] = [A]^t \left[ \underline{a}^+ - \underline{a}^- \right] \quad (8)$$

The complex amplitudes  $a_i^+$ ,  $a_i^-$ ,  $b_j^+$ , and  $b_j^-$  are combined to form the column vectors  $\underline{a}^+$ ,  $\underline{a}^-$ ,  $\underline{b}^+$ , and  $\underline{b}^-$ , respectively. The elements of the matrices are given by:

$$[\lambda_p]_{ij} = \delta_{ij} P_i, \quad 1 \leq i, j \leq N \quad (9)$$

$$[\lambda_q]_{ij} = \delta_{ij} Q_i, \quad 1 \leq i, j \leq M \quad (10)$$

$$[A]_{ij} = \int_S \left( \underline{e}_{b,j} \times \underline{h}_{a,i} \right) \cdot \underline{u}_z \, dS, \quad 1 \leq i \leq N, 1 \leq j \leq M. \quad (11)$$

Independent of the number of eigenmodes in regions "a" and "b", M or N, respectively, the number of equations (M + N) equals the number of unknowns. So the relation between M and N is still a free parameter. To satisfy the boundary conditions on the magnetic conducting wall,  $\underline{b}^+$  and  $\underline{b}^-$  are related by the following matrix equation:

$$\underline{b}^- = [\lambda_s] \underline{b}^+ \quad (12)$$

The elements of the matrix  $[\lambda_s]$  are:

$$[\lambda_s]_{ij} = \delta_{ij} \exp(-2\gamma_{b,j} L), \quad 1 \leq i, j \leq M. \quad (13)$$

Substituting (12) into (7) and (8), the resonance condition can easily be derived:

$$\det \left( [\lambda_p] + [A] [\lambda_{\coth}] [\lambda_q]^{-1} [A]^t \right) = 0 \quad (14)$$

$[\lambda_{\coth}]$  contains the elements:

$$[\lambda_{\coth}]_{ij} = \delta_{ij} \coth(\gamma_{b,j} L), \quad 1 \leq j \leq M. \quad (15)$$

## III. RESULTS AND DISCUSSION

To justify the validity of the above analysis, we consider the cross-sections of the waveguide and the dielectric resonator as shown in figure 2. The calculations are simplified by taking only angularly independent TE-modes into account. Furthermore we restrict

ourselves to resonant frequencies of the dielectric resonator which are below the cut-off frequency of the  $TE_{01}$ -mode of the circular waveguide. This guarantees a purely real formulation of the resonance condition which reduces the computational efforts considerably. To evaluate the resonance condition we calculate the elements of the matrices  $[P]$ ,  $[Q]$ , and  $[A]$ . For  $[P]$  this can simply be done because the eigenmodes of the empty circular waveguide are well known. The calculation of  $[Q]$  and  $[A]$  needs the eigenmodes of a circular waveguide which is partially filled with a coaxial circular dielectric insert. They can be determined as described in [2]. All integrations required by the calculations of  $[P]$ ,  $[Q]$ , and  $[A]$  can be done analytically.

In practice the infinite matrices  $[P]$ ,  $[Q]$ , and  $[A]$  have to be truncated. That means that the numbers of eigenmodes in regions "a" and "b",  $N$  or  $M$ , respectively, are limited to finite values. Then a difficulty known as relative convergence problem arises in choosing the correct ratio  $N/M$ . As was demonstrated in [6] an incorrect choice of  $N/M$  can yield a totally wrong description of the discontinuity, even if  $N$  and  $M$  are very large. Considering [9],  $N$  and  $M$  have to be adjusted so that a "similarity balance" at both sides of the discontinuity is obtained. The mode coupling coefficients  $(A)_{ij}$  defined by (11) represent a measure of the degree of similarity between the  $i$ -th mode in region "a" and the  $j$ -th mode in region "b". The effect of the dielectric inhomogeneity on the field distribution becomes negligible if we take a sufficiently large number of higher-order eigenmodes into account. Hence the similarity between the eigenmodes at both sides of the discontinuity increases with the order of the eigenmodes. Therefore the relative convergence problem is solved here by the identity  $N = M$ .

Figure 3 shows the convergence of the normalized resonant wavenumbers  $k_0 = k_0 a_2$  for a typical case where  $k_0$  denotes the free-space wavenumber. The convergence is very good for  $M = N > 5$  although the relative permittivity of the dielectric insert  $\epsilon_{r1} = 20$  is considerably high.

Figure 4 presents the normalized resonant wavenumbers for some dielectric resonators with different relative permittivities as functions of the normalized radius of the resonators  $a_1 = a_1/a_2$ . The normalized length of the resonator  $L = L/a_2 = 0.5$  and the numbers of eigenmodes  $N = M = 20$  are kept constant in all cases.

The results obtained are now compared with those of [9]. Table 1 shows the good agreement. Maximum relative deviations between both methods are of the order of 1 %.

#### REFERENCES

- [1] Guillon, P., Proc. 15'th EuMC (Paris), 1985, pp. 77-86.
- [2] Zaki, K. and Atia, A., IEEE MTT, vol. MTT-31, 1983, pp. 1039-1045.
- [3] Zaki, K. and Chen, C., IEEE MTT, vol. MTT-33, 1985, pp. 1442-1447.
- [4] Zaki, K. and Chen, C., IEEE MTT, vol. MTT-33, 1985, pp. 1448-1452.
- [5] Zaki, K. and Chen, C., IEEE MTT, vol. MTT-34, 1986, pp. 815-824.
- [6] Mittra, R., Itoh, T. and Li, T., IEEE MTT, vol. MTT-20, 1972, pp. 96-104.
- [7] Omar, A. and Schünemann, K., IEEE MTT, vol. MTT-35, 1987, pp. 268-275.
- [8] Omar, A. and Schünemann, K., IEEE MTT, vol. MTT-33, 1985, pp. 765-770.

- [9] Omar, A. and Schünemann, K., IEEE MTT, vol. MTT-34, 1986, pp. 1508-1514.
- [10] De Smedt, R., AEU, Band 38, , 1984, pp. 113-120.

$\epsilon_{r1}$	$L$	$\bar{k}_0$ of [9]	$\bar{k}_0$	$\Delta/\bar{k}_0$
5	1.0000	1.940	1.941	0.05
5	0.7519	2.014	2.016	0.10
5	0.6000	2.042	2.049	-0.37
10	1.0000	1.379	1.380	0.07
10	0.7519	1.446	1.449	-0.21
10	0.5000	1.510	1.519	-0.64
10	0.2500	2.063	2.062	-2.76
20	1.0000	0.970	0.970	0.00
20	0.7519	1.020	1.020	0.01
20	0.5000	1.062	1.060	-0.23
20	0.2500	1.200	1.218	-0.99

Table 1:

Relative deviation  $\Delta$  of the calculated normalized resonant wavenumber  $\bar{k}_0$  from that of [9].

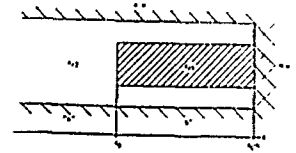


Figure 1:

Longitudinal section of the analysed structure.

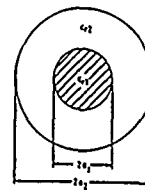


Figure 2:

Cross section of the analysed structure.

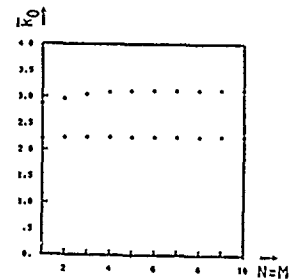


Figure 3:

The normalized wavenumber  $\bar{k}_0$  as a function of the number of eigenmodes in regions "a" and "b"  $N = M = 20$ .

Parameter:

$\epsilon_{r1} = 20$ ,  $\epsilon_{r2} = 1$ ,  $a_1 = 0.25$ ,  $L = 0.5$ .

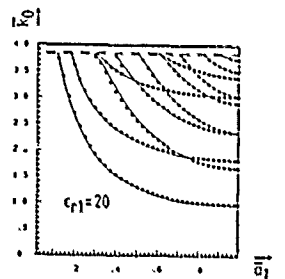
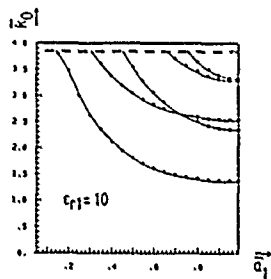
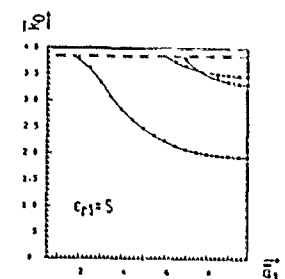
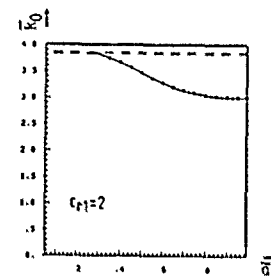


Figure 4:

The normalized resonant wavenumber  $\bar{k}_0$  as a function of the normalized radius of the dielectric resonator  $a_1$  with  $\epsilon_{r1}$  as a parameter. Other parameters:  $\epsilon_{r2} = 1$ ,  $L = 0.5$ ,  $N = M = 20$ .

## NON-LINEAR TLM MODELLING OF HIGH-FREQUENCY VARACTOR MULTIPLIERS AND HALVERS™

S.A.Kosmopoulos, W.J.R.Hoefer  
Lab. for Electromagnetics and  
Microwaves  
Dept. of Elect. Engineering  
Ottawa, Ont., Canada, K1N 6N5

A. Gagnon  
Telemus Electronic Systems Inc.  
310 Moodie Dr.  
Nepean, Ont.  
Canada, K2H 8G3

### ABSTRACT

A numerical modelling procedure in the time-domain of microstrip circuits containing non-linear devices such as varactor multipliers and halvers™, is described. The two-dimensional Transmission Line Matrix (TLM) method has been extended to model elements with voltage-dependent capacitance (varactors). Waveforms and spectra computed with the TLM model compare well with measured results.

### INTRODUCTION

At microwave and millimeter-wave frequencies, non-linear reactance is usually achieved by means of the depletion capacitance, in varactor diodes [1]. One of the simplest applications of varactors is harmonic generation or frequency multiplication. The varactor is excited at a frequency  $f_{in}$ , and power is delivered to a load at a frequency  $f_{out} = m f_{in}$  for some fixed integer  $m$ . Typical varactor multipliers deliver from a few watts of power at 10 GHz to several hundred milliwatts at 100 GHz [1][2]. Another more recent application of varactors involves subharmonic generation or frequency division. The varactor is excited at  $f_{in}$ , and power is delivered to the load at  $f_{in}/m$  for some fixed integer  $m$ . The case of  $m = 2$  (HALVER™) is of special interest and will be studied in the following.

Both frequency and time-domain methods are available for designing varactor circuits [2]. Their constituent parts are usually modelled by equivalent lumped elements and/or transmission line circuits. However, the circuit equivalent of components realized in planar and quasi-planar technology, and the interaction between the passive and active parts are difficult to evaluate. Particularly, in the case of circuits of high complexity, such as frequency halvers™, it is advantageous to model directly the field behavior, thus avoiding the ambiguity of impedance definitions and the difficulties of specifying equivalent circuit elements over a large frequency band.

In this study, we take a first step towards the TLM-modelling of microstrip varactor multipliers and dividers. Both the passive and the active components are modelled by two-dimensional TLM (2D-TLM) networks. In spite of the required simplifications, the results obtained with a 2D-TLM simulation agree very well with measurements, thus demonstrating the validity of our approach.

### NON-LINEAR 2D-TLM MODEL FOR A VARACTOR DIODE

The voltage-dependent capacitance of a varactor diode is given by [1]:

$$C_j(v) = \frac{C_j(0)}{(1 - \frac{v}{\phi_o})^\gamma} \quad (1)$$

where  $C_j(0)$  is the depletion capacitance at zero bias,  $\phi_o$  is the built-in potential ( $\phi_o \approx 0.7$  Volt for Si)[1], and  $\gamma$  is a constant depending on the type of the pn junction ( $\gamma = 1/2$  for an abrupt diode)[1]. The voltage  $v$  across the diode usually contains a dc-component and a time-dependent part:

$$v = V_{bias} + v(t) \quad (2)$$

For forward bias ( $0 \leq V_{bias} \leq \phi_o$ ) the varactor's diffusion capacitance ( $C_d$ ), derived directly by the continuity equation for a forward-biased pn junction [2], is becoming important as well. Thus, the varactor's equivalent circuit consists of the parallel combination of the depletion capacitance, the diffusion capacitance and the parasitic capacitance due to packaging ( $C_p$ ); i.e.

$$C_{TOT} = C_j + C_d + C_p \quad (3)$$

In the 2D-TLM simulation of a microstrip varactor multiplier or divider, the passive circuit part is modelled by a parallel-plate equivalent circuit which is easily represented by a standard 2D-TLM mesh. The non-linear device is represented by a rectangular submesh covering essentially the same area  $A$  as the packaged diode, as illustrated in Fig.1. This figure shows the simplest passive arrangement, consisting of a microstrip line terminated in a varactor diode.  $w'$  is the width of the equivalent parallel-plate waveguide model (Fig.1a). For convenience, the width of the representative submesh can be made equal to  $w'$  (Fig.1b), and its length  $L$  is then obtained from the condition that both areas should be identical:

$$L = \frac{D^2 \pi}{4w'} \quad (4)$$

The dielectric constant in the submesh must then be modified in such a way that its total capacitance ( $C_{TOT}$ ) is related to the capacitance of the equivalent microstrip section as follows:

$$\epsilon_r = \frac{\epsilon_{eff}}{\epsilon_{effm}} = \frac{C_{TOT}}{C_A} \quad (5)$$

where  $\epsilon_{eff}$  is the effective dielectric constant of the submesh representing the diode,  $\epsilon_{effm}$  is the effective dielectric constant of the microstrip section equal area  $A$ , and  $C_A$  is given by:

$$C_A = \frac{\epsilon_0 \epsilon_{effm} A}{h} \quad (6)$$

where  $h$  is the substrate thickness. The modification is accomplished by loading the nodes of the submesh with open-ended  $\frac{\Delta l}{2}$  stubs of non-linear characteristic admittance  $y_o$  given in [4]:

$$y_o = 4(\epsilon_r - 1) \quad (7)$$

Since the diode capacitance depends on the diode voltage which, in turn, is a function of time, the time-dependent stub admittance in the submesh can be written as:

$$y_o = 4 \left[ \frac{1}{C_A} \left( \frac{C_j(0)}{(1 - \frac{v(t)}{\phi_0})^\gamma} + C_d + C_p \right) - 1 \right] \quad (8)$$

This value is updated at each iteration, after the total voltage at each node has been computed.

## SIMULATION RESULTS

### a) Frequency Multiplier

In order to verify the validity of this model, a simple microstrip varactor multiplier was simulated and tested. It consisted of a 50 Ohm microstrip line with a shunt-connected varactor diode. A 3x14 submesh was used to simulate the diode. The output spectra computed and measured at the output port, are compared in Fig.2, indicating that the 2D-TLM method performs very well in analysing the behavior of this frequency multiplier. Note that the simulation does not include losses in the microstrip and in the device, which is considered to account for the difference in the magnitude of the second harmonic.

### b) Frequency Halver™

The lossless frequency halver™ simulated here, is a unbalanced frequency divider [3] consisting of a rectangular microstrip resonator and a pair of varactor diodes, simulated by a 7x14 submesh each. For  $V_{bias} = 0.24$  Volt and an even-mode sinusoidal excitation, the half-frequency appeared (odd-mode) at  $0.50684f_0$  (see Fig.3). The small error in the computed half-frequency is mostly due to the velocity error inherent in the TLM procedure [4].

## CONCLUSION

A 2D-TLM computer simulation of microstrip varactor multipliers and halvers™ has been carried out here. In contrast to other known methods, it allows a direct field analysis in the time-domain and is particularly promising for millimeter-wave components realized in planar and quasi-planar technology. Extension to 3D simulation and inclusion of losses are presently being studied in view of developing millimeter-wave halvers™ in E-plane configuration.

## REFERENCES

- [1] P.Penfield Jr., R.P.Rufuse "Varactor Applications" The M.I.T. Press, Cambridge, MA, 1962.
- [2] I.Bahl, P.Bhartia "Microwave Solid State Circuit Design" J.Wiley & Sons, New York, 1988.
- [3] A.Gagnon "Microstrip / Varactor Halvers™" Internal Report, Telemus Electronic Inc., Nepcan, Canada, 1987.
- [4] W.J.R.Hoefer "The Transmission-Line Matrix Method -Theory and Applications" IEEE Trans. on Micr. Theor. and Tech., Vol. MTT-33, No.10, Oct. 1985, pp 882-893.

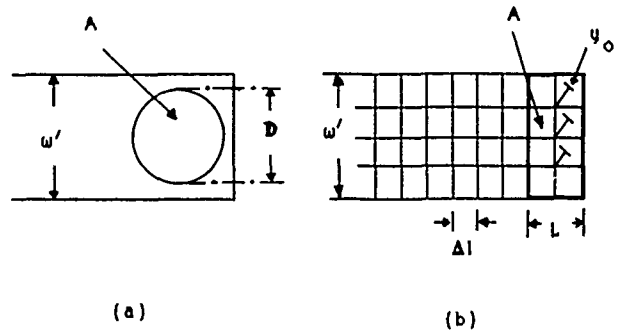


Fig.1: 2D-TLM simulation of microstrip varactor multiplier. a) Package diode in equivalent microstrip model. b) TLM mesh with stub-loaded submesh, simulating the diode.

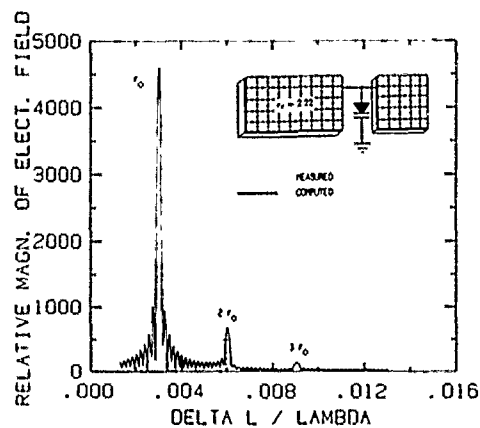


Fig.2: Multiplier's output spectra.

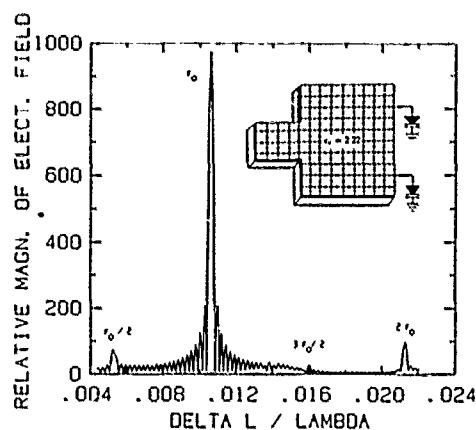


Fig.3: Halver's™ output spectra.

# NUMERICAL MODELING OF GENERALIZED MILLIMETER-WAVE TRANSMISSION MEDIA WITH FINITE ELEMENT AND TRANSMISSION LINE MATRIX METHODS

By

Eswarappa, G. Costache, and W. J. R. Hoefer

Laboratory for Electromagnetics and Microwaves, Dept of Electrical Engineering, Univ. of Ottawa, Ottawa, Ontario, Canada, K1N 6N5.

## I. Abstract

In this paper, a general finite element method as well as a graded-mesh TLM procedure for determining the dispersion characteristics, field distribution, pseudo-impedance and losses of generalized millimeter-wave transmission media are described. These methods cover arbitrary cross-sections and account for realistic features (finite metallization thickness, substrate mounting grooves etc.) that are often neglected in theoretical analysis. Dispersion characteristics and characteristic impedances obtained for dielectrically loaded ridged waveguides compare well with the available data. Conductor and dielectric losses are also computed for these structures. A modified finline structure called "ridged finline" is also analysed. The main advantage of this structure are its large monomode bandwidth and reduced dispersion. The cutoff frequencies of bilateral finlines in circular waveguides are also computed.

## II. Introduction

Knowledge of the propagation characteristic impedance, field distribution, monomode bandwidth, attenuation constant, power handling capacity etc., are necessary to design microwave and millimeter wave transmission systems. Various analytical methods have been used to obtain the design data, but cannot be applied to transmission lines of arbitrary cross-section, and the realistic features cannot be easily accounted for. On the other hand, powerful computing facilities make numerical methods such as finite element, transmission line matrix, and time domain finite difference techniques more attractive. Generalized programs based on these techniques can be applied to design novel structures with excellent electrical characteristics, or to study the second order effects on their characteristics. Furthermore, these methods are suitable for lookup table generation for CAD applications.

## III. Finite Element Method

### a. Theory

The finite element method is based on a variational principle. We have used variational expressions which are formulated in terms of the longitudinal components of the electric field,  $E_z$ , and the magnetic field,  $H_z$ , [1]. Consider a wave-guide of arbitrary shape uniform in the  $z$  direction, which consists of isotropic, lossless dielectric media. Assume propagation along the  $z$ -axis of the form  $\exp[j(\omega t - \beta z)]$  with longitudinal field components  $H_z$  and  $E_z$ . The functional to be made stationary is

$$\begin{aligned} \delta I = 0, \text{ where } I &= \sum_{p=1} I_p \quad (1) \\ &= \sum_{p=1} \iint \left( \tau_p |\nabla H_z^{(p)}|^2 + \gamma^2 \tau_p \frac{\epsilon_p}{\epsilon_0} \left[ \frac{1}{\gamma} \left( \frac{\epsilon_0}{\mu_0} \right)^{\frac{1}{2}} \nabla E_z^{(p)} \right]^2 \right. \\ &\quad \left. + 2\tau_p \epsilon_z \gamma^2 \cdot \left[ \frac{1}{\gamma} \left( \frac{\epsilon_0}{\mu_0} \right)^{\frac{1}{2}} \nabla E_z^{(p)} \times \nabla H_z^{(p)} \right] \right. \\ &\quad \left. - \left( \frac{\omega}{c} \right)^2 (1 - \gamma^2) \cdot \left\{ [H_z^{(p)}]^2 + \gamma^2 \frac{\epsilon_p}{\epsilon_0} \left[ \frac{1}{\gamma} \left( \frac{\epsilon_0}{\mu_0} \right)^{\frac{1}{2}} E_z^{(p)} \right]^2 \right\} \right) dx dy \quad (2) \end{aligned}$$

where  $\tau_i = (\gamma^2 - 1)/(\gamma^2 - \epsilon_i/\epsilon_0)$ ,  $\gamma = (\beta c)/\omega$ .

At the stationary point, the functional yields as its Euler equations and natural boundary conditions the Helmholtz equations and continuity conditions of the tangential electric and magnetic fields along the common interface for all regions comprising the waveguide cross-section.

The basis for generating the finite element algorithm are equation (1) with the functional (2). The initial step is the discretization of the waveguide cross-section into a large number of triangular subregions. The final form of (1) after discretization can be reduced to a generalized eigenvalue problem

$$[A]\{\theta\} - \left( \frac{\omega}{c} \right)^2 (1 - \gamma^2) [B]\{\theta\} = 0 \quad (3)$$

where  $\{\theta\}$  is an ordered array of the longitudinal electromagnetic nodal

variables. The parameter  $\gamma$  is present in the matrices  $[A]$  and  $[B]$ . For a given value of  $\gamma$ , the above generalized eigenvalue equation is solved for the frequency and the longitudinal electromagnetic nodal variables. All other field components can be derived from these longitudinal field values.

The perturbational approach is employed to solve for the attenuation constants due to dielectric and conductor losses

$$\alpha_d = \frac{P_d}{2P_{av}}, \alpha_c = \frac{P_c}{2P_{av}} \quad (4)$$

Where  $P_{av}$  is the time-average power flow along the line, and  $P_d$  and  $P_c$  are the time-average powers dissipated in the dielectric and conductors, respectively. The parameters  $P_{av}$ ,  $P_d$  and  $P_c$  have been expressed in terms of special finite element matrices, so that no numerical integration or differentiation is involved in the computation of losses. The most appropriate definition of characteristic impedance for our applications is given by

$$Z_0 = V^2/(2P_{av}) \quad (5)$$

### b. Application to Dielectrically loaded Ridge Waveguides and Finline

On the basis of this finite element procedure, a computer program has been developed. The computed values of the normalised propagation constant, characteristic impedance and losses of a dielectric loaded ridged waveguide are plotted in Figs. 1(a) and 1(b). The results for propagation constant and characteristic impedance compare well with the available data [2]. It is seen that with the dielectric present, the cutoff frequencies are reduced, and the propagation constants are increased.

The computed dispersion characteristics of the dominant and higher-order modes in a bilateral finline with and without the ridge are shown in Fig. 2. The results for zero ridge thickness are in good agreement with the results obtained using the Spectral Domain Method. With the ridge present, the cutoff frequency of the dominant mode is not affected, as expected. This is because the capacitive loading of the fins dominate that of the ridge. However, the effective dielectric constant comes down as the frequency increases. The cutoff frequency of the higher-order mode is increased considerably, thus increasing the monomode bandwidth. Note that in this operating range the dispersion is very small. The conductor loss is not expected to be highly influenced by the ridge. A PIN-diode attenuator in this technique has been realized successfully by AEG [3] with a bandwidth of two octaves.

## IV. 2D Graded Transmission Line Matrix Method

### a. Theory

Transmission Line Modeling is a time-domain numerical technique for solving networks and fields. The details of this method can be found in [4]. The 2-D TLM method can be applied to obtain the cutoff frequencies and field distributions of various modes of any transmission line of arbitrary cross-section. In this method, the propagation space is represented by a mesh of TEM transmission lines. The numerical calculation usually starts by exciting the mesh at specific points by voltage or current impulses and follows the propagation of these impulses over the mesh as they are scattered by the nodes and bounce back at boundaries.

To achieve time synchronism with least programming effort, square elements are used in the 2-D model. In planar and quasi-planar circuits, there are field singularities around the fin edges. To represent such complex fields we should have fine mesh deployment around the fin edges. If we use a conventional TLM model, large computer run time and memory are required. To reduce these, we can use a fine mesh around the fin edges, and a coarse mesh elsewhere. To achieve time synchronism in such cases, the algorithm must be modified. Such graded TLM models have been proposed by P. Saguet [5] and Al-Mukhtar [6]. The graded TLM model proposed in [5] is adopted for this study.

### b. Application to Bilateral Finline

The bilateral finlines in rectangular and circular waveguide enclosures are shown in Fig.3. The cutoff frequencies computed for a bilateral





## Polarization Conversions in Dielectric Strip Waveguides

Z. M. Lu, S. L. Wang, and S. T. Peng

New York Institute of Technology, Old Westbury, NY 11568

and

Howard Jenkinson

U. S. Army Armament Research, Development & Engineering Center  
Picatinny, NJ 07806-5000

## ABSTRACT

A new phenomenon of coflow coupling between guided waves of opposite polarizations has been discovered. Numerical results are given to illustrate the effect of polarization conversions on guiding characteristics of dielectric strip waveguides.

modified. Furthermore, in the region of strong coflow interaction, the polarization of a guided wave can not be clearly defined. Such a phenomenon could cause undesirable effects in a practical system where the mode purity is important. The practical implications of such a phenomenon remains to be explored.

## INTRODUCTION

Dielectric strip waveguides belong to the class of open structures with inhomogeneous dielectrics. Such a class of waveguides supports only hybrid modes, which can be considered as consisting of basic TE and TM polarized surface wave modes being coupled together. The guiding characteristics of dielectric strip structures have been analyzed in the literature[1,2,3,4] and many methods of analysis have been employed. In particular, the effective-dielectric-constant method is simple to use for obtaining approximate results. On the other hand, the method of mode matching provides an exact formulation of the dielectric strip waveguides as a rigorous electromagnetic boundary-value problem. Although it requires elaborate numerical computations which are rather time consuming, the exact formulation yields more accurate data on the waveguiding characteristics. More importantly, it is based on a set of basic guided modes which are well understood, so that any wave phenomenon taking place in a structure can be easily predicted and clearly explained. For example, by such a method, the phenomenon of energy leakage from a uniform dielectric waveguide had been predicted on the basis of polarization conversions[3,4] taking place at boundary discontinuities in a waveguide structure.

In this paper, we report a new phenomenon of strong coflow in a uniform dielectric waveguide. Such a new phenomenon arises also from the polarization conversions at the boundary discontinuities in a dielectric waveguide, as the phenomenon of energy leakage mentioned above. By a proper design of the waveguide, a TE and a TM mode may propagate at the same velocity along the structure. Due to the inherent process of polarization conversions, these two modes propagating in the same direction are coupled under the phase-matching condition. As a result, a strong coflow coupling occurs between guided waves of opposite polarizations, and the dispersion characteristics are thus substantially

## FORMULATION

The cross-sectional geometry of a rib waveguide is shown in Fig. 1. It consists of a cover region of infinite extent and with a dielectric constant  $\epsilon_c$ ; a guiding region consisting of a uniform film and a rectangular rib, with a dielectric constant  $\epsilon_r$ ; a uniform buffer layer with a dielectric constant  $\epsilon_b$ ; and finally a substrate region of infinite extent and with a dielectric constant  $\epsilon_s$ . Such a structure may be treated as a three dimensional boundary value problem to determine the propagation characteristics of waves guided by the structure. The boundary-value problem can be formulated in two steps: (1) determining a general solution for each constituent region that comprises the cross-section of the structure and (2) matching the continuity conditions of tangential electromagnetic fields on the boundaries separating the constituent regions. The guiding characteristics can then be determined by the eigenvalues of the boundary value problem.

For the class of structures under consideration, the cross-section of a waveguide may be divided into subregions in such a way that each constituent subregion can be taken as a planar waveguide by itself. Therefore, the general solution for each constituent region may be represented as a superposition of a complete set of mode (eigen) functions of the planar waveguide. Since the structure is of the open type, the complete set of mode functions consists of those of both discrete and continuous spectrum. The formulation of the boundary-value problem for the open structure generally leads to an integral equation from which the guiding characteristics of the waveguide are determined. Since the electromagnetic energy of a guided wave is mostly confined in the vicinity of the rib and decays exponentially in the vertical direction in the cover and substrate regions, we may place the dielectric waveguide inside a metallic parallel-plate waveguide. In doing so, the structure is open horizontally but closed

vertically, resulting in a semi-open dielectric waveguide. Such a structure may be divided laterally into subregions, each of which can be considered as a metallic parallel-plate waveguide filled with multilayer dielectrics. The modes of a parallel-plate waveguide are discrete and the boundary-value problem of the semi-open dielectric waveguide will then lead to a system of linear equations, instead of an integral equation in the case of an open structure. The system of linear equations is relatively easier to handle than the integral equation. Therefore, in this work, our analysis is based on the semi-open dielectric waveguides, instead of the open ones.

### NUMERICAL RESULTS

To illustrate the new phenomenon of coflow coupling, we have carried out an analysis of the structure shown in Fig. 1. By the simple method of effective dielectric constant, the approximate propagation characteristics of the waveguide are computed, and the results are shown in the form of dispersion curves in Fig. 2, with the structure parameters indicated therein. These numerical results are shown here for two purposes: (1) They provide an easy way of predicting the occurrence of the new phenomenon of strong coflow coupling. (2) They are used as initial values for the analysis by the elaborate method of mode matching. It is pointed out that in Fig. 2, the region enclosed by a box marked by A contains an intersection between dispersion curves for  $TE_{21}$  and  $TM_{11}$  modes which belong to the same symmetry configuration of the fields. Physically, these two modes may exist simultaneously in the same bisected structure, with almost equal phase constants. From the coupled-mode theory[1], a strong interaction may occur, if the two modes are coupled. As pointed out earlier, the modes of dielectric waveguides are hybrid and the polarization conversions taking place at boundary discontinuities of a dielectric waveguide provide the coupling mechanism that results in the previously unexpected phenomenon of strong interaction between the two modes. By the exact method of mode matching that includes both TE and TM surface waves, the propagation characteristics of the same waveguide are computed and the results are depicted in Fig. 3. It is observed that although numerically different, the general behaviors of the dispersion curves so obtained resemble those obtained by the simple effective dielectric constant method as shown in Fig. 2. However, in the region enclosed by Box A, the dispersion curves are changed markedly in character, as exhibited in the inset. In contrast to those in Fig. 2, the two dispersion curves do not cross over each other. This means physically that the two modes are strongly coupled and original designations of  $TE_{21}$  and  $TM_{11}$  modes lose their meanings in this region.

### ACKNOWLEDGEMENT

This work was sponsored by the U.S. Army Research Office under the Contract No. DAAL03-86-D-0001.

### REFERENCES

- [1] D. Marcuse, Theory of Dielectric Optical Waveguides (Academic Press, New York, 1974).
- [2] W.M. McLevige, T. Itoh and R. Mittra, *IEEE Trans. Microwave Theory and Tech.*, 1975, vol.MTT-23, pp.788-794.
- [3] S.T. Peng and A.A. Oliner, *IEEE Trans. Microwave Theory and Tech.*, 1981, vol.MTT-29, pp.843-855.
- [4] A.A. Oliner, S.T. Peng, Y.I. Hsu and S. Sanchez, *IEEE Trans. Microwave Theory and Tech.*, 1981, vol.MTT-29, pp.855-869.

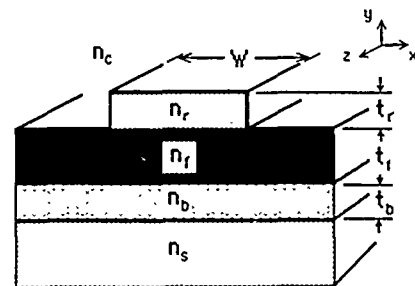


Fig. 1 Geometrical configuration of rib waveguide

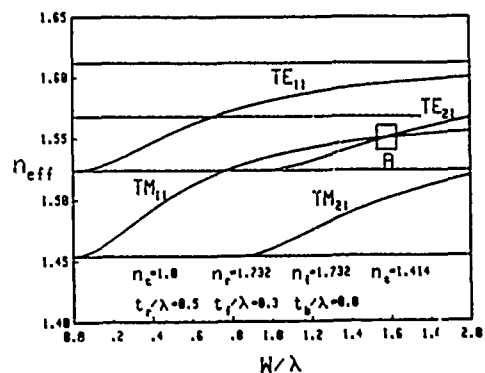


Fig. 2 Approximate Dispersion Curves

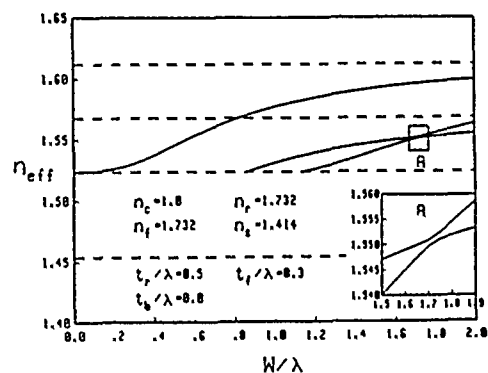


Fig. 3 Accurate Dispersion Curves Showing Coflow Coupling

# THE SOLUTION OF END EFFECTS OF SLOT LINE BY OPEN CAVITY METHOD

Yi-yuan Chen  
(Southeast University)  
Nanjing, P.R.China

## ABSTRACT

An open cavity model is developed to analyse end effects of slot line. Both the reactance and radiation effects are taken into account. The numerical results are compared with the published data.

## INTRODUCTION

Slot line is a transmission medium for microwave and millimeter wave applications. Much work has been done for its guided-wave properties [1] [2]. Only few work, however, has contributed to its discontinuities, such as step or shorted end. A slot line shorted end is needed to build slot line transitions or filters. As far back as 1973, experimental characteristics of a slot line shorted end have been reported by Knorr et al [3]. Until last year no theoretical work was presented. Yang et al [4] [5] reported their results about slot line shorted end by dynamic model.

In this paper an open cavity model is presented for analysing shorted end of slot line. The reactance and radiation effects are both considered. The numerical results show that the reactance parts of the end effects by cavity model agree well with that in [4] [5] and radiation resistances are different from that in [5].

## CAVITY MODEL FOR SLOT LINE SHORTED END

The slot line cavity is shown in Fig. 1, which is composed of a uniform slot line with two shorted ends. The equivalent circuit for it is shown in Fig. 2. As well known, resonance frequency of this cavity is a complex value, because of radiation losses, and can be denoted as

$$\omega = \omega_r + j\omega_i$$

where  $\omega_r$  is the oscillation frequency of the cavity.

$\omega_i$  stands for losses.

For a half-wave cavity the normalized equivalent reactance can be found from following expression

$$X = j \operatorname{tg} \beta \frac{L' - L}{2}$$

where  $\beta$  is the propagation constant at  $\omega = \omega_r$  for uniform slot line.

$$L' = \frac{\pi}{\beta}$$

The radiation resistance  $R$  can be found by following procedure.

It is known that the power losses caused by radiation from one end in this cavity can be written as

$$P = W\omega_i \quad (1)$$

where  $W$  is the stored energy in the cavity.

On the other hand, the group velocity is defined as

$$V_g = \frac{P_F}{E} \quad (2)$$

where  $P_F$  is the power flow on the entire cross-section.

$E$  is the energy per unit length.

$W$  can be expressed as

$$W = 2EL' \quad (3)$$

The reflection coefficient  $\Gamma$  at the end plane, with the eqs. (1), (2) and (3) considered, can be related to the equations

$$1 - |\Gamma|^2 = \frac{P}{P_F} = \frac{2\omega_i L'}{V_g}$$

$$|\Gamma| = \left| \frac{1-Y}{1+Y} \right|$$

$$\text{where } Y = \frac{1}{R} + \frac{1}{X}$$

It is evident that radiation resistance can be found from the two previous equations once  $X$  has

been known.

The complex resonance frequency of slot line cavity can be determined by a full-wave analysis method [6]. In this method the two-dimensional Fourier transformation is taken to solve Helmholtz equation, and then form characteristic equation. It is noted that only the complex frequency can be considered as its solution.

#### NUMERICAL RESULTS

Fig. 3 is the normalized reactance of slot line shorted end, which is agreement well with [5]. Fig. 4 is its normalized resistance. The results by cavity model show that the radiation effects are less significant than the results from [5].

#### ACKNOWLEDGMENT

The author thanks Prof. S.-F. Li for preparing this manuscript.

#### REFERENCES

- [1] S. B. Cohn, "Slot-line on a dielectric substrate", IEEE Trans, Vol. MTT-17, 1969, pp.768-778
- [2] T. Itoh et al, "Dispersion characteristics of slot line", Electron. Lett. Vol. 7, 1971, pp.364-365
- [3] J. B. Knorr et al, "End effect in a shorted slot", IEEE Trans, Vol. MTT-21 1973, pp.579-580
- [4] H.-Y. Yang et al, "A dynamic model for microstrip-slot line transition and related structures", IEEE MTT-Symposium, U.S.A. 1987, pp.773-775
- [5] H.-Y. Yang et al, "A dynamic model for microstrip-slot line transition and related structures", IEEE Trans, Vol. MTT-36, 1988, pp.286-293
- [6] T. Itoh et al, "A full-wave analysis method for open microstrip structures", IEEE Trans, Vol. AP-29, pp.63-67, 1981

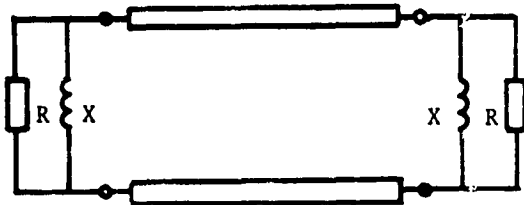


Fig.2

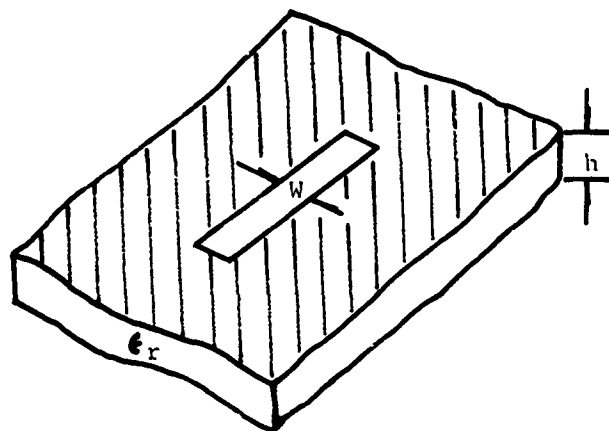


Fig.1

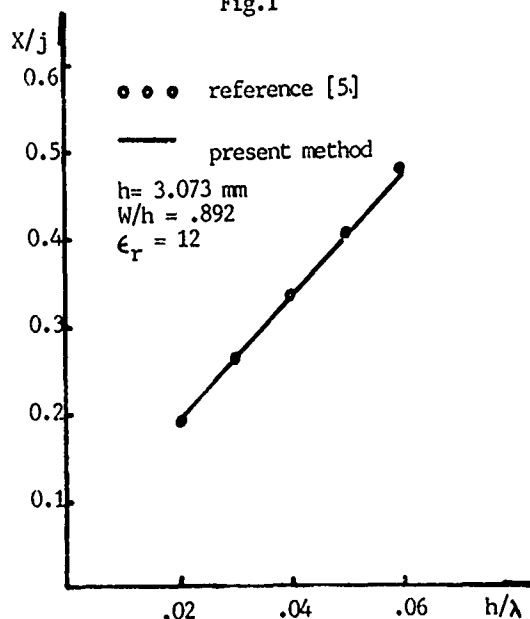


Fig.3

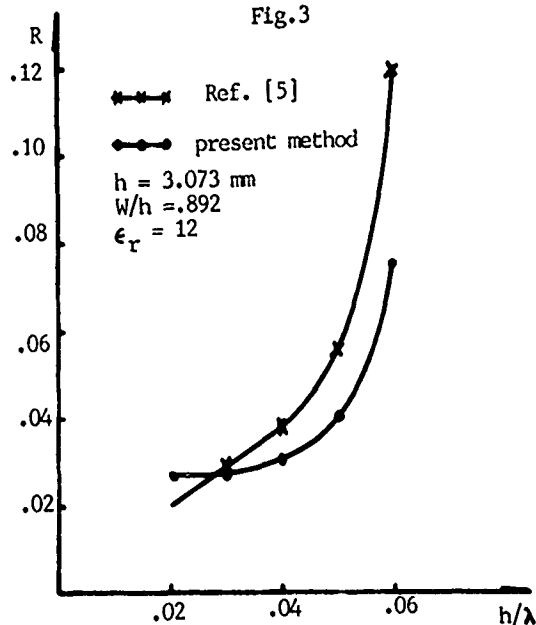


Fig. 4

## ANALYSIS OF MICROSTRIP LINES ON FERRITE AND ANISOTROPIC DIELECTRIC SUBSTRATES

M.R.M.L. Albuquerque, A.G. d'Assunção, M.R.G. Maia  
Electrical Engineering Department, Federal University of Rio Grande do Norte  
Natal, RN, Brazil

A.J. Giarola  
School of Electrical Engineering, State University of Campinas  
Campinas, SP, Brazil

## ABSTRACT

Spectral domain analyses of microstrip transmission lines on anisotropic layers are presented. Dielectric and magnetic anisotropies are considered. The dyadic Green's function in a matrix form, in combination with Galerkin's method, are used to obtain the propagation characteristics of the microstrip on ferrite and on anisotropic dielectric substrates. Curves of effective permittivities as functions of frequency are shown for microstrip lines on anisotropic dielectric substrates.

## INTRODUCTION

The analysis of a variety of planar transmission line structures has been necessary for the consolidation of microwave and millimeter wave integrated circuit technology [1]-[5]. The initial studies were dedicated to the analysis of planar transmission lines on isotropic dielectric substrates [1]. The need of a higher precision and/or flexibility in circuit designs at microwave frequencies has enhanced the study of planar transmission lines on anisotropic substrates. Both dielectric and magnetic anisotropies have been investigated.

The dielectric anisotropy in planar transmission lines may be used for improving the design of coupled transmission line circuits and neglecting its existence may lead to appreciable errors [2], [3]. On the other hand, the magnetic anisotropy in planar transmission line substrates allows the design of non-reciprocal devices in a compact form, of easy integration, when compared with circuits that use waveguides loaded with ferrite rods [4], [5].

In this paper, single and coupled microstrip lines on dielectric and magnetic anisotropic substrates are analyzed. The effective permittivity as a function of frequency is shown for microstrip lines on anisotropic dielectric substrates.

## THEORY AND RESULTS

The dielectric substrate is assumed to be uniaxial, linear and homogeneous, with a dielectric permittivity tensor,  $\hat{\epsilon}$  having its optical axis along a general  $\xi$  transverse direction. The ferrite substrate is assumed to be linear, homogeneous, and magnetized along the propagating  $z$  direction of the microstrip line, with a permeability tensor  $\hat{\mu}$ . Losses in the conductors and anisotropic substrates, as well as the metal thickness are neglected. A harmonic time dependence of the type  $\exp(j\omega t)$  is assumed for the electric and magnetic fields.

The Hertz potential in the Fourier transform spectral domain, proposed by Lee and Tripathi [6] for the analysis of microstrip lines and generalized in [2], is used here for the calculation of the dyadic

Green's function in a form of an impedance matrix. This function, in combination with Galerkin's method, is used for the evaluation of the main characteristic of the structure. The effective permittivity as a function of frequency was obtained for a variety of microstrip lines on anisotropic dielectric substrate. As an example, Fig. 1 shows the result for a coupled microstrip line on a double layer anisotropic substrate consisting of boron nitride and sapphire. The upper layer, with a thickness  $H_2$  is sapphire, while the lower layer is boron nitride, with a thickness  $H_1$ . The effective permittivity was obtained for the even and odd modes and for  $H_1 + H_2 = 0.1$  cm,  $H_1/H_2 = 1.777$ , spacing between strips  $S = 0.037$  cm and values of metal strip widths,  $w = 0.075$  cm and  $0.105$  cm. Note that at a frequency near 20 GHz the effective permittivity for the odd mode is the same for both values of  $w$  while for the even mode its value is higher for the wider value of  $w$ .

## REFERENCES

- (1) T.C. Edwards, Foundations for Microstrip Circuit Design. New York: Wiley, 1985
- (2) M.R.G. Maia, A.G. d'Assunção and A.J. Giarola, "Dynamic analyses of microstrip lines and finlines on uniaxial anisotropic substrates", IEEE Trans. Microwave Theory Tech., 1987, vol. MTT-35, pp. 881-886.
- (3) H.Y. Yang and N.G. Alexopoulos, "Uniaxial and biaxial substrate effects on finline characteristics", IEEE Trans. Microwave Theory Tech., 1987, vol. MTT-35, pp. 24-29.
- (4) Y. Hayashi and R. Mittra, "An analytical investigation of finlines with magnetized ferrite substrate", IEEE Trans. Microwave Theory Tech., 1983, vol. MTT-31, pp. 495-498.
- (5) M. Geshiro and T. Itoh, "Analysis of double-layered finlines containing a magnetized ferrite", IEEE Trans. Microwave Theory Tech., 1987, vol. MTT-35, pp. 1377-1381.
- (6) H. Lee and V.K. Tripathi, "Spectral domain analysis of frequency-dependent propagation characteristics of planar structures on uniaxial medium", IEEE Trans. Microwave Theory Tech., 1982, vol. MTT-30, pp. 1188-1193.

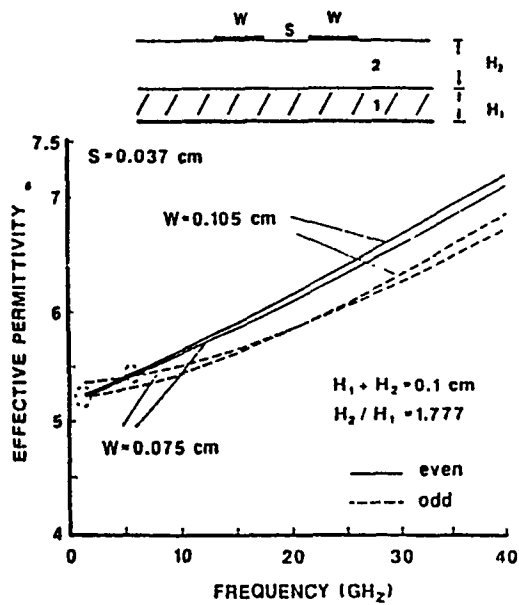


Figure 1

Effective permittivity as a function of frequency for the even and odd modes of a microstrip on double layers. Medium 1 is boron nitride and medium 2 is sapphire.

## ANALYSIS OF FINLINES ON BIAXIAL ANISOTROPIC DIELECTRIC

F.A.F. Tejo

Electrical Engineering Department, Federal University of Paraíba  
Campina Grande, PB, Brazil

A.G. d'Assunção

Electrical Engineering Department, Federal University of Rio Grande do Norte  
Natal, RN, Brazil

A.J. Giarola

School of Electrical Engineering, State University of Campinas  
Campinas, SP, Brazil

## ABSTRACT

An analysis of finlines on layered biaxial anisotropic dielectric substrate using the finite element method is developed. The spurious modes are eliminated by imposing the restriction  $\int_{\Omega} |\nabla \cdot \vec{H}|^2 d\Omega = 0$  to the used functional with a consequent reduction of matrix size of the resultant eigenvalue problem. The basic formulation is presented and the eigenvalue equation for the calculation of the effective dielectric constant is given.

The transverse section,  $\Omega$ , of the structure is decomposed into a summation of finite elements. The vector magnetic fields in each element,  $\Omega_0$ , are interpolated in terms of the nodal values of the magnetic fields in this element by [2]

$$\{H(x,y,z)\}^e = [N]^e T \{h\}^e \exp(-j\beta z) \quad (6)$$

where

$$[N]^e = \begin{bmatrix} \{N\} & \{0\} & \{0\} \\ \{0\} & \{N\} & \{0\} \\ \{0\} & \{0\} & j\{N\} \end{bmatrix}^e \quad (7)$$

$$\{h\}^e T = [\{h_x\}^e \quad \{h_y\}^e \quad \{h_z\}^e] \quad (8)$$

and  $\{-\}^T$  denotes a transposed matrix.

The variation of the functional of the wave equation (1) with respect to the nodal variables leads to the following eigenvalue problem [2]

$$[S] \{h\} - k_0^2 [T] \{h\} = \{0\} \quad (9)$$

From (6) and with the restriction  $\int_{\Omega} |\nabla \cdot \vec{H}|^2 d\Omega$ , the variation of the functional leads to

$$[B] \{h\} = \{0\} \quad (10)$$

The spurious modes, one of the most serious difficulties when using the finite element method [2] - [5], are eliminated with the restriction (10).

With the change of variables  $\vec{x} = \beta \vec{x}$  and  $\vec{y} = \beta \vec{y}$  one obtains  $[S] = [\tilde{S}]$  and  $[T] = (1/\beta^2) [\tilde{T}]$ , such that (9) and (10) are written as

$$[\tilde{S}] \{h\} = (k_0/\beta)^2 [\tilde{T}] \{h\} \quad (11)$$

$$[\tilde{B}] \{h\} = \{0\} \quad (12)$$

With the partition of (12) one obtains:

$$[\tilde{B}]_{tt} \{h\}_t + [\tilde{B}]_{tz} \{h\}_z = \{0\} \quad (13)$$

$$[\tilde{B}]_{zt} \{h\}_t + [\tilde{B}]_{zz} \{h\}_z = \{0\} \quad (14)$$

From (14)  $\{h\}_z$  is obtained as

$$\{h\}_z = [\tilde{D}] \{h\}_t, \text{ with } [\tilde{D}] = -[\tilde{B}]_{zz}^{-1} [\tilde{B}]_{zt}$$

However, since,

$$\{h\}_t = [I] \{h\}_t + [0] \{h\}_z \quad (15)$$

$$\{h\}_z = [\tilde{D}] \{h\}_t + [0] \{h\}_z \quad (16)$$

the following is obtained:

## INTRODUCTION

With the increment of activities in the millimeter wave technology the finlines have emerged among other alternatives for the construction of millimeter wave integrated circuits [1]. In this paper, a dynamic analysis of typical finlines on transverse non-homogeneous anisotropic substrates is developed using the finite element method. By imposing the restriction  $\int_{\Omega} |\nabla \cdot \vec{H}|^2 d\Omega = 0$  to the functional associated with the vector wave function, the matrices used to obtain the eigenvalues are reduced. These eigenvalues correspond to the inverse of the effective dielectric constant and the eigenvectors correspond to the fields configuration for the respective finline modes.

## THEORY AND RESULTS

From Maxwell's equations, for harmonic time dependent electromagnetic fields, the wave equation for the magnetic field  $\vec{H}$  in a biaxial anisotropic dielectric medium is given by

$$\nabla \times (\vec{p} \cdot \nabla \times \vec{H}) - k_0^2 \vec{H} = 0 \quad (1)$$

where  $k_0 = \omega^2 \mu_0 \epsilon_0$  is the free space wavenumber and  $\vec{p}$  is the inverse of the relative permittivity tensor:

$$\vec{p} = \vec{\epsilon}_r^{-1} = \vec{\epsilon}^{-1} / \epsilon_0 \quad (2)$$

The material is assumed to be lossless and source free, such that it is Hermitean:

$$\vec{p}^* T = \vec{p} \quad (3)$$

In addition, a non-magnetic material ( $\mu = \mu_0$ ) is assumed.

The boundary conditions are:

$$\vec{n} \times \vec{p} \cdot \nabla \times \vec{H} = 0, \text{ on an electric boundary} \quad (4)$$

$$\vec{n} \times \vec{H} = 0, \text{ on a magnetic boundary} \quad (5)$$

$$\{\tilde{h}\} = [D] \{h\}_t \quad (17)$$

$$[D]^T = [[I] \ [\tilde{D}]] \quad (18)$$

With (17) in (11) the result is:

$$[\tilde{S}]_{tt} \{\tilde{h}\}_t = (1/\epsilon_{eff}) [\tilde{T}]_{tt} \{h\}_t \quad (19)$$

where,  $\epsilon_{eff} = (\beta/k_0)^2$  is the desired effective dielectric constant and

$$[\tilde{S}]_{tt} = [D]^T [\tilde{S}] [D] \quad (20)$$

$$[\tilde{T}]_{tt} = [D]^T [\tilde{T}] [D] \quad (21)$$

Eq. (19) is a generalized eigenvalue matrix problem and the solutions are eigen-pairs  $(1/\epsilon_{effi}, \{h\}_{ti})$ ,  $i=1, 2, \dots NN$ , where  $NN$  is the total number of interpolation modes of  $\Omega_h$ . It may be solved by means of appropriate algorithms [6].

We should note that the condition  $\int_{\Omega} |\nabla \cdot H|^2 d\Omega = 0$ , that eliminates the spurious modes, is implicitly included in (19) and that the final size of matrices  $[\tilde{S}]_{tt}$  and  $[\tilde{T}]_{tt}$  is only two thirds of the size of matrices  $[\tilde{S}]$  and  $[\tilde{T}]$  that appear in (11). Thus, the numerical problem is substantially reduced. It is important to note also that all values  $\{h\}_{zi}$ ,  $i = 1, 2, \dots NN$ , may be obtained using (16).

#### REFERENCES

- (1) P.J. Meir, "Integrated finline millimeter components", IEEE Trans. Microwave Theory Tech., 1974, vol. MTT-22, pp. 1209-1216.
- (2) M. Koshiba, K. Hayata and M. Suzuki, "Improved finite-element formulation in terms of the magnetic-field vector for dielectric waveguides", IEEE Trans. Microwave Theory Tech., 1985, vol. MTT-33, pp. 227-233.
- (3) A. Konrad, "Vector variational formulation of electromagnetic fields in anisotropic media", IEEE Trans. Microwave Theory Tech., 1976, vol. MTT-24, pp. 553-559.
- (4) A. Konrad, "Higher-order triangular finite elements for electromagnetic waves in anisotropic media", IEEE Trans. Microwave Theory Tech., 1977, vol. MTT-25, pp. 353-360.
- (5) M.A.B. Melo, "Finite Element Method Applied to the Solution of Vector Wave Equation in Waveguides and Cavities Containing Lossy Media" (In Portuguese), MS - Thesis, Federal University of Paraíba, Brazil, 1985.
- (6) B.T. Smith et al., "Matrix Eigensystem Routines-EISPACK Guide. Second Ed., Heidelberg: Springer-Verlag, 1976.



## SINGLE MODE PROPAGATION IN MAGNETOOPTICAL WAVEGUIDES

J. Hernández Marco, Lluís Grau, Lluís Torner, F. Canal

Departamento Teoría de la Señal y Comunicaciones  
E.T.S.E. de Telecomunicación (UPC)  
Barcelona (Spain)

## ABSTRACT

It is well known that single-mode behaviour of plane optical waveguides made of magneto-optical materials is of great importance in the implementation of an isolator. In this work we are going to analyze the propagation in a single mode magneto-optical waveguide by means of the "Transfer Matrix" method, which can be directly applied to any multi-layer structure.

## INTRODUCTION

The utility of optical devices working at monomodal regime in widely known (1). A multi-layer structure is usually required in order to achieve this type of operation (2). So far the six-layer guide in which one of them is highly absorbent seems to present the best features (3).

The structure of this guide is as follow: the active layer, with the refractive index equal to  $n_1$ , is placed between two layers with the same index  $n_2$  ( $n_1, n_2 \sim 0.001$ ). The lower layer has the function of avoiding the fundamental modes attenuation, and the upper layer is set to maintain the guide symmetry. At last a highly absorbent layer ( $n_3$ ) is placed between these three layers and the substrate.

Mode coupled theory (4) can't be applied in the analysis due the existence of the absorbent medium and a numerical method is required. In this work the 'Transfer Matrix' technique has been used (5,6,7).

We will begin the analysis with the study of the fundamental modes propagation constants as a function of the imaginary part of the magneto-optical material complex index in a waveguide formed by a Bi-YIG epitaxied onto an isotropic substrate of GGG.

Afterwards, the propagation in the six-layer magneto-optical waveguide will be studied, paying a special attention at the attenuation undergone by the modes.

## PROPAGATION IN A THREE-LAYER MAGNETOOPTICAL WAVEGUIDE

Let us to take a waveguide formed by a Bi-YIG layer, five microns thickness, epitaxied onto a GGG substrate, which refractive index is 1.945 at 1.152 microns.

The Bi-YIG refractive index, in absence of a external magnetic field, has a complex value of  $2.2505 + jn_i$ . When a magnetic field induces an internal imantation in the medium (with a direction given by both zenithal and azimuthal angles of 45° degrees), its permittivity tensor

(relative values) is

$$\epsilon_{xx} = 5.0650989 - n_i^2 + j4.501 n_i$$

$$\epsilon_{xy} = (2.59155 - j8.57508) 10^{-4} = \epsilon_{yx}^*$$

$$\epsilon_{xz} = (3.56601 + j6.06350) 10^{-4} = \epsilon_{zx}^*$$

$$\epsilon_{yy} = 5.0650849 - n_i^2 + j4.501 n_i$$

$$\epsilon_{yz} = (3.51651 - j6.06350) 10^{-4} = \epsilon_{zy}^*$$

$$\epsilon_{zz} = 5.0653476 - n_i^2 + j4.501 n_i$$

In these conditions, the eigenvalues obtained throughout "Transfer Matrix" method for the fundamental modes are:

$n_i$	TE	TM
0	2.236025756095010	2.234497700032020
$10^{-5}$	2.236025756091943 +j9.96170610 <sup>-6</sup>	2.234497700032942 +j1.00784710 <sup>-6</sup>
$510^{-5}$	2.236025756064118 +j5.00434910 <sup>-5</sup>	2.234497700017248 +j5.01492910 <sup>-6</sup>
$10^{-4}$	2.236025755994935 +j1.00145710 <sup>-4</sup>	2.234497699950111 +j1.0023782010 <sup>-4</sup>
$510^{-4}$	2.236025754051248 +j5.00963610 <sup>-4</sup>	2.234497697521083 +j5.0094602010 <sup>-4</sup>
$10^{-3}$	2.236025748146640 +j1.00198510 <sup>-3</sup>	2.234497689756267 +j1.0018312910 <sup>-3</sup>
$510^{-3}$	2.236025561980340 +j5.01016710 <sup>-3</sup>	2.234497438536141 +j5.0089171310 <sup>-3</sup>
$10^{-2}$	2.236024982430313 +j1.00204110 <sup>-2</sup>	2.234496652346924 +j1.0017797010 <sup>-2</sup>

## SINGLE MODE MAGNETOOPTICAL WAVEGUIDE

We will analyze the structure shown in Figure 1

1	
$n_2 = 2.245$	3 $\mu\text{m}$
$n_1 = 2.2505$	5 $\mu\text{m}$
$n_2 = 2.245$	5 $\mu\text{m}$
$n_3 = 2.249 + j0.01$	3 $\mu\text{m}$
1.945	

where the active layer ( $n_1$ ) is the same that in the last case. We will consider attenuation being only in the last layer, closed to substrate.

Under these conditions effective index ( $\alpha$ ) values for zero and one order modes are

$$TE_0 \alpha = 2.249228544666399 + j2.08610025 \cdot 10^{-7}$$

$$TM_0 \alpha = 2.249278098520466 + j8.98159500 \cdot 10^{-8}$$

$$TE_1 \alpha = 2.245746253443725 + j1.19297992 \cdot 10^{-5}$$

$$TM_1 \alpha = 2.245771114716105 + j1.11161263 \cdot 10^{-5}$$

From these values it is possible to show that fundamental modes only propagate in the active layer ( $n_3 < \text{Re}(\alpha) < n_1$ ), whereas upper modes travel by the absorbent layer too.

If we define the mode attenuation as

$$20 \log \exp[k_0 \text{Im}(\alpha)]$$

where  $k_0$  is the wave number in the vacuum and  $\text{Im}(\alpha)$  is the imaginary part of effective mode index, it can be seen that the fundamental modes undergo 0.1 dB/cm of attenuation, and the other modes of 5.23 dB/cm.

#### CONCLUSIONS

We have applied the transfer matrix method in the calculation of the effective index dependence with the attenuation in a three-layer magneto-optical slab waveguide.

Furthermore, these method has been applied in order to establish the monomodal behaviour of the described six-layer waveguide. In a numerical case, an attenuation of 0.1 dB/cm in the fundamental modes and of 5.23 dB/cm for upper order modes, has been obtained.

#### REFERENCES

- (1) R. Wolfe et al. Appl. Phys. Lett. 48, 508, 1986
- (2) J. Hernández et al. Infrared and Millimeter Waves, vol. 9, no. 3, 1988
- (3) H. Dammann et al. Appl. Phys. Lett. 49(26), 1986
- (4) A. Yariv, IEEE Journal Of Quantum Electronics QE-9, 919, 1973
- (5) D. W. Berreman J. Opt. Soc. Am., 62, 502, 1972
- (6) M. O. Vassel, J. Opt. Soc. Am., 64, 166, 1974
- (7) L. L. Torner, J. Hernández, F. Canal (preprint)

## MAKING SENSE OF SUPERCONDUCTING INFRARED SENSORS

S. A. Wolf

Naval Research Laboratory  
Washington DC 20375-5000

## ABSTRACT

Superconducting films have been shown to be very sensitive, broadband, low noise infrared sensors. Granular, low dimensional superconducting films of Nb, NbN, Nbn/BN as well as the high transition temperature cuprates have been studied over the last decade and shown to have unusual physical properties that make them especially suitable for use as mm-wave and infrared detectors. In this paper, this work will be reviewed with an eye toward projecting the ultimate utility of superconducting sensors

Superconducting films have low thermal mass and a typically large value of the derivative of resistance with respect to temperature ( $dR/dT$ ) in the transition region. This in general makes them suitable as bolometric detectors of any radiation that is coupled into them. Granular superconducting films of Nb and NbN can be made extremely thin ( $<50 \text{ \AA}$ ), so that their heat capacity is vanishingly small at low temperatures, with a  $dR/dT$  that is very large over an extended temperature region below the superconducting transition temperature  $T_c$ . These films were shown to be excellent phonon detectors and have been used for many years to look at phonon propagation in various semiconductor substrates [1]. These detectors were sensitive and very fast ( $<10^{-9}$  sec response time).

Although the detectors discussed above were very useful, they were difficult to fabricate because each one had to be made granular by a tedious anodization process that is described in ref. [1]. In order to overcome the fabrication difficulties, a new method of detector fabrication was invented several years ago in which both Nb and BN are cosputtered onto a heated substrate in the presence of a mixed nitrogen and argon plasma. The resulting films were a phase segregated mixture of small ( $<50 \text{ \AA}$ ) superconducting grains of NbN surrounded by a matrix of amorphous BN [2]. These new

materials were not only useful as phonon detectors but were shown to be very fast and very sensitive, broadband detectors of infrared radiation [2]. The response of these granular films to radiation is quite complicated involving both a bolometric response in the superconducting transition region as well as a non-bolometric response at lower temperatures that is certainly related to the weak coupling of the superconducting grains and the tenuous nature of the overall phase coherence that exists only at low temperatures. It also turns out that these materials are better absorbers of far infrared radiation than one might have expected from the homogenous form of the Bardeen-Cooper-Schrieffer (BCS) theory as used to calculate infrared absorption. The inhomogeneous nature of these materials drastically affects their infrared properties as was clearly shown in Ref. [3].

With this background in granular detectors utilizing the more conventional lower transition temperature superconductors, we have been studying the properties of films of the new high transition temperature cuprates as they relate to infrared detectors. We recently discovered that off stoichiometric films of Y-Ba-Cu-O deposited on sapphire will respond to optical and infrared radiation both bolometrically and non-bolometrically in analogy with the NbN/BN materials [4]. In the course of our detailed study of both the NbN/BN and the Y-Ba-Cu-O materials we discovered that the photoconductive response at low temperatures could be significantly enhanced by the application of a moderate magnetic field [5]. This enhancement must be due to the very strong effect that a magnetic field has on the phase difference of the superconducting wave function from grain to grain. In fact, these materials often behave like a very large array of Josephson junctions.

In summary, granular superconducting films have been shown to be excellent photoconductors in the optical and infrared portions of the electromagnetic spectrum and may in some cases be the detectors of choice for their broadbandness or their response.

## REFERENCES

- [1] K. Weiser, U. Strom, S. A. Wolf and D. U. Gubser, *J. Appl. Phys.*, 1981, vol 52, 4888.
- [2] M. Leung, U. Strom, J. C. Culbertson, J. H. Claassen, S. A. Wolf and R. W. Simon, *Appl. Phys. Lett.*, 1987, vol 50, 1691
- [3] D. R. Karecki, G. L. Carr, S. Perkowitz, D. U. Gubser and S. A. Wolf, *Phys. Rev.* , 1983, vol B27, 5460.
- [4] M. Leung, P. R. Broussard, J. H. Claassen, M. Osofsky, S. A. Wolf and U. Strom, *Appl. Phys. Lett.*, 1987, vol 51, 2046.
- [5] U. Strom, J. C. Culbertson, E. S. Snow, P. R. Broussard, J. H. Claassen, S. A. Wolf, M. Leung and R. W. Simon, *J. Appl. Phys.*, to be published.

**FAR-INFRARED REFLECTIVITY AND MAGNETIC FIELD DEPENDENCE OF  
HIGH  $T_c$  SUPERCONDUCTORS**

Mohammed Nurul Afsar and Hua Chi  
Department of Electrical Engineering  
Tufts University  
Medford, Massachusetts 02155

**ABSTRACT**

Far-Infrared reflectivity technique over the wavenumber region 10 - 800 per centimeter was utilized to observe the surface reflection of a Y-Ba-Cu-O high temperature superconductor specimen. The specimen was introduced inside a liquid helium dewar, the tail of which passes through a two inch bore Bitter solenoid high intensity d.c. magnet.

FAR INFRARED REFLECTIVITY OF CERAMIC HIGH- $T_c$  SUPERCONDUCTORS  
AND OF AN ORIENTED  $\text{YBa}_2\text{Cu}_3\text{O}_7$  THIN FILM

K.F. Renk, W. Ose, J. Schützmann, T. Zetterer, H.H. Otto, and J. Keller  
Fakultät Physik, Universität Regensburg, 8400 Regensburg, FRG

B. Roas and L. Schultz  
Siemens AG, Research Laboratories, 8520 Erlangen, FRG

A far infrared study for ceramic high- $T_c$  superconductors,  $\text{Ti}_2\text{Ba}_2\text{CaCu}_2\text{O}_8$  and  $\text{YBa}_2\text{Cu}_3\text{O}_7$ , and for an oriented  $\text{YBa}_2\text{Cu}_3\text{O}_7$  thin film is reported. We present for the ceramics, that consist of strongly anisotropic crystallites, a new method of analysis that allows to extract properties of phonons and of charge carriers. We find that the dynamical conductivity of both the ceramics and the film in the normal state can be described by Drude's theory. The reflectivity of the film in the superconducting state corresponds to a Mattis-Bardeen like behavior with an energy gap  $2\Delta(0)/kT_c = 4.2$ .

Far infrared reflectivity studies have been performed for ceramic samples of  $\text{La}_{2-x}(\text{Ba},\text{Sr})_x\text{CuO}_{4-y}$ ,<sup>1</sup>  $\text{YBa}_2\text{Cu}_3\text{O}_7$ ,<sup>1-5</sup> and  $\text{Bi}_2\text{Sr}_2\text{CaCu}_2\text{O}_8$ ,<sup>6</sup> and for  $\text{YBa}_2\text{Cu}_3\text{O}_7$  thin films<sup>7,8</sup> and mosaics of crystals.<sup>9</sup> However, there is not yet a clear understanding of the dynamical properties of the high- $T_c$  superconductors. In this paper we report on a study of a  $\text{Ti}_2\text{Ba}_2\text{CaCu}_2\text{O}_8$  ceramic sample and of a  $\text{YBa}_2\text{Cu}_3\text{O}_7$  ceramic sample and we present a new method of analysis of far infrared reflection spectra of ceramic samples. Furthermore, we report on a study of an oriented  $\text{YBa}_2\text{Cu}_3\text{O}_7$  thin film.

We have prepared and analyzed ceramic samples according to standard procedures. An oriented  $\text{YBa}_2\text{Cu}_3\text{O}_7$  thin film was prepared, on a  $\text{SrTiO}_3$  substrate, by a laser evaporation technique.<sup>10</sup> The far infrared reflectivity was determined by use of an infrared Fourier spectrometer.

Experimental reflection spectra for ceramic  $\text{Ti}_2\text{Ba}_2\text{CaCu}_2\text{O}_8$  are shown in Fig. 1. The reflectivity has a high level at small frequencies and decreases to a lower level at large frequencies. At very large frequencies diffuse reflection sets in (inset). There is pronounced phonon structure, with narrow reflection minima at small frequencies and a Reststrahlen like behavior at large frequencies.

The reflectivity of  $\text{YBa}_2\text{Cu}_3\text{O}_7$  (Fig. 2) shows a similar behavior. The reflectivity drops from a high level at small frequencies to a low level at high frequencies. Phonons appear also as minima at small frequencies. At large frequencies the structure is less pronounced.

Both spectra have in common that the reflectivity increases with decreasing temperature and that the phonon structure becomes more pronounced at low temperature. Superconductivity is indicated by an increase of reflectivity at small frequencies at temperatures below  $T_c$ .

For an analysis of the reflection spectra we take into account that the ceramic samples consist of strongly anisotropic crystallites. A crystallite appears metallic if the electric field vector  $E$  of the radiation is perpendicular to the crystal  $c$ -axis, but it appears dielectric for  $E||c$ . This leads us to a new model: A metal ceramic can be described as a metal plate that contains holes filled with dielectric material. We can describe the hole regions by the dielectric constant  $\epsilon = \epsilon_\infty + \sum_j S_j v_j^2 (v_j^2 - v^2 - i\Gamma_j v)^{-1} - v^2/4d^2$  where the first term describes the high-frequency dielectric constant, the second term the phonon resonances for  $E||c$  ( $S_j$  = strength,  $v_j$  = eigenfrequency,  $\Gamma_j$  = damping constant,  $v$  = frequency), and the third term the influence of the structure ( $d$  = dimension of a square shaped hole). A theoretical curve, with two phonon resonances, is shown in Fig. 3; two third of the material is assumed to be metallic with a reflectivity of 1. At small frequencies the structure is almost totally reflecting and has a cutoff frequency (with a cutoff wavelength  $\lambda_c = 2nd$  where  $n$  is the refractive index of the dielectric medium). At large frequencies the reflectivity has a lower level. A phonon resonance appears below the cutoff as a narrow reflection minimum and above the cutoff as a Reststrahlen like band.

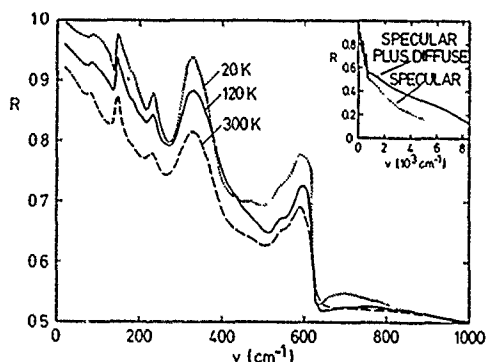


Fig. 1 Far infrared reflectivity of  $\text{Ti}_2\text{Ba}_2\text{CaCu}_2\text{O}_8$  ( $T_c = 105$  K).

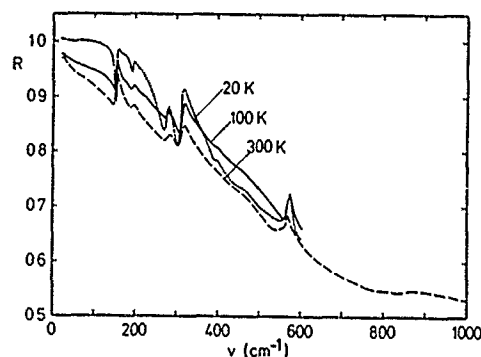


Fig. 2 Far infrared reflectivity of  $\text{YBa}_2\text{Cu}_3\text{O}_7$  ( $T_c = 86$  K).

Using our model, taking into account more than two phonon resonances and also finite conductivity, we found a characteristic dimension  $d \approx 8 \mu\text{m}$  for  $\text{Ti}_2\text{Ba}_2\text{CaCu}_2\text{O}_8$  and a dynamical (low-frequency) resistivity ( $\approx 300 \mu\Omega\text{cm}$ ) comparable to the dc value ( $\approx 150 \mu\Omega\text{cm}$ ). Similar results were obtained for  $\text{YBa}_2\text{Cu}_3\text{O}_7$ ; however, for this material it has to be taken into account that a weak conductivity occurs also for E1c, thus leading to a smearing of the phonon structure above cutoff. For the phonons we find similar strengths ( $S \approx 1$ ) for the Ba vibrations (near  $150 \text{ cm}^{-1}$ ) and for characteristic Cu-O vibrations (near  $300 \text{ cm}^{-1}$  and  $600 \text{ cm}^{-1}$ ). The conductivity for E1c (for  $T > T_c$ ) can be described by Drude's dynamical theory of conductivity.

Reflection spectra of  $\text{YBa}_2\text{Cu}_3\text{O}_7$  thin films are shown in Figs. 4 and 5. We can describe the reflectivity in the normal state by Drude's theory (solid lines) with a conductivity  $\sigma = \sigma_0 (1 - i\nu/\nu_\tau)^{-1}$  where  $\sigma_0$  is the low frequency conductivity. We find values for  $\sigma_0^{-1}$  (inset of Fig. 5) that correspond almost to the dc values ( $\sigma_0^{-1} \approx 60 \mu\Omega\text{cm}$  at 100 K). Our results indicate furthermore that  $\nu_\tau$  increases proportional to the temperature. For 100 K we find  $\nu_\tau \approx 2700 \text{ cm}^{-1}$ , which corresponds to a mean free path of about  $20 \text{ \AA}$ .

The reflectivity in the superconducting state can be described (dashed in Fig. 4) by the theory of Mattis and Bardeen,<sup>12</sup> with  $2\Delta(0)/kT_c \approx 4.2$ ; this value is characteristic also for other strong coupling superconductors. The reflectivity is, however, smaller than 1 still below the assumed gap frequency (at  $300 \text{ cm}^{-1}$ ), possibly because of remaining imperfections of our (high quality) film.

The work was supported by the Bundesministerium für Forschung und Technologie.

- 1 T.W. Noh et al., Phys. Rev. B **36**, 8866 (1987).
- 2 G.A. Thomas et al., Phys. Rev. B **36**, 846 (1987).
- 3 D.A. Bonn et al., Phys. Rev. Lett. **58**, 2249 (1987).
- 4 L. Genzel et al., Solid State Commun. **63**, 843 (1987).
- 5 W. Ose et al., Z. Phys. B - Condensed Matter **70**, 307 (1988).
- 6 Z.V. Popovic et al., Solid State Commun. **66**, 965 (1988).
- 7 G.A. Thomas et al., Jap. J. Appl. Phys. **26**, 1001 (1987).
- 8 R.T. Collins et al., Phys. Rev. Lett. **59**, 704 (1987).
- 9 Z. Schlesinger et al., Phys. Rev. Lett. **59**, 1958 (1987).
- 10 B. Roas et al., submitted to Appl. Phys. Letters.
- 11 F. Keilmann, Intl. J. IR and MM Waves **2**, 259 (1981).
- 12 D.C. Mattis and J. Bardeen, Phys. Rev. **111**, 412 (1958).

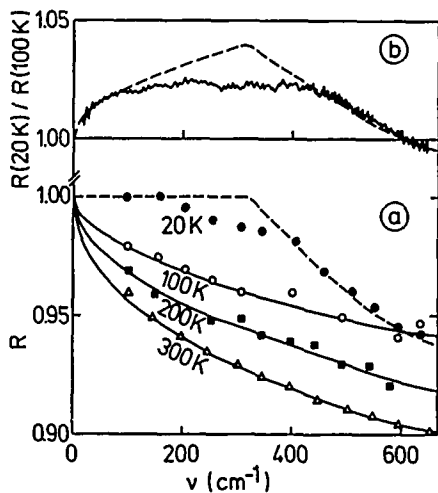


Fig. 4 Far infrared reflectivity of an oriented  $\text{YBa}_2\text{Cu}_3\text{O}_7$  thin film (a) and reflectivity ratio (b).

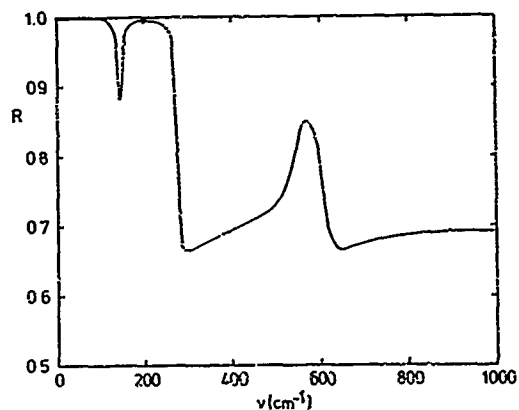


Fig. 3 Calculated reflectivity for a metallic structure with dielectric holes; phonon resonances  $\nu_1 = 143 \text{ cm}^{-1}$ ,  $\nu_2 = 570 \text{ cm}^{-1}$ ,  $S_1 = S_2 = 0.8$ ,  $\Gamma_j/\nu_j = 0.05$ .

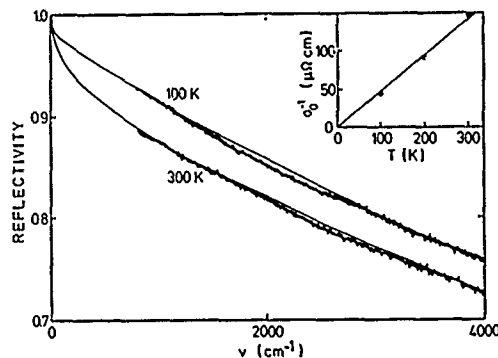


Fig. 5 Infrared reflectivity of the  $\text{YBa}_2\text{Cu}_3\text{O}_7$  film.

FAR INFRARED OPTICAL PROPERTIES OF HIGH  $T_c$  SUPERCONDUCTORS $\text{LnBa}_2\text{Cu}_3\text{O}_x$  (Ln = Y, Ho, Er, Sm, Gd, Dy, Eu, Pr)

S. Onari, T. Hiroaki, A. Ono, S. Hidaka and T. Arai

Institute of Applied Physics, University of Tsukuba,  
Tsukuba 305, Japan

## ABSTRACT

Systematic measurements of the far infrared reflection spectra of high  $T_c$  superconductors  $\text{LnBa}_2\text{Cu}_3\text{O}_x$  for various Ln as shown in the title were performed. Infrared reflection spectra of tetragonal  $\text{LnBa}_2\text{Cu}_3\text{O}_x$  exhibit Reststrahlen vibration at 640, 590, 530, 355 and 250  $\text{cm}^{-1}$ , common to these materials, and the spectra of the orthorhombic  $\text{LnBa}_2\text{Cu}_3\text{O}_x$  exhibit the characteristics of free carriers except  $\text{PrBa}_2\text{Cu}_3\text{O}_x$  with weak phonon structures at 617, 570, 317 and 285  $\text{cm}^{-1}$ .  $\text{PrBa}_2\text{Cu}_3\text{O}_x$  is not a superconductor, and it has no characteristic broad band due to free carriers for all x in the range of 6 to 7.

## INTRODUCTION

Ever since Bednorz and Muller reported the possible existence of a percolative superconductivity in La-Ba-Cu-O system in the 30 K range, Y-Ba-Cu-O, Ho-Ba-Cu-O, Er-Ba-Cu-O and so on were found to be high temperature superconducting materials. The crystal structure of these materials has been studied in detail, and the main difference between the orthorhombic and tetragonal structures is related to the oxygen concentration [1].

Study of the lattice vibration and the free carriers is important for understanding the physical nature of the high  $T_c$  superconductors. Infrared reflection spectrum of the orthorhombic  $\text{YBa}_2\text{Cu}_3\text{O}_x$  has been reported by Bonn et al. [2], and that of the tetragonal  $\text{YBa}_2\text{Cu}_3\text{O}_x$  has been reported by Onari et al. [3]. Infrared spectra of  $\text{YBa}_2\text{Cu}_3\text{O}_x$  and so on for various oxygen concentration have been studied [4-10].

In this report infrared reflection spectra of the tetragonal and orthorhombic  $\text{LnBa}_2\text{Cu}_3\text{O}_x$  (Ln = Y, Ho, Er, Sm, Gd, Dy, Eu, Pr) are reported systematically, and phonon structures are discussed.

## EXPERIMENTAL

Properly weighted mixed powder of  $\text{Ln}_2\text{O}_3$ ,  $\text{BaCO}_3$  and  $\text{CuO}$  is sintered at 930°C for 24 h in the air. After it is pulverized, pellets of 10 mm diameter with a thickness of ca. 1 mm are made by a 4 ton press. The sample pellets with tetragonal crystal structure are obtained by quenching the pellets into the liquid nitrogen after sintering at 930°C for 24 h. The sample pellets with orthorhombic crystal structure are obtained as follows. The pellets are first sintered at 930°C for 4 h and then they are annealed again at 500°C for 20 h before they are cooled in the air.

Infrared reflection spectra from the surfaces which are polished with carborandom #1200 and finished with 1  $\mu\text{m}$  alumina were measured by Digilab Fourier transform spectrometer FTS 16B.

The X-ray diffraction patterns are measured, and the samples which are sintered at 930°C and quenched into liquid nitrogen exhibit a tetragonal structure.

The samples, which are cooled after sintering at 500°C, exhibit the different lattice constants a and b, and these are shown to be in the orthorhombic structure.

## RESULTS AND DISCUSSION

In Fig. 1, the infrared reflection spectra of the tetragonal and orthorhombic  $\text{SmBa}_2\text{Cu}_3\text{O}_x$ ,  $\text{GdBa}_2\text{Cu}_3\text{O}_x$ ,  $\text{DyBa}_2\text{Cu}_3\text{O}_x$ ,  $\text{PrBa}_2\text{Cu}_3\text{O}_x$ ,  $\text{YBa}_2\text{Cu}_3\text{O}_x$  and  $\text{EuBa}_2\text{Cu}_3\text{O}_x$  are shown. The tetragonal polycrystalline samples of  $\text{SmBa}_2\text{Cu}_3\text{O}_x$ ,  $\text{GdBa}_2\text{Cu}_3\text{O}_x$ ,  $\text{DyBa}_2\text{Cu}_3\text{O}_x$ ,  $\text{YBa}_2\text{Cu}_3\text{O}_x$  and  $\text{EuBa}_2\text{Cu}_3\text{O}_x$  have the structures in reflection spectra at 640, 590, 530, 355 and 250  $\text{cm}^{-1}$  common to these materials, and the orthorhombic polycrystalline samples have rather smaller structures in the reflection spectra at 630, 570, 317 and 285  $\text{cm}^{-1}$  also common to these materials.

The difference between tetragonal and orthorhombic  $\text{LnBa}_2\text{Cu}_3\text{O}_x$  is strongly correlated with the oxygen concentration x [1]. The occupation probability of oxygen on (0,1/2,0) site is reported for  $\text{YBa}_2\text{Cu}_3\text{O}_x$  to be ca. 80% at 400°C and ca. 65% at 600°C, and that on (0,1/2,0) site is ca. 13% at the temperature above 900°C.

The infrared active vibration bands at 590, 355 and 250  $\text{cm}^{-1}$  which are observed in the tetragonal structure disappear in the orthorhombic structure common to  $\text{SmBa}_2\text{Cu}_3\text{O}_x$ ,  $\text{GdBa}_2\text{Cu}_3\text{O}_x$ ,  $\text{DyBa}_2\text{Cu}_3\text{O}_x$  and  $\text{EuBa}_2\text{Cu}_3\text{O}_x$ , and new vibration bands appear at 317 and 285  $\text{cm}^{-1}$  in the orthorhombic structure.

As the oxygen concentration is changed largely with the orthorhombic-tetragonal structure change, these experimental facts suggest that the infrared active bands at 590, 355 and also at 250  $\text{cm}^{-1}$  are strongly influenced by the oxygens around the Cu atom which is surrounded by four Ba atoms.

Tetragonal  $\text{PrBa}_2\text{Cu}_3\text{O}_x$  has the structures at 640, 540, 355 and 250  $\text{cm}^{-1}$ . The orthorhombic  $\text{PrBa}_2\text{Cu}_3\text{O}_x$  shows no superconductivity, and corresponding to these fact, the infrared reflection spectra shows no broad band due to free carriers. Therefore, the screening effect on the vibration by the free carriers is eliminated for the orthorhombic  $\text{PrBa}_2\text{Cu}_3\text{O}_x$ .

The mass of Sm, Gd, Dy and Eu atoms is about 1.9 times larger than that of Y atom, however, the reflection spectra of the tetragonal and also orthorhombic  $\text{YBa}_2\text{Cu}_3\text{O}_x$ ,  $\text{SmBa}_2\text{Cu}_3\text{O}_x$ ,  $\text{GdBa}_2\text{Cu}_3\text{O}_x$ ,  $\text{EuBa}_2\text{Cu}_3\text{O}_x$  are quite similar in shape and wave number of the vibration modes to each other. These quite interesting experimental results suggest that the vibration of Y, Sm, Gd, Eu and Dy atoms may play no role in the infrared spectra in the wave number range of 210-700  $\text{cm}^{-1}$ .

As  $\text{LnBa}_2\text{Cu}_3\text{O}_x$  (Ln = Sm, Gd, Dy, Eu) have very similar phonon structures with  $\text{YBa}_2\text{Cu}_3\text{O}_x$ , the vibrational mode assignment for  $\text{YBa}_2\text{Cu}_3\text{O}_x$  may also apply to  $\text{LnBa}_2\text{Cu}_3\text{O}_x$ . The phonon assignments for the tetragonal crystal by Thomsen et al. are as follows [4]. Oxygen of Ba-O plane has the vibration mode  $A_{2u}$  in



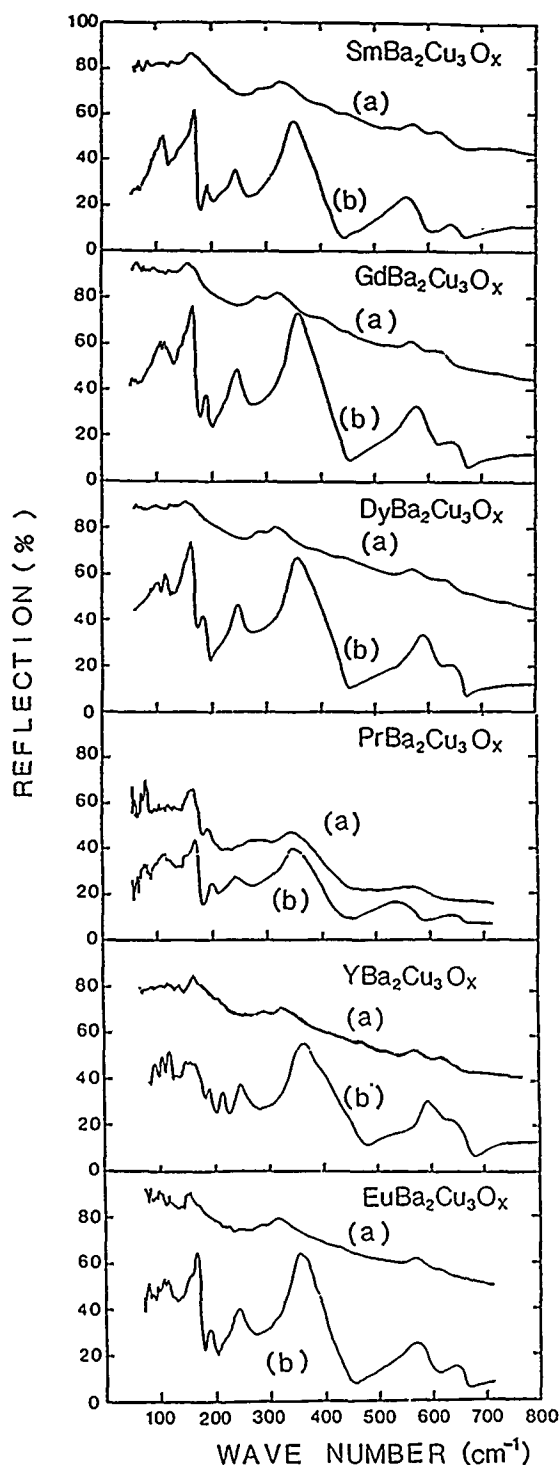


Fig. 1

Infrared reflection spectra of  $\text{SmBa}_2\text{Cu}_3\text{O}_x$ ,  $\text{GdBa}_2\text{Cu}_3\text{O}_x$ ,  $\text{DyBa}_2\text{Cu}_3\text{O}_x$ ,  $\text{PrBa}_2\text{Cu}_3\text{O}_x$ ,  $\text{YBa}_2\text{Cu}_3\text{O}_x$ , and  $\text{EuBa}_2\text{Cu}_3\text{O}_x$ ,

(a) : Orthorhombic sample.

(b) : Tetragonal sample.

c-axis direction at  $530\text{ cm}^{-1}$ , and has the vibration mode  $E_u$  in ab plane at  $355\text{ cm}^{-1}$ . Oxygen vibration in Cu-O plane has the  $E_u$  mode at  $250\text{ cm}^{-1}$ . The phonon assignments for the orthorhombic crystal are as follows. Oxygen of Ba-O plane has the vibration mode  $B_{1u}$  in c-axis direction at  $550\text{ cm}^{-1}$ , and has the vibration mode  $B_{3u}$  in ab plane at  $320\text{ cm}^{-1}$ . Oxygen vibration in Cu-O plane has  $B_{2u}$ ,  $B_{3u}$  modes in ab plane at  $280\text{ cm}^{-1}$ .

The high frequency mode of  $640\text{ cm}^{-1}$  in the tetragonal crystal is hard to explain from the results of the lattice dynamics.

## REFERENCES

- (1) D.J.Jorgensen, M.A.Beno, D.G.Hinks, L.Soderholm, J.K.Volin, R.L.Hitterman, J.D.Grace, I.K.Schuller, C.U.Serge, K.Zang & M.S.Kleefish, *Phys. Rev. B* 36 (1987) 3608
- (2) D.A.Bonn, J.E.Greedan, C.V.Stager, T.Timusk, M.G.Doss, S.L.Herr, K.Kamras & D.B.Taner, *Phys. Rev. Lett.* 58 (1987) 2249
- (3) S.Onari, M.Iioka, K.Ohshima, T.Arai & T.Sakudo, *Jpn. J. Appl. Phys.* 26 (1987) L1052
- (4) C. Thomsen, M.Cardona, W.Kress, R.Liu, L.Genzel, M.Bauer, E.Schönherr & U. Schrodter, *Solid State Commun.* 65 (1988) 1139
- (5) M.Cardona, L.Genzel, R.Liu, A.Wittlin, H.J.Mattausch, F.G.Alvarado, E.G.Gonzalez, *Solid State Commun.* 64 (1987) 727
- (6) M. Cardona, R.Liu, C.Thomsen, M.Bauer, L.Genzel, W.Konig, A.Wittlin, U.Amador, M.Barahona, F.Fernandez, C.Otero and R.Saez, *Solid State Commun.* 65 (1988) 71
- (7) G.Burns, F.H.Dacol, P.P.Freitas, W.Konig, T.S. Plaskett, *Phys. Rev. B* 37 (1988) 5171
- (8) M.K.Crawford, W.E.Farneth, R.K.Bordia and E.M. McCarron III, *Phys. Rev. B* 37 (1988) 3371
- (9) S.Sugai, *Phys. Rev. B* 36 (1987) 7133
- (10) W.Ose, P.E.Dermayer, H.H.Otto, T.Zetterer, H. Lengfellner, J.Keller and K.F.Renk, *Z. Phys.* B70 (1988) 307

MICROWAVE CHARACTERIZATION OF BULK AND POWDERED HIGH- $T_c$  SUPERCONDUCTORS\*

A. Meulenberg, H-L. A. Hung and G. H. Tough

COMSAT Laboratories  
Clarksburg, Maryland 20871-9475

## ABSTRACT

A versatile microwave/millimeter-wave characterization technique using cylindrical resonance cavities has been implemented which allows measurement of the absorption and sheet resistivity of high-temperature superconductor (HTS) powders, films, and bulk samples. Copper and  $\text{YBa}_2\text{Cu}_3\text{O}_{7-x}$  (1-2-3) powders were compared with bulk samples to provide input for a simple model of microwave conductivity in bulk HTS materials. While the conductivity of copper metal is more than twice that of bulk  $\text{YBa}_2\text{Cu}_3\text{O}_{7-x}$  at 77 K, the conductivity of copper powder at this temperature is less than that of the HTS powder.

## INTRODUCTION

Currently only single crystals, or an occasional oriented high-temperature superconductor (HTS) thin film, have exhibited microwave properties superior to those of copper (Cu) at 77 K. Both forms are generally impractical for many microwave applications. Measurements utilizing resonance cavities are a useful approach to determining microwave conductivity and absorption (1),(2). The less-than-predicted conductivity of HTS bulk materials at microwave frequencies is studied by using a single-port cylindrical cavity near 16 GHz. The ability of the system to analyze bulk, thin-film, and powdered materials permits comparison of superconductors with normal conductors in various forms. Experiments were performed based on a hypothesis describing the nature of microwave conductivity in bulk HTS materials. Appropriate application of the results obtained from work with conductive powders should lead to HTS materials with much improved microwave properties.

## MEASUREMENT SYSTEM

Microwave conductivity is determined by measuring the quality factor,  $Q$ , of a reflecting resonance cavity operating in the  $\text{TE}_{011}$  mode. The cavity  $Q$  is obtained in an automated system by sweeping the frequency range of interest. Results for a cavity having an endplate replaced with the sample are referenced against those for a cavity with an absorbing endplate. To accelerate data acquisition, a computer program was developed to control the step frequency, permitting large step sizes away from a resonance and reduced step size as the resonance peak is approached. The resolution of full-width-at-half-maximum (FWHM) points was found to be excellent, since data points are concentrated about the resonance peak.

The  $Q$  of a cavity is determined by measuring the loss in reflected power at resonance, calculating the level at half maximum (or some other fixed percentage level), and interpolating between data points to determine the frequencies corresponding to this

level (3). The value obtained from the center frequency ( $f_c$ ) divided by the frequency difference between the half-maximum points ( $\Delta f$ ) is the loaded  $Q$  ( $Q_L$ ) of the system. The  $Q_L$  value is then converted to the unloaded  $Q$  after determining the coupling coefficient and whether the cavity is overcoupled or undercoupled.

## MATERIAL MODEL

The HTS bulk materials have not yet demonstrated the predicted high microwave conductivity. Possible causes are non-single-phase composition, grain-boundary problems, anisotropic conductivity, and twin-planes within crystals. Another cause, suggested by observations of very thin tin films, is the inhomogeneous structure in which low-temperature superconducting islands are connected by resistive paths (5).

The conductivity model proposed here for bulk HTS materials involves superconducting paths that are nonlinear and, particularly just below the critical temperature ( $T_c$ ), may be very circuitous. For DC measurements, such meandering paths have only a small effect, which is seen during the onset of superconducting behavior. At this stage, intense magnetic fields from high local current densities can quench the superconductivity and force the current to flow, for short distances, through alternative paths, which may include resistive material. At high frequencies, circuitous paths which result in self- and mutual inductance can generate back-emfs that oppose current flow along the path and thus divert current through resistive channels. These inductive effects will increase with frequency. As temperatures are lowered below  $T_c$  and more superconducting paths are opened up, the current flows become more linear and self-inductance is reduced. (Capacitance effects are not included in the first-order model.)

Most microwave applications require high conductivity, not zero resistance. Therefore, a means of reducing the inductive element of HTS materials, even at the expense of slightly increased resistive components, would be highly desirable. This could be accomplished by filling the voids in bulk HTS materials with high-conductivity materials, such as silver.

## EXPERIMENT AND RESULTS

A reference is established for these experiments by using a Cu disk in the cavity to calibrate the changes in both  $Q$  and center frequency as the cavity is reduced from room temperature to 77 K ( $\text{LN}_2$ ). Figure 1 shows the increase in unloaded  $Q$  of one such disk as a function of decreasing temperature. In comparison, a disk of  $\text{YBa}_2\text{Cu}_3\text{O}_{7-x}$  (1-2-3) has a much lower  $Q$  until the temperature is just below  $T_c$ . At 77 K, the  $Q$  is much closer to that of Cu ( $Q_{123}/Q_{\text{Cu}} = 0.9 \pm 0.05$ ) and the resulting resistivity ratio is

\*This paper is based on work performed at COMSAT Laboratories under the sponsorship of the Communications Satellite Corporation.

$\rho_{123}/\rho_{Cu} = 2.1 \pm 0.4$ . Other samples of HTS bulk material (2122 bismuth and 1-2-3 compounds) have been tested, but with poorer results (Figure 1).

To evaluate the effects of material fabrication, rather than the elemental and crystalline composition or the material, samples of HTS powder and Cu powder were compared. Both the HTS and conducting materials were observed to be absorbent and to lower the  $Q$  of a cavity without changing its center frequency. The microwave energy is reflected from the plate behind the powder and, if the powder layer is too thick, no resonance is observed.

Figure 2 compares powder samples of  $YBa_2Cu_3O_{7-x}$  and Cu at room temperature and near  $T_C$ . The superconductive transition is clearly observed, and relative changes should be indicative of material quality.

The first attempt to reconstitute the Cu powder into a bulk form involved using mercury as a conductive lubricant and binder, without removing oxides from the powder surfaces. Figure 3 shows the increase in  $Q$  and reduction in  $f_c$  as a function of compacting pressure.

The second experiment used indium-silver (90 percent In plus 10 percent Ag) solder as a binder for the Cu powder. This solder has a large plastic temperature range and very high conductivity. The layer was clearly conductive, with a resulting  $Q$  near 10,000, and the reflecting surface (as determined from  $f_c$ ) shifted to the front surface of the layer. This  $Q$  was still significantly less than that of a Cu disk (15,000), or even an InAg solder disk (15,000 when freshly polished and 12,000 when oxidized), but clearly shows the improvement possible for "dirty" powders. Experiments with  $YBa_2Cu_3O_{7-x}$  powders are in progress.

#### CONCLUSIONS

Several experiments have been carried out to study the microwave properties of conductive materials in the full range from dense metals to fine powders. Use of a resonance cavity, with an automated data

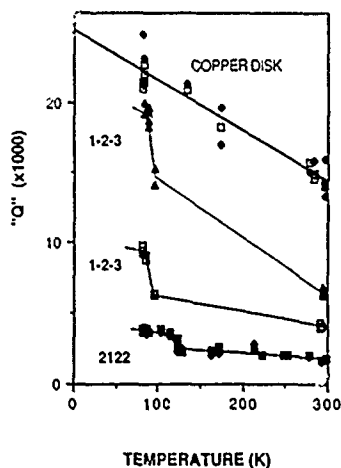


Figure 1. Cavity  $Q$  of Cu,  $YBa_2Cu_3O_{7-x}$  (1-2-3) HTS, and Bismuth (2122) HTS Endplates as a Function of Cavity Temperature

acquisition system and with the normal endplate coated, covered, or replaced by test material or sample, provides a simple means of obtaining comparative results.

Results of conductivity measurements in the 15- to 16-GHz range for copper powder with mercury or indium-silver solder as a binder have supported a material model for some limitations of RF conduction in bulk HTS.

#### ACKNOWLEDGMENTS

The authors would like to thank R. Bonetti and L. Holdeman for their technical support.

#### REFERENCES

- (1) T. M. P. Percival, J. S. Thorn, and R. Driver, "Measurements of High- $T_C$  Superconductivity in a Microwave Cavity," *Electron Lett*, Vol. 23, No. 23, November 1987, pp. 1225-1226.
- (2) J. S. Martens, J. B. Beyer, and D. S. Ginley, "Microwave Surface Resistance of  $YBa_2Cu_3O_{6.9}$  Superconducting Films," *Appl Phys Lett*, Vol. 52, No. 21, May 1988, pp. 1822-1824.
- (3) M. Sucher, "Measurement of  $Q$ ," *Handbook of Microwave Measurements*, Ch. 8, New York: John Wiley, 1963.
- (4) S. Ramo, J. Whinnery, and T. Van Duzen, "Resonant Cavities," *Fields and Waves in Communication Electronics*, Ch. 10, New York: John Wiley, 1965.
- (5) S. Sridhar, "Microwave Response of Thin-Film Superconductors," *J Appl Phys*, Vol. 63, No. 1, January 1988, pp. 159-166.

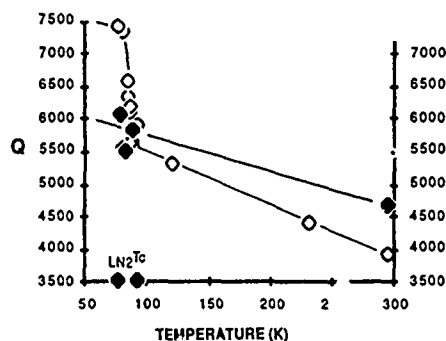


Figure 2. Comparison of Powder Samples on the Endplate

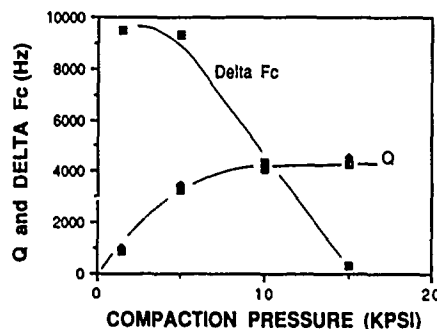


Figure 3. Increase in  $Q$  as a Function of Pressure Applied During Compaction of Cu Powder With Hg Binder

## RF MEASUREMENTS OF HIGH TEMPERATURE SUPERCONDUCTING MATERIAL

K. Chang, R. K. Pandey, M. K. Skrehot, M. Li, G. R. Gilbert,  
K. W. Goeking, B. L. Gries, D. L. Mabus, and J. C. McCleary

Department of Electrical Engineering  
Texas A&M University  
College Station, Texas 77843

### ABSTRACT

A simple RF measurement method using a resonant strip in a waveguide has been developed. The method has been used to measure the RF properties of different superconducting materials. The results of  $Q$  and loss measurements will be presented.

### INTRODUCTION

The recent discovery of superconducting materials, with transition temperatures above 77 K, has excited the technical community with the possibility of a new class of microwave devices. The successful development of these devices will rely on the RF and microwave characterization of these materials.

Little work has been reported on the RF characterization of these new superconducting materials. Hagen et al. [1] used a cavity method to measure a sample at 3 GHz. Tateno and Masaki [2] reported a method to measure the VSWR of a specimen in a waveguide. Both experiments required fairly big samples. Belohoubek and Kalokitis [3] used a disk resonator for  $Q$ -measurement. The resonator was excited by a coaxial probe that penetrated the large disk in close proximity of the smaller disk. At Texas A&M, we have developed a simple method to measure the loaded  $Q$  by using a resonant strip [4]. The method has the advantage of simplicity and provides both resonance and loss information. It can be used to measure a very small sample. With little modification, this method can also be used for the measurement of thin film samples.

### MEASUREMENT TECHNIQUE

The measurement technique is very simple and straightforward. A sample of superconducting material is placed inside a rectangular waveguide as shown in Figure 1. The waveguide has a width of  $a$  and height of  $b$ . As the material becomes conductive, the equivalent circuit can be represented by a  $L$ - $R$ - $C$  resonant network.  $L$  is due to the excitation of  $TE_{no}$  modes, and  $C$  is attributed to the excitation of  $TE_{nm}$  modes. The resistance  $R$  accounts for the conductor losses. From the field analysis [5], the resonant frequency is a function of the strip depth and strip width. By designing the strip dimensions, the desired resonant frequency can be obtained.

The superconducting sample could be placed inside a Teflon dielectric holder to avoid the direct contact with moisture. The holder does not affect the resonant frequency significantly due to its low dielectric constant.

### MEASUREMENT RESULTS

The method was used to measure a high-temperature 123  $YBaCu$ -oxide bulk sample. The sample was processed by hot pressing. A charge material consisting of high purity grade powders of  $Y_2O_3$ ,  $BaCO_3$ , and  $CuO$ . The charge was prepared by reacting the powders at elevated temperatures and then by sintering and annealing the final product at 950 and 550°C, according to carefully developed temperature programming steps in order to obtain and stabilize the orthorhombic phase of the material. The 90 K superconducting transition is obtained when the 123  $YBCO$  is stabilized in the orthorhombic phase.

Typical RF measurement results are shown in Figure 2. At room temperature, there was no significant resonance. As the temperature was lowered to the liquid nitrogen temperature, a strong resonance occurred at 11.3 GHz indicating that the strip had become conductive. The loaded  $Q$  calculated from this resonance is about 750, which is comparable to that obtained from a copper strip. This is in agreement with other results reported recently for bulk samples operated at liquid nitrogen temperature [3,6].

The same method can be applied to measure other superconducting material such as  $BiCaSrCuO_x$  ( $BCSCO$ ) which has two transition temperatures at 80 K and 110 K. This measurement method can also be used for thin film superconducting material measurements. Work with these materials is currently in progress.

### ACKNOWLEDGMENTS

The authors acknowledge the support of this program by the Board of Regents of Texas A&M University (Grant No. AUF 24424-V to RKP), Texas Engineering Experiment Station (Grant No. 32125-92870 to RKP), DARPA (Grant No. MDA-972-88G-0002 to RKP), and to Texas Instruments, Inc. for granting a Fellowship to M. K. Skrehot. Furthermore, we express our thanks also to K. L. Cuerton, T. Sauter, and S. C. Blanton of Electronic Materials Laboratory of Electrical Engineering Department at Texas A&M University for their technical assistance.

### REFERENCES

- [1] M. Hagen, M. Hein, N. Klein, A. Michalke, G. Muller, H. Piel and R. W. Roth, "Observation of RF Superconductivity in  $Y_1Ba_2Cu_3O_{7-\delta}$  at 3 GHz," *Journal of Magnetism and Magnetic Materials*, Vol. 68, pp. L1-L5, 1987.
- [2] J. Tateno and N. Masaki, "Measurement of RF Superconductivity in  $YBa_2Cu_3O_{7-x}$  with the standing-wave method at 9 GHz," *Japanese J. Appl. Phys.*, Vol. 26, No. 10, pp. L 1654-1656, October 1987.
- [3] E. Belohoubek, A. Fathy and D. Kalokitis, "Microwave Characteristics of Bulk High-Tc Superconductors," in 1988 IEEE MTT-S International Microwave Symposium Digest, pp. 445-448.

- [4] K. Chang, R. K. Pandey, M. K. Skrehot, M. Li, and G. R. Gilbert, "RF Characteristics of a High Temperature Superconductive Resonant Strip in Waveguide," to appear in *Microwave and Optical Technology Letters*, Vol. 1, No. 6, August 1988.
- [5] K. Chang and P.J. Khan, "Analysis of a Narrow Capacitive Strip in Waveguide," *IEEE Trans. on Microwave Theory and Tech.*, Vol. MTT-22, pp. 536-541, May 1974.
- [6] K. Fitzgerald, "Superconductivity: Fact vs. Fancy," *IEEE Spectrum*, Vol. 25, No. 5, pp. 30-41, May 1988.

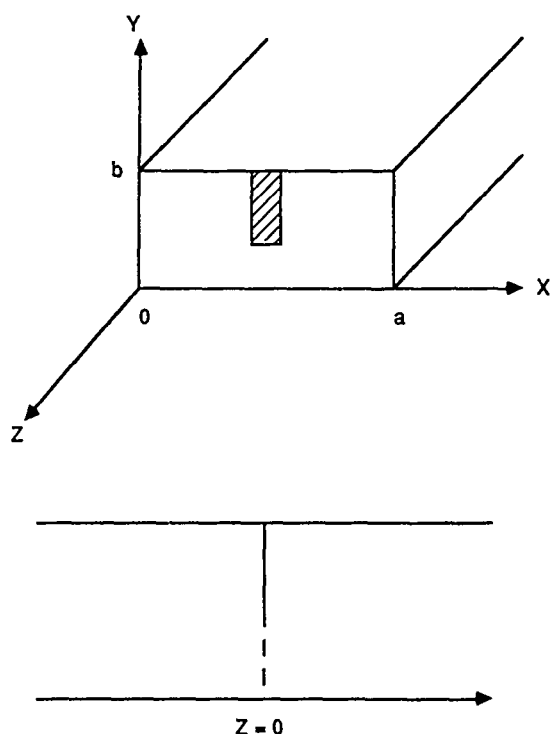


Figure 1 A resonant strip in a rectangular waveguide

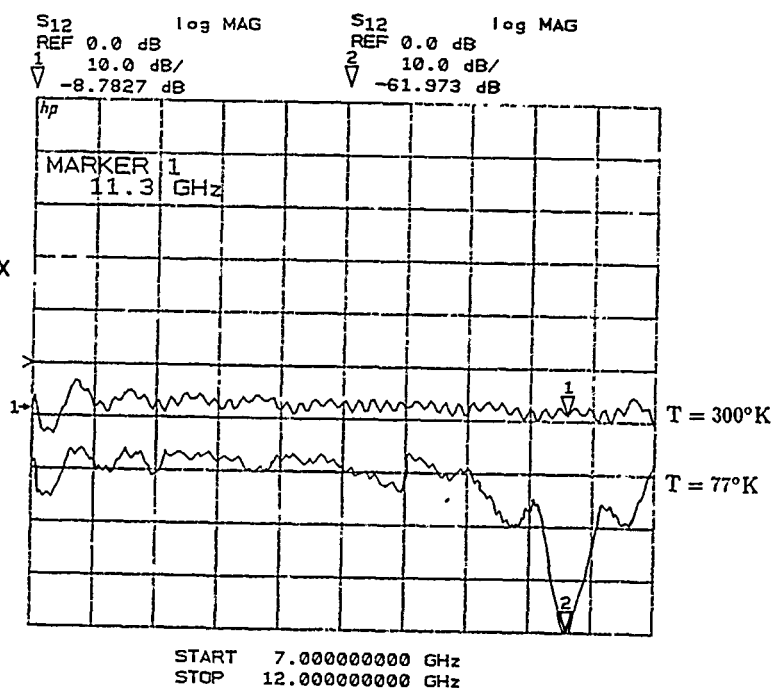


Figure 2 RF measurements of a superconducting resonant strip in waveguide at T=300K and 77 K

Characteristics and Performance of the National Synchrotron Light Source  
Infra-Red Beamline\*

Gwyn P. Williams, Carol J. Hirschmugl, D. Peter Siddons & Erin A. Sullivan  
National Synchrotron Light Source  
Brookhaven National Laboratory  
Upton, New York, 11973 USA

K. D. Moeller, P. Petrone & E. Angelides  
Physics Department, Fairleigh Dickinson University  
Teaneck, New Jersey, 07666 USA

Y. J. Chabal  
AT&T Bell Laboratories  
Murray Hill, New Jersey 07974 USA

F. M. Hoffmann  
Exxon Research and Engineering Center,  
Corporate Research Laboratories,  
Annandale, New Jersey, 08801 USA

The National Synchrotron Light Source (NSLS) is a very bright, pulsed, broadband IR source. Continuously covering the spectral range from the visible to the mm wave region, it has been calculated<sup>1,2</sup> to be one to three orders of magnitude brighter than a black-body source. At wavelengths longer than  $100\mu$ , ( $100\text{ cm}^{-1}$ ) the NSLS provides more flux than a standard globar source, due to the different power laws governing black-body radiation and synchrotron radiation emission.

We now report measurements of the spectral characteristics of the infra-red beamline.<sup>3</sup> In the measurements, the NSLS was compared with globar and mercury sources using instruments with well defined etendue (area, solid angle products). Two spectrometers were used for the measurements. For the region  $25\text{-}700\text{ cm}^{-1}$  we used a rapid-scan Michelson Interferometer using a silicon beamsplitter. For the longer wavelength region from  $5\text{-}40\text{ cm}^{-1}$  we used an interferometer with a scanning lamellar grating.



Figure 1. Photograph of the infra-red facility at the National Synchrotron Light Source, Brookhaven. The instrumentation is on a platform 11 feet above the 750 MeV electron storage ring.

In addition to its brightness properties, the synchrotron radiation source has a high degree of spatial coherence. Since the source dimensions are only  $200\mu$  high by  $400\mu$  wide, there is less than a wavelength of wavefront error across the entire f10 emission cone at long wavelengths. We have verified this by recording an interferogram using a novel scanning lamellar "grating" with only one fixed and one scanning plate.

\*Research performed under the auspices of the U.S. Department of Energy under contract #DE-AC02-76CH00016.

#### References

1. Gwyn P. Williams, Int. Journal of Infra-red and Submillimeter Waves, 5 829 (1984).
2. W.D. Duncan and G.P. Williams, Applied Optics 22 2914 (1983).
3. G.P. Williams, P.Z. Takacs, R.W. Klaffky and M. Shleifer, Nucl. Instr. and Methods A246 168 (1986).

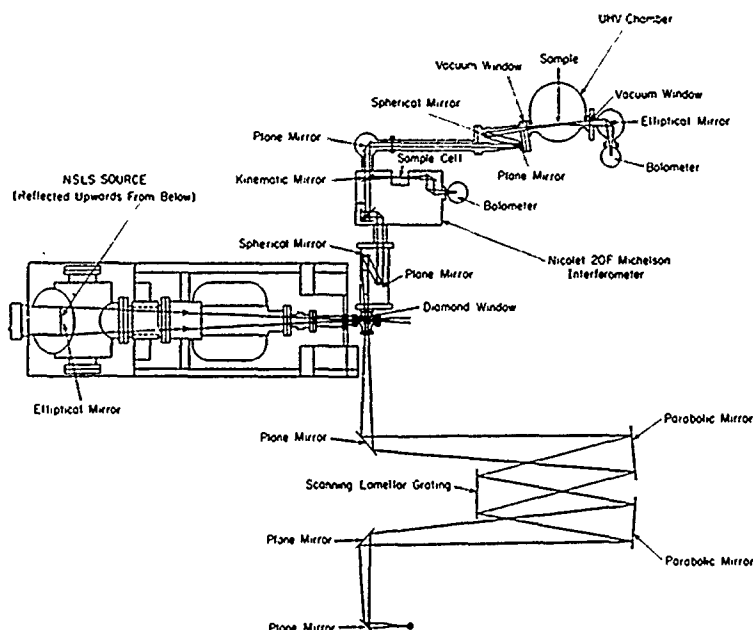


Figure 2. Schematic of the optical layout of the infra-red beamline at the National Synchrotron Light Source, Brookhaven.

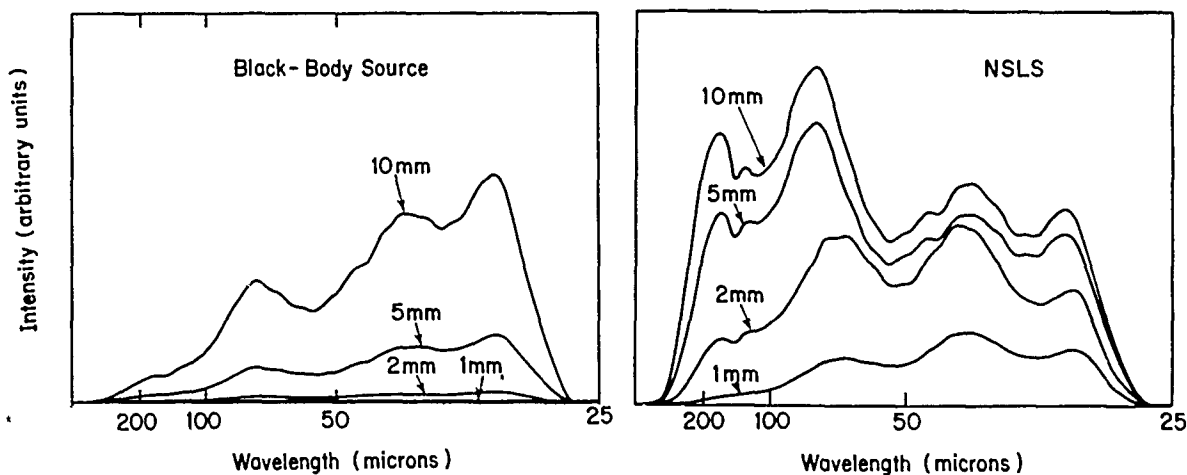


Figure 3. Comparison spectra taken at the National Synchrotron Light Source, Brookhaven using f4 optics in the sample cell, and apertures whose sizes are indicated. The spectra are plotted on the same vertical scale, for a stored beam of 330 mA. The black-body is a standard Nicolet 20F silicon carbide source at 1000K. The advantage of the NSLS at long wavelengths can clearly be seen.

OPTICALLY-PUMPED  $\text{NH}_3$  LASERS - A VERY STABLE FREQUENCY SOURCE

J. Reid

Engineering Physics Department, McMaster University,  
Hamilton, Ontario, Canada L8S 4M1

and K.J. Siemsen

NRC, Montreal Road,  
Ottawa, Ontario, K1A 0R8

## ABSTRACT

A beat-note stability of 500 Hz over 1 second has been observed between two free-running optically pumped  $\text{NH}_3$  lasers. The  $12\text{ }\mu\text{m}$  laser frequency is strongly isolated from cavity-mirror motion, and is relatively insensitive to perturbations in the pump lasers. The  $\text{NH}_3$  lasers have been used to observe Lamb-dips in external  $\text{NH}_3$  cells.

## INTRODUCTION

In the past, a variety techniques have been successfully employed to develop frequency stable lasers. However, most of these techniques are based on one general principle. Ultra-stable lasers are usually of very rigid construction, and are placed in a carefully shielded environment. These precautions ensure that the free-running laser linewidth, as determined by perturbations in the optical cavity length, is minimized. The free-running laser is then locked to an external reference to control long term drift.

In this paper, we describe a new approach to the construction of an ultra-stable laser, in which the properties of the gain medium itself help to isolate the laser frequency from external perturbations. We have successfully demonstrated this approach by developing an optically-pumped  $\text{NH}_3$  laser which is almost immune to perturbations in the pump radiation, and which shows an order of magnitude isolation from the frequency shifts induced by cavity length changes.

We have constructed two identical cw  $\text{NH}_3$  lasers operating on the  $\text{sp}(7,0)$  transition at  $12.08\text{ }\mu\text{m}$ . By heterodyning the two lasers with a fast  $\text{HgCdTe}$  detector, and measuring the frequency-tuning characteristics, we have identified an operating regime which gives very stable laser operation. Figure 1 compares the free-running frequency stability of the  $\text{NH}_3$  lasers with that of the pump  $\text{CO}_2$  lasers. Note that the stability of the  $\text{NH}_3$  lasers is a factor of 50 better than that of the  $\text{CO}_2$  lasers operating in the same environment. We find that the  $\text{NH}_3$  frequency is insensitive to perturbations in either the power or the frequency of the pump laser. A 1% change in pump power gives a  $12\text{ }\mu\text{m}$  frequency shift of  $<500\text{ Hz}$ , while a frequency shift of  $250\text{ kHz}$  in the pump produces  $5\text{ kHz}$  shift in the  $12\text{ }\mu\text{m}$  laser. In addition, the dispersion associated with the narrow  $12\text{ }\mu\text{m}$  gain profile produces a strong

frequency pulling which isolates the  $12\text{ }\mu\text{m}$  laser from the effects of cavity mirror vibration. We have directly measured isolation factors as high as 15. At present, our  $\text{NH}_3$  laser linewidth is limited by the cavity design. When the cavities are operated as conventional infrared lasers, they give a beat width of  $\geq 20\text{ kHz}$ . The same cavities give a beat width of  $500\text{ Hz}$  to  $1\text{ kHz}$  when operating on  $\text{NH}_3$ , due to the strong frequency pulling.

In recent work, the  $\text{NH}_3$  lasers have been used to observe Lamb-dips in external low-pressure  $\text{NH}_3$  cells. The  $12.08\text{ }\mu\text{m}$  emission wavelength is exactly in coincidence with the  $\text{sp}(7,0)$  absorption line in  $\text{NH}_3$ , and Lamb-dips with widths as small as  $240\text{ kHz}$  (HWHM) have been measured in a  $1\text{ m}$  absorption cell. By locking to these dips, the  $\text{NH}_3$  laser can attain good long-term stability.

We have developed a detailed theory of operation of these lasers based on a density-matrix formulation. This theory has been validated by comparison with gain measurements made in an  $\text{NH}_3$  amplifier cell. A  $9\text{ }\mu\text{m}$  beam is used to saturate the  $\text{sr}(5,0)$  transition, while the  $12\text{ }\mu\text{m}$  beam acts as a probe. Measurements made with both co- and counter-propagating beams will be presented, and plans for improving both the short and long term stability of the  $\text{NH}_3$  laser will be discussed.

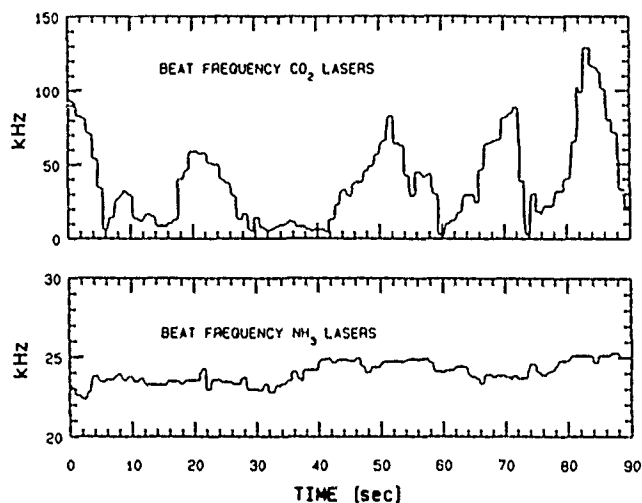


FIGURE 1: Beat frequencies of the free-running  $9\text{ }\mu\text{m}$  pump lasers and the  $12\text{ }\mu\text{m}$   $\text{NH}_3$  lasers as a function of time.



# PRESSURE EFFECTS ON THE FREQUENCY OF OPTICALLY PUMPED FAR INFRARED LASERS

Richard L. Crownover and Frank C. De Lucia

*Department of Physics, Duke University, Durham, NC 27706*

David D. Skatrud

*Army Research Office, Research Triangle Park, NC 27709*

## ABSTRACT

We have used millimeter/submillimeter spectroscopic techniques to investigate the pressure dependence of the absorption and gain frequencies of several optically pumped far infrared lasers. Pump offset effects on the gain frequencies were also investigated. These measurements are free from obfuscating effects such as cavity pulling and competing lasing lines which are present in measurements of oscillating laser systems.

## INTRODUCTION

Optically pumped far infrared (OPFIR) lasers are frequently used as fundamental sources for spectroscopy and as local oscillators for various heterodyne systems. For these and other metrologic applications, the accuracy and precision with which the frequency of OPFIR lasers can be reproducibly set is of considerable importance. A number of physical processes affect the frequency of OPFIR lasers. Chief among these are cavity pulling due to the OPFIR resonator, variations in the CO<sub>2</sub> pump laser frequency, and pressure shifts from the OPFIR laser gas. The magnitude of the latter mechanism has been a subject of recent debate. Lawandy and coworkers [1] have measured an anomalously large pressure shift of approximately 15 MHz/Torr for the 170  $\mu$ m line of CH<sub>3</sub>OH. Evenson, Inguscio, Strumia, and coworkers [2,3] have reported measurements to the contrary and have found an uncertainty in the frequency reproducibility of  $\sim 2 \times 10^{-7}$ . We have used our millimeter/submillimeter (mm/submm) spectroscopic techniques to investigate the fundamental physical processes which affect the frequency of OPFIR lasers.

## EXPERIMENTAL SYSTEM

The mm/submm wave probe was generated by a point contact harmonic multiplier driven with a phase-locked klystron and detected by a helium cooled bolometer. Useful probe radiation can be produced and detected continuously in the range from 100 to 1000 GHz by these techniques [4]. The probe radiation was copropagated with the CO<sub>2</sub> pump radiation through a mirrorless gain cell. The mm/submm probe frequency was swept over the region of the emission frequency. Two detection methods were used: direct detection with a cw pump and lock-in detection referenced to a chopped pump.

These measurements provide a direct probe of the OPFIR gain curve which is independent of cavity pulling affects and other possible obscuring affects arising from measurements on oscillating lasers (e.g. output from competing lines). The independence from cavity effects greatly simplifies the interpretation of the data in terms of the fundamental physical processes. Although our experiments are not sensitive to cavity effects, this is not a problem since cavity pulling is a well understood process. Given the width of the gain profile and Q of the cavity, the size of the cavity pulling effect and the resulting reproducibility limits are easily and accurately predicted.

## MEASUREMENTS AND DISCUSSION

At the relatively low pressures typically used in CW OPFIR lasers, the rovibrational pump transition is inhomogeneously broadened. Therefore when the pump is not exactly coincident with the energy spacing, a velocity subset in the wings of the Doppler profile is selectively pumped and the gain frequency for the OPFIR transition is shifted away from rotational line center.

Figure 1 shows the measured peak gain frequency for the 496  $\mu$ m <sup>12</sup>CH<sub>3</sub>F OPFIR line while being pumped by approximately 3 W of 9P20 CO<sub>2</sub>. The proportionality of the Doppler shift with frequency has been used to scale the actual pump offset frequency at the vibrational frequency to the effective offset frequency at the rotational transition frequency. Since the cross section for rotationally inelastic collisions is much

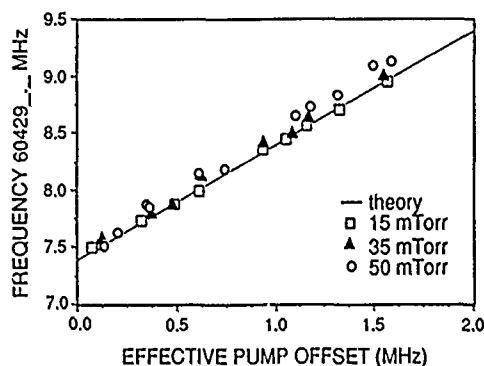


FIG. 1. Experimental frequency of the peak gain as a function of the effective pump offset.

larger than that for velocity changing collisions, the excited molecules will tend to remain in the velocity subclass in which they were pumped until they have reached rotational states far from those involved in the OPFIR laser transition. This implies that for longitudinally pumped systems (where the OPFIR radiation is parallel to the pumped velocity component) the gain offset should be proportional to the pump offset with a slope of one as plotted by the solid line in Figure 1. The data are seen to be in good agreement with this expectation; however, close inspection shows a systematic deviation with pressure for the three different pressures groups that are plotted. This effect is more readily apparent in Figure 2 where the proportionality with the pump has been subtracted and only the remaining shift plotted — higher pressures clearly exhibit a larger shift.

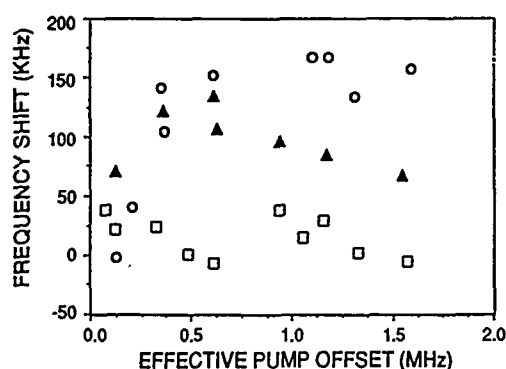


FIG. 2. Shift in frequency of the peak gain from simple theory. The pressures are labeled as in Figure 1.

We performed pressure broadening measurements in pure absorption for this  $^{12}\text{CH}_3\text{F}$  OPFIR laser transition,  $J = 12 - 11$ ,  $K = 2$ . Data were collected over a range of 25 - 110 mTorr. The pressure broadening coefficient was measured to be  $17.8 \pm 0.7$  kHz/mTorr. No observable pressure shift was found to within the experimental uncertainty which was conservatively estimated to be 0.4 kHz/mTorr. Therefore the gain shifts of Figure 2 cannot be attributed to a pressure induced shift.

In addition to the pumped, nonthermal molecules in the rotational states of the pumped excited vibrational state, there also exists a thermal distribution in these rotational states. This distribution absorbs radiation at the rotational energy spacings, including that of the OPFIR laser frequency. The net gain is equal to the gain from the nonthermal excitation minus the absorption from the thermal molecules (note that the number density of the thermal molecules can greatly exceed its normal unpumped value because of the rapid rotational equilibration compared to the slower vibrational decay). When the pump is not exactly coincident with the rotational state, the gain from the nonthermal molecules will not be centered at the same frequency as the competing absorption. The resulting decrease in the net gain is larger nearer rotational line center, and thus skews the net gain away from line center. This is illustrated in Figure 3.

We have implemented a numerical simulation to verify this effect. The gain and absorption lines were subtracted from

each other for a number of thermal/nonthermal amplitude ratios. The resulting frequency for the peak net gain was plotted as a function of pump offset. The solid lines in Figure 4 shows the results at a pressure of 35 mTorr. With the appropriate ratio choice, good agreement with the experimental data (the triangles) is obtained. The shift can be seen to peak and then decrease for effective pump offsets greater than about 500 kHz. This is due to passing through the inflection point of the absorption line.

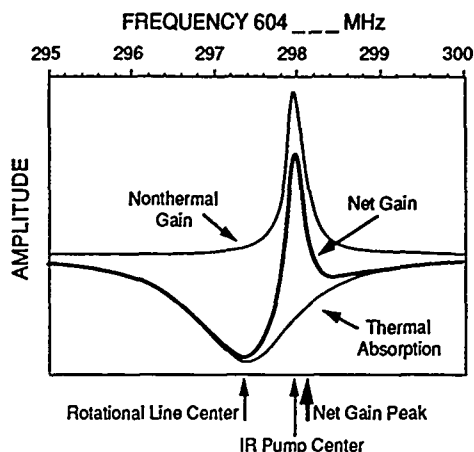


FIG. 3. Shift in the net gain due to the thermal absorption.

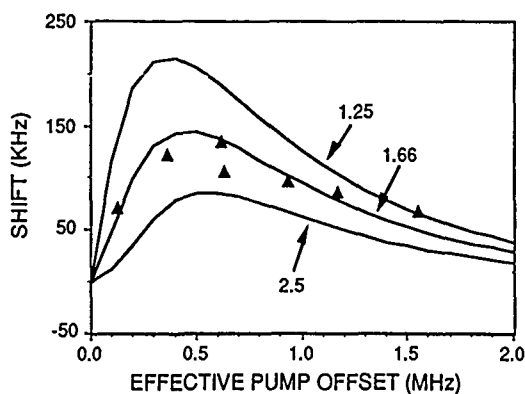


FIG. 4. Theoretical gain shifts (solid lines) for three thermal/nonthermal amplitude ratios compared with experimental data (triangles).

## REFERENCES

- [1] N. M. Lawandy, G. A. Koeff, and D. L. MacFarlane, *Infrared Phys.*, 1985, vol. 25, pp. 751-754.
- [2] M. Inguscio, N. Ioli, A. Moretti, F. Strumia, and F. D'Amato, *Appl. Phys. B*, 1986, vol. 40, pp. 165-169.
- [3] M. Inguscio and K. M. Evenson, *Optics Letters*, 1984, vol. 9, pp. 443-444.
- [4] P. Helminger, J. K. Messer, and F. C. De Lucia, *Appl. Phys. Lett.*, 1983, vol. 42, pp. 309-310.

## LASER RADAR RANGE OPTIMIZATION FOR DETECTING AND TRACKING

## AIRBORNE COOPERATIVE TARGETS

Dr. J. Gavan

Center for Technological Education Holon  
P.O.B. 305, Holon 58102, IsraelA. Korman  
Techno Science Ltd.  
P.O.B. 1784, Ramat Gan, Israel.

## ABSTRACT

A high resolution Nd-YAG pulsed Laser Radar "LIDAR" system is proposed for detecting and tracking Airborne cooperative retro-reflector carrying targets against noise, clutter and back-scatter sources. A previous range computation method is improved and new possibilities of coherent heterodyne detection and phase conjugate elements are discussed.

## INTRODUCTION

High angular resolution Laser Radar (LADAR) systems can supplement or extend conventional radar techniques and systems. Radar technology had borrowed many techniques from well known approaches in optics [1].

Modern LADAR systems are used for many applications where long distances and higher angular resolution is required which exceeds the known capabilities of microwave radars. The orders of magnitude decrease in wavelength allowing for very small apertures with very high beam collimation capabilities [1;2].

The increase in frequency provides for very high bandwidth and time resolution capabilities in the order of several nano-seconds [2].

LADAR operation in the atmosphere, however, is subject to various degrees of absorption, scattering and coherence degradation due to the shorter wavelength used [1;3;4].

It was found necessary to develop a straight forward approach in which one can predict the required Radar system physical parameters, based on standard Radar operational parameters [3], which are range, probability of detection  $P_d$  and False Alarm Rate (FAR) or equivalent probability  $P_f$ .

#### Analysis and computation of interferences limitations for the Proposed LADAR system

The tracked cooperative targets, whose geometry is shown in Figure 1, use retro-reflectors, thereby increasing system efficiency and ranging.

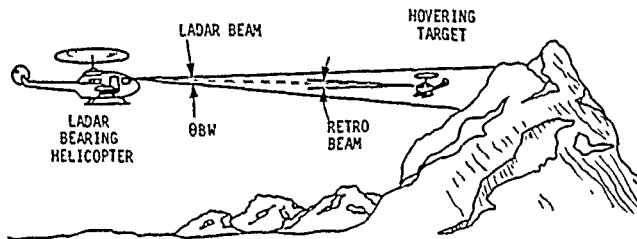


Figure 1. Geometry of a Retro-carrying Target against Typical Background

The desired signal Power Ratio from the cooperative target with retroreflector, related to signal from the cluttering, is significantly more critical than related to the scattering interference source [3]. This power ratio can be calculated from equation (1) [2;3].

$$\frac{P_{\text{retro}}}{P_{\text{clutter}}} = S_c = \frac{\pi^2 \cdot K_{1,0} \cdot D_{(r)}^4 \cdot \rho_{(1,0 \text{ retro})}}{4 \lambda^2 \cdot K_{2,0} \cdot \rho_{(0,1 \text{ diff})} \cdot \theta^2 \cdot R^2 \cdot 10^6} \quad (1)$$

where:

$R$  is the cooperative target operative range in km.

$K_{1,0} = \frac{0,65}{e}$  The target attenuation factor due to atmospheric turbulences;

$D_{(r)}$  Cooperative aperture diameter is 0,038 m;

$\rho_{(1,0 \text{ retro})}$  Attenuation factor of the cooperative target  $K_{2,0}$  Retro factor for the circular cross section is 3,7.

The clutter or scattering causes an equivalent reflection factor [3] of  $\rho_{(0,1 \text{ diff})} = 0,6$  typical and  $\rho_{(0,1 \text{ diff})} = 0,8$  for realistic worst case value applied for the computation of minimum range.

The critical ranges limitations in the far field regions above 1 km are provided only by the background clutter interferences,

$$S_c = \frac{2350}{R^2} \quad (2)$$

and the (back) scattering interference effects can be neglected [3].

The clutter returns, as in the thermal noise case, is modeled after a Rician Distribution [3].

The log normal distribution approximation, however, can be applied for computing the detection probability of the LADAR system when the clutter signals are much stronger than the quantum noise power levels [3;4].

The false alarm probability is given by [3]

$$\frac{b}{\sqrt{2N}} = \sqrt{\ln \left( \frac{1}{P_f} \right)} \quad (3)$$

where  $N$  is the total clutter power average at the detector input and  $b$  is the threshold voltage for false alarm detection.

The probability of detecting a signal in the presence of clutter is then given by

$$P_d = \frac{1}{\sqrt{\pi}} \int_{\left( \frac{b-A}{\sqrt{2N}} \right)}^{\infty} e^{-y^2} dy \quad (4)$$

which is the tabulated standard normal error function [5].

$$\text{If } y = \frac{r-A}{\sqrt{2N}} \quad (5)$$

For any given  $b < A$ , therefore [3]

$$P_d = 0,5 + 0,5 \operatorname{erf} \left( \sqrt{s} - \frac{b}{\sqrt{2N}} \right) \quad (6)$$

which gives the mathematical relations between  $P_f$ ,  $P_d$ ,  $b$ ,  $s$  and  $R$ .

The LADAR system required parameters  $P_d = 0,99$  and  $P_f = 10^{-5}$ , for example.

Using the developed method:

$$\frac{b}{\sqrt{2N}} = 3,393 \text{ and } 0,01 = \operatorname{erfc}(\sqrt{s} - 3,393)$$

and from [5]:

$$\frac{2,33}{\sqrt{2}} = \sqrt{s} - 3,393 \text{ yielding } s = 25,4 \text{ (14,05 dB)}$$

Using equations (1) and (2) we obtain:

$$R_{\min} = 9,60 \text{ km; } R_{\max} = 11,10 \text{ km}$$

In this case the effective system range is not sufficient and  $n$  pulses integration is required [3].

Choosing  $n = 8$ , the worst case signal to clutter improvement is 7,5 dB. Therefore the necessary  $s_{\min} = 14,05 - 7,5 = 6,55$  dB.

$$\text{Then, } R_{\min} = \sqrt{\frac{2350}{10^{0,655}}} = 22,80 \text{ km}$$

and  $R_{\max} = 26,40$  km.

The computer method can provide useful graph plots representing the  $R_{\min}$  and  $R_{\max}$  as function of  $P_f$  and  $P_d$  and  $n$  as parameters. Such a typical graph family for  $P_d = 0,99$  is presented in Figure 2.

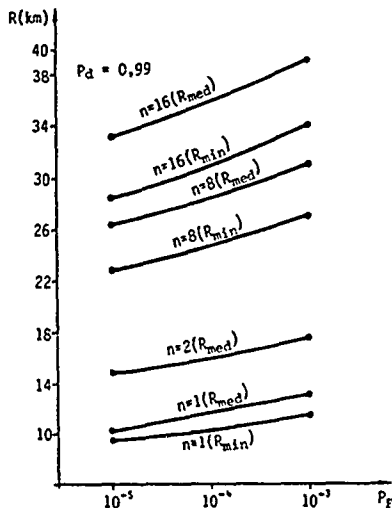


Figure 2. Computed Optimal Target Range ( $R$ ) as a function of False Alarm Rate ( $P_f$ ) using  $P_d$  and  $n$  as parameters.

#### Methods for increasing the LADAR system detection range

Remarkable improvements of " $P_d$ " and " $s$ " can be obtained by signal pulse integration [3;6]. It can be proved that increased LASER power or retroreflectors cross section are less effective.

Special signal processing and clutter reduction methods using Analog and digital technologies [7] can be implemented in the final LADAR system to increase significantly the effective detection and tracking ranges. Future development in LADAR coherent systems, even for Nd Yag LASER's, will permit a more than 10 decibels increase in the receiver system sensitivity. The heterodyne operation complemented by smart clutter reduction methods may increase significantly the system

range even for reduced LADAR transmitter power [7]. Better receiver sensitivity and system improvements can be obtained by Homodyne coherent detection instead of Heterodyne. The homodyne method is, however, more difficult to implement and requires an accurate optical Phase-Locked-Loop [8]. Further range improvements can be achieved due to the new techniques of phase conjugate materials and mirror elements [9]. The choice of special retro-reflectors implementing phase conjugate technology would enable significant reduction in the atmospheric effects concerning our proposed LADAR system. The reduced attenuation would lead to a significant increase in the system range operation specially for ground or low altitude applications.

#### CONCLUSIONS

The developed computation method indicated that LADAR systems can detect cooperative targets, against clutter and backscatter, from fairly long distances with high detection and low False Alarm probabilities. The power required for the LASER transmitters, the price, weight and volume of the equipments will be significantly reduced for equal or even better operation ranges by using the following improvements: Special Signal Processing and Clutter Reduction Methods Coherent heterodyne LADAR receivers instead of the direct detection method.

Homodyne detection method more efficient than the heterodyne but difficult to implement. Phase Conjugate materials and mirror elements technology which may be used in future projects.

#### REFERENCES

- [1] M. Skolnik, Introduction to RADAR systems, International Student Edition 1980, Chapters: 2,10,13,14.
- [2] W. Wolfe, G.J. Zissis, The infrared Handbook Office of Naval Research, 1978, Chapter 23.
- [3] J. Gavan and A. Korman, False alarm, detection probability factors implementations on LIDAR design. IEEE 12th International conference on Millimeter Waves and IR digest, December 1987.
- [4] RCA Electro optics Handbook, Section 7, 1974.
- [5] B. Sklar, Digital Communications, Prentice Hall, 1988, pp. 87-88, 156, 742-743.
- [6] M. Schwartz, Information, Transmission, Modulation and Noise, McGraw Hill, 1970, pp. 442-454.
- [7] J. Salz, Modulation and detection for Coherent lightwave communications, IEEE Com. Magazine, Vol.24, No.6, June 1986, pp. 38-49.
- [8] L.G. Kozovsky, Balanced Phase-Locked Loops for Optical Homodyne receivers performance analysis design considerations, IEEE Journal of L.T., Vol.4, Feb. 1986, pp.182-195.
- [9] A. Yariv et.al, Real time phase conjugate window for one way optical field imaging through a distortion, Appl. Phys. Lett. 41(2), July 1982, pp. 141-143.

# INITIAL ATTEMPTS TO OBSERVE LONG WAVELENGTH PHASE CONJUGATION IN AN ARTIFICIAL KERR MEDIUM

Peter A. Krug

University of Sydney  
Sydney, N.S.W. 2006  
Australia

Dennis K. Mansfield  
Princeton University Plasma Physics Laboratory  
Princeton, New Jersey 08543 USA

## ABSTRACT

Stable, well-dispersed suspensions of dielectric particles have been prepared for use as long wavelength artificial Kerr media. However, initial attempts at FIR degenerate four wave mixing using these suspensions have been frustrated because of the intrinsic loss of the host liquids.

## REFERENCES

- (1) D.K. Mansfield and J.F. Federici, Int. J. of Infrared and Millimeter Waves 9, (1988) 419.

Recently, the feasibility of long wavelength phase conjugation via degenerate four wave mixing in an artificial Kerr medium has been considered (1). Indeed, it has been suggested that, for wavelengths near 100 microns, a collection of micron size particles suspended in a transparent liquid would exhibit phase conjugate reflectivities approaching or exceeding unity in the DFM geometry, assuming pump power levels that are available from the present generation of FIR lasers.

Attempts to suspend large particles of transparent materials (Si, Ge, diamond, ...etc.) in transparent non-polar liquids (decalin, cyclohexane...etc.) using commercially available surfactants have been successful. In addition, long wavelength Fourier transform spectroscopy of these suspensions has shown that some of them retain their transparency in the FIR. However recent attempts to use these media in degenerate four wave mixing experiments have met with failure because of the intrinsic loss of the host liquid ( $0.5 \text{ cm}^{-1}$ ).

Experiments were carried out in which the particle motions of these suspensions were observed with a microscope while the suspension was illuminated with the output of a FIR laser operating at 119 microns. For FIR power levels ranging from 10 to 100 mW the particles were observed to swirl in convective cells rather than to form the spatial gratings needed for phase conjugation to occur. This behavior is attributed to the intrinsic loss of the host material and must be overcome before long wavelength phase conjugation in this medium can succeed. In that regard, attempts are being made to find lower loss liquids than those employed in this work.

This work supported by US DOE Contract No. DE-AC02-76-CH0-3073.

In addition, one of us (PAK) acknowledges the Australian National Research Fellowships - Queen Elizabeth II Awards Scheme for supporting both this work and his attendance at this Conference.

# SUBMILLIMETER WAVE LOW TEMPERATURE ADMITTANCE OF N-GaAs AND InP DIODE STRUCTURES USING TRANSPORT ANALYSIS

Clifford M. Krowne

Electronics Science and Technology Division  
Naval Research Laboratory  
Washington, DC 20375-5000

## ABSTRACT

Numerical simulation results for n-nn+ GaAs and InP diode structures in the 1-3 THz frequency range are presented. Cryogenic temperatures from 4 through about 77 K are examined to obtain the two-terminal admittance. Earlier work has suggested possible negative differential conductivity (NDC) at or below 4.2 K, but no consistent NDC above 77 K. Implications of the Monte Carlo data for generation of submillimeter waves at these intermediate temperatures is discussed.

## INTRODUCTION

The ability of submicron n-nn+ GaAs diodes to generate submillimeter waves has been previously studied over a variety of lattice temperatures  $T_L$  and signal amplitude conditions [1,2]. At terahertz frequencies, the signal period is on the order of magnitude of the intervalley relaxation time, making negative differential conductance (NDC) behavior only weakly dependent on intervalley effects. Instead, carrier inertial effects dependent upon other material and structural properties of the device take over beyond a few hundred gigahertz. This physical behavior is reflected in the difficulty of obtaining NDC in the diodes at high  $T_L$ . Indications of NDC seem to occur at cryogenic temperatures, in particular, at or below 77 K.

Here we look at device length, dc bias voltage, and doping density variations which may influence the NDC in GaAs. The III-V sister material to GaAs, InP, is also examined because its material properties [3-5], such as enhanced saturation velocity and increased threshold voltage for intervalley transfer, could change the NDC device characteristics. Terminal admittance  $Y$  is obtained numerically for both GaAs and InP using a large signal, time domain Monte Carlo transport simulation approach on a CRAY X-MP/12 supercomputer.

## GaAs ADMITTANCE

Device terminal admittance  $Y$  at 4.2 K is given in Fig. 1 for a 0.30, 0.30, 0.30  $\mu\text{m}$  n-nn+ structure having  $10^{17}$ ,  $10^{14}$ ,  $10^{17}/\text{cc}$  doping  $N_d$ . Mesh points are separated by  $\Delta x = 200 \text{ \AA}$  and the time increment  $\Delta t$  is 5 fs. Calculated data points using 20,000 superparticles are provided every 0.2 THz, connected by straight lines, and given in the  $f = 0.8\text{-}3.0$  THz frequency range. The ac modulation voltage  $V_{ac} = 0.03 \text{ V}$  and dc bias voltage  $V_{dc} = 0.42 \text{ V}$ . The contour is similar to the central region doping  $N_{dc} = 10^{15}/\text{cc}$  result found earlier [1]. However, between 2.2 and 2.8 THz, the  $Y_r$  is now larger,

reducing the NDC. When the device size is uniformly doubled (and  $\Delta x = 400 \text{ \AA}$ ), Fig. 2 is obtained at 4.2 K ( $N_{dc} = 10^{15}/\text{cc}$ ). Maximum NDC is reduced by a factor of two. Elevating  $T_L$  to 77 K again reduces NDC (by a factor of two) as seen in Fig. 3. Going back to the smaller structure, and applying a much larger  $V_{dc} = 2.5 \text{ V}$ , does noticeably alter the contour shape, but NDC is not improved (Fig. 4).

## InP ADMITTANCE

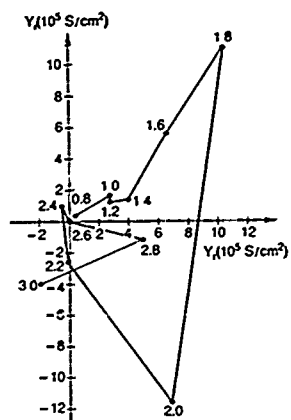
The InP admittance contours are created for the smaller device of 4.2 and 77 K. For  $V_{dc} = 0.40 \text{ V}$  and  $V_{ac} = 0.03 \text{ V}$ , Figs. 5 and 6 give the results. It is seen that NDC is reduced upon raising  $T_L$ . When  $V_{dc}$  is increased by a factor of 2.7 (the InP to GaAs threshold voltage ratio for intervalley transfer), the negative  $Y_r$  excursion is increased at 4.2 K, (Fig. 7) but at 77 K (Fig. 8) no NDC is apparent.

## SUMMARY

The above numerical results plus admittance contour plots done for GaAs at  $T_L = 8, 16, 24, 32, 40, 50$ , and 60 K and for InP at 200 and 300 K suggest that NDC below about 3 THz, if it is to be found at all, will likely occur for  $T_L < 20 \text{ K}$ . No consistent improvement of InP over GaAs for producing NDC below 3 THz is found.

## REFERENCES

- [1] C. M. Krowne and P. A. Blakey, "On the Existence of Submillimeter-Wave Negative Conductance in n-Gallium Arsenide Diodes," J. Appl. Phys., Vol. 61, pp. 2257-2266: Mar. 1987.
- [2] C. M. Krowne, "Nonlinear Large Signal Admittance in n-GaAs Diodes at Terahertz Frequencies Based Upon Transport Analysis," J. Appl. Phys., Vol. 64, Aug. 1988.
- [3] D. C. Herbert, W. Fawcett and C. Hilsum, "High-Field Transport in Indium Phosphide," J. Phys. C: Solid State Phys., Vol. 9, pp. 3969-3975: 1976.
- [4] T. J. Maloney and J. Frey, "Transient and Steady-State Electron Transport Properties of GaAs and InP," J. Appl. Phys., Vol. 48, pp. 781-787: Feb. 1977.
- [5] K. Brennan and K. Hess, "High Field Transport in GaAs, InP and InAs," Solid-State Electronics, Vol. 27, pp. 347-357: Apr. 1984.



# ANALYSIS OF SCATTERING FROM OIL FILM ON SEA SURFACE WITH A MODEL OF STRATIFIED MEDIUM WITH SLIGHTLY ROUGH INTERFACES

Sun Liguang and Xu Shanjia

Department of Radio and Electronics  
University of Science and Technology of China  
Hefei, Anhui  
The People's Republic of China

## ABSTRACT

A model of stratified medium with the slightly rough interfaces is presented for analysis of scattering from oil film on sea surface. Because the thickness of oil film is considered, the model is more realistic than that raised in other paper in which only single rough surface is assumed. In this paper, the coupled differential equations are derived and solved by using full wave approach, and the simple expressions of back scattering cross section for oil film on sea surface have been obtained. According to these expressions some curves are given for different thickness of oil film. It is shown that the results obtained by the present model are in better agreement with the experimental data than those obtained by single surface model.

## INTRODUCTION

The problem of remote sensing of oil film on sea surface has been studied extensively. In previous work [1] the model of a single rough sea surface was used to treat the problem by perturbation approach, in which the effect of thickness of oil film was neglected. However, in actual cases the oil film always has some thickness. Therefore, more accurate model is needed for practical applications. In the paper a model of stratified medium with slightly rough interfaces is presented. Because the oil film on sea surface is considered as multilayered structure of arbitrary thickness. It is obvious that the presented model is more realistic than the single surface model.

In the paper the coupled differential equations for the scattering problem are derived and solved by means of full wave approach. The simple expressions of backscattering cross section of oil film on sea surface are obtained. The scattering characteristics of different oil film thicknesses are calculated. It is shown that the scattering characteristics are quite different for different thicknesses. A practical example is calculated with different models. Due to considering effect of the thickness of oil film, the results obtained by present model are in better agreement with experimental data than those obtained by single surface model, and the utility of the present model is justified.

## THEORETICAL ANALYSIS

There are three regions used to describe the oil film on sea surface, let  $\epsilon_0$ ,  $\epsilon_1$ , and  $\epsilon_2$  are complex permittivity of upper medium (air), middle medium (oil film), and lower medium (sea), respectively, and  $\mu_1 = \mu_2 = \mu_0$  is assumed. The upper interface (air/oil film) and lower interface (oil film/sea) are defined by  $z = \zeta_0(x, y)$  and  $z = \zeta_1(x, y)$ , which are random variables. The distance between upper and lower interface is  $H_1(x, y) = \zeta_1(x, y) - \zeta_0(x, y)$ , and  $H_1$  is the mean of  $H_1$ , that is  $H_0 = \langle H_1 \rangle$ .

First, the field is expanded by the basis functions consisting of the radiative, lateral, and surface-wave terms. Using exact boundary conditions and properties of basis functions. Maxwell's equations are converted into rigorous sets of ordinary coupled first-order differential equations. The iterative approach is used to solve the coupled differential equations. By employing the steepest descent method, the expressions of scatter field are derived for the case in which the source and the receiver are far from the irregular boundary [2].

To simplify the problem, following three are assumed in analyzing the scattering problem: (a) upper and lower interface have same fluctuation, i.e.  $H_1 = H_0$ , (b) the spectral density of the random rough surface is that of sea surface, which is defined by  $W(p, q) = K(|p|^2 + |q|^2)^{-k_1}$ , (c) the surface is slightly rough. It is obtained that the backscattering cross section of oil film on sea surface is as:

$$\sigma_{pa} = \sigma_{pa}^1 g_{pa} \quad P, Q = V \pi H \quad (1)$$

where  $\sigma_{pa}^1$  is the backscattering cross section for single rough surface (corresponding to  $K, H_0 \rightarrow \infty$ ), which is the same as the results obtained in other paper [1].  $g_{pa}$  is a factor for stratified medium with slightly rough interfaces, which is main result of this paper different from others, and  $\sigma_{pa}^1$  is defined as:

$$\sigma_{pa}^1 = k_1 C_0^{-1} S_0^{-k_2} \alpha_{pa} \quad P, Q = V \pi H \quad (2)$$

where

$$\alpha_{VV} = \left| \frac{(\epsilon_{1r} - 1)(\epsilon_{1r} - 1) S_0^{1/2} + \epsilon_{1r}}{(\epsilon_{1r} C_0^2 + |\epsilon_{1r} - 1| S_0^{1/2})^2} \right|^2$$

$$\alpha_{HV} = \alpha_{VH} = 0$$



$$\alpha_{HH} = \left| \frac{(\epsilon_{1V} - 1)}{(C_0^2 + \sqrt{\epsilon_{1V} - S_0^2})^2} \right|^2$$

and  $g_{HH}$  is given by:

$$g_{VV} = \left| (1 + A_1^{VV} e^{\theta_i} + A_2^{VV} e^{2\theta_i}) / (1 + A_3^{VV} e^{\theta_i})^2 \right|^2 \quad (3)$$

where

$$A_1^{VV} = \frac{2(\epsilon_{2V} - \epsilon_{1V})[2\epsilon_{1V}(\epsilon_{1V} - S_0^2)(\epsilon_{1V}\epsilon_{2V} + S_0^2(\epsilon_{2V} - \epsilon_{1V}))]}{(\epsilon_{1V} - 1)(\epsilon_{1V} + S_0^2(\epsilon_{1V} - 1))(\epsilon_{2V}\epsilon_{1V} - S_0^2 + \epsilon_{1V}\sqrt{\epsilon_{2V} - S_0^2})} \\ - \frac{2(\epsilon_{2V} - \epsilon_{1V})(\epsilon_{1V} - 1)(\epsilon_{1V}C_0^2 - S_0^2)(\epsilon_{1V}\epsilon_{2V} - S_0^2(\epsilon_{1V} + \epsilon_{2V}))}{(\epsilon_{1V} - 1)(\epsilon_{1V} + S_0^2(\epsilon_{1V} - 1))(\epsilon_{2V}\epsilon_{1V} - S_0^2 + \epsilon_{1V}\sqrt{\epsilon_{2V} - S_0^2})}$$

$$A_2^{VV} = \left( \frac{\epsilon_{2V}\sqrt{\epsilon_{1V} - S_0^2} - \epsilon_{1V}\sqrt{\epsilon_{2V} - S_0^2}}{\epsilon_{2V}\epsilon_{1V} - S_0^2 + \epsilon_{1V}\sqrt{\epsilon_{2V} - S_0^2}} \right)^2$$

$$A_3^{VV} = \frac{(\epsilon_{1V}(C_0^2 - \sqrt{\epsilon_{1V} - S_0^2})(\epsilon_{2V}\epsilon_{1V} - S_0^2 - \epsilon_{1V}\sqrt{\epsilon_{2V} - S_0^2}))}{(\epsilon_{1V}C_0^2 + \sqrt{\epsilon_{1V} - S_0^2})(\epsilon_{2V}\epsilon_{1V} - S_0^2 + \epsilon_{1V}\sqrt{\epsilon_{2V} - S_0^2})}$$

$$B_1 = -j\sqrt{\epsilon_{1V} - S_0^2}(2k_0H_0)$$

Similar results for  $g_{HH}$  are obtained. Because of space limitation, they are omitted here.

In above formulae the subscripts V and H denote vertical and horizontal polarization, respectively.  $\theta_i$  is the incident angle,  $C_0^2 = \cos^2\theta_i$ ,  $S_0^2 = \sin^2\theta_i$ .  $K_1$  and  $K_2$  are parameters of sea surface, and  $k_0 = \omega\sqrt{\mu_0\epsilon_0}$ .

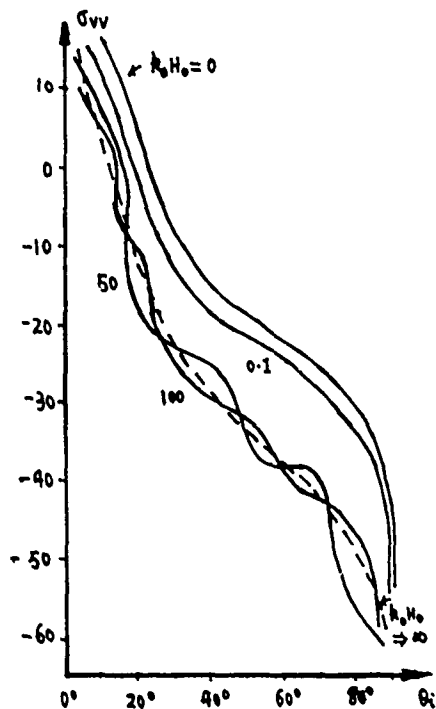


Fig.1

## NUMERICAL CALCULATION

We have obtained the formulae of backscattering cross section for oil film on slightly rough sea surface, as shown in Eqs. (1), (2) and (3). Here, some numerical results are given.

Supposing  $\epsilon_{1V} = 2.06 - j0.021$ ,  $\epsilon_{2V} = 58.11 - j28.86$ , and  $K_1 = 0.003$ ,  $K_2 = 5.5$ , we plot the backscattering cross section  $g_{VV}$  as a function of  $\theta_i$  and  $k_0 H_0$  in Fig.1. It has been seen that when  $k_0 H_0$  increases the curves approach the curve corresponding to  $k_0 H_0 \rightarrow \infty$ , when  $k_0 H_0$  decreases the curves approach the curve of  $k_0 H_0 = 0$ . For different  $k_0 H_0$ , the curves appear great differences. It indicates that the return power from lower interface always affects the total power. That is why  $H_0$ , as an important parameter in calculating the scattering problem should be considered for general case.

Fig.2 gives the scattering characteristics of oil film on sea surface, which are calculated with different models. The solid line shows the results calculated by present model, and the dotted line denotes the results obtained by the single surface model using the relative formula given in [1] and  $\times$  denotes the experimental point. The good agreement between theoretical and experimental results justifies that the present model is more reasonable than single surface model for analyzing the oil film scattering problem.

## REFERENCES

- [1]. K. Krishen, Proceeding of the 8-th International symposium on remote sensing of environment, October, 1972.
- [2]. Sun Ligu and Xu Shanjia, Proceedings of APMC'88, 1988.

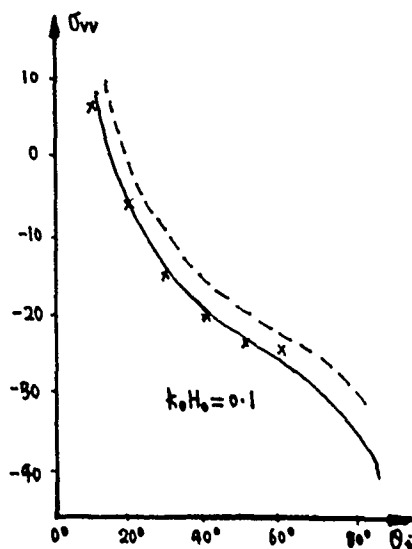


Fig.2

## Operation of a Quasi-Optical Gyrotron with Variable Output Coupling

A.W. Fliflet, T.A. Hargreaves<sup>†</sup>, W.M. Manheimer,  
R.P. Fischer, and M.L. Barsanti<sup>†</sup>

Naval Research Laboratory  
Washington, D.C.

### ABSTRACT

Results from a quasi-optical gyrotron experiment with a 20 – 28 cm mirror separation will be presented showing operation from 95 – 130 GHz at powers up to 150 kW and efficiencies up to 11%. The output coupling can be controlled by varying the mirror separation. Efficiency optimization by variation of output coupling and by tapering the magnetic field has been demonstrated.

### INTRODUCTION

The quasi-optical gyrotron (QOG) has been under development as a megawatt average power source of 100-300 GHz radiation for ECRH of fusion plasmas.<sup>1-3</sup> It differs from conventional gyrotrons by having an open resonator formed by a pair of spherical mirrors instead of a waveguide cavity. The QOG operates in one or more of the  $TEM_{00n}$  gaussian modes of the resonator. To obtain low mirror ohmic losses consistent with CW operation at millimeter wavelengths, the axial mode index  $n$  must be large ( $> 100$ ) and the relative mode separation must be small compared to the interaction bandwidth. This leads to the possibility of several interacting axial modes with attendant mode competition. This paper presents results from an experimental study of this operating regime. The separation of the resonator mirrors is adjustable which allows independent variation of the resonator output coupling. The QOG has operated from 95 – 130 GHz at powers up to 150 kW and efficiencies up to 11%. Efficiency optimization by variation of output coupling and by tapering the magnetic field has been demonstrated. Operation in single and multimode steady-states has been observed. These results point the way to the realization of megawatt level devices.

### EXPERIMENTAL SETUP

A schematic of the experiment is shown in Figure 1. A 13  $\mu$ sec pulselength annular electron beam with a velocity pitch ratio  $\alpha \equiv v_{\perp}/v_{\parallel} \sim 1$  is generated by a Varian temperature-limited MIG-type gun which operates at voltages up to 78 kV and currents up to 25 Amp. A magnetic field of up to 50 kG is provided by superconducting coils in a modified Helmholtz configuration. The magnet dewar incorporates a 6 inch axial bore and a 4 inch crossbore which contains the resonator mirrors and output waveguides. The mirrors used in the experiment have a 38.7 cm radius of curvature and a diameter of 5 cm. The mirror separation is adjustable from 20-28 cm while under vacuum by means of six micrometers which also provide for mirror alignment and translation with respect to the electron beam. The resonator output coupling is via diffraction around the mirror edges and depends on the operating frequency as well as the mirror separation as shown in Figure 2. The theoretical results shown in Figure 2 were obtained using a code based on a scalar diffraction theory discussed in Ref. 3. The results show how the diffraction losses increase with increase in mirror separation. The microwave power is taken out equally around each mirror and

is output through a pair of 0.013 cm thick mylar windows which are essentially transparent to all frequencies produced by the device. Frequency measurements were obtained using a heterodyne system in which the QOG output was beat against the signal from a 12-15 GHz tunable oscillator via a harmonic mixer. Power measurements were made with a laser calorimeter with is estimated to be 95% absorptive at 120 GHz based on reflectivity measurements.

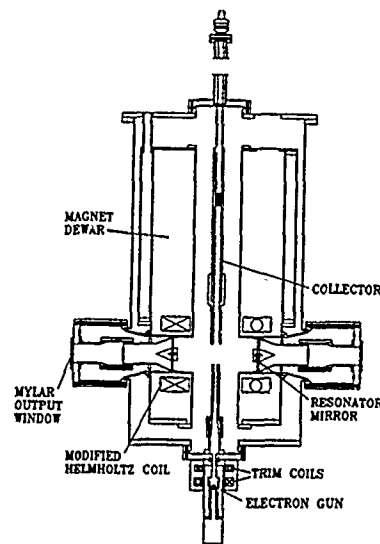


Figure 1: Schematic of QOG experiment.

Large volume resonant cavities are inherently over-moded, however, the present resonator and output coupling scheme effectively discriminates against higher order transverse modes ( $TEM_{mnl}$  with  $m > 0$  or  $n > 0$ ) leaving only the lowest order gaussian modes of the form  $TEM_{00l}$ , where  $l \sim 150 - 200$  depending on the operating frequency and mirror separation. The radiation waist radius  $w_0 \approx 4.5\lambda$ , where  $\lambda$  is the wavelength of the radiation. The frequency separation between adjacent axial modes is  $\sim 0.5\%$  which is much less than the interaction bandwidth ( $\sim 5\%$ ). Thus multimode effects, which are an issue for cw devices can be investigated. On the other hand, the frequency separation between modes,  $\sim 600$  MHz, was easily resolvable by our frequency diagnostic system.

### RESULTS

Extensive measurements have been carried out for this configuration including threshold current studies, output power and efficiency measurements, and oscillation frequency measurements. The threshold current studies included investigation of the effect of resonator translation, as well as variation of the magnetic field and mirror separation. These

measurements were generally in agreement with small signal theory. Threshold currents as low as a few tenths of an Ampere were observed. The best fit between theory and experiment was obtained by assuming  $\alpha \sim 1.5$  which is considered achievable at currents below an Ampere. At higher currents  $\alpha \sim 1$  is considered achievable with some drop-off expected for currents above 10 Amp.

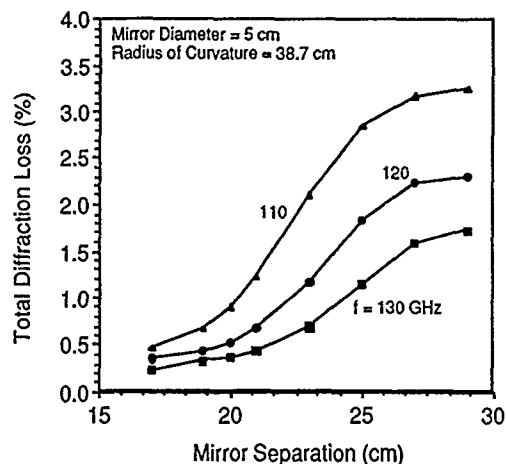


Figure 2: QOG resonator output coupling.

Initial power and efficiency measurements were taken at the minimum mirror separation of 20 cm. This minimizes the output coupling and so leads to the optimum saturated efficiency at the lowest current where beam quality should be highest. The measured efficiency as a function of beam current is shown in Figure 3 for three magnetic fields. At a beam voltage of 75 kV, a magnetic field of 47 kG leads to operation at  $\sim 120$  GHz. A maximum efficiency of 11% is obtained at a beam current of 6 Amps. A disadvantage of low output coupling is that it maximizes the effect of ohmic heating of the mirrors. This is estimated to absorb over 30% of the total power generated during 120 GHz operation and 20 cm mirror separation. Correcting for ohmic heating, the peak electronic efficiency is estimated to be 17%. This is in good agreement with nonlinear, multimode simulations using the parameters of this experiment.

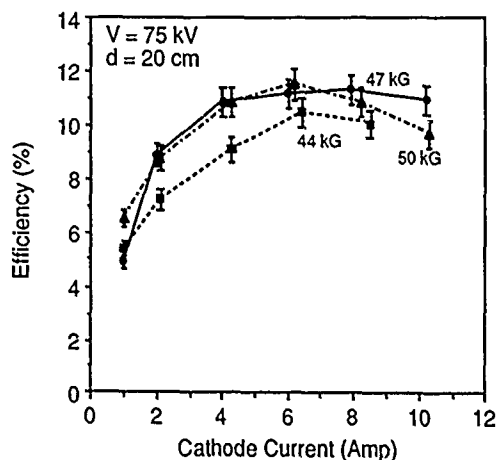


Figure 3: QOG efficiency for 20 cm mirror separation.

For a magnetic field of 50 kG and a mirror separation of 20 cm, the efficiency decreases as the current is increased

beyond 6 Amp. This effect of overdriving the resonator is well known from cavity gyrotrons. Increased efficiency at currents above 6 Amps can be obtained in the QOG by increasing the output coupling until the optimum RF field amplitude is re-established in the cavity. This effect is illustrated in Figure 4 which shows output power optimization by variation of the mirror separation and thus the output coupling.

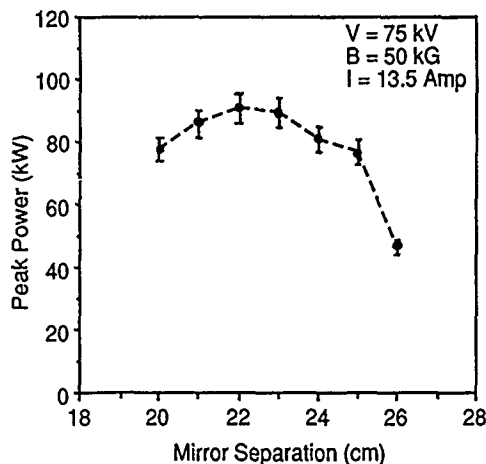


Figure 4: Output power vs. mirror separation.

The optimum measured output power was obtained by operating the gun at maximum power: about 78 kV and 24 Amp. A peak power of 125 kW at 23 Amps beam current was obtained for a 47 kG magnetic field. Optimum efficiency operation at 47 kG was generally characterized by the excitation of 1 - 3 adjacent longitudinal modes. No evidence of oscillation in higher order transverse modes was observed. The highest measured power was 148 kW at a beam voltage of 78 kV and a current of 24 Amps. This power was obtained for a magnetic field of 50 kG at the cavity midpoint and a negative 2% taper across the interaction region.

#### ACKNOWLEDGEMENT

This work was supported by the U.S. Department of Energy.

#### REFERENCES

- <sup>†</sup> Mission Research Corporation, Newington, VA
- <sup>‡</sup> Jaycor, Inc., Vienna, VA
- <sup>1</sup> P. Sprangle, J.L. Vomvoridis, and W.M. Manheimer, Phys. Rev. A, vol. 23, pp. 3127-3138, 1981.
- <sup>2</sup> T.A. Hargreaves, K.J. Kim, J.H. McAdoo, S.Y. Park, R.D. Seeley, and M.E. Read, Int. J. Electronics, vol. 57, pp. 977-984, 1984.
- <sup>3</sup> A. Perrenoud, T.M. Tran, M.Q. Tran, C. Rieder, M. Schleipen, and A. Bonderson, Int. J. Electronics, vol. 57, pp. 985-1001, 1984.

# Nonlinear Theory of Quasi-Optical Gyrotron with an Electron Beam at an Oblique Angle

C. Y. Wang, K. E. Kreischer, R. J. Temkin

Plasma Fusion Center  
Massachusetts Institute of Technology  
Cambridge, MA 02139

## ABSTRACT

In quasi-optical gyrotrons the angle between the electron and radiation beams has considerable influences on gain, harmonic operation and efficiency. This paper investigates the effect on the efficiency. Numerical simulations show that the efficiency peaks at particular angles and is acceptable even for the seventh harmonic. So the quasi-optical gyrotron is suitable for harmonic operation.

## FIELD AND PARTICLE EQUATIONS

In this paper the formulation in Ref.2 which was developed for a perpendicular injection geometry is extended to include geometries with arbitrary injection angles.

In the primed frame which is affiliated to the resonator the E and B fields can be expressed as

$$\mathbf{E} = e_x' E_0 \exp(-z^2 \sin^2 \alpha / r_0^2) \cos \omega t \sin(k_{\perp} y - k_{\parallel} z)$$

$$\mathbf{B} = e_y' E_0 \exp(-z^2 \sin^2 \alpha / r_0^2) \sin \omega t \cos(k_{\perp} y - k_{\parallel} z)$$

where  $\alpha$  is the angle between the electron and radiation beams.

Using as independent variables  $p_{\perp}, \psi$ , (transverse momentum and angle)  $x_g$  and  $y_g$  (guiding center coordinates) the equations of motion then reduce to

$$\frac{dp_{\perp}}{dz} = -\frac{em\gamma}{p_z} E(z) J_n'(Q) \cos(\omega t - n\psi) \cos(k_{\perp} y_g - k_{\parallel} z - n\pi/2) - \frac{ec \cos \alpha}{c} E(z) J_n'(Q) \sin(\omega t - n\psi) \sin(k_{\perp} y_g - k_{\parallel} z - n\pi/2)$$

$$\frac{dp_z}{dz} = \frac{ep_{\perp} \cos \alpha}{cp_z} E(z) J_n'(Q) \sin(\omega t - n\psi) \sin(k_{\perp} y_g - k_{\parallel} z - n\pi/2)$$

$$\frac{d\psi}{dz} = \frac{m\omega}{p_z} - \frac{eE(z)m\gamma}{p_z p_{\perp}} \frac{n J_n(Q)}{Q} \left( 1 - \frac{p_{\perp} \sin \alpha}{m\gamma c} \frac{Q}{n} \right) \sin(\omega t - n\psi) \cos(k_{\perp} y_g - k_{\parallel} z - n\pi/2) + \frac{eE(z) \cos \alpha}{cp_{\perp}} \frac{n J_n(Q)}{Q} \cos(\omega t - n\psi) \sin(k_{\perp} y_g - k_{\parallel} z - n\pi/2)$$

$$\frac{dy_g}{dz} = \frac{c\gamma E(z)}{p_z \Omega} J_n(Q) \left\{ \left( \frac{n\Omega}{\gamma\omega} - 1 \right) \cos(\omega t - n\psi) \sin(k_{\perp} y_g - k_{\parallel} z - n\pi/2) + \frac{p_z \cos \alpha}{\gamma mc} \sin(\omega t - n\psi) \cos(k_{\perp} y_g - k_{\parallel} z - n\pi/2) \right\}$$

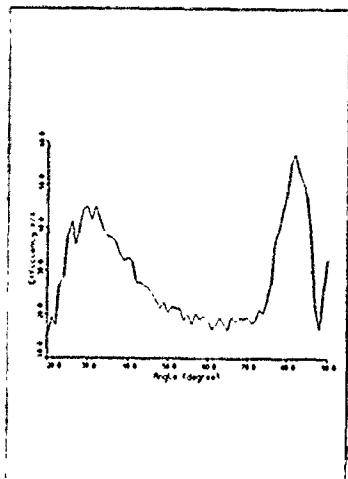
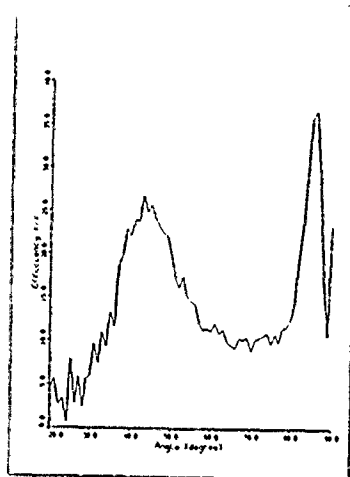
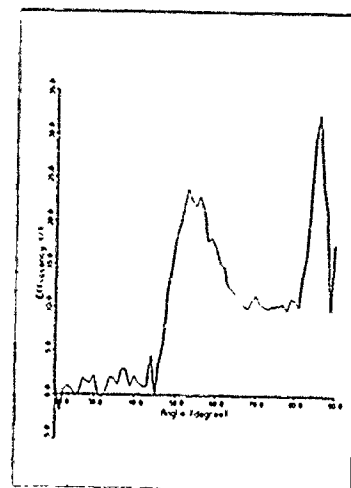
where  $Q = k_{\perp} p_{\perp} / m\Omega$ .

## CALCULATION AND ANALYSIS

Plots with efficiency versus angles ranging from  $20^\circ$  to  $90^\circ$  for the first three harmonics with  $U = 80kv$ ,  $p_{\perp}/p_{\parallel} = 1.93$ ,  $B_0 = 50kG$ , and the waist radius  $r_0 = 1cm$  are shown in Figs. (1) to (3) where the normalized E field amplitude  $\varepsilon = eE_0 r_0 / mc^2 \sin \alpha$  and the detuning  $\xi = l(\omega_c - \omega + k_{\parallel} v_z) / v_z$ . One can see that the maximum doesn't reach at  $90^\circ$  but at a smaller angle. This is because although at  $90^\circ$  the opposing Weibel instability is gone<sup>(5)</sup>, the interaction length which is in fact the waist diameter of the rf is too short. So there is a compromise between. Also one can see that below some angle the efficiency is low. There are two distinct regimes with noticeably different efficiencies. This is consistent with our linear theory in Ref.(5) where two gain regimes were identified.

## REFERENCES

- (1) J.L.Vormvoridis, P.Sprangle and W.M.Manheimer, in *Infrared and Millimeter Waves*, Vol.7, New York: Academic, 1983, ch.9, p.487
- (2) A.Bondeson, W.M.Manheimer and E.Ott, *ibid.* Vol.9, Chap.7, Academic Press, Inc. 309(1983)
- (3) C.M.Tang, S.Riyopoulos, P.Sprangle and B.Levush, *Nucl. Instrum. Methods*, Vol.A259, p.192(1987)
- (4) S.Riyopoulos, C.M.Tang, P.Sprangle and B.Levush, *Phys. Fluids* 31(4), 924(1988)
- (5) C.Wang, K.Kreischer and R.Temkin, *IEEE Trans. Electron Devices*, Vol.35, No.7, 1166(1988)

Figure 1  $n = 1, \epsilon = 0.38, \xi = -7.5$ Figure 2  $n = 2, \epsilon = 0.72, \xi = -9.5$ Figure 3  $n = 3, \epsilon = 1.48, \xi = -12.5$ 

Efficiency versus Angles for the First Three Harmonics

# A 120 GHz Axisymmetric Quasi-Optical Gyrotron

Y. Itoh, M. Komuro, K. Hayashi, and T. Sugawara

Toshiba Corp.

4-1, Ukishimacho, Kawasaki-ku, Kawasaki 210, Japan

## ABSTRACT

An axisymmetric quasi-optical gyrotron was designed, constructed, and operated. Its cavity resonator was composed of a conical mirror and a plane slotted mirror. The observed oscillation frequencies were in a range from 114 to 123 GHz. Output waves were transmitted quasi-optically to a water load. The measured output power was more than 20 kW at a frequency of 120 GHz.

## INTRODUCTION

Toshiba has been developing a concept of axisymmetric quasi-optical gyrotron [1-3] to realize 1 MW cw millimeter wave sources. The gyrotron has a quasi-optical system composed of coaxial annular reflection mirrors, two of which are for a cavity resonator. As shown in Fig. 1, one of the mirrors forming the cavity is conical and the other is plane. Waves are excited in this cavity by a co-axially injected hollow electron beam, which propagate back and forth along the ray path from point 1 to 4. Near the axis of the conical mirror, the wave function can be expressed by

$$\Phi(r, \theta, z) = \Phi_0 [J_m'(kr) e_{\theta} + i m / kr \cdot J_m(kr) e_r] \cdot \exp(-\nu z \pm i m (\theta - \theta_0))$$

where  $k = 2\pi/\lambda$ , ( $\lambda$ : wavelength),  $m$  is the azimuthal mode number, and  $\nu$  can be obtained by the equation in Ref. [2]. The plane mirror is radially slotted to serve as a partially and uniformly transparent mirror [4]. The field leaking out of the cavity through the slot array propagates in the form of a hollow Gaussian radiation beam, which can be transmitted by using a series of the annular reflection mirrors [2].

A 120 GHz-20 kW test tube was designed and constructed to demonstrate this quasi-optical gyrotron concept.

## DESIGN

Figure 2 shows the configuration of the present quasi-optical gyrotron. The electron gun produces a hollow electron beam of 2.3 A at a voltage of 30 kV. Its radius becomes 0.8 mm at the cavity in a magnetic field of 4.5 T. As shown in Fig. 1, the cavity is designed with the following three parameters: cavity radius  $R$ , mirror spacing  $l$ , and radius of curvature  $\rho$ .

In the present design,  $R = l = 7.5$  cm,  $\rho = 42.4$  cm. The plane mirror forming the cavity has 250 slots to serve as a partially transparent mirror with a voltage reflection coefficient of 95 % at 120 GHz. The output waves propagate into the transmission channel consisting of 5 mirrors and finally into a water load.

## EXPERIMENTAL RESULTS

Oscillation frequencies were observed at the water load section. Resonant frequencies  $f$  in the present cavity are given by  $f = f_0(1 \pm n \Delta f / f_0)$ , ( $n$ : integer), where  $\Delta f / f_0 = \lambda / [2(l + R)]$  and  $f_0$  is the reference frequency. For  $f_0 = 120$  GHz and  $l + R = 15$  cm, we obtain  $\Delta f / f_0 = 0.83$  %, i.e.,  $\Delta f = 1$  GHz.

Figure 3 shows the observed oscillation frequencies in the tube for various cavity magnetic fields. They were in a range from 114 to 123 GHz with a frequency spacing of  $\sim 1$  GHz, i.e., the excited waves propagated along the designed ray path shown in Fig. 1.

A numerical calculation was carried out for the field profiles and resonant frequencies in the present cavity with Huygens' principle. Figure 4 shows the calculated phase  $\psi(f)$  of the wave at the cavity axis relative to that at the plane mirror. The relative phase must satisfy the condition of  $\psi = n\pi$ , ( $n$ : integer). We see from Fig. 4 that the calculated resonant frequencies were in good agreement with the observed values.

The power was measured for an output wave with a frequency of 120.4 GHz oscillated by the electron beam of 30 kV 3.5 A, (3 ms pulse) and which was evaluated to be  $24 \pm 2$  kW (efficiency  $23 \pm 2$  %).

Figure 5 shows the calculated starting currents and output powers for various azimuthal modes  $m$  under the present experimental condition. We see from Fig. 5 that the modes  $m = 0-3$  were able to be oscillated and the optimum power had a nearly equal value as that obtained in the experiment. However, the oscillated azimuthal mode was not clarified by the experiment.

## CONCLUSIONS

A concept of an axisymmetric quasi optical gyrotron has been demonstrated by constructing a 120 GHz 20 kW test tube. Observed oscillation frequencies were in a range from 114 to 123 GHz with a frequency spacing of  $\sim 1$  GHz. This result indicates that the resonated waves propagate back and forth along the designed ray path in the cavity.

The output wave power, transmitted quasi-optically by annular reflection mirrors to the water load, was in good agreement with the calculated value. However, its azimuthal mode was not clarified. The mode number would be in the range from 0 to 3.

It should be noted that the quasi-optical system in the present tube would have sufficient size to generate 1 MW RF power with coaxially injected dual electron beams [3].

## ACKNOWLEDGMENT

The authors would like to thank Dr. H. Yamato for his valuable discussions.



# DESIGN OF A QUASI-OPTICAL GYROTRON WITH A SHEET ELECTRON BEAM

M.E. Read and A.J. Dudas  
Physical Sciences Inc., Alexandria, VA. 22314

J.J. Petillo and A. Drobot  
Science Applications Int'l Corp., McLean, VA. 22102

## ABSTRACT

An electron gun has been designed to produce dual sheet electron beams to be used in a 1 MW, 120 GHz quasi-optical gyrotron. Initial design work was performed using the Herrmannsfeldt Code EGN. Final design and simulation was performed using the 3-dimensional ARGUS code. Use of a segmented sheet beam to optimize the efficiency has been examined.

## INTRODUCTION

The quasi-optical (QO) gyrotron is a promising source of high power mm wave radiation. With a klystron configuration, efficiencies up to 45% are predicted. Due to the large resonator mirrors, output powers of several megawatts at 300 GHz may be possible.

Presently, QO gyrotrons are constructed using cylindrically symmetric MIG-type electron guns. This type of electron gun is a holdover from more traditional cylindrical cavity gyrotrons. Unlike the resonator of a cylindrical cavity gyrotron, the resonator axis of a QO gyrotron is oriented at right angles to the direction

than that of an annular beam. This allows the beam current and consequently the output power of the QO device to be larger.

Additionally, we have examined the feasibility of segmenting this sheet beam into "beamlets", such that each beamlet will pass through the resonator at the position of a peak of the standing electric field pattern. This is expected to increase the efficiency of the device by ~30% because little or no beam current will pass through the standing wave in the resonator at a position where the electric field is zero.

## DESIGN

The geometry of the proposed design and experiment is inherently 3-dimensional. While the geometries of the gun and the beam are rectangular, the magnetic field in which they are immersed and compressed is cylindrical. Further, the edge effects and any segmentation of the beam will require 3-D modeling. However, for the present problem, the "radial" component of the magnetic field is much smaller than the axial component and thus the beam (without including beamlets or edge effects) can be approximately modeled using 2-D Cartesian geometry. Thus initial modeling has been performed in 2-D, with more expensive 3-D modeling used as a check.

### 2-D Design

The 2-D simulation was performed using the Herrmannsfeldt Code EGN run in the rectangular geometry mode with the cylindrical magnetic field information input as an axial array. This produces a good modeling in the gun region, where the magnetic field is essentially constant along the axis, and is an inexpensive method of optimizing the electrodes. In the drift region, where the magnetic field increases, the modeling is not strictly correct. Conservation of canonical angular momentum requires that, in the Cartesian geometry, the guiding centers of the beam electrons

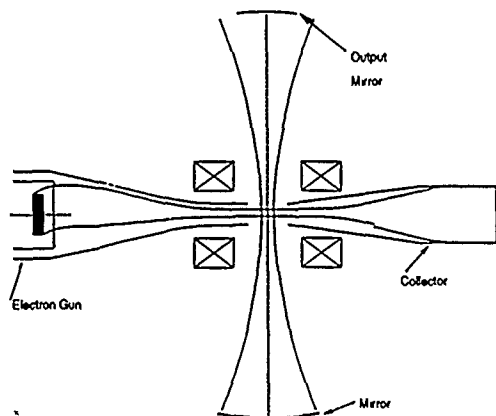


Figure 1. Schematic of a Quasi-Optical Gyrotron

of beam propagation, as shown in Figure 1. For good efficiency the radiation beam waist must be on the order of 10 wavelengths in diameter. Since the beam extent must be significantly less than this dimension, this limits the diameter of an annular electron beam. This limitation is significant for megawatt operation at wavelengths approaching 1 mm.

This paper describes the design of an electron gun with a rectangular geometry capable of producing an electron beam which is thin in one direction, thus satisfying the need for the beam to lie within the waist of the radiation beam. The beam can be quite wide in the direction of the radiation beam axis; therefore the cross-sectional area of "sheet" beam can be significantly greater

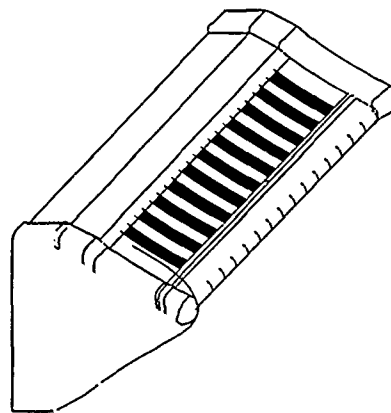


Figure 2. Schematic of the Sheet Beam Cathode



compress as  $1/B_z$ , while in the axial cylindrical geometry, the compression goes as  $1/B_z^{0.5}$ . This clearly gives an incorrect modeling of the beam trajectories. However, the beam current density is correctly modeled, and thus space charge effects can be observed. In addition, based on earlier experience with cylindrical beams, the trajectories of the guiding center radii can be quite accurately determined using analytic calculations based on adiabatic compression.

The gun geometry is shown in Figure 2.

The results of the simulations are summarized in Table 1 and

Table 1. Gun Parameters

Voltage	80 kV
Current (Both beams, unsegmented)	130 A
Magnetic Field Compression	38
Cathode	
half angle	27°
slant length	24 mm
width	78.8 mm
beamlet width/spacing	3.75/7.5 mm
current density	4.4 A/cm <sup>2</sup>

Figure 3. Figure 3 shows the spread of  $V_{\text{perp}}$  as a function of axial position along the beam. Due to the relatively low current density, the 38:1 area compression of the beam was adiabatic, and the perpendicular velocity spread remained largely constant. (In earlier designs, with a cathode current density of 10 A/cm<sup>2</sup>, an increase in the perpendicular velocity spread with magnetic field was observed, consistent with other reported experience.) The cooling of the beam is not well understood, but was observed in most of the designs modeled. The velocity spread is expected to

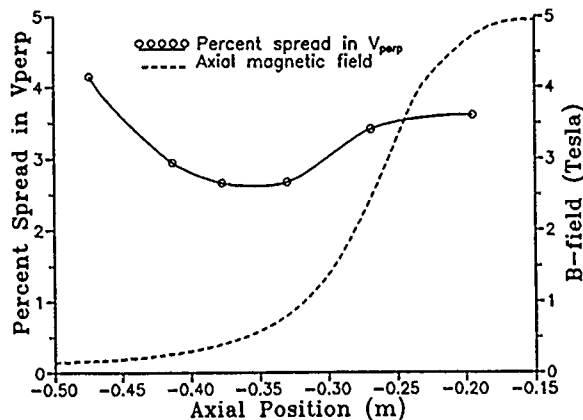


Figure 3. Spread in  $V_{\text{perp}}$  vs Axial Position

be low enough to avoid either degradation in the gyrotron efficiency or significant beam mirroring, and is similar to the velocity spread predicted for the "MIT" megawatt gun. A symmetric cathode, not masked into beamlets, would yield a total beam current of 130 A and beam power of 10.4 MW. The fully compressed height of the beam is 4.2 mm, 34% of the beam waist of a 120 GHz gyrotron, and thus the rf electric field would vary no more than 10% across the beam.

#### ExB Drifts

One of the principal concerns with the sheet beam is that ExB drifts will cause distortion. There are three types of distortion: (1) Due

to the self field  $E_y$ , the (y) edges of the beam will move in the x direction, causing a curling of the beam. This motion occurs primarily in the drift region, due to its length. It has been modeled using a Poisson solver, 2-D in the plane of beam, and integrating the particle motion, assuming the axial electric fields to be zero. This simulation showed a noticeable, but not important distortion. (2) The electric fields in the anode-cathode gap will produce a sliding of the beam in the y direction. This motion is modeled by EGN. The average drift for the present design is 1.8 cm. Of course, the beams from the two sides of the cathode will move in opposite directions, and this must be taken into account in the design. (3) Since the electrons originating near the back of the cathode spend much more time in the diode fields than those starting near the nose, there will be a difference in the drifts, and a corresponding skewing of the beam. This is important only if the beam is segmented into beamlets for efficiency enhancement, as the beamlets could be tilted such that they overlap and thus become ineffective. EGN can be used to estimate the skewing, and indicates a 1.2 cm difference in the drifts. This is an unacceptable amount because the beamlet separation at the cathode is only 0.75 cm. However, this can be easily corrected by slanting the emitters in the opposite direction.

#### 3-Dimensional modeling

Three dimensional modeling is being accomplished using ARGUS, a 3-dimensional Poisson solver. The simulation has been carried past the point in the compression cycle where the EGN code shows complete thermalization of the beam. Figure 4, a view looking down on the beam (y-z plane), shows the degree of mixing of the beamlets as they propagate through the compression and drift region. The initial ExB drift is seen near the diode region.

#### CONCLUSIONS

Extensive 2-D and initial 3-D calculations indicate that a sheet beam electron gun for a quasi-optical gyrotron will produce a beam with a low velocity spread. Pending further 3-D modeling, the formation of beamlets for enhancement of efficiency and/or second harmonic operation appears feasible. An 80 kV, 130 A gun is presently being fabricated.

This work was sponsored by the Department of Energy under contract number DE-AC05-87ER80523.

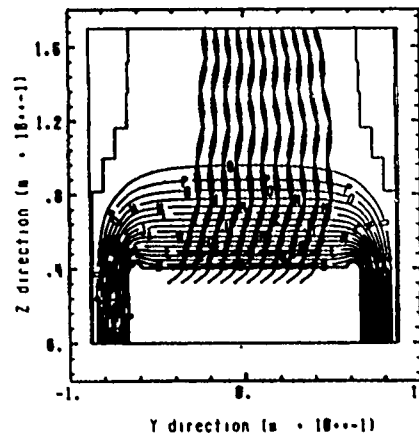


Figure 4. Plot of the beam trajectories in the y-z plane.

# "Mode Stability in a Quasi-Optical Gyrotron"

Wallace Manheimer, Code 4740  
Naval Research Laboratory, Washington, D.C.

Thomas Antonsen and Baruch Levush  
University of Maryland, College Park, Maryland

The stability of modes in a quasi-optical gyrotron is examined analytically and numerically for both free running, mode locked and phase locked equilibria. One key to the analysis is the fact that the mode eigenfrequencies are nearly integral multiples of a fundamental frequency corresponding to the reciprocal of the radiation transit time between mirrors. Analytically, results are obtained with the use of a klystron model.<sup>1,2</sup> Here, the radiation field in the optical resonator is approximated as essentially two delta functions separated by the radiation waste length. It is not exactly two delta functions because the field must be square integrable. However, if the separation is sufficiently large ( $\mu \gg 1$ , where  $\mu$  is the dimensionless length unit in normalized gyrotron parameters) the klystron model is approximately valid. This model gives a good approximation to the linear and nonlinear behavior of a single moded quasi-optical gyrotron with realistic field profile as long as  $0 < \mu \delta < \pi$  where  $\delta$  is the dimensionless frequency mismatch parameter in normalized gyrotron parameters. Using the klystron model, one may solve analytically for the time dependence of the field amplitude. For instance one can calculate the frequency shift in the initial linear regime, as well as in the final nonlinear regime. By going to a multimode state, one can calculate analytically the condition for instability. The instability takes one of two possible characteristics. In one case the phase may be unstable; here the nearest mode is always unstable. In other cases, the amplitude may be unstable; here, it is generally not the nearest mode which is unstable. With the klystron model, one can determine the parameter space of stable and unstable single mode equilibria.

One way to control the mode in a quasi-optical gyrotron is to mode lock it in some manner. There are two basic methods of doing this which we consider. First one may directly inject a signal into the optical cavity, or second one may prebunch the beam with a separate prebunching cavity.<sup>3</sup> In either case, the frequency shift of the injected signal from that of the free running oscillator (or equivalently, the phase shift between the injected signal and oscillator signal) adds one additional dimension to the parameter space. If the signal used is obtained from a separate rf source, the equilibrium produced will be phase locked to this separate source. On the other hand, if the signal is obtained in some way from quasi-optical gyrotron itself<sup>4</sup>, the signal will be mode locked. Whether a phase locked or mode locked source is desired

depends on the application. The klystron model is also analytically tractable in examining the stability of a directly injected phase locked equilibrium. We find that the effect of the directly injected signal into the cavity has a small stabilizing effect on the equilibrium, principally in the stabilizing effect it has on the phase unstable mode. However the use of a directly injected signal also could have the effect of setting up the oscillator in one preferred mode out of many possible stable equilibria. For the case of the prebunched beam, the klystron model is analytically tractable only for the case of the 'ultimate prebunching', that is all particles entering at a particular phase. For this case, the stability boundary for the quasi-optical gyrotron is significantly affected.

For a more realistic field profile in the resonator, the stability is computed numerically with a modification of the multimode simulation developed earlier.<sup>4</sup> Once the equilibrium is obtained, perturbed orbits are calculated and inserted in the equations for the two sidebands. The growth rates for these two modes are then computed numerically. For the free running oscillator case, for a particular value of  $\mu$ , a plot of the stable regions in the space of  $\delta$  and field amplitude parameter  $F$  is obtained. Typically a mode can be stable for values of current as high as twenty times the start oscillation threshold current. Results will be presented for direct injection phase locked equilibria and prebunched beam phase locked equilibria, and the results will be compared with the results for free running equilibria.

\* This work supported by the Department of Energy.

1. N.S. Ginzburg and S.P. Kuznetsov, in *Relativistic High Frequency Electronics*, p 101 IPF USSR Acad. Sci. Gorky (1981)

2. T.M. Antonsen and B. Levush, to be published; also see U.Md. Plasma Preprint 88-039

3. A. W. Fliflet and W.M. Manheimer, to be published; also see NRL Memo 6180

4. A. Bondeson, B. Levush, W. Manheimer, and E. Ott, *Int. J. Electronics*, 53, 547, (1982)

## FREQUENCY STEP-TUNABLE GYROTRON

O. Dumbrajs  
Arbeitsbereich Hochfrequenztechnik,  
Technische Universität Hamburg-Harburg,  
D-2000 Hamburg 90, Federal Republic of Germany

B. Piosczyk  
Kernforschungszentrum Karlsruhe GmbH,  
Institut für Technische Physik,  
Postfach 36 40, D-7500 Karlsruhe 1,  
Federal Republic of Germany

## ABSTRACT

A resonator consisting of three successive cavities with different radii is proposed for a step-tunable gyrotron. Different frequencies of the operating mode can be excited in individual cavities by means of changing the beam radius and the strength of the external magnetic field. A resonator for the frequencies 120 GHz, 140 GHz, and 150 GHz, as desired by the JET, is considered for the operating mode as an example. Mode competition in this resonator is investigated theoretically.

## INTRODUCTION

In applications it is sometimes desirable that the operating frequency of a gyrotron can be varied. Gyrotron frequency can be changed by changing the guiding external magnetic field or/and the voltage of the applied accelerating field. A gyrotron operates under the condition  $\omega/c \approx x_{mp}/R$ , where  $\omega$  is frequency,  $c$  is light velocity,  $x_{mp}$  is zero of the derivative of the Bessel function, which specifies the operating mode, and  $R$  is the cavity radius. Here three cases should be distinguished. 1)  $x_{mp} = \text{const}$  and  $R = \text{const}$ . This is the so-called frequency pulling by the electron beam. It has been shown recently [1] that here the frequency can be changed at most twice of the natural width  $\Delta\omega/\omega \approx 2/Q$ , where  $Q$  is the quality factor. 2)  $x_{mp} \neq \text{const}$  and  $R = \text{const}$ . In this case frequency change is accompanied by the mode change [2]. 3)  $x_{mp} = \text{const}$  and  $R \neq \text{const}$ . In this case frequency changes with  $R$  for the prescribed mode. Here one should distinguish the fine tuning [2] and the step-tuning which is the subject of the present note. Step-tunable gyrotrons are desired by JET, where the frequencies 120 GHz, 140 GHz, and 150 GHz are specified.

## METHOD

We propose a resonator consisting of three successive cavities with different radii (Fig. 1). In this resonator the principal TE<sub>06</sub> mode can be excited in different parts of the cavity at different frequencies by adjusting optimally the electron beam radius by changing appropriately magnetic fields. The values of the corresponding

parameters are given in Table I. In this scheme the problem of mode competition may be very severe if the principal mode is higher than TE<sub>01</sub>. Indeed, in addition to the "ordinary" mode competition in each individual cavity, mode competition between the modes in different cavities must be also considered.

## RESULTS

We have treated mode competition with the method described in [3]. The results of the calculations are shown in Figs. 2 - 4 where the indices - and + correspond to co-rotating and contra-rotating HF fields, respectively. In the calculations we used the external parameters which are close to the KfK experiment:  $U = 70$  kV and  $V_{\perp}/V_{\parallel} = 1.5$ .

## CONCLUSION

With the resonator proposed it should be possible to operate a gyrotron at three different frequencies with the TE<sub>06</sub> mode. If such a gyrotron is supposed to be used for plasma heating one should solve the problem of delivering the output power to plasma in the form of the TE<sub>01</sub> mode. The existing mode converters [4] have a very narrow bandwidth. However, it should be much easier to exchange mechanically a mode converter than a resonator in a gyrotron.

## Acknowledgement

This work has been performed in the framework of the Nuclear Fusion Project of the Kernforschungszentrum Karlsruhe and is supported by the European Communities within the European Fusion Technology Program.

## REFERENCES

- [1] E.V. Zasyrkin, Radio Physics Quantum Electronics, 1988, vol. 33.
- [2] G.F. Brand, Infrared and Millimeter Waves, 1985, vol. 14, 371-409
- [3] O. Dumbrajs, G.S. Nusinovich, and A.B. Pavelyev, International Journal of Electronics, 1988, vol. 64, 137-145.
- [4] H. Kumric, M. Thumm, and R. Wilhelm, International Journal of Electronics, 1988, vol. 64, 77-94.

Table I

Cold cavity resonant frequencies, quality factors and optimal electron beam radii for the TE06 mode excited in different parts of the resonator.

Cavity	F (GHz)	Q	$R_{el}$ (mm)
I	150.048	1495	1.70
II	140.248	903	1.82
III	120.197	892	2.13

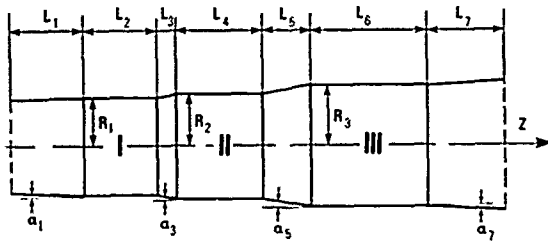


Figure 1

Geometry of a resonator for a frequency step-tunable gyrotron. In the study of the TE06 mode we fixed

$R_1 = 6.25$  mm,  $R_2 = 6.70$  mm,  $R_3 = 7.81$  mm  
 $L_1 = 10$  mm,  $L_2 = 10$  mm,  $L_3 = 2.5$  mm,  
 $L_4 = 12$  mm,  $L_5 = 6.3$  mm,  $L_6 = 16$  mm,  
 $L_7 = 10$  mm,  $\alpha_1 = 0.5^\circ$ ,  $\alpha_2 = 0^\circ$ ,  
 $\alpha_3 = 10^\circ$ ,  $\alpha_4 = 0^\circ$ ,  $\alpha_5 = 10^\circ$ ,  $\alpha_6 = 0^\circ$ ,  
 and  $\alpha_7 = 3^\circ$ .

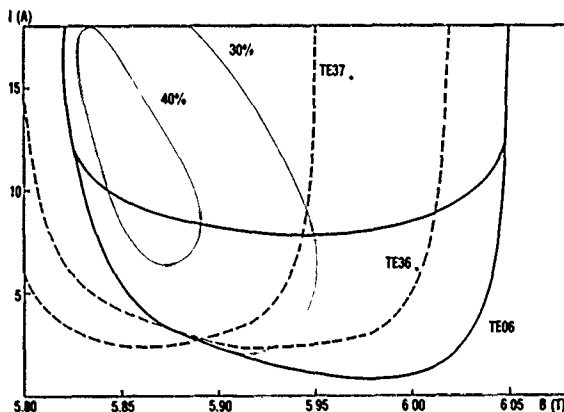


Figure 2

Gyrotron map in the case of excitation of the operating TE06 mode in the first cavity. The boundary of the self-excitation region of the parasitic TE36 mode in the second cavity in the presence of oscillation of the operating mode in the first cavity is marked by dots from the side of self-excitation. The parasitic TE37 mode in the third cavity is completely suppressed by the operating mode. Starting currents of other parasitic modes (TE17<sub>+</sub>, TE18<sub>-</sub>, and TE85<sub>+</sub>) are larger than 18 A and are not shown. The external magnetic field is homogenous.

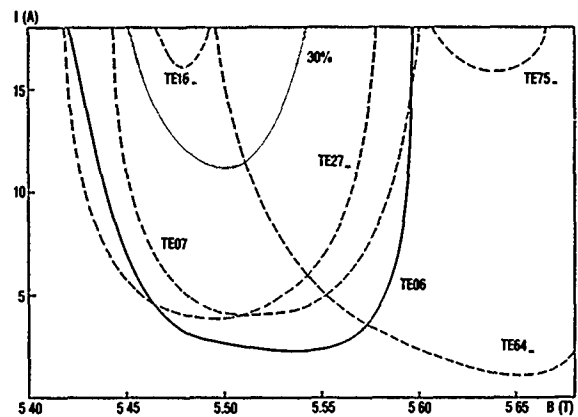


Figure 3

Gyrotron map in the case of excitation of the operating TE06 mode in the second cavity. The parasitic TE64 and TE16 modes in the first cavity cannot be excited in those regions where the corresponding starting currents are higher than the starting current of the operating mode. The parasitic TE27, TE07 and TE75 in the third cavity are completely suppressed by the operating mode. The external magnetic field is homogenous.

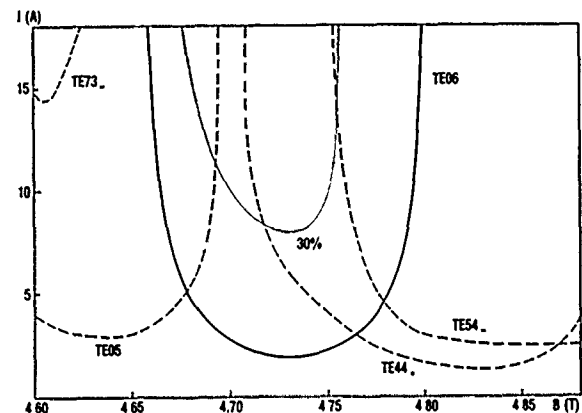


Figure 4

Gyrotron map in the case of excitation of the operating TE06 mode in the third cavity. The parasitic TE44 mode in the first cavity and the parasitic TE73, TE05, and TE54 modes in the second cavity cannot be excited in those regions where the corresponding starting currents are higher than the starting current of the operating mode. The external magnetic field is homogenous.

## MILLIMETRE-WAVE, MONOLITHIC AND HYBRID INTEGRATED CIRCUIT TECHNOLOGY

J.W. Archer  
Division of Radiophysics, CSIRO  
PO Box 76, Epping, NSW 2121, Australia

## ABSTRACT

Discrete devices made from GaAs have been used for many years in sensitive receivers in the microwave and millimetre-wave (mm-wave) bands (1-300 GHz). An extensive international research effort is now under way to develop GaAs monolithic integrated circuits (MMICs) for microwave and mm-wave frequencies. This paper will review recent developments in mm-wave integrated circuit technology.

## INTRODUCTION

The greatest impetus to the growth of mm-wave technology has arisen from military radar, communications and passive imaging applications. However, commercial mm-wave requirements for collision avoidance radars, remote sensing and communications are expected to grow. Traditional, waveguide-mounted devices and components have been shown to be inadequate for these applications in terms of size, cost and reliability. A more viable approach - mm-wave hybrid integrated circuit technology (MIC) - which utilises several discrete GaAs semiconductor devices on a subsidiary dielectric substrate, has been developed to maturity in recent years. An international effort is now under way to develop high-performance monolithic GaAs integrated circuits to replace the hybrid ICs currently available, reducing unit costs and enhancing performance and reliability. As a consequence, a rapid growth in the use of mm-wave systems is to be expected. The conference presentation will review recent research and development results in the fields of hybrid (MIC) and monolithic (MMIC) integrated circuit receiver technology, and present the results of the Division's research programme aimed at developing MMICs and MICs for application in low-noise receivers.

## MILLIMETRE-WAVE MESFET AND HEMT AMPLIFIERS

Much progress has been made in recent years in extending the operating frequency of MESFETs and HEMTs into the mm-wave regime. These advances came about through the use of direct-write electron beam lithography to prepare the sub-half-micron gate lengths which are essential for mm-wave amplification. Table 1 summarises performance achieved with MESFETs and HEMTs in the mm-wave bands.

In general, GaAs/AlGaAs HEMTs provide lower noise at higher frequencies when compared with MESFETs of the same gate geometry. Further improvement in device performance has been achieved using InGaAs/AlGaAs pseudomorphic HEMTs, which offer improved transport properties over GaAs/AlGaAs devices because of the higher carrier saturation velocity and mobility and lower source resistance. In the mm-wave bands HEMT and MESFET MMIC amplifiers offer obvious performance advantages compared with a hybrid IC approach.

## MILLIMETRE-WAVE SCHOTTKY DIODE TECHNOLOGY

Considerable effort has been expended in developing Schottky diode devices for monolithic

integration on GaAs with sufficiently low parasitic series resistance and shunt capacitance for successful mm-wave operation. Most of the work reported to date has been oriented towards the development of Mott diodes for mixer applications. Air bridge technology has been widely used for anode interconnects, and both ion-implantation and MBE growth have been used to prepare the epitaxial structures on which the diode is formed. However, small-area planar devices (less than about 30 square microns) and planar integrated varactor diodes have not been reported. The reduction of diode area and hence junction capacitance, without significantly increasing series resistance, will be necessary if the planar diode technology is to rival the performance of conventional whisker-contacted diodes. Typical performance achieved with both hybrid and monolithic integrated circuit mixers and frequency multipliers incorporating planar Schottky diodes is summarised in Table 2 and 3.

TABLE 1

Low-noise, millimetre-wave MESFET and HEMT amplifiers at room temperature

Device type	Freq (GHz)	Fmin (dB)	Gav (dB)	Gmax (dB)
MESFET	30	2.0	6.2	-
	40	2.6	6.9	-
	60	3.4	3.8	-
	60	7.0	4.0	-
Conventional HEMT	40	1.8	7.5	12.5
	62	2.5	4.4	9.0
	70.0	7.8	5.0	-
	94.0	-	-	3.6
Pseudomorphic HEMT	62	2.4	4.4	11.7
HEMT MMIC Amplifier	44	5.0	5.5	-

Refs: 1,2,3,4.

TABLE 2

Integrated circuit mixers using planar Schottky diodes

Device type	LO (GHz)	Signal (GHz)	FDSB (dB)	LDSB (dB)
<u>Single Ended</u>				
MMIC	93.7	94.0	-	6.5
<u>Balanced</u>				
MIC	34.0	31.5-36.5	-	5.5-7.5
	94	91-96	-	6.0
	124	126-142	-	8.0-9.0
	138	138.5	4.2	4.9
MMIC	34.8	34.5	6.5	6.5
	94.0	94.97	5.7	6.5
<u>Cross-Bar</u>				
MIC	33.0	26-40	-	6.0-7.0
	92.0	94.0	5.5	5.7
MMIC	93.6	84.91	-	8.0
<u>Subharmonic</u>				
MIC	98.6	100	9.2 (SSB)	8.4 (SSB)

Refs: 5,6,7,8,9

TABLE 3

Integrated circuit frequency multipliers using planar Schottky diodes

Device type	Pump freq. (GHz)	Output freq. (GHz)	Effic. (%)	Output power (mW)
<b>Doubler</b>				
MIC	40	80	22.4	22.4
	45-46.5	90-93	~15.0	~15.0
	33-47	66-94	5.0	5.0
<b>Quadrupler</b>				
MIC	10	40	15.8	31.6

Refs: 10,11

#### RESEARCH AT DIVISION OF RADIOPHYSICS

The goal of this research programme is to develop an indigenous Australian capability in mm-wave and microwave GaAs technology, and to transfer aspects of it to industry. The Division has installed: an MBE system; a research-scale e-beam lithography system; a combined RIE/PECVD system; and a microwave wafer prober combined with an HP 8510B network analyser. A complete range of conventional mask alignment, metallization, bonding and packaging equipment is also installed. A capability for monolithic integration of active and passive components on GaAs has been developed and successfully demonstrated. Techniques for air-bridge and via-hole fabrication have been developed and incorporated along with spiral inductors, m-o-m capacitors and transmission line structures into prototype MMIC amplifiers and mixers.

MESFETs and HEMTs with gate lengths as short as 0.25 micron have been fabricated on MBE-grown material. Processes using either electron-beam or optical lithography have been developed which result in this gate geometry. Extrapolation of on-wafer measurements (up to 26.5 GHz) predicts MESFET/HEMT noise figures of 3.8/3.0 dB and gain of 5.0/5.5 dB at 40 GHz, respectively. MICs and MMICs incorporating similar MESFET and HEMT devices will be fabricated in the near future. Planar Schottky diodes, which can readily be integrated with MESFETs and HEMTs, have been produced at the Division. An air-bridge is used for the anode contact. Devices with diameters as small as 2 microns have been fabricated on MBE material using Ti/Pt/Au contacts. The process allows the simultaneous fabrication of varactor diodes and Mott mixer diodes on a single wafer. The varactor devices exhibit a half-power capacitance variation with reverse bias, whereas for the mixer diodes, the capacitance is nearly constant. The total zero-bias capacitance of a 2 micron mixer diode is typically 6.0 fF, including parasitics of <1 fF. Mixer diode DC-IV and noise ( $T_{dc}$ ) behaviour is comparable with the best available whisker-contacted devices produced by other laboratories, as shown in Table 4. The planar diodes have been incorporated in a number

TABLE 4

Planar Schottky-diodes fabricated at CSIRO Division of Radiophysics

Device	Diam. ( $\mu$ m)	$\eta$ (%)	$R_s$ ( $\Omega$ )	$T_{phys}$ (K)	$T_{dc}$ (K) at		
					100 $\mu$ A	1mA	10mA
Mott-6A3	2	1.09	11.3	295	186	220	1467
		1.47	14.1	78	73	102	1318
SHM-4-1	2	1.10	13.8	295	196	237	719
SHM-4-2	2	1.09	13.3	295	196	234	681

of hybrid integrated circuit mixers and multipliers. An MMIC subharmonically pumped mixer (SHPM) for 75-110 GHz has been fabricated on GaAs, incorporating a matched diode pair, transmission lines and capacitors. Table 4 demonstrates the excellent diode match achieved in these SHPM MMICs - an undoubted benefit of monolithic integration. Table 5 summarises performance achieved with CSIRO's mm-wave components. Designs are in progress for an expanded range of MMIC mixers, frequency doublers and triplers.

TABLE 5

MM-wave components fabricated at CSIRO Division of Radiophysics

#### MIXERS

Device	LO (GHz)	Signal (GHz)	F (dB)	L (dB)
MIC-S-6A2	40	38.45	5.3(SSB)	5.5(SSB)
MIC-S-6A3	106	104.5/107.5	2.8(DSB)	3.7(DSB)
MMIC-SHM-5	43	84.5/87.5	5.6(DSB)	5.9(DSB)

MIC-S-6A2 has >20 dB image rejection.

#### FREQUENCY TRIPLER

Device	Output freq. (GHz)	Power in (mW)	Power out (mW)	Effic. (%)
MIC-T-3B1	110	10.0	1.20	12.0

#### CONCLUSIONS

Substantial progress has been made in recent years towards the realization of fully monolithic mm-wave integrated circuits. However, most of the advances have been at frequencies below 110 GHz and a major challenge exists for solid-state physicists and microwave engineers to extend the capabilities of MMICs to frequencies as high as 300 GHz.

#### ACKNOWLEDGEMENTS

The author wishes to acknowledge the substantial contribution made by Mr R.A. Batchelor and Mr C.J. Smith to the development and fabrication of the Division's mm-wave devices.

#### REFERENCES

- (1) A.W.Swanson, *Microwaves & RF*, Vol. 26, March 1987, pp. 139-150.
- (2) D.W.Ball and L.Q.Bui, *Proc SPIE*, Vol. 544, pp. 89-94, 1985.
- (3) M.Sholley and A.Nichols, *IEEE MTT-S Conference Digest*, pp. 463-465, 1986.
- (4) J.Berenz, H.C.Yen, R.Esfanolari, K.Nakano, T.Sato, J.Velebir and K.Ip, *IEEE 1987 MMIC Symp. Digest*, pp. 15-18.
- (5) Y.Ngan, Y.Yen, D.English, A.Grote, T.Pham, G.Hayashibara, L.Wandinger, E.Freibergs, *Proc. SPIE*, Vol. 791, pp. 141-147, 1987.
- (6) T.N.Trinh, W.S.Wong, D.Li and J.R.Kessler, *IEEE 1987 MMIC Symp. Digest*, pp. 89-92.
- (7) B.Jarry, J.S.K.Mills, F.Azan, *Elec. Letters*, Vol. 22, 4 December 1986, pp. 1328-1329.
- (8) E.Carlson, M.Schneider, T.McMaster, *IEEE Trans. on MTT*, Vol. MTT-26, pp. 706-715, 1978.
- (9) A.G.Cardiasmenos, *MSN*, Vol. 10, pp. 33-53, Aug. 1980.
- (10) R.Tahim and G.Chan, *12th Inter I.R. and mm-wave Conf Digest*, pp. 40-41, 1987.
- (11) L.Nguyen, *Microwave Journal*, Vol. 30, pp. 232-235, 1987.

# BROADBAND PHASE MODULATORS IN INTEGRATED FIN-LINE TECHNIQUE FOR MILLIMETRE-WAVE APPLICATIONS

Elias Kpodzo  
Bolriet Technologies Inc.  
150 Mill Street  
Carleton Place  
Ontario, Canada K7C 3P3

## ABSTRACT

Three structures of broadband reflection type phase modulators in unilateral fin-line are presented. The circuits have been analysed assuming ideal transmission line equivalent circuits for the fin-line sections, while the switching element, a pin-diode is represented by a typical equivalent circuit at Ka-band. The measured insertion loss is better than 1.5 dB.

## 1. INTRODUCTION

For a 180 degrees reflection type phase modulator to operate in a bi-phase P.S.K. (phase shift keying) system, the impedance in the two states of the switching element, in this case of the pin-diode, must be matched in such a way that, the reflection coefficients at the input of the modulator are equal in magnitude and opposite in phase. The important factors for a 180 degrees phase modulator are the amplitude imbalance between the two states and the phase error relative to the phase shift. The bandwidth here is defined in respect to deviations in the desired phase shift of 4 degrees and to an amplitude imbalance of less than 10%. For 90 degrees phase shift the phase deviation should be 2 degrees.

The broadband performance of phase modulators realized utilizing fin-line structures as matching networks have been demonstrated first in [1] and [2]. The new fin-line modulators being introduced in this paper are shown in Figures 1a, 2a and 3a and are made up of various types of symmetrical discontinuities, which have been analysed in [3]. These circuits are printed on one side of the substrate and can be manufactured at low-cost.

## 2. CIRCUIT DESCRIPTION

The matching networks realized in unilateral fin-line technique have been etched on a 0.254 mm (10 Mils) thick RT-Duroid 5880. A thin gap of .0254 mm (1 Mil) in width in the fin-line structure provides the required dc-block for the pin-diode, which is biased via a low pass filter in microstrip technique. The circuits have been tested with the pin-diodes DSG6474E (ALPRA) and DC2603 (MARCONI).

### 2.1. REFLECTION TYPE PHASE MODULATOR I

The imbedding of the pin-diode for the phase modulator I is the fin-line network in Fig. 1a. With reference to the matching network applied in [1], which had a single notch followed by a short circuited line section behind the diode, the structure of Fig. 1a consists of a symmetrical notch, which is essentially inductive. Between the tapered fin-line section and the notch is a section of length  $l$ . The diode is mounted across the fin-line slot immediately behind the notch, followed by a short circuited fin-line of length  $l$ . The slot width is chosen to be the same as that of the notch and is equal to  $2d$ .  $l$  is the notch height.

Fig. 1b represents the transmission line equivalent circuit of the phase modulator I, while Fig. 1c shows the equivalent circuit of the discontinuity (a notch) based on [3]. The circuit has been theoretically analysed by assuming the equivalent circuits in Fig. 1b and Fig. 4 together with the diode data given by the manufacturer. Tuning of the modulator is achieved by adjusting the geometrical parameters  $l$  and  $l$ .

The performance of the 180 degrees biphasic modulator I from 27 to 33 GHz is shown in Fig. 1d. The modulator bandwidth is seen to be about 12% and the insertion loss is better than 1.5 dB.

### 2.2. REFLECTION TYPE PHASE MODULATOR II

The circuit pattern of the phase modulator II is sketched in Fig. 2a. This structure makes use of a symmetrical inductive strip discontinuity. The corresponding equivalent circuit is shown in Fig. 2c. The pin-diode is mounted across the fin-line slot in the middle of the strip. The line sections before and after the strip have the same wave impedance, which is about two times the impedance in the region of the strip. The strip is followed by a short circuited fin-line section of length  $l$ . This modulator is tuned for 90 degrees phase shift by properly adjusting the parameter  $l$ .

In Fig. 2d is the performance of the modulator II over the frequency range 27 to 33 GHz. The insertion loss is less than 1.5 dB. The bandwidth amounts to 16%, a factor larger than results reported at Ka-band.

### 2.3. REFLECTION TYPE PHASE MODULATOR III

The structure for the 180 degrees phase modulator III is shown in Fig. 3a. This matching network utilizes a symmetrical step discontinuity, which is short circuited at the end of the fin-line. This step discontinuity can be modelled as shown in Fig. 3c. The pin-diode is directly soldered across the fin-line slot at a distance  $l$  from the step discontinuity. The geometrical parameter for tuning the modulator III is the height of the step discontinuity  $l$ .

The performance curves of the modulator III are shown in Fig. 3d. Over 12% bandwidth the phase error is below 4 degrees and the insertion loss is about 1.4 dB.

## 3. CONCLUSIONS

Three different configurations of fin-line bi-phase modulators have been realized at Ka-band. The performance of these fin-line structures are broadband compared to those obtained in waveguide technique. The overall insertion loss is of the order of 1.4 dB while the bandwidth around 31 GHz for 90 and 180 degrees phase shift are 16% and 12% respectively.

## 4. ACKNOWLEDGEMENT

The author gratefully acknowledge the National Research Council of Canada for financial support.

## 5. REFERENCES

1. E. Kpodzo, K. Schuenemann and H. El-Hennawy, "A Quadrature Phase Modulator in Fin-Line Technique", Proc. Int. Microwave Symp., Orlando, FL., 1979.
2. E. Kpodzo, K. Schuenemann and G. Begemann, "A Quadrature Fin-Line Modulator", IEEE Trans. Microwave Theory Tech., Vol. MTT-28, NO.7, July 1980, pp. 747-752.
3. H. El-Hennawy and K. Schuenemann, "Impedance Transformation in Fin Lines", IEE Proc., Vol. 129, Pt. H, No. 6, Dec. 1982, pp. 342-350.

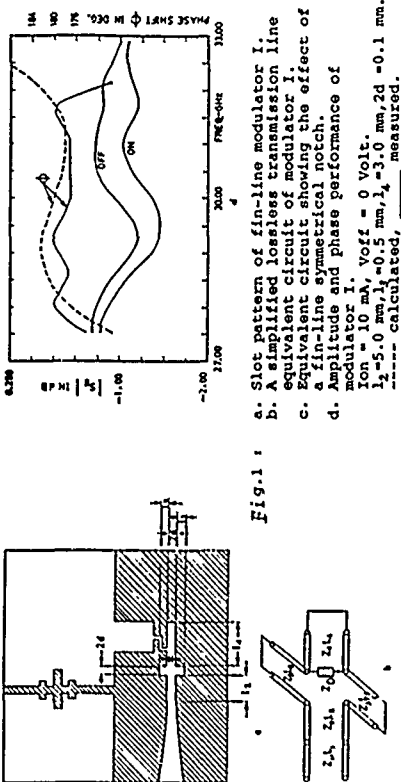
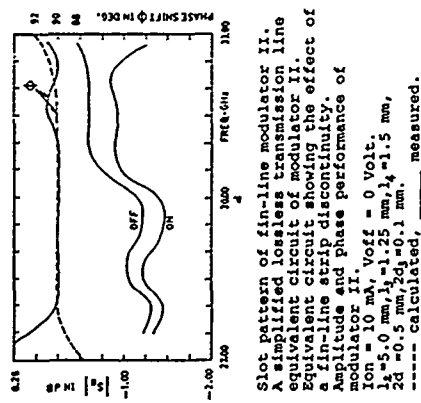
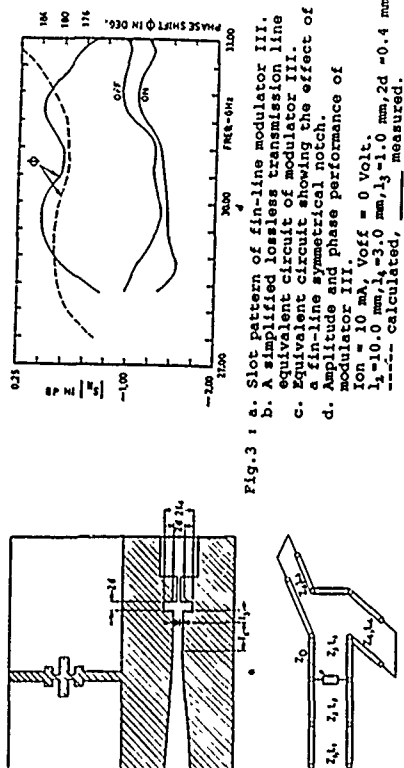


Fig. 1 :

a. Slot pattern of fin-line modulator I. b. A simplified lossless transmission line equivalent circuit of modulator I. c. A fin-line symmetrical notch showing the effect of a fin-line strip discontinuity. d. Amplitude and phase performance of modulator I. Ion = 10 mA, Voff = 0 Volt. l1 = 5.0 mm, l2 = 0.5 mm, l3 = 3.0 mm, l4 = 0.1 mm. --- calculated, — measured.



a. Slot pattern of fin-line modulator II. b. A simplified lossless transmission line equivalent circuit of modulator II. c. A fin-line strip discontinuity showing the effect of a fin-line strip discontinuity. d. Amplitude and phase performance of modulator II. Ion = 10 mA, Voff = 0 Volt. l1 = 5.0 mm, l2 = 1.25 mm, l3 = 1.5 mm, l4 = 0.5 mm, l5 = 0.1 mm. --- calculated, — measured.



a. Slot pattern of fin-line modulator III. b. A simplified lossless transmission line equivalent circuit of modulator III. c. A fin-line asymmetrical notch showing the effect of a fin-line strip discontinuity. d. Amplitude and phase performance of modulator III. Ion = 10 mA, Voff = 0 Volt. l1 = 10.0 mm, l2 = 3.0 mm, l3 = 1.0 mm, l4 = 0.4 mm. --- calculated, — measured.

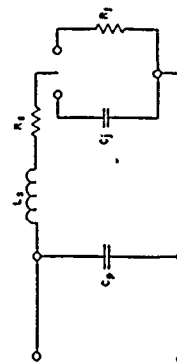


Fig. 4 : A typical equivalent circuit of a pin-diode at Ka-band.

R = 1.5 Ohm Contact Resistance  
R = 1.5 Ohm Series Resistance  
L = 0.1 nH Contact Inductance  
C = 0.006 pF Junction Capacitance  
C = 0.1 pF Package Capacitance



## GaAs TRAVELLING WAVE SCHOTTKY CONTACT COPLANAR WAVEGUIDE WITH APPLICATIONS TO MIMIC

D.R. Singh  
Honeywell, Defense Systems Group  
Minnetonka, MN 55434

K.S. Champlin  
Dept of Electrical Engineering  
University of Minnesota,  
Minneapolis, MN 55454

### Abstract

A unique "Travelling Wave" GaAs Schottky Contact Coplanar Waveguide device has been developed which has application to MIMICs. The device is useful as wide band voltage variable phase shifter, voltage variable attenuator and frequency multiplier and has the advantage of small size, low cost and simple structure. Additionally, it also has the unique feature of incorporating the complete circuit function into one elemental device.

### Introduction

In recent years, there has been considerable progress in the development of millimeter-wave integrated components and subsystems for applications in precision weapons radar systems. The present trend is to concentrate on planar integrated circuits for low-cost system requirements. This hybrid planar technology on either hard or soft substrate, is attractive due to its light weight and small size as well as its potential for high-volume, repeatable manufacturing. However, for repeatable large scale manufacturing, the current trend is towards Microwave and Millimeter-Wave Monolithic ICs (MIMIC).

Present MIMIC technology is based on MESFET process, where the submicron features greatly effect the yield. Moreover, useful functions such as mixing, frequency multiplication, phase shifting and detection have been performed by lumped non-linear devices where the interactions take place over distances which are small in comparison with a wavelength. As frequency increases these devices necessarily become smaller and ultimately reach fundamental limitation of power and frequency. These factors have motivated the need to develop devices which incorporate novel operational processes to overcome these limitation and at the same time be compatible with current MIMIC technology.

Distributed non-linear device structures, on the other hand, do not have the same limitation in dimensions on account of the fact that interactions take place over distances which are comparable to, or even greater than, a wavelength. Instead, the fundamental problem of distributed devices is that of obtaining structures having sufficiently low losses that distributed non-linearities can be properly exploited. This paper describes a unique GaAs Schottky Contact Coplanar Waveguide (SCCPW) device structure, incorporating a distributed non-linearity and operating on the principle of travelling "slow-wave". In such a structure considerable wavelength reduction occurs in the "slow-wave" region, thereby reducing the physical size of the device. Furthermore, such structures are compatible with the present MIMIC processing technology and also offer the possibility of combining all circuit functions into one elemental device, which satisfies the criterion of circuit simplicity and size.

### Technical Discussions

Figure 1 shows the layout and cross-section of the SCCPW device. Although such structures support the propagation of different types of modes [1,2], the most important is the well known "slow-wave mode" [3]. In this region the electric energy is largely confined to the schottky depletion region immediately under the centre conductor; whereas the

magnetic field penetrates the semiconductor layers as the cross-sectional dimensions of the structure are less than the semiconductor skin depth. Thus the magnetic field distribution is nearly that of a coplanar waveguide on a dielectric substrate and the magnetic energy can be said to be mainly confined to the semiconductor region. This spatial separation of the electric and magnetic energies results in the wave velocity "slowing down" owing to the energy transfer that must occur at the semiconductor-depletion region interface.

The "slow-mode" region is of considerable importance as it represents a relatively low-loss mode of propagation [4]. The schottky depletion width can be easily varied by varying the bias and in effect altering the slow-wave properties. In the small signal case this leads to phase shifting properties; whereas in the large signal case, frequency multiplication, parametric amplification and mixing occurs. Moreover, considerable wavelength reduction occurs in this region, thereby reducing the physical size of the device.

The limit of the "slow-wave" region is defined to be the frequency which is both smaller than the skin effect frequency,  $f_g$ , and the dielectric relaxation frequency,  $f_e$ . Here  $f_g$  is the frequency for which the skin depth equals the transverse dimensions of the structure [4]. Typically, the SCCPW transverse dimensions are of the order of a few microns on a GaAs substrate having a nominal doping of  $\sim 10^{17} \text{ cm}^{-3}$ . For these parameters  $f_g = 500 \text{ GHz}$  and  $f_e \sim 7000 \text{ GHz}$ . Thus, in relation to  $f_g$  and  $f_e$ , the "slow-wave" mode of propagation extends well into the millimeter wave region.

### Device Fabrication and Experimental Results

Figure 1 shows the device layout and cross-section, wherein the centre conductor and ohmic contacts form the Schottky contact and ground plane of the coplanar waveguide (CPW), respectively. The N and N<sup>+</sup> layers were formed using selective ion implantation process. Moreover, the N layer is shallow ( $< 0.2 \mu\text{m}$ ) with a peak doping of  $\sim 5 \times 10^{17} \text{ cm}^{-3}$ . A thick ( $\sim 3 \mu\text{m}$ ) gold layer is selectively plated on the device to reduce conductor losses. The length of the active region is  $1200 \mu\text{m}$  which in turn is cascaded with  $50 \Omega$  CPW on semi-insulating GaAs for the purpose of measurements, giving a total device length of  $2700 \mu\text{m}$ , as shown in figure 1. Broadband Cascade Microtech probes [5] were used to perform on-wafer measurements.

Small signal measurements indicated a phase shift of  $> 150$  degree/mm for a voltage variation of 0-5V at 20 GHz, as shown in figure 2(a). For a similar voltage change and frequency of operation the losses varied from 2-20 db/mm (Fig 2(b)). These results indicate a broadband voltage variable phase shifting and attenuating properties. Large signal measurements showed for the first time the harmonic generation properties of these devices. Second harmonic efficiencies of the order of 6% were observed for input frequencies of 2-8 GHz at input power levels of about 50mW. This is shown in figure 3. The low harmonic efficiencies can be attributed to the thin N layer which increases the device losses. Nevertheless, small and large signal models were developed which showed good agreement with the

measured results. Furthermore, optimised device structures, developed on the basis of these models, predict excellent phase shifting and harmonic generation properties well into the millimeter-wave region.

### Summary

This paper has described a unique Schottky Contact Coplanar Waveguide device, operating on the principle of travelling waves and having applications to MIMIC. Measured results in the frequency range of 1-20 GHz have shown that the device is useful as broadband voltage variable phase shifter, voltage variable attenuator and frequency multiplier, and has the advantage of small size, low cost and simple structure. Moreover, it also has the unique feature of incorporating the complete circuit function into one elemental device.

### References

- (1) H. Hasegawa, M. Furukawa and H. Yan, "Properties of microstrip line on Si-SiO<sub>2</sub> system," IEEE Trans Microwave Theory Tech., Vol MTT-19, pp 869-881, Nov 1971.
- (2) H. Hasegawa and H. Okizaki, "M.I.S and Schottky slow-wave coplanar striplines on GaAs substrates," Electron. Lett., Vol 13, no.22, pp 663-664, Oct 1977.
- (3) D. Jager, "Slow-wave propagation along variable schottky-contact micro-strip line," IEEE Trans Microwave Theory Tech., vol. MTT-24, pp. 566-572, Sept 1976.
- (4) Y.R.Kwon, V.M.Hietala and K.S.Champlin, "Quasi-TEM Analysis of "slow-wave" mode propagation on Coplanar Microstructure MIS Trans-mission lines," IEEE Trans Microwave Theory Tech., Vol MTT-35, pp. 545-551, June 1987.
- (5) V.M.Hietala, Y.R.Kwon and K.S.Champlin, "Broadband continuously variable phase shifter employing a distributed schottky contact on silicon," Electron Lett. vol 23. no 13, pp. 675-677, June 1987.

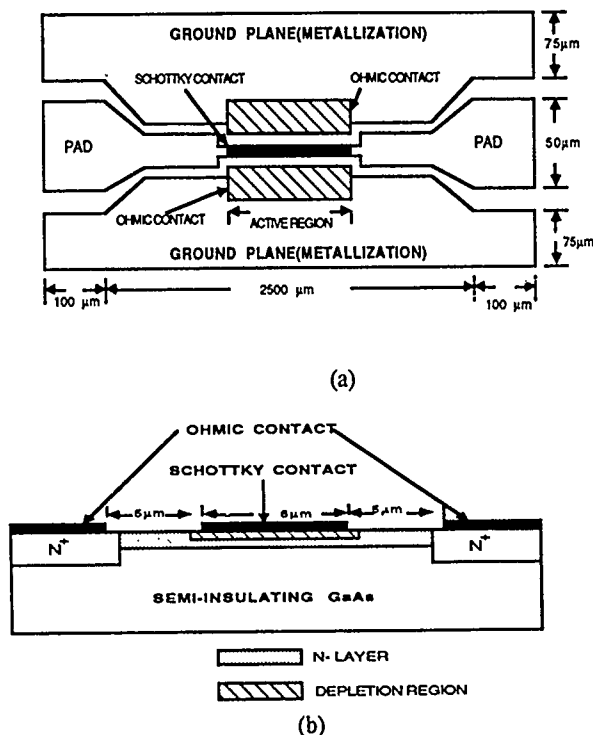


Figure 1. Layout and Cross-section of a SCCPW Device

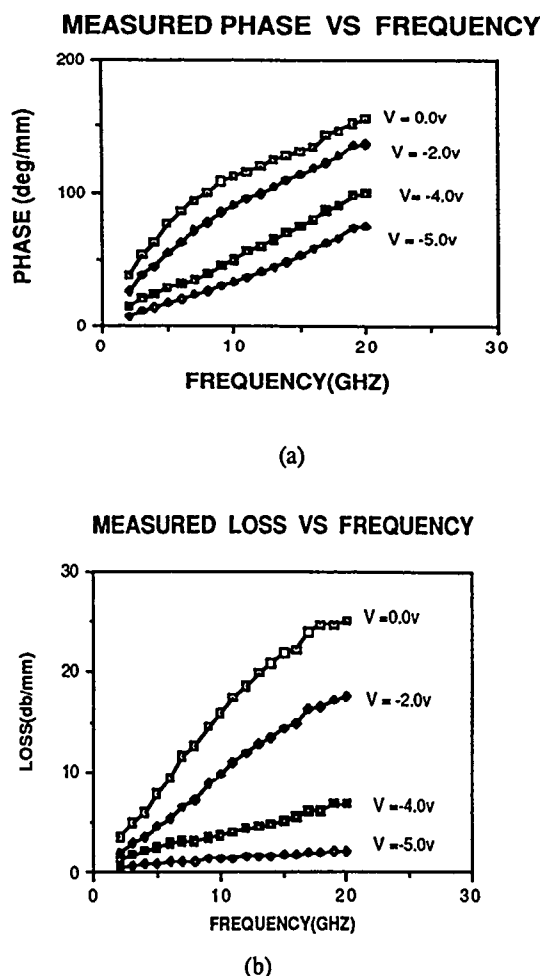


Figure 2. Measured Phase and Loss vs Frequency of SCCPW Device

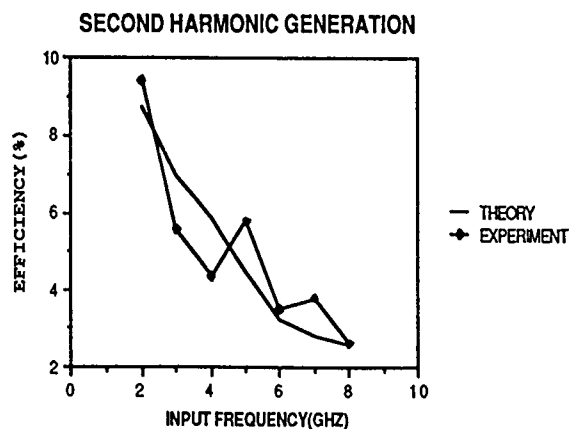


Figure 3. Measured and Calculated Second Harmonic Generation of SCCPW

## OPTIMAL DESIGN OF MILLIMETER-WAVE INTEGRATED

## E-PLANE DIPLEXERS

Jia Sheng Hong and Jun Ming Shi

Dept of Radio Engineering, Fuzhou University

People's Republic of China

## ABSTRACT

An optimal design of waveguide E-plane diplexers for millimeter-wave applications is described. In order to increase the design flexibility and to achieve the higher performance, the dimensions of two channel filters and the spaces to the common junction are optimized at the same time according to their sensitivity information.

## INTRODUCTION

In recent years the development of small size, high-performance diplexers and multiplexers for millimeter-wave applications has drawn researchers' more attention/1-4/. The E-plane diplexer/4/, which consists of two E-plane bandpass filters with all metal inserts and a waveguide E-T junction shown in Fig.1, has advantages of simple-structure, easy-fabrication, low-insertion-loss and low-cost. In addition, this type of diplexer is most suitable for development of a waveguide manifold-type multiplexer/5/.

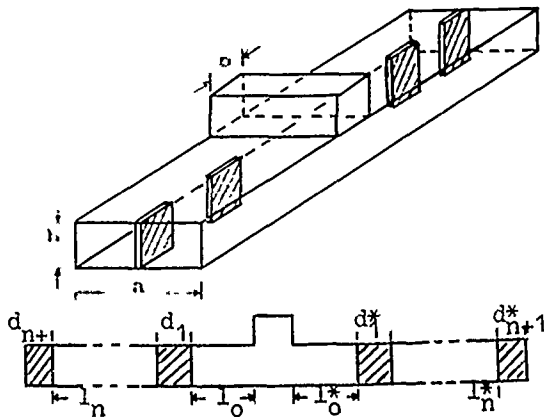


Fig.1 A waveguide E-plane diplexer

In the previous design/4/, the two channel filters are separately designed by a computer program based on a field-theory method, and then placed in the T-junction arms so as to reduce the channel interaction effect. This design approach has two disadvantages. One is it involves the complicated and time-consuming numerical computations so that requires large computer-facilities. The

other is it involves no information about optimisation of the spaces to the junction and in fact, it is difficult to adjust them alone for compensation of the frequency-dependence reactances of the junction as the guard band is getting smaller or the channel bands are getting wider. In order to solve such problems, the presented paper describes another simplified and optimisation-oriented design method based on an efficient dominant-mode equivalent circuit of the diplexer. The agreement between the theory and the measurement is demonstrated by an E-plane diplexer at X-band.

## DESIGN AND RESULTS

Fig.2 shows the dominant-mode (TE<sub>10</sub>) equivalent circuit of E-plane diplexer. The calculations of the reactances of E-T junction, which does not involve any design parameters, are available in the publication/6/. The computations of S-matrix of air-filled waveguide sections and its sensitivities w.r.t. their lengths are also found elsewhere. The S-matrix of E-plane metal septum and its first- and second-order sensitivities has been derived as follow

$$S^M = \frac{1}{Z} \begin{vmatrix} -(1+X_s^2 + 2X_sX_p) & j2X_p \\ j2X_p & -(1+X_s^2 + 2X_sX_p) \end{vmatrix}$$

$$\frac{\partial S^M}{\partial d} = \frac{1}{Z^2} \begin{vmatrix} d_{11} & d_{12} \\ d_{12} & d_{11} \end{vmatrix} \quad \frac{\partial^2 S^M}{\partial d^2} = \frac{1}{Z^2} \begin{vmatrix} h_{11} & h_{12} \\ h_{12} & h_{11} \end{vmatrix}$$

with

(1)

$$d_{11} = 4AX_p - 4(A+B)X_s + j(2(A+B)(1-X_sX_s) - 4AX_p(X_s+X_p))$$

$$d_{12} = 4AX_p - 4BX_s + j(4A(X_p^2 + X_sX_p) + 2B(1-X_s^2))$$

$$h_{11} = U_1 + jV_1, \quad h_{12} = U_2 + jV_2$$

$$U_1 = (4A^2(1-3X_p^2) - 12A^2(X_s+X_p)^2 + E)/Z - 4c(X_s+X_p) - 4DX_s$$

$$V_1 = (F+G+4A^2X_s(3-X_s^2))/Z + 2D(1-X_s^2) + 2C(1-X_s^2-2X_p^2-2X_sX_p)$$

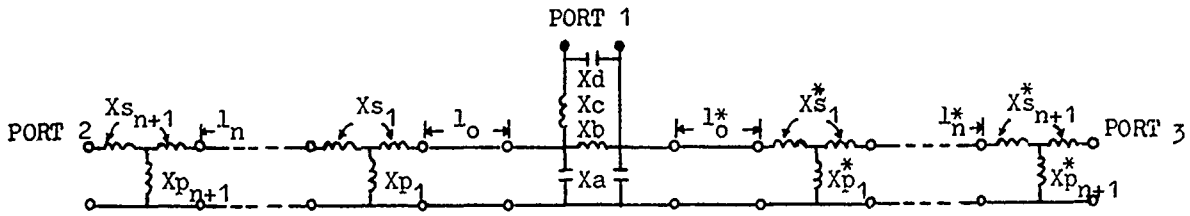


Fig.2 The equivalent circuit of E-plane diplexer

$$U2 = (24A^2 X_p (X_s + X_p) + E) / Z + 4C X_p - 4D X_s$$

$$V2 = (G - F) / Z + 4C (X_p^2 + X_s X_p) + 2D (1 - X_s^2)$$

where

$$X_s = s(1) e^{s(2)d'} + s(3)$$

$$X_p = p(1) e^{p(2)d'} + p(3) \ln(d')$$

$$A = s(1)s(2)/\lambda_0 e^{s(2)d'}$$

$$B = X_p/\lambda_0 (p(2) + p(3)/d')$$

$$C = As(2)/\lambda_0$$

$$D = X_p/\lambda_0 ((p(2) + p(3)/d')^2 - p(3)/d'^2)$$

$$E = 8B(A+B)(1 - 3X_s^2)$$

$$F = 4A^2 X_p (3 - 6X_s X_p - 3X_s^2 - 4X_p^2)$$

$$G = 8B(A+B)X_s(3 - X_s^2)$$

$$Z = (1 - X_s^2 - 2X_s X_p) + j2(X_s + X_p)$$

$$d' = d/\lambda_0 \quad (\lambda_0 : \text{wave length in free space})$$

The remaining unknown coefficients  $s(i)$  and  $p(i)$  ( $i=1,2,3$ ) can be obtained from the author's another paper/7/.

A computer program has been developed for fast computation of S-matrix of the diplexer and its sensitivities/8/ to minimize the objective function

$$U(\Phi) = \max_{\Phi} \left( \frac{|S_{k1}(\Phi, f)| - |S_{k1}|}{|S_{k1}|} \right) \quad (2)$$

where  $\Phi$  is a set of design parameters indicated in Fig.1 by  $d_1 \dots d_{n+1}$ ,  $d_1^* \dots d_{n+1}^*$ ,  $l_0 \dots l_n$  and  $l_0^* \dots l_n^*$ ,  $f$  represents the sampled frequencies.  $|S_{k1}|$  and  $|S_{k1}(\Phi, f)|$  ( $k=1,2,3$ ) denote the required and predicted performances.

Notice that all design parameters of the diplexer, i.e., the dimensions of the two channel filters and their spaces to the common junction, are optimized at the same time so as to increase the design flexibility and to achieve the higher performances.

To verify the presented design method, a diplexer at X-band was designed, fabricated and tested. The computer predicted and measured frequency responses are shown in Fig.3 where good agreement between the theory and the measurement can be observed.

## CONCLUSION

The optimal design of waveguide E-plane diplexer has been proposed and demonstrated. Owing to the use of the simple but efficient models for the diplexer, the computer program is small and can be run on mini desk computers. The design method can be extended for CAD of E-plane multiplexers/5/.

We acknowledge financial support from the Fujian Education Commission.

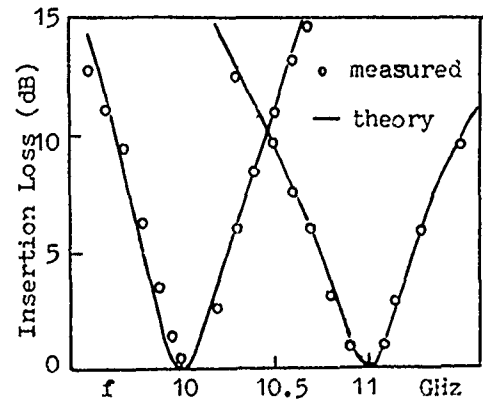


Fig.3 Frequency responses of E-plane diplexer at X-band

$$l_0 = 10.36 \quad d_1 = 5.11 \quad l_1 = 14.42 \quad d_2 = 4.41$$

$$l_0^* = 13.46 \quad d_1^* = 4.68 \quad l_1^* = 11.35 \quad d_2^* = 5.68 \text{ mm}$$

## REFERENCES

- /1/ K.D.Breuer & N.Worontzoff, 1980 IEEE MTT-S Digest, pp.150-152
- /2/ L.D.Cohen et.al., 1984 IEEE MTT-S Digest, pp.233-235
- /3/ Y.C.Shih et.al., IEEE Trans., 1985 MTT-33, pp.1465-1469
- /4/ F.Arndt et.al., Electron. Lett., 1985 Vol.21 No.14, pp.615-617
- /5/ J.S.Hong, to be published
- /6/ N.Marcuvitz: "Waveguide Handbook", McGRAW-Hill, 1951
- /7/ J.S.Hong, "An effective model of E-plane metal septum for millimeter wave integrated circuit design", The 13th Int. Conf. on Infrared & Millimeter Waves
- /8/ J.S.Hong, Electron. Lett., 1988 Vol.24 No.12, pp.764-765

# INTEGRATED CIRCUIT ACTIVE ARRAYS AND SPATIAL POWER COMBINERS USING APERTURE COUPLED PATCH ANTENNAS

Kai Chang, Kenneth A. Hummer and James L. Klein  
Department of Electrical Engineering  
Texas A&M University  
College Station, Texas 77843

## ABSTRACT

Integrated circuit active arrays and spatial power combiners using aperture coupled patch antennas have been developed. Results from a prototype element and a two-element combiner are very encouraging. Methods for achieving phase coherency have been developed.

## INTRODUCTION

Recent developments in microwave/millimeter-wave integrated circuits and solid-state devices have opened up many applications by integrating the antennas and sources (or transmit-receive modules). The integration has advantages of low cost, small size, and good compatibility to monolithic implementation. The circuits should have many applications in radar, communication, and EW systems.

In this paper, we report an aperture coupled patch antenna element which is useful for construction of active phase arrays and spatial power combiners. If a transmit-receive (T/R) module is connected to the antenna element, many of these elements form an active phased array. The circuit can be used for spatial power combiners if the T/R module is replaced by a source. A theoretical analysis has been developed to model the equivalent coupling circuit based upon the aperture coupling theory and a 6-port network S-parameters. A prototype two-element array was designed, fabricated and tested at 2.4 GHz for concept demonstration. Injection locking using either mutual coupling or an external source has been successfully demonstrated for achieving phase coherency.

## CIRCUIT DESCRIPTION

One practical difficulty with active arrays is in isolating the input and output signals and maintaining the stability of the array. Another problem is to maintain unidirectional radiation and to avoid spurious feed radiation. To overcome these problems, a two-sided substrate circuit has been proposed [1]. As shown in Figure 1, the active circuits which could include the oscillators, amplifiers, phase shifters, etc., are fabricated on GaAs substrate located on one side of the ground plane. The antenna elements are fabricated on low dielectric constant substrate located on the other side of the ground plane. The ground plane provides good heatsinking for active devices. The coupling between the two layers is accomplished by a circular coupling aperture in the ground plane. The ground plane separates the radiating aperture from the feed network, eliminating the possibility of spurious signal radiation from the source. Because of the good isolation between the radiating antenna and active device, the antenna and active circuits can be optimized separately. The circuit is compatible to monolithic implementation. For better efficiency, low dielectric constant material can be used for antenna elements and GaAs substrate for T/R circuitry.

Based on the aperture coupling and scattering theory, a  $2 \times 2$ -port equivalent network was developed [2]. The equivalent circuit is shown in Figure 2. All reference of the ports are taken at the center of the coupling aperture.

After calculating the electric and magnetic field at the aperture excited by the input microstrip line, the scattered fields can be found from the aperture coupling theory [3-6]. From the

scattered fields, the coupling coefficients and the S-parameters can be determined [2]. The details of the analysis can be found in reference 2.

A computer program has been developed to facilitate the calculation. Figure 3 shows a typical comparison between the theoretical and experimental results. The agreement is very good.

## CIRCUIT PERFORMANCE

To demonstrate the concept, a two-element array was designed and built. The two antennas are separated by a quarter-wavelength in order to have about 20 dB mutual coupling [7]. The antennas were designed to operate at 2.36 GHz. One antenna is connected to a sweeper and the other to a free running oscillator. The oscillator is a transistor oscillator manufactured by EMF Systems, Inc. The sweeper is used to injection-lock the free running oscillator by mutual coupling.

Figure 4 shows the E-plane pattern of the active array when only the sweeper is "on", when only the oscillator is "on", and when both sources are "on". When one of the sources was disengaged, a 3 dB beamwidth of about 90 degrees was measured. This beamwidth was reduced to 65 degrees when both sources are "on". Furthermore, the power with both sources operating was about 2 dB higher than for the power with any single source operating. This shows that the array is exhibiting good power combining properties.

One problem that does exist is that with both sources on, the main lobe is centered at roughly 25°. This could be caused by the phase difference between the two sources.

Injection-locking through mutual coupling was also demonstrated. The locking bandwidth was measured to be 2.15 MHz. This narrow locking bandwidth is due to the high-Q transistor oscillator.

## CONCLUSIONS

Aperture coupled active patch antenna elements have been developed for phased array and power combining applications. A two-element array has been demonstrated to have good power combining efficiency. Injection locking for phase coherency has also been demonstrated.

## ACKNOWLEDGEMENTS

The authors would like to thank Mr. X. Gao for technical assistance and helpful discussions. This work was supported in part by Army Research Office under contract No. DAAL03-88-K-0151 and a grant from TRW.

## REFERENCES

- [1] D. Pozar and D. H. Schaubert, "Comparison of Architectures for Monolithic Phased Array Antennas", *Microwave Journal*, March 1986, pp. 93-104.
- [2] X. Gao and K. Chang, "Network Modeling of an Aperture Coupling Between Microstrip Line and Patch Antenna for Active Array Applications", *IEEE Trans. on Microwave Theory and Tech.*, Vol. MTT-36, March 1988, pp. 505-513.

- [3] D. James, G. R. Painchaud and W. J. R. Hoefer, "Aperture Coupling Between Microstrip and Resonant Cavities", *IEEE Trans. on Microwave Theory and Tech.*, Vol. MTT-25, May 1977, pp. 392-398.
- [4] J. Miao and T. Itoh, "Coupling Between Microstrip Line and Image Guide Through Small Apertures in the Common Ground Plane", *IEEE Trans. on Microwave Theory and Tech.*, Vol. MTT-28, April 1983, pp. 361-363.
- [5] R. Levy, "Improved Single and Multiaperture Waveguide Coupling Theory, Including Explanation of Mutual Interactions", *IEEE Trans. on Microwave Theory and Tech.*, Vol. MTT-28, April 1980, pp. 331-338.
- [6] R. E. Collin, *Foundations for Microwave Engineering*, McGraw-Hill, pp. 183-197.
- [7] R. P. Jedlica, M. T. Poe and K. R. Carver, "Measured Mutual Coupling Between Microstrip Antennas", *IEEE Trans. on Antennas and Propagation*, Vol. AP-29, Jan. 1981, pp. 147-149.

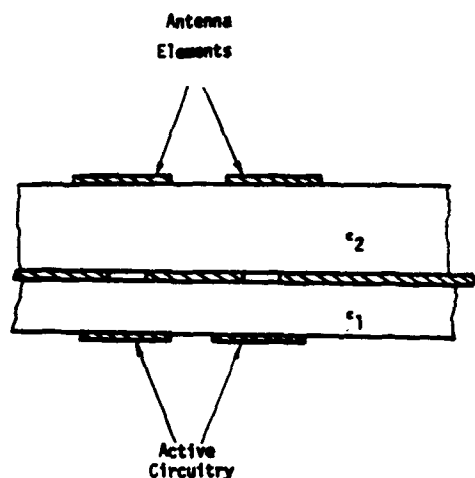


Figure 1. Aperture coupled microstrip to patch antenna circuit for active array.

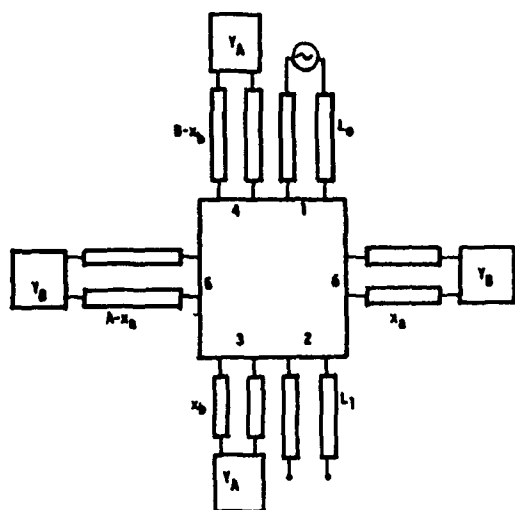


Figure 2. Equivalent circuit for aperture coupled microstrip to patch antenna circuit.

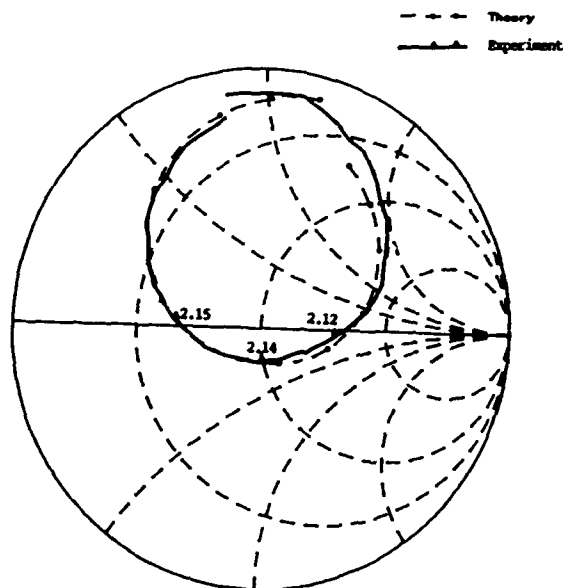


Figure 3. Comparison of calculated and experimental results for input impedance as a function of frequency.

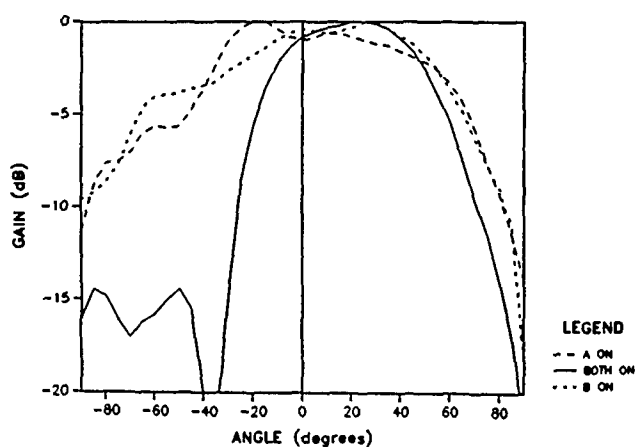


Figure 4. E-plane power pattern of a two-element aperture coupled active array.

## A UNIVERSAL TEST FIXTURE FOR CHARACTERIZING MM-WAVE SOLID STATE DEVICES

## USING A NOVEL DEEMBEDDING PROCEDURE

Robert R. Romanofsky and Kurt A. Shalkhauser  
National Aeronautics and Space Administration  
Lewis Research Center  
Cleveland, Ohio 44135

## ABSTRACT

The design and evaluation of a novel fixturing technique for characterizing mm-wave solid state devices, including monolithic microwave integrated circuits, is presented. The technique utilizes a cosine tapered ridge guide fixture and a one-tier deembedding procedure to provide accurate and repeatable device level data. Advanced features include "nondestructive" testing, full waveguide bandwidth operation, a high degree of universalism, and rapid yet repeatable chip-level characterization. Furthermore, only one set of calibration standards is required regardless of device geometry.

## INTRODUCTION

Accurate characterization of solid state devices at millimeter wavelengths is hindered by limited metrological techniques due to unpredictable parasitics, diminutive physical dimensions, and inconvenient interface methods (1). Typically, devices are characterized by S-parameters using an automatic network analyzer (ANA). To be accessible to the ANA and amenable to characterization, the device must be mounted in a fixture. This fixture introduces substantial insertion and return loss effects, both in magnitude and phase, often masking the true device characteristics. Hence, it would be desirable to devise a mathematical scheme to reposition the reference (measurement) plane adjacent to the device terminals. This procedure is known as deembedding and requires chip level microstrip standards to shift the reference plane from the fixture-to-ANA interface to the device area.

Drawbacks of existing fixtures include non-repeatability, fixturing and calibration complexity, and limited bandwidth. Most techniques require cumbersome device mounting arrangements and are labor intensive. The fixture presented here utilizes a cosine tapered ridge guide transition to match the high waveguide impedance to the 50  $\Omega$  microstrip. The taper length and profile have been analytically determined to provide maximum bandwidth and minimum insertion loss. Discrete devices and integrated circuits are mounted on a customized carrier which is inserted between the bottom of the ridge and the base of the waveguide. The electric field is concentrated by the ridge and launched onto the carrier by direct pressure contact. Control voltages are applied to the carrier using a self-aligned bias module with integral spring loaded contacts. Deembedding is accomplished using a modified "through, short, delay" (TSD) calibration algorithm.

## DESIGN

Since the fixture itself is mechanically rigid, the required versatility was built into the carrier.

A 0.020 in. alumina substrate was chosen for ease of manufacturability, good dielectric properties, and relatively good thermal and mechanical characteristics. The thickness was constrained to a narrow range due to certain electrical features and a concern about the generation of higher order modes. DC blocks are required since the carrier microstrip is in contact with the fixture body. A coupled line section 0.032 in. long with 0.0029 in. wide fingers and 0.002 in. gaps was found to be optimum (2,3). Bias can be fed directly to the chip input and output microstrip lines through two high RF impedance bias filters. The chip is mounted in a laser machined well in the center of the carrier and is supported by a gold plated kovar subcarrier.

The ridge waveguide transition can be described by dividing the design into three calculations, first outlined in (4). First, the ridge waveguide cutoff wavelength must be obtained. At cutoff, propagation may be considered to be restricted to a wave traveling transversely across the guide with no longitudinal component. The cutoff wavelength is derived by solving for the input impedance of a simple equivalent network (5). Next, the ridge thickness is determined by evaluating the infinite frequency characteristic impedance for the TE<sub>10</sub> mode as given in (6). Finally, the profile of the physical taper must be determined. A sinusoidal variation is assumed since this geometry outperforms most other candidates in terms of optimizing return loss in the shortest electrical length. Based on the above calculations, a taper length of 1.366 in. and a ridge thickness of 0.0695 in. was chosen.

Due to its practical implementation in microstrip, a TSD calibration routine was chosen for deembedding. The technique, first proposed by Franzen and Special (7) used a one-tier calibration approach and assumes an eight term error model. Based on measurements of the three standards, all 16 terms (magnitude and phase) of the error networks can be determined. The topography of the model consists of three cascaded two port networks; hence, the S-parameters of the error networks and device are converted to T-parameters for mathematical convenience. The T-matrix of the model is equal to the product of the individual T matrices; therefore, the matrix of the deembedded device can be extracted and reconverted to S-parameters (8). Subsequent to the initial calibration, the ancillary reference plane is mathematically shifted to the device boundaries through the translation  $\exp(-\gamma \ell)$ . Gamma ( $\gamma$ ), the complex propagation constant, is determined from the "through" and "delay" measurements. The physical length of the device,  $\ell$ , must be known. It is this feature which permits the use of only one set of calibration standards.

## PERFORMANCE

The RF characteristics of the fixture were measured using a Hewlett-Packard 8510 ANA configured using a WR-28 waveguide test set. The fixture was calibrated and the error correction verified by re-inserting the "through" standard. Figures 1 and 2 highlight the performance of the fixture from 26.5 to 40.0 GHz. The fixture achieved an insertion loss of approximately 0.1 dB and an insertion phase of less than 0.5° across the band. A corresponding return loss in excess of 40 dB was also measured.

The fixture is being used to evaluate 30 GHz MMICs as well as advanced discrete millimeter wave devices. Designs for similar fixtures for frequencies up to 75 GHz have been initiated.

## REFERENCES

1. R.R. Romanofsky, K.A. Shalkhauser, G.E. Ponchak, and K.B. Bhasin, "RF Characterization of Monolithic Microwave and mm-Wave IC's," NASA TM-88948 (1986).
2. G. Matthaei, L. Young, and E.M.T. Jones, Microwave Filters, Impedance-Matching Networks, and Coupling Structures, Artech House, Dedham, MA (1980).
3. T.Q. Ho, and Y.C. Shih, "Broadband Millimeter-Wave Edge-Coupled Microstrip DC Blocks," *MSN Microwave Syst. News Commun. Technol.* 17(4), 74-78 (1987).
4. D.R. Singh, and C.R. Seashore, "Straightforward Approach Produces Broadband Transitions," *Microwaves RF* 23(9), 113-118 (1984).
5. N. Marcuvitz, Waveguide Handbook, McGraw Hill, New York (1951).
6. S.B. Cohn, "Properties of Ridge Wave Guide," *Proc. IRE* 35(8), 783-788 (1947).
7. N.R. Franzen, and R.A. Speciale, "A New Procedure for System Calibration and Error Removal in Automated S-Parameter Measurements," 5th European Microwave Conference, Microwave Exhibitions and Publishers, Kent, England, 69-73 (1975).
8. D. Brubaker and J. Eisenberg, "Measure S-Parameters With the TSD Techniques," *Microwaves RF* 24(12), 97-101, 159 (1985).

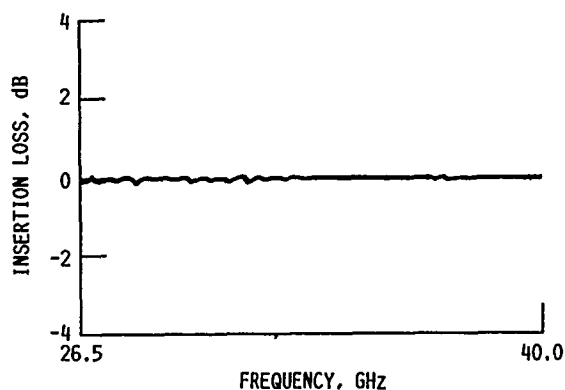


FIGURE 1. - RESULTANT INSERTION LOSS AT KA-BAND FOR THE "THROUGH" STANDARD FOLLOWING TSD CALIBRATION.

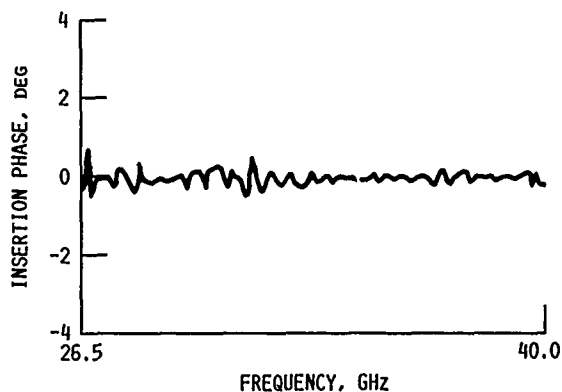


FIGURE 2. - RESULTANT INSERTION PHASE AT KA-BAND FOR THE "THROUGH" STANDARD FOLLOWING TSD CALIBRATION.



# On the measurement of mm-wave propagation characteristics of GaAs microstrip lines

Robert R. Romanofsky, Kim Adaway and Kul B. Bhasin

National Aeronautics and Space Administration  
Lewis Research Center  
Cleveland, Ohio 44135

## ABSTRACT

A thorough analytical procedure is developed for evaluating the frequency dependent loss characteristics and effective permittivity of millimeter-wave microstrip lines. The technique is based on the measured reflection coefficient of microstrip resonator pairs. Experimental data including Q factor, effective relative permittivity, and fringing for 50  $\Omega$  lines on GaAs was obtained. Effects of an imperfect open circuit, coupling losses, and loading of the resonant frequency are considered. A cosine tapered ridge guide fixture was used to characterize the resonators.

## 1. INTRODUCTION

Numerous theoretical formulations have been proposed to describe the microwave performance of strip transmission lines. Accurate analysis is hindered by the inhomogeneous geometry of microstrip which causes a field discontinuity at the air-dielectric interface. Short cuts to a full-wave analysis are often employed, particularly when closed form solutions are desirable. Furthermore, measurement techniques beyond ~25 GHz are not well established and tend to be cumbersome and unreliable. This paper proceeds through the straight forward calculation of the necessary parameters using a relatively simple but effective model and an innovative measurement technique. Many of the procedures described are based on principles outlined by Ginzton,<sup>1</sup> with the adaptation to microstrip "cavities" and modern measurement techniques. Additional work by Aitken<sup>2</sup> developed alternative methods for evaluating Q from swept frequency network analysis. The derivations evolved from cavity equivalent circuits at "detuned open" and "detuned short" measurement planes. In this paper, the usual assumption regarding small losses is adopted. Specifically, it is assumed that  $G \gg \omega C$ ,  $1/\omega L$  where G, C, and L are the distributed conductance, capacitance, and inductance per unit length along the transmission line. Swept frequency measurements are performed using a Hewlett-Packard 8510 automatic network analyzer and a cosine tapered ridge guide test fixture. The technique is used to determine loss (in terms of Q), dispersion (the variation of phase velocity with frequency), and fringing effects from the microstrip discontinuities.

## 2. EXPERIMENTAL PROCEDURE

Linear open circuit  $n/2$  microstrip resonators were fabricated on 2 in. semi-insulating GaAs wafers along the (100) crystallographic plane in the [010] direction. Both evaporated and electroplated gold films were evaluated in an attempt to determine the effects of metalization on conductor loss. Initially,

a 200 Å titanium layer was deposited on the wafers to enhance adhesion. A number of wafers were lapped to either 0.010 or 0.005 in. using a silicon carbide slurry and subsequently polished using a sodium hypochlorite/colloidal silica mixture. The technique to determine effective permittivity utilizes two 50  $\Omega$  lines on a single die; a short line of length  $L_1$  with a fundamental  $\lambda/2$  resonance at  $f_1$ , and a long line of length  $L_2 \approx 2L_1$  with a first harmonic resonance at  $f_2 \approx f_1$ . Each line was separated from an adjacent line by 0.100 in. to avoid coupling effects. By using two lines, the end (fringing) effects can be excluded from the results.<sup>3,4</sup> The resonators are coupled to the feed line via a critical symmetric gap. The gap dimensions ranged from 0.00075 to 0.001 in. for 0.005 in. thick wafers and from 0.0015 to 0.00175 in. for 0.010 in. thick wafers. Losses were evaluated in terms of the quality factor Q. The unloaded ( $Q_0$ ) must be derived from the raw data which includes the loading effects of the coupling mechanism.

To obtain the reflection coefficient of the resonators, S-parameter measurements were performed using an automatic network analyzer equipped with a synthesized source. The system was calibrated in microstrip using the technique discussed in Ref. 5. By judiciously positioning the reference plane, complications from the feed line can be avoided.

## 3. ANALYTICAL PROCEDURE

The microstrip cavity can be modeled as a resonant R,L,C circuit in the vicinity of resonance. Since the microwave cavity must be excited by a transmission line to perform the measurements, the input impedance will be modified. In general, the coupling between the resonator and feed line contains resistive ( $R_L$ ) and reactive ( $jX_L$ ) elements. The coupling loss component and the transmission line characteristic impedance load the resonant circuit. Coupling, in the case of a microstrip structure, is accomplished using a narrow ( $\ll \lambda_g$ ) gap. This discontinuity can be modeled by a capacitive pi network, or equivalently, by an ideal transformer. The input impedance of this equivalent circuit is:

$$Z_i(j\omega) = R_L + jX_L + \frac{\kappa Z_0}{1 + jQ_0 \left\{ \frac{\omega}{\omega_0} - \frac{\omega_0}{\omega} \right\}}$$

The variable  $\kappa$  is referred to as the coupling coefficient and is equal to the ratio of coupled conductance to resonator conductance. It is apparent that the coupling gap functions as an impedance inverter resulting in a small reflection coefficient at resonance.

Based on this model, it can be shown that the unloaded  $Q$  is given by:

$$Q_0 = Q_L \left\{ \frac{1 + \kappa + \sigma}{1 + \sigma} \right\}$$

where  $\sigma$  is the coupling loss which can be calculated from the reflection coefficient far off resonance. The loss component modifies the coupling coefficient and also influences the location "3 dB" bandwidth which is required to evaluate the loaded  $Q$ . The effect of the loss can be observed on a Smith chart as a linear displacement of the impedance locus. As a consequence of the modified input impedance, the level at which to determine the correct bandwidth becomes:

$$P_{1/2} = 10 \log_{10} \left\{ \frac{\left[ \frac{\kappa + \sigma - 1}{\kappa + \sigma + 1} \right]^2 + \left[ \frac{\sigma - 1}{\sigma + 1} \right]^2}{2} \right\} \text{ dB}$$

Additionally, losses associated with the abrupt open circuited line can be evaluated using two resonators. The technique is analogous to the method used to obtain the  $Q$  of waveguide cavities with lossy endplates. A complete derivation of the material which has been described is available in Ref. 6.

#### 4. REFERENCES

1. E.L. Ginzton, Microwave Measurements, McGraw-Hill, New York (1957).
2. J.E. Aitken, "Swept Frequency Microwave Q-Factor Measurement," *Proc. IEE*, 123(9), 855-862 (1976).
3. R.A. Pucel, D.J. Masse, and C.P. Hartwig, "Losses in Microstrip," *IEEE Trans. Microwave Theory Tech.*, MTT-16(6), 342-350 (1968).
4. T.C. Edwards, Foundations for Microstrip Circuit Design, John Wiley and Sons, Ltd., New York (1981).
5. R.R. Romanofsky and K.A. Shalkhauser, "A Universal Test Fixture for mm-Wave Solid State Devices Using a Novel Deembedding Algorithm," to be presented at the 13th International Conference on Infrared and Millimeter Waves, Honolulu, Hawaii, SPIE, Dec. 1988.
6. R.R. Romanofsky, "Analytical Experimental Procedures for Evaluating Propagation Characteristics of mm-Wave Microstrip Lines," NASA TP- , 1988, to be published.

INTERNATIONAL SAMPLE EXCHANGE FOR THE COMPARISON OF NEAR-MILLIMETER-  
WAVE CHARACTERIZATIONS OF MATERIALS\*

George J. Simonis

LABCOM, Harry Diamond Laboratories  
2800 Powder Mill Road  
Adelphi, MD 20783-1197

and

James P. Birch

National Physical Laboratory  
Teddington, Middlesex, UK

ABSTRACT

The National Physical Laboratory and Harry Diamond Laboratories have organized and are conducting an international sample exchange of materials to compare near-millimeter-wave (NMMW) characterizations made by different laboratories on exactly the same samples. The materials used comprise a cross section of NMMW properties in order to more completely test the various modes of analysis used. Results obtained up to the present and plans for the future will be provided in the oral presentation.

The near-millimeter wavelength (NMMW) range is understood to be approximately 1 to 10 mm in wavelength, 300 to 30 GHz in frequency, or 10 to 1  $\text{cm}^{-1}$  in wavenumber (or reciprocal wavelength). This range is very high in frequency compared to the normal microwave range. The implementation of many standard microwave techniques for characterizing materials, such as the insertion of samples in waveguides, is found to be very difficult and inaccurate in this range. The normal optical techniques, such as Fourier transform spectroscopy, are also difficult to implement in this range. A number of different techniques are employed for the characterizing the NMMW properties of materials. Unfortunately, many different values of complex index of refraction or complex dielectric constant can be found in the literature for a given material [1]. Some of these discrepancies are due to variations in sample properties, and some are due to poorly understood systematic or random errors in the measurement process.

There are no standards available for the measurement of the NMMW properties of materials and, because demand for such standards is limited, it is unclear when such standard materials or measurement techniques will be available. A group of researchers active in this subject area has therefore collaborated in measuring, in turn, exactly the same set of samples in order to avoid possible discrepancies due to sample-to-sample variations. The participants in this sample

exchange and the measurement techniques that they employed are presented in Table I. A variety of measurement techniques are represented, involving researchers from five countries. Seven samples having a range of NMMW property values were selected and measured. The samples selected and their nominal characteristics are presented in Table II.

A workshop involving the exchange participants was held just prior to the 12th International Conference on Infrared and Millimeter Waves in Orlando, Florida, in December 1987. The observations and conclusions of this workshop will be presented. prepared samples, a number of different techniques can provide NMMW real index of refraction values (or real dielectric constant values) accurate to better than 1 percent, with 0.1 percent readily achievable. Such accuracy is sufficient for many purposes. Also, the index of refraction changes only very slowly as a function of frequency so the value can be readily extrapolated to a useful accuracy from values at other frequencies. Unfortunately, the results regarding material loss measurements were not nearly as consistent and are not as easily extrapolated. Large unexplained discrepancies occurred in the frequency range below 120 GHz, particularly when the absorption loss was small and the index of refraction was large, such as for important window materials like beryllia or crystal quartz. The use of calorimetric techniques involving illumination by powerful NMMW sources and measurement of resultant sample heating should be explored for the measurement of low-loss materials, as has been done in the past for low-loss window materials for infrared lasers.

The sample exchange activity will be continued and the characterized samples will be made available to other researchers. An additional set of samples will be prepared with different dimensions machined from a common piece in order to provide optimal sample dimensions for different measurement techniques while insuring similar NMMW properties among the samples. Emphasis will be placed on improving the loss measurements for materials in the 35 to 120 GHz range where the discrepancies are the largest and the need for data is the most urgent.

REFERENCES

- (1) G. J. Simonis, "Index to the Literature Dealing with the Near-Millimeter Wave Properties of Materials," Intl. J. of IR and Millimeter Waves 3, 439-469 (1982).

\*Partial support provided by the U.S. Army Research, Development, and Standardization Group (UK), London, England.

TABLE I. Sample Exchange Participants

Laboratory	Researchers	Measurement Technique
<u>England</u>		
National Physical Laboratory Teddington Middlesex	Dr. J. R. Birch Dr. R. Clark	Dispersive PTS - (nondispersive PTS) Open Resonator
<u>France</u>		
Universite Nancy Nancy	Prof. A. Hadni Dr. X. Gerbaux	Nondispersive PTS
<u>United States</u>		
LABOON, Harry Diamond Laboratories Adelphi, Maryland	Dr. G. J. Simonis M Stead	Nondispersive PTS (dispersive PTS)
Georgia Institute of Technology Atlanta, Georgia	Dr. R. Moore Dr. T. Wells	Open resonator
Rockwell International Corp. Thousand Oaks, California	Dr. W. W. Ho Dr. W. F. Hall	Coherent source trans/reflect.
Los Alamos National Laboratory Los Alamos, New Mexico	Dr. H. Prost	Coherent source trans/reflect.
North Carolina Central Durham, North Carolina	Dr. J. M. Dutta Dr. C. R. Jones	245 GHz laser interferometer/trans.
National Bureau of Standards Boulder, Colorado	Dr. R. Baird	(Cognizance)
Tufts University Medford, Massachusetts	Prof. M. N. Afsar	Dispersive PTS
<u>West Germany</u>		
Physikalisch-Technische Bundesanstalt Braunschweig	Dr. U. Stumper	6-port reflectometer
University of Karlsruhe Karlsruhe	Dr. R. Heidinger	Open resonator
<u>Japan</u>		
Osaka University Osaka	Dr. K. Sakai	Nondispersive PTS

TABLE II

NOMINAL CHARACTERISTICS OF SAMPLES

Material	Aperture Diameter  (cm)	Thickness  (cm)	35 To 600 GHz			
			n	$\epsilon$	$\alpha$ ( $\text{cm}^{-1}$ )	$\tan \delta$ ( $10^{-3}$ )
Macor	5	0.2	2.38	5.7	0.1-35	10-80
Polyethylene	4	1.0	1.52	2.3	0.001-0.2	0.1-1
Rexolite I	5	1.2	1.59	2.5	0.01-1.4	1-5
Rexolite II	5	1.9				
Ferroflow	5	0.04	3.6	13.0	10-300	-400
Beryllia	5x5	0.5	2.59	6.7	0.01-1.0	0.6-2
Quartz, Crystal (x-cut)	5	0.8	0-2.106 2-2.153	4.44 4.64	0.001-0.08 0.001-0.08	0.08-0.2 0.08-0.2

Note: n is the real component of the index of refraction,  $\epsilon$  is the real component of the dielectric constant and  $\alpha$  is the power absorption coefficient.

# SOLID STATE SPECTROSCOPY IN FAR INFRARED AND MILLIMETER WAVE REGIONS BY SYNCHROTRON RADIATION

Takao Nanba

*Department of Physics, Faculty of Science, Tohoku University  
Sendai 980, Japan*

## ABSTRACT

The utilization of the synchrotron radiation from the UVSOR storage ring of the Institute for Molecular Science at Okazaki in Japan for the far infrared and millimeter wave spectroscopy has started since 1986. The experience at the UVSOR proved that the synchrotron radiation is a very bright light source over a black body source. To demonstrate the advantage to use the synchrotron radiation in the far infrared region instead of a conventional source, experiment under high pressure using a diamond anvil cell is described.

## INTRODUCTION

Synchrotron radiation is a new light source which covers a very wide energy region from the microwave to the x-ray. However, the synchrotron radiation has not been employed in the long wavelength spectroscopy although the synchrotron radiation has many excellent properties such as high brightness (photon numbers per unit area-solid angle product), continuous spectral distribution over the entire energy region, its precise time structure in the nano-second time domain and so on.

After precursory experiments at the storage ring of the SRS (Daresbury) [1] and the BESSY (Berlin) [2], a spectroscopic system was constructed in 1985 at the beam line BL6A1, which is dedicated exclusively for the far infrared spectroscopy, of the UVSOR and its practical utilization has started since 1986 [3].

The purpose of the present paper is to describe the recent advance in experiment on solid state spectroscopy in the far infrared and the millimeter wave regions at the UVSOR.

## INTENSITY MEASUREMENT

The far infrared radiation from the UVSOR in a solid angle of  $4.8 \times 10^{-3}$  sr was introduced into a Martin-Puplett interferometer by light collection mirrors. The emitting solid angle of the synchrotron radiation is by about twenty times smaller than that of the usual optics of  $f/3$  by a conventional light source. The incident light beam into the sample chamber after the interferometer was reflected a toroidal mirror and focussed on the sample position in the sample chamber. The interferometer is equipped with its own light source of a 125 W high pressure mercury lamp with the light collection of the solid angle of 0.075 sr. Thus, either the synchrotron or the light from the mercury lamp is selective [3]. Therefore, we can

directly compare the intensities of the two sources using the same spectroscopic system.

By this system, the light intensities from the two sources were measured as the function of the aperture at the sample position through which the light passed. Fig.1 shows the ratios of the light intensity at 100  $\mu\text{m}$  of the synchrotron radiation to that of the mercury lamp through different apertures. The intensities of the synchrotron radiation were normalized to that in operation of 100 mA. This result shows that more photon flux with the synchrotron radiation than with the mercury lamp is acceptable into a detector in experiment where a sample acceptance is limited. The UVSOR is designed for a ring current of 500 mA. Therefore, the synchrotron radiation should serve as a superior intense continuum light source over any other conventional source in the entire far infrared region.

## EXPERIMENT UNDER HIGH PRESSURE

The response of the phonon spectrum of material due to the phase transition on its crystal structure has been widely studied by laser Raman spectroscopic method. However, the change in the phonon spectrum of the materials which possesses the inversion crystal symmetry such as alkali halides has not been reported because its optic phonon mode has Raman inactive character. In such a case, an absorption measurement under high pressure using a diamond anvil cell is required to observe it. Such an experiment has been difficult particularly in the far infrared region because of the lack of the brightness of a conventional source.

At the UVSOR, the experiment under high pressure using a diamond anvil cell in the far infrared region is possible owing to the high brightness of the synchrotron radiation. The precise description of the spectroscopic system under high pressure combined with the UVSOR was given elsewhere [4]. We made a so-called lever-arm type of a diamond anvil cell. The pressure induced in the diamond anvil cell was measured by a conventional fluorescence measurement technique of a ruby. A ruby chip was immersed as a pressure sensor together with the sample in the liquid paraffin within the pressure cell. By use of this high pressure apparatus, we measured the change in the phonon spectrum of alkali halides due to the phase transition with the pressure. It is well known that alkali halide shows a first order phase transition from the B1 phase (rock salt structure) to the B2 (cesium chloride) under pressure. However, the measurement of the far infrared spectrum under

pressure has not been done.

Fig. 2 shows the changes of the phonon spectra of KI with the pressure at room temperature. A KI film of 2  $\mu\text{m}$  thickness was evaporated in advance onto the one culet surface of the diamond. The pressure is shown at each spectrum. The dip which corresponds to the TO phonon absorption is shown by a downward arrow in each curve. The TO phonon showed a blue energy shift with the pressure in the B1 phase (curves a-c). It was suddenly reduced after the phase transition to the B2 which occurs at 1.8 GPa. In the B2 phase, the TO phonon showed a blue shift.

From the energy shift of the TO phonon versus the pressure, the mode Gruneisen parameters ( $\gamma_{\text{TO}}$ ) in the both phases and the TO phonon energy ( $\omega_{\text{TO}}$ ) in the B2 phase were reduced for the first time. They are  $\gamma_{\text{TO}}^{\text{B1}} = 1.66$ ,  $\gamma_{\text{TO}}^{\text{B2}} = 2.7$  and  $\omega_{\text{TO}}^{\text{B2}} = 108 \text{ cm}^{-1}$ . The details of the experimental results on other alkali halide crystals will also be given.

## CONCLUSIONS

1) The practical utilization of the synchrotron radiation in the far infrared region has started since 1988 at the UVSOR. The available spectral region for the measurement covers 3 to  $250 \text{ cm}^{-1}$ . 2) The absorption measurement of alkali halide under high pressure using a diamond anvil cell is now carried out at the UVSOR. The change in the phonon spectrum of alkali halides under high pressure was done to demonstrate an advantage of the utilization of the synchrotron radiation in the far infrared region. 3) By the experiment under high pressure, the mode Gruneisen parameters and the TO phonon energy of the alkali halides in the B1 and B2 phases were determined for the first time.

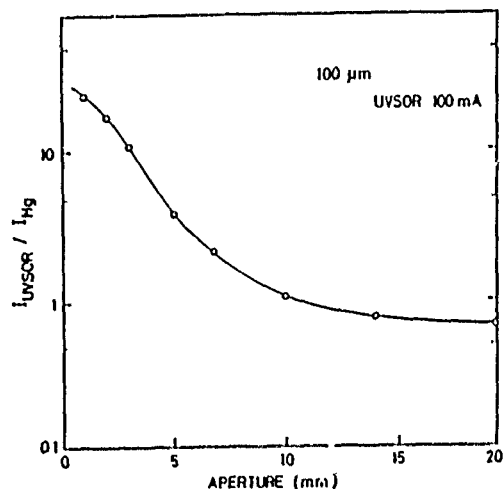


Fig. 1 The ratio of the light intensity of the synchrotron radiation at 100  $\mu\text{m}$  to that of the mercury lamp which pass through the same aperture is shown versus the diameter of the aperture. The intensities of the synchrotron radiation were normalized to that in operation at 100 mA.

## ACKNOWLEDGMENTS

This work has been done in collaboration with Professor M. Ikezawa of Tohoku University and Professor M. Watanabe, Dr. K. Fukui and Professor H. Inokuchi of the Institute for Molecular Science. The author is grateful to them for their useful discussions and encouragement through this work.

## REFERENCES

- [1] J. Yarwood, T. Shuttleworth, J. B. Hasted and T. Nanba: *Nature* 317 (1984) 743.
- [2] E. Schweizer, J. Nagel, W. Braun, E. Lippert and A. M. Bradshaw: *Nucl. Instrum. Meth. A239* (1985) 630.
- [3] T. Nanba, Y. Urashima, M. Ikezawa, M. Watanabe, E. Nakamura, K. Fukui and H. Inokuchi: *Int. J. Infrared and Millimeter Waves* 7 (1986) 1769.
- [4] T. Nanba: submitted to *Rev. Sci. Instrum.* (1988)

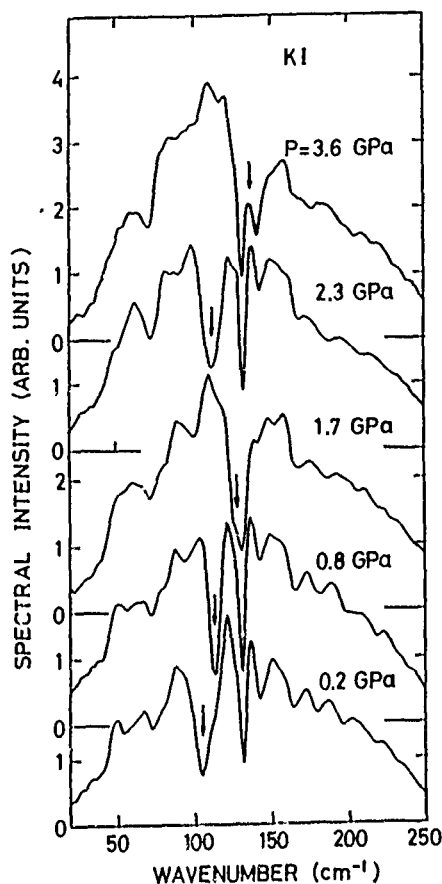


Fig. 2 Transmission spectra of a KI evaporated film of 2  $\mu\text{m}$  thickness measured at room temperature under high pressure. The pressure monitored by the energy shift of the fluorescence R1 line of ruby is shown on each spectrum. The dip due to the absorption of the TO phonon mode of KI is shown by the downward arrow. A sharp dip at  $130 \text{ cm}^{-1}$  is due to the absorption of the crystalline quartz filters of the detector.

## MILLIMETER WAVE MEASUREMENT OF COMPLEX PERMITTIVITY

## BY IMPROVED DIELECTRIC DISK RESONATOR METHOD

Yoshio KOBAYASHI and Junya SATO

Saitama University  
Department of Electrical Engineering  
Urawa, Saitama 338, Japan

## ABSTRACT

A resonance method using a dielectric disk resonator, consisting of a plate sample clamped between two conductor cylinders, is described for measuring the temperature dependence of the complex permittivity in the millimeter wave region. An alumina substrate is measured at 36 GHz by this method.

## INTRODUCTION

A  $TE_{0m0}$ -mode dielectric disk resonator, constituted by inserting a circular disk sample into a  $TE_{0m}$ -mode circular cutoff waveguide, is used to accurately measure the complex permittivity of solid dielectric materials [1]-[3]. Recently, this method was improved to measure a plate or sheet sample of any size nondestructively, although the measurement of loss tangent was not discussed sufficiently [4]. This paper discusses a more complete treatment of this method to measure the temperature dependence of the complex permittivity in the millimeter wave region.

## MEASUREMENT PRINCIPLE

Fig. 1 shows a resonator structure used in this measurement. Two conductor cylinders of the diameter  $D \approx 16.4$  mm and the length  $M \approx 19.3$  mm were machined from brass and copper plated. A plate sample is placed between these cylinders and clamped with clips to fix this structure; hence, the sample can be quickly removed and replaced by another one to be measured. The axially symmetric  $TE_{0m0}$  modes are used to avoid air gap effects at the plate-cylinder

interfaces and the higher order values of  $m$  are chosen to increase the  $D$  value ( $m=4$  in this case). The cylinders constitute the  $TE_{0m}$ -mode cutoff waveguides; hence the fields decay exponentially on either side of the sample. The required  $M$  value can be determined from Fig. 5 in [3]. Under test, two conductor plates are removed from the cylinders.

This structure is excited by two 2.4 mm semi-rigid coaxial cables, each of which has a small loop at the top; this system permits the measurement up to 50 GHz. The transmission-type resonator is constituted and undercoupled equally to the input and output loops. The resonant frequency  $f_0$  and unloaded  $Q$ ,  $Q_u$  are measured using HP series devices (8340B sweeper, 8349B amplifier, 53554A millimeter wave head, R281 waveguide-coax. adapter, 85025D coaxial detector, and 8757A scalar network analyzer) by means of the swept-frequency method.

For this structure the resonant frequency and unloaded  $Q$  of the  $TE_{0m0}$  mode can be calculated accurately by the rigorous analysis based on Ritz-Galerkin method. Therefore, we can determine  $\epsilon_r$  and  $\tan \delta$  from the measured values of  $f_0$  and  $Q_u$  on the basis of this analysis. This numerical calculation, however, is rather tedious. Then we first determine relative permittivity  $\epsilon_r$  and loss tangent  $\tan \delta$  by using simple formulas for the dielectric disk resonator method described in [3], where the fringing effect for Fig. 1 is neglected. In the following we obtain  $\epsilon_r$  and  $\tan \delta$  from the graphical correction of  $\epsilon_r$  and  $\tan \delta$ , using charts calculated from this analysis. This simplified treatment will be discussed below.

The  $\epsilon_r$  value is given by [3]

$$\epsilon_r = \left( \frac{c}{\pi f_0 L} \right)^2 [X^2 + Y^2] + 1 \quad (1)$$

where the first root  $X$  for a given value  $Y$  is calculated from

$$X \tan X = Y \quad Y = \frac{L}{2} \sqrt{k_r^2 - k_0^2} \quad (2)$$

with  $k_0 = 2\pi f_0 / c$ ,  $k_r = 2j_{0m}' / D$ , and  $J_0'(j_{0m}') = 0$ .

The  $\tan \delta_r$  value is given by [3]

$$\tan \delta_r = \frac{A}{Q_u} - B \sqrt{\frac{\pi f_0 \mu_0}{\sigma}} [1 + \alpha(T - T_0)] \quad (3)$$

where  $\sigma = \bar{\sigma}_0$  and  $\bar{\sigma}$  are the conductivity and the relative conductivity at the temperature  $T_0$  °C,  $\sigma_0 = 58 \times 10^6$  S/m, and  $\alpha$  is the temperature coefficient of  $\sigma$ . Also the values  $A$  and  $B$  are given by [3]

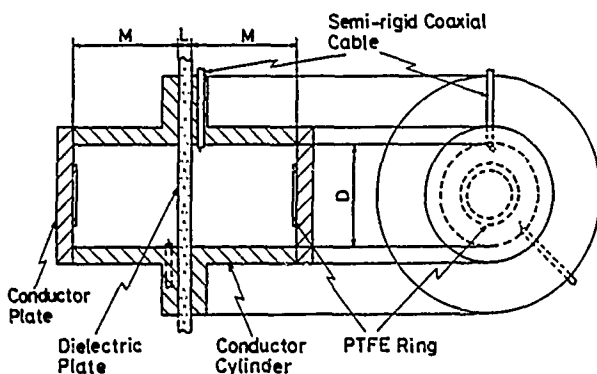


Fig. 1 Resonator structure for measurement.

$$A = 1 + \frac{W}{\epsilon_r} \quad B = \left( \frac{c j_0 m}{\pi f_0 D} \right)^3 \frac{1+W}{60 \pi j_0 m \epsilon_r} \quad W = \frac{\cos^2 X}{Y + \sin^2 X} \quad (4)$$

Then, the  $\epsilon_s$  and  $\tan \delta_s$  values are given by

$$\epsilon_s = \epsilon_r \left( 1 - \frac{\Delta \epsilon}{\epsilon_r} \right) \quad (5)$$

$$\tan \delta_s = \frac{A}{Q_u} \left( 1 + \frac{\Delta A}{A} \right) B \left( 1 + \frac{\Delta B}{B} \right) \sqrt{\frac{\pi f_0 H_0}{\sigma} [1 + \alpha(T - T_0)]} \quad (6)$$

respectively, where the correction terms due to the fringing field  $\Delta \epsilon / \epsilon_r$ ,  $\Delta A / A$  and  $\Delta B / B$  are can be obtained from the charts, which are omitted here.

The mean square errors of  $\epsilon_r$  and  $\tan \delta_r$  can be estimated by means of the first-order approximation [3]. Then, we assume that  $\Delta \epsilon_s \approx \Delta \epsilon_r$  and  $\Delta \tan \delta_s \approx \Delta \tan \delta_r$ .

## EXPERIMENT

### A. Cylinder Parameters Measurement

We can determine the cylinder parameters such as  $D$ ,  $2M$ ,  $\sigma$ ,  $\tau_c$ , and  $\alpha$  from the measurement for the  $TE_{011}$  mode of an empty cavity, which is constructed by attaching two conductor plates to both ends of the cylinders after removing the sample as in Fig. 1. PTFE rings are attached on the end plates to separate the degenerate  $TM_{112}$  modes from the  $TE_{011}$  modes [3].

At first,  $D$  and  $2M$  are determined from the measured two resonant frequencies,  $f_1$  for the  $TE_{011}$  mode and  $f_3$  for the  $TE_{013}$  mode, by using

$$D = \frac{2c j_0}{\pi} \sqrt{\frac{2}{9f_1^2 - f_3^2}} \quad 2M = c \sqrt{\frac{2}{f_3^2 - f_1^2}} \quad (7)$$

derived from the resonance conditions.

Secondly,  $\sigma$  is determined from the measured unloaded  $Q$ ,  $Q_{uc}$  at  $f_1$  by using equation (1) in [3].

Thirdly, the temperature coefficient of the cylinder  $\tau_c$  is determined from the measurement of temperature dependence of  $f_1$  by using

$$\tau_c = -\frac{1}{f_1} \frac{\Delta f_1}{\Delta T} \quad (8)$$

Finally,  $\alpha$  is determined from the measurement of temperature dependence of  $\sigma$  by using

$$\alpha = \frac{1}{\sigma} \frac{\Delta \sigma}{\Delta T} \quad (9)$$

For this cavity, we obtained  $D=16.417$  mm and  $2M=38.689$  mm from the measured values  $f_1=22.606$  GHz and  $f_3=25.122$  GHz at room temperature ( $23^\circ\text{C}$ ), and  $\bar{\sigma}=82.5$  percent from  $Q_{uc}=17300$  at  $f_1$ . In the following, we placed the cavity in a temperature-stabilized oven and measured the temperature dependences of  $f_1$  and  $Q_{uc}$ . These results yield  $\tau_c=18.4$  ppm/ $^\circ\text{C}$  and  $\alpha=0.00354$  between  $10^\circ\text{C}$  and  $90^\circ\text{C}$ . As a result,  $D$  and  $\bar{\sigma}$  are given by

$$D = 16.415 [1 + 18.4 \times 10^{-6} (T - 20)] \text{ mm} \quad (10)$$

$$\bar{\sigma} = 83.4 / [1 + 0.00354 (T - 20)] \%$$

### B. Measurement of Temperature Dependence of Complex Permittivity

The resonator structure with a 99.9% alumina ceramic plate having  $L=0.776 [1 + 5.4 \times 10^{-6} (T - 20)]$  mm,

was placed in the temperature-stabilized oven and the temperature dependences of  $f_0$  and  $Q_u$  were measured. These results are shown in Fig. 2. The  $\epsilon_r$  and  $\tan \delta_r$  values determined from these results by using (1), (3), and (10) are shown in Fig. 3 by broken lines. Considering the fringing effect terms  $\Delta \epsilon / \epsilon_r = 0.0176$ ,  $\Delta A / A = 6.7 \times 10^{-4}$ , and  $\Delta B / B = 0.57$  calculated in this case, we obtain  $\epsilon_s$  and  $\tan \delta_s$ , shown in Fig. 3 by solid lines.

The root mean square error of  $\epsilon_s$  is  $\pm 0.14$  which is estimated from  $\Delta D = \pm 0.0002$  mm,  $\Delta L = \pm 0.018$  mm, and  $\Delta f_0 = \pm 0.02$  GHz. The root mean square error of  $\tan \delta_s$  is  $\pm 1.2 \times 10^{-6}$  which is estimated from  $\Delta Q_u = \pm 91$  and  $\Delta \bar{\sigma} = \pm 1.4$  percent.

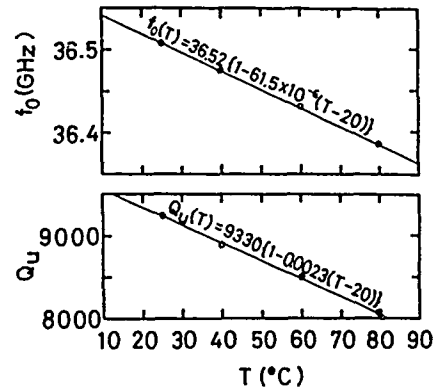


Fig. 2 Temperature dependence of  $f_0$  and  $Q_u$  for 99.9 percent alumina sample.

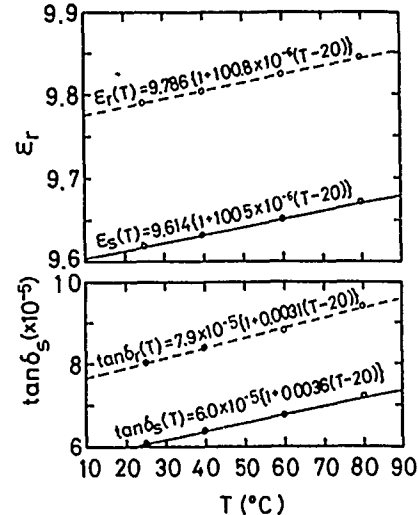


Fig. 3 Temperature dependence of  $\epsilon_r$ ,  $\epsilon_s$ ,  $\tan \delta_r$ , and  $\tan \delta_s$  for 99.9 percent alumina sample.

## REFERENCES

- [1] E. T. Jaynes; Proc. IRE, 46, p. 415, Feb. 1958.
- [2] S. B. Cohn and K. C. Kelly; IEEE Trans., MTT-14, p. 406, Sept. 1966.
- [3] Y. Kobayashi and T. Hataguchi; 1984 IR&MM Waves Digest, p. 374 (Takarazuka).
- [4] G. Kent; 1988 IEEE MTT-S Int. Microwave Symp., OF-2-7 (New York).



## SOME NEW PROPERTIES OF LOADED RESONATORS

Dr. Louis F. Libelo and Guy Pisane  
Harry Diamond Laboratories

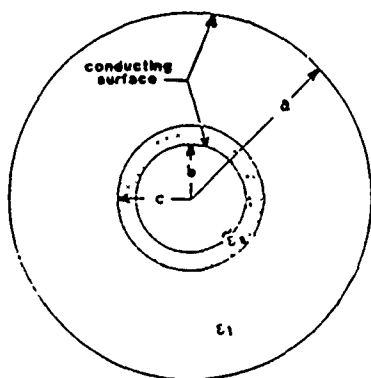
## ABSTRACT

We have been investigating the effects of loading resonator systems in the interior as well as accessing them from the exterior. We present some new properties that have been brought to light as a result of the methods used to study systems loaded in the interior. Mode charts and eigenfield distributions are to be shown for the concentric spherical resonator. The form of the representation of these mode charts illustrates the power of the techniques used and the richness of the results obtained.

## INTRODUCTION

We investigated analytically a simple resonator system in such a manner that the many interesting and useful results obtained are immediately applicable in the millimeter wave and in other regimes. Furthermore, the properties found for the relatively simple system can be extrapolated to more general, highly complex resonator systems. The system we report on here is the ideal, concentric, spherical cavity with ideal walls. In this system, the inner conductor is loaded with a lossy dielectric layer, while the remainder of the cavity is homogeneously filled with a lossless dielectric. Zaki and collaborators [1,2], to mention one research effort, have established the value of mode charts for millimeter resonator systems in their studies of cylindrical systems. Since space limitations constrain us to present a small fraction of our results, we have selected for this report several representative mode charts for our system. These mode charts are in dimensionless form and hold for all ranges of the geometric parameters of the system. We show results for the dielectric load ranging continuously from an ideal, lossless dielectric, to an ideal (infinitely lossy) conductor. In addition to the mode charts, we show representative eigenfield component distributions, but only for lossless loads.

Figure 1. The concentric cavity with dielectric  $\epsilon_1$  and load  $\hat{\epsilon}_2 = \epsilon_2 - i\sigma/\omega$ .



## THEORY AND RESULTS

Figure 1 illustrates the geometry of the concentric spherical system. Application of the boundary conditions at the metal walls and the dielectric interface to the fields obtained from the Debye potentials yields the characteristic equation whose roots are the propagation constants. In all we discuss here, we have suppressed the angular dependencies of all physical quantities since they are quite well known. Extensive calculations of the system TM and TE eigenvalues have been carried out. In the special case of a non-lossy dielectric load, mode charts were developed separately for the TM and the TE modes for different values of the load layer thickness and for a number of choices of relative dielectric constants. Figure 2 is an example of one such chart, namely, the TM modes for relative dielectric constant 10, and a load layer thickness one-tenth the radius of the outer metal wall. Each trajectory contains, for a specific TM mode, the value of the propagation constant (or the resonance frequency) of the system for any size outer conductor wall for the entire permissible range of inner conductor wall radius. An inspection of this mode chart reveals some very surprising properties in the variation of the resonances with respect to the different parameters. In particular, note that there is one and only one family of modes (the TM<sub>1p</sub>) for the system whose frequencies do not become quite large as  $c/a$  approaches unity. The lower lying trajectories in Figure 2 illustrate this. For a concentric cavity with no dielectric layer, the resonances of the higher modal families approach infinity as  $b$  approaches  $a$ .

Figures 3 and 4 are simple mode charts for the ratio of inner to outer conductor radii of 0.8 and a lossy load dielectric of thickness equal to one-tenth the outer metal radius, and whose real parts have ratios equal to 3 and 10, respectively. In each case these figures give the value of the complex frequency as the loss in the load ranges continuously from zero to infinity for any value of outer conductor radius. Note that in Figure 3 there is an intermediate range of conductivity for the load for which the damping constant decreases with increasing conductivity. Considerably more intricate variation has been found for other cases. This is all in marked contrast to the monotonic behavior for the cavity homogeneously filled with a lossy dielectric.

A normalized set of the radial dependence of TM<sub>11</sub> and TE<sub>11</sub> eigenfield distributions will be shown for a non-lossy case. The variation of the eigenfields with the various system parameters proves to be an interesting study in its own right.

Figure 2. TM eigenvalues,  $k_{np}a$ , for the loaded concentric cavity, filled with dielectric  $\epsilon_1$ . The inner conductor is clad with dielectric  $\epsilon_2 = 10\epsilon_1$  of thickness  $1/10$  the outer conductor radius.

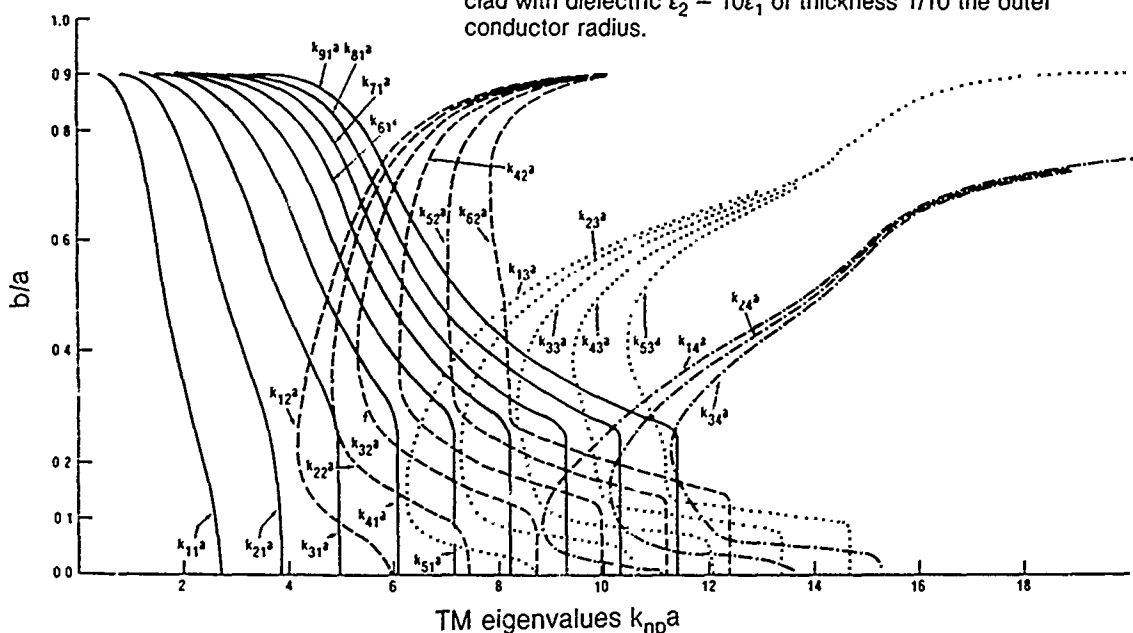


Figure 3. TM11 spatial eigenvalues,  $\gamma_1 a = \omega a \sqrt{\mu \epsilon_1}$ , in medium  $\epsilon_1$ , with normalized conductivity  $\hat{\sigma} = \sigma a \sqrt{\mu \epsilon_1}$  as parameter, for  $b = 0.8a$  and  $c = 0.9a$ . Layer with relative dielectric constant  $\epsilon = \tilde{\epsilon}_2/\epsilon_1 = 3 - i\hat{\sigma}/\gamma_1 a$ .

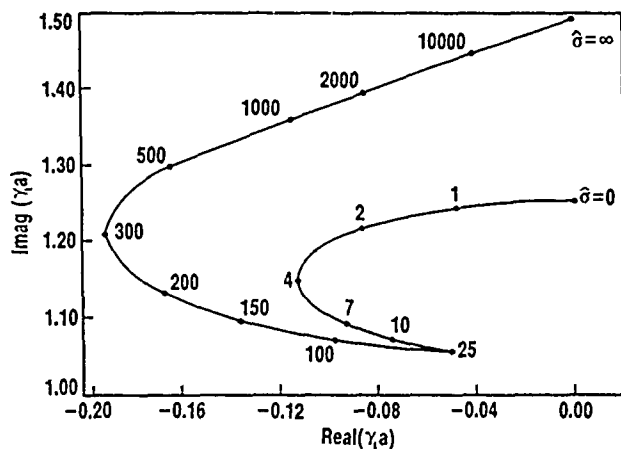
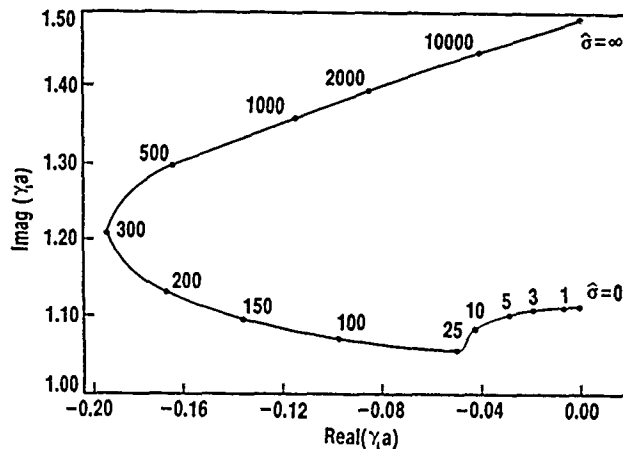


Figure 4. TM11 spatial eigenvalues,  $\gamma_1 a = \omega a \sqrt{\mu \epsilon_1}$ , in medium  $\epsilon_1$ , with normalized conductivity  $\hat{\sigma} = \sigma a \sqrt{\mu \epsilon_1}$  as parameter, for  $b = 0.8a$  and  $c = 0.9a$ . Layer with relative dielectric constant  $\epsilon = \tilde{\epsilon}_2/\epsilon_1 = 10 - i\hat{\sigma}/\gamma_1 a$ .



The spherical cavity loaded with a dielectric sphere has also been thoroughly analyzed. This work relates to, but is more extensive than that of Julien and Guillon [3], and is to be presented later. Extensive results were obtained when there is an aperture in the outer wall to access the resonator interior. These results are also to be presented elsewhere. Further work is under way to include the effects of finite wall conductivity and finite wall thickness to make the study complete. These results can be of use to workers in many different areas of electromagnetics.

1. K. A. Zaki and C. Chen, IEEE Trans. Microwave Theory and Techniques, vol MTT 34, pp 815-824, July 1986
2. K. A. Zaki and A. Alia, IEEE Trans. Microwave Theory and Techniques, vol MTT 31, pp 1039-1040, Dec. 1983
3. A. Julien and P. Guillon, IEEE Trans. Microwave Theory and Techniques, vol MTT 34, pp 723-729, June 1986

# NEAR-MILLIMETER-WAVELENGTH MEASUREMENTS OF COMPLEX INDEX VALUES OF SEVERAL POLYMER MATERIALS

Michael Stead and George J. Simonis

LABCOM, Harry Diamond Laboratories  
2800 Powder Mill Road  
Adelphi, MD 20783-1197

## ABSTRACT

We have determined the near-millimeter-wavelength (100 to 500 GHz) values of the complex indices of refraction of several polymer materials. A polarizing Fourier transform spectrometer was used in making the measurements. Results include error analyses and comparisons with other reported measurements.

Today, polymers are being considered for applications which in the past were closed to them. The new generation of polymers and composites are strong, resistant to heat and many chemicals, lightweight, insulating, moldable, and machinable [1]. These properties make them improved candidates for use as windows, radomes and waveguides. It is the purpose of this discussion to present the near-millimeter-wave (NMMW) characteristics of some of these materials.

For each material tested, the index of refraction and the absorption coefficient,  $\alpha$ , were determined as a function of frequency using Fourier transform spectroscopy (FTS). The experimental configuration is shown in Fig. 1. First, the average index was determined in the range of 3 to 10  $\text{cm}^{-1}$  using dispersive FTS [2]. Then  $\alpha$  was determined using nondispersive FTS [3]. It is sufficient for most purposes to find the average index, since the index changes by less than a percent over the frequency range tested [4]. All the samples tested were large enough to be placed in the collimated beam. This avoided the possible error caused by different portions of the beam travelling different optical path lengths if the sample had been placed in the focussed beam [5]. A brief description of each material will be given with the results.

Eight materials were tested. Table 1 displays the index of refraction,  $n$  at 94 GHz, and loss tangent at 94 GHz of each sample. We found the value of sample thickness variation,

$\Delta t$ , by making several thickness measurements at different points on each sample. The number given is the standard deviation. This value was incorporated into our calculation of the uncertainty of the index,  $\Delta n$ . Also contributing to  $\Delta n$  is the resolution of the interferometer. Interpolations can be made in the dispersive interferogram to find the index to within a quarter of the resolution, given a uniform sample. If greater accuracy is needed, smaller step sizes can be used. However, as polymer samples properties are not generally highly consistent, the resolution used was deemed sufficient. Both

$\Delta t$  and  $\Delta n$ , and also the uncertainties in the transmission data were used to find  $\Delta \alpha$  and  $\Delta \tan \delta$ . Standard propagated-error calculations were made to determine uncertainties. Fig. 2 is a plot of

the absorption coefficient of acrylonitrile-butadiene-styrene (ABS) and polyether-etherketone (PEEK) from 3 to 12  $\text{cm}^{-1}$ . Fig. 3 displays the absorption coefficient of polyimide quartz (PIQ) and glass-fiber-loaded polycarbonate (Lexan 3414) from 3 to 12  $\text{cm}^{-1}$ . Fig. 4 is a comparison of three types of polyether imide (Ultem). The plot shows the absorption coefficient from 3 to 12  $\text{cm}^{-1}$  of pure Ultem, and Ultem with 20% and 30% by weight concentrations of glass fibers. We see that the least lossy is the pure Ultem. We also see that the sample with the higher concentration of glass fibers, Ultem 2300, is the most lossy, as might be expected. Fig. 5 compares the least lossy sample tested, poly-4-methyl pentane (TPX), with another low-loss window material, sapphire [4]. The absorption coefficient is presented from 3 to 15  $\text{cm}^{-1}$ . Our loss data for TPX compares well with that of Afsar [6,7]. The differences may be due to different impurities in the samples, as TPX is produced with different additions for different purposes.

The error bounds plotted in figures 2 through 5 demark a 95% confidence interval for the value of the absorption coefficient, with respect to statistical fluctuations. There is also a possibility of systematic error that could be as large as 0.03 Np/cm.

We see that none of the materials tested exhibit catastrophic losses. The very low absorption coefficient of TPX makes it worth considering for waveguide applications. The other materials, with losses an order of magnitude larger, would have virtually no use in waveguides at this frequency. However, in cases where ample signal is available, they would be of use as windows or radomes. This judgement is made in consideration of the fact that none of the materials has an absorption coefficient above 0.7 Np/cm at 94 GHz. This value corresponds to a 50% reduction in transmission for every centimeter of thickness.

Another conclusion can be drawn from the Ultem results. The incorporation of glass fibers in the material makes the material more lossy. The fibers are included to add strength to the material. So, for reinforced Ultem, in this frequency range there is a tradeoff involved between strength and transmission. Both fiber dimensions and fiber composition may contribute to the absorption coefficient. Experimentation with different fibers, would be enlightening.

## REFERENCES

- (1) J. A. Mock, *Plast. Eng.* **40**, n2, 25 (1984).
- (2) J. Chamberlin, J. Gibbs, and H. Gibbie, *IR. Phys.*, **9**, 185 (1969).
- (3) E. V. Loewenstein and D. R. Smith, *Appl. Opt.*, **10**, 577 (1971).
- (4) M. Stead and G. Simonis, "Near Millimeter Wave Characteristics of Dual Mode Materials," publication pending.
- (5) G. Simonis, J. Sattler, T. Worchesky, R. Leavitt, *Int. J. of IR and MMW*, **5**, 57 (1984).
- (6) M. N. Afsar, *IEEE Trans, on MTT*, **33**, 1410 (1983).

Table 1: Index data for 94-350 GHz and loss data at 94GHz for samples tested.

Material	t (cm)	$\Delta t$	n	$\Delta n$	$\alpha$	$\Delta \alpha$	$\tan \delta$	$\Delta \tan \delta$
TPX	5.0794	0.0015	1.458	0.004	0.038	0.011	0.0015	0.0004
	1.3580	0.0004	1.458	0.004	0.038	0.011	0.0015	0.0004
Ultem 1000	1.1417	0.0006	1.730	0.005	0.194	0.044	0.0056	0.0013
Ultem 2200	1.0669	0.0004	1.819	0.006	0.274	0.055	0.0075	0.0015
Ultem 2300	1.0299	0.0007	1.865	0.006	0.341	0.065	0.0092	0.0018
ABS	1.1072	0.0007	1.636	0.005	0.217	0.043	0.0066	0.0013
PEEK	1.0376	0.0006	1.777	0.004	0.225	0.049	0.0063	0.0014
PIQ	1.1455	0.0004	1.733	0.006	0.55	0.14	0.016	0.004
Lexan 3414	1.0675	0.0006	1.655	0.005	0.68	0.30	0.018	0.008

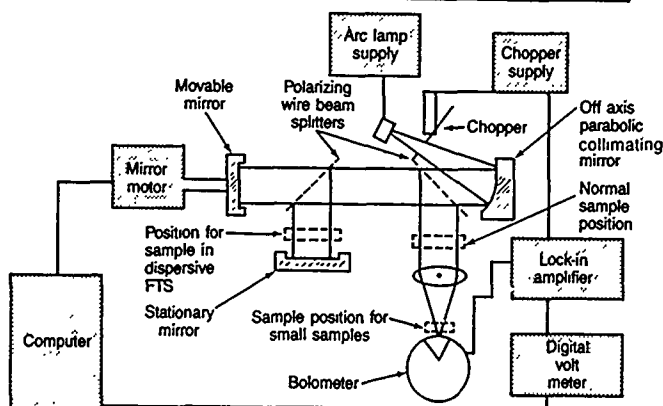


Fig. 1. Polarizing interferometer used to perform Fourier Transform Spectroscopy (FTS).

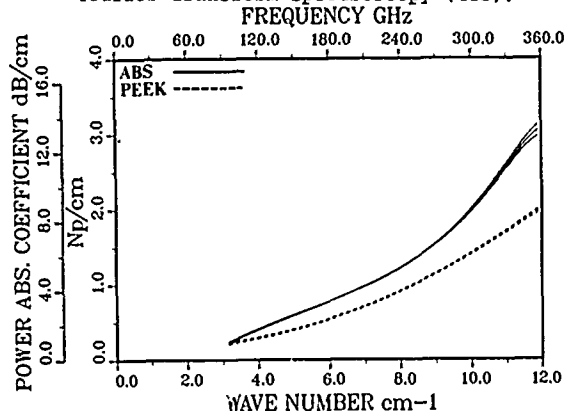


Fig. 2. Absorption coefficient for acrylonitrile butadiene styrene (ABS), solid, and polyether etherketone (PEEK), dashed. As with Figs. 3-5, the upper and lower lines demark a 95% confidence.

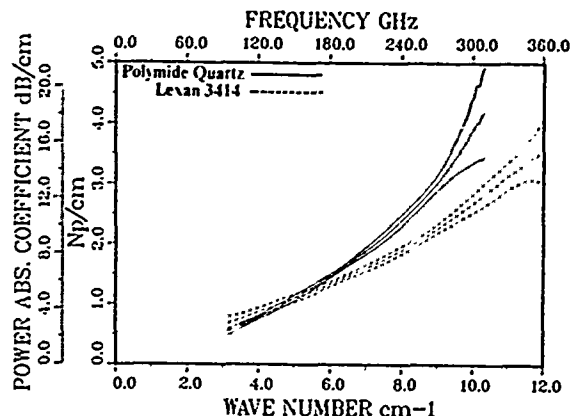


Fig. 3. Absorption coefficient for polyimide quartz (PIQ), solid, and Lexan 3414, dashed.

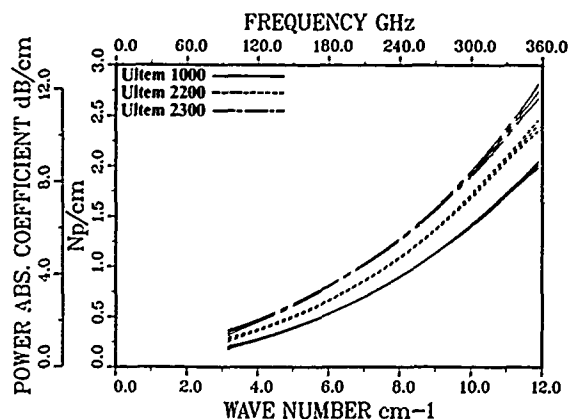


Fig. 4. Absorption coefficient for three Ultem samples, Ultem 1000, solid, Ultem 2200, dashed, Ultem 2300 chain-dashed.

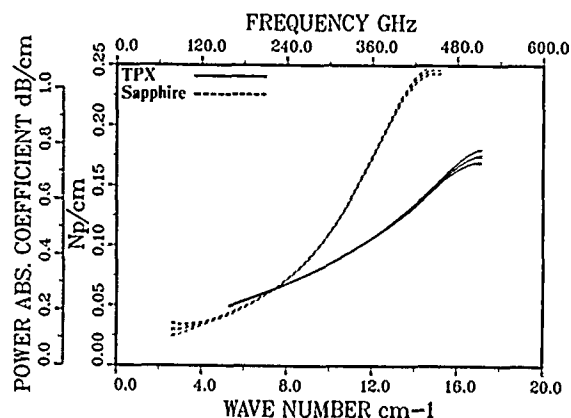


Fig. 5. A comparison between the absorption coefficients of poly-4 methyl pentane (TPX), solid, and sapphire, dashed.

# PHYSICAL PROCESSES AND DEVELOPMENT OPPORTUNITIES IN FAR-INFRARED LASERS

Frank C. De Lucia

*Department of Physics, Duke University, Durham, NC 27706*

## ABSTRACT

The physical processes of both discharge excited and optically pumped far infrared lasers will be discussed. Experimentally this work is based on the use of a tunable millimeter and submillimeter spectrometer as a diagnostic probe of the internal energy transfer mechanism in these lasers. Quantitative numerical models whose parameters describe fundamental energy transfer processes will be discussed. Emphasis will be on results which have the potential to lead to new or improved laser systems.

## INTRODUCTION

Far infrared lasers have played an important role in the development of this spectral region. As a result there have been extensive development efforts aimed at the discovery of new lasers, and the improvement and characterization of existing lasers. This presentation is based upon a number of diagnostic experiments and modeling efforts carried out in our laboratory on both discharge and optically pumped lasers. In these experiments millimeter and submillimeter (mm/submm) radiation from a tunable spectrometer<sup>1-3</sup> was used to probe the active laser media. From the cw and time resolved emission/absorption responses of rotational transitions in a number of vibrational states, it has been possible to deduce in some detail the important excitation and relaxation pathways of these lasers. Numerical models, whose parameters are basic energy transfer rates between thermal pools of states or individual states, have been developed to describe these results. In addition to the detailed description of these lasers, a number of new results have been obtained that provide opportunities for further progress in this field.

## EXPERIMENTAL

The basic method common to all of the diagnostic studies is the use of a modified mm/submm spectrometer to probe both the cw and time resolved spectra of the active laser media. The figure below shows the configuration used for the study of time resolved energy transfer in optically pumped systems. In it a Q-switch was used to produce  $\sim 0.5 \mu\text{s}$  pulses of  $\text{CO}_2$  laser radiation. Alternatively, the laser could be gated on for longer periods, typically 200  $\mu\text{s}$  for the observation of more slowly varying states. The laser power was copropagated with the mm/submm diagnostic probe through a 2 cm diameter, 1.37 m long gain cell. The mm/submm probe radiation was phase locked to a harmonic of a frequency synthesizer. This system was extremely stable and provided absolute power levels constant to a few percent with minimum attention. For studies of discharge systems, the optically pumped gain cell was replaced by a tube characteristic of discharge far lasers,<sup>4,5</sup> which for time resolved studies<sup>6</sup> could be gated on and off by a modulator.

## RESULTS

Extensive experimental and theoretical results have been obtained on both optically pumped and discharge driven far

infrared lasers. In this section, we will describe a few selected examples from work on both types of lasers to illustrate the nature of the results and to provide a basis for discussing possible avenues for further advances.

**Discharge driven systems:** Lide and Maki showed that the HCN discharge laser was dependent on a Coriolis enhanced rotation-vibration transition between the 110 vibrational state (which contains the upper lasing level) and the 040 vibrational state (which contains the lower lasing level). Its inversion is thus primarily a vibrational inversion and the important variables are the chemical concentrations and vibrational state populations. This Coriolis mechanism is very important because it provides a means to have inverted populations between levels whose energy difference are  $\ll kT$  without a highly selective laser pump. Extensive measurements of the chemical compositions and vibrational excitations have been made and it has been established that: (1) The population of the 100 vibrational mode is in equilibrium with the vibrational temperature of the  $\text{N}_2$  in the discharge; (2) The population of the 110 state relative to the 100 state is in thermal equilibrium with the R/T temperature; (3) The population of 040 is very small and approximates being in thermal equilibrium with 000; (4) There is very little CN in the discharge and its lifetime is much shorter than the decay time of the population inversion of the laser levels. Figure 2 shows an example of the experimental basis for the second conclusion above, a comparison of the time dependent decay of the vibrational temperature of CO (which is used as a tracer for  $\text{N}_2$ ) and the temperature of the 100 state of HCN. It can be seen that they are identical.

All of this leads to a simple model, with no adjustable parameters, which quantitatively explains both the extensive data obtained in this work and the results of a substantial body of

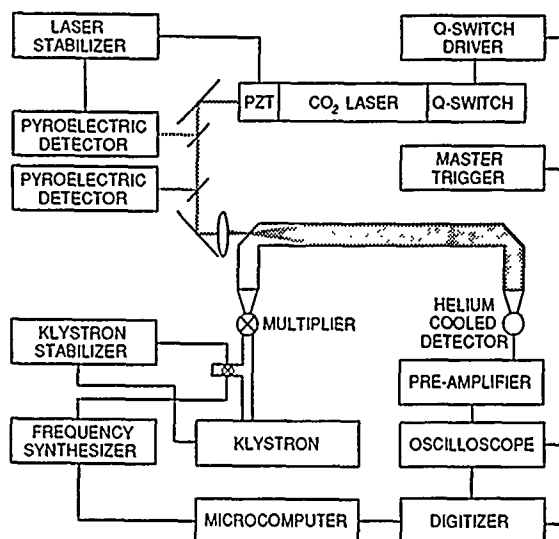


Figure 1. Block diagram of system.

work in the literature. In this model the energy from the discharge is first deposited in the  $N_2$  and comes to reside primarily in the  $v=1$  state. It is then efficiently transferred via near resonant collisions to the 100 state of HCN. The population of 110 (which contains the upper lasing state) is tied thermally to the R/T temperature of the discharge. Thus, a combination of vibrational energy and thermal energy replenish the upper laser state as the lasing transfers population to the rapidly relaxing 040 state.

**Optically pumped systems:** The collisional physics of optically pumped systems is very different because rotational energy transfer, rather than vibrational, is of first order importance. This is because the energy deposition associated with the optical pumping can be specific and fast enough to produce population inversions between rotational states that are connected by electric dipole allowed collisional relaxation pathways. These are typically orders of magnitude faster than the vibrational processes discussed above. As a result, to first order, optically pumped systems are simple to understand. However, it is well known that the processes which return the population to the lower pump level are very important in cw systems and that they are the cause of some of the major limitations of optically pumped far infrared lasers.

These important relaxation mechanisms will be discussed in the context of the  $CH_3F$  laser systems. The first group of these involves processes which move the population away from the lasing levels into the rest of the  $v_3$  rotational manifold. In addition to being of fundamental interest, these rates and selection rules govern the effective partition function of the states that must hold the molecules until they can be vibrationally relaxed. If this pool is large, the absorption that the laser gain must overcome is small. We have found that a very good model of this rotational relaxation in  $CH_3F$  can be based on three distinct relaxation processes: (1) the electric dipole allowed  $\Delta J = \pm 1$  transitions, (2) the  $\Delta K = 3n$  transitions that are allowed by spin statistic selection rules, and (3) a fast vibrational swapping mechanism that transcends the spin selection rule of (2) and rapidly populates the other rotational symmetry species of the  $v_3$  vibrational state. In addition, we have found that true vibrational transfer to nearby vibrational states also increases the effective rotational partition function.

Because all of the above process are orders of magnitude faster than most fundamental vibrational deactivation mechanisms in not only  $CH_3F$  but also in most laser systems, the vibrational deactivation is ordinarily considered as a separate, sequential step. This difference in rates is especially valid at higher pressures where wall deactivation is less important. This leads naturally to the concept of a "vibrational bottleneck," a pressure above which the threshold for oscillation can not be obtained, irrespective of pump power. This cutoff pressure  $P_c$  is given by<sup>8</sup>

$$P_c = \left(\frac{1}{d}\right) \sqrt{\frac{D}{f_2 \Gamma} \left(\frac{kT}{hv}\right)}$$

where  $d$  is the cell diameter,  $D$  the diffusion coefficient,  $\Gamma/2\pi$  the pressure broadening parameter, and  $f_2$  the fraction of the Boltzman population of the rotational pool in the upper laser state. It is ordinarily assumed that none of the terms in this equation have a significant pump power dependence, thus, the "cutoff" concept. However, consider  $f_2$ . In the vibrational bottlenecking limit the population of the vibrational state containing the lasing levels increases as molecules are trapped in the excited state. This corresponds to an increased vibrational temperature. In a real molecule the vibrational rates which redistribute the population among the excited states can be very fast. In this circumstance, the effective value of  $f_2$  decreases because many more states share the molecules. This

reduces the absorption which the laser gain must overcome. Similar considerations lead to the conclusion that the effective value of  $D$  increases with pump power. Both of these effects cause the "cutoff" pressure to increase without bound with increased pump intensity. We have demonstrated the validity of this result by operating a small laser about an order of magnitude above the "cutoff" pressure.<sup>9</sup>

## DISCUSSION

From the point of view of discharge laser development, perhaps the most significant results of our study of the HCN laser are those related to the excitation mechanism. Although it is possible in other systems that the commonly accepted chemical excitation via CN is important, under all conditions that we have investigated the concentrations of CN and its lifetime are both far too small to make significant contributions. Our observations have shown that vibrational energy transfer from  $N_2$  at  $\sim 2100 \text{ cm}^{-1}$  to the 100 state of HCN, followed by thermal excitation to the upper lasing state 110 quantitatively accounts both for observed laser behavior and a wide range of diagnostic data. Since only a few polyatomic molecules that have the requisite Coriolis interaction can survive a discharge environment that would provide chemical driven excitation via species such as CN, the possibility of transferring excitation from the long lived  $v=1$  state of  $N_2$  offers attractive alternatives.

For laser development, the most interesting results of our studies on optically pumped systems are those which relate to the "vibrational bottleneck" in diffusion relaxed systems. It would appear that engineering extensions of the demonstration laser discussed above are especially interesting because they could lead to a class of moderately tunable cw OPFIR lasers. A very simple system has exhibited tunability of  $\sim 100 \text{ MHz}$ , with high spectral purity. Extension to  $\sim 1 \text{ GHz}$  seems reasonably straightforward.

## REFERENCES

- [1] W. C. King and W. Gordy, *Phys. Rev.* **90**, 319 (1953).
- [2] P. Helminger, F. C. De Lucia, and W. Gordy, *Phys. Rev. Lett.* **25**, 1397 (1970).
- [3] P. Helminger, J. K. Messer, and F. C. De Lucia, *Appl. Phys. Lett.* **42**, 309 (1983).
- [4] F. C. De Lucia, *Appl. Phys. Lett.* **31**, 606 (1977).
- [5] D. D. Skatrud and F. C. De Lucia, *Appl. Phys. B* **35**, 179 (1984).
- [6] D. D. Skatrud and F. C. De Lucia, *Appl. Phys. Lett.* **46**, 631 (1985).
- [7] D. R. Lide and A. G. Maki, *Appl. Phys. Lett.* **11**, 62 (1967).
- [8] D. T. Hodges, *Infrared Phys.* **18**, 375 (1978).
- [9] H. O. Everitt, D. D. Skatrud, and F. C. De Lucia, *Appl. Phys. Lett.* **49**, 995 (1986).

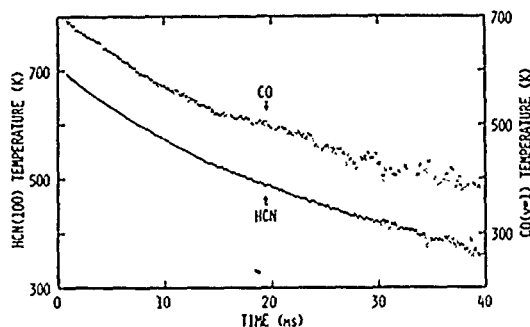


Figure 2. Vibrational temperatures of HCN(100) and CO( $v=1$ ) as a function of time after the end of a 2.5 A current pulse. The vertical scales are off set in order to separate the data points.

OPTICALLY PUMPED MID-INFRARED  $\text{NH}_3$  LASERS

J. Reid\*

Engineering Physics Department, McMaster University,  
Hamilton Ontario, Canada L8S 4M1

## ABSTRACT

An overview of recent experiments carried out at McMaster University on optically pumped  $\text{NH}_3$  lasers will be given. Both pulsed and cw lasers have been investigated, and conversion efficiencies  $\sim 40\%$  have been measured. More than sixty laser transitions have been generated in the 10 to 30  $\mu\text{m}$  region, with cw power as high as 10 W and pulse energies  $>4.5$  J on the strongest lines.

## INTRODUCTION

Optically-pumped  $\text{NH}_3$  lasers have been widely investigated as sources of line-tunable radiation in the 11 to 13  $\mu\text{m}$  region. Initial experiments used pulsed TE  $\text{CO}_2$  lasers as pump sources [1], and efficient operation of these pulsed lasers was soon demonstrated [2]. However, the dynamics of the  $\text{NH}_3$  laser system was not fully understood in this early work. In particular, it was not clear if the  $\text{NH}_3$  laser was a Raman laser or a conventional inversion laser, and the details of line-tunability could not be characterized from device to device.

CW  $\text{NH}_3$  LASERS

In 1980, we undertook a comprehensive study of optically-pumped  $\text{NH}_3$  lasers at McMaster University. It soon became clear that the threshold pump power required to operate these lasers was much lower than expected, and in 1982 we reported the first cw  $\text{NH}_3$  laser operating in the 12  $\mu\text{m}$  region [3]. The behaviour of this cw laser could only be explained if laser action occurred by means of a two-photon Raman transition, and striking confirmation of this mechanism was obtained by probing the gain in an  $\text{NH}_3$  amplifier with a tunable diode laser [4]. Optimisation of the cw Raman laser followed, and more than 10 Watts of output was achieved at 12.08  $\mu\text{m}$ , with a conversion efficiency of 28% [5]. Further work led to a variety of cw  $\text{NH}_3$  Raman lasers with pump offsets as large as 1.35 GHz [6].

While the Raman lasers were efficient sources of radiation in the 12  $\mu\text{m}$  region, they were of limited utility for spectroscopic purposes, as only a single laser wavelength could be obtained for each pump

transition. We therefore examined the case of resonance pumping using a cw  $\text{CO}_2$  laser operating on the 9 R(30) transition, and shifted by 180 MHz in an acoustooptic modulator to bring the pump frequency into exact co-incidence with the  $\text{sr}(5,0)$  transition in  $\text{NH}_3$ . This resonance pumping turned out to be an extremely powerful technique for creating inversion in the entire  $\nu_2$  band of  $\text{NH}_3$ . Dilute mixtures of  $\text{NH}_3$  in a buffer gas were used to ensure thermalisation of the rotational levels in  $\text{NH}_3$ , and once again tunable diode lasers were used to probe the dynamics of the laser system. A simple model of the  $\nu_2$  inversion laser was developed, and this model enabled us to optimise laser operation. Ultimately, more than sixty lasing transitions were observed from 10.3 to 13.8  $\mu\text{m}$  and output powers as high as 5.5 W with conversion efficiencies of 33% were attained on the strongest lines [7]. Lasing was also observed in  $^{15}\text{NH}_3$ , and heterodyne frequency measurements made of several of the transitions [8].

PULSED  $\text{NH}_3$  LASERS

Recently, we have re-visited the pulsed  $\text{NH}_3$  laser. Our improved understanding of the dynamics of the  $\text{NH}_3$  system has enabled us to develop a rate-equation model with no adjustable parameters. This model has been validated by making detailed measurements of the performance of pulsed  $\text{NH}_3$  amplifiers under both small-signal and saturated gain conditions. Good agreement with experiment was obtained over a wide range of amplifier pressures (170-700 Torr), temperatures (200-300 K), mixtures (0.05-0.2%  $\text{NH}_3$ ) and buffer gases (Ar,  $\text{N}_2$  and He). Optically-pumped  $\text{NH}_3$  makes an ideal amplifier in the mid-infrared. We measured small-signal gain co-efficients of  $\sim 20\%/cm$ , and conversion efficiencies of  $>50\%$ .

In the most recent experiments, a 13 J TE  $\text{CO}_2$  laser was used to pump an  $\text{NH}_3$  oscillator. The oscillator could be tuned over more than 70  $\text{NH}_3$  transitions, and 12  $\mu\text{m}$  pulses with energies  $>4.5$  J were observed.

## REFERENCES

- (1) T.Y. Chang and J.D. McGee, "Laser Action at 12.812  $\mu\text{m}$  in Optically Pumped  $\text{NH}_3$ ", Appl. Phys. Lett., 28, 526 (1976).

\*Lumonics Inc., 105 Schneider Road,  
Kanata, Ontario, Canada K2K 1Y3

- (2) P.K. Gupta, A.K. Kar, M.R. Taghizadeh, and R.G. Harrison, "12.8  $\mu\text{m}$   $\text{NH}_3$  Laser Emission with 40-60% Power Conversion and Up to 28% Energy Conversion Efficiency", Appl. Phys. Lett., 39, 32 (1981).
- (3) C. Rolland, B.K. Garside and J. Reid, "A cw Optically Pumped 12  $\mu\text{m}$   $\text{NH}_3$  Laser", Appl. Phys. Lett., 40, 655-657 (1982).
- (4) C. Rolland, J. Reid, B.K. Garside, H.D. Morrison and P.E. Jessop, "Investigation of cw Optically Pumped 12-  $\mu\text{m}$   $\text{NH}_3$  Lasers Using a Tunable Diode Laser", Appl. Opt., 23, 87-93 (1984).
- (5) C. Rolland, J. Reid, B.K. Garside, "10 W cw Optically Pumped 12-  $\mu\text{m}$   $\text{NH}_3$  Laser", Appl. Phys. Lett., 44, 725-727 (1984).
- (6) D.F. Kroeker, J. Reid and B.K. Garside, "Operation of Continuous Wave 12-  $\mu\text{m}$  Raman Lasers in  $\text{NH}_3$  with Pump Offset as Large as 1.35 GHz", Optics Lett., 11, 300 (1986).
- (7) D.F. Kroeker and J. Reid, "Line-Tunable cw Ortho- and Para-  $\text{NH}_3$  Lasers Operating at Wavelengths of 11 to 14  $\mu\text{m}$ ", Appl. Opt., 25, 2929 (1986).
- (8) K.J. Siemsen and J. Reid, "Heterodyne Frequency Measurements of  $^{14}\text{NH}_3$  and  $^{15}\text{NH}_3$   $\nu_2$ -Band Transitions", Opt. Lett., 10, 594-596 (1985).



# SUBMILLIMETER-WAVE LASER PUMPED BY AN EMQ-SWITCHED CO<sub>2</sub> LASER

Hirokazu Shirai, Jongsuck Bae, Takashi Nishida, and Koji Mizuno

Research Institute of Electrical Communication  
Tohoku University, Sendai 980, Japan

## ABSTRACT

Submillimeter wave (SMM) laser with a high peak power ( $> 80$  W) and a high repetition rate ( $> 9$  kHz) has been developed. The laser is pumped by a newly developed current-pulsed, mechanical shutter type Q-switched (EMQ-switched) CO<sub>2</sub> laser.

In this paper, we describe the experimental results obtained from the SMM laser pumped by the EMQ-switched CO<sub>2</sub> laser.

## INTRODUCTION

The inverse Smith-Purcell (ISP) effect [1] which was proposed by us in 1975 is a candidate for laser-driven linear accelerator. A SMM laser is used as a driving source to demonstrate the effect experimentally [2]. The SMM laser for the experiment of the ISP effect has to have the following characteristics [3]; output pulses of 1) a high peak power ( $> 1$  W), 2) a high repetition rate ( $> 500$  Hz), 3) a TEM<sub>00</sub> single mode of operation, and 4) a reproducible clean pulse shape. A conventional Q-switched CO<sub>2</sub> laser [4] as a pump source is insufficient for producing such the SMM pulses. An EMQ-switched CO<sub>2</sub> laser which is Q-switched by a mechanical beam shutter in combination with a pulsed discharge excitation has been newly developed for pumping SMM laser. This CO<sub>2</sub> laser produces a very stable output with a peak power greater than 1 kW at a repetition rate of 1 kHz for all transitions in the P and R branches of the CO<sub>2</sub> spectrum. Using it as a pump for a CH<sub>3</sub>F laser, we have obtained 496  $\mu$ m radiation in 40 W peak, 20 ns pulses at 1 kHz in the lowest loss EH<sub>11</sub> cavity mode.

## EXPERIMENT

Fig. 1 shows a schematic of the experimental setup. The CO<sub>2</sub> laser is a conventional low-pressure ( $\sim 3$  kPa) gas-flow discharge tube laser. Its cavity length is 1.9 m. Two lenses concentrate the laser beam. The shutter wheel is placed at the focus of the beam to make the switching time as small as possible. The shutter has a RF motor usually used in molecular turbo-vacuum-pumps, and the maximum rotation rate is 70,000 rpm. These are contained in a vacuum chamber. The discharge is synchronized to the shutter with a current modulator.

The SMM laser is a dielectric-waveguide laser. The output mirror is a double silicon Fabry-Perot coupler [5] which can vary the reflectivity for a SMM emission line. Peak power of both lasers were determined from the pulse shape and the average power.

Fig. 2 shows the peak power of the pumping CO<sub>2</sub> laser pulse as a function of the shutter velocity for three different gas pressures. It is seen that the peak power saturates at a high shutter velocity of above 400 m/s. The result shows that the shutter velocity is sufficient enough to develop the laser pulse fully. Fig. 3 demonstrates that the saturated output power is maintained even for repetition rate of above 1 kHz. Peak power of greater than 13 kW has been obtained at a repetition rate of 1 kHz. It should be noted that the pulses of 2 kW are obtainable even at repetition rate of 9.2 kHz. Fig. 4 shows a variation of the peak power of the 496  $\mu$ m radiation of the SMM CH<sub>3</sub>F laser versus that of the pump laser. We have obtained a 86 W peak pulse of 496  $\mu$ m in duration of 20 ns at a repetition rate of 90 Hz with a 21 kW peak power pump on the 9P(20) line. The quantum conversion efficiency is 6 %, which is 1.5 times better than the best efficiency previously reported for a CW laser [6].

## ACKNOWLEDGMENT

This work was partially supported by a Grant-in-Aid for Scientific Research from the Ministry of Education, Science and Culture.

## REFERENCES

- [1] K. Mizuno, K. Ono, and O. Shimoe, "Interaction between coherent light waves and free electrons with a reflection grating," *Nature*, vol. 253, pp. 184-185, 1975.
- [2] K. Mizuno, J. Bae, T. Nozokido, and K. Furuya, "Experimental evidence of the inverse Smith-Purcell effect," *Nature*, vol. 328, pp. 45-47, 1987.
- [3] J. Bae, K. Furuya, H. Shirai, T. Nozokido, and K. Mizuno, "The Inverse Smith-Purcell Effect in the Submillimeter Wave Region," *Jpn. J. Appl. Phys.*, vol. 27, pp. 408-412, 1988.
- [4] H. J. A. Bluyssen, A. F. Van Etteger, J. C. Maan, and P. Wyder, "Very Short Far-Infrared Pulses from Optically Pumped CH<sub>3</sub>OH/D, CH<sub>3</sub>F, and HCOOH Lasers Using an EQ-Switched CO<sub>2</sub> Laser as a Pump Source," *IEEE J. Quantum Electron.*, QE-16, pp. 1347-1351, 1980.
- [5] F. Julien and J-M. Lourtioz, "SILICON FABRY-PEROT INTERFEROMETER AS AN OPTICAL FIR COMPONENT: APPLICATION TO VARIABLE

COUPLERS WITH UNIFORM TRANSMISSION OF FIR OPTICALLY PUMPED LASERS," Int. J. of Infrared and Millimeter Waves, vol. 1, No. 2, pp. 175-194, 1980.

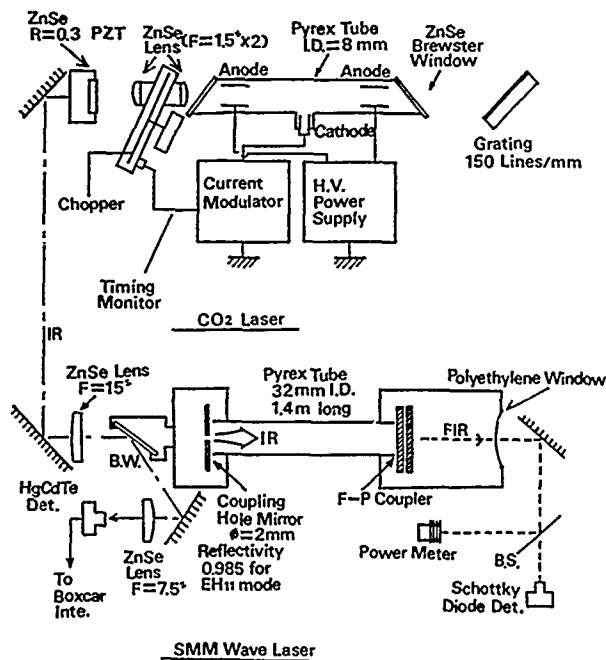


Fig.1 Experimental setup of the SMM waveguide laser pumped by an EMQ-switched CO<sub>2</sub> laser

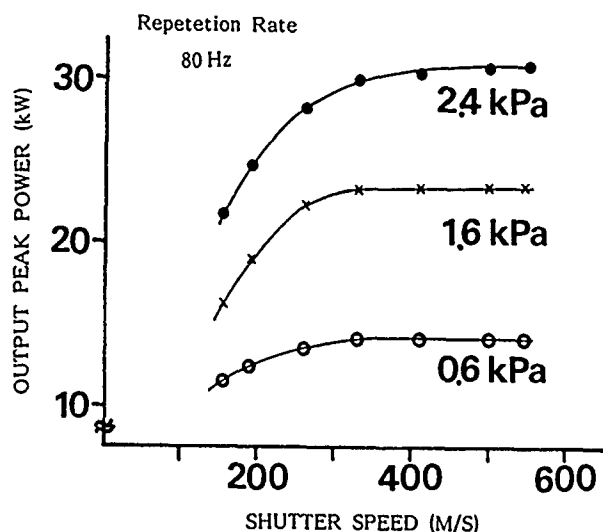


Fig.2 Output peak power of the CO<sub>2</sub> laser for three different gas pressures in 9P(20) branch as a function of a shutter speed of a mechanical shutter.

- [6] D. T. Hodges, F. B. Foote, and R. D. Reel, "Efficient high power operation of the cw far-infrared waveguide laser," Appl. Phys. Lett., vol. 29, pp. 662-664, 1976.

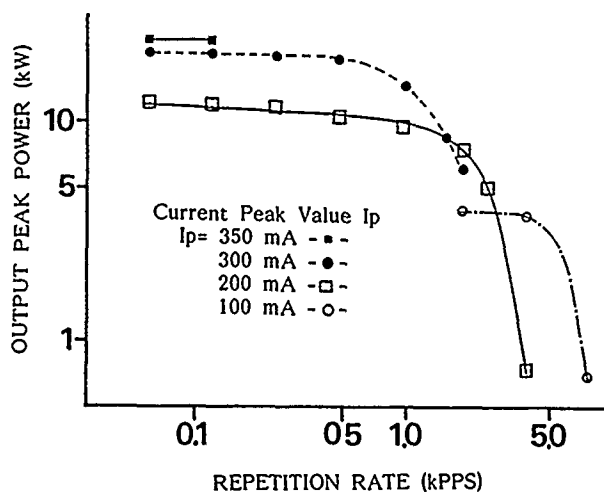


Fig.3 Output Peak power versus repetition rate in the EMQ-switched mode for the 9P(20) transition for various discharge currents. The shutter speed was 454(m/s) and the pressure was 1.7kPa.

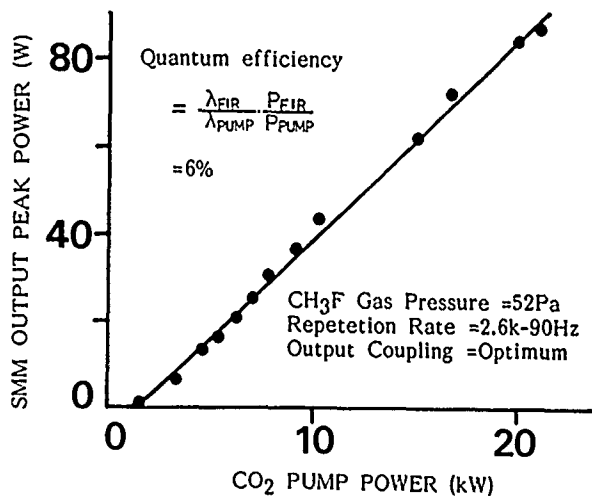


Fig.4 Variation of the output peak power of the CH<sub>3</sub>F SMM laser versus CO<sub>2</sub> pump peak power

# **LINEWIDTH AND POLARIZATION OF AN OPTICALLY-PUMPED GaAs SURFACE EMITTING LASER WITH INTEGRATED BRAGG REFLECTORS**

J.Faist, F.Morier-Genoud, D.Martin, M.A.Dupertuis, J.D.Ganière, F.K.Reinhart

Institut de Micro- et Optoélectronique, Ecole Polytechnique Fédérale de Lausanne,  
PHB Ecublens, CH-1015 Lausanne, Switzerland

**Abstract:** Operation of an infrared (880 nm) optically-pumped room temperature cw surface emitting vertical laser made of a GaAs active layer and Bragg AlAs/(AlAs)<sub>2</sub>(GaAs)<sub>9</sub> reflectors is reviewed. Pump threshold power is 16 mW and the quantum efficiency 7%. Output polarization and linewidth are discussed.

**Introduction:** Surface emitting lasers are attractive candidate sources for optoelectronics since they provide a single mode light beam with reduced divergence which can be easily coupled to fibers and may eventually be produced in high density 2-D arrays. Owing to the absence of surface recombination these lasers can withstand very high powers. Moreover, due to the small active volume, they have potentially low threshold and a low capacitance promising high speed applications. Recently, some electrically pumped structures have been reported [1-2], as well as an optically-pumped structure. In this paper we will recall the main results of the first room temperature cw optically-pumped surface laser [3], and discuss in detail the polarization and linewidth behaviour. This structure has potential applications for wavelength switching and as a bistable optical device.

**Laser design and characterization:** The whole laser structure is grown by molecular beam epitaxy on a (001) oriented GaAs substrate at 680 °C. As shown in the Scanning Electron Microscope (SEM) picture of Fig.1, it consists of a central active layer (1.78 μm thick) sandwiched between two quarter wave Bragg mirrors (2.86 μm thick). The GaAs active layer is lightly n-doped ( $n \sim 4.5 \cdot 10^{16} \text{ cm}^{-3}$ ) and provides gain in the vicinity of the Fabry-Perot resonance. The two quarter wave dielectric Bragg structures are made of 20 alternating pairs of AlAs and (AlAs)<sub>2</sub>(GaAs)<sub>9</sub> superlattice layers with widths of 640 Å and 734 Å respectively. This material is non absorbing at the pump and laser frequencies. The use of superlattices in the Bragg mirrors, instead of Al<sub>x</sub>Ga<sub>1-x</sub>As, allowed us to keep the Al oven temperature constant during the growth which improves greatly the regularity and the quality of the layers.

The reflectance spectrum of the whole structure provides information on the quarter wave Bragg dielectric mirror performance, as well as on the Fabry-Perot resonance inside the structure. The most recent measurement [4] of the reflectance spectrum is shown on Fig.2 and agrees quite well with theoretical design calculations. As expected the mirrors provide a high reflectivity which falls off rapidly outside the 80 nm stopband peaked around 890 nm. The two dips at 880 and 910 nm in the reflectance curve are due to the resonant modes of the Fabry-Perot cavity. Long wavelength thickness fluctuations on the 2" wafer shift the position of the stopband between 730 nm and 900 nm. As a result lasing could occur only on the regions where all the resonance conditions were satisfied.

**Laser operation and power characteristics:** Operation of the laser requires optical pumping at wavelengths shorter than the lasing wavelength. Moreover, in order to maximize the transmission of the pump radiation into the active layer it is advantageous to use one of minimum reflectivity regions of Fig.2 (9% at 837 nm). The beam of a Styril 9M cw dye laser has been focused on a 20 (μm)<sup>2</sup> area with a microscope objective. The lowest threshold power, 16 mW has been obtained at 880 nm. However these values depend very sensitively again on the position on the wafer because of short wavelength thickness fluctuations (100 Å over 0.5 μm). As the structure does not involve any kind of lateral confinement the surface laser mode is laterally gain-guided and its width is limited by the ambipolar diffusion of the carriers. The carrier peak density has been estimated to be  $3 \cdot 10^{18} \text{ cm}^{-3}$ . From the reflectivity measurements and the active layer thickness the gain is estimated to be  $\leq 200 \text{ cm}^{-1}$ . The laser linear characteristic curve was always observed: the differential quantum efficiency for both facets ( $\alpha$  slope) varied from 1 to 7%. This low value must be attributed to the lack of lateral carrier confinement and possibly to scattering of light by mirror imperfections.

**Laser linewidth:** The laser emission spectrum was measured with a high resolution (0.20 Å) THR 1000 Jobin-Yvon spectrometer. As shown on Fig.3 the laser linewidth decreased as a function of laser power until a seemingly constant value (1.8 Å) but still varying as a function of the position on the wafer. We analysed this value with the help of the Henry formula [5] for quantum limited noise in semiconductor lasers: at a power of 0.1 mW one finds a linewidth of 0.15 Å. This value, which is well below our measured value at this power (2.5 Å), as well as its power dependence, indicates that one must search for other limiting factors. Pump fluctuations and occupation fluctuation noise [6] can be excluded since the well stabilized pump spectrum stays narrow (0.75 Å) and because this ultimate linewidth depends on the position of the lasing spot on the wafer. Possible explanations include carrier diffusion effects [7], or the formation of an unstable resonator (resulting

from transverse refractive index variations or from mirror imperfections) which is a well-known factor introducing a broadening of the quantum fluctuations [8]. Further studies are needed to fully elucidate the origin of the linewidth.

**Laser polarization:** The laser polarization has been measured with the help of a simple polarizer (Glan Thompson) inserted in front of the spectrometer. We searched for coherent effects [9] inside the active medium by rotating the linear pump polarization, but it was difficult to change the angle of polarization without introducing a slight shift of the pumping laser spot on the sample. Due to the layer roughness, significant on a scale of 0.1  $\mu\text{m}$ , the laser characteristics may have changed slightly between two measurements. However we have always observed that the laser polarization aligned itself along the crystallographic axes of the crystal, (110) or (1-10), instead of the pump polarization axis. This result agrees with the findings obtained on electrically-pumped surface lasers [10]. The selection of polarization is due to small anisotropies creating different cavity losses in the two crystallographic directions, which could arise intrinsically like slightly different matrix elements or extrinsically like oriented defects or the formation of a slight wedge. The polarization ratio always increased with the pump power, the maximum ratio observed was 3:1.

**Conclusions:** The detailed operation characteristics of the optically-pumped GaAs surface emitting laser with integrated Bragg reflectors have been reviewed. Single mode output has been satisfactorily obtained cw at room temperature. The linewidth and polarization measurements both confirmed the necessity to improve the interface quality and to have a better control over layer thickness fluctuations.

- [1] S.Kinoshita, K.Iga, IEEE J.Quant. Electron. QE-23, pp.882-888 (1987)
- [2] P.Gourley, T.J.Drummond, Appl. Phys. Lett. 50, p.1225 (1987)
- [3] J.Faist, F.Morier-Genoud, D.Martin, J.D.Ganière, F.K.Reinhart, Electron. Lett. 24, p.629 (1988)
- [4] J.Faist, J.D.Ganière, P.Buffat, S.Sampson, F.K.Reinhart, "Characterization of GaAs/(GaAs)<sub>n</sub>(AlAs)<sub>m</sub> photopumped surface-emitting lasers through reflectivity, laser linewidth and high resolution electron microscopy measurements", to be published.
- [5] C.H.Henry, IEEE J. Lightwave Techn. LT-4(3), pp.298-311 (1986)
- [6] K.Vahala, A.Yariv, Appl. Phys. Lett. 43(2), pp.140-142 (1983)
- [7] P.Brosson, B.Fernier, D.Leclerc, J.Benoit, IEEE J. Quant. Electron. QE-21, p.700 (1985)
- [8] A.E.Siegman, "Excess spontaneous emission in unstable resonator lasers", Technical digest of the International Quantum Electronics Conference IQEC'86, Invited paper WCC3, p.106, June 9-13, 1986, San Francisco, California, USA
- [9] Z.Drozdzowicz, R.J.Temkin, B.Lax, IEEE J. Quant. Electron. QE-15(3), pp.170-178 (1979)
- [10] Z.Drozdzowicz, R.J.Temkin, B.Lax, IEEE J. Quant. Electron. QE-15, pp.865-869 (1979)
- [10] M.Shimizu, F.Koyama, K.Iga, "Polarization characteristics of MOCVD grown GaAs/GaAlAs CBH surface emitting lasers", Paper WA3-1, Proceedings of Integrated and Guided Wave Optics, Santa Clara, Barbara, California USA, 1988

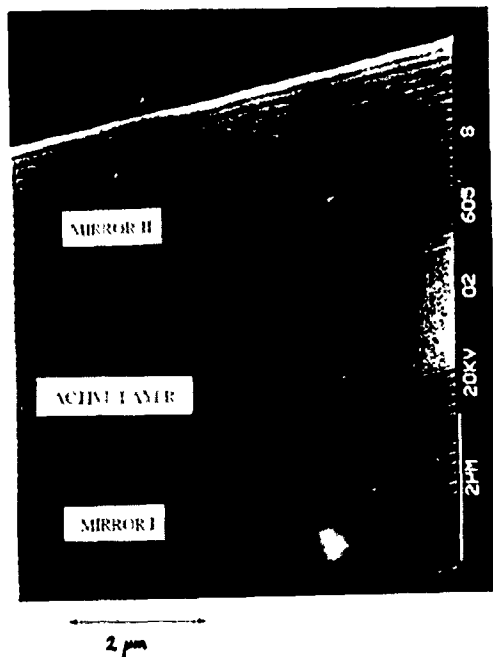


Fig.1

Fig.2:

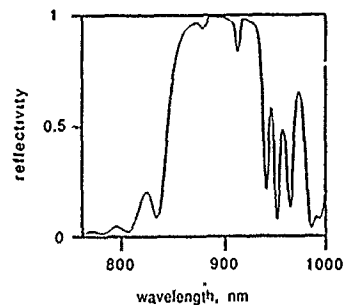
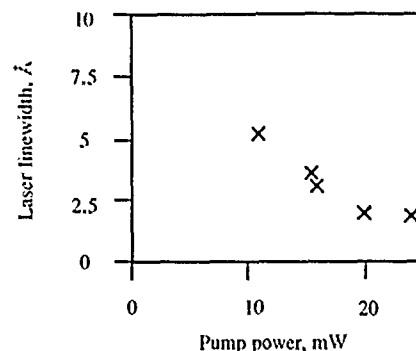


Fig.3:



# Millimeter Wave CARM Amplifier Experiment

B.G. Danly, K.D. Pendergast, and R.J. Temkin

Plasma Fusion Center,  
Massachusetts Institute of Technology, Cambridge, MA 02139

## ABSTRACT

A high power, 140 GHz, cyclotron autoresonance maser (or CARM) amplifier is under development at the Plasma Fusion Center at M.I.T. Theory, simulations, and the experimental design are discussed. The experiment will employ a high voltage (450 – 700 kV) Pierce-type beam and a helical wiggler to produce the required electron beam. The initial experiment will be carried out using a 450 kV electron gun; the second phase of the experimental program will employ a 700 kV electron gun. First experimental operation is anticipated shortly. The details of the experimental design and theoretical analysis will be presented.

## 1. INTRODUCTION

The cyclotron autoresonance maser has received considerable attention in the past several years as a promising alternative to the free-electron laser and the gyrotron for the generation of high power radiation in the millimeter and sub-millimeter wave region of the electromagnetic spectrum. In particular, the CARM may prove to be a promising millimeter wave source for ECRH of fusion plasmas in the 280 – 560 GHz frequency range, or as a high peak power 17 – 35 GHz driver for the next generation electron linear colliders. Considerable progress in the theory [1,2] and simulation [3,4] of the CARM in both oscillator and amplifier configurations has been achieved. In spite of the considerable amount of theoretical work on the CARM, few experimental devices have been built. Two oscillator experiments have been reported [5,6], and a 35 GHz superradiant CARM has also been reported [7] (see also Bekefi, *et al.*, this digest).

Currently, a 140 GHz CARM amplifier experiment is under development at the Massachusetts Institute of Technology (MIT). It will employ a high voltage Pierce gun and will include a helical wiggler region that will produce the required perpendicular velocity on the electron beam. The CARM will be designed to operate in either the TE<sub>11</sub> or the TE<sub>12</sub> mode, as will be discussed later.

## 2. THEORY

Our theoretical investigation of CARM amplifiers contains several parts. Separate one- and two-dimensional, slow-time-scale codes for modeling the CARM amplifier convective instability are employed for the basic design of the M.I.T. CARM amplifier experiment. A Bers-Briggs type pinch point analysis of the CARM dispersion relation has yielded stability criteria for the design of the CARM amplifier [8].

The CARM interaction occurs when electrons undergoing cyclotron motion in an axial magnetic field ( $\mathbf{B} = B\hat{z}$ ) interact with an electromagnetic wave ( $\omega, \mathbf{k}$ ) with wavevector nearly parallel to the axial field  $\mathbf{B}$ . The resonance condition is then  $\omega - \mathbf{k} \cdot \mathbf{v} = s\Omega_c$ , where  $s$  is the harmonic number and  $\Omega_c$  is the relativistic cyclotron frequency defined by  $\Omega_c \equiv \Omega_{c0}/\gamma \equiv eB/\gamma mc$ . The well-known resonance condition for the CARM is thus

$$\omega = \frac{s\Omega_{c0}}{\gamma(1 - \beta_{\parallel}/\beta_{ph})},$$

where  $\gamma$  and  $\beta_{\parallel}$  are the electron energy and velocity in the  $\hat{z}$  direction. The wave phase velocity is given by  $\beta_{ph} \equiv v_{ph}/c \equiv k/k_{\parallel}$ . As is apparent from the resonance condition, the CARM is capable of operation at a large Doppler upshift from the cyclotron frequency (in contrast to the gyrotron). For  $\gamma_0^2 \gg 1$ ,  $\beta_{\perp 0} \approx 1/\gamma_0$ ,  $\beta_{ph} \approx 1$ , and  $\beta_{\parallel 0} \approx 1$ , there is a  $\gamma_0^2$  frequency upshift from the relativistic cyclotron frequency. For this reason, the CARM is also referred to as a Doppler-shifted cyclotron resonance maser. In this paper we consider only CARM operation at the fundamental of the cyclotron frequency ( $s = 1$ ).

Using a two-dimensional code discussed elsewhere [9], detailed simulations of a 140 GHz CARM amplifier have been carried out. The baseline design parameters for the 450 kV M.I.T. CARM experiment are outlined in Table 1. Simulation results for the parameters in Table 1 are presented in Fig. 1 for three different current values. The efficiency ( $\eta$ ) is plotted as a function of the standard deviation in  $p_{\parallel}$ . The energy spread has been taken to be effectively zero, and thus  $\sigma_{p_{\parallel}} \approx \sigma_{p_{\parallel}}/\gamma$ . The well known sensitivity of the CARM to velocity spread is apparent. Nevertheless, for  $\sigma_{p_{\parallel}}/\beta_{\parallel} \lesssim 2\%$ , the efficiency remains reasonable for a high power amplifier.

Table 1  
450 kV CARM Amplifier  
Baseline Design

Parameter	Design Value
$\gamma$	1.88
$\beta_{\perp}/\beta_{\parallel}$	0.3 – 0.5
$I$	10 – 50 A
$\nu$	140 GHz
$P_{INPUT}$	50 W / 10 kW
Mode	TE <sub>11</sub>
$\beta_{ph}$	1.02 – 1.06

A 700 kV CARM amplifier experiment is also planned, with design parameters similar to the 450 kV design. Efficiency and sensitivity to velocity spread are comparable to the 450 kV case, but higher voltage operation is more stable for equivalent beam power. For a 700 kV beam, the nonlinear 3 dB bandwidth is approximately 10%.

Analysis of absolute instabilities in the CARM amplifier have been carried out using a Bers-Briggs pinch-point analysis [8]. This analysis has yielded conditions for amplifier stability in infinite systems in the absence of reflections. A second treatment of the stability of the CARM amplifier is by numerical calculation of the starting current for a backward-wave oscillator solution on the same beam. Such an analysis can incorporate finite length and wave mismatch effects. Results will be presented.

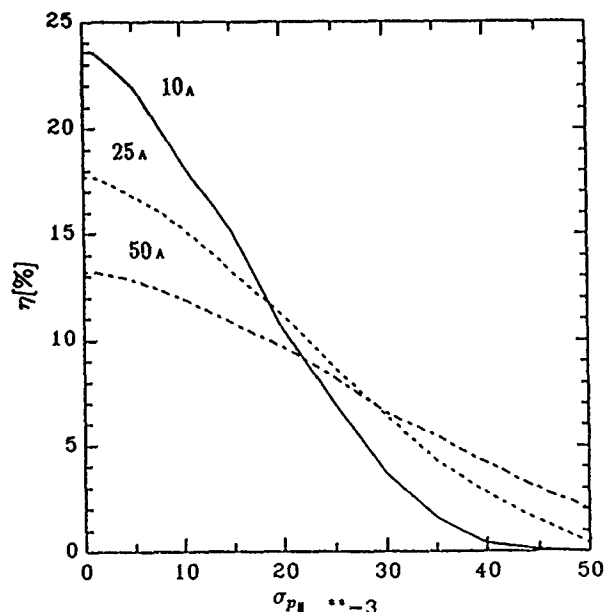


Fig. 1 CARM amplifier efficiency ( $\eta$ ) versus  $\sigma_{p||}$  for a 450 kV beam with currents of 10, 25, and 50 A,  $\beta_{ph} = 1.04$ , and  $\beta_{\perp}/\beta_{||} = 0.5$ .

### 3. EXPERIMENTAL DESIGN

The two-dimensional model [9] and the stability analysis presented in reference [8] are being used to design the 140 GHz CARM amplifier experiment planned at MIT, a schematic of which is shown in Fig. 2. Operation in both the  $TE_{11}$  and  $TE_{12}$  modes is being considered at present, although it appears that operation in the  $TE_{11}$  mode will be less problematic. Although the  $TE_{12}$  mode yields no  $TE_{12}$  absolute instability for the parameters under consideration, the beam is unstable in the  $TE_{11}$  mode. If this absolute instability cannot be suppressed, then operation in the  $TE_{11}$  mode is the only alternative. The first experiments planned will operate in the  $TE_{11}$ .

The electron beam will be formed by a combination of a Pierce gun and a helical wiggler. Such guns are known colloquially as helix (H-) guns or Pierce-Wiggler guns. The first experiments will be carried out using a 5045 SLAC klystron gun and a dc bifilar helical wiggler for production of the beam. The principle advantages of this type of helical beam formation compared with MIG type electron guns are its low cost, interchangeability, and variable  $\beta_{\perp}/\beta_{||}$  capability. The 450 kV experiment will utilize a wiggler of 7 cm periodicity and an axial guide field of 2.5 kG to produce the required  $\beta_{\perp}$  on the beam.

A superconducting magnet with two independently variable magnetic field regions is being constructed for the CARM experiment. The first magnetic field region will be variable from 2 - 6 kG, and will contain the helical wiggler for production of  $\beta_{\perp}$  on the electron beam. The beam will then be compressed into the high-field (2 - 6 T) region, where the CARM amplifier interaction circuit will be located. The lengths of the two field regions in the magnet are 50 cm and 60 cm, respectively. The magnet will have the capability of magnetic field tapering in the interaction region for the purpose of efficiency enhancement [3].

Two different drivers are available for the amplifier experiments: a Varian 140 GHz extended interaction oscillator, which is capable of delivering 300 W at its output, and a 140 GHz gyrotron, capable of delivering 10 kW. Both quasioptical launchers and hole-coupled launchers are under consideration.

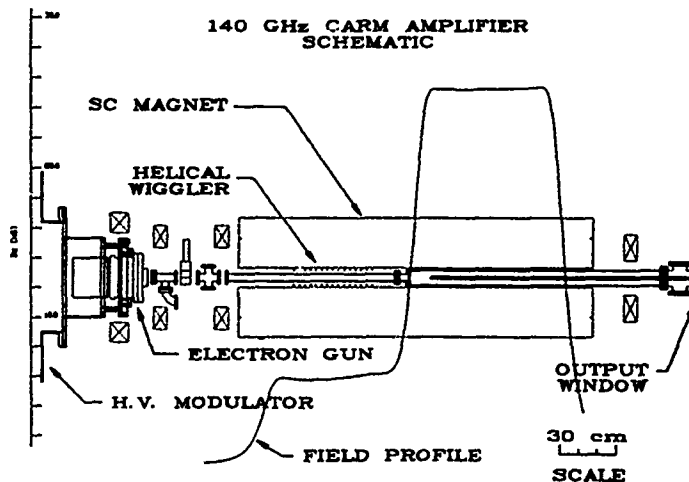


Fig. 2 Schematic of CARM amplifier experiment.

### 4. CONCLUSIONS

A 140 GHz CARM amplifier experiment is presently under design at M.I.T., and first results are expected in early 1989. Theoretical analysis of CARM amplifiers indicate that they are attractive sources for high power millimeter wave applications.

### 5. ACKNOWLEDGEMENT

This work is supported by the Innovative Science and Technology Office of the Strategic Defense Initiative Organization and managed by the Harry Diamond Laboratories.

### 6. REFERENCES

- [1] A.W. Fliflet, *Int. J. Electron.*, **61**, 1049-1080 (1986).
- [2] V.L. Bratman, N.S. Ginzburg, G.S. Nusinovich, M.I. Petelin, and P.S. Strelkov, *Int. J. Electron.*, **51**, 541-567 (1981).
- [3] K.D. Pendergast, B.G. Danly, R.J. Temkin, and J.S. Wurtele, *IEEE Trans. Plasma Sci.*, **PS-16**, 122 (1988).
- [4] A.T. Lin, *Int. J. Electron.*, **57**, pp. 1097-1108 (1984).
- [5] I.E. Botvinnik, V.L. Bratman, A.B. Volkov, N.S. Ginzburg, G.G. Denisov, B.D. Kol'chugin, M.M. Ofitserov, and M.I. Petelin, *Pis'ma Zh. Eksp. Teor. Fiz.*, **35**, 418-420, (1982).
- [6] I.E. Botvinnik, V.L. Bratman, A.B. Volkov, G.G. Denisov, B.D. Kol'chugin, and M.M. Ofitserov, *Pis'ma Zh. Eksp. Teor. Fiz.*, **8**, 1376-1378, (1982).
- [7] G. Bekefi, A. Dirienzo, C. Liebovitch, and B.G. Danly, *Proc. 10<sup>th</sup> International Conference on Free-Electron Lasers*, Jerusalem, Israel, 1988.
- [8] J.A. Davies, Submitted for Publication.
- [9] B.G. Danly, K.D. Pendergast, R.J. Temkin, and J.A. Davies, *Proc. S.P.I.E.*, **873**, 143-147 (1988).

## The NRL 100 GHz Cold-Cathode CARM\*

R. B. McCowan<sup>†</sup>, C. A. Sullivan<sup>†</sup>, D. A. Kirkpatrick<sup>†</sup>, S. H. Gold, W. M. Manheimer,  
A. W. Fliflet, W. M. Black<sup>x</sup>, A. K. Kinkead, and M. Sucky<sup>s</sup>

High Power Electromagnetic Radiation Branch  
Plasma Physics Division, Naval Research Laboratory  
Washington, DC 20375-5000

### ABSTRACT

The design of a 10-20 MW, 40 nsec cyclotron auto-resonance maser experiment is presented. The basic components of the CARM are a novel 600 kV, 200 A. field emission gun and a "whispering gallery" mode rippled wall cavity.

### INTRODUCTION

High power millimeter waves have many important applications. For example, millimeter wave radar systems have higher gain and target resolution than will lower frequency radars for a given antenna aperture. Electron cyclotron heating of fusion plasmas will require high frequency radiation when strong magnetic fields are used to confine the plasma<sup>1</sup>.

The cyclotron auto-resonance maser (CARM) is a promising source of high power radiation in the 100 GHz to 500 GHz frequency range that may impact the requirements of advanced systems for applications such as those mentioned above. The requirements for guide field strength and electron energy in a CARM may be advantageous when compared with competing devices. Compared with a gyrotron, the required magnetic field strength requirement is substantially reduced. For example, a planned experiment at the Naval Research Laboratory will produce powers in excess of 10 MW at 100 GHz with a magnetic field of only 25 kG, while a fundamental harmonic gyrotron operating at 100 GHz with a 600 kV beam requires a magnetic field of over 70 kG. Compared with a Free-Electron-Laser (FEL), only moderate voltages are required for the CARM at millimeter and submillimeter wavelengths; the NRL experiment will use a 600 kV, 200 A. electron beam. Finally, the CARM is efficient; computer simulations indicate that the device will operate at efficiencies greater than 20%.

The CARM oscillator, like the gyrotron oscillator, is a cyclotron maser. In contrast to the gyrotron, which requires an electron beam with a high pitch angle, the CARM has an electron beam with a moderate pitch angle and a substantial amount of axial momentum. The CARM benefits from the doppler upshift provided by the axial velocity of the beam; the operating frequency of the CARM is approximately  $\gamma f_c$ , where  $f_c$  is the nonrelativistic cyclotron frequency associated with the axial magnetic field, and  $\gamma$  is the usual relativistic factor.

Currently, a 100 GHz CARM oscillator is under development at the Naval Research Laboratory (NRL). The 600 kilovolt, 200 ampere beam is provided by a Marx bank-Blumlein configuration (the TRITON machine). The magnetic field is provided by a pulsed solenoid and can be varied up to a field strength of 30 kilogauss. The predicted power of the CARM is 20 megawatts, with an operating efficiency of 25% in the TE<sub>61</sub> mode.

The chief components of a CARM, besides a strong magnet, are the electron gun and the microwave cavity. The nature of the CARM interaction results in much more stringent requirements on both of these components than there are for the gyrotron; the beam for the CARM must meet roughly the same requirements as must the beam for a Free Electron Laser (FEL)<sup>2</sup>.

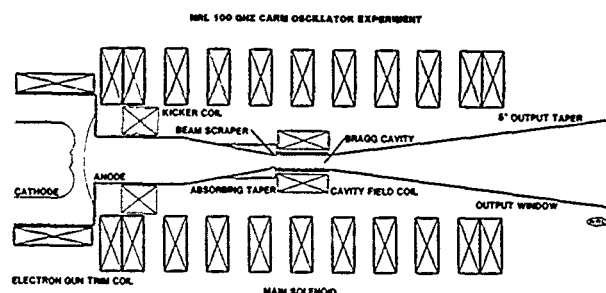


Figure 1. Schematic of the CARM oscillator experiment

### THE CARM ELECTRON GUN

In order that the efficiency of the CARM be high, the electron beam must have a small velocity spread. For the current experiment the spread in axial velocity of the electron beam must be less than 3%. To interact effectively with the whispering gallery modes, the beam must be concentrated near the walls of the cavity. The ratio of beam transverse momentum to beam axial momentum is 0.6

The electron gun designed to match these criteria has been designed. In order to match the power supply for the experiment a field emission diode is used. The rough electrode shapes were determined using an electrode synthesis code developed by Finn, Fliflet, and Manheimer<sup>3</sup>. These shapes were then entered into the SLAC electron trajectory code<sup>4</sup>, a ray tracing code commonly used in the design of electron guns. The cathode-anode shape provides a nearly cold electron beam with an axial velocity spread that can be controlled by small changes in the anode shape.

A magnetic 'dip' is used to provide the required beam transverse momentum<sup>5</sup>. The spatial variation of the magnetic field is fast enough to be nonadiabatic; therefore the beam picks up transverse momentum as it traverses the 'dip'. The reduction of the field is approximately 50% and occurs with a scale length of 1.5 cm. This dip, coupled with magnetic compression, produces an electron beam strength of the 'dip', and a velocity spread of less than 2%.

An absolutely-calibrated Rogowski coil is used to measure the total beam current. In addition, we use a witness plate to provide beam location and to detect density variations on the beam. This witness plate aids in the alignment of the magnetic fields. Another beam diagnostic is a current probe that can measure the current in selected spatial areas of the beam. We have designed a diagnostic which will allow only a small portion of the beam to propagate through to a witness plate. By measuring the spot size on the witness plate as a function of distance from the mask, we will be able to determine the energy ratio.

### THE CARM CAVITY

Because the CARM is a device that depends on a convective instability, the oscillator operation must take place in a cavity that provides feedback of the radiation onto the electron beam. For typical CARM operation, the resonator reflectors must provide high reflectivity for modes that are far from cutoff. Furthermore, mode selectivity is desirable, preferably with discrimination between modes differing in either transverse or axial structure. In addition, modes that are near cutoff must be suppressed in order to minimize competition from the gyrotron interaction. Finally, the CARM cavity must allow unrestricted passage of an electron beam parallel to the axis.

A suitable realization of CARM resonator reflectors may be achieved by using a small periodic corrugation of the waveguide surface. Each ripple provides a small reflection of wave amplitude. If the corrugation period is such that the radiation reflected from each of the corrugations adds in phase, the corrugated section can be highly reflective and is known as a Bragg reflector.

For the NRL CARM, a  $TE_{61}$  Bragg cavity was designed<sup>6</sup>. The cavity is 12 cm. long, 1.6 cm. in diameter, with ripple depths of approximately 0.15 mm. The upstream ripple is longer than the downstream ripple; this restricts the energy losses to the proper direction. The cavity is constructed using precision electroforming techniques, in order that the necessary tolerances can be met.

The important microwave radiation parameters are the frequency, the power, and the operating mode. The frequency of operation is expected to be 100 GHz, the mode is predicted to be the  $TE_{61}$ , and the power in excess of 10 MW.

Preliminary mode determination efforts will be primarily the measurement of radiation mode patterns in a gas breakdown cell. Breakdown techniques have been successfully by Gold et al. at NRL.<sup>5</sup> When viewed looking back into the output waveguide, the breakdown light pattern photographed reveals the transverse mode structure of the radiation, and hence the mode. When viewed transverse to the output waveguide, the standing wave pattern provides an estimate of the wavelength of the radiation, and hence

the frequency. A more precise measure of the oscillating frequency will be obtained with a grating spectrometer and with waveguide filters.

The duration of the pulse and the power of the radiation will be determined by using a calibrated crystal detector along with a series of calibrated attenuators and couplers. Detector output is recorded on a high speed digital oscilloscope.

### CONCLUSIONS

A 10-20 MW, 40 nsec CARM has been designed at NRL. The design consists of a novel electron gun and electron beam diagnostics, a  $TE_{61}$  Bragg resonator, and various microwave diagnostics. The electron gun is undergoing testing.

### REFERENCES

- 1) Granatstein, V. L., 1987, *Proc. of the 1987 Particle Accelerator Conf.*, Washington, D. C., To Be Published.
  - 2) Sprangle, P., Smith, R. A., and Granatstein, V. L., 1979, in *Infrared and Millimeter waves*, (K. Button, ed.) Vol 1. Academic Press, New York.
  - 3) Finn, J. M., Fliflet, A. W., and Manheimer, W. M., 1986, *NRL Memorandum Report 5727*, Naval Research Laboratory, Washington, D.C.
  - 4) Herrmannsfeldt, W. B., 1979, *SLAC Report SLAC-226, UC-28 (A)*. Stanford University, Stanford, CA.
  - 5) Gold, S. H., Fliflet, A. W., Manheimer, W. M., McCowan, R. B., Black, W. M., Lee, R. C., Granatstein, V. L., Kinkead, A. K., Hardesty, D. L., and Sucy, M., 1987, *Phys. Fluids* 30(7), p 2226.
  - 6) McCowan, R. B., Fliflet, A. W., Gold, S. H., Granatstein, V. L., Wang, M. C., *International Journal of Electronics*, To be published., 1988
- 
- † Science Applications International Corporation, McLean, VA 22102.
- ¥ Also Dept. of Electrical and Computer Engineering, George Mason University, Fairfax, VA 22030
- § JAYCOR, Inc. Vienna, VA 22180
- \* Work supported by the Office of Naval Research



# CARM EC Heating Source for High Field Tokamaks

Q.S.Wang, A.T.Lin, N.C.Luhmann, Jr. and D.B.McDermott  
University of California, Los Angeles, CA 90024

K.R.Chu  
National Tsing Hua University, Hsinchu, Taiwan, ROC

## ABSTRACT

Theory and experimental design of a 2 MW, 560 GHz CARM as well as a 1 MW, 90-140 GHz, 400 kV proof of principle experiment will be presented.

## INTRODUCTION

ECRH has proven to be a successful method to heat magnetically confined fusion plasmas. Second harmonic EC heating in the future 100 kG CIT tokamak will require a multi-MW cw source at 560 GHz. The gyrotron is not appropriate here due to the requisite high magnetic fields and extreme wall loading. This naturally leads to the interest in the cyclotron autoresonance maser (CARM).

A CARM amplifier is similar to a gyro-TWT but operated far above cutoff, making high power operation possible, since the attenuation is low. For  $\beta_{ph} = \omega/ck_z = 1$ , gyrating electrons remain in synchronism with the wave even as they lose energy, allowing complete energy transfer to the wave and resulting in the potential for high efficiency, which is proportional to  $(1-\beta_{ph}^2)^{-1}$ . The large axial velocity also allows a large Doppler upshift of the output frequency, permitting the requisite magnetic field to be considerably reduced.

## THEORY

Figure 1 shows the intersections of the cyclotron resonance line with the waveguide mode for three situations, a relativistic gyro-TWT, a stable CARM and an unstable CARM. The particle wave interaction is strongest in a gyro-TWT, because the resonance line is tangent to the electromagnetic mode, and thus the axial velocity of the beam is equal to the group velocity of the wave. As the magnetic field is increased above  $B_g$ , which gives this grazing condition, the device is stable until it reaches some highest magnetic field,  $B_{osc}$ , beyond which oscillation due to an absolute instability occurs. Figure 2 shows a 50% range of stable magnetic field exists for a beam of  $\alpha = 0.5$  interacting with the  $TE_{11}$  mode of cylindrical waveguide. In the stable range, the upper intersection excites a wave with a larger  $\beta_{ph}$  than for the grazing condition and thus higher efficiency can be expected.

The available range of frequency upshift over the cutoff,  $\omega_c$ , for the stable operating region of Fig. 2 appears in Fig. 3. The upshift for the gyro-TWT case,  $B = B_g$ , is  $\omega/\omega_c = \gamma_r$ . The maximum stable upshift is approximately four.

Figure 4 plots the linear gain in one free space cutoff wavelength ( $\lambda = 2\pi c/\omega_c$ ) as a function of the beam current. As expected, the gyro-TWT's grazing intersection yields a stronger interaction than the CARM near the oscillation threshold. However, the growth rate of the gyro-TWT is roughly only 25 % larger, while the efficiency of the CARM is enhanced by more than 50 % from that of the gyro-TWT, as can be seen from Fig. 5.

## EXPERIMENTAL DESIGN

The design of the 2 MW, 560 GHz  $TE_{01}$  CARM has been previously presented <sup>(1)</sup>. Although the waveguide's lowest order mode,  $TE_{11}$ , unfortunately is not appropriate for high power generation, the  $TE_{01}$  mode yields an acceptable level of dissipation.

At 3 MW, the wall loading is 2.5 kW/cm<sup>2</sup>. One may suppress the lower order modes by using a helical waveguide, a washer-stack waveguide, etc. As in any high  $k_z$  traveling wave interaction, the CARM requires a high quality electron beam for efficient wave generation. The axial velocity spread should be less than 2 %<sup>(2)</sup>. A magnetron injection gun will serve as the beam source. The numerical design of the gun using an electron gun code is currently underway with the proposed parameters listed in Table 1.

Studies have shown that an alternate choice is also possible. The almost perfectly linearly polarized  $HE_{11}$  hybrid mode can propagate in a circumferentially corrugated guide of quarter-wavelength corrugation depth with an attenuation substantially lower than that of any other mode, even lower than that of the  $TE_{01}$  mode in smooth-walled circular waveguide of comparable size. The low attenuation of the  $HE_{11}$  mode is clearly exhibited in Fig. 6 for the case of  $ka = 13.55$  and  $a/b = 0.894$  which yields a quarter-wavelength corrugation depth at frequency 560 GHz. In addition to the low dissipation, the  $HE_{11}$  mode can efficiently couple power into a Gaussian beam for launching the wave into the plasma due to the fact that the field distribution of the  $HE_{11}$  mode is very close to that of an ideal  $TEM_{00}$  mode. The dispersion of the corrugated waveguide is shown in Fig. 7. Techniques of discriminatively suppressing the lower order modes must be developed to minimize the effects of absolute instabilities from the lower order modes. The electron gun geometry most appropriate for this mode is a combination of a Pierce gun and a gyro-resonant undulator.

## PROOF OF PRINCIPLE EXPERIMENT

In order to separate the physics issues from the engineering issues, we have scaled the experiment to a lower frequency and voltage and propose a proof of principle CARM as described in Table 2.

The operating waveguide mode is the lowest order mode, the  $TE_{11}$ , with a cutoff frequency of 60 GHz. The grazing condition for the gyro-TWT occurs at a frequency of 90 GHz and  $B_g = 25.7$  kG. At 30 kG the CARM will amplify 140 GHz. A specially designed coupler <sup>(3)</sup> will be used to couple rf power into the tube.

Since the electric fields of the  $TE_{11}$  mode peak on axis, a pencil beam will be launched by a 400 kV Pierce gun from the SLAC 5045 high power klystron, with an axial velocity spread of less than 1%, and passing through a gyro-resonant undulator with an undulator period,  $l$ , such that the axial velocity,  $v_z = l\Omega_c / 2\pi$ . At 400 kV, the gun emits 500 A, but only the inner 2 % of the beam will be used.

The electron beam from the 8.9 cm diameter cathode will be squeezed to a 2.4 cm diameter at the gun exit with a magnetic compression 30 over this region. The undulator should be positioned in the weakest magnetic field possible to minimize the velocity spread caused by the inhomogeneity of the pump field. A further 10-20 fold compression occurs before the beam enters the CARM interaction tube. Efficiency enhancement <sup>(4)</sup> will be attempted with a 13 % taper gradient coil.

For this proof of principle experiment we have built a 45 kV modulator, obtained a 800 kV 20:1/40:1 dual purpose step-up transformer, a 65 kG, 0.4 m long ( $\pm 0.1\%$ ) and a 6 kG, 0.5 m long ( $\pm 0.1\%$ ) superconducting solenoid. Our mm-wave center's 94 GHz and 140 GHz 25 W cw EIOs are to be used as the signal input.

## CONCLUSION

The stability, reduced magnetic field requirement, high efficiency and wall loading of the CARM have been discussed. The major development tasks have been identified. Also, the design of a proof principle experiment to test the fundamental properties of the CARM has been presented.

## ACKNOWLEDGEMENTS

This work was supported by AFOSR under Grant No. 86-0199, NRL under Contract No. N00014-87-K-2032 and ATRI under Contract No. F30602-87-C-0201.

## REFERENCES

1. A.T. Lin, et al., "Cyclotron Autoresonant Maser (CARM) EC Heating Source for High Field Tokamaks", Proc. of the 1987 Int. Conf. IR and mm-Waves.
2. A.T. Lin, W.W. Chang and C.C. Lin, Phys. Fluids 27, 1054(1984).
3. C.S. Kou, et al., "Design of a 100 kW TE<sub>11</sub> Gyro-TWT", Proc. of the 1988 Int. Conf. IR and mm-Waves.
4. K.D. Pendergast, et al., IEEE Trans. Plasma Sci. 16, 122(1988)

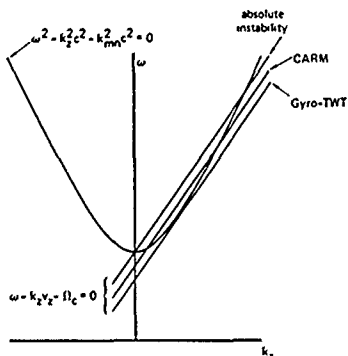


Figure 1 Intersection of waveguide mode with cyclotron resonance lines for gyro-TWT, stable CARM and unstable CARM.

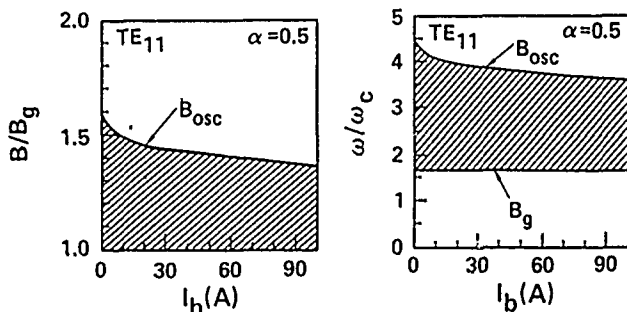


Fig. 2

Fig. 3

Figure 3 Range of normalized frequency corresponding to stable region of Fig. 2.

Figure 2 Dependence of stable range of normalized magnetic field on beam current.

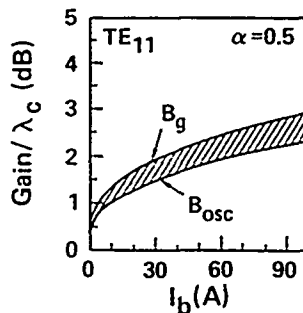


Fig. 4

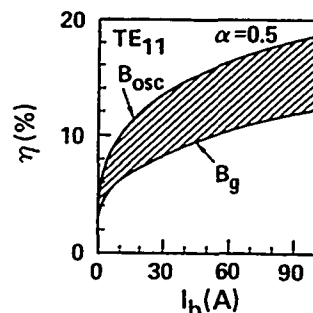


Fig. 5

Figure 4 Range of growth rate corresponding to stable region of Fig. 2.

Figure 5 Range of efficiency corresponding to stable region of Fig. 2.

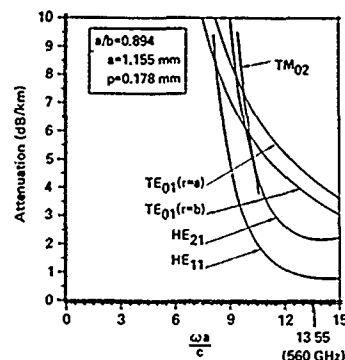


Figure 6 Dependence of attenuation in corrugated guide on normalized frequency.

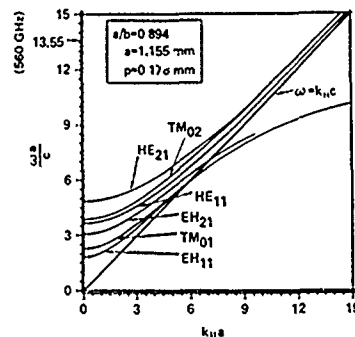


Figure 7 Dispersion of the corrugated waveguide.

TABLE 1

MIG Parameters

Cathode Radius	0.44	cm
Emitter Strip Width	2.7	cm
Mod Anode-Cathode Gap	0.76	cm
Mod Anode Voltage	23.5	kV
Cathode Magnetic Field	1.7	kG
Cathode Angle	4.7°	
Emission Current Density	5.4	A/cm <sup>2</sup>
Emission Current Density Normalized to Limiting Current Density	0.15	

TABLE 2

Proof of Principle

Electron Energy	400	keV
Beam Current	10	A
Beam Radius	0.05	cm
α	0.5	
Magnetic Field (Cathode)	90	G
Magnetic Field (Wiggler)	2.7	kG
Magnetic Field (CARM)	30	kG
Frequency	140	GHz
Waveguide Mode	TE <sub>11</sub>	
Waveguide Radius	0.15	cm
B / B <sub>c</sub>	1.17	
ω / ω <sub>c</sub>	2.3	

## OPTICAL GUIDING IN THE CYCLOTRON AUTORESONANCE MASER

Robert G. Kleva, Baruch Levush, and P. Sprangle\*  
 Laboratory for Plasma Research  
 University of Maryland  
 College Park, MD 20742

## ABSTRACT

The effect of the electron beam on the propagation of a three-dimensional radiation beam in a cyclotron autoresonance maser (CARM) amplifier is investigated numerically. In the exponential gain regime, it is shown that the natural tendency of the radiation beam to spread diffractively is overcome and the radiation beam is focused due to the interaction with the electron beam. The nature of the focusing is found to depend on the relative magnitude of the Doppler-shifted wave frequency,  $\omega_D \equiv \omega - k_z v_z$ , and the relativistic gyrofrequency,  $\Omega$ . The radiation beam can be transported without defocusing following saturation only if  $\omega_D$  is slightly larger than  $\Omega$ . Efficiencies in excess of 50% can be attained through the use of a tapered magnetic field.

## INTRODUCTION

An electromagnetic wave can be amplified by interaction with an electron beam which is injected along an applied magnetic field when there is a resonance between the electron's cyclotron motion and the Doppler-shifted wave frequency. In a CARM the electron beam is injected along the direction of wave propagation and the interaction frequency is Doppler-shifted to  $\omega \sim \gamma \Omega$ , where  $\gamma = (1 - \beta_z^2)^{-1/2}$ ,  $\Omega = \Omega_0/\gamma$  and  $\Omega_0 = eB_0/mc$  is the nonrelativistic gyrofrequency. In some frequency ranges, the CARM has an advantage over the free electron laser (FEL) for moderate energy electron beams because it is difficult to create a magnetic field with a small wiggler period. The radiation beam in an FEL can be focused, and this has been an important point in favor of the FEL. However, since the wave and the electron beam are co-propagating in a CARM, it may also be possible to focus the radiation beam in a CARM.

## EQUATIONS

Consider a CARM in cylindrical coordinates  $(r, \theta, z)$  with the electron beam propagating in the  $z$ -direction along the applied magnetic field. Our analysis proceeds from the wave equation for the vector potential  $A_z$  of a right-hand circularly polarized wave,  $A_z(r, z, t) = \frac{1}{2} A(r, z) \times$

$\exp[i(k_z z - \omega t)](\hat{y} - i\hat{x}) + \text{c.c.}$ , where the complex amplitude  $A(r, z)$  is assumed to vary slowly in  $z$ ,  $|(k_z A)^{-1} dA/dz| \ll 1$ , the frequency  $\omega = k_z c$ , and c.c. denotes the complex conjugate. The wave equation is conveniently solved by the use of a source-dependent modal expansion [1] for the normalized vector potential  $a(r, z) = eA/mc^2$ . In the source-dependent expansion, the structure of the current source is incorporated into the functional dependence of the radiation spot size  $r_s(z)$  and the wave front curvature  $\alpha(z)$ , as well as in the complex amplitude. The advantage of the

source-dependent expansion over an expansion in the vacuum modes is that far fewer modes are needed to accurately describe the radiation. Due to the source-dependent nature of the expansion, the lowest order fundamental mode,  $a(r, z) \approx a_0(z) \times \exp[-i\alpha(z)r^2/r_s^2(z)]$ , provides a good approximation to the evolution of the radiation. Equations of evolution for  $a_0$ ,  $r_s$ , and  $\alpha$  can be obtained by inserting this expression for  $a(r, z)$  into the wave equation. In the source-dependent technique [1],  $r_s(z)$  and  $\alpha(z)$  are chosen to obey the equations [2]

$$\frac{dr_s}{dz} = \frac{2}{k_z r_s} \alpha - \frac{4v\beta_z z_0}{k_z r_s |a_0|} H(z) \langle \frac{\beta_z}{\beta_z} \cos\psi \rangle, \quad (1)$$

$$\frac{d\alpha}{dz} = \frac{2}{k_z r_s^2} (1 + \alpha^2) + \frac{8v\beta_z z_0}{k_z r_s^2 |a_0|} H(z) \left[ \langle \frac{\beta_z}{\beta_z} \sin\psi \rangle - \alpha \langle \frac{\beta_z}{\beta_z} \cos\psi \rangle \right], \quad (2)$$

where  $\langle \rangle$  denotes an average over the electrons, the total phase  $\psi$  is the sum of the particle phase and the wave phase, and  $H(z) = (1-f)/(1+f)^2$  with  $f = (r_b/r_s)^2$ . In deriving Eqs. (1) and (2) we have taken the radial electron density to be Gaussian,  $n(r) = n(0)\exp[-(r/r_b)^2]$ . The quantity  $v =$

$\omega_p^2(0)r_b^2/4c^2$  is Budker's parameter with  $\omega_p^2(0) =$

$4\pi n(0)e^2/m$ . The structure of the current has been incorporated into  $r_s$  and  $\alpha$  through the terms proportional to  $v$ . Writing the amplitude  $a_0(z) = |a_0(z)|\exp[i\chi(z)]$ , we find the following equations for  $|a_0(z)|$  and  $\chi(z)$ :

$$\frac{d}{dz} |a_0| = -\frac{2}{k_z r_s^2} \alpha |a_0| + \frac{8v\beta_z z_0}{k_z r_s^2 |a_0| (1+f)^2} \langle \frac{\beta_z}{\beta_z} \cos\psi \rangle, \quad (3)$$

$$\frac{d}{dz} \chi = -\frac{2}{k_z r_s^2} - \frac{8v\beta_z z_0}{k_z r_s^2 |a_0| (1+f)^2} \langle \frac{\beta_z}{\beta_z} \sin\psi \rangle. \quad (4)$$

Equations which describe the self-consistent evolution of the electron momenta  $U_z = \gamma\beta_z$  and  $U_z = \gamma\beta_z$ , and the phase  $\psi$  are obtained from the Lorentz force law [2].

## COMPUTATIONAL RESULTS

We find that the behavior of the radiation beam depends on two important parameters: the frequency detuning parameter,  $\Delta\omega/\omega = 1 - \beta_z - (\Omega_0/\gamma\omega)$ , which measures the difference between the Doppler-shifted wave frequency and the gyrofrequency, and the index of refraction  $\bar{n} = (c/\omega)(k_z + d\chi/dz) = 1 + k_z^2 d\chi/dz$ . The wave is in resonance with the electrons and gains energy when  $\omega - (k_z + d\chi/dz)v_z \approx \Omega_0/\gamma$ . Therefore, in order

\*Naval Research Laboratory, Washington, DC.

that the wave be resonant with the electrons, the wave phase  $\chi$  must change to compensate for the frequency detuning such that  $d\chi/dz \approx (\Delta\omega/\omega)(k_z/\beta_z)$ . When  $\Delta\omega > 0$ ,  $d\chi/dz > 0$  and the phase velocity of the wave decreases so as to maintain resonance and the index of refraction  $\bar{n} > 1$ . Conversely, when  $\Delta\omega < 0$ ,  $d\chi/dz < 0$  and the phase velocity increases ( $\bar{n} < 1$ ) to maintain resonance.

In Fig. 1 we show the results of a simulation for a CARM amplifier with a positive frequency detuning parameter  $\Delta\omega/\omega = 5 \times 10^{-3}$  [ $\omega/\Omega_0 = 3.7$ ] and with parameters  $\gamma_0 = 4$ ,  $\beta_{10}/\beta_{z0} = .3$ , electron beam radius  $r_b/r_s(0) = .5$ , beam density  $v = 0.1$ , and a wavelength given by  $k_z z_R = 1 \times 10^3$  where  $z_R = (1/2)k_z r_s^2(0)$  is the Rayleigh length. The solid curve in Fig. 1a is a plot of the axial dependence of the efficiency  $\eta$  with which the electrons transfer their energy to the wave, where  $\eta(z) \equiv |\langle \Delta\gamma(z) \rangle|/(\gamma_0 - 1)$  with  $\langle \Delta\gamma(z) \rangle$  being the average over the beam electrons of the change in  $\gamma$  from its initial value  $\gamma_0$ . In this simulation, the magnetic field was linearly tapered between  $z = 11 z_R$  and  $z = 21 z_R$ , its magnitude increasing by a total of  $\Delta B/B = 30\%$  in this interval. The electron beam transfers 50% of its energy to the wave. In contrast, in the absence of magnetic field tapering the efficiency is only one or two percent. The solid curve in Fig. 1b shows the variation in the normalized spotsize  $\bar{r}(z) = r(z)/r_s(0)$  along the axis of the amplifier. The radiation beam is focused by its interaction with the electron beam. By way of comparison, the diffractive spreading of the radiation beam in a vacuum, obtained from Eqs. (1) and (2) with  $v = 0$ , is given by  $\bar{r}(z) = [1 + (z/z_R)^2]^{1/2}$  for  $z \gg z_R$ . For simulations with  $\Delta\omega < 0$ , the index of refraction is less than one, but the radiation beam is still focused in the exponential gain regime due to the growth of the wave [2]. However, following saturation the radiation beam defocuses and spreads diffractively.

The dashed curves in Figs. 1a and 1b show the results of a simulation with the same parameters as before except that the magnitude of the magnetic field is increased by a total of  $\Delta B/B = 45\%$  between  $z = 11 z_R$  and  $z = 26 z_R$ . Although the efficiency is in excess of 50%, the radiation beam becomes defocused as a result of the increase in magnetic field tapering. An explanation for this is provided by the plots of the axial dependence of  $\bar{n} - 1 = k_z^{-1} d\chi/dz$  in Figs. 1c and 1d. In Fig. 1c, which corresponds to the case in which  $\Delta B/B = 30\%$ ,  $d\chi/dz$  initially increases so that  $k_z^{-1} d\chi/dz \approx \Delta\omega/(\omega\beta_z)$  in the exponential gain regime and the index of refraction is larger than one. During the interval  $11 < z/z_R < 21$  in which the applied magnetic field is increased,  $d\chi/dz$  decreases and  $\bar{n}$  decreases towards one. However, at the end of this interval, the index of refraction is still slightly larger than one so the radiation beam is focused. For the case in which  $\Delta B/B = 45\%$  (Fig. 1d), the applied magnetic field is increased to the point at which the index of refraction is no longer larger than one and the beam begins to spread diffractively.

In conclusion, we have shown that the radiation beam in a CARM amplifier can be transported without defocusing following saturation only if the Doppler-shifted wave frequency is slightly larger than the relativistic gyrofrequency ( $\Delta\omega > 0$ ) and the magnetic field taper is not excessive.

## REFERENCES

- (1) P. Sprangle, A. Ting, and C. M. Tang, Phys. Rev. Lett., 1987, vol. 59, p. 202; Phys. Rev., 1987, vol. A36, p. 2773.
- (2) R. G. Kleva, B. Levush, and P. Sprangle, to be published in Phys. Fluids, 1988.

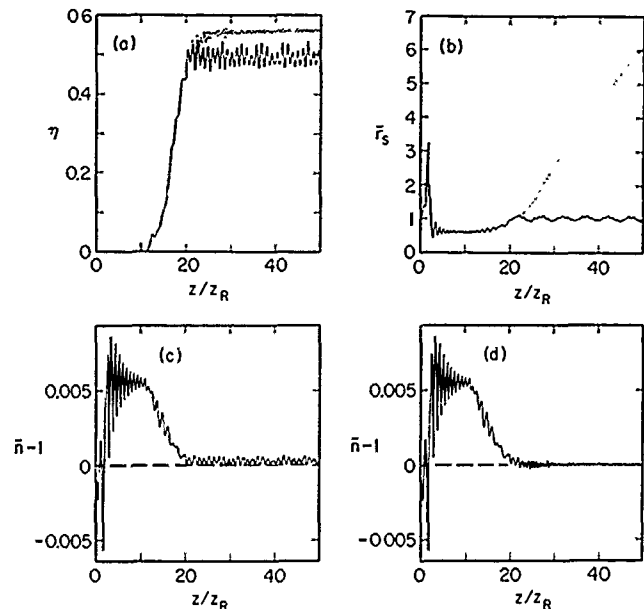


Figure 1. Optical Guiding in CARM

The axial dependence of the (a) efficiency  $\eta$  and (b) normalized spotsize  $\bar{r}(z) = r(z)/r_s(0)$  are plotted for a tapered magnetic field  $\Delta B/B = 30\%$  (solid line) and  $\Delta B/B = 45\%$  (dashed line). The axial dependence of  $\bar{n} - 1$ , where  $\bar{n}$  is the index of refraction, is plotted for  $\Delta B/B =$  (c) 30% and (d) 45%.

## INITIAL OPERATION OF A CHERENKOV CARM

H.B. Cao, D.B. McDermott and N.C. Luhmann, Jr.  
Department of Electrical Engineering, University of California  
Los Angeles, California 90024

### ABSTRACT

The advantages of high efficiency and high frequency from a CARM can be obtained even with a low energy electron beam by incorporating a slow wave structure. Interaction on the light-line of a Cherenkov CARM has been achieved in an oscillator configuration.

### INTRODUCTION

The CARM<sup>(1,2)</sup> is a novel variation of the cyclotron resonance maser. It is designed so that the electrons remain in synchronism with the electromagnetic wave even as they lose energy. The resonance condition, as for all fundamental gyro-tubes, is:

$$\omega = \Omega_{ce}/\gamma + k_z v_z \quad (1)$$

where  $\Omega_{ce} = eB/m_0$  is the rest mass cyclotron frequency,  $k_z$  and  $v_z$  are the axial wavevector and velocity, respectively. Synchronism can be maintained if the longitudinal velocity decreases at the same rate as the energy. This occurs for  $\beta_{ph} \equiv \omega/ck_z = 1$ . The dynamic phase shift of an electron relative to the wave can be written as<sup>(2)</sup>

$$\Delta\phi = (\Delta\gamma/\gamma)\omega\tau(\beta_{ph}^2 - 1) \quad (2)$$

Notice that the phase slippage occurs less slowly as  $\beta_{ph}$  approaches unity. This enables particles to interact with the wave with a high efficiency.

Another feature of the CARM is that the Doppler-upshift of frequency is significant, which can be shown as

$$\omega = (1 - \beta_z)^{-1} \Omega_{ce}/\gamma \quad (3)$$

A highly relativistic electron beam is required for a fast wave CARM in order to avoid the competition from backward wave oscillation. However, by incorporating a slow wave structure we can still achieve the advantages of a CARM while using a low energy beam<sup>(3)</sup>.

The guiding structure of a Cherenkov CARM is a dielectric cylinder within the cavity. The mode of interest is the hybrid  $HE_{11}$  mode which peaks on axis as the phase velocity approaches the speed of light. Thus the wave is strong in the central vacuum region for the values of phase velocity which yield the highest efficiency. Yet, the required beam energy is substantially reduced.

### EXPERIMENT

An appropriate gun geometry to excite the  $HE_{11}$  mode is a pencil beam which acquires its transverse energy by passing through a gyroresonant wiggler. The initial CARM was designed as an oscillator. The principal design of the experimental system is shown in Fig. 1.

A linearly polarized wiggler was constructed with permanent magnets. The pump field on axis can be adjusted from 10 to 200 Gauss. Figure 2 shows the measured field strength for the wiggler. The detrimental "edge field" was eliminated by configuring the magnets with a reduced period at the ends.

The solenoid was configured such that the magnetic fields for the wiggler and the CARM interactions were separately adjustable so that both interactions could be optimized independently. The magnetic field profile is shown in Fig. 3.

A diagnostic experiment examined the performance of gyroresonant velocity transformation in the wiggler. Using an aperture, an extremely thin beam was passed through the wiggler and impacted on a uranium glass plate, so that the Larmor radius of the electrons could be measured and the  $\alpha$  could be calculated. The experimental results with different pump field and varying background field are shown in Fig. 4. The result is fairly consistent with simulation (Fig. 5).

The Cherenkov CARM experiment was then performed with a 4 A, 100 keV beam. The wiggler fields were adjusted so that the electron had an  $\alpha$  of 0.8 in the CARM region. The CARM's magnetic field was then swept so that the cyclotron resonance line (Eq. 1) moved along the  $HE_{11}$  dispersion curve, exciting both forward and backward modes. Figure 6 shows the cold test measurement of the  $HE_{11}$  dispersion along with the power emitted through one of the two output ports. A peak power of 24.6 kW was generated for the fourth order axial mode. The 15th order mode, which is on the light-line, was excited with an output power of 300 W.

### CONCLUSION

A wave with  $\beta_{ph} = 1$  has been excited. However, the experiment is far from optimized. It is known that a high quality electron beam ( $\Delta v_z/v_z \lesssim 2\%$ ) is required for efficient CARM interaction<sup>(2)</sup>. The velocity spread is presently about 8%, given by the inhomogeneity of the pump field. By reducing the size of the beam, the velocity spread will be reduced. Also, the coupling of the power from the cavity must be improved. Presently, wall coupling is being used. However, as the operating point approaches the light line, the electromagnetic energy tends to concentrate near the axis of the cavity and to be a null near wall, yielding minimal coupling.

### ACKNOWLEDGEMENT

This work is supported by NRL under Contract N00014-87-k-2032, Mod. 00001, and AFOSR under Grant 86-0199, Amd. A.

## REFERENCES

1. V.L. Bratman, N.S. Ginzburg, G.S. Nusinovich, M.I. Petelin and P.S. Strelkov, *Int. J. Elect.* **51**, 541 (1981)
2. A.T. Lin, *Int. J. Elect.* **57**, 1097 (1984)
3. D.B. McDermott, H.B. Cao and N.C. Luhmann, Jr., "A Cherenkov Cyclotron Autoresonance Maser", *Int. J. Elect.* to be published (1988)

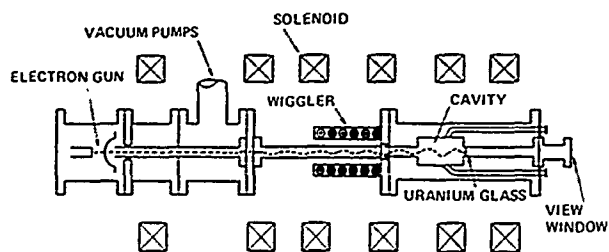


Figure 1 Schematic of the Cherenkov CARM oscillator system.

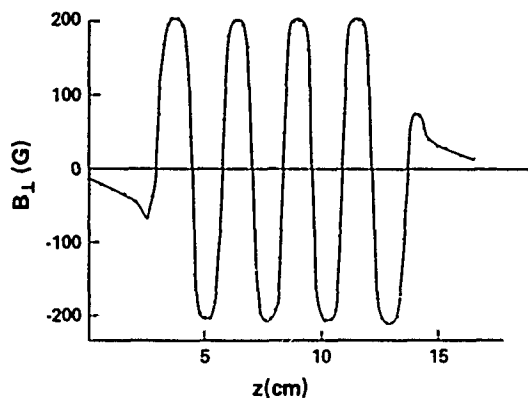


Figure 2 Measured transverse magnetic field strength on axis of the permanent magnet wiggler.

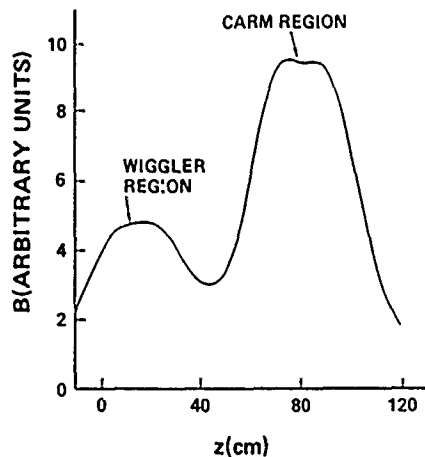


Figure 3 Magnetic field profile of the Cherenkov CARM system.

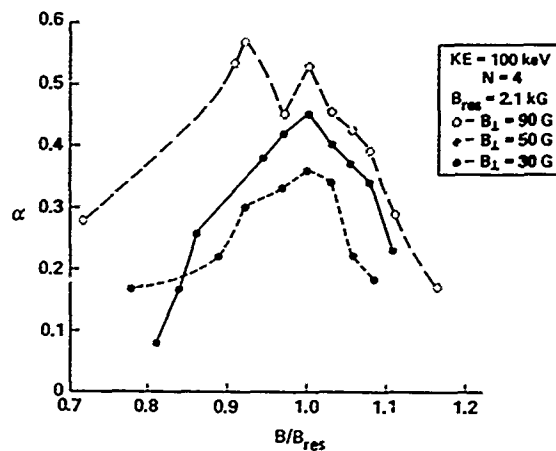


Figure 4 Experimental results of  $\alpha$  for several pump fields with varying background field.

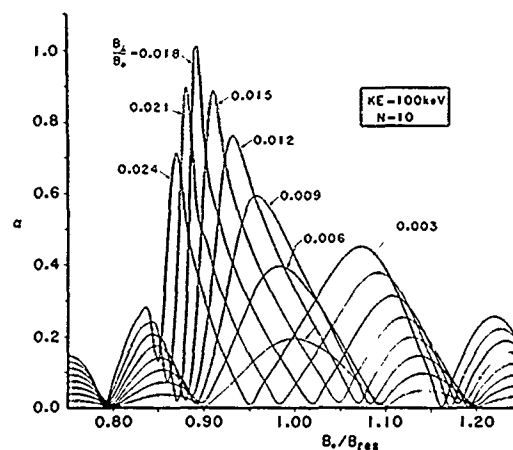


Figure 5 Simulation results of  $\alpha$  for several pump fields with varying background field.

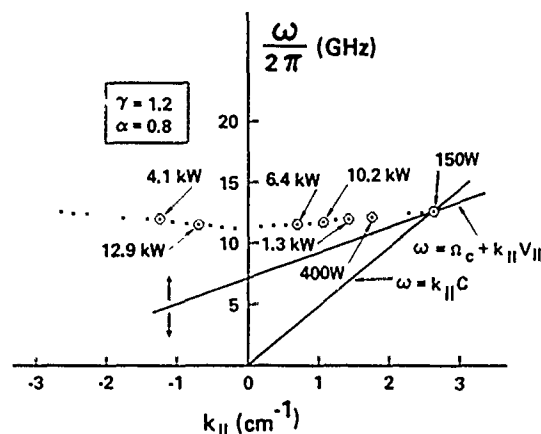


Figure 6 Measured dispersion relation of  $HE_{11}$  mode along with power emitted from several axial modes through one of two output ports.

## HIGH POWER MULTI-CAVITY PHASE-LOCKED GYROTRON OSCILLATOR EXPERIMENT

S.H. Gold, A.W. Fliflet, W.M. Black, D.A. Kirkpatrick,\* and W.M. Manheimer

Naval Research Laboratory  
Washington, DC

## ABSTRACT

A high-peak-power 35 GHz multi-cavity phase-locked gyrotron based on a solid 1 MeV, 100 Amp, 30 nsec electron beam has been designed. The required beam transverse momentum is produced by a helical wiggler and increased to a beam pitch ratio  $\alpha=0.75$  by magnetic field compression. The locking signal, provided by a 20 kW magnetron, drives a slotted cylindrical  $TE_{111}$  prebunching cavity. The azimuthal phase bunching of the beam, is enhanced by means of a second passive bunching cavity. The  $TE_{121}$  output cavity, which will self-oscillate in the absence of beam prebunching, is expected to produce output powers of ~10 MW and have a locking frequency bandwidth of 0.1 percent.

## INTRODUCTION

This paper describes the design for an experimental high power, phase-locked gyrotron oscillator. The electron beam is generated by a 1 MV pulseline accelerator, and the reference signal is provided by a 35 GHz, 20 kW magnetron. The expected output power is approximately 10 MW. The experiment is intended to serve as a test bed for the development of very high peak power phase-locked gyrotron oscillators. Such oscillators are of interest as sources for high-accelerating-gradient RF accelerators and phased-array directed-energy antenna systems. The experiment should allow the investigation of important elements of the design of these devices and of the diagnostics required for demonstrating phase-locked operation under short pulse, low repetition-rate conditions.

## EXPERIMENTAL DESIGN

A schematic of the experimental configuration is shown in Fig. 1. A solid 1 MeV, ~100 A electron beam is produced by the NRL VEBA pulseline accelerator, with a voltage pulse length (FWHM) of ~55 nsec and a voltage flat-top of ~30 nsec, using an apertured diode previously used to produce a high quality, low transverse velocity beam for millimeter-wave free-electron laser (FEL) experiments [1]. The transverse momentum required for the gyrotron interaction is produced initially by a bifilar helical wiggler and then increased to a final momentum pitch ratio  $\alpha$  of ~0.75 by adiabatic compression of the axial magnetic field. The locking signal from the magnetron is introduced via a prebunching cavity. A second passive bunching cavity is used to increase the locking frequency bandwidth obtainable with a given locking power.

The bunching cavities are designed to operate in the fundamental  $TE_{111}$  cylindrical cavity mode. However, some competition from the  $TE_{112}$  mode could not be avoided due to the constraint on the minimum drift tube diameter set by the requirement to propagate the electron beam. The bunching cavities include two axial slots to control the cavity Q

factor and suppress competing modes [2]. Additional slots and apertures are used to suppress oscillation in the drift spaces. The output cavity operates in the  $TE_{121}$  mode, and is also slotted to reduce competing mode excitation.

Figure 2 shows calculated axial RF-field profiles for the  $TE_{111}$  and  $TE_{112}$  modes for one of the prebunching cavities as well as the location of the apertures and slots used both to suppress higher-order transverse modes, and to linearly-polarize and control the Q of the desired  $TE_{111}$  mode and the competing  $TE_{112}$  mode. Since the drift spaces separating the cavities are weakly cut off to these modes, their fields extend well into the drift spaces. Thus, the effective RF cavity extends well beyond the nominal cavity length defined by the enlarged diameter section. The length of the main 44° axial slots of the cavity region is three times the length of the enlarged section of the cavity, in order to extend everywhere that the  $TE_{111}$  mode has substantial rf fields. In order to further suppress the  $TE_{112}$  mode, which extends much further into the cutoff regions, additional pairs of "key-hole" slots were placed in the walls of the cutoff section, beginning just beyond the main cavity slots, but at an angle of 90° from them. The combination of large slots at 90° intervals in different regions of the cutoff section helps both to limit the spatial extent of the rf fields of the  $TE_{112}$  mode of the cavity, and also to substantially lower the Q of the  $TE_{111}$  mode of the drift spaces, of any polarization, in order to prevent the build-up of oscillation in these regions.

## THEORY

A linear theory of gyrotron oscillator phase locking via a prebunching cavity has been presented by Manheimer [3]. The nonlinear theory of gyrotron phase locking has been investigated by Fliflet and Manheimer [4]. As shown in [4], a simple estimate from perturbation theory for the locking bandwidth using a prebunching cavity is:

$$\frac{\Delta\omega}{\omega_0} \leq 2\sqrt{\pi} \frac{\mu I_0}{2QF} J_1(q) e^{-\left[\frac{\mu\Delta}{4}\right]^2} J_1'(\beta_{\perp 0}) \quad (1)$$

where  $\mu$ ,  $\Delta$ ,  $I_0$ , and  $F$  are the normalized interaction length, detuning parameter, current, and steady state field amplitude, respectively,  $Q$  is the quality factor of the output cavity,  $J_1$  is the regular Bessel function of order 1,  $J_1'$  is its derivative,  $q$  is the beam azimuthal phase bunching parameter, and  $\beta_{\perp 0}$  is the initial transverse velocity of the electron beam divided by the speed of light. The normalized gyrotron parameters are defined as in Danly and Temkin [5]. Eq. (1) assumes that the cavity axial rf-field profile has a gaussian form  $f(z)=\exp\{-[3^{1/2}(2z/d-1)]^2\}$ , where  $z$  ranges from 0 to  $d$  and  $d$  is the effective interaction

length. It neglects axial velocity modulation generated by the bunching cavity and the effects of initial beam velocity spread. As discussed in [3], the effect of beam velocity spread is to reduce the resonance detuning parameter at which a given locking bandwidth can be obtained. If the expected beam quality is obtained ( $\Delta v_z/v_z < 5\%$ ), this effect should be small. The maximum bandwidth corresponds to the maximum value (0.58) of  $J_1$ , which occurs for  $q=1.83$ . This bunching parameter appears feasible with multiple bunching cavities.

Figure 3 shows the start oscillation current for the prebunching cavities and the output cavity as a function of magnetic field. While the  $TE_{11}$  mode of the prebunching cavity is stable at all magnetic fields, the  $TE_{12}$  remains a problem. It appears stable at the design voltage and magnetic field, but may oscillate during the rise and fall of the voltage waveform. The free-running oscillator parameters for the output cavity have been calculated. The peak efficiency of 13% occurs at 32 kG and corresponds to  $\Delta=0.91$  and  $F=0.43$ . The normalized beam current is 0.35. Based on these parameters, and assuming optimum bunching, the locking frequency bandwidth is 0.16%. Some increase in bandwidth at lower efficiency could be achieved at higher magnetic field. These analytic results are supported by simulations using a time-dependent slow-time-scale code described in [4].

In summary, a circuit design has been obtained for a phase-locked intense beam gyrotron oscillator with a locking frequency bandwidth of  $\sim 0.1\%$ . The effective gain of output power to the locking power needed to achieve this bandwidth is  $\sim 28$  dB. The circuit makes use of a novel arrangement of slots and apertures to control the Q of the bunching cavities and to prevent oscillation in spurious modes. These cavities have been constructed and cold tested, and have shown the desired combinations of Q-values, center frequencies, and frequency tunability. A method has been identified to produce an electron beam with the desired current,  $\alpha$ , and velocity spread. The successful conclusion of this design effort [6], and our success in fabricating cavities with the desired combination of properties, points the way to an experimental test of our design for a high voltage multi-cavity 35 GHz phase-locked gyrotron oscillator.

This work was supported in part by the Office of Innovative Science and Technology, Strategic Defense Initiative Organization, and managed by the Harry Diamond Laboratories, and in part by the Office of Naval Research

#### REFERENCES

- \*D.A. Kirkpatrick is with SAIC, McLean, VA 22102.
- [1] R.H. Jackson, et al., *IEEE J. Quantum Electron.*, vol. QE-19, pp. 346-356, 1983.
- [2] S.W. McDonald, et al., *Int. J. Electron.*, vol. 61, pp. 795-822, 1986.
- [3] W.M. Manheimer, *Int. J. Electron.*, vol. 63, pp. 29-47, 1987.
- [4] A.W. Fliflet and W.M. Manheimer, to be published.
- [5] B.G. Danly and R.J. Temkin, *Phys. Fluids*, vol. 29, pp. 561-567, 1986.
- [6] A.W. Fliflet, S.H. Gold, and W.M. Manheimer, *Int. J. Electron.*, to be published.

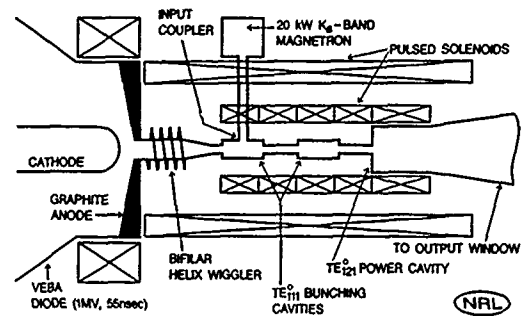


Fig. 1. Schematic diagram of the three-cavity phase-locked gyrotron oscillator experiment.

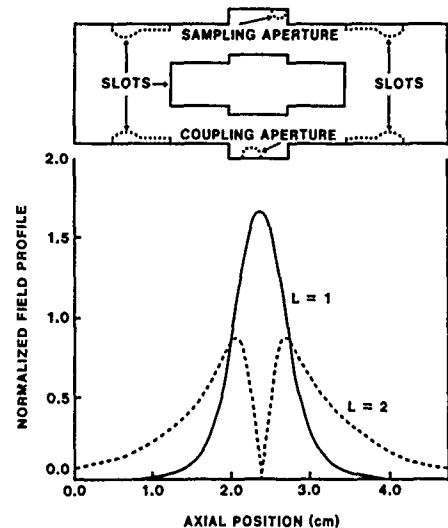


Fig. 2. Calculated axial profile functions for the  $TE_{111}$  and  $TE_{112}$  modes of the prebunching cavities, showing the location of apertures and slots.

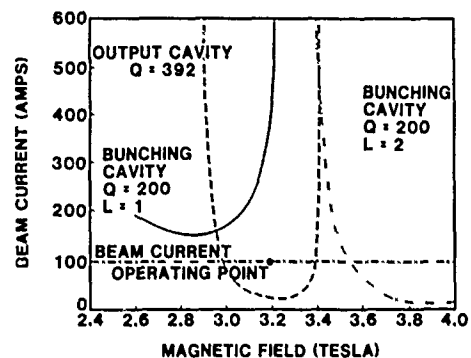


Fig. 3. Start oscillation current for the pre-bunching cavity ( $l=1$  and  $l=2$  modes) and the main output cavity.



# Monolithic Watt-Level Millimeter-Wave Barrier-Intrinsic-N<sup>+</sup> (BIN) Diode-Grid Frequency Tripler Array

R. J. Hwu, N. C. Luhmann, Jr.  
University of California, Los Angeles  
Department of Electrical Engineering  
D. B. Rutledge  
CIT, Pasadena  
D. Streit, T. O'Neill  
TRW, Redondo Beach  
U. Lieneweg  
JPL, Pasadena

## ABSTRACT

Thousands of barrier-Intrinsic-N<sup>+</sup> diodes are monolithically integrated by a metal grid as a highly efficient frequency tripler which promises watt-level CW output power throughout the millimeter wave region.

## INTRODUCTION

A serious problem in the development of millimeter and submillimeter wavelength receivers for atmospheric and space spectroscopy is the availability of suitable local oscillators required for heterodyne mixing. Such local oscillators must have reasonable power output and efficiency, and are required to cover a range of wavelengths of interest to spectroscopy. Available solid-state oscillators, such as GaAs Gunn diodes and IMPATTs, are highly efficient and tunable, but are currently limited to frequencies up to about 75 and 150 GHz, respectively (for output power  $\geq 0.1$  W).

Much higher frequencies can be obtained by generating harmonics of the fundamental frequency from these solid-state oscillators. To overcome the power limitations of a single-diode multiplier, our design of a diode grid for frequency multiplication is motivated (1). This approach is attractive because a metal grid is monolithically integrated with thousands of diodes thereby resulting in potentially low-cost, small-size and realization. Power is distributed among many diodes making possible watt-level output power throughout the millimeter and submillimeter wave region.

The feasibility of this approach has been demonstrated by a frequency doubler arrays of GaAs Schottky diodes (see Fig. 1) with 0.5 W output power at 66 GHz (2). However, the Schottky diodes have serious limitations at higher frequencies. These stem mainly from the parasitic resistance introduced by the ohmic front contact. Furthermore, the weak dependence of the capacitance on the voltage limits the efficiency in harmonic generation, especially for higher harmonics.

## SILICON BIN DIODE DOUBLER

The approach we have taken to overcome these deficiencies is the thin metal-oxide-silicon diode (3). The T-MOS diode, which has an undoped thin epitaxial layer, exhibits an exponential dependence of the capacitance on voltage and thus is much more efficient in producing harmonics. This concept has been tested with a single-diode in a whisker-coupled waveguide configuration for frequency

doubling. A doubling efficiency of 14.7% at 95 GHz was obtained experimentally which is in good agreement with the theoretical predictions (4,5). Furthermore, due to the blocking barrier, two diodes can be operated back-to-back generating a sharp spike in the C-V curve. This symmetric C-V characteristic provides cancellation of even harmonics favoring the tripling and quintupling operation. In addition, the height and width of this C-V curve can, in principle, be adjusted by doping control alone thus eliminating the need for an external dc bias. This arrangement results in a highly efficient frequency tripler. However, defects in the epitaxial silicon layer deteriorated the thin oxide and limited the yield of the devices making array construction difficult.

## GaAs BIN DIODE-GRID TRIPLER

Recently, a GaAs barrier-Intrinsic-N<sup>+</sup> (BIN) diode has been developed as shown in Fig. 2. This structure does not require an insulator layer as in the T-MOS structure, but instead relies on a Mott-type barrier formed in the semiconductor between the metal gate and a sheet of positive charge formed by a doped atomic plane. The active region is an intrinsic layer between the Mott-barrier and a heavily doped electron injecting zone. Accumulation and depletion of electrons at the barrier produce nonlinearities in the C-V characteristic which, especially at low temperature, are much stronger than in a Schottky diode. This structure also takes advantage of the higher mobility of GaAs. The maximum cut-off frequency is determined by the time it takes electrons to transit the active layer at the saturation velocity. For a 100 nm GaAs layer the cut-off frequency is  $f_c \approx 1$  THz. A tripling efficiency of 35% at an output frequency of 100 GHz is predicted.

The metal grid we designed for the BIN diode tripler consists of a columnar mesh of aluminum strips with Schottky electrodes on each end as shown in Fig. 3. The small dimension and rectangular shape of the Schottky electrode are designed to minimize the zero-voltage capacitance and series resistance of the device, respectively. The two neighboring Schottky electrodes are designed to give the back-to-back configuration for two BIN diodes. This arrangement requires only one metal pattern, which greatly facilitates the ease of fabrication.

The quasi-optical diode-grid tripler design has been developed as shown in Fig. 4, where power at the fundamental frequency enters from the bottom, through an input tuner. The grating plate (which

functions as a high-pass transmission filter) reflects the incident pump power at the fundamental frequency to the diode grid on the left of it, and the metal mirror behind the diode grid again reflects all the harmonics back to the grating plate. Different harmonics are then diffracted in different directions. The third harmonic is designed to exit in the desired direction passing through an output tuner. The tripling configuration has been tested with one of the remaining Schottky diode grids.

The experimentally measured C-V curve from two back-to-back BIN diodes with the structure shown in Fig. 5, demonstrates the back-to-back tripling configuration. The efficiency of the BIN diode tripler is also calculated using this C-V data by a large-signal multiplier analysis program (6). The computation results as shown in Fig. 6 verify the utilization of the BIN diode as a highly efficient frequency tripler.

This work is supported by TRW under the California MICRO program.

#### REFERENCES

- (1) D. B. Rutledge, and S. E. Schwarz, IEEE J. Quantum Electronics, QE-17, P. 407, 1981.
- (2) C. F. Jou, W. W. Lam, H. Chen, K. Stolt, N. C. Luhmann, Jr., and D. B. Rutledge, to be published on IEEE Trans. on Microwave Theory and Tech.
- (3) C. F. Jou, Ph.D. Thesis, Chap. 6, UCLA, 1987.
- (4) R. P. Rause, D. H. Steinbrecher, International Solid-State Circuit Conf., Digest of Technical Papers, P. 68, 1966.
- (5) K. Schunemann, B. Schiek, A. E. U. 22, P. 293, 1968.
- (6) H. Siegel, A. R. Kerr, and W. Hwang, NASA Tech. Paper 2287, 1987.

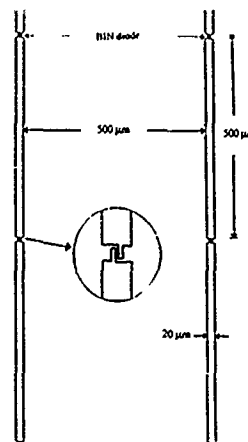


Fig. 3 The design of metal grid for the BIN diode-grid tripler.

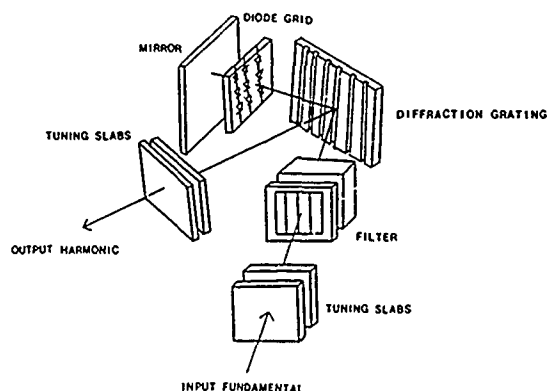


Fig. 4 The quasi-optical diode-grid tripler design.

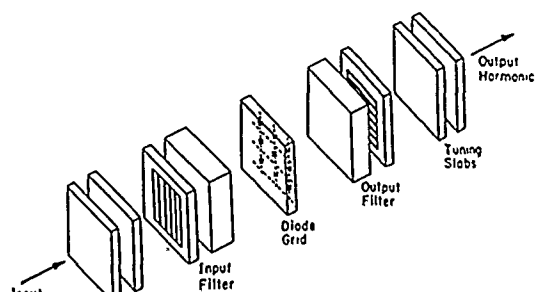


Fig. 1 The quasi-optical diode-grid doubler design.

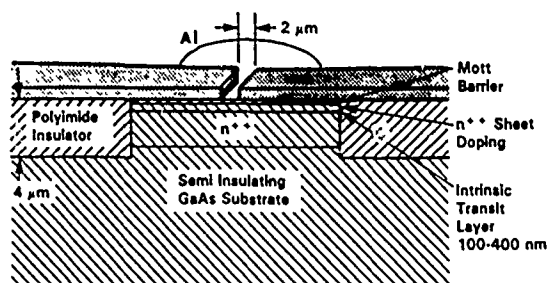


Fig. 2 The BIN diode structure.

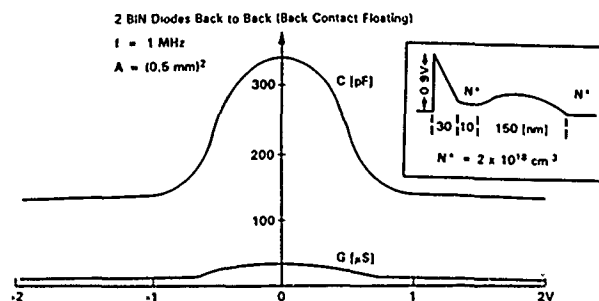


Fig. 5 Symmetric C-V characteristic from the experimental measurement of two back-to-back BIN diodes.

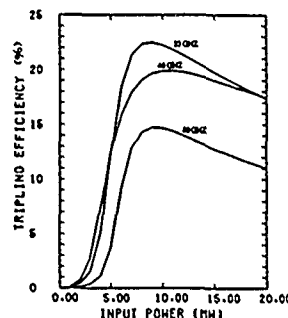


Fig. 6 Tripling efficiencies of the BIN diode from the large-signal multiplier analysis using the experimentally measured C-V data of Fig. 5.

## ANALYSIS OF A NOVEL MONOLITHIC GaAs MIS PHASE SHIFTER

M. E. McKaughan and F. C. Jain

Department of Electrical and Systems Engineering  
University of Connecticut  
Storrs, CT.

## ABSTRACT

Analysis of a novel monolithic GaAs MIS phase shifter is presented. A quasi-TEM transmission line model, valid for the slow-wave regime, is used to predict operation of the device as an electronically controllable phase shifter. Device parameters such as phase shift, characteristic impedance, and insertion loss are computed.

## INTRODUCTION

Electronically steerable antenna arrays for use in the millimeter and submillimeter wavelength ranges are being developed for defense and civilian requirements in the 1990s and beyond. A major goal of millimeter wavelength systems is to integrate a majority of the electronics onto a single microchip. Such systems will no doubt include transceiver and control circuits as well as the antenna array.

One novel monolithic phased array antenna system has been presented by Jain and Bansal (1984) (1). Their idea is to construct individual antenna elements of doped semiconductor material directly on a semi-insulating gallium arsenide (GaAs) substrate. This scheme will simplify synthesizing the desired antenna radiation pattern. Work is presently in progress to fabricate and test antenna elements of these arrays in the Microelectronics Laboratory at the University of Connecticut. However, steering the radiation intensity of the array will require additional electronic adjustment of the phase of the electromagnetic wave reaching the individual antenna element. This paper describes a MIS type phase shifter for GaAs based integrated systems. In particular, theoretical analysis using quasi-TEM model of the slow-wave structure, and numerical computations are presented.

## QUASI-TEM ANALYSIS

Kwon, et al (2) have presented a straight forward method for analyzing coplanar microstrip transmission lines using a quasi-static TEM approximation. Their experimental data agree well with their theoretical results. We have used this model to analyze our structure shown in Figure 1. Determining the model parameters was modified to correspond with the physical structure of this new device. Figure 2a and 2b show the schematics of the circuit models used by Kwon et al and by the authors, respectively. Components, equivalent in the two models, were

evaluated using Kwon et al's formulas. These components include the metal conductor losses per unit length,  $R_m$ , and the transverse resistance,  $R_t$ . To compute the line inductance,  $L_m$ , a modified procedure was used to account for the multiple layered geometry in our phase shifter.

The line inductance is determined from the static line capacitance. The usual method (3) to determine the static line capacitance neglects the thickness of the conductors. A simple method to include the effect of conductor thickness subdivides the capacitance into three parts; the bottom-half, the top-half, and the edge capacitances (4). Using the Schwartz-Christophel conformal mapping, the top half and bottom half capacitances may be computed. The edge capacitance is computed using a parallel plate approximation. The total static line capacitance is the parallel combination of these three components. Using this value, the per unit length inductance,  $L_m$ , of the transmission line is determined.

Kwon et al account for the loss in the semiconductor material directly beneath the conductor strip by introducing a resistance,  $R_s$  in parallel with the  $R_m + jL_m$  impedance of the conductor strips. The value for the semiconductor loss resistance is determined from the conductivity of the material and the skin depth. We have determined that for a multiple layer structure, the loss resistance must be replaced by a series resistance and inductance. This impedance is found by applying Schelkunoff's (5) definition of surface impedance. The result of this computation is an impedance connected in parallel with the impedance used by Kwon et al as seen by comparing Figures 2a and 2b. The results of the calculations for surface impedance of a two-layer device are:

$$Z_{ti}(0) = \frac{1+j}{\sigma_1 \delta_1 \left\{ 1 + \left( \frac{\sigma_2 \delta_2}{\sigma_1 \delta_1} - 1 \right) e^{-(1+j)(d_i/d_1)} \right\}} \quad (1)$$

where:

$Z_{ti}(0)$  = total internal impedance for a device with  $i$  layers

$E_z(0)$  = electric field at the surface

$J_{Total}$  = total current density

$\sigma_i$  = conductivity of layer  $i$

$\delta_i$  = skin depth in layer  $i$

$d_i$  = thickness of layer  $i$

The resistive and inductive components are determined from the real and imaginary parts of the surface impedance:

For the shunt transverse capacitance, this model uses the capacitance due to both the insulation/oxide and the depleted layer created by bias on the device.

Using this model, slowing factor and attenuation are computed and presented in Figures 3, and 4 respectively. It is important to note that the slowing factor, and hence the phase shift per unit length can be adjusted by varying the DC bias on the gate of this MIS structure.

### CONCLUSIONS

The Quasi-static analysis presented by Kwon et al has been extended to a multi-layer device where the slowing factor can be controlled by DC bias. The improved model includes the thickness of the conductors and losses in multiple layers of semiconducting material. The entire analysis is straight forward and does not require extensive use of numerical analysis. Results obtained to date are in close agreement with published results for similar structures. The availability of electronically controllable monolithic phase shifters which can be integrated directly onto the wafer will open new horizons for the millimeter wave antenna array designer.

### References

- (1) F. C. Jain, and R. Bansal, "Semiconductor Antenna: A New Device in Millimeter- and Submillimeter-Wave Integrated Circuits," IEEE Transactions on Microwave Theory and Techniques, vol. MTT-32, no. 2, pp. 204-208, Feb. 1984.
- (2) Y. R. Kwon, V. M. Hietala, and K. S. Champlin, "Quasi-TEM Analysis of 'Slow-Wave' Mode Propagation on Coplanar Microstructure MIS Transmission Lines," IEEE Transactions on Microwave Theory and Techniques, vol. MTT-35, pp. 545-551, Jun. 1987.
- (3) K. C. Gupta, R. Garg, and I. J. Bahl, Microstrip Lines and Slotlines, Artech House, Inc., 1979.
- (4) A. Schwarzmann, "Microstrip Plus Equations Adds Up to Fast Designs," Electronics, Oct 2, 1967.
- (5) S. A. Schelkunoff, "The Electromagnetic Theory of Coaxial Transmission Lines and Cylindrical Shields," The Bell System Technical Journal, vol. 13, pp. 532-579, Oct. 1934.

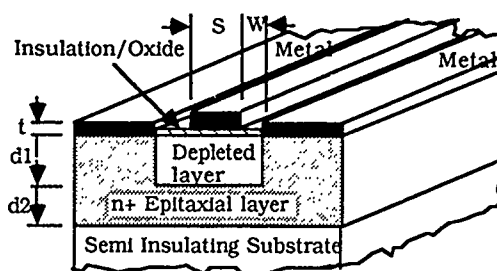


Figure 1. Cross sectional geometry of the proposed monolithic phase shifter

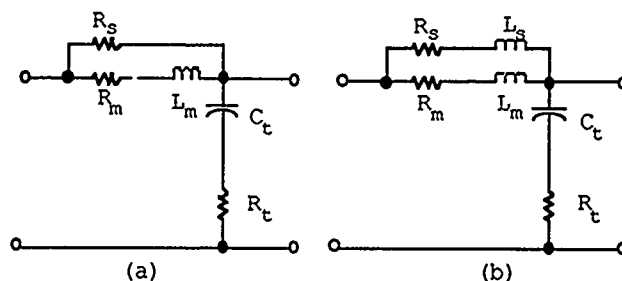


Figure 2. Schematic of the models used by Kwon et al, (a) and the present work (b).

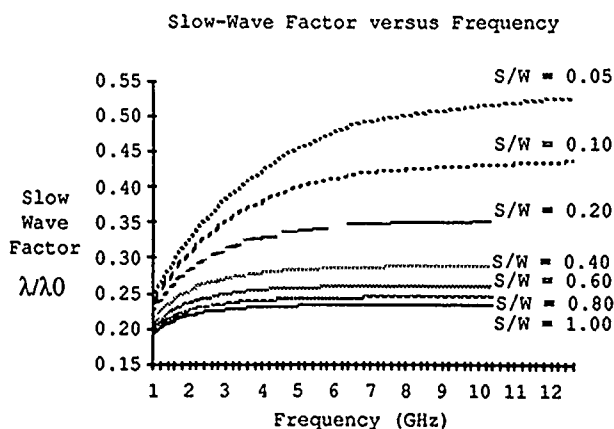


Figure 3. Slowing factor versus frequency for various line configurations.

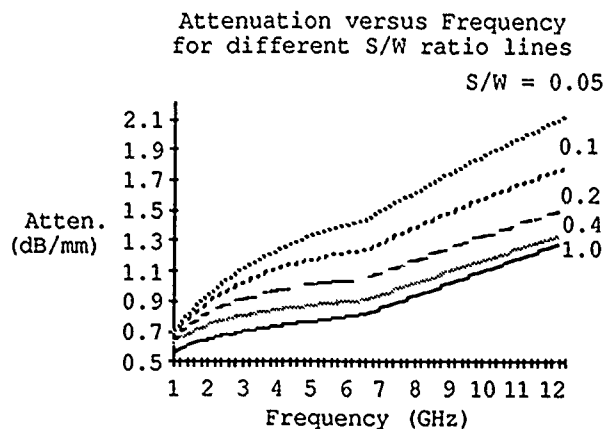


Figure 4. Attenuation versus frequency for various line configurations

## Scattering of Plane Wave by Microstrip Lines

S. T. Peng

New York Institute of Technology, Old Westbury, NY 11568

and

Robert T. Kinasewitz

U. S. Army Armament Research, Development &amp; Engineering Center, Picatinny, NJ 07806-5000

## ABSTRACT

The scattering of a plane wave by a microstrip line is formulated under the most general conditions, including the finite conductivities of the metal strip, substrate and ground plane, in order to determine accurately the absorption of energy by the microstrip structure. It is shown that a new class of modes in the metal is needed for a formulation of the microstrip structure as a rigorous boundary-value problem by the method of mode matching.

## INTRODUCTION

A rigorous formulation is presented for the scattering of a plane wave by a uniform microstrip line which is composed of a metal strip placed on top of a dielectric substrate which is backed by a ground plane. The metal strip is made of a good conductor with a finite thickness and a finite conductivity. The substrate has a complex dielectric constant with a small imaginary part to represent its absorption effect. Finally, the ground plane is assumed to be very large and is taken as a semi-infinite medium. This is the most realistic characterization of a microstrip structure for a theoretical analysis. In terms of the complex dielectric constants, the microstrip structure can be taken as a dielectric strip waveguide which has been rigorously formulated, by the method of mode matching, as a boundary-value problem in the literature[1,2].

For a low-loss structure composed of good conductors and a good dielectric material for the substrate, the absorption is generally expected to be small. However, for the guiding structure of concern here, the incident energy may be converted or coupled into the guided modes of the microstrip line, under appropriate conditions on the incident-wave and structure parameters. The energy of a guided (microstrip) mode is trapped mostly in the substrate around the strip and is ultimately absorbed by the lossy materials comprising the structure. If the coupling of the incident energy into the microstrip modes is substantial, the phenomenon of anomalous absorption may occur in the scattering of an incident plane wave by the microstrip structure. We show here that there exists a new class of modes in the metal-dielectric layered structure, which has to be included in order to treat the structure as a whole, including the effect of loss in every constituent part of the structure.

## FORMULATION

The geometrical configuration of the microstrip line is shown in Fig. 1(A). The metal strip has a width  $2w$ , a thickness  $t$ , and a complex dielectric constant  $\epsilon_m$ . The substrate has a complex dielectric constant  $\epsilon_s$  and a thickness  $t_s$ . The ground plane has a complex dielectric constant  $\epsilon_g$ . To facilitate the

formulation of the problem, we enclose the microstrip line inside an ideal parallel-plate waveguide, so that the basic modes of the structure are totally discretized. Furthermore, by the reflection symmetry in the lateral direction, the structure is bisected, and only one half of it is considered. At the bisection plane, we have a perfect magnetic conductor (PMC) for the symmetric modes and a perfect electric conductor (PEC) for the antisymmetric modes. Thus, we may consider only the bisected structure with an appropriate termination at the bisection or symmetry plane, as shown in Fig. 1(b).

With the structure vertically confined, the scattering problem now becomes the determination of the reflection and transmission of energy along the parallel-plate waveguide. The structure may be divided into four regions: the air region,  $x < 0$ ; the microstrip region,  $0 < x < x_1$ ; the substrate region,  $x_1 < x < x_2$ ; and the grounding region,  $x < x_2$ . We first find the general field solutions in each region and then require the continuity of tangential field components at the boundary between two adjacent regions. Among the four regions, the microstrip region is considered as a parallel-plate waveguide filled with two different layers of dielectric, whereas the other three regions as being filled with a uniform dielectric. The mode functions of the three parallel-plate waveguides filled with a uniform dielectric are well known; they are simply the sine or cosine functions, independent of the dielectric constant. The mode functions of the microstrip region consisting of two uniform layers can also be easily determined. Because of the presence of metal with a large imaginary part of the dielectric constant, there exist two classes of modes, one being well understood but not the other. The new class of modes is responsible for many interesting behaviors of the fields in the structure. With the complete set of modes determined, the boundary-value problem can now be rigorously formulated by the method of mode matching, as previously employed.

## MODES IN MICROSTRIP REGION

It is well known that the mode functions in a parallel-plate waveguide may be determined from a transverse equivalent network, as shown in Fig. 2, together with the waveguide structure. Here,  $\kappa_i$  is the propagation constant and  $Z_i$  is wave impedances of the transmission line representing the  $i^{\text{th}}$  medium, where the subscript  $i$  may stand for either "a" or "m" to denote the air or metal region;  $\kappa_0$  is the phase constant of plane wave in free space;  $\epsilon_i$  is the dielectric constant of the  $i^{\text{th}}$  (air or metal) region; and  $\epsilon_{\text{eff}}$  is the effective dielectric constant of a guided wave supported by the structure. The resonance condition of the transverse network defines the dispersion relation of the waveguide. For example, the dispersion relation is given by

$$Z_{\text{air}} \tan k_z w_a - Z_m \cot k_z w_m = 0 \quad (1)$$

for TE and TM symmetric modes and a similar equation can be obtained for the antisymmetric modes.

Consider the general case where both air and metal regions are present,  $w_a \neq 0$  and  $w_m \neq 0$ . In the limit of infinite conductivity of the metal, the air region itself becomes an ideal parallel-plate waveguide with a uniform medium. In this case, the energy of a mode is totally within the air region. When the conductivity of the metal region is very high, but finite, most of the energy of a guided mode will remain in the air region, with an evanescent tail penetrating into the metal. For simplicity, such a mode will be referred to as an air mode. The class of air modes has been well understood and easily accepted. With the metal taken as a perfect conductor, the fields can not exist inside the metal and it is irrelevant to talk about modes in a metal layer. To see the effect of the metal as a good conductor here, it is necessary to look for another class of modes which are less understood in the past.

In the extreme case where the air region is absent, we have a parallel-plate waveguide and the transverse propagation constant in the metal is given, for an  $n^{\text{th}}$  TE or TM mode, by

$$k_m w_m = (n - \frac{1}{2})\pi, \quad (2)$$

If such an extreme case is taken as an unperturbed structure, the presence of an air region can then be regarded as a small perturbation. Thus, a metal mode should have an almost real transverse propagation constant as in the case of the unperturbed waveguide. In view of (1), the transverse propagation constant of the air region must have a very large imaginary part. This means that the fields of each metal mode vary sinusoidally in the metal region and decay exponentially at a very fast rate in the air region. Therefore, the energy of the mode is distributed mainly in the metal region, with an evanescent tail penetrating into the air region. For simplicity, a mode with most of its energy in the metal region will be referred to as a metal mode.

To invoke the concept of small perturbation for the analysis of metal modes, the dispersion relation in (1) can be manipulated to yield

$$k_m w_m = \begin{cases} (n - \frac{1}{2})\pi - p_m, & \text{for TE modes} \\ n\pi - p_m, & \text{for TM modes} \end{cases} \quad (3)$$

for the case of symmetric bisection. Comparing (3) with (2), we see that the perturbation of the air region on a metal mode depends critically on the thickness of the air region for TM modes, but not for TE modes. Physically, when the thickness of the air region is vanishingly small, the upper perfect electric conductor is sitting directly on the metal and has the effect of a perfect electric conductor on a mode in the metal region. On the other hand, when the air region is sufficiently thick, the effect of the upper conductor is negligible because the fields are evanescent in the air region. Since the wave impedance of a TM mode is very large, an air region of large thickness has the effect of a perfect magnetic conductor, instead of a perfect electric

conductor, sitting directly on top of the metal. For the case of interest here, the unperturbed waveguide is taken as a metal layer with a semi-infinite air region above it; the concept of small perturbation is still applicable, as invoked in arriving at analytic expressions given in (3).

With the two types of modes systematically enumerated above, the boundary-value problem for the structure depicted in Fig. 2 can then be solved by the method of mode matching at the three interfaces separating the constituent regions, as in the case of dielectric strip waveguides[1,2].

#### REFERENCES

- [1] S.T. Peng and A.A. Oliner, IEEE Trans. Microwave Theory and Tech., 1981, vol.MTT-29, pp.843-855.
- [2] A.A. Oliner, S.T. Peng, T.I. Hsu and A. Sanchez, IEEE Trans. Microwave Theory and Tech., 1981, vol.MTT-29, pp.855-869.

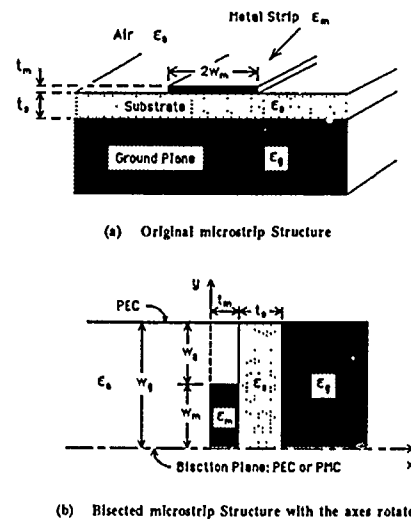


Fig. 1. Geometrical configuration of microstrip line

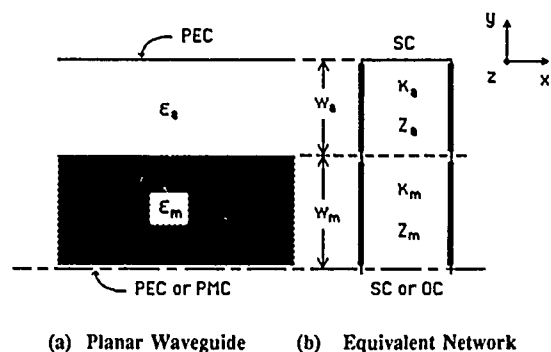


Fig. 2 Planar waveguide and its transverse network

# FINLINE-DISPLACEMENT ISOLATOR —THE THEORETICAL AND EXPERIMENTAL INVESTIGATION

Jifu Huang and Quanrang Yang

Southeast University  
Nanjing, China

**ABSTRACT**—In this paper, finline-displacement isolator with partial-heighted ferrite slab has been analysed. The finline isolator is fabricated. The measured band width at 8 mm waveband is 5 GHz.

## I. INTRODUCTION

With the development of millimeter wave technique, a number of passive and active integrated components have been investigated. However, relatively little attention has been paid to the development of nonreciprocal devices such as circulators and isolators. In many communication and radar systems, the millimeter wave integrated isolator is one of the key devices. The theoretical investigation of finline isolator has been published.<sup>[1-4]</sup> But most of the papers investigated only simple models of isolator with full-heighted ferrite slabs. In this paper finline-displacement isolator with partial-heighted ferrite slab has been analysed. the direction of magnetized field is parallel to the broad side of ferrite slab.

A set of curves of the relations between propagation constants and parameters of ferrite material and isolator configuration are given. The theoretical prediction agrees well with experimental results. The measured band width of a finline-displacement isolator at 8 mm waveband is 5 GHz.

## II. THEORETICAL INVESTIGATION

The waveguide structure with the coordinate system is shown in Fig.1. When an external d.c. magnetic field is applied in x-direction, the permeability of ferrite is the tensor permeability.

$$\hat{\mu} = \begin{bmatrix} \mu_0 & 0 & 0 \\ 0 & \mu_1 & -j\mu_2 \\ 0 & j\mu_2 & \mu_1 \end{bmatrix} \quad (1)$$

First, we analyse the structure for  $0 < y < h_2$  in Fig.1. The hybrid modes of the region are assumed to be classified into  $E_{pq}$  and  $H_{pq}$ . It is noted here that only  $E_{pq}$  modes are of interest because  $H_{pq}$  modes do not exhibit nonreciprocity. The analysis is based on the modified effective dielectric constant method for the structure containing ferrite layer.

The structure for  $0 < y < h_2$  is divided into three regions. Applying the transverse resonance method (TRM), each region replaces with an effective medium in the y-direction. We have

$$\epsilon_{e2} = \epsilon_f - (k_f/k_0)^2 \quad (2)$$

$$\epsilon_{e1} = \epsilon_{e3} = \epsilon_1 - (k_1/k_0)^2 \quad (3)$$

Applying the TRM again in the x-direction, we obtain

$$\beta_z^2 = \epsilon_{e1} k_0^2 - k_{x1}^2 = \epsilon_{e2} k_0^2 - k_{x2}^2 \quad (4)$$

The normal structure is replaced with a hypothetical medium in which the effective dielectric constant is

$$\epsilon_{eff} = (\beta_z/k)^2 \quad (5)$$

Next, the structure in Fig.1 is replaced by a shield slot line structure. Hence, the analysis procedure is based on Galerkin's method applied in the Fourier transform domain. The characteristic equation is obtained by employing spectral domain admittance approach as usual.

$$\begin{bmatrix} G_{xx} & G_{xz} \\ G_{zx} & G_{zz} \end{bmatrix} \begin{bmatrix} \tilde{E}_x \\ \tilde{E}_z \end{bmatrix} = \begin{bmatrix} \tilde{J}_x \\ \tilde{J}_z \end{bmatrix} \quad (6)$$

The propagation constants are calculated by putting the matrix determinant equal to zero.

The accuracy of the equation solutions has been checked. Curves in Fig.2 show the dispersion characteristics of the dominant mode propagating in the positive and negative z-directions. With introduction of a dielectric layer, a larger nonreciprocity has been achieved. Fig.3 shows curves for the differential phase shift as a function of finline substrate location in the waveguide wall. It is worthwhile to note that every curve takes its peak at the approximately same  $h_1$  value.

## III. EXPERIMENTAL FINLINE-ISOLATOR

Starting with the knowledge of the theoretical analysis of the ferrite loaded finline, several cross sectional structures for the finline isolator using a ferrite slab are investigated experimentally. Finally, the sizes of structure are as

follows: The finline is fabricated on RT/Duroid 5880 dielectric medium with a thickness of 0.25 mm. The thickness of the ferrite slab is 1.2 mm. Whereas the thickness of dielectric spacer is 1.4 mm. Thin resistive sheet is placed on the left side in the ferrite slab. The total length of the ferrite slab is 17.8 mm. The value of the d.c. magnetic field  $H_0$  is 7300 Oe. Fig. 4 shows the measured results of the forward and the reverse loss.

#### IV. CONCLUSIONS

Finline structures with partial-heighted ferrite slabs are studied for theory and experiment. It is found that an optimum

condition exists for the dielectric layer and the finline location in the waveguide. Furthermore, it has been shown that material parameters of dielectric spacer and ferrite samples need to be chosen for the design procedure.

#### REFERENCES

- [1] A.Beyer, K.Solback, IEEE MTT-29, Dec. 1981, pp. 1344-1348.
- [2] F.Lang, AEÜ, No.3, 1982, PP. 95-100.
- [3] A.Beyer, IEE Proceedings, Part H, July 1985, PP. 244-258.
- [4] D.Guan, R. Hoffmann, Electronics Lett. 13 March 1986, Vol. 22, No.6, PP. 298-299.

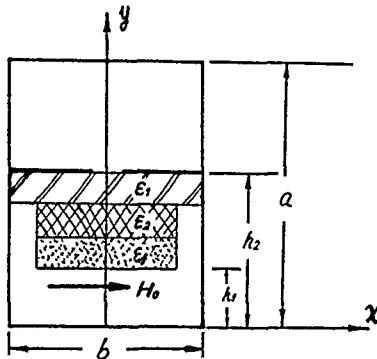


Fig.1 Cross-sectional view of the finline isolator.

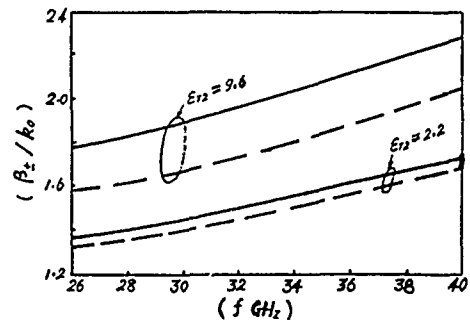


Fig.2 Dispersion characteristics of the dominant mode in the z direction.

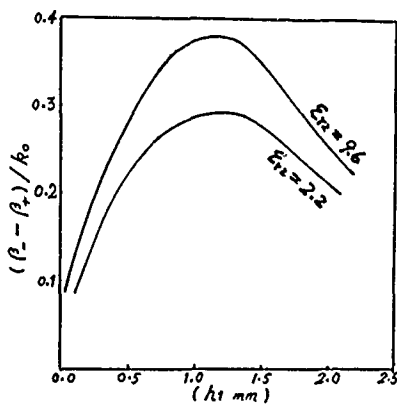


Fig.3 Differential phase shift versus distance  $h_1$ .

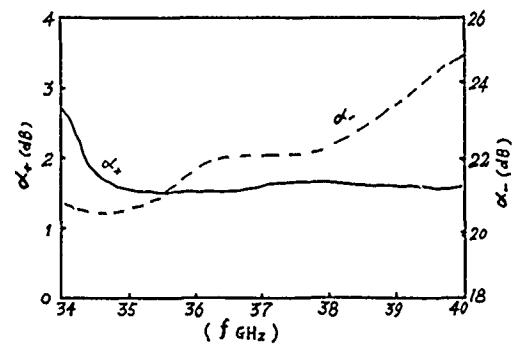


Fig.4 Characteristics of the finline ferrite isolator.



## DESIGN AND PERFORMANCE OF 20 AND 45 GHZ MMIC LANGE COUPLERS

Jack E. Wallace and Grant A. Ellis

High Technology Center  
Boeing Electronics Company  
Seattle, Washington

### ABSTRACT

Experimental results are presented for GaAs MMIC Lange coupler designs in both the 15 to 25 GHz and 33 to 50 GHz frequency ranges. Coupler insertion loss, return loss, isolation, and differential insertion phase are included.

### INTRODUCTION

This paper describes MMIC Lange couplers that have been built and tested for use in the 20 and 45 GHz frequency ranges. Performance of Lange couplers fabricated on semi-insulating GaAs substrates has been previously documented (1), (2). With the aid of improved measurement capability (3) and on-wafer thru-reflect-line (TRL) calibration standards, it was possible to make precise coupler measurements to 50 GHz without de-embedding the microstrip transitions or accounting for test fixture losses.

### DESIGN

Six Lange coupler designs were built and tested. The physical parameters of each coupler including coupler length, line and gap widths, and metallization thickness are summarized in Table 1. Substrate thickness was 100  $\mu\text{m}$ . Line crossovers were implemented with 5.0  $\mu\text{m}$  wide air bridges. The transition from the coupler to 50 $\Omega$  microstrip was a 45 degree bevel for couplers 1, 2, 4, and 5 as shown in Figure 1a. The transition for couplers 3 and 6 was a stepped transition as illustrated in Figure 1b (50  $\mu\text{m}$  length of 70 $\Omega$  microstrip and a 45 degree bevel to 50 $\Omega$  microstrip). Capacitors were placed across each end of the coupling section of coupler 4 (25 fF) and coupler 6 (15fF).

### PERFORMANCE

The key to accurate coupler measurements was an accurate calibration with the measurement reference plane located just prior to the microstrip to coupler transition. As shown in Figure 1, couplers are accessed through ground-signal-ground probe patterns. Three different coupler layouts were required for each design since only 2-port measurements were possible. Two assumptions were made to generate a 4-port s-parameter matrix from the three sets of 2-port measurements. The unused terminated ports must be

terminated with 50 $\Omega$  loads and the coupler must be symmetrical (i.e.,  $S_{11}=S_{22}=S_{33}=S_{44}$ ;  $S_{12}=S_{21}=S_{34}=S_{43}$ ;  $S_{23}=S_{32}=S_{41}=S_{14}$ ; and  $S_{13}=S_{31}=S_{24}=S_{42}$ ).

Plots of measured insertion loss, isolation, and return loss are shown in Figures 2 and 3 for couplers 1 and 4 respectively. These data represent the best performance in each frequency band. The loss at 20 GHz for coupler 1 was 1.3 dB compared to 1.7 dB for couplers 2 and 3. The return loss for coupler 1 was 2 to 4 dB better than that for couplers 2 or 3. The isolation of couplers 1 and 2 was 3 dB better than the isolation of coupler 3. The measured coupler characteristic impedances were 61 $\Omega$  for coupler 1 and 65 $\Omega$  for couplers 2 and 3. At 45 GHz, couplers 4 and 5 exhibited very similar performance except that coupler 4 had better return loss. The loss at 45 GHz for couplers 4 and 5 was 1.2 dB compared to 1.7 dB for coupler 6. The isolation of couplers 4 and 5 was 17 dB compared to 14 dB for coupler 6. The measured coupler characteristic impedances were 58 $\Omega$  for coupler 4 and 64 $\Omega$  for couplers 5 and 6.

Figures 4 and 5 illustrate the differential phase between the through and coupled ports for all six couplers. The phase offset at 20 GHz was 97 degrees for couplers 1 and 2 and 101 degrees for coupler 3. The phase offset at 45 GHz was 95 degrees for couplers 4 and 5 and 99 degrees for coupler 6.

### CONCLUSIONS

Accurate measurements of several coupler designs have been presented. Insertion loss and coupler impedance were higher than predicted and isolation was lower than predicted using commercial CAD software. This can be explained by the metallization thickness which was approximately one skin depth at 20 GHz. Increasing conductor line width and thickness should reduce the insertion loss (as suggested in (2)) and optimize the coupler characteristic impedance. The coupler should be designed with a coupler impedance which is lower than the system impedance by an amount corresponding to the skin effect losses. The phase offset from phase quadrature has not been fully evaluated, but (4) suggests that it is due to asymmetrical configuration of the air bridge crossovers.

## ACKNOWLEDGMENTS

The authors are grateful to G. Fitzsimmons and M. Florian for their valuable discussions and interest during this work.

## REFERENCES

- (1) R. C. Waterman, W. Fabian, R. A. Pucel, Y. Tajima, and J. L. Vorhaus, GaAs Monolithic Lange and Wilkinson Couplers, IEEE Trans. Elec. Dev., 1981, vol. ED-28, pp. 212-216.
- (2) M. Kumar, S. N. Subbarao, R. J. Menna, and H. Huang, Monolithic GaAs Interdigitated Couplers, IEEE Trans. MTT, 1983, vol. MTT-31, pp. 29-32.
- (3) D. Harvey and M. Virtue, Millimeter Wave TRL Calibration with a Modified Test Set, to be published Microwaves and RF, Oct. 1988.
- (4) C. Y. Ho and L. Moser, Symmetrical Coupler Reduces Phase Error, Microwaves, Apr. 1981, pp. 82-84.

Coupler #	Line Width ( $\mu\text{m}$ )	Line Spacing ( $\mu\text{m}$ )	Line Thickness ( $\mu\text{m}$ )	Coupler Length ( $\mu\text{m}$ )	Discontinuity Compensation	Capacitive Compensation
1	5.5	7.0	0.5	1300.	No	No
2	4.5	6.5	0.5	1300.	No	No
3	4.5	6.5	0.5	1300.	Yes	Yes (25 fF)
4	5.5	7.0	0.5	600.	No	No
5	4.5	6.5	0.5	600.	No	No
6	4.5	6.5	0.5	600.	Yes	Yes (15 fF)

Table 1. Physical Parameters for 6 Lange Coupler Designs

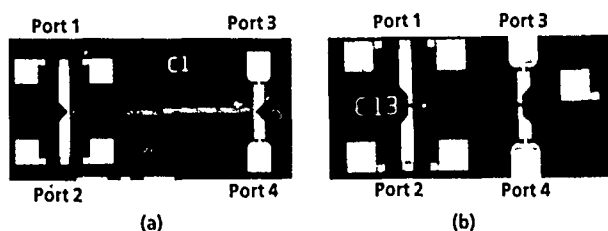


Figure 1. GaAs MMIC Lange Couplers for Use at (a) 20 GHz and (b) 45 GHz

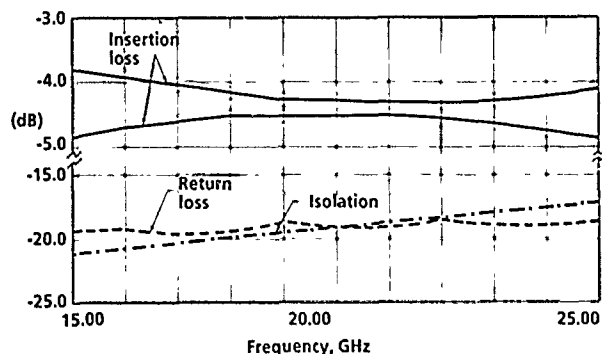


Figure 2. Insertion Loss, Isolation, and Return Loss for Coupler 1

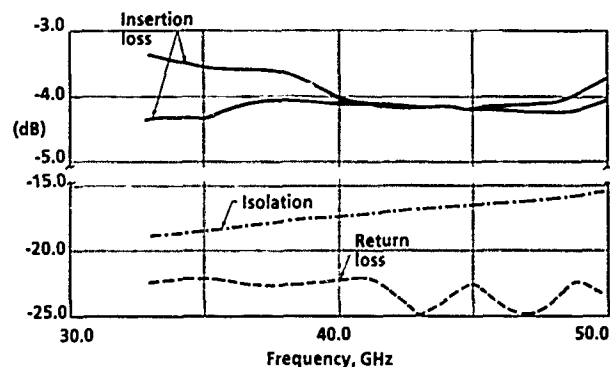


Figure 3. Insertion loss, Isolation, and Return Loss for Coupler 4

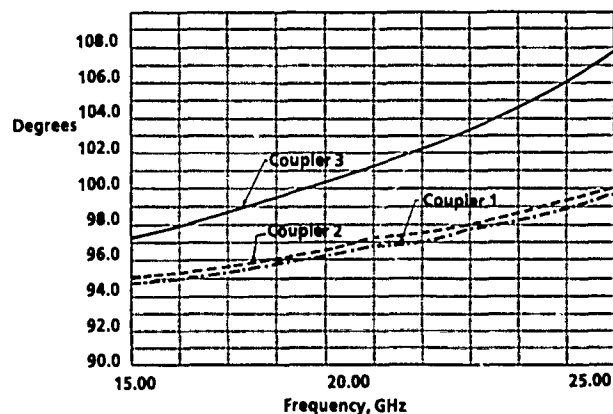


Figure 4. Differential Insertion Phase for Couplers 1, 2, and 3

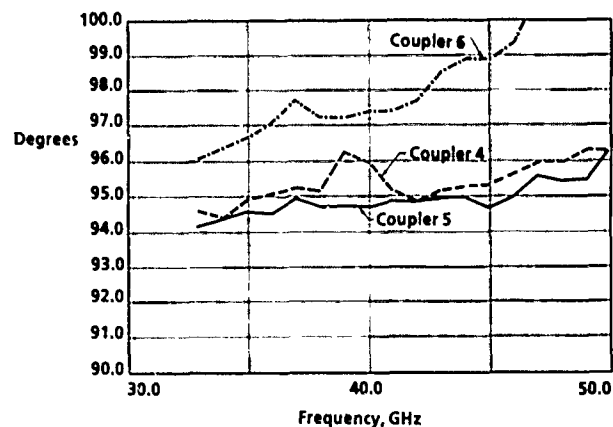


Figure 5. Differential Insertion Phase for Couplers 4, 5, and 6

## FAR IR AND SURFACE LAYERS (REVIEW)

A. Hadni and X. Gerbaux

University of Nancy 1

BP 259 54509 Vandoeuvre les Nancy France

At a solid surface, the atoms rearrange with respect to their periodic position such as to establish equilibrium with the adjacent vacuum (1-2). Rearrangement seems to go beyond the atomic scale for polar materials and experimental hints have been given by different methods (3-4-5-6-7-8-9-10).

Far IR spectroscopy may also be considered for this difficult problem since it is very sensitive to small modifications in the crystal structure. Far IR data obtained at low temperature where the absorption lines can be very sharp, will be discussed for some hydrogen bonded crystals: TGS, TGSe, GASH and Rochelle Salt (11-12-13).

## REFERENCES

- (1) T.P. Martin, Phys. Rev. B, 1970, vol.1, p. 3480.
- (2) K. Binder and P.G. Hohenberg, Phys. Rev. B, 1974, vol.9, p. 2194.
- (3) U.T. Höchli, J. Phys. C, 1975, vol.8, p. 3896.
- (4) W.N. Lawless, Phys. Rev. B, 1976, vol.14, p. 134.
- (5) W.N. Lawless, Phys. Rev. B, 1981, vol.23, p. 2421.
- (6) N.I. Agladze, B.P. Antonyuk, V.M. Burlakov, E.A. Vinogradov and G.N. Zhizhin, Sov. Phys. Solid State, 1981, vol.2-3, p. 1911.
- (7) P. Marquardt and H. Gleiter, Phys. Rev. Lett., 1982, vol.48, p. 1423.
- (8) U.T. Höchli and H. Rohrer, Phys. Rev. Lett., 1982, vol.48, p. 188.
- (9) A. Hadni and R. Thomas, Ferroelectrics, 1984, vol. 59, p. 221.
- (10) J.F. Scott, Ming-Sheng Zhang, R. Bruce Godfrey, C. Araujo and L. Mc Millan, Raman Spectroscopy of Submicron  $KNO_3$  films, Phys. Rev. B, 1987, vol. 35, p. 4044.
- (11) X. Gerbaux, A. Hadni and A. Kitade, Phys. Status Solidi a, 1985, vol.88, p. 165.
- (12) X. Gerbaux and A. Hadni, Comptes Rendus Acad. Sc, Paris, 1988, vol.307, p. 745.
- (13) A. Hadni and X. Gerbaux, J. Phys. C, 1988, vol. 21, p. 2045.

# CHARACTERIZATION OF THE INFRARED AND FAR-INFRARED PROPERTIES OF SAPPHIRE AND QUARTZ

Michael E. Thomas and Richard I. Joseph

The Johns Hopkins University Applied Physics Laboratory  
Laurel, Maryland 20707-6080

George J. Simonis and Michael Stead

Harry Diamond Laboratories, 2800 Powder Mill Road  
Adelphi, Maryland 20783-1197

## ABSTRACT

High-quality room-temperature data have been obtained on single-crystal sapphire and quartz in the far infrared ( $\nu = 50\text{--}200\text{ cm}^{-1}$ ) and found to follow the expected  $\nu^2$  variation (based on the fluctuation-dissipation theorem, e.g., Huber and Van Vleck). An extrapolation to lower frequencies following the  $\nu^2$  curve is found to be consistent with experimental data down to  $1\text{ cm}^{-1}$ . It has been physically argued in the past that the absorption mechanism in this region arises from broad phonon difference bands. We find that a substantial fraction of the observed absorption is consistent with a red-wing extrapolation from the dominant one-phonon modes seen in the reflection spectrum. A combination of these two mechanisms is believed to account for the smooth falloff in absorption that is observed.

## INTRODUCTION

The ability to grow high-quality sapphire and quartz makes these two materials desirable for many applications in the infrared and far infrared. A simple, but descriptive, model of multiphonon sum bands has been developed to describe infrared absorption in the region of transparency for these materials and others (1,2) on the blue side of the lattice vibrational bands. However, the far-infrared window region (red side of the lattice vibrational bands) does not in general lend itself to a simple description. Many materials exhibit extrinsic absorption features or pronounced multiphonon difference band absorption. Because of the purity of sapphire and quartz single crystals, virtually no extrinsic absorption has been experimentally observed, and difference bands are broad and show no structure. Because of this, a simple approach is taken to characterize the absorption coefficient from  $1\text{ to }100\text{ cm}^{-1}$  for single-crystal sapphire and quartz.

On the basis of theoretical work of Van Vleck and Huber (3) the absorption coefficient, as the frequency becomes small, goes to zero as  $\nu^2$  ( $\nu$  is a wave number with units  $\text{cm}^{-1}$ ) multiplied by the line shape function. A simple  $\nu^2$  falloff will dominate in two cases. The first is the far red wing of an absorption band (4) and the second is for broad line shape functions featuring very little frequency dependence throughout a band. It is our contention that these conditions are met for sapphire and quartz in the far infrared, because the absorption is dominated by intrinsic processes. Thus, the simple formula

$$\kappa(\nu) = A\nu^2 \quad (1)$$

can be used to represent experimental data on these two materials.

## BACKGROUND

Specifically, we will consider the far red wing and the difference bands of the lattice vibrational bands that occur in the far

infrared. A phenomenological one-phonon model is used to represent the vibrational bands in terms of the relative complex permittivity,  $\epsilon(\nu)$ :

$$\epsilon(\nu) = \epsilon_\infty + \sum_j \frac{\Delta\epsilon_j \nu_j^2}{\nu_j^2 - \nu^2 + i\gamma_j\nu} \quad (2)$$

where  $\Delta\epsilon_j$ ,  $\gamma_j$ ,  $\nu_j$ , and  $\epsilon_\infty$  are the  $j$ th mode strength, line width, transverse optical frequency, and high-frequency permittivity, respectively. This model satisfies the Kramers-Kronig relation and accurately represents experimental reflection data and the index of refraction. The absorption coefficient is related to the complex permittivity by the formula

$$k(\nu) = 4\pi\nu \text{Im} [\sqrt{\epsilon(\nu)}] \quad (3)$$

It is straightforward to show that

$$k(\nu \rightarrow 0) = B\nu^2 \quad (4)$$

based on this formula. Thus the far-red-wing absorption of the lattice vibrational bands has the correct theoretical frequency dependence using this model. The parameters in the model have been experimentally determined for sapphire (5) and quartz (6) for both the ordinary and extraordinary rays. The  $B$  coefficient can be computed on the basis of this work. However, it must be emphasized that this is a phenomenological model that contains some correct physics but not everything needed to make a definitive statement on the far red wing of the lattice vibrational bands.

The difference phonon bands in these materials are broad with no experimentally observed structures. Thus, they also feature a  $\nu^2$  falloff as argued earlier. The difference bands are at least two-phonon processes; as the number of phonons in an interaction increases, so does the width of the difference band. In summary, if the difference bands are broad structures, then the net absorption coefficient (the sum of far wing and difference bands absorption) must follow a  $\nu^2$  falloff as  $\nu \rightarrow 0$ . This will occur until the coefficient gets so low that minor defects and impurities become important or the difference band terminates.

An extensive experimental database exists for sapphire and quartz between  $50\text{ and }200\text{ cm}^{-1}$  (7,8,9). The data follow a  $\nu^2$  falloff as expected, with the one exception of the ordinary ray of quartz that features a minor absorption band at  $128\text{ cm}^{-1}$ . In fact Roberts and Coon (7) fit their data to a function of the form as expressed by Eq. (1) based on Eq. (2). Of course, their parameters are not consistent with the work on the one-phonon bands by Barker (5) and Spitzer and Kleinman (6) because they have not accounted for difference bands.

## RESULTS

The first point of this paper is that the formula used by Roberts and Coon (7) can be extrapolated below  $50\text{ to }1\text{ cm}^{-1}$

with reasonable confidence. This is illustrated in Figs. 1 and 2 for sapphire and quartz, respectively. Recent experimental data taken below  $20 \text{ cm}^{-1}$  on the ordinary rays of sapphire and quartz are also presented on the plots (10-14). The experimental data points from Birch represent a mean value based on several measurements of the same sample by different laboratories

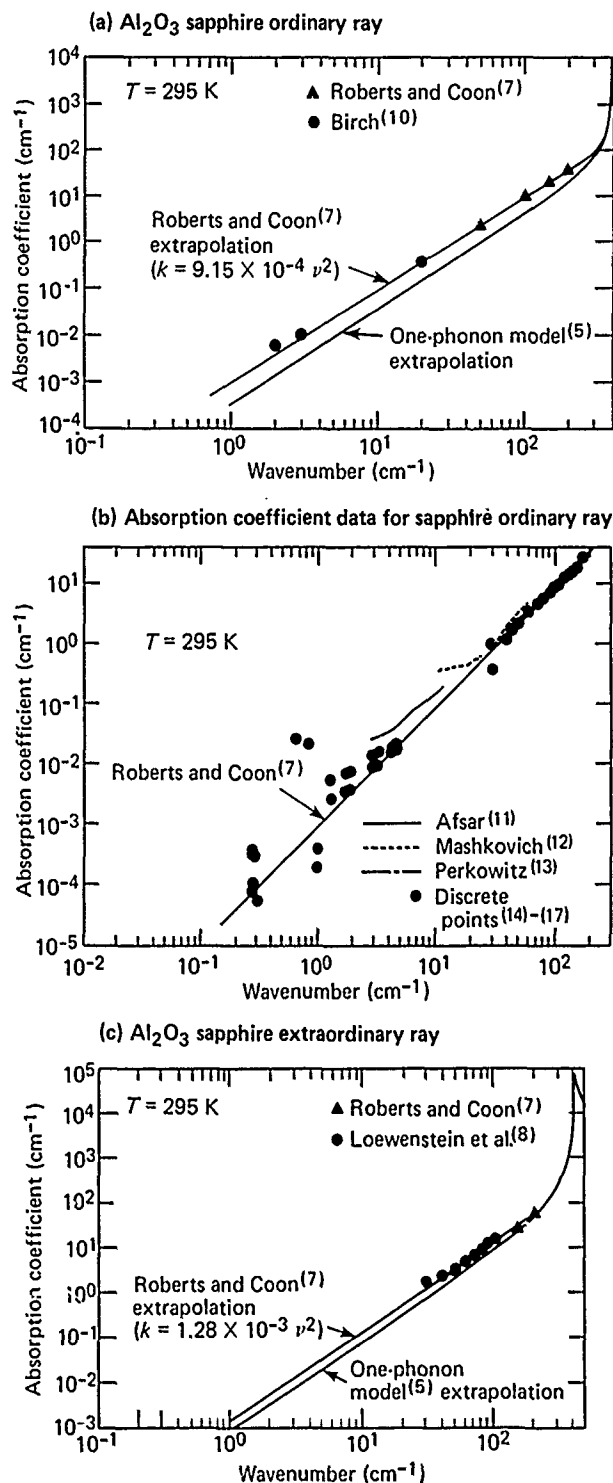


Figure 1

The far-infrared absorption coefficient of sapphire:  
(a) ordinary ray, (b) ordinary ray, (c) extraordinary ray.

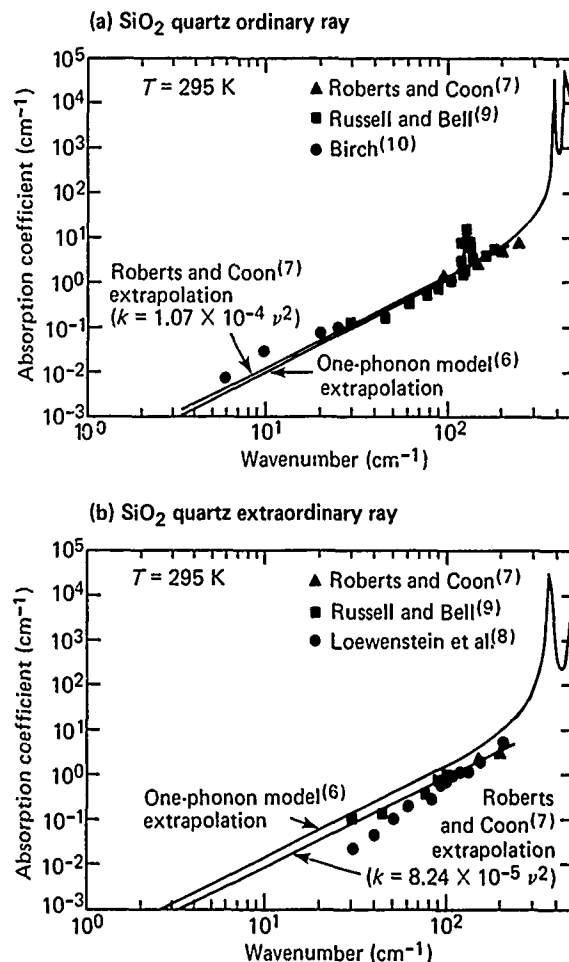


Figure 2

The far-infrared absorption coefficient of quartz:  
(a) ordinary ray, (b) extraordinary ray.

(10). The data support the extrapolation. The large error in data is demonstrated by the scatter, yet the  $\nu^2$  curve is representative of the mean result (see Fig. 1b especially). Also, appreciating the difficulty in collecting accurate data, one can see the need for knowing the frequency dependence of the absorption coefficient in this region. Unfortunately, no experimental data exist for the extraordinary rays of sapphire and quartz.

The second point is that a substantial portion of the absorption that is observed in the far infrared is coming from the red wing of the one-phonon bands (Figs. 1a, 1c, 2a and 2b). In the case of sapphire, roughly 50% of the absorption is from the red wing, on the basis of the one-phonon model of Barker for both the ordinary and extraordinary rays. In the case of quartz, the ordinary ray is dominated by the red wing of the one-phonon bands, as expected, because the one-phonon bands are roughly an order of magnitude weaker than sapphire and thus the difference bands in quartz should be correspondingly weaker. However, the one-phonon model red wing overpredicts the absorption for the extraordinary ray of quartz, indicating a problem possibly in the one-phonon model parameters but also in the model itself. Thus the one-phonon red-wing extrapolations are suggestive but not conclusive. It is clear that both the difference bands and the one-phonon far wings contribute in this region.

## CONCLUSIONS

A case is made for a simple physical model of far-infrared absorption for sapphire and quartz based on the fluctuation-dissipation theorem and detail balance. This allows extrapolations based on accurate measurements ( $50\text{--}200\text{ cm}^{-1}$ ). Since only transmission techniques have been used thus far, it is strongly recommended that calorimetry techniques using high-power microwave and millimeter wave sources be attempted in the future. Such techniques will greatly improve the accuracy of data in the near-millimeter region.

## REFERENCES

- (1) M. E. Thomas, R. I. Joseph, and W. J. Tropf, "Infrared Transmission Properties of Sapphire, Spinel, Yttria and ALON as a Function of Temperature and Frequency," *Appl. Opt.*, 1988, vol. 27, pp. 239-245.
- (2) M. E. Thomas and R. I. Joseph, "A Comprehensive Model for the Intrinsic Transmission Properties of Optical Windows," *Proc. SPIE*, 1988, vol. 929, *Infrared Optical Materials VI*, pp. 87-93.
- (3) J. H. Van Vleck and D. L. Huber, "Absorption, Emission, and Linebreadths: A Semihistorical Perspective," *Rev. Mod. Phys.*, 1977, vol. 49, pp. 939-959.
- (4) G. Birnbaum, "The Shape of Collision Broadening Lines from Resonance to the Far Wings," *J. Quant. Spectrosc. Radiat. Transfer*, 1979, vol. 21, pp. 597-607.
- (5) A. S. Barker, Jr., "Infrared Lattice Vibrations and Dielectric Dispersion in Corundum," *Phys. Rev.*, 1963, vol. 132, pp. 1474-1484.
- (6) W. G. Spitzer and A. Kleinman, "Infrared Lattice Bands of Quartz," *Phys. Rev.*, 1961, vol. 121, pp. 1324-1335.
- (7) S. Roberts and D. D. Coon, "Far-Infrared Properties of Quartz and Sapphire," *J. Opt. Soc. Am.*, 1962, vol. 52, pp. 1023-1029.
- (8) E. V. Loewenstein, D. R. Smith, and R. L. Morgan, "Optical Constants of Far Infrared Materials. 2: Crystalline Solids," *Appl. Opt.*, 1973, vol. 12, pp. 398-406.
- (9) E. E. Russell and E. E. Bell, "Measurements of the Optical Constants of Crystal Quartz in the Far Infrared with the Asymmetric Fourier-Transform Method," *J. Opt. Soc. Am.*, 1967, vol. 57, pp. 341-348.
- (10) J. R. Birch, "Errors in NMM Wavelength Dielectric Measurements: A Discussion of a Recent International Measurement Intercomparison," *Proc. Twelfth Int. Conf. on Infrared and Millimeter Waves, 14-18 Dec 1987*, J. R. Temkin, ed., IEEE Cat. No. 87CH2490-1.
- (11) M. N. Afsar and K. J. Button, *Digest of Millimeter and Submillimeter Wave Materials*, 1983, U.S. Army Research Office contract DAAG-29-81-K-009 and Dept. of Energy contract W-7405-ENG-26.
- (12) M. D. Mashkovich and A. I. Demenshina, *Sov. Phys. Soli State*, 1965, vol. 7, pp. 1323-1327.
- (13) W. B. Cook and S. Perkowitz, Conf. Digest, Eighth Int. Conf. on Infrared and Millimeter Waves, 12-17 Dec 1983, IEEE Cat. No. 83CH1917-4.
- (14) W. W. Ho, "Millimeter Wave Dielectric Property Measurement of Gyrotron Window Materials," *Program Status Report, June-July 1984*, Dept. of Energy Subcontract Purchase Order 11Y-51926C.
- (15) E. E. Russell and E. E. Bell, "Optical Constants of Sapphire in the Far Infrared," *J. Opt. Soc. Am.*, 1967, 57, pp. 543-544.
- (16) R. E. Jaeger and E. M. Gyorgy, *Rev. Sci. Instr.*, 1970, pp. 820-823.
- (17) W. B. Westphal, *Dielectric Constant and Loss Data*, Final Report, Jan 1977-May 1980, AFML-TR-74-250, Part IV.

# SOFT MODE SPECTROSCOPIC STUDY OF FERROELECTRIC PHASE TRANSITION IN $\text{Li}_2\text{Ge}_7\text{O}_{15}$

Mitsuo WADA, Akikatsu SAWADA<sup>+</sup> and Yoshinori ISHIBASHI<sup>+</sup>

Department of physics, Faculty of Liberal Arts,  
Shinshu University, Matsumoto 390, JAPAN  
and

<sup>+</sup>Synthetic Crystal Research Laboratory, Faculty of Engineering  
Nagoya University, Nagoya 464, JAPAN

## 1 Introduction

Far-infrared and submillimeter wave measurements are very important in the study of ferroelectric phase transitions because the soft mode which concerns the ferroelectricity should be infrared active both in the paraelectric and ferroelectric phases.

Recently, in some ferroelectrics the critical slowing down of the dielectric constant has been observed as well as the soft phonon mode. In order to interpret the dynamics of this kind of phase transition, the following two models should be proposed:

A) There is only one phonon which concerns the transition. As transition temperature is approached, the soft phonon becomes overdamped and then in the vicinity of  $T_c$  becomes a pseudo-relaxational mode.

B) There exists a relaxational mode as well as the soft phonon. Firstly, the frequency of the phonon decreases as  $T_c$  is approached, by the coupling effect with the soft phonon the relaxational mode becomes soft near  $T_c$ .

Ferroelectrics lithium heptagermanate  $\text{Li}_2\text{Ge}_7\text{O}_{15}$  (abbreviated to LGO) undergoes the phase transition such as mentioned above at  $T_c = 283.5\text{K}^{1-3}$ . The space group in paraelectric phase belongs to  $D_{2h} - \text{Pbcn}$  and that in the ferroelectric phase to  $C_{2v} - \text{Pbc2}_1$  with the spontaneous polarization along the c-axis. The size of the unit cell does not change at the transition ( $Z=4$ ), so that the soft mode should locate at Brillouin zone center. From the symmetry consideration of the space group, the soft mode should be both infrared and Raman active in the ferroelectric phase, whereas it should be infrared active and Raman inactive in the paraelectric phase.

## 2 Experimental results

The details of the Raman scattering<sup>2-5)</sup> and far-infrared measurements<sup>6,7)</sup> have been previously reported. Fig.1 shows spectra observed for the  $-a+c(bb)-a-c$  geometry at various temperatures, where the  $A_1$  pure LO modes propagating along the polar c-axis were observed. The frequency of lowest-lying mode at  $43.5\text{ cm}^{-1}$  at 201 K decreases as  $T_c$  is approached

from below. This behaviour is very similar to that of the pure TO mode. The LO-TO splitting of the soft phonon is smaller than  $1.0\text{ cm}^{-1}$  in the temperature region below 273 K.

Figure 2 shows the FTIR transmission spectra at various temperatures measured for the orientation where the electric field  $E$  is parallel to the polar c-axis. The lowest frequency mode should be taken as the soft phonon corresponding to that observed by Raman scattering. The frequency, damping constant and oscillator strength for the soft mode at 553 K are  $28\text{ cm}^{-1}$ ,  $7.5\text{ cm}^{-1}$  and 0.05, respectively. The oscillator strength of the soft phonon is very small and its contribution to the dielectric constant does not exceed 0.1 even at  $T_c$ .

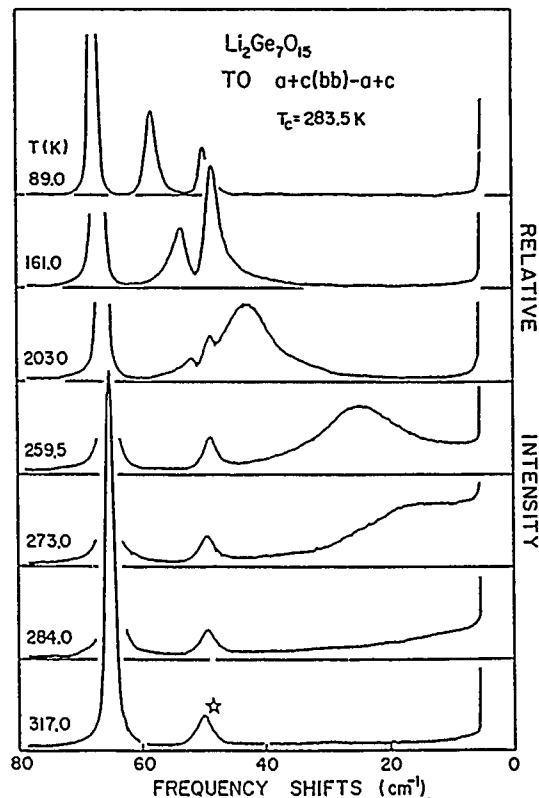


Fig.1 Raman spectra of LGO at various temperatures.

Figure 3 shows the temperature dependence of the frequencies of the soft phonons and the hard modes obtained by Raman scattering, MP-FTIR, and BWO measurements.<sup>2-7)</sup>

#### 4 Discussion

In the paraelectric phase the  $B_{1u}$  soft phonon mode and in the ferroelectric phase the corresponding totally symmetric soft phonon mode have been observed. Their small oscillator strength and small contribution to the dielectric constant suggest that there must be a relaxation mode which should concerns the phase transition as well as the soft phonon mode.

The critical slowing-down has been observed by the dielectric dispersion measurements. The relaxational frequency is about  $0.03 \text{ cm}^{-1}$ .<sup>8)</sup> In addition, the existence of the relaxational mode is suggested in terms of the Brillouin scattering study.<sup>9)</sup>

Consequently, the ferroelectric phase transition of LGO is associated with the polar  $B_{1u}$  soft phonon mode, and in the vicinity of the transition point the character of soft mode is "transferred" from the phonon to the relaxational mode.

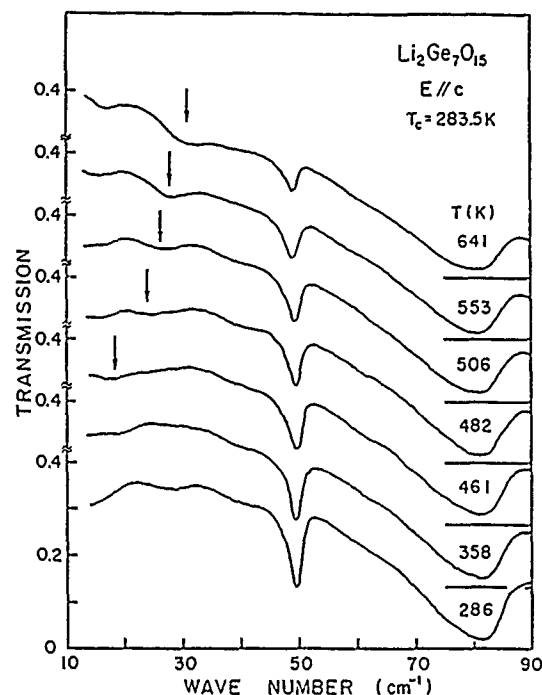


Fig.2 Far-infrared transmission spectra of LGO at various temperatures.

#### Acknowledgement

The authors wish to thank M.Horioka, A.Sakai, T.Yagi, Y.Morioka and Y. Iwata for many fruitful and helpful discussions. This work was partially supported by Misuzu Matsuko Foundation.

#### References

- 1) Haussuhl S., Wallrafen F., Recker K. & Eckstein J.: Z. Kristallogr. 153 (1980) 329.
- 2) Wada M., Sawada A. & Ishibashi Y.: J. Phys. Soc. Jpn. 50 (1981) 1811.
- 3) Wada M. & Ishibashi Y.: J. Phys. Soc. Jpn. 52 (1983) 193.
- 4) Vollenkle H., Wittman A. & Nowotny H.: Monatsh Chem. 101 (1970) 46.
- 5) Wada M., Sawada A. & Ishibashi Y.: J. Phys. Soc. Jpn. 53 (1984) 818.
- 6) Volkov A. A., Kozlov G. V., Gondharov Yu. G., Wada M., Sawada A. & Ishibashi Y.: J. Phys. Soc. Jpn. 54 (1985) 818.
- 7) Sawada A., Wada M., Fujita K., & Toibana H.: Jpn. J. Appl. Phys. 24 (1985) (Suppl. 24-2), 534.
- 8) Horioka M., Sawada A. & Wada M.: to be published in Jpn. J. Appl. Phys.
- 9) Arai M., Arima M., Sakai A., Wada M., Sawada A. & Yagi T.: J. Phys. Soc. Jpn. 56 (1988) 3213.

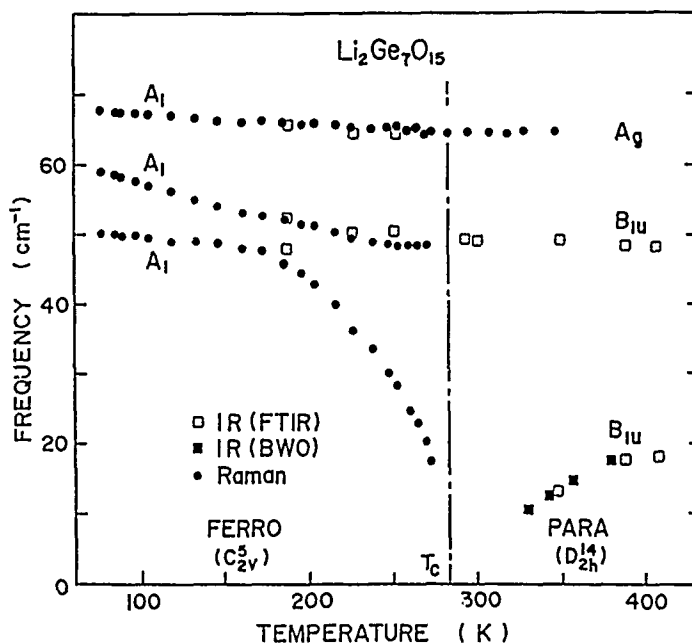


Fig.3 Frequencies of low-lying phonon modes of LGO as a function of temperature.



## FAR IR TRANSMISSION SPECTRA OF ROCHELLE SALT AT 5 K.

X. Gerbaux and A. Hadni

University of NANCY I  
BP. 239 - 54506 VANDOEUVRE LES NANCY  
FRANCE

Ferroelectricity has been uncovered in Rochelle Salt (RS) by Valasek in 1920 (1). RS is a complicated crystal with four molecules  $[\text{NaKC}_4\text{H}_4\text{O}_6 \cdot 4\text{H}_2\text{O}]$  in the primitive unit cell (2). Several external lattice vibrations have been observed in the  $10 - 100 \text{ cm}^{-1}$  far infrared range at 80 K and 5 K in crystal plates of increasing thickness : 160-550 and 6,500  $\mu\text{m}$ . At 80 K absorption increases with thickness according to Beer's law. At 5 K, the lower frequency absorption line ( $21 \text{ cm}^{-1}$ ) seems independent of thickness. This line had been shown to shift to a lower frequency at  $T = 130 \text{ K}$ , and to disappear from the FIR range at a still higher temperature (3). More recently (4) it has been ascribed to the soft mode responsible for the FE transition with a resonant behaviour at 5 K and 80 K. It is softening into a relaxation mode whose frequency goes to zero when temperature increases up to the lower Curie temperature ( $T_1 = 255 \text{ K}$ ). At 5 K the soft mode is a very weakly damped one, and we have to take into account the instrumental function for the discussion of the effect of plate thickness.

## REFERENCES

- (1) J. Valasek, Phys. Rev., 1920, vol. 15, p. 537
- (2) M.E. Lines and A.M. Glass, Principles and Applications of ferroelectrics, Clarendon Press, Oxford 1977, p. 1-2.
- (3) M. Malineau, P. Strimer et A. Hadni, J. Chimie Phys. 1972, vol. 2, p. 343
- (4) A.A. Volkov, G.V. Koslov, E.B. Kryukova, J. Petzelt, SOV. Phys. J.E.T.P., 1986, vol. 63, p. 110.

# MEASUREMENT OF THE SPECTRAL THERMAL EMISSION FROM TECHNICAL INFRARED RADIATORS

A. Leupin, H. Vetsch and F.K. Kneubühl  
Infrared Physics Laboratory  
ETH (Swiss Federal Institute of Technology)  
CH-8093 Zurich, Switzerland

## ABSTRACT

We have designed a spectroscopic system for the measurement of the spectral emissivities at wavelengths between 1  $\mu\text{m}$  and 16  $\mu\text{m}$  of solid surfaces at temperatures from 1000 K to 1500 K. As reference infrared radiator we have designed a blackbody whose emissivity agrees within 1% with commercial standards. We have applied our system to measure the spectral emissivities and the characteristics of blackbodies and various commercial infrared radiators.

## INTRODUCTION

Two experimental procedures are commonly chosen for measuring the spectral thermal emissivity of a surface. The choice depends on the temperature of the surface. For room temperature and below a method based on Kirchhoff's law [1,2] is favoured. This law states that the spectral directional emissivity of a surface equals its spectral directional absorptivity. At room temperature and temperatures below the experimental determination of the absorptivity and the related reflectivity is simpler and more reliable than the direct measurement of the emissivity. As a consequence, the experimenters measure absorptivities and reflectivities in this temperature range and rely on Kirchhoff's law when evaluating the emissivity. Most of the optical and infrared data of surfaces concern room temperature and temperatures below and, consequently, result from absorption and reflection measurements. In a few cases, Kirchhoff's law has also been applied to determine the emissivity of a surface at higher temperatures, e.g. ref[3]. For high temperatures absorption measurements are cumbersome because of the self-radiation of the surfaces [3]. At these temperatures it is more convenient to determine the spectral directional emissivity by direct measurement of the radiation from the surface and its comparison with the spectral intensity of blackbody radiation. The spectral emissivity is then calculated with the aid of the following equation:

sent measured temperature and spectral intensity of the sample,  $T_{\text{BB}}$  and  $S_{\text{BB}}(\lambda, T_{\text{BB}})$  those of the blackbody. Furthermore,  $T_A$  is the ambient air temperature,  $\lambda$  the wavelength,  $c$  the speed of light,  $h$  Planck's constant and  $k$  Boltzmann's constant. The direct experimental determination of the emissivity based on this equation is well known and described in various papers [4-9]. This method requires well-defined blackbody reference sources for the spectral range in consideration.

## SPECTROMETRIC ARRANGEMENT

For the measurement of the spectral emissivity  $\epsilon(\lambda, T_s)$  of solid surfaces we apply the following optical system: The thermal radiation emitted by the sample in the direction perpendicular to the surface is adapted and focused to the entrance slit of a McPherson RS-10 grating spectrophotometer with the aid of a Cassegrain system. At the entrance slit the radiation is chopped and passed through a low-pass filter which transmits only the spectral range corresponding to the first order of the grating. The grating of the spectrometer is exchangeable. For our measurements we use four reflecting Echelette gratings with 600, 300, 150 and 75 lines per mm. Thus, we cover the spectral range between 10'000  $\text{cm}^{-1}$  and 625  $\text{cm}^{-1}$  or 1  $\mu\text{m}$  and 16  $\mu\text{m}$  wavelength. In order to match this wide spectral range we make use of four different detectors, i.e. a PbS-, a liquid-nitrogen cooled InSb-, a liquid-nitrogen cooled HgCdTe-, and a pyroelectric detector. They are mounted alternately in a position close to the exit slit of the grating spectrophotometer. For amplification of the detector signal and filtering of noise we apply a lock-in amplifier with an integration time between 1 and 10 s. The wavelength-dependent signals are read in and stored by a desk computer for subsequent evaluation. This computer also controls the spectrophotometer and auxiliary devices. Because of the long integration time of the lock-in amplifier which is required by the detectors, the measurements of the spectral emissions of sample and black-

$$\epsilon(\lambda, T_s) = G \cdot \frac{S_s(\lambda, T_s) \cdot ((\exp(hc/k\lambda T_{\text{BB}}) - 1)^{-1} - (\exp(hc/k\lambda T_A) - 1)^{-1})}{S_{\text{BB}}(\lambda, T_{\text{BB}}) \cdot ((\exp(hc/k\lambda T_s) - 1)^{-1} - (\exp(hc/k\lambda T_A) - 1)^{-1})}$$

In this relation,  $G$  indicates the ratio of the geometrical factors of sample and blackbody.  $T_s$  and  $S_s(\lambda, T_s)$  repre-

body reference have to be performed alternately. In order to avoid drift-effects of the detectors the periods of measurements

and those between are kept as short as possible. Remaining drift-effects are eliminated by the evaluation program of the desk computer.

### BLACKBODY REFERENCE SOURCE

There exists a large variety on theoretical and numerical calculations on the characteristics of blackbody sources as function of size, shape and wall materials of the cavities, e.g. [10-25], yet instructions on their practical design are less frequent, e.g. [26-32]. Since commercially available blackbody radiators do not satisfy our demands, we had to design our own reference radiator [33]. Its cavity exhibits a cylindrical and a conical part. This shape is preferable to a spherical or a purely conical or cylindrical form because of its smaller dependence on effects related to specular reflections on the inner cavity walls. From calculations we performed according to ref. [16] and experience with our own measurements on commercial blackbodies we assume that our blackbody exhibits a spectral emissivity  $\epsilon(\lambda, T_{\text{gg}})$  better than 0.99 over the entire spectral range considered [33].

### STUDY OF COMMERCIAL INFRARED RADIATORS

With our spectrometric system we attempted to determine the spectral emissivity of the radiating components of four different technical infrared radiators, namely radiators by "Krelus", Hirschthal, Switzerland, by "Matherm", Villeurbanne, France, by "Heraeus", Hanau, FRG and by "Salamander", Infrared International, England. The two radiators first mentioned consist of thin metal foils mounted on a ceramic support and heated electrically. These foils are used as primary radiation source.

We have preoxidized the stainless-steel foils on the "Krelus" radiator for at least 12 hours at 1173 K in order to prevent drifts on the thermal emissivity due to oxidation during the measurement. The measurement itself was performed on a flat section of the heating foils at 1073 K. Between 1  $\mu\text{m}$  and 12  $\mu\text{m}$  wavelength the emissivity of this section varies slightly between 0.8 and 0.9 and reaches almost 1.0 above 12  $\mu\text{m}$ , yet it drops significantly above 14  $\mu\text{m}$ . The emissivity at these long wavelengths may be affected by the phenomenon of residual radiation ("Reststrahlen") from oxides on the heating foil.

The radiator by "Matherm" is very similar to that of "Krelus", but Kanthal-like foils are used as radiation source instead of stainless-steel foils. Since it was not possible to measure the emissivity on the radiator itself we determined the emissivity of separate Kanthal-Al samples. We performed two types of measurements: The

foils were preoxidized either at a temperature of  $\approx 1473$  K for 2 hrs or at  $\approx 1173$  K for 15 hrs. The emissivities of both samples are significantly lower than that of the "Krelus" foils. Furthermore, both show strong quasi-periodic variations with wavelength due to interferences in the aluminum-oxide layer on the foils. The observed periods correspond to a layer thickness of  $\approx 2$   $\mu\text{m}$  or 0.3  $\mu\text{m}$  respectively. The measured spectral emissivities are in reasonable agreement with the published total emissivity of  $\approx 40\%$  for Kanthal-Al [34].

Infrared radiators with quartz tubes are common and wide spread. The radiator of "Heraeus" is an example. In this radiator an electrically heated metal helix inside a quartz tube acts as primary radiation source. The back side of the tube is gold coated to prevent radiation losses in the back direction. Because of this gold coating this type of radiator exhibits a strong directional dependence of the radiation. Hence, we oriented the radiator for our measurements in the direction of maximum radiation intensity. Nevertheless, the measured emission power is smaller than that of a "Krelus" radiator at the same temperature. In addition, the spectral emissivity begins to drop at wavelengths longer than 3  $\mu\text{m}$  because of the decrease of the quartz transmissivity in this wavelength range.

The heating element of the "Salamander" radiator consists of a ceramic surface which is heated by inlaid helices. Because of very strong temperature variations along its surface we have not been able to perform reliable measurements on the spectral emission of this radiator.

### CONCLUSION

We have built a spectrometric system including a reference blackbody in order to measure spectral emissivities of technical infrared radiators at wavelengths between 1  $\mu\text{m}$  and 16  $\mu\text{m}$ . The comparison of our reference blackbody with commercial blackbodies shows agreement within 1%. With our spectrometric system we have succeeded to measure the emissivities and to determine the characteristics of various commercial radiators.

### ACKNOWLEDGEMENTS

This study is supported by the Kommission zur Förderung der wissenschaftlichen Forschung, Krelus AG and ETH Zürich.

## REFERENCES

- [1] NICODEMUS, F.E.,  
Applied Optics, 4 (1965), 767-773.
- [2] SIEGEL, R.H. and HOWELL, J.R.,  
Thermal Radiation Heat Transfer,  
59-61. Mc Graw-Hill, N.Y.
- [3] SHCHERBINA, D.M.,  
High Temp. (USA), 5 (1967), 438-444.
- [4] DMITRIEV, V.D. and KHOLOPOV, G.K.,  
High Temp. (USA), 6 (1968), 527-528.
- [5] SLOBODKIN, L.S. and SOTNIKOV-YUZHNIK,  
YU.M., J. Eng. Phys. (USA), 27  
(1974), 918-921.
- [6] KÄLIN, R. and KNEUBÜHL, F.K.,  
Infrared Physics, 16 (1976), 491-508.
- [7] MASTRYUKOV, B.S., KRIVANDIN, V.Z. and  
ZUBOV, V.V., High Temp. (USA), 14  
(1976), 662-666.
- [8] FUCHS, F. and KNEUBÜHL, F.K.,  
Infrared Physics, 21 (1981), 127-147.
- [9] BRÖNNIMANN, R. and KNEUBÜHL, F.K.,  
Infrared Physics, 26 (1986), 179-195.
- [10] DE VOS, J.C.,  
Physica, 20 (1954), 669-689.
- [11] FECTEAU, M.L.,  
Applied Optics, 7 (1968), 1363-1364.
- [12] NICODEMUS, F.E.,  
Applied Optics, 7 (1968), 1359-1362.
- [13] BALTES, H.P., MURI, R. and KNEUBÜHL,  
F.K., Revue Int. de Hautes  
Températures et Réfractaires, 7  
(1970), 192-196.
- [14] BALTES, H.P. and KNEUBÜHL, F.K.,  
Helv. Phys. Acta, 45 (1972), 481-529.
- [15] BEDFORD, R.E. and MA, C.K.,  
J. Opt. Soc. Am., 64 (1974), 339-349.
- [16] BEDFORD, R.E. and MA, C.K.,  
J. Opt. Soc. Am., 65 (1975), 565-572.
- [17] BEDFORD, R.E. and MA, C.K.,  
J. Opt. Soc. Am., 66 (1976), 724-730.
- [18] BEDFORD, R.E., MA, C.K., CHU, Z.,  
SUN, Y. and CHEN, S., Applied Optics,  
24 (1985), 2971-2980.
- [19] CHANDOS, R.J. and CHANDOS, R.E.,  
Applied Optics, 13 (1974), 2142-2152.
- [20] BARTELL, F.O. and WOLFE, W.L.,  
Applied Optics, 15 (1976), 84-88.
- [21] CHEN, S., CHU, Z. and CHEN, H.,  
Metrologia, 16 (1980), 69-72.
- [22] CHU, Z., CHEN, S. and CHEN, H.,  
J. Opt. Soc. Am., 70 (1980),  
1270-1274.
- [23] BERRY, K.H.,  
J. Phys. E.: Sci. Instrum., 14 (1981),  
629-632.
- [24] OHWADA, Y.,  
Applied Optics, 20 (1981), 3332-3335.
- [25] REDGROVE, J.S. and KEITH, H.B.,  
High Temperature - High Pressure,  
15 (1983), 1-11.
- [26] YAMADA, H.Y.,  
Applied Optics, 6 (1967), 357-358.
- [27] GRAY, W.T.,  
ISA Transactions, 6 (1967), 242-251.
- [28] FRIEDE, G. and MANNKOPFF, R.,  
Z. angew. Physik, 28 (1970), 357-362.
- [29] BLISS, F.E., DAVIS, S. and STEIN, B.,  
Applied Optics, 9 (1970), 2023-2027.
- [30] NAGASAKA, T. and SUZUKI, M.,  
Applied Optics, 16 (1977), 2358-2359.
- [31] RAST, J., KNEUBÜHL, F.K. and  
MÜLLER, E.A., Astron. Astrophys.,  
68 (1978), 229-238.
- [32] VLASOV, L.V. et al.,  
Meas. Tech. (USA), 25 (1982),  
396-398.
- [33] LEUPIN, A., VETSCH, H. and  
KNEUBÜHL, F.K., Proc. Workshop Opt.  
Prop. Measurement, Ispra, Oct. 27-29  
(1987), 243-251.
- [34] SALA, A.,  
Radiant Properties of Materials, 205,  
Elsevier (Amsterdam, 1986).

## THE RELATION BETWEEN IR AND VIS SPECTRAL PROPERTIES OF GLASSES AND THE ENERGY TRANSFER THROUGH WINDOWS

R. Furler, P. Williams and F.K. Kneubühl  
Infrared Physics Laboratory  
ETH (Swiss Federal Institute of Technology)  
CH-8093 Zurich, Switzerland

### ABSTRACT

We report on an extensive experimental and theoretical study of the influence of ir and vis characteristics of glasses, design and position of fenestrations, atmospheric and solar conditions, free and forced convection on the energy transfer through windows.

### INTRODUCTION

The energy transfer through windows has a significant influence on the energy consumption of buildings. After an extended study of the influence of infrared and solar radiation on the energy balance of windows [e.g. 1-3] we have therefore investigated the energy performance of conventional and advanced multiple-glazed windows [4]. The aim of our study was to gain a detailed knowledge of the physical phenomena controlling the energy transfer through different types of fenestrations. Consequently, we have devised a simple characterization of multiple glazings, which allows us to compare different windows subject to arbitrary environmental conditions and to discuss their energy performance.

### EXPERIMENTAL STUDIES

In order to determine the spectral properties of windows we have first measured the spectral transmittance and reflectance of many commercial glazings with two double-beam spectrometers in the wavelength range between 200 nm and 45  $\mu$ m. From these spectra we have calculated the data of single and multiple glazings relevant with respect to solar and thermal radiation.

In addition, we have performed in-situ measurements on a test cabin at EMPA, Dübendorf, Switzerland. This cabin has been equipped with two different windows, a "Float" triple glazing and a "Silverstar" double glazing. We have measured the surface temperature of the individual glass panes with thermocouples and with radiometers. Simultaneously, we have determined ambient air temperatures, global wind speed and direction as well as solar and thermal background radiation. The data have been stored by a personal computer.

Furthermore, we have determined the

forced convective heat transfer at the outside surface of the multiple glazings of our test cabin. We have derived these specific data from additional investigations on the convective heat loss of the glazings on scaled models of the test cabin in a water channel and in a wind tunnel. Thus, we have demonstrated that the forced-convective-heat-transfer coefficient strongly depends on the wind direction, the position on the building envelope and the shape of the building. We have observed a maximum convective-heat-transfer coefficient when the air flow is turbulent at the windows. However, we have to emphasize that the relation between this coefficient and the global wind velocity presented in this study is valid only for buildings with shapes corresponding to our test cabin. Therefore, there still exists the need for a general relation which is valid approximately for all building geometries.

### COMPUTER MODEL

Finally, we have designed a theoretical computer model of the energy transfer through fenestrations based on the assumptions of steady-state conditions. It includes heat transfer by convection, conduction and radiation and allows us to simulate the performance of windows. We have found excellent agreement between the simulated data of the glass-pane temperatures and the in-situ measured glass temperatures. Nevertheless, it should be noticed, that this model, which is applicable to arbitrary fenestration systems, is restricted to slowly varying environmental conditions. With the described computer model we have investigated the energy performance, i.e. the U-value, of three selected multiple glazings for a wide range of environmental conditions for missing solar radiation. In these cases we have not found a simple relation between the U-value and the environmental parameters, except for the situation where the outdoor surroundings are at the outdoor-air temperature. Our latest investigations on the energy performance of fenestrations took into account incident solar radiation. This resulted in a nearly linear relationship between the intensity of incident solar radiation and the solar-heat gain. Therefore, we have introduced a solar-heat-gain coefficient which in a good approximation is independent of environmental parameters.

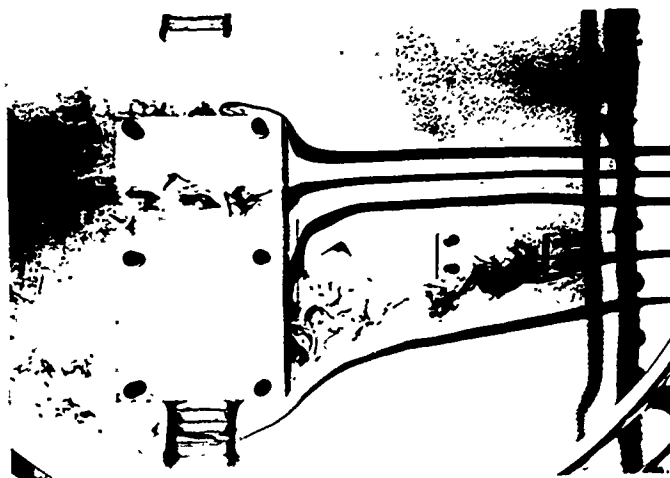
## CONCLUSIONS

In conclusion our investigations have demonstrated that low-emissivity coatings applied in double glazings improve significantly the energy performance in the absence of solar radiation. Yet, clear double glazings allow better utilization of solar energy. Finally, we have to mention that only an annual energy analysis with respect to the special requirements of each individual building can take into account in detail energy gains, losses and the wide variation of U-values of fenestrations. Our computer model can be extended to this kind of analysis.

This study was supported by NEFF (National Energy Research Foundation) and ETH Zurich.

## REFERENCES

- [1] F.K. Kneubühl, Ch. Zürcher, F. Thiébaud, G. Finger, R. Sagelsdorff, Th. Frank: 2nd Int. CIB Symposium on Energy Conservation in the Built Environment, Copenhagen (1979)
- [2] F.K. Kneubühl, G. Finger, F. Thiébaud, Ch. Zürcher, R. Sagelsdorff, Th. Frank: Dig. Fifth Int. Conf. on Infrared and Millimeter Waves, Würzburg, Oct. 6-10, 85-89 (1980)
- [3] Ch. Zürcher, G. Finger, F.K. Kneubühl, F. Thiébaud, H. Vetsch, R. Sagelsdorff, Th. Frank: Proc. Conference on New Energy Conservation Technologies, Berlin, April 6-10, J.P. Millhone & E.H. Willised, Springer 1037-1043 (1981)
- [4] Ch. Zürcher, G. Finger, F.K. Kneubühl, F. Thiébaud, H. Vetsch: Infrared Physics 22, 277-291 (1982)
- [5] Ch. Zürcher, G. Finger, F.K. Kneubühl, F. Thiébaud, H. Vetsch: Proc. CIB 83 Stockholm, August 15-19, 3A, 431-442 (1983)
- [6] R. Furler, P. Williams and F.K. Kneubühl: NEFF Report Project No 177.1 (1988) (ETH-PhD Thesis R. Furler) to be published



Model of test cabin in the water tank:  
Water flow 0.13 m/s normal to the front surface with the two windows. The obstacles in front of the cabin cause a turbulent flow on one window whilst the flow on the other window remains laminar.

## EFFECT OF TEMPERATURE ON IR-ABSORPTION OF DIPHENYL

By: M.I. Nasser & M.A. Moharram , Physics Department  
Natl Research Ctr.  
Dokki, Cairo, Egypt.

Abstract:

In this work, the temperature dependence of the intensities of the IR absorption bands corresponding to the fundamental vibrations, overtones and combination frequencies of diphenyl is presented. A thorough discussion of the interpretation of the fundamental modes of vibration has been made on the basis of the temperature dependence of the intensities of these absorption bands.

The structure of the diphenyl molecule has been the subject of numerous investigations. Despite a considerable amount of work on the Raman <sup>(1)</sup>, IR <sup>(3,4,5)</sup> and ultraviolet <sup>(2)</sup> spectra, the assignment of the fundamental frequencies has not yet been established with certainty. Some assistance can be obtained from the temperature dependence of the IR spectrum of this material.

Discussion:

The effect of various peculiarities of an intramolecular vibration, namely its symmetry, form unharmonicity, etc., on the temperature variation of the shape, halfwidth and frequency location of the corresponding absorption bands is of substantial interest for the theory of vibrational spectra and the practice of molecular spectral investigations.

This work presents a wide investigation of the effect of temperature on the infrared absorption bands of liquid diphenyl between its melting and boiling points (70- 254°C ). In the discussion of the spectra of Diphenyl, one has to consider the  $D_{2h}$  model. On the basis of the interpretations of Katon, Kovner and Pergudov, the discussion of the results of the present work is given. Tables (1, 2 & 3) show the results of the effect of temperature on the liquid diphenyl.

Conclusion:

It could be concluded that all the bands belonging to  $B_{1u}$  symmetry class whether they are non-planar C-C vibrations or C-H bending vibrations are temperature dependent. The intensity of each band decreases by 32.8% per 100°C.

The planar C-C absorption bands whether they belong to  $B_{2u}$  or  $B_{3u}$  symmetry classes are less temperature dependent and the decrease in intensity of each band is about 14.4% per 100°C.

The planar C-H bending vibrations at 1075  $cm^{-1}$  belongs to the symmetry class  $B_{2u}$ . This band is temp. dependent and its intensity decreases by nearly 32.8% per 100°C which is similar to the decrease in the bands belonging to the symmetry class  $B_{1u}$ . The band at 1180  $cm^{-1}$  was assigned by Kovner to belong to the symmetry class  $B_{3u}$  and has been confirmed by the present work. Its temperature dependence resembles that of the band at 1043  $cm^{-1}$ , which belongs to the symmetry class  $B_{3u}$  and decreases by about 26.5% per 100°C Fig. (2A) line(c) It could also be noticed that the decrease in intensity for all these bands is linear. The changes of the intensities of the C-H stretching vibrations, overtones and combinations with temperature are different as discussed earlier in this work.

References :

1. Aziz S.A.  
Indian J. Phys. 12, 247. (1939).
2. Braude E.A. et al.  
Nature, 173, 117 (1954).
3. Lippinott E.R., Edward J. Orelli JR.  
J. Chem. Phys., 23, 285. (1955).
4. Katon J.E., Lippinott ER  
Spec. Chim. Acta 15, 267 (1959).
5. Peregudov G.V.  
Opt. & Spect. 9, 155 (1960).

# MEASUREMENT OF THE DIELECTRIC CONSTANT OF FERROELECTRIC $\text{KH}_2\text{PO}_4$ AT $35\text{GHz}$ BY TRANSMISSION IN A WAVEGUIDE

M. Horioka

Department of Electronics  
Kanazawa Institute of Technology  
Kanazawa 921 Japan

## ABSTRACT

The apparatus to measure precisely dielectric constant of a high loss material at  $f=35\text{GHz}$  has been composed. By using this the complex dielectric constant ( $\epsilon = \epsilon' - j\epsilon''$ ) of  $\text{KH}_2\text{PO}_4$  (KDP) has been determined in the temperature region from  $-160^\circ\text{C}$  to  $0^\circ\text{C}$ . The temperature dependence of  $\epsilon'$  shows a double peaks around the Curie temperature  $T_C$ , which characterizes the critical slowing down of the dielectric response. The maximum values of  $\epsilon'$  and  $\epsilon''$  reach 480 and 350 near  $T_C$ , respectively.

## INTRODUCTION

Recently dielectric measurements of a high loss material at frequencies from microwave range to millimeter wave range have been required in the various researches. In the study of the ferroelectric phase transition, the dielectric measurements [1,2] for the lossy substances in the wide frequency range ( $10^3 - 10^{12}\text{Hz}$ ) have central importance to clarify the behavior of soft mode, which represents the main concept of all dynamical theories of structural phase transition. So far the measurements at frequencies from microwave to millimeter wave range have not been fully done. In the present report the complex dielectric constant of KDP attracting intense interest in the phase transition mechanism was determined at  $35\text{GHz}$  by measuring the transmission coefficient of a slab of KDP inserted into a rectangular waveguide. This method is similar to that used by Jackle [3]. Several improvements have been done for the measuring apparatus.

## EXPERIMENTAL

The transmission coefficient  $T$  of the sample with thickness  $d$  is given for the  $\text{TE}_{10}$  mode by the following relation:

$$T = t \cdot \exp(-i\eta) = \frac{(1-r^2)\exp(-i2\pi bd/\lambda)}{1-r^2\exp(-i4\pi bd/\lambda)} \quad (1)$$

with

$$r = \frac{b_0 - b}{b_0 + b}, \quad b_0 = \sqrt{1 - (\lambda/2a)^2}$$

and

$$b = \sqrt{\epsilon - (\lambda/2a)^2},$$

where  $t$  and  $\eta$  are respectively the amplitude

ratio of the transmitted wave to the incident wave and the phase change caused by the insertion of the sample. The wavelength  $\lambda$  is the free space wavelength,  $a$  the width of the waveguide. As the quantities  $\lambda$ ,  $d$  and  $a$  are known,  $\epsilon$  can be determined by measuring  $\eta$  and  $t$ .

Transmission coefficient was measured by using the millimeter wave bridge shown in Fig. 1. The measurement was done by adjusting the attenuator and the phase shifter for zero voltmeter reading, when the sample is present and when it is not present. The differences of the attenuation and the phase corresponding to these settings are  $(S_2 - S_1)\text{dB}$  and  $(\eta_2 - \eta_1)$  radian, respectively. Thus  $t$  and  $\eta$  in eq(1) are given by the following relations:

$$t = \frac{t_2}{t_1} = 10^{(S_2 - S_1)/20} \quad (2)$$

$$\eta = \eta_2 - \eta_1 + 2\pi b_0 d/\lambda, \quad (3)$$

where  $2\pi b_0 d/\lambda$  shows the phase change caused by air of the same thickness as the sample. Improved points in the present experiment are as follows: {1} The attenuators were inserted in the waveguide of both sides of the sample. These are effective to remove unwanted multireflections between the sample and the others, such as the isolator, the H-bend and the coupler, so that  $T$  becomes independent to the position of the sample mounted to the waveguide. {2} To compensate for the variations in temperature and humidity in the waveguide, the reference arm was kept at the same condition as the sample arm. Thus the phase and the attenuation, when the sample is not present, do not depend on temperature and constant within the experimental errors as shown in Fig.2.

The crystal slab of the sample was  $0.44 \times 3.60 \times 7.10 \text{ mm}^3$  in size. Silver paste was used to fit the sample tightly to the waveguide wall. Some reference samples, such as teflon, micalex were used to check the accuracy of this apparatus. The errors in  $\epsilon'$  and  $\epsilon''$  were less than 3% and 5%, respectively. The temperature in the thermostat was controlled within  $\pm 0.1^\circ\text{C}$ .

Figure 3 shows the temperature dependence of  $\epsilon'$  along the ferroelectric  $c$  axis of KDP. The curve shows a double peaks around  $T_C$ , which characterizes the critical slowing down of the dielectric response. The maximum value of  $\epsilon'$  reaches 450 and the one of  $\epsilon''$  about 350. The latter value will



be reported in the conference in detail.  $\epsilon'$  over the wide temperature region is shown by small circles in Fig. 4 together with that in the submillimeter range obtained by Volkov et al. [4]. The value of  $\epsilon'$  in the present measurement is fairly large around  $T_c$  in comparison with the values in the submillimeter measurements. This fact indicates that remarkable frequency dispersion is expected in the frequency region from micro-wave to millimeter wave.

#### REFERENCES

- [1] R. Blinc and B. Zeks, *Soft Modes in Ferroelectrics and Antiferroelectrics* (North-Holland, Amsterdam, American Elsevier, New York, 1974) pp175-187.
- [2] J. Petzelt, G. V. Kozlov and A.A. Volkov, *Europhysics News*, 1984, vol.15, pp.1-4.
- [3] W. Jackle, *Z. Angew. Phys.* 1959, vol.12, pp.148-155.
- [4] A. A. Volkov, G. V. Kozlov and Lebedev, *Sov. Phys. Solid State*, 1978, vol.20(7), pp.1166-1169.

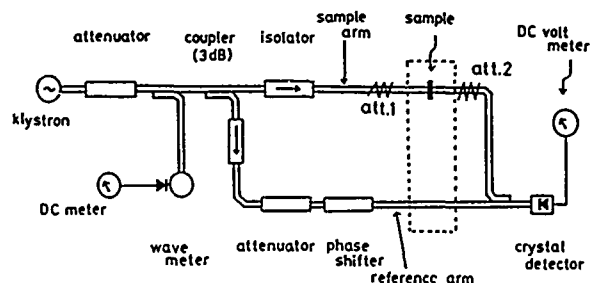


Figure 1  
Block diagram of millimeter wave bridge

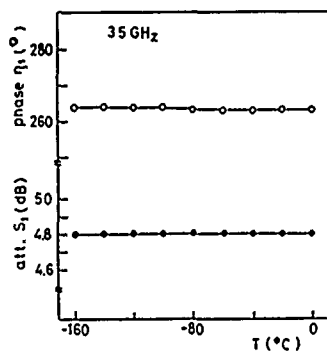


Figure 2  
Temperature dependences of the phase  $\eta_1$  and the attenuation  $S_1$

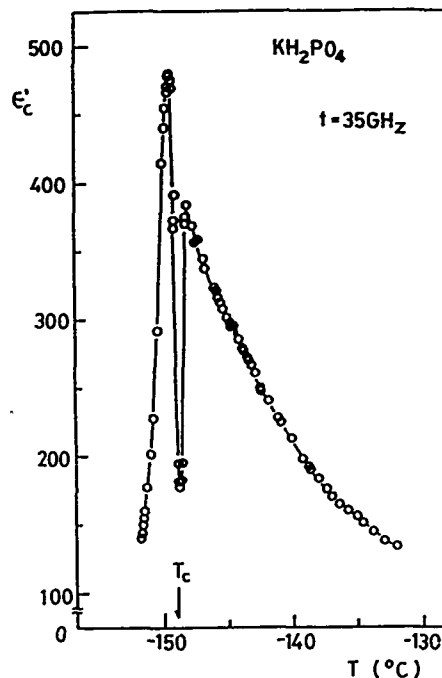


Figure 3  
Temperature dependence of  $\epsilon'$  along the ferroelectric c axis of  $\text{KH}_2\text{PO}_4$  at 35GHz

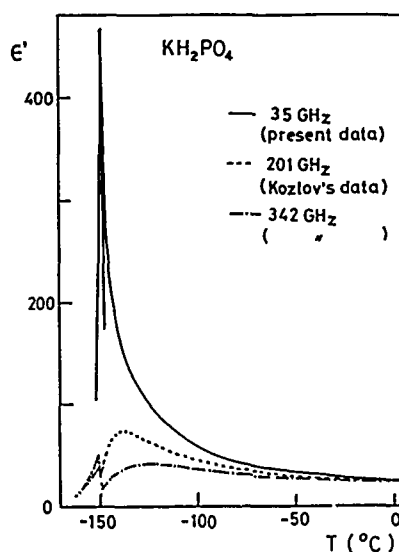


Figure 4  
Comparison of the present data with the submillimeter ones

## SPECTROSCOPY AND FIR LASER EMISSION: PERISCOPE TO THE VIBRATIONAL WORLD OF METHANOL AND METHYLAMINE

R.M. Lees

Dept. of Physics, University of New Brunswick, Fredericton, N.B., Canada E3B 5A3

The methyl alcohol and methylamine molecules both are notable for their large-amplitude  $\text{CH}_3$  torsional motions, while methylamine has a second large-amplitude motion in the inversion or "wagging" of the  $\text{NH}_2$  group. As well, both molecules are notable in having strong infrared (IR) C-O or C-N stretching bands which overlap well with the  $\text{CO}_2$  laser bands, and thereby provide numerous opportunities for optical pumping and FIR laser line emission. Although the torsion-rotation structure of the ground and excited state energy level manifolds is quite complex, sustained spectroscopic effort over the last decade has led to a reasonable understanding and accurate mapping of substantial portions of these manifolds. In addition to the principal species of  $\text{CH}_3\text{OH}$  (1-8) and  $\text{CH}_3\text{NH}_2$  (9-11) several isotopic variants of the former have been studied, including  $^{13}\text{CH}_3\text{OH}$  (12, 13),  $\text{CH}_3^{18}\text{OH}$  (14, 15) and  $\text{CD}_3\text{OH}$  (16).

There are, however, other vibrational modes of these molecules, as well as highly-excited torsional modes of the ground state, which also have IR bands in the  $\text{CO}_2$  laser region but of very much lower intensity than the C-O or C-N stretching fundamental. These bands are not readily amenable to observation by normal high-resolution IR absorption spectroscopy, so that the energy level structures of their parent modes are not yet well understood. Their presence and locations can nevertheless be revealed on the one hand by a variety of interactions with the stretching modes resulting in observable perturbations to particular levels of the latter, and on the other by occasional coincidences with  $\text{CO}_2$  laser lines which are strong enough to pump the weak absorptions to give detectable FIR laser lines (17) or to yield laser Stark spectra (18). Thus, for these weak modes, the IR and FIR spectroscopic observations do not generally give an overall view of the energy manifolds, but rather permit periscopic peeks up into the excited states for small localized regions of the energy level structure.

The presence of apparent perturbations was first observed for the  $(n\tau K) = (010)$  levels of A torsional symmetry in the diode laser spectrum of the C-O stretch band of  $\text{CH}_3\text{OH}$  by Sattler et al. (1). Subsequently, Henningsen observed and characterized other strong perturbation-induced shifts and mixings in this band from assignments and analysis of FIR laser lines (2, 4). The analogous C-O stretch band of  $\text{CD}_3\text{OH}$  was studied by Weber and Maker (16), who pointed out the possibility of Fermi resonance between the C-O stretch state and high-lying torsional levels of the ground state and were thereby able to account for observed shifts in both  $\text{CD}_3\text{OH}$  and  $\text{CH}_3\text{OH}$ . Henningsen then made further significant progress in accounting for the anomalous torsional barrier height in the  $n=1$  torsional state of the C-O stretch as the result of interaction with the O-H bending mode, (5) and particularly in identifying the strong mixing and shift of  $(n\tau K) = (025)$  and  $(016)$  levels as due to Coriolis interaction with the  $\text{CH}_3$  rocking mode, the mysterious "X-state" (3).

In this paper, we will review the information on vibrational interactions so far obtained from perturbations and FIR laser emission, and present some recent new data on additional perturbations observed for several isotopic species of methanol and for methylamine.

## ACKNOWLEDGEMENTS

The research described here has proceeded with the active assistance and collaboration of Drs. W. Lewis-Bevan, J.W.C. Johns, G. Moruzzi and I. Mukhopadhyay, whose help is gratefully acknowledged. Financial support was provided by the Natural Sciences and Engineering Council of Canada and the University of New Brunswick Research Fund.

## REFERENCES

- (1) J.P. Sattler, W.A. Riessler, and T.L. Worchesky, *Infrared Phys.* **19**, 217-224 (1979).
- (2) J.O. Henningsen, *Infrared and Millimeter Waves*, Vol. 5 (ed. K.J. Button), Ch. 2, pp. 29-128, Academic Press 1982.
- (3) J.O. Henningsen, *J. Mol. Spectrosc.* **91**, 430-457 (1982).
- (4) J.O. Henningsen, *IEEE J. Quantum Electron.* **QE-18**, 313-317 (1982).
- (5) J.O. Henningsen, *J. Mol. Spectrosc.* **102**, 399-415 (1983).
- (6) G. Moruzzi and F. Strumia, *Infrared Phys.* **24**, 257-260 (1984).
- (7) G. Moruzzi, F. Strumia, C. Bonetti, B. Carli, F. Mencaraglia, M. Carlotti, G. DiLionardo, and A. Trombetti, *J. Mol. Spectrosc.* **105**, 24-52 (1984).
- (8) R.M. Lees, *Far Infrared Science and Technology*, ed. J.R. Izatt, *Proc. SPIE* **666**, 156-171 (1986).
- (9) M.S. Malghani, R.M. Lees, and J.W.C. Johns, *Int. J. IR & MM Waves* **8**, 803-825 (1987).
- (10) N. Ohashi, K. Takagi, J.T. Hougen, W.B. Olson, and W.J. Lafferty, *J. Mol. Spectrosc.* **126**, 443-459 (1987).
- (11) R.M. Lees, W. Lewis-Bevan, R.R.J. Goulding, and C. Young, *Proc. Fourth Int. Conf. IR Phys.*, Zurich, 1988, pp. 587-589.
- (12) I. Mukhopadhyay, Ph.D. Thesis, University of New Brunswick, 1986.
- (13) I. Mukhopadhyay, R.M. Lees, and W. Lewis-Bevan, *Proc. 4th Int. Conf. IR Physics*, Zurich, 1988, pp. 721-723.
- (14) R.R.J. Goulding, Ph.D. Thesis, University of New Brunswick, 1987.
- (15) R.R.J. Goulding, C. Young, R.M. Lees, W. Lewis-Bevan, and J.W.C. Johns, *Infrared Phys.*, in press.
- (16) W.D. Weber and P.D. Maker, *J. Mol. Spectrosc.* **77**, 298-309 (1982).
- (17) J.O. Henningsen, *Int. J. IR & MM Waves* **7**, 1605-1629 (1986).
- (18) S. Petersen and J.O. Henningsen, *Infrared Phys.* **26**, 55-71 (1986).

# HOMOGENEOUS LINEWIDTHS AND LEVEL-CROSSING SIGNALS OF SOME PUMP TRANSITIONS OF $^{12}\text{CH}_3\text{OH}$ CW LASER LINES

N.Sokabe, K.Matsushima and A.Murai

Department of Applied Physics  
Osaka City University  
Sumiyoshiku, Osaka 558 Japan

## ABSTRACT

Electric field effect on absorption in some pump transitions of  $\text{CH}_3\text{OH}$  fir laser lines is analysed in terms of zero-field level-crossing effect with reference to homogeneous linewidths observed in intermodulated absorption method with photoacoustic detection.

## INTRODUCTION

Since the first report on Stark effect on the 496- $\mu\text{m}$  laser line of  $\text{CH}_3\text{F}$  pumped with the  $\text{CO}_2$  9P(16) by Tobin and Jensen[1], electric field effect on optically pumped FIR laser lines has attracted considerable attention. It has been reported on many fir laser lines exhibiting first order Stark effect that the output power is enhanced when an weak static electric field is applied to laser medium perpendicular to the direction of polarization of both pump and fir laser fields[1,2,3]. Such an enhancement is accompanied with an increase in absorption of the  $\sigma$ -component of infrared pump transition of a given fir laser line. In the meantime, Zeeman laser theory has been applied to an  $\text{HCOOH}$  fir laser operating under the influence of static electric field[4]. Electric field dependence of the fir output power can be reproduced on some fir laser lines for which no absorption increase in pump transition nor fir power enhancement is observed. Therefore, the fir power enhancement seems to be the direct consequence of the absorption increase in pump transition.

The absorption increase in infrared pump transition has been reported on several fir lines of  $\text{CH}_3\text{OH}$  and  $\text{CH}_3\text{F}$  by Inguscio et al[2]. Nonlinear Hanle effect caused by different saturation of Stark components of an inhomogeneously broadened transition has been proposed for the origin of the absorption increase[5,6].

## LEVEL-CROSSING SIGNALS IN SATURATED ABSORPTION

We have recently reported absorption profile for  $\sigma$ -transition in a degenerate two-level system as a function of applied electric field in an approximation to fourth order of incident radiation field in density matrix formalism[7]. The expression for power absorbed per unit volume of a medium under the influence of applied static electric field contains two narrow and two broad Lorentzians as a function of sublevel splitting in the upper and lower levels. The narrow ones come from purely coherent effect, while the broad ones from population effect. All of them give rise to level crossing signals. A typical absorption profile is shown in Fig.1. The central dip is the manifestation of level-crossing.

In order to compare the theoretical absorption profile with experimental observation, we need relaxation constants and sublevel splitting. The former quantities are not available even now except

for on a very limited number of fir laser lines. One of the most well-investigated lines may be the 118.8- $\mu\text{m}$  line of  $^{12}\text{CH}_3\text{OH}$  pumped with  $\text{CO}_2$  9P(36). Therefore, we focus upon this line for a while. The pump transition of this line was assigned as  $\nu_5$  0-1,  $qQ(018,16)$  by Henningsen[8]. The sublevel splitting in the upper and lower levels can be calculated from effective rotational quantum number[9]. The relaxation constants of the upper( $\tau_1$ ), the lower( $\tau_2$ ) and optical coherence( $\tau$ ) were estimated by Heppner et al[10]. No relaxation constants ( $\tau'$ ) between sublevels in the upper and lower levels have been reported.

## HOMOGENEOUS LINEWIDTHS

In this work, we report homogeneous width of the pump line of the 118.8- $\mu\text{m}$  line measured with intermodulated saturated-absorption method incorporated with photoacoustic detection. The beam from a cw  $\text{CO}_2$  laser operating on 9P(36) line splits into two beams in a beam splitter. The two beams, chopped at different frequencies of 360 Hz and 540 Hz, respectively are let into an absorption cell with approximately 12 cm in length in a counter propagation scheme. Absorption in the cell was detected as photoacoustic signal at the sum frequency of 900 Hz with an electret microphone whose output was fed into a lock-in amplifier. As the frequency of the  $\text{CO}_2$  laser was scanned across the Doppler gain curve, Doppler-free absorption signal was recorded on a chart recorder. Typical Doppler-free profiles are reproduced in Fig.2 for different pressures (no buffer gas used). The absorption line offset from the 9P(36) line center by  $+23.0 \pm 5$  MHz which is compared with the value of  $+23 \pm 2$  MHz reported by Henningsen. The absorption profiles are asymmetric owing to intensity variation of the  $\text{CO}_2$  line. After taking this effect into account, linewidth (HWHM) is plotted as a function of pressure in Fig.3. One obtains a value of 17.9 MHz/Torr for pressure coefficient of  $7/2\pi$ . This value is smaller compared with a value of 24 MHz/Torr that is calculated from the values of  $\tau_1$  and  $\tau_2$  in [10], under the assumption that all collisions are energy-changing. It is noted that there is an uncertainty in the linearity in frequency scanning in this work. In Fig.4, an observed level-crossing signal is compared with theoretical ones calculated from two sets of relaxation constants.

Calculated level-crossing signals for some pump transitions of  $\text{CH}_3\text{OH}$  cw fir laser lines are shown in Fig.5. All the relaxation constants are assumed to be equal with each other with pressure coefficient of 20 MHz/Torr.

## CONCLUSION

Electric field effect on some fir transitions in  $\text{CH}_3\text{OH}$  which produce fir laser lines are reported. Level-crossing signals may be used for determining

relaxation constants  $\tau$  and  $\tau'$ , and also be useful for assignment of transitions.

### REFERENCES

- [1] M.S. Tobin and R.E. Jensen, IEEE J. Quantum Electron. QE-13 (1977) 481.
- [2] M. Inguscio, A. Moretti and F. Strumia, IEEE J. Quantum Electron. QE-16 (1980) 955.
- [3] P. Janssen and H. Vanderstraeten, Conf. Digest, 11-th Int. Conf. IR and MM Waves, Pisa, 1986, ed. G. Moruzzi, p. 21.
- [4] N. Sokabe, K. Horikawa, N. Zumoto and A. Murai, Int. J. IR and MM Waves 6 (1985) 893.
- [5] F. Strumia, M. Inguscio and A. Moretti, Laser Spectroscopy, eds. A.R.W. McKellar et al. (Springer, Berlin, 1981) p. 255.
- [6] F. Strumia, Advances in Laser Spectroscopy, eds. F. T. Arecchi et al. (Plenum, N.Y., 1983) p. 267.
- [7] N. Sokabe, Y. Tamura, K. Matsushima and A. Murai, Int. J. IR and MM Waves 8 (1987) 1145.
- [8] J. Henningsen, IEEE J. Quantum Electron. QE-13 (1977) 435.
- [9] J. Henningsen, Private communication.
- [10] J. Heppner, C.O. Weiss, U. Hülmer and G. Shinn, IEEE J. Quantum Electron. QE-16 (1980) 392.

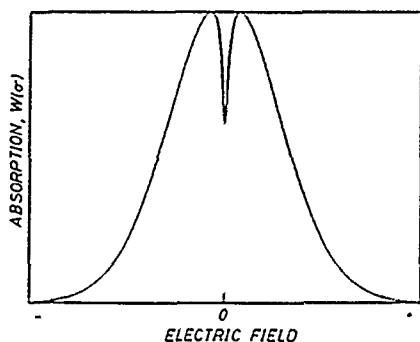


Figure 1. Typical level-crossing signal (central dip).

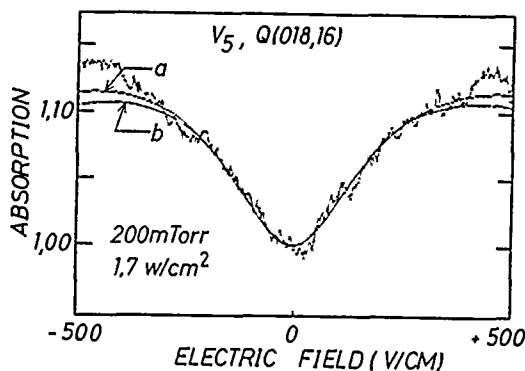


Figure 2. Level-crossing signal of  $^{12}\text{CH}_3\text{OH}$ , Q(018,16) along with calculated profiles. (a)  $\tau_1/2\pi=2.9$ ,  $\tau_2/2\pi=6.7$ ,  $\tau/2\pi=4.8$  MHz,  $\tau'=1.3\tau$ , (b)  $\tau_1/2\pi=2.9$ ,  $\tau_2/2\pi=4.3$ ,  $\tau/2\pi=3.6$  MHz,  $\tau'=1.7\tau$ .

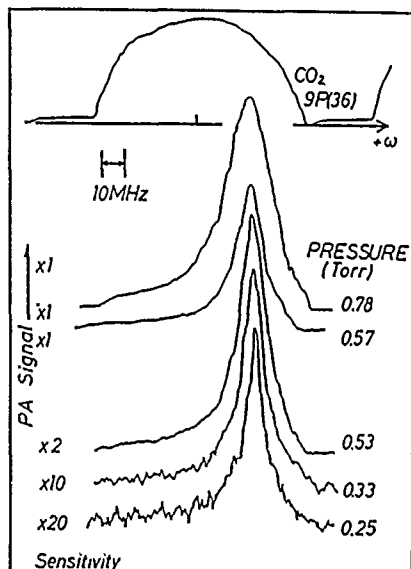


Figure 3. Intermodulated Doppler-free absorption signals of Q(018,16) at various pressures.

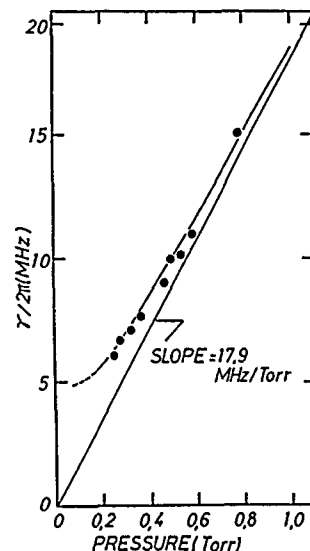


Figure 4. Homogeneous linewidth (HWHM) as a function of pressure.

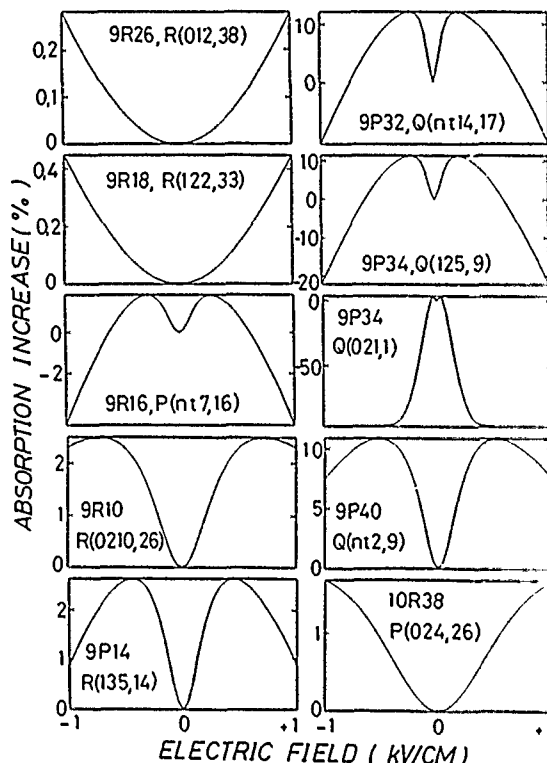


Figure 5. Calculated level-crossing signals of some pump transitions of  $^{12}\text{CH}_3\text{OH}$  cw fir laser lines. All the relaxation constants are assumed to have the same pressure coefficient of 20 MHz/Torr. The saturation parameter is taken as 0.2.

## IR SPECTRA AND FIR LASER ASSIGNMENTS FOR O-18 METHANOL

R.M. Lees<sup>a</sup>, W. Lewis-Bevan<sup>b</sup>, J.W.C. Johns<sup>c</sup>, R.R.J. Goulding<sup>a</sup>, D.P. Donovan<sup>a</sup> and C. Young<sup>a</sup><sup>a</sup>Dept. of Physics, University of New Brunswick, Fredericton, N.B., Canada E3B 5A3<sup>b</sup>Dept. of Chemistry and Biochemistry, Southern Illinois University, Carbondale, IL 62901<sup>c</sup>Herzberg Institute of Astrophysics, National Research Council, Ottawa, Canada K1A 0R6

## ABSTRACT

The high-resolution Fourier transform IR spectrum of the C-O stretch band of O-18 methanol has been investigated. Assignments have been determined for a number of FIR laser lines optically pumped by CO<sub>2</sub> lasers.

## INTRODUCTION

The various isotopic species of methanol are among the most important sources of optically pumped far-infrared (FIR) laser emission. This is due both to the good coincidences between the methanol C-O stretching IR bands and the CO<sub>2</sub> laser bands and to the density of the torsion-rotation spectral structure. The most recent species to be investigated is CH<sub>3</sub><sup>18</sup>OH, for which 100 FIR laser lines have been observed covering a wide range of frequencies (1). For O-18 methanol, although the Q branch of the C-O stretch band is located at 1008 cm<sup>-1</sup> in the gap between the 9.6 μm and 10.6 μm CO<sub>2</sub> laser bands, the P and R branches overlap well with the 10R and 9P laser bands, respectively.

In order to seek quantum number assignments for the FIR laser transitions, the IR spectrum of the CH<sub>3</sub><sup>18</sup>OH was recorded at high resolution from 900 to 1100 cm<sup>-1</sup> (2,3). Analysis of the spectrum has permitted identification of much of the structure for the n=0 and n=1 torsional states, and has led to proposed assignments for 7 IR-pump/FIR-laser transition systems so far. Although the assignments have not yet been confirmed definitively by the combination loop technique using complementary FIR spectra as was done for the analogous case of C-13 methanol (4), the assigned FIR laser frequencies seem quite consistent with calculated energy levels for the excited C-O stretch state.

## IR SPECTRUM OF THE C-O STRETCH BAND

The Fourier spectrum of the C-O stretch band of CH<sub>3</sub><sup>18</sup>OH was originally recorded at a resolution of 0.004 cm<sup>-1</sup> on a Bomem DA3.002 spectrometer at the University of British Columbia. From this spectrum, many of the torsion-rotation branches in the n=0 torsional ground state were assigned (3). When coupled with an optoacoustic study showing the strong coincidences with CO<sub>2</sub> laser lines, the results suggested good possibilities for FIR laser lines, but severe IR line overlap led to some

ambiguity as to the assignments (2). Accordingly, the spectrum was reexamined at 0.002 cm<sup>-1</sup> resolution on the modified Bomem DA2.002 spectrometer at the Herzberg Institute of Astrophysics.

With the higher resolution data, the assignment uncertainties have been substantially reduced, and the spectral identifications have been extended to higher K and to the n=1 excited torsional state. All series have been assigned up to K=6 and J values of about 35 for the A, E<sub>1</sub> and E<sub>2</sub> torsional symmetries for the n=0 state, with the exception of the (nτK) = (015) E<sub>1</sub> series. For n=1, branches up to K=3 have been assigned, with the exception of the (1 3 2) E<sub>2</sub> series. Analysis of the branches to determine power-series expansion coefficients is underway.

## FIR LASER ASSIGNMENTS

At about the same time as the analysis of the new CH<sub>3</sub><sup>18</sup>OH spectrum was in progress, a preprint was received from Prof. F. Strumia containing observations of FIR laser lines. From our IR results, it proved possible to identify a number of the IR pump transitions coincident with the CO<sub>2</sub> laser lines. Then, calculations of the excited C-O stretch energy levels were performed to determine the FIR laser frequencies associated with the proposed IR pump transitions to see if the assignments were realistic. In the calculations, the torsional barrier and effective rotational constant were taken for the vibrational ground state as  $V_3^0 = 374.9146$  cm<sup>-1</sup> and  $B_3^0 = 0.77450$  cm<sup>-1</sup>, and for the first excited C-O stretch state as  $V_3^1 = 394.3$  cm<sup>-1</sup> and  $B_3^1 = 0.76776$  cm<sup>-1</sup>. For both states, identical values of certain a-type torsion-rotation interaction and centrifugal distortion constants were used, as determined from a previous microwave study (5).

The assignments proposed so far are presented in Table 1, showing the comparison first between the frequencies of the reported CO<sub>2</sub> laser pump plus offset (in MHz) and the spectroscopic IR transition, and then between the observed and calculated FIR laser frequencies. Given the IR and FIR measurement uncertainties, plus the significant uncertainty in the excited state energy calculations, the agreement is very encouraging, with the possible exception of the heavily overlapped IR transitions in the enigmatic 10R(20) pump systems (2). Thus, the assignments

for the 7 IR-pump/FIR-laser transition schemes look quite plausible. In Fig. 1, the systems are illustrated for the 9P(14) and 10P(24) pumps involving closely related levels of A symmetry with A+/A- asymmetry splittings.

### CONCLUSIONS

The IR C-O stretch band Fourier transform spectrum of  $\text{CH}_3^{18}\text{OH}$  has been investigated from  $900\text{--}1100\text{ cm}^{-1}$  at a resolution of  $0.002\text{ cm}^{-1}$ , and nearly all branches have been assigned for K values up to 6 for the  $n=0$  torsional ground state, and K up to 3 for the  $n=1$  excited state, up to J values of typically 35.

With the IR spectroscopic results plus calculated C-O stretch energy levels, it has been possible to determine plausible assignments for 7 IR-pump/FIR-laser transition schemes, and thereby to identify 17 of the 100 FIR laser lines so far reported.

### ACKNOWLEDGEMENTS

We wish to thank Drs. M.C.L. Gerry and A.J. Merer for their hospitality at the University of British Columbia, and Drs. F. Strumia and N. Ioli for providing the list of FIR laser frequencies of  $\text{CH}_3^{18}\text{OH}$  prior to publication. Support of the research by the Natural Sciences and Engineering Research Council of Canada and the University of New Brunswick Research Fund is gratefully acknowledged.

### REFERENCES

- (1) N. Ioli, A. Moretti, D. Pereira, F. Strumia, and G. Carelli, Proc. Fourth Int. Conf. on Infrared Physics, Zurich, Switzerland, August, 1988, pp. 382-384.
- (2) R.R.J. Goulding, R.M. Lees, W. Lewis-Bevan, and C. Young, Infrared Phys., in press.
- (3) R.R.J. Goulding, Ph.D. Thesis, University of New Brunswick, 1987.
- (4) I. Mukhopadhyay, R.M. Lees, W. Lewis-Bevan, J.W.C. Johns, F. Strumia, and G. Moruzzi, Int. J. IR and MM Waves **8**, 1483-1502 (1987).
- (5) M.C.L. Gerry, R.M. Lees, and G. Winnewisser, J. Mol. Spectrosc. **61**, 231-242 (1976).

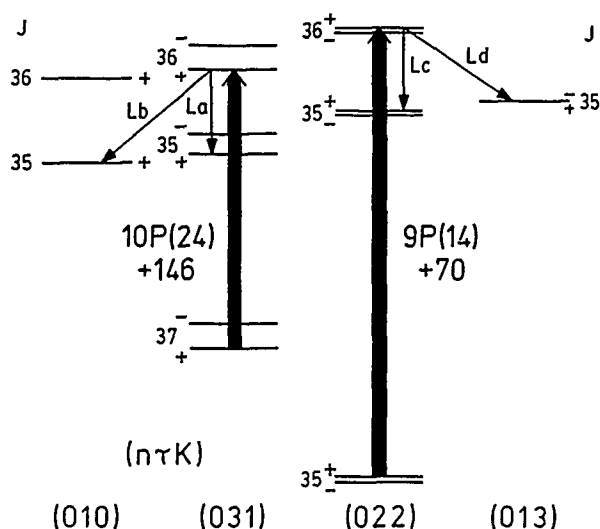


Figure 1. Proposed energy level systems for the 10P(24) and 9P(14)  $\text{CO}_2$  pump lines in  $\text{CH}_3^{18}\text{OH}$ . FIR laser frequencies (in  $\text{cm}^{-1}$ ) are:  $L_a = 54.11$ ,  $L_b = 58.79$ ,  $L_c = 54.89$  and  $L_d = 46.69$ .

Table 1. Assignments of FIR Laser Lines in O-18 Methanol

CO2 Pump	Offset	$\nu_{\text{pump}}$	IR Assgt	$\nu_{\text{IR obs}}$	$\nu_{\text{laser}}$	Pol.	FIR Assgt	$\nu_{\text{calc}}$
9P(14)	+70	1052.19788	R(022+,35)	1052.19729	54.89 46.69	 	(022+,36)-(022+,35) -(010, 35)	55.09 59.00
9P(26)	+10	1041.27941	R(026, 24)	1041.27932	38.11 44.94 83.45	 ⊥ 	(026, 25)-(026, 24) -(035, 25) -(035, 24)	38.23 44.65 82.89
9P(32)	+90	1035.47662	R(025, 19)	1035.47698	30.53 39.70 70.21	 ⊥ 	(025, 20)-(025, 19) -(034, 20) -(034, 19)	30.61 39.30 69.93
10R(20)	+21	975.93114	P(014, 19)	975.929608	27.48 17.99 45.47	 ⊥ 	(014, 18)-(014, 17) -(023, 18) -(023, 17)	27.56 18.41 45.97
10R(20)	-31	975.92941	P(033, 19)	975.925238	27.58 45.49	 	(033, 18)-(033, 17) -(012, 17)	27.59 45.09
10R(6)	-118	966.24642	P(022+,24)	966.24611	35.15 55.07	 	(022+,23)-(022+,22) -(031+,22)	35.26 54.78
10P(24)	+146	940.55297	P(031+,37)	940.55194	54.11 58.79	 	(031+,36)-(031+,35) -(010, 35)	54.30 59.00

⊥ Overlapped line

## FAR INFRARED LASER ASSIGNMENTS FOR METHYLAMINE

R. M. Lees

Department of Physics, University of New Brunswick, Fredericton, N.B., Canada E3B 5A3

and

W. Lewis-Bevan

Dept. of Chemistry and Biochemistry, Southern Illinois University, Carbondale, IL 62901

## ABSTRACT

High-resolution FTIR spectroscopy of the C-N stretching band of  $\text{CH}_3\text{NH}_2$  has permitted location of several coincidences with  $\text{CO}_2$  laser lines, and identification of FIR laser transitions optically pumped by these lines. With the use of previous FIR spectroscopic results, it has been possible to form closed frequency combination loops to support the assignment of one of the IR-pump/FIR laser transition systems and improve the accuracy of one of the FIR laser frequencies.

## INTRODUCTION

The infrared spectrum of methylamine was originally reported at low resolution by Gray and Lord (1). They found the C-N stretching band to be centered around  $1044\text{ cm}^{-1}$ , with the usual P, Q and R branch structure expected for a parallel vibration. This band thus overlaps very well with the  $9.6\text{ }\mu\text{m}$  band of the  $\text{CO}_2$  laser, and might be expected to yield good possibilities for optical pumping and far-infrared (FIR) laser emission. Indeed, FIR laser lines from  $\text{CH}_3\text{NH}_2$  were detected early on by Plant et al. in 1973 (2), and further pump systems giving FIR emission were reported by Radford (3,4), Landsberg (5), and Dyubko et al. (6). During the same period, an optoacoustic study by Walzer et al. (7) revealed a rich spectrum of signals, showing that a substantial number of  $\text{CO}_2$  laser lines must overlap with methylamine IR transitions.

The identification of the quantum numbers for the IR pump and FIR laser transitions in methylamine, however, presents a very difficult spectroscopic problem. In addition to the complex structure introduced into the spectrum by the internal rotation (torsion) of the  $\text{CH}_3$  group relative to the  $\text{NH}_2$  group, there is also a significant and irregular splitting of the energy levels due to the inversion or wagging motion of the  $\text{NH}_2$  (analogous to the well-known inversion in ammonia). The two levels of an inversion doublet can be labelled as "a" or "s", for antisymmetric or symmetric rotational states, and have spin weights of 3 and 1, respectively. Thus, there are twice as many lines in the spectrum as one would get for methanol, already a complex situation, and with widely differing and relative intensities.

A vibration-torsion-rotation-inversion energy level of methylamine can conveniently be denoted as

$$E(n\tau K^{\pm}-a, J)^v \quad \text{or} \quad E(n\tau K^{\pm}-s, J)^v$$

where  $n$  is the torsional quantum number,  $\tau$  is an index equal to 1, 2 or 3 which specifies the torsional symmetry,  $K$  is the axial component of the rotational angular momentum  $J$ , and  $v$  is the vibrational state. The  $\pm$  superscript indicates a particular component of an asymmetry doublet for levels of A symmetry only. Substantial progress has been made recently (8-11) in the understanding of the FIR spectrum and the IR C-N stretching band of  $\text{CH}_3\text{NH}_2$ , but it does not yet appear possible to calculate the energy levels with real accuracy from the available model Hamiltonians, even for the ground vibrational state. Thus, assignment of the FIR laser lines must still depend to a large extent on direct spectroscopic observations. Furthermore, the low value of the  $\mu_a$  parallel dipole component makes the  $\Delta K=0$  a-type FIR transitions very weak, so that for  $\text{CH}_3\text{NH}_2$  one does not see the familiar patterns of triads of FIR laser lines that are such a help to assignments in methanol.

## FIR LASER TRANSITION SYSTEMS

Our high-resolution Fourier transform spectrum of the C-N stretch band (11), in conjunction with previous FIR results for the vibrational ground state (8, 10), has yielded some insight into the FIR laser emission from  $\text{CH}_3\text{NH}_2$ . The  $9\text{P}(24)$   $\text{CO}_2$  laser line, which produces a particularly intense optoacoustic signal (7), falls within the dense Q-branch of the band and lies about 45 MHz below a strong observed IR line. From our results, it appears that the latter is the  $^9\text{Q}(029-a, 15)$  IR transition, with the FIR laser lines reported at  $45.9\text{ cm}^{-1}$  (2) and  $67.638548\text{ cm}^{-1}$  (2, 4) being assigned as the  $(029-a, 15)^1 \rightarrow (038-a, 15)^1$  and  $(029-a, 15)^1 \rightarrow (039-a, 14)^1$  excited transitions, respectively. These assignments are based on the consistency of the following independent closed-loop combination relations which can be formed from the transition scheme shown in Fig. 1:

$$\begin{aligned} b &= a+l-d = 45.7153\text{ cm}^{-1} \\ &= i+k-e = 45.7143\text{ cm}^{-1} \end{aligned}$$

$$\begin{aligned} c+h-k-i &= 0.0015\text{ cm}^{-1} \\ c+g-l-a &= -0.0021\text{ cm}^{-1} \\ c+f-m-j &= -0.0004\text{ cm}^{-1} \end{aligned}$$

The values of the frequency of laser line b agree to within the experimental uncertainty, and are significantly more accurate than the previous wavelength measurement. The residual loop defects involving line c, which has been precisely measured by heterodyne techniques (4), are zero to within experimental accuracy, so also serve to tie down the assignment through the well-determined ground state FIR assignments of lines k, l and m.

Similarly, the 9P(46) CO<sub>2</sub> line has been found to pump two IR transitions. One is the <sup>9</sup>P(022<sup>+</sup>-a,15) line, for which we assign the FIR laser line at 28.5 cm<sup>-1</sup> (5) to the (022<sup>+</sup>-a,14)<sup>1</sup> → (031<sup>-</sup>-a,13)<sup>1</sup> transition. The other is a <sup>9</sup>P(0r7,15) transition, with the FIR lines reported (5) at 35.3 and 56.2 cm<sup>-1</sup> assigned to (0r'7,14)<sup>1</sup> → (0r6,14)<sup>1</sup> and (0r'7,14)<sup>1</sup> → (0r6,13)<sup>1</sup> transitions, respectively. Here, we have not confirmed the (nrK) assignment through combination loops, but the most likely possibilities appear to be (017-s) or (037-s) for the pumped levels.

Tentative J-numbering has been determined for a few further pump transitions, but definite assignment proposals await additional analysis of the IR spectra.

#### CONCLUSIONS

High-resolution FTIR observations coupled with previous FIR spectral analysis have permitted complete or partial assignment of those FIR laser line systems pumped by the 9P(24) and 9P(46) CO<sub>2</sub> laser lines. The assignment for one of the systems is supported by forming closed frequency combination loops. Thus, the interplay between IR and FIR spectroscopy and FIR laser emission measurements has again given important clues to the assignment, particularly valuable for the transitions of high K.

#### ACKNOWLEDGEMENTS

Support of the research by the Natural Sciences and Engineering Research Council of Canada and the University of New Brunswick Research Fund is gratefully acknowledged. We also thank Dr. J.W.C. Johns of the Herzberg Institute, NRC of Canada, for his collaboration in obtaining a recent FTIR spectra of CH<sub>3</sub>NH<sub>2</sub> at higher resolution, from which our final numbers were taken.

#### REFERENCES

- (1) A.P. Gray and R.C. Lord, J. Chem. Phys. **26**, 690-705 (1957).
- (2) T.K. Plant, P.D. Coleman, and T.A. DeTemple, IEEE J. Quantum Electron. **QE-9**, 962-963 (1973).
- (3) H.E. Radford, IEEE J. Quantum Electron. **QE-11**, 213-214 (1975).

- (4) H.E. Radford, F.R. Peterson, D.A. Jennings, and J.A. Mucha, IEEE J. Quantum Electron. **QE-13**, 92-94 (1977).
- (5) B.M. Landsberg, Appl. Phys. **23**, 127-130 (1980).
- (6) S.F. Dyubko, L.D. Fesenko, A.S. Shevyrev, and V.I. Yartsev, Sov. J. Quantum Electron. **11**, 1248-1249 (1981).
- (7) K. Walzer, M. Tacke, and G. Busse, Infrared Phys. **19**, 175-177 (1979).
- (8) M.S. Malghani, R.M. Lees, and J.W.C. Johns, Int. J. IR & MM Waves **8**, 803-825 (1987).
- (9) N. Ohashi and J.T. Hougen, J. Mol. Spectrosc. **121**, 474-501 (1987).
- (10) N. Ohashi, K. Takagi, J.T. Hougen, W.B. Olson, and W.J. Lafferty, J. Mol. Spectrosc. **126**, 443-459 (1987).
- (11) R.M. Lees, W. Lewis-Bevan, R.R.J. Goulding, and C. Young, CIRP4, Proc. 4th Int. Conf. on IR Physics, Zurich, 1988, pp. 587-589.

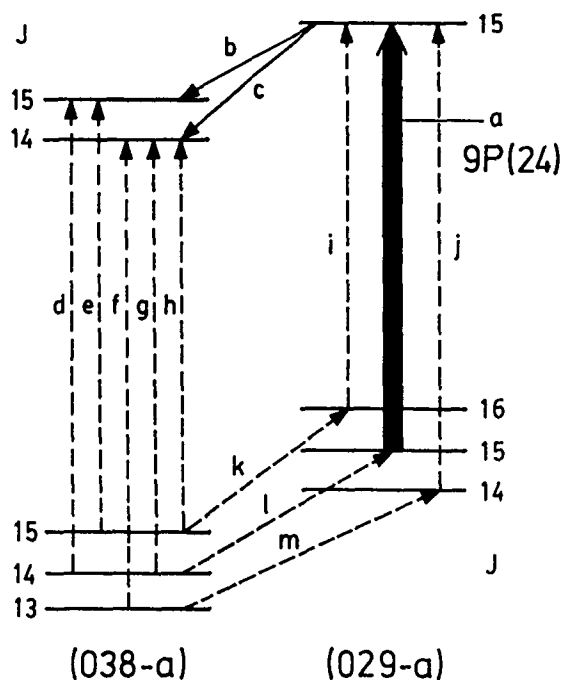


Figure 1. CH<sub>3</sub>NH<sub>2</sub> energy level system for the 9P(24) CO<sub>2</sub> pump. Frequencies are (in cm<sup>-1</sup>): a = 1043.1647, b = 45.9, c = 67.638546, d = 1065.4631, e = 1043.3040, f = 1064.2230, g = 1043.5378, h = 1021.3813, i = 1019.5343, j = 1065.3198, k = 69.4840, l = 68.0137, m = 66.5421.



## Experimental Results on Relativistic Gyrodevices

R.B. McCowan, S.H. Gold, W.M. Black and W.M. Manheimer

High Power Electromagnetic Radiation Branch  
Naval Research Laboratory  
Washington, DC 20375

### Abstract

Experimental work at the Naval Research Laboratory has proceeded on three different relativistic gyrodevices, the cyclotron autoresonance maser (CARM), the three cavity phase-locked gyrotron oscillator, and the high power free running gyrotron oscillator. Experimental results relating to these projects will be presented.

### The CARM

The CARM is a Doppler-shifted cyclotron maser. The interaction takes place at the upper intersection of the beam cyclotron wave with the dispersion relation of the waveguide. Like a free electron laser, it has the advantage of the Doppler-upshift in frequency, and also like an FEL, the beam must have a small spread in parallel velocity. A CARM oscillator has been designed and constructed at NRL and experimental work on it is under way. There are two key issues for this CARM experiment, first producing a beam with sufficiently small velocity spread, and second, developing a cavity which will favor the CARM interaction rather than the competing low frequency gyrotron interaction. To address the former issue, an electron gun has been fabricated which has a velvet emitting region and anodized aluminum to suppress emission on the remainder of the cathode, which serves also as a focusing electrode. To address the second issue, a Bragg resonator cavity has been designed and constructed. This cavity is designed to select the high frequency CARM interaction and should suppress the gyrotron interaction. The experiment has been designed to run on the NRL TRITON accelerator, and is expected to generate about 10 MW at 100 GHz in the  $TE_{61}$  mode. A schematic of the CARM experiment is shown in Fig 1.

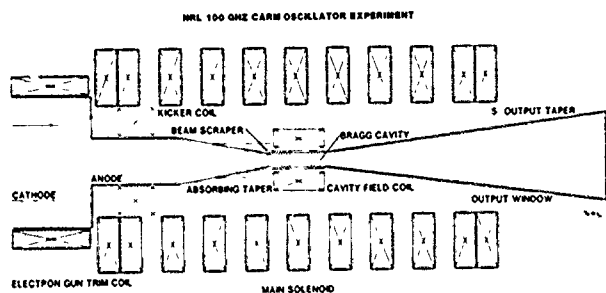


Figure 1

### The Phase Locked Gyrotron Oscillator

To investigate the issues of phase locking a gyrotron oscillator at high power, a fundamental mode three-cavity gyrokystron oscillator has been designed and constructed. The Q values of the individual cavities are controlled with axial slots. These slots also permit squash tuning of the cavity. This tuning is necessary so that the cavities can all be tuned to the same frequency. The individual cavities have all been designed and their design has been confirmed with cold tests. The actual cold cavity frequencies have to account for the effects of beam loading also, and this, of course cannot be cold tested. It is important to realize that the first two prebunching cavities contain a linear beam wave interaction implying a particular frequency shift, while the last cavity contains a nonlinear beam wave interaction with a different frequency shift. The design of the cavity must account for all of this, because the magnitude of these frequency shifts exceeds the predicted phase-locking bandwidth.

The cavity and slot widths must be chosen so that the two prebunching cavities are stable to all modes, while the oscillator cavity is unstable only to the intended  $TE_{12}$  mode of oscillation. The stability of the prebunching cavities is a difficult constraint, particularly because the rf electric fields of the bunching cavities extend fairly far into the drift regions, which can be made only weakly cut off in order to allow passage of the electron beam through clear the drift region. Because of the axial extent of the electric field, these cavities must be designed to suppress higher order axial modes also. This is done with 'keyhole' shaped slots  $90^\circ$  away from the main slots in the cavity wall. The final design has the prebunching cavities below the start oscillation threshold current for all possible modes at the design current, voltage, beam alpha, and magnetic field, while the oscillator cavity is designed to generate 10 MW at 35 GHz in the  $TE_{12}$  mode. The prebunching cavity is driven with a 20 kW magnetron at 35 GHz. A schematic of the three cavity phase locked gyrokystron oscillator is shown in Fig 2.

### NRL 35 GHz MULTI-CAVITY PHASE-LOCKED GYROTRON

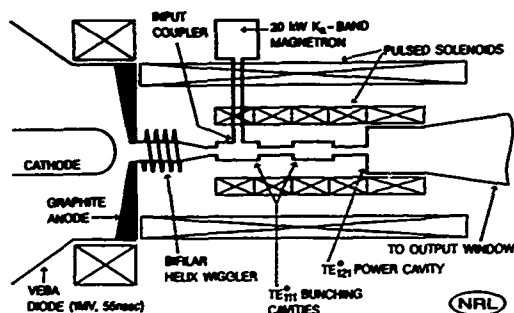


Figure 2

#### High Power Free Running Gyrotron Oscillator

The experimental study of high power gyrotron oscillators has been under way at the Naval Research Laboratory for about four years. The initial studies were carried out on a compact Febetron accelerator, and achieved 100 MW with 8% efficiency at 35 GHz in a  $TE_{62}$  mode.<sup>1</sup> More recently, experimental work has moved to the VEBA accelerator in order to investigate higher voltages and currents as well as longer pulse widths. Initial experiments have generated 100 MW, but with a longer, more robust (that is about 50 nsec) microwave pulse, a microwave pulse whose duration is apparently limited by the duration of the beam voltage pulse. Increasing the voltage to 1.2 MV increased the power to 200 MW, but the efficiency dropped to about 6%. The next series of experiments attempted to improve the performance by improving the beam quality. Since VEBA has the capability of generating about twenty times the current necessary for gyrotron operation, a beam scraper diode was utilized. Of the 30 kA generated by the accelerator, only about 4 kA gets through the anode aperture. This significantly improves the beam quality. With the new diode configuration, power of about 250 MW has been generated with an efficiency in excess of 10%. The microwave pulse is still robust and still lasts for the entire duration of the voltage and current flat-top. A schematic of the VEBA gyrotron is shown in Fig 3.

### VEBA GYROTRON EXPERIMENT

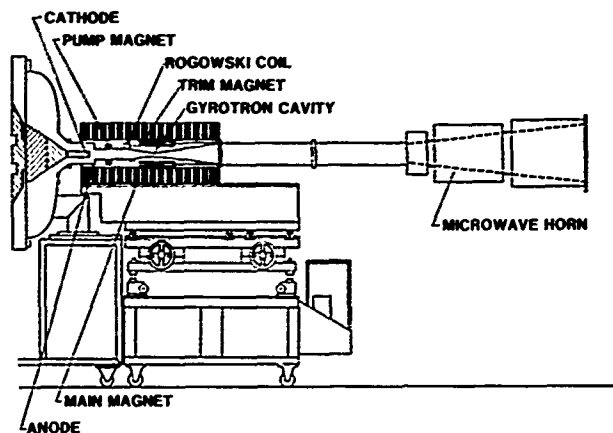


Figure 3

\* This work was supported in part by the Office of Naval Research, and in part by the Office of Innovative Science and Technology of the Strategic Defense Initiative, and managed by the Harry Diamond Laboratories.

#### References

1. S.H. Gold, et al., Phys. Fluids 30, 2226 (1987).

## INTENSE ELECTRON BEAM CYCLOTRON MASERS WITH MICROSECOND PULSELENGTHS

R. M. Gilgenbach, J. G. Wang, J. J. Choi, C. A. Outten,  
and T. A. Spencer

Intense Energy Beam Interaction Laboratory  
Nuclear Engineering Department  
The University of Michigan  
Ann Arbor, MI 48109-2104

### ABSTRACT

Experiments have been performed in which MW microwave power levels have been produced by means of the cyclotron maser resonance on high current, relativistic electron beams from a generator with parameters: 0.4 MV, 1.2 kA, and 0.4  $\mu$ s. In the first series of experiments, a nonadiabatic dip in the magnetic field imparted large ratios of perpendicular to parallel momentum ( $\alpha > 1$ ) in a transported beam current of typically 20 - 60 A. X-Band microwave power ( $> 0.6$  MW) was sustained over nearly the full e-beam pulselength and 85% variation in electron beam generator voltage. In more recent experiments, MW power levels in X-band have been generated using an improved magnetic field profile which increased the transported electron beam current to 500 - 1000 A, but with lower  $\alpha$  (0.2 - 0.3). A wiggler has been utilized to increase the ratio of perpendicular to parallel momentum. Data show a strong (up to a factor of 40) enhancement in peaks of K-band microwaves when the e-beam energy is near a resonance condition with the wiggler. Design studies are underway for a multimewatt, microsecond, intense electron beam cyclotron maser which will operate on the Michigan Electron Long Beam Accelerator (MELBA) at parameters: 0.7-1 MV, 1-10 kA, and voltage compensated pulselength of 1-1.5  $\mu$ s.

### 1. INTRODUCTION

In recent years a number of researchers have investigated the generation of MW to GW microwave power levels from intense, relativistic electron beam sources [1]. These sources have applications to new compact accelerators as well as fusion plasma heating [2,3]. A parameter regime of particular importance concerns kilojoule delivered energy, with 0.1-1 GW microwave power over pulselengths of 1-10  $\mu$ s. Several different physical mechanisms have been exploited for high power microwave generation from intense e-beams, including: relativistic magnetron [4], magnetically insulated line oscillator (MILO) [5], the virtual cathode oscillator (vircator), Cerenkov effects, and the electron cyclotron maser instability [6-8]. A major difficulty in extending to  $\mu$ s pulselengths in many of these devices concerns the generation of plasma in the microwave interaction region. The cyclotron

maser has an advantage in this regard, since the microwave interaction section can be separated from the e-beam collector and its associated plasma. However, a number of fundamental issues need to be addressed concerning the scaling of cyclotron masers to the 100 MW to 1 GW regime.

### 2. EXPERIMENTAL CONFIGURATION

In order to guide the design studies for the MELBA maser, a smaller pulseline type electron beam generator was utilized with a peak voltage of 0.4-0.5 MV and pulselength of 0.4  $\mu$ s. An annular velvet cathode produced a flat current pulse of about 1.2 kA. Two types of e-beam transport systems were employed:

1) Nonadiabatic dip in the pulsed magnetic field by means of a thick, aluminum anode plate, and 2) a thin stainless steel anode plate, field shaping coils, and a permanent magnet wiggler (shown in Figure 1). The first system imparted a large ratio of perpendicular to parallel electron beam momentum (estimated  $\alpha > 1$ ), but only transported 20- 60 A e-beam current into the device. The second system transported 500 - 1000A through the maser, but with a lower transverse to parallel velocity ratio (estimated  $\alpha \sim 0.2-0.3$  without the wiggler). A smooth bore waveguide ( $L = 97$  cm, I.D. = 2.84 cm) was initially employed in these experiments, although other cavity structures are under investigation. Pulsed magnetic field coils wound directly on the beam tube generated uniform fields of 2.2-4.8 kG.

### 3. EXPERIMENTAL RESULTS

Microwave emission data for the high  $\alpha$  maser configuration gave peak power levels of about 0.6 MW for an e-beam current of 20-60 A, corresponding to peak electronic efficiencies in the range of 6 %. High power microwave emission was maintained for 0.35  $\mu$ s, over voltage deviations of greater than 85%. For these high  $\alpha$  experiments, the tuning range in magnetic field for long pulse emission was very broad (Figure 2). The emission frequency (6.5-7.5 GHz) corresponds to the cyclotron maser interaction with the TE<sub>11</sub> waveguide mode. Sharp spikes in the microwave power with upward frequency chirping (due to drooping generator voltage) suggest that the maser operates on a number of closely spaced

( $\sim 0.1$  GHz) axial cavity modes. Operation with the second maser configuration gave higher X-band power ( $>1$  MW) with transported e-beam currents of 500–1000 A, in the absence of the wiggler. In order to increase the e-beam transverse energy, a 4.3 cm period, planar, permanent magnet wiggler was installed on the maser. Preliminary experiments with the wiggler showed large enhancements (factor of 40) of microwave emission in the K-band ( $>0.5$  MW). The wiggler-enhanced peaks in the emission consisted of short spikes as the rapidly drooping voltage passed through the conditions corresponding to beam energy near resonance with the wiggler period.

These preliminary experiments suggest that in future experiments utilizing the regulated voltage output from the MELBA accelerator [9], it should be possible to generate multimewatt microwave emission for microsecond pulses.

#### 4. ACKNOWLEDGMENTS

This research was sponsored in part by the Air Force Office of Scientific Research (Bolling AFB), Air Force Weapons Laboratory, and by a Presidential Young Investigator Award from the National Science Foundation. T. Spencer was supported by an Air Force Laboratory Graduate Fellowship. C. Outten received support from a DOE Magnetic Fusion Technology Fellowship.

#### 5. REFERENCES

- (1) IEEE Trans. on Plasma Science, Second Special Issue on High Power Microwave Generation 16 (1988)
- (2) R. M. Gilgenbach, et al., Phys. Rev. Lett. 44 647 (1980)
- (3) R. M. Gilgenbach, et al., Nuclear Fusion 21 319 (1981)
- (4) G. Bekefi and T. J. Orzechowski, Phys. Rev. Lett., 37 379 (1976)
- (5) M. C. Clark, B. M. Marder, and L. D. Bacon, Appl. Phys. Lett. 52 78 (1988)
- (6) A. N. Didenko, et al., Sov. J. Plasma Phys. 2 283 (1976)
- (7) S. Gold, et al, Phys. Fluids 30 2226 (1987)
- (8) R. M. Gilgenbach, et al., Proc. of 12th Int. Conf. on IR&MM Waves, Dec. 14–18, 1987
- (9) R. M. Gilgenbach, et al., Invited Paper, Proc. 5th IEEE Pulse Power Conf., p126 (1985)

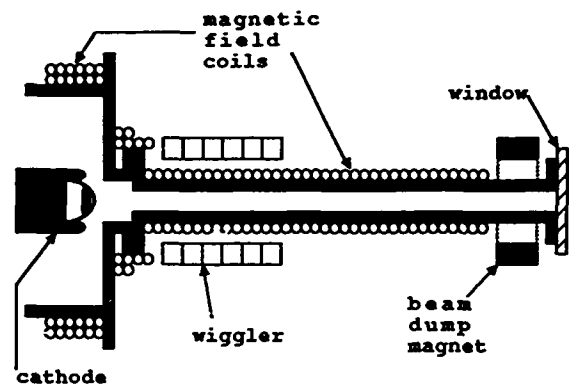


Figure 1  
Experimental configuration for high current maser.

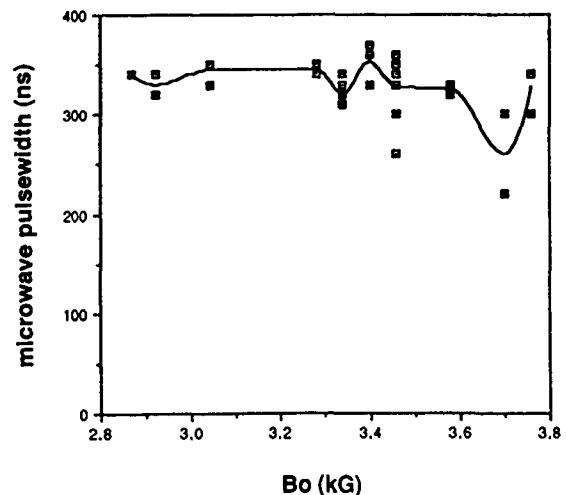


Figure 2.  
Data for high  $\alpha$  maser driven by  $0.4 \mu$ s pulseline generator.

# EXPERIMENTAL INVESTIGATION OF THE EFFECTS OF A NEUTRALIZING BACKGROUND PLASMA ON THE OPERATION OF A HIGH CURRENT GYROTRON\*

D.A. Kirkpatrick<sup>†</sup>, S.H. Gold, A.K. Kinkead, W.M. Manheimer,  
C.A. Sullivan<sup>†</sup>, T.M. Antonsen<sup>†</sup>, and B. Levush<sup>†</sup>

High Power Electromagnetic Radiation Branch  
Plasma Physics Division  
Naval Research Laboratory  
Washington, DC 20375-5000

## ABSTRACT

We present plans for an experiment to investigate the effects of a neutralizing background plasma on the operation of a high current gyrotron. A neutral plasma filling the electron beam transport and gyrotron cavity regions allows for the propagation of super-vacuum currents and for tuning of the interaction frequency through the neutralizing plasma density  $\omega_p^0$ . The background plasma is completely ionized before the passage of the high current electron beam, and the plasma density (in the absence of the electron beam) is a known, measured quantity.

## INTRODUCTION

Recent developments in high current electron beams have led to substantial increases in the output powers of devices based on the electron-cyclotron-maser[1] such as the gyrotron. The electron beam current propagated in these devices is approaching the vacuum limit, where the space-charge field of the beam depresses the electron beam energy and prohibits any further increase in the current transmitted. Well before this strict limit is reached, the space charge field interacts with the beam electrons to increase their velocity spread, reducing the device efficiency and limiting the output power.

Several experiments have already been carried out which use a neutralizing background plasma as a means to transcend these difficulties[2,3]. The background plasma which fills the beam transport and radiation interaction regions must be dense enough to neutralize and screen the charge in the high current electron beam, while at the same time it must be tenuous enough to allow for the free propagation of the output radiation and not have a deleterious effect on the desired beam interaction. An earlier experiment[3] with a 320 keV, 1.2 kA electron beam noted an increase in the output 10 GHz gyrotron power from 7 MW to 60 MW when the neutral plasma density was increased from  $n_p \sim 10^9 \text{ cm}^{-3}$  to  $n_p \approx 2 \times 10^{11} \text{ cm}^{-3}$ . Increasing the plasma density further to  $n_p \approx 5 \times 10^{11} \text{ cm}^{-3}$  resulted in a rapid reduction in the output power to about 10 MW. The beam current of 1.2 kA was greater than the vacuum current limit  $I_{vac} = 640 \text{ A}$  by slightly less than a factor of two. The plasma in this experiment was produced by a secondary, low voltage electron gun which was used to pre-ionize a background gas. Residual neutral gas which might be ionized by the passage of the high voltage electron beam would contribute to an uncertainty in  $n_p^0$ .

## EXPERIMENT

We are presently modifying a 35 GHz gyrotron oscillator experiment[4] to operate in the presence of a neutralizing background plasma. A 1–10 kA,  $\sim 1 \text{ MeV}$  electron beam is generated by a masked, cylindrical diode. The electron beam is spun up by means of a rapid drop in the axial magnetic field caused by a small field-reversed coil placed well after the cathode-anode gap. The beam is compressed into the gyrotron interaction region and then dumped on the downstream side by the fringing magnetic fields. Recent experiments in the absence of a neutralizing background plasma

have produced 200 MW of RF power at a frequency of 35 GHz. The maximum intracavity beam current was approximately 2 kA.

A neutralizing background plasma is added to this system by plasma guns[5] situated after the anode mask and before the field-reversed coil. The plasma guns are ideal for this application in that they are compact and produce a highly directional, almost completely ionized neutral plasma. Different plasma densities can be realized by firing the VEBA accelerator ( $\tau \sim 40 \text{ ns}$ ) at different times after firing the plasma guns. The plasma inventory as a function of time after the firing of the plasma guns is measured *in situ* by pairs of electrostatic probes. The plasma density available from four plasma guns situated symmetrically in the azimuth is then variable between  $n_p \sim 10^{11} - 10^{13} \text{ cm}^{-3}$ , corresponding to  $\omega_p^0/2\pi \sim 3 - 30 \text{ GHz}$ . The number density of the high energy electron beam is  $n_{beam} \sim 6 \times 10^{11} \text{ cm}^{-3}$  for  $J \sim 3 \text{ kA/cm}^2$ , and the available range in neutral plasma density should be able to scan through shielding the beam self-fields and approach cutting off the desired 35 GHz gyrotron interaction.

- (1) P. Sprangle and A.T. Drobot, IEEE Trans. Microwave Theory Tech., MTT-25(6):528 (1977).
- (2) V.I. Kremmentsov, M.S. Rabinovich, A.A. Rukhadze, P.S. Strelkov, and A.G. Shkvarunets, Sov. Phys.-JETP, 42(4):622 (1976).
- (3) V.I. Kremmentsov, M.I. Petelin, M.S. Rabinovich, A.A. Rukhadze, P.S. Strelkov, and A.G. Shkvarunets, Sov. Phys.-JETP, 48(6):1084 (1978).
- (4) W.M. Manheimer, S.H. Gold, J. Burke, A.W. Fliflet, and W.M. Black, Microwave and Particle Beam Sources and Propagation, N. Rostoker Ed., Proc. SPIE 873, p. 2 (1988).
- (5) R.J. Commisso, D.D. Hinshelwood, J.M. Neri, W.F. Oliphant, and B.V. Weber, NRL Memo Report 6057 (1987).

\*Work supported by the Office of Naval Research.

<sup>†</sup>Permanent address: Science Applications International Corporation, McLean, VA 22102.

<sup>†</sup>Permanent address: University of Maryland, Plasma Physics Laboratory, College Park, MD 20742.

## Design of a 100 kW Gyro-TWT

C.S. Kou, D.B. McDermott, C.K. Chong and N.C. Luhmann, Jr.

Dept. of Electrical Engineering, University of California  
Los Angeles, California 90024

## ABSTRACT

A gyro-TWT is often plagued by absolute instabilities in lower order modes and even in the operating mode itself. These problems will be avoided by performing the experiment in the lowest order mode in cylindrical waveguide (TE<sub>11</sub>) and using a low  $\alpha$  beam to excite a wave with large  $k_{\parallel}$ . A gyroresonant wiggler will partially transform the axial velocity of a high quality Pierce beam into transverse velocity. A 100 keV, 5 A,  $\alpha = 0.5$  beam will generate 9 GHz rf in a 3 kG magnetic field. Magnetic tapering will be used to enhance the efficiency. The theoretical gain is predicted to be 60 dB with a bandwidth over 20%.

## INTRODUCTION

A Gyro-TWT utilizes a moderately relativistic electron beam to interact with a fast waveguide mode near the grazing point where the beam's velocity is equal to the wave's group velocity. The interaction mechanism is based on the convective electron cyclotron maser instability which originates from the relativistic energy dependence of the electron cyclotron frequency<sup>(1)</sup>. Unfortunately, this convective instability can become absolutely unstable if the beam current exceeds a critical value which is a sensitive function of magnetic field and  $\alpha (= v_{\perp}/v_{\parallel})$ . The absolute instability is due to the coupling between the backward wave and the electron beam. The mismatch between the rf coupler and the waveguide circuit will also induce oscillation if the system's gain exceeds a certain value determined by the reflection from the rf couplers<sup>(2)</sup>.

The previous experimental investigations have been performed at NRL and by Varian Associates. The NRL experiments used the TE<sub>01</sub> mode of a circular waveguide of cutoff frequency 34.30 GHz with lossless interaction waveguide. Linear gain up to 32 dB was achieved with a 70 kV, 9 A electron beam. The best efficiency observed was 7.8 % with a 16.6 kW output power, 20 dB gain, and 1.4 percent bandwidth for a 3 A electron beam. The experiments performed by Varian Associates with a TE<sub>11</sub> circular polarized mode obtained impressive results. Substantial improvement was obtained by tapering the magnetic field by 4.4%. Small signal gain was 26 dB with a peak power of 120 kW at 26% efficiency. Saturated gain was 20 dB with a bandwidth of 7.25%<sup>(3)</sup>.

The goal of our experiment is to demonstrate the gyro-TWT as a high gain, wideband source. A low  $\alpha$  electron beam and the fundamental TE<sub>11</sub> mode will be used to stabilize the absolute instability. A tapered magnetic field will be used to enhance the efficiency.

## CALCULATED PERFORMANCE

The dispersion relation of the gyro-TWT interaction for a circular TE<sub>11</sub> mode and an axis-encircling cold electron beam is given by<sup>(4)</sup>,

$$(\omega^2 - k^2 c^2 - \omega_{nc}^2) \chi \omega - k v_{\parallel} - n \Omega_c)^2 = -\epsilon \quad (1)$$

where the coupling factor is

$$\epsilon = 4\beta_{\perp}^2 (I/I_A) \chi q_{n1}^2 - n^2)^{-1} (J'_n(q_{n1}r/a)/J_n(q_{n1}))^2 \quad (2)$$

$q_{n1}$  is the first zero of  $J'_n(y)$ ,  $\omega_{nc} = cq_{n1}/a$  is the cutoff frequency of the TE<sub>11</sub> wave, and  $I_A$  is the Alven current ( $\approx 17A$ ).

The spatial growth rate is obtained by solving Eq. 1. for the imaginary part of  $k_{\parallel}$ . The growth rates are plotted as a function of frequency for different values of electron beam current as shown in Fig. 1. Here a TE<sub>11</sub> mode with  $\gamma = 1.2$ ,  $\beta_{\parallel} = 0.5$ ,  $\alpha = 0.5$ ,  $\Omega_c/\omega_{nc} = 0.87$  is considered. The absolute instability will occur for an electron beam current of 15 A. From Fig. 1, we know that very high gain over 60 dB/m and with a bandwidth over 20% can be obtained with these design parameters. To avoid oscillation due to coupling mismatches, a sever may be necessary.

The predicted dependence of spatial growth rate on frequency for different values of magnetic field are plotted in Fig. 2. If the magnetic field is too large, oscillation will occur, but the gain will become too small when the magnetic field is too far beneath the grazing point. For this design, the tolerance is 7%, easily satisfied by our solenoid with a ripple of 1.5%.

## EXPERIMENTAL DESIGN

The experimental configuration with an interaction length of 1 m is shown in Fig. 3.

A modified version of the SLAC 5045 klystron gun will be used in this experiment. The dimension is scaled from the SLAC design by a factor of 3.5. This electron gun is operated at 100 kV and generates about 50 A. A small aperture will be used such that only a 5 A electron beam with low velocity spread can pass through. Simulation results of this design by Herrmannsfeldt's gun code have shown that the electron beam has characteristics very similar to that of the SLAC gun.

The transverse energy of the electrons which is needed for gyro-TWT interaction is obtained by passing the pencil electron beam through a gyro-resonant wiggler (i.e.,  $v_{\parallel} = \ell\Omega_c/2\pi$  where  $\ell$  is the wiggler's period). A 5 period permanent magnet wiggler has been built. A wiggler of the same design has been successfully used on another experiment performed at UCLA<sup>(5)</sup>.

A wideband coupler is required which will also allow the electron beam to pass through. Also the coupler must launch a circular polarized TE<sub>11</sub> mode. A design which satisfies these requirements is shown in Fig. 4, which is a modified version of the design by L.R. Barnett<sup>(6)</sup>. Preliminary tests show that a linear polarized TE<sub>11</sub> mode has been efficiently coupled from rectangular waveguide to circular wave guide with a bandwidth over 10%. The frequency response of the coupler is shown in Fig. 5.

A polarization converter is then used to transform a linear polarized wave into a circular polarized wave. It is based on the fact that the cut-off frequency of even mode and odd TE<sub>11</sub> modes of the elliptical waveguide are different<sup>(6)</sup>. By squeezing the circular waveguide by a certain eccentricity and length, the linear polarized wave is decomposed into these two modes, and a circular polarized wave can be obtained when the phase difference between this two modes becomes 90 degrees.

## ACKNOWLEDGEMENTS

We wish to acknowledge several stimulating discussion with Dr. K.R. Chu. This work is supported by ARO under contract DAAG29-84-K-0015.

## REFERENCES

1. P. Sprangle and A.T. Drobot, IEEE Trans. Microwave Theory Tech. MTT-25, 528-544 (1977).
2. Y.Y. Lau, K. R. Chu, L.R. Barnett and V.L. Granatstein, Int. J. IR and mm-Waves 2, 373 (1981)
3. V.L. Granatstein, M. Read, and L.R. Barnett, Infrared and mm waves, Vol. 5, K.J. Button Ed. New York, Academic, 1984, pp. 267-304
4. Y.Y. Lau, IEEE Trans. Electron Devices, 29, 320 (1982)
5. H. Cao, D.B. McDermott and N.C. Luhmann, Jr., "Initial Operation of a Cherenkov CARM," Proceedings of the 13th Int. Conf. on Infrared and mm-waves, 1988.
6. K.R. Chu, private communication.

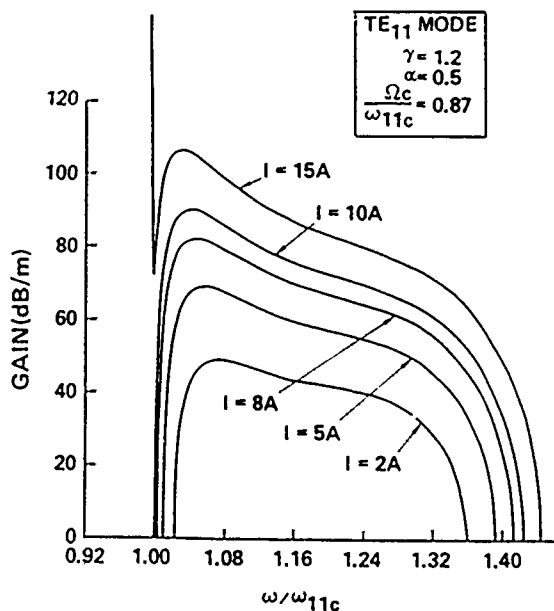


Fig. 1. Predicted dependence of spatial growth rate on frequency for several values of beam current.

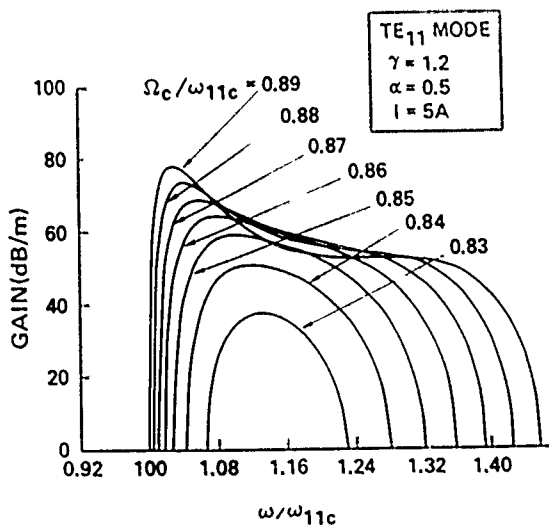


Fig. 2. Predicted dependence of spatial growth rate on frequency for several values of magnetic field.

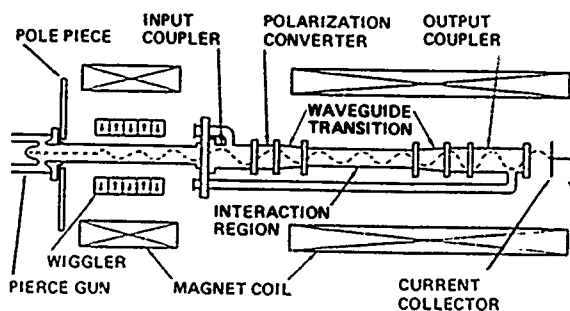


Fig. 3. 100-kW Gyro-TWT experiment configuration.

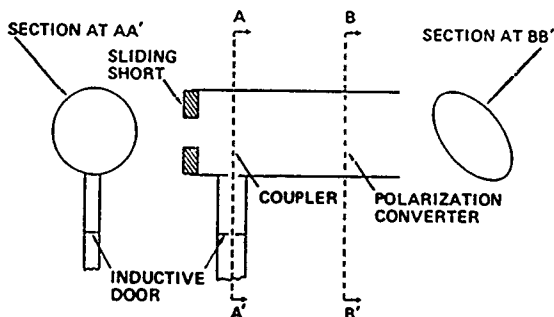


Fig. 4. Schematic of coupler

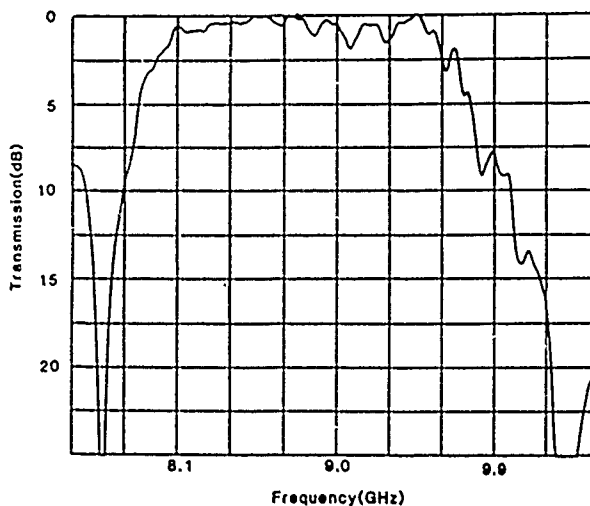


Fig. 5. Frequency dependence of the coupler's transmission.

## EFFICIENCY ENHANCEMENT IN GYRO-BWO BY TAPERED MAGNETIC FIELD

A. K. Ganguly and S. Ahn  
Code 6840, Naval Research Laboratory  
Washington, D.C. 20375

### ABSTRACT

A three dimensional self-consistent theory of the gyrotron backward wave oscillator has been developed in slow-time-scale formulation. The efficiency of gyro BWO is nearly 10% in a uniform magnetic field but can be enhanced to exceed 25% by tapering the magnetic field. Results are shown for TE<sub>10</sub> mode in rectangular waveguide and TE<sub>11</sub> mode in cylindrical waveguide.

### INTRODUCTION

Gyrotron backward wave oscillators (gyro-BWO) have great potential as tunable sources at mm-wave frequencies and can serve as drivers for ultra-high power gyrotron, CARM and FEL amplifiers. Initial experiment [1] of gyro-BWO at K<sub>a</sub>-band has shown a tuning range of over 15%. Backward wave amplification with internal positive feedback occurs when a forward cyclotron wave excited on a beam is in synchronism with a backward TE waveguide mode. Oscillations set in when the current exceeds a critical value. Calculations [2] of the efficiency in gyro-BWO give a modest value in the range of 10-15% in a uniform magnetic field. In this paper, we show that efficiency can be significantly enhanced by tapering the magnetic field as in gyrotrons and FEL.

### NON-LINEAR THEORY AND SIMULATION OF GYRO-BWO

The non-linear behavior and efficiency of gyro-BWO are calculated from a self-consistent set of coupled equations for the evolution of the electron trajectories and the RF field amplitude in the slow-time-scale formulation [3] which are commonly employed in gyro-devices. The electron beam is assumed to be monoenergetic but can have an axial velocity spread. The tapering of the external magnetic field is included in the theory. The boundary conditions for the RF electric field (F) correspond to two experimental situations:

$$F=0 \text{ at } z=L, \text{ and } \frac{dF}{dz} = -ik_z F \text{ at } z=0 \quad (1)$$

where L is the interaction length and  $k_z$  the axial wave vector. These boundary conditions apply to the case where the power is coupled out at the input end ( $z=0$ ) as is done in conventional BWO.

Perfect reflection at  $z=0$ , and  $\frac{dF}{dz} = ik_z F$  at  $z=L$  (2)  
These boundary conditions refer to reflection type BWO.

Numerical results are presented in the parameter ranges corresponding to the experiment [1] at NRL with TE<sub>10</sub> rectangular mode in the K<sub>a</sub>-band and the TE<sub>11</sub> (cylindrical) mode discussed in ref [2] for frequencies near 102 GHz. These examples considered the excitations in the fundamental cyclotron harmonic. The calculations were done for a monoenergetic and "cold" beam. Figs 1-3 refer to the TE<sub>10</sub> (rectangular) mode and a 33KV, 0.6A beam with  $\alpha = v_1/v_z = 1.3$ . The start oscillation condition in BWO is satisfied by a discrete set of frequencies with corresponding critical lengths. These modes are equivalent to the axial modes in gyrotron oscillator. In

Fig.1, the efficiency ( $\eta$ ) for the lowest axial mode is shown as a function of the interaction length (L) in a uniform magnetic field  $B_0 = 12kG$ . The guiding center of the beam is located at  $r_0 = 0.17L_x$ , where  $L_x = 0.22in$  is the width of the waveguide in the x-direction. The aspect ratio  $L_y/L_x = 0.636$ . The wave propagation is along the z-axis. The critical length for this mode is found to be  $L_c/L_x = 10.9$ . A maximum efficiency ( $\eta_{max}$ ) of 14% is obtained in this mode when the power is coupled out at the input end ( $z=0$ ) but  $\eta_{max}$  has a slightly lower value of 11% for the reflection-type BWO. In the latter case,  $\eta$  oscillates as a function of L due to the interference between the forward and the backward waves. The efficiency of the next higher mode (axial) for the reflection-type BWO is also shown in the figure. This mode has a higher critical length ( $L_c/L_x = 17.9$ ) and higher frequency. The variation of the output frequency with the interaction length is plotted in Fig 1b. The enhancement of efficiency in a tapered magnetic field is shown in Fig.2 for a reflection-type BWO. We consider a linearly tapered magnetic field of the form  $B = B_0(1 + sz/L_x)$  for  $0 \leq z < L$ . Fig. 2a is a plot of the efficiency as a function of the slope (s) of the magnetic field taper. Three values of  $B_0 = 11.0, 11.25$  and  $11.5$  are used. The interaction length  $L = 17L_x$  and the other parameters are the same as in Fig.1.

As seen in the figure,  $\eta$  increases sharply from 8% to 25% as s is raised to 0.004 ( $\Delta B/B_0 = 6.8\%$ ). The frequency of oscillation slowly shifts to higher values as shown in Fig. 2b. The results for magnetic tuning are given in Fig. 3 where  $\eta$  is plotted as a function of frequency (f). The corresponding magnetic field ( $B_0$ ) is also indicated in the figure. A tapered magnetic field  $B = B_0(1 + 0.00362z/L_x)$  is used in the calculation. Other parameters are the same as in Fig.2. The frequency tuning range at the 3-dB level is found to be 14.9% with a magnetic field tuning of 20.5%. We now consider the TE<sub>11</sub> cylindrical mode. The calculations were done for the boundary condition in Eq.(1) with  $V = 50kV, I = 3A, \alpha = 1.5, \Delta v/v_z = 0.0$  and  $B_0 = 44.93kG$ . The radius of the waveguide  $R_{wall} = 0.113$  cm. Fig 4a shows the efficiency as a function of the interaction length for a uniform magnetic field as well as a linearly tapered field with  $s=0.003$ . The efficiency increases from 14% to 34% in the tapered field. The frequency of the oscillations are shown in Fig. 4b.

### CONCLUSION

The efficiency of gyro-BWO with a cold beam is calculated to have a modest value of 10-15% in a uniform magnetic field. But the efficiency can be enhanced to over 25% by a suitable taper in the magnetic field. The efficiency of the gyro-BWO in the configuration where the power is extracted at the input end is higher than the reflection-type BWO. The frequency is magnetically tunable over a wide range of 15%. The effects of non-zero axial velocity spread and finite thickness of the beam will be discussed in a detailed publication.



## REFERENCES

- [1] Park, S.Y., Kyser, R.H., Armstrong, C.M., and Parker, R.K., "Experimental Study of Gyro-BWO", IEDM Digest Paper No. 35-4 (1987).  
 [2] Caplan, M., "Design of an Electronically Tunable Millimeter Wave Gyrotron Backward Wave Oscillator", 12th Int'l Conf. on Infrared and mm Waves, Orlando, Florida, p.276 (1987).

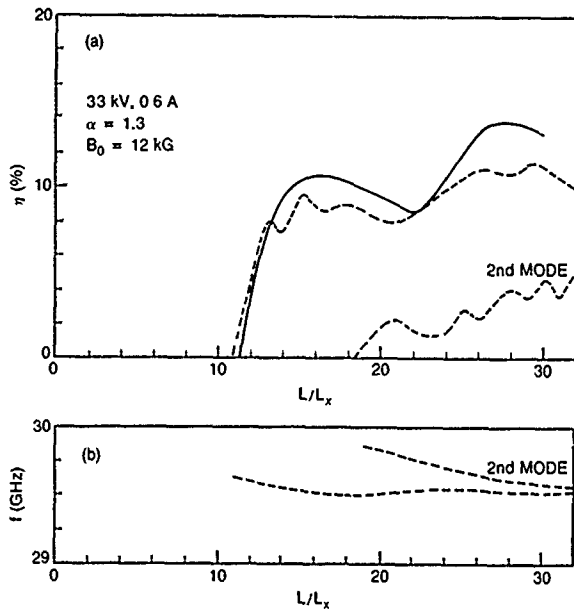


Fig 1. Efficiency ( $\eta$ ) and frequency ( $f$ ) vs interaction length ( $L$ ). Solid curve is for boundary conditions in eq.(1) and dashed curve for those in eq.(2).

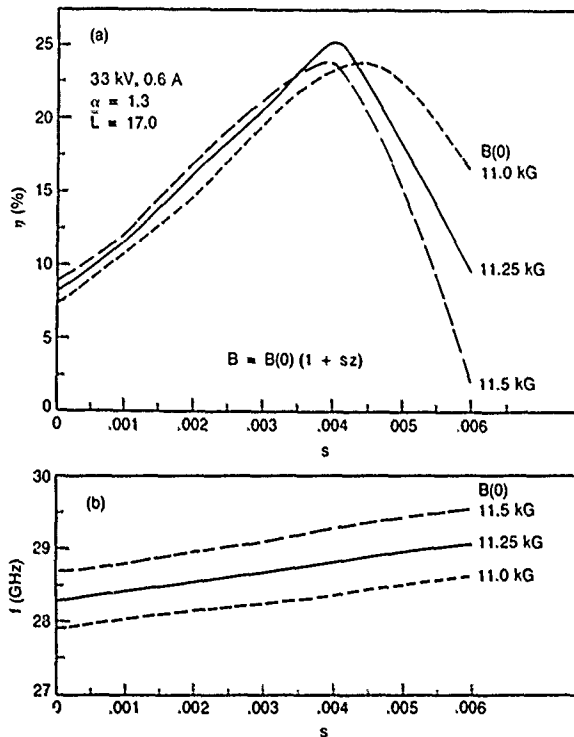


Fig 2. Efficiency and frequency as functions of the slope ( $s$ ) of the magnetic field taper.

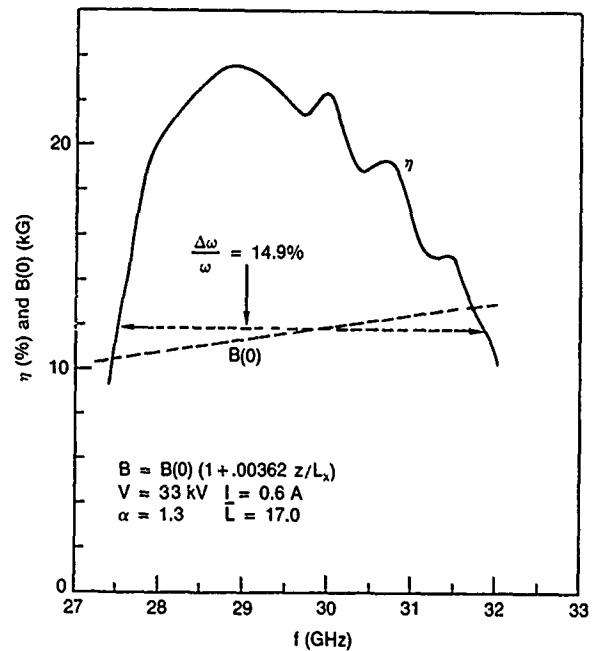


Fig 3. Magnetic tuning.

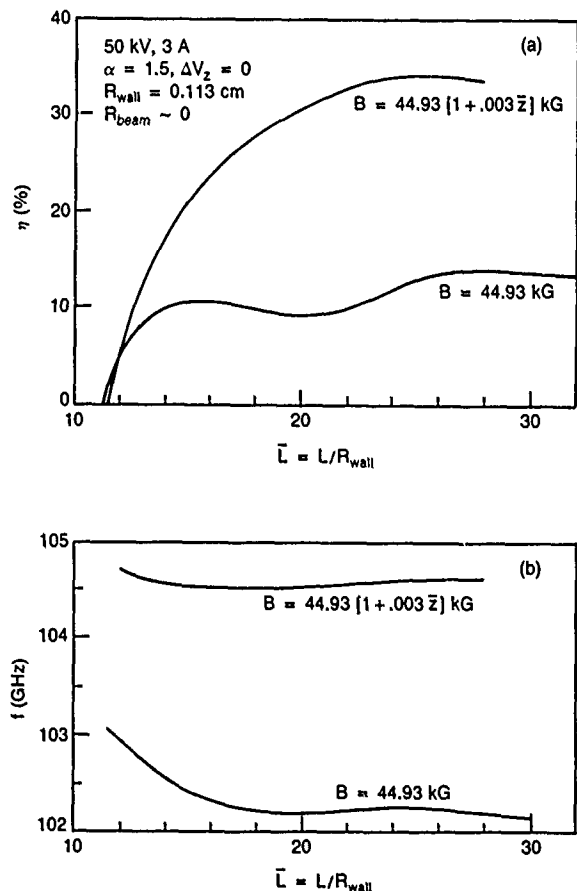


Fig 4.  $\eta$  and  $f$  as functions of  $L$  for  $TE_{11}$  mode in uniform and tapered magnetic field.

# OPERATION OF A 140 GHz TUNABLE BACKWARD WAVE GYROTRON OSCILLATOR

W.C. Guss, K.E. Kreischer, and R.J. Temkin

Massachusetts Institute of Technology, Cambridge, MA 02139

M. Caplan

Lawrence Livermore National Laboratory, University of California  
Livermore, CA 94550

D. Pirkle

Varian Assoc. Inc., Microwave Tube Division, Palo Alto, CA 94303

## ABSTRACT

A tunable backward-wave oscillator (BWO) gyrotron is currently being operated at MIT which is a prototype for a FEL driver at high frequency. Novel features of this design are the overmoded  $TE_{12}$  cylindrical cavity, a wide band mothe-eye window, and the use of a Pierce-wiggler gun. The design objectives are voltage tuning from 130-140 GHz with 10 kW output power. The interaction region is  $10\lambda_0$  long where  $\lambda_0$  is the free space wave length. A linear  $2^\circ$  uptaper is used to maintain mode purity and a broadband mothe-eye window is used for maximum transmission.

## INTRODUCTION

Plasma heating experiments using a FEL as the power source require a tunable driver whose frequency can be varied fast compared to the heating pulse length. Backward wave oscillators have this ability and some experimental results[1] have been already obtained for an oscillator using a fundamental rectangular interaction region with a hollow electron beam from a MIG source. A 3% voltage tunability centered at about 28 GHz was demonstrated with  $\approx 15\%$  efficiency. Caplan has performed a design study[2] using a nonlinear self-consistent computer code for an overmoded cylindrical interaction region using a Pierce-wiggler gun for 250-265 GHz. In that design, radiation is totally reflected at the gun end of the interaction region and exits the device in the direction of the beam propagation. We have selected another design point, 130-140 GHz, and produced a similar BWO gyrotron design.

The experimental program has as its goals the construction of the interaction circuit, tapers, and a broad band window and the subsequent operation of the tube. Initial operation will be at a single frequency and the power and efficiency optimized. Then the BWO gyrotron efficiency will be studied and optimized with respect to beam voltage (50-70 kV), wiggler period, and  $\alpha$  (.8- 2.0).

## EXPERIMENTAL DESIGN

The Pierce-wiggler gun was selected because of its relatively strong coupling to the  $m=1$  modes, specifically to the  $TE_{11}$  mode which would eliminate mode competition problems. The gun specifications are listed in Table I.

Table I

Parameter	Specification
Beam Voltage	60-80 kV
Beam Current	4 A
Perveance	.272 $\mu$ perv
Axial Field	2800 G max
Helical Field	10-12 G
Beam Radius	.127 cm at 2500 G

The helical field is produced by flexible permanent magnets that can be easily removed for pitch modification. Approximately six periods will be used in the 15 cm wiggler length. The gun is a unconventional because of its compact design.

Although the  $TE_{11}$  mode is most desirable, the resulting circuit size is small and virtually the same radius as the beam tunnel, so that it is impractical to implement. Consequently the cylindrical interaction region was designed for a  $TE_{12}$  mode. The dispersion relationship for this mode is shown in Fig. 1 along with several other nearby modes. For the case shown,  $\omega_{BWO}/\omega_c = 1.22$  and  $\omega_0/\omega_c = 1.36$ , where  $\omega_{BWO}$ ,  $\omega_0$ , and  $\omega_c$  are the BWO frequency, the electron gyro-frequency, and the cavity cutoff frequency ( $TE_{12}$ ) respectively. The slope of the beam line is proportional to  $v_{||}$  so that voltage tuning changes the slope, and therefore the intersection, and the resulting frequency and wavelength. Of the other modes, the modes with  $m \neq 1$  should not couple strongly. For  $m=1$  modes lower than the  $TE_{12}$ , the required length is greater than that for the  $TE_{12}$ , since the critical length for BWO oscillations is proportional to  $k_{||}$ .

A non-linear self-consistent electromagnetic simulation program[2], was used to determine the specifications of the interaction circuit and to predict operational characteristics of the tube. Comparison of experimental results with the code predictions benchmarks the code and bolsters our confidence in its further use. In the design phase, the code was used primarily to determine the circuit length. The efficiency as a function of length is shown in Fig. 2 for several values of axial velocity spread. Beam voltage and current were 60 kV and 4 A respectively; and  $\alpha=2$  was assumed. Anticipated values for the experimental velocity spread is  $\approx 8\%$  so an efficiency of  $\approx 10\%$  is expected. And Fig. 3 shows the output efficiency as a function of beam current for several values of  $\alpha$ . Table II summarizes the interaction region specifications.

Table II

Parameter	Specification
Cavity Radius	.214 cm
Cavity Length	2.141 cm
Beam Radius	.026 cm at 6.45 T
Beam Tunnel Radius	.055 cm

The output window is a mothe-eye window[3] which has about 90% transmission over a wide frequency range. Figure 4 shows the measured transmission from a quartz window ultrasonically machined with the shapes of small pyramids. Mode conversion and reflected power from the window may effect the operation of the BWO gyrotron and its effects will be studied.

A significant issue is the axial location of the termination of the interaction. In the results presented above it is assumed for computational and analytic convenience that it stops at the end of the circuit. This question was examined computationally with the non-linear BWO code since it can model varying wall radius. Solutions were found for cases where the interaction extended beyond the circuit end into the uptaper. Lower efficiencies were found, compared to the interaction ceasing at the circuit end, indicating that some reabsorption by the beam in the uptaper existed.

### ACKNOWLEDGEMENTS

We would like to acknowledge the assistance of Dr. M. Afsar for the window transmission measurement. We also thank Drs. S.Y. Park and A. Ganguly for useful discussions. This work was performed under DOE Contract No. W-7405-ENG-48 Subcontract No. 2698003.

### References

- [1] S.Y. Park, R.H. Kyser, C.M. Armstrong, and R.K. Parker, *International Electron Devices Meeting*, Dec. 6-9, 1987, p. 933
- [2] M. Caplan, *Twelfth International Conference on Infrared and Millimeter Waves*, Dec. 14-18, 1987, p. 274
- [3] J.Y.L. Ma, and L.C. Robinson, *Optica Acta* **30**, 1685(1983)

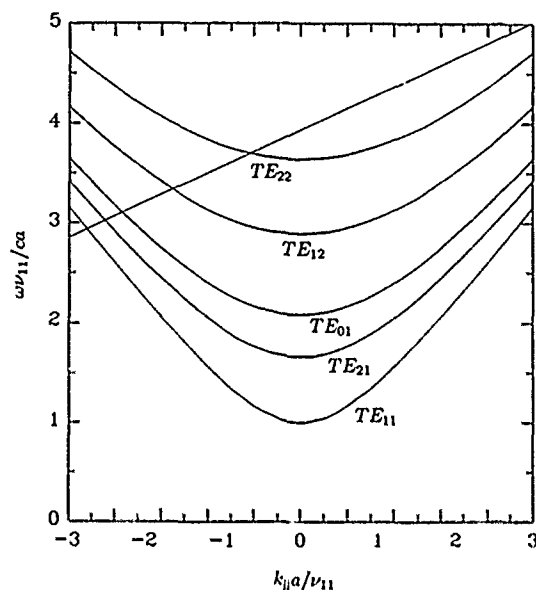


Figure 1. Dispersion diagram for BWO gyrotron with normalization to  $TE_{11}$  mode. Beam line assumes  $V_b=60$  kV and  $\alpha=2.0$ .

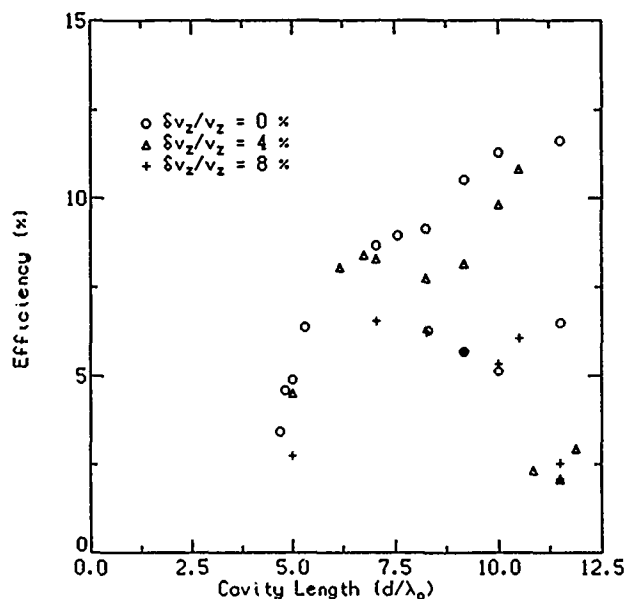


Figure 2. Oscillator efficiency as a function of length.

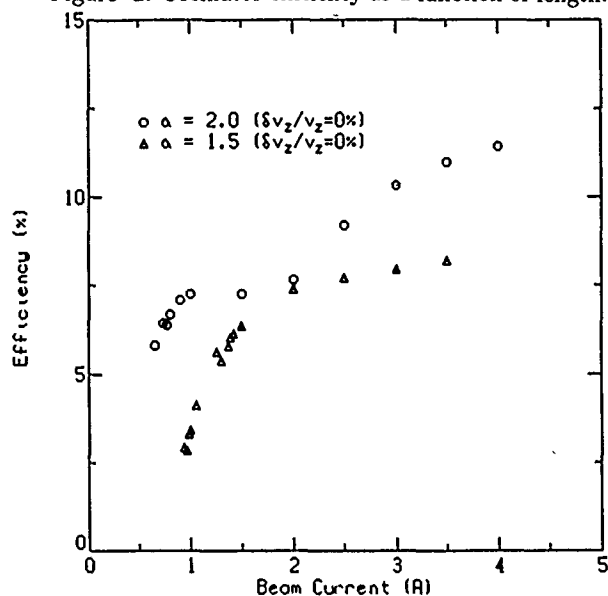


Figure 3. Oscillator efficiency as a function of beam current.

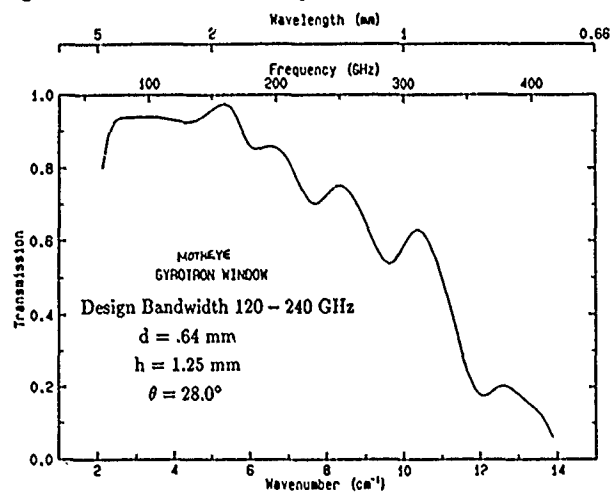


Figure 4. Window transmission as a function of wavenumber.

## AN EXPERIMENTAL SIXTEENTH HARMONIC CUSPTRON DEVICE

S.P. Kuo, K.K. Tiong and P.E. Miller  
Polytechnic University, Farmingdale, New York 11735

## ABSTRACT

A cusptron device operating at sixteenth cyclotron harmonic has been set up for the development of a compact and high power microwave source. An axis-encircling electron beam of 22Kev ( $\gamma=1.044$ ) as the radiation source is produced from an annular thermionic cathode of 1.4 cm radius and 0.16 cm radial thickness with a pierce-type focusing electrode together with a cusp magnetic field.

A 16-slotted waveguide with  $b/a=1.23$  is used for the  $2\pi$  mode operation where  $b$  and  $a$  are the radii of the slots and the inner wall of the waveguide respectively.  $a=1.7$  cm is designed so that the operating magnetic field is 364 Gauss and the radiation frequency is 15.6GHz. 11% efficiency is achieved from particle simulation. The results of our experimental study will be presented and a comparison of the experimental results with those of particle simulation will be made.

## INTRODUCTION

In recent years, there has been considerable effort in gyrotron development (1,2). A gyrotron is tuned by varying the magnitude of the axial magnetic field; a high frequency gyrotron requires a large magnetic field when it is operated at the low harmonic mode. The magnetic field requirement is, however, reduced if the device is operated efficiently at a high cyclotron harmonic. A promising way to enhance the harmonic interaction is to maximize the finite Larmor radius effect by using an axis-encircling beam (3-7). Such a rotating electron beam can be produced by passing an axially moving hollow beam through a cusp magnetic field. In addition, if slots on the waveguide wall are introduced, it would allow efficient operation even at low beam energy (8-10). The cusptron is a device being developed to carry these features. It is designed to operate at the sixteenth cyclotron harmonic; an experimental set up has been constructed to demonstrate its feasibility.

Similar to magnetron device, cusptron can also have  $\pi$  mode and  $2\pi$  mode operations. The tube currently being operated will work in the  $2\pi$  mode. Though the results of particle simulations show that  $\pi$  mode operation can lead to a better output efficiency than  $2\pi$  mode operation, the difficulty in constructing a 32 vane waveguide for  $\pi$  mode operation forces us to choose the  $2\pi$  mode operation at the present stage. The machining work for the slotted waveguide is further reduced if the ratio  $b/a$  is not too large, hence,  $TE_{02}$  is chosen in the design to be the dominant mode of radiation.  $TE_{02}$  represents the dispersion branch of the slotted waveguide which becomes  $TE_{02}$  mode at  $b/a=1$ . The purpose of this work is to pave a way for the further development of a compact high power and high frequency millimeter wave source.

## EXPERIMENT

The experimental set up is shown in Figure 1a. Ten individually wound copper wire coils connected to three power supplies are used to produce the desired

magnetic field profile. A cusp field centered at the anode place is produced by the three coils positioned in the upstream region together with the first three of the remaining seven placed in the downstream region. The other four coils in the downstream region are used to produce a uniform field inside the waveguide for cyclotron harmonic resonance interaction. Each coil can sustain a maximum of 20 amperes current ( $\sim 1$ kG magnetic field) without overheating for an extended period of operation. The cusp transition width is narrowed substantially by a soft iron plate positioned between the upstream and downstream regions and jointed as part of the anode. The axial distribution of the magnetic field along the neutral axis is measured as plotted in Figure 1b, where the cusp transition length is found to be about 0.5 cm. The system vacuum is maintained by an ion pump at about  $10^{-8}$  torr.

A hollow electron beam will be produced from an annular thermionic cathode of 1.4 cm radius and 0.16 cm radial thickness with a Pierce-type focusing electrode. The electron axial energy is provided by a hard tube modulator with a maximum capability of 30 eV and 10 A current. The pulse width and pulse repetition rate is adjustable from 10-2 $\mu$ s and 200 Hz-1Kz respectively. The cathode is mounted on a bellow coupled tubing to facilitate alignment and the adjustment of the cathode-anode gap without breaking the vacuum system. The anode with an annular slit of width 0.2 cm supported by three bridges is attached to the iron plate. The slit will allow the hollow electron beam to pass through the magnetic cusp transition region, where the  $v_z \times B_r$  force converts the beam axial velocity  $v_z$  into the azimuthal velocity  $v_\theta$  on the downstream side of the cusp transition. The 16-vane waveguide for the beam-wave interaction is placed immediately behind a high voltage break in the downstream region.

The slotted waveguide is designed based on the results of numerical particle simulations. Shown in Figure 2 are the dependences of  $ka$  and  $\eta$  on  $b/a$  for  $TE_{02}$  mode, where  $k$  and  $\eta$  are the transverse wave number of the  $TE_{02}$  mode and the solution efficiency of the radiation respectively. It shows that the first peak of the efficiency is located near  $b/a=1.23$ . The corresponding  $ka$  value is 5.55. The other peaks are not considered because they require larger  $b/a$  value and also operate at lower output frequencies (i.e. smaller  $ka$  values). A photographic picture of the waveguide with  $b/a=1.23$  is shown in Figure 3. Since the radius  $r_L$  of an ideal E-layer is equal to the radius of the hollow beam, it is, thus, fixed by the radius of the annular cathode  $r_c$ , i.e.  $r_L=r_c$ . From the relations  $kc = 16 \Omega_0 / \gamma_0$ ,  $v_\perp = (\Omega_0 / \gamma_0) r_L$ , and  $\gamma_0 = (1 - v_\perp^2 / c^2)^{-1/2}$ , we obtain  $\gamma_0 = [1 - (kr_c/16)^2]^{-1/2}$ ,  $\Omega_0 = \gamma_0 \omega / 16$  and  $\omega = kc$ . Using the specific values  $r_c=1.4$  cm and  $k=3.267\text{cm}^{-1}$ , the operating voltage, magnetic field and output frequency are determined to be 22kV (i.e.  $\gamma_0=1.044$ ),

364 Gauss, and 15.6GHz respectively. The operational characteristics of the tube are summarized in Table I. At present, very weak signal in the expected frequency region has been observed. We are in the process of doing fine tuning for the operational parameters in order to achieve the expected output power.

#### REFERENCES

- (1) J.L. Hirschfield and V.L. Granatstein, IEEE Trans. Microwave Theory Tech., MTT-25, 528 (1977).
- (2) K.E. Kreischer and R.J. Temkin, Phys. Rev. Lett., 59, 547 (1987).
- (3) W. Lawson, W.W. Destler, and C.D. Striffler, Appl. Phys. Lett., 38, 570 (1981).
- (4) H.S. Uhm, C.M. Kim, and W. Namking, Phys. Fluids, 27, 488 (1984).
- (5) K.R. Chu and D. Dialetti, Int. J. IR & MM Waves, 5, 37 (1984).
- (6) S.P. Kuo, S.C. Kuo, B.R. Cheo and M.C. Lee, Int. J. IR & MM Waves, 7, 635 (1986).
- (7) W. Lawson and C.D. Striffler, Phys. Fluids, 29, 1682 (1986).
- (8) Y.Y. Lau and L.R. Barnett, Int. J. IR & MM Waves, 3, 618 (1982).
- (9) W. Namkung, Phys. Fluids, 27, 329 (1984).
- (10) K.K. Tiong, S.P. Kuo and S.C. Kuo, Int. J. Electronics, 64 (1988), September issue.
- (11) S.P. Kuo, K.K. Tiong, P.E. Miller and W. Namking, Phys. Fluids, 31, 1821 (1988).

#### ACKNOWLEDGEMENT

This work is supported by the Air Force Office of Scientific Research, Grant No. AFOSR-85-0316. Useful discussion with Dr. W. Namkung is appreciated. The computational work was performed at the Pittsburgh Supercomputing Center of NSF.

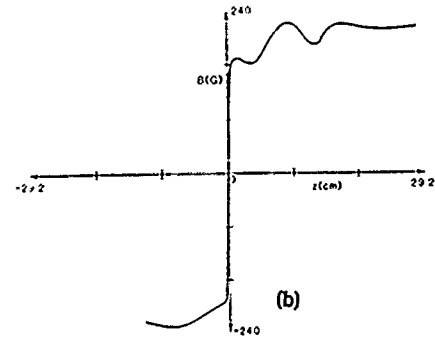
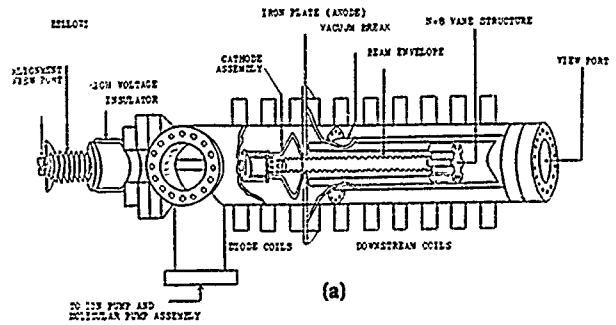


Fig 1 Schematic of the Cusptron device and axial magnetic field distribution

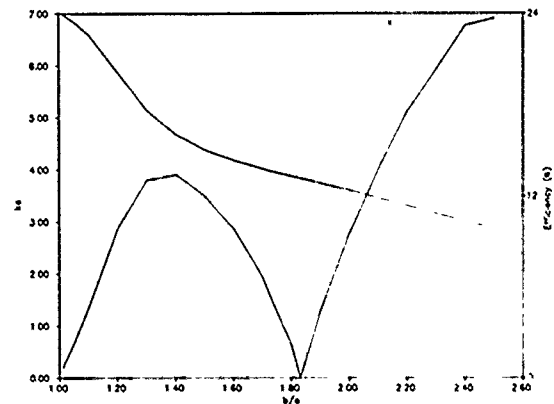


Fig 2  $ka$  and Efficiency versus  $b/a$  with  $r_1/a = 0.8$  for the Efficiency curve



Fig 3 Photograph of 16 vane waveguide with  $b/a = 1.23$

Table I

N	b/a	a (cm)	ka	$f_0$ (GHz)	magnetic field (G)	$\gamma$	Beam current (Amp)	$\eta$ (%)	Expected Output Power
16	1.23	1.7	5.55	15.6	364	1.044	#1	11	2.42kW

# RESONATOR WITH A CURVED WALL FOR A GYROTRON

O. Dumbrajs  
Arbeitsbereich Hochfrequenztechnik,  
Technische Universität Hamburg-Harburg,  
D-2000 Hamburg 90, Federal Republic of Germany

H. Wenzelburger  
Kernforschungszentrum Karlsruhe,  
Institut für Datenverarbeitung in der Technik,  
Postfach 36 40, D-7500 Karlsruhe 1,  
Federal Republic of Germany

## ABSTRACT

The influence of the curvature of the resonator wall on the frequency, quality factor, efficiency, current and the optimum magnetic field is studied within the framework of a simple resonator model for a gyrotron operating at 150 GHz in the TE03 mode with the output power 200 kW.

## INTRODUCTION

A design of a resonator with a curved wall for a gyrotron was reported as early as 1974 in [1], where it was shown that resonators with a rather complicated curvature can, indeed, increase efficiency of a gyrotron. Obviously, the most general method of study of resonator geometry can be posed in the form of the inverse problem [2]: determining the geometry of a cavity for a desired (for example, optimized with respect to maximum efficiency and minimum mode competition) field profile. In this approach the problem (as yet unsolved) of choice of a class of test functions for field profiles arises. In recent years several investigations of the direct problem (finding field profile on the basis of given geometry) for resonators with special forms have been carried out (see the review [3] and references therein). In the present work we investigate theoretically the influence of the curvature of a resonator wall on the frequency, quality factor, efficiency, current and the optimum magnetic field with a simple resonator model for a gyrotron operating under the conditions close to the KfK experiment:  $F = 150$  GHz, TE03 mode,  $P_{out} = 200$  kW,  $v_1/v_m = 1.5$ , and  $U = 70$  kV.

## RESONATOR

The geometry of the resonator studied is shown in Fig. 1. It consists of the input and output straight tapered sections and of the curved main part in the form of a circular arc. In the study the maximum resonator radius  $R_{max}$  was varied between  $R_0$ , which corresponds to the straight main section and 3.314 mm.

## CALCULATIONS

The calculations were performed both in the cold cavity approximation and self-consistently using the gyrotron theory developed at Gorky [4] with the formalism described by us in detail in [5].

## RESULTS

The results of the calculations are presented in Figs. 2 - 6 as functions of  $\Delta R = R_{max} - R_0$ . As expected, the frequency decreases linearly (Fig. 2) and the quality factor increases (Fig. 3) with increase of  $R_{max}$ . On the other hand, the efficiency and, therefore, the current are highly nonlinear functions of  $R_{max}$ . For  $R_{max} > R_0 + 0.05$  mm efficiency drops and current rises dramatically (Figs. 4 and 5). The optimum magnetic field decreases with increase of  $R_{max}$ . The calculations in the cold cavity approximation agree qualitatively with the results obtained in the self-consistent approach. In the latter case no solutions were found for large  $\Delta R$ .

## CONCLUSIONS

In the model studied the curvature of the resonator wall has a negative effect, and if it is large enough  $R_{max} - R_0 > 0.05$  mm it may very seriously deteriorate the gyrotron operation. This makes stringent demands on manufacturing methods of resonator and on cooling conditions which should prohibit any mechanical deformation of a resonator. The influence of the curvature on the mode competition between the principal TE03 mode and the parasitic TE32 and TE52 modes is under study and will be reported.

## REFERENCES

- [1] A. A. Kuraev, F. G. Shevchenko, and V. P. Shestakoich, Radio Eng. Electron. Phys. **19**, 96 (1974).
- [2] S. N. Vlasov, G. M. Zhislin, I. M. Orlova, M. I. Petelin, and G. G. Rogacheva, Radiofizika **12**, 1236 (1969).

- [3] Cheng-he Xu and Le-zhu Zhou, *Infrared and Millimeter Waves* 10, 311 (1983).
- [4] Gyrotron, Academy of Sciences of the USSR, Institute of Applied Physics, Gorky, 1981.
- [5] O. Dumbrajs and H. Wenzelburger, *Int. J. Infr. Mill. Waves* 9 (1988), (in print).

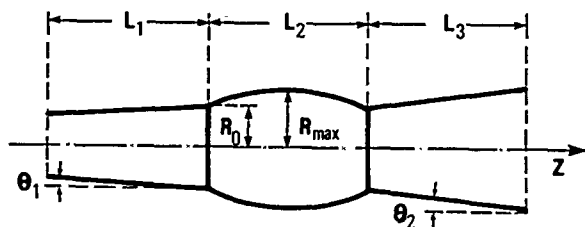


Figure 1

Geometry of the resonator studied:  $L_1 = 19$  mm,  $L_2 = 10$  mm,  $L_3 = 15$  mm,  $R_0 = 3.242$  mm,  $\theta_1 = 0.5^\circ$  and  $\theta_2 = 3^\circ$ .

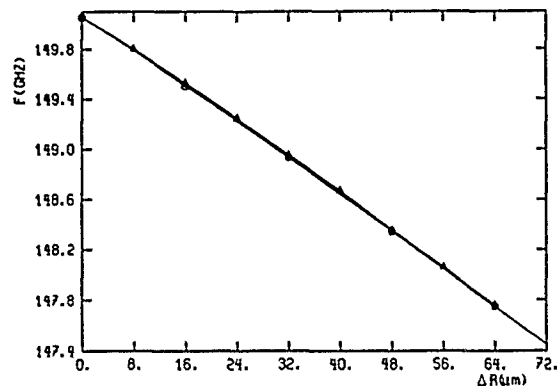


Figure 2

Frequency as a function of  $\Delta R$ ; o: cold cavity approximation,  $\Delta$ : self-consistent calculation.

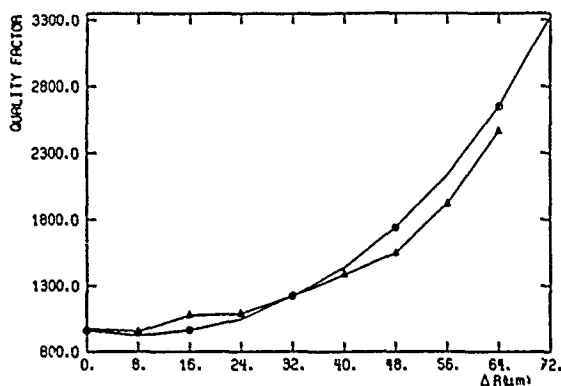


Figure 3

Quality factor as a function of  $\Delta R$ ; o: cold cavity approximation,  $\Delta$ : self-consistent calculation.

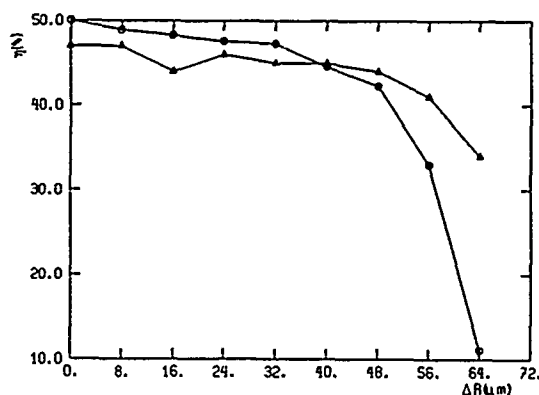


Figure 4

Efficiency as a function of  $\Delta R$ ; o: cold cavity approximation,  $\Delta$ : self-consistent calculation. The results are for  $P_{out} = 200$  kW and optimum magnetic field.

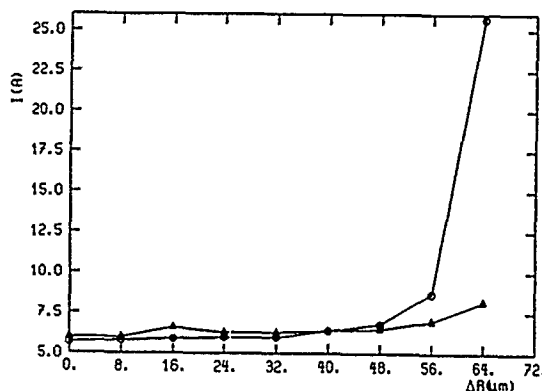


Figure 5

Current as a function of  $\Delta R$ ; o: cold cavity approximation,  $\Delta$ : self-consistent calculation. The results are for  $P_{out} = 200$  kW and optimum magnetic field.

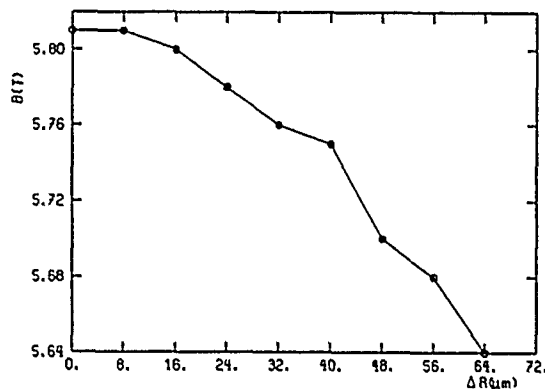


Figure 6

Optimum magnetic field as a function of  $\Delta R$ . The results are for  $P_{out} = 200$  kW.

## MILLIMETER-WAVE SUSPENDED PARALLEL-COUPLED FILTERS AT Ka AND W-BAND

Thomas Chen-Chou Ho and Kan Chou

Chung Shan Institute of Science and Technology  
Lung-Tan, Taiwan, Republic of China

### ABSTRACT

The design and development of Ka-band (26.5-40 GHz) and W-band (75-110 GHz) parallel-coupled filters with suspended stripline structure is described. The measured insertion loss at the passband is about 1 dB for Ka-band and 2 dB for W-band. The return losses are more than 12 dB in the passbands for both frequency bands.

### INTRODUCTION

Technological advances in millimeter-wave field have contributed to the growth of millimeter-wave systems during the last several years. Almost all millimeter-wave receiver systems require input bandpass filter for image or harmonic rejection. Therefore, a need for reliable low cost millimeter-wave components has lead to the development of integrated printing circuits. The printed circuit technology is used to reduce the size and cost, and to improve the performance and reproducibility in the production of millimeter-wave systems.

This paper describes the design and performance of the parallel-coupled line filters with suspended stripline structure at Ka and W-band. The filters are designed on the suspended substrates with built in transitions to waveguide input and output.

### TRANSITIONS

Before the development of the filter networks, techniques that allow for the transition from waveguide to suspended stripline must be formulated. The electric probe transition was chosen because it can be fabricated as an integral part of the stripline and the difficulty of making reliable electrical contacts is avoided.

Ka-band printed circuit transitions have been previously demonstrated with various Fin-line mixers [1]. W-band transition circuit is designed on an 5-mil-thick RT-5880 substrate with 1/8 oz. roll copper. The dielectric constant is 2.2. We fabricated and tested two such transitions connected back to back by a 0.6-inch-long suspended stripline. Good measured results are shown in Figure 1. The return loss is better than 12 dB, and the total insertion loss is about 1 dB over the entire W-band (75-110 GHz). The insertion loss of each transition is about 0.3 dB. The test fixture of this type transition is relatively simple, and sliding short can be used to optimized the performance at the specified narrow band frequency.

### DESIGN AND RESULTS

The suspended parallel-coupled line filter is designed by using a distributed prototype. The design procedures have been published in several papers [2]-[4]. However, in the practical realizations at millimeter-wave frequencies, several design iterations are normally

required to alleviate the end-step discontinuities, the transmission lines and the prototype problems.

Figure 2 shows a typical layout and equivalent circuit of coupled-line filter. In our design, a cascade of five parallel-coupled resonators with a half-wavelength at center frequency is chosen for both Ka and W-band. Six sections of quarter-wavelength long coupled transmission line connected in series can be also seen in the equivalent circuit. The K inverters in the prototype are first from the synthesis procedures [2][4]. Then the even-and add-mode impedances ( $Z_{oe}$  and  $Z_{oc}$ ) of the coupled lines are computed from the impedance inverter values. The line width and spacing of each coupled-line section are determined by the even- and odd-mode impedances. Finally, the coupled length of each section was determined by the Dell-Imagine formula [5].

Figure 3 and 4 are the pictures of two complete filters at Ka (26.5-40 GHz) and W-band (75-110 GHz). It can be viewed that parallel-coupled line filter at the center and two waveguide-to-suspended-stripline probe transitions at both sides of waveguide input and output ports. The complete circuit is fabricated on a single substrate, which is then cut to size and placed into a split-block housing. The W-band filter was fabricated on 5-mil-thick Duroid 5880 using chemical etching, and the Ka-band filter was also fabricated on Duroid 5880 substrate with the thickness of 10-mil.

The Ka-band filter was evaluated over the frequencies of interest, and its performance is shown in Figure 5. The insertion loss is about 1 dB and return loss is 12 dB over the 7-GHz passband (28.5-35.5 GHz). Figure 6 shows the performance of W-band filter with 10-GHz passband (84.5-94.5 GHz). The measured insertion loss is approximately 2 dB and return loss is more than 15 dB in the passband.

### CONCLUSIONS

Millimeter-wave Parallel-coupled line filters have been designed and developed with suspended stripline structure. Good performances have been achieved at Ka and W-band. A simple split-block housing with printed circuit makes these filters highly reproducible. These light weight, small size and low cost filters are suitable for millimeter-wave systems.

### ACKNOWLEDGEMENT

The authors gratefully acknowledge the technical assistance of many colleagues in MIC Laboratory at CSIST.

### REFERENCES

- [1] T.C. Ho and K. Chou "High Performance mm-Wave Balanced Mixers for Ka-Band Down-Converters," in IEEE Int'l conf. Dig. of IR & MM-WAVE pp. 118-120, Dec. 1987.



- [2] S.B. Cohn, "Parallel-Coupled Transmission-Line Resonator Filters," IRE. Trans., Microwave Theory Tech., Vol.MTT-6, pp.223-231, April 1958.
- [3] D. Rubin and A. Hislop, "Millimeter-Wave Coupled Line Filters Design Techniques for Suspended Substrate and Microstrip," Microwave Journal, Vol. 23, pp.67-68, Oct. 1980.
- [4] J.D. Rhodes, "Design Formula for Stepped Impedance Distributed and Digital Wave Maximally Flat and Chebyshev Low-Pass Prototype Filters," IEEE Trans. Circuit Systems, Vol. CAS-22, pp.866-876, Nov. 1975.
- [5] R.A. Dell-Imagine, "A parallel Coupled Microstrip Filter Design Procedure," 1970 IEEE Int'l Microwave Symp. Dig., pp.29-31, May 1970.

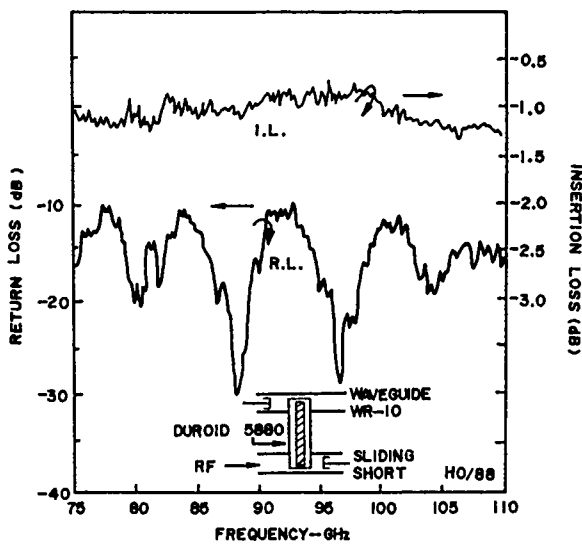


Figure 1. Performance of W-band electric probe type transition ( Loss including two transitions and 0.6-inch suspended stripline ).

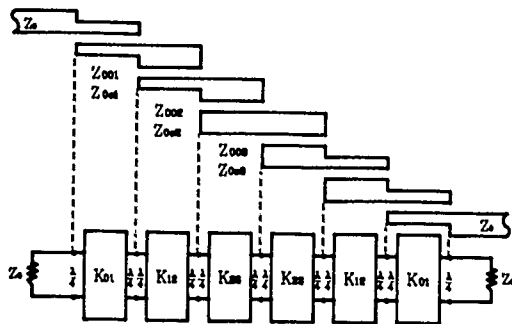


Figure 2. Layout and equivalent circuit of parallel-coupled line filter

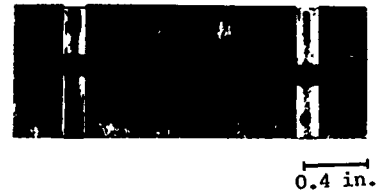


Figure 3. Photograph of a completed Ka-band filter.

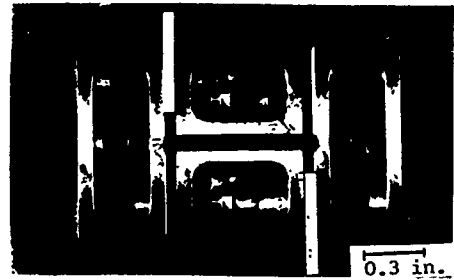


Figure 4. Photograph of a completed W-band filter.

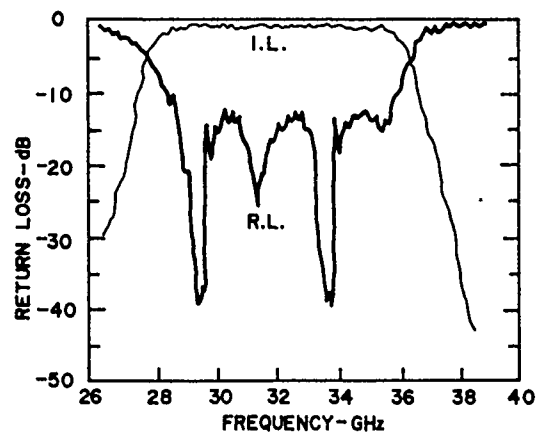


Figure 5. The Measured return loss and insertion loss of a Ka-band filter with 7-GHz passband.

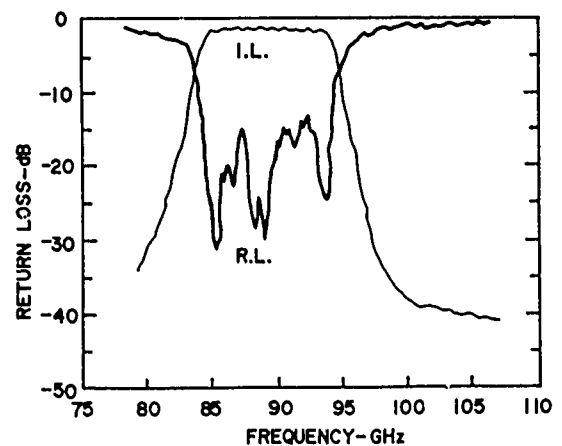


Figure 6. The measured return loss and insertion loss of a W-band filter with 10-GHz passband.

# PRINTED-CIRCUIT RAT-RACE-TYPE DIRECTIONAL COUPLERS FOR LARGER POWER-SPLIT RATIO

Isao OHTA, Ichiro HAGINO, and Takenori KANEKO

Faculty of Engineering, Himeji Institute of Technology  
2167 Shosha, Himeji-shi, 671-22 Japan

## ABSTRACT

Two different types of  $5\lambda/2$ -wavelength rat-race-type directional couplers with a remarkably increased power-split ratio for a realizable ring-impedance, in particular which are useful for millimeter-wave circuits suffering from the severe restriction on the usable impedance range, are described. Experimental corroboration is provided in the microwave region (at 8 GHz).

## INTRODUCTION

The  $3\lambda/2$  rat-race-type (or hybrid ring) directional coupler with 3-dB (1) or an arbitrary coupling (2) has been employed as an important circuit element in microwave communications systems and radar systems. However, this conventional coupler, especially when constructed of printed-circuits, suffers from a deterioration of accuracy in manufacturing and lastly falls into impossibility to manufacture with increasing of power-split ratio, because a pair of lines between its two adjacent arms is required to have a higher characteristic impedance and lastly the width of the lines becomes unrealizable. This problem becomes more serious in the millimeter-wave region owing to severer restriction on the usable impedance range.

This paper deals successfully with the above difficulty by designing  $5\lambda/2$  rat-race circuits with  $\lambda/4$  impedance steps on the ring.

## CONFIGURATIONS AND SCATTERING MATRICES

In this section, we consider the two types of  $5\lambda/2$  couplers illustrated in Fig. 1. The characteristic admittance of the four arms is normalized to unity. The variable parameters are the three normalized admittances  $Y_1$ ,  $Y_2$  and  $Y_{2\Delta}$  for type-A, and  $Y_1$ ,  $Y_{1\Delta}$  and  $Y_2$  for type-B. The impedance matching conditions and the scattering matrices of both the types at the design frequency are given as follows:

$$\text{(type-A)} \quad Y_1^2 + (Y_2^2/Y_{2\Delta})^2 = 1 \quad (1)$$

$$[S] = \begin{bmatrix} 0 & 0 & jY_2^2/Y_{2\Delta} & jY_1 \\ 0 & 0 & -jY_1 & jY_2^2/Y_{2\Delta} \\ jY_2^2/Y_{2\Delta} & -jY_1 & 0 & 0 \\ jY_1 & jY_2^2/Y_{2\Delta} & 0 & 0 \end{bmatrix} \quad (2)$$

$$\text{(type-B)} \quad (Y_1^2/Y_{1\Delta})^2 + Y_2^2 = 1 \quad (3)$$

$$[S] = \begin{bmatrix} 0 & 0 & -jY_2 & -jY_1^2/Y_{1\Delta} \\ 0 & 0 & jY_1^2/Y_{1\Delta} & -jY_2 \\ -jY_2 & jY_1^2/Y_{1\Delta} & 0 & 0 \\ -jY_1^2/Y_{1\Delta} & -jY_2 & 0 & 0 \end{bmatrix} \quad (4)$$

Defining the coupling factors of type-A and B as

$C = 20 \log_{10} |S_{31}|$  and  $C = 20 \log_{10} |S_{41}|$  (or  $= 20 \log_{10} |S_{32}|$ ), respectively, we have

$$C = 40 \log_{10} Y_2 - 20 \log_{10} Y_{2\Delta} \quad (5a)$$

$$C = 40 \log_{10} Y_1 - 20 \log_{10} Y_{1\Delta} \quad (5b)$$

On the other hand, the coupling factor of a conventional  $3\lambda/2$  coupler can be described by

$$C = 20 \log_{10} Y_2 \text{ or } C = 20 \log_{10} Y_1 \quad (6)$$

according as  $Y_1 > Y_2$  or  $Y_2 > Y_1$  (2). A close look at eqs. (5) and (6) indicates that if  $Y_{2\Delta} = 1$  and  $Y_{1\Delta} = 1$ , the maximum absolute values in dB of the realizable coupling factors for both the  $5\lambda/2$  couplers are twice as large as that of the conventional coupler for the same realizable impedance.

Now, if, as an example, we consider a coupler with four equal arms of  $50 \Omega$  constructed of a microstrip line on a 0.2-mm-thick alumina substrate in U-band, the minimum coupling factor of a conventional  $3\lambda/2$  coupler is limited to approximately -8.9 dB but that of the present couplers is allowed to -19.8 dB because of the usable impedance range of 40-140  $\Omega$  (3).

Figs. 2 and 3 show the frequency characteristics of the scattering parameters of type-A and B couplers with a coupling factor of -15 dB. From these figures it is found that type-A is more favorable than type-B in the bandwidths of power split and isolation, but in the phase behavior type-B is much more excellent.

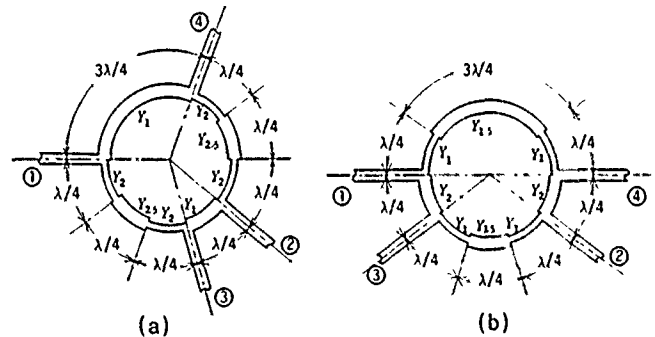


Fig. 1 Schematic configurations of  $5\lambda/2$  rat-race-type directional couplers. (a) Type-A. (b) Type-B.

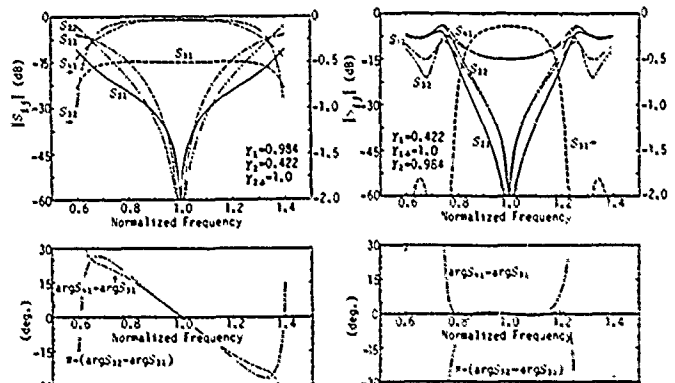


Fig. 2 Computed scattering parameters of type-A.

Fig. 3 Computed scattering parameters of type-B.

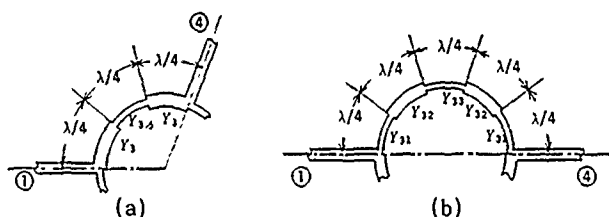


Fig. 4 Impedance steps inserted between arms 1 and 4.  
(a) Type-A. (b) Type-B.

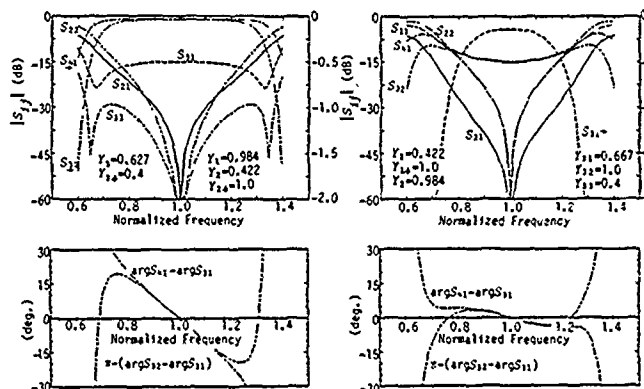


Fig. 5 Computed scattering parameters of an improved type-A.

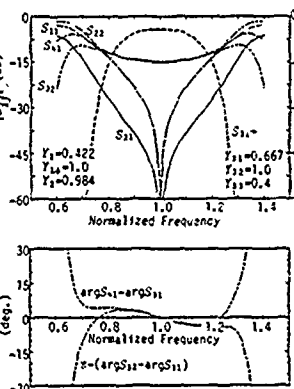


Fig. 6 Computed scattering parameters of an improved type-B.

### EFFECT OF ADDITIONAL IMPEDANCE STEPS ON CHARACTERISTICS

In this section, as illustrated in Fig. 4, we deal with couplers having  $\lambda/4$  impedance steps added between arms 1 and 4 for the purpose of improving on bandwidths of some scattering parameters. The characteristic admittances of the additional steps have to satisfy the following equations from the matching condition at the center frequency:

$$Y_3^2/Y_{32} = Y_1 \quad (7)$$

$$Y_{33}Y_{31}^2/Y_{32}^2 = \sqrt{1 - Y_2^2} \quad (8)$$

Figs. 5 and 6 exhibit the frequency dependency of each scattering parameter of the two improved couplers. For type-A, as can be seen in Fig. 5, a broadband matching of the input arm yielding geometrically symmetric and in-phase outputs (i.e., an improvement of  $|S_{11}|$ ) is obtained almost without degrading the other parameters. Fig. 6 shows considerable improvements in power split and isolation for type-B.

### EXPERIMENTAL RESULTS

An improved type-B coupler with a coupling factor

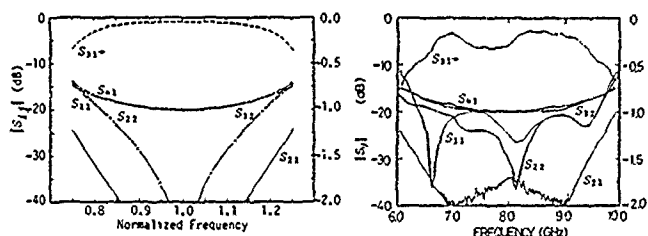


Fig. 7 Computed values of  $|S_{ij}|$  vs. frequency for a tested coupler.  
 $Y_1=0.316, Y_{31}=1.0, Y_2=0.995, Y_{32}=0.447, Y_{33}=1.0, Y_{34}=0.5$

Fig. 8 X-Y recording of  $|S_{ij}|$  of the tested coupler with a coupling factor of -20dB.

of -20dB at 8GHz was fabricated using a stripline on a 1/16-inch Rexolite 1422 substrate and tested as an example. The calculated and measured scattering parameters are shown in Figs. 7 and 8, respectively. A close agreement between both the results is observed.

### CONCLUSIONS

Two types of  $5\lambda/2$  rat-race-type directional couplers realizable of larger power-split ratio than any other rat-race coupler and methods of improvement on their bandwidths have been presented. The configurations of these couplers are useful to construct a coupler of a narrow stripline or microstrip line fabricated on a substrate of a small thickness and/or with a high dielectric constant. Experimental corroboration in the millimeter-wave region and an examination of excessive transmission loss caused by the additional ring line of a wavelength would be important subjects for further work.

### ACKNOWLEDGMENT

The authors would like to thank H. Taniguchi and R. Kagawa for contributions in computations and experiments.

### REFERENCES

- (1) W. A. Tyrrell: "Hybrid circuits for microwave", Proc. IRE, 35, 11, pp.1294-1306 (Nov. 1947).
- (2) C. Y. Pon: "Hybrid-ring directional coupler for arbitrary power divisions", IRE Trans. Microwave Theory & Tech. MTT-9, 11, pp.529-535 (Nov. 1961).
- (3) M. Muraguchi, T. Yukitake and Y. Naito: "Optimum design of 3-dB branch-line couplers using microstrip lines", IEEE Trans. Microwave Theory & Tech., MTT-31, 8, pp.674-678 (Aug. 1983).

## CIRCULATOR USING GaAs DUAL GATE FETs

Sachihiro Toyoda

Department of Electrical Engineering

Osaka Institute of Technology

5-16-1 Omiya Asahi-Ku Osaka 535 JAPAN

## Abstract

This paper describes active circulators for microwave band. Using three dual-gate FETs, a 2 GHz band circulator was constructed. The bandwidth of this circulator is 1.3 GHz, and the insertion loss and the isolation are 0.3 dB and 30 dB, respectively. Further, the circulator for 5 - 18 GHz band is proposed and tested. Three amplifiers for 5 - 18 GHz and three power dividers are used. The frequency range of this circulator is from 5 to 18 GHz. The circulator exhibit the insertion loss of 0.3 dB and the isolation of 30 dB. The circulator for 5 - 18 GHz band can be used for the input power up to 19 dBm.

## Introduction

Many studies of the microwave-band circulators using rectangular waveguides, coaxial lines or strip lines have been reported. The circulators using microstrip line, which are small in size and have broadband characteristics, have been commercially available. With the advancement of MMIC of microwave-band amplifiers and oscillators, the circulators at the input and output terminals of MMIC become necessary. In a conventional circulator, a permanent magnet is placed on the ferrite. When this type of circulator is used in MMIC, the magnetic field may induce Hall effect in the semiconductors, which is harmful to the MMIC. Although an active circulator requires power, no magnetic field is associated with it. Hence this type of circulator is desirable for the MMIC. Concerning an active circulator, Tanaka et al.(1) constructed the circulator for 500 Hz - 3 MHz band using three transistors.

The author constructed the 2 GHz band active circulator using three dual-gate FETs by the method of Tanaka et al. and proposes one type of active circulator. Three amplifiers for 5 - 18 GHz and three power dividers are used. This circulator exhibit broadband characteristic, and the bandwidth is 5 - 18 GHz. The isolation and the insertion loss are 30 dB and 0.3 dB, respectively. The active circulator has broadband characteristics which are beyond comparison with those of the conventional one using ferrite. Moreover, around 1 GHz, the conventional circulator is bulky and its bandwidth is narrow, whereas the active

circulator is compact and has wide bandwidth.

## Structures of the active circulators and experimental results

Figure 1 shows the circuit of an active circulator constructed using three dual-gate FETs(FET1 - FET3). In the circuit, FET4 - FET6 are single-gate FETs and are used as variable resistances. GaAs dual-gate FET is MGF-1100 and signal-gate FET is 2sk273. When the signal-gate FETs were used in place of FET1 - FET3, the oscillation occurred. The three dual-gate FETs were used to prevent this oscillation. In Fig. 1, the power incident on terminal 1 appears at terminal 3 and not at terminal 2. Likewise, the power incident on terminal 3 appears only at terminal 2, and the power coming to terminal 2 emerges only from terminal 1. When the voltages

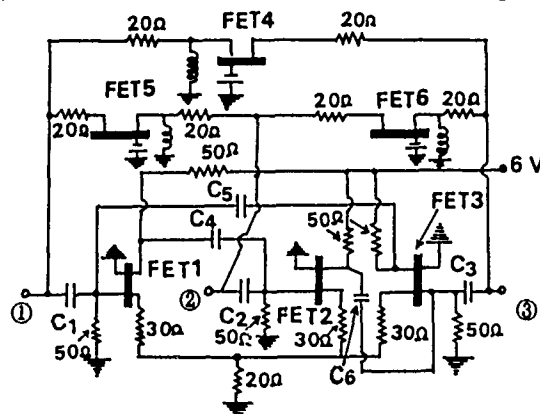


Fig. 1 Circuit diagram of an active circulator using FETs.

across gate and source of single-gate FETs (FET4 - FET6) are changed, the inner resistances of the FETs are also changed. By changing the voltages, the inner resistances were adjusted to the values for which the isolation of the circulator becomes large.

Figure 2 shows a photograph of the circulator of Fig. 1. As shown in this figure,  $\lambda/4$  open transmission lines were employed at the input and output terminals to obtain the impedance matching at both terminals. The experiment on this circulator was carried out in 2 GHz band. Figs. 3a, 3b and 3c show the characteristics of the circulator of Fig. 2. As seen from Fig. 3a, the frequency range is from 1.3 to 2.6

GHz, and the insertion loss is 0.3 dB. Since three dual-gate FETs have the same characteristics, the experimental results obtained for any two of the three terminals are almost the same. We see from Fig. 3b that the isolation is 20 dB in the range of 1.3 - 2.6 GHz. The input vs output characteristics are shown in Fig. 3c, which indicates that the output power is 2.35 mW when the input power is 2.6 mW and it saturates for the input power larger than 2.6 mW.

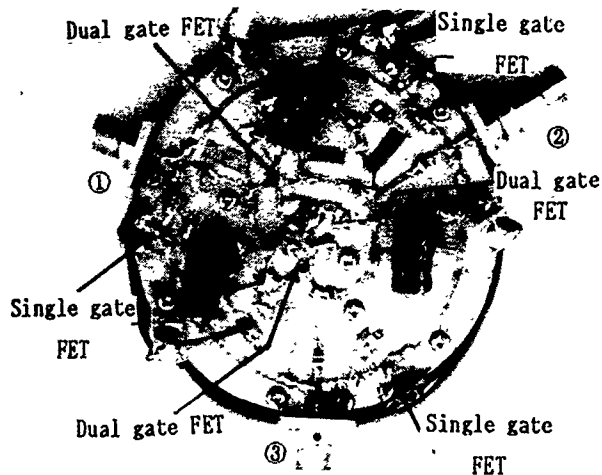


Fig. 2 Photograph of the circulator of Fig. 1.

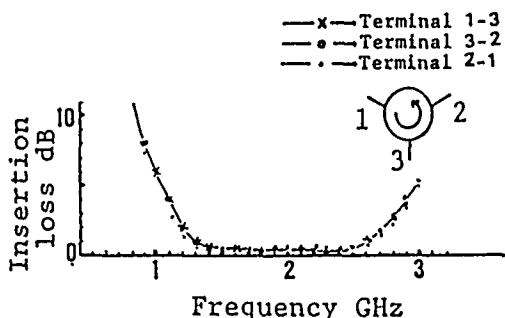


Fig. 3a Insertion loss of the circulator.

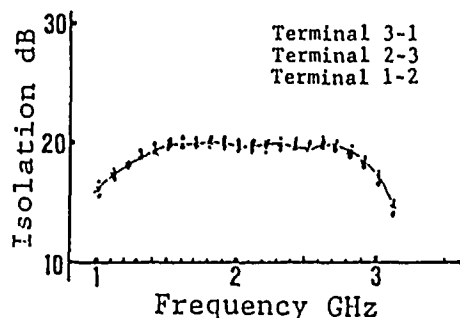


Fig. 3b Isolation of the circulator.

The circulator shown in Fig. 4 was constructed by using three amplifiers and three power dividers. The three amplifiers are the products of Fujitsu, and they operate in the range 5 - 18 GHz. As shown in Fig. 4, the attenuators are connected at the output terminals of the amplifiers. As the gain of these amplifiers cannot be con-

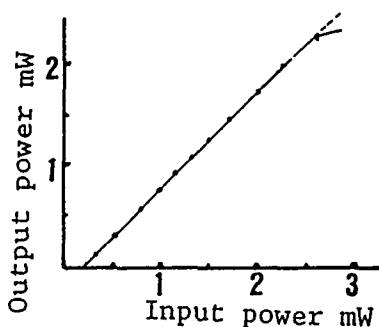


Fig. 3c Input vs output power characteristics of the circulator.

trolled, we must use attenuators. If we do not use them, the oscillation occurs. The amount of attenuation was so chosen that the insertion loss became 0.3 dB for the same reason as that explained before.

Figure 5 shows the characteristics of the circulator of Fig. 4. As seen from the figure, it works in the range of 5 - 18 GHz. The insertion loss and the isolation are 0.3 dB and 30 dB, respectively. The output power of this circulator is 18.7 dBm for the input power of 19 dBm, which is the maximum input power with no saturation. It depends on the input-power level that which type of the amplifier, either small-signal or medium-power amplifier, should be used in the circulator.

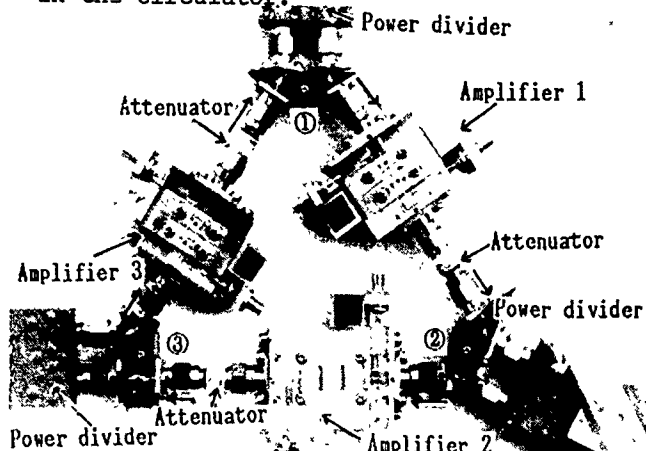


Fig. 4 photograph of the 5 - 18 GHz band active circulator.

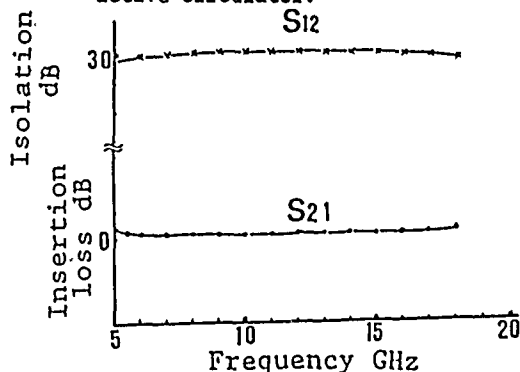


Fig. 5 Frequency characteristics of the 5-18 GHz band active circulator.

(1) S. Tanaka et al. PROC. IEEE, Vol. 53, No. 3 PP. 260-267, Mar. 1965.

## A SIMPLE AND LOW COST 3-PROBE MEASUREMENT TECHNIQUE USING MICROSTRIP CIRCUITS

Kai Chang, Ming-Yi Li and Thomas Sauter  
Department of Electrical Engineering  
Texas A&M University  
College Station, Texas 77843

### ABSTRACT

A simple and low cost measurement system using 3-probe microstrip circuits has been developed for impedance and S-parameter measurements. The coupling coefficients for the three probes can be unequal and only one power meter is required. The measured results agree very well with those obtained from an HP 8510 automatic network analyzer.

### INTRODUCTION

The impedance and S-parameter measurements at microwave and millimeter-wave frequencies are very challenging since both phase and amplitude need to be determined. The conventional slotted line measurement is tedious and slow. Measurements using the modern automatic network analyzer are fast and accurate, but the equipment is very expensive and difficult to extend into millimeter-wave frequencies.

A microstrip 3-probe measurement system has been developed providing an alternative for low cost impedance measurements [1]. The 3-probe measurement techniques have been proposed before for coaxial and waveguide systems [2,3]. The use of microstrips has the advantages of small size, light weight and low cost.

### MEASUREMENT SETUP

The measurement setup is shown in Figure 1. A stable source is connected to a 3-probe microstrip circuit. The system only requires to measure the amplitude or power of the signals at the 3 ports. Using a switch, only one power meter is needed to detect the output power level of the three probes. The microstrip circuit layout is shown in Figure 2.

The measured power level at each port corresponds to the standing wave along the terminated transmission line. The power measured at the  $i$ th port is given by

$$P_i = q_i P_0 |1 + \alpha_i \Gamma_L e^{-j2\beta z_i}|^2 \text{ for } i = 1, 2, 3$$

where  $\Gamma_L$  is the reflection coefficient due to the unknown load.  $\beta$  is the propagation constant.  $z_i$  are the locations of probes.  $\alpha_i$  and  $q_i$  are the calibration factors which will be determined by calibration. Three calibration standards are used to determine  $\alpha_i$  and  $q_i$ . They are a perfectly matched load, a short circuit, and an open load.

### RESULTS

A circuit was built using Duroid 5870 substrate with a thickness of 1.524 mm. With  $\Delta z_1 = 14.35$  mm and  $\Delta z_2 = 15.5$  mm, a bandwidth of 8 to 10.5 GHz can be achieved for the measurement. The same circuit can be used to measure other bandwidths with new calibration. To demonstrate the technique, the measured results for a mismatch load are shown in Figure 3. The results obtained from the HP 8510 network analyzer are shown in the same figure for comparison.

The use of this circuit for S-parameter measurements is under development. Some results will be presented in the conference.

### ACKNOWLEDGEMENTS

The authors would like to thank Dr. Charles Jackson of TRW for many helpful suggestions.

### REFERENCES

- [1] K. Chang, M. Li, and T. Sauter, "A Three-Port Microstrip Impedance Measurement System", *Microwave and Optical Technology Letters*, Vol. 1, pp. 90-93, May 1988.
- [2] W. J. Duffin, "Three-Probe Method of Impedance Measurement", *Wireless Engineer*, pp. 317-320, Dec 1952.
- [3] C. J. Hu, "Microwave Automatic Impedance Measuring schemes Using Three Fixed Probes", *IEEE Trans on Microwave Theory and Tech.*, Vol. MTT-31, pp. 756-762, September 1983.

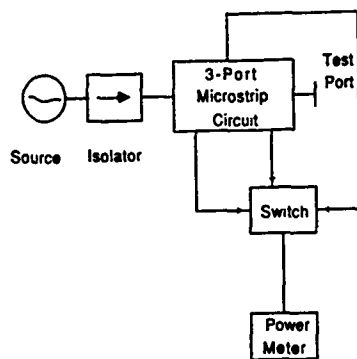


Figure 1. Measurement System Setup

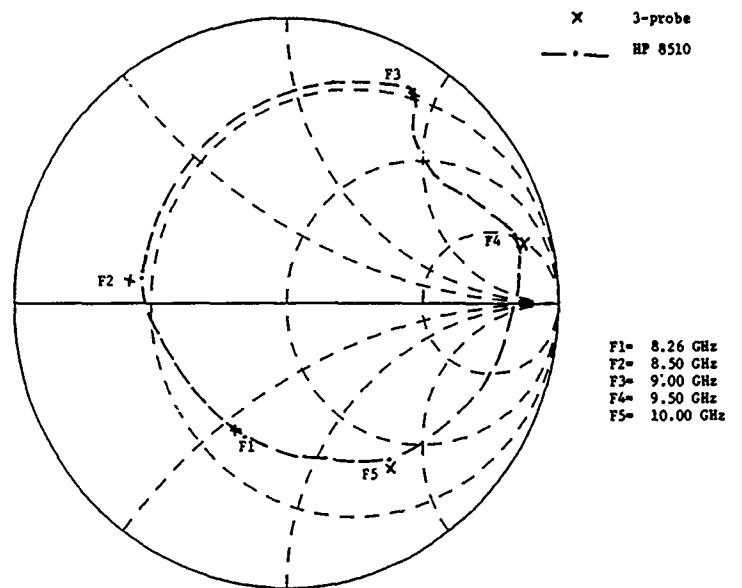


Figure 3. Measurement Results for a Mismatch Load

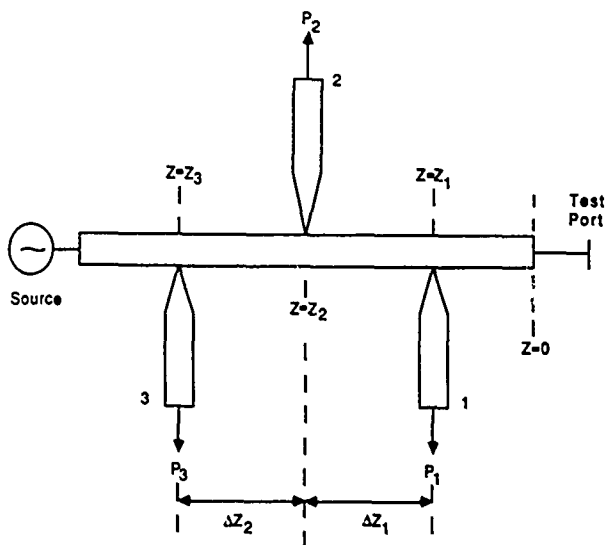


Figure 2. Microstrip Circuit Arrangement

## EXPERIMENTAL RESULTS OF A HIGH Q QUASI-OPTICAL REFLECTION CAVITY

Karen A. Lee and Margaret A. Frerking  
Jet Propulsion Laboratory  
California Institute of Technology  
Pasadena, CA 91109

## ABSTRACT

A quasi-optical reflection cavity has been designed, constructed, and tested and consists of three elements in cascade. a high  $Q$  folded Fabry-Perot resonator, a lower  $Q$  Fabry-Perot resonator, and a diffraction grating. The resonator exhibits a  $Q$  of 6700 and 1.6 dB of loss at 63 GHz. The design can be scaled to 1 THz to serve as the resonator for high frequency quantum well resonant tunneling device oscillators.

TABLE I. COMPARISON OF RESULTS.

	DESIGN	MEASUREMENT	DESIGN WITH LOSSES
<b>HIGH Q FABRY-PEROT</b>			
$FSR(\text{MHz})$	401	$401 \pm 1.5$	401
$\Delta f(\text{MHz})$	8.0	$9.5 \pm 1.5$	8.1
$R$	—	.940	—
$\alpha$	—	.0014	.001†
$F$	50.8	$42.2 \pm 8.1$	49.8
$Q$	8000	$6631 \pm 844$	7827
<b>LOW Q FABRY-PEROT</b>			
$FSR(\text{MHz})$	1000	$974 \pm 4.5$	1000
$\Delta f(\text{MHz})$	272	$288 \pm 4.5$	283
$R$	—	.436	—
$\alpha$	—	.020	.006†
$F$	3.68	$3.38 \pm 0.07$	3.53
$Q$	231	$219 \pm 3.6$	223
<b>DIFFRACTION GRATING</b>			
$\Delta\theta(^{\circ})$	2.6	$4.1 \pm 0.4$	3.2
$\theta_{\text{peak}}(^{\circ})$	72.67	$71.13 \pm 0.2$	—
$\alpha$	—	.12	.01†
$\Delta f(\text{MHz})$	1.0	$1.6 \pm 0.15$	1.2
$Q$	63	$40 \pm 3.6$	56

†Loss calculated from spillover and resistivities.

## INTRODUCTION

A single mode, high  $Q$ , quasi-optical, tunable resonator has been designed, fabricated, and tested at 63 GHz. The resonator is easily scalable to frequencies as high as 1000 GHz. Such a structure could serve as the resonator for a quasi-optical oscillator employing a resonant tunneling device, which exhibits negative resistance at submillimeter wavelengths [1]. The quasi-optical design consists of three elements in cascade. A high finesse Fabry-Perot interferometer with a  $Q$  of 6700 defines the  $Q$  of the system. It is followed by a low finesse Fabry-Perot interferometer and a Littrow mounted diffraction grating to filter all but the single desired mode. The transmission of each element was measured at a fixed frequency of 63 GHz, and the measured loss of each combine for a total round trip loss of less than 1.7 dB. Deviation from the design parameters can be understood when the various loss mechanisms are accounted for.

## RESONATOR DESIGN

In the quasi-optical oscillator, the resonant tunneling device biased in the negative resistance region generates broad band white noise. This white noise is coupled to the high  $Q$  quasi-optical resonator which filters and reflects a narrow band signal. This signal is fed back onto the device, amplified and re-reflected through the resonator to provide frequency stabilization. Fabry-Perot mirror spacing and diffraction grating angle can be varied for frequency tuning.

The quasi-optical resonator shown schematically in Figure 1(a) performs the filtering and reflection: Figure 1(b) shows the spectra at specified locations, and Table I contains the design parameters for each element. The system uses optical coupling and was designed assuming Gaussian beam propagation. Each element refocuses the beam to the beamwaist of the subsequent element.

A folded Fabry-Perot interferometer [2] is illustrated schematically for two of the structures shown in Figure 1. The cavity resonance is tuned by moving the plane solid mirror. The transmission curve is a comb pattern of peaks and can be characterized by their full widths at half maximum ( $FWHM$ ) and their spacing, or free spectral range ( $FSR$ ), yielding a  $Q$  and finesse for the cavity.

The high  $Q$  folded Fabry-Perot was designed to have a  $Q$  of 8000 and a  $FSR$  of 401 MHz, and a finesse of 50.8. The low  $Q$  folded Fabry-Perot was designed to filter half of the longitudinal modes passed by the high  $Q$  Fabry-Perot resonator, with an  $FSR$  of 1 GHz, a finesse of 3.68, and a  $Q$  of 231.

The diffraction grating reflects the radiation back upon itself and performs the final filtering in the cavity. To carry out the first function the diffraction grating is Littrow mounted. The blaze angle, the number of gratings, and the grating spacing are determined given the beam taper edge and  $Q$ .

## MEASUREMENTS

Three types of measurements were performed to determine the  $Q$  and the finesse of the folded Fabry-Perot interferometers and the  $Q$  of the diffraction grating; the transmissivity of each mesh, the transmissivity of each Fabry-Perot resonator, and the reflectivity of the diffraction grating. The finesse and  $Q$ s determined from the measurements and the loss in each element are summarized in Table I.

The transmissivity of the high  $Q$  Fabry-Perot resonator shown in Figure 2 was measured as a function of relative Fabry-Perot mirror spacing. The smaller peaks are due to higher order transverse modes. The loss at the design spacing is 0.2 dB. The distance between the major peaks resulting from the longitudinal modes was converted to an equivalent  $FSR$  of 401.4 MHz, and the width of the peak to an equivalent  $FWHM$ ,  $\Delta f$ , of 9.5 MHz. The  $Q$  is  $\frac{FSR}{\Delta f} = 6631$ , and the finesse is  $\frac{FSR}{\Delta f} = 42.2$ .

Figure 3 is the transmissivity of the low  $Q$  Fabry-Perot resonator versus mirror spacing. The asymmetry in the peaks arise from unresolved higher order modes. This measurement yields an  $FSR$  of 974 MHz and a  $FWHM$  of 288 MHz, corresponding to a finesse of 3.38 and

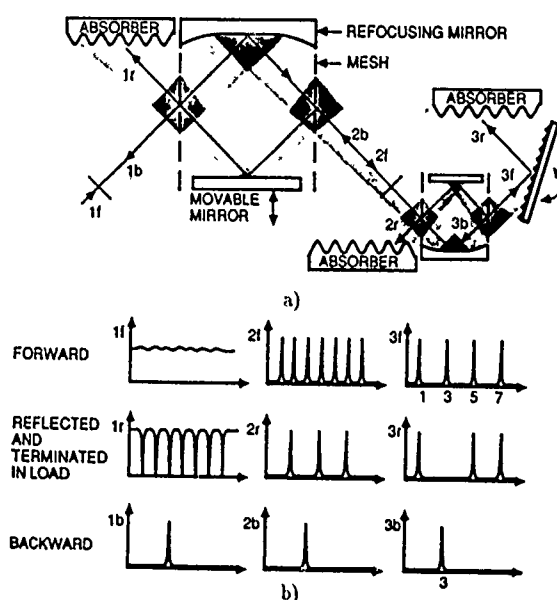


FIGURE 1. The quasi-optical resonator.



a  $Q$  of 219. The loss at the design spacing is 0.32 dB. The higher ordered transverse modes are also evident in this resonator.

The  $Q$  of the diffraction grating was determined from the reflectivity as a function of incident angle shown in Figure 4. The loss at the peak was 0.56 dB. Half power angles were converted to frequencies using the diffraction grating equation, yielding a  $FWHM$  of 1.6 GHz, for a  $Q$  of 40.

#### EFFECTS OF LOSSES

A number of factors were not accounted for in the design of the resonator. These factors contributed to deviation of the measurements from the design. For example, in the Fabry-Perot resonators, truncation of the beam will cause spillover loss, and can introduce loss to unwanted transverse modes. The meshes, the mirrors, and the diffraction grating incur ohmic losses. The total loss measured in the two Fabry-Perot resonators were 4.5% in the high  $Q$ , and 7.1% in the low  $Q$  cavity. The total loss in a Fabry-Perot resonator can be converted to a loss per pass, given in Table I. The measured loss per pass  $\alpha=0.14\%$  in the high  $Q$  cavity and 2% in the low  $Q$  cavity.

Losses in the Fabry-Perots result from a number of entities. Two loss mechanisms, ohmic losses from the finite conductivity of the mirrors and meshes and spillover losses from the design taper edge, can be calculated. Mirror and mesh ohmic losses per pass for the high  $Q$  and low  $Q$  Fabry-Perot resonators were 0.098 and 0.106% respectively. A 23 dB edge taper for the low  $Q$  Fabry-Perot resonator results in 0.5% loss, a 45 dB edge taper results in 0.02% loss in the high  $Q$  Fabry-Perot resonator.

The theoretical  $Q$  will differ from the design  $Q$  if loss is accounted for. A more accurate comparison would be with the loaded  $Q$ , where  $\frac{1}{Q_L} = \frac{1}{Q_0} + \frac{1}{Q_{ext}}$ . The external  $Q$ ,  $Q_{ext} = \frac{2\pi d}{\lambda \alpha}$ , the geometrical phase shift divided by the loss per pass. The loaded  $Q$ , based on measured losses, for the high and low  $Q$  Fabry-Perot resonators is 7827 and 223 respectively.

Transmission plots were generated by changing the mirror spacing, deviating from a square cavity which will cause transverse modes. The desired frequency is at the  $(q, 0, 0)$  mode. Frequencies at for the  $(q, 0, 1)$  and  $(q, 1, 0)$  modes, the next lowest order are given by

$$f_{qmn} = \frac{c}{2L} \left[ q + \frac{m+n+1}{\pi} \right] \tan^{-1} \frac{1}{\sqrt{\frac{R}{L} - 1}},$$

where  $L$  is the cavity length and  $R$  is the mirror radius of curvature [3]. The mode separation is 0.148 GHz for the high  $Q$  cavity, or a shift in mirror spacing of 1.3 mm. It can be seen in Figure 2 that the secondary transmission peaks occur at 1.3 mm from the associated fundamental peak. The mode separation for the low  $Q$  Fabry-Perot resonator was calculated to be a 0.79 mm shift in mirror spacing. This is evident in the asymmetric broadening of the lower longitudinal modes in Figure 3.

Secondly, the design of the diffraction grating assumed uniform illumination. The effective grating width will be somewhat smaller when illuminated with a Gaussian beam. The  $Q$  of the diffraction grating is proportional to the grating width. The effective grating width is calculated by integrating the Gaussian curve.  $\int_0^\infty e^{-(r/W)^2} dr = W\sqrt{\pi}/2$ . Therefore the  $Q$  is reduced to 56.

The total loss measured in the diffraction grating was 12%. Spillover and resistive losses in the diffraction grating were calculated to be 0.5% each. Additional loss can be attributed to phase errors since the beam incident angle differs from the blaze angle. These losses give an effective  $Q$  of 53 for the diffraction grating.

#### CONCLUSIONS

We have demonstrated the operation of a quasioptical reflection cavity resonator that can be scaled for use as a frequency tuner and stabilizer in a submillimeter wavelength oscillator. Extremely high  $Q$ s can be obtained and losses are minimal in the quasioptical components. Each element of the resonator was characterized and its performance found to be consistent with the design, accounting for loss, within measurement tolerances. The performance of the Fabry-Perots was limited by spillover losses, power in transverse modes, and ohmic losses. The diffraction grating design needs to account for the difference between uniform and Gaussian beam illumination. The loss in the high  $Q$  Fabry-Perot is 0.2 dB, in the low  $Q$  is 0.32 dB, and in the diffraction grating is

0.56 dB yielding an overall roundtrip loss of 1.68 dB for the entire resonator. The  $Q$  at 63 GHz is 6700 and with a modified design accounting for the effects of loss and illumination could be as high as 10,000 with similar loss.

#### ACKNOWLEDGEMENTS

This research was performed by the Jet Propulsion Laboratory, California Institute of Technology under contract with the National Aeronautics and Space Administration.

#### REFERENCES

- [1] T. C. L. G. Sollner, E. R. Brown, W. D. Goodhue, and H. Q. Le, *Appl. Phys. Lett.* 50 (6), Feb 1987, pp. 332-334.
- [2] J. J. Gustincic, *IEEE MTT-S Int. Microwave Symp. Dig.*, 1977, pp. 99-101.
- [3] A. E. Siegman, *An Introduction to Lasers and Masers*, Chapter 8, McGraw-Hill, New York, 1971.

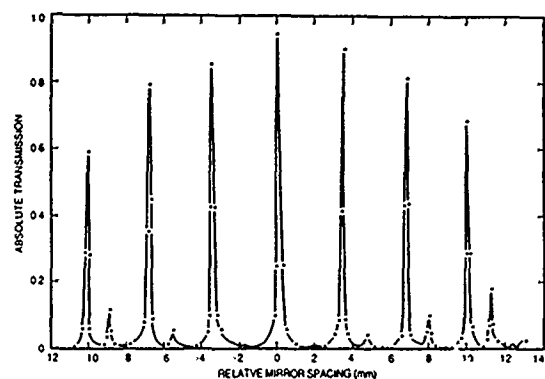


FIGURE 2. Measured transmission of the high  $Q$  Fabry-Perot resonator.

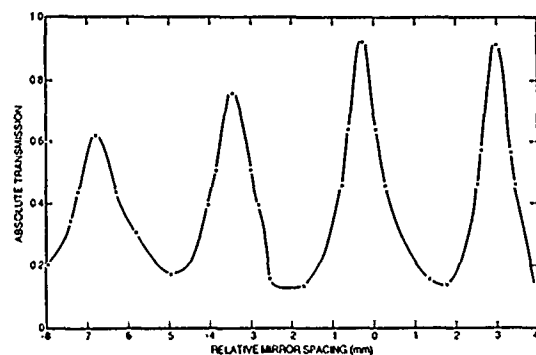


FIGURE 3. Measured transmission of the low  $Q$  Fabry-Perot resonator.

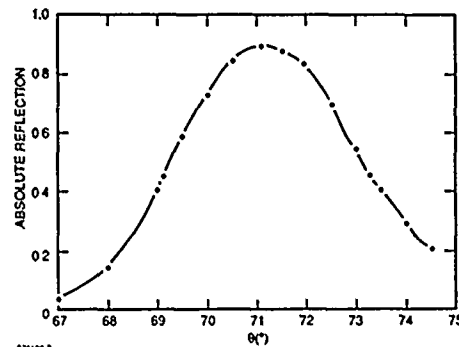


FIGURE 4. Measured reflection of the diffraction grating.

# CW DOPPLER SYSTEMS FOR EXTERNAL URODYNAMIC STUDY, COMPARISON BETWEEN ELECTROMAGNETIC WAVE AND AIRBORNE ULTRASOUND

Y. Takeuchi

Yokogawa Medical Systems, Ltd.  
Tachikawa, Japan

## ABSTRACT

Urination behavior indicates a series of important information for urologist Doctors to find, for example, prostatic hypertrophy. External, non-contact urodynamic monitors using CW-Doppler principle were built in similar wavelengths with 24GHz electromagnetic wave ( $\lambda=12.5\text{mm}$ ) and 40KHz airborne ultrasound ( $\lambda=8.5\text{mm}$ ). Both systems were found having almost equivalent excellence in detecting the Doppler return from urinary flow simulated by water ejector. However, airborne ultrasound system seems slightly less expensive although its electronics are more complicated.

acoustical output seems about half of that. The transducers themselves have relatively broad directivity like  $\pm 45^\circ$  (fig.3), Doppler cross section spans for similar wide angle when they are juxtaposed in parallel in a foam plastic baffle(fig.4). With such arrangement the system has quite sufficient sensitivity for simulated urine flow across the air given by water ejector(fig.5). Even a single drop with quiescent starting was detected clearly together with water surface ripple caused by the drop(fig.6). Additional pair of external horn projector will increase sensitivity much more, but seems unnecessary for subject purpose. It is an obvious advantage for patient and paramedical safety to use hazard-free low level airborne ultrasound energy as a probing means.

## INTRODUCTION

Urodynamic studies in past time generally have been semi-invasive when using catheter type cystometer, or with slightly poor reproducibility when using funnel-and-cup type flowmeter (1)(2). These primitive means are still used widely, however, Doctors are first to ask question to the patient for his subjective impression how he can void easily or with any difficulty.

Uroflowmetry should be carried out in conditions as natural as possible because any slight strange feeling tends to create additional bias for his voiding behavior, which may result in misdiagnosis. From this point of view author developed a completely non-contact method using either mm-wave or airborne ultrasound. The principle is well known simple CW-Doppler method, which detects the running liquid drops across the air. The air to water reflectivity in both mm-wave and ultrasound is great, the system has an excellent sensitivity for subject matter. However, careful considerations are placed upon patient safety as well as practical sensitivity and quality of the information yielded by the system.

## 24GHZ MICROWAVE CW DOPPLER SYSTEM

A K-band Doppler unit (ND610AAM/NEC,fig.7) containing of gunn diode oscillator and shottkey-barrier diode detector was used to construct a CW-Doppler system for same purpose. In this case the waveguide mount Doppler unit itself has so wide directivity, like almost  $\pm 135^\circ$ , a small horn was added to form adequate sensitivity angle(fig.8). Without such horn its sensitivity is slightly poor than ultrasound system, however with horn, sensitivity gets 6-12 dB higher than it. A subaudio Doppler filter-amplifier is sole external circuit to the Doppler unit(fig.9). Specified irradiating output is 3-10mW, although the gunn diode eats a 5Vx100mA dc power. Its detectability and characteristics are almost 100% compatible to the ultrasound system. Flow (fig.10) and drop and ripple (fig.11) are also well detected. However, from patient safety standpoint and possible interferences to other systems, and related regulations, some may concern about its feasibility for clinical screening practice.

## 40KHZ AIRBORNE ULTRASOUND CW DOPPLER SYSTEM

A pair of 40KHz airborne ultrasound transducer, one for transmission and the other for reception, was used to construct a CW-Doppler system (fig.1). The transducer used here (MA40B6/Murata,fig.2) was selected from generally available types for intruder detection or simple ranging device or telemetry-telecontrol purposes. A 5vpp square wave from CMOS power gate is fed for the transmitting transducer, while the receiver consists of a tuned RF amplifier with AGC/ALC followed by a coherent demodulator and subaudio Doppler filter-amplifier. Electrical input power to the transmit transducer is about 30-40mW,

## SIGNAL ANALYSIS FOR QUANTITATIVE FLOWMETRY

Under an adequate setup the system is well expected to be able to measure, not only flow velocity but also flow volume rate with certain accuracy. This is because the media, i.e. atm. air, is very well transparent to both of these waves and frequencies. This is big advantage compared with inside-body Doppler study/diagnosis for vascular system seen in diagnostic ultrasound devices suffering from inherent tissue attenuation and dispersion which deteriorate measurement quality very much. A trial FFT spectrum analysis of the signal, after 1:10 time compression so to hire conventional diagnostic Doppler device spectrum analysis and display subsystem, indicates this signal looks very

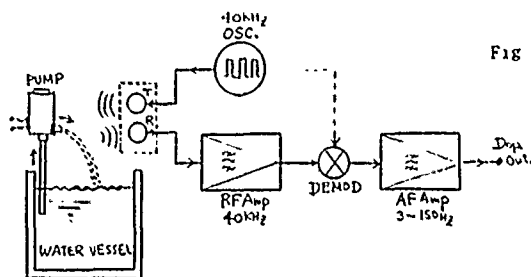


Fig 1 Block diagram of 40KHz airborne ultrasound CW Doppler system and general test setup for the same.

Fig 2



Fig.3

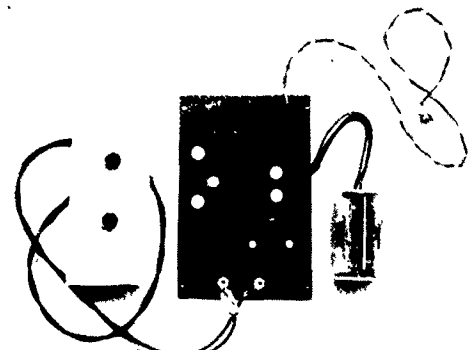


Fig.4 Transducer assembly and circuit to accommodate fig.1.

similar to the venus flow signal(fig.12). It was suggested that under an adequate setup the Doppler signal power can be interpreted as instantaneous running fluid volume within sampling site i.e. Doppler cross-section. This will yield, when combined with instantaneous velocity data from FFT analysis, the flow-rate vs. time curve which is necessary for urologist Doctors' diagnosis.

#### SAFETY AND OTHER CONSIDERATIONS

Since both system having almost compatible and fairly excellent performance in terms of subject purpose, next considerations are for safety, cost/performance and other points. Although either system merely irradiates far less power density of wave energy to the object field than known hazardous levels(3)(4), some people may concern about electro-magnetic wave much more than ultrasound. Interference and compatibility from or to other systems or environments seems, in general, slightly better for ultrasound than electro-magnetic wave, however, this will not be practical problem. Material cost and operating power consideration tends to conclude a definite advantage of ultrasound system because at least presently gunn oscillator mixer module is much expensive and power consuming than a pair of ultrasound transducer plus additional transmit-receive electronics.

#### CONCLUSION

For external non-contact urodynamics study, CW Doppler systems in similar wavelengths (8-12mm) of electromagnetic wave and airborne ultrasound were tried. Although both systems having compatible good performance to monitor and possibly measure the urinary flow as desired, safety and cost considerations promote ultrasound system slightly more than electromagnetic wave system. Further evaluation might be necessary for more dedicated prototyping and clinical evaluation in screening practices. Proposed direction includes to use much shorter wavelength like 3mm (100GHz mm-wave or 100KHz ultrasound) where urinary flow Doppler signal comes up to audible range and signal analysis makes much easier.

#### REFERENCES

- (1) P.Abrams and M.Torrens, Symposium of clinical urodynamics. Urologic Clinics of North America, vol.6, (1), pp.71-79 (1979)
- (2) F.Sanchez-Doblado and J.C.Matoes, "Computerised Analysis of Urological Parameters", Medical & Biological Engineering and Computation, vol.26, pp325-327 (1988)
- (3) Safety Code 24, "Guidelines for the Safe Use of Ultrasound, part 2, Industrial and Commercial Applications", Authority of the Minister of National Health and Welfare, Canada, Doc. No. 80-EHD-60. (1980)

Fig.9 Doppler unit with horn antenna and subaudio filter-amplifier

Fig.7 ND610AAM/NEC  
24GHz CW Doppler unit

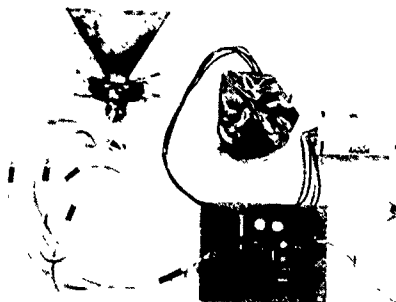


Fig 5(US)

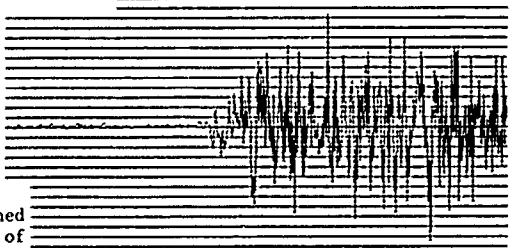
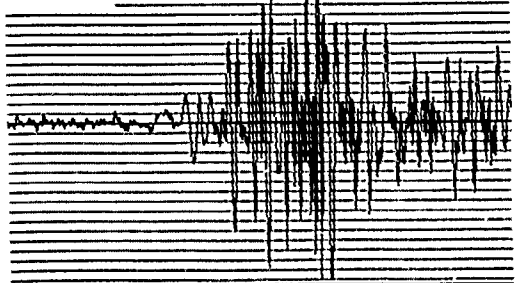


Fig 10(MW)



Figs 5 and 10  
Signals obtained  
by test setup of  
fig 8, pump off  
to on Left to  
right = 1sec

Figs 6 and 11  
Single drop  
Doppler  
followed by  
water surface  
ripple.

Fig. 6(US)

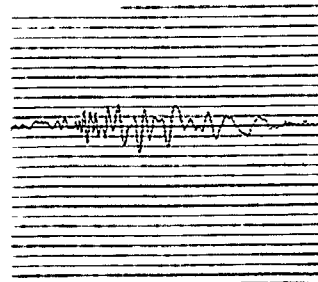


Fig.11(MW)

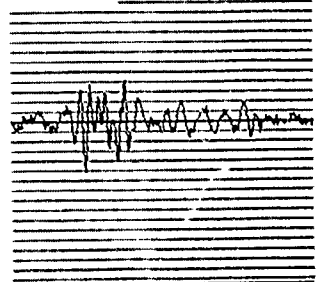


Fig.12  
Spectrogram of  
the Doppler  
signal. Starts  
and stops.  
Upper half is  
fold back of  
lower half.  
totally about  
40sec

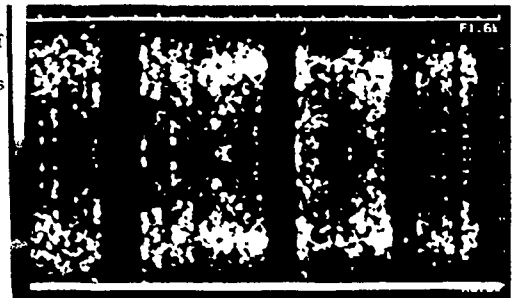


Fig.8  
test  
setup



# DEVELOPMENT OF A BROADBAND 3-mm PHF H-PLANE WAVEGUIDE CIRCULATOR

Zhang Dengguo Wu Zhengde

Applied phys. Inst. Box 83 Chengdu  
Sichuan P.R. China

## ABSTRACT

The exact operation mode of PHF H-plane waveguide circulator is given to be  $HE_{11L}$ , where  $L=n+\delta_{n+1}$ ,  $n=0,1,2,\dots$  and  $\delta_{n+1}$  can be determined numerically. A broadband 3-mm circulator operating in the lowest mode  $HE_{11\delta_1}$  is reported for the first time.

The center frequency of waveguide circulator agrees well with the resonance frequency of the dielectric ferrite resonator if no magnetic bias is applied(1). At  $r=R_1$  and  $r=R_2$  in Fig.1 the

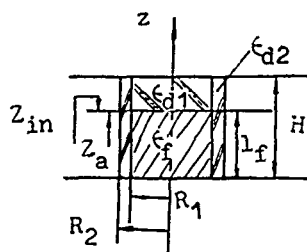


Fig.1

characteristic equations of HE mode is

$$\left[ \frac{1}{u} \frac{J'_m(u)}{J_m(u)} + \frac{1}{w_1} \frac{I'_m(w_1)}{I_m(w_1)} + DK'_m(w_1) \right] \left[ \frac{k_z^2 J'_m(u)}{u J_m(u)} + \frac{k_z^2 I'_m(w_1)}{w_1 I_m(w_1)} + DK'_m(w_1) \right] = \pi^2 \beta^2 \left[ \frac{1}{w_1^2} + \frac{1}{u^2} \right]^2 \quad (1)$$

$$\left[ \frac{1}{w_2} \frac{K'_m(w_2)}{K_m(w_2)} - \frac{R_1}{w_1 R_2} \frac{I'_m(w_1 R_2/R_1)}{I_m(w_1 R_2/R_1)} + DK'_m(w_1 R_2/R_1) \right] \left[ \frac{k_z^2 K'_m(w_2)}{w_2 K_m(w_2)} - \frac{k_z^2 R_1}{w_1 R_2} \frac{I'_m(w_1 R_2/R_1)}{I_m(w_1 R_2/R_1)} + DK'_m(w_1 R_2/R_1) \right] = \pi^2 \beta^2 \left[ \frac{R_1^2}{w_2^2 R_2^2} - \frac{1}{w_2^2} \right]^2 \quad (2)$$

where  $D$  is a constant and

$$u = R_1 (k_z^2 - \beta^2)^{1/2} \quad (3)$$

$$w_1 = R_1 (\beta^2 - k_{d1}^2)^{1/2} \quad (4)$$

$$w_2 = R_2 (\beta^2 - k_{d1}^2)^{1/2} \quad (5)$$

Resonance condition of  $z=l_f$  makes  $Z_{in}$  and  $Z_a$  be complex conjugates

$$\tanh sx = V \tanh x \quad (6)$$

where  $x = pl_f = \alpha(H-l_f)$ ,  $s = \beta/p$  (7)

$$\alpha^2 = k_f^2 - k_{d1}^2 - \beta^2 \quad (8)$$

$$V = (-w \mu_0 \alpha + \alpha / w \epsilon_0 \epsilon_{d1}) / (w \mu_0 \beta + \beta / w \epsilon_0 \epsilon_f) \quad (9)$$

From Fig.2 we can get the height of the ferrite cylinder

$$l_f = x/p = \pi L/\beta = (n + \delta_{n+1})\pi/\beta \quad n=0,1,2,\dots \quad (10)$$

where  $\delta_{n+1} < \frac{1}{2}$  for  $n$  can be found out from (1) (2) (6) numerically. Thus the exact operation modes of partial height ferrite (PHF) H-plane waveguide circulator are determined to be  $HE_{11L}$  hybrid modes and the center frequency

$$f = (u_{11}^2 + (L R_1 \pi)^2)^{1/2} / 2\pi \sqrt{\epsilon_s \epsilon_f \mu_s \mu_f} R_1 \quad (11)$$

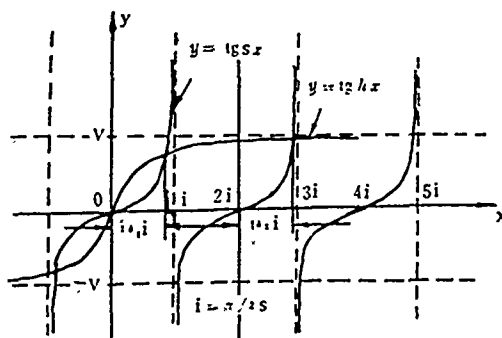


Fig.2

Employing the lowest possible mode and shortest associated path length implies broadband. A 8-mm broadband circulator in the lowest mode  $HE_{11L}$ , defined here had been reported (2), and for the first time we have developed a broadband 3-mm H-plane waveguide circulator operating in the same mode  $HE_{11L}$ , shown in Fig.3 is the device's structure. The performance of the circulator can meet the needs of a majority of MMW systems.



Fig.3

#### References

- (1) B.Owen, Bell syst.Tech.J.,vol 51(1972),pp595-627.
- (2) W.S.Piotrowski et al ,IEEE on MTT,vol.MTT-24,no.11,1976, pp863-866.

DETERMINATION OF I-V CHARACTERISTICS OF NEGATIVE CONDUCTANCE  
DEVICES FROM MICROWAVE REFLECTION COEFFICIENTS

P. Huang, A. Botula, N.C. Luhmann, Jr. and D.S. Pan

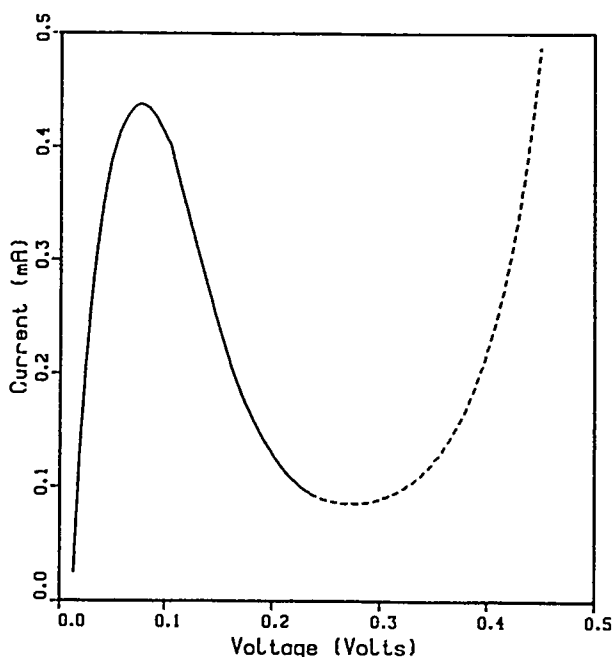
Electrical Engineering Department  
University of California, Los Angeles  
Los Angeles, California 90024

Negative differential conductance (NDC) devices have stimulated intensive research activities since the first acknowledged work on the tunnel diode, also referred to as the Esaki diode<sup>1</sup>. In recent years, the interest in NDC devices has been revived by the successful fabrication of various double barrier resonant tunneling (DBRT) structures<sup>2,3</sup>. The interest in these DBRT structures is due primarily to their high potential as high frequency devices. For the design of high frequency devices, the necessary information is provided by the detailed shape of the dc I-V characteristics, especially the negative conductance regime. Unfortunately, the NDC regime of the I-V curve has always made the dc I-V measurement difficult because of its nature to oscillate. A direct dc measurement of the I-V characteristics by a conventional curve tracer only shows the positive conductance portion of the entire I-V curve. Various methods have been proposed to measure the I-V characteristics.

Chua et. al. have devised a curve tracer from a stability analysis<sup>4</sup>. Shewchuk et. al. have used damped microwave circuit to prevent oscillations<sup>5</sup>. In this paper, we discuss a novel approach to calculate the NDC regime of the I-V characteristics using microwave reflection coefficients and the measurable portion of the I-V curve.

This method uses microwave network analyzer techniques to measure the reflection coefficients,  $S_{11}$ , of the device. The ac conductance is de-embedded from the measured  $S_{11}$  as a function of the rf signal and dc bias; the ac conductance thus obtained can serve to determine the "local" slope of I-V curve. By dc biasing the device near the valley voltage and varying the rf signal until it swings beyond the peak voltage, the entire NDC regime can then be reconstructed. This method has been tested on a packaged tunnel diode with  $V_p = 0.06$  volt,  $I_p = 0.45$  mA,  $V_v = 0.28$  volt, and  $I_v = 0.086$  mA. The diode is mounted on a 50-ohm microstrip test fixture. With the diode biased at 0.2357 volt, and the largest rf signal equal to 0.220 volt, the I-V characteristics less than 0.2357 volt is calculated and shown in Fig. 1.

Since this method only requires the device being biased at a point where it is still dc measurable and large enough rf signal to cover the whole NDC regime, there is no need to worry about the device oscillation. Because no conventional tracing circuit is required in this rf method, the difficulty occurred in most curve tracer for large NDC can be avoided here. Furthermore, since the de-embedding of



I-V characteristics is well developed at microwave frequencies, the accuracy of this approach can be very satisfactory. Fine structures have been found in the NDC regime of some DBRTs<sup>6</sup>. When these fine structures are reflected in the  $S_{11}$  measurement, the detailed shape of the I-V curve can be calculated.

The accuracy of this method depends on the device model and the de-embedding used in the microwave S-parameter measurement. For the tunnel diode tested, the simple model of a nonlinear resistor defined by the dc I-V curve in parallel with a nonlinear capacitor has been used<sup>7</sup>. For DBRT devices, the transit time effect of adjacent depletion region needs to be considered in the device modeling<sup>8</sup>. The accuracy of this method can be further improved if higher harmonics is included in the Fourier analysis when calculating the I-V characteristics.

In conclusion, we have devised a method that measures the I-V characteristics of a negative resistance device from a microwave approach. This method has proved useful and provides valuable information in the NDC regime that is otherwise unobtainable with conventional methods.

### Acknowledgements

This work was supported by TRW under the California MICRO Program.

### Reference

1. L. Esaki, Phys. Rev. 109, 603 (1958)
2. L. L. Chang, L. Esaki, and R. Tsu, Appl. Phys. Lett. 24, 593 (1974)
3. T.C.L.G. Sollner, W. D. Goodhue, P. E. Tannenwald, C. D. Parker, and D. D. Peck, Appl. Phys. Lett. 43, 588 (1983)
4. L. O. Chua, G. Zhong, IEEE Circuits and Systems CAS-32, 569 (1985)
5. T. J. Shewchuk, J. M. Gering, P. C. Chapin, and P. D. Coleman, Appl. Phys. Lett. 47, 986 (1985)
6. G. S. Lee, K. Y. Hsieh, and R. M. Kolbas, Appl. Phys. Lett. 49, 1528 (1986)
7. S. M. Sze, Physics of Semiconductor Devices, 2nd ed., Wiley & Sons, N.Y. 1981
8. I. Song and D. S. Pan, IEEE Electron Device Lett., EDL-8, 560 (1987)

## SUBMILLIMETER WAVE EMISSION FROM SEMICONDUCTOR SUPERLATTICES

M. Helm, E. Colas, P. England, F. DeRosa, and S.J. Allen, Jr.

Bellcore  
Red Bank, N.J. 07701, U.S.A.

## ABSTRACT

Far infrared emission due to electronic transitions between subbands in semiconductor superlattices is observed for the first time. The electrons are excited by applying an electric field in the plane of the layers. The generated radiation is coupled out of the sample by a metallic grating on the surface.

## INTRODUCTION

The lack of coherent solid state far infrared sources has been overcome recently by the realization of the crossed field p-germanium laser (1). Its wide application, however, could remain limited because the operation requires the use of a magnetic field and is restricted to pulsed mode. For that reason, the search for other possible FIR sources is still going on. One of the most promising systems is the semiconductor superlattice made feasible by modern layered semiconductor growth. It is well known that transitions between subbands in such structures, originating from the confinement of the carriers, exhibit a large electric dipole moment (2), and can be engineered to give transition frequencies in the far infrared, thus making them attractive as the active medium in an infrared source. Although the polarization of the light has to be perpendicular to the layers in order to interact with the confined electrons (3), this system has already been demonstrated to be very powerful as infrared detector (4).

We report the first observation of submillimeter wave emission due to subband transitions in a semiconductor superlattice (5). The emission is observed only with a metal grating on the surface of the superlattice, which converts the radiation polarized perpendicular to the interface into a plane wave radiating from the surface.

## EXPERIMENT

The  $\text{GaAs}/\text{Al}_{0.3}\text{Ga}_{0.7}\text{As}$  superlattice was grown by organometallic chemical vapor deposition (OMCVD) on a semi-insulating substrate and consists of 400 Å wide wells and 50 Å wide barriers, with a total thickness of 6  $\mu\text{m}$ . The superlattice was nominally undoped, which gave the desired n-background of  $1 \times 10^{15} \text{ cm}^{-3}$ . The relatively wide wells were chosen in order to keep several subbands below the optical phonon energy (36 meV). This is important because it enhances the ratio of radiative to nonradiative relaxation rate, which is proportional to the quantum efficiency. The energy levels for the present superlattice are calculated to be  $E_1 = 3 \text{ meV}$ ,  $E_2 = 11.9 \text{ meV}$ , and  $E_3 = 26.7 \text{ meV}$ , thus the lowest subband transition is expected to occur at 8.9 meV, or at a wavelength of 139  $\mu\text{m}$ .

In order to increase the effective radiating area, we deposited metal gratings onto the surface of the superlattice. Diffraction gratings, having roughly the same period as the wavelength of the subband radiation in the GaAs, have been suggested by Goossen and Lyon (6) to enhance the efficiency of a quantum well detector. Heitmann et al. (7) observed intersubband absorption in Si-MOSFETs induced by a grating with much smaller period than the corresponding wavelength. In the present superlattice the wavelength of the subband radiation in the GaAs is calculated to be 40  $\mu\text{m}$ . Accordingly, we deposited Ti:Au gratings with periods of 40  $\mu\text{m}$ , 30  $\mu\text{m}$ , 22  $\mu\text{m}$  and 16  $\mu\text{m}$  which were defined photolithographically. Ohmic contacts to the sample were achieved by alloying Ni:AuGe. The area between the contacts was typically  $4 \times 4 \text{ mm}^2$ . A schematic of the sample is shown in Fig. 1.

In the experiment the electron distribution function is heated by an electric field in the plane of the layers. The subsequent radiation is detected with a high-sensitivity Si-bolometer (sensitivity =  $3.6 \times 10^5 \text{ V/W}$ , noise equivalent power =  $7 \times 10^{-14} \text{ W/Hz}^{1/2}$ ) operated at 1.5 K. Facing the problem of spectrally resolving weak radiation, we used a novel technique to analyze the emission spectrum. A slab of InSb ( $n \approx 10^{14} \text{ cm}^{-3}$ , thickness 0.5 mm) was placed between the superlattice and the bolometer in the center of a superconducting magnet. By application of a magnetic field the cyclotron resonance absorption in the InSb (width  $\approx 20 \text{ cm}^{-1}$  or 0.3 Tesla) was varied and provided a tunable far infrared filter. The rejection of the filter was 50% for unpolarized light. The superlattice temperature was between 5 and 10K, voltage pulses of about 1ms duration were applied to the sample.

## RESULTS

Curve (a) in Fig. 2 shows the emission signal from a sample without grating as a function of the magnetic field for an electric field of  $E = 20 \text{ V/cm}$ . This curve represents the emission spectrum of the superlattice convoluted with the InSb cyclotron resonance line. The minimum is detected when the InSb cyclotron resonance frequency equals the peak frequency of the emitted radiation. The emission spectrum consists of one line at about 5 meV. We ascribe this line to the 2p - 1s shallow donor transition (8). No intersubband emission is observed, because the polarization of the subband radiation requires that it leaves the sample mainly at the edges, which is only a very small radiating area. (Note, however, that subband emission has been observed from Si-MOSFETs in a similar situation (9).) Curve (b) in Fig. 2 shows the emission from the superlattice with a 30  $\mu\text{m}$  - period Ti:Au grating. Besides the 2p - 1s emission a second line is clearly observed at a magnetic field of  $B = 1.1 \text{ T}$ . Since this



corresponds to a photon energy of about 9 meV, we ascribe this line to radiative decay of electrons in the second subband into the first subband. Fig.3 illustrates the donor and the subband transition causing the observed emission. Different grating periods do not change the position of the line, but only the strength due to different coupling efficiencies. Most efficient coupling is not achieved when the grating period matches the wavelength in the GaAs (which would correspond to simple diffraction of a plane wave by 90 degrees), but rather, at shorter periods. In the present case the 30  $\mu\text{m}$  grating provides the best coupling, followed by the 22  $\mu\text{m}$ , and finally the 40  $\mu\text{m}$  and 16  $\mu\text{m}$  gratings, where the subband emission is hardly seen. This can be understood, if an evanescent surface wave rather than a plane wave is propagating in the superlattice (4). The optimal coupling would then be achieved when the decay length of the surface wave matched the superlattice thickness.

### CONCLUSIONS

We have demonstrated that intersubband transitions in semiconductor superlattices are potentially useful for the development of novel submillimeter sources. Future work will have to concentrate on more efficient ways of exciting higher subbands than simple carrier heating in an electric field. Advanced semiconductor growth allows us to engineer structures, where electrons are injected directly in highly excited levels. The possible range of emission wavelengths is then only limited by material properties: It extends from 5  $\mu\text{m}$  (limited by the conduction band offset) to 300  $\mu\text{m}$  (limited by the achievable linewidth). More sophisticated injection schemes could also lead to population inversion and thereby to a new class of infrared semiconductor lasers.

### REFERENCES

- (1) A.A. Andronov, I.V. Zverev, V.A. Kozlov, Yu.N. Nozdryn, S.A. Pavlov, and V.N. Shastin, Sov. Phys.-JETP Lett., 1984, vol. 40, p. 804
- (2) F. Stern, Phys. Rev. Lett. 1974, vol. 33, p. 960
- (3) L.C. West and S.J. Eglash, Appl. Phys. Lett., 1985, vol. 46, p. 1156
- (4) B.F. Levine, C.G. Bethea, G. Hasnain, J. Walker, and R.J. Malik, Appl. Phys. Lett., 1988, vol. 53, p. 296
- (5) M. Helm, E. Colas, P. England, F. DeRosa, and S.J. Allen, Appl. Phys. Lett., in press
- (6) K.W. Goossen and S.A. Lyon, Appl. Phys. Lett., 1985, vol. 47, p. 1257
- (7) D. Heitmann, J.P. Kotthaus, and E.G. Mohr, Solid State Commun., 1982, vol. 44, p. 715
- (8) I. Melngailis, G.E. Stillman, J.O. Dimmock, and C.M. Wolfe, Phys. Rev. Lett., 1969, vol. 23, p. 1111
- (9) E. Gornik and D.C. Tsui, Phys. Rev. Lett., 1976, vol. 37, p. 1425

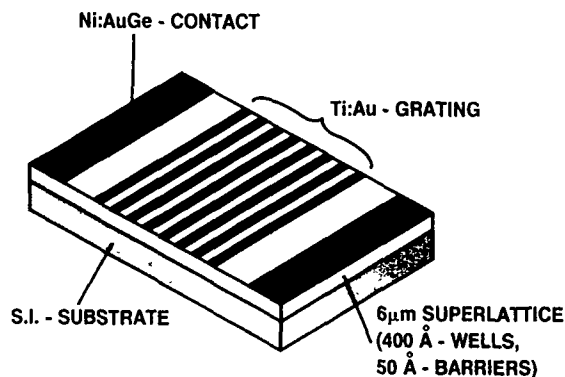


Figure 1

Structure of the sample

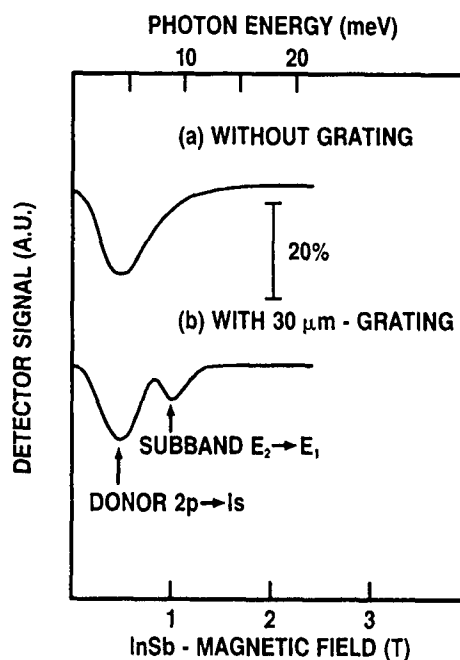


Figure 2

Detector signal versus magnetic field of InSb - filter and corresponding photon energy. The 2p-1s donor transition and  $E_2-E_1$  subband transition are indicated.

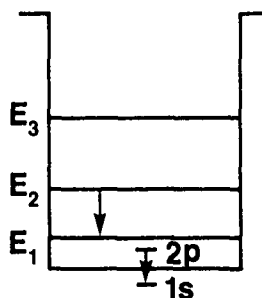


Figure 3

2p - 1s donor transition and  $E_2 - E_1$  subband transition in a quantum well.

# FAR INFRARED NON-ASTIGMATIC CZERNY-TURNER MONOCHROMATOR FOR STRESSED Ge:Ga PHOTOCONDUCTOR EXPERIMENTS

N. Hiromoto, H. Takami\* and T. Itabe

Communications Research Laboratory  
Koganei, Tokyo 184, Japan

and

H. Okuda, H. Matsuhara, H. Shibai and T. Nakagawa

Institute of Space and Astronautical Science  
Sagamihara, Kanagawa 229, Japan

\*Present address is National Astronomical Observatory of Japan, Mitaka, Tokyo 181, Japan

## ABSTRACT

A far infrared monochromator of Czerny-Turner type has been devised which has an output optical system comprising two small spherical mirrors to obtain non-astigmatic image. The far infrared monochromator covers both 50-120  $\mu\text{m}$  and 100-240  $\mu\text{m}$  wavelengths ranges and can be used to measure spectral response of stressed Ge:Ga photoconductors having response up to 200  $\mu\text{m}$ , which we have fabricated to apply them to far infrared astronomical observations by balloons and by satellites. Experimental performance of the stressed Ge:Ga photoconductors under low photon fluxes conditions also will be given.

## INTRODUCTION

Stressed Ge:Ga photoconductors are very sensitive detectors in the far infrared wavelengths shorter

than 200  $\mu\text{m}$ [1], and they have now become very important devices for precise detection of weak far infrared radiation. Because of the high detectivity under low background conditions, the stressed Ge:Ga photoconductors have been studied mainly for applications to far infrared astronomy in space[1,2,3,4].

We have fabricated a sensitive stressed Ge:Ga photoconductor with a compact and stable stressing assembly[5], and the detector have successfully used in the far infrared Fabry-Perot spectroscopy to observe astronomical CII line (158  $\mu\text{m}$ ) by a balloon-borne telescope[6].

In stressed Ge:Ga performance tests, we have constructed a far infrared monochromator of Czerny-Turner type with an astigmatism compensation optical system to measure spectral responsivity of the stressed Ge:Ga simply and quickly. The principle of the non-astigmatic optical system and a design of the far-infrared monochromator are explained in the next section.

And moreover, experimental results of performance tests of the stressed Ge:Ga at 2K under low background photon fluxes is briefly given in the third section. The low background experiments are very important in space applications, as the Japanese infrared astronomical satellite project (IRTS).

## FAR INFRARED CZERNY-TURNER MONOCHROMATOR WITH NON-ASTIGMATISM

A grating spectrometer with Czerny-Turner mounts is widely used as a monochromator because of its flexibility, and we have fabricated a far-infrared monochromator of this type to use in stressed Ge:Ga experiments.

A Czerny-Turner spectrometer with collimating and condensing spherical mirrors has the aberrations of astigmatism, coma and spherical aberration[7]. Since the astigmatism is the largest in usual configurations, some improvement to reduce the aberration is necessary especially when a single detector is placed at focus.

In order to compensate the astigmatism of the Czerny-Turner spectrometer, we have introduced an optical system comprising two concave spherical mirrors after focus of the spectrometer. Two mirrors of the compensation optical system act as a re-collimator and re-condenser, and they are placed on a plane perpendicular to an optical plane of the Czerny-Turner spectrometer (Fig.1). The spectrometer

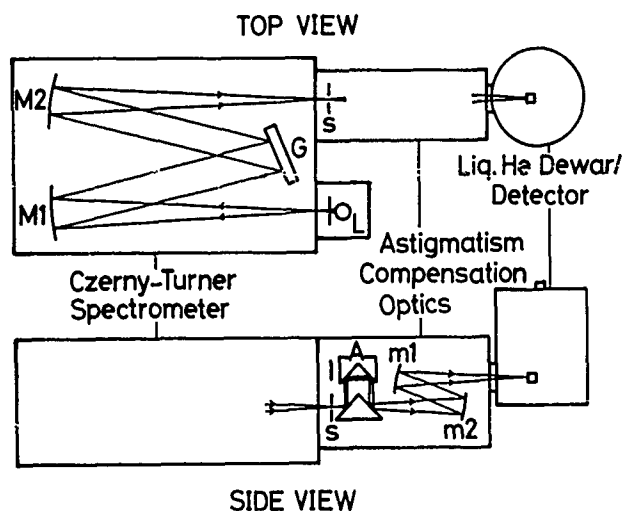


Figure 1

Configurations of the Czerny-Turner Monochromator with an astigmatism compensation optical system.

L is a high-pressure mercury lamp, G is a diffraction grating, and M1 and M2 are collimating and condensing mirrors, respectively, of the spectrometer. m1 and m2 are re-collimating and re-condensing mirrors of the compensation optical system. s is a slit.

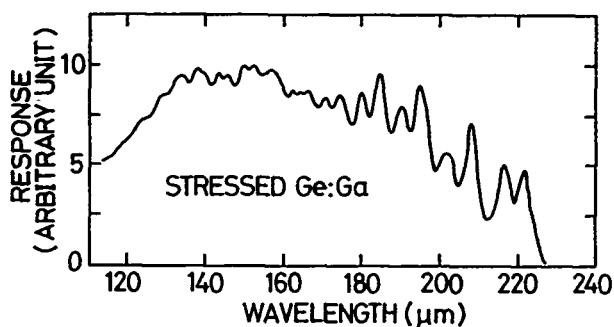


Figure 2  
Spectral responsivity of  
a stressed Ge:Ga photoconductor at 2 K.

optical system and the compensation optical system are arranged to have a common focus between two where a point source is imaged as two line segments perpendicular to each other separated by an interval due to the astigmatism. After a spectrometer condensing mirror images a point as two separated line segments, a compensation optical system images two line segments as a point. The reason why the total system can be almost non-astigmatic is that two parts of the optical systems have a common astigmatism.

The far infrared monochromator can emit radiation in 50-120  $\mu\text{m}$  and 100-240  $\mu\text{m}$  wavelengths ranges using two diffraction gratings and a high-pressure mercury lamp. The resolution is between 50 and 300 according to the slit size 6 mm to 1 mm. The monochromator can be pumped down to a vacuum to eliminate atmospheric absorption in the instrument. Using the monochromator, spectral responsivity of Ge:Ga photoconductors has been measured (Fig.2).

#### PERFORMANCE OF STRESSED Ge:Ga PHOTOCONDUCTORS UNDER LOW BACKGROUND CONDITIONS

Stressed Ge:Ga photoconductors fabricated by us have high detectivity: responsivity is 15 A/W and NEP is better than  $2 \times 10^{-18}$  W/√Hz at 2 K under low background photon fluxes of  $1.1 \times 10^6$  photons/sec. The good NEP is due to both low dark current of  $4.5 \times 10^{-14}$  A at 2 K (Fig.3) and high responsivity[5].

Under conditions of low photon fluxes, cooled extrinsic photoconductors show transient response with long time constant and nonlinear response[8,9]: the behavior limits performance of the detectors.

We have observed very slow anomalous transient response with time constant of several seconds in the stressed Ge:Ga photoconductor, though we have not found large responsivity dependence upon photon influxes between  $7.2 \times 10^{12}$  and  $1.1 \times 10^6$  photons/sec. The experimental results will be discussed.

#### REFERENCES

- (1) E.E.Haller, M.R.Hueschen, and P.L.Richards, 1970, Appl. Phys. Lett., vol. 34, pp. 495-497.

- (2) D.Lutz, D.Lemke, and J.Wolf, 1986, Appl. Opt., vol. 25, pp. 1698-1700.
- (3) J.Leotin, C.Laverny, M.Goiran, S.Askenazy, and J.R.Birch, Intl. J. Infrared Millimeter Waves, vol. 6, pp. 323-337.
- (4) J.-Q.Wang, P.L.Richards, J.W.Beeman and E.E.Haller, 1987, Appl. Opt., vol. 26, 4767-4771.
- (5) N.Hiromoto, T.Itabe, T.Aruga, H.Okuda, H.Matsuhara, H.Shibai, T.Nakagawa, M.Saito, 1988, to be submitted to Infrared Phys..
- (6) H.Okuda, H.Shibai, T.Nakagawa, T.Mtsuhara, T.Maiharu, K.Mizutani, Y.Kobayashi, N.Hiromoto, F.J.Low and T.Nishimura, 1988, Proc. IAU Symp. No.136, The Galactic Center, D.Reidel, Jordrecht.
- (7) D.J.Schroeder, 1974, Method of Experimental Physics, vol.12, Astrophys. Part A: Optical and Infrared, Ed. N.Carleton, Academic Press, New York.
- (8) N.M.Haegel and E.E.Haller, 1986, Infrared Phys., vol.26, pp. 247-261.
- (9) P.R.Bratt, 1977, Semiconductors and Semimetals, vol. 12 Infrared Detectors II, Eds. R.K. Willardson and A.C.Beer, Academic Press, New York.

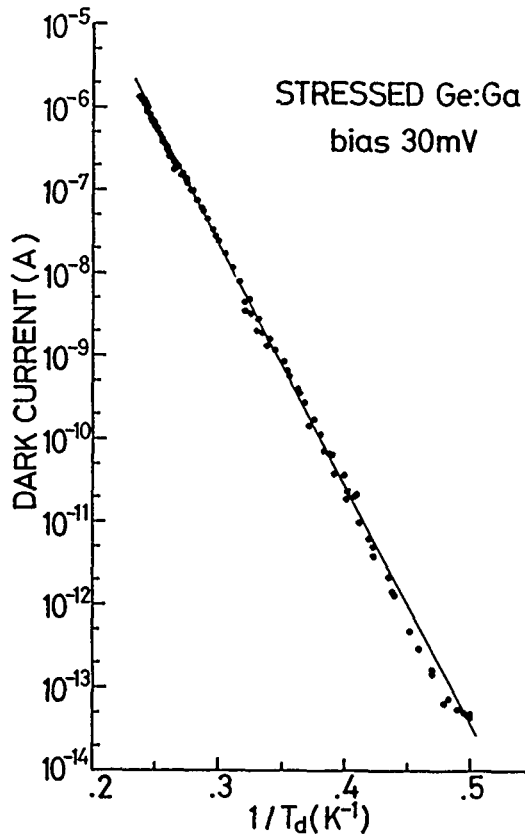


Figure 3  
Dark current versus inverse of the detector temperature. Minimum background photon flux was  $1.1 \times 10^6$  photons/sec at measurements. A solid line is a theoretical curve with  $E_a = 5.06$  meV fitted to the data[5].

## HIGH FREQUENCY SEMICONDUCTOR HETEROSTRUCTURE DEVICE ANALYSIS

Clifford M. Krowne and Gregory B. Tait

Electronics Science and Technology Division  
 Naval Research Laboratory  
 Washington, DC 20375-5000

## ABSTRACT

Two-terminal heterostructure diodes present many potential opportunities for high frequency operation, even into the millimeter wave frequency regime. Motivated by this fact, we have developed an algorithm which is globally convergent for solving the nonlinear Poisson equation. By appropriate numerical techniques, the nonlinear Poisson equation is coupled to the current continuity equations which can then be employed for high frequency, small signal, ac simulations. Numerical results for the  $\text{Al}_y\text{Ga}_{1-y}\text{As}$  system with layers as thin as a few hundred angstroms in thickness are provided.

## INTRODUCTION

Techniques which are both time efficient and accurate are of great interest to heterostructure device analysis if they can be implemented easily. We describe here such a procedure for obtaining ac two-terminal heterostructure device characteristics including internal device behavior as well as terminal current and voltage. The ac small-signal problem can be approached by first solving the coupled dc transport system of equations, namely the dc nonlinear Poisson equation and the dc current continuity equations. These dc solutions provide the position dependent dc variables necessary in the ac equations, along with the field dependency of the mobility. In order to calculate realistic starting values for the coupled dc system of equations which is solved iteratively, it is very useful to employ solutions of the nonlinear Poisson equation obtained by a globally convergent method.

## THEORY

The dc nonlinear heterostructure Poisson equation (using a single carrier species as is done below for all discussion to follow for illustrative purposes) is given by

$$d[\epsilon(x)dV/dx]/dx =$$

$$[n_{ir} \exp \{q(V + V_n - \phi_n)/kT\} - N_d^+] = f(V). \quad (1)$$

Here,  $V$ ,  $V_n$ ,  $\phi_n$ , and  $\epsilon$  are the electrostatic, heterostructure material, and electron quasi-Fermi potentials, and the dielectric constant [1]. If (1) is discretized and solved by a Jacobi-Newton iterative process, the solution can be shown to exist, be unique, converge to the continuous solution, and be globally convergent. Thus, if  $\phi_n$  is selected beforehand, or if equilibrium conditions are assumed ( $\phi_n = 0$ ), (1) can be solved for the starting potential distribution  $V$ .

Starting dc values of the variables are next applied to the dc system of equations,

$$dD/dx = -f(V) \quad (2); \quad dV/dx = -D/\epsilon \quad (3); \quad dJ_n/dx = 0 \quad (4)$$

$$d\phi_n/dx = -[J_n/q\mu_n(\delta)n_{ir}] \exp\{-q(V + V_n - \phi_n)/kT\}. \quad (5)$$

Here  $\mathcal{E}$  is the effective field utilized in the mobility  $\mu_n$  expression,

$$\mathcal{E} = -(dV/dx + dV_n/dx). \quad (6)$$

Equations (2) and (3) constitute the Poisson equation ( $D$  is the displacement field), (4) the continuity equation, and (5) the particle current  $J_n$  expression. After obtaining the continuous Jacobian matrix, the (2)-(5) system is solved employing a Newton numerical method subject to boundary conditions (BCs)  $n(0) = n_c(0)$  and  $n(l) = n_c(l)$  for the ohmic contacts giving conditions on  $V$  and  $\phi_n(0) = V_c$  and  $\phi_n(l) = 0$ .

Solutions to the dc equations yield the spatially dependent coefficients in the ac current equation, necessary for solving the ac system,

$$d\tilde{D}/dx = -q\tilde{n} \quad (7); \quad d\tilde{V}/dx = -\tilde{D}/\epsilon \quad (8); \quad d\tilde{J}_n/dx = j\omega q\tilde{n} \quad (9)$$

$$[qn_0\mu_{n0}/J_{n0}]d\tilde{\phi}_n/dx = -\tilde{J}_n/J_{n0} + \tilde{n}/n_0$$

$$+ \tilde{D}[d\mu_{n0}/d\mathcal{E}]/(\mu_{n0}\epsilon) \quad (10)$$

where  $\tilde{n} = qn_0(\tilde{V} - \tilde{\phi}_n)/kT$  eliminates  $\tilde{n}$  in the above formulas, subscript 0 denotes a dc value, and  $\mu_{n0} = \mu_n(\mathcal{E}_0)$ . The ac system is also solved using the BCs  $\tilde{V}(0) = \tilde{\phi}_n(0) = \tilde{V}_c$ ,  $\tilde{V}(l) = \tilde{\phi}(l) = 0$ .

## NUMERICAL EXAMPLE

Consider an isotype heterostructure diode having a sawtooth shaped compositional grading [2] of  $\text{Al}_y\text{Ga}_{1-y}\text{As}$  between two 0.75  $\mu\text{m}$  thick GaAs layers. Doping is uniform with  $N_d = 10^{16}/\text{cc}$  and the 0.25  $\mu\text{m}$  thick graded layer has a maximum  $y = 0.3$  on the right-hand-side. The heterojunction discontinuity rule applied at the  $y = 0.3$  interface is that  $0.62\Delta E_g = \Delta E_c$ . For a reverse bias situation ( $V_c = 0.4$  V) and  $T = 300$  K, Figs. 1 and 2 give the dc,  $\mathcal{E}$  and  $-dV/dx$ , and the energy band diagram versus  $x$ . Figure 3 gives the dc I/V curve for a 10 mil diameter cross-section, which shows rectification and a noticeable reverse leakage current due to doping and room temperature effects. AC  $|\tilde{J}_n|$  is given in Fig. 4 for 50 GHz. Figures 5 and 6 show the ac reverse bias terminal admittance components for the simulation (points) and an equivalent circuit fit (—) consisting of a series  $R_1$  and ( $R_2 \parallel C$ ) network with  $R_1 = 0.027 \Omega$ ,  $R_2 = 13.79 \Omega$ , and  $C = 21.5$  pf.

## REFERENCES

- [1] M. S. Lundstrom and R. J. Schuelke, IEEE Trans. Electron Devices, Vol. ED-30, pp. 1151-1159: Sept. 1983.
- [2] C. L. Allyn, A. C. Gossard, and W. Wiegmann, Appl. Phys. Lett., Vol. 36, pp. 373-376, Mar. 1980.

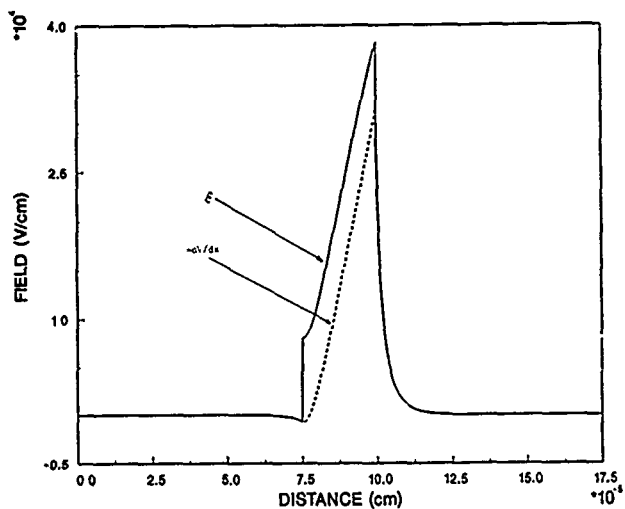


Figure 1

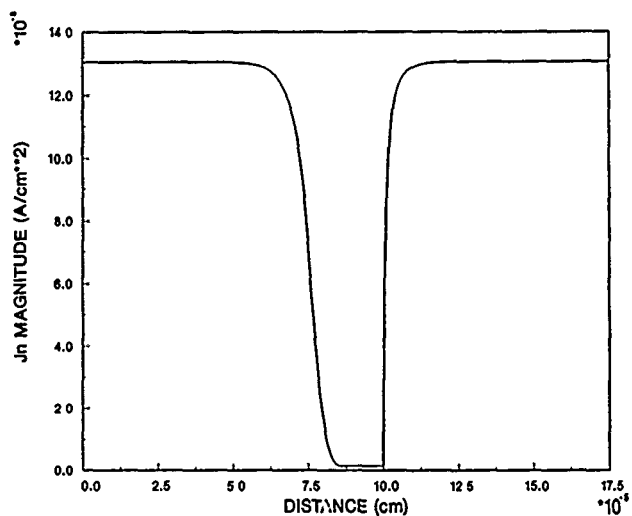


Figure 4

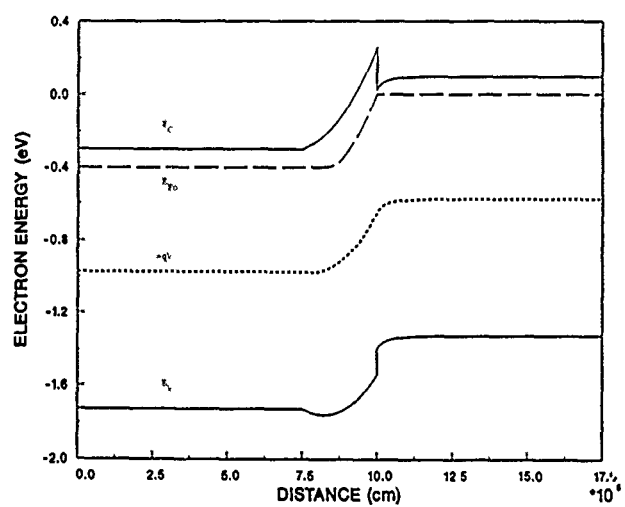


Figure 2

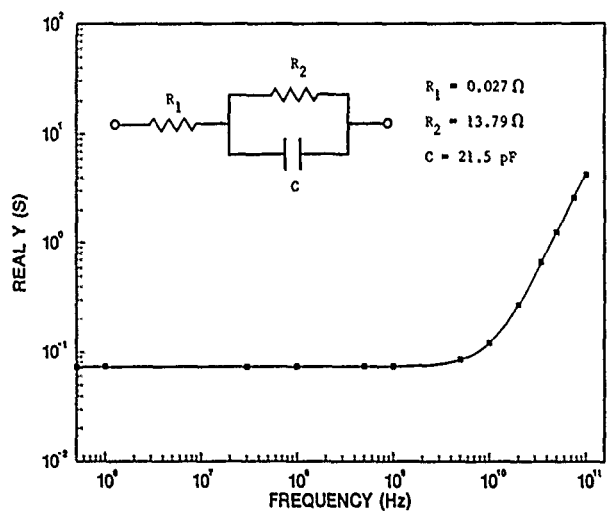


Figure 5

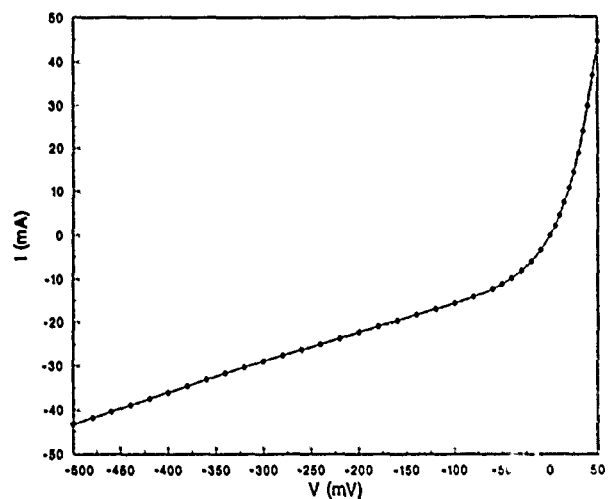


Figure 3

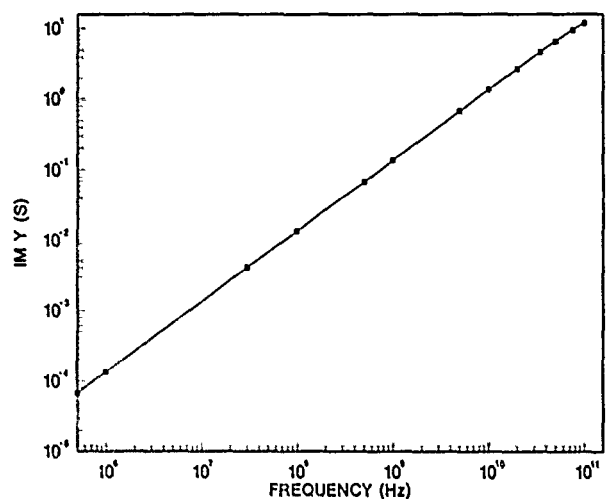


Figure 6

# FAR INFRARED ABSORPTION SPECTRA OF AMORPHOUS $(As_2S_3)_{1-x}(Sb_2S_3)_x$ SEMICONDUCTORS AND THE SPATIAL CHARGE FLUCTUATION

K. Matsuishi, T. Anzaki, S. Onari and T. Arai

Institute of Applied Physics, University of Tsukuba  
Tsukuba, Ibaraki 305, Japan

## ABSTRACT

Far infrared absorption spectra of amorphous  $(As_2S_3)_{1-x}(Sb_2S_3)_x$  system ( $x=0.0\sim 0.6$ ) were measured in the wavenumber region  $7\sim 25\text{ cm}^{-1}$  with Lamellar grating far infrared Fourier Transform Spectrometer, and the spatial fluctuation of charges and its correlation range were estimated with charge fluctuation model. The charge fluctuation of  $(As_2S_3)_{1-x}(Sb_2S_3)_x$  system increases with  $Sb_2S_3$  concentration  $x$ . On the other hand, the correlation length of the charge fluctuation decreases from 7 Å to 4.5 Å with an increase in  $x$ . As a result, it can be found that the medium range order of  $As_2S_3$  changes drastically with an increase in  $Sb_2S_3$  concentration  $x$ .

## INTRODUCTION

For the amorphous materials, charge fluctuation due to disorder induces acoustic phonon-photon coupling. As a result, the optical absorption at low frequency region far beyond the Reststrahlen band is much larger in magnitude than that in the corresponding crystalline solids, and its frequency-dependence reflects the spatial correlation of charge fluctuation [1,2,3]. The correlation length of charge fluctuation obtained from the frequency-dependence of very far infrared absorption is quite sensitive to medium range structure in amorphous, and provides the additional information of medium range order which cannot be sufficiently obtained from X-ray or neutron diffraction measurement. The knowledge about medium range order is very important for the understanding of many kinds of features of amorphous materials, for example electronic and vibrational states. For amorphous  $As_2S_3$  and  $As_2Se_3$ , the presence of an intralayer correlation ranging over about 7 Å as a medium range order has been confirmed from correlation effect of the charge fluctuations [4,5], in addition to the interlayer correlation which extends to four layers (15~20 Å) obtained from diffraction measurement.

Our purposes in this study are to investigate how the medium range order changes with an increase in  $x$  for  $(As_2S_3)_{1-x}(Sb_2S_3)_x$  system, and how the degree of disorder increases with the substitution of Sb for As atoms. In this report, we estimate the magnitudes and the correlation lengths of the spatial fluctuations of charges for  $(As_2S_3)_{1-x}(Sb_2S_3)_x$  system with the charge fluctuation model, and investigate the changes of those with an increase in  $x$ . From the correlation effect of the charge fluctuations, the medium range order is discussed. The magnitudes of the charge fluctuations for this system are considered from the effective charge and the degree of disorder.

## EXPERIMENTAL AND ANALYSES

The samples used were prepared by the melt quenching

method for  $(As_2S_3)_{1-x}(Sb_2S_3)_x$  ( $x=0.0,0.1,0.2,0.3,0.4,0.5,0.6$ ) system. The far-infrared absorption spectra in energy range  $7\sim 25\text{ cm}^{-1}$  were measured by the Lamellar grating far-infrared Fourier transform spectrometer constructed in our laboratory [6]. In this instrument, an ark-stabilized high pressure mercury lamp (~1 kw) was used as a light source, and the signal was detected by the liquid helium-cooled Ge bolometer of composite type.

For glasses, the disorder-induced far-infrared absorption coefficient  $\alpha(\omega)$  is expressed by the charge fluctuation model as follows

$$\alpha(\omega) = \frac{(n^2 + 2)^2}{9\rho cnVt^3} \omega^2 g(\omega/\omega_0) Nq_i^2 \quad (1)$$

where  $Vt$  is the transverse acoustic velocity,  $\rho$ ,  $n$  and  $c$  are the mass density, the refractive index and the velocity of light, respectively [3]. In this equation,  $N$  is the density of the point charge fluctuation  $q_i$  which is given by the difference from the average charge, and  $g(\omega/\omega_0)$  is the correlation factor proposed by Schlömann [1]. If the compensating charge distribution, which surrounds a charge fluctuation  $q_i$ , is assumed to fall off exponentially as  $q_i \exp(-r/\iota)$ ,  $g(\omega/\omega_0)$  is given as

$$g(\omega/\omega_0) = 1 - (1 + (\omega/\omega_0)^2)^{-2} \quad (2)$$

where  $\omega_0 = Vt/\iota$ . The "correlation length"  $\iota$  is a parameter which characterizes the strength of the correlation of the charge fluctuation. When the phonon wavelength is larger than the correlation length of the spatial fluctuation of charge, such a correlation interaction arises as known from equation (2). We can estimate the spatial fluctuation  $q_i$  and the correlation length  $\iota$  for the spatial fluctuation due to disorder from the best fit of the equations (1) and (2) to the experimentally obtained absorption spectra.

## RESULTS AND DISCUSSION

In Fig. 1, the spectra of  $n\alpha/(\hbar\omega)^2$  for  $(As_2S_3)_{1-x}(Sb_2S_3)_x$  system are shown together with the calculated best fit curves of equations (1) and (2). These  $n\alpha/(\hbar\omega)^2$  spectra show that the optical coupling coefficient in this energy region increases drastically with  $Sb_2S_3$  concentration  $x$  and strongly depends on frequency. We obtained the values of  $Nq_i^2$  and  $\omega_0 (=Vt/\iota)$  in equation (1) from the above procedure.

In Fig. 2, the magnitudes of  $Nq_i^2$  for  $(As_2S_3)_{1-x}(Sb_2S_3)_x$  are shown as a function of the concentration  $x$ . They increase superlinearly with the concentration  $x$ . With a view to explain the remarkable increase of the charge fluctuation with concentration  $x$ ,  $Nq_i^2$  can be expressed for convenience as

$$Nq_1^*{}^2 = (Nq_1^*{}^2)_{x=0} \cdot \frac{N_0 e_{\text{eff}}^2}{(N_0 e_{\text{eff}}^2)_{x=0}} + \Delta D \quad (3)$$

where  $e_{\text{eff}}$  is the effective charge obtained from the Reststrahlen bands and  $N_0$  is the number of oscillators with  $e_{\text{eff}}$  per unit volume. The first term in equation (3), shown as the line ② in Fig. 2, represents the contribution of charge fluctuation induced in proportion to effective charge. On the other hand, the second term  $\Delta D$  in equation (3), shown as the curve ③ in Fig. 2, corresponds to excess of charge fluctuation which might be created by the substitution of Sb for As atoms in this system. The value of  $\Delta D$  is related to the increment of the degree of disorder.

The correlation lengths  $\iota$  derived from the relation  $\iota = Vt/\omega_0$  are listed in Table 1. The value of  $\iota$  decreases from 7 Å to 4.5 Å with an increase in concentration  $x$ .

The local structure of glassy  $\text{Sb}_2\text{S}_3$ , which is a 3-2 covalent network composed of trigonal pyramids  $\text{SbS}_3$ , is similar to that of  $\text{As}_2\text{S}_3$  glass with respects to the coordination number and the basic structural unit. For this reason, it could be considered that there is no remarkable change in short range order for  $(\text{As}_2\text{S}_3)_{1-x}(\text{Sb}_2\text{S}_3)_x$  system. On the other hand, the network structure is based on 2D-clusters (layers) in  $\text{As}_2\text{S}_3$  glass, but on more or less 1D clusters (bands) in  $\text{Sb}_2\text{S}_3$  glass. This difference between the medium range structures of them suggests that the increase of  $\text{Sb}_2\text{S}_3$  concentration  $x$  prompts chain-branching and the interconnection of layer-forming configurations. Namely, the substitution of Sb for As atoms in glassy  $\text{As}_2\text{S}_3$  creates a gradual transition from a glassy layer-like structure of  $\text{As}_2\text{S}_3$  to a different kind of continuous random network structure. This is why the correlation length of the charge fluctuation decreases with an increase in  $\text{Sb}_2\text{S}_3$  concentration. This conclusion is consistent with the assertion by Červinka through the analysis of the RDF of electron density calculated from X-ray diffraction data [7].

## REFERENCES

- [1] E. Schlömann, Phys. Rev. 135 (1968) A413.
- [2] W. Bagdade and R. Stolen, J. Phys. Chem. Solids 29 (1968) 2001.
- [3] U. Strom and P.C. Taylor, Phys. Rev. B16 (1977) 5512.
- [4] K. Matsuishi, S. Onari and T. Arai, Jpn. J. Appl. Phys. 25 (1986) 1144.
- [5] K. Matsuishi, S. Onari and T. Arai, J. Non-Cryst. Solids 97&98 (1987) 1187.
- [6] S. Onari, K. Matsuishi and T. Arai, J. Non-Cryst. Solids 86 (1986) 22.
- [7] L. Červinka and A. Hruby, J. Non-Cryst. Solids 48 (1982) 231.

$(\text{As}_2\text{S}_3)_{1-x}(\text{Sb}_2\text{S}_3)_x$

concentration

$x$	0.0	0.1	0.2	0.3	0.4	0.5	0.6
$\iota$	7.2	5.8	4.8	4.4	4.5	4.4	4.6

Table 1

Correlation length  $\iota$  obtained from the best fit in Fig. 1.

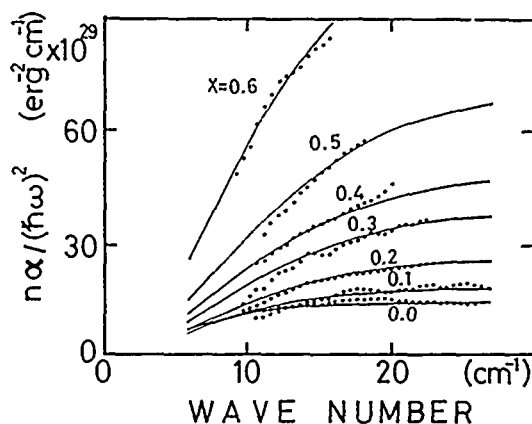


Figure 1  
Fitting of the theoretical curves by equations (1) and (2) with the spectra of  $n\alpha/(\hbar\omega)^2$  obtained experimentally.

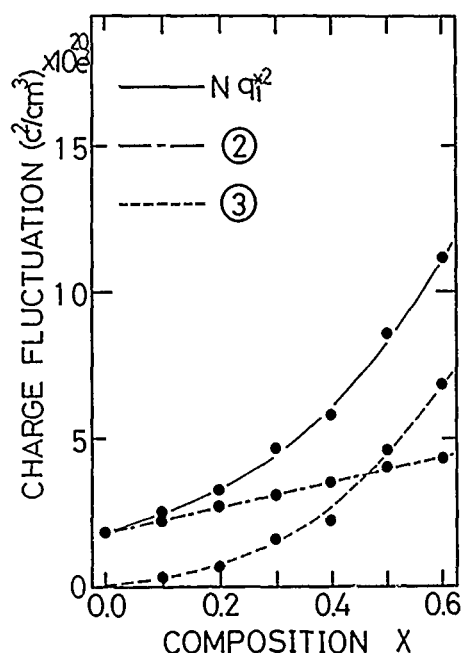


Figure 2  
Magnitude of  $Nq_1^*{}^2$  derived from equation (1). The lines ② and ③ are related to the first and second terms in equation (3), respectively.

EFFECTS OF ANNEALING ON THE ELECTRICAL PROPERTIES OF P-Cd<sub>0.2</sub>Hg<sub>0.8</sub>Te GROWN BY LPE

K. Yasumura and K. Sato  
Materials and Electronic Devices Lab., Mitsubishi Electric Corp.  
(1-1-8, Tsukaguchi-honmachi, Amagasaki, 661, Japan)

Y. Yoshida and Y. Komine  
LSI R & D Lab., Mitsubishi Electric Corp.  
(4-1, Mizuhara, Itami, 664, Japan)

## ABSTRACT

The effects of annealing on the electrical properties of Cd<sub>0.2</sub>Hg<sub>0.8</sub>Te(CMT) grown by liquid phase epitaxy technique are investigated. We show that the annealing at the temperature as low as 250°C under the vacuum condition is superior to the conventional technique, annealing at the temperature higher than 400°C under Hg over-pressure, to obtain high quality p-CMT layers. Hole concentration and mobility of the resultant p-CMT are  $7.2 \times 10^{15} \text{ cm}^{-3}$  and  $787 \text{ cm}^2/\text{V}\cdot\text{sec}$ , respectively.

## INTRODUCTION

The as-grown CMT epitaxial layers by liquid phase epitaxy from Te solution are generally p-type with high hole concentration (over  $10^{17} \text{ cm}^{-3}$ ) and low mobility (below  $300 \text{ cm}^2/\text{V}\cdot\text{sec}$ ) (1),(2). In order to adjust these electrical properties to suit the device requirement, the annealing under Hg over-pressure at high temperature ( $T > 400^\circ\text{C}$ ) has been pursued (4),(9),(11). In terms of p-type crystal, it is generally accepted that Hg vacancy is the dominant acceptor in CMT. However, there is such a dispute that the redistribution of residual acceptor impurities from the gettering site converts n-CMT crystal to p-type due to the annealing (3).

In this paper, the electrical properties in CMT are investigated as a function of annealing condition. We demonstrate that low temperature annealing below 250°C under the vacuum makes CMT layers higher quality superior to the conventional high temperature annealing under Hg over-pressure, and that not only Hg vacancy, but also residual impurities are the dominant acceptor in CMT.

## EXPERIMENTAL

CMT ( $X=0.2$ ) epitaxial layers were grown on CdTe(111)B substrates by LPE technique using a slider boat as shown Figure 1. HgTe ingot, which plays the role of exerting the Hg pressure on a grown layers, was loaded in the slider boat. The furnace temperature was lowered at the rate of  $0.5^\circ\text{C}/\text{min}$ , and the growth temperature was  $480^\circ\text{C}$ .

As-grown CMT layers were annealed under two conditions; one is under the constant temperature of  $400^\circ\text{C}$  under Hg pressure ranging from 20 to 150 torr, the other is under various temperature from 130 to  $350^\circ\text{C}$  under vacuum condition. Carrier concentration and Hall mobility in annealed CMT layers were measured at 77K by van der Pauw method.

## RESULTS AND DISCUSSION

Annealing under Hg over-pressure

Figure 2 shows the electrical properties of CMT at 77K as a function of the partial pressure of Hg. The hole concentration is shown to be inversely proportional to Hg pressure, which agrees with the relationship deduced from the theory of defects chemistry equilibrium (8). This agreement suggests that the hole concentration is dominated by Hg vacancy.

Since the concentration of hole increases with the annealing temperature at the constant Hg pressure (5),(8),(10), higher quality p-CMT layers should be obtained by the annealing condition at lower temperature.

Annealing under vacuum condition

Figure 3 shows the relationship between the electrical properties of CMT and the annealing temperature under vacuum condition. The temperature dependence of the hole concentration in the region above  $190^\circ\text{C}$  is given empirically, by

$$[h'] = 9.2 \times 10^{21} \exp(-0.6 \text{ eV} / kT) \text{ cm}^{-3}.$$

The activation energy,  $E=0.6 \text{ eV}$ , which is believed to be the formation energy of Hg vacancy under vacuum condition. Similar experiments have been reported by S.H.Shin (7) and H.Wiedeneier (6): their values are 0.9, 0.43 eV, respectively, these disparities from our value due to the difference of the experimental condition.

While in the region below  $190^\circ\text{C}$ , the slope of the curve is opposite to that above  $190^\circ\text{C}$ , indicating that dominant acceptor is not Hg Vacancy, but another factor such as residual impurities (3). During the annealing, Te precipitate being present in CMT getters residual impurities such as Cu, Na, which behave acceptor. Thus the high quality p-CMT layers are obtained at minimum point of the curve, where hole concentration and mobility at 77K are  $7.2 \times 10^{15} \text{ cm}^{-3}$  and  $787 \text{ cm}^2/\text{V}\cdot\text{sec}$ , respectively.

Diffusion experiment at  $150^\circ\text{C}$  for an hour shows that diffusion depth of In for the layers under Hg over-pressure is five times larger than that under vacuum condition. This result agrees with our conclusion that p-CMT annealed at lower temperature has lower defects concentration.

## CONCLUSION

- (1) High quality p-CMT layers are obtained by low temperature annealing technique under the vacuum condition.



- (2) There are two types of acceptor. One is Hg vacancy being dominant at high temperature, the other is residual impurities at low temperature.
- (3) The annealing temperature should be as low as possible, to lower the concentration of defects in CMT layers.

#### REFERENCES

- (1) M. Chu : Southcon. Conf. Rec., 4, 99 (1984).
- (2) J. C. Tranchart, B. Latorre, C. Foucher, and Y. Le Gouge : J. Crystal Growth, 72, 468 (1985).
- (3) J. Tregilgas, J. Beck, and B. Gnade : J. Vac. Sci. Technol., A3 (1), 150 (1985).
- (4) C. E. Jones, K. James, J. Merz, R. Braunstein, M. Burd, M. Etemadai, S. Hutton, and J. Drumheller : J. Vac. Sci. Technol., A3(1), 131(1985).
- (5) J. Yang, Z. Yu, and D. Tang : J. Crystal Growth, 72, 275 (1985).
- (6) H. Wiedemeier, S. B. Trivedi, R. C. Whiteside, and W. Polosz : J. electrochem. Soc., 133, No. 11, 2399 (1986).
- (7) S. H. Shin, M. Khoshnevisan, C. Morgan-Pong, and R. Raghavan : J. Appl. Phys., 58(4), 1470 (1985).
- (8) H. R. Vydyanath, J. C. Donovan, and D. A. Nelson : J. Electrochem. Soc., 128, 2625 (1981).
- (9) M. Chu : J. Appl. Phys., 51(11), 5876 (1980).
- (10) C. G. Morgan-Pond : Phys. Rev., B31, 6616 (1985).
- (11) C. L. Jones, M. J. T. Quelch, P. Capper, and J. J. Gosney : J. Appl. Phys., 53(12), 9080 (1982).

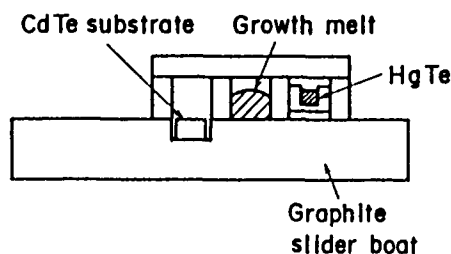


Figure 1

A slider boat with the HgTe room.

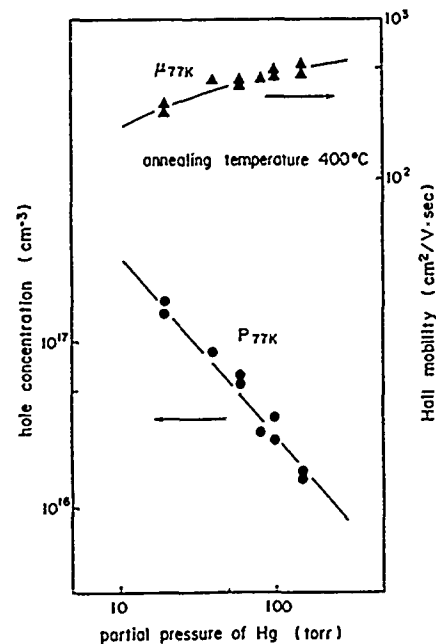


Figure 2

Electrical properties, hole concentration and Hall mobility, as a function of partial pressure of Hg.

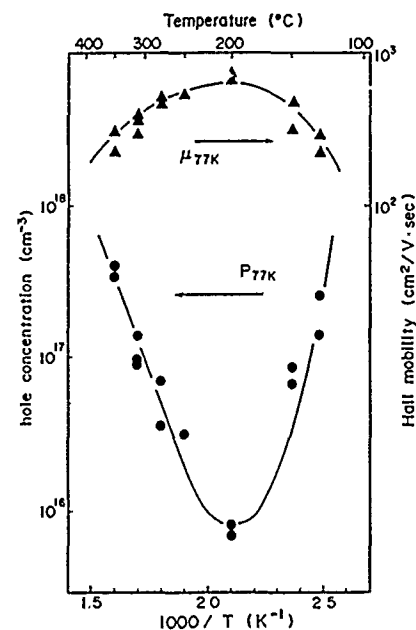


Figure 3

Electrical properties, hole concentration and Hall mobility, as a function of annealing temperature under vacuum condition.

**MILLIMETER AND SUBMILLIMETER WAVE OPTICAL AND  
DIELECTRIC PROPERTIES OF SINGLE CRYSTAL HIGH PURITY SILICON**

Mohammed Nurul Afsar  
Department of Electrical Engineering  
Tufts University  
Medford, Massachusetts 02155

**ABSTRACT**

The single crystal silicon is a monatomic material. The lattice vibration absorption peaks appear around 18,000 GHz (600 wavenumber per centimeter). The only other absorption process present in the entire millimeter and submillimeter wave region is the free carrier absorption which centers around 60 GHz (5 mm in wavelength, 2 wavenumber per centimeter). The free carrier absorption can be reduced in two way: by making the material ultra pure or by introducing deep trap impurities while manufacturing. The resistivity increases in both cases. Complex refractive index, complex dielectric permittivity and loss tangent spectra on several hyperpure silicon specimens will be presented as a function of frequency and resistivity and compared.

# BAND DEGE STRUCTURE OF $Pb_{1-x}Sn_xTe$ DOPED WITH INDIUM BY FAR-INFRARED MAGNETOPLASMA REFLECTION METHOD

S. Takaoka, S. Shimomura, H. Takahashi and K. Murase

Department of Physics, Faculty of Science, Osaka University  
1-1 Machikaneyama, Toyonaka 560 Japan

## ABSTRACT

Far-infrared magnetoplasma reflection spectra of In doped  $Pb_{1-x}Sn_xTe$  are measured across the band inversion region ( $0.15 < x < 0.40$ ). From the spectra, the temperature dependences of photo-carrier concentrations and cyclotron masses are determined below 20K, where large photoconduction is observed. By using the two bands theory with observed masses and carrier concentrations, it is found that the band edge masses become much heavier even by 1% In doping, while the band gaps do not change appreciably as compared with those of undoped  $Pb_{1-x}Sn_xTe$ .

## INTRODUCTION

The IV-VI compound semiconductors such as  $PbTe$ ,  $SnTe$  and  $PbSe$  are well-known narrow gap semiconductors[1]. Especially, it has been believed that the band gap ( $E_g$ ) of  $Pb_{1-x}Sn_xTe$  decreases with increasing tin composition ( $x$ ) and the conduction and valence bands cross each other i.e.  $E_g$  becomes zero near  $x=0.35$  at 4.2K and then  $E_g$  increases again with larger  $x$ [1]. However, it is very difficult to investigate the band edge structure near the band inversion region, since a only high carrier concentration more than  $10^{18}cm^{-3}$  specimen with low density of states due to the small effective mass is available[2] and the edge structure is hidden by the high carrier concentration in normal  $Pb_{1-x}Sn_xTe$ .

When In is doped in  $Pb_{1-x}Sn_xTe$ , the chemical potential (Fermi level) is pinned and moves down from the conduction band ( $x < 0.23$ ) to the band gap ( $0.23 < x < 0.30$ ) and then to the valence band ( $x > 0.30$ ) with increasing  $x$ [3]. The low carrier concentration specimens with  $10^{15}cm^{-3} - 10^{17}cm^{-3}$  are obtained in the band inversion region. Further a remarkable strong photoconduction sensitive to infrared radiation is observed below 20K[3,4]. With changing temperatures, the photocarrier concentration varies greatly. We can obtain the information of the band parameters in a wide range of carrier concentration in a same specimen.

## EXPERIMENTS

The specimens used in this study were single crystals grown by a vapor transport method. Indium was introduced to the sliced crystal by isothermal annealing in In vapor[3]. The amount of In dopant is estimated to be 1 at.%. The far-infrared magnetoplasma reflection spectra were measured using a strip-line method with HCN laser light ( $337\mu m$ ) and a split type superconducting magnet up to 4T[4]. A magnetic field direction can be changed from the Faraday to the Voigt configuration. The specimens were exposed to room temperature black body radiation.

In Fig.1, the typical spectra in the Faraday configuration with a magnetic field parallel to a  $\langle 100 \rangle$

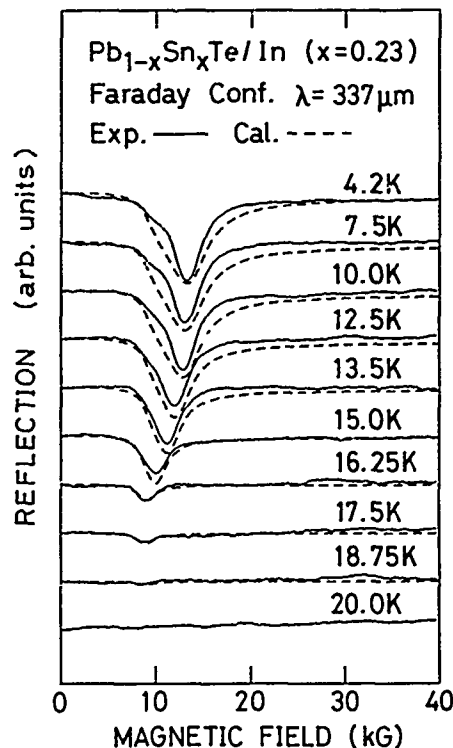


Fig.1. Temperature dependence of magnetoplasma reflection spectra of In doped  $Pb_{1-x}Sn_xTe$  ( $x=0.23$ ).

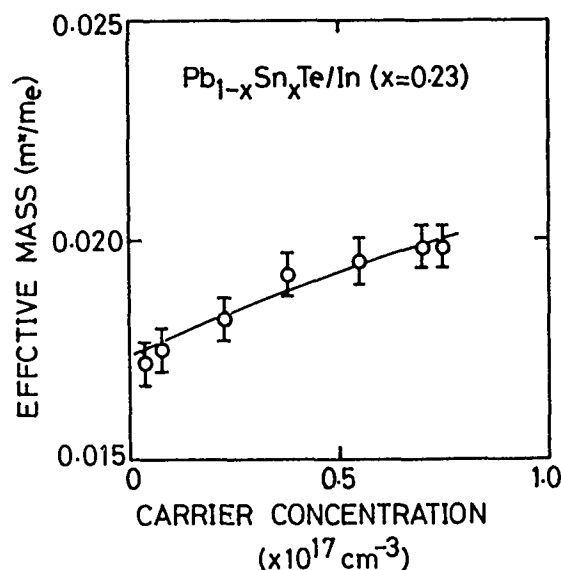


Fig.2. Carrier concentration dependence of effective masses. Solid curve is calculation.

direction for  $x=0.23$  are shown with changing temperatures between 4.2K and 20K. With increasing temperatures, the dip positions shift to lower magnetic fields and dip depths become smaller due to reduction of the photocarrier concentration and cyclotron mass. The broken curves in Fig.1 are calculated spectra using dielectric functions derived from the Drude model[4]. From such a fitting procedure, the photocarrier concentration and the cyclotron mass are obtained for each temperature. In Fig.2, the photocarrier concentration dependence of the effective mass is plotted again by using previously obtained concentrations and masses for various temperatures. The temperature dependence of photocarrier concentration is discussed in other papers[4,5].

### DISCUSSION

The effective mass becomes smaller with decreasing carrier concentration, as shown in Fig.2, probably due to the band non-parabolicity. Since the band gaps are very small ( $E_g < 80\text{meV}$ ) in the present specimens, the two bands theory is applicable to describe the band edge structure. According to the two bands theory, the effective mass with energy  $E$  is expressed as[6]

$$m^* = m_0(1 + 2E/E_g), \quad (1)$$

where  $m_0$  is the band edge mass. The relation between the carrier concentration ( $N$ ) and the Fermi energy ( $E_f$ ) is given as

$$N = \int D(E, E_f, m_0) f(E, E_f, T) dE, \quad (2)$$

where  $D(E, E_f, m_0)$  is the density of states,  $f(E, E_f, T)$  is the Fermi distribution function and  $T$  is temperature. The solid curve in Fig.2 is the calculated non-parabolicity of effective mass to reproduce the experiments using eqs.(1) and (2). The fitting parameters are  $E_g$  and  $m_0$ . Thus determined  $E_g$  and  $m_0$  are plotted vs. tin composition ( $x$ ) in Figs. 3 and 4, respectively. The broken curves are the expected values of undoped  $\text{Pb}_{1-x}\text{Sn}_x\text{Te}$ [3,7].

As seen in these figures,  $m_0$  are much heavier than those of undoped  $\text{Pb}_{1-x}\text{Sn}_x\text{Te}$ , while  $E_g$  do not change remarkably within experimental uncertainty. In the two bands theory, the band edge mass is expressed as  $m_0 = E_g/2P^2$ , where  $P$  is a momentum matrix element between the conduction and valence bands[6]. The enhancement effect of  $m_0$  by doping In was already reported in  $\text{Pb}_{1-x}\text{Sn}_x\text{Te}$  film ( $x=0.25$ )[8]. However there were some complicated situations such as the valley splitting due to the strain in the film sample and only one sample was measured, we could not trace the enhancement effect to its origin. From this study, it is considered that the enhancement of  $m_0$  by doping In is mainly due to the reduction of the matrix element.

### ACKNOWLEDGEMENTS

We wish to thank Mr. T.Itoga for the sample preparations. This work was partially supported by the 22nd Science and Technology of Toray Science Foundation and the 10th Nippon Sheet Glass Foundation for Materials Science.

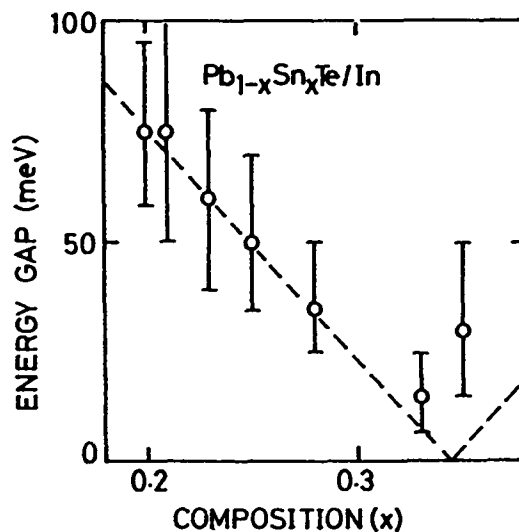


Fig.3. Composition dependence of  $E_g$  of  $\text{Pb}_{1-x}\text{Sn}_x\text{Te}$  doped with In. Broken curve is expected value of undoped  $\text{Pb}_{1-x}\text{Sn}_x\text{Te}$ .

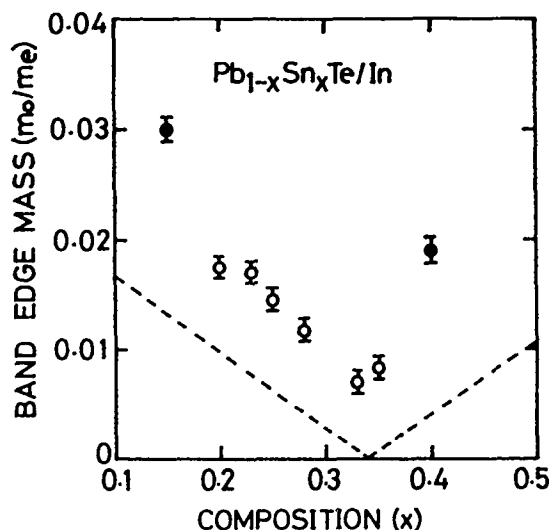


Fig.4. Composition dependence of band edge masses of In doped  $\text{Pb}_{1-x}\text{Sn}_x\text{Te}$ . Broken curve is expected value of undoped  $\text{Pb}_{1-x}\text{Sn}_x\text{Te}$ .

### REFERENCES

- (1) G. Nimtz and B. Schricht in: *Narrow Gap Semiconductors* (Springer-Verlag, Berlin, 1983) p.1.
- (2) T.C. Harman, *J. Nonmetals* **1** (1973) 183.
- (3) S. Takaoka, T. Itoga and K. Murase, *Jpn. J. Appl. Phys.* **23** (1984) 216.
- (4) S. Shimomura: Dr. Thesis, Osaka University, 1988.
- (5) S. Shimomura, H. Takahashi, S. Takaoka and K. Murase, *Proc. 19th Intern. Conf. Phys. Semicond. Warsaw, Poland, August, 15-19, 1988.*
- (6) P.A. Wolff, *J. Phys. Chem. Solids*, **25** (1964) 1057.
- (7) C.R. Hew and M.S. Adler and S.D. Senturia, *Phys. Rev. B* **7** (1973) 5195.
- (8) S. Takaoka, T. Hamaguchi, S. Shimomura and K. Murase, *Proc. 17th Intern. Conf. Phys. Semicond. San Francisco, 1984* (Springer-Verlag, New York, 1985) p.663.

## LOW FREQUENCY IMPURITY VIBRATION MODES IN II-VI SEMICONDUCTOR

Lu Wei, Ye Hongjuan, Xu Wenlan, Shen Xuchu(S.C.Shen)

(Laboratory for Infrared Physics, Shanghai Institute of Technical Physics, Academia Sinica, Shanghai, China)

W.Giriat

(Centra de Fisica, Caracas, Venezuela)

## ABSTRACT

The quasi-local modes induced by light impurities in CdTe and observed by use of the far infrared spectroscopy have been reported. The theoretical analysis of these modes by combining the Green's function with Recursion calculation has shown an obvious acoustic phonon behavior of quasi-local modes.

## INTRODUCTION

In recent years, there have been a lot of theoretical and experimental studies on the lattice vibrations induced by impurities in semiconductors and other solids[1,2]. Many quasi-local modes related with impurities and located just above the TA acoustic phonon band of host crystal have been reported in element semiconductor Si and Ge and in III-V group compound semiconductor GaAs and GaP, in addition to the local modes induced by impurities above the optical phonon band of host crystal[3,4]. In order to see the generalization of this phenomenon, here we report a systematical study on the low frequency impurity vibration modes in II-VI semiconductor CdTe.

## EXPERIMENTS AND RESULTS

The mixed crystal  $\text{Cd}_{1-x}\text{Fe}_x\text{Te}$ ,  $\text{Cd}_{1-x}\text{Zn}_x\text{Te}$  and  $\text{CdTe}_{1-x}\text{Se}_x$  used in our experiments are grown by modified Bridgman method. Their composition  $x$  is between 0.005 and 0.05. So our samples can be considered as CdTe doped with impurity Fe, Zn and Se because we only study their lattice vibration behavior.

The far infrared reflection spectra and transmission spectra of our samples have been measured by Fourier transform spectrometer in the wavenumber region of 20 - 360  $\text{cm}^{-1}$  with a resolution of 1 - 2  $\text{cm}^{-1}$  at different temperature from 4.2K to 300K. The typical absorption spectra are shown in Fig.1. By analysing the temperature effect of the absorption peaks in Fig.1 we have identified that one of lower frequency is one phonon absorption and the other is two phonon absorption. The dielectric function  $\tilde{\epsilon}(\omega)$  of our samples is derived from their reflection spectra by K-K relation calculation and random element isodisplacement model fitting. From the peaks in  $\text{Im}(\tilde{\epsilon}(\omega))$  and

absorption peaks, we distinguished the quasi-local modes at 56  $\text{cm}^{-1}$ , 54  $\text{cm}^{-1}$  and 55  $\text{cm}^{-1}$  related to the impurities Fe, Zn and Se; local modes at 196  $\text{cm}^{-1}$ , 174  $\text{cm}^{-1}$  and 176  $\text{cm}^{-1}$  induced by Fe, Zn and Se in addition to the band modes of CdTe. Similar with the properties of quasi-local modes observed in Si, Ge, GaAs and GaP, the frequencies of the quasi-local modes observed in our samples are also just above the critical point of the TA phonon band of CdTe.

## DISCUSSION

With the harmonic approximation, the equation for lattice vibration can be written in the matrix form as

$$H|u\rangle = \omega^2 |u\rangle \quad (1)$$

where

$$u_{kx} = m_k u'_{kx} \\ H_{kk'xx'} = \tilde{H}_{kk'xx'} / (m_k m_{k'})$$

$u'_{kx}$  is the vibrational amplitude component in  $x$  direction at the  $k$ -th atom,  $\tilde{H}_{kk'xx'}$  is the  $xx'$  element in the interaction matrix between  $k$ -th and  $k'$ -th atom,  $m_k$  the mass of  $k$ -th atom,  $\omega$  is the frequency. The Green's function related to matrix  $H$  is defined as

$$G(\omega^2) (H - \omega^2 I) = I \quad (2)$$

where  $I$  is the unit matrix. Transforming the matrix  $H$  into a tri-diagonal matrix  $H'$  and calculating the imaginary part of the diagonal elements of Green's function one can get the local densities of states (LDOSs) of the lattice vibration[4].

Applying this theoretical procedure on our system - II-VI group compound semiconductor CdTe doped with impurities Fe, Zn and Se, we have got the local density of states (LDOSs) of impurity atoms Fe, Zn and Se and their surrounding atoms. The comparison of LDOSs of impurity atoms with the LDOS of host atom shows that there are two peaks of density of states located above TA phonon band and optical phonon band respectively. The frequencies of these two peaks are the same as those observed in our experiments. The both theoretical and experimental values are listed in table 1. The LDOSs of impurity atom and its surrounding atoms have been shown in Fig.2. Considering that LDOSs is proportional to the vibration amplitude of correspond atom, we see from Fig.2 that the amplitude of the local mode decreases so quickly that at the second

neighbour atoms it has been fairly weak, but for the quasi-local mode the amplitude decays to a constant value which is the amplitude of vibration for atom replaced by impurity at this frequency in perfect crystal. This is a resonance mode behavior. The correlation functions of impurity atom with its surrounding atoms show that the impurity atom vibrates in the same direction with its nearest neighbour atom but in the opposite direction with its second neighbour atom. So contrast to the local mode which behaves as an optical phonon, the quasi-local mode behaves as an acoustic phonon of fair large wave vector. This difference makes that the dipole formed by local mode is much larger than that formed by quasi-local mode. This fact is the major reason for why the absorption intensity of local mode is much higher than that of quasi-local mode as observed in our experiment.

Table 1  
Frequencies of local and quasi-local mode in doped CdTe\*

impurity	Fe	Zn	Se
$\omega_{le}(\text{cm}^{-1})$	196	174	176
$\omega_{lt}(\text{cm}^{-1})$	196	171	177
$\omega_{qe}(\text{cm}^{-1})$	56	54	55
$\omega_{qt}(\text{cm}^{-1})$	56	54	55

\*  $\omega_{le}$  and  $\omega_{lt}$  represent the experimental and theoretical values of frequencies for local modes respectively;  $\omega_{qe}$  and  $\omega_{qt}$  are same as  $\omega_{le}$  and  $\omega_{lt}$  respectively but for quasi-local modes.

#### REFERENCES

- (1) A.S.Barker, Jr. and A.J.Sievers, Rev. of Modern Phys., 47, Suppl., No.2, S1 (1975).
- (2) M.Vanderyver and D.N.Talwar, Phys. Rev., B21, (1980), 3405.
- (3) M.Cardona, S.C.Shen and S.P.Varma, Phys. Rev., B23, (1981), 5329.
- (4) Y.Fu, W.L.Xu and Z.B.Zheng, Sol. Sta. Comm., 62, (1987), 163.

Figure 1  
Absorption spectra of CdTe doped with (a)Fe (b)Se (c)Zn.

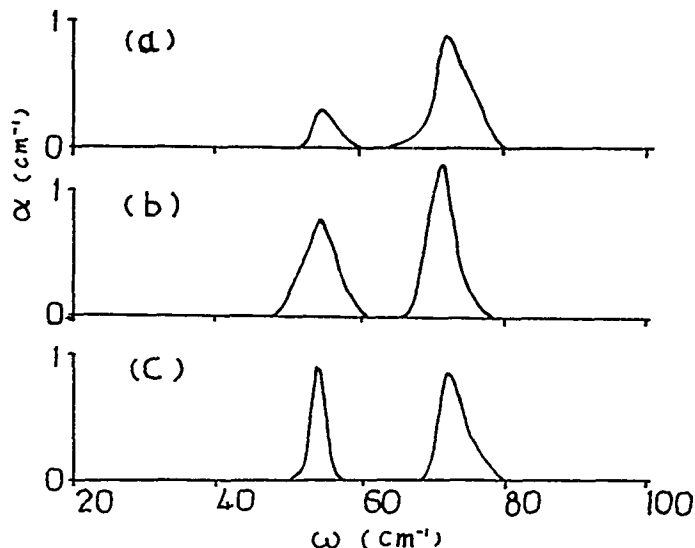


Fig. 1

Figure 2

LDOSs for impurity Fe (F1), nearest neighbour atom of Fe (F2), second nearest neighbour atom of Fe (F3), third nearest neighbour atom of Fe (F4) and Cd in pure CdTe (F5).

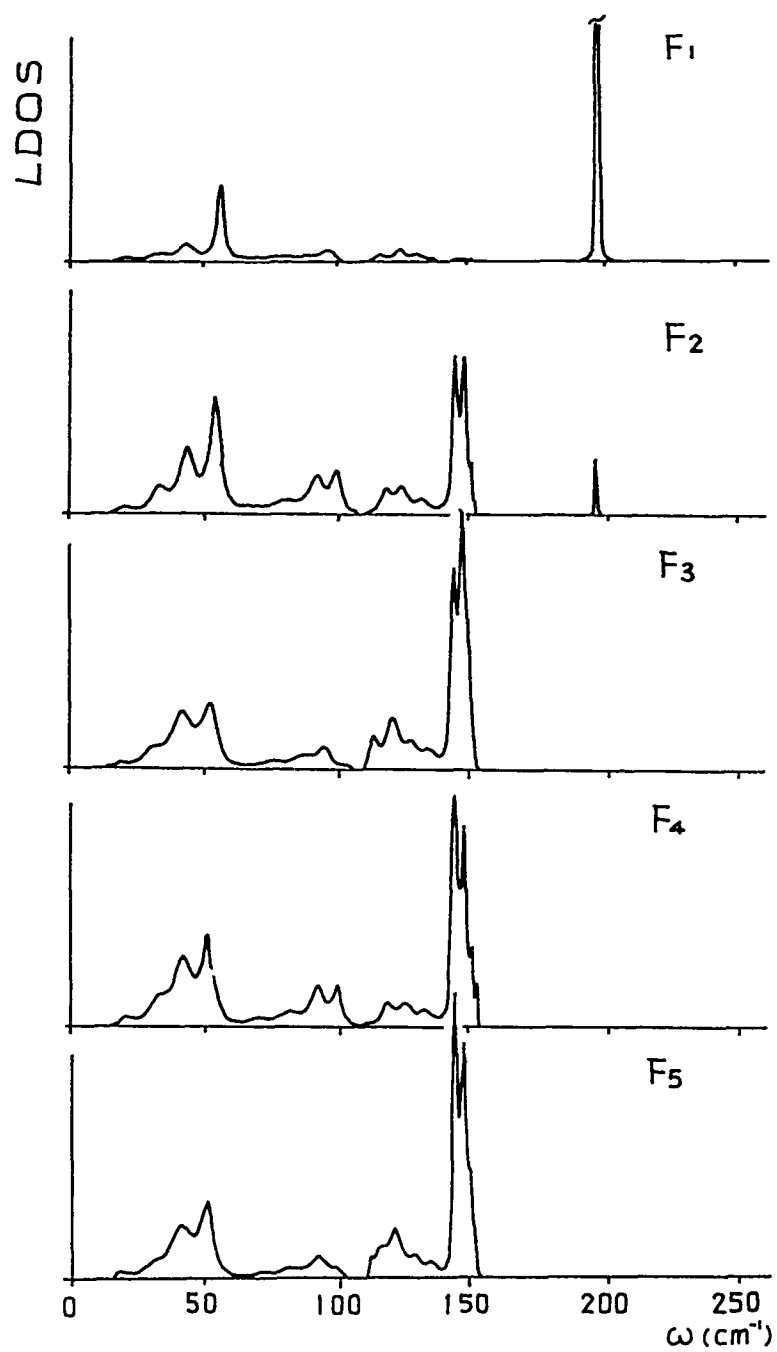


Fig. 2

## NOVEL ASPECTS OF FAR-INFRARED GAS LASERS

Fritz K. Kneubühl  
Infrared Physics Laboratory  
Institute of Quantum Electronics  
ETH (Swiss Federal Institute of Technology)  
CH-8093 Zurich, Switzerland

## ABSTRACT

A review is given on actual applications of far-infrared gas lasers in basic laser physics. These concern the various aspects of distributed feedback and deterministic chaos.

## INTRODUCTION

In recent years far-infrared gas lasers evolved as valuable tools for the experimental study of two different basic concepts in laser science, i.e. distributed and helical feedback on one hand as well as deterministic chaos on the other hand.

With respect to the experimental investigation of the mode properties of distributed and helical feedback laser systems and the comparison of the results with the theoretical predictions the optically pumped far-infrared lasers have proven to be superior to semiconductor and dye lasers mainly due to their narrow gain profile. Thus, it was possible to test the coupled-wave theory relevant to distributed feedback (DFB) with weak periodic modulation of the index of refraction or waveguide cross-section, to investigate the in-gap modes occurring in distributed feedback with phase matching achieved by gaps in the periodic laser structure, to realize helical feedback (HFB) with waveguide structures of the symmetries of the helix and the double helix, and finally, to verify quantitatively nonlinear gain saturation in distributed and helical feedback lasers.

In 1975 Haken proved that the theoretical model of deterministic chaos postulated by Lorenz in 1963 can also be applied to the nonlinear dynamics of lasers under specific conditions. In the meanwhile it was realized that specifically designed optically pumped far-infrared gas lasers exhibit the phenomena characteristic for deterministic chaos. These include the transition from the stationary oscillation through subharmonic instabilities to chaos as well as the intermittent route of Manneville-Pomeau. Therefore, the current research concentrates on the quantitative interpretation of instabilities and chaos in far-infrared gas lasers in view of the theory on deterministic chaos.

## DISTRIBUTED AND HELICAL FEEDBACK LASERS

In lasers the optical feedback is usually provided by the reflections on the two mirrors of the conventional laser resonators. The main handicap of these resonators with the optical feedback localized at the mirrors is the similarity of the losses of their fundamental longitudinal modes which are separated by  $c/2R$  in frequency.  $R$  indicates the length of the resonator and  $c$  the velocity of light. This handicap impedes the single-mode operation of lasers with a broad-band gain of the active medium, i.e. of dye, semiconductor and high-pressure gas lasers. This can be avoided by replacing the conventional optical resonators by axially periodic or helical laser structures. In these laser structures the optical feedback is provided by backward Bragg scattering from periodic or helical modulations of the waveguide, the refraction index and/or the gain of the laser medium. In this arrangement the optical feedback is distributed along the entire laser structure. Therefore, it is called distributed feedback (DFB) for axially periodic and helical feedback (HFB) for helical laser structures. The relevant feature of DFB and HFB is the high spectral selectivity inherent in the Bragg effect which permits easy selection among the fundamental longitudinal laser modes even for laser-active media with broad-band gain.

Distributed feedback (DFB) was accomplished first in a dye laser [1], later in a solid-state laser [2] and in a gas laser [3-5]. The DFB gas laser is an optically pumped far-infrared 496  $\mu\text{m}$   $\text{CH}_3\text{F}$  laser [6-8] with a periodic waveguide acting as optical feedback system.

The majority of calculations on DFB lasers are based on perturbation theory. It can be applied to lasers with weak axially periodic modulations of waveguide cross-section, refraction index or/and gain of the laser medium. The successful coupled-wave theory [9-11] is relevant for the far-infrared DFB gas lasers. Therefore, these have been applied to test this theory [4, 5, 12-16]. On the other hand, they are not suited for a study of DFB with strong axially periodic modulations [16-17].

DFB lasers with low gain and pure index modulation, e.g. DFB far-infrared gas lasers exhibit frequency gaps without modes. They correspond to the energy gaps of solids. However, it is possible to generate modes within these frequency gaps by phase



matching with the aid of a spatial gap in the continuous periodic laser structure. Also this phenomenon can be demonstrated theoretically by coupled-wave theory [10, 11, 15] and experimentally with far-infrared gas lasers [15]. The in-gap modes are of special interest in the design of semiconductor DFB lasers.

The concept of helical feedback (HFB) which is based on group theory [13, 19] was first verified on an optically pumped far-infrared gas laser equipped with a helical waveguide for optical feedback [13, 18, 19]. In the meanwhile it was noticed that HFB is also present in dye lasers with cholesteric liquid crystals serving as optical feedback [10, 11, 16, 20].

Only recently it was discovered that the power distributions of the modes near the frequency gaps of far-infrared DFB gas lasers manifest nonlinear gain saturation [21]. This opens new aspects in the study of DFB and HFB lasers.

#### DETERMINISTIC CHAOS

Instabilities in laser emission notably in the form of coherent pulsations have been observed almost since the first demonstration of laser action. The first laser operated in 1960 by Maiman [22] generated noisy spiked output even under condition of quasi steady excitation. Subsequent theoretical efforts towards understanding these phenomena remained on a modest level until Haken [23] demonstrated that the Lorenz model [24, 25] of deterministic chaos can also be applied to the nonlinear dynamics of lasers. In the meanwhile, a large variety of experiments on pulsating instabilities and chaos in lasers has been performed [26-29]. Optically pumped far-infrared lasers have proven to be predestinated for this kind of experiment. This was first recognized by Weiss et. al. [29-32]. For this purpose they applied  $81.5 \mu\text{m}$   $\text{NH}_3$  [30-31] and  $117 \mu\text{m}$   $\text{CH}_2\text{F}_2$  [32] lasers. Laser-pumped gas lasers are usually not properly described by the three Lorenz equations of a two-level laser derived by Haken [23]. The coherent coupling of the three levels of a laser-pumped gas laser includes nine equations. The conditions for the reduction of these nine equations to the three Lorenz equations have been formulated by Dupertuis et. al. [33]. This reduction is possible for optically pumped far-infrared lasers with some restrictions.

In summary, optically pumped far-infrared lasers are especially suited for the study of pulsating instabilities and chaos in lasers. In this context it should be mentioned that they permit to demonstrate the sequence of subharmonic instabilities to chaos in detail [31]. Other phenomena of deterministic chaos are under investigation.

#### CONCLUSION

Actually, the optically pumped far-infrared gas lasers developed in the seventies prove to be the predestinated tool for the study of two basic concepts of laser physics. This was not expected at the time of their discovery.

#### REFERENCES

- [1] H. Kogelnik, C.V. Shank: Appl. Phys. Lett. 18, 152 (1971)
- [2] N. Nakamura, A. Yariv, H.W. Yen: Appl. Phys. Lett. 22, 515 (1973)
- [3] E. Affolter, F.K. Kneubühl: Phys. Lett. 74A, 407 (1979)
- [4] E. Affolter, F.K. Kneubühl: IEEE J. of Quantum Electronics QE-17, 1115 (1981)
- [5] F.K. Kneubühl, E. Affolter: in "Infrared and Millimeter Waves", K.J. Button, ed. Academic Press, N.Y., Vol. 5, Ch. 6, 305 (1982)
- [6] T.Y. Chang, T.J. Bridges: Optics Comm. 1, 423 (1970)
- [7] T.A. De Temple: in "Infrared and Millimeter Waves", K.J. Button, ed., Academic Press, N.Y., Vol. 1, Ch. 3, 129 (1979)
- [8] T.A. De Temple and E.J. Danielewicz: in "Infrared and Millimeter Waves", K.J. Button, ed., Academic Press, N.Y., Vol. 7, Ch. 1, 1 (1983)
- [9] H. Kogelnik, C.V. Shank: J. Appl. Phys. 43, 2327 (1972)
- [10] F.K. Kneubühl: Revue Roumaine de Physique 33, 691 (1988)
- [11] F.K. Kneubühl, Cui Dafu: (in Chinese) Chinese J. of Infrared Research 7A, 241-251 (1988)
- [12] X. Zheng, S. Gnepf, H.P. Preiswerk, D. Wildmann, F.K. Kneubühl: Chinese J. of Infrared Research 3, 81 (1984), in Chinese
- [13] H.P. Preiswerk, M. Lubanski, F.K. Kneubühl: Applied Physics B33, 115-131 (1984)
- [14] F.K. Kneubühl: Optica Acta, special issue in commemoration of the 25th anniversary of the first laser, 32, 1055 (1985)

- [15] D. Wildmann, S. Gnepf, F.K. Kneubühl: Applied Physics, B42, 129-145 (1987)
- [16] F.K. Kneubühl, M.W. Sigrist: "Laser" (in German), Teubner, Stuttgart (1988)
- [17] S. Gnepf, F.K. Kneubühl: in "Infrared and Millimeter Waves", K.J. Button, ed., Academic Press, N.Y., Vol. 16, Ch. 2, 35 (1986)
- [18] H.P. Preiswerk, G. Küttel, F.K. Kneubühl: Physics Lett. 93A, 15 (1982)
- [19] H.P. Preiswerk, M. Lubanski, S. Gnepf, F.K. Kneubühl: IEEE J. of Quantum Electron., QE-19, 1452-1457 (1983)
- [20] F.K. Kneubühl: Infrared Physics, 23, 115-117 (1983)
- [21] J. Arnesson, Cui Dafu, S. Gnepf and F.K. Kneubühl: Proc. 4th Intern. Conf. on Infrared Physics (CIRP 4), Zurich, August 1988, 358-360
- [22] T.H. Maiman: Nature 187, 493 (1960)
- [23] H. Haken: Phys. Lett. 53A, 77 (1975)
- [24] E.N. Lorenz: J. Atmos. Sci. 20, 130 (1963)
- [25] C.T. Sparrow: The Lorenz Equations: Bifurcations, Chaos and Strange Attractors", Springer, Berlin (1982)
- [26] R.G. Harrison, D.J. Biswas: Progress in Quantum Electronics 10, 147 (1985)
- [27] R.G. Harrison, D.J. Biswas: Nature 321, 394 (1986)
- [28] D.J. Biswas, R.G. Harrison, C.O. Weiss, W. Klische, D. Dangoisse, P. Glorieux, N. Lawandy: in "Instability and Chaos in Quantum Optics", ed. R.G. Harrison, F.T. Arecchi, Vol. 34, 109 (1987)
- [29] C.O. Weiss: Proc. 4th Intern. Conference on Infrared Physics (CIRP 4), Zurich, August 1988, 208
- [30] C.O. Weiss, W. Klische: Opt. Comm. 51, 47 (1984)
- [31] C.O. Weiss, W. Klische, P.S. Ering, M. Cooper: Opt. Comm. 52, 405 (1985)
- [32] C.O. Weiss, W. Klische: Opt. Comm. 50, 413 (1984)
- [33] M.A. Dupertuis, R.R.E. Salomaa, M.R. Sigrist: Opt. Comm. 57, 410 (1986)

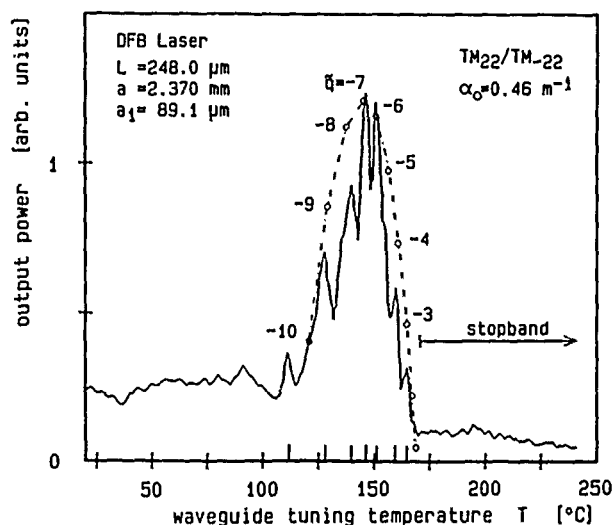


Figure:

Experimental demonstration of non-linear gain saturation in an optically pumped  $496 \mu\text{m}$   $\text{CH}_3\text{F}$  DFB laser (PhD thesis J. Arnesson, ETH, Zurich, 1988). Tuning is performed by thermal expansion of the periodic laser waveguide.

## THEORY OF OPTICALLY PUMPED FIR LASERS

Lin Yikun

Zhongshan University, P.R. China

## ABSTRACT

So far, the optically pumped FIR laser was a useful and cheap coherent source for FIR techniques. The drawbacks of this kind of laser source are: (1) Provides only discrete FIR discrete FIR spectral lines. (2) It lase with relatively low efficiency. (3) It occupies too large space as compared with the conventional electronic equipments. In this review, the theory of optically pumped FIR laser actions in the multi-level quantum system will be introduced as follows:

- 1) Density matrix equations of the laser system.
- 2) The solutions of the density matrix equations.
- 3) Tuning characteristics and gain response of Raman laser.
- 4) Solution of the density equations with  $I_s \ll I_p$ .
- 5) Calculation of output power density of OPFIRL.
- 6) Gain saturation effect.
- 7) Interactions between multiphoton processes.

- 8) Further study of AC Stark effect in OPFIRL.
- 9) Optimization of the operating parameter of OPFIRL.
- 10) The features of the two longitudinal modes pumped OPFIRL.

## REFERENCES:

1. Acta Optica Sinica, 2, 201 (1982)
2. Int. J. IR - MM Waves, 3, 553 (1982)
3. Ibid, 6, 1061 (1985)
4. Ibid, 6, 1071 (1982)
5. Ibid, 8, 673 (1987)
6. Acta Optica Sinica, 6, 688 (1986)
7. Acta Scientiarum Naturalium Universitatis Sun Yasei, No.3, p.9 (1985)
8. 4th Int. Conf. IR Phys. Digest 365 (1988)

# LINE SELECTION IN OFF-RESONANTLY PUMPED SYSTEMS

(Invited Keynote)

M.A. Dupertuis

Institut de Micro- et Optoélectronique, Ecole Polytechnique Fédérale de Lausanne,  
PHB Ecublens, CH-1015 Lausanne, Switzerland

**Abstract:** The problem of line competition in off-resonantly pumped systems is reviewed. The theoretical predictions are compared with recent experimental results in the FIR.

**Introduction:** Numerous lasers in the far-infrared (FIR) are optically-pumped. This is due to the fact that the small energy separation between the ground and excited energy level of the FIR transitions is typically smaller than  $kT$ , making electrical pumping difficult (selectivity larger than  $kT$ ), and because the lifetime of the rotational levels in molecules is short, making energy storage impossible [1]. Optical pumping, on the other hand, is very attractive because cheap, efficient and powerful sources exist (the  $CO_2$  laser) and provide an excellent selectivity and a high pumping rate. In addition pump tuning off resonance often permits to achieve tunable Raman emission inside the active medium. On the coarsest spectral scale different laser transitions may compete with each other in the medium (Fig.1 reproduced from [2]). On the next scale (when the cavity mode density is high enough) resonant line-center emission may compete against stimulated Raman-type emission. Finally, on the finest scale, several competing cavity eigenmodes can appear within each type of lines (especially in inhomogeneously broadened situations) (Fig.2). Line competition is an important issue when it is desirable to ensure tunability, to obtain high spectral purity radiation (or single-mode operation), or to have maximum efficiency when different lines couple in parallel in the energy diagram.

In the present study we will rigorously define the line-competition problems where parametric (Raman-like) processes compete against resonant (laser-like) processes and study the non linear interaction mechanisms between them. FIR lasers are privileged testbeds for this theory but it is also of relevance for Mid-IR lasers [3] and dimer lasers [4].

**Line competition:** The main peculiarities of the systems pumped by off-resonant coherent light are certainly coherence effects and coupled Doppler effects. Both arise from the fact that the active medium is at least a three-level system interacting with two classical fields. To illustrate our generalized concept of line competition let us consider the gain spectrum of such a system. In general three conditions are required to have two distinct gain peaks as in Fig.2, one at the Raman frequency, and the other at the line-center:

- (i) To create the Raman gain the system must be pumped off-resonantly,
- (ii) The pump should not be so intense as to induce excessive AC-Stark shifts. (If this were the case, the peaks would tend to occupy symmetric positions around line center and their nature would become mixed rendering the problem more complicated),
- (iii) The Doppler broadening should not mix up the peaks (on both transitions).

The line competition approach consist of studying the combined effects due to the modes under the Raman line onto the line center modes or vice versa. The interaction between modes within the two gain peaks will be neglected. Hence the competition situation is described by the effective two-mode model of Fig.2 b). The problem of mode competition under one of the peaks and its relation to laser instabilities is a subject of interest which has been studied elsewhere ([5-8] and [9-11]). For convenience we assume a single pass amplifier configuration. To some extent the results are qualitatively valid for the time development of the oscillation in a resonator structure which does not favor any particular oscillation type and in which the quasi steady state approximation applies.

**Predictions and experimental results:** Within the approximations detailed above we have been able to explain the dominance of Raman emission in most three level FIR lasers [12,1]. Three effects (a population effect, population pulsations, a coherence effect) participate in the creation of a very strong absorption at the FIR resonance frequency in the presence of a strong Raman mode. On Fig.3, time resolved experiments in  $D_2O$  [7] show that both the slightly AC-Stark shifted line center and Raman emission start to grow out of noise. As predicted we can see that as soon as the Raman mode comes into saturation, the line center mode is quickly reabsorbed and "noise quietening" is observed in this channel.

In more complicated situations where a refill transition becomes simultaneously active a four level model must be used and a simple explanation of the overall behaviour in terms of the three level behaviour can be given only in certain cases. Surprisingly the complex behaviour of the whole system can be interpreted as resulting from the complex interaction of simple effects [13]. In this case it is possible to disentangle unambiguously each effect from each other. Moreover only two possible asymptotic states are predicted to be possible within our approximations, and these states are unusual because they include a simultaneous oscillation at the Raman and line-center frequencies on the same transition. A review of the literature allowed us to show [14] that exactly this oscillation state had indeed been observed by De Martino, Frey and Pradère [15] in conditions compatible with our

theory. These results spurred a detailed study of a variety of other level configurations [14,16], as well as on the influence of a number of additional effects. However the complexity of the results lead to the formulation of intuitive guidelines [14,16] to the general line selection problem instead of rigorous prescriptions which we summarize below:

- 1) Raman emission is strongly favoured on all transitions coupled to the off-resonantly pumped ones,
- 2) Raman oscillation tends to suppress line-center oscillation on the same transition,
- 3) Raman oscillation may strongly assist line-center oscillation on another transition,
- 4) Cascade oscillation is generally expected to be resonant,
- 5) Interference effects are associated with closed paths within the system of active transitions. As a consequence, a phase equation has to be added to the set of evolution equations. In this case transverse may become extremely important since Raman and line-center fields can have different directions of propagation,
- 6) Closed multiphoton resonant paths are strongly favoured.

**Conclusions:** The study of line competition in off-resonantly pumped systems carried out in this paper is feasible only as long as the concept of a line is well defined. The requirements for this have been formulated. This approach is attractive because it allows one to study the start up of the oscillation as well as the development of the competition in the saturation regime. The final very highly saturated regime may not be always fully described (typically if Eq.(23) of [16] is not satisfied), however it is believed that the final oscillation mode is often determined by the early phase of the competition. Moreover, as emphasized, in this case the concept of a "line" is not anymore well defined. A few experimental results have been carried out in such conditions that some of the original predictions of the theory could be tested and confirmed. Many experimental and theoretical situations remain, however, out of reach of a detailed study. Recent measurements have been recently completed and are still under way [7,17,18] and we hope that the new insights in the complex spectral behaviour of FIR lasers offered by the study of line competition effects will prove useful.

**Acknowledgements:** The author express his appreciation to Dr.M.Siegrist, his PhD thesis advisor, for his counsels and encouragements during this work, and to Dr.R.Salomaa for his collaboration.

- [1] B.G.Danly, S.G.Evangelides, R.J.Temkin, B.Lax, Infrared and Millimeter waves, Vol.12, Ed. K.J.Button, New York: Academic 1984, pp.195-278
- [2] G.Dodel, N.G.Douglas, IEEE J. Quant. Electron. QE-18(8), pp.1294-1301 (1982)
- [3] B.Welleghausen, IEEE J. Quant. Electron. QE-15, p.1108 (1979)
- [4] M.S.Malcuit, D.J.Gauthier, R.W.Boyd, Phys. Rev. Lett. 55, p.1086 (1985)
- [5] M.A.Dupertuis, R.R.E.Salomaa, M.R.Siegrist, IEEE J. Quant. Electron. QE-23(7), pp.1217-1232 (1987)
- [6] R.G.Harrison, D.J.Biswas, Phys. Rev. Lett. 55(1), pp.63-66 (1985)
- [7] R.Behn, M.A.Dupertuis, P.Krug, I.Kjelberg, A.Salito, M.R.Siegrist, IEEE J. Quant. Electron. QE-24(3), pp.549-557 (1988)
- [8] C.O.Weiss, J.Brock, Phys. Rev. Lett. 57(22), pp.2804-2806 (1986)
- [9] M.A.Dupertuis, M.R.Siegrist, R.R.E.Salomaa, Opt. Commun. 57(6), pp.410-414 (1986)
- [10] J.Pujol, J.Laguarta, R.Vilaseca, R.Corbala, J.Opt.Soc. Am. B5(5), pp.1004-1010 (1988)
- [11] N.M.Lawandy, J.C.Ryan, Opt. Commun. 63(1), pp.53-56 (1987)
- [12] M.A.Dupertuis, M.R.Siegrist, R.R.E.Salomaa, Phys. Rev. A30(5), pp.2824-2826 (1984)
- [13] M.A.Dupertuis, R.R.E.Salomaa, M.R.Siegrist, Opt. Commun. 54(1), pp.27-32 (1985)
- [14] M.A.Dupertuis, R.R.E.Salomaa, M.R.Siegrist, Phys. Rev. A36(2), pp.669-682 (1987)
- [15] A.DeMartino, R.Frey, F.Pradère, Opt. Commun. 27(2), pp.262-266 (1978)
- [16] M.A.Dupertuis, R.R.E.Salomaa, J. Opt. Soc. Am. B5(1), pp.130-137 (1988)
- [17] J.R.Izatt, B.K.Deka, W.Zhu, IEEE J. Quant. Electron. QE-23(1), pp.117-122 (1987)
- [18] S.G.Evangelides, L.Carson, B.G.Danly, R.J.Temkin, IEEE J. Quantum Electron. QE-24(1), pp.99-104 (1988)

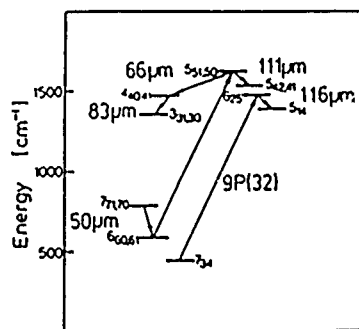


Fig.1

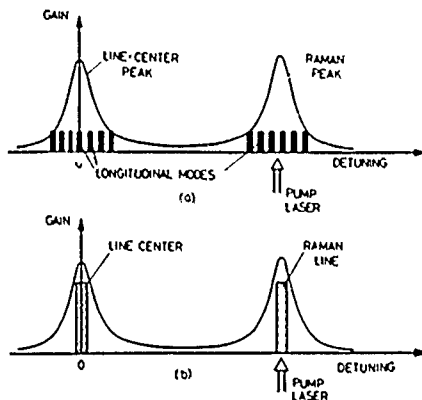


Fig.2

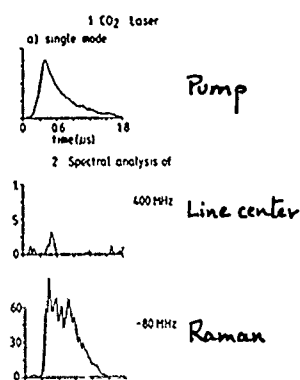


Fig.3

## THE INVERSE SMITH-PURCELL EFFECT AT SUBMILLIMETER WAVELENGTHS

J. Bae, K. Furuya, H. Shirai, T. Nishida, T. Nozokido, and K. Mizuno

Research Institute of Electrical Communication  
Tohoku University, Sendai 980, Japan

## ABSTRACT

The inverse Smith-Purcell (ISP) effect is a candidate for laser-driven linacs with an accelerating gradient of several GeV/m. It uses a metallic grating as an interaction circuit. For the first time, we observed the ISP effect using a submillimeter wave (SMM) laser as the driving source in 1987. Since then, we have improved the signal-to-noise ratio in the electron energy measurements to verify the theoretical predictions in more detail.

In this paper, we describe our experimental apparatus and newly obtained experimental results of this effect. These agreed with the theory.

## THE INVERSE SMITH-PURCELL EFFECT

In 1953 Smith and Purcell [1] demonstrated the light is emitted when a high voltage electron beam moves parallel and close to a metallic diffraction grating. The light is emitted in the plane perpendicular to the rulings. The dispersion relationship is given by a synchronous condition between the electrons and the wave on the grating. In the inverse effect [2-3], the same relationship holds, and there is an extended interaction between the electrons and an incident light beam (Fig. 1).

## EXPERIMENT

Fig. 2 shows our experimental setup. The submillimeter-wave  $\text{CH}_3\text{F}$  laser produces single mode,  $496\mu\text{m}$  radiation pulses up to 80 W peak power and 9 kHz repetition rate [4]. The laser is pumped by newly developed current-pulsed mechanical shutter type Q-switched (EMQ-switched)  $\text{CO}_2$  laser [5]. The grating with a rectangular groove shape was designed and fabricated on a milling machine [6]. The grating has a pitch of  $246\mu\text{m}$ , a groove-width of  $40\mu\text{m}$ , and a groove-depth of  $104\mu\text{m}$ . The retarding field electron energy analyzer has a resolving power of 0.8 eV FWHM at an electron-energy of 80 keV and a current of 3 nA, when the intrinsic thermal energy spread of the electron beam is taken into account.

The SMM laser beam fell on the grating at the incidence angle  $\theta = \pi/2$  (Fig. 1). The pulsed laser beam modulates the energy of the electron beam, so that the electron current through the analyzer changes during the pulse. The change in the anode current is measured by an amplifier and box-car averager that is triggered by the  $\text{CO}_2$  laser pulses.

The change of the width of the electron-energy spectrum  $\Delta W$  is shown in Fig. 3 as a function of the

initial electron accelerating voltage. The largest spread is produced at 80 keV. We can deduce the effective interaction length by a curve fit to the data, and this indicates that the interaction length is 3 mm. This is shown by the fitted curve in Fig. 3. For comparison, theory [7] predicts values of 78 kV and 2.4 mm for our grating dimensions. Fig. 4 shows  $\Delta W$  as a function of the peak power of the laser. It is seen that a laser power of 30 W produces a 100-eV spread in the electron energy. The dotted line has a slope of 0.5, indicating that the energy spread is proportional to the square root of the peak power of the laser, as predicted by theory [7].

## ACKNOWLEDGMENTS

This work was partially supported by a Grant-in-Aid for Scientific Research from the Ministry of Education, Science and Culture.

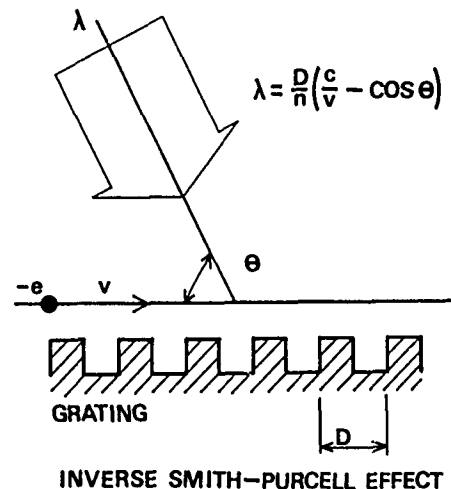


Fig. 1 The inverse Smith-Purcell effect. When a metallic grating is illuminated by laser light with wavelength  $\lambda$  at an incident angle  $\theta$ , an infinite number of evanescent space harmonics are induced on the grating surface. If the phase velocity of the  $n$ th order space harmonic is equal to the velocity of electron which moves parallel and close to the grating surface, an effective interaction between the electron and the  $n$ th harmonic can be obtained. The synchronous condition is represented in the figure, where  $D$  is the pitch of the grating ruling and  $c$  is the velocity of light.

## REFERENCES

- [1] S. J. Smith and E. M. Purcell, "Visible Light from Localized Surface Charges Moving across a Grating," *Phy. Rev.*, vol. 92, pp. 1069, 1953.
- [2] K. Mizuno, K. Ono, and O. Shimoe, "Interaction between coherent light waves and free electrons with a reflection grating," *Nature*, vol. 253, pp. 184-185, 1975.
- [3] K. Mizuno, J. Bae, T. Nozokido, and K. Furuya, "Experimental evidence of the inverse Smith-Purcell effect," *Nature*, vol. 328, pp. 45-47, 1987.
- [4] H. Shirai, J. Bae, T. Nishida, and K. Mizuno, "SUBMILLIMETER-WAVE LASER PUMPED BY AN EMQ-SWITCHED CO<sub>2</sub> LASER," this conference digest.
- [5] J. Bae, K. Furuya, H. Shirai, T. Nozokido, and K. Mizuno, "Mechanical Chopper Type EQ-Switched CO<sub>2</sub> Laser as a Pumping Source for a Submillimeter Wave Laser," Paper of Tech. Group, IECE, OQE86-50, Japan, 1986 [in Japanese].
- [6] J. Bae, K. Furuya, H. Shirai, T. Nozokido, and K. Mizuno, "FIRST OBSERVATION OF THE INVERSE SMITH-PURCELL EFFECT," Tech. Digest of int'l Electron Devices meeting, IEDM 87-307, 1987.
- [7] J. Bae, K. Furuya, H. Shirai, T. Nozokido, and K. Mizuno, "The Inverse Smith-Purcell Effect in the Submillimeter Wave Region," *Jpn. J. Appl. Phys.*, vol. 27, pp. 408-412, 1988.

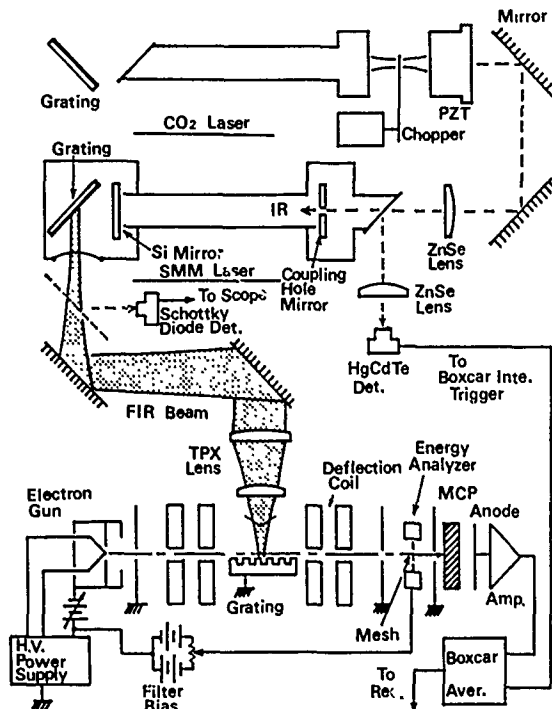


Fig. 2 Experimental setup to demonstrate the ISP effect.

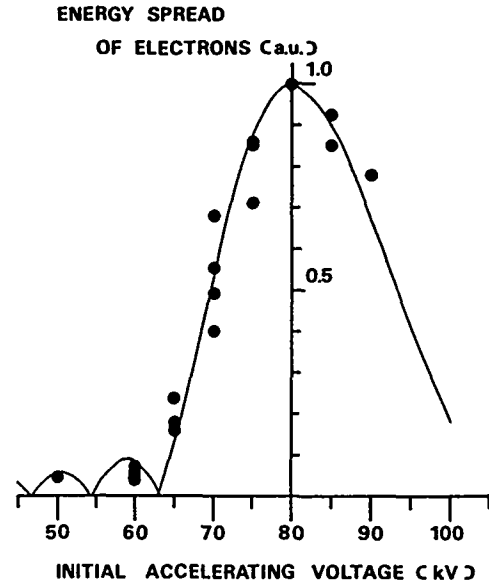


Fig. 3 The change of electron-energy spread vs. the initial accelerating voltage of electron. The points represent the experimental values normalized by the maximum values. The solid line is theoretically predicted change of  $\Delta W$  for an interaction length of 3 mm.

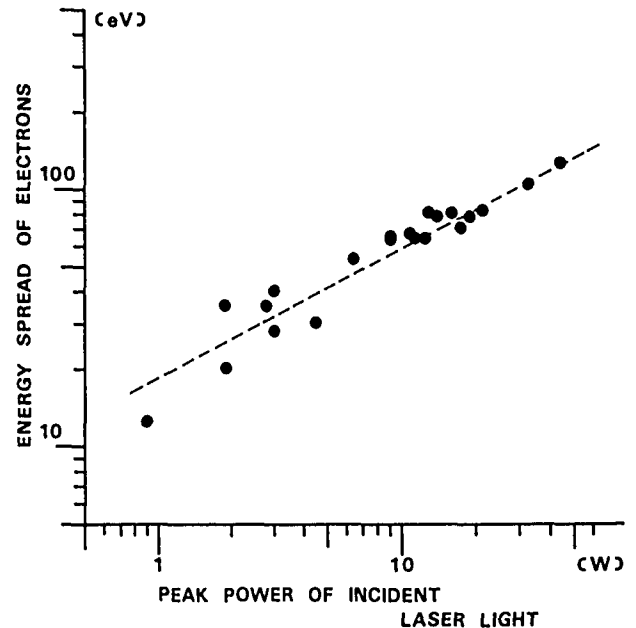


Fig. 4 The energy spread of electrons as a function of the peak power of the incident laser light. The dotted line has a slope of 0.5, indicating that the energy spread is proportional to the square root the laser power.

COPPER AND MOLYBDENUM MIRRORS FOR HIGH POWER TEA CO<sub>2</sub> LASER

Y. Tsunawaki\*, K. Yoshida\*\*, K. Ohta\*\*\*, S. Aramaki\*\*\*, H. Okamoto\*\*\*, M. Yamanaka\*\* and S. Nakai\*\*

\*Dept. of Electrical Engineering & Electronics, Osaka Industrial University, Daito, Osaka 574, Japan; \*\*Institute of Laser Engineering, Osaka University, Suita, Osaka 565, Japan; \*\*\*Central Research Laboratory, Nippon Mining Co., LTD. Toda, Saitama 335, Japan.

## Abstract

Various kinds of copper (Cu) and molybdenum (Mo) mirror were studied on the damage induced by a TEA CO<sub>2</sub> laser. Cu mirror had a damage threshold<sup>2</sup> to 2.4 times higher than that of a Mo mirror. As suggested in the previous work<sup>1</sup>, a single-crystalline mirror was stronger than a polycrystalline one while TEA CO<sub>2</sub> laser was irradiated onto the mirror surface, because most of the damages originated at the grain boundaries of the poly-crystalline surface.

## Introduction

Metallic mirrors are interesting for high power TEA CO<sub>2</sub> laser system<sup>2</sup> because of the higher laser damage threshold. In the previous work<sup>1</sup>, the laser induced damage of electron beam melting Mo mirror and powder metallurgy Mo mirror were investigated for TEA CO<sub>2</sub> laser, and then it was found that the difference between these mirrors at the laser damage threshold was due to the fine surface without voids and the small amount of impurities. In this study, poly- and single-crystalline Cu and Mo mirrors with fine surface, which contain different amounts of impurities, were studied on the damage threshold for pulsed TEA CO<sub>2</sub> laser. Moreover, a Cu mirror coated with ZnSe instead of Au was also tried to be irradiated with high power CO<sub>2</sub> laser.

## Experimental

The surfaces of Cu and Mo mirrors were ground by a diamond turning machine and by an oscillation type machine, respectively. The experimental method of laser induced damage was the same as previous work<sup>1</sup>. The 9R(22) TEA CO<sub>2</sub> laser with pulse length of 50 ns was focused onto a mirror surface by a ZnSe lens with 10 cm focal length. The incident laser energy was varied by changing the distance between the lens and the mirror.

The laser induced damages of three kinds of Mo mirror and five kinds of Cu mirror were studied for TEA CO<sub>2</sub> laser. Polycrystalline Mo mirrors were prepared from low carbon content (LC) Mo and electron beam melting (EB) Mo, and a single-crystalline (SC) Mo mirror was obtained from conventional one. On the Cu mirror, oxygen free (OF) Cu and high purity (HP) Cu were used for polycrystalline mirrors. The

latter one was also used for a single-crystalline (OFS) Cu mirror. In order to clarify the effect of residual strain on a mirror surface due to the turning, thermal treated oxygen free (OFT) Cu mirror was compared with usual OF Cu mirror.

## Results and Discussion

It is known that the surface condition of a mirror is important for laser induced damage threshold. The surface roughness of all mirrors was within 100 Å rms by Talystep measurement. The flatness of a whole mirror surface was 0.3 µm. The reflectivity of Mo and Cu mirrors was around 98.3 and 99.2 % at 9.26 µm, respectively. Singlecrystalline mirrors had a reflectivity a little bit larger than poly-crystalline one.

When the laser energy density was high enough, one shot irradiation of the laser onto any kind of mirror homogeneously melted the surface. A poly-crystalline mirror had cracks along the grain boundaries but a single-crystalline mirror only melted without any crack. Tables 1 and 2 show the damage threshold for some kinds of Mo and Cu mirrors under one shot irradiation of TEA CO<sub>2</sub> laser, respectively. These results (2nd column) are in agreement with calculated ones by theory<sup>3</sup> (3rd col.). Cu mirror has a threshold about twice larger than Mo mirror. The tendency is seen that the damage threshold becomes higher as the impurity content in a mirror is lower and the surface is single- rather than polycrystalline state. Although ZnSe coated (ZS) Cu mirror had a reflectivity almost same as Au coated mirror, the damage threshold was not so high due to the peeling of ZnSe layer. If the coating method is improved, we will be able to expect stronger and more practical mirror coated with ZnSe.

To study the damage by multi shots of laser radiation, the focused TEA CO<sub>2</sub> laser beam was irradiated with 0.5 pps.<sup>2</sup> At a certain number of shots, depending on the incident energy density, a plasma was produced on the mirror surface. The number of shots, at which the plasma was produced on the surface of Mo mirror and the reflectivity abruptly decreased, is plotted in Fig.1. It is seen that SC Mo mirror has the longest life time in three kinds of Mo mirrors as expected in our previous work<sup>1</sup>. The micrograph of damaged surface of SC Mo mirror and LC Mo mirror are shown in Figs.2 and 3, respectively. It is seen that the damage is waved on the SC Mo mirror. On the



other hand, in the LC Mo mirror the neighbour portion of grain boundaries is pushed up and the center of them has pit. Furthermore, impurities in the grain boundaries seem to be spouted out as a plasma. These phenomena would be caused by repeating of thermal expansion and shrinkage of the grains at each shot of CO<sub>2</sub> laser. And then the thermal strain would be trapped at the grain boundaries in LC Mo mirror and at the irradiated portion in SC Mo mirror without any grain, respectively. Some similar results were obtained on Cu mirrors.

In conclusion, at one shot irradiation of TEA CO<sub>2</sub> laser the damage threshold would have weak tendency of becoming higher with decreasing of impurity content in a mirror. On the other hand, at multi shots of CO<sub>2</sub> laser radiation the life time of a mirror would strongly depend on the amount of impurities in a mirror surface and also depend on its crystalline state.

#### References

- 1) Y. Ichikawa et al., Appl. Opt. 26(1987) 3671.
- 2) Y. Ichikawa et al., Infrared Phys. 27 (1987) 317.
- 3) A. I. Barchukov et al., Sov. Phys. JETP. 39 (1974) 469.

Table 1 Surface damage threshold vs 9.26- $\mu$ m R(22) TEA CO<sub>2</sub> laser beam (50ns) of Mo mirrors.

Mo mirror	threshold (J/cm <sup>2</sup> )	
	experimental	calculated
LC Mo	45.7 - 54.4	55.8
EB Mo	46.7 - 57.4	59.0
SC Mo	52.8 - 61.7	62.7

Table 2 Surface Damage threshold vs 9.26- $\mu$ m R(22) TEA CO<sub>2</sub> laser beam (50 ns) of Cu mirrors.

Cu mirror	threshold (J/cm <sup>2</sup> )	
	experimental	calculated
OF Cu	76.2 - 112	121
OFT Cu	115	-
HP Cu	107 - 120	129
HPS Cu	115 - 121	138
ZS Cu	53.5 - 62.9	-

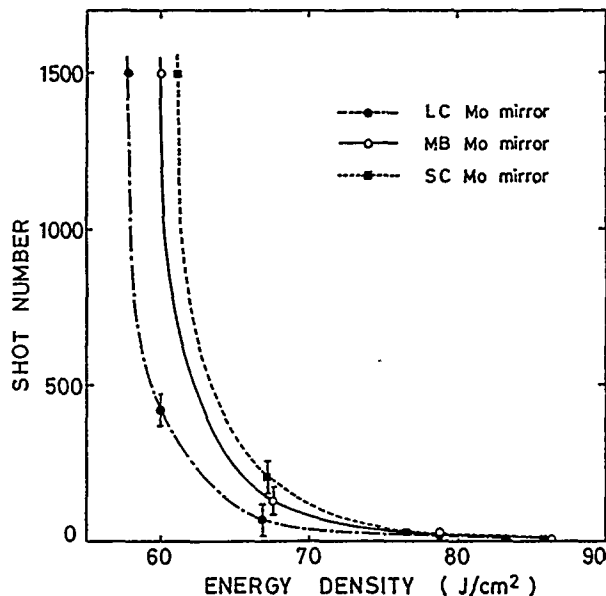


Fig.1 Shot number N at which the reflectivity abruptly changed as a function of illumination energy density for LC, EB, SC Mo mirrors.

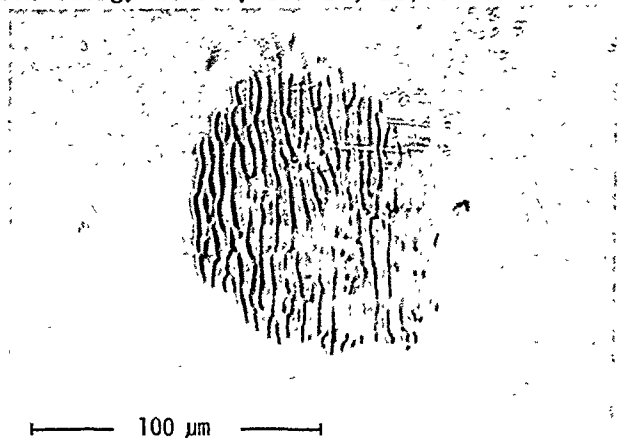


Fig.2 Damaged microstructure of the SC Mo mirror surface after the repetitive irradiation of 25 shots vs the energy density of 75.8 J/cm<sup>2</sup>.

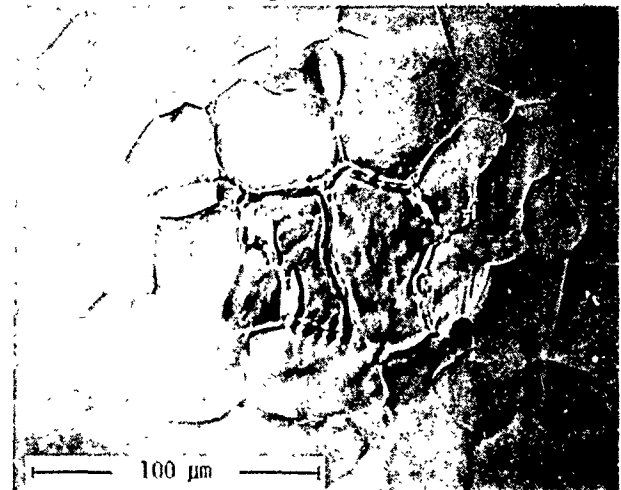


Fig.3 Damaged microstructure of the LC Mo mirror surface after the repetitive irradiation of 43 shots vs the energy density of 68.3 J/cm<sup>2</sup>.

MICROWAVE AND MILLIMETER-WAVE SPECTRA OF  $^{13}\text{CD}_3\text{OH}$ 

K.V.L.N. Sastry, I. Mukhopadhyay, R.M. Lees, J. VanderLinde and D. Donovan  
 Department of Physics, University of New Brunswick  
 Fredericton, N.B., Canada E3B 5A3

## ABSTRACT

The microwave absorption spectrum of  $^{13}\text{CD}_3\text{OH}$  has been investigated in the frequency region 18-80 GHz. The a-type R-branch transitions have been measured for J=1-0 and J=2-1 for the lowest three torsional states. Asymmetry splittings were observed for the K=1, A transitions. In addition, frequencies have been measured for a substantial number of b-type transitions, including the K=1-0 E1 and K=3-2 A Q branches. The frequencies have been fitted to a semi-empirical torsion-rotation model, and a-type and b-type parameters are reported. Stark effect measurements were made for the J=1-0 A and E transitions in the three lowest torsional states, and J=3-2 E1 in the ground torsional state.

## INTRODUCTION

Methanol, because of the coincidence between its C-O stretch band and the  $\text{CO}_2$  laser bands, is an excellent source for FIR laser lines. Recently, Inguscio et al. (1) reported strong laser emission line at 127  $\mu\text{m}$  for  $^{13}\text{CD}_3\text{OH}$  when optically pumped with the 10P(8) CO laser line. This observation motivated the present investigation of the microwave spectrum of this molecule. This study, in addition to contributing to the fundamental understanding of the torsion-rotation interactions in methanol, will be helpful in the identification of FIR emission lines of this species. Furthermore, the accurate measurement of the dipole moments will be useful in the understanding of relative intensities and Stark splittings of the FIR lines.

SPECTRUM OF  $^{13}\text{CD}_3\text{OH}$ 

The microwave spectrum of  $^{13}\text{CD}_3\text{OH}$  was observed on a standard Stark modulation spectrometer (2) employing a 6-ft K-band absorption cell, phase-stabilized microwave sources, and signal averaging. Frequency measurements were made with a Hewlett-Packard 5340A frequency counter, referenced to an EFROTOM 5-MHz rubidium frequency standard. A methanol sample with 99%  $^{13}\text{C}$  and 98% D was obtained from MSD Isotopes. All measurements were made at room temperature, with pressures varying from 10 to 100 mTorr as appropriate to optimize frequency accuracy. The estimated accuracy of these line measurements is  $\pm 100$  KHz.

The Stark effect measurements were made using a parallel plate Stark cell (3). For these

measurements, low pressures ranging from 5 to 15 mTorr were used to obtain narrow lines of approximately 150 KHz FWHM. With the parallel plate cell, Stark components did not broaden significantly up to a maximum shift of 30 MHz, and we were able to measure the Stark shifted frequencies to accuracies of  $\pm 20$  KHz or better.

The a-type R-branch transitions were measured for J=1-0 and J=2-1 for the lowest three torsional states. Also several b-type Q branches series were assigned, including the K=1-0 E1, K=1-2 E1 and K=3-2 A series. The Q branch origins for these and the Q-branch expansion coefficients for the K=3-2 A series are given in Table 1. The frequencies were then fitted to a semi-empirical torsion-rotation model (4). The molecular parameters obtained from the least squares fit are given in Table 2, in which the parameters shown in parentheses were fixed at their estimated values. In general, the parameters in Table 2 are in excellent agreement with the values calculated by I. Mukhopadhyay et al. (5). Asymmetry splitting parameters were determined also for A levels, and are given in Table 3.

The transitions in the Stark effect study include J=1-0 A-E pairs and J=3-2 E1 for the ground torsional state, and J=1-0 A-E pairs for the V=1 and 2 torsional states. For each transition, first and second order Stark coefficients were determined by least squares, and are given in Table 4. Analysis of the results to determine accurate dipole moment components is in progress.

## REFERENCES

- (1) M. Inguscio, K.M. Evenson, F.R. Peterson, F. Strumia, and E. Vasconcellos, *Int. J. IR and MM Waves* 5, 1289-1296 (1984)
- (2) R.M. Lees and M.A. Mohammadi, *Canad. J. Phys.* 58, 1640-1648 (1980)
- (3) K.V.L.N. Sastry, R.M. Lees and J. VanderLinde, *J. Mol. Spectrosc.* 88, 228-230 (1981)
- (4) R.M. Lees and J.G. Baker, *J. Chem. Phys.* 48, 5299-5318 (1968)
- (5) I. Mukhopadhyay, R.M. Lees and W. Lewis-Bevan, *Int. J. IR and MM Waves* 9, 545-553 (1988)

TABLE 1

Q-Branch Origins (MHz)					
TS	K'	K''	obs.	Assy. Shift	Corrected
E1	1	0	79703.500	0.833	79704.333
E1	1	2	75896.57	5.165	75901.74
A	3	2	19052.782	33.073	19085.855
K=3-2 Q-Branch Expansion					
$Q(J) = v_0 + aJ(J+1) + BJ^2(J+1)^2 + CJ^3(J+1)^3$					
$v_0 = 19052.782$ $a = 2.84067$					
$b = 0.036432$ $c = 4.25539 \times 10^{-7}$					

TABLE 2

<sup>13</sup> CD <sub>3</sub> OH Molecular Parameters	
a-Type	b-Type
$(B+C)/2 = 19270.28(7)$	$I_{a_1} = (0.75526)$
$F_v = -54.09(8)$	$I_{a_2} = 6.39073$
$G_v = -2.270(7)$	$V_3 = 369.67$
$L_v = 0.31(2)$	$V_6 = (-2.27)$
$D_J = 0.027(6)$	$D_K = (0.2998)$
$D_{JK} = 0.20(3)$	$k_1 = (0.05996)$
$B-C = 556.35$	$k_2 = (-18.947)$
$D_{ab} = -89.34$	$k_3 = (-90.747)$
$I_b = 25.8525$	$k_4 = (-281.98)$
$I_c = 26.6092$	$k_5 = (288.16)$
$I_{ab} = -0.1182$	$k_6 = (243.91)$
$\delta_v = 496.79$	$k_7 = (0.0)$

TABLE 3

<sup>13</sup> CD <sub>3</sub> OH Asymmetry Splitting Parameters			
n	K	S(MHz)	T(MHz)
0	1	248.397	
0	2	.053498	$1.4993 \times 10^{-6}$
0	3	$3.644 \times 10^{-5}$	$4.662 \times 10^{-8}$
1	1	22.351	
2	1	59.153	

TABLE 4

Stark Coefficients				
n	$J'_{K'} \leftarrow J_K$	TS	Observed Frequency (MHz)	$A \cdot 10^{-5} \text{MHz}/(V/\text{cm})^2$
0	$1_0 \leftarrow 0_0$	A	38485.298	$4.4158 \pm .0030$
0	$1_0 \leftarrow 0_0$	E	38488.523	$4.3969 \pm .0027$
0	$2_1 \leftarrow 3_0$	E <sub>1</sub>	35399.951	$12.366 \pm .0091^*$
1	$1_0 \leftarrow 0_0$	A	38403.600	$4.1210 \pm .0029$
1	$1_0 \leftarrow 0_0$	E	38392.746	$5.0073 \pm .0030$

$\Delta v = AE^2$ . Indicated errors correspond to a 90% confidence interval approximately 4 standard deviations. \*The splitting of this state is fitted by  $\Delta v = CME + (A+BM^2)E^2$  with B and C found to be  $B = (1.657 \pm .195) \times 10^{-5} \text{ MHz}/(V/\text{cm})^2$  and  $C = .26867 \pm (9 \times 10^{-5}) \text{ MHz}/(V/\text{cm})$ .

## A BROADBAND GYRO-TWTA EXPERIMENT\*

S. Y. Park<sup>+</sup>, R. H. Kyser<sup>++</sup>, C. M. Armstrong, A. K. Ganguly and R. K. Parker

Naval Research Laboratory  
Code 6840  
Washington, DC 20375

### ABSTRACT

A tapered reflection-type gyrotron amplifier (33 kV, 1.2 A) has been designed and built. The amplifier incorporates precise axial tapering of both the magnetic field and the interaction circuit for stable broadband operation (27-34 GHz). Cold test results show that the tube presents an excellent RF match over the entire operating band. This device will be used to explore the performance characteristics of low voltage operation.

### INTRODUCTION

The Electronics Science & Technology Division of the Naval Research Laboratory is actively investigating the potential of gyrotron TWT amplifiers for high power broadband mm-wave applications. Since the gyrotron amplifier does not require a slow wave interaction structure its power handling capability at mm-wave frequencies is greatly enhanced over its conventional slow wave counterpart. The intrinsic bandwidth of the gyrotron amplifier however is small and must be broadened to be attractive for many applications. The approach taken in this program is to taper both the interaction circuit and the magnetic field profile to maintain the resonance interaction over a wide frequency range.<sup>(1)</sup> For moderate voltage operation (30 kV) the cyclotron resonance interaction occurs very near the local cutoff point of the circuit where the interaction impedance is strong and relatively insensitive to beam velocity spread. The main disadvantage of operating near cutoff however is the onset of spurious oscillations due to the absolute instability. The key issue therefore facing the successful development of efficient low voltage fast wave gyrotron amplifiers is amplifier stability.

The approach taken in this study employs careful control of the circuit, magnetic field and beam parameters for stable low voltage operation. For broadband low voltage operation in the fundamental waveguide mode TE<sub>10</sub> and at the fundamental cyclotron frequency the cyclotron beam line is extremely close to cutoff over the entire operating frequency band. Small imperfections in the circuit taper and/or the magnetic field profile therefore can result in the onset of oscillations near cutoff. Similarly the interaction circuit must present an excellent RF match across the band to avoid cavity mode oscillations. A previous experiment conducted with a tapered circuit having a constant aspect ratio exhibited a large return loss at the high frequency end of the band. This anomalously high return loss was attributed to mode coupling between the TE<sub>10</sub> and TE<sub>01</sub> modes. In the tapered guide the TE<sub>10</sub> and TE<sub>01</sub> modes are no longer perfectly orthogonal and mode coupling and subsequent trapping of the unwanted TE<sub>01</sub> mode in the output circuit/transition region can occur. This problem has been eliminated in the present experiment by employing a interaction circuit which only supports the

TE<sub>10</sub> mode over the operating frequency band.

Stable amplifier operation near cutoff requires careful balancing of the magnetic field detuning parameter and the electron beam alpha, i.e. the perpendicular to axial velocity ratio. A previous gyro-twt study<sup>(2)</sup> demonstrated over 20 dB stable small signal gain using an electron beam with a relatively low alpha of around 0.5. For an alpha this small, however, the efficiency is expected to be only a few percent. The purpose of this study is to optimize the system parameters to maximize the efficiency. The extensive experimental database on the electron beam alpha values developed in a previous gyro-BWO<sup>(3)</sup> experiment will be of considerable assistance in this task.

### EXPERIMENTAL SETUP

The schematic of the experimental device is shown in Fig. 1. A MIG-type electron gun, operating at a relatively low voltage (nominal voltage 33 kV and current 1.2 A) is used to produce a small annular gyrating beam of alpha value ( $v_{\perp}/v_{\parallel}$ ) 1.5 and axial velocity spread ( $\Delta v_{\parallel}/v_{\parallel}$ ) 5 %. A specially designed lossy section consisting of interspaced Ceralloy and SS-304 discs is provided to suppress oscillations in the beam tunnel. A sapphire window is located in the back of the gun to detect the presence of oscillations in the gun or beam tunnel regions.

The interaction circuit is a simple rectangular waveguide whose broad wall is linearly tapered from 240"x.140" to .150"x.140" over a length of 20.5". The cutoff frequency of the TE<sub>10</sub>-mode thus varies continuously from 24.6 GHz to 39.4 GHz. The height of the circuit is held constant so that the circuit only supports the TE<sub>10</sub> mode over the 27-37 GHz operating band. The degree of the tapering is made much larger than the previous tube to improve the stability. A 4" long tapered transition section connects the interaction circuit to standard Ka-band output waveguide. Both the circuit and the transition sections are made of two pieces joined together along the center line of the E-plane. Each halves were machined out of solid OFHC copper rods with an accuracy within .0005" over the entire length. A thin mica sheet (.0008" thick) is used for the RF output window. The return loss characteristics of the completely assembled tube is shown in Fig. 1. There is no evidence of any trapped mode and the ~2 dB return loss is comparable to that obtained using a similar length section of standard Ka band waveguide.

As shown in Fig. 2 the amplifier is a single port reflection-type device. A high power isolator serves to protect the 1-20W drive chain from the amplifier output signal. Power and frequency measurements are made using directional couplers and calibrated Ka-band components. The magnetic field is provided by a superconducting magnet consisting of 14 individually

controllable magnet coils. A synthesizer code is used to determine the coil currents required for the desired magnetic field profile. The magnetic field profile is measured to an accuracy of 0.1%.

### EXPERIMENT

The tube is currently being prepared for installation in the experimental test stand. The initial studies will be used to map out the regimes of stable operation of the device. The dependence of the start oscillation current on electron beam alpha and on the magnetic field detuning parameter will be detailed. The stability map will then be used to optimize the small signal gain of the amplifier at full beam current (1.2A) operation. Large signal characterization of the amplifier and subsequent device optimization will follow.

### DISCUSSION

This experiment is designed to evaluate the potential of the tapered gyrotron amplifier approach for producing broadband high power mm-wave radiation.

The fundamental obstacle facing efficient low voltage fast wave operation remains amplifier stability. The present experiment has been designed to explore the basic stability limits imposed by the absolute instability near cutoff.

### REFERENCES

- 1) M. A. Moiseev, *Izv. Vyssh. Uchebn. Zaved.m Radiofiz.*, 20, No. 8, 1218 (1977); L. R. Barnett, Y. Y. Lau, K. R. Chu and V. L. Granatstein, *IEEE Trans. Electron Devices*, ED-28, 872 (1981)
- 2) S. Y. Park, R. H. Kyser, C. M. Armstrong, A. K. Ganguly, S. Ahn and R. K. Parker, 1986 Microwave Power Tube Conference, Monterey, CA
- 3) S. Y. Park, R. H. Kyser, C. M. Armstrong, R. K. Parker and V. L. Granatstein, to be published

\* Work supported by ONT  
+ Omega-P, Inc., New Haven, CT  
++ B-K Systems, Rockville, MD

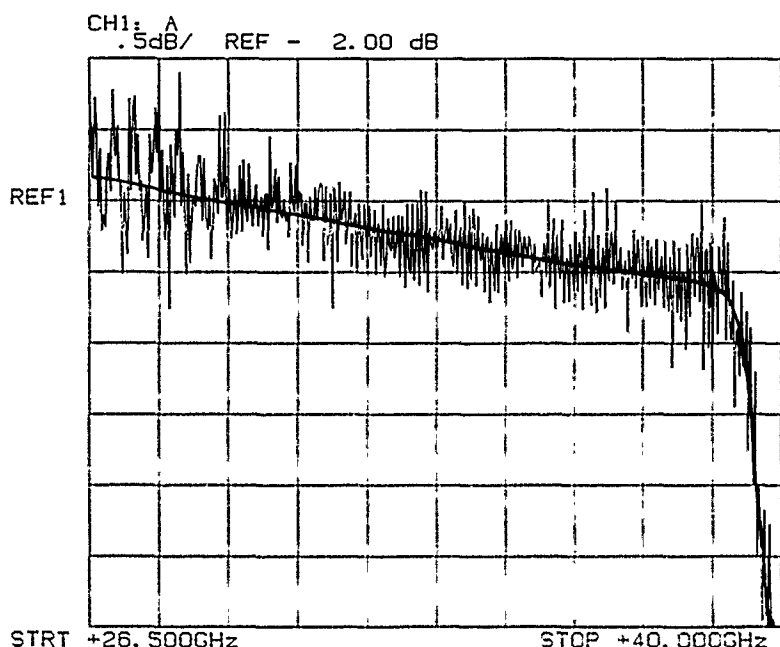


Figure 1; Return loss characteristics of assembled tube.

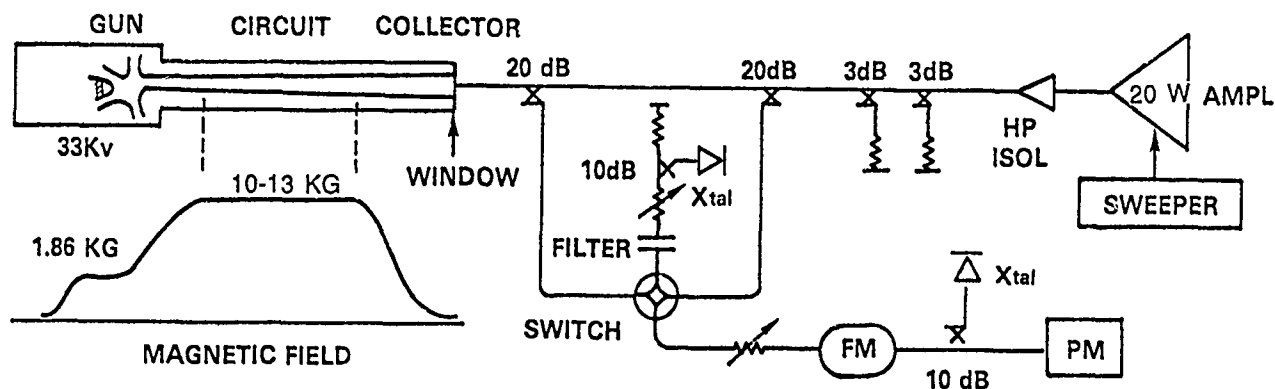


Figure 2; Schematic of experimental setup.

## HIGH CURRENT DENSITY CATHODES FOR MICROWAVE TUBES

M.E. Read and A.J. Dudas

Physical Sciences, Incorporated

635 Slaters Lane, Suite G-101, Alexandria, Va. 22314

and

P.E. Oettinger

Thermo Electron Technologies Corporation

74 West Street, Waltham MA 02254-9046

There has been a recent resurgence in the research and development of high power microwave sources, spurred by the growth of pulse power technology, wherein advances in energy storage and pulse forming have made possible the generation of electron beams with peak powers over 4 Terawatts. These beams can generate microwaves and millimeter waves with impressive intensity over a wide frequency range. Unfortunately, these high peak powers have been achieved, with few exceptions, with pulse lengths less than 100 ns, and, therefore low energy content. Moreover, the pulse repetition rate has been very low, with a measured peak of approximately 50 Hz. Such limitations in pulse length and repetition rate have been due to the characteristics of the accelerators and the nature of the cathode sources of the electron beams. However, lately, significant advances have been made in accelerator technology allowing the generation of pulses with microsecond pulse lengths and peak powers of 10 GW.

Advances in cathode development have been less substantial. Field emission cathodes are used in almost all the high peak power accelerators. These cathodes provide current densities well over  $1 \text{ kA/cm}^2$ , much higher than can be obtained with the thermionic emitters used in conventional, lower power microwave tubes. However, field emission cathodes operate via the formation of a plasma at the cathode surface, which limits both the pulse length and pulse repetition frequency.

In contrast, for barium oxide or dispenser cathodes, there is no limit on the pulse length or prf, since the emission is continuous. However, the DC current density generated from such cathodes is nominally below  $14 \text{ A/cm}^2$ . Higher densities have been achieved, but at the expense of cathode lifetime.[1] Of course, beam current densities can be increased by compressing the beam. However, compression causes an increase in the perpendicular "temperature" of a beam, a direct consequence of the conservation of phase space (Liouville's theorem.) This transverse velocity spread can cause a significant drop in the performance of several types of microwave tubes, such as free electron masers (FEM), cyclotron autoresonance masers (CARM), and relativistic backward wave oscillators (BWO).

Because of the above, there has been a great deal of interest in high pulse-current emitters. In particular, photoemissive cathodes such as  $\text{Cs}_3\text{Sb}$  have been used to produce beams with  $600 \text{ A/cm}^2$  [2]. Driven by a pulsed laser, these types of cathodes have been used to produce pulse lengths of 10's of picoseconds, and calculations based on thermal considerations indicate that pulse lengths over 100 microseconds with duty cycles over 1% are possible. However, in even carefully prepared tube environments, the lifetime of such cathodes has been on the order of hours.[2] Photoemitters which are more robust have been examined, but have been found to have substantially lower quantum efficiencies

and require short wavelength laser-drivers. The characteristics of several emitters are summarized in Table 1.

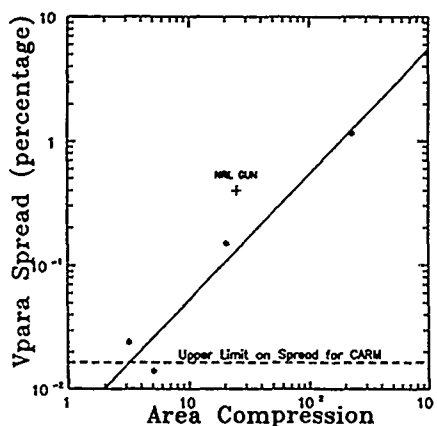


Figure 1. Parallel velocity spread vs area compression. For a Pierce gun with  $V=700 \text{ kV}$ ,  $I=50 \text{ A}$ , and beam radius of 2.2 mm.

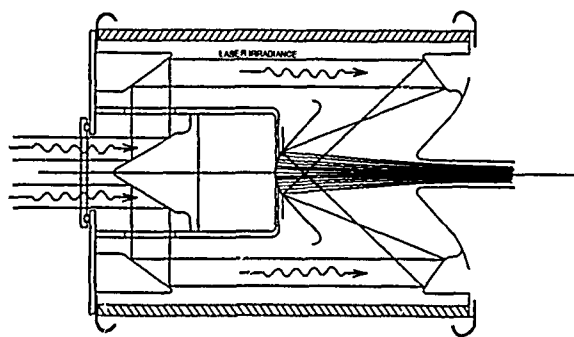


Figure 2. Schematic of the 700 kV Pierce gun, showing laser irradiation of the cathode.

An alternative approach, recently studied, is the use of pulse laser driven thermionic emitters. In this approach, the cathode is heated to the high temperature required for the emission of densities of several hundred  $\text{A/cm}^2$  only during the pulse(s). This avoids the high average barium loss which would unacceptably reduce the lifetime with continuous heating. For example,  $200 \text{ A/cm}^2$ , requiring a temperature of approximately 1700 degrees K, could be produced with a 10% duty factor while maintaining a barium loss

(and lifetime) equivalent to that with  $20 \text{ A/cm}^2$  via continuous heating.

A survey of the beam requirements for various pulsed high power microwave devices is summarized in Table 2. Two classes of interest for application of high current density cathodes emerge: (1) those that require moderately high beam current densities, but also very low velocity spread; (2) those requiring very high beam current densities, but with moderate velocity spread requirements. The FEM and CARM fall into the first category, while the BWO and REDITRON are characteristic of the second.

As an illustration of the use of a laser driven thermionic cathode, a design was realized for a gun to produce a beam for a CARM being developed at MIT.[3] For this device, the beam is to be formed by a Pierce gun, followed by a helical wiggler to give the beam the perpendicular motion required in the CARM interaction. The velocity spread at the output of the wiggler is related to the emittance  $\epsilon_n$  of the beam produced by the Pierce gun by  $(\Delta v_z/v_z)_f = 1.25 \epsilon_n (\text{p cm-rad})$  [3]. For monoenergetic beam,  $(\Delta v_z/v_z)_p = 0.5(\epsilon_n/\gamma\beta r)^{-1}$ . The beam voltage is 700 kV, with a current of 50 A. The radius at the input to the wiggler is 2.2 mm. The final value of the spread must be lower than 1% in order to avoid a significant degradation of the efficiency. Thus, velocity spread in the beam from the pierce gun must be less than 0.014%. ( $\epsilon_n = 40 \text{ mm-mrad}$ ). A series of simulations was performed using EGN, by W. Herrmannsfeldt. The velocity spread at the output of the gun as a function of area compression is plotted in Figure 1. As

can be seen, a compression of less than approximately 3 is required to realize the required velocity spread. This implies a cathode current density of  $\sim 100 \text{ A/cm}^2$ . A current density of  $10 \text{ A/cm}^2$ , typical of a space charge limited continuously heated cathode, would require a compression of 32, resulting in a velocity spread an order of magnitude higher than required. That our results are not simply the result of poor optics is confirmed by the results of a design, confirmed by measurement, for a Pierce gun for an NRL FEM,[4] noted on the figure.

To raise the dispenser cathode to the required 1700 deg K, from an idle temperature of 1400 deg K in 1 microsecond, approximately 2 MW of laser power is required. The laser wavelength is not critical, and this power can easily be obtained with a commercially available laser. A schematic of the gun is shown in Figure 2.

This work was supported by the U.S. Army, ET and D Laboratory.

## REFERENCES

1. M.C. Green, Tech. Digest, Int. Electron Dev. Meeting, Dec, 1987, pp 925-928.
2. J.S. Fraser, et al., LANL preprint LA-UR-87-863, presented at 1987 Particle Accel. Conf., Wash, DC, March, 1987.
3. B.G. Danley, et al., Proc. SPIE, 873 (1988).
4. G. Meriam, et al., Tech Dig., Int. Electron Dev. Meeting, Dec, 1985, pp. 188-191.

**Table 1 Beam Requirements for Microwave Tubes**

Tube	Freq (GHz)	Voltage (kV)	Current (A)	Perve- ance ( $\mu$ perts)	Current Density ( $\text{kA/cm}^2$ )	Velocity Spread (%)	Radius (cm)	Pulse Width ( $\mu$ s)
Gyroklystron	10	500	160	0.5	0.08	8	$0.8 \times 0.4$	sp
Gyromonotron	60-300	80	50	2.2	0.6	10	$1.2 \times 0.034$	cw
	35	800	600	0.8		1.1	$1.2 \times 0.2$	sp
CARM	140	700	50	0.09	1	.5*	0.12	sp
	100	600	200	0.4	0.5	$\sim 1$	$0.6 \times 0.1$	sp
FEL (FEM)	35	250	100	0.8	0.2	0.3	0.4	sp/cw
	35	3500	700	0.1				
Relativistic BWO	10	750	3300	5	3	10+	0.6	sp

\* at output of helix. A much lower spread is required at the input of the helix (see text.)

**Table 2 Summary of Cathode Characteristics**

Cathode Material	Type	Max Current <sup>++</sup> Density ( $\text{A/cm}^2$ )	Max Pulse <sup>+</sup> Length ( $\mu$ s)	Max <sup>+</sup> Duty	Laser Required P (W/A)	Laser Required $\lambda$ (nm)	Vacuum Required (Torr)
Cs3Sb	Photo	~00	300	0.02	60	300-500	$10^{-9}$
GaAs(Cs,O)	Photo	60	1000	0.15	10	400-900	$10^{-10}$
Metal (Au;Cu)	Photo	~500	10	$10^{-5}$	$\sim 10^6$	<200	$\sim 10^{-6}$
LaB6	Photo	50	~5	.01	$\sim 10^3$	<350	$\sim 10^{-7}$
Dispenser	Thermionic	200	NA	0.1	$\sim 10^6$ *	NA	$\sim 10^{-7}$

<sup>++</sup>Achieved to date. <sup>+</sup> Pulse length and duty cycle calculated for  $200 \text{ A/cm}^2$ .

## A NON-ADIABATIC ELECTRON GUN FOR GYROTRONS

B. Piosczyk  
Kernforschungszentrum Karlsruhe  
Institut für Technische Physik  
Postfach 36 40, D-7500 Karlsruhe 1  
Federal Republic of Germany

## Introduction

The hollow electron beams in gyrotrons are normally generated in magnetron injection type (MIG) guns. In these guns the transverse velocity of the electrons is mainly determined by the  $\mathbf{E} \times \mathbf{B}$ -drift at the emitter. Non-adiabatic effects during the acceleration do not give a major contribution. Several properties of the electron beam, such as the sensitivity to space charge effects and to conditions of the emitter surface, are related to this kind of extraction.

In the following a non-adiabatic (NA) type of an electron gun suitable for gyrotron application is presented. In contrast to MIG-guns the electrons are extracted parallel to the magnetic field in a manner similar to that described in Ref.2. The electrons gain their transverse velocity as a result of non-adiabatic effects during acceleration in a strong inhomogeneous electric field around the modulation anode. The extraction of the electrons parallel to the magnetic field results in several advantages of the NA-gun, which will be discussed later.

## Geometrical arrangement and operation

The geometrical dimensions as well as the magnetic field  $B = 0.118T$  around the emitter have been chosen in order to fulfill the requirements for a 140GHz gyrotron operated in a  $TE_{03}$ -mode with an electron beam at the second radial field maximum. To avoid high voltage problems the maximum electric field at the electrode surface was limited to about 50kV/cm. Fig.1 gives a schematic layout of the geometrical arrangement of the NA-gun. In addition to the shape of the electrodes the electron trajectories and potential lines are shown. The voltage  $U_{mod}$  between the cathode and the modulation anode and  $U_a$  between the cathode and the anode are 30kV and 70kV respectively. The magnetic field increases within the acceleration up to  $B = 0.218T$  at the end of the gun. The emitting surface consists of a concentric ring placed around a cathode finger. The modulation anode is a disc with a spherical aperture. In order to create a region with a strong inhomogeneous electric field the modulation anode is positioned around the end of the cathode finger. The anode consists of a spherical aperture in front of the modulation anode.

At the emitter surface the electrons are extracted parallel to the magnetic field. In the region of the modulation anode the electric field varies strongly over distances which are short compared with the longitudinal Larmor period  $l_L = p_z / (eB)$  with  $p_z$  being the longitudinal momentum of the electrons. Therefore, the electron motion becomes non-adiabatic and the electrons acquire a transverse momentum  $p_t$ . The motion

in the adjacent acceleration region between the modulation anode and the anode as well as in the magnetic compression region is adiabatic with  $p_t^2/B$  being a constant of motion.

## Numerical results

An extensive numerical parameter studies has been done using the SIAC-code. The results are summarized in the following:

- the transverse velocity  $\beta_t$  is roughly proportional to the square of the voltage  $U_{mod}$  between the cathode and the modulation anode,  $\beta_t \propto (U_{mod})^2$ ;
- the electron current is suppressed when the potential of the modulation anode is 2kV or more negative than the cathode potential;
- the electron flow is laminar;
- for a given value  $B_e$  of the magnetic field at the emitter surface the beam properties are not sensitive to a variation of the magnetic field within the acceleration region;
- for a given value  $B_{res}$  of the magnetic field at the resonator the transverse velocity decreases with increasing magnetic field at the emitter according to  $\beta_t \propto B_e$ . This strong decrease of  $\beta_t$  with the field  $B_e$  requires relatively low magnetic fields at the emitter ( $B_e \leq 0.15T$ ) corresponding to high magnetic compression ratios  $b = B_{res}/B_e$ ;
- by varying the geometrical dimensions a very low velocity spread ( $< 0.3\%$ , standard deviation) has been achieved numerically;
- the amount of the anode voltage  $U_a$  has nearly no influence on the transverse momentum  $p_t$  of the electrons;
- Influence of space charge:

Space charge effects around extraction do not influence the beam properties thus allowing an operation over the full range from zero current up to the space charge limited case. Fig.2 shows the numerical results.  $\beta_{tg}$  is the transverse velocity at the end of the gun,  $\Delta\beta_t/\beta_t$  is the relative spread of the transverse velocity and  $E_z$  the electric field at the emitter surface.  $j_e$  and  $I_e$  are the current density at the emitter and the total emitted current. The transverse velocity and the velocity spread are nearly not influenced by the emitted current from zero current up to the space charge limited case ( $E_z \rightarrow 0$ ).

## -2- Influence of the emitting surface conditions:

As discussed in Ref.4 the temperature and especially the roughness of the emitter surface may have a significant influence on the velocity spread of the electron beam in MIG-guns. The velocity spread within the electron beam limits the maximum achievable velocity ratio  $\alpha = \beta_2/\beta_1$  inside the interaction region. In order to investigate the velocity spread the trajectories of electrons leaving the emitter surface at an angle of  $45^\circ$  with an energy  $W_g$  has been calculated in



addition to the trajectories of electrons leaving the emitter in the normal direction with an energy of 0.1 eV. Fig.3 gives the results of the numerical simulation.  $|\Delta\beta_t/\beta_t|$  is the relative deviation of the transverse velocity at the resonator between the electrons with different starting conditions. In that figure  $|\Delta\beta_t/\beta_t|$  represents the total value and not the standard deviation. The MIG-gun used for comparison has been designed and built for a 140GHz gyrotron which is now under test. The results in Fig.3 show that for the same conditions the velocity spread at the NA-gun is by a factor of about 3 less than at the MIG-gun. The starting energy  $W_s$  is caused either by temperature effects or by surface roughness<sup>4</sup> of the emitter. For a given roughness the corresponding  $W_s$  is proportional to the electric field  $E_z$  at the emitter surface. A numerical calculation for a cone-shaped roughness with an height  $h_0$  and an opening angle of  $50^\circ$  resulted in a starting energy  $W_s \approx 6h_0 E_z$ . However, at the NA-gun the surface electric field  $E_z$  is by a factor of about 10 lower than for a MIG-gun. This causes a corresponding lower influence of the roughness on velocity spread.

### Summary

The NA-gun has several interesting features for an application in gyrotrons. In comparison with MIG-guns the main advantages are seen in the possibility of operation over the full current range and in the reduced influence of the emitter surface roughness on the velocity spread. A low velocity spread is a necessary condition for electron beams with a high  $\alpha$ . As a consequence of the perpendicular arrangement of the emitter surface to the magnetic field lines an enhanced emitter current density  $j_e$  is needed. However,  $j_e$  may be reduced, when a higher compression ratio is accepted.

### Acknowledgement

This work has been performed in the framework of the Nuclear Fusion Project of the Kernforschungszentrum Karlsruhe and is supported by the European Communities within the European Fusion Technology Program.

### References

1. e.g. J.M.Baird, W.Lawson, Int. J. Electronics, 1986, Vol.61, No.6, 953-967
2. J.Y.L.Ma, IEEE Trans. on Microwave Theory and Techniques, Vol.MTT-33, No.4, April 1985
3. W.B.Hermannsfeldt, Electron Trajectory Programm, Stanford University, Stanford, California, SLAC\_226, November 1979
4. Sh.E.Tsimring, Radiophysics and Quantum Electronics, 1972, Vol.15
5. B. Piosczyk, Kernforschungszentrum Karlsruhe, Primärbericht 03.04.02P09G, Juni 1987

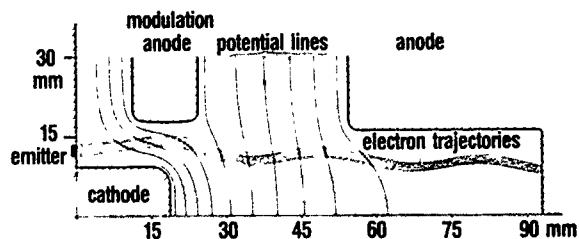


Fig.1: Geometrical arrangement of the NA-gun with electron trajectories and potential lines.  $U_a=70\text{ kV}$ ,  $U_{\text{mod}}=30\text{ kV}$ .

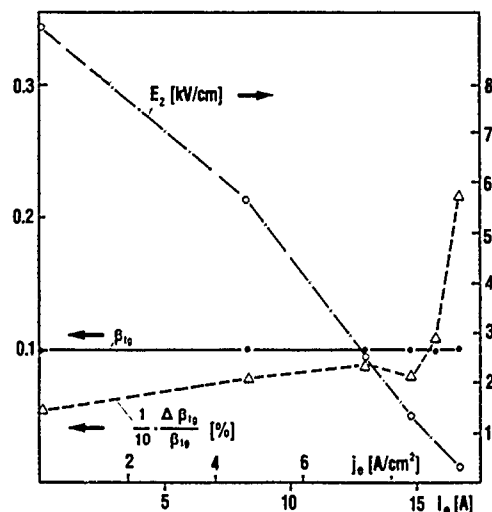


Fig.2: Influence of the extracted current  $I_e$  and current density  $j_e$  on the transverse velocity  $\beta_t$ , the velocity spread (standard deviation)  $\Delta\beta_t/\beta_t$  and the electric field  $E_z$  at the emitter surface.  $U_a=70\text{ kV}$ ,  $U_{\text{mod}}=30\text{ kV}$ .

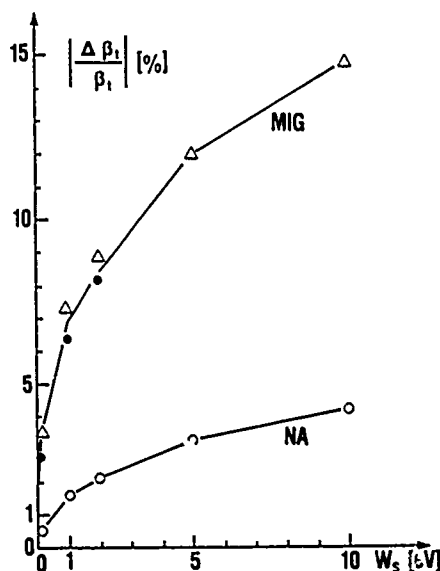


Fig.3: The relative velocity spread (total value) in dependence of the starting energy  $W_s$  under  $45^\circ$  for the NA-gun and a MIG-gun.

## FREQUENCY DOMAIN ANALYSIS OF A GYROTRON

E. Jensen and K. Schünemann

Technische Universität Hamburg-Harburg  
Arbeitsbereich Hochfrequenztechnik  
Postfach 90 14 03, D-2100 Hamburg 90, West-Germany

### ABSTRACT

For this analysis, the gyrotron is divided into an active, nonlinear "amplifier" and a passive, linear "resonator" part. At the interface between these parts, voltages and currents may be defined from modal expansion. Both the linear and the nonlinear network are then characterized by immittance matrices. The method is applied to a sample gyrotron.

### INTRODUCTION

A variety of methods for the theoretical investigation of oscillators exists in literature (see e.g. [1]). These methods concern locking phenomena, stability analysis, and noise. In order to apply them to the gyrotron, the formulation of its theory in terms of frequency dependent impedances or admittances is unavoidable. Our frequency domain analysis is such a formulation. By means of a sample gyrotron we present this analysis in the following.

### FIELD REPRESENTATION

In this model, the total field in the gyrotron is represented as an expansion in terms of empty cavity modes. These modes will be coupled by the electron beam, and therefore one has to take into account more than one of these to represent the distortion of the field by the beam. But due to the usually quite high quality factors involved, the number of modes might be restricted to those with eigenfrequencies near cyclotron resonance. The advantage of this approach is that the computations of cavity properties and electronic interaction are totally separated from each other. For the latter, the electromagnetic field appears only in terms of the known eigenfunctions and some complex amplitudes.

A problem with the modal field expansion in the source region is that the electric field of each mode is divergenceless while the total electric field is not.

This can be solved by not expanding  $\vec{E}$  directly, but the expression  $\nabla \times \vec{E}$ .

The empty cavity modes are found numerically by solving an eigenvalue problem imposed by the resonator boundary conditions. Due to the separate calculation, even complicated resonator structures (complex cavities) are possible. The eigenvector for a certain eigenvalue (complex frequency) corresponds to the field distribution of this mode.

### FIELD EXCITATION

The excitation of a mode  $i$  by the current density  $\vec{J}$  is described by the coupling coefficient  $c_i = \int \vec{J} \cdot \vec{E}_i^* dV$ , where  $\vec{E}_i^*$  is the complex conjugate of the eigenfield of mode  $i$ , and the integration is extended to the total cavity volume. If the electric field amplitude of mode  $i$  is denoted  $a_i$ , the resonance behaviour of the cavity is completely described by the ratios  $Y_{Li} = -c_i/a_i$ . The negative sign assures that the real part of  $Y_{Li}$  becomes positive when power flows from the excitation to the field, i.e. when  $Y_{Li}$  is passive. We call these ratios  $Y_L$  for load admittance because the functions  $Y_{Li}(\omega)$  resemble the admittances of parallel resonance circuits. Carrying on this analogy leads to the interpretation of  $a_i$  as voltages and  $c_i$  as currents. In our normalization,  $a_i$  have the dimension  $\sqrt{\text{energy}}$ ,  $c_i$  the dimension  $\sqrt{\text{energy}}/\text{time}$ ; hence the  $Y_{Li}$  are measured in  $1/\text{time}$ . The energy stored in the electric field of mode  $i$  might now directly be expressed as  $1/2 |a_i|^2$ , the power transfer from beam to field as  $\text{Re}\{a_i \dot{c}_i^*\}$ . If  $a_i$  and  $c_i$  are written in vector notation, all  $Y_{Li}$  appear as the elements of a diagonal matrix  $Y_L$ .

With this simple load admittance matrix, the question arises what the device admittance is in this model. Apart from the frequency dependence of  $Y_D$ , essentially given by the cyclotron resonance, we have a dependence of  $Y_D$  on the amplitudes. This is the

primary effect of the nonlinearity of the equations of motion.  $Y_D$  is calculated numerically for given  $\omega$  and amplitude vector.

#### THE SINGLE MODE CASE

For the sake of illustration, we restrict ourselves at first to the simplest, single mode case. Stepping through the amplitude-frequency-plane, we represent the result as loci in the complex  $Y_D$ -plane. Fig. 1 was calculated for a 35-GHz-gyrotron with a 6 % bias magnetic field taper. The  $\omega$ -loci for constant amplitudes are shown as solid lines, while the amplitude loci for constant  $\omega$  are dashed.  $Y_D$  is normalized to  $\omega_0/Q_0$  which is the real part of  $Y_L$  at resonance. The frequency range shown is 20 % in steps of 1 %, the amplitude range is 36 dB in steps of 3 dB. The outmost solid curve corresponds to small amplitudes. At this limit,  $Y_D$  becomes independent of the amplitude (linear regime). The curve is traced clockwise with frequency. From simple considerations one finds that the electron beam behaves purely inductive at the cyclotron frequency. At higher frequencies,  $Y_D$  gets a negative real part, and hence can transfer power to a real load. The oscillation condition,  $Y_L + Y_D = 0$ , can be illustrated by plotting the locus of  $-Y_L(\omega)$ , the load line, into this same diagram. Thus stable oscillations are - roughly

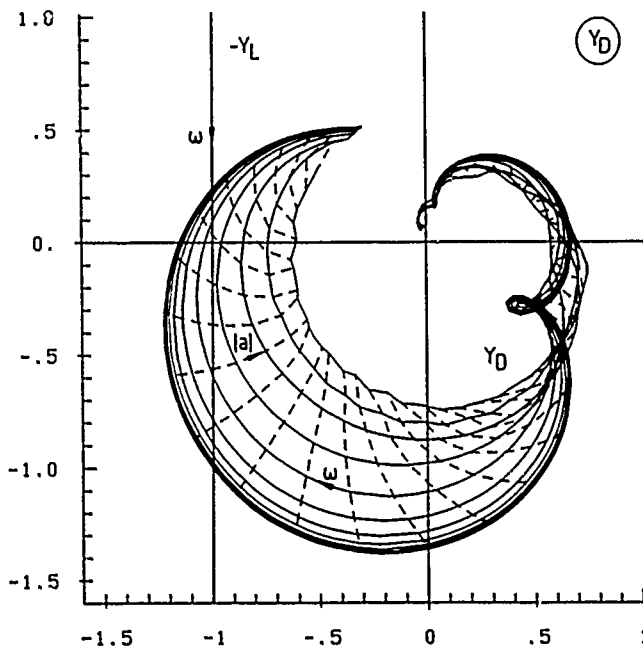


Fig. 1: Loci of the normalized gyrotron device admittance

speaking - given as intersections of load and device line.

Due to the high resonator  $Q$ , the locus of  $-Y_L$  is passed through very rapidly with frequency ( $\text{Im}(Y_L)$  changes from  $-j$  to  $+j$  in a frequency range of  $1/Q$ ). Hence,  $Y_L$  determines essentially the oscillation frequency. The resulting amplitude is read from the proper  $Y_D$ -locus.

#### THE MULTIMODE CASE

In the single mode case, the state of oscillation is thus determined quite easily. Considering the total field composed of several modes, one may start from this single (dominant) mode solution in an iteration.  $Y_L$  is now written as a diagonal matrix,  $Y_D$  contains off diagonal elements which represent the coupling of modes due to the beam. These exist even in the limit of small amplitudes, and depend basically on beam positioning. It should be noted here that modes with azimuthal dependence exist as a pair of degenerate modes in all rotational symmetric cavities.

The oscillation condition may now be written in matrix form as  $\{Y_D(a, \omega) + Y_L(\omega)\} \cdot a = 0$ , where  $a$  denotes the amplitude vector. This nonlinear equation can have more than one stable solution, but if we assume that essentially the amplitude of the dominant mode determines  $Y_D$ , the following algorithm will converge towards this solution. Starting from the single mode solution,  $(a_0, \omega_0)$ , in the  $n$ 'th iteration the equation  $\det(Y_D(a_{n-1}, \omega_{n-1}) + Y_L(\omega)) = 0$  is solved for complex  $\omega$ .  $a_n$  is the associated eigenvector, its length being determined by the amplitude of the dominant mode. It is increased (decreased) if the imaginary part of  $\omega$  is negative (positive). For the next iteration,  $\omega_n = \text{Re}(\omega)$  is set. If this algorithm converges, the imaginary part of  $\omega$  will tend to 0.

#### ACKNOWLEDGEMENT

The authors would like to thank the Deutsche Forschungsgemeinschaft for financial support.

#### REFERENCES

- [1] K. Kurokawa, "Injection Locking of Microwave Solid-State Oscillators," Proc. IEEE, vol.61, 1973, pp. 1386-1410

# EXPERIMENTS WITH A 35 GHz CYCLOTRON AUTORESONANCE MASER (CARM) AMPLIFIER

G. Bekefi, A. DiRienzo, C. Leibovitch and B. Danly

Massachusetts Institute of Technology  
Cambridge, Massachusetts 02139 USA

## ABSTRACT

Studies of a cyclotron autoresonance maser (CARM) are presented. The measurements are carried out at a frequency of 35 GHz using a mildly relativistic electron beam of 1.5 MeV energy and a 200 A current. The beam is generated by a field emission electron gun followed by an emittance selector that removes the outer, hot electrons. The entire system length ( $\sim 2.0$  meter), including the field emission gun, is immersed in a uniform solenoidal guide field of 7 kG. Perpendicular energy is imparted to the electrons by means of a bifilar helical wiggler having a period of 7 cm and a length of 56 cm. The cyclotron radiation is generated in a 1 meter long wiggler free region. Initial superradiant measurements give a small signal gain of 91 dB/m. Experiments are also underway in which a 35 GHz, 100 kW magnetron is used as the driver for our CARM amplifier.

## INTRODUCTION

The cyclotron autoresonance maser (CARM) has been subjected to extensive theoretical<sup>1,2</sup> studies and numerical simulations.<sup>3,4,5</sup> However, unlike the gyrotron and the free electron laser, its capabilities as a source of coherent millimeter wavelength radiation remain virtually untested in the laboratory. To the best of our knowledge, only CARM oscillator experiments<sup>6,7</sup> have been reported in the literature. We present here what we believe to be the first, albeit preliminary studies of a CARM amplifier.

The emission from a CARM results through an interaction between the Doppler upshifted cyclotron wave on the electron beam

$$\omega = \frac{\Omega_0}{\gamma} + k_{\parallel} v_{\parallel} \quad (1)$$

and an electromagnetic waveguide mode

$$\omega^2 = k_{\parallel}^2 c^2 + \omega_c^2; \quad (2)$$

$\omega$  and  $k_{\parallel}$  are the frequency and axial wavenumber, respectively;  $\Omega_0 = eB_{\parallel}/m$  is the nonrelativistic electron cyclotron frequency associated with an axial guide magnetic field  $B_{\parallel}$ ;  $\gamma = [1 - (v_{\parallel}/c)^2 - (v_{\perp}/c)^2]^{-1/2}$  is the relativistic energy factor; and  $\omega_c$  is the cutoff frequency of the waveguide mode in question. Maximum gain of the CARM instability occurs near phase velocity synchronism of the two waves. This yields the radiation frequency:

$$\omega \simeq \Omega_0 \frac{\gamma_{\parallel}^2}{\gamma} \left\{ 1 \pm \beta_{\parallel} \left[ 1 - \left( \frac{\omega_c \gamma}{\Omega_0 \gamma_{\parallel}} \right)^2 \right]^{1/2} \right\} \quad (3)$$

Here  $\beta_{\parallel} = v_{\parallel}/c$ ,  $\gamma_{\parallel} = (1 - \beta_{\parallel}^2)^{-1/2}$ , and the positive sign refers to the sought after Doppler upshifted CARM mode of operation.

## EXPERIMENT

A schematic of the CARM amplifier is shown in Fig. 1. The accelerator potential is supplied by a Marx generator (Physics International Pulserad 110A) with a maximum capability of 1.5 MV and 20 kA. The electron beam is generated by a field emission gun composed of a hemispherical graphite cathode and conical anode, which also acts as an emittance selector. The entire two meter long system is immersed in a uniform solenoidal magnetic field of 7 kG.

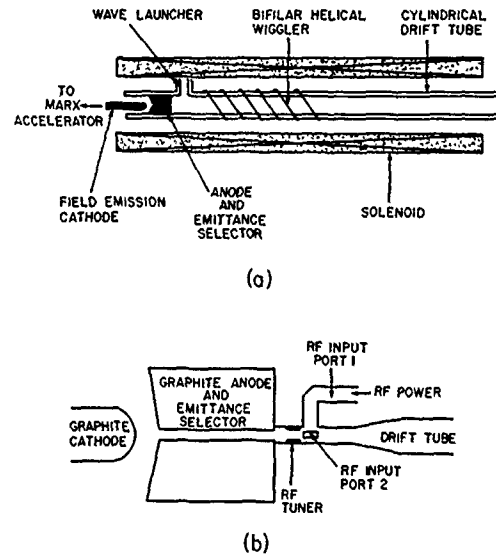


Fig. 1. Schematic of the experimental setup.

The 260 A, 1.5 MV beam that issues from the emittance selector has a radius of 0.254 cm and a measured normalized beam brightness equal to  $2.4 \times 10^4 \text{ A cm}^{-2} \text{ rad}^{-2}$ . This corresponds to a normalized RMS emittance of  $4.9 \times 10^{-2} \text{ cm-rad}$  and an RMS energy spread  $\Delta\gamma_{\parallel}/\gamma_{\parallel} \simeq 0.019$ . We note that by sacrificing current, considerably higher beam brightness is achieved. When the radius of the emittance selector is reduced to 0.076 cm, the current drops to 8.4 A but the brightness increases to  $9.5 \times 10^4 \text{ A cm}^{-2} \text{ rad}^{-2}$ . The corresponding emittance is now  $4.5 \times 10^{-3}$  and the energy spread  $\Delta\gamma_{\parallel}/\gamma_{\parallel} \simeq 0.0017$ .

The aforementioned electron beam is injected into a bifilar helical wiggler which imparts perpendicular energy

to the electrons. The wiggler has a periodicity of 7 cm and is six periods long. Within the first four periods, the wiggler magnetic field increases slowly and thereby provides an adiabatic input for the electron beam; the last two periods provide a uniform wiggler field with an amplitude on axis equal to 460 G. The resulting transverse electron velocity  $v_{\perp} \approx 0.3v_{\parallel}$ .

The downstream end of the wiggler is terminated abruptly by means of a metal shorting ring and the spinning electrons are allowed to drift into the 86 cm long CARM interaction region where they are subjected to the uniform axial magnetic field only.

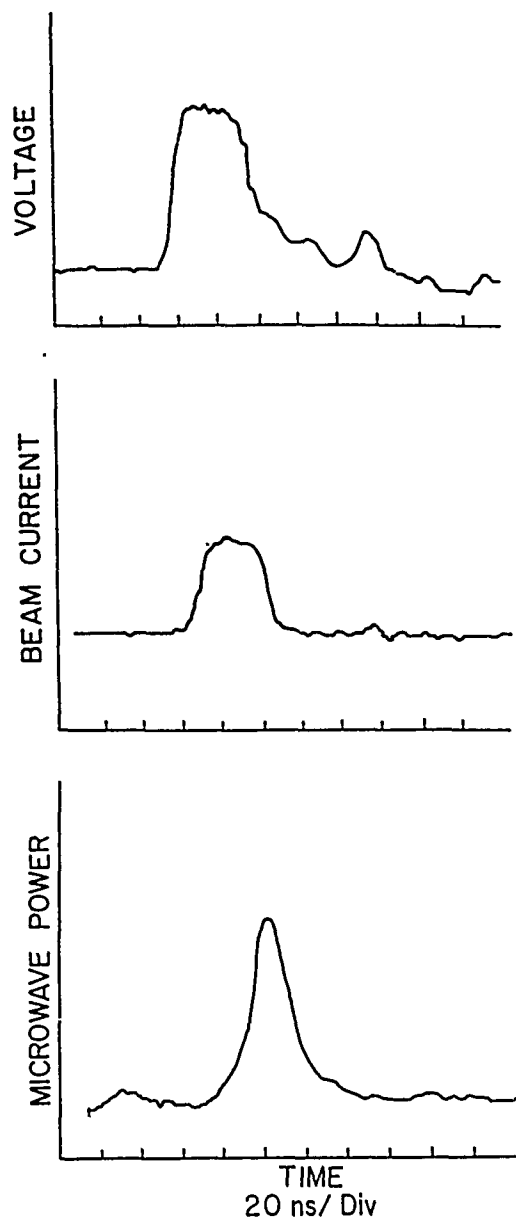


Fig. 2. Oscilloscope traces of the voltage, current and radiation intensity.

The  $\sim 2$  m long, 0.787 cm radius evacuated drift tube acts as a cylindrical waveguide whose fundamental  $TE_{11}$  mode has a cutoff frequency  $\omega_c/2\pi = 11.16$  GHz. Substituting this value of  $\omega_c$  in Eq. 3 together with the remaining experimental parameters yields the desired 35 GHz radiation frequency.

Figure 2 illustrates the time history of the voltage, current and radiation characteristics of the device. To date, the CARM has been operated in the superradiant mode in which the signal is allowed to grow out of background RF noise.

At the output end of the CARM, a mica window transmits the circularly polarized radiation generated in the drift tube, where it is measured by means of standard calibrated crystal detectors and its spectrum is analyzed by means of a 98 m long dispersive line. In order to determine the growth rate of the wave, the output intensity is measured as a function of the length of the interaction region. This is accomplished by means of an axially movable horseshoe "kicker" magnet that deflects the electron beam into the waveguide wall at any desired position  $z$ , thereby terminating the interaction at that point. Figure 3 shows how the RF power output measured at the far downstream end varies with the "kicker" magnet position  $z$ . The slope of the curve yields a single pass gain of 91 dB/m.

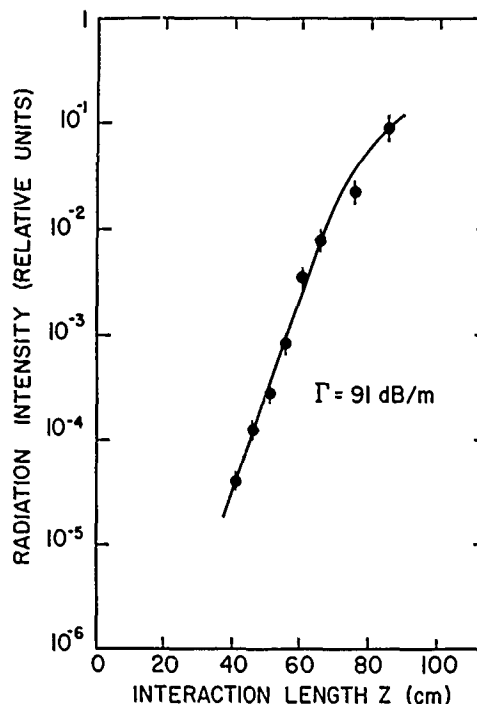


Fig. 3. Radiation intensity as a function of the interaction length.

## CONCLUSIONS

We have reported on the linear gain characteristics of a 35 GHz CARM amplifier giving a single pass, superradiant gain of 91 dB/m. We plan to study the efficiency and non-

linear characteristics of the CARM amplifier by injecting a monochromatic, circularly polarized wave into the system from a 100 kW magnetron driver (see Fig. 1).

#### ACKNOWLEDGEMENTS

This work was supported by the Air Force Office of Scientific Research.

#### REFERENCES

- [1] A.W. Fliflet, *Int. J. Electron.*, **61**, 1049-1080 (1986).
- [2] V.L. Bratman, N.S. Ginzburg, G.S. Nusinovich, M.I. Petelin, and P.S. Strelkov, *Int. J. Electron.*, **51**, 541-567 (1981).
- [3] K.D. Pendergast, B.G. Danly, R.J. Temkin, and J.S. Wurtele, submitted to *IEEE Trans. Plasma Sci.*, April (1988).
- [4] A.T. Lin, *Int. J. Electron.*, **57**, 1097-1108 (1988).
- [5] B.G. Danly, K.D. Pendergast, R.J. Temkin, and J.A. Davies, *Proc. SPIE* **873**, (1988).
- [6] I.E. Botvinnik, V.L. Bratman, A.B. Volkov, N.S. Ginzburg, G.G. Denisov, B.D. Kol'chugin, M.M. Ofitserov, and M.I. Petelin, *Pis'ma Zh. Eksp. Teor. Fiz.*, **35**, 418-420 (1982).
- [7] I.E. Botvinnik, V.L. Bratman, A.B. Volkov, G.G. Denisov, B.D. Kol'chugin, and M.M. Ofitserov, *Pis'ma Zh. Eksp. Teor., Fiz.*, **8**, 1376-1378 (1982).

# OPERATION OF HARMONIC GYROTRONS IN THE SUBMILLIMETER REGION

S.E. Spira, K.E. Kreischer and R.J. Temkin

Plasma Fusion Center  
Massachusetts Institute of Technology  
Cambridge, Ma.

## ABSTRACT

High power, submillimeter, second harmonic emission has been achieved with a 10 A, 75 kV, 1  $\mu$  sec pulse electron gun. In an iris cavity configuration, using a motheye window, second harmonic modes were observed at 12 frequencies in the range 301-503 GHz, with 15 kW at 417 GHz and 4-7 kW at 9 of the other modes.

## INTRODUCTION

The development of a high power submillimeter gyrotron is important for applications as electron cyclotron resonance heating for thermonuclear fusion, tokamak, plasma diagnostics, radar and astronomy. Gyrotrons are particularly suited for these applications, since they operate efficiently in the frequency gap between lasers and conventional microwave devices.

The submillimeter gyrotron program was established to achieve single mode second harmonic submillimeter emission with an existing gun that can emit up to 10 A at 75 kV with 2  $\mu$ sec pulse lengths. Second harmonic operation requires a smaller magnetic field than the fundamental. With fundamental operation, a field of 12 T is needed to generate 300 GHz, while second harmonic operation requires only 6 T. Present day Nb-Ti superconducting magnets with a large ( $\leq 10$  cm) room temperature bore can produce up to 10 T.

Second harmonic modes are harder to excite than the fundamental. Usually the fundamental modes have a lower starting current than the second harmonic modes. Therefore, the fundamental is excited first and it tends to suppress the second harmonic. Higher order axial modes of the fundamental ( $TE_{mpq}$ ,  $q=2,3$ ) and other second harmonic modes can also stifle the desired second harmonic mode. As the design frequency increases, larger cavities are required to reduce ohmic losses, but this increases the mode density and further aggravates mode competition problems. Mode competition problems also arise from the fact that our electron beam is actually quite thick and therefore can couple to several different modes simultaneously. When operating at higher magnetic fields the beam is more compressed and thicker, thereby able to couple to more unwanted modes. These difficulties were successfully overcome by using a cavity with an output iris and a motheye window.

## EXPERIMENTS

In the initial experiment a cavity with an output iris<sup>1</sup> was used with an ordinary quartz window to generate second harmonic emission. Design parameters for the output iris cavity are listed in Table 1. The output iris traps the second harmonic more, due to its shorter wavelength, than the fundamental. This lowers the starting current of the second harmonic mode and facilitates the suppression of

the fundamental by the second harmonic.

Seven second harmonic modes were observed ranging from 301 GHz to 417 GHz. At 417 GHz, 15 kW of second harmonic, single mode emission was generated, and the other six modes produced 4-7 kW. As frequency increased the region of excitation for the second harmonic modes decreased. The design mode of the cavity,  $TE_{13,2,1}$ , that oscillates at 410 GHz was not observed. Possible reasons for reduced harmonic emission include mode competition, beam degradation, or beam thickness. Degradation of beam quality could be occurring at the higher compression ratios,  $B_m/B_g$  (where  $B_g$  is the field at the gun and  $B_m$  is the field at the cavity), experienced when operating at higher magnetic fields. Due to the thickness of our electron beam, it could have coupled strongly to the nearby fundamental modes, thereby lowering fundamental mode starting currents, and enabling them to suppress the desired second harmonic mode. This problem can be overcome in two ways. A thinner beam or better fundamental mode suppression techniques must be used. Modifying our gun to produce a thinner beam was not possible so using additional mode suppression devices, like a motheye window, is preferable.

The motheye window<sup>2</sup> only provides positive feedback for the second harmonic, and using it in the system requires very little system adjustment. Reflectivity of our motheye window is low ( $\leq 0.2$ ) at frequencies below 300 GHz and very high ( $\geq 0.8$ ) above 400 GHz, with the transition region between 300-400 GHz, so only the diffractive Q of the second harmonic is raised significantly. Measurement of reflectivity as a function of frequency was done with a Fast Fourier spectrometer. For the next phase of this experiment this window was used successfully as a method to suppress the fundamental. Five new second harmonic frequencies were observed, including the design mode, the  $TE_{13,2,1}$ . The results are summarized in Table 2, where the observed power, frequency and theoretical modes are listed. With more second harmonic modes being excited, one notices the step tunable behavior in the second harmonic, similar to that observed in fundamental megawatt experiments<sup>3</sup> for the fundamental modes. When the harmonic is not suppressed by a strong fundamental mode, the  $p = 1,2,3$  ( $TE_{m,p,q}$ ) sequences are being excited. The highest second harmonic frequency attainable is no longer limited by cavity design, but rather by the transition region of the window's transmission characteristic as a function of frequency. At higher fields, the fundamental and second harmonic spectrum become sparser, since beam compression is increasing, and therefore beam quality is diminished. Poorer beam quality means that the ratio  $\beta_{\perp}/\beta_{\parallel}$  decreases, so less of

the beam energy can couple to the rf-wave. Also velocity and energy spread increase in more compressed beams. These effects raise the starting currents. However for the second harmonic, this is counterbalanced somewhat by the increase of  $Q_D$  due to the motheye window. For example, the  $TE_{17,2,1}$  mode at 503 GHz was observed, but not until beam current was increased to 5-6 A. The effects of the motheye window can also be seen in Figure 1, where the regions of second harmonic have increased considerably at higher frequencies, which correspond to low window transmission coefficients. Second harmonic modes with frequencies less than 390 GHz did not have regions of excitation bigger than that observed with an ordinary quartz window. This agrees with the measurement of transmission coefficient as a function of frequency, which shows that the transition region between good and bad transmission is between 300-400 GHz.

Operating at second harmonic requires more sophisticated diagnostics than those needed for the fundamental. One must be able to detect the harmonic modes when the fundamental is present, and also estimate the fraction of fundamental present. Two custom made filter horns with cutoff frequencies of 280 GHz and 300 GHz were used with a WR-3 video diode, to prevent that diode from detecting fundamental radiation. With this modified WR-3 diode system and a WR-6 video diode to detect fundamental radiation, the harmonic mode can be optimized. Frequency is measured with a heterodyne receiver that uses a Hughes harmonic mixer diode. The filter horns are also attached to the mixer diode so that a stronger fundamental signal will not swamp the system. Power is measured by a Scientech calorimeter<sup>4</sup>. Second harmonic measurements were taken, with and without a 1.27 cm thick sheet of plexiglass in front of the calorimeter. Since the sheet of plexiglass is a calibrated low pass filter, the fraction of second harmonic radiation can be estimated. For example, when the measurement at 417 GHz was taken, 15 kW of power was measured without the plexiglass sheet. With the plexiglass sheet in front of the calorimeter minimal power was measured, indicating that virtually all the power was in second harmonic emission. Also during this measurement, even with a WR-6 horn on the mixer diode (which will allow the mixer to detect fundamental radiation), no other frequencies were found, so one concludes that to the accuracy of the calorimeter, single mode harmonic emission was observed. In the frequencies above 390 GHz the harmonic modes tended to be pure second harmonic emission, while the lower frequency modes tends to have varying amounts of fundamental mixed in.

This research is partially sponsored by the Strategic Defense Initiative Organization, Office of Innovative Science and Technology, and managed by Harry Diamond Laboratories, and partially by the U.S. Department of Energy. We are grateful to the Francis Bitter National Magnet Laboratory for the use of their high field Bitter magnet and facilities. The authors would like to thank W. Mulligan, C.Y. Wang, P. Lentini, and S. Chu.

## REFERENCES

- (1) S.E. Spira, K.E. Kreischer and R.J. Temkin, "Sub-millimeter gyrotron for space-based radar", Sensing, Discrimination, and Signal Processing and Superconducting Materials and Instrumentation, Roy Nichols, James A. Ionson, Editors, Proc. SPIE 879 58-61 (1988).
- (2) J.Y.L. Ma and L.C. Robinson, *Optica Acta* **30**, 1685 (1985).
- (3) K.E. Kreischer and R.J. Temkin, *Phys. Rev. Lett.* **59**, 547 (1987)
- (4) K.E. Kreischer, J.B. Schutkeker, B.G. Danly, W.J. Mulligan, and R.J. Temkin, *Int. J. Electronics*, 1984, vol. 57, pp. 835-850.

TABLE 1

### OUTPUT IRIS CAVITY DESIGN PARAMETERS

#### Second Harmonic

Frequency=410 GHz	$Q_T=3800$
Power=100 kW	$\eta_T=18\%$
Cavity Radius=0.232 cm	Beam Current=9 Amps
Magnetic Field=8.3 Tesla	

TABLE 2

#### Second harmonic emission observed in the output iris cavity

Frequency (GHz)	Magnetic Field (T)	Power (kW)	Probable Mode
301.6	6.1	4	$TE_{3,4,1}$
329.6	6.7	5	$TE_{14,1,1}$
339.3	6.9	4	$TE_{10,2,1}$
363.3	7.4	7	$TE_{11,2,1}$
366.9	7.4	4	$TE_{8,3,1}$
372.6	7.6	3	$TE_{16,1,1}$
392.5	7.8	4	$TE_{9,3,1}$
410.6	8.2	1	$TE_{13,2,1}$
417.1	8.4	15	$TE_{10,3,1}$
457.1	9.1	7	$TE_{15,2,1}$
467.2	9.3	6	$TE_{12,3,1}$
503.3	10.0	1	$TE_{17,2,1}$

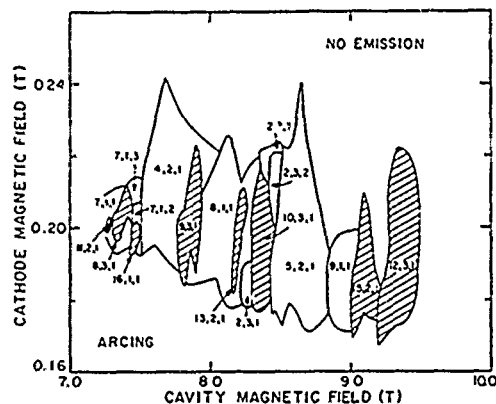


Figure 1

Regions of emission using the output iris cavity with the motheye window. Shaded regions correspond to second harmonic modes



## NON-LINEAR ANALYSIS OF A GYRO-PENIOTRON OSCILLATOR\*

P. Vitello

SCIENCE APPLICATIONS INTERNATIONAL CORPORATION  
MCLEAN, VA 22102 USA

## ABSTRACT

We present here the results of a non-linear numerical investigation of a high-harmonic gyro-peniotron oscillator design which uses a slotted cylindrical magnetron-type cavity. Our modeling shows that very high efficiency ( $\gtrsim 60\%$ ) can be achieved at high harmonics ( $s > 3$ ), and that the operation current can be dramatically reduced by the addition of slots. We find that the start oscillation current may decrease with harmonic number in a slotted device, unlike the smooth walled gyrotron where start oscillation current always increases with increasing harmonic number. This greatly favors the use of a slotted cavity for high harmonic operation. The gyro-peniotron oscillator in a slotted cavity appears attractive as a means of achieving millimeter wave emission.

## INTRODUCTION

The gyro-peniotron has an excellent potential as a high efficiency, high harmonic microwave source. Recent theoretical modeling [1-5] has shown that efficiencies (as great as 80-90%) can be gotten for electron beams with finite velocity and guiding center spread. Although the peniotron interaction may lead to higher saturated efficiencies than the electron cyclotron interaction, in the weak field linear limit the cyclotron maser interaction is generally a stronger interaction. This relative weakness of the peniotron interaction can lead to high start oscillation currents, and therefore, significant mode competition and interference from cyclotron maser modes with lower start oscillation beam powers. Use of a slotted, magnetron-type cavity presents a means of overcoming these problems by both enhancing the interaction between the electron beam and the field at high harmonics (which lowers the operating current), and at the same time reducing mode competition from unwanted modes [6]. In this paper we present the results of a numerical non-linear investigation of a slotted cylindrical cavity gyro-peniotron oscillator operating in a  $TE_{m11}$  "whispering gallery" mode. The modes  $m = 2-5$  were studied at the peniotron interaction harmonics  $s = m - 1$ . As expected from smooth walled and previous slotted cavity studies, we find that high efficiencies are possible at high harmonics for the gyro-peniotron. We also find that the use of a slotted cavity can lead to a decrease in the operating beam current with increasing harmonic number.

## GYRO-PENIOTRON MODEL

We consider a magnetron-type slotted cavity with  $N$  slots each of width  $2\theta_0$  interacting with an axis encircling beam (see Figure 1). The cavity inner radius, outer radius, and axial length are respectively  $a$  and  $b$ , and  $L$ . The axial length of the cavity contains two tapered regions, the input and output regions,  $z_1$  and  $z_3$ , with a straight interaction region,  $z_2$ , between them (see Figure 2). Using the initial cavity radius,  $a_0$ , as our scale factor, the radius in the first tapered region varies from 1-1.111, while in the output ta-

pered region the radius goes from 1.111-1.688. The input, interaction, and output tapered regions are respectively  $2a_0$ ,  $8a_0$ , and  $a_0$  in length.

The transverse RF field is calculated by treating the cavity proper and the slots as separate expansions which are matched across the slot openings [6]. We take the relative phase dependence of each of the  $N$  slots as being  $e^{i2\pi mq/N}$   $q = 0, \dots, N - 1$ . The value of the mode number  $m$  determines the general mode. The  $2\pi$  mode corresponds to  $m = 0$ , while the  $\pi$  mode is given by  $m = N/2$ . The  $\pi$  mode, which we will consider here, has the same symmetry as a  $TE_{m11}$  smooth walled mode, but the radial peak may be strongly displaced towards the axis. This inward shift in the field maximum allows the placement of the electron beam in the region of high field and greatly enhances the interaction between the beam and the cavity mode [6].

An additional advantage with a  $N$  slotted magnetron-type cavity is the imposed  $N$ th fold symmetry which is lacking in a smooth walled cavity. The cavity symmetry leads to an enhancement of the  $Q$  for modes which have the same symmetry as the cavity, relative to the cavity modes that do not "fit" well into the cavity symmetry. This results in a lower start oscillation current for the wanted  $\pi$  mode and a reduction in the mode competition.

To explore the non-linear behavior of this gyro-peniotron oscillation we have developed a self-consistent numerical model based on the slow-time scale formulation of Ganguly and Ahn [7]. We use guiding center coordinates  $u_\perp, u_z, r_{gc}, \psi_{gc}$ , and slow-time scale variables,  $\omega t - s\psi_{gc} - \xi(z)$ , where the RF field axial profile is given by  $F(z)e^{-i\xi(z)}$ . By averaging over a cyclotron period the interaction is limited to a single  $s$  harmonic. Integrating Maxwell's equations for the RF field over the cavity cross section then results in complex, non-linear second order ordinary differential equations for  $F(z)$  and  $\xi(z)$ , where the coupling between the RF field and the beam is governed by  $\vec{v} \cdot \vec{E}$ . This RF field equation is solved numerically with the three-dimensional beam particle equations of motion. The equations contain sums over the RF field harmonics which are truncated, and involve high order Bessel functions evaluated in line for speed and accuracy. The RF field solution is subject to oscillator boundary conditions, with an initial effervescent field where the beam interaction starts and an outgoing wave field at the output end of the cavity. The need to satisfy the RF field boundary conditions constitutes an eigenvalue problem for the field amplitude and mode frequency which is solved iteratively. A spread in the initial beam parameters, such as the guiding center radius or the axial velocity is also treated by using a weighted average when calculating the beam current. As the full RF fields for TE modes is used, including all  $(E_\theta, E_r, B_\theta, B_r, B_z)$  components, both the electron cyclotron maser and the peniotron interactions are accurately calculated. The gyro-peniotron oscillator is assumed to be in steady state operation.

We have used this model to analyze both the weak field linear regime, and the high field non-linear saturated efficiency regime. We feel that the calculation of the field profile and cavity  $Q$  is needed to accurately determine the oscillator operating current behavior. Variations in the model param-

eters can lead to large changes in  $Q$ . Using the quantity  $QI$ , as is often done in models which are not self-consistent, can therefore lead to erroneous predictions for the optimum operating beam currents.

## RESULTS

We have made a parameter study of the start oscillation and saturated efficiency for the  $TE_{m11}$  modes for  $m = 2-5$  and at the peniotron resonance harmonics  $s = 1-4$ . The parameters varied include the cavity length and slot depth, and the beam energy, transverse to axial velocity ratio,  $\alpha$ , axial velocity spread, and guiding center spread. Figure 3 shows the minimum start oscillation current for the modes as a function of  $b/a$  for  $\alpha = 1.5$  and beam energy 70 keV. For the smooth walled cavity,  $b/a = 1$ , the start oscillation current increases with mode number. As  $b/a$  increases, however, this trend then reverses and the start oscillation current decreases with increasing mode number. The curves for  $TE_{311}$ – $TE_{511}$  are stopped when the ratio of the beam Larmor radius,  $r_L$ , to the cavity radius in the interaction region which reaches 80%. This gives room for a reasonable amount of initial guiding center spread. For the  $TE_{211}$  mode, the Larmor radius was only about half of the interaction radius even with  $b/a$  as large as 2.25. Larger values of  $b/a$  lead to very low values of  $k_{\perp}$  and the extension of the RF field excessively into the input region. We note from Figure 3 that the start oscillation current at the optimum 80% Larmor radius point decreases slowly with mode number for large  $m$ . The addition of slots therefore, dramatically reduces the high harmonic operating current, and favors operation at high harmonics. We find that for the  $TE_{511}$  mode operating at the 4th harmonic, efficiencies of  $\approx 50\%$  can be gotten even with a guiding center spread of  $\approx 10\%$  of the interaction region radius. The gyro-peniotron oscillator in a slotted cavity is therefore, a device with excellent potential as a high harmonic microwave source.

## REFERENCES

- [1] S.P. Kuznetsov, D.I. Trubetskov, and A.P. Chetverikov, "Nonlinear analytic theory of the peniotron," *Sov. Tech. Phys. Lett.*, vol. 6, pp. 498–499, 1980.
- [2] P. Vitello, "Cyclotron maser and peniotron-like instabilities in a whispering gallery mode gyrotron," *IEEE Trans. Microwave Theory Tech.*, vol. MTT-32, pp. 917–921, 1984.
- [3] S. Cno, K. Tsutaki, and T. Kageyama, "Proposal of a high efficiency tube for high power millimeter or sub-millimeter wave generation: The gyro-peniotron," *Int. J. Electron.*, vol. 56, pp. 507–520, 1984.
- [4] P. Vitellò, "Design considerations for the gyro-peniotron oscillator," *Int. J. Infrared Millimeter Waves*, vol. 8, pp. 487–515, 1987.
- [5] P. S. Rha, L. R. Barnett, J. M. Baird, and R. W. Grow, in *Int. Electron Device Meet.*, pp. 525–538, 1985.
- [6] K. R. Chu and D. Dialetis, "Kinetic theory of harmonic gyrotron oscillator with slotted resonant structure," *Infrared Millimeter Waves*, vol. 13, 45, 1985.
- [7] A.K. Ganguly, S. Ahn, and S.Y. Park, "Three dimensional nonlinear theory of the gyro-peniotron amplifier," in press, *Int. J. Electronics*, September 1988.

\* Supported by NRL under Contract N00014-87-C-2448.

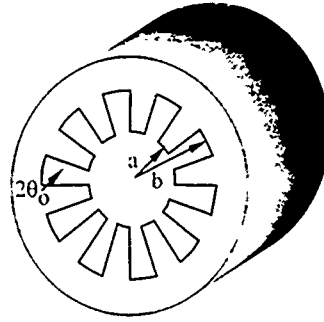


Figure 1. Slotted Cavity Gyro-peniotron Oscillator

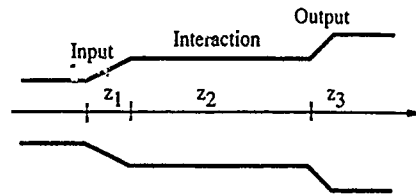


Figure 2. Gyro-peniotron Oscillator axial cross section

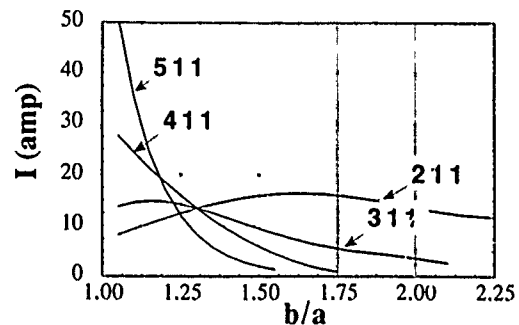


Figure 3. Start Oscillation Current

# Prebunched High Harmonic Gyrotron

C.S. Kou, D.B. McDermott and N.C. Luhmann, Jr.

Dept. of Electrical Engineering, University of California  
Los Angeles, California 90024

## ABSTRACT

A prebunched beam has been used to further increase the efficiency of our axis-encircling high harmonic gyrotron. The experiment was performed at the third harmonic with a  $TE_{3,12}$  mode at 27.7 GHz. The conversion power was 6.7 kW which was significantly greater than that of the non-prebunched experiment. Also, mode competition was substantially reduced. The dependence of the output power on the square of current has been verified. The start of oscillation current is effectively zero.

## INTRODUCTION

A high harmonic gyrotron has been developed at UCLA which is based on the resonant interaction between a large orbit axis-encircling electron beam with a high order azimuthal  $TE_{n,1}$  mode. Since the electrons are in resonance with the wave when  $\omega = n\Omega_c$ , the magnetic field requirement has been substantially reduced (by a factor of  $n$ )<sup>(1)</sup>.

Since the fields of high order  $TE_{n,1}$  modes are strongly localized near the wall of the cavity, strong interaction between the electrons and wave requires an electron beam with a high transverse velocity (Fig. 1). At UCLA, the high energy axis encircling electron beam is produced by a gyro-resonant rf accelerator. A pencil beam is accelerated up to 1 MeV in a  $TE_{1,1}$  cavity, becoming a high energy axis-encircling helical beam<sup>(2)</sup>.

Notable high harmonic gyrotron results using this RF accelerator have been a conversion efficiency of 16% in a 2 kW, fourth harmonic, 32 GHz tube with mode control, saturation at 1 kW by an eleventh harmonic tube and emission at 65 GHz by an eighth harmonic tube<sup>(3)</sup>.

Here, a novel interaction has been developed based on the fact that the RF accelerator transforms a pencil beam into a helical electron beam rotating with the accelerator's frequency. If the gyrotron's frequency is a harmonic multiple of the accelerator's frequency, the angular velocity of the wave is the same as the rotating velocity of the helical beam and each electron will see the same phase when entering the interaction cavity. This results in a prebunched electron beam. The accelerator behaves like the buncher cavity of a klystron and higher power can be obtained.

## LINEAR THEORY

In order to simultaneously satisfy the prebunching condition

$$\omega = n\omega_{acc} \quad (1)$$

and the gyro-resonance condition

$$\omega - k_{||}v_{||} - n\Omega_c/\gamma = 0 \quad (2)$$

we must achieve

$$\omega_{acc} = \frac{\Omega_c}{\gamma} + k_{||} \frac{v_{||}}{n} \quad (3)$$

However, we know the optimal operating condition is<sup>(4)</sup>

$$\Omega_c \approx 2\Omega_c/(\gamma + 1) \quad (4)$$

Condition (3), and (4) are not easily achieved without using a tapered magnetic field or utilizing the Doppler shift term. Unfortunately, the former will cause reflection of the electrons due to their high  $\alpha$ . By using a high axial mode, Eq.(3) can be satisfied while the cavity's length can still be long enough to allow the interaction to saturate.

A small signal, linear theory of the prebunched harmonic gyrotron can be derived by considering the generation of a  $TE_{n,1}$  wave whose azimuthal electrical field is given by

$$E_\theta = E_0 J'_n(k_\perp z) \sin(n\theta - \omega t) \quad (5)$$

The change in energy of an electron is given by  $dU/dt = evE$ . Taking into account the  $\sin(k_\perp z)$  dependence of the mode, the energy change of an optimally phased, axis-encircling electron rotating synchronously with the wave is  $\Delta U = ev_\perp (E_0/2) \ell / v_{||}$  where  $\ell$  is the length of the cavity. The power flow into the wave is given by  $P = \Delta U I / e$ , or

$$P = \frac{\ell}{2} (v_\perp / v_{||}) E_0 J'_n(k_\perp r_\perp) \quad (6)$$

Meanwhile, the power lost by the field with total energy,  $U$ , is given by  $P = \frac{\omega}{Q} U$ , where

$$U = \frac{\pi \epsilon_0^2}{4} \ell E_0^2 \left(1 - \left(\frac{n}{q_{n1}}\right)^2\right) J_n^2(q_{n1}) \quad (7)$$

At equilibrium, the power gained from the electrons must equal the dissipated power. Consequently, the expected power level is given by

$$P = (Q \ell^2 / \pi \epsilon_0 \omega a^2) \chi_{v_\perp / v_{||}}^2 (J'_n(q_{n1} r_\perp / a) / J_n(q_{n1}))^2 (1 - (n/q_{n1})^2)^{-1} \quad (8)$$

Notice that the power scales with the square of the current, which is a characteristic of an amplifier.

## EXPERIMENT

The geometry of the prebunched high harmonic gyrotron is shown in Fig. 2. A low energy pencil beam is injected along the magnetic field into the cylindrical cavity  $TE_{1,1}$  gyro-resonant accelerator. The resulting helix of high energy electrons strikes a uranium glass plate after propagating through the interaction cavity. Because the radius of the resulting fluorescent image is just the Larmor radius, the perpendicular velocity can be determined within 2.5%.

Our first experiment was performed at the third harmonic with a  $TE_{3,12}$  mode at 27.7 GHz which is exactly three times the RF accelerator's frequency. The maximum output power is 3.4 kW. The dependence of the output power on the beam current is shown in Fig. 3. As Eq.(8) predicts, the output power scales with the square of the current and no start of oscillation current exists. Also, the prebunching mechanism has substantially suppressed mode competition. The level of the competing mode is never more than 30 dB below the level of the main mode.

## DISCUSSION

A rough estimate of the maximum efficiency is given by the change of  $\gamma$  by which the electrons advance in the wave by 180 degrees. It can be shown that the efficiency is then given by

$$\eta \equiv \frac{\Delta\gamma}{\gamma-1} = \left(\frac{\gamma}{\gamma-1}\right) \frac{\pi c \beta_{\parallel}}{\omega L} \quad (9)$$

For our parameters the predicted maximum efficiency is 13%, whereas a peak efficiency of 10.5% was obtained. For the linear region, Eq.(8) predicts an output power of 245kW/A<sup>2</sup> for our experimental parameters, whereas we have measured a power of 125kW/A<sup>2</sup>. The discrepancy can be accounted for by the fact that the guiding center spread leads to some electrons entering the cavity at improper phase angles. A small aperture in front of the accelerator reducing the beam's guiding center spread would improve the agreement. Axial velocity spread together with the large  $k_{\parallel}$  will also reduce the formation of a prebunched electron beam and the efficiency of the interaction. The influence of velocity spread will be studied in the future. A comparative experiment with a non-prebunched gyrotron is also being performed.

## ACKNOWLEDGEMENTS

We wish to acknowledge several stimulating discussion with Dr. K. R. Chu. This work is supported by AFOSR Grant 86-0199 Amd A.

## REFERENCES

1. D.B. McDermott, N.C. Luhmann, Jr., A. Kupiszewski and H.R. Jory, Phys. Fluids, **26**, 1936(1983).
2. D.B. McDermott, Jr., D.S. Furuno and N.C. Luhmann, Jr., J. Appl. Phys. **58**, 4501(1985).
3. D.B. McDermott, N.C. Luhmann, Jr., D.S. Furuno, A. Kupiszewski and H.R. Jory, Int. J. IR and MM-waves, **4**, 639 (1983).

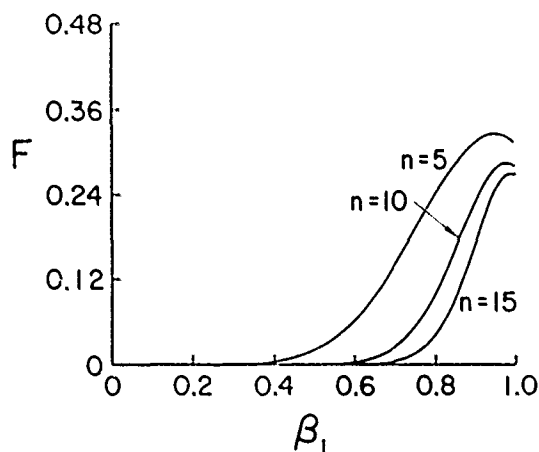


Fig. 1. Dependence of the normalized rf field strength squared on  $\beta_{\parallel}$  for high harmonic interaction.

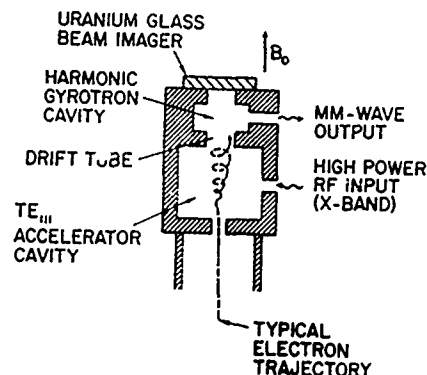


Fig. 2. Schematic of prebunched high harmonic gyrotron.

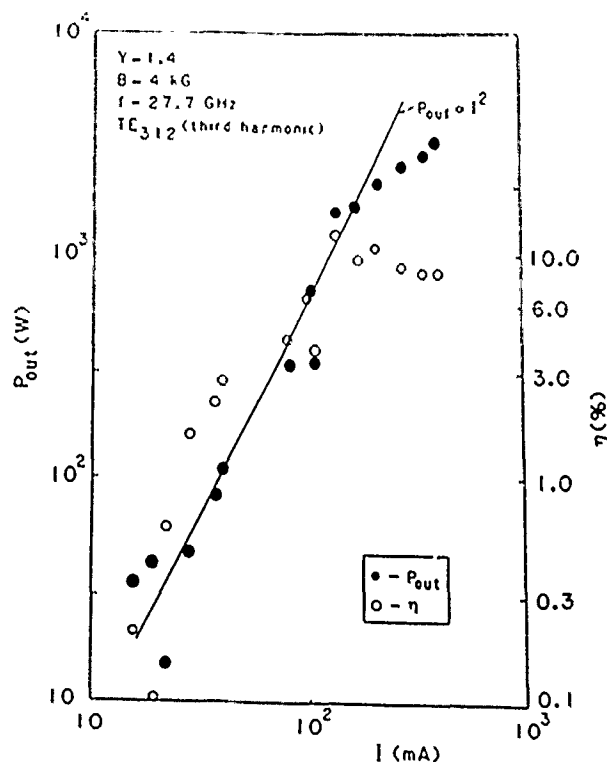


Fig. 3. Dependence of output power on beam current in prebunched third harmonic gyrotron.

# LINEAR ANALYSIS OF THE HIGH-POWER MAGNETRON

R. A. Stark and H. S. Uhm  
Naval Surface Warfare Center  
White Oak Laboratory  
Silver Spring, MD 20903-5000

## ABSTRACT

A linear stability analysis of the extraordinary mode in a high-power (>GW) planar magnetron is developed using a cold-fluid model of the electron flow. The eigendifferential equation for arbitrarily intense electron flow is found and solved numerically through finite differencing techniques. As a sample of some initial results, a calculation of growth rates versus cavity depth is shown.

## I. INTRODUCTION

The magnetron has attracted much attention lately as a means of efficiently generating high-power electromagnetic radiation. Although many successful applications of the magnetron exist, including radar and the microwave oven, the theory of the magnetron is very primitive and ad hoc. In particular, a self-consistent theory of the high-power (>GW) magnetron has yet to be developed. The major difficulties to such a theory are the presence of anode resonators and the intense self field of the electron flow at the cathode.

Previously, in an effort to develop the first self-consistent theory of the magnetron, a linear stability analysis of the extraordinary mode in both a planar and a cylindrical magnetron was performed, using a macroscopic cold-fluid model for the electron flow<sup>1</sup>. A closed analytic dispersion relation was found for each geometry in the limit of a tenuous electron flow ( $\omega_{pb}^2 \ll \omega_c^2$ ). In the present work we will present, we have lifted this tenuous flow restriction by numerically solving the eigendifferential equation characterizing an intense electron flow ( $\omega_{pb}^2 > \omega_c^2$ ) at the cathode. Details of this theoretical development, numerical techniques and initial results are presented below.

The remainder of this paper is organized as follows. Section II details the geometry employed and the development of the linearized eigendifferential equation for extraordinary mode oscillations for arbitrarily intense electron flow. It also explains the boundary conditions used to model the effect of the anode resonators. Section III describes the code developed to solve the eigendifferential equation. Section IV gives sample initial results. Finally, Section V gives the conclusion.

## II. LINEARIZED EIGENMODE ANALYSIS OF THE PLANAR MAGNETRON

The geometry employed in our analysis of the

planar magnetron is shown in Figure 1. The Brillouin electron flow is in the y-direction along the cathode whose surface lies in the y-z plane. The x-direction gives the distance from the cathode, while the applied magnetic field lies in the z-direction.

We assume extraordinary mode (TM) perturbations, since it is these perturbations that both propagate perpendicular to the applied magnetic field and have an electric field component in the direction of the electron flow:

$$\vec{\mathcal{E}} = \mathcal{E}_x(x, y, t) \hat{x} + \mathcal{E}_y(x, y, t) \hat{y}, \quad (1)$$

$$\vec{\mathcal{B}} = \mathcal{B}_z(x, y, t) \hat{z}.$$

For simplicity, a cold macroscopic fluid treatment is used for the electron flow. The resulting eigendifferential equation is the same as that found by Davidson, Tsang and Swegle<sup>2</sup> for extraordinary-mode stability of a smooth-wall planar diode, although the boundary conditions are different. These are found by the usual procedure: the fluid and Maxwell equations are linearized and Fourier decomposed ( $\sim \exp(iky - i\omega t)$ ); the eigendifferential equation follows from the consistency condition. We do not show the eigendifferential equation or its derivation here. Rather the reader is referred to Section III of reference 2. It suffices here to say that it is a second order linear eigendifferential equation for the perturbed axial electric field as a function of x, with coefficients that are non-linear function of  $\omega$ , k, x and the plasma parameters. The code written to solve this eigendifferential equation is outlined in Section III.

The boundary conditions outside the electron flow are determined from the usual admittance matching calculation at the resonator openings. In this way, the form of the perturbed axial electric field in the vacuum region is found. While this perturbed field is expressed as an infinite series of components, its interaction with the electron flow is dominated by the longest wavelength component. The perturbed electric field in this vacuum region is seen to be of the form

$$\mathcal{E}_y \sim \frac{p}{\omega} [\sin px - G(\omega, k) \cos px], \quad (2)$$

where  $p^2 = (\omega^2/c^2) - k^2$  and  $G(\omega, k)$  is a complicated function<sup>3</sup> of  $\omega$  and k. The other boundary conditions are  $\mathcal{E}_y = 0$  at the cathode, and  $\mathcal{E}_y$  and its x derivative are continuous across the plasma-vacuum interface.

### III. THE EIGENDIFFERENTIAL EQUATION CODE

The eigendifferential equation is solved in its (tridiagonal) matrix form, which results from the usual finite differencing techniques. At an  $x$  coordinate in the vacuum region the boundary condition of equation (2) is applied in the form

$$\frac{1}{\delta E_y} \frac{\partial}{\partial x} [\delta E_y] = \text{function}(\omega, k). \quad (3)$$

The desired eigenfrequencies are given by the zeroes of the determinate of the matrix, which are found by iteration from an initial guess using Mueller's method. The code can automatically find  $\omega$  over a range in any other parameter. The accuracy of the code has been successfully tested by reproducing the results of Davidson<sup>2</sup> et al for a smooth-wall diode.

### IV. RESULTS

Application of the eigendifferential equation code to the planar magnetron is now underway. An example of some early results is given in Figure 2, which shows the growth rate,  $\omega_i$ , versus the depth of the resonator cavities for two cases of intense electron flow. In this case the magnetron was

"heavily loaded": The factor  $s \equiv \omega_{pe}^2 / \omega_{ce}^2$  was 1.0 for the upper curve and 0.5 for the lower; in both cases the width of the electron for ( $x_b$ ) was 2/3 of anode-cathode spacing ( $x_a$ ). Here, the separation between the cathode surface and the back surface of a vane is denoted by  $x_c$ . Hence,  $x_c/x_b = 1.5$  implies  $x_c = x_a$  and a smooth wall.

As expected, the growth rate,  $\omega_i$ , in Figure 2 is higher for  $s=1$  than  $s=1/2$ . Also as expected,  $\omega_i$  is seen to increase with increasing cavity depth, but saturates when the resonator depth becomes comparable to the beam-anode spacing. However, the phase velocity (not shown) varies only slightly (< .5%) over this range of cavity depths, which is contrary to the expected role of the resonators as a slow wave structure. This discrepancy is probably a consequence of the intense loading of the resonator structure: the modes are determined primarily by the electron flow and not the waveguide structure.

A detailed examination of magnetron behavior over a wide range of values for the electron flow and resonator geometry is now underway, using the eigendifferential equation code.

### V. CONCLUSION

A linear stability analysis of the extraordinary mode oscillation in a planar magnetron has been developed. A cold fluid model is used for the electron flow. The resulting eigendifferential equation for the perturbed axial electric field is the same as that found previously<sup>2</sup> for arbitrarily intense electron flow in a smooth bore magnetron. However, in our treatment, boundary conditions characterizing the effect of the anode resonators (equation (3)) must be applied in the vacuum region. A code to solve this eigendifferential equation via finite difference techniques has been developed and is now operational. An initial application of the code, shown in this

paper, featured the increase of growth rates with increasing cavity depth. A thorough exploration of planar magnetron behavior over a wide range of parameters characterizing the electron flow and the geometric configuration is in progress. A similar analysis of the cylindrical magnetron is also planned.

This work was supported by IR at NSWC and SDIO-IST.

### REFERENCES

1. H. Uhm and H. Brandt, "Dispersion Relation of the Diocotron Instability in a High-Power Cylindrical Magnetron," to be published.
2. R. Davidson, et al, Phys. Fluids 27 (9), p. 2332, 1984.
3. H. Uhm and H. Brandt, "Linear Dispersion Relation for High Power Magnetron," Proc. of High Power Microwave Workshop, May 1987.

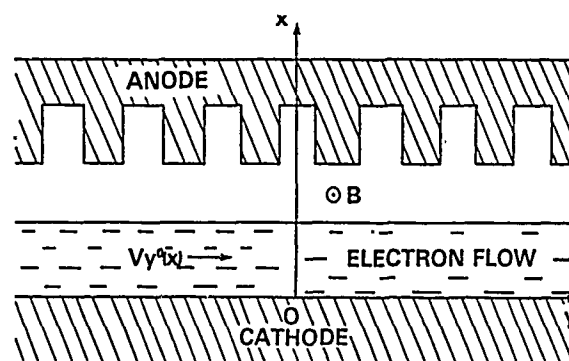


Figure 1 Growth rate versus cavity depth. Here,  $s \equiv \omega_{pe}^2 / \omega_{ce}^2$ , and the anode cathode separation is  $1.5 x_b$ .

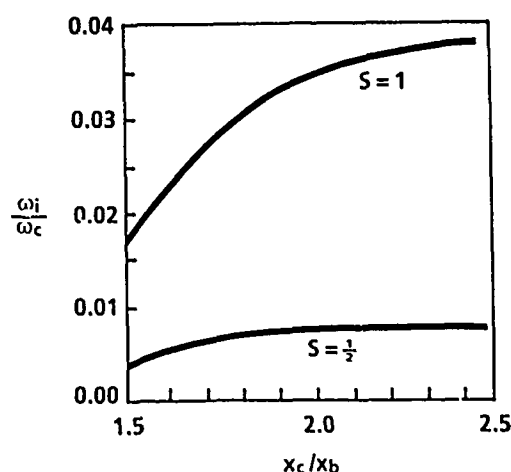


Figure 2 Geometry for Planar Magnetron Analysis

## SYMMETRY AND PERIODICITY FOR MILLIMETER WAVE DEVICES

W. N. Cain and R. W. Grow

Microwave Device and Physical Electronics Laboratory  
 Department of Electrical Engineering  
 University of Utah  
 Salt Lake City, Utah 84112

## ABSTRACT

Symmetry and periodicity is discussed as it pertains to wave propagation, with particular emphasis on Floquet's theorem and Bloch's theorem. Floquet's theorem in three dimensions is applied to a circular waveguide with screw periodicity. The resulting dispersion characteristics of the uncoupled modes are compared to those of a normal circular waveguide.

## INTRODUCTION

The topic of symmetry and periodicity is fundamental in the analysis of millimeter wave circuits. To take advantage of symmetry, a structure is often broken down mathematically to its smallest possible unit cell and analyzed accordingly. Similarly in a periodic structure, the solution is restricted to a specific form obeying Floquet's theorem, and the analysis is performed over one period only. Furthermore, the orthogonality criteria is defined over the same period.

When symmetry and translational periodicity are simultaneously present, the fundamental periodicity is assumed to be that unique transformation which describes the geometric relation (translation and rotation) between any two consecutive unit cells. Orthogonality is then defined over the unit cell.

As an example, the interdigital structure shown in Fig. 1 is invariant with respect to the transformation

$$(x, y, z) \rightarrow (x, -y, z + p/2)$$

with the result that the fundamental periodicity involves a translation of  $p/2$  and a rotation of  $\pi$  about the  $z$  axis.

## THE THEOREMS OF FLOQUET AND BLOCH

The solution to a differential equation involves the differential equation itself, as well as its boundary conditions (and/or initial conditions). When periodicity is present within the differential equation, the form of the solution is appropriately restricted. The family of periodic differential equations of the form

$$\frac{d^2\psi(x)}{dx^2} + f(x)\psi(x) = 0 \quad (1)$$

where  $f(x)$  is a periodic function with period  $p$ , are known as Hill equations. Solutions to these equations take the form

$$\psi(x + np) = \Gamma\psi(x) \quad (2)$$

$\Gamma$  being a (complex) constant and  $n$  an integer. Equation 2 is Floquet's theorem, which can be verified by linear algebra [1]. The familiar corollary to Floquet's theorem follows directly from Eq. 2; it asserts that a solution to a Hill equation can always be found of the form

$$\psi(x) = e^{jkx} u(x) \quad (3)$$

where  $u(x)$  is periodic such that

$$u(x + np) = u(x) \quad (4)$$

and  $j = \sqrt{-1}$ .

Bloch's theorem is the generalization to three dimensions of Floquet's theorem [2]. The differential equation is written in three dimensions as

$$\nabla^2\psi(\underline{r}) + f(\underline{r})\psi(\underline{r}) = 0 \quad (5)$$

where

$$f(\underline{r}) = f(\underline{r} + n\underline{R}) \quad (6)$$

The solution to Eq. 5 then takes the form

$$\psi(\underline{r}) = e^{j\underline{k}\cdot\underline{r}} u(\underline{r}) \quad (7)$$

in which

$$u(\underline{r} + n\underline{R}) = u(\underline{r}) \quad [3, 4] \quad (8)$$

Periodicity may also enter a problem through its boundary conditions. It can be shown by matrix methods that the solution to the wave equation under the constraint of a periodically varying boundary must also be of the form given in Eqs. 3 and 7 [5]. Consequently, periodic structures may be classified into two basic types: structures with periodic boundary conditions and structures with periodically varying physical properties (an example of which is a waveguide filled with a dielectric material whose dielectric constant varies in a periodic manner along the axial direction). For the latter case, the differential equation will be of the form given in Eq. 5, and in both cases, the solutions will obey Bloch's (Floquet's) theorem.

THE CIRCULAR CYLINDRICAL WAVEGUIDE  
WITH IMPOSED SCREW PERIODICITY

The gyrotron backward-wave oscillator proposed by Bunch, Grow, and Baird [6] is simply a cylindrical waveguide, with wall perturbations evenly spaced along a helical path and with azimuthal spacing of  $2\pi/\ell$ ,  $\ell$  being an integer. The case of  $120^\circ$  separation,  $\ell = 3$ , is shown in Fig. 2. The fundamental periodicity is then a translation of  $p/3$  coupled with a rotation of  $2\pi/3$ .

Assuming a homogeneous, source-free medium and harmonic time variation, the solution to the scalar Helmholtz equation

$$\nabla^2 \psi(r) + k^2 \psi(r) = 0 \quad (9)$$

is written in terms of a complete set of basis functions, each of which satisfies the differential equation and together satisfying the screw periodicity criteria:

$$\psi \sim \sum_{l,n=-\infty}^{\infty} J_l(\gamma_r) e^{j l \phi} e^{-j \beta_{l,n} z} \quad (10)$$

Application of Bloch's theorem to Eq. 10 [7] restricts the axial prepropagation constant  $\beta_{l,n}$  to the form

$$\beta_{l,n} = \beta_0 + \frac{2\pi}{p} (l - 3n) \quad (11)$$

while application of the boundary conditions restricts the radial propagation constant  $\gamma$  in the Bessel function  $J_l$  to the values

$$\gamma = \gamma_{l,i} = \begin{cases} x_{l,i}/a, & \text{TM to } z \\ x'_{l,i}/a, & \text{TE to } z \end{cases} \quad (12)$$

where  $x_{l,i}$  is the  $i$ th root of  $J_l$ , and  $x'_{l,i}$  is the  $i$ th root of  $J'_l$ . The separation equation yields the relationship

$$\gamma^2 = k^2 - \beta_{l,n}^2 \quad (13)$$

where  $k$  is the wave number of the homogeneous medium. By considering Eqs. 11 and 13,  $\beta_0$  may be written as

$$\beta_0 = k^2 - \gamma^2 - \frac{2\pi}{p} (l - 3n) \quad (14)$$

thereby providing a dispersion relationship between  $\beta$  and  $k$ . The corresponding dispersion equation for the unperturbed waveguide is

$$\beta_0 = k^2 - \gamma^2 \quad (15)$$

The lowest order mode in a normal circular waveguide is the  $TE_{11}$  or the  $TE_{-11}$  mode, each having the same dispersion characteristics, and therefore indistinguishable from one another. Equation 15 is used to obtain these dispersion characteristics for

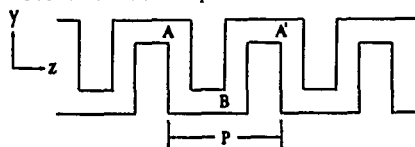


Fig. 1. Schematic of an interdigital line. The fundamental periodicity  $A + B$  involves a rotation as well as a translation. The axial periodicity  $A + A'$  is simply a linear translation.

the two modes, and these are plotted as the familiar dashed hyperbola shown in Fig. 3. Equation 14 can be used to analyze how the dispersion for these modes is affected when  $120^\circ$  screw periodicity is imposed.

For the  $TE_{\pm 11}$  modes, the dispersion equation in Eq. 14 has the form

$$\beta_0 = k^2 - \gamma_{1,1}^2 - \frac{2\pi}{p} (\pm 1 - 3n) \quad (16)$$

which results in the solid dispersion curves shown in Fig. 3. As a consequence of the screw periodicity, the two unperturbed modes have shifted -- the  $TE_{11}$  by  $-2$  and the  $TE_{-11}$  by  $2$  -- and each now consists of a complete set of space harmonics. For illustrative purposes, these modes are shown uncoupled, though coupling would occur for wall perturbations of finite size [8].

#### REFERENCES

- [1] J. Mathews and R. L. Walker, Mathematical Methods of Physics, W. A. Benjamin, Inc., Menlo Park, California, 1970.
- [2] L. Brillouin, Wave Propagation in Periodic Structures, McGraw-Hill Book Company, New York, 1946.
- [3] A. B. Boardman, D. E. O'Connor, and P. A. Young, Symmetry and Its Applications in Science, John Wiley and Sons, Inc., New York, 1973.
- [4] M. Lax, Symmetry Principles in Solid State and Molecular Physics, John Wiley and Sons, Inc., New York, 1974.
- [5] R. E. Collin, Field Theory of Guided Waves, McGraw-Hill Book Company, New York, 1960.
- [6] K. J. Bunch and R. W. Grow, "Backward-Wave Interaction Using Step-Periodic Structures," International Journal of Infrared and Millimeter Waves, Plenum Press, New York, 1988.
- [7] W. N. Cain, "The Effects of Dielectric and Metal Loading on the Dispersion Characteristics for Contrawound Helix Circuits Used in High Power Traveling-Wave Tubes," Technical Report AFTER-30, Microwave Device and Physical Electronics Laboratory, Department of Electrical Engineering, University of Utah, Salt Lake City, Utah, 1988.
- [8] M. H. Chen, Electromagnetic Wave Propagation Characteristics of Periodic Structures with Screw Symmetry, Ph.D. Dissertation, Polytechnic Institute of Brooklyn, Brooklyn, New York, 1969.

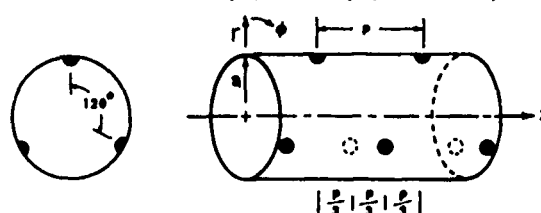


Fig. 2. Schematic of  $120^\circ$  screw periodicity imposed on a circular waveguide.

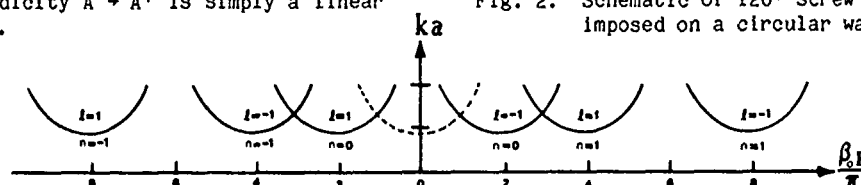


Fig. 3. The dispersion characteristics of the  $TE_{11}$  and the  $TE_{-11}$  modes. The  $TE_{\pm 11}$  mode of the unperturbed waveguide (dashed curve) separates into two distinct modes and their associated space harmonics when screw periodicity is imposed.



# MICROWAVE LOSSES IN HIGH T<sub>c</sub> SUPERCONDUCTING MICROSTRIP RING RESONATORS

June Takemoto, Floyd Oshita, Harold Fetterman

Department of Electrical Engineering  
University of California, Los Angeles  
Los Angeles, CA

Paul Kobrin, Emilio Sovero

Rockwell International Corporation Science Center  
1049 Camino Dos Rios  
Thousand Oaks, CA

## ABSTRACT

Microwave properties of high T<sub>c</sub> superconducting films sputtered on MgO were measured using a closed-loop ring resonator circuit. Unloaded Q values of Y-Ba-Cu-O and Bi-Sr-Ca-Cu-O resonators were compared to gold plated resonators of identical design. The attenuation of yttrium-barium-copper oxide films on a MgO substrate is approximately 31% lower than gold films at 6.6 GHz and 33% lower at 19.2 GHz for temperatures below 50 K.

## INTRODUCTION

High T<sub>c</sub> superconductors have received considerable interest for possible thin film applications in microwave integrated electronics. The absence of dc resistivity and reduced microwave attenuation offer performance advantages over devices and circuits made with conventional gold conductors. Experiments have been performed to characterize these new superconductors at microwave and millimeter-wave frequencies on high Q cavity resonators [1] - [5]. In this paper we report results on microwave attenuation in Y-Ba-Cu-O (YBCO) and Bi-Sr-Ca-Cu-O (BSCCO) superconductors based on Q factor measurements of microstrip ring resonators. This is the first reported experimental implementation of microstrip to obtain results on microwave losses in thin film high T<sub>c</sub> superconductors.

## MICROSTRIP RING RESONATORS

Microstrip resonators have been used extensively to study dispersion, effective dielectric constant, and microwave attenuation on dielectric substrates. The most widely used resonators are the ring resonator and the open-ended linear resonator. Open-ended linear resonators suffer from considerable losses due to radiation from the open ends, which can complicate the determination of microstrip conductor losses. The ring resonator, however, offers the advantage of no open end effects so that the attenuation sources result primarily from dielectric and conductor losses. The resonance mode is governed by the multiple lengths of the mean ring diameter which is given by  $D_0 = n\lambda_g/\pi$ , where  $\lambda_g$  is the guide wavelength and  $n$  is the resonance mode.

## FABRICATION OF SAMPLES

The samples tested had a mean diameter of 213 mils, ring width of 20 mils, conductor thickness of 1  $\mu$ m for YBCO and 1/2  $\mu$ m for BSCCO, and a MgO substrate thickness of 20 to 30 mils with a dielectric constant of 10. The microstrip input lines were designed to match the 50  $\Omega$  impedance of the rf power source. The superconducting thin films were sputtered at 700°C and then annealed at 850°C in oxygen for YBCO and at 880°C for BSCCO samples. Ring resonator patterns were printed onto the films by using standard semiconductor photolithographic techniques. Etching of unwanted films was accomplished with argon ion milling. Due to difficulties encountered with the fabrication of superconducting thin films on both sides, a plated gold layer was used for the microstrip ground plane. As a comparison identical gold plated ring resonators were also fabricated. Since the resonator design was not optimized for maximum Q, higher Q values are achievable through careful design of coupling gap, ring geometry, and characteristic impedance.

## ANALYSIS

From swept frequency reflection measurements, the unloaded Q is calculated [6]. The unloaded Q may be derived from either the reflection-amplitude response or the reflection-phase response taken from either port of the resonator.

The unloaded Q of a microstrip resonator is related to the various loss mechanisms in a microstrip line

$$\frac{1}{Q_t} = \frac{\lambda_g}{\pi} (\alpha_c + \alpha_d) + \frac{1}{Q_r} \quad (1)$$

where  $\alpha_c$  and  $\alpha_d$  are the conductor and dielectric loss constants in Np/m,  $\lambda_g$  the guide wavelength, and  $Q_r$  the radiation quality factor [7]. The conductor loss constant  $\alpha_c$  is estimated from the expression

$$4\pi\alpha_c Z_0 = B \{ (C+D) R_{S1} + C R_{S2} \} \quad (2)$$

where,

$$B = 1 - \frac{w^2}{16h^2}$$

$$C = \frac{1}{h} \left( 1 - \frac{1}{\pi w} \right)$$

$$D = \frac{2}{w'} \left( 1 + \frac{1}{\pi} \ln \frac{2h}{t} \right)$$

$$w' = w + \frac{t}{\pi} \left( \ln \frac{2h}{t} + 1 \right)$$

and  $Z_0$  is the characteristic impedance,  $R_{S1}$  and  $R_{S2}$  are the surface resistivity of the strip and ground plane metallization, and  $w$ ,  $h$ , and  $t$  are the microstrip width, substrate height, and metallization thickness, respectively [8].

In order to separate out the loss contribution due to a gold ground plane in the superconducting sample, the following first order procedure is used. It is assumed that the dielectric and radiation losses are identical in both the superconducting and gold samples, so that a difference in the unloaded  $Q$ 's arises from a difference in conductor losses. Combining equations (1) and (2) yields an expression for the surface resistivity  $R_{ss}$  of the superconductor,

$$R_{ss} = R_{sa} - \frac{4 \pi Z_0}{B(C+D)} (\alpha_{ca} - \alpha_{cs}) \quad (3)$$

where  $\alpha_{cs}$  is the conductor loss in the superconducting sample,  $\alpha_{ca}$  the conductor loss in the gold sample, and  $R_{sa}$  the surface resistivity of plated gold.  $R_{sa}$  is computed from equations (1) and (2) with the assumption that dielectric and radiation losses are negligible at cryogenic temperatures. Once  $R_{ss}$  is obtained, the above equations can be used to compute the attenuation  $\alpha_{css}$  and the unloaded  $Q_{ss}$  in an ideal sample with superconductors on both sides.

## RESULTS AND DISCUSSION

The ring resonators were mounted in test fixtures and placed in a closed cycle refrigerator. The fixture is connected via semirigid coaxial cables to a Hewlett Packard 8510A automatic network analyzer. In addition, a four point probe is attached to a strip of superconductor on the same substrate to monitor the DC resistivity.

The YBCO and BSSCO samples had transition temperatures of 72 K and 69 K, respectively. A comparison of the unloaded  $Q$  vs. temperature for both the gold and YBCO samples is shown in Figure 1. The unloaded  $Q$  obtained from the YBCO sample is higher than the gold sample by 39% at 6.6 GHz and 42% at 19.2 GHz at 40 K. Since the superconducting sample was fabricated with a gold ground plane, a higher  $Q$  is expected for a superconducting ground plane.

Figure 2 plots the temperature dependence of conductor attenuation  $\alpha_c$  for the gold and YBCO samples. The conductor loss for YBCO is lower than gold by 31% at 6.6 GHz and 33% at 19.2 GHz at 40 K. The sharp drop in  $\alpha_c$  below the transition temperature and subsequent gradual decline below 60 K is consistent with the qualitative two fluid picture, in which the fraction of electrons in the normal state decreases rapidly below the transition temperature. The relatively high attenuation in both samples can be attributed to the high surface

roughness of the commercial MgO substrates. The BSSCO sample was measured to have 2 times higher conductor loss than gold. The higher loss could be due to the current sputtering technique for this particular compound or the inherent two-phase nature of the new material.

The results of this investigation have demonstrated that the microstrip performance of certain high  $T_c$  superconductors is better than conventional gold conductors at microwave frequencies. Characterization of attenuation losses in superconducting microstrips can also be extended to the millimeter-wave range. Higher performance is expected as the fabrication quality of superconducting thin films is improved.

## REFERENCES

- [1] T. M. P. Percival, J. S. Thom, and R. Driver, *Elec. Lett.* 23 (23), 1225 (1987).
- [2] M. Poirier, G. Quirion, K. R. Poeppelmeier, and J. P. Thiel, *J. Appl. Phys.* 63 (5), 1646 (1988).
- [3] J. S. Martens, J. B. Beyer, and D. S. Ginley, *Appl. Phys. Lett.* 52 (21), 1822 (1988).
- [4] J. P. Carini, A. M. Awasthi, W. Beyermann, G. Gruner, T. Hylton, K. Char, M. R. Beasley, and A. Kapitulnik, *Phys. Rev. B* 37 (16), 9726 (1988).
- [5] C. Zahopoulos, W. L. Kennedy, and S. Sridhar, *Appl. Phys. Lett.* 52 (25), 2168 (1988).
- [6] J. Aitken, *Proc. IEE*, 123 (9), 885 (1976).
- [7] A. Gopinath, *IEEE Trans. Microwave Theory Tech.* 29 (2), 128 (1981).
- [8] R. A. Pucel, D. J. Masse, and C. P. Hartwig, *IEEE Trans. Microwave Theory Tech.* 16 (6), 342 (1968).  
-----, *ibid.*, 16 (12), 1064 (1968).

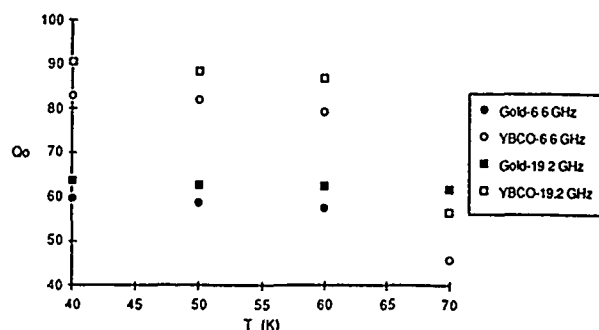


Figure 1. Unloaded  $Q$  vs. temperature plot shows that the YBCO film has a sharp transition to saturated  $Q_0$  below  $T_c$ .

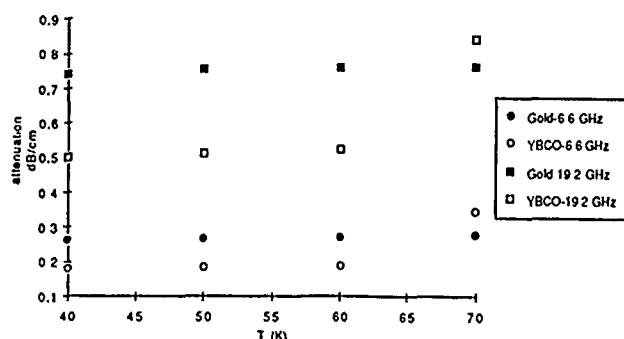


Figure 2. Conductor attenuation vs. temperature plot shows that the YBCO microstrip has a lower microwave loss than the gold microstrip.

## MICROWAVE PHASE CONJUGATION IN ARTIFICIAL KERR MEDIA

Robert Shih, Harold R. Fetterman, Bradley Bobbs  
Department of Electrical Engineering, University of California  
Los Angeles, California 90024

William W. Ho, Robert McGraw, Dan Rogovin  
Rockwell International Science Center  
1049 Camino dos Rios, Thousand Oaks, California 91360

### ABSTRACT

One dimensional phase conjugation of microwaves via degenerate four-wave mixing in an artificial Kerr medium has been demonstrated. The medium consisting of a liquid suspension of elongated graphite particles is confined within a single mode waveguide. The decay of the nonlinear refractive index grating is shown to agree with previous relaxation time measurements.

### INTRODUCTION

Recent interest in degenerate four-wave mixing in artificial Kerr media to produce a phase conjugate wave has concentrated on the visible spectrum [1-6]. Attempts to extend this technique to the millimeter wave and microwave spectral regions encounter severe difficulties. A much greater medium nonlinearity is required to offset the limitation in the number of interference fringes that can be fit into practical interaction lengths. Large diffraction effects limit the intensities and interaction lengths obtainable by focussing. The former problem may be solved by the use of artificial Kerr media, the latter by confinement in a waveguide. In a single mode waveguide, however, wavefront perturbations cannot propagate. Phase conjugation therefore reduces in this case to a one-dimensional conjugation capable only of correcting for piston error. Observation of this conjugate wave with a slow response medium has been proposed using a two-step procedure illustrated in Figure 1 [7]. In 1(a) a nonlinear refractive index grating is written by counterpropagating pump and probe waves. In 1(b), both these waves have been turned off, and a pump wave approaching from the opposite side reads (scatters off) the grating to produce a wave which is the conjugate of the probe. This conjugate signal will decay in intensity as thermal equilibration of the medium washes out the grating.

### EXPERIMENT

The nonlinear medium used in the present study contains short elongated graphite fibers with a diameter of 7 to 8 microns and aspect ratio of 3 to 5. These particles are suspended in a mixture of 60% mineral oil and 40% heptane. This medium has been characterized [8] as having an unsaturated nonlinear refraction coefficient of  $2.6 \times 10^{-4} \text{ cm}^2/\text{W}$  produced by an orientational mechanism. Excellent agreement was obtained between theory

and experiment for the time response of the medium [9]. The suspension is highly transparent, having a loss length ( $1/e$  attenuation) of 140 cm at 18 GHz.

The schematic of the experimental setup is shown in Figure 2. An RF oscillator at roughly 18 GHz is used to drive a TWT amplifier producing a maximum of 20 W of continuous power. A 3 dB directional coupler splits the power to form pump and probe waves. The probe wave passes through the 35 cm sample chamber containing the nonlinear medium from right to left in Figure 2, with the pump wave counterpropagating. After allowing about a minute for buildup of the nonlinear grating, the pump wave is turned off using a variable attenuator. What was previously the probe wave now functions as the second pump wave in Figure 1(b). The conjugate wave reflected from the grating is measured at power meter #2. Sensitivity is maximized by tuning the RF oscillator frequency to minimize the signal reflected by the sample chamber windows after the grating has completely decayed.

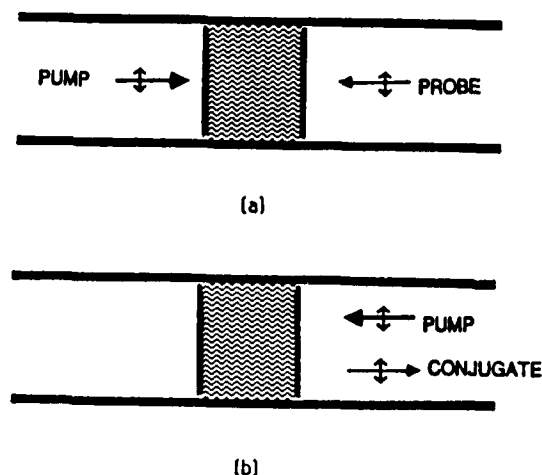


Fig. 1. Schematic diagrams of write and read of the phase conjugate grating. (a) The phase conjugate grating is written by the pump and the probe waves. (b) The phase conjugate grating is read by the pump wave to form the conjugate wave.

Figure 3 shows the time evolution of the reflected wave after turning off the first pump wave. It follows an exponential decay with a time constant of 20 sec. This value is roughly independent of power, indicating operation within the low power regime, and agrees with the previously determined [8] relaxation time for this medium. We therefore identify this signal as being reflected from the nonlinear grating and hence a phase conjugate wave produced by four-wave mixing.

### CONCLUSION

We have observed direct evidence of the nonlinear refractive index grating responsible for one-dimensional phase conjugation of microwaves. The temporal decay of the return signal agrees with previous measurements for the artificial Kerr medium used, confirming its production by four-wave mixing and hence its phase conjugate nature. We are currently pursuing the possibility of detecting simultaneous microwave phase conjugation inside a waveguide via polarization discrimination to separate the pump and conjugate signals [10]. Three-dimensional phase conjugation using free space propagation is also currently under investigation.

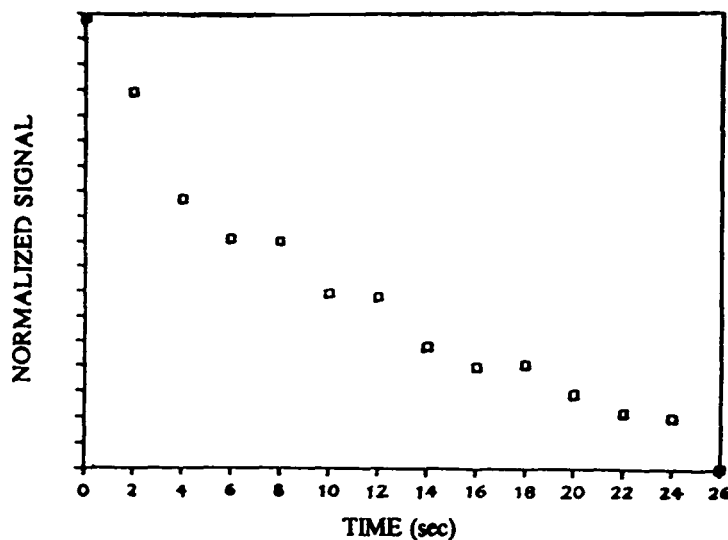


Fig. 3. Normalized phase conjugate signal as a function of time. The decay of the signal corresponds to the relaxation of grating formed by the particles to their equilibrium positions.

### ACKNOWLEDGEMENTS

This work was supported in part by the U. S. Air Force Office of Scientific Research.

### REFERENCES

- [1] P.W. Smith, A. Ashkin, and W.J. Tomlinson, *Opt. Lett.* 6, 284 (1981).
- [2] D. Rogovin and S. Sari, *Phys. Rev. A* 31, 2375 (1985).
- [3] S. Sari and D. Rogovin, *Opt. Lett.* 9, 414 (1984).
- [4] D. Rogovin, *Phys. Rev. A* 32, 2837 (1985).
- [5] R. McGraw and D. Rogovin, *Phys. Rev. A* 34, 689 (1986).
- [6] D. Rogovin, R. McGraw, and P. Yeh, *Phys. Rev. Lett.* 55, 2864 (1985).
- [7] B. Bobbs, Ph.D. dissertation, University of California, Los Angeles (1988).
- [8] B. Bobbs, R. Shih, H. Fetterman, and W. Ho, *Appl. Phys. Lett.* 52, 4 (1988).
- [9] R. McGraw, D. Rogovin, W. Ho, B. Bobbs, R. Shih, H. Fetterman, *Phys. Rev. Lett.* Aug (1988).
- [10] D. Pepper, D. Fekete, and A. Yariv, *Appl. Phys. Lett.* 33(1), 1978.

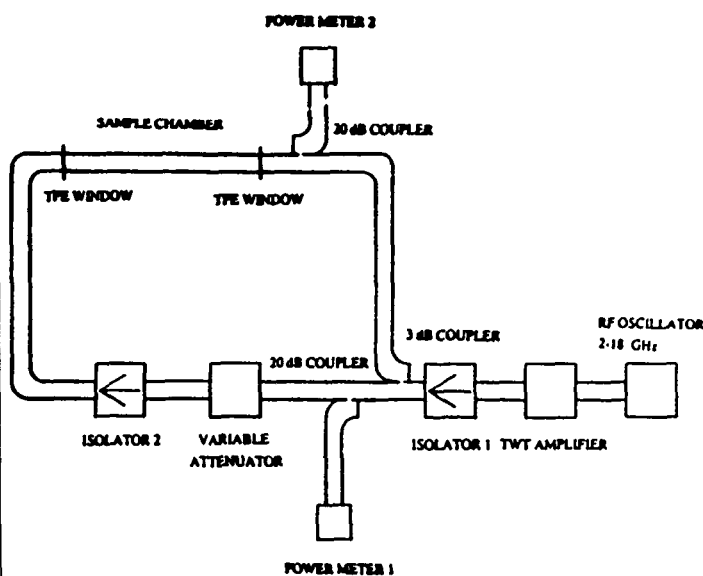


Fig. 2. Schematic diagram of the experimental setup.

## MAGNETOPOLARON EFFECTS IN CdTe

J. Oberti, M. Goiran, M. Bouchelagem, R. Triboulet\*, J. Léotin

Laboratoire de Physique des Solides, associé au CNRS  
INSA, Avenue de Rangueil, 31077 Toulouse-Cedex (France)

\* Laboratoire de Physique des Solides CNRS, 92190 Meudon.

## ABSTRACT

The electron cyclotron effective mass in CdTe was measured with photons having energy ranging from 12 to 250  $\text{cm}^{-1}$ . The expected dramatic decrease of the mass when the photons energy exceeds that of the LO phonons is shown for the first time. Accurate measurements at 4K were made possible by a free carrier persistent effect occurring in the samples investigated. The magnetic field resonance values at various photons excitation energies were fitted by using a recent accurate calculation of the magnetooptic absorption by Peeters and Devreese. This new theory produces a good fit with the data when taking the electron Frölich constant value  $\alpha = 0.3$  and adjusting the band mass to the value  $m_b = 0.092 m_0$ . Previous results and theory favours the values  $\alpha = 0.4$  and  $m_b = 0.089 m_0$ .

## INTRODUCTION

Cadmium Telluride is recognized as the most suitable semiconductor material to study the polaron effect which originates from the electron coupling to the LO phonons. This effect gives rise to the polaron (electron + lattice distortion) having a mass value higher than the electron band mass in absence of coupling.

The relevant parameter to be measured is the cyclotron mass performed by exciting the cyclotron resonance with radiation ranging from a few wavenumber to well above the LO phonon wavenumber  $\nu_{LO} = 171 \text{ cm}^{-1}$ . However previous experiments (1, 2) failed to measure above the LO phonon, missing the interesting frequency range where the cyclotron effective mass should exhibit a substantial decrease. The resonant magnetic fields are above the crossing value  $B_{LO}$  for which the

LO phonon energy equals the cyclotron energy in absence of coupling. In addition, only recently it exists a realistic model developed by Peeters and Devreese (hereafter PD) accurate enough to account for the effective mass value in the whole range of magnetic fields.

The experimental difficulty is twofold. First the magnetic field crossing value  $B_{LO}$  is 16.8 teslas, therefore magnetic fields in the 40 teslas range are required. Second the exciting radiation energy falls above  $170 \text{ cm}^{-1}$  where infrared sources poorly exist. The new magnetooptic spectrometer built at Toulouse enables to overcome part of the problems (3). Finally high purity ingots having an ionized free carriers density  $N_D - N_A = 10^{13} \text{ cm}^{-3}$  were grown at the CNRS-Meudon Laboratory. These samples offer the advantage of a persistent effect giving at helium temperatures after band gap illumination a free carriers density above  $10^{12} \text{ cm}^{-3}$  (4). At 4K the mobility is value high enough than to give rise to Landau quantization even at very low magnetic fields values. Consequently, sharp resonance signals were obtained corresponding to the transition from  $N = 0$  to  $N = 1$  Landau Level. Accurate determinations of the cyclotron masses with exciting radiation at the frequencies  $\omega$  are simply obtained with the relation  $m = eB/\omega$ , where  $B$  is the resonant magnetic field. The band electron mass  $m_b$  at the band edge could be deduced by the relation  $m^* = m_b (1 + \frac{\alpha}{2})$  which is accurate for  $\alpha \ll 1$ .  $\alpha$  is the electron-LO phonon coupling constant  $m^*$  is the measured cyclotron mass in the limit of low energy of exciting photons. One should recall the Frölich coupling constant expression :

$$\alpha = \frac{1}{2} \frac{e^2}{\sqrt{k/2m_b\omega_{LO}}} \left( \frac{1}{\epsilon_\infty} - \frac{1}{\epsilon_0} \right) \frac{1}{\hbar\omega_{LO}}$$

$\epsilon_0$  and  $\epsilon_\infty$  are the static and high frequency dielectric constants. In CdTe  $\epsilon_0 = 9.4 - 10.6$ ,  $\epsilon_\infty = 7.1 - 7.4$ ,  $\alpha = 0.22 - 0.35$ .

### RESULTS AND DISCUSSION

- Fig.1 displays cyclotron absorption signals for several wavelength values of the exciting radiation at the temperature 10 K. The resonance at 20.7 teslas is excited with the  $41 \mu\text{m}$  wavelength radiation having a frequency higher than the LO phonons. A broadening and a decrease of the absorption occurs above the crossing field  $B_{LO}$ .

- Fig.2 shows the measured effective mass value at various magnetic fields. The vertical dashed line indicates the crossing field value  $B_{LO}$  at which the LO phonon and the electron cyclotron frequency (not the polaron) are the same. Previous experimental points obtained by Waldman et al and by Mears et al are also reported. The solid line is a theoretical fit of our data by Peeters and Devreese when taking the coupling constant  $\alpha = 0.3$ . They found the electron band mass value  $m_b = 0.092m_0$  at the band edge (5). The PD approach calculates the CR absorption spectrum using the real part of the conductivity tensor expressed in terms of a memory function (6). Earlier theoretical calculations by Larsen underestimated the polaron correction. A higher value of  $\alpha = 0.4$  was necessary to achieve the best fit of Waldman et al results (2).

In conclusion, we expect that in the near future more data points above  $B_{LO}$  become available. In this case, it is likely that both the band mass parameters and the Frölich constant could be adjusted for the best fit of data. If so, a narrower range of appropriate values of  $\alpha$  would give a higher accuracy for the dielectric constant.

### REFERENCES

- [1] A.L. Mears and R.A. Stradling, Solid. Stat. Comm. **7**, 1267, (1969).
- [2] J. Waldman, D.M. Larsen, P.E. Tannewald, C.C Bradley, D.R. Cohn and B. Lax, Phys. Rev. Lett. **23**, 1033 (1969).
- [3] J. Oberti, thèse de Doctorat INSA Avenue de Rangueil, Toulouse (1988).
- [4] K. Pastor, E. Goldys, Solid. State Comm. **55**, 671 (1985).
- [5] J.T. Devreese and F.M. Peeters, A.R.W. on Growth and Optical properties of Widedag I

I-VI, Lowdimensional S.C., Regensburg, August 1988.

[6] F.M. Peeters and J.T. Devreese, Phys. Rev. B-34, 7246 (1986).

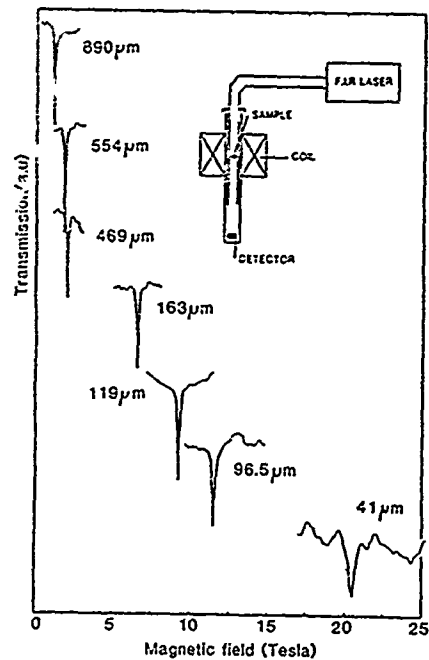


Figure 1

CR Transmission signals measured at 10 K in CdTe. The insert shows a schematic view of the spectrometer.

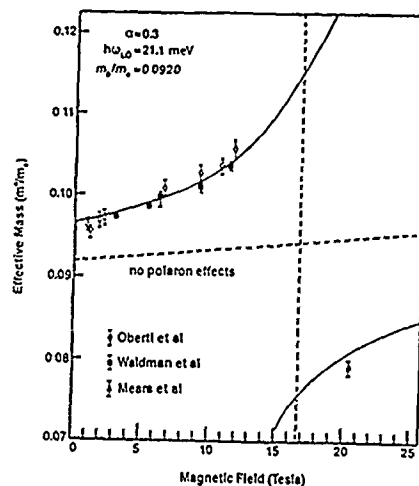


Figure 2

Experimental results and theoretical calculation of the polaron effective mass versus magnetic field in CdTe (after J.T. Devreese and F.M. Peeters, ref.5).

## QUANTUM LIMIT ELECTRON-PHONON SCATTERING STUDIES IN SEMICONDUCTORS BY FAR-INFRARED CYCLOTRON RESONANCE

H.Kobori, T.Ohyama and E.Otsuka

College of General Education, Osaka Univ., Toyonaka, Osaka 560, Japan

## ABSTRACT

Extensively systematic studies of the cyclotron resonance linewidth in the quantum limit have been performed on electron-phonon scattering in basic semiconductors (Ge, CdS, GaAs). Far-infrared (119 to 513  $\mu\text{m}$ ) laser cyclotron resonance experiments have been carried out in photo-excitation by pulsed band gap light or in thermal excitation. We present the temperature and magnetic field dependences of cyclotron resonance linewidth for electron-phonon scattering in the quantum limit with respect to various samples.

## INTRODUCTION

Cyclotron Resonance Line-Width (CRLW) is directly connected with the information of transport relaxation mechanism of carriers. It represents the total sum of transport relaxation probabilities from various scatterings. As the cyclotron resonance is a resonant absorption of AC electric field in magnetic field, the quantum effect due to magnetic field is expected on transport relaxation of carriers. If the electron gas is non-degenerate, the threshold of the quantum effect will be  $\hbar\omega_c \sim k_B T$  ( $\omega_c$ : cyclotron angular frequency and  $T$ : temperature). In the classical limit  $\hbar\omega_c \ll k_B T$ , a large number of cyclotron resonance experimental studies have been reported at microwave frequencies, particularly those in Ge and Si [1][2]. The relaxation time derived from CRLW has been describable by the prediction from DC transport theory in the absence of a magnetic field.

In the quantum limit  $\hbar\omega_c \gg k_B T$ , the effect of the magnetic field cannot be neglected. Semi-classical treatment is unsatisfactory and a quantum statistical one is required. There have been extensive experimental theoretical studies, particularly for the ionized impurity scattering in InSb. Experimental and theoretical aspects are frequently inconsistent and even internally contradictory to each other. Accordingly, extensively systematic experimental studies are long hoped for in basic semiconductors. Meyer[3] first pointed out, in the quantum regime, that CRLW for acoustic deformation potential scattering could not be explained by the classical transport relaxation time and intuitively deduced quantum formulae assuming that transport relaxation time in the quantum limit was determined by inter-Landau level scattering from  $n=1$  to 0 ( $n$ : Landau quantum number). Arora-Spector[4] and Suzuki et al.[5] obtained equivalent results to each other apart from a constant multiplying factor for the same scattering using density operator and proper connected diagram expansion methods, respectively, assuming elastic and intra-Landau level scatterings from  $n=0$  to 0 and  $n=1$  to 1. subsequently Suzuki-Dunn[6] removed the assumption of elastic scattering by taking numerical analysis. Saitoh-Kawabata [7] obtained a formula for acoustic piezo-electric scattering with the help of Mori's projection operator method.

We present CRLW in the quantum limit for both acoustic deformation potential and acoustic piezo-electric scatterings in Ge, CdS and GaAs as a function of temperature and magnetic field for various samples. Analysis of CRLW in GaAs contains impurity and carrier-carrier scatterings as well as phonon scatterings, since the former ones cannot be neglected for employed GaAs samples. Details of impurity and carrier-carrier scatterings are given in the next paper[8].

## EXPERIMENTAL RESULTS AND DISCUSSIONS

The CRLW or the inverse relaxation time caused by various scatterings has been derived making use of the following relation:

$$\Gamma \equiv 1/\langle\tau\rangle = \omega_c \Delta B / 2B_r \quad (1)$$

where  $\omega_c = eB_r/m^*c$  with the effective mass of conduction electron  $m^*$ ,  $\Delta B$  the cyclotron resonance half-width and  $B_r$  the resonance magnetic field. The brackets denotes an appropriate thermal average.

Figure 1 shows the temperature dependence of the inverse relaxation time in pure Ge for a wavelength of 119  $\mu\text{m}$  in photo-excitation by a xenon flash lamp. The impurity concentration of employed pure Ge sample is such that  $N_A - N_D = 10^{12} \text{ cm}^{-3}$ , where  $N_A$  is the acceptor and  $N_D$  the donor concentration[9]. The contribution of carrier-carrier scattering has been excluded by taking signal at a sufficiently long interval between photo-excitation and aperture, where CRLW becomes constant in time. Therefore we expect that acoustic deformation scattering is dominant under the condition we have carried out experiments. As seen from Fig. 1, the inverse relaxation time for acoustic deformation potential scattering is larger in the quantum limit than the classical limit and proportional to temperature.

Figure 2 indicates the temperature dependence of the inverse relaxation time in n-CdS for a wavelength of 220  $\mu\text{m}$  in photo- and thermal excitations. Acoustic piezo-electric scattering is supposed to be dominant in CdS because of large piezo-coupling constant. Certainly for CdS, it is known that this scattering is more dominant than acoustic deformation potential one from DC Hall measurements. The contribution from impurity and carrier-carrier scatterings seems to be small in comparison with one from acoustic piezo-electric scattering. Indeed we have observed that CRLW of former scatterings is almost independent of temperature. As shown from Fig. 2, the inverse relaxation time for acoustic piezo-electric scattering is nearly proportional to temperature like acoustic deformation potential scattering.

Figure 3 shows the temperature dependence of the inverse relaxation time in n-GaAs for a wavelength of 119  $\mu\text{m}$  in thermal excitation. The impurity concentration is such that  $N_D = 5.5 \times 10^{15} \text{ cm}^{-3}$  and  $N_A = 1.5 \times 10^{15} \text{ cm}^{-3}$ . Designated "ND, C-C, II, DP, PE and  $\rho O$ " indicates the neutral donor, carrier-

carrier, ionized impurity, acoustic deformation potential, acoustic piezo-electric and polar optical phonon scatterings, respectively. The assumption of linear temperature dependence of the inverse relaxation times for both acoustic deformation potential and acoustic piezo-electric scatterings in the quantum limit reproduce our experimental results. Other parameter dependences, eg, magnetic field, different samples, for phonon scatterings will be presented and discussed in the later proceeding. Magnetic field dependence of the inverse relaxation time is given in Fig. 4 on acoustic deformation potential scattering in the quantum limit.

#### REFERENCES

- [1] E.Otsuka, K.Murase and J.Iseki: J.Phys.Soc.Jpn. 19 30 (1964)
- [2] T.Ohyama, K.Murase and E.Otsuka: J.Phys. Soc.Jpn. 29 912 (1972)
- [3] H.J.G.Meyer: Phys.Lett. 2 259 (1962)
- [4] V.K.Arora and H.N.Spector: Phys.Stat.Sol. (b) 94 701 (1979)
- [5] A.Suzuki, S.D.Choi and S.Fujita: J.Phys.Chem. Sol. 41 735 (1980)
- [6] A.Suzuki and K.Dunn: Phys.Rev. B25 7754 (1982)
- [7] H.Saitoh and A.Kawabata: J.Phys.Soc.Jpn 23 1006 (1967)
- [8] H.Kobori, and T.Ohyama and E.Otsuka: the subsequent paper
- [9] H.Kobori, and T.Ohyama and E.Otsuka: Sol. Stat.Comm. 64 35 (1987)

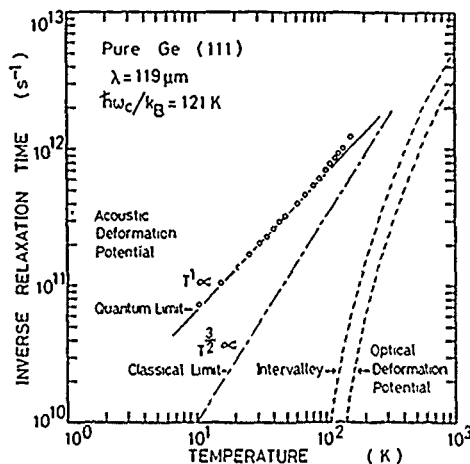


Fig. 1 Dependence on temperature of the inverse relaxation time is taken between 10 and 160 K in pure Ge sample at  $\langle 111 \rangle$  magnetic field direction for a wavelength of  $119 \mu\text{m}$  in photo-excitation.

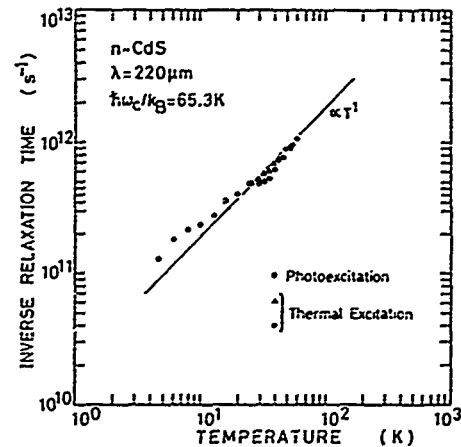


Fig.2 Temperature dependence of the inverse relaxation time between 4.7 and 60 K in n-CdS sample at magnetic field direction parallel to c-axis for a wavelength of  $220 \mu\text{m}$  in both photo- and thermal excitation.

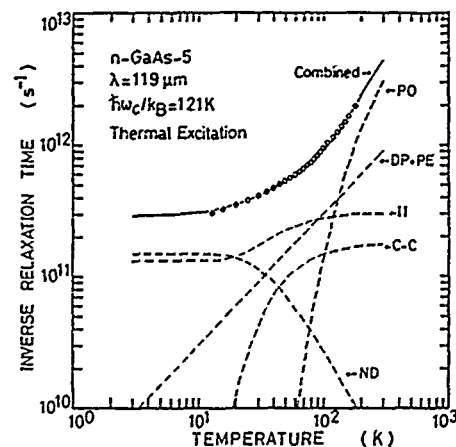


Fig.3 Temperature dependence of the inverse relaxation time between 13 and 180 K in n-GaAs sample for a wavelength of  $119 \mu\text{m}$  in thermal excitation.

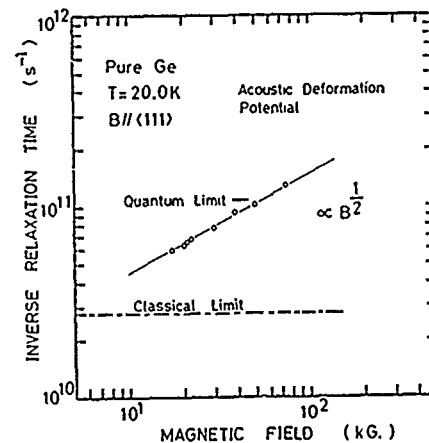


Fig.4 Magnetic field dependence of the inverse relaxation time in pure Ge sample at the  $\langle 111 \rangle$  magnetic field direction for a wavelength of 513, 433, 419, 394, 295, 220, 172 and  $119 \mu\text{m}$  at 20 K.



# FAR-INFRARED CYCLOTRON RESONANCE STUDIES OF IMPURITY SCATTERING IN Ge, GaAs AND InSb

Hiromi Kobori, Tyuzi Ohyama and Eizo Otsuka

College of General Education, Osaka University, Toyonaka, Osaka 560, Japan

## ABSTRACT

Contribution of impurity scattering to the electron cyclotron resonance linewidth (inverse relaxation time) has been studied in the quantum limit, after subtracting the contribution of phonon scattering, for typical semiconductors Ge, GaAs and InSb. To our surprise, dependence of inverse relaxation time on temperature, magnetic field and impurity concentration is the same for neutral and ionized impurities.

## INTRODUCTION

Linewidth of cyclotron resonance is comprised by phonon scattering and impurity scattering. Now that the contribution of phonon scattering, to be more exact acoustical deformation potential phonon scattering, has been precisely determined [1], it is easy to discuss the behavior of impurity scattering. The genuine contribution of impurity scattering can be derived simply by subtracting the phonon scattering contribution from the observed linewidth. At low temperatures, where the quantum limit condition  $\hbar\omega_c \gg k_B T$  all the more prevails, the free carriers can generally be produced only by band-gap photoexcitation. The free carriers thus produced promptly neutralize the impurities. Thus the impurity scattering is generally due to neutral impurities. At higher temperatures, free carriers can be generated thermally from the impurity sites, which are left in ionized states. Then one can observe cyclotron

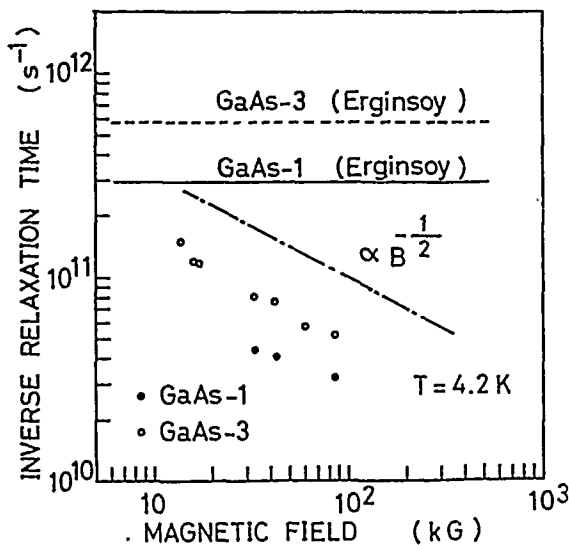


Fig. 1. Magnetic field dependence of the electron inverse relaxation time due to neutral impurities obtained for two n-type GaAs samples (GaAs-1:  $N_D = 7.5 \times 10^{14} \text{ cm}^{-3}$ ,  $N_A = 5.0 \times 10^{14} \text{ cm}^{-3}$ ; GaAs-3:  $N_D = 1.5 \times 10^{15} \text{ cm}^{-3}$ ,  $N_A = 1.0 \times 10^{15} \text{ cm}^{-3}$ ). Horizontal lines indicating "Erginsoy" are field independent classical predictions [3].

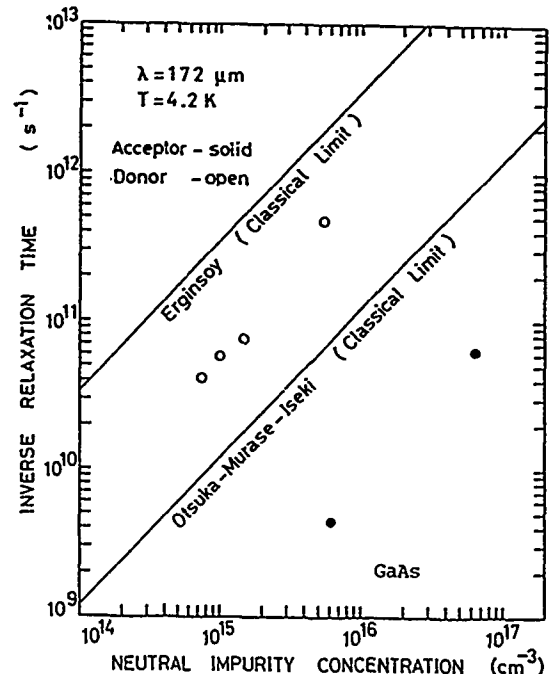


Fig. 2. Concentration dependence of the electron inverse relaxation time due to neutral donors (open circles) and acceptors (solid circles). Solid lines are classical predictions for donors (Erginsoy) [3] and acceptors (Otsuka et al.) [2,4].

resonance without the help of band-gap photoexcitation and, at the exhaustion range, all we are observing is the ionized impurity scattering.

What is said above is the general argument. There exists, of course, exception. Typically, InSb is a material in which total neutralization of impurities is hard even by band-gap photoexcitation. This character, however, offers us an advantage of seeing difference between attractive and repulsive electron scatterings.

## EXPERIMENTAL

Experimental details are more or less the same with the preceding paper. Far-infrared laser wavelength varies 519 to 119  $\mu\text{m}$  (578 to 2521 GHz). Time resolution technique has been essential to avoid the carrier-carrier scattering. Germanium crystals have been those doped only with antimony. Gallium arsenide samples are both n- and p-type with different impurity concentrations. Indium antimonide sample is an almost fully compensated n-type one.

## NEUTRAL IMPURITIES

For studying neutral impurity scattering, GaAs has been employed. With Ge, it is difficult to secure low cyclotron mass electrons enough to observe a good cyclotron resonance signal at low

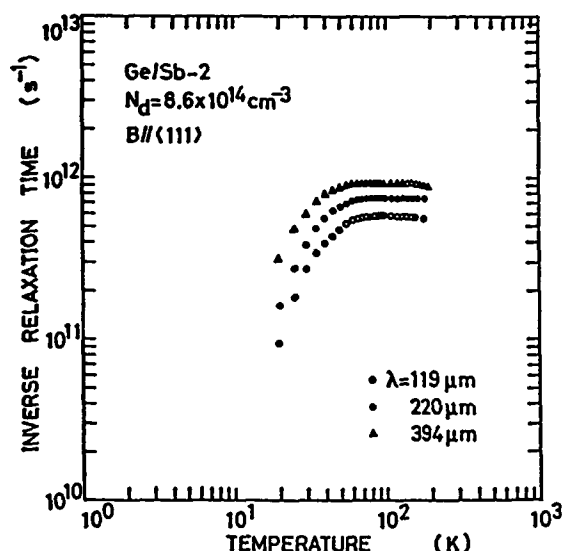


Fig. 3. Temperature dependence of the electron inverse relaxation time due to ionized impurity scattering from an Sb-doped Ge sample, without photoexcitation, for three FIR wavelengths. Contribution of phonon scattering has been subtracted.

temperature and high field on account of the valley elevation. Magnetic field dependence has been observed for two n-type samples with different donor concentrations (Fig. 1). Concentration dependence is shown both for donors and acceptors (Fig. 2). So far no dependence on temperature has been observed. The dramatic size difference between electron-donor and electron-acceptor scattering observed in classical (millimeter wave) cyclotron resonance [2,4] is carried over to the quantum limit. The effect of the magnetic field in the form of  $B^{-1/2}$  is quite obvious.

#### IONIZED IMPURITIES

Antimony-doped Ge crystals are heated to yield the extrinsic electron cyclotron resonance. Inverse relaxation time due to scattering by ionized donors (and electrons) is plotted in Fig. 3 against temperature for three FIR wavelengths. The flat portion at higher temperatures corresponds to the exhaustion range. Magnitude of the inverse relaxation time drops to that by neutral impurities at low temperatures below 10 K, where signals are not obtained. Ionized impurity scattering is seen more prominent at longer wavelength (lower field). Concentration dependence is found linear. We obtain  $NB^{-1/2}T^0$  dependence.

In the case of InSb, our crystal contains almost equal number of ionized donors and ionized acceptors. Nevertheless, the magnetic field and temperature dependence is found exactly the same with the Ge case where only ionized donors are present. The magnetic field dependence is shown in Fig. 4.

#### CONCLUSIONS

In the quantum limit ( $\hbar\omega_c \gg k_B T$ ) cyclotron resonance, we have seen  $T^0 B^{-1/2} N$  dependence of the inverse relaxation time due to impurity scattering both for neutral and ionized impurities. The effect of ionized impurities is by more than an

order of magnitude larger than that of neutral impurities. Size difference between donor and acceptor scatterings is conserved for neutral impurities even in the quantum limit. Magnetic field dependence of impurity scattering is opposite to that of phonon scattering [1]. So it is not surprising to have a minimum in magnetic field dependence if we measure the linewidth for an appropriately doped sample and at an appropriate temperature.

#### REFERENCES

- 1) H. Kobori, T. Ohya and E. Otsuka, the preceding paper.
- 2) E. Otsuka, Jpn. J. Appl. Phys. 25, 303 (1986).
- 3) C. Erginsoy, Phys. Rev. 79, 1913 (1950).
- 4) E. Otsuka, K. Murase and J. Iseki, J. Phys. Soc. Jpn. 21, 1104 (1966).

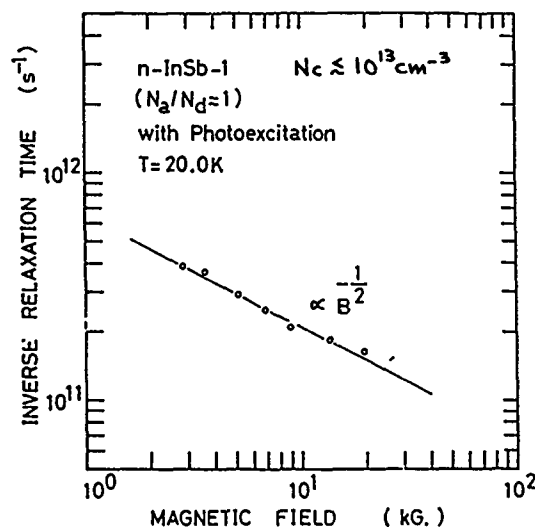


Fig. 4. Magnetic field dependence of the electron inverse relaxation time due to ionized impurities (both donors and acceptors) in a heavily compensated InSb. Free carriers have been available only by weak photoexcitation.

## Broadband Dielectric Measurements with Picosecond Transient Radiation

G. Arjavalingam, Y. Pastol, J.-M. Halbout, and G.V. Kopcsay

IBM Research Division, T.J. Watson Research Center  
P. O. Box 218, Yorktown Heights, NY 10598

### ABSTRACT

Picosecond transient radiation from optoelectronically pulsed integrated antennas is used for coherent microwave spectroscopy in the 10 to 125 GHz frequency range. The experimental apparatus is characterized using samples with predictable loss and dispersion properties. We present measurements of the frequency dependent absorption coefficient and refractive index of materials performed using this set-up.

### INTRODUCTION

Traditionally, the microwave dielectric properties of materials are measured at discrete frequencies where sources and related hardware are available using techniques such as the cavity perturbation method [1]. The data is then inter- and extrapolated for use at other frequencies. While these methods have been used for many years, they are time consuming and require a different sample configuration for each frequency. This is becoming a more acute problem in recent times as electronic devices are demonstrating risetimes of less than 10 ps, and the frequencies of interest cover a wide range (10-100 GHz). Several new insulators are being investigated for use in these circuits, as well as in the packaging structures used to interconnect them. In both cases the performance critically depends on the dielectric properties of these materials. In this paper we describe a new technique for making broadband dielectric measurements in the 10 to 125 GHz frequency range using a single experimental set-up. The coherent microwave transient spectroscopy (COMITS) is performed using the picosecond transient radiation from optoelectronically pulsed broadband integrated antennas. A COMITS experiment consists of transmitting and receiving antenna structures with the sample to be characterized located between them.

### EXPERIMENTS AND RESULTS

We use exponentially tapered coplanar stripline antennas in our experiments. [2]. They are particularly useful for the application discussed here due to their broad bandwidth, their directivity, and their transmission line nature. The antennas are fabricated by lift-off lithography on 0.5  $\mu\text{m}$  thick epitaxial silicon layers on 430  $\mu\text{m}$  thick sapphire substrates (Fig.1). The uniform coplanar-strip feedline, 4 mm in length with 5  $\mu\text{m}$  wide lines separated by a 10  $\mu\text{m}$  gap, is terminated at one end by bonding pads. The other end of the transmission line is prolonged by an exponential flare which forms the antenna

part of the structure. In order to reduce the carrier lifetime, the silicon epilayer is heavily implanted with  $\text{O}^+$  ions. Ion energies of 100 and 200 keV at implant doses of  $10^{15} \text{ cm}^{-2}$  are used [3].

The transient radiation properties of the antennas described above were investigated and the results are presented here. We also characterized the dependence of the antenna bandwidth on its geometry, the H-plane radiation pattern and the polarization of the radiation [4]. The experiments are carried out in the following manner: two identical antennas, the transmitter and the receiver, face each other, and are separated by a fixed distance. A 5 V bias is supplied to the transmitter; the receiver is unbiased. The exciting optical pulses of 2.5 ps duration at a 100 MHz repetition rate are obtained from a mode-locked, pulse-compressed, and frequency-doubled Nd:YAG laser. The 532 nm wavelength output beam has an average power of 250 mW and is split into two beams of equal intensity. The first beam (pump) is focused on the feedline of the transmitter, close to the edge of the antenna part. There it generates the electrical transient which radiates as it propagates in the antenna section. The second optical beam (probe) is delayed with respect to the pump by a variable amount, and is focused at the edge of the antenna part in the receiver. The transient voltage induced by the received field is measured as a function of time by photoconductive sampling. Mechanical chopping of the pump beam and standard lock-in detection are used to recover the signal. The two antennas are separated by 4 cm for the results presented here. The observed  $1/r$  dependence of the received signal verifies that at this spacing the receiver is in the far-field region of the transmitter. A typical received waveform is shown in Fig.2. The amplitude spectrum of the received signal, obtained by Fourier transforming the temporal data, is plotted in inset. Its frequency components extend up to 150 GHz, and tend to zero at low frequency, which is expected since dc signals cannot be radiated in the far-field.

For a standard coherent microwave spectroscopy (COMITS) measurement a reference recording is first taken without any sample between the transmitter and the receiver (see Fig.1). Subsequently the sample, with a cross section exceeding that of the receiving pattern, is introduced close to the receiver and a second recording is taken. The two sets of temporal data are then Fourier-transformed and the second spectrum is divided by the reference to obtain the complex amplitude transmission function of the sample. Since the measured voltage is proportional to the electric field, both

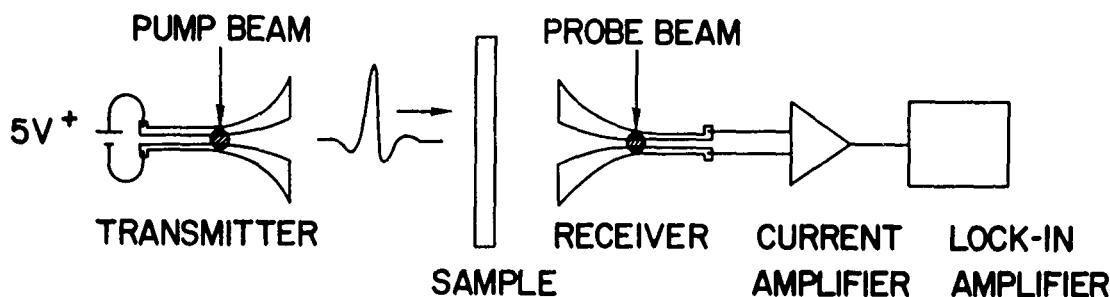


Figure 1. Schematic of the COMITS experimental setup

the amplitude  $\Lambda(f)$  and the phase  $\Phi(f)$  of the transmission function are obtained experimentally. The former yields the absorption of the sample and the latter gives its dispersion.

We use two different samples with well known and predictable behavior to characterize the spectroscopy apparatus. First, a 100 Å thick titanium film evaporated on a 125 µm thick glass slide was used as a sample. As might be expected for a thin metal film on a transparent substrate, the measured amplitude  $\Lambda(f)$  and phase  $\Phi(f)$  spectra decrease with increasing frequency,  $\Lambda(f)$  because of the skin effect losses in the metal, and  $\Phi(f)$  primarily because of the phase delay in the glass substrate. We then used a Fabry-Pérot interferometer, built with two of the Ti coated glass slides described previously, as the sample. The transmission function (amplitude and phase) for a Fabry-Pérot interferometer with  $d = 5$  mm is shown in Fig. 3. The maxima in the amplitude spectrum, and the corresponding variations in the phase follow the expected behavior for the electric field transmission function. The overall decrease of the envelope of  $\Lambda(f)$  and  $\Phi(f)$  with frequency is expected from the increasing metal losses at high frequencies. Finally, since the reflectivity of the metal films increases with frequency, the modulation depth of  $\Lambda(f)$  should also increase, which is clearly observed in Fig. 3. The transmission spectra of Fabry-Pérot interferometers with other spacings exhibit the above behavior as well.

This spectroscopy apparatus has been used to make measurements of the dielectric properties of several materials. The results of these measurements will be presented. For instance, we measured the microwave refractive index of fused silica to be  $1.94 \pm 1\%$  from 10 to 125 GHz. This is consistent with earlier data. The experimental set-up is particularly useful for measuring the dielectric properties of low loss materials, many of which are of interest for the fabrication of high-speed circuits.

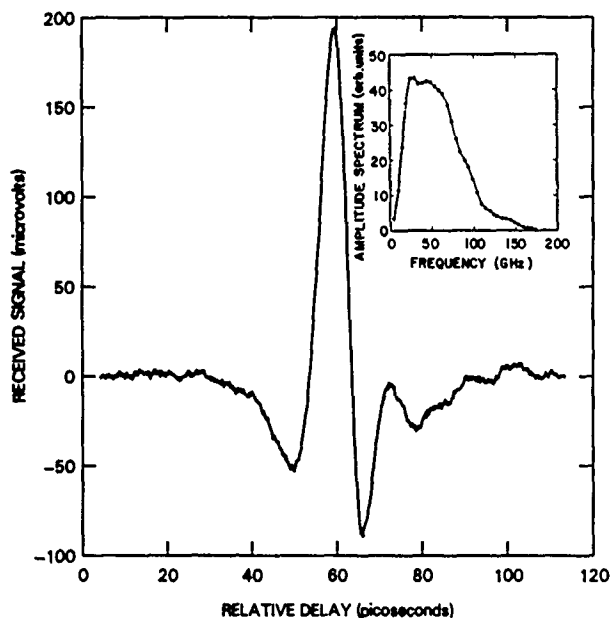


Figure 2. Received waveform with no sample between the transmitter and the receiver. The corresponding amplitude spectrum is shown in inset. Only the dots correspond to experimental data, the continuous line is a guide to the eye.

## SUMMARY

In summary we have described broadband coherent microwave spectroscopy experiments using the transient radiation from optoelectronically pulsed antennas. The effectiveness of this set-up for measuring the dielectric properties of materials over a wide frequency range in the microwave and millimeter wave spectrum is demonstrated using filters with predictable behaviour. Though all the experiments described in this paper are done in transmission, reflection spectroscopy experiments can also be carried out by placing two antennas in front of the sample and exciting them as described above. In terms of spectral range, our COMITS technique is complementary to other existing methods, and is of immediate technological interest for the measurement of the dielectric properties of materials used in the microelectronics industry.

We acknowledge several illuminating discussions with Professor J.R. Whinnery of the University of California, and Professor D.B. Rutledge of the California Institute of Technology.

## REFERENCES

1. See for instance "Microwave Engineering" ed. A.H. Harvey, Academic Press (London), 1963.
2. A.P. De Fonzo, M. Jarwala, and C. Lutz, *Appl. Phys. Lett.* **50**, 1155 (1987); A.P. De Fonzo and C. Lutz, *Appl. Phys. Lett.* **51**, 212 (1987).
3. M.B. Ketchen, D. Grischkowsky, T.C. Chen, C.-C. Chi, I.N. Duling, N.J. Halas, J.-M. Halbout, J.A. Kash, and G.P. Li, *Appl. Phys. Lett.* **48**, 751 (1986).
4. Y. Pastol, G. Arjavalingam, J.-M. Halbout and G.V. Kopsay, Submitted for publication.

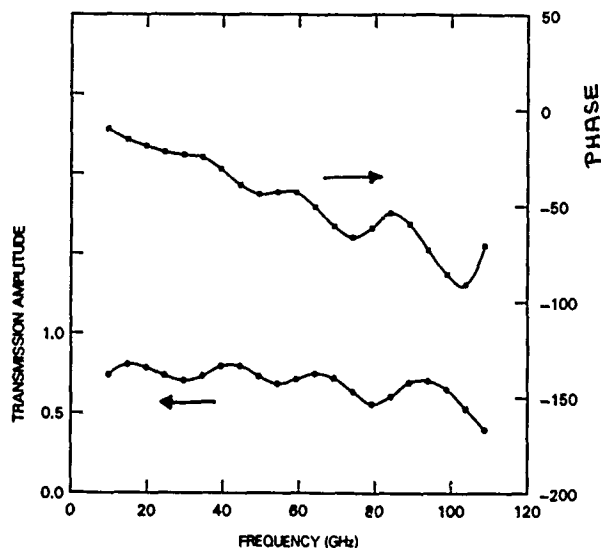


Figure 3. Amplitude and phase of the transmission function of a Fabry-Pérot interferometer with the two reflecting surfaces 5 mm apart. Only the dots correspond to experimental data, the continuous lines are a guide to the eye.

## MILLIMETRE-WAVELENGTH PULSE PROPAGATION THROUGH THE EARTH'S ATMOSPHERE

C J Gibbins

Rutherford Appleton Laboratory, Chilton, Didcot, Oxfordshire, OX11 0QX, UK

## ABSTRACT

The effects on pulse propagation at millimetre wavelengths of both atmospheric absorption and dispersion are calculated. For sub-nanosecond pulses, severe broadening of the pulse occurs at frequencies near to atmospheric absorption lines, whilst around the centres of such lines, in regions where the second derivative of the absorption coefficient is negative, pulse compression is found to occur. Furthermore, the frequency at which maximum energy in the pulse is received shifts from the carrier frequency towards regions of lower atmospheric attenuation, while the pulse itself acquires a modulation in the form of a chirp frequency.

## INTRODUCTION

The propagation through the Earth's atmosphere of continuous-wave (CW) or narrow-bandwidth signals in the microwave and millimetre-wavelength regions of the electromagnetic spectrum has been the subject of much investigation during recent years, leading to the development of propagation models which can now provide a reasonably accurate description of the effects of the clear atmosphere on the transmission of such electromagnetic waves, for example [1].

In contrast to these extensive studies, however, rather less attention has been directed, in the open literature, towards the propagation of pulsed or wideband signals, the applications of which would include high data-rate digital communications systems, high-resolution radar systems and those systems employing spread-spectrum techniques. Recent advances in the development of components and devices, stimulated by spectrum congestion at lower frequencies and requirements for covert systems operation, are now making feasible such applications in the millimetre-wavelength regions of the electromagnetic spectrum.

At such wavelengths, the clear atmosphere can impose significant constraints on the transmission of signals, through interactions with the polar molecules of oxygen and water vapour, not only in terms of signal attenuation, now generally well understood, but also in terms of signal dispersion, which introduces a frequency dependent propagation delay. These effects can vary significantly over the wide signal bandwidths required by very short pulses; thus, the spectrum of the pulsed signal may experience differential attenuation and

dispersion (i.e. propagation delay), resulting in distortions in the received pulse waveform. These distortions can appear as a broadening or compression of the pulse, through variations in group velocity, together with changes in the phase of signals and shifts in the frequency at which maximum energy is received (the "mode" frequency). The magnitude and sign of these effects clearly depend on the particular carrier frequency being transmitted.

## OUTLINE OF THEORY

Consider a pulsed signal with a spectrum  $F(\omega)$ , transmitted at a carrier frequency  $\omega_0$ , travelling through the Earth's atmosphere, characterised by a complex propagation constant  $\gamma$ . The envelope of the received pulse, as a function of time, at a distance  $L$  from the transmitter, may be expressed as a Fourier integral, thus:

$$E(t, L) = \frac{1}{\sqrt{2\pi}} \int_{-\infty}^{\infty} F(\omega) \exp \{j(\omega + \omega_0)t - \gamma L\} d\omega \quad (1)$$

where  $\gamma(\omega) = \alpha(\omega) + j\beta(\omega)$

and  $\alpha(\omega)$  is the frequency-dependent absorption coefficient,  $\beta(\omega)$  the frequency-dependent phase-delay coefficient.

At millimetric wavelengths, a Gaussian pulse shape of the form  $\exp(-bt^2)$ , where  $b$  is a function of the pulse width, can be assumed as fairly representative of very short pulses achievable with current technology. The frequency spectrum of such a pulse is also Gaussian, i.e.

$$F(\omega) = \frac{1}{\sqrt{2b}} \exp\left(-\frac{\omega^2}{4b}\right) \quad (2)$$

Forrer [2], and later Terina [3], have shown that, in this case, the Fourier integral in Equation 1 can be solved in closed form by assuming that the absorption and phase-delay coefficients can be expanded as a Taylor series around the carrier frequency  $\omega_0$ , retaining only the first three terms, e.g.

$$\alpha(\omega) = \alpha(\omega_0) + \alpha'(\omega_0)(\omega - \omega_0) + \frac{1}{2} \alpha''(\omega_0)(\omega - \omega_0)^2 \quad (3)$$

where the primes represent the first and second derivatives, with respect to frequency, evaluated at the carrier frequency. Thus, with the condition that  $(1 + 2b\alpha''L) > 0$ , the solution

is found of the form

$$E(t^*, L) \propto \exp[-kb(t^* + \zeta)^2] \exp[-j(\omega^* t^* + \delta)] \quad (4)$$

which shows that the received pulse envelope is still Gaussian in shape, on a new time scale  $t^*$ , but now has a pulse width  $kb$ , where

$$k = \frac{1 + 2b\alpha''L}{(1 + 2b\alpha''L)^2 + (2b\beta''L)^2} \quad (5)$$

The mode frequency  $\omega^*$ , given by

$$\omega^* = \omega_0 + \Delta\omega + \chi\tau^* \quad (6)$$

shows that the frequency at which maximum energy is received has shifted by an amount  $\Delta\omega$  and now has imposed on it a chirp frequency modulation  $\chi$ .

#### RESULTS OF CALCULATIONS

The effects of attenuation and dispersion on the propagation of pulses through the Earth's atmosphere have been calculated using the Microwave Propagation Model of Liebe [1] to evaluate the attenuation and phase-delay coefficients ( $\alpha, \beta$ ) and their derivatives. A variety of pulse widths, ranging from 0.1 ns to 2 ns (at the 10 dB level) have been considered,

propagating over path lengths between 1 and 50 km. As an example, Figure 1 shows the pulse distortion (either broadening or compression) as a percentage for 0.1 ns and 2 ns pulses propagating over a path of 10 km at carrier frequencies between 10 and 200 GHz. Pulse compression, i.e.  $k < 1$ , is found to occur, from Equation (5), when  $\alpha'' < 0$ , i.e. when the second derivative of the attenuation coefficient is negative.

Calculations have also been carried out to determine the shifts in mode frequency and to evaluate the magnitude of the chirp frequencies, along terrestrial line-of-sight paths, while pulse distortions have further been assessed on Earth-space paths at 90° and 10° elevation.

#### REFERENCES

1. H. J. Liebe, *Radio Sci.*, 1985, vol. 20, pp 1069 - 1089.
2. M. P. Forrer, *Proc. IRE*, 1958, vol. 46, pp 1830 - 1835.
3. G. I. Terina, *Radio Eng. Electron. Phys.*, 1967, vol. 12, pp 109 - 113.

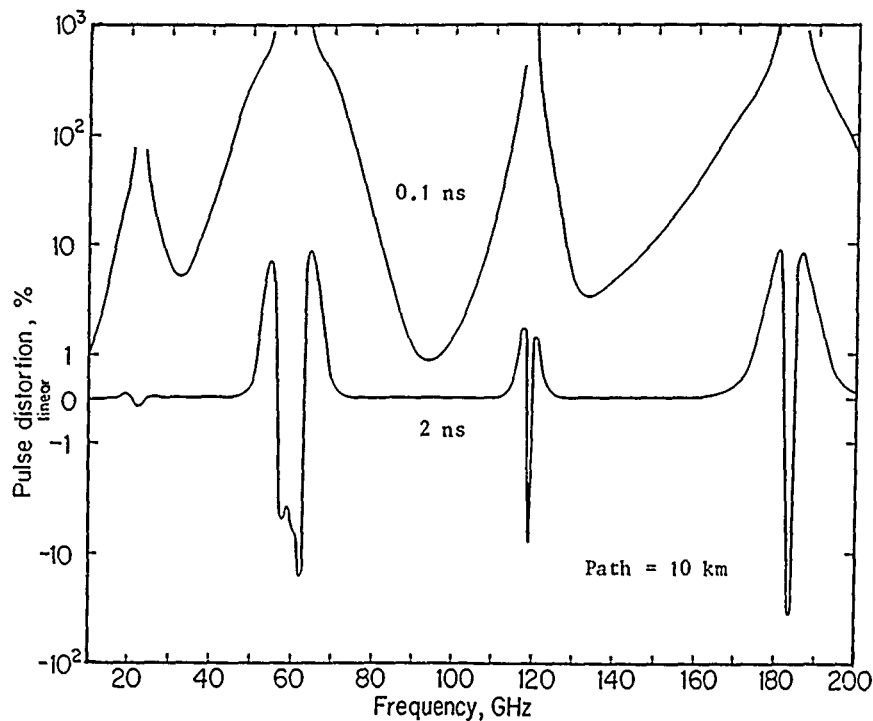


Fig. 1. Pulse distortions, as a percentage, for 0.1 and 2 ns pulsewidths and a propagation path of 10 km. Note the change of scale from logarithmic to linear between  $\pm 1$  %.

## STATISTICS OF PROPAGATION AT MILLIMETRIC, INFRARED AND OPTICAL WAVELENGTHS

C J Gibbins

Rutherford Appleton Laboratory, Chilton, Didcot, Oxfordshire, OX11 0QX, UK

## ABSTRACT

This paper describes the results of an investigation into the statistics of propagation measurements made at millimetric, infrared and optical wavelengths over a 500m path. The analysis includes an evaluation of the distribution of attenuation levels and rainfall rates exceeded during the 12 month period analysed, together with an examination of the distribution of fades and rainfall rates of various durations and intensities, and the return periods between such events.

## INTRODUCTION

At millimetric wavelengths and shorter, the Earth's atmosphere imposes numerous constraints and limitations to the transmission of signals. Dominant, and well known, are the effects of molecular oxygen and water vapour. Numerous models exist to enable the designer of communications and other systems operating at such wavelengths to evaluate with acceptable precision the omnipresent transmission losses thus imposed by the propagation medium.

More problematic, however, are the additional effects of hydrometeors, in the form of precipitation and fog. Such effects are not present all the time and depend particularly on the climate and prevailing meteorology at the location of planned systems. To facilitate systems design, attenuation by precipitation is generally considered in a statistical manner, rather than analytically, particularly as rain, etc., are stochastic phenomena. From the standpoint of the reliability of a communications system, it therefore becomes important to determine a fade margin appropriate to a specified level of reliability, generally in the form of a level of attenuation which will be exceeded for a percentage of time, over a period of a year, for example, determined by the system reliability requirement.

In order to provide such information at millimetre wavelengths, and shorter, the Rutherford Appleton Laboratory has operated a 500m transmission range to obtain propagation and relevant meteorological data continuously over long periods of time.

## INSTRUMENTATION

The 500m range, which has been described in detail elsewhere (1), comprises six single-pass transmission links situated 4m above flat grassland, operating at frequencies of 37, 57,

97 and 137 GHz, with vertical polarization and at wavelengths of 10.6 $\mu$ m and 0.6 $\mu$ m in the infrared and optical regions respectively, with random polarization. An extensive set of meteorological instruments complement the propagation measurements and include rapid-response rain gauges at three locations along the path, a rapid-response snow/hail gauge, measurements of temperature and humidity at a variety of locations and heights above the ground, a distrometer to measure the distribution of rain drop sizes, a microwave refractometer, surface pressure and wind speed and direction.

Data from all sensors and links are recorded on magnetic tape at a rate of 0.1 Hz for subsequent calibration and analysis. The links are calibrated automatically every 6 hours by inserting additional, known, levels of attenuation.

## RESULTS

The data are being analyzed to provide a variety of statistical results of relevance and importance to the planning and design of future communications systems. Basic probability distributions of the levels of attenuation which have been exceeded, of the type shown earlier (2) are now available for longer periods of time, covering a complete 12 month period, and have been supplemented by similar distributions of rainfall rate exceeded during the period. Comparisons of such data yield important information on the relationships between attenuation at the various frequencies and rainfall rates, thus yielding an insight into the interactions between electromagnetic waves and raindrops, in addition to facilitating the scaling of statistical data at one frequency to another, higher, frequency. As noted earlier (2), such data can also be applied to the evaluation of the relative merits of the different wavebands, of importance to the increasing consideration and deployment of multi-spectral sensors.

More detailed analyses of propagation have further been carried out to investigate the probability distributions of the durations of events at various levels of attenuation and rainfall rates. Such data is of importance in assessing systems unavailability. As an example, Figure 1 shows the distribution, as a percentage, of the durations of fades of 2, 4, 6 and 8 dB km<sup>-1</sup> measured over a period of 1 year at 97 GHz, normalized to the number of 30 second fades,  $N_{30}$ .

In an analogous way, the distribution of return period i.e., the times between fades, has also been examined. Figure 2 shows the distribution of return periods for the same fade depths as Figure 1, for 97 GHz transmissions. The distributions of both durations and return periods are found to be similar, functionally, to a log-normal probability distribution, and suggest that it may be possible to develop a model to predict attenuation/rainfall rate - duration - return period relationships, which would assist the design and operation of terrestrial communications systems, in particular those employing space diversity techniques to improve systems reliability.

## REFERENCES

1. C J Gibbins, D G Cater, P A Eggett, K A Lidiard, M G Pike, M A Tracey, E G White, J M Woodroffe, and U M Yilmaz, *J IERE*, 1987, Vol 57, pp 227-234.
2. C J Gibbins, Proc. 12th Int.Conf. on Infrared and Millimeter Waves, Lake Buena Vista, Fl. December 14-18, 1987

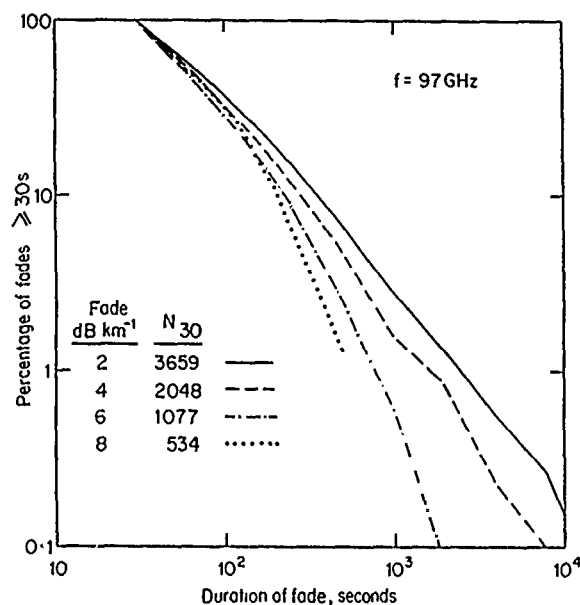


Fig. 1. Distribution of fade durations longer than 30 seconds, normalised to the number of 30 second fades, measured at 97 GHz.

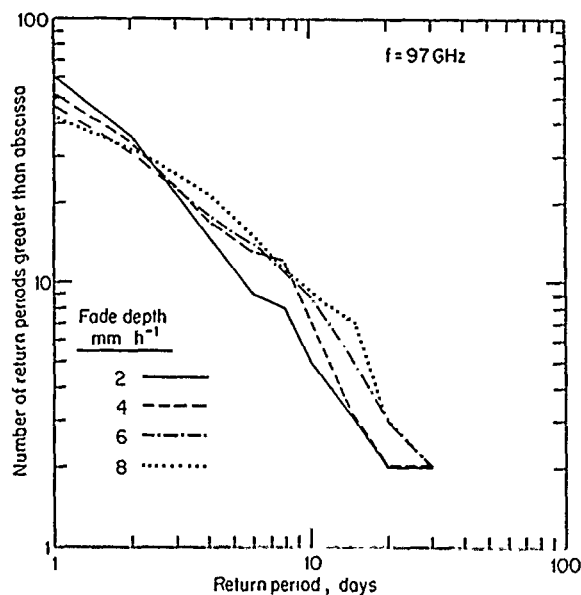


Fig. 2. Distribution of return periods between fades of depths 2 - 8  $\text{dB km}^{-1}$ , measured at 97 GHz.



# FAR-INFRARED DETECTOR USING $\text{BaPb}_{0.7}\text{Bi}_{0.3}\text{O}_3$ THIN FILM JOSEPHSON ELEMENT

A. Sawada, K. Sato, Y. Enomoto\* and T. Murakami\*

Synthetic Crystal Research Laboratory,  
Faculty of Engineering, Nagoya University,  
Nagoya 464-01, JAPAN

\*NTT Electrical Communication Laboratory,  
Tokai, Ibaraki-ken, 319-11, JAPAN

## ABSTRACT

A new detector using  $\text{BaPb}_{0.7}\text{Bi}_{0.3}\text{O}_3$  thin film Josephson element has been found to detect far-infrared light in the range of wavelength from  $50\ \mu$  to  $500\ \mu$  (wavenumber from  $200\ \text{cm}^{-1}$  to  $20\ \text{cm}^{-1}$ ). The optimum conditions are searched by changing the temperature of the element, the bias current through the element, and the chopping frequency of incident light.

## INTRODUCTION

Recently Enomoto and Murakami have developed a new detector using  $\text{BaPb}_{0.7}\text{Bi}_{0.3}\text{O}_3$  (BPB) thin film Josephson element which is very sensitive in the infrared region of wavelength from  $1\ \mu$  to  $8\ \mu$  (1). Detection principle is as shown in Fig. 1. The I-V characteristic of Josephson junction changes when infrared light is irradiated on the Josephson element. When the constant bias current  $I_B$  is applied, light signal is detected as the change of voltage  $\Delta V$  across the Josephson junction. The purpose of the present paper is to report a new detector which works in far-infrared region from  $50\ \mu$  to  $500\ \mu$  using the same detection principle.

## EXPERIMENTS

Fig. 2 shows the schematic diagram of the Josephson element used in the present experiment. Polycrystalline BPB thin films were deposited on sapphire substrates using RF sputtering method. Grain boundaries in sputtered films have been found to work as tunneling barriers and to make Josephson junctions. This is called as boundary Josephson junctions (BJJ) (1). In order to detect far-infrared light, active area on which incident light beam is irradiated was enlarged to  $1\ \text{mm} \times 1\ \text{mm}$  in size. Furthermore, in order to increase the number of BJJ and to increase the detection sensitivity, the total length of the active part was increased by inserting very narrow slits of about  $10\ \mu$  in width as shown in Fig. 2.

Fig. 3 shows the I-V characteristics of the present BPB element where the superconducting transition temperature is  $T_c = 8.0\ \text{K}$ . It is noticed that the scale of  $V_c$  is very large (10V). This shows that a number of BJJ are connected in series in the present BPB element.

Fig. 4 shows the capacitance  $C_p$  of the BPB element at various frequencies under DC bias voltage (6V) as a function of temperature. Above  $T_c$ , capacitance  $C_p$  is zero as is expected. Just around  $T_c$ , however,  $C_p$  becomes nonzero and increases as

the temperature is lowered. Furthermore,  $C_p$  is found to be very large (about  $10^4\ \text{pF}$ ) at  $T = 5\ \text{K}$  in the frequency of 120 Hz.

Martin-Puplett type Fourier spectrometer (2) was used to study detector properties in

the far-infrared region from  $20\ \text{cm}^{-1}$  to  $200\ \text{cm}^{-1}$ . Constant bias current  $I_B$  was applied to the BPB element, and the light signal was detected as output voltage of lock-in amplifier.

Fig. 5 shows the output voltage of lock-in amplifier as a function of bias current  $I_B$  when the temperature of the BPB element is  $T = 6.7\ \text{K}$ .

The optimum conditions of the present BPB element have been found to be  $I_B = 74\ \mu\text{A}$  and  $T = 6.7\ \text{K}$ . As the temperature is raised, sensitivity decreases and becomes zero above  $T_c$ . As the temperature is lowered, noises increase greatly. This is because the I-V characteristic becomes tunneling type.

Fig. 6 shows a far-infrared spectrum which was obtained using our Martin-Puplett spectrometer and the present BPB detector. It is seen that the present detector can detect far-infrared light in the wavenumber range from  $20\ \text{cm}^{-1}$  to  $200\ \text{cm}^{-1}$ .

## REFERENCES

- (1) Y. Enomoto and T. Murakami, J. Appl. Phys. 1986, Vol. 59, pp. 3807-3814.
- (2) A. Sawada, M. Wada and K. Fujita, Conference Digest of 9th International Conference on Infrared and Millimeter Waves, 1984, pp. 236-237.

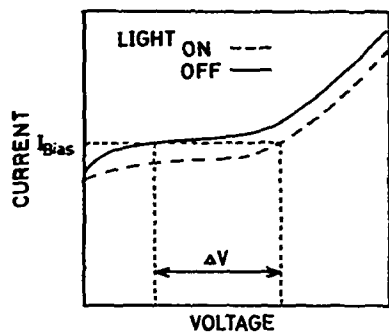


Fig. 1. Detection principle of infrared light.

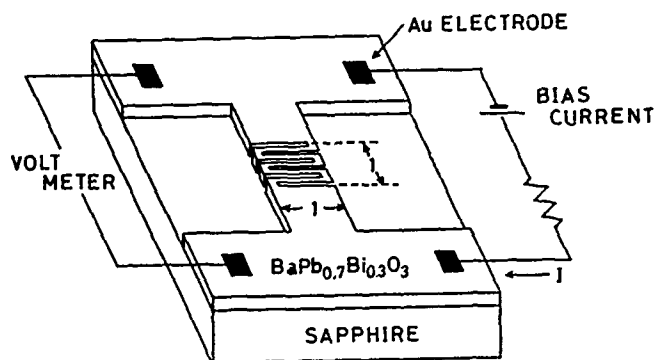


Fig. 2. BPB Josephson element for far-infrared detection.

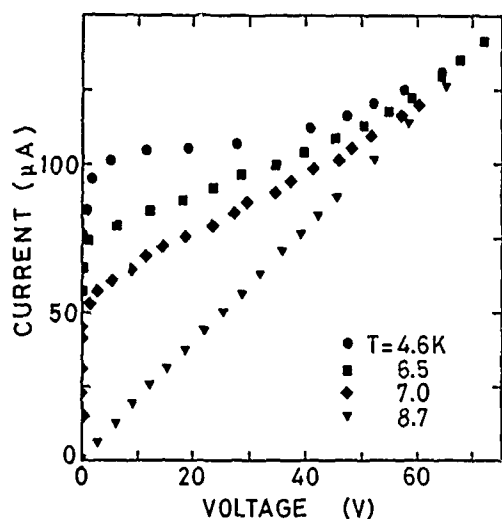


Fig. 3. I-V characteristics of the BPB element.

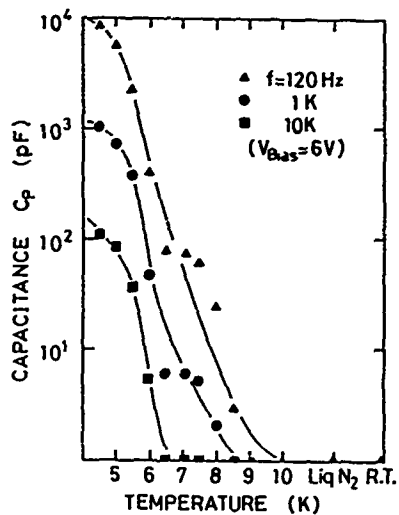


Fig. 4. Capacitance of the BPB element as a function of temperature.

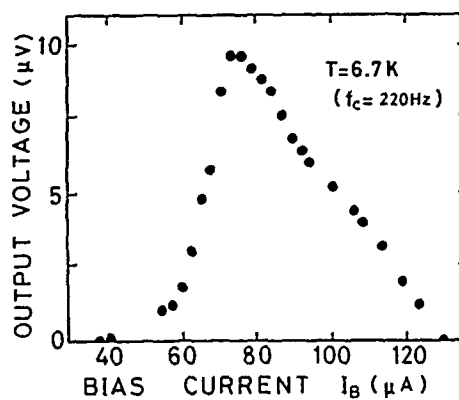


Fig. 5. Output voltage of lock-in amplifier as a function of bias current.

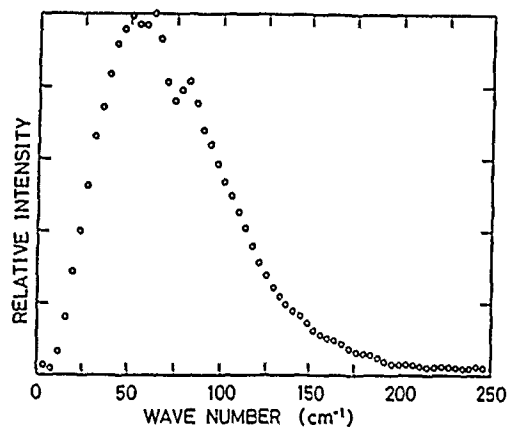


Fig. 6. Spectrum obtained by the BPB detector.

# COHERENT MECHANICAL FIR DOPPLER SHIFTING FOR HETERODYNE APPLICATIONS

U.H.W. Lammers  
R.A. Marr  
J.B. Morris

Rome Air Development Center  
Hanscom AFB, MA

## ABSTRACT

Frequency shifting of a single far infrared laser source by mechanical means is investigated to obtain highly correlated transmit and local oscillator signals for narrowband heterodyne reception. The analysis refers to a radar but applies to other systems as well.

## INTRODUCTION

A parameter of particular concern to Doppler radar is coherency. Coherency determines the frequency resolution that a radar can achieve, and in turn its ability to resolve radial target velocities. The Doppler shift measurement is accomplished with either a homodyne or a heterodyne receiver. The coherency of transmit and local oscillator signals determines the accuracy with which the shift can be measured and the sensitivity of the receiver. Both are directly proportional to the receiver's coherent bandwidth.

Because of the high atmospheric attenuation at these wavelengths, a terrestrial FIR radar is only practical for target measurements in the laboratory. Incoherent systems with cooled detectors have been used successfully in this country and abroad for the measurement of scattering properties. It is our objective to explore critical parameters necessary to design a similar but coherent radar for Doppler imaging.

Due to the short round-trip time of tens of nanoseconds or less for radar signals of interest, it is advantageous to derive transmit and local oscillator signals from a single FIR laser source. The stability of a good laser signal over such time span is sufficient to resolve Doppler shifts on the order of 1 Hz or better. For example, laser frequency jitter at a 2 MHz/sec rate causes a Doppler frequency error of 0.1 Hz over a 50 nsec round-trip time.

## METHOD OF COHERENT DOPPLER SHIFTING

One possibility of generating a frequency offset to a laser signal is through mechanical Doppler shifting. Note, that this is different from the Doppler shift generated by target motion. The major advantage of a mechanical Doppler shifter at FIR lies in its power efficiency. The major disadvantage lies in the limited amount of frequency shift achievable. It is well known that mixer output noise is inversely proportional to IF frequency at low IF. That is, a receiver with 100 kHz IF is 20 dB less sensitive than one with 10 MHz IF, all else being equal. The highest possible mechanical frequency shift is therefore important.

Continuous mechanical frequency shifting of an FIR signal in order to generate well correlated transmit and local oscillator signals involves, by necessity, a repetitive process. A Doppler shift is imparted on the FIR signal by a moving (generally rotating) metallic reflector. After some time, another reflector substitutes for the first one and repeats its motion, and so on. In a rotating system it is possible to have only a single reflector. Phase and amplitude continuity of the Doppler shifted signal between repetitions of the process characterize an ideal frequency shifter. Phase continuity requires that the phase between repetitions of the process advance by integer multiples  $m$  of  $2\pi$ . Then and only then a pure offset frequency of  $m N$  Hz is generated, where  $N$  is the number of repetitions of the process per second. A non-perfect process, such as one of discontinuous phase, leads to a spectrum of lines spaced  $N$  Hz apart. The consequence is a power loss at the desired frequency and potential aliasing. The latter results as the radar target's own Doppler spectrum modulates all spectral lines generated in the frequency shifter, causing spectral overlap.

Figure 1 presents a qualitative picture of the situation. The frequency shifter offsets the laser signal by an amount equal to the IF. Due to its imperfections, additional equally spaced spectral lines occur, whose amplitude distribution (the outer dashed envelope) depends on the specific shifter operation. The radar signal from a rotating stationary target then modulates every line of the shifter spectrum in the heterodyning process. As drawn in Figure 1, the target spectrum (the line spectrum with the inner dashed envelope) does not result in aliasing.

Phase discontinuity is the more serious phenomenon with regard to spectral broadening. Amplitude discontinuity, brought about at FIR by a variable Gaussian beam geometry, must also be minimized through an appropriate design.

Several mechanical frequency shifters have been described in the literature. Veron [1] uses a cylindrical rotating blazed grating. He recognizes the need for phase continuity. However, limitations in his reflection geometry require a large number of grooves on a slowly rotating grating. The result is a densely crowded spectrum unsuited for our purpose. Manuccia [2] describes the basic function of the device shown in Figure 2. He is concerned with laser isotope separation for which a monochromatic signal is not required. Consequently, he does not address the issue of phase and amplitude continuity. The same essentially holds for a device, for which a patent was issued to Guers and Boscher[3].

## EXAMPLE OF MECHANICAL SHIFTER

We have analyzed the performance of the mechanical frequency shifter shown in Figure 2. Basically, it consists of two rotating mirrors and a stationary reflector, circumferentially shaped according to the involute of a circle of radius  $r$ . The first mirror deflects the laser beam, which enters along the axis of rotation, at a  $90^\circ$  angle. The second mirror, rotating at radius  $r$ , deflects the beam by another  $90^\circ$ , this time tangentially with the disk. The disk, with holes along the beam's path, is only a mechanical means to hold the mirrors and to reduce drag. In Figure 2 the stationary reflector takes the shape of four identical involute segments. Its important properties are a) retroreflection of the laser beam at all angles of rotation, b) linear phase progression with angle of rotation, and c) phase continuity, if the steps between segments are chosen equal to integer multiples of half the wavelength  $\lambda$ . Each stationary segment can be rotated slightly around one shoulder screw for best phase match at any FIR wavelength. Mechanical size and amplitude stability make it preferable to use four involute segments (or some other number greater than one). Discontinuities in amplitude and phase, which are generated equally by all four segments, contribute power to only every fourth line in the spectrum.

Consider this example. At  $\lambda = 0.471$  mm,  $r = 19.04$  mm, and  $N = 400$  Hz, the frequency offset generated by the device in Figure 2 is  $\Delta f = 4\pi r N / \lambda = 203.2$  kHz. Typical base plate dimensions for such a design are 230 by 230 mm.

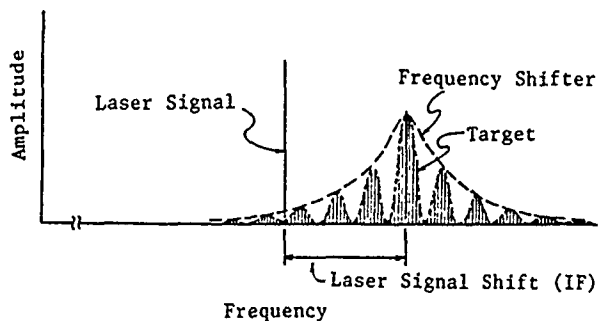


Figure 1 Frequency Shifter/Target Spectrum

In order to avoid aliasing, the maximum radial target velocity is  $v = N\lambda/4 = 47$  mm/sec. At a target rotation rate  $n = 0.1$  Hz, this corresponds to a maximum radial target dimension of  $d = v/(2\pi n) = 75$  mm. A receiver with 1 Hz coherent bandwidth integrates over many frequency shifter revolutions. In contrast, it responds to target Doppler shifts within one tenth of a target revolution. It can be shown that effects on  $\Delta f$  by fluctuations in the disk's rate of rotation cancel ideally through an appropriate heterodyning scheme.

Although the discussion has stressed Doppler resolution in radar, there are broader implications. The quasi self-mixing technique permits narrowband coherent IF processing for any system, where signal path delay is short. Since it is a heterodyne and not a homodyne scheme, spectrum foldover can be avoided in many cases. Likewise, imperfections in the frequency shifting process can be overcome by proper frequency selection. A mechanical frequency shift of several hundred kHz is relatively simple to achieve at FIR. Despite the fact that this is not optimal in terms of system noise, the sensitivity of a receiver with a room temperature Schottky barrier mixer should at least match that of a helium-cooled detector with comparable integration time. A mechanical frequency shifter as described is currently under construction.

## REFERENCES

1. D. Veron, Optics Communications, 1974, Vol. 10, pp. 835-850.
2. T.J. Manuccia, Laser in Chemistry, 1977, Elsevier Sci. Pub. Co., pp. 210-215.
3. K. Guers and J. Boscher, U.S. Patent No. 4 264 141, 1981.

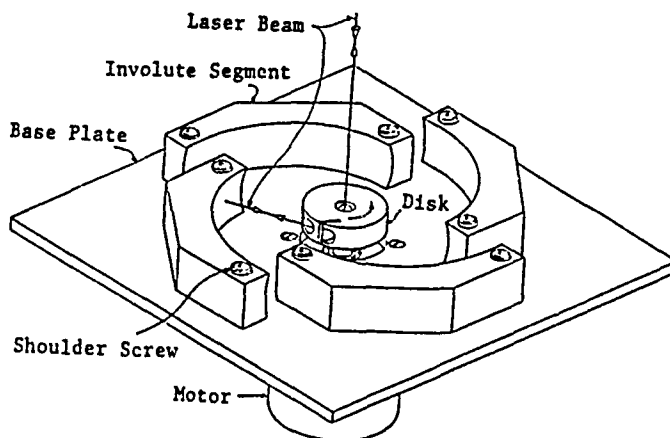


Figure 2 Rotating Frequency Shifter

## SELF-CONSISTENT TRANSMISSION LINE ANALYSIS OF THE GYROTRON TRAVELING-WAVE AMPLIFIER

J. E. Arrington, R. W. Grow, J. M. Baird, and L. R. Barnett

Microwave Device and Physical Electronics Laboratory  
 Department of Electrical Engineering  
 University of Utah  
 Salt Lake City, Utah 84112

## ABSTRACT

A self-consistent analysis of the gyrotron traveling-wave amplifier is performed using a single particle theory and an exact transmission-line field analysis to yield a nonlinear large signal theory able to describe the effects of tapered, nonideal wall waveguides and tapered dc magnetic fields. Guiding center drift is considered, as well as efficiency as a function of input power, RF detuning, dc detuning, current, and beam size.

## INTRODUCTION

The gyrotron traveling-wave amplifier (GTWA) has been studied in some depth by several authors [1, 2, 3] who have shown that two fundamental problems limit the usefulness of the standard configurations of the GTWA in which the beam and the RF are both launched in the +z direction [4, 5]. The first of these problems is the limited beam current at which the device may operate without breaking into oscillation. The second problem is related to the narrow bandwidth of the CRM interaction. Device-based solutions to each of these problems have been posed by previous researchers [4, 5]. The proposed solution for the oscillation problem is the use of frequency selective, spatially located loss mechanisms. The proposed solution for the bandwidth problem is the use of a reverse-injection scheme in a tapered waveguide (see Fig. 1). These two device-

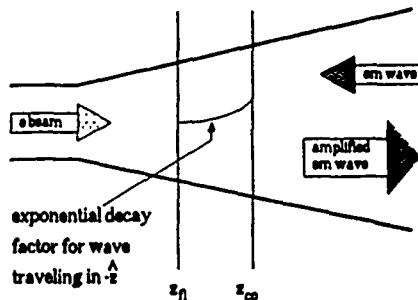


Fig. 1. Schematic diagram of the reverse injection GTWA. The transverse plane at  $z_{c0}$  is the cutoff plane for perfect reflection. The wave will penetrate into the region  $z_{f1} < z < z_{c0}$ , so that a wave launched at  $z_{f1}$  will have the same apparent starting point as the reflected wave.

based solutions have not been subject to analysis by previous analytic theories, indicating the need for a new theory capable of addressing both standard and new configurations of the GTWA.

## THEORETICAL DEVELOPMENT

The two standard methods of analyzing gyrotron devices are kinetic theory and single particle

ballistic theory. The kinetic theory method results in a linear dispersion relationship via consideration of a linearized form of the Vlasov equation, and is, primarily, a study of the RF electromagnetic fields. The single particle method results in a set of differential equations yielding values for the change in important beam particle quantities, and thus is primarily a study of the beam particle characteristics. The kinetic theory, being a linear theory, can not study the fundamentally nonlinear saturation processes which occur in GTWA amplifiers. The normal implementation of the single particle theory suffers from limitations on the complexity of the interaction region and on the nature of the RF fields. Neither of these theoretical approaches are capable of addressing the device-based solutions mentioned above.

The theory presented in this work is a self-consistent, large signal, nonlinear theory for GTWA devices based on a combination of a transmission line analysis for the RF fields and a single particle theory for the electron beam. The transverse electromagnetic fields are represented as

$$\vec{E}_t(\vec{r}) = \sum_k V_k(z, t) \vec{e}_k(r, \theta) \quad (1a)$$

$$\vec{H}_t(\vec{r}) = \sum_k I_k(z, t) \vec{h}_k(r, \theta) \quad (1b)$$

and the expansion coefficients,  $V_k$  and  $I_k$ , have units of volts and amps, respectively. Maxwell's curl relations are separated into longitudinal and transverse equations, and Eqs. 1a and 1b are substituted into the transverse equations. After extensive analysis, the following exact expressions result:

$$\frac{dV_n}{dz} = -jk_z Z_n I_n + \sum_k T_{kn} V_k + jk \sum_k Z_{nk} I_k \quad (2)$$

$$\frac{dI_n}{dz} = -j \sum_k \frac{k}{Z_n} V_n - \sum_k T_{nk}^* I_k - jk \sum_k Y_{nk} V_k \quad (3)$$

$$- \int_{S(z)} \vec{J}_t \cdot \vec{e}_n^* ds \quad (3)$$

where terms (a) and (d) are the ideal waveguide terms, terms (b) and (e) represent the influence of a tapered waveguide wall, and terms (c) and (f) represent the influence of an electrically nonideal (i.e., lossy) waveguide wall. Term (g) is the beam-field coupling term, which may be written as a sum over the  $N$  individual charge carrying macroparticles

used to represent the electron beam, as shown in Eq. 4,

$$\int_{S(z)} \vec{j}_t \cdot \vec{e}_n^* ds = -|e| \frac{\omega}{2\pi} \sum_{i=1}^N \frac{\vec{v}_{ti}}{v_{zi}} \cdot \vec{e}_n^*(\vec{r}_{ti}) e^{-j\omega t_i} \quad (4)$$

The electron beam, represented by a collection of charge carrying macroparticles having the same ballistic properties as electrons, is assumed to propagate in the presence of a strong dc magnetic field of the form:

$$\vec{B}_0 = B_{0z} \hat{z} + B_{0r} \hat{r} = B_{0z} \hat{z} - \frac{r}{2} \frac{\partial B_{0z}}{\partial z} \hat{r} \quad (5)$$

The electron beam is represented in the coordinate system shown in Fig. 2. A slow time scale transform

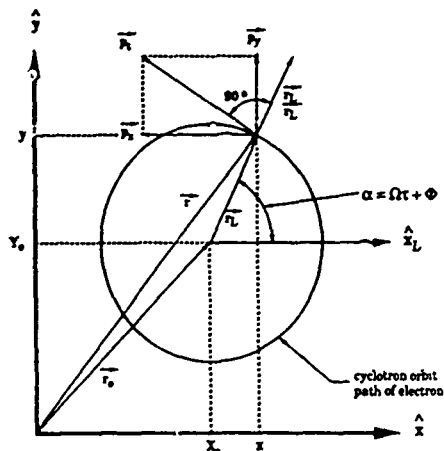


Fig. 2. Diagram of the trajectory of a single electron with phase  $\alpha = \Omega t + \phi$  and transverse momentum  $p_t$ .  $p_t$  is always at right angles with  $\vec{r}_L$ , and leads it by  $90^\circ$ .  $\hat{z}_L$  is a unit vector in the  $\hat{z}$  direction, located in the Larmour radius. Rectangular coordinate points  $(x_0, y_0)$  and  $(x, y)$  are the guiding center and electron positions, respectively.

is used in the representation of the transverse momentum components. A formulation for the motion of the dc guiding center of the electrons is included in the theory. The equation for the electron energy is derived for use in the verification of the primary calculations of the electron quantities. The particle trajectory analysis results in a set of 7 first order, nonlinear differential equations per particle, so that the interaction is represented by a system of order  $7N + 2$  [6].

#### NUMERICAL IMPLEMENTATION AND RESULTS

The analytic theory has been implemented into a numerical simulation program. An extensive verification study, establishing the ability of the program to simulate conventional GTWA configurations, was carried out by comparison of numerical results against work by Chu [2] and Fliflet [3]. Also, analysis has established the validity of the beam-coupling coefficient, since the total power error, represented by the change in the beam power compared to the change in field power, is always less than 0.9 percent [6].

The code has been applied to the study of GTWA operational parameters. It was found that the saturated efficiency peaks at approximately 96 percent of the synchronous value of the dc magnetic field. The saturated efficiency is improved by RF detuning either above or below the synchronous value. The optimum beam size was studied, and results were found to be slightly different than predicted by linear theory [2]. The guiding center motion for  $TE_{0n}$  modes was studied, and it was found that several modes cause significant drift, so that theories which neglect such motion may be in error for particular modes [6].

#### SUMMARY

In summary, the theory discussed in this work presents several distinct advantages to researchers when compared to earlier work. Specifically, the present theory has the ability to consider the simultaneous presence of electrically nonideal walls and tapered waveguide walls. The CRM interaction may be analyzed below the conventional cutoff frequency. The beam-field coupling term derived in the analysis is straightforward, simple, and very accurate. The single particle ballistic theory addresses electron beam propagation in the presence of a strong tapered dc magnetic field.

#### ACKNOWLEDGMENTS

This research received support from the United States Air Force under AFTER Contract F30602-84-C-0153, the University of Utah Development Fund, and Hughes Aircraft, Electron Dynamics Division, in the form of a fellowship arrangement and sponsorship in the AFTER program.

#### REFERENCES

1. J. M. Baird, "Gyrotron Theory," *High Power Microwave Sources*, V. L. Granatstein and I. Alexeff, Editors, Artech House, Inc., Boston, Massachusetts, Chapter 4, 1987.
2. K. R. Chu, A. T. Drobot, H. H. Szu, and P. Sprangle, "Theory and Simulation of the Gyrotron Traveling-Wave Amplifier Operation at Cyclotron Harmonics," *IEEE Transactions on Microwave Theory and Techniques*, Vol. MTT-28, No. 4, 1980, pp. 313-317.
3. A. W. Fliflet, "Linear and Nonlinear Theory of the Doppler-Shifted Cyclotron Resonance Maser Based on TE and TM Waveguide Modes," *International Journal of Electronics*, Vol. 61, No. 6, 1986, pp. 1049-1080.
4. Y. Y. Lau and K. R. Chu, "Gyrotron Traveling-Wave Amplifier: III. A Proposed Wide-Band Fast Wave Amplifier," *International Journal of Infrared and Millimeter Waves*, Vol. 2, No. 3, 1981, pp. 415-425.
5. Y. Y. Lau, K. R. Chu, L. R. Barnett, and V. L. Granatstein, "Gyrotron Traveling-Wave Amplifier: I. Analysis of Oscillations," *International Journal of Infrared and Millimeter Waves*, Vol. 2, No. 3, 1981, pp. 373-393.
6. J. E. Arrington, "Development of Theoretical and Numerical Techniques for Achieving Stability in Gyrotron Traveling-Wave Amplifiers," Technical Report AFTER-32, Microwave Device and Physical Electronics Laboratory, Department of Electrical Engineering, Salt Lake City, Utah, 1988.

# THE SURFACE-MATCHING METHOD FOR SOLVING PERIODIC AND HELICALLY-PERIODIC SLOW WAVE STRUCTURES FOR TRAVELING-WAVE SIMULATION

K. J. Bunch and R. W. Grow

Microwave Device and Physical Electronics Laboratory  
Department of Electrical Engineering  
University of Utah  
Salt Lake City, Utah 84112

## ABSTRACT

A method is presented for solving electromagnetic fields problems with application to the design and simulation of millimeter traveling-wave devices.

## DISCUSSION

The surface-matching method is an extension and generalization of the "point-matching" and "boundary residual" methods used successfully in two-dimensional propagation and scattering electromagnetic problems [1-7]. Whereas the point-matching method satisfies the field boundary conditions at a finite number of points, the surface-matching method best fits the fields to the entire boundary in the least-squares sense. Because of its best fit properties, the method is compact and gives relatively accurate results using a small number of field functions.

This method casts the field solution into matrix form; the determinant of this matrix creates the dispersion equation, and the roots of this equation provide the normal modes of the system. The elements of this matrix are determined by matching the components of the electric and magnetic fields to the boundary of the problem, and in the limiting case of an exact solution, the matrix created is infinite in extent. For the periodic boundaries typically found in microwave devices, the matrix form need match the fields only across a single period. Any symmetries present in the problem are easily handled through restricting elements of the determinantal matrix. For the particular class of problems with helical symmetry, the problem can be reformulated to minimize the size of the resulting matrix using methods similar to those used by Sensiper in solving the tape helix problem [8].

Results using this method are shown for several guiding structures. Dispersion results obtained using this method are compared to past theoretical and experimental work. Several examples include the helical waveguide and the scalloped waveguide [9], and the circular waveguide with step-periodic symmetry [10]. The first two examples are suitable for '0'-type traveling-wave devices, whereas the last is geared towards solving gyrotron devices. Numerical methods used to efficiently solve the matrix problem are discussed, including the use of Householder transformations [11] and the use of Aitken extrapolation to accelerate convergence [12]. Extending the method to the more difficult problems of the ring-bar structure [13] and the cross-wound helix [14] is also presented.

Since the fields are matched across an entire surface, a natural extension of this method is to

simulate beam-wave interaction in a microwave amplifier. Both the boundary conditions of the slow-wave structure and that of the electron beam can be satisfied simultaneously. The advantage of this technique is that the beam need not be sliced up, but can be simulated entirely over one or more periods of the slow wave structure.

## REFERENCES

- [1] H. Y. Lee and N. F. Audeh, "Uniform Waveguides with Arbitrary Cross Section Considered by the Point-Matching Method," IEEE Transactions on Microwave Theory and Techniques, Vol. MTT-13, No. 6, November 1965, pp. 847-851.
- [2] P. A. Laura, "Application of the Point-Matching Method in Waveguide Problems," IEEE Transactions on Microwave Theory and Techniques (correspondence), Vol. MTT-14, May 1966, p. 251.
- [3] H. Y. Yee, "Attenuation Constants of Waveguides with General Cross Sections," IEEE Transactions on Microwave Theory and Techniques (correspondence), Vol. MTT-14, May 1966, pp. 252-253.
- [4] R. H. T. Bates, "The Point-Matching Method for Interior and Exterior Two-Dimensional Boundary Value Problems," IEEE Transactions on Microwave Theory and Techniques, Vol. MTT-15, March 1967, pp. 185-187.
- [5] E. J. Rothwell and L. L. Frasc, "Propagation Characteristics of Dielectric-Rod-Loaded Waveguides," IEEE Transactions on Microwave Theory and Techniques, Vol. 36, No. 3, March 1988, pp. 594-600.
- [6] R. H. T. Bates, "The Theory of the Point-Matching Method for Perfectly Conducting Waveguides and Transmission Lines," IEEE Transactions on Microwave Theory and Techniques, Vol. MTT-17, No. 6, June 1967, pp. 294-301.
- [7] J. B. Davies, "A Least-Squares Boundary Residual Method for the Numerical Solution of Scattering Problems," IEEE Transactions on Microwave Theory and Techniques, Vol. MTT-21, No. 2, February 1973, pp. 99-104.
- [8] S. Sensiper, Electromagnetic Wave Propagation on Helical Conductors, D.Sc. Dissertation, Massachusetts Institute of Technology, Cambridge, Massachusetts, 1951.
- [9] K. J. Bunch and R. W. Grow, "The Helically-Wrapped Circular Waveguide," IEEE Transactions on Electron Devices, Vol. ED-34, August 1987, pp. 1873-1884.

- [10] K. J. Bunch and R. W. Grow, "Backward-Wave Interaction Using Step-Periodic Structures," International Journal of Infrared and Millimeter Waves, Plenum Press, New York, July 1988, pp. 609-629.
- [11] A. Ralston and P. Rabinowitz, A First Course in Numerical Analysis, McGraw-Hill Book Company, Inc., New York, 1978, pp. 451-457.
- [12] Ibid., pp. 358-359.
- [13] W. N. Cain, "The Effects of Dielectric and Metal Loading on the Dispersion Characteristics for Contrawound Helix Circuits Used in High Power Traveling-Wave Tubes," Technical Report AFTER-30, Microwave Device and Physical Electronics Laboratory, Department of Electrical Engineering, University of Utah, Salt Lake City, Utah, 1988.
- [14] M. Chodorow and E. L. Chu, "Cross-Wound Twin Helices for Traveling-Wave Tubes," Technical Report No. 249, Microwave Laboratory, Stanford University, Stanford, California, 1954.



## RADIATION PATTERNS WITH SUPPRESSED SIDELOBES FOR QUASI-OPTICAL MODE CONVERTERS

M. Thumm, L. Rebuffi<sup>†</sup>, H.J. Barkley, A. Jacobs, G.A. Müller

Institut für Plasmaforschung, Universität Stuttgart  
D-7000 Stuttgart 80, Fed. Rep. of Germany

### ABSTRACT

By superposition of appropriate phase-matched mixtures of specific waveguide modes it is possible to obtain intensity distributions with very low sidelobes, radiated from highly overmoded waveguides. Such desirable mode compositions have been studied in order to improve the conversion efficiency (reduction of diffraction losses) of quasi-optical mode transducing antennas (Wengenroth- and Vlasov-type) for use with circular symmetric and rotating asymmetric gyrotron output modes. It is demonstrated, that Wengenroth-type output couplers can also be used for optimum mixtures of rotating asymmetric  $TE_{mn}$  (dominant) /  $TE_{m,n-1}$  /  $TE_{m,n+1}$  modes which exhibit pure azimuthal electric fields.

### INTRODUCTION

Wengenroth-type quasi-optical mode transducing antennas [1] have been used to directly produce a linearly polarized radiation pattern from  $TE_{0n}$  modes generated by 200 kW gyrotrons for application as launcher for electron cyclotron resonance heating (ECRH) of plasmas in thermonuclear fusion experiments. Such appropriately grooved twist reflectors have worked quite well on low-order circular modes [2]. Vlasov-type quasi-optical mode converters [3] can generate a concentrated, linearly polarized microwave beam from rotating, asymmetric  $TE_{mn}$  whispering gallery modes, where  $m$  is large and  $n = 1$  or  $2$  (e.g.  $TE_{15,2}$ ). Such modes may be particularly useful in designing very high-power CW gyrotrons (with low mode competition [4]) for future fusion-reactor type ECRH systems.

Diffraction losses at the radiating waveguide-antenna cut of such simple quasi-optical mode transducers limit their efficiency in the conversion from the gyrotron output mode to a free-space Gaussian beam ( $TEM_{00}$ ). The efficiency of a non-improved Vlasov-type coupler is about 80 % [3-5], and for a Wengenroth-type mode transducing antenna it is between 80 % and 90 % [2].

The present paper shows, that by superposition of appropriate phase-matched mixtures of other waveguide modes to the dominant gyrotron output mode it is possible to synthesize desirable aperture distributions with tapered electric fields at the radiating waveguide cut. This reduces the diffraction and strongly suppresses sidelobes (reduced spillover), making possible the design of quasi-optical mode transducers with higher conversion efficiency.

In the case of multimode horn antennas [6] it has been shown, that this approach can yield impressive results of sidelobe suppression, beam-width equalization, and cross-polarization reduction. In the dual-mode conical horn the dominant  $TE_{11}$  mode (87.5 %) and the orthogonal, higher-order mode  $TM_{11}$  (12.5 %) are superimposed in such a way as to create a high degree of axial pattern symmetry [6]. An appropriate phasing section accounts for the correct relative phases of the modes. This part is not necessary in a corrugated horn antenna where the optimum mode mixture is the propagating fundamental normal mode (hybrid mode  $HE_{11}$ ) [6]. The advantage of the corrugated horn, in terms of operating bandwidth, can easily be appreciated.

### SYNTHESIS OF FAR-FIELD RADIATION PATTERNS

One approach to synthesize desirable radiation distributions is to consider the superposition of the patterns of individual modes. By

varying the relative amplitude and phases of these modes, the resulting radiation pattern can be modified in order to reduce the level of sidelobes. For this purpose we have developed a far-field pattern code for radiation from a circular overmoded waveguide which handles mode-compositions with fixed or rotating polarization.

Experimentally, pure modes or mixtures of them can be easily obtained using appropriate sections of mode converters with periodically perturbed waveguide wall [7]. Higher-order  $HE_{mn}$  or  $EH_{mn}$  hybrid modes can be generated in the similar way as  $HE_{11}$  [7]. The validity of our far-field pattern code has been checked using measured radiation distributions radiated from such mode transducer sections (fixed and rotating modes, TE and TM) at IPF Stuttgart and Thomson-CSF Velizy.

#### 1 Circular Electric $TE_{0n}$ Modes

The far-field patterns of circular symmetric  $TE_{0n}$  modes exhibit the following common features [7]:

- all patterns have the same location of the minima between the sidelobes,
- the maximum of the mainlobe is close to the angular position corresponding to the  $n$ -th zero of the Bessel function  $J_1$ ,
- the phase of the mainlobe in the  $TE_{0n}$ -mode series is alternating.

These properties allow the reduction of the inner and outer sidelobes of a given dominant  $TE_{0n}$ -mode pattern by superimposing the correct percentage of power in the  $TE_{0,n-1}$  and  $TE_{0,n+1}$  modes (both modes with opposite phase with respect to  $TE_{0n}$ ), respectively. In the case of the fundamental  $TE_{01}$  mode, the superposition of  $TE_{02}$  (approx. 85 %  $TE_{01}$  and 15 %  $TE_{02}$ ) alone leads already to a nearly total suppression of the outer sidelobes. The calculated (dashed curve) and measured far-field patterns of this phased mode mixture are shown in Fig. 1 for an aperture diameter of 27.8 mm at 70 GHz. A comparison of both distributions reveals excellent agreement between theory and experiment. The tapering of the electric field distribution at the radiating aperture (see Fig. 2) leads to reduced wall currents and thus to low sidelobes. Near-field measurements showed that this desirable low-sidelobe feature of the radiation pattern also exists in the Fresnel region.

In order to obtain nearly sidelobe-free higher  $TE_{0n}$  (dominant) mode radiation patterns the following mode compositions are needed:

	relative power (%)	relative phase
$TE_{0n}$	70 - 80	0
$TE_{0,n-1}$	10 - 15	$\pi$
$TE_{0,n+1}$	10 - 15	$\pi$

#### 2 Rotating Asymmetric $TE_{mn}$ Modes

The result of the preceding table can be generalized for phased mixtures of rotating asymmetric  $TE_{mn}$  (dominant) /  $TE_{m,n-1}$  /  $TE_{m,n+1}$  modes using the same rule. In any case the result is an azimuthally symmetric radiation pattern with a maximum sidelobe level of -30 dB to -50 dB. The computed radiation pattern of a 80 % / 10 % / 10 % mixture of  $TE_{15,2}$  /  $TE_{15,1}$  /  $TE_{15,3}$  is presented in Fig. 3 (I.D. = 27.8 mm, 140 GHz). This pattern which has only an azimuthal ( $E_\phi$ ) component of the electric field (obvious for circular electric modes) is a fundamental result for rotating

<sup>†</sup>present address: "Thomson-CSF", F-78141 Velizy Villacoublay, France, detached to "The NET Team", D-8046 Garching, Fed. Rep. of Germany.

asymmetric TE mode mixtures. The theoretical maximum level of cross-polarization is  $-49\text{ dB}$  (dashed curve). For comparison, Fig. 4 shows the two co-polar patterns of a pure rotating  $\text{TE}_{15,2}$  mode.

### 3 Rotating Higher-Order $\text{HE}_{mn}$ and $\text{EH}_{mn}$ Hybrid Modes

With the exception of  $\text{EH}_{n1}$  surface modes, all balanced hybrid modes in corrugated circular waveguide whose internal wall is grooved with resonant slots [6, 7] exhibit the important common feature, that the ohmic skin losses are drastically reduced (reduction of fields at the inner waveguide surface). This means that, as in the case of corrugated  $\text{HE}_{11}$  horn antennas, the diffraction losses for higher-order hybrid modes will be significantly reduced. This property has been demonstrated for  $\text{HE}_{15,2}$  (modelled by various mixtures of  $\text{TE}_{15,2}$  and  $\text{TM}_{15,2}$  with  $\Delta\phi = 180^\circ$ ).

### CONCLUSIONS

The design of high-performance quasi-optical mode transducing antennas of the Wengenroth-type for use with high-power gyrotrons will be possible with the help of nearly sidelobe-free axisymmetric radiation patterns generated by appropriately phase-matched specific mixtures of circular electric  $\text{TE}_{0n}$  modes or rotating asymmetric  $\text{TE}_{mn}$  modes.

For a Vlasov-type quasi-optical mode converter, its long axial waveguide cut causes problems with the correct phasing of the different modes. In this case, the diffraction losses should be preferably reduced by rounding the edges of the cut (optimized by geometrical optics/rays [8, 9]—or geometrical theory of diffraction [10]) or as proposed in the present paper, by using a corrugated waveguide propagating its natural, rotating asymmetric hybrid modes (e.g.  $\text{HE}_{15,2}$  or  $\text{EH}_{15,2}$ ).

### REFERENCES

- [1] R. D. Wengenroth, *IEEE Trans. MTT*, 1978, **26**, p. 332.
- [2] H.-S. Yang et al., *IEEE Trans. AP*, 1985, **33**, p. 26.
- [3] S.N. Vlasov et al., *Radio Eng. Elect. Phys.*, 1975, **20**, p. 14.
- [4] B. G. Danly et al., *IEEE Trans. PS*, 1985, **13**, p. 383.
- [5] H. J. Barkley, *this Conference Digest*.
- [6] A. W. Love, ed., *Electromagnetic Horn Antennas*, IEEE Press, New York, 1976.
- [7] M. Thumm, *Int. J. Electronics*, 1986, **61**, p. 1135.
- [8] B. Ye. Kinber, *Radio Eng. Elect. Phys.*, 1963, **8**, p. 1923.
- [9] L. V. Piskunova et al., *Izvestiya Vuzov, Radiofizika*, 1987, **30**, p. 440.
- [10] J. B. Keller, *J. Opt. Soc. Am.*, 1962, **52**, p. 116.

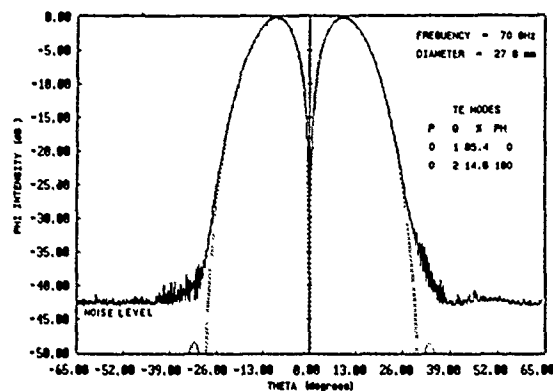


Fig. 1: Computed (dashed curve) and measured far-field pattern of the optimum  $\text{TE}_{01}/\text{TE}_{02}$  mode mixture.

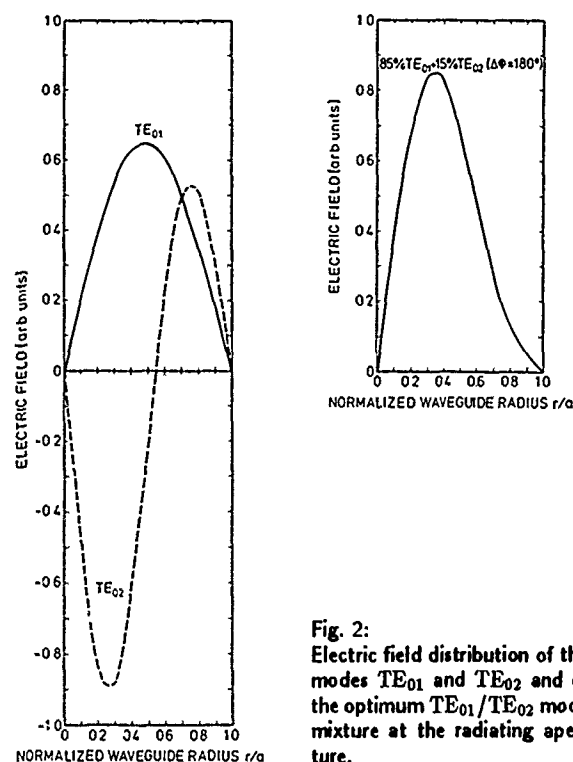


Fig. 2: Electric field distribution of the modes  $\text{TE}_{01}$  and  $\text{TE}_{02}$  and of the optimum  $\text{TE}_{01}/\text{TE}_{02}$  mode mixture at the radiating aperture.

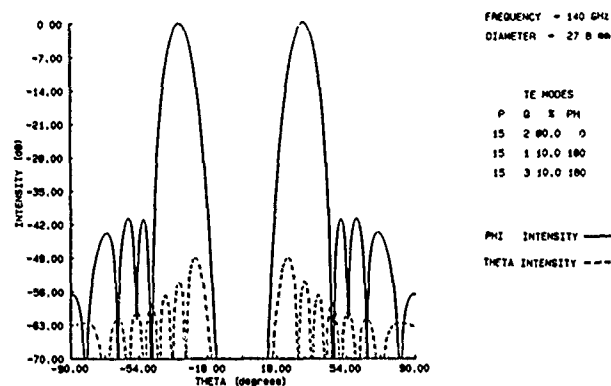


Fig. 3: Co-polar phi- and theta intensity distributions of the optimum rotating  $\text{TE}_{15,n}$  mode (dominant  $\text{TE}_{15,2}$ ) mixture.

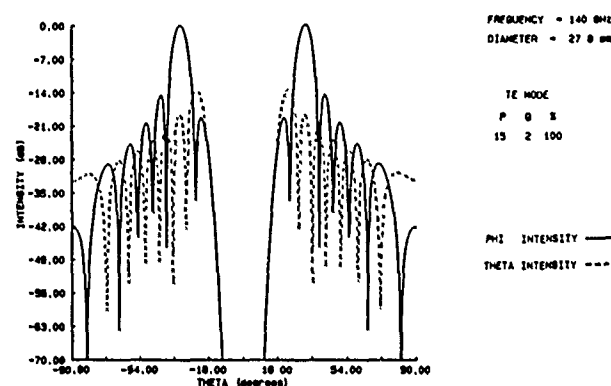


Fig. 4: Co-polar phi- and theta far-field pattern of a rotating  $\text{TE}_{15,2}$  whispering gallery mode.

## IN-WAVEGUIDE TE<sub>01</sub>-TO-WHISPERING GALLERY MODE CONVERSION USING PERIODIC WALL PERTURBATIONS

Manfred Thumm and Annemarie Jacobs

Institut für Plasmaforschung, Universität Stuttgart  
D-7000 Stuttgart 80, Fed. Rep. of Germany

### ABSTRACT

This paper reports numerical optimization calculations on mode converters to generate pure, rotating TE<sub>12,2</sub> (at 120 GHz) and TE<sub>15,2</sub> (at 140 GHz) whispering gallery modes (WGM) in oversized circular waveguides, for conversion efficiency optimization studies on high-power quasi-optical WGM gyrotron output mode transducers. Two-stage TE<sub>01</sub>-to-TE<sub>0n</sub>-to-TE<sub>m2</sub> conversion sequences ( $n = 6$  at 120 GHz,  $n = 7$  at 140 GHz) using periodic radius and  $m$ -fold helical (corkscrew type) wall deformations, respectively, provide output mode purities of almost 99%.

### INTRODUCTION

The development of megawatt high-frequency ( $> 100$  GHz) CW gyrotrons for future fusion-reactor type electron cyclotron resonance heating (ECRH) systems requires the use of high-order asymmetric cavity modes, such as the so-called whispering gallery modes (WGM) [1, 2]. The down conversion of these complicated output modes by using conventional in-waveguide mode transducers with highly oversized waveguide diameter is practically impossible due to the extreme mode competition involved. At reduced diameters, the possibility of RF breakdown in the waveguide may be inevitable. Thus the improvement of the conversion efficiency of quasi-optical mode transducing antennas ( $\eta \approx 80\%$ ) [3] which directly convert rotating WGM into a linearly polarized collimated free-space Gaussian beam is of particular importance for the future prospects of ECRH. For cold-test measurements on such improved high-power quasi-optical WGM-to-TEM<sub>00</sub> mode transformers pure WGM are required.

Gyrotrons capable of generating power levels up to 1 MW at 120 GHz or 140 GHz are currently under development at VARIAN [2]. The design of these tubes is based on an interaction circuit which employs TE<sub>12,2,1</sub> at 120 GHz and TE<sub>15,2,1</sub> at 140 GHz, respectively. The present paper describes optimization computations on two-stage in-waveguide mode converters with suitable periodic wall deformations to generate these rotating modes (at the corresponding frequencies) from the easily available circular electric TE<sub>01</sub> mode. At low power levels this in-waveguide mode conversion from the lowest order circular electric mode to very high-order asymmetric modes is feasible, since optimum waveguide diameters can be chosen.

### GENERAL DESIGN CONSIDERATIONS

Wall deformations with suitable azimuthal symmetry that rotate around the waveguide axis (corkscrew type) may be used to directly convert an unpolarized circular electric TE<sub>0n</sub> mode to a given rotating TE<sub>m,n</sub> mode [4, 5]. At the waveguide wall the phases of two modes with phase constants  $\beta_1$  and  $\beta_2$  and

azimuthal mode numbers  $m_1$  and  $m_2$  are at any time equal on a helix of the  $\Delta m$ -th order such as:

$$\Delta\beta \cdot z + \Delta m \cdot \phi = \text{const}, \quad (1)$$

where  $\Delta\beta = \beta_2 - \beta_1$  and  $\Delta m = m_2 - m_1$ . Small wall distortions with a constant amplitude along this helix:

$$a(z, \phi) = a_0[1 + \epsilon \cos(\Delta\beta \cdot z + \Delta m \cdot \phi)] \quad (?)$$

create a periodic coherent (selective) coupling between the two considered modes. This perturbation has both cosine and sine oriented components.  $P_{\text{eff}} = 2\pi/\Delta\beta = \lambda_B$  (beat wavelength) is the effective period (pitch) of the deformation. The shape of one period of a 12-fold distortion is shown in Fig. 1. The effective coupling factor in this conversion process is reduced by  $\sqrt{2}$  [4]. For periodic coupling between a stationary polarization and TE<sub>0n</sub> using a non-rotating deformation, however, the effective coupling is reduced by a factor of two [6]. The difference between the effect of the rotating deformations and that of non-rotating perturbations lies in the possibility of discriminating against one sense of rotating polarization [4, 5]. Conversion to the other sense of polarization requires a deformation rotating with the opposite sense.

Contrary to some expectations, a rotating distortion does not, in general, permit conversion between a rotating polarization of one mode and a stationary polarization of a different mode. In particular, the direct conversion TE<sub>11</sub> (stationary) to TE<sub>m,n</sub> (rotating) does not seem possible [4]. Nevertheless, conversion with high efficiency between a circular symmetric TE<sub>0n</sub> mode and a rotating TE<sub>m,n</sub> mode is possible [5]. The choice of the intermediate TE<sub>0n</sub> mode in the two-step TE<sub>01</sub>-to-TE<sub>0n</sub>-to-TE<sub>m2</sub> conversion sequence is totally determined by the requirements of the 2nd stage since highly efficient rippled-wall TE<sub>01</sub>-to-TE<sub>0n</sub> mode transducers are feasible [7].

### COMPUTATIONAL MODE CONVERTER OPTIMIZATION

Due to the competition from unwanted spurious modes, the parameters of the inner waveguide surface in a mode transducer with periodically perturbed walls, such as the perturbation amplitude  $a_0\epsilon$ , converter length  $L = N \cdot \lambda_w$  ( $N$  being the number of geometrical periods  $\lambda_w$ ) and shape of wall deformation, have to be optimized in order to get a very high conversion efficiency. In the case of small waveguide distortions (low coupling per wavelength) the optimization of the improved converter structure can be studied by solving the proper coupled-wave differential equations. The optimum number of perturbations is determined by the need for limiting the conversion to undesired modes as well as by limitations on the conversion rate to the desired modes; this depends on the

values of  $|c_{mn}/\Delta\beta_{mn}|$  for the different modes ( $c_{mn}$  are the coupling coefficients). The coupling coefficients that we use [8] are somewhat different from those of [4]. Mechanical tolerances and machining facilities have to be taken into account during the optimization calculations. The average inner converter diameters were chosen to be  $D_0 = 2a_0 = 17.475$  mm (waveguide norm C120) and  $D_0 = 2a_0 = 16.25$  mm (C129) since these diameters are below the cutoff diameters of  $TE_{12,2}$  at 120 GHz and  $TE_{15,2}$  at 140 GHz, respectively.

The optimization computations for the two conversion stages:  $TE_{01}$ -to- $TE_{0n}$  and  $TE_{0n}$ -to- $TE_{m2}$  revealed, that the most appropriate  $TE_{0n}$  mode is  $TE_{06}$  for generation of  $TE_{12,2}$  at 120 GHz and  $TE_{07}$  for production of  $TE_{15,2}$  at 140 GHz.

The parameters of the corkscrew type  $TE_{0n}$ -to- $TE_{m2}$  (rotating) mode converters including input and output taper sections were optimized by numerically integrating the coupled-mode equations for the following modes:

$TE_{06}/TE_{12,2}$ at 120 GHz	$TE_{07}/TE_{15,2}$ at 140 GHz
$TE_{01}, \dots, TE_{06}$	$TE_{01}, \dots, TE_{07}$
$TE_{12,1}$ and $TE_{12,2}$	$TE_{15,1}$ and $TE_{15,2}$
$TM_{01}, \dots, TM_{07}$	$TM_{01}, \dots, TM_{07}$
$TM_{12,1}$ and $TM_{12,2}$	$TM_{15,1}$

The radial coordinate of the optimum wall contour which is schematically plotted in Fig. 2 is described by: input taper ( $0 \leq z \leq \lambda_w$ ):

$$a(z, \phi) = a_0 \left[ 1 + \frac{\epsilon \Delta\beta_w}{2\pi} z \cdot \cos(\Delta m \cdot \phi - \Delta\beta_w \cdot z) \right] \quad (3)$$

central part ( $\lambda_w \leq z \leq (N-1)\lambda_w$ ):

$$a(z, \phi) = a_0 [1 + \epsilon \cos(\Delta m \cdot \phi - \Delta\beta_w \cdot z)] \quad (4)$$

output taper ( $(N-1)\lambda_w \leq z \leq N\lambda_w$ ):

$$a(z, \phi) = a_0 \left[ 1 + \left( \epsilon - \frac{\epsilon \Delta\beta_w}{2\pi} z \right) \cos(\Delta m \cdot \phi - \Delta\beta_w \cdot z) \right] \quad (5)$$

with	$TE_{06}/TE_{12,2}$ at 120 GHz	$TE_{07}/TE_{15,2}$ at 140 GHz
$\Delta m$	12	15
$\epsilon$	0.00849	0.00491
$\Delta\beta_w$	$0.17169 \text{ mm}^{-1}$	$0.20588 \text{ mm}^{-1}$
$N$	3	3
length $L$	109.79 mm	91.556 mm
mode purity	99.9 %	99.8 %
ohmic losses	1.4 %	2.2 %

The computed normalized power in the  $TE_{06}$  and  $TE_{12,2}$  modes and the total transmitted power ( $P_{TOT}$ ) as a function of  $z$  along the optimum 120 GHz  $TE_{06}$ -to- $TE_{12,2}$  mode converter are shown in Fig. 3. The maximum internal level of unwanted spurious modes is very low. The slightly changed perturbation period (wall perturbation period  $\lambda_w \neq \lambda_B$ ) results in a continuous phase rematching within the converter which causes a reduction of the remaining  $TE_{0n}$  mode content [6].

The calculations showed, that in the case of  $TE_{12,2}$  generation at 120 GHz an accuracy of 0.01 mm is required, whereas for  $TE_{15,2}$  at 140 GHz mechanical tolerances  $< 0.01$  mm are mandatory (milling machine with numerical control and correction with respect to the shape of the cutting tool).

## OVERALL $TE_{01}$ -to- $TE_{m2}$ ( $m = 12, 15$ ) CONVERSION EFFICIENCY

The predicted conversion efficiency for direct  $TE_{01}$ -to- $TE_{06}$  (or  $TE_{07}$ ) transformation is approximately 98 % [7]. The large number of ripple periods ( $N \approx 100$ ) makes those transducers very narrow band devices, so that the bandwidth of the total  $TE_{01}$ -to- $TE_{m2}$  ( $m = 12, 15$ ) conversion is only determined by these rippled-wall mode transformers (approximately 1 GHz FWHM). The overall conversion efficiency is calculated to be 98 %, including ohmic losses. The output mode purity of the WGM is almost 99 %.

## REFERENCES

- [1] A. Sh. Fix et al., *Int. J. Electronics*, 1984, **57**, p. 821.
- [2] L. J. Craig, *J. Fusion Energy*, 1987, **6**, p. 351.
- [3] S.N. Vlasov et al., *Radio Eng. Electron. Phys.*, 1975, **20**, p. 14.
- [4] J.L. Doane, *Int. J. Electronics*, 1986, **61**, p. 1109.
- [5] Garin et al., *Conf. Digest 12th Int. Conf. Infrared and Millimeter Waves*, Orlando, Florida, 1987, p. 194.
- [6] M. Thumm, *Int. J. Electronics*, 1984, **57**, p. 1225.
- [7] H. Kumric et al., *Int. J. Electronics*, 1988, **64**, p. 77.
- [8] M. Thumm et al., *Conf. Digest 12th Int. Conf. Infrared and Millimeter Waves*, Orlando, Florida, 1987, p. 336.

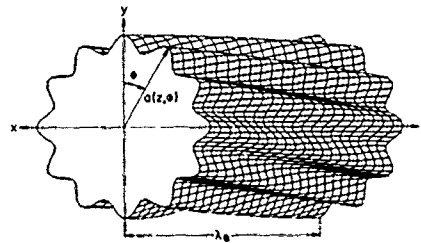


Fig. 1: Schematic of 12-fold helical deformation.

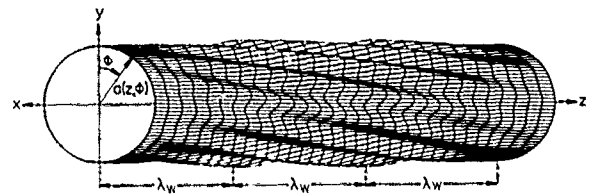


Fig. 2: Schematic of the complete helical  $TE_{06}$ -to- $TE_{12,2}$  mode converter wall contour, including input and output taper sections.

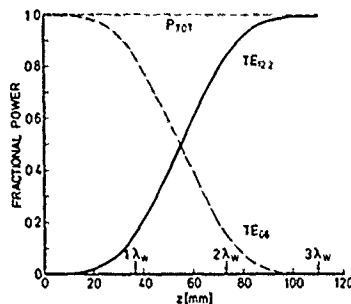


Fig. 3: Calculated fractional power in  $TE_{06}$  and  $TE_{12,2}$  modes and total transmitted power ( $P_{TOT}$ ) as a function of  $z$  along the corkscrew type 120 GHz mode transducer with average diameter  $D = 2a_0 = 17.475$  mm.

THE DIRECT CONVERSION TO A GAUSSIAN BEAM FROM  $TE_{03}$  GYROTRON MODES

H.J. Barkley

Institut für Plasmaforschung, Universität Stuttgart,  
D-7000 Stuttgart 80, Fed. Rep. of Germany

## ABSTRACT

The use of quasi-optical Vlasov converters to produce directly Gaussian output beams from  $TE_{03}$  waveguide modes has been studied at 70 GHz. The far-field measurements presented here of various types of these converters, with and without their parabolic mirrors, indicate inherent efficiency limitations in the simplistic design originally proposed.

## INTRODUCTION

The conversion of the whispering gallery (WG) output modes (e.g.  $TE_{15,2}$ ), of the next generation of megawatt power, high frequency microwave sources, to lower order, simple modes (e.g. a fundamental Gaussian beam) is, at this moment in time, particularly topical since great interest is being shown in the development of high power (> 1 MW), higher frequency (> 100 GHz) microwave beams for plasma heating and plasma diagnostics.

The use of quasi-optical Vlasov converters to directly convert the WG modes to Gaussian beams (first proposed as early as 1975, (1)) shows great potential; it is simple and requires no conversions to various intermediate modes as is currently the case for efficient Gaussian mode conversion even from a low order  $TE_{02}$  mode (2). The overall efficiency, however, can be relatively low, only ~ 80 % (1), although some recently reported results (3) show enhanced efficiencies up to 88 %.

The focus of the work presented here is the understanding of the operation and limitations of Vlasov converters. Since pure WG modes are both complicated to model and hard to produce in the laboratory, we have used for the time being circularly symmetric modes and studied the conversion efficiencies of various types of Vlasov converters (all results given here are for  $TE_{03}$  modes).

Purely for reasons of nomenclature, we have called the cut end of the waveguide a Vlasov antenna and this, together with a parabolic mirror, forms a Vlasov converter.

## MEASURED OUTPUTS OF VLASOV ANTENNAE

Four different types of Vlasov antennae have been studied: a conventional stepped-cut (4), an oblique-cut (5) and two hybrid combinations of the two previous cuts (see figure 1). The far-field radiation pattern measurements of only one of these antennae, the oblique-cut one, are presented in figures 2a,b & c. It is easily seen that diffraction effects are quite strong in the development of the far-field radiation pattern; only, the power in the central crescent can be regarded as important since only it can be converted by a parabolic mirror into a fundamental Gaussian beam.

The measured proportions of the total power which is contained in this central semi-circle is given in Table I.

Table I

Proportions of the transmitted power within various power levels for four Vlasov antennae.

	Simple-Step	Oblique-Cut (I)	Hybrid (II)	Hybrid
-3dB	69.5%	43.7%	54.9%	59.0%
-10dB	84.5%	80.3%	81.8%	81.3%
-15dB	86.2%	86.8%	84.5%	84.7%

Thus with these types of Vlasov antennae about 86 % of the total power can be regarded as useful.

## MEASURED OUTPUTS OF VLASOV CONVERTERS

The output beams from combinations of the four Vlasov antennae and a number of parabolic mirrors have been studied. Figures 3a,b & c show the measured output patterns using an oblique-cut antenna and a parabolic mirror, whose focal length equalled the outer waveguide radius (here, 16 mm).

The measured output beams are normally not circular and often have irregularities, thus it is not immediately obvious what percentage of the power will couple to fundamental Gaussian beams. As a guide to the overall efficiency, the proportions of the total power which occur in the central output beam are shown in Table II, for the four different antennae types.

Table II.

Proportions of the transmitted power within various power levels for four Vlasov converters, each with a 16 mm focal length parabolic mirror.

	Simple Step	Oblique-Cut (I)	Hybrid (II)	Hybrid
- 3dB	60.3%	63.2%	50.8%	50.6%
-10dB	78.0%	76.8%	76.2%	77.1%
-15dB	81.6%	80.7%	80.6%	80.6%

These results lead one to anticipate only about 80 % total efficiency for conventional Vlasov antennae and parabolic mirrors.

## CONCLUSIONS

We have considered here one of the simplest cases of a Vlasov converter, i.e. conversion from the symmetric  $TE_{03}$  mode to a Gaussian beam, and still the overall efficiency is estimated to be only about 80 %. Even with a phase corrected "parabolic" mirror, the efficiency should not be more than 86 % (the useful power shown in Table I).

One way to improve the conversion efficiency is to tailor the edges of the Vlasov antenna so as to decrease the diffraction effects (as done in (3)).

Ultimately one can say that Vlasov converters are particularly promising, even with the presently reported low efficiencies of  $\sim 80\%$ , since at high power densities and high frequencies there are few alternatives, but the full potential of these converters has not yet been achieved.

#### REFERENCES

- [1] S.N. Vlasov et al., *Radio Eng. Electron Phys.*, **21**, pp. 14-17 (1975).
- [2] M. Thumm, *Int. J. Electronics*, **61**, pp. 1135-1153 (1986).
- [3] V.A. Flyagin and M.I. Petelin, "Technics of EC (H+CD): Sources and Transportation of EM Radiation". ITER CD+H Tech. Meeting, July 1988.
- [4] S.N. Vlasov and I.M. Orlova, *Radiophys. Quantum Electronics*, **17**, pp. 115-119 (1974).
- [5] O. Wada and M. Nakajima, *Space Power*, **6**, pp. 213-220 (1986).

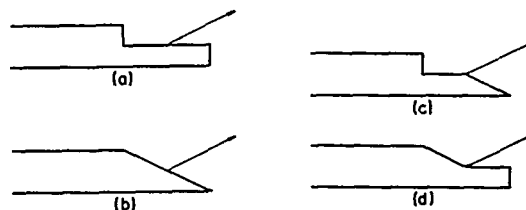


Fig. 1: Four different Vlasov Antennae:  
(a) Simple-Step, (b) Oblique-Cut,  
(c) (I) Hybrid and (d) (II) Hybrid.

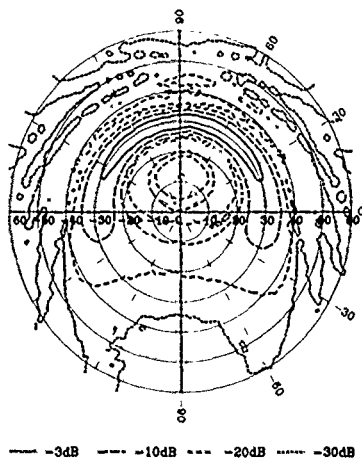


Fig. 2(b): Power contour levels for the Oblique-Cut antenna.

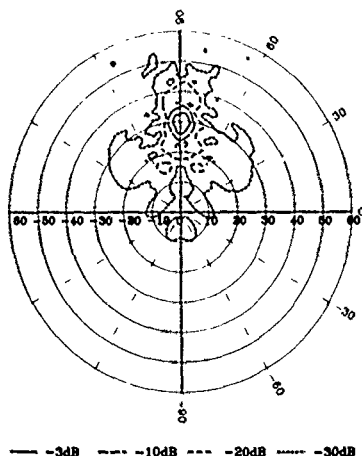


Fig. 3(b): Power contour levels for the Oblique-Cut converter.

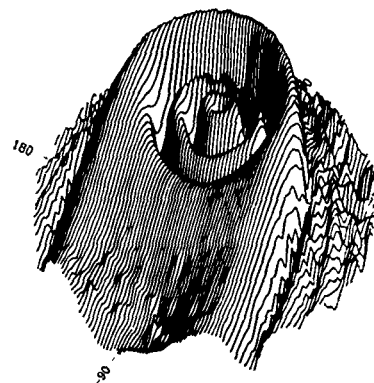


Fig. 2(a): 3 D projection of the far-field pattern power for an Oblique-Cut antenna.

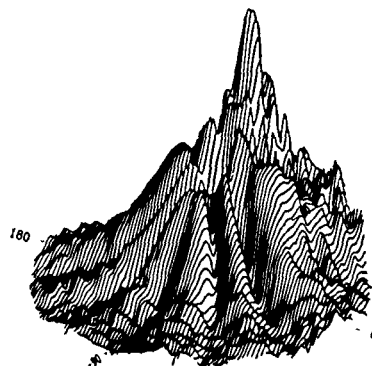


Fig. 3(a): 3 D projection of the far-field pattern power for an Oblique-Cut converter, with 16 mm focal length mirror.

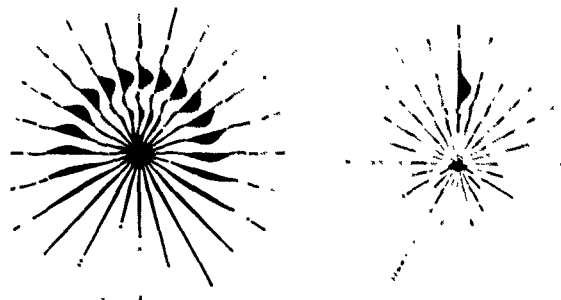


Fig. 2(c):  
Measured electric fields  
for the Oblique-Cut  
antenna.

Fig. 3(c):  
Measured electric fields  
for the Oblique-Cut  
converter.

## WINDOW MATERIALS FOR 280 GHz CONTINUOUS WAVE GYROTRON

Mohammed Nurul Afsar  
Department of Electrical Engineering  
Tufts University  
Medford, Massachusetts 02155

### ABSTRACT

The high frequency absorption in crystalline and polycrystalline materials arises mainly from sharp lattice vibrations, or due to the tail effect of the intense lattice vibration absorption peak. In polycrystalline material there are also other sources of absorption such as amorphous region continuum. A monatomic material such as diamond or diamond like silicon has a simple cubic structure and the lattice vibration absorption peak appears at a very high frequency (Infrared frequency region 20,000 - 40,000 GHz). The 280 GHz region is then completely free from the tail effect of lattice vibration absorption peak. If one can prepare a specimen of such a material in which other millimeter wave absorption processes are compensated, the window will have negligible absorption at 280 GHz.

New results on varieties of classes of window materials such as alumina, sapphire, boron nitride and high resistivity silicon will be compared. The loss tangent value of a hyperpure compensated silicon at 280 GHz is about 40 percent less compared to presently used window material, the single crystal sapphire.

Small-signal Analysis of  
a Free Electron Cyclotron Resonance Laser

Changbiao Wang  
Research Laboratory of Microwave Electronics  
Chengdu Institute of Radio Engineering  
People's Republic of China

The free electron cyclotron resonance laser, based on conversion of synchrotron radiation to a coherent oscillation, operates at an extremely high harmonic with a frequency of about  $0.39\gamma^3\omega_c$ , with  $\gamma$  the transverse relativistic factor and  $\omega_c$  the relativistic cyclotron angular frequency. By introduction of the field amplitude spontaneous modified coefficient and by local expansion of the interaction light field, the linear efficiency and the start-up current are derived. It is shown that this device possesses a striking narrow width of the efficiency profile and so can successfully oscillate on a single longitudinal mode to produce light output of good coherence.